Nanotechnology for Sustainable Development

Mamadou S. Diallo · Neil A. Fromer · Myung S. Jhon
Editors

Nanotechnology for Sustainable Development

First Edition

Previously published in *Journal of Nanoparticle Research*
Topical Collection on Nanotechnology for Sustainable Development

Springer

Editors
Mamadou S. Diallo
Howard University,
Pasadena, CA, USA

Neil A. Fromer
California Institute of Technology
Pasadena, CA, USA

Myung S. Jhon
Carnegie Mellon University
Pittsburgh, PA, USA

ISBN 978-3-319-05040-9
e-ISBN 978-3-319-05041-6
DOI 10.1007/978-3-319-05041-6
Springer New York Heidelberg Dordrecht London

Library of Congress Control Number: 2014931659

Printed on acid-free paper

Springer is part of Springer Science+Business Media (www.springer.com)

Dedication

We dedicate this special issue of the Journal of Nanoparticle Research to the late Professor Mark A. Shannon, the James W. Bayne Professor in the Department of Mechanical Science and Engineering of the University of Illinois at Urbana-Champaign (UIUC). Professor Shannon served both as Director of the Center of Advanced Materials for the Purification of Water with Systems and the Micro-Nano-Mechanical Systems Laboratory at UIUC. He made significant contributions to many areas of "Nanotechnology for Sustainable Development" including water purification, micro/nanofabrication, micro/nanofluidics and analytical chemistry. Professor Shannon was also the co-founder of Cbana Labs, Inc, a UIUC spin off company that is developing and commercializing micro-gas chromatograph analyzers. In addition to being an exceptional scientist/engineer, Mark was a great human being who cared about others. He was a passionate advocate for global water sustainability and worked tirelessly to advance the science, technology and availability of clean water. Mark also worked hard to promote international collaboration in water science and technology. During his last international trip, he traveled to South Korea to give a keynote presentation on "The Coming Revolution in Water Impacting Energy and Health" for the 2010 KAIST EEWS International Workshop. Professor Shannon passed away on Sunday, October 14, 2012 in Urbana-Champaign. We miss his leadership and deep insight into water science, engineering and technology.

Acknowledgements

This edition of the special issue of the Journal of Nanoparticle Research (JNR) devoted to "Nanotechnology for Sustainable Development" is a timely effort in an exciting research area where groundbreaking technological developments are taking place. The content of this special JNR issue is based primarily on invited articles derived from the presentations and discussions during two international conferences that were held at the California Institute of Technology in 2011:

1) The *Eighth US-Korea Forum on Nanotechnology:* (http://www.andrew.cmu.edu/org/nanotechnology-forum/Forum_8/GeneralInfo.htm).
2) The *Resnick Sustainability Institute Workshop on Critical Materials for Energy Generation and Storage* (http://resnick.caltech.edu/e-critical-materials.php).

We thank all the participants and speakers of both meetings. For the Eight US-Korea Nanotechnology Forum, we thank the Korean co-organizers of the conference: 1) Prof. Jo Won Lee of Hanyang University, Mr. Chang Woo Kim, Director General of the National Nanotechnology Policy Center (NNPC) of Korea and Dr. Dae Sup So of Korea Institute of Science and Technology Information (KISTI). For the Resnick Institute Critical Materials Workshop, we thank the session leaders and report co-editors: Prof. Roderick Eggert (Colorado School of Mines) and Jack Lifton (Co-founding Principal of Technology Metals Research). We also thank Dr. Mihail Roco (NSF Senior Advisor for Nanotechnology and JNR Editor-In-Chief) and the JNR staff for their constant support throughout the edition of this special issue. We greatly appreciate Dr. Roco's leadership in helping bring sustainable development to the forefront of the nanotechnology research agenda worldwide. Finally, we thank the NNPC of KISTI (South Korea) and the Caltech Resnick Sustainability Institute (USA) for their financial and in-kind support of this project.

Contents

About the Editors

Prof. Mamadou S. Diallo holds a joint faculty appointment between the Korea Advanced Institute of Science and Technology (KAIST) and the California Institute of Technology (Caltech). At KAIST, Prof. Diallo serves as Associate Professor in the Graduate School of Energy, Environment, Water and Sustainability (EEWS). At Caltech, Prof. Diallo is a visiting Faculty Associate in the Environmental Science and Engineering Department of the Division of Engineering and Applied Science. During the last 10 years, Prof. Diallo and his collaborators have been pioneering the applications of dendrimer nanotechnology to challenging problems in environmental and industrial separations. His current research interests and activities focus on the development of advanced separations materials and systems for sustainable chemistry, engineering and materials (SusChEM) using dendritic macromolecules and polymeric micro/nanofibers as building blocks. Prof. Diallo is also the co-founder and Chief Technology Officer of AquaNano, LLC, a California spin-off company that is developing high performance media for water treatment and environmental remediation. In 2011, he became a member of the Editorial Advisory Board of *Environmental Science and Technology*. In 2012, Prof. Diallo was appointed as Associate Editor of the *Journal of Nanoparticle Research*.

Dr. Neil A. Fromer is the Executive Director of the Resnick Institute, Caltech's endowed program for energy and sustainability. Neil works with the faculty, staff and students across the entire campus to develop new ideas and research technologies related to a clean energy future. Dr. Fromer received his PhD in semiconductor physics from UC Berkeley, and his BS in Engineering/Physics from Brown University. Neil's scientific background is in the interactions of light and matter, and he has over a decade of experience working on solar energy technologies. However, lately he has also been very interested by energy storage, clean fuel generation and use, smarter energy distribution systems, and energy efficiency. Prior to his arrival at the Resnick Institute, Neil Fromer was the Director of Advanced Projects and the Director of Reliability and Testing for Soliant Energy, a concentrating photovoltaic company. While at Soliant, Neil directed the development, testing and certification of a new solar panel, designed specifically to generate the most energy on commercial rooftops. During this time, Neil was actively involved in defining the certification process of this new panel, and was responsible for Soliant receiving the first certification to the UL8703 safety certification for concentrating PV systems. Neil is still active on the technical review panel for UL8703. Previously, Neil worked at Lawrence Berkeley National Laboratory, developing new low-cost solar cells from inorganic semiconductor nanoparticles, and also on the commercialization of energy efficient LED light bulbs and fixtures.

Dr. Myung S. Jhon is a Professor of Chemical Engineering, a member of the Data Storage Systems Center and the Institute for Complex Engineered Systems at Carnegie Mellon University in Pittsburgh, PA. Professor Jhon received his B.S. in Physics from Seoul National University, Korea, and his Ph.D. in Physics from the University of Chicago. He served as a visiting professor at the U.S. Department of Energy (National Energy Technology Laboratory and Sandia National Laboratories), University of California at Berkeley, IBM Almaden Research Center, and the Naval Research Laboratory. He also served as a consultant to the United Nations Industrial Development Organization. During his leave of absence from Carnegie Mellon, he served as the President & CEO of Doosan DND Co., Ltd and also served as a World Class University Professor at Sungkyunkwan University in Korea. Professor Jhon's research focuses on the fundamentals in engineering science and their application to the state-of-the-art engineering problems. He has contributed over 400 publications in the areas of nanotechnology, computational methods, information storage systems, semiconductors, equilibrium and non-equilibrium statistical mechanics, nucleation, fluid and solid mechanics, interfacial dynamics, polymer engineering, rheology, fuel cell, multiphase flow, tribology, chemical kinetics, and organic light-emitting devices & chemical mechanical polishing equipment.

DOI 10.1007/978-3-319-05041-6_1
Reprinted from the *Journal of Nanoparticle Research*, DOI 10.1007/s11051-013-2044-0

EDITORIAL FOR SPECIAL ISSUE ON NANO-SUSTAINABILITY

Nanotechnology for sustainable development: retrospective and outlook

Mamadou S. Diallo · Neil A. Fromer · Myung S. Jhon

Received: 17 July 2013 / Accepted: 3 October 2013 / Published online: 1 November 2013

Abstract The world is facing great challenges in meeting rising demands for basic commodities (e.g., food, water and energy), finished goods (e.g., cell phones, cars and airplanes) and services (e.g., shelter, healthcare and employment) while reducing and minimizing the impact of human activities on Earth's global environment and climate. Nanotechnology has emerged as a versatile platform that could provide efficient, cost-effective and environmentally acceptable solutions to the global sustainability challenges facing society. This special issue of the *Journal of Nanoparticle Research* is devoted to the utilization of nanotechnology to improve or achieve sustainable development. We highlight recent advances and discuss opportunities of utilizing nanotechnology to address global challenges in (1) water purification, (2) clean energy technologies, (3) greenhouse gases management, (4) materials supply and utilization, and (5) green manufacturing and chemistry. In addition to the technical challenges listed above, we also discuss societal perspectives and provide an outlook of the role of nanotechnology in the convergence of knowledge, technology and society for achieving sustainable development.

Keywords Nanotechnology · Sustainability · Natural resources · Manufacturing · Societal needs

Special Issue Editors: Mamadou Diallo, Neil Fromer, Myung S. Jhon

This article is part of the Topical Collection on Nanotechnology for Sustainable Development

M. S. Diallo
Graduate School of Energy, Environment, Water and Sustainability (EEWS), Korea Advanced Institute of Science and Technology (KAIST), 373-1 Guseong Dong, Yuseong Gu, Daejeon 305-701, Republic of Korea

M. S. Diallo (✉)
Environmental Science and Engineering, Division of Engineering and Applied Science, California Institute of Technology, Pasadena, CA, USA
e-mail: mdiallo@kaist.ac.kr; diallo@wag.caltech.edu

N. A. Fromer
Resnick Sustainability Institute, California Institute of Technology, Pasadena, CA, USA

M. S. Jhon
Department of Chemical Engineering, Carnegie Mellon University, Pittsburgh, PA, USA

Introduction

Every human being needs food, water, energy, shelter, clothing, healthcare, employment, etc., to live and prosper on Earth. One of the greatest challenges facing society in the twenty-first century is providing better living standards to all people while minimizing the impact of human activities on the global environment and climate as the world population reaches 8–10 billion by 2050 (Diallo et al. 2013). The Brundtland

Commission of the United Nations defined "sustainable development" as "that which meets the needs of the present without compromising the ability of future generations to meet their own needs" (Brundtland 1987). Currently, the world is facing great challenges to meet rising demands for basic commodities (e.g., food, water and energy), finished goods (e.g., cars, airplanes and cell phones) and services (e.g., shelter, healthcare and employment) while reducing the emission of greenhouse gases and the environmental footprint of agriculture and industry (Godfray et al. 2010; Diallo and Brinker 2011; Brinker and Ginger 2011; Diallo et al. 2013). Soon after the inception of the National Nanotechnology Initiative (NNI), it was envisioned that nanotechnology could provide more sustainable solutions to the global challenges facing society. During a presentation made at the Cornell Nanofabrication Center on September 15, 2000, Roco (2001) discussed how nanotechnology could help improve agricultural yields, provide more efficient and cost-effective water treatment and desalination technologies, and enable the development of clean and renewable energy sources including highly efficient solar photovoltaic cells. As nanotechnology continues to advance, the research agenda is increasingly focused on addressing two key questions related to sustainability over the next 10–20 years:

- Can nanotechnology help address the challenges of improving global sustainability in energy, water, food, shelter, transportation, healthcare and employment?
- Can nanotechnology be developed in a sustainable manner with maximum societal benefits and minimum impact on Earth's global environment and climate?

In this special issue of the *Journal of Nanoparticle Research* (JNR), we highlight and discuss the utilization of nanotechnology to advance and achieve sustainable development. Two key goals of this special issue are to:

1. Provide a retrospective and an outlook of the state-of-the-field for interested scientists, engineers, policy makers and business leaders.
2. Bring into focus crosscutting scientific, technological and societal issues associated with the development and implementation of nanotechnology-based solutions for societal challenges in clean water and energy supplies, greenhouse gases management and materials and manufacturing.

The content of this JNR special issue is based on invited article from the presentations and discussions during two international meetings that were held at the California Institute of Technology in 2011: the *Eighth US-Korea Forum on Nanotechnology* (http://www.andrew.cmu.edu/org/nanotechnologyforum/Forum8/GeneralInfo.htm) and the *Resnick Sustainability Institute Workshop on Critical Materials for Energy Generation and Storage* (http://resnick.caltech.edu/e-critical-materials.php). In addition, the editors of this special issue have included selected articles published by JNR during 2012 and 2013 to provide a broader discussion of the contributions of nanotechnology to sustainable development. Table 1 provides a list of the thirty (30) core articles that are featured in this JNR special issue. Building upon the research findings and perspectives of selected articles listed in Table 1, this editorial provides a retrospective and outlook of nanotechnology for sustainable development. Following the "Introduction" section, "Nanotechnology for sustainable development: overview of recent advances" section highlights recent advances in the utilization of nanotechnology to address global challenges in water purification, clean energy technologies, greenhouse gases management, materials supply and utilization, and green manufacturing and chemistry. "Nanotechnology for sustainable development: Societal perspectives and outlook" section discusses key societal perspectives and provides an outlook of the role of nanotechnology in the convergence of knowledge, technology and society (CKTS) for achieving sustainable development.

Nanotechnology for sustainable development: overview of recent advances

As noted above, nanotechnology has emerged as a versatile platform for addressing global sustainability challenges facing the world (Diallo and Brinker 2011; Brinker and Ginger 2011). Nanomaterials exhibit key physicochemical properties that make them particularly attractive as functional materials for sustainable technologies. On a mass basis, they have much larger and more active surface areas than bulk materials. Nanomaterials can be functionalized with various

Table 1 List of thirty (30) core research, review and perspectives articles that are highlighted in this JNR Special Issue

Title	Authors	Citation
Water purification		
1. Ionic transport in nanocapillary membrane systems	Vikhram V. Swaminathan, Larry R. Gibson II, Marie Pinti, Shaurya Prakash, Paul W. Bohn and Mark A. Shannon	J Nanopart Res (2012) 14:951
2. Nanofiltration membranes based on polyvinylidene fluoride nanofibrous scaffolds and crosslinked polyethyleneimine networks	Seong-Jik Park, Ravi Kumar Cheedrala, Mamadou S. Diallo, Changmin Kim, In S. Kim and William A. Goddard III	J Nanopart Res (2012) 14:884
3. Composite polyester membranes with embedded dendrimer hosts and bimetallic Fe/Ni nanoparticles: synthesis, characterization and application to water treatment	Soraya P. Malinga, Omotayo A. Arotiba, Rui W. Krause, Selweyn F. Mapolie, Mamadou S. Diallo and Bhekie B. Mamba	J Nanopart Res (2013) 15:1698
4. A new approach for determination of fouling potential by colloidal nanoparticles during reverse osmosis (RO) membrane filtration of seawater	Ji Yeon Park, Sungil Lim and Kihong Park	J Nanopart Res (2013) 15:1548
5. Multiwalled carbon nanotubes decorated with nitrogen, palladium co-doped TiO_2 (MWCNT/N, Pd co-doped TiO_2) for visible light photocatalytic degradation of Eosin Yellow in water	Alex T. Kuvarega, Rui W. M. Krause and Bhekie B. Mamba	J Nanopart Res (2012) 14:776
6. Synthesis and characterization of carbon-covered alumina (CCA) supported TiO_2 nanocatalysts with enhanced visible light photodegradation of Rhodamine B	Mphilisi M. Mahlambi, Aay K. Mishra, Shivani B. Mishra, Rui W. Krause, Bhekie B. Mamba and Ashok M. Raichur	J Nanopart Res (2012) 14:790
7. Improvement of the structural, morphology and optical properties of TiO_2 for solar treatment of industrial wastewater	Mona Saif, Sameh Mohammed Aboul-Fotouh, Sahar A. El-Molla, Marwa M. Ibrahim and Laila F. M. Ismail	J Nanopart Res (2012) 14:1227
8. Shape-controlled synthesis of α-Fe_2O_3 nanostructures: engineering their surface properties for improved photocatalytic degradation efficiency	Subramaniasiva Bharathi, Devaraj Nataraj, Karuppanan Senthil and Yoshitake Masuda	J Nanopart Res (2012) 15:1346
9. Protein-functionalized magnetic iron oxide nanoparticles: time efficient potential water treatment	Chuka Okoli, Magali Boutonnet, Sven Järås and Gunaratna Rajarao-Kuttuva	J Nanopart Res (2012) 14:1194
10. Fabrication of amine functionalized magnetite nanoparticles for water treatment processes	Candace C. P. Chan, Hervé Gallard and Peter Majewski	J Nanopart Res (2012) 14:828
11. Manganese-incorporated iron(III) oxide–graphene magnetic nanocomposite: synthesis, characterization and application for the arsenic(III)-sorption from aqueous solution	Debabrata Nandi, Kaushik Gupta, Arup Kumar Ghosh, Amitabha De, Sangam Banerjee and Uday Chand Ghosh	J Nanopart Res (2012) 14:1272
12. Arsenic removal by magnetic nanocrystalline barium hexaferrite	Hasmukh A. Patel, Jeehye Byun and Cafer T. Yavuz	J Nanopart Res (2012) 14:881
13. Removal of heavy metals from aqueous solutions using Fe_3O_4, ZnO and CuO nanoparticles	Shahriar Mahdavi, Mohsen Jalali and Abbas Afkhami	J Nanopart Res (2012) 14:846
14. Kaolin-supported nanoscale zero-valent iron for removing cationic dye-crystal violet in aqueous solution	Zheng-xian Chen, Ying Cheng, Zuliang Chen, Mallavarapu Megharaj and Ravendra Naidu	J Nanopart Res (2012) 14:899
15. Aqueous phosphate removal using nanoscale zero-valent iron	Talal Almeelbi and Achintya Bezbaruah	J Nanopart Res (2012) 14:900

Table 1 continued

Title	Authors	Citation
Clean energy and greenhouse gas management		
16. Poly(vinyl chloride)-g-poly(2-(dimethylamino ethyl methacrylate) graft copolymer templated synthesis of mesoporous TiO_2 thin films for dye-sensitized solar cells	Rajkumar Patel, Sung Hoon Ahn, Jin Ah Seo, Sang Jin Kim and Jong Hak Kim	J Nanopart Res (2012) 14:845
17. SnO_2, IrO_2, Ta_2O_5, Bi_2O_3 and TiO_2 nanoparticle anodes: electrochemical oxidation coupled with the cathodic reduction of water to yield molecular H_2	Jina Choi, Yan Qu and Michael R. Hoffmann	J Nanopart Res (2012) 14:983
18. Preparation of proton conducting membranes containing bifunctional titania nanoparticles	Ayse Aslan and Ayhan Bozkurt	J Nanopart Res (2013) 15:1781
19. Nanotechnology convergence and modeling paradigm of sustainable energy system using polymer electrolyte membrane fuel cell as a benchmark example	Pil Seung Chung, Dae Sup So, Lorenz T. Biegler and Myung S. Jhon	J Nanopart Res (2012) 14:853
20. Thermally rearranged (TR) polymer membranes with nanoengineered cavities tuned for CO_2 separation	Seungju Kim and Young Moo Lee	J Nanopart Res (2012) 14:949
21. Local intermolecular interactions for selective CO_2 capture by zeolitic imidazole frameworks: energy decomposition analysis	Ji Young Park, Yoon Sup Lee and Yousung Jung	J Nanopart Res (2012) 14:793
Materials, manufacturing and green chemistry		
22. Nanotechnology and clean energy: sustainable utilization and supply of critical materials	Neil Fromer and Mamadou S. Diallo	J Nanopart Res (2013) XXX
23. Recovery of silica from electronic waste for the synthesis of cubic MCM-48 and its application in preparing ordered mesoporous carbon molecular sieves using a green approach	Tzong-Horng Liou	J Nanopart Res (2012) 14:869
24. Sustained release of fungicide metalaxyl by mesoporous silica nanospheres	Harrison Wanyika	J Nanopart Res (2013) 15:1831
25. Nanomanufacturing and sustainability: opportunities and challenges	Ahmed Busnaina, Joey Mead, Jacqueline Isaacs, and Sivasubramanian Somu	J Nanopart Res (2013) 15:1984
26. Synthesis, characterization and mechanistic insights of mycogenic iron oxide nanoparticles	Arpit Bhargava, Navin Jain, Manju Barathi L, Mohd S Akhtar, Yeoung-Sang Yun and Jitendra Panwar	J Nanopart Res (2013) 15:2031
27. Electrochemical synthesis of gold nanorods in track-etched polycarbonate membrane using removable mercury cathode	Manoj K. Sharma, Arvind S. Ambolikar and Suresh K. Aggarwal	J Nanopart Res (2012) 14:1094
28. Filtration behavior of silver nanoparticle agglomerates and effects of the agglomerate model in data analysis	Jelena Buha, Heinz Fissan and Jing Wang	J Nanopart Res (2013) 15:1709
Societal perspectives		
29. Nanotechnology for sustainability: what does nanotechnology offer to mitigate complex sustainability problems?	Arnim Wiek, RiderFoley and David Guston	J Nanopart Res (2012) 14:1093
30. Nanotechnology policy in Korea for sustainable growth	Dae Sup So, Chang Woo Kim, Pil Seung Chung and Myung S. Jhon	J Nanopart Res (2012) 14:854

chemical groups to increase their affinity toward a given compound including dissolved solutes and gases. They can also be functionalized with chemical groups that selectively target key biochemical constituents and metabolic/signaling networks of waterborne bacteria and viruses. Nanomaterials are also providing unprecedented opportunities to develop functional materials with superior electronic, optical, catalytic and magnetic properties. These novel functional materials can be processed into various form factors including water-soluble supramolecular hosts, particles, fibers and membranes. Figures 1, 2 and 3 show selected classes of nanomaterials, nanotechnology-based processes/systems and multi-scale modeling tools that are, respectively, being employed/developed to design and build the next generation of sustainable products and technologies. Below, we provide an overview of recent progress in the utilization of nanotechnology to address global challenges in (1) water purification, (2) clean energy technologies, (3) greenhouse gases management, (4) materials supply and utilization and (5) green manufacturing and chemistry.

Water purification

The availability of clean water has emerged as one of the most critical problems facing society and the global economy in the twenty-first century (Savage and Diallo 2005; Shannon et al. 2008; Diallo and Brinker 2011). Many regions of the world face multiple challenges in sustainably supplying potable water for human use and clean water for agriculture, food processing, energy generation, mineral extraction, chemical processing, and industrial manufacturing (Shannon et al. 2008; Diallo and Brinker 2011). Demand for water is increasing due to population growth at the same time as water supplies are being stressed by the increasing contamination and salinization of freshwater sources including lakes, rivers and groundwater aquifers. A report published by the Intergovernmental Panel on Climate Change (Bates et al. 2008) suggests that global climate change will adversely impact the world's freshwater resources in several ways: (1) increase the frequency of droughts and floods; (2) decrease the amount of water stored in snowpack and glaciers; and (3) decrease the overall water quality due to salinity increase and enhanced sediment, nutrient, and pollutant transport in many watersheds throughout the world. Thus, a significantly larger amount of clean water needs to be produced from impaired water (e.g., wastewater, brackish water and seawater) to meet the growing demand throughout the world in the next decade and beyond. The convergence between nanotechnology and water science and technology is leading to revolutionary advances in water treatment, desalination and reuse technologies (Savage and Diallo 2005; Shannon et al. 2008; Diallo and Brinker 2011). In this special issue, we have selected fifteen (15) published JNR articles (Table 1) to highlight significant advances that have resulted from the application of nanotechnology to water purification.

Pressure-driven membrane processes such as reverse osmosis (RO), nanofiltration (NF), ultrafiltration (UF) and microfiltration (MF) are becoming the key components of advanced water treatment, reuse and desalination systems worldwide (Savage and Diallo 2005; Shannon et al. 2008). Four (4) articles of this JNR special issue are devoted to fundamental investigations of membrane processes, materials and systems. The article *Ionic transport in nanocapillary membrane systems* by Swaminathan et al. (2012) reviews the state-of-the-art of nanocapillary array membranes (NCAMs) as model systems for probing ion and particle transport in nanopores of characteristic length scales ranging from 1 to 100 nm. NCAMs consist of nanoporous membranes with tunable pore sizes that are fabricated by track etching using base polymers such as polycarbonate. The authors reported that pore geometry, surface charge and nonlinear electrokinetic effects arising from the interplay between surface charge density and surface energy control the transport of ions and charged particles in nanopores with diameters below 100 nm. They also discussed how basic knowledge derived from fundamental studies of NCAMs is providing new opportunities to design (1) biomimetic membranes for water desalination and (2) 3D micro-/nanofluidic systems for sustainability applications including chemical separations, analysis sensing and energy conversion. The article *Nanofiltration membranes based on polyvinylidene fluoride nanofibrous scaffolds and crosslinked polyethyleneimine networks* by Park et al. (2012a) describes the preparation, characterization and evaluation of a new family ion-selective nanofiltration (NF) membranes using polyvinylidene fluoride (PVDF) and hyperbranched polyethylenimine (PEI) as building

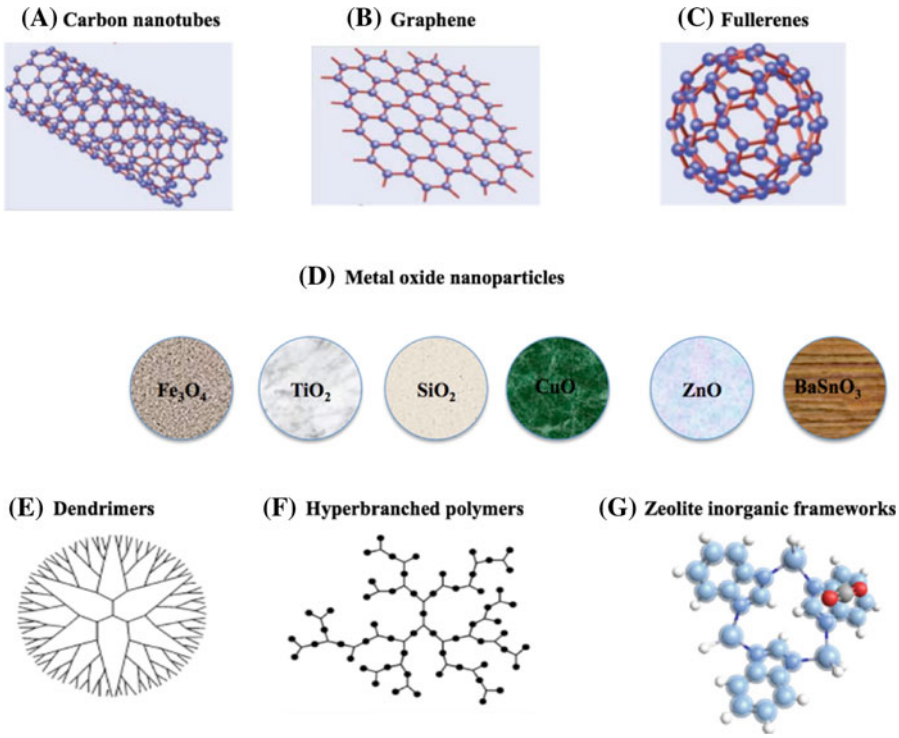

Fig. 1 Selected nanomaterials that are currently being utilized as building blocks to develop the next generation of sustainable products and technologies in water purification, energy generation, conversion and storage, greenhouse gas management, materials supply and utilization and green manufacturing and chemistry

blocks. These new nanofibrous composite (NFC) membranes consist of crosslinked hyperbranched PEI networks supported by PVDF nanofibrous scaffolds that are electrospun onto commercial PVDF microfiltration (MF) membranes. A major objective of this work was to develop positively charged NF membranes that can be operated at low pressure (i.e., less than 10 bar) with high water flux and improved rejection for monovalent salts such as NaCl, compared to the commercially available membranes. The proof-of-concept experiments show that the NFC–PVDF membrane with crosslinked PEI/trimesoyl chloride networks has a high water flux ($\sim$30 L m^{-2} h^{-1}) and high rejections for $MgCl_2$ (88 %) and NaCl (65 %) at pH 6 and pressure of 7 bar. The overall results of this study suggest that PVDF nanofibers and hyperbranched PEI are promising building blocks for the fabrication of a new generation of high performance NF membranes for (1) water purification Park et al. (2012a) and (2) metal extraction from non-traditional sources including mine tailings and industrial wastewater (Fromer and Diallo 2013).

Metal oxide nanoparticles (Fig. 1D) have great potential as catalyst materials for water purification due their large surface areas and superior optical/electronic properties (Savage and Diallo 2005). During the last decade, titanium dioxide (TiO_2) nanoparticles have emerged as promising photocatalysts for water treatment. TiO_2 nanoparticles are versatile and can serve both as oxidative and reductive catalysts for organic and inorganic pollutants. Three (3) articles of this JNR special issue are devoted to the synthesis, characterization and evaluation of TiO_2-based photocatalysts for water treatment. The article *Multiwalled carbon nanotubes decorated with nitrogen, palladium co-doped TiO_2 (MWCNT/N, Pd co-doped TiO_2) for visible light photocatalytic degradation of Eosin Yellow in water* by Kuvarega et al. (2012) investigates the photocatalytic activity of MWCNT/N, Pd co-doped TiO_2 nanocomposites. To probe catalyst reactivity, the authors measured the photodegradation of Eosin Yellow under simulated solar and visible light irradiation. They reported that the 0.5 wt% MWCNT/N, Pd co-doped TiO_2 composite gave high degradation rate constants of 3.42×10^{-2} and 5.18×10^{-3} min^{-1} using simulated solar light and visible light, respectively. The article *Synthesis and characterization of carbon covered alumina (CCA) supported TiO_2 nanocatalysts with enhanced visible light photodegradation of Rhodamine B* by Mahlambi et al. (2012)

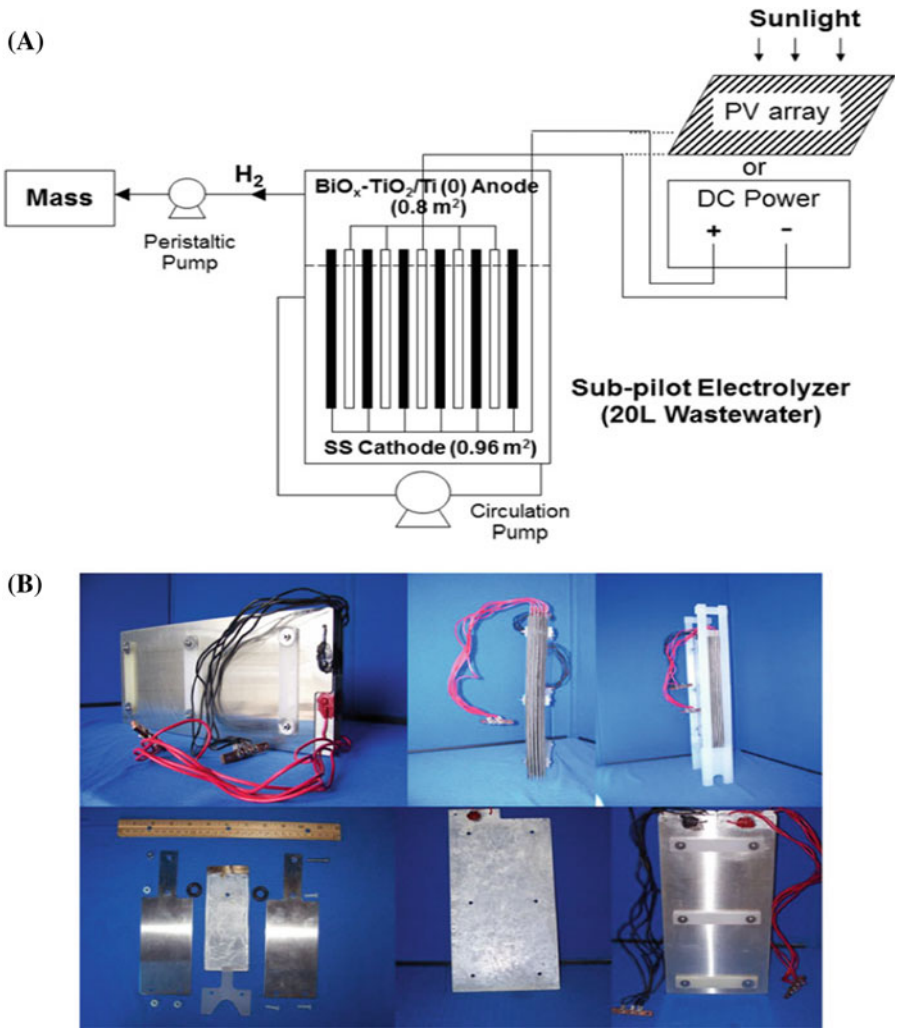

Fig. 2 **A** Schematic diagram of a hybrid photovoltaic–electrochemical system, which utilizes semiconductor nanoparticles coated on to metal substrates as electrodes for the generation of hydrogen coupled with the oxidation of wastewater. **B** Photographs of the electrode arrays showing the anodic semiconductor coatings on the Ti-metal base support [Choi et al. J Nanopart Res (2012) 14:983]

illustrates the preparation of TiO_2 nanocatalysts on CCA supports. The authors reported that the CCA-TiO_2 photocatalysts show higher reactivity under visible light compared to their unsupported counterparts. Metal oxide nanoparticles are also providing new opportunities to leverage the efficiency of magnetic separations technology in water purification (Ge et al. 2011; Ling and Chung 2011). Four (4) articles of this JNR special issue are devoted to the synthesis, characterization and evaluation of MNPs for water treatment. The article *Protein-functionalized magnetic iron oxide nanoparticles: time efficient potential-water treatment* by Okoli et al. (2012) discusses the synthesis, characterization and evaluation of composite magnetic nanoparticles (MNPs) with an iron oxide core and a shell consisting of sorbed *Moringa oleifera* proteins. The authors reported that their protein-stabilized MNPs could be utilized as recyclable media in water treatment to remove turbidity (i.e., suspended solids) from surface water. Okoli et al. (2012) also showed that the MNPs could be combined with magnetic separations to remove more 90 % of the turbidity from a test surface water sample within 12 min. In contrast, only 70 % of turbidity removal was achieved within 60 min using conventional gravity separation with a synthetic and non-recyclable coagulant such as alum.

Clean energy technologies

Global climate change is one of the greatest challenges facing the twenty-first century (Solomon et al. 2007). During the last two decades, a consensus has gradually

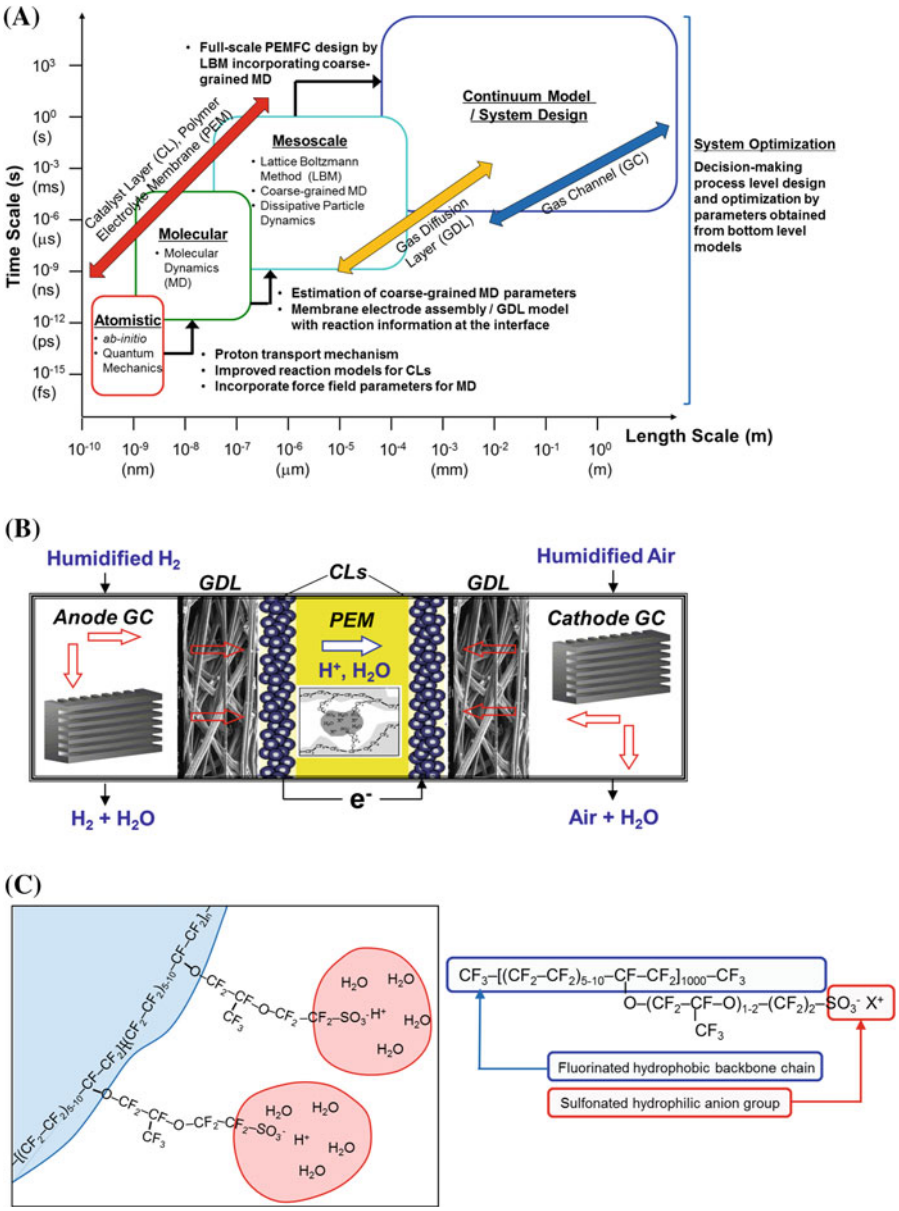

Fig. 3 **A** Multi-scale modeling strategy for designing and optimizing polymer electrolyte membrane fuel cells (PEMFC). **B** Components of a single stack hydrogen PEMFC. **C** Structure a polymer electrolyte membrane (Nafion) [Chung et al. J Nanopart Res (2012) 14:853]

emerged that increasing emissions of greenhouse gases such as carbon dioxide (CO_2) from the combustion of fossil fuels (e.g., coal and petroleum) are the key drivers of global climate change (Solomon et al. 2007). Meeting the growing demand for energy while significantly reducing CO_2 emissions will require the deployment of orders of magnitude more clean and renewable energy systems than what is now in place as the world population reaches 8–10 billion by 2050 (Brinker and Ginger 2011; Fromer et al. 2011; Diallo et al. 2013). Nanotechnology provides unprecedented opportunities to advance the development of clean and renewable energy technologies (Fromer and Diallo 2013). Four (4) articles of this JNR special issue are devoted to clean energy technologies. Solar photovoltaics has emerged the most attractive source of renewable electrical energy due to its abundance, versatility, and ease of implementation with minimum environmental impact in terms of water consumption and land usage (Lewis 2007; Brinker and Ginger 2011). The article *Poly(vinyl chloride)-g-poly(2-(dimethylamino ethyl methacrylate) (PVC-g-PDMAEMA) graft copolymer templated synthesis of mesoporous TiO_2 thin films for dye-sensitized solar*

cells by Patel et al. (2012b) investigates the utilization of graft copolymers as structure-directing agents for the fabrication of mesoporous thin films containing titanium dioxide (TiO_2) layers used as anodes. The authors subsequently employed these new mesoporous TiO_2 films to fabricate a photoanode for a dye-sensitized solar cell (DSSC) that achieved an energy conversion efficiency of 3.2 % at 100 mW/cm^2. This performance was higher when using a TiO_2 film with a higher porosity and lower interfacial resistance between the anode and the electrolyte. According to the authors, they achieved one of the highest reported energy conversion efficiency for a quasi-solid-state DSSC with a 600-nm-thick TiO_2 film. The article *SnO_2, IrO_2, Ta_2O_5, Bi_2O_3, and TiO_2 nanoparticle anodes: electrochemical oxidation coupled with the cathodic reduction of water to yield molecular H_2* by Choi et al. (2012) discusses hydrogen generation by solar water splitting using organic contaminants in wastewater as sacrificial electron donors. This work is potentially important since solar radiation is intermittent and the large-scale implementation of solar power will require efficient systems that convert solar energy into high-density chemical fuels. The authors demonstrated the feasibility of a scaled-up rooftop prototype of a hybrid photovoltaic electrolysis system (Fig. 2), which utilizes semiconductor nanoparticles coated onto metal substrates as electrodes for the generation of hydrogen coupled with the oxidation of organic compounds in wastewater.

In industrialized countries such as the USA, transportation is responsible for approximately 66 % of oil consumption and 33 % of CO_2 emissions (Davis et al. 2008; EPA 2008). Thus, fuel cell cars could meet the world's growing demand for transportation vehicles while significantly reducing CO_2 emissions. Polymer electrolyte membrane fuel cells (PEMFCs) have emerged as the most promising energy conversion devices for automotive applications (http://www.nextgreencar.com/fuelcellcars.php). Two (2) articles of this JNR special issue are devoted to PEMFCs. The article *Preparation of proton conducting membranes containing bifunctional titania nanoparticles* by Aslan and Bozkurt (2013) discusses the preparation and characterization of novel proton conducting nanocomposite membranes. These new polymer electrolyte (PE) membranes consisted of poly(vinyl alcohol) (PVA) membrane matrices that are embedded with sulfated TiO_2 nanoparticles (TS) and nitrilotri(methyl phosphonic acid) (NMPA). The authors reported that one of their new PE membranes [PVA–TS–$(NMPA)_3$] achieved a proton conductivity of 0.003 S cm^{-1} at 150 °C. This membrane also showed improved mechanical strength, which is critical for applications such as PEMFCs. The article *Nanotechnology convergence and modeling paradigm of sustainable energy system using polymer electrolyte membrane fuel cell as a benchmark example* by Chung et al. (2012) discusses nanotechnology convergence for clean energy generation and novel multi-scale modeling paradigms using the fuel cell system as a benchmark example (Fig. 3). This approach includes understanding and modeling complex multi-physics phenomena at different time and length scales along with the introduction of an optimization framework for application-driven nanotechnology research trends. The new modeling paradigm introduced by the authors covers the novel holistic integration from atomistic/molecular phenomena to meso-/continuum scales. The authors also discuss system optimization with respect to the reduced order parameters for a coarse-graining procedure in multi-scale model integration as well as system design.

Greenhouse gases management

Currently, fossil fuels provide approximately 80 % of the energy used worldwide (IPCC 2005). Although many non-CO_2-emitting energy sources are being developed, the world will continue to burn significant amounts of fossil fuels in the foreseeable future. Thus, carbon capture and storage is emerging as a viable short-to-medium term alternative for reducing the amounts of anthropogenic CO_2 released into the atmosphere (IPCC 2005). Nanotechnology has the potential to provide efficient, cost-effective and environmentally acceptable solutions for CO_2 separation, capture and storage (Diallo and Brinker 2011). Two (2) articles of this JNR special issue are devoted to CO_2 separation and storage. The article *Thermally rearranged (TR) polymer membranes with nanoengineered cavities tuned for CO_2 separation* by Kim and Lee (2012) reviews recent developments in CO_2 separation technologies utilizing various membranes including thermally rearranged (TR) polymeric membranes with CO_2 selective nanocavities. The authors reported that these new TR polymeric membranes show high gas permeability as well as good selectivity, especially in CO_2 separation from post-combustion flue gases. Zeolitic imidazolate frameworks (ZIFs) have emerged

as promising building blocks for high capacity and selective CO_2 capture and storage media (Wang et al. 2008; Banerjee et al. 2008). The article *Local intermolecular interactions for selective CO_2 capture by zeolitic imidazole frameworks: energy decomposition analysis* by Park et al. (2012b) utilizes density functional theory (DFT) calculations to investigate the binding of CO_2 with ZIFs. The overall objective of this work was to provide a molecular level interpretation of experimental measurements of CO_2 uptake (capacity and selectivity) by ZIFs. The DFT calculations suggest that the local electronic interactions of CO_2 and the substituent groups of ZIFs, which is mainly characterized by frozen density and polarization interactions with little charge transfer, are the primary binding interaction. Park et al. (2012b) also reported that electron correlation effects are also important depending on the binding geometry and functional groups.

Materials supply and utilization

Innovations in the sustainable supply and utilization of materials will also be critical to developing the next generation of sustainable technologies and products (Diallo et al. 2013). Metals are used to fabricate the critical components of numerous products and finished goods, including airplanes, automobiles, cell/smart phones and biomedical devices (NRC 2008; Diallo and Brinker 2011). Carbon-based materials derived from petroleum are also the building blocks of a broad range of essential products and finished goods, including plastics, solvents, adhesives, fibers, resins, gels, and pharmaceuticals (Diallo et al. 2013). Four (4) articles of this JNR special issue are devoted to materials supply and utilization. The article *Nanotechnology and clean energy: sustainable utilization and supply of critical materials* by Fromer and Diallo (2013) discusses the utilization of nanotechnology to improve or achieve materials sustainability for energy generation, conversion and storage. There is a growing realization that the development and large-scale implementation of clean energy technologies will also require sizeable amounts of technology metals (Diallo and Brinker 2011; Fromer et al. 2011; Diallo et al. 2013). In their perspectives article, the authors argue that many current problems involving the sustainable utilization and supply of *critical materials* in clean/renewable energy technologies could be addressed using (1) nanostructured materials with enhanced electronic, optical, magnetic and catalytic properties (Table 2) and (2) nanotechnology-based separation materials and systems that can recover *critical materials* from non-traditional sources including mine tailings, industrial wastewater and electronic wastes with minimum environmental impact.

The article *Recovery of silica from electronic waste for the synthesis of cubic MCM-48 and its application in preparing ordered mesoporous carbon molecular sieves using a green approach* by Liou (2012) deals with the recovery of valuable elements/materials from electronic wastes (e-wastes) consisting of mixtures of epoxy resin, phenolic resin, silica and additives. In this case, the author utilized resin ash from electronic packaging wastes to synthesize mesoporous silica (MCM-48) with high purity (99.87 wt%), high surface area (1 317 m^2/g) and mean pore size of 3.0 nm. Converting e-wastes into mesoporous materials (e.g., MCM-48) could help alleviate waste disposal problems associated with the use of consumer electronics products. Nanotechnology has also emerged as a versatile platform for addressing materials sustainability in agriculture through the development of smart systems for controlled/precision release of nutrients, fertilizers and pesticides (Scott and Chen 2003; Diallo and Brinker 2011). The article *Sustained release of fungicide metalaxyl by mesoporous silica nanospheres* by Wanyika (2013) discusses the utilization of silica nanoparticles for the storage and controlled release of the pesticide metalaxyl. The author found that the silica (SiO_2) nanoparticles (average particle diameters of 162 nm and mean pore sizes of 3.2 nm) could load about 14 wt% of metalaxyl. He also reported a "sustained release behavior" in water-saturated soil columns over a period of 30 days with a release into the soil media of 11.5 wt% of the metalaxyl trapped into the SiO_2 nanoparticles compared to 76 wt% when metalaxyl is used without initial storage into the nanoparticles.

Green manufacturing and chemistry

Manufacturing is critical to a sustainable world economy. It is the key engine that drives innovation and creates higher value jobs in both developed and developing countries (Liveris 2012). Industrial manufacturing has a heavy environmental footprint. First, it requires a significant amount of materials, energy and water. Second, it generates a lot of wastes (gaseous, liquid and solid) and toxic by-products that need to be disposed of or converted into harmless products. Nanotechnology is emerging as an enabling platform

Table 2 Nanotechnology and materials criticality reduction strategies in clean and renewable energy systems (Fromer and Diallo, J Nanopart Res (2013) 15:2011)

Systems	Components	Critical materials	Materials criticality reduction strategies
Wind turbines	Generators	Neodymium dysprosium	Develop nanostructured REPMs that utilize less amounts of neodymium and dysprosium
			Use non-critical materials and earth-abundant elements to develop nanocomposite "exchange spring magnets" by coupling nanoparticles with s hard and soft magnetic domains to achieve high energy density and coercivity
Electric vehicles	Motors	Neodymium, dysprosium	Same strategy as above
	Li-ion batteries	Lithium, cobalt	Use electrospun nanofibers of earth-abundant elements to prepare more efficient anodes, cathodes and separators for Li-ion batteries
	NiMH batteries	REEs, cobalt	Develop magnesium batteries and new batteries using nanomaterials based on earth-abundant elements
Solar cells	Thin film	Tellurium, gallium, germanium, indium, silver, cadmium	Find new nanostructured and absorbing materials that match the solar spectrum without using critical materials
			Exploit quantum confinement to tune and improve the optical properties of solar cells materials built using non-critical materials
			Exploit advances in nanophotonics and plasmonics to build thin-film solar cells that utilize orders of magnitude less active materials
Solid state lighting devices	LED devices	Gallium, indium	See strategy as above
			Utilize nanoparticles and quantum confinement to improve light emitting efficiency throughout the visible spectrum
	Phosphors	Yttrium, europium, terbium, other REEs	Switch from fluorescent lights to LED lights to decrease the use of phosphors (REEs) by an order of magnitude
			Utilize nanoparticle light emitters to reduce or replace REEs in phosphors
Solar fuel generators	Catalysts	Platinum, palladium, iridium, yttrium	Develop hydrogen/oxygen evolution catalysts using nanomaterials based on earth-abundant elements
			Optimize grain size and exploit quantum size effects to tune band energies/surface states/thermal properties to increase catalyst activity and reactivity

for green manufacturing and chemistry in the semiconductor, chemical, petrochemical, materials processing, pharmaceutical and many other industries (Schmidt 2007; Diallo and Brinker 2011). The article *Nanomanufacturing and sustainability: opportunities and challenges* by Busnaina et al. (2013) discusses the state-of-the-art of nanomanufacturing. The authors argue that rapid and directed assembly based processes (Fig. 4), which are carried out at room temperature and ambient pressure, could significantly decrease the cost of manufacturing equipment and tools and achieve "long-term sustainability" by reducing the consumption of materials, water, energy and the generation of wastes. The convergence between nanotechnology and biotechnology is also providing new opportunities to develop non-toxic and environmentally acceptable "green chemistry" routes for the synthesis of functional nanomaterials using bacteria, fungi and plants (Mohanpuria et al. 2008). The article *Synthesis, characterization and mechanistic insights of mycogenic iron oxide nanoparticle*s by Bhargava et al. (2013) discusses the biosynthesis of ion oxide nanoparticles (IONPs) using an *Aspergillus japonicus* fungus (AJP01) that was isolated from an iron-rich soil. The authors reported that the AJP01 fungus isolate could utilize a mixture of potassium ferricyanide and ferrocyanide as precursor salt solution to synthesize IONPs with size raging from 60 to 70 nm. They showed that extracellular proteins play a key role in the synthesis and stabilization of the IONPs (Fig. 5). The

authors believe that their approach could be utilized to synthesize other classes of nanomaterials.

Nanotechnology for sustainable development: societal perspectives and outlook

Societal perspectives

Brundtland's Commission called the three pillars of sustainability social, economic and environment—suggesting that sustainability requires convergence of all three (Brundtland 1987). Thus, two important goals of global sustainability are to achieve inclusive economic and societal development, which benefits all people while minimizing the impact of human activities on Earth's climate and ecosystems (UN 2012; Diallo et al. 2013). Two articles of this JNR special issue are devoted to societal perspectives associated with the utilization of nanotechnology to advance sustainable development. The article *Nanotechnology for sustainability—what does nanotechnology offer to mitigate complex sustainability problems?* by Wiek et al. (2012) argues that the current research on nanotechnology for sustainable development narrowly "focuses on end-of-pipe applications" such as water purification and energy efficiency. The authors make the case that nanotechnology-based solutions are often proposed without seriously considering other alternatives and/or negative side effects of these technologies. To support their arguments, Wiek et al. (2012) combined the results of discussions form focused interdisciplinary workshops and literature reviews to evaluate the utilization of nanotechnology to address three urban sustainability problems in the Gateway Corridor Community of Phoenix in Arizona (USA): (1) water contamination, (2) energy utilization and (3) childhood obesity. The authors reported that "there is potential for nanotechnology to contribute to a sustainable future, but those

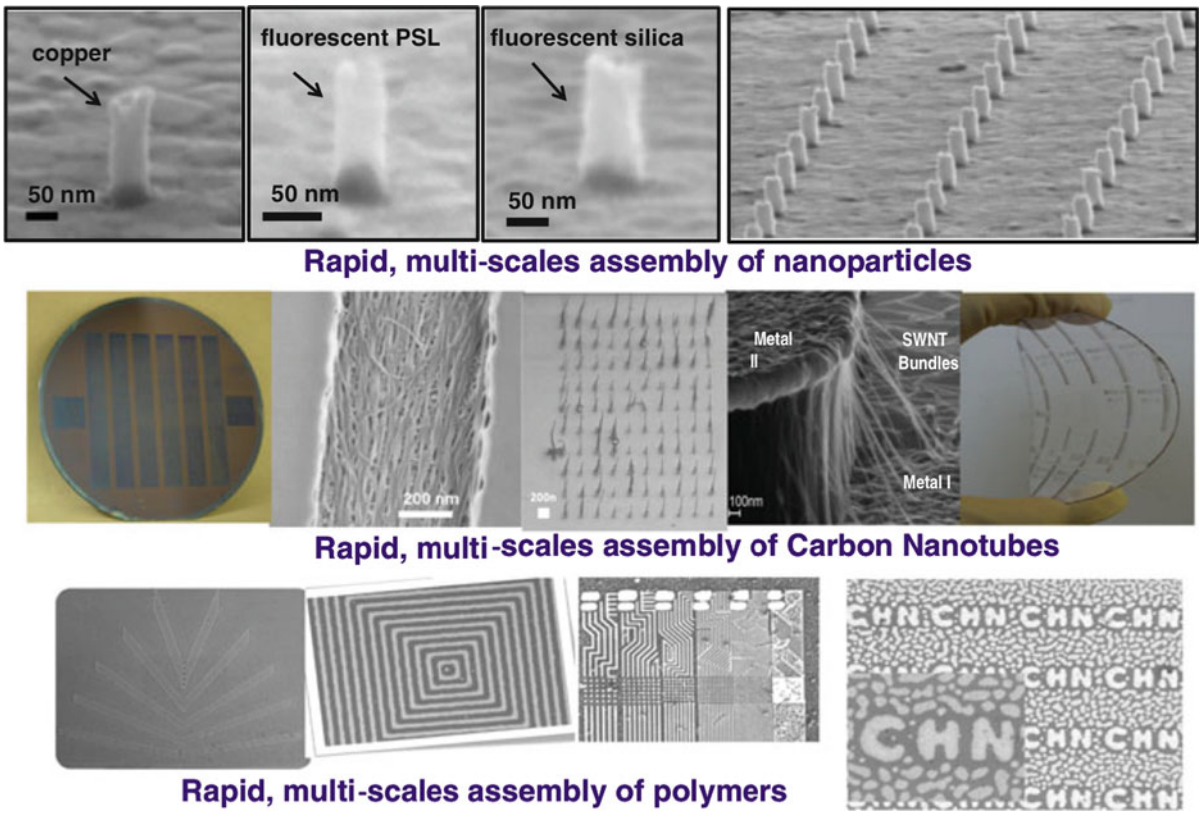

Fig. 4 Sustainable nanomanufacturing processes: rapid assembly of nanoparticles, carbon nanotubes, and polymers in various configurations and orientations [Busnaina et al. J Nanopart Res (2013) 15:1984]

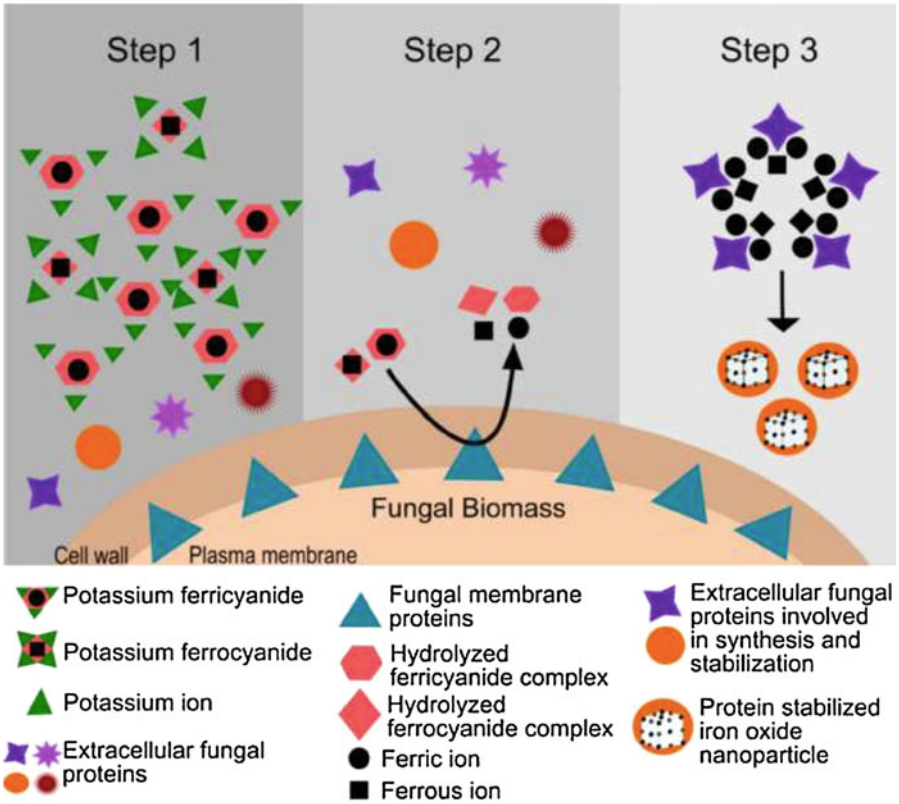

Fig. 5 Biosynthesis of iron oxide nanoparticles using an *Aspergillus japonicus* fungal isolate [Bhargawa et al. J Nanopart Res (2013). In press]

interventions must be coupled with and embedded in systemic intervention strategies, which are not solely reliant on nanotechnology as the silver bullet."

Because sustainability entails considering social, economic and environmental factors, it is critical in all cases to integrate fundamental science (e.g., materials synthesis, characterization and modeling) with engineering research (e.g., system design, fabrication and testing), commercialization (e.g., new products) and societal benefits (e.g., new jobs and cleaner environment) (Diallo and Brinker 2011; Diallo et al. 2013). Thus, nanotechnology solutions for sustainable development cannot simply be addressed at the level of small- and single-investigator funded research grants. Sustainability R&D has to be integrated with broader research goals and included from the beginning in large interdisciplinary programs to be carried out by interdisciplinary teams of investigators and/or dedicated government funded research and development centers (Diallo and Brinker 2011; Diallo et al. 2013). The article *Nanotechnology policy in Korea for sustainable growth* by So et al. (2012) reviews nanotechnology policy for sustainability in South Korea over the past decade. The authors reported that several key policy enactments fostering both fundamental and application-driven research have helped South Korea become one of the leading countries in nanotechnology R&D along with the USA, Japan and Germany. The authors also discuss the current (Third Phase) of Korea's nanotechnology program (2011–2020), which focuses on nanotechnology convergence and integration with the information technology, energy and environmental sectors.

Outlook

The global sustainability challenges facing the world are complex and involve multiple interdependent areas. Nanotechnology has emerged as a versatile platform for the development of technical solutions to global sustainability challenges facing the world. In this JNR special issue, we provided a retrospective of the utilization of nanotechnology to advance sustainable development. More specifically, we discussed the results/findings of selected articles from this special issue to highlight key advances in the following topical areas of global sustainability: (1) water

purification, (2) clean energy technologies, (3) greenhouse gases management, (4) materials supply and utilization, (5) green manufacturing and chemistry and (6) societal perspectives. Our retrospective confirms that nanotechnology continues to provide unprecedented opportunities to develop functional materials for sustainable technologies/products with superior electronic, optical, catalytic and magnetic properties. These novel nanomaterials can be processed into various form factors including water-soluble supramolecular hosts, particles, fibers and membranes. Thus, they have emerged as promising building blocks for a broad range of sustainability applications including (1) water treatment, reuse and desalination, (1) energy generation, conversion and storage, (3) CO_2 capture, storage and conversion, (4) environmental monitoring and remediation, (5) material extraction, purification and recovery and (6) manufacturing (Diallo and Brinker 2011; Diallo et al. 2013).

Because sustainability is determined by the coupled interactions between (1) population growth and human needs, (2) societal and cultural values and (3) the human-built environment and Earth system's boundaries (Diallo et al. 2013; Tonn et al. 2013), it is vital to take into account the complex linkages between the "social system" (i.e., the institutions that support human existence on Earth), the "global system" (i.e., the Earth's ecosystems that support human life) and the "human system" (i.e., all the other factors that impact the health and well being of humans) to achieve global sustainability (Rapport 2007; Diallo et al. 2013). Following the June 2012 Rio Conference on Sustainable Development, the United Nations began developing its post-2015 development agenda (UN System Task Team 2012). Three guiding principles of this new agenda are (1) human rights, (2) equality, and (3) sustainability. The implementation of the post-2015 UN development agenda will require transformative changes in the ways we produce and consume goods, manage our natural resources, and govern our society. In addition, the convergence of knowledge, technology and society (CKTS) will also be required to produce the transformative advances and revolutionary technology/products critical to realizing a sustainable, healthy, secure, and peaceful world (Diallo et al. 2013). We expect that nanotechnology to continue to be a critical component of CKTS as its offers the potential to expand the limits of sustainability and address all critical needs of human development on Earth including basic commodities (e.g., energy, water and food), finished goods (e.g., cell phones, cars and airplanes) and services (e.g., shelter, healthcare and employment). However, it is critical to make sure that any potential adverse effects of nanotechnology on human health and the environment are effectively assessed and addressed before the large-scale deployment of nanotechnology-based solutions and products for the global sustainability challenges facing the world in the next 10–20 years.

Acknowledgments The edition of this JNR special issue on "Nanotechnology for Sustainable Development" was a timely effort in an area where exciting breakthroughs are occurring and paradigm shifting technologies are being developed. As Guest Editors, we really enjoyed working on this JNR special issue. We thank the authors and reviewers for making the edition of this issue possible through their responsiveness and high quality work. We thank Dr. Mihail Roco (NSF Senior Advisor for Nanotechnology and Editor-in-Chief of JNR) and the JNR staff for their constant support throughout the edition of this special issue. We greatly appreciate Dr. Roco's leadership in bringing sustainable development to the forefront of the nanotechnology research agenda worldwide. We thank the National Nanotechnology Policy Center (NNPC) of the Korea Institute of Science and Technology Information (KISTI) of the Republic of Korea and the Resnick Sustainability Institute of the California Institute of Technology for their financial support to the printing of a hardbound book of this JNR special issue. Mamadou Diallo thanks the KAIST EEWS Initiative (Grant # NT080607C0209721), the National Research Foundation of Korea (NRF) [MEST grant No. 2012M1A2A2026588] and the US National Science Foundation (NSF) (CBET Grants 0948485 and 0506951) for funding his research on sustainable chemistry, engineering and materials (SusCHEM). Neil Fromer thanks the Resnick Sustainability Institute, as well as the LMI-EFRC, Rod Eggert, and Jack Lifton and the other attendees of the Resnick Institute critical materials workshop for helpful discussions. Myung Jhon's research was partially supported by the Korea Science & Engineering Foundation through the WCU Project.

References

Almeelbi T, Bezbaruah A (2012) Aqueous phosphate removal using nanoscale zero-valent iron. J Nanopart Res 14:900

Aslan A, Bozkurt A (2013) Preparation of proton conducting membranes containing bifunctional titania nanoparticles. J Nanopart Res 15:1781

Banerjee R, Phan A, Wang B, Knobler C, Furukawa H, O'Keeffe M, Yaghi O (2008) High-throughput synthesis of zeolitic imidazolate frameworks and applications to CO_2 capture. Science 319:939–943

Bates BC, Kundzewicz ZW, Wu S, Palutikof JP (eds) (2008) Climate change and water. Technical paper of the intergovernmental panel on climate change, IPCC Secretariat, Geneva, p 210

Bharathi S, Nataraj D, Senthil K, Masuda Y (2012) Shape controlled synthesis of α-Fe_2O_3 nanostructures: engineering their surface properties for improved photocatalytic degradation efficiency. J Nanopart Res 15:1346

Bhargava A, Jain N, Barati ML, Akhtar MS, Yu YS, Panwar J (2013) Synthesis, characterization and mechanistic insights of mycogenic iron oxide nanoparticles. J Nanopart Res 15:2031

Brinker JC, Ginger D (2011) Nanotechnology for sustainability: energy conversion, storage, and conservation. In: Roco MC, Mirkin MC, Hersham M (eds) Nanotechnology research directions for societal needs in 2020: retrospective and outlook. Science Policy Reports, Springer, Dordrecht, pp 261–303

Brundtland H (1987) Toward sustainable development. In our common future (chap 2). From A/42/427. Our common future: report of the world commission on environment and development. Available online: http://www.un-documents.net/ocf-02.htm

Buha J, Fissan H, Wang J (2013) Filtration behavior of silver nanoparticle agglomerates and effects of the agglomerate model in data analysis. J Nanopart Res 15:1709

Busnaina A, Mead J, Isaacs J, Somu S (2013) Nanomanufacturing and sustainability: opportunities and challenges. J Nanopart Res 15:1984

Chan CCP, Gallard H, Majewski P (2012) Fabrication of amine functionalized magnetite nanoparticles for water treatment processes. J Nanopart Res 14:828

Chen ZX, Cheng Y, Chen Z, Megharaj M, Res Naidu R (2012) Kaolin-supported nanoscale zero-valent iron for removing cationic dye-crystal violet in aqueous solution. J Nanopart 14:899

Choi J, Qu Y, Hoffmann MR (2012) SnO_2, IrO_2, Ta_2O_5, Bi_2O_3, and TiO_2 nanoparticle anodes: electrochemical oxidation coupled with the cathodic reduction of water to yield molecular H_2. J Nanopart Res 14:983

Chung PS, So DS, Biegler LT, Jhon MS (2012) Nanotechnology convergence and modeling paradigm of sustainable energy system using polymer electrolyte membrane fuel cell as a benchmark example. J Nanopart Res 14:853

Davis SC, Diegel SW, Boundy RG (2008) Transportation energy data book, Ed 27. Oak Ridge National Laboratory (ORNL-6981): Oak Ridge, TN, USA

Diallo MS, Brinker JC (2011) Nanotechnology for sustainability: environment, water, food, minerals and climate. In: Roco MC, Mirkin MC, Hersham M (eds) Nanotechnology research directions for societal needs in 2020: retrospective and outlook. Science Policy Reports, Springer, Dordrecht, pp 221–259

Diallo MS et al (2013) Implications: convergence of knowledge and technology for a sustainable society. In: Roco MC, Bainbridge WS, Tonn B, Whitesides G (eds) Convergence of knowledge, technology, and society: beyond convergence of nano-bio-info-cognitive technologies. Science policy reports. Springer, Dordrecht, pp 311–356

EPA (Environmental Protection Agency) (2008) Inventory of US greenhouse gas emissions and sinks: 1990–2006. EPA, Washington, DC

Fromer N, Diallo MS (2013) Nanotechnology and clean energy: sustainable utilization and supply of critical materials. J Nanopart Res 15:2011

Fromer N, Eggert RG, Lifton J (2011) Critical materials for sustainable energy applications. Resnick Institute Report, California Institute of Technology. Available online at http://resnick.caltech.edu/programs/critical-materials/index.html

Ge QC, Su JC, Chung TS, Amy G (2011) Hydrophilic superparamagnetic nanoparticles: synthesis, characterization, and performance in forward osmosis processes. Ind Eng Chem 50:382–388

Godfray HCJ, Beddington JR, Crute IR, Haddad L, Lawrence D, Muir JF, Pretty J, Robinson JS, Thomas SM, Toulmin C (2010) Food security: the challenge of feeding 9 billion people. Science 327:812–818

IPCC (Intergovernmental Panel on Climate Change) (2005) IPCC special report on carbon dioxide capture and storage. In: Metz B, Davidson O, de Coninck HC, Loos M, Meyer LA (eds) Prepared by working group III of the intergovernmental panel on climate change. Cambridge University Press, Cambridge, p 442

Kim S, Lee YM (2012) Thermally rearranged (TR) polymer membranes with nanoengineered cavities tuned for CO_2 separation. J Nanopart Res 14:949

Kuvarega AT, Krause RW, Mamba BB (2012) Multiwalled carbon nanotubes decorated with nitrogen, palladium co-doped TiO_2 (MWCNT/N, Pd co-doped TiO_2) for visible light photocatalytic degradation of Eosin Yellow in water. J Nanopart Res 14:776

Lewis NS (2007) Toward cost-effective solar energy use. Science 315:798–801

Ling MM, Chung TS (2011) Desalination process using super hydrophilic nanoparticles via forward osmosis integrated with ultrafiltration regeneration. Desalination 278:194–202

Liou TZ (2012) Recovery of silica from electronic waste for the synthesis of cubic MCM-48 and its application in preparing ordered mesoporous carbon molecular sieves using a green approach. J Nanopart Res 14:869

Liveris A (2012) Make it in America: the case for reinventing the economy. Wiley, Hoboken, NJ

Mahdavi S, Jalali M, Afkhami A (2012) Removal of heavy metals from aqueous solutions using Fe_3O_4, ZnO, and CuO nanoparticles. J Nanopart Res 14:846

Mahlambi MM, Mishra AK, Mishra SB, Krause RW, Mamba BB, Raichur AM (2012) Synthesis and characterization of carbon-covered alumina (CCA) supported TiO_2 nanocatalysts with enhanced visible light photodegradation of rhodamine B. J Nanopart Res 14:790

Malinga SP, Arotiba OA, Krause RW, Mapolie SF, Diallo MS, Mamba BB (2013) Composite polyester membranes with embedded dendrimer hosts and bimetallic Fe/Ni nanoparticles: synthesis, characterisation and application to water treatment. J Nanopart Res 15:1698

Mohanpuria P, Rana NK, Yadav SK (2008) Biosynthesis of nanoparticles: technological concepts and future applications. J Nanopart Res 10:507

Nandi D, Gupta K, Ghosh AK, De A, Banerjee S, Ghosh UC (2012) Manganese-incorporated iron(III) oxide–graphene magnetic nanocomposite: synthesis, characterization, and application for the arsenic(III)-sorption from aqueous solution. J Nanopart Res 14:1272

NRC (National Research Council) (2008) Minerals, critical minerals, and the US economy. ISBN: 0-309-11283

Okoli C, Boutonnet M, Järås S, Rajarao-Kuttuva G (2012) Protein-functionalized magnetic iron oxide nanoparticles: time efficient potential-water treatment. J Nanopart Res 14:1194

Park SJ, Cheedrala RK, Diallo MS, Kim CH, Kim IS, Goddard WA (2012a) Nanofiltration membranes based on polyvinylidene fluoride nanofibrous scaffolds and crosslinked polyethyleneimine networks. J Nanopart Res 14:884

Park JY, Lee YS, Jung Y (2012b) Local intermolecular interactions for selective CO_2 capture by zeolitic imidazole frameworks: energy decomposition analysis. J Nanopart Res 14:793

Park JY, Lim S, Park K (2013) A new approach for determination of fouling potential by colloidal nanoparticles during reverse osmosis (RO) membrane filtration of seawater. J Nanopart Res 15:1548

Patel HA, Byun J, Yavuz CT (2012a) Arsenic removal by magnetic nanocrystalline barium hexaferrite. J Nanopart Res 14:881

Patel R, Ahn SH, Seo JA, Kim SJ, Kim JH (2012b) Poly(vinyl chloride)-g-poly(2-(dimethylamino ethyl methacrylate) graft copolymer templated synthesis of mesoporous TiO_2 thin films for dye-sensitized solar cells. J Nanopart Res 14:845

Rapport DJ (2007) Sustainability science: an ecohealth perspective. Sustain Sci 2:77–84

Roco MC (2001) From vision to the implementation of the US national nanotechnology initiative. J Nanopart Res 3:5

Roco MC, Bainbrige WS (1946) The new world of discovery, invention and innovation: convergence of knowledge, technology, and society. J Nanopart Res 15:1–17 (Paper 1946)

Saif M, Aboul-Fotouh SM, El-Molla SA, Ibrahim MA, Ismail LFM (2012) Improvement of the structural, morphology, and optical properties of TiO_2 for solar treatment of industrial wastewater. J Nanopart Res 14:1227

Savage N, Diallo MS (2005) Nanomaterials and water purification: opportunities and challenges. J Nanopart Res 7:331–342

Schmidt KF (2007) Green nanotechnology: it is easier than you think. Project on Emerging Nanotechnologies (Pen 8), Washington, DC: Woodrow Wilson International Center for Scholars. Available online at http://www.nanotechproject.org/file_download/files/GreenNano_PEN8.pdf

Scott NR, Chen H (2003) Nanoscale science and engineering for agriculture and food systems. Roadmap report of the national planning workshop, Washington DC, November 18–19, 2002. Available online: http://www.nseafs.cornell.edu/web.roadmap.pdf

Shannon MA, Bohn PW, Elimelech M, Georgiadis J, Marinas BJ, Mayes A (2008) Science and technology for water purification in the coming decades. Nature 54:301–310

Sharma MK, Ambolikar AS, Aggarwal SK (2012) Electrochemical synthesis of gold nanorods in track-etched polycarbonate membrane using removable mercury cathode. J Nanopart Res 14:1094

So DS, Kim CW, Chung PS, Jhon MS (2012) Nanotechnology policy in Korea for sustainable growth. J Nanopart Res 14:854

Solomon S, Quin D, Manning M, Chen Z, Marquis M, Averyt KB, Tignor M, Miller HL (eds) (2007) Climate change 2007: the physical science basis. Cambridge University Press, Cambridge

Swaminathan VV, Gibson LR II, Pinti M, Prakash S, Bohn PW, Shannon MA (2012) Ionic transport in nanocapillary membrane systems. J Nanopart Res 14:951

Tonn B et al (2013) Convergence platforms: earth-scale systems. In: Roco MC, Bainbridge WS, Tonn B, Whitesides G (eds) Convergence of knowledge, technology, and society: beyond convergence of nano-bio-info-cognitive technologies. Science policy reports. Springer, Dordrecht, pp 103–135

UN (United Nations) (2012) Realizing the future we want for all. Report to the Secretary-General. Available online: http://www.un.org/millenniumgoals/pdf/Post_2015_UNTTreport.pdf

Wang B, Cote AP, Furukawa H, O'Keeffe M, Yaghi OM (2008) Colossal cages in zeolitic imidazolate frameworks as selective carbon dioxide reservoirs. Nature 453:207–211

Wanyika H (2013) Sustained release of fungicide metalaxyl by mesoporous silica nanospheres. J Nanopart Res 15:1831

Wiek A, Foley R, Guston D (2012) Nanotechnology for sustainability: what does nanotechnology offer to mitigate complex sustainability problems? J Nanopart Res 14:1093

DOI 10.1007/978-3-319-05041-6_2
Reprinted from the *Journal of Nanoparticle Research*, DOI 10.1007/s11051-012-0951-0

REVIEW

Ionic transport in nanocapillary membrane systems

Vikhram V. Swaminathan · Larry R. Gibson II · Marie Pinti · Shaurya Prakash · Paul W. Bohn · Mark A. Shannon

Received: 11 March 2012 / Accepted: 23 May 2012 / Published online: 4 July 2012

Abstract Species transport in nanocapillary membrane systems has engaged considerable research interest, presenting technological challenges and opportunities, while exhibiting significant deviations from conventionally well understood bulk behavior in microfluidics. Nonlinear electrokinetic effects and surface charge of materials, along with geometric considerations, dominate the phenomena in structures with characteristic lengths below 100 nm. Consequently, these methods have enabled 3D micro- and nanofluidic hybrid systems with high-chemical selectivity for precise manipulation of mass-limited quantities of analytes. In this review, we present an overview of both fundamental developments and applications of these unique nanocapillary systems, identifying forces that govern ion and particle transport, and surveying applications in separation, sensing, mixing, and chemical reactions. All of these developments are oriented toward adding important functionality in micro-total analysis systems.

Keywords Membranes · Nanostructures · Nanofluidics · Microfluidics · Ion transport · Electrokinetics · μ-TAS · Nanopore · Nanocapillary · Water filtration · Sustainable development

Special Issue Editors: Mamadou Diallo, Neil Fromer, Myung S. Jhon

This article is part of the Topical Collection on Nanotechnology for Sustainable Development

Introduction

The development of nanofluidic systems containing nanocapillary array membranes (NCAMs) is strongly motivated by the interesting phenomena that occur at length scales between 1 and 100 nm. NCAMs consist

V. V. Swaminathan · M. A. Shannon (✉)
Department of Mechanical Science and Engineering, University of Illinois at Urbana-Champaign, Urbana, IL 61801, USA
e-mail: mshannon@illinois.edu

L. R. Gibson II · P. W. Bohn
Department of Chemical and Biomolecular Engineering, University of Notre Dame, Notre Dame, IN 46556, USA

M. Pinti · S. Prakash
Department of Mechanical and Aerospace Engineering, The Ohio State University, Columbus, OH 43210, USA

P. W. Bohn
Department of Chemistry and Biochemistry, University of Notre Dame, Notre Dame, IN 46556, USA

M. A. Shannon
Department of Chemical and Biomolecular Engineering, University of Illinois at Urbana-Champaign, Urbana, IL 61801, USA

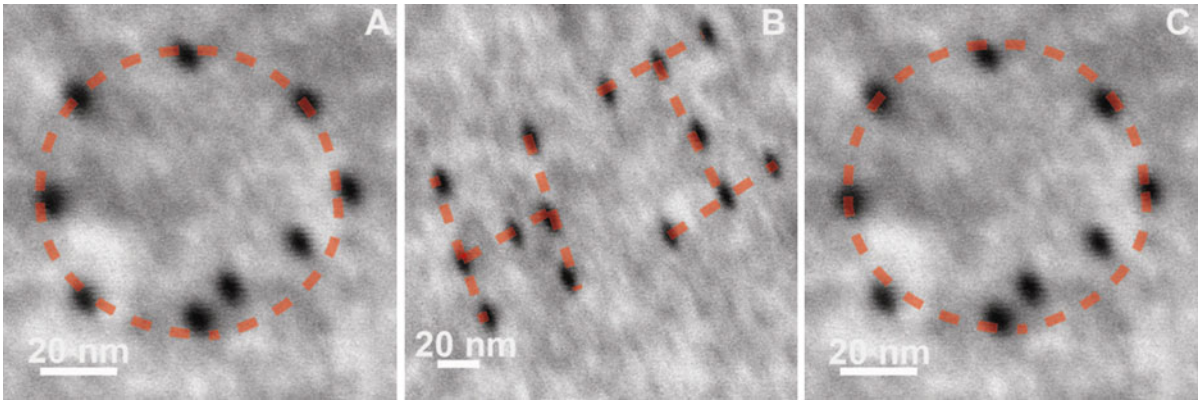

Fig. 1 Fabrication of nanopore arrays using a transmission electron microscope (TEM). Ordered arrangements were fabricated to illustrate the word "OHIO" with elliptical cross-section nanopores. The *red-dotted line* is meant to serve as an eye-guide. The pores in **a** and **c** are 4 ± 0.4 x 2.6 ± 0.6 nm The nanopores that spell out "H" and "I" are 5.8 ± 0.7 x 3.0 ± 0.5 nm as shown in **b**. This figure is taken from Prakash et al. 2012

of monodisperse nanopores fabricated in a polymer membrane, most commonly composed of polycarbonate sheets with thickness on the order of 6–10 μm, with nanopores produced from the damage tracks created by high-energy (∼2 MeV) alpha particles, followed by chemical etching to produce nanopores ranging in diameter from 10 to 800 nm. These NCAMs are commercially available. Next generation NCAMs are fabricated with various geometries, in different polymers and in multi-lamellar structures. For example, fabrication of solid-state nanopores similar to NCAMs with a transmission electron microscope has been achieved in silicon nitride membranes with controlled cross-section geometry and ordered arrangement of the nanopores (Prakash et al. 2012a, b) (Fig. 1).

The influence of surface charge, surface potentials, and subsequent electrostatic forces lead to hindered transport, selectivity, and partitioning of chemical and biological species. Such systems draw advantage from enhanced surface area-to-volume (SA/V) scaling that leads to reduced diffusion time scales in contrast to conventional microfluidic systems for transport toward surfaces and rapid kinetics. The ability to capture and manipulate extremely small quantities of analytes (zeptoliter to attoliter volumes) with high precision and flexibility approaching the molecular level, and to execute multiple analytical unit operations on-chip, has strongly driven several fundamental studies and applications of separation, concentration, and sensing systems aimed toward developing better tools of chemical analysis and biological diagnostics.

In recent years, numerous articles have reviewed concepts of nanofluidic transport phenomena and their applications in chemical and biological analysis, (Han et al. 2008; Schoch et al. 2008; Prakash et al. 2008, 2009; Sparreboom et al. 2009; Bohn 2009; Piruska et al. 2010a, b; Mulero et al. 2010). Technological advancements in micro- and nanofabrication have facilitated the realization of systems integrated with nanocapillary arrays in microfluidic devices, and methods of surface modification of pore surfaces (Nishizawa et al. 1995) have enabled excellent control and modulation of factors governing nanoscale transport. The purpose of this review is to present a broad overview of nanoscale transport phenomena in NCAMs, highlighting outcomes of fundamental studies, along with advancements in a variety of application areas.

Background

Flow characteristics through nanostructures such as nanopores, NCAMs, nanochannels, and nanotubes are largely determined by the size, geometry, and surface chemistry (i.e., surface charge density and surface energy) of the nanostructure. The characteristic dimension of a nanocapillary is its pore diameter, a, which lies typically in the range of 1–100 nm for nanofluidic phenomena. The Debye length, λ_D, is a critical scaling parameter that captures the extent of surface charge shielding in nanoscale geometries. As physical feature dimensions approach this value new phenomena such as perm selectivity (Nishizawa et al. 1995) come into play

with the primary driving forces for transport being electrokinetic flow or surface mediated transport (Prakash et al. 2008). While this condition can intersect with the transition between continuum and molecular models, it can be used to address individual molecules (Bohn 2009). On one hand, fluid dynamics within high-aspect ratio nanocapillaries is beset with size effects—shielding and apparent electro viscosity that lead to hindered transport. However, surfaces and their characteristic properties such as charge and potential distributions determine the environment and forces experienced by ions and cause effects of selectivity and partitioning.

Transport equations in cylindrical capillaries

Even though the basis for most modern-day electrokinetics arises from colloidal theories developed well over 100 years ago, detailed analytical studies of electrokinetic flow in fine capillaries date back to 1964, where it was demonstrated for rectangular slit geometries that, for large values of the surface potential, Ψ_0, and sufficiently small κa, where κ equals $1/\lambda_D$, electrokinetic retardation effects opposed pressure-induced flow when capillary dimensions shrink down to 100 nm (Burgreen and Nakache 1964). Rice and Whitehead derived the analytical solution to the potential distribution, Ψ, inside a cylindrical capillary, for small surface potential, Ψ_0, using a Poisson-Boltzmann distribution equation (Rice and Whitehead 1965)

$$\frac{1}{r}\frac{\partial}{\partial r}\left(r\frac{\partial \psi}{\partial r}\right) = \kappa^2\psi, \tag{1}$$

where

$$\kappa = \sqrt{\frac{8\pi n e^2}{\varepsilon kT}}, \tag{2}$$

with n representing the bulk concentration of ions per unit volume, e is the fundamental charge, ε is the electrical permittivity, k is the Boltzmann's constant, and T is the temperature. The solution for potential distribution follows

$$\psi = \psi_0 \frac{I_0(\kappa r)}{I_0(\kappa a)}, \tag{3}$$

where I_0 is the modified Bessel equation of the first kind. This analytical solution was valid to within 3 % accuracy for small values of $\Psi_0 < \mathrm{kT} \approx 25$ mV, and later extended up to 50 mV based on asymptotic approximations. Combining this with the steady-state Navier–Stokes' equation for fluid motion

$$\eta\nabla^2 v + (v\cdot\nabla)v + \nabla p = F, \tag{4}$$

where η is the viscosity, p is the pressure, and F is the body force, yields the electroosmotic velocity, $v(r)$, as follows

$$v(r) = \frac{a^2 - r^2}{4\eta}p_z - \Omega E_z\left[1 - \frac{I_0(\kappa r)}{I_0(\kappa a)}\right], \tag{5}$$

where $\Omega = \dfrac{\varepsilon\psi}{4\pi\eta}$, and E_z is the axial electric field that represents the body force.

Advanced computational techniques and molecular dynamics simulations have been incorporated to validate analytical and numerical models for ionic transport (Conlisk et al. 2002; Qiao and Aluru 2003; Conlisk 2005). Furthermore, the effects of surface charge/wall potentials, ionic size, and differential transport on electroosmotic flow (EOF) in nanochannels and membranes have been studied both computationally (Qiao and Aluru 2004; Qiao et al. 2006; Conlisk et al. 2007) and experimentally (Sadr et al. 2006).

The local potential distribution shown in Eq. 3 is strongly dependent on length scales and Fig. 2 shows schematic profiles for different values of κa with a more detailed discussion found in several textbooks (Conlisk 2012) and recent reviews (Prakash et al. 2012a, b). When pores are sufficiently large, or the ionic strength is large and membrane potential small, so that κa >> 1 (Fig. 2a), the electrochemical double layers (EDLs) are compact and the core region of the

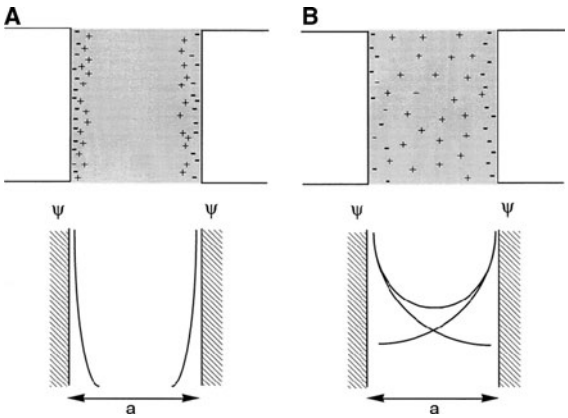

Fig. 2 Schematic representation of the formation of the EDLs and potential profiles within nanopores at the extreme conditions where **a** κa >> 1 when the EDLs are compact and **b** κa $\leq$ 1 when the EDLs overlap and lead to permselectivity. Reprinted with permission, (Kemery et al. 1998). Copyright 1998 American Chemical Society

pore retains bulk-like concentration and plug-flow electrophoretic characteristics (Kemery et al. 1998). On the other hand, narrow pores with dilute media, corresponding to $\kappa a \leq 1$, form overlapped EDLs with radial velocity following Poiseuille flow-like parabolic characteristic. Consequently, counter-ions are drawn into the pore and co-ions rejected to maintain charge neutrality (Fig. 2b), and give rise to perm selectivity by the exclusion-enrichment effect (Plecis et al. 2005). Local asymmetry in solute distribution causes deviations from bulk electrostatic behavior—most notably, the EOF arising from interactions with the wall charge dominating over electrophoresis.

The electroviscous effect and enhanced conductivity

At length scales of $\kappa a \leq 10$, it has been estimated through flow-rate measurements fit to conventional Poiseuille flow that the apparent viscosity is enhanced over that of Poiseuille flow due to back flow from EOF effects. The resulting enhanced viscosity is often referred to as electroviscosity since surface charge has been shown to cause increased structuring or layering of water near the pore walls through molecular dynamics simulations (Qiao and Aluru 2003). Further in the case of nanopores, when $\kappa a \leq 1$, interacting double layers cause decreased solvent flow and may also contribute to the apparent viscosity. Huisman et al. (2000) calculated the electroviscous effect from measurements of streaming potential and showed that differences in ionic mobilities in binary electrolytes broke zeta potential (ζ-potential) symmetry and enhanced the electroviscosity. A Knudsen number based on the ratio of molecular interaction length over system characteristic dimension has been suggested for modeling fluidic resistance under Stokes' flow in nanochannels (Sparreboom et al. 2010). Backflow of ions under the electric field arising from electroosmotic pressure is also enhanced by the surface conductance, G_s, due to the presence of the EDLs, and contributes to increased conductivity of the electrolyte inside the pore, λ_{pore}, than in bulk, λ_{bulk}, such that

$$\lambda_{\text{pore}} = \lambda_{\text{bulk}} + \frac{2G_s}{a}. \tag{6}$$

It should be noted here that electroviscosity is an effect that has been used to explain deviations from conventional theory, and some molecular dynamics simulations have shown fluid layering as one possible reason for enhanced viscosity, but independent experimental verification of increased fluid viscosity have not yet been reported.

Streaming potential

The streaming potential, a measurable quantity, serves as a useful experimental tool used in gauging separation performance of ultrafiltration (UF) and nanofiltration (NF) membranes (Nystrom et al. 1989; Agerbaek and Keiding 1995; Fievet et al. 2000; Datta et al. 2010). Surface charge of membranes is often characterized using ζ-potential at slip planes derived from streaming potential measurements. Experimentally determined ζ-potentials in both aqueous and non-aqueous media (Chowdiah et al. 1983) substantially exceeded the calculations from Helmholtz–Smoluchowski theory using analytical correction factors (Rice and Whitehead 1965). Nystrom and colleagues reported a 10-fold increase in apparent ζ-potentials when correction factors and the influence of membrane surface charge and double layer were suitably taken into account. In pH-dependent transport experiments of chlorolignin through polyvinylidene fluoride (PVDF) UF membranes, strong electrostatic repulsions were observed when the polyelectrolyte was fully dissociated, whereas neutral molecules passed through when they were un-dissociated at a low pH of 3. Determining a true ζ-potential from experimental measurements required extending Rice and Whitehead's model to account for larger pore potentials by numerical calculations using the space-charge model (Szymczyk et al. 1999). Especially in the case of nanocapillary membranes with hydrophilic surfaces, the strong coupling between transport phenomena presents a hard challenge for the measurement of ζ-potential with overlapped EDLs. Furthermore, in the case of overlapped EDLs, the notion of slip planes and hence ζ-potential loses physical significance (Prakash et al. 2008).

Transport of macromolecules

Besides the effect of capillary size and λ_D, a third length scale, based on the ionic size, R_i, affects transport characteristics of NCAMs. Incorporating the

finite size of ions, particularly for systems with $\kappa a \sim 1$, was found to have significant effect in suppressing average ionic concentrations and electrical conductance inside pores while increasing selectivity and streaming potential (Cervera et al. 2010). The Renkin equation (Renkin 1954) captures the effect of ionic size relative to pore radius in decreased species diffusion coefficient, D_i, within a confined pore in comparison with bulk values, D_0, such that

$$D_i = D_0\left[1 - 2.104\frac{R_i}{a} + 2.09\left(\frac{R_i}{a}\right)^2 - 0.95\left(\frac{R_i}{a}\right)^5\right]. \quad (7)$$

Studies of peptide concentration using NCAMs (Zhang and Timperman 2003) and, more recently, protein dynamics in silicon nitride nanopores have clearly demonstrated the hindered macromolecular transport effect (Oukhaled et al. 2011). Dwell-times measured for proteins were found to be on the order of milliseconds while diffusion-based calculations predicted microsecond timescales, which is attributed to the protein-wall adsorption interactions as well as EOF retardation. Further, anomalous protein dynamics in nanopores, including longer dwell-times for compact proteins than those of unfolded structures, are indicative of entropic energy costs associated with size, unfolding, and interactions of heterogeneous charge macromolecule structures with nanocapillary surfaces (Talaga and Li 2009; Napoli et al. 2010) that are not yet fully understood.

Transport studies at NCAM-microchannel interfaces

One of the challenges in microfluidics (and even more so in nanofluidics) is the ability to provide controlled metering of fluid and chemical or biological species for specific unit operations. The interface between microchannels and NCAMs can lead to strong discontinuity in electrokinetic characteristics, and various parameters—pore size, pH, ionic strength, and functionality—can be used to control and regulate molecular transport. Kuo et al. (2001), investigated these effects on flux through NCAMs with both hydrophobic and hydrophilic surfaces. In high-ionic strength, diffusion dominated the transport in hydrophilic membranes while hydrophobic membranes were controlled by ion migration. Transport direction could be reversed, under the same applied electric field, by modifying surface charge or ionic strength. At low-ionic strength, EOF effects dominated transport as surface charge determined the direction, with pH acting as a fine-tuning parameter. The choice of many control variables enables a high degree of control over nanofluidic gated injections, a powerful strategy capable of enhancing several applications discussed in section 5.

Molecular gating

Molecular gating refers to the selective transport of ions or molecules based on electrical interactions with an externally applied potential and the surface charge of the NCAM. The ion gating concept was studied as early as 1982 with the use of embedded electrodes and redox polymer membranes in a macroporous system (Burgmayer and Murray 1982). The device depicted in Fig. 3 consists of an NCAM placed between two polydimethylsiloxane (PDMS) microfluidic channels and is used to illustrate the way selection of properties such as pore size and surface chemistry allow for electrically biased flow manipulation within the device (Kuo et al. 2003a, b). An applied potential between the source and receiving channels drives the flow, with forward bias defined as the configuration that causes depletion in the source channel and enrichment in the receiving channel. The direction of the fluid flow for the same applied potential is determined by the choice of pore diameter, pore surface chemistry, channel surface charge, and ionic strength of the buffer. The pores used in this study had a positive surface charge corresponding to negative mobile counter-ions within the pores, while PDMS microchannels had negative surface charge. It was found that for the 200 nm pores the surface charge of the channels dictated the applied voltage that corresponded to forward bias rather than the surface charge of the pores themselves. The opposite was true for an array of 15 nm diameter pores indicating that nanopore EOF dominated in 15 nm pores while channel EOF dominated in 200 nm pores. In such devices, fabrication limitations place constraints on materials and surface properties; however, sizing of the molecular gates can be tuned for desired transport characteristics. Aluru and co-workers (Chatterjee et al. 2005) analyzed the same problem using circuit models to

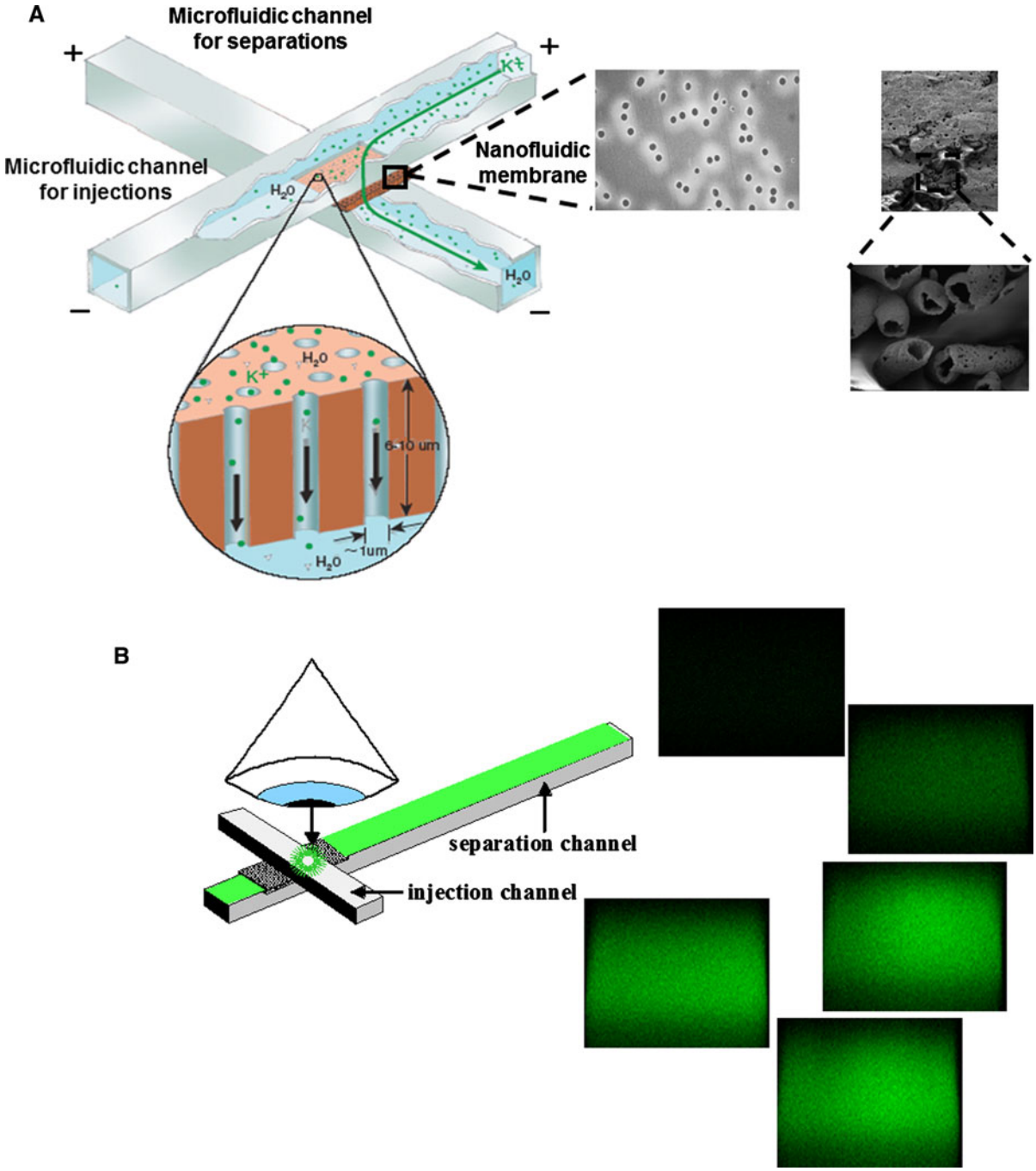

Fig. 3 **a** A schematic for the molecular gate developed using NCAMs. A NCAM with positive surface charge is sandwiched between two PDMS microchannels with negative surface charge, with the inserts showing fluorescence images of the injected samples collected over a period of time. The device is used to illustrate electrically-controlled fluid flow through the NCAM. **b** Demonstrates rapid injection from the source to the receiving channel, with the inserts showing fluorescence images of the injected samples collected over a period of time. Figure from IEEE (Prakash et al. 2008)

determine impedances and calculate ionic currents. The size of the nanopores have a dramatic effect; while, the 200 nm pores contribute as little as 1 % of the total impedance, a 36-fold increase in the case of 15 nm pores highlights the role of nanocapillary EOF in reversing the effective biasing conditions. Subsequently, NCAMs have been integrated within microfluidic devices for quantification of ionic transport regimes (Prakash et al. 2007) and have also been used to develop impedance measurements as a tool.

Switchable fluidic communication in NCAMs used in molecular gates demonstrates diode-like characteristics, with the additional capability of tuning size-dependent fractionation and injection (Kuo et al. 2003a, b). Novel injection strategies have been incorporated for improving peak reproducibility and separation resolution by the use of floating injection methods in NCAM hybrid devices (Gong et al. 2008a, b). Floating injection, albeit lower throughput than the biased injection schemes, addresses non-uniformities in electric field distribution at NCAM-separation channel interfaces to offset issues of broadening and excess injection. The fabrication of such multilayer hybrid microfluidic devices with 3-D NCAM nanofluidic interconnects as molecular gates (Flachsbart et al. 2006) could be used to build lab on a chip (LoC) devices with several stages for multiple unit operations on mass-limited samples.

Transport in metallic NCAMs

Continuously coated Au-NCAMs

Over the last decade there has been increased interest in the use of metal-coated (particularly Au) membranes as a means of extending the range of applications of NCAMs. The motivation stems from the potential for imparting multiple functionalities to the metal-coated membranes: metal-mediated electrokinetic transport in the nanocapillaries (Martin et al. 2001a, b; Lee and Martin 2002; Chun et al. 2006; Buyukserin et al. 2007; Piruska et al. 2008; Piruska et al. 2010a, b), Faradaic electrochemistry (Contento et al. 2011), self-assembly chemistry on coinage metals for specific surface decoration (Chun and Stroeve 2002; Kohli et al. 2004; Huang and Yin 2006; Kim et al. 2007; Jagerszki et al. 2007), and plasmonic behavior when the pores form a translationally symmetric array. Furthermore, these properties can be exploited by itself or in various combinations, for example, using a plasmonic array to sense the change in solution conditions upon carrying out electron transfer reactions.

There are a number of approaches to realizing metallic nanopores. As shown by Martin and co-workers over a decade ago, electroless deposition of thin Au films affords selective control over transport of a range of molecular entities based on their size, charge, and unique chemical properties. Starting from either cylindrical or conical nanopore membranes, simply varying the plating time during electroless deposition enables reproducible fabrication of Au-coated nanopores with varying internal diameters, producing pores as small as several nm in optimal cases (Martin et al. 2001a, b). Elegant experiments using these structures as effective molecular sieves or filters have been described. However, determinations in complex mixtures frequently dictate that additional molecular selection criteria, beyond size exclusion, be employed.

Taking advantage of robust Au-thiol chemistry, Au-coated nanopore surfaces can be functionalized to effect selective passage based on molecular recognition principles. For example, Huang et al. altered the hydrophobicity within Au nanopores using either cysteine or carbamidine terminated thiols to separate tryptophan and vitamin B_2 (Huang and Yin 2006). Au-coated nanopores functionalized with DNA oligonucleotides have been used to capture, and thus selectively retard, complementary strands via DNA hybridization (Jagerszki et al. 2007; Kohli et al. 2004). In addition, the behavior of thiol-terminated Au nanopore modifiers can be conditionally controlled to mediate molecular transport (Chun and Stroeve, 2002). Stroeve and co-workers controllably modulated amino acid transport across Au-NCAMs by varying pH and ionic strength of an electrolyte solution within a nanopore to regulate the structure of the double layer and the charge state of the analyte (Ku et al. 2007).

Modulation of transport is by no means limited to small molecules. Kim et al. immobilized F_{ab}' fragments of anti-insulin in an Au-NCAM using self-assembly through the exposed disulfide. The resulting affinity-NCAM was competent for molecular recognition of its antigen, insulin, as shown by selective release followed by MALDI mass spectrometry (Kim et al. 2007). Finally, as a highly conductive metal, Au

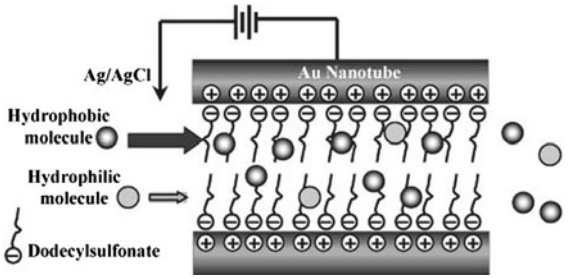

Fig. 4 Surfactant/double layer charging approach for electromodulating neutral molecule transport in Au-NCAMs. Reproduced with permission, (Lee and Martin 2002). Copyright 2002 American Chemical Society

can also be electrostatically charged using an applied potential (Martin et al. 2001a, b), as demonstrated by the electromodulated transport of both small molecules and proteins across Au-NCAMs (Buyukserin et al. 2007; Chun et al. 2006; Lee and Martin 2002). Figure 4 illustrates the strategy: the application of an appropriate electrochemical potential to the Au-coated nanopore results in modulation of the surface density of oppositely charged surfactant molecules, which in turn retard transport of hydrophobic molecules by a mobile-stationary phase partitioning mechanism. Taken together, just this small collection of examples shows how these versatile structures can mimic the behavior of electrophoretic, affinity, and partitioning-based separations used routinely in larger-scale structures.

Partially coated Au-NCAMs

In the previous section, several techniques that have been employed to selectively modulate the diffusive transport of specific molecules across fully coated Au-NCAMs were discussed, but there is a compelling technological motivation for introducing convective transport, in order to significantly improve throughput. However, hydrodynamic strategies employing pressure-driven flow are undesirable for portable applications and are unworkable for pores in the sub-500 nm diameter range, in any case. Furthermore, electrokinetic pumping is limited in continuously coated Au-NCAMs, because the electric fields established by external potentials across these structures are severely distorted by continuous Au layers, thus obviating electrically-controlled transport across these membranes (Piruska et al. 2008). However, NCAMs featuring a thin embedded Au layer are capable of facilitating electrokinetic transport with efficiencies comparable to that of all-dielectric NCAMs (Piruska et al. 2010a, b). Fortunately, NCAM pore dimensions favor rapid EOF driven by applied potentials at the embedded metallic layer of ~ 1 V. Although, injection efficiency across asymmetric NCAMs depends on the orientation of the asymmetric membrane relative to the driving potential, with efficient injections being enabled when the Au coating is on the receiving side of the membrane, reproducible high-quality electrokinetic transport is also achieved in symmetric Au-NCAMs having an embedded gold nanoband region within the nanopores. In addition, embedded Au-layers may serve as working electrodes to drive electrochemical reactions. For example, Contento et al. (2011) reduced water to generate H_2 at nanochannel-embedded electrodes, the hydrogen then being transported by induced electroosmotic flow downstream where it is available for catalytic hydrogenation reactions. Figure 5 depicts the electrochemical generation of H_2 and subsequent transport in planar nanochannels. The abilities discussed here to modulate transport in metallic NCAMs based on molecular recognition and to carry out reactive processing emphasize the fact that nanoband Au-NCAMs are excellent candidates for a range of applications, including high-efficiency electrochemical sensing, electrochemically catalyzed conversion, or pretreatment and label free sensing utilizing extraordinary optical transmission based plasmonic responses.

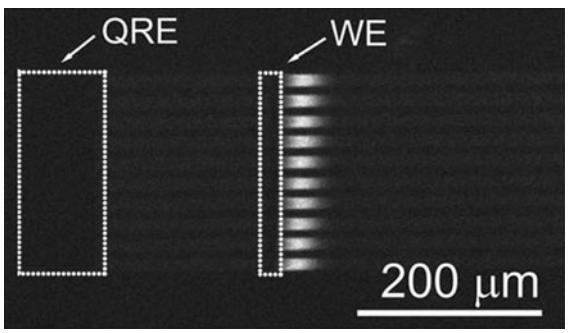

Fig. 5 Generation of H_2 within nanochannel arrays at working electrode (WE), evidenced by an increase in fluorescein indicator fluorescence caused by the rise in pH, and electroosmotic transport downstream (*left* to *right*) by electric field established between the embedded working and quasi-reference (QRE) electrodes. Reproduced from (Contento et al. 2011), by permission of The Royal Society of Chemistry

Applications

Transport through nanostructures has allowed many interesting and innovative applications such as fluidic transistors and diodes, rapid fluid injections, high-throughput reactions, separations, sample mixing, sample concentrating, filtering and sieving, and molecular gating as discussed in detail below. Several of these unit operations can be combined on a single platform to create a micro-total analysis (μ-TAS) system or LoC.

Fundamental studies

NCAMs have been used since the early 1990s to conduct a variety of studies for probing fundamentals of confined nanofluidic transport. Such studies were enabled by the relatively monodisperse pore size distribution achieved during the alpha particle tracking and subsequent etching to make the NCAMs. Initial studies evaluated perm selectivity of ionic species due to surface charge shielding as a function of Debye length (Kemery et al. 1998; Kuo et al. 2001; Nishizawa et al. 1995; Lee and Martin 2002; Jirage et al. 1999; Martin et al. 2001a, b; Hulteen et al. 1998). In the last 5 years or so, as the overall knowledge base for nanofluidic transport phenomena has grown, NCAMs have been integrated within model systems to predict geometry of nanocapillaries using impedance measurements (Vitarelli et al. 2011), to study redox activity of surface functional groups and enhanced transport through nanopores using cyclic voltammetry (CV) (Perera and Ito 2010), and also for studies of electric field mediated wetting phenomena (Powell et al. 2011).

Sample injection/separation

An NCAM sandwiched between two microfluidic channels can be used to electrokinetically inject samples from a source microchannel to a separation microchannel, where electrophoretic separations are performed (see Fig. 3b). Initially a potential is applied across the separation channel with the waste reservoir of the separation channel grounded. During this step the source channel is allowed to float. A picoliter volume from the source side is injected through the NCAM by applying equal potential to either side of the source channel and grounding the waste reservoir of the separation channel. This results in the injection of a well-defined sample plug into the separation channel. Injection times are short, typically a few hundred ms. Electrophoretic separation is then performed on the sample plug before another sample injection (Cannon et al. 2003). This design can also be adapted for sample collection. If a third channel is added and separated by an NCAM from the separation channel, following injection the sample plug can be transferred down the separation channel by electroosmosis and then collected in the third channel by applying an equal bias to both reservoirs of the separation channel and grounding the collection channel (Kuo et al. 2003a, b). These studies illustrate the ability to manipulate flows of mass-limited samples (Shannon et al. 2005; Tulock et al. 2004). The transport of target molecules through NCAMs can be controlled by ionic strength, magnitude, and polarity of the applied potential, pore size, and surface chemistry (i.e., surface charge density and surface energy). NCAMs allow for electrically-controlled valving and rapid sample injections (Wernette et al. 2006; Gong et al. 2008a, b; Wang et al. 2009) with high-sample plug reproducibility, and separation resolution, and reproducibility approaching 1 % for some studies (Cannon et al. 2003). Following the success of these initial demonstrations of molecular gates, new planar microchannel–nanochannel hybrid devices have been developed that allow for controlled dosing of a variety of transfection agents to single cells through electroporation at the microchannel–nanochannel interface (Boukany et al. 2011) with potential applications in high-throughput drug delivery.

Similar injection/collection strategies have been implemented to perform two-stage sample separation. The first stage is electrophoretic separation based on electrophoretic mobilities of varying species, while the second stage involving chiral amino acid mixture separation is achieved through micellar electrokinetic chromatography with a chiral selector. Separation depends critically on injection and collection capabilities in the device. Such separations are important to biochemical studies that require the separation of complex mixtures of analytes with orthogonal separation principles (Kim et al. 2009).

Sieving/filtration

Nanoscale structures such as nanopores and nanochannels allow for the fabrication of molecular filters

of sieves since the size of many biomolecules is on the same order as the characteristic size of these structures themselves. Transport through pores is affected by steric hindrance or exclusion due to molecular entropy, hydrodynamic hindrance, caused by viscous forces associated with the walls of the pores, and charge interactions between the molecule and the surface of the nanopore or nanochannel. Molecules that are larger than the size of the pores themselves can be electrically driven through the pore forcing the molecules to change their shape and conformation. Pore/channel size, surface chemistry (i.e., charge), applied potentials, and multi-step filtrations with different membranes can be used to perform highly efficient separations (Yan et al. 2009; Karnik et al. 2006). Furthermore, methods for active manipulation of the pore geometry using stimulus-responsive polymers, through temperature-mediated shape changes in polymer brushes (Lokuge et al. 2007) and pressure-induced insertion of ion-channels in lipid bilayers (Schibel et al. 2011), have been demonstrated that permit actively-controlled size-selective transport across NCAMs.

Rapid reagent mixing

Incorporating NCAMs into microfluidic structures affords a highly tunable, nanoscale pathway for the transport of molecules from one chemical environment to another (Fa et al. 2005). Typically 5–50 μm thick, NCAMs support rapid electroosmotic flow with relatively low-electrical potentials. Under such conditions linear velocities of order $\sim$1 mm s^{-1} can be achieved across the nanopore. In addition, permitting the digital switching of fluid packets across the nanopores, and coupling of rapid flow in the nanopores to the microfluidic channels feeding those results in advantageous mixing behavior, as well. In general, electrokinetic transport in microfluidic channels occurs at low Reynolds number (10^{-3}–10^{-2}), and as a result, mixing of molecular entities across streamlines relies on Fickian diffusion. However, nanochannel mediated electroosmotic flow encourages convective mixing at the micro/nanochannel junction, as demonstrated by effective mixing within 3D structures comprised of orthogonal microfluidic channels surrounding a polymeric NCAM (Kuo et al. 2004). This strategy has been successfully used for injecting Ca^{2+} into a channel containing a fluorogenic Ca^{2+} probe or molecular beacon action by introducing Pb^{2+} into a channel containing a DNA aptazyme, which is quenched in its native state but unquenched after analyte-mediated dehybridization (Chang et al. 2005). Similarly, large biomolecules, such as enzymes suspended in a microfluidic channel can be electrokinetically injected across an NCAM into an orthogonal microchannel containing the substrate, where the two entities convectively mix and react at the nanopore/microchannel junction (Gong et al. 2008a, b). These operations, which exploit the rapid response to control signal for electrokinetic transport and rapid mixing, mimic the behavior of stopped-flow reactors, but on volumes that are orders of magnitude smaller than bench-top stopped-flow instruments.

Analyte pre-concentration

NCAMs integrated into microfluidic devices can be used to pre-concentrate the sample before injecting it through the NCAM. In one demonstration, fluorescein, a negatively charged dye, was combined with a buffer solution. A positive potential was applied to the source side of the device while the receiving side (other side of NCAM) was grounded. The fluorescein dye was repelled away from the positive electrode and collected on the source side of the NCAM. The surface of the NCAM was positively charged corresponding to negative mobile counter-ions in the pores. This prevented fluorescein from simply passing through the pore for the initial voltage configuration. The dye collected near the NCAM after 40 min was 300 times the initial concentration of the fluorescein for both 1 μM or 0.1 μM initial concentrations, indicating that the concentration was independent of the repulsive forces between the fluorescein molecules (Zhang and Timperman 2003). When the bias was reversed, the pre-concentrated sample was transported through the NCAM to the receiving side. Pre-concentration has applications in biochemical studies where small amounts of biomolecules can be pre-concentrated before detection, allowing lower detection limits. Studies have used techniques based on pre-concentration in a T-shaped device for pre-concentration of DNA (Khandurina et al. 1999).

One interesting phenomenon that takes place at the micro-nanochannel interface is that of concentration polarization, with one end being enriched and the other depleted for a given species (Piruska et al. 2010a, b).

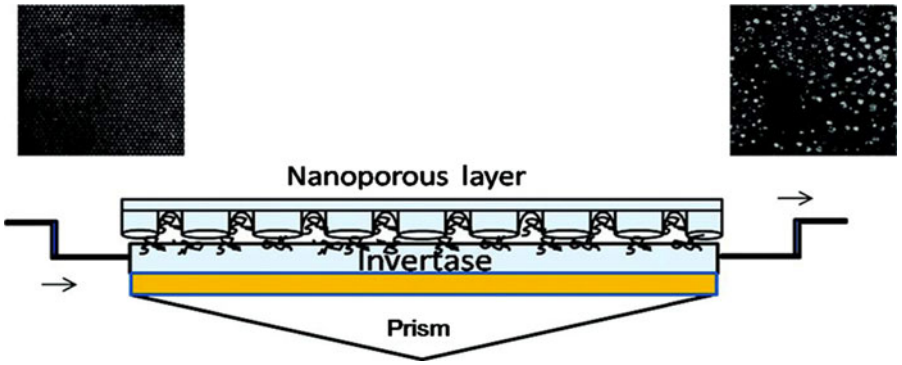

Fig. 6 Flow cell to monitor real-time production of glucose and fructose. Substrate (sucrose) is introduced convectively to nanoporous anodic alumina featuring immobilized invertase from left to right. Sucrose/invertase interaction is monitored by surface plasmon resonance (SPR) measurement. Reproduced with permission, (Dhathathreyan 2011). Copyright 2011 American Chemical Society

Gradients in ionic concentration cause added impedance to solute rejection, and the resulting concentration polarization serves as a limiting factor for water flux through reverse osmosis membranes. Bio-inspired systems are envisaged for energetically favorable pumping of hydrated ions through membranes by modulating pore potentials (Shannon et al. 2008). The phenomenon of concentration polarization, in combination with pressure-driven flow, has also been used to create ion and particle depletion zones around membranes to develop devices for water desalination (Kim et al. 2010). Similar strategies exploiting the space-charge region at the microfluidic-nanofluidic interface have shown concentration polarization factors in excess of 10^6 (Wang et al. 2005).

Improved enzyme reaction kinetics

With pore dimensions as small as several nanometers, the fluid transport properties of NCAMs differ considerably from those in microfluidic structures. In particular, lateral (radial) diffusion can efficiently deliver molecules from the center of the channel to the walls at the nanoscale and, thus, can effectively be combined with electrokinetically-driven axial flow. Applications employing nanochannel-immobilized enzymes are particularly attractive. With relatively short distances for substrates to traverse, it is expected that they will encounter surface-bound enzymes many times during transit through the nanochannel, thereby rendering enzyme kinetics within confined geometries superior to those in bulk solution (Dhathathreyan 2011). Figure 6 illustrates the immobilization of the enzyme, invertase, onto a nanoporous membrane for the conversion of sucrose into glucose and fructose. The flow cell device used in this study not only exhibits a higher rate of enzyme/substrate interaction than in bulk (Bowski et al. 1971), but also requires a lower substrate concentration for product detection. In another study, reaction–diffusion modeling was combined with measurements of enzymatic reaction velocities during injection-relaxation cycles across an NCAM to show that the enzymatic activity of immobilized horseradish peroxidase in NCAMs is up to 10^2 times higher than in free solution (Wang et al. 2009). Most notably, electrokinetic transport in NCAMs affords rapid convective delivery of substrates to active sites to improve turnover of mass transport limited enzymatic reactions. Thus, enzyme-functionalized NCAMs utilized within microfluidic devices, as described above, show great promise for in situ generation of biological reagents for downstream reactions.

Sensors

There is a growing interest in portable detection devices that can perform complete measurements including sample manipulation and detection in a matter of minutes using increasingly smaller sample volumes approaching the picoliter or smaller sample volumes, especially for point-of-use applications. Nanopores and nanofluidic devices allow for manipulation of such small sample volumes. Several sensors based on nanopores have been developed, for example one for hydrogen peroxide (Ali et al. 2011). Furthermore, a transducer can be integrated directly into a nanofluidic

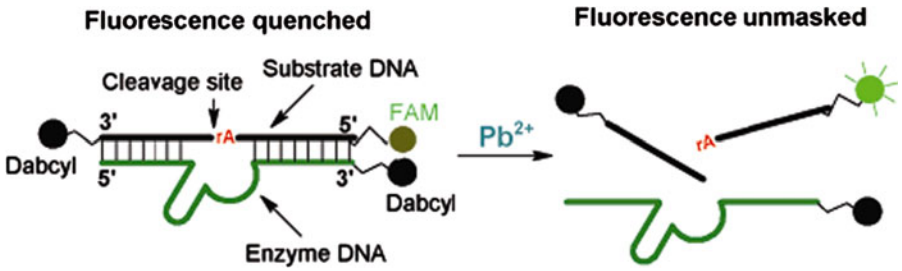

Fig. 7 Sensing using dehybridization reactions of DNAzyme immobilized inside NCAMs. FAM fluorescence from the substrate is initially suppressed by Dabcyl quencher on the enzyme. Cleavage of DNA in the presence of Pb^{2+} releases fluorescent product for subsequent detection. Reproduced with permission, (Chang et al. 2005). Copyright 2005 American Chemical Society

device, for the detection of either biomolecules such as proteins and nucleic acids or heavy metal contaminants in water (Prakash et al. 2012a, b). A further demonstration of the utility of carrying out molecular recognition reactions in nanopores utilizes the catalytic DNA molecular beacon introduced above. Catalytic DNA molecules, or DNAzymes, facilitate multiple turnover reactions (Lu and Liu 2006), but in this chemical sensing application the enzyme strand facilitates recognition of the analyte that occurs on the complementary substrate strand. Figure 7 illustrates the operating principle, in which Pb^{2+}-mediated cleavage of DNA leads to the release of the FAM conjugate. FAM fluorescence, originally quenched by Dabcyl, is enhanced by orders of magnitude upon dehybridization. Recognition reactions are most frequently implemented as homogeneous reactions, however it was discovered that immobilization of DNAzymes within NCAMs greatly enhanced sensitivity and lowered limits of detection—a promising strategy for biosensing applications (Adiga et al. 2009). In addition to the potential in vivo detectors, DNAzyme functionalized NCAMs have been incorporated into microfluidic devices for real-time detection of harmful toxins (Chang et al. 2005; Wernette et al. 2006).

Fluidic transistors and diodes

Nanofluidic channels and nanopores allow for ion transport manipulation that parallels electronic devices such as field effect transistors (FETs) (Nam et al. 2009) and diodes (Yan et al. 2009). The ability to control charge movement is due to the fact that the characteristic length of the channel is on the same order as the size of the EDL. An applied potential across the length of a channel drives an electroosmotic flow. A perpendicular electric field is created by controlling the surface charge through a third electrode on the channel wall. The magnitude of this electric field serves to increase, decrease or even reverse the EOF velocity (Karnik et al. 2005; Schasfoort et al. 1999; Kuo et al. 2003a, b). These devices are known as flow FETs. Such devices have been used for selective protein transport allowing for manipulation of biomolecules in picoliter size samples (Karnik et al. 2006). A nanofluidic channel that has a surface charge of equivalent magnitude but opposite polarity on the left and right halves of the channel can serve as a fluidic diode, allowing electrolyte to pass under forward bias but blocking flow during reverse bias as long as the double layers do not overlap (Daiguji et al. 2005; Vlassiouk and Siwy 2007). Recently, tunable transport characteristics and diode-behavior have been demonstrated in NCAMs through induced charge inversion (He et al. 2009) and electrostatic gating (Pardon and van der Wijngaart 2011).

Summary

Nanofluidic systems that combine NCAMs and microfluidic elements benefit from physical phenomena interacting on multiple length scales. NCAMs with microfluidics exploit the role of surface properties and geometric characteristics that govern physical phenomena, such as molecular diffusion and electrostatic forces, and electrokinetic effects arising from their coupling with physical device dimensions. While ongoing fundamental studies continue to refine the

state-of-art in understanding nanofluidic transport, our growing ability to create well-defined periodic nanometer scale capillary arrays, define their surface functionality, and address them in ways to separate diverse chemical environments and control fluidic communication between them have enabled experiments using NCAMs to mimic biological membrane processes. Advancements from the last decade have brought us a step closer to realizing systems capable of manipulating molecules one-by-one, thus affording processes of extraordinary power for chemical sensing, analysis, separation, and energy conversion.

Acknowledgments Mark Shannon and Vikhram Swaminathan acknowledge support through WaterCAMPWS, Center for Advanced Materials for the Purification of Water with Systems, a US National Science Foundation funded Science and Technology Center under contract CTS-0120978, and the US Defense Advanced Research Projects Agency under grant W911NF-09-C-0079. The portion of this study conducted at the University of Notre Dame was supported by the US National Science Foundation under grants DBI 0852741 and CBET 0120978, by the US Department of Energy Office of Basic Energy Sciences DE FG02 07ER15851, and by the US Army Corps of Engineers contract W9132-10-0010. Shaurya Prakash and Marie Pinti acknowledge partial support through the US Defense Advanced Research Projects Agency grant W911NF-09-C-0079.

References

Adiga SP, Jin CM, Curtiss LA, Monteiro-Riviere NA, Narayan RJ (2009) Nanoporous membranes for medical and biological applications. WIREs Nanomed Nanobiotechnol 1:568–581

Agerbaek M, Keiding K (1995) Streaming potential during cake filtration of slightly compressible particles. J Colloid Interface Sci 169:255–342

Ali M, Tahir MN, Siwy ZS, Neumann R, Tremel W, Ensinger W (2011) Hydrogen peroxide sensing with horseradish peroxidase-modified polymer single conical nanochannels. Anal Chem 83:1673–1680

Bohn PW (2009) Nanoscale control and manipulation of molecular transport in chemical analysis. Annu Rev Anal Chem 2:279–296

Boukany PE, Morss A, Liao W, Henslee B, Jung H, Zhang X, Yu B, Wang X, Wu Y, Li L, Gao K, Hu X, Zhao X, Hemminger O, Lu W, Lafyatis GP, Lee LJ (2011) Nanochannel electroporation delivers precise amounts of biomolecules into living cells. Nat Nanotechnol 6:747–754

Bowski L, Saini R, Ryu D, Vieth W (1971) Kinetic modeling of hydrolysis of sucrose by invertase. Biotechnol Bioeng 13:641–656

Burgmayer P, Murray RW (1982) An ion gate membrane: electrochemical control of ion permeability through a membrane with an embedded electrode. J Am Chem Soc 4:6139–6140

Burgreen D, Nakache F (1964) Electrokinetic flow in ultrafine capillary slits. J Phys Chem 68:1084–1091

Buyukserin F, Kohli P, Wirtz M, Martin C (2007) Electroactive nanotube membranes and redox-gating. Small 3:266–270

Cannon DM Jr, Kuo T-C, Bohn PW, Sweedler JV (2003) Nanocapillary array interconnects for gated analyte injections and electrophoretic separations in multilayer microfluidic architectures. Anal Chem 75:2224–2230

Cervera J, Patricio R, Manzanares JA, Mafe S (2010) Incorporating ionic size in the transport equations for charged nanopores. Microfluid Nanofluid 9:41–53

Chang I-H, Tulock JJ, Liu J, Cannon DM Jr, Bohn PW, Sweedler JV, Cropeck DM (2005) Miniaturized lead sensor based on lead-specific DNAzyme in a nanocapillary interconnected microfluidic device. Environ Sci Technol 39:3756–3761

Chatterjee AN, Cannon DM Jr, Gatimu EN, Sweedler JV, Aluru NR, Bohn PW (2005) Modeling and simulation of ionic currents in three-dimensional microfluidic devices with nanofluidic interconnects. J Nanopart Res 7:507–516

Chowdiah P, Wasan D, Gidaspow D (1983) On the interpretation of streaming potential data in nonaqueous media. Colloids Surf 7:291–299

Chun K-Y, Stroeve P (2002) Protein transport in nanoporous membranes modified with self-assembled monolayers of functionalized thiols. Langmuir 18:4653–4658

Chun K-Y, Mafe S, Ramirez P, Stroeve P (2006) Protein transport through gold-coated, charged nanopores: Effects of applied voltage. Chem Phys Lett 418:561–564

Conlisk AT (2005) The Debye-Huckel approximation: Its use in describing electroosmotic flow in micro- and nanochannels. Eletrophoresis 26:1896–1912

Conlisk AT (2012) Essentials of micro- and nanofluidics: with applications to the biological and chemical sciences. Cambridge University Press, Cambridge

Conlisk AT, McFerran J, Zheng Z, Hansford D (2002) Mass transfer and flow in electrically charged micro- and nanochannels. Anal Chem 74:2139–2150

Conlisk AT, Kumar A, Rampersaud A (2007) Ionic and biomolecular transport in nanochannels. Nanoscale Microscale Thermophys Eng 11:177–199

Contento NM, Branagan SP, Bohn PW (2011) Electrolysis in nanochannels for in situ reagent generation in confined geometries. Lab Chip 11:3634–3641

Daiguji H, Oka Y, Shirono K (2005) Nanofluidic diode and bipolar transistor. Nano Lett 5:2274–2280

Datta S, Conlisk AT, Kanani DM, Zydney AL, Fissell WH, Roy S (2010) Characterizing the surface charge of synthetic nanomembranes by the streaming potential method. J Colloid Interface Sci 348:85–95

Dhathathreyan A (2011) Real-time monitoring of invertase activity immobilized in nanoporous aluminum oxide. J Phys Chem B 115:6678–6682

Fa K, Tulock JJ, Sweedler JV, Bohn PW (2005) Profiling pH gradients across nanocapillary array membranes connecting microfluidic channels. J Am Chem Soc 127:13928–13933

Fievet P, Szymczyk A, Aoubiza B, Pagetti J (2000) Evaluation of three methods for the characterisation of the membrane-solution interface: streaming potential, membrane potential and electrolyte conductivity inside pores. J Membr Sci 168:87–100

Flachsbart BR, Wong K, Iannacone JM, Abante EN, Vlach RI, Rauchfuss PA, Bohn PW, Sweedler JV, Shannon MA (2006) Design and fabrication of a multilayered polymer microfluidic chip with nanofluidic interconnects via adhesive contact printing. Lab Chip 6:667–674

Gong M, Flachsbart BR, Shannon MA, Bohn PW, Sweedler JV (2008a) Fluidic communication between multiple vertically segregated microfluidic channels connected by nanocapillary array membranes. Electrophoresis 29:1237–1244

Gong M, Kim BY, Flachsbart BR, Shannon MA, Bohn PW, Sweedler JV (2008b) An on-chip fluorogenic enzyme assay using a multilayer microchip interconnected with a nanocapillary array membrane. IEEE Sens J 8:601–607

Han J, Fu J, Schoch RB (2008) Molecular sieving using nanofilters: past, present and future. Lab Chip 8:23–33

He Y, Gillespie D, Boda D, Vlassiouk I, Eisenberg RS, Siwy ZS (2009) Tuning transport properties of nanofluidic devices with local charge inversion. J Am Chem Soc 131:5194–5202

Huang S, Yin Y (2006) Transport and separation of small organic molecules through nanotubules. Anal Sci 22:1005–1009

Huisman IH, Pradanos P, Calvo JI, Hernandez A (2000) Electroviscous effects, streaming potential, and zeta potential in polycarbonate track-etched membranes. J Membr Sci 178: 79–92

Hulteen JC, Jirage KB, Martin CR (1998) Introducing chemical transport selectivity into gold nanotubule membranes. J Am Chem Soc 120:6603–6604

Jagerszki G, Gyurcsanyi R, Hofler L, Pretsch E (2007) Hybridization-modulated ion fluxes through peptide-nucleic-acid-functionalized gold nanotubes. A new approach to quantitative label-free DNA analysis. Nano Lett 7:1609–1612

Jirage KB, Hulteen JC, Martin CR (1999) Effect of thiol chemisorption on the transport properties of gold nanotubule membranes. Anal Chem 71:4913–4918

Karnik R, Fan R, Yue M, Li D, Yang P, Majumdar A (2005) Electrostatic control of ions and molecules in nanofluidic transistors. Nano Lett 5:943–948

Karnik R, Castelino K, Majumdar A (2006) Field-effect control of protein transport in a nanofluidic transistor circuit. Appl Phys Lett 88:123114

Kemery PJ, Steehler JK, Bohn PW (1998) Electric field mediated transport in nanometer diameter channels. Langmuir 14:2884–2889

Khandurina J, Jacobson SC, Waters LC, Foote RS, Ramsey JM (1999) Microfabricated porous membrane structure for sample concentration and electrophoretic analysis. Anal Chem 71:1815–1819

Kim BY, Swearingen CB, Ho JA, Romanova EV, Bohn PW, Sweedler JV (2007) Direct immobilization of Fab' in nanocapillaries for manipulating mass-limited samples. J Am Chem Soc 129:7620–7626

Kim BY, Yang J, Gong M, Flachsbart BR, Shannon MA, Bohn PW, Sweedler JV (2009) Multidimensional separation of chiral amino acid mixtures in a multilayered three-dimensional hybrid microfluidic/nanofluidic device. Anal Chem 81:2715–2722

Kim S, Ko S, Kang K, Han J (2010) Direct seawater desalination by ion concentration polarization. Nat Nanotechnol 5: 297–301

Kohli P, Harrell CC, Cao Z, Gasparac R, Tan W, Martin CR (2004) DNA-functionalized nanotube membranes with single-base mismatch selectivity. Science 305:984–986

Ku J-R, Lai S-M, Ileri N, Ramirez P, Mafe S, Stroeve P (2007) pH and ionic strength effects on amino acid transport through Au-nanotubule membranes charged with self-assembled monolayers. J Phys Chem C 111:2965–2973

Kuo T-C, Sloan LA, Sweedler JV, Bohn PW (2001) Manipulating molecular transport through nanoporous membranes by control of electrokinetic flow- effect of surface charge density and Debye length. Langmuir 17:6298–6303

Kuo T-C, Cannon DM Jr, Chen Y, Tulock JJ, Shannon MA, Sweedler JV, Bohn PW (2003a) Gateable nanofluidic interconnects for multilayered microfluidic separation systems. Anal Chem 75:1861–1867

Kuo T-C, Cannon DM Jr, Shannon MA, Bohn PW, Sweedler JV (2003b) Hybrid three-dimensional nanofluidic/microfluidic devices using molecular gates. Sens Actuators, A 102: 223–233

Kuo T-C, Kim H-K, Cannon DM Jr, Shannon MA, Sweedler JV, Bohn PW (2004) Nanocapillary arrays effect mixing and reaction in multilayer fluidic structures. Angew Chem 116:1898–1901

Lee SB, Martin CR (2002) Electromodulated molecular transport in gold-nanotube membranes. J Am Chem Soc 124: 11850–11851

Lokuge I, Wang X, Bohn PW (2007) Temperature-controlled flow switching in nanocapillary array membranes mediated by poly(*N*-isopropylacrylamide) polymer brushes grafted by atom transfer radical polymerization. Langmuir 23: 305–311

Lu Y, Liu J (2006) Functional DNA nanotechnology: emerging applications of DNAzymes and aptamers. Curr Opin Biotechnol 17:580–588

Martin CR, Nishizawa M, Jirage K, Kang MS, Lee SB (2001a) Controlling ion-transport selectivity in gold nanotubule membranes. Adv Mater 13:1351–1362

Martin CR, Nishizawa M, Jirage K, Kang M (2001b) Investigations of the transport properties of gold nanotubule membranes. J Phys Chem B 105:1925–1934

Mulero R, Prabhu AS, Freedman KJ, Kim MJ (2010) Nanopore-based devices for bioanalytical applications. JALA 15: 243–252

Nam S-W, Rooks MJ, Kim K-B, Rossnagel SM (2009) Ionic field effect transistors with sub-10 nm multiple nanopores. Nano Lett 9:2044–2048

Napoli M, Eijkel J, Pennathur S (2010) Nanofluidic technology for biomolecule applications: a critical review. Lab Chip 10:957–985

Nishizawa M, Menon VP, Martin CR (1995) Metal nanotubule membranes with electrochemically switchable ion-transport selectivity. Science 268:700–702

Nystrom M, Lindstrom M, Matthiasson E (1989) Streaming potential as a tool in the characterization of ultrafiltration membranes. Colloids Surf 36:297–312

Oukhaled A, Cressiot B, Bacri L, Pastoriza-Gallego M, Betton J-M, Bourhis E, Jede R, Gierak J, Auvray L, Pelta J (2011) Dynamics of completely unfolded and native proteins

through solid-state nanopores as a function of electric driving force. ACS Nano 5:3628–3638

Pardon G, van der Wijngaart W (2011) Electrostatic gating of ion and molecule transport through a nanochannel-array membrane. Proc IEEE Solid-State Sens Actuators Microsyst Conf (Transducers) Beijing, China, pp 1610-1613

Perera DNT, Ito T (2010) Cyclic voltammetry on recessed nanodisk-array electrodes prepared from track-etched polycarbonate membranes with 10-nm diameter pores. Analyst 135:172–176

Piruska A, Branagan SP, Cropek DM, Sweedler JV, Bohn PW (2008) Electrokinetically driven fluidic transport in integrated three-dimensional microfluidic devices incorporating gold-coated nanocapillary array membranes. Lab Chip 8:1625–1631

Piruska A, Branagan SP, Minnis AB, Wang Z, Cropeck DM, Sweedler JV, Bohn PW (2010a) Electrokinetic control of fluid transport in gold-coated nanocapillary array membranes in hybrid nanofluidic-microfluidic devices. Lab Chip 10:1237–1244

Piruska A, Gong M, Sweedler JV, Bohn PW (2010b) Nanofluidics in chemical analysis. Chem Soc Rev 39:1060–1072

Plecis A, Schoch RB, Renaud P (2005) Ionic transport phenomena in nanofluidics: experimental and theoretical study of the exclusion-enrichment effect on a chip. Nano Lett 5:1147–1155

Powell MR, Cleary L, Davenport M, Shea KJ, Siwy ZS (2011) Electric-field-induced wetting and dewetting in single hydrophobic nanopores. Nat Nanotechnol 6:798–802

Prakash S, Yeom J, Jin N, Adesida I, Shannon MA (2007) Characterization of ionic transport at the nanoscale. Proc ASME IMECE, N: J Nanoeng Nanosyst 220:45–52

Prakash S, Piruska A, Gatimu EN, Bohn PW, Sweedler JV, Shannon MA (2008) Nanofluidics: Systems and Applications. IEEE Sens J 8:441–450

Prakash S, Karacor M, Benerjee S (2009) Surface modification in microsystems and nanosystems. Surf Sci Rep 64: 233–254

Prakash S, Pinti M, Bellman K (2012a) Variable cross-section nanopores fabricated in silicon nitride membranes using a transmission electron microscope. J Micromech Microeng in press

Prakash S, Pinti M, Bhushan B (2012b) Theory, fabrication and applications of microfluidic and nanofluidic biosensors. Philos Trans R Soc London, Ser A 370:2269–2303

Qiao R, Aluru N (2003) Ion concentration and velocity in nanochannel electroosmotic flows. J Chem Phys 118: 4692–4701

Qiao R, Aluru N (2004) Charge inversion and flow reversal in a nanochannel electroosmotic flow. Phys Rev Lett 92: 198301

Qiao R, Georgiadis J, Aluru N (2006) Differential ion transport induced electroosmosis and internal recirculation in heterogeneous osmosis membranes. Nano Lett 6:995–999

Renkin E (1954) Filtration, diffusion, and molecular sieving through porous cellulose membranes. J Gen Physiol 38: 225–243

Rice C, Whitehead R (1965) Electrokinetic flow in a narrow cylindrical capillary. J Phys Chem 69:4017–4024

Sadr R, Yoda M, Gnanaprakasam P, Conlisk AT (2006) Velocity measurements inside the diffuse electric double layer in electro-osmotic flow. Appl Phys Lett 89:044103

Schasfoort RB, Schlautmann S, Hendrikse J, van den Berg A (1999) Field-effect flow control for microfabricated fluidic networks. Science 286:942–944

Schibel AE, Heider EC, Harris JM, White HS (2011) Fluorescence microscopy of the pressure-dependent structure of lipid bilayers suspended across conical nanopores. J Am Chem Soc 133:7810–7815

Schoch RB, Han J, Renaud P (2008) Transport phenomena in nanofluidics. Rev Mod Phys 80:839–883

Shannon MA, Flachsbart BR, Iannacone JM, Wong K, Cannon Jr DM, Fa K, Sweedler JV, Bohn PW (2005) Nanofluidic interconnects within a multilayer microfluidic chip for attomolar biochemical analysis and molecular manipulation. Proc 3rd Ann IEEE Int EMBS Special Topic Conf Microtechnol Medicine Biology Kahuhu, pp 257-259

Shannon MA, Bohn PW, Elimelech M, Georgiadis JG, Marinas BJ (2008) Science and technology for water purification in the coming decades. Nature 452:301–310

Sparreboom W, van den Berg A, Eijkel J (2009) Principles and applications of nanofluidic transport. Nat Nanotechnol 4: 713–720

Sparreboom W, van den Berg A, Eijkel J (2010) Transport in nanofluidic systems: a review of theory and applications. New J Phys 12:015004

Szymczyk A, Aoubiza B, Fievet P, Pagetti J (1999) Electrokinetic phenomena in homogeneous cylindrical pores. J Colloid Interface Sci 216:285–296

Talaga DS, Li J (2009) Single-Molecule Protein Unfolding in Solid State Nanopores. J Am Chem Soc 131:9287–9297

Tulock JJ, Shannon MA, Bohn PW, Sweedler JV (2004) Microfluidic Separation and Gateable Fraction Collection for Mass-Limited Samples. Anal Chem 76:6419–6425

Vitarelli M, Prakash S, Talaga D (2011) Determining nanocapillary geometry from electrochemical impedance spectroscopy using a variable topology network circuit model. Anal Chem 83:533–541

Vlassiouk I, Siwy ZS (2007) Nanofluidic diode. Nano Lett 7: 552–556

Wang Y-C, Stevens A, Han J (2005) Million-fold preconcentration of proteins and peptides by nanofluidic filter. Anal Chem 77:4293–4299

Wang Z, King TL, Branagan SP, Bohn PW (2009) Enzymatic activity of surface-immobilized horseradish peroxidase confined to micrometer- to nanometer-scale structures in nanocapillary array membranes. Analyst 134:851–859

Wernette DP, Swearingen CB, Cropek DM, Lu Y, Sweedler JV, Bohn PW (2006) Incorporation of a DNAzyme into Au-coated nanocapillary array membranes with an internal standard for Pb(II) sensing. Analyst 131:41–47

Yan R, Liang W, Fan R, Yang P (2009) Nanofluidic diodes based on nanotube heterojunctions. Nano Lett 9:3820–3825

Zhang Y, Timperman AT (2003) Integration of nanocapillary arrays into microfluidic devices for use as analyte concentrators. Analyst 128:537–542

DOI 10.1007/978-3-319-05041-6_3
Reprinted from the *Journal of Nanoparticle Research*, DOI 10.1007/s11051-012-0884-7

RESEARCH PAPER

Nanofiltration membranes based on polyvinylidene fluoride nanofibrous scaffolds and crosslinked polyethyleneimine networks

Seong-Jik Park · Ravi Kumar Cheedrala · Mamadou S. Diallo · Changmin Kim · In S. Kim · William A. Goddard III

Received: 1 February 2012 / Accepted: 20 April 2012 / Published online: 28 June 2012

Abstract In this article, we describe the synthesis of new and ion-selective nanofiltration (NF) membranes using polyvinylidene fluoride (PVDF) nanofibers and hyperbranched polyethylenimine (PEI) as building blocks. These new nanofibrous composite (NFC) membranes consist of crosslinked hyperbranched PEI networks supported by PVDF nanofibrous scaffolds that are electrospun onto commercial PVDF microfiltration (MF) membranes. A major objective of our study was to fabricate positively charged NF membranes that can be operated at low pressure with high water flux and improved rejection for monovalent cations. To achieve this, we investigated the effects of crosslinker chemistry on membrane properties (morphology, composition, hydrophobicity, and zeta potential) and membrane performance (salt rejection and permeate flux) in aqueous solutions (2,000 mg/L) of four salts (NaCl, $MgCl_2$, Na_2SO_4, and $MgSO_4$) at pH 4, 6, and 8. We found that an NFC–PVDF membrane with a network of PEI macromolecules crosslinked with trimesoyl chloride has a high water flux (~ 30 L m^{-2} h^{-1}) and high rejections for $MgCl_2$ (~ 88 %) and NaCl (~ 65 %) at pH 6 using a pressure of 7 bar. The overall results of our study suggest that PVDF nanofibers and hyperbranched PEI are promising building blocks for the fabrication of high performance NF membranes for water purification.

Special Issue Editors: Mamadou Diallo, Neil Fromer, Myung S. Jhon

This article is part of the Topical Collection on Nanotechnology for Sustainable Development

S.-J. Park · R. K. Cheedrala · M. S. Diallo (✉) · W. A. Goddard III
Graduate School of Energy, Environment, Water and Sustainability (EEWS), Korea Advanced Institute of Science and Technology (KAIST), Daejeon, Republic of Korea
e-mail: mdiallo@kaist.ac.kr; diallo@wag.caltech.edu

Present Address:
S.-J. Park
Department of Bioresources and Rural Systems Engineering, Hankyong National University, Anseong, Greonggi-do 456-749, Republic of Korea

M. S. Diallo
Environmental Science and Engineering, Division of Engineering and Applied Science, California Institute of Technology, Pasadena, CA, USA

C. Kim · I. S. Kim
Department of Environmental Science and Engineering, Gwangju Institute of Science and Technology (GIST), Gwangju, Korea

W. A. Goddard III
Materials and Process Simulation Center, Division of Chemistry and Chemical Engineering, California Institute of Technology, Pasadena, CA, USA

Keywords Nanofibers · Polyethylenimine · Polyvinylidene fluoride · Hyperbranched · Polymer networks · Membranes · Nanofiltration · Water purification · Nanotechnology sustainable development

Introduction

The availability of clean water has emerged as one of the most critical problems facing society and the global economy in the twenty-first century. Many regions of the world are already experiencing higher demands for clean water while freshwater supplies are being stressed (Service 2006; Shannon et al. 2008). According to the World Resources Institute, 40 % of the world's population lives in water-stressed areas. The United Nations Environment Program (UNEP) predicts that freshwater will be scarcer in many regions of the world by 2030 (UNEP 2006). The problem will get much worse unless we develop more efficient, cost-effective and environmentally sound technologies to extract clean water from impaired water including wastewater, brackish water, and seawater (Shannon et al. 2008; Diallo and Brinker 2011). Pressure-driven membrane processes such as reverse osmosis (RO), nanofiltration (NF), ultrafiltration (UF), and microfiltration (MF) have become the key components of advanced water reuse and desalination systems throughout the world. RO is considered as the best commercially available desalination technology (Shannon et al. 2008; Elimelech and Philipp 2011). In RO, a high pressure is applied to force saline water through a semi-permeable membrane that retains salts (e.g., dissolved ions) while allowing the pure water to pass through the membrane. Due to its lower pressure requirements, NF is increasingly being used as alternative to RO in water softening and water reclamation (Schäefer et al. 2005). Today, the vast majority of commercial NF membranes are thin film composite (TFC) membranes with three components (Schäefer et al. 2005): (1) a nonwoven polymeric support [polyethylene terephthalate], (2) a microporous polymeric support [polysulfone], and (3) a thin separation layer consisting of crosslinked polyamide (PA). Commercial TFC-PA NF membranes have small pores (0.5–1.5 nm) and are negatively charged (Schäefer et al. 2005). Because of this, their mechanisms of ion rejection include (i) size exclusion, (ii) Donnan exclusion, and (iii) dielectric exclusion (Vezzani and Bandini 2002; Escoda et al. 2010; Déon et al. 2011). Although TFC-PA NF membranes are effective in most cases at retaining (>95 %) divalent anions (e.g., SO_4^{2-} and PO_4^{3-}), they have limited retention capability for monovalent anions (e.g., Cl^-) and cations (e.g., Na^+) (Schäefer et al. 2005). Thus, there is great need for novel, low pressure and robust NF membranes with enhanced rejection capability for monovalent cations/anions.

Recent advances in nanotechnology such as the fabrication of polymeric nanofibers (PNFs) by electrospinning (ES) are providing unprecedented opportunities to develop a new generation of high performance filtration media and membranes for water purification (Ramakrishina et al. 2005; Yoon et al. 2008). During the last decade, ES has emerged as a versatile technique for synthesizing a broad range of nanofibers including PNFs, inorganic nanofibers, and hybrid polymeric–inorganic nanofibers (Ramakrishina et al. 2005). With ES, polymeric fibers with diameters ranging from 10–100 nm to 1–10 μm can be produced. Electrospun PNFs have several unique characteristics such as large surface area to unit volume, large porosity (up to over 80 %), and versatile chemistry. Several investigators have begun exploiting these unique properties of electrospun PNFs to develop novel MF, UF, and NF membranes for water purification. Gopal et al. (2006) have reported the synthesis of electrospun nanofibrous membranes using polyvinylidene fluoride (PVDF) and polysulfone as base polymers. They showed that these new MF membranes could reject more than 90 % of polystyrene (PS) microparticles (5, 7, 8, and 10 μm in diameter) in solution with high water flux and no significant fouling using a transmembrane pressure of ~0.5 bar. Wang et al. (2005) have reported the fabrication of a new UF membrane consisting of a thin layer of crosslinked poly(vinyl alcohol) nanofibers that were electrospun onto an electrospun polyacrylonitrile (PAN) nanofibrous substrate. Their filtration experiments showed that the new thin film nanofibrous composite (TFNC) UF membrane could separate a model soybean oil–water emulsion with high rejection (99.5 %) and high water flux (210 L m^{-2} h^{-1}) using a pressure of 3 bar. Yoon et al. (2009) have fabricated a new TFNC NF membrane consisting of an electrospun PAN nanofibrous support with a PA layer that was

synthesized by interfacial polymerization of piperazine and bipiperidine. They evaluated the performance of the new membrane using cross-flow filtration of aqueous solutions of $MgSO_4$ (2,000 mg/L) at a pressure of 4.8 bar. Yoon et al. (2009) reported that the $MgSO_4$ rejection (~98 %) of their new TFNFC membrane was comparable to that of the commercial NF270 TFC NF membrane from DOW-FILMTEC™. However, its permeate flux was 38 % higher than that of the NF270 membrane.

Despite these promising results, a great deal of fundamental research remains to be done to advance the basic science and engineering knowledge needed to fabricate viable NF membranes using electrospun PNFs as building blocks (Yoon et al. 2008). A key challenge includes the identification and selection of PNFs with the robust chemical, thermal and mechanical properties and the versatile chemistry required to fabricate high performance NF membranes for water treatment, reuse, and desalination. In this article, we describe the preparation of novel nanofibrous composite (NFC) membranes using PVDF and hyperbranched polyethylenimine (PEI) as building blocks. These new NFC–PVDF–PEI membranes consist of crosslinked hyperbranched PEI networks supported by PVDF nanofibrous scaffolds that are electrospun onto commercial PVDF MF membrane supports (Fig. 1). A key driver of our study was to fabricate positively charged NF membranes with high water flux and improved rejection for monovalent cations. Such membranes are needed to expand the applicability of NF to the treatment/reclamation of acid mine drainage and industrial wastewater contaminated by toxic metal ions (e.g., Cu^{2+}, Zn^{2+}, and Pb^{2+}) and cationic organic compounds (e.g., dye and biopharmaceuticals) (Cheng et al. 2011; Ji et al. 2011; Sun et al. 2011; Ba et al. 2009). In our efforts to develop low pressure, ion selective and positively charged NFC membranes, we investigated the effects of crosslinker chemistry on membrane properties (morphology, composition, hydrophobicity, and zeta potential) and membrane performance (salt rejection and permeate flux). Three crosslinkers were evaluated including trimesoyl chloride (TMC), 1,3-dibromo propane (DBP), and epichlorohydrin (ECH). Four salts (NaCl, $MgCl_2$, Na_2SO_4, and $MgSO_4$) were tested. The overall results of our study suggest that PVDF nanofibers and hyperbranched PEI are promising building blocks for the fabrication of high performance NF membranes for water purification.

Experimental methods and procedures

Materials

PVDF MF membrane supports (0.45 μm pore size) were purchased from Millipore (USA). PVDF powder (Kynar 761) was provided by Arkema (USA). Hyperbranched PEI [M_w: 25,000 and M_n: 10,000] was provided by BASF (Germany). Dimethylformamide (DMF), *n*-methyl-2-pyrrolidone (NMP), TMC, 1,3-DBP, and ECH were purchased from Sigma-Aldrich. Analytical grade NaCl, $MgCl_2$, Na_2SO_4, and $MgSO_4$ were purchased from Samchon Chemicals (Korea). All chemicals were used as received. Deionized (DI) water (18.2 MΩ cm resistivity) was used to rinse the membranes and prepare the salt solutions.

Nanofiber and membrane synthesis

We utilized blends of PVDF + PEI to spin the nanofibrous scaffolds of the NFC–PVDF–PEI membranes. A typical polymer blend was prepared by dissolving PVDF (18.5 wt%) and PEI (2.5 wt%) in a mixture of DMF and NMP (1:1 w/w). The mixture was sonicated for 4 h to obtain a homogeneous PVDF/PEI solution. A NANON-01A ES machine (MECC, Japan) was employed to spin the PVDF nanofibrous scaffold of each membrane. The PVDF MF support was first mounted on the NANON-01A drum collector. Following this, the PVDF/PEI blend was electrospun onto the PVDF membrane support using a solution flow rate of 0.7 mL/h and a voltage of 29 kV. During the ES process, the distance between the needle and the collector drum was kept constant at 7.5 cm. The speed of the collector was also kept constant 500 rpm. After the completion of the ES process, 1.0 mL of a solution of hyperbranched PEI in methanol (50 wt%) was electrosprayed onto the electrospun nanofibrous PVDF membranes using a solution flow rate 0.3 mL/h, a voltage of 29 kV, a needle to collector distance of 7.5 cm, and a collector speed of 2,500 rpm. Table 1 shows the process parameters used to (i) spin the PVDF nanofibers and (ii) spray them with PEI. Following electrospraying, the PEI-coated PVDF nanofibrous scaffolds were reacted with the crosslinkers to generate three different types of membranes (Fig. 1). To synthesize the NFC–PVDF–PEI-1 membranes, the PEI-coated nanofibrous scaffolds were reacted with a solution of TMC

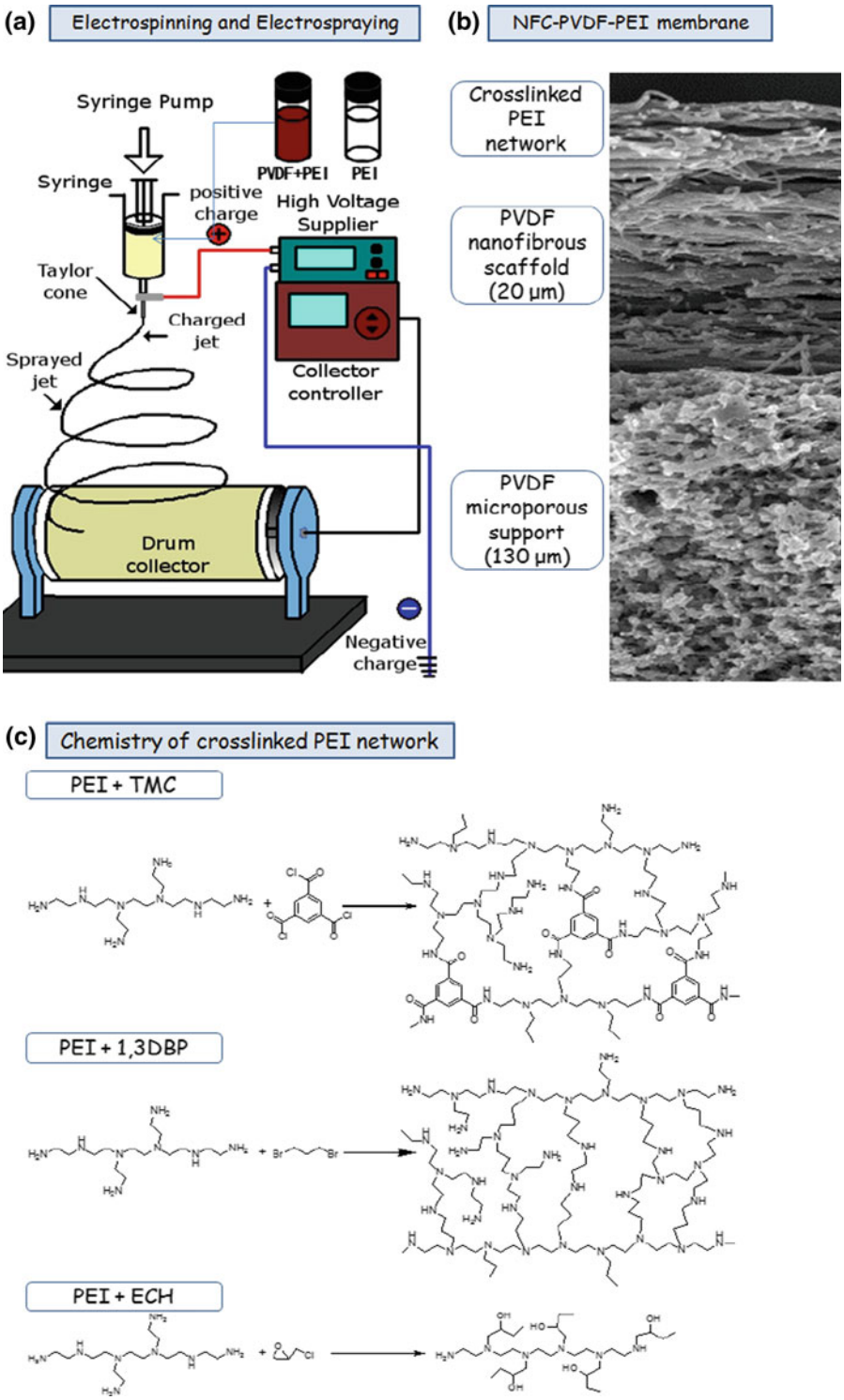

Fig. 1 Schematic diagram of the fabrication of nanofibrous composite (NFC–PVDF–PEI) membranes with PVDF microporous support, PVDF nanofibrous scaffolds, and crosslinked PEI networks

in toluene (1 % w/v) in a glass vessel at room temperature for 5 min (Fig. 1). Similarly, the NFC–PVDF–PEI-2 and NFC–PVDF–PEI-3 membranes were synthesized by reacting the PEI-coated PVDF nanofibrous scaffolds, respectively, with 20 wt% solutions of 1,3-DBP and ECH in toluene for 1 h at

Table 1 List of electrospinning and electrospraying process parameters

Process parameters	Electrospinning	Electrospraying
Concentration of polymer solution	18.5 % (w/w) PVDF and 2.5 % (w/w) PEI in a mixture (5:5 w/w) of DMF and NMP	Hyperbranched PEI (50 % w/w) in methanol
Amount of polymer solution (mL)	6	1
Solution flow rate (mL/h)	0.7	0.3
Applied voltage (kV)	29	29
Needle diameter (mm)	0.394	0.394
Needle collector distance (cm)	7.5	7.5
Drum collector speed (rpm)	500	2,500

45 °C. Following this, the membranes were rinsed three times with DI water and stored in DI water at room temperature.

Nanofiber and membrane characterization

The morphology, chemical composition, hydrophobicity, and zeta potential of the PVDF nanofibers and NFC–PVDF–PEI membranes were characterized using various analytical tools. The cross-sectional and surface morphologies of the nanofibers and membranes were imaged using a field emission scanning electron microscope (FESEM, FEI, SIRION-100, USA). Before imaging, all samples were coated with gold at 30 mA for 120 s to minimize the charging effect. To obtain the FESEM images, the membranes were frozen and fractured following immersion in liquid nitrogen. The SEM images were subsequently analyzed to estimate the thickness of the membrane surface layers using the ImageJ software (Abramoff et al. 2004). The compositions of the surface layers of the NFC–PVDF–PEI membranes were characterized by attenuated total reflectance-Fourier transform infrared spectroscopy (ATR-FTIR) using a JASCO 4100 FT-IR spectrometer (Japan). All samples were scanned from 500 to 4000 cm^{-1} with a scanning speed of 2 mm/s using a zinc selenide ATR crystal plate with an aperture angle of 45°. The hydrophobicity of each NFC–PVDF–PEI membrane was determined from contact angle measurements using a Phoenix 300 contact angle analyzer (SEO cooperation, Korea). A microsyringe was utilized to place a water droplet on the surface of each membrane. After 30 s, the image was captured and analyzed using the instrument's image processing software. Each reported contact angle is the average of 10 different measurements. The zeta potentials of the membranes were determined using the electrophoresis method (Shim et al. 2002). This involves measuring the electrophoretic mobility of monitoring particles inside an electrophoresis chamber consisting of a membrane and quartz cells (Shim et al. 2002). Due to the sorption and accumulation of ions at the surface of the membranes, an electro-osmotic flow occurs inside the electrophoresis chamber. This induced electro-osmotic flow causes the particles to undergo electrophoretic flow (Shim et al. 2002). An ELS-8000 electrophoretic light scattering spectrophotometer with a plate quartz cell (Otsuka Electronics, Japan) was employed to measure the electrophoretic mobility of the monitoring particles in 0.01 M KCl solutions as a function of pH. The monitoring particles consisted of PS latex particles (Otsuka Electronics, Japan) with a hydroxy propyl cellulose surface coating and diameter of 520 nm. The PS particles were dispersed in 0.01 N KCl solutions. The pH of the KCl solutions was adjusted with 0.1 N HCl or KOH as needed. The measured electrophoretic mobilities (U) [cm^2/(V s)] were employed to calculate the zeta potentials (ζ_{EP}) (mV) of the membranes using the Smoluchowski equation as given below (Shim et al. 2002):

$$\zeta_{EP} = 4\pi\eta U/\varepsilon_r\varepsilon_0 \quad (1)$$

where η is the liquid viscosity (0.89×10^{-3} Pa s), ε_r is the relative permittivity of liquid (78.38), and ε_0 is the vacuum permittivity (8.854×10^{-12} s m^{-1}).

Filtration experiments

A costume-built cross-flow filtration system with an effective membrane area of 24 cm^2 was employed to measure the salt rejection and permeate flux of each NFC–PVDF–PEI membrane. During each filtration

experiment, we used a feed solution of 10 L with a salt concentration of 2,000 mg/L. The pH of the feed solution was adjusted with a solution of 0.1 N HCl or 0.1 N NaOH as needed. All filtration experiments were carried out at room temperature and at a constant pressure of 7.0 bar. The salt rejection (R) of each membrane was assayed by electric conductivity measurements. R was expressed as:

$$R = \left(1 - C_p/C_f\right) \times 100 \quad (2)$$

where C_f and C_p are, respectively, the conductivity of the feed and permeate solutions. The permeate flux [J] (L m^{-2} h^{-1}) at time t through each membrane was expressed as:

$$J = V_p/(A \times \Delta t) \quad (3)$$

where V_p is the volume of permeate (L) collected during the sampling time Δt (h) and A is the effective membrane (m^2).

Results and discussion

Nanofiber synthesis and characterization

Hyperbranched PEI and PVDF were utilized, respectively, as building blocks for the ion-selective networks, nanofiborous scaffolds, and microporous supports of our new NFC membranes (Fig. 1). Due its high density of reactive amine groups and ready availability from commercial sources (Frechet et al. 2010; Diallo and Yu 2011), hyperbranched PEI is a versatile building block for preparing ion-selective thin films and networks. Recent studies have shown that hyperbranched PEI can be used to synthesize NF membranes with positively charged separation layers (Ba et al. 2009; Chiang et al. 2009; Sun et al. 2011). The selection of PVDF as base polymer to fabricate the nanofibrous scaffolds and microporous supports of the NFC membranes was motivated by two key considerations. First, PVDF is widely used as base polymer in the fabrication of commercial UF/MF membrane because of its high thermal/chemical resistance and tensile strength (Oh et al. 2009; Choi et al. 2011). Second, PVDF is soluble in a broad range of solvents including DMF, NMP, and dimethyl acetamide (DMAc) (Gopal et al. 2006; Choi et al. 2011). This provides many degrees of freedom for optimizing the properties of the microporous supports and nanofibrous scaffolds of our new NFC membranes (Fig. 1) by selecting the appropriate synthesis conditions. However, proteins and other hydrophobic macromolecular assemblies present in water/wastewater can easily foul PVDF membranes due to their hydrophobicity. Compared to membrane surface treatment methods such as chemical oxidation, plasma treatment and polymer grafting (Strathmann 2011), blending hydrophobic polymers such as PVDF with more hydrophilic polymers is versatile and easy to implement method for decreasing the hydrophobicity of polymeric membranes (Mansouri et al. 2010). Because hyperbranched PEI and PVDF are both soluble in DMF and NMP, we utilized blends of PVDF (18.5 wt%) and PEI (2.5 wt%) to synthesize the nanofibrous scaffolds of the NFC–PVDF–PEI membranes (Fig. 1). The blends were prepared by dissolving the required amounts of PVDF and PEI in mixtures of DMF and NMP (1:1 w/w). Consistent with literature data (Ramakrishina et al. 2005), we found that the average diameter (155.8 ± 44.4 nm) of PVDF nanofibers electrospun using mixtures DMF/NMP (1:1 w/w) was larger than that of the corresponding PVDF

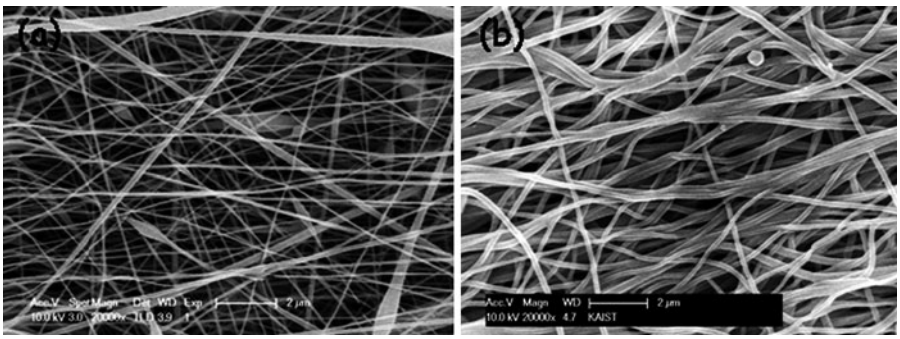

Fig. 2 Electrospun nanofiber from polymer solution dissolved in **a** DMF solvent and **b** NMP/DMF mixed solvent

nanofibers (81.4 ± 21.4 nm) that were prepared using pure DMF (Fig. 2).

The utilization of mixtures of as ES solvents provides several advantages (Ramakrishina et al. 2005; Yung et al. 2010). First, this can eliminate the formation of beaded nanofibers (Ramakrishina et al. 2005). Beads are defects that are formed during the ES of PNFs when low viscosity solvents are utilized to dissolve the base polymers (Ramakrishina et al. 2005). In NFC membranes, beaded nanofibers decrease the membrane porosity and interrupt the flow of water through the membrane nanofibrous scaffolds (Ramakrishina et al. 2005). Note that the viscosity of NMP (1.7 cps) is larger than that of DMF (0.9 cps). Consistent with the observations of Ramakrishina et al. (2005), we have found the use of pure DMF as spinning solvent resulted in the formation of beaded PVDF nanofibers (Fig. 2a). In contrast, no beaded nanofibers were observed when mixtures of DMF and NMP (1:1 w/w) were utilized as spinning solvents (Fig. 2b). Second, the use of mixtures as spinning solvents can also increase both the adhesion/tensile strength of PNFs as well as the strength of their adhesion to nonwoven microporous supports. Yung et al. (2010) have investigated the adhesion/tensile strength of PNFs and their delamination from nonwowen microporous polymeric supports. They reported that the adhesion between poly(ethersulfone) (PES) nanofibrous layers and a nonwoven poly(ethylene terephthalate) (PET) microporous support was stronger when the base PES polymer was dissolved in mixtures of DMF and NMP (6:4 w/w). We have also found that the use of mixtures of DMF and NMP increases the adhesion strength of PVDF nanofibers to PVDF microporous supports. Consistent with the observations of Yung et al. (2010), we have found the use of pure DMF as spinning solvent resulted in the formation of PVDF nanofibrous scaffolds that are easily peeled off by hand from the PVDF microporous supports. In contrast, none of the PVDF nanofibrous scaffolds could be peeled off by hand from their supports when the fibers were electrospun using mixtures of DMF and NMP (1:1 w/w).

Membrane synthesis and characterization

To fabricate our new ion-selective NFC membranes (Fig. 1), we first employed electrospraying to deposit films of hyperbranched PEI onto PVDF nanofibrous scaffolds that were electrospun onto commercial PVDF MF membrane supports using 1:1 w/w mixtures of DMF + NMP. Electrospraying has emerged as a versatile technique for depositing films onto a broad range of substrates including polymeric membranes (Jaworek and Sobczyk 2008). These films can be deposited from solutions or suspensions of microparticles/nanoparticles with controlled thickness ranging from 10 nm to 100 μm. Rosso et al. (2008) have successfully combined ES with electrospraying to fabricate novel catalytic membranes consisting of polysulfone nanofibrous scaffolds with embedded TiO_2 nanoparticles. Table 1 shows the process parameters used to spray the PVDF nanofibrous scaffolds with hyperbranched PEI. Based on SEM images (data not shown), we found that we can fully cover the surfaces of the PVDF nanofibrous scaffolds by spraying them with 1.0 mL of a 50 wt% solution of PEI in methanol. Following electrospraying, the PEI-laden nanofibrous PVDF were reacted, respectively, with TMC, 1,3-DBP, and ECH to produce NFC membranes with crosslinked PEI networks (Fig. 1) as described in the section "Experimental methods and procedures." Table 2 shows selected properties of the NFC–PVDF–PEI membranes that were measured in this study including contact angle, zeta potential, isoelectric point, and surface layer thickness. Figure 4 shows the FESEM images of the surface and cross-section morphology of the NFC–PVDF–PEI membranes. As shown in Fig. 4a and b, the surface of the NFC–PVDF–PEI-1 membrane (with TMC crosslinker) consists of a film of PVDF nanofibers with crosslinked PEI macromolecules. Due to its rough/wiggly surface morphology, it was difficult to measure the thickness of the surface layer of the NFC–PVDF–PEI-1 membrane with high precision. Using the ImageJ software (Abramoff et al. 2004), we estimate the thickness of the membrane surface layer is equal to 240 ± 100 nm (Table 2). This value is within the range of the observed thickness (150–2,000 nm) of the surface layers of conventional polymeric NF membranes (Baker 2004; Ji et al. 2011). Figure 3 shows that both the surface of the NFC–PVDF–PEI-2 membrane (with DBP crosslinker) and that of the NFC–PVDF–PEI-3 membrane (with ECH crosslinker) consist also of films of PVDF nanofibers with crosslinked PEI macromolecules. We estimate the thickness of the separation layers of the NFC–PEI-2 and NFC–PEI-3 membranes are, respectively, equal to 10 and 13 μm (Table 2). We

Table 2 Selected properties of the NFC–PVDF–PEI membranes synthesized in this study

Membrane	Surface layer	Contact angle[a]	Isoelectric point	Zeta potential (pH 6)	Surface layer thickness
NFC–PVDF–PEI-1	Crosslinked PEI/TMC	38.6 ± 1.4°	7.8	39.7 ± 3.7 mV	240 ± 100 nm
NFC–PVDF–PEI-2	Crosslinked PEI/DBP	54.9 ± 0.5°	6.4	9.0 ± 3.0 mV	10 μm
NFC–PVDF–PEI-3	Crosslinked PEI/ECH	50.2 ± 1.3°	5.7	−4.5 ± 0.9 mV	13 μm

[a] All the contact angles were measured in water. The contact angle of the PVDF MF membrane support is equal to 130.2 ± 0.9°

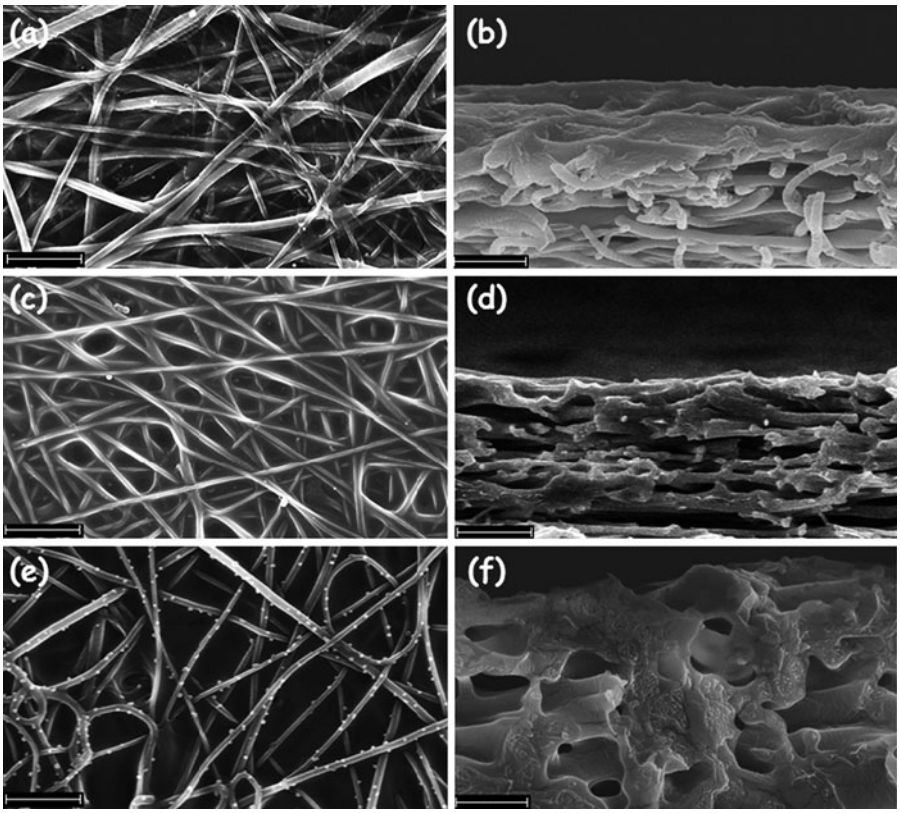

Fig. 3 FE-SEM images of the surfaces and cross-section morphologies of an NFC–PEI-1 membrane crosslinked with trimeosyl chloride (**a**, **b**), NFC–PEI-2 membrane crosslinked with 1,3-dibromopropane (**c**, **d**), and NFC–PEI-3 crosslinked with epichlrohydrin (**e**, **f**). The length of the scale bar in each panel is equal to 5 μm

attribute the large thickness of the surface of these membranes to longer crosslinking reaction times (1 h) at higher temperature (45 °C) in the presence of excess reagents (i.e., solutions of 20 wt% of DBP/ECH in toluene).

Figure 4 shows the ATR-FTIR spectra of a PDVF membrane support, a blended PVDF/PEI nanofibrous scaffold and those of the NFC–PVDF–PEI membranes. Figure 3a highlights several characteristic peaks of PVDF surfaces including CF_2 bending (615 and 766 cm^{-1}), CH_2 rocking (840 cm^{-1}), CH stretching (976 cm^{-1}), and CF stretching (1234 and 1279 cm^{-1}) (Bormashenko et al. 2004). Figure 3b shows that the blended PVDF/PEI nanofibrous scaffold exhibits two major peaks including (i) NH_2 bending (1655 cm^{-1}) from primary amines and (ii) NH stretching (3255 cm^{-1}) from primary/secondary amines. We assign these peaks to PEI macromolecules that are embedded inside PVDF nanofibrous scaffold (Fig. 1). As shown in Fig. 4c, the FT-IR spectrum of the NFC–PVDF–PEI-1 membrane exhibits some characteristic features of NF membranes with

amide groups including CN stretching (1641 cm^{-1}) and C=O stretching (1532 cm^{-1}) (Setiawan et al. 2011; Sun et al. 2011). These amide groups are generated when the PEI macromolecules that are embedded in the membrane PVDF nanofibrous scaffold react with TMC molecules (Fig. 1). Note that the FT-IR spectrum of the NFC–PVDF–PEI-2 membrane (Fig. 4d) shows no new characteristic peak. This observation is consistent with the fact that mostly secondary/tertiary amines are generated when the embedded PEI macromolecules of the membrane PVDF nanofibrous scaffold reacts with 1,3-DBP molecules (Fig. 1). In contrast, the FT-IR spectrum of the NFC–PVDF–PEI-3 membrane exhibits a new peak, i.e., OH stretching at 3257 cm^{-1} indicating that hydroxyl groups are produced when the PEI macromolecules that are embedded inside the membrane PVDF nanofibrous scaffold reacts with ECH molecules (Fig. 1). Table 2 shows significant differences between the hydrophilicity and zeta potential potentials of NFC–PVDF–PEI membranes. Note that the contact angle of the PVDF membrane support is equal to 130.2 ± 0.9° thereby indicating that the support is very hydrophobic. In contrast, the contact angles for the NFC–PVDF–PEI-1, NFC–PVDF–PEI-2, and NFC–PVDF–PEI-3 membranes are equal, respectively, to 38.6 ± 1.4°, 54.9 ± 0.5°, and 50.2 ± 1.3° thereby suggesting these membranes are hydrophilic and less susceptible to fouling via sorption of proteins and other hydrophobic macromolecular assemblies present in water/wastewater. It is worth mentioning that the contact angle of the NFC–PVDF–PEI-1 membrane (38.6 ± 1.4°) is smaller by ~10–20° than those of commercial TFC PA NF/RO membranes with crosslinked PA separation layers. These membranes have contact angles of 50–60° (Elimelech and Philipp 2011). Figure 5 shows the zeta potentials of the NFC–PVDF–PEI membranes measured at various pH. Table 2 shows their estimated isoelectric points and zeta potentials. The isoelectric points of the NFC–PVDF–PEI-1, NFC–PVDF–PEI-2, and NFC–PVDF–PEI-3 membranes are, respectively, equal to 7.8, 6.4, and 5.7. Their zeta potentials at pH 6 are equal to 39.7 3.7, 9.0 ± 3.0, and −4.5 ± 0.9 mV, respectively.

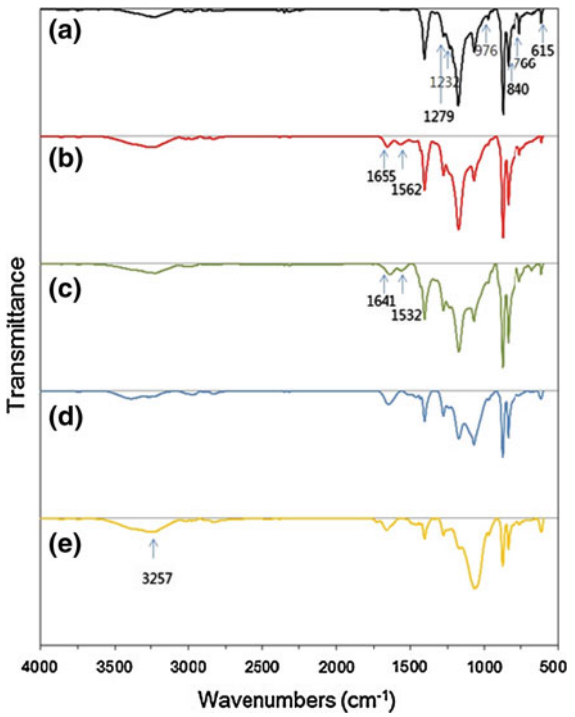

Fig. 4 FTIR-ATR spectra of a PVDF microporous support (**a**), a PVDF + PEI nanofibrous scaffold (**b**), NFC–PVDF–PEI-1 membrane crosslinked with trimeosyl chloride (**c**), NFC–PVDF–PEI-2 membrane crosslinked with 1-3 dibromopropane (**d**), and NFC–PVDF–PEI-3 membrane crosslinked with epichlorohydrin (**e**)

Evaluation of membrane performance

The overall results of the characterization experiments indicate that the NFC–PVDF–PEI-1 membrane (with TMC crosslinker) is more hydrophilic than commercial TFC-PA RO/NF membranes. The large and positive zeta potential of the NFC–PVDF–PEI-1 membrane at pH 6–7 (Fig. 5) suggests that it has good potential for high water flux and improved rejection for monovalent cations. To evaluate the performance of this new membrane, we carried out

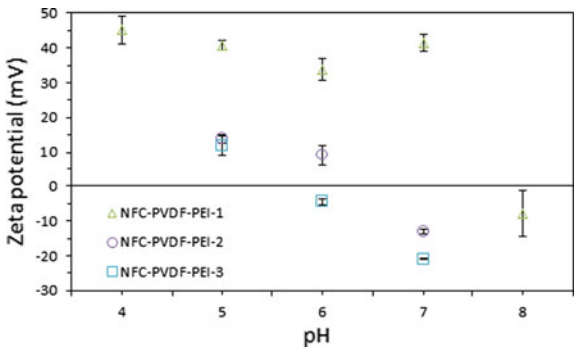

Fig. 5 Zeta potentials of NFC–PEI membranes at various pH values

cross-flow filtration experiments to measure its ion rejection and permeate flux in saline solutions as described in the section "Experimental methods and procedures." Aqueous solutions (2,000 mg/L) of four salts (NaCl, $MgCl_2$, Na_2SO_4, and $MgSO_4$) were evaluated. Figure 6 shows the salt rejection and permeate flux of the NFC–PVDF–PEI-1 membrane during the course of a typical 12 h filtration experiment. In all cases, we found that the membrane salt rejection and permeate flux reached constant values after 2 h of filtration. Figure 7 shows that the NFC–PVDF–PEI-1 membrane exhibits higher rejections for the 2-1 salt ($MgCl_2$) and 2-2 salt ($MgSO_4$) than for the 1-1 salt (NaCl) and 1-2 salt (Na_2SO_4) at pH 4 and 6. This rejection profile is consistent with that of a Donnan exclusion membrane with a positive surface charge (Schäefer et al. 2005). As indicated in Table 1, the NFC–PVDF–PEI-1 membrane has an isoelectric point of 7.8. The isoelectric point of a membrane is the pH at which it has no net charge in solution. Thus, the

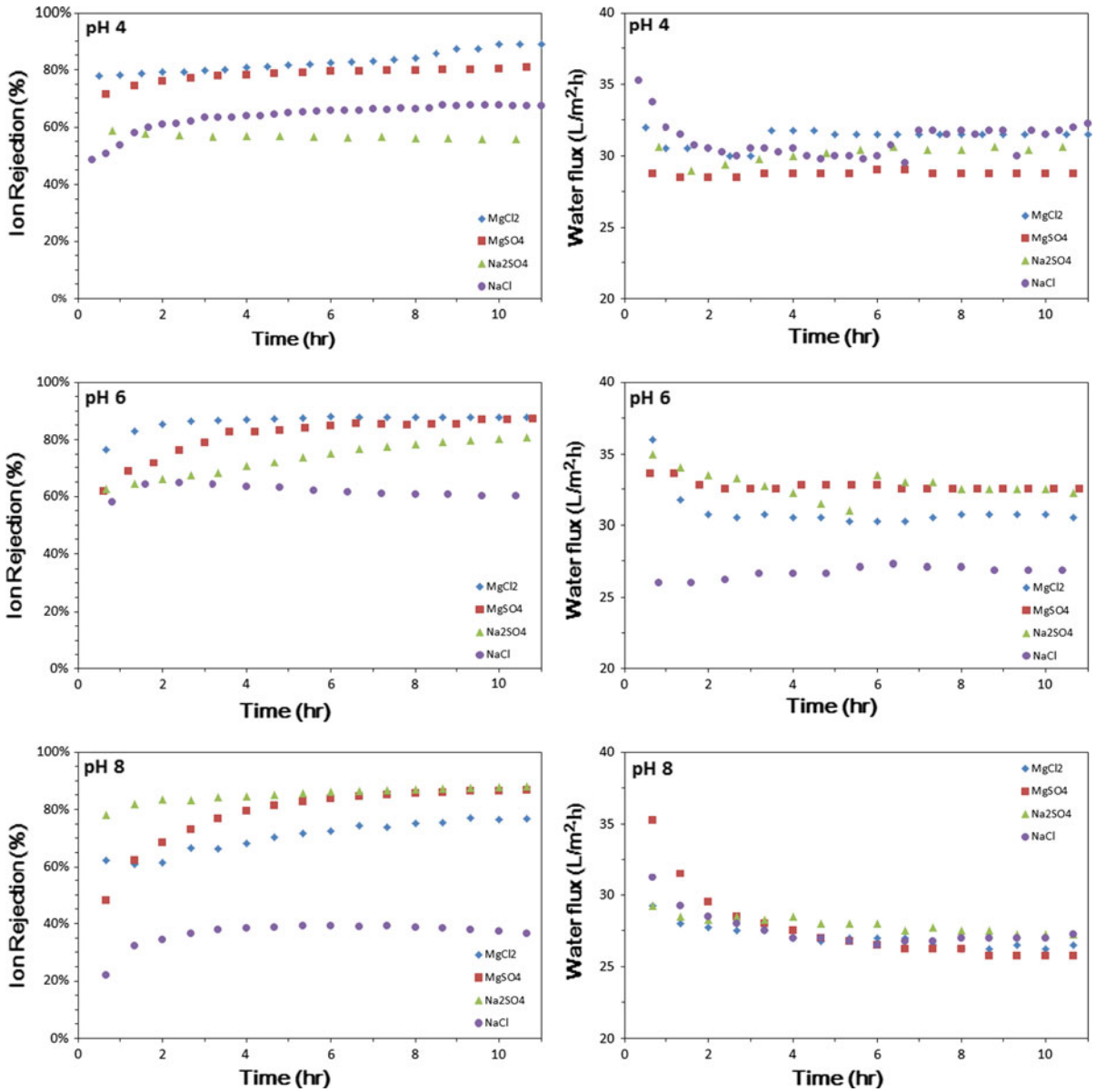

Fig. 6 Ion rejection and water flux of NFC–PEI-1 at pH 4, 6, and 8 as a function of time at room temperature. A cross-flow filtration system was utilized to measure the ion rejection and permeate flux of the membrane

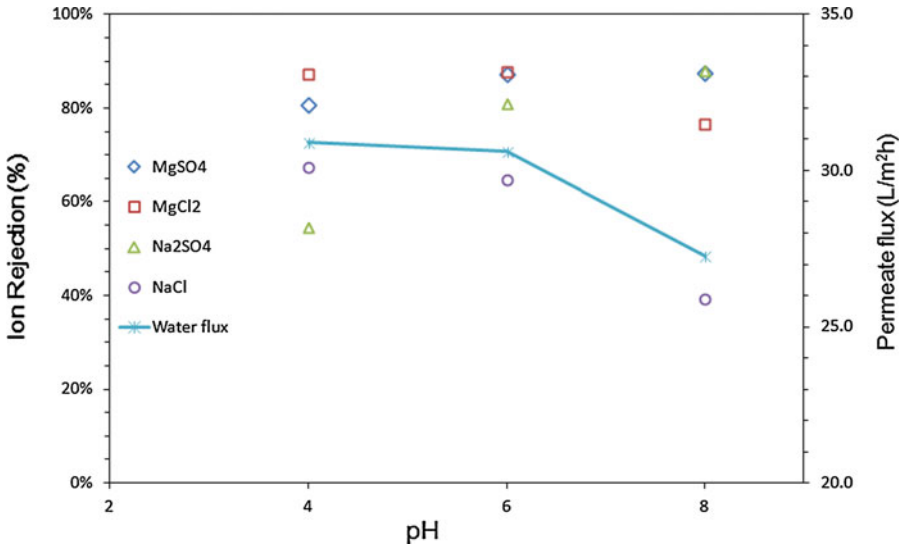

Fig. 7 Salt rejection and water flux for NFC–PEI-1 membrane as a function of pH at room temperature

NFC–PVDF–PEI-1 membrane is (i) positively charged at pH 4 and 6 and (ii) negatively charged at pH 8 (Fig. 6). Consistent with the Donnan effect, the NFC–PVDF–PEI-1 membrane will have a higher rejection for divalent cations (e.g., Mg^{2+}) over monovalent cations (e.g., Na^{+}) at pH 4 and 6 (Schäefer et al. 2005; Escoda et al. 2010; Déon et al. 2011). Note that a positively charged membrane will also reject an equivalent amount of anions to maintain overall solution electroneutrality. Because of this, we expect the rejection of a magnesium salt (e.g., $MgCl_2$ and $MgSO_4$) by a NFC–PVDF–PEI-1 membrane will be larger than that of a sodium salt (e.g., Na_2SO_4) in aqueous solutions at pH 4 and 6. At pH 8, however, Fig. 7 shows that the salt rejection order of the NFC–PVDF–PEI-1 membrane is $Na_2SO_4 > MgCl_2 >$ NaCl. We found that the $MgCl_2$ rejection of the NFC–PVDF–PEI-1 membrane decreased from 87.2 to 76.7 % as solution pH water increased from 4 to 8. In contrast, its Na_2SO_4 rejection increased significantly from 54.5 to 88.0 % with increasing pH from 4 to 8. At pH 8, the rejection of $MgSO_4$ (87.4 %) is comparable to that of Na_2SO_4 (88.0 %). However, it is significantly larger than that (76.7 %) of $MgCl_2$ at pH 8. The observed higher rejections of Na_2SO_4 and $MgSO_4$ by the NFC–PVDF–PEI-1 membrane are also consistent with those of Donnan exclusion membranes with negative surface charges including TFC PA NF membranes (Schäefer et al. 2005; Verissimo et al. 2005; Pontié et al. 2008) and sulfonated polyethersulfone asymmetric NF membranes (Tsuru et al. 1991; Schaep et al. 1998).

We also measured the salt rejections and permeate fluxes of the NFC–PVDF–PEI-2 and NFC–PVDF–PEI-3 membranes (Table 3). Table 3 shows the $MgCl_2$/NaCl rejections and permeate fluxes of the NFC–PVDF–PEI membranes at pH 6. The $MgCl_2$/NaCl rejections and permeate fluxes of selected NF membranes with positively charged surface layers are also listed in Table 3 (Ji et al. 2011). As shown in Table 3, the $MgCl_2$ rejection of the NFC–PVDF–PEI-1 membrane (87.8 %) is higher than those of the NFC–PVDF–PEI-2 membrane (75.5 %) and NFC–PVDF–PEI-3 membrane (76.4 %). Note that NaCl rejection of the NFC–PVDF–PEI-1 and NFC–PVDF–PEI-3 membranes are comparable. They are equal to 64.8 and 62.6 %, respectively. However, the NaCl rejection of the NFC–PVDF–PEI-2 is lower and equal to 22.9 %. Table 3 indicates that the permeate flux of the NFC–PVDF–PEI-3 membrane is relatively low (8–9.0 L m^{-2} h^{-1}). In contrast, the permeate flux of the NFC–PVDF–PEI-1 membrane is relatively high (27–30 L m^{-2} h^{-1}). As shown in Table 3, the permeate flux of the NFC–PVDF–PEI-2 membrane (25–30 L m^{-2} h^{-1}) is comparable to that of the NFC–PVDF–PEI-2 membrane. This result is surprising as the NFC–PVDF–PEI-1 membrane has a higher surface charge at pH 6 (39.7 mV versus 9.0 mV) with a lower contact angle (38.6° versus 54.9°) and a thinner surface layer (200 nm versus 10 μm). At the

Table 3 Comparative test results of ion rejection and water flux for positively charged nanofiltration membranes (modified from Ji et al. 2011)

Membrane	R_{MgCl_2} (%)	J_{MgCl_2} (L m^{-2} h^{-1})	R_{NaCl} (%)	J_{NaCl} (L m^{-2} h^{-1})	Separation layer	Experimental conditions	Reference
NFC–PVDF–PEI-1	87.8	30.5	64.8	27.1	Crosslinked PEI/TMC	2,000 ppm $MgCl_2$; 2,000 ppm NaCl; 7.0 bar	This study
NFC–PVDF–PEI-2	75.5	29.8	22.9	24.8	Crosslinked PEI/1,3-DBP	2,000 ppm $MgCl_2$; 2,000 ppm NaCl; 7.0 bar	This study
NFC–PVDF–PEI-3	76.4	9.3	62.6	8.0	Crosslinked PEI/ECH	2,000 ppm $MgCl_2$; 2,000 ppm NaCl; 7.0 bar	This study
PPO	73.0	63.0	36.0	63.0	Poly(2,6-dimethyl-1,4-phenylene oxide)	1,000 ppm $MgCl_2$; 1,000 ppm NaCl; 3.5 bar	Tongwen and Weihua (2003)
PDMAEMA/PSF	98.0	8.3	77.8	7.6	Poly(*N*,*N*-dimethylaminoethyl methacrylate)	1,000 ppm $MgCl_2$; 1,000 ppm NaCl; 8.0 bar	Du and Zhao (2004)
HACC/PAN NF-1	94.1	6.9	47.3	12.9	2-hydroxypropyltrimethyl ammonium chloride chitosan/hexane diacid/acetic anhydride	2,000 ppm $MgCl_2$; 2,000 ppm NaCl; 5.0 bar	Huang et al. (2008)
QAPPESK	84.0	49.0	31.0	54.0	Quaternized poly(phthalazinone ether sulfone ketone)	1,000 ppm $MgCl_2$; 1,000 ppm NaCl; 4.0 bar	Yan et al. (2008)
GCTACC/PAN	91.7	8.5	57.0	8.6	A graft copolymer of trimethylallyl ammonium chloride onto chitosan	2,000 ppm $MgCl_2$; 2,000 ppm NaCl; 12.0 bar	Huang et al. (2009)
PEI modified membrane	91.2	15.0	82.2	15.0	PEI coating on polyamide thin film composite membrane	75 ppm $MgCl_2$; 90 ppm NaCl; 8.0 bar	Zhou et al. (2009)
PCNFM3	94.3	19.1	60.7	20.6	Poly(2-methacryloyloxy ethyl trimethylammonium chloride-co-2-hydroxyethyl acrylate)	1,000 ppm $MgCl_2$; 1,000 ppm NaCl; 6 bar	Ji et al. (2011)
M-40	63.3	30.2	36.6	30.2	Poly(arylene ether sulfone) with pendant tertiary amine group	1,000 ppm $MgCl_2$; 1,000 ppm NaCl; 5 bar	Zhang et al. (2011)

present time, we have no definite explanation for this observation. The overall results of our study suggest that NFC membranes with PVDF nanofibrous scaffolds and crosslinked PEI networks are promising building blocks for the fabrication of high performance NF membranes for water purification. Without optimization, our new NFC–PVDF–PEI-1 membrane (Fig. 1) already exhibit a high water flux ($\sim$30 L m^{-2} h^{-1}) and good rejections for $MgCl_2$ ($\sim$88 %) and NaCl ($\sim$65 %) rejection in salt solutions (2,000 mg/L) at pH 6 using a pressure of 7 bar (Table 3). It is worth mentioning that the all the nanofiltration membranes listed in Table 3 that have higher $MgCl_2$/NaCl rejections than those of NFC–PVDF–PEI-1 membrane have also lower permeate fluxes ($\sim$15.0–19.0 L m^{-2} h^{-1}). Additional experiments are being carried out to improve the performance of the NFC–PVDF–PEI membranes (Fig. 1).

Summary and conclusions

In this study, we described the synthesis of a new generation of NFC membranes for water purification. These new NFC membranes consisted of crosslinked hyperbranched PEI networks supported by PVDF

nanofibrous scaffolds that were deposited onto commercial PVDF MF membrane supports. To fabricate these new NFC membranes, we first utilized ES to deposit blends of PVDF/PEI nanofibers onto commercial PVDF MF membranes. Following completion of the ES process, we deposited films of hyperbranched PEI onto PVDF nanofibrous scaffolds using electrospraying. The PEI-laden nanofibrous PVDF scaffolds were then reacted with TMC, 1,3-DBP, and ECH, respectively, to produce NFC membranes with crosslinked PEI separation layers. The morphology, composition, hydrophobicity, and surface charge of the new NFC–PVDF–PEI membranes were subsequently characterized using FESEM, ATR-FTIR, contact angle, and zeta potential measurements. The salt rejection and permeate flux of the new membranes were evaluated using a costume-built filtration system with an effective membrane area of 24 cm^2. During each filtration experiment, we used a feed solution of 10 L with a salt concentration of 2,000 mg/L. The pH of the feed solution was adjusted with a solution of 0.1 N HCl or 0.1 N NaOH as needed. All filtration experiments were carried out at room temperature and at a constant pressure of 7.0 bar. Aqueous solutions (2,000 mg/L) of four salts (NaCl, $MgCl_2$, Na_2SO_4, and $MgSO_4$) were evaluated. We found that our NFC–PVDF membrane with crosslinked PEI/TMC networks has a high water flux ($\sim$30 L m^{-2} h^{-1}) and high rejections for $MgCl_2$ ($\sim$88 %) and NaCl ($\sim$65 %) at pH 6 using a pressure of 7 bar. The overall results of our study suggest that PVDF nanofibers and hyperbranched PEI are promising building blocks for the fabrication of high performance NF membranes for water purification.

Acknowledgments This study was carried out at Korea Advanced Institute of Science and Technology (KAIST) and at the California Institute of Technology (Caltech). Selected materials characterization studies (zeta potential measurements) were carried out at the Gwangju Institute of Science and Technology (GIST). Funding for KAIST was provided by the EEWS Initiative (NT080607C0209721). Funding for Caltech was provided by the U.S National Science Foundation (NSF) [CBET EAGER Award 0948485]. W. A. Goddard III was supported partially by the KAIST World Class University (WCU) program (NRF-31-2008-000-10055).

References

Abramoff MD, Magalhaes PJ, Ram SJ (2004) Image processing with ImageJ. Biophotonics Int 11:36–42

Ba C, Langer J, Economy J (2009) Chemical modification of P84 copolyimide membranes by polyethylenimine for nanofiltration. J Membr Sci 327:49–58

Baker RW (2004) Membrane technology and applications, 2nd edn. Wiley, Chichester

Bormashenko Y, Pogreb R, Stanevsky O, Bormashenko E (2004) Vibrational spectrum of PVDF and its interpretation. Polym Test 23:791–796

Cheng S, Oatley DL, Williams PM, Wright CJ (2011) Positively charged nanofiltration membranes: review of current fabrication methods and introduction of a novel approach. Adv Colloid Interface Sci 164:12–20

Chiang Y-C, Hsub Y-Z, Ruaan R-C, Chuang C-J, Tung K-L (2009) Nanofiltration membranes synthesized from hyperbranched polyethyleneimine. J Membr Sci 326:19–26

Choi H, Kwon Y, Jung Y, Hong S, Tak T (2011) Preparation and characterization of antifouling poly(vinylidene fluoride) blended membranes. J Appl Polym Sci 123:286–291

Déon S, Escoda A, Fievet P (2011) A transport model considering charge adsorption inside pores to describe salts rejection by nanofiltration membranes. Chem Eng Sci 66:2823–2832

Diallo MS, Brinker JC (2011) Nanotechnology for sustainability: environment, water, food, minerals and climate. In: Roco MC, Mirkin C, Hersham M (eds) Nanotechnology research directions for societal needs in 2020: retrospective and outlook. Science Policy Reports, Springer, pp 221–259

Diallo MS, Yu C (2011) Soluble anion exchangers from hyperbrannched macromolecules. US Patent Application Pub. No: 2011/0315636 A1

Du R, Zhao J (2004) Properties of poly (N,N-dimethylaminoethyl methacrylate)/polysulfone positively charged composite nanofiltration membrane. J Membr Sci 239:183–188

Elimelech M, Philipp WA (2011) The future of seawater desalination: energy, technology and the environment. Science 333:712–717

Escoda A, Lanteri Y, Fievet P, Déon S, Szymczyk A (2010) Determining the dielectric constant inside pores on nanofiltration membranes from membrane potential measurements. Langmuir 26:14628–14635

Frechet JMJ, Boz E, Diallo MS, Chi Y (2010) Extraction of anions from solutions and mixtures using hyperbranched macromolecules. US Patent Application No.: 20100181257

Gopal R, Kaur S, Ma ZW, Chan C, Ramakrishna S, Matsuura T (2006) Electrospun nanofibrous filtration membrane. J Membr Sci 281:581–586

Huang R, Chen G, Sun M, Gao C (2008) Preparation and characterization of quaterinized chitosan/poly(acrylonitrile) composite nanofiltration membrane from anhydride mixture cross-linking. J Membr Sci 58:393–399

Huang R, Chen G, Sun M, Gao C (2009) Preparation and characterization of composite NF membrane from a graft copolymer of trimethylallyl ammonium chloride onto chitosan by toluene diisocyanate cross-linking. Desalination 239:38–45

Jaworek A, Sobczyk AT (2008) Electrospraying route to nanotechnology: an overview. J Electrostat 66:197–219

Ji Y, An Q, Zhao Q, Chen H, Gao C (2011) Preparation of novel positively charged copolymer membranes for nanofiltration. J Membr Sci 376:254–265

Mansouri J, Harrisson S, Chen V (2010) Strategies for controlling biofouling in membranefiltration systems: challenges and opportunities. J Mater Chem 20:4567–4586

Oh SJ, Kim N, Lee YT (2009) Preparation and characterization of PVDF/TiO_2 organic–inorganic composite membranes for fouling resistance improvement. J Membr Sci 345: 13–20

Pontié M, Dach H, Leparc J, Hafsi M, Lhassani A (2008) Novel approach combining physico-chemical characterizations and mass transfer modelling of nanofiltration and low pressure reverse osmosis membranes for brackish water desalination intensification. J Membr Sci 221:174–191

Ramakrishina S, Fujihara K, Teo W-E, Lim T-C, Ma Z (2005) An introduction to electrospinning and nanofibers. World Scientific Publishing Co., Singapore

Rosso M, Sundarrajan S, Pliszka D, Ramakrishina S, Modesti M (2008) Multifunctional membranes based on spinning technologies: the synergy of nanofibers and nanoparticles. Nanotechonology 19:285707 (6 pp)

Schäefer A, Fane AG, Waite TD (2005) Nanofiltration: principles and applications. Elsevier, New York

Schaep J, Bruggen BVD, Vandecasteele C, Wilms D (1998) Influence of ion size and charge in nanofiltration. Sep Purif Technol 14:155–162

Service RF (2006) Desalination freshens up. Science 313:1088–1090

Setiawan L, Wang R, Li K, Fane AG (2011) Fabrication of novel poly(amide-imide) forward osmosis hollow fiber membranes with a positively charged nanofiltration-like selective layer. J Membr Sci 369:196–205

Shannon MA, Bohn PW, Elimelech M, Georgiadis J, Marinas BJ, Mayes A (2008) Science and technology for water purification in the coming decades. Nature 54:301–310

Shim Y, Lee HJ, Lee SY, Moon SH, Cho J (2002) Effects of natural organic matter and ionic species on membrane surface charge. Environ Sci Technol 36:3864–3871

Strathmann H (2011) Introduction to membrane science and technology. Wiley-VCH Verlag & Co, Weinheim

Sun SP, Hatton AT, Chung TS (2011) Hyperbranched polyethyleneimine induced cross-linking of polyamide-imide nanofiltration hollow fiber membranes for effective removal of ciprofloxacin. Environ Sci Technol 45: 4003–4009

Tongwen X, Weihua Y (2003) A novel positively charged composite membranes for nanofiltration prepared from poly(2,6-dimethyl-1,4-phenylene oxide) by in situ amines crosslinking. J Membr Sci 215:25–32

Tsuru T, Urairi M, Nakao S, Kimura S (1991) Negative rejection of anions in the loose reverse osmosis separation of mono- and divalent ion mixture. Desalination 81:219–227

UNEP (2006) Challenges to international waters—regional assessments in a global perspective. United Nations Environment Programme, Nairobi

Verissimo S, Peinemann KV, Bordado J (2005) New composite hollow fiber membrane for nanofiltration. Desalination 184:1–11

Vezzani D, Bandini S (2002) Donnan equilibrium and dielectric exclusion for characterization of nanofiltration membranes. Desalination 149:477–483

Wang X, Chen X, Yoon K, Fang D, Hsiao BS, Chu B (2005) High flux filtration medium based on nanofibrous substrate with hydrophilic nanocomposite coating. Environ Sci Technol 39:7684–7691

Yan C, Zhang S, Yang D, Jian X (2008) Preparation and characterization of chloromethylated/quaternized poly(phthalazinone ether sulfone ketone) for positively charged nanofiltration membranes. J Appl Polym Sci 107:1809–1816

Yoon K, Hsiao BS, Chu B (2008) Functional nanofibers for environmental applications. J Mater Chem 18:5326–5334

Yoon K, Hsiao BS, Chu B (2009) High flux ultrafiltration nanofibrous membranes based on polyacrylonitrile electrospun scaffolds and crosslinked polyvinyl alcohol coating. J Membr Sci 338:145–152

Yung L, Ma H, Wang X, Yoon K, Wang R, Hsiao BS, Chu B (2010) Fabrication of thin-film nanofibrous composite membranes by interfacial polymerization using ionic liquids as additives. J Membr Sci 365:52–58

Zhang Q, Wang H, Zhang S, Dai L (2011) Positively charged nanofiltration membrane based on cardo poly(arylene ether sulfone) with pendant tertiary amine groups. J Membr Sci 375:191–197

Zhou Y, Yu S, Gao C, Feng X (2009) Surface modification of thin film composite polyamide membranes by electrostatic self-deposition of polycations for improved fouling resistance. Sep Sci Technol 66:287–294

DOI 10.1007/978-3-319-05041-6_4
Reprinted from the *Journal of Nanoparticle Research*, DOI 10.1007/s11051-013-1698-y

RESEARCH PAPER

Composite polyester membranes with embedded dendrimer hosts and bimetallic Fe/Ni nanoparticles: synthesis, characterisation and application to water treatment

S. P. Malinga · O. A. Arotiba · R. W. M. Krause · S. F. Mapolie · M. S. Diallo · B. B. Mamba

Received: 27 November 2012 / Accepted: 4 May 2013 / Published online: 21 May 2013

Abstract This study describes the preparation, characterization and evaluation of new composite membranes with embedded dendrimer hosts and Fe/Ni nanoparticles. These new reactive membranes consist of films of cyclodextrin–poly(propyleneimine) dendrimers (β-CD–PPI) that are deposited onto commercial polysulfone microporous supports and crosslinked with trimesoyl chloride (TMC). The membranes were subsequently loaded with Fe/Ni nanoparticles and evaluated as separation/reactive media in aqueous solutions using 2,4,6-trichlorophenol as model pollutant. The morphology and physicochemical properties of the composite membranes were characterised using high-resolution transmission electron microscopy (HR-TEM), atomic force microscopy and measurements of contact angle, water intake, porosity and water permeability. The sorption capacity and catalytic activity of the membranes were evaluated using ion chromatography, atmospheric pressure chemical ionisation-mass spectrometry and UV–Vis spectroscopy (UV–Vis). The sizes of the embedded Fe/Ni nanoparticles in the membranes ranged from 40 to 66 nm as confirmed by HR-TEM. The reaction rates for the dechlorination of 2,4,6-trichlorophenol ranged from 0.00148 to 0.00250 min^{-1}. In all cases, we found that the reaction by-products consisted of chloride ions and mixtures of compounds including phenol ($m/z = 93$), 2,4-dichlorophenol ($m/z = 163$)

Special Issue Editors: Mamadou Diallo, Neil Fromer, Myung S. Jhon

This article is part of the Topical Collection on Nanotechnology for Sustainable Development

Electronic supplementary material The online version of this article (doi:10.1007/s11051-013-1698-y) contains supplementary material, which is available to authorized users.

S. P. Malinga (✉) · O. A. Arotiba · M. S. Diallo · B. B. Mamba
Department of Applied Chemistry, University of Johannesburg, P.O. Box 17011, Doornfontein 2028, South Africa
e-mail: sitholespr@yahoo.com

B. B. Mamba
e-mail: bmamba@uj.ac.za

R. W. M. Krause
Department of Chemistry, Rhodes University, P.O. Box 94, Grahamstown 6140, South Africa

S. F. Mapolie
Department of Chemistry and Polymer Science, University of Stellenbosch, Private Bag X1, Matieland 7602, South Africa

M. S. Diallo
Graduate School of EEWS, Korea Advanced Institute of Science and Technology (KAIST), Daejeon 305-701, Republic of Korea

M. S. Diallo
Division of Engineering and Applied Science, Environmental Science and Engineering, California Institute of Technology, Pasadena, CA 91125, USA

and 4-chlorophenol ($m/z = 128$). The overall results of this study suggest that β-CD–PPI dendrimers are promising building blocks for the synthesis of composite and reactive membranes for the efficient removal of chlorinated organic pollutants from water.

Keywords β-Cyclodextrin · Fe/Ni nanoparticles · Poly(propyleneimine) dendrimer · Polysulfone · 2,4,6-Trichlorophenol

Introduction

Membranes have gained a lot of attention in the chemical technology industry and these have been used in a wide range of applications such as the production of high quality water, removal and recovery of toxic and valuable components from industrial effluent (Abedini et al. 2011). The introduction of membrane technology in separation and concentration has become industrially viable due to the low energy of operation, high efficiency of separation and simplicity of operation (Abedini et al. 2011). Traditionally, membranes have been used in separation based on size exclusion, solution diffusion or Donnan exclusion (Smuleac et al. 2010). However, the fabrication of membranes with novel materials such as nanostructured dendrimer–cyclodextrin (Fig. 1a) Ni–Fe bimetalics can extend their application towards advanced separation and catalysis.

Dendrimers are highly branched, globular, nanoscopic macromolecules with numerous terminal groups (Sarkar et al. 2010). Dendrimers have been regarded as high performance material over the past decade and have received greater attention due to their exquisite structure have found many possible applications in the field of catalysis, drug delivery and biomimetics (Lianchao et al. 2006; Wei et al. 2008). Poly(propyleneimine) (PPI) dendrimers are macromolecules with three-dimensional structures which consist of an interior diaminobutane core, interior branching units (propylene imine) and peripheral functional groups (NH_2 groups in the unfunctionalised polymer) (Vassilev et al. 2009). The use of dendrimers in bimetallic and monometallic nanoparticle synthesis is well established and this has led to the production of nanoparticles which are cone-, spherical- or disc-like shaped, soft and have very low polydispersity and sizes in the range of 1–3 nm (Diallo et al. 2005; Bao et al. 2003; Weir et al. 2010; Scott et al. 2004). A number of key factors make dendrimers particularly interesting in nanoparticle and macromolecular synthesis. First, dendrimers have a high number of internal amine functional groups, which can act as ligands to complex metal ions such as Cu, Fe, Ag and Ni for nanoparticle synthesis (Huang et al. 2008; Diallo et al. 2005). Second, the presence of nanocavities in the dendrimer structure acts as hosts/templates for the preparation of narrow and stable nanoparticles (Bai et al. 2009). The quasispherical hyperbranched structure of the dendrimers (generation 4 and above) also provides a shell to prevent aggregation of the nanoparticles (Huang et al. 2008). Third, the nanocavities can act as catalytic and adsorption sites for the degradation and removal of organic pollutants. Lastly, the highly branched peripheral amine functional groups can be grafted with other molecules (such as cyclodextrins) to prepare a new generation of multifunctional material. The incorporation of β-cyclodextrin to dendrimers provides a unique polymer structure that exhibits the combination of the two-type of molecular cavities as well as characteristics of both the cyclodextrin and the dendrimer (Fig. 1a) (Li et al. 2011).

Recent advances in membrane research such as the fabrication of nanoparticles within structures has been reported. Lee et al. (2008) fabricated a novel polyamide nanocomposite membrane containing TiO_2 nanoparticles synthesised via in situ polymerisation. The membrane was found to have very high rejection towards $MgSO_4$ (95 %) and a permeate flux of 9.1 L m^{-2} h^{-1}. Smuleac and co-workers (2010; 2011) prepared Fe/Pd nanoparticles in a polymer film consisting of polyacrylic acid coated on a polyvinylidene fluoride membrane for the degradation of trichloroethylene and 2,2-dichlorobiphenyl. The inclusion of Fe/Pd bimetallic system into the polymeric film was found to improve the degradation rate from 0.005 (for Fe only) to 0.008 L m^{-2} h^{-1} when Fe/Pd bimetallic system was used for the degradation of trichloroethylene (Smuleac et al. 2010). On the other hand, 2,2-dichlorophenyl was converted to phenyl in <40 s (Smuleac et al. 2010).

Despite these promising results a great deal of work still needs to be done to develop more efficient technologies to extract clean water from industrial runoff, wastewater and sea water. Thus, in this study, a new generation of multifunctional membranes

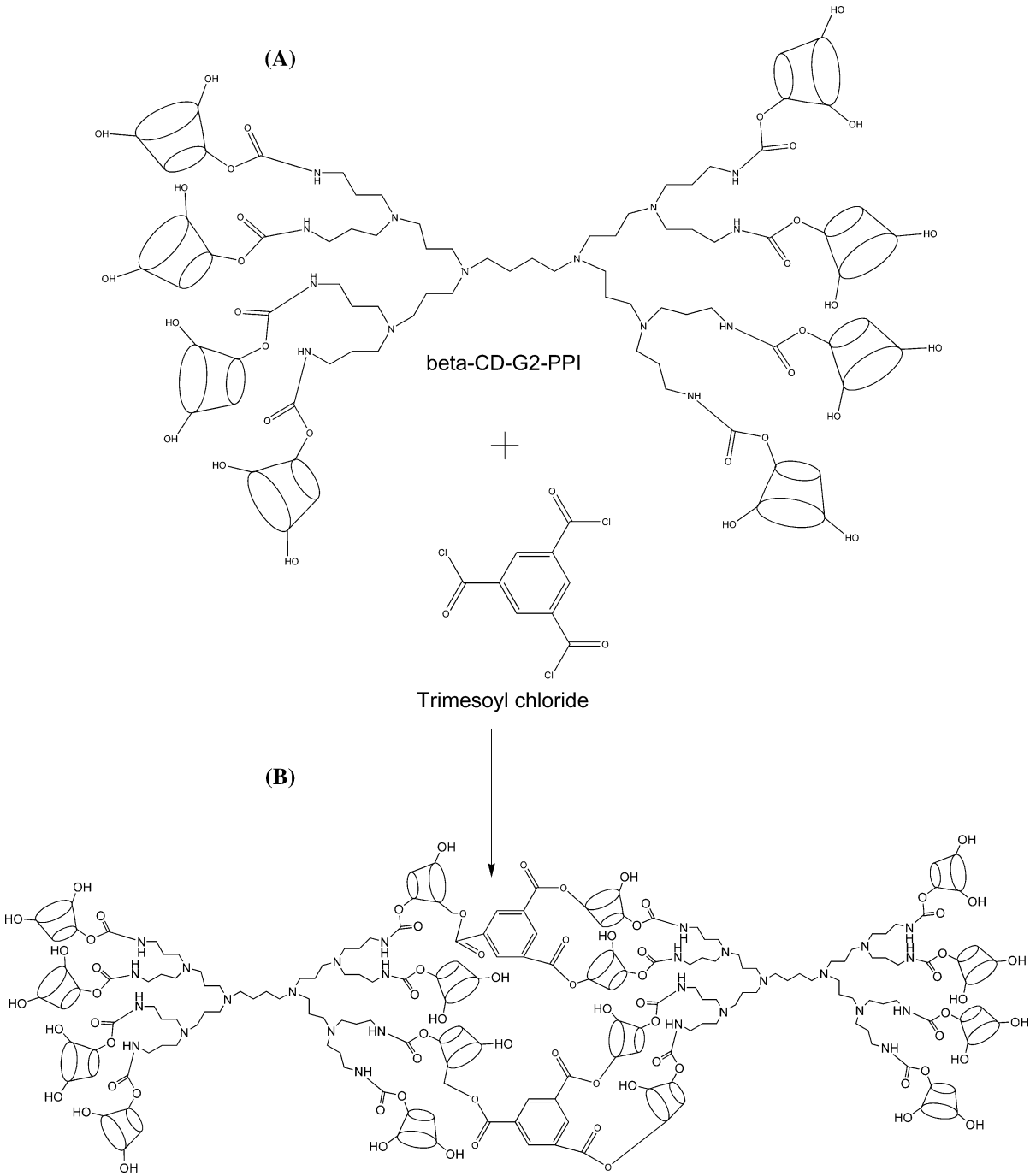

Fig. 1 β-CD–G2-PPI (**a**) reaction with trimesoyl chloride to produce a highly crosslinked β-CD–G2-PPI structure (**b**)

embedded with β-cyclodextrin–poly(propyleneimine) dendrimer and catalytic Ni/Fe centres were prepared and used to carry out both catalysis and adsorption. Specifically, β-cyclodextrin and generation 3 (G3)/ generation 4 (G4) poly(propyleneimine) (PPI) (β-CD–G3 and β-CD–G4) were incorporated on polysulfone (PSf) as a coating layer to form a thin film composite using trimesoyl chloride. These membranes (β-CD–G3-PSf and β-CD–G4-PSf) were then dip coated in Fe and Ni solution followed by metal reduction using

$NaBH_4$ to prepare the catalytic membranes (β-CD–G3-PSf-Fe/Ni and β-CD–G4-PSf-Fe/Ni). The synthesis of Ni/Fe bimetallic system in a β-cyclodextrin–dendrimer PSf domain has not been reported before. To further demonstrate the usefulness of these membranes, the membranes were applied in the dechlorination and adsorption of 2,4,6-trichlorophenol (TCP).

Experimental methods and procedures

Materials

Generation 3 (G3) and generation 4 (G4) poly(propylene imine) dendrimers were purchased from SyMO-Chem B.V (Netherlands). *N,N*-carbonyldiimidazole(CDI) was purchased from Sigma Aldrich (USA). The purification of the β-CD–dendrimer conjugates was carried out using benzoylated dialysis tubing with molecular weight cut off of 1,200 g mol^{-1}, from Sigma, Aldrich (USA). Commercial ultrafiltration flat sheet of PSf membrane was supplied by Marsi water (Pty) Ltd (Northriding, South Africa). 1,3,5-Benzenetricarbonyl trichloride (TMC) and *N*-(3-dimethylamino propyl)-*N*-ethyl-carbodiimide hydrochloride (EDC) were purchased from Sigma Aldrich Company (St. Louis, USA). 2,4,6-Trichlorophenol, Ni (II) nitrate hexahydrate (Ni $(NO_3)_2{\cdot}6H_2O$), Ferric nitrate (Fe $(NO_3)_3{\cdot}9H_2O$) and sodium borohydride were purchased from Fluka. All chemicals and materials were used as received.

Host synthesis (β-CD–PPI)

A typical conjugation reaction of precursor β-cyclodextrin carbonylimidazole and poly(propyleneimine) dendrimer (generations 3 and 4) was carried out as follows: generation 3 poly(propyleneimine) (G3-PPI) (0.211 g, 0.125 mmol) was dissolved in dimethylsulphoxide (3 mL); β-cyclodextrin imidazole (2.446 g, 1.9 mmol) and triethylamine (3 mL) were added to this dendrimer solution. This solution was stirred at room temperature for 24 h and purified using dialysis against deionised water for 2 days. Lyophilization of the solution for 2 days resulted in a white fluffy solid. A similar procedure was used for the preparation of β-CD–G4-PPI host. Figure 1a shows an example of the host material β-CD–G2-PPI (i.e., 8 β-CD molecules). For β-CD–G3-PPI and β-CD–G4-PPI, 16 and 32 β-CD molecules are attached to the periphery, respectively. Figures S1, S2, S3 and S4 show the FTIR, HNMR and MS–ESI analysis, respectively, confirming that the host structure was successfully synthesised.

Membrane synthesis

The membranes were prepared using an interfacial polymerisation reaction. The aqueous phase solution was prepared by dissolving β-cyclodextrin–poly(propyleneimine) (β-CD–PPI) (6 %, w/v) (generation 3 or 4) in water. The microporous commercial PSf membrane was then dip coated in the aqueous solution for 24 h at room temperature. The residual liquid was drained and *N*-(3-dimethylamino propyl)-*N*-ethyl-carbodiimide hydrochloride solution (5 % w/v) in a phosphate buffer solution (pH = 5.6) was poured over the membrane and left to react for 3 h. This solution was used as a coupling agent to promote esterification. The membrane was then placed in the organic phase, i.e., trimesoyl chloride (1 % w/v) in n-hexane and the reaction time was set to 60 s. The membrane was dried in the oven at 60 °C for 30 min to promote further polymerisation. The modified PSf membranes were then washed with deionised water to remove any residual trimesoyl chloride and stored in deionised water. The reaction between the host (β-CD–G2-PPI) and trimesoyl chloride generates a crosslinked structure shown in Fig. 1b. Figure S5 shows FTIR analysis of the membrane confirming successful crosslinking of the β-CD–PPI host with trimesoyl chloride to give a polyester membrane.

Preparation of Fe/Ni-modified membranes

Prior to the Fe/Ni nanoparticle preparation, the membranes were immersed in NaCl (5 wt%) solution (pH = 10) overnight to deprotonate the hydroxyl groups (Smuleac et al. 2010). The deprotonation was carried out to facilitate metal binding with the membrane. The membrane was thoroughly washed with deionised water until the pH became neutral. It was then immersed in an aqueous solution containing $NiNO_3{\cdot}9H_2O$ (2.4 wt%) and $FeNO_3{\cdot}9H_2O$ (7.8 wt%) and shaken overnight to provide efficient deposition of the metal ions onto the membrane. Argon was purged into the solution to prevent oxidation. The encapsulated Fe^{2+}/Ni^{2+} ions were simultaneously reduced with

aqueous $NaBH_4$ (0.4 M, 25 mL) for 20 min and this resulted in the catalytic membrane (Xu et al. 2005). The membrane was stored in ethanol to prevent oxidation.

Membrane characterisation

Fourier transform infrared-attenuated total reflection (FTIR-ATR)

The membrane samples were analysed with a Perkin Elmer 100 FTIR spectrophotometer. Powder and membranes samples (with active side facing down) were placed on the ATR and analysed in the range 650–4,000 cm^{-1} averaging 32 scans at a spectral resolution of 4 cm^{-1}.

Atomic force microscopy (AFM)

Multimode Atomic Force Microscope (Nano Scope Version (IV) was used to determine surface morphology and roughness (Rq) of the membranes. The membrane sample (1 cm × 1 cm) was placed on a sample holder and a RTESPW tip with a radius of curvature of <10 nm (Veeco instruments) was used. The tip was mounted on a 125-μm-long cantilever with the spring constant of 40 N/m and this was employed for the tapping mode experiment. The height and phase images were obtained using a scan rate of 0.5 Hz and the tip frequencies ranged from 280 to 310 kHz.

Scanning electron microscopy (SEM)

Scanning electron microscopy was used to determine the cross-sectional images of the thin film composite. The samples were frozen and fractured in liquid nitrogen, coated with carbon and mounted on the instrument. The samples were then examined using Field emission scanning electron microscopy (Joel, JSM, 7500F).

Contact angle analysis

Contact angle analyses were measured using the sessile drop method with a Data Physics optical contact angle instrument. About ten measurements were conducted at different sites per sample and all measurements were recorded at room temperature. These analyses were carried out in order to determine the hydrophilicity of the membranes.

High-resolution transmission electron microscopy (HR-TEM)

The membrane samples were prepared by sectioning with a diamond knife to give very thin sections. These thin sections were examined using HRTEM JOEL JEM-2100 coupled to an energy dispersive X-ray spectroscopy (EDS).

Water intake capacity and porosity measurements

Water intake capacity was performed to evaluate the adsorption of water by the fabricated membranes. The water intake capacity of the membrane was obtained after soaking the membrane in deionised water for 24 h. The membranes were weighed after mopping with paper to obtain the wet weight. The membranes were dried in an oven at 60 °C for 24 h to obtain the dry weight. The percent water intake capacity (WIC) was calculated using Eq. (1) (Adams et al. 2012);

$$\mathrm{WIC}(\%) = \frac{W_w - W_d}{W_w} \times 100 \quad (1)$$

where w_w and w_d are the wet and dry weights of the membrane, respectively.

Membrane porosity was determined by immersing the membrane in water for 24 h followed by blotting the membrane with paper and the wet weight of the membrane was measured. The membrane was dried in an oven at 60 °C for 24 h and the weight was measured again. The porosity of the membrane (P) was measured by using Eq. 2 (Adams et al. 2012):

$$P(\%) = \frac{(W_0 - W_1)}{Ah} \times 1000 \quad (2)$$

where w_0 and w_1 are the weight of the wet and dry membrane, respectively, A is the area of the membrane (cm^2) and h is the membrane thickness (mm).

Membrane performance evaluation

The separation performance tests for β-CD–PPI–PSf, β-CD–PPI–PSf-Fe/Ni and native PSf membranes were carried using a six-cell crossflow parallel membrane system shown in Scheme 1. The membranes were stabilised with distilled water at 2.4 MPa for 2 h with deionised water before testing. The six-cell crossflow system has a set of membrane cells fed in parallel from a single feed tank (Jin et al. 2009). The water in the

feed tank was maintained by magnetic stirring and was pressurised into the system by a hydra cell pump. A laboratory recirculating heater chiller (Poly Science digital temperature controller) maintained the feed water at 22 °C. Back pressure regulators (Swagelok) and bypass valves controlled the feed water hydraulic pressure and crossflow velocity for each side individually (Jin et al. 2009). After sampling, the permeate and retentate were returned to the feed tank in order to maintain a constant concentration of 2,4,6-TCP.

The membrane permeability was determined from pure water flux using deionised water. The water flux was (J_w) is expressed in Eq. 3 (Adams et al. 2012):

$$J_w = \frac{V}{At} \tag{3}$$

where v is the permeate volume (m^3), A is the effective membrane area (0.00129 m^2) and t is the time (hours) to collect the permeate volume. To evaluate the dechlorination performance of the membrane towards 2,4,6-TCP, the feed solution (50 mg $L^{-1)}$ was passed through the membrane at a pressure of 0.69 MPa. The permeate was collected at constant time intervals and analysed using an UV–Vis spectrophotometer at 293 nm. The amount of 2,4,6-TCP adsorbed per unit area of the membrane was calculated using Eq. 4:

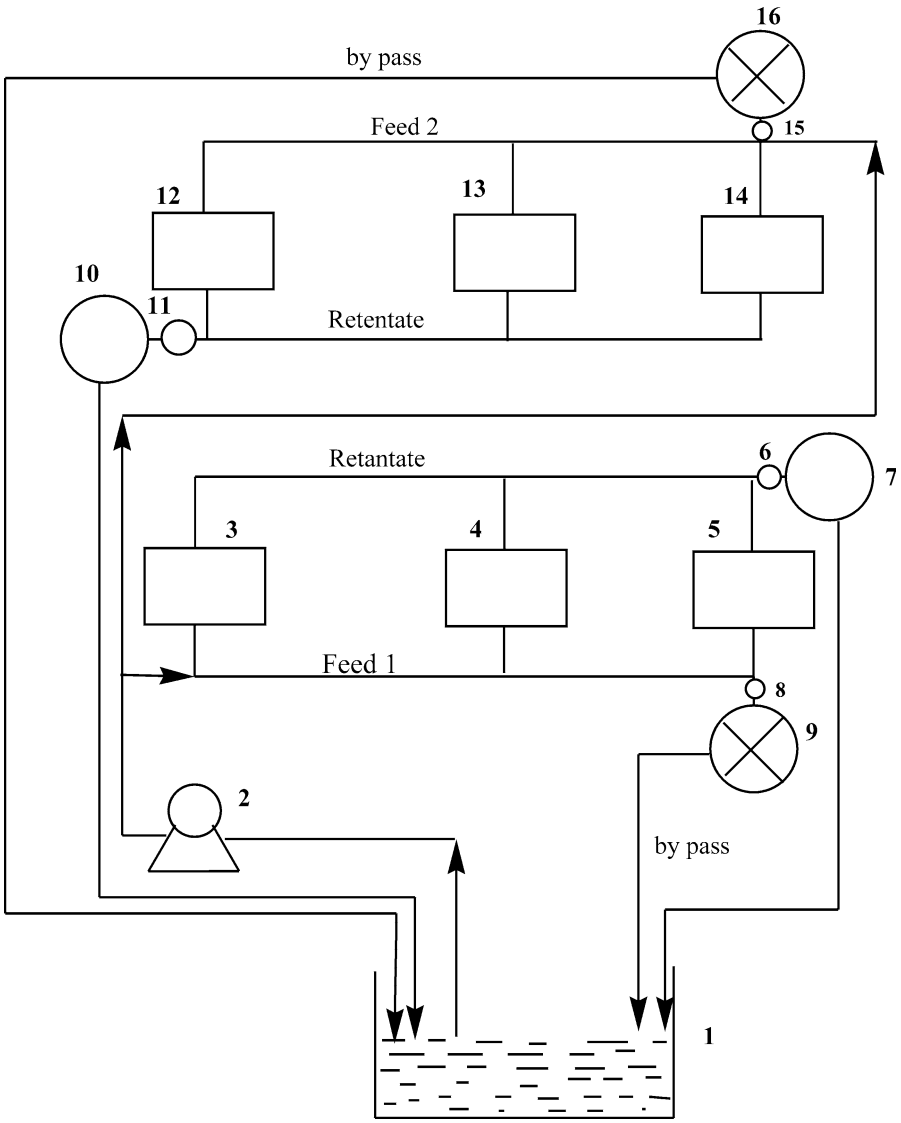

Scheme 1 A schematic representation of a six-cell crossflow system (*1*) feed solution (10 L, 22 °C), (*2*) feed pump (*3–5*), and (*12–14*) membrane cell, (*6* and *11*) back pressure regulators, (*7* and *10*) flow meter, (*8* and *15*) by pass valves, (*9* and *16*) pressure gauges

$$\text{TCP adsorption} = \frac{C_f - C_p}{A} \times V \quad (4)$$

where c_p is the concentration of the permeate, c_f is the concentration of the feed (mg L^{-1}), A is the membrane area in cm^2 and V is the total volume of the solution (L).

Batch analysis for evaluation of kinetics

Membranes containing Fe/Ni nanoparticles were immersed in a sealed erlenmeyer flask containing 2,4,6-triclorophenol (50 mg L^{-1}) solution under argon gas. This solution was shaken on a shaker at a speed of 180 rpm. The samples were collected at different time intervals using a syringe and analysed using an UV–Vis spectrophotometer at 293 nm.

Ion chromatography analysis

The concentration of chlorine ions was determined using Ion chromatography (Dionex ICS-2000 equipped with a Dionex Ionpac AS18 (2 × 250 mm) column) and the samples were first filtered through polyvinylidene fluoride syringe filters (0.45 μm) before analysis.

Atmospheric pressure chemical ionisation-mass spectrometry (APCI-MS) analysis

The dechlorination by-products (2,4-dichlorophenol, 4-chlorophenol and phenol) were analysed by liquid chromatography–mass spectrometry (Waters e2695, Separations). A methanol (80 %):water (20 %) mobile phase was used and the injection volume was set at 1 μL using direct infusion.

Results and discussion

HR-TEM analysis

The morphology of Fe/Ni nanoparticles was determined by HR-TEM cross-sectional images illustrated in Fig. 2a, c. The TEM micrographs illustrate that the nanoparticles were uniformly and densely dispersed within the structure of the membrane. The particle sizes ranged from 59 to 66 nm for β-CD–G3-Ni/Fe and 47–58 nm for β-CD–G4-PSf-Ni/Fe. The mean diameters of the synthesised nanoparticles were 66 nm (Fig. 2b) and 59 nm (Fig. 2d) for β-CD–G3-Fe/Ni and β-CD–G4-PSf-Fe/Ni, respectively. The corresponding EDS (Fig. 2e) affirmed the presence of Fe/Ni within the membranes; the Ni and Fe were detected at 7.5 and 6.2 keV, respectively. Xu et al. (2005) also observed the same EDS line profile for Fe/Ni synthesised in polyacrylic acid/polyethersulfone membranes. The synthesised nanoparticles were bigger in size than the Fe/Ni nanoparticles individually prepared in generation 2 and generation 3 poly(propyleneimine) dendrimers which were in the quantum dot size range (1–4 nm) (Malinga et al. 2012). In this nanoparticle range, the Fe/Ni nanoalloy is said to have been formed inside the dendrimer cavities. In a similar study by Meyer and Bhattacharyya (2007) where Fe/Ni was imbedded on cellulose acetate membrane the particle sizes were found to range from 18 to 80 nm within the membrane cross-section. Formation of large nanoparticles sizes after synthesis in membranes has been reported is attributed to the fact that membranes have a more open structure (Meyer and Bhattacharyya 2007). Fe/Pd nanoparticles were also synthesised in polyacrylic acid embedded in a polyvinylidene fluoride membrane and these nanoparticles were reported to be in the range of 20–30 nm (Smuleac et al. 2010). However, the Fe/Ni nanoparticles synthesised in this study were still in the nanometer range (1–100 nm). EDS mapping shown in Fig. S6 gave evidence that the Fe and Ni were distributed uniformly in the membrane therefore bimetallic Fe/Ni nanoparticles were fabricated within the membranes.

AFM analysis

The surface morphology of the membranes were further characterised by AFM. The AFM topography and roughness measurements revealed that the change in roughness was a result of various membrane fabrication processes. In general, the morphology of the membranes changes after coating with cyclodextrin–dendrimer material followed by subsequent loading of Fe/Ni nanoparticles (Fig. 3b–e) as compared to the unmodified PSf (Fig. 3a). There is appearance of protrusions which form a ridge and valley structures and these morphological changes are complemented by the increase in roughness measurements observed in Fig. 4. The roughness increased in the following sequence: PSf < β-CD–G3-PSf and β-CD–G4-PSf < β-CD–G3-PSf-Fe/Ni and β-CD–G4-PSf-Fe/Ni. Wei et al. (2008) also found that the roughness

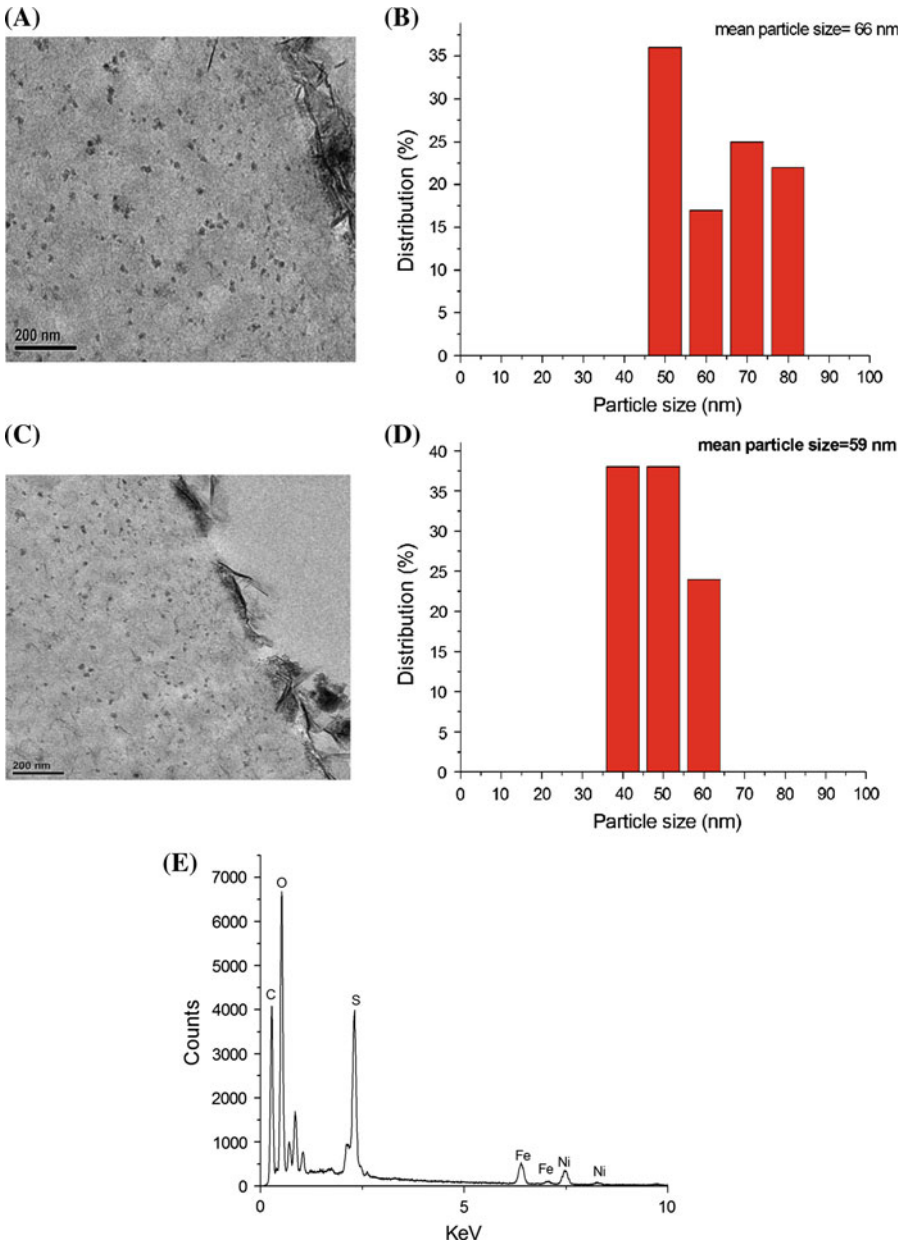

Fig. 2 HR-TEM for **a** β-CD–G3-PSf-Fe/Ni and **b** corresponding size distribution histogram. **c** β-CD–G4-PSf-Fe/Ni and **d** corresponding size distribution histogram. **e** EDS spectrum

increased after each fabrication process step, i.e., PSf–ultrafiltration membrane (5.5 nm) to PSf–ethanol membrane (5.7 nm) and finally PSf–hyperbranched polyether membranes (6.5–12.5 nm).

Water intake capacity, contact angle and pure water flux

Figure 5 shows that generally the water flux increased with increasing operating pressure and the water permeability was calculated using the four different applied pressures. Table 1 shows the water intake capacity, contact angle, porosity and pure water permeability of the β-CD–PPI–PSf with Fe/Ni nanoparticles. After nanoparticle incorporation of the β-CD–G3/G4-PSf membrane, the pure water permeability was found to decrease from 26 to 20 m h^{-1} MPa^{-1} for β-CD–G3-PSf-Fe/Ni and from 46 to 16 m h^{-1} MPa^{-1} for β-CD–G4-PSf-Fe/Ni. Introduction of the nanoparticle in the membrane matrix reduced pure

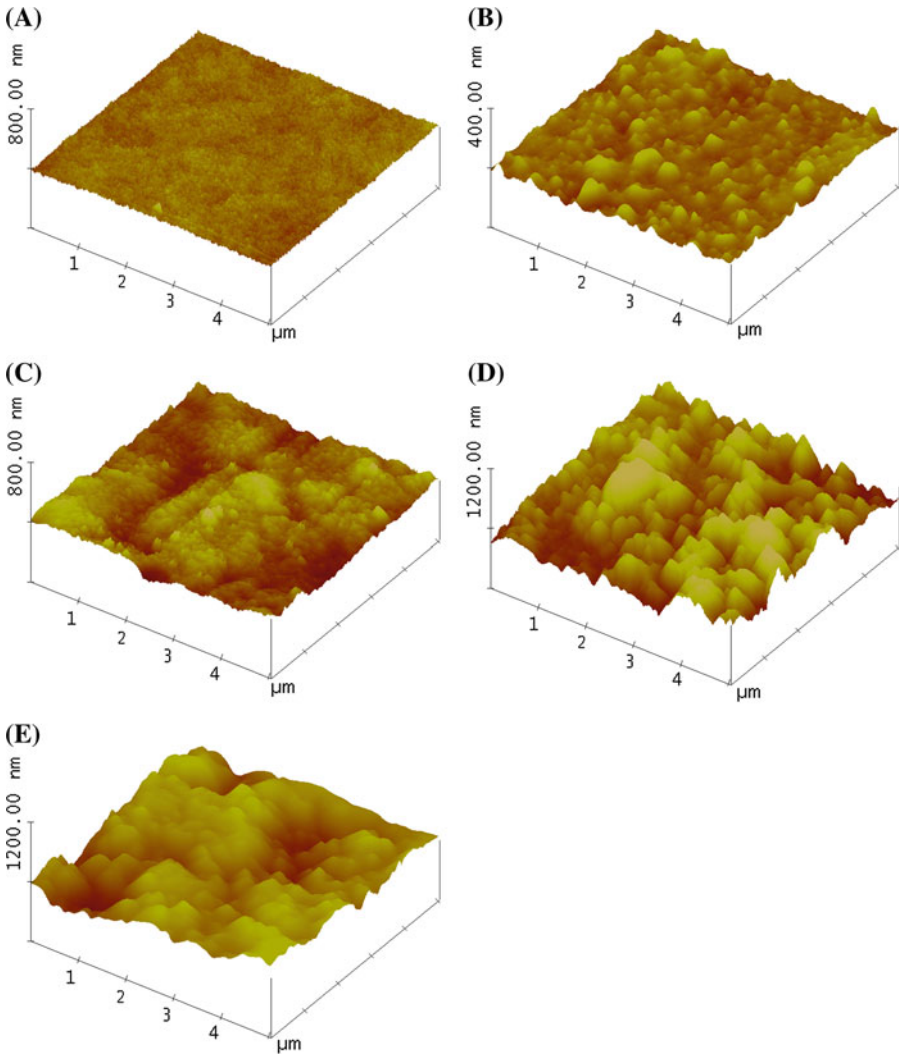

Fig. 3 AFM images of **a** Commercial PSf, **b** β-CD–G3-PSf, **c** β-CD–G4-PSf, **d** β-CD–G3-PSf-Fe/Ni, **e** β-CD–G4-PSf-Fe/Ni

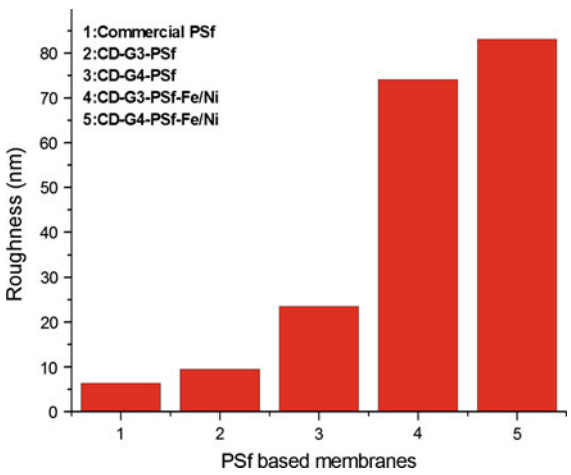

Fig. 4 Roughness of PSf-based membranes

water permeability. It also had a slight effect in the porosity and water content. This trend was also reported by Xu et al. (2005) when Fe/Ni nanoparticles were synthesised on polyacrylic acid polyether sulfone composite membrane. The pure water permeability of the polyacrylic acid/polyethersulfone (PAA/PES) with Fe/Ni had the lowest pure water permeability (0.27×10^{-4} cm^3 cm^{-2} bar^{-1} s^{-1}) as compared to the PAA/PES (3.03×10^{-4} cm^3 cm^{-2} bar^{-1} s^{-1}) and PES (76.9×10^{-4} cm^3 cm^{-2} bar^{-1} s^{-1}) (Xu et al. 2005). This was attributed to the resistance from the PAA coating layer and Fe/Ni immobilised in the membrane which affects the membrane pore matrix thus reducing the membrane pore size and porosity as demonstrated by our results (Table 1) (Xu et al. 2005). Smuleac et al. (2010) also obtained similar results

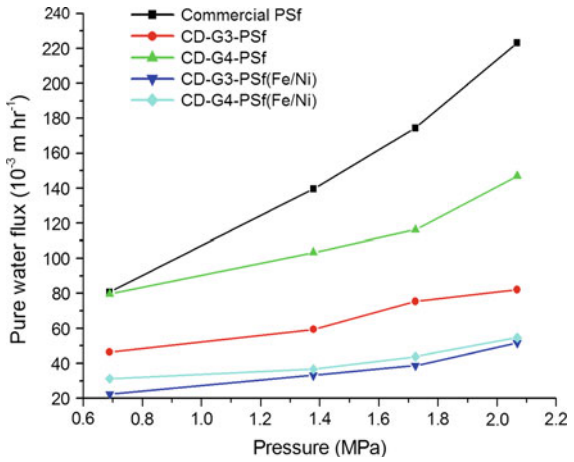

Fig. 5 The relationship between pure water flux and pressure

where the membrane permeability was found to decrease after each functionalisation step. The water permeability of bare polyvinylidene fluoride membrane was 4,824 × 10^{-4} cm^3 cm^{-2} s^{-1} bar^{-1} which decreased after the addition of iron to 468.7 × 10^{-4} cm^3 cm^{-2} s^{-1} bar^{-1}. Liu et al. (2010) also observed that as more components or layers are added to the membrane the pure water flux gradually decreases. In this study, crosslinking of the base membrane chitosan with activated carbon fibre and then dip coating in TiO_2 reduced the water flux from 34.35 to 19.56 m^3 m^{-2} h^{-1} (Liu et al. 2010). As illustrated in Table 1, there is decrease in permeability as components are introduced to the base PSf membrane. This is because the addition of nanoparticles reduces the membrane pore voids resulting in increase in resistance to water permeation. The membranes coated with nanoparticles maintained their hydrophilicity as the contact angle remained below that of PSf membrane.

Adsorptive removal of 2,4,6-trichlorophenol from water using PSf, β-CD–G3-PSf and β-CD–G4-PSf

Figure 6a shows 2,4,6-trichlorophenol adsorption of the base membrane (PSf), β-CD–G3-PSf and β-CD–G4-PSf. The removal efficiency of all the modified membranes was higher as compared to the PSf. As the reaction progressed the removal efficiencies decreased and reached a steady state. The modified membranes exhibit cyclodextrin–dendrimer nanocavities which can efficiently adsorb and encapsulate organic pollutants such as 2,4,6-trichlorophenol and this network system is present in all the membranes tested except PSf. In a study conducted by Li et al. (2011), polyamidoamine–cyclodextrin (PAMAM–CD) copolymer was found to have high adsorption efficiencies towards organic compounds such as 2,4,6-trichlorophenol (up to 92 %), 2,4-dichlorophenol (69 %) and poceau 4R (up to 99.6 %). It was concluded that these adsorbents were adsorbed to a large extent onto the surface or into the PAMAM–CD through interactions with nitrogen and oxygen available within the PAMAM–CD copolymer (Li et al. 2011). The high removal efficiency of modified membranes could be due to the interaction of 2,4,6-TCP with the nitrogen and oxygen available from the poly(propyleneimine)–cyclodextrin structure (Fig. 1a) which are active sites on the surface and within β-cyclodextrin–poly(propyleneimine) conjugate.

The corresponding solute fluxes of the membranes are depicted in Fig. 6b. The modified β-CD–PPI–PSf-Fe/Ni membranes exhibited a lower flux than β-CD–PPI–PSf and native PSf and this was attributed to the increase in the thickness of the thin film layer. The thickness of the selective layer estimated using Imagej software (Park et al. 2012) from the cross-section SEM images are shown in Fig. 7. The thickness of the film was found to be 45 and 39 μm β-CD–G3-PPI–PSf and β-CD–G4-PPI–PSf, respectively. Upon addition of Fe/Ni nanoparticle, the layer thickness increased to 259 μm for β-CD–G3-PPI–PSf-Fe/Ni and 109 μm for β-CD–G4-PPI–PSf-Fe/Ni. According to Singh et al. (2011), composite membranes which have a thicker selective layer exhibit a lower flux. In this study, composite membranes were prepared by crosslinking L-arginine and piperazine with trimesoyl chloride (1 and 0.5 %) (Singh et al. 2011). Membranes that were prepared using 0.5 % trimesoyl chloride with layer thickness of 0.4 μm exhibited a lower flux (Singh et al. 2011).

Dechlorination studies

One of the by-products formed during the dechlorination of 2,4,6-TCP is chloride ions (Fig. 8). The chloride ions generated by β-CD–G3-PSf-Fe/Ni were of lower concentration (∼0.5 mg L^{-1}) than β-CD–G4-PSf-Fe/Ni (∼1.5 mg L^{-1}) and remained at a constant concentration for the time tested. Low chlorine ions were reported by Schrick et al. (2002) for trichloroethylene dechlorination using Fe/Ni

Table 1 Water intake capacity, contact angle and pure water permeability for PSf, β-CD–PPI–PSf and β-CD–PPI–PSf-Fe/Ni membranes

Membranes	Water intake capacity (%)	Contact angle (°)	Porosity (%)	Pure water permeability (10^{-3} m h^{-1} MPa^{-1})	Thickness of surface layer (nm)
Commercial PSf	17	76	15	101	–
β-CD–G3-PPI–PSf	29	36	23	26	45
β-CD–G4-PPI–PSf	47	41	42	46	39
β-CD–G3-PSf-Fe/Ni	22	70	18	20	259
β-CD–G4-PSf-Fe/Ni	34	64	27	16	109

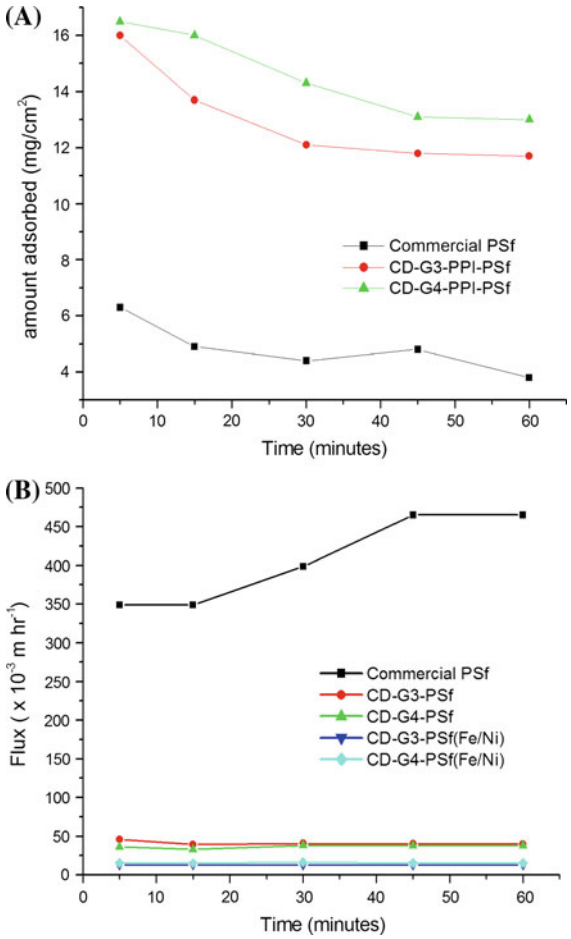

Fig. 6 **a** Adsorption efficiency of membranes overtime and **b** permeate flux at 0.69 MPa

nanoparticles. The low chloride ion concentration could be explained by the formation of insoluble chlorine containing hydroxides or adsorption of chloride by metal corrosion products (green rust) thus leading to low detection of the ion (Schrick et al. 2002). According to Smuleac et al. (2010), dechlorination reaction can be affected by two factors, i.e., iron oxide and Ni (or catalyst) deactivation due to coverage of oxide or hydroxides (Smuleac et al. 2010). Fe (0) can be corroded releasing ferrous ions and these ions cause an increase pH which in turn results in the formation of iron oxide (Yang et al. 2011; Meyer and Bhattacharyya 2007). The iron oxide deposits on the surface of the Fe (0) thus causing a decrease in dechlorination efficiency of the bimetallic system (Meyer and Bhattacharyya 2007: Yang et al. 2011). Therefore, the iron cannot produce hydrogen which can be deposited on the Ni to create active sites for dechlorination of 2,4,6-TCP. This can lower the dechlorination reactivity of the bimetallic Fe/Ni as seen for β-CD–G3-PSf-Fe/Ni membrane. Also as the 2,4,6-TCP is dechlorinated to other intermediate by-products, the nanocavities of the catalytic membranes maybe occupied by these molecules thus inhibiting further interaction of the 2,4,6-TCP with the catalytic membranes hence lowering dechlorination. This trend was also observed by Liu et al. (2010) where in situ photocatalytic regeneration of chitosan/activated carbon fibre/TiO_2 (CS/ACF/TiO_2) was affected by the presence of small molecules intermediate from oxidation of 2,4-dichlorophenol which inhibited the adsorption of 2,4-dichlorophenol onto the adsorption site of the CS/ACF/TiO_2 composite membrane.

To further confirm dechlorination, the permeate was analysed for the presence of other products using APCI-MS. The dechlorination products of 2,4,6-TCP were 4-chlorophenol (m/z 128.5), phenol ($m/z = 93.0$) and 2,4-dichlorophenol ($m/z = 162.9$) as illustrated in Fig. 9. Specifically for β-CD–G3-PSf-Fe/Ni 2,4-dichlorophenol was the only by-product detected after 60 min and for β-CD–G4-PSf-Fe/Ni, 4-chlorophenol (after 45 min) and phenol (after 60 min) were also detected. These products have also been reported by

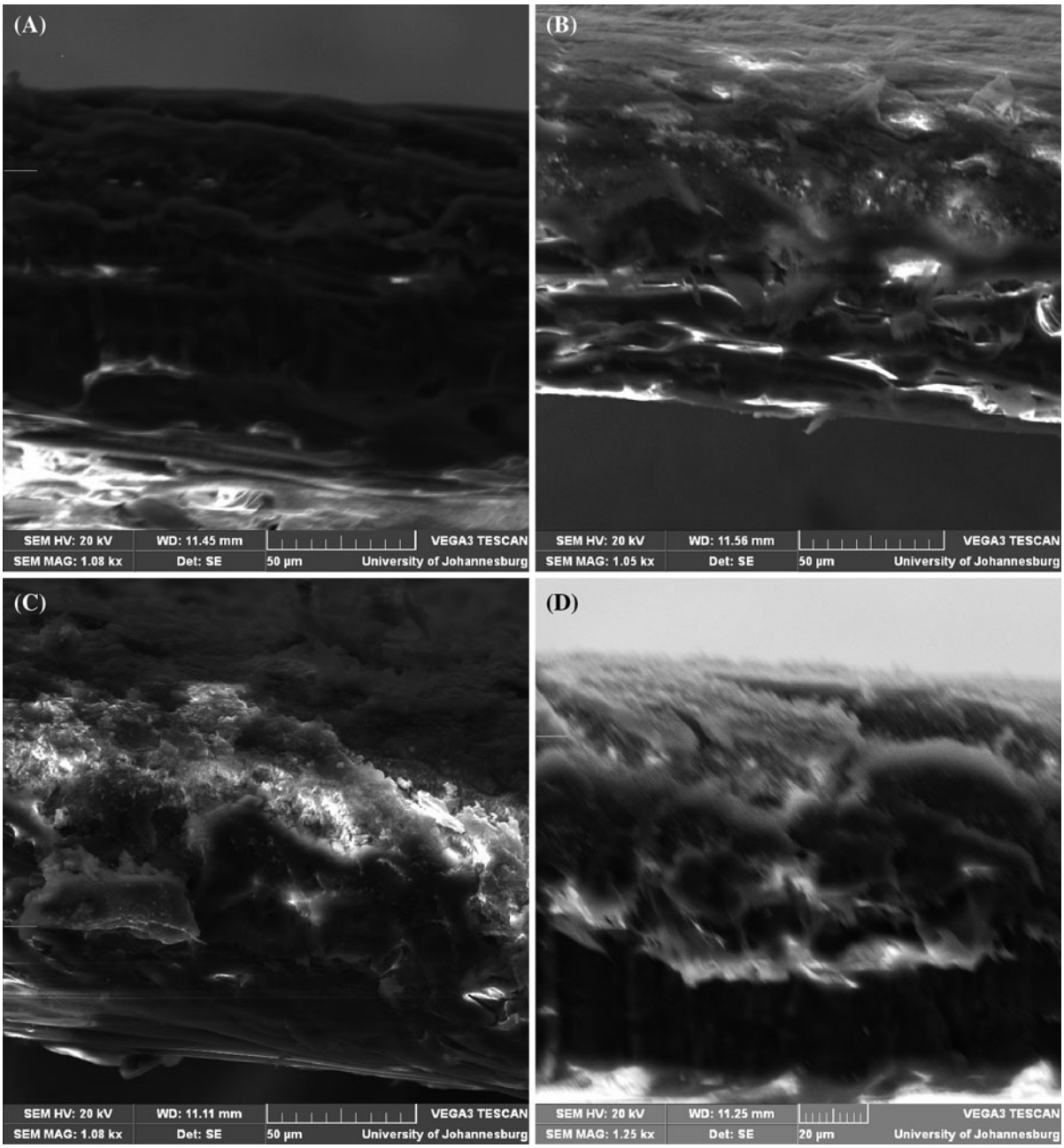

Fig. 7 Cross-section images for **a** β-CD–G3-PPI–PSf, **b** β-CD–G4-PPI–PSf, **c** β-CD–G3-PPI–PSf-NiFe, **d** β-CD–G4-PPI–PSf-NiFe

other researchers who have used different materials either for degradation or dechlorination of 2,4,6-TCP. Choi et al. (2007) detected phenol after reductive dechlorination of 2,4,6-TCP using a Fe/Pd-coated reactive barrier. Mun et al. (2008) used an acidogenic sequencing batch reactor to successfully dechlorinate 2,4,6-trichlorophenol to 4-chlorophenol. Gaya et al. (2010) used ZnO powder for the photocatalytic degradation of 2,4,6-trichlophenol, gas chromatography–mass spectrometry and high performance-liquid chromatography revealed the presence of 4-chlorophenol and phenol as the degradation intermediates and complete minerilisation of these intermediates was observed after 120 min.

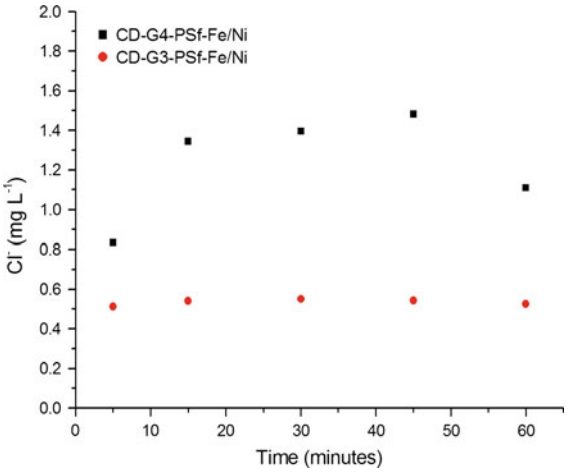

Fig. 8 Concentration of chlorine ions as a function of time for the dechlorination of 2,4,6-TCP under convection mode using β-CD–G3-PSf-Fe/Ni and β-CD–G4-PSf-Fe/Ni

Kinectic studies for the dechlorination of 2,4,6-TCP using batch studies

Data for kinetic evaluation based on the convective mode analysis were not used since the rate constant calculations are based on assumptions as reported by other investigators (Smuleac et al. 2010, 2011). Therefore, in this study we opted for the batch analysis to calculate the rate of the reaction and this was evaluated using Eq. 5 (Kuvarega et al. 2011) (Meyer and Bhattacharyya 2007):

$$\ln\frac{C}{C_0} = k_{\text{obs}}t \tag{5}$$

where k is the observed reaction rate constant, C and C_0 represent the concentration at initial time and time t, respectively. The values of k_{obs} obtained from the linear fit of the data are shown in Fig. 10. The rate constants for the dechlorination of 2,4,6-TCP was found to be 0.0015 and 0.0025 min^{-1} for β-CD–G3-PSf-Fe/Ni and β-CD–G4-PSf-Fe/Ni, respectively. These rate constants were found to be comparable with those reported by researchers who have prepared Ni/Fe nanoparticles using cellulose acetate membranes (Meyer and Bhattacharyya 2007). Meyer and Bhattacharyya (2007) reported a reaction rate constant of 0.29 h^{-1} (0.00483 min^{-1}) for the dechlorination of trichloroethylene for Fe/Ni nanoparticles embedded on cellulose acetate membranes which were prepared by phase inversion.

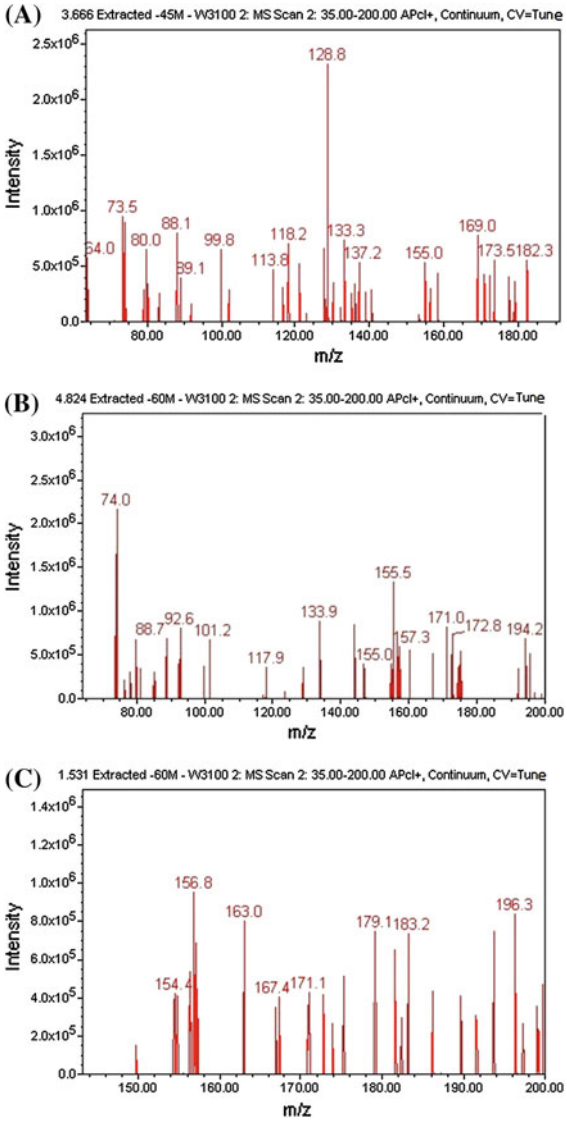

Fig. 9 APCI-MS analysis of 2,4,6-TCP dechlorination products **a** 4-chlorophenol, **b** phenol, **c** 2,4-dichlorophenol

Conclusion

The current study reports for the first time the synthesis of Fe/Ni nanoparticles in the presence of the β-cyclodextrin–dendrimer. HR-TEM demonstrated even distribution of the Fe/Ni nanoparticles and this feature is very important in the dechlorination of organic compounds such as 2,4,6-TCP. Dechlorination efficiency towards 2,4,6-TCP was comparable with other studies for the catalytic membranes and the presence of chloride ions, phenol, 4-chlorophenol and

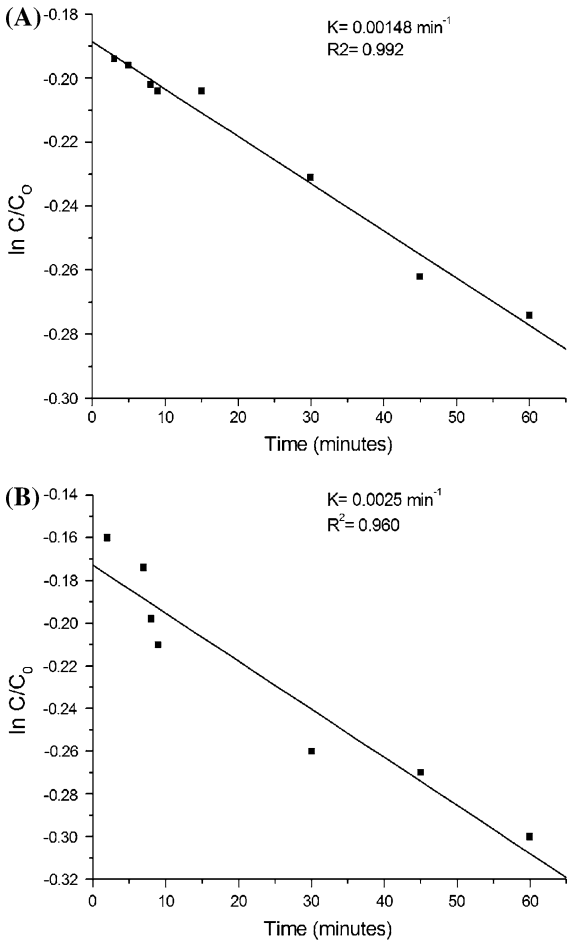

Fig. 10 Kinetics for the dechlorination of 2,4,6-TCP using β-CD–G3-PSf-Fe/Ni (**a**) and β-CD–G4-PSf-Fe/Ni (**b**)

2,4-dichlorophenol as by-products indicated that the membrane is feasible as a support for Fe/Ni nanoparticles.

Acknowledgments The author would like to thank the University of Johannesburg new generation scholarship for funding.

References

Abedini R, Mousavi SM, Aminzadeh R (2011) A novel cellulose acetate membrane using TiO2 nanoparticles: preparation, characterisation and permeation studies. Desalination 277:40–45

Adams FV, Nxumalo EN, Krause RWM, Hoek EMV, Mamba BB (2012) Preparation and characterization of polysulfone/β-cyclodextrin polyurethane composite nanofiltration membranes. J Membr Sci 405–406:291–299

Bai L, Wan H, Street SC (2009) Preparation of ultrafine FePt nanoparticles by chemical reduction in PAMAM-OH template. Coll Surf A 349:23–28

Bao C, Jin M, Lu R, Zhang T, Zhao YY (2003) Preparation of Au nanoparticles in the presence of low generational poly (amidoamine) dendrimer with surface hydroxyl groups. Mater Chem and Phys 81:160–165

Choi J, Kim Y, Choi SJ (2007) Reductive dechlorination and biodegradation of 2,4,6-trichlorophenol using sequential permeable reactive barriers: laboratory studies. Chemosphere 67:1551–1557

Diallo MS, Christie S, Swaminathan P, Jnr Johnson JH, 111 Goddard WA (2005) Dendrimer enhanced ultrafiltration.1. Recovery of Cu (II) from aqueous solutions using PAMAM dendrimers with ethylene diamine core and terminal NH_2 groups. Environ Sci Technol 39:1366–1377

Gaya UB, Abdullah AH, Hussein MZ, Zainal Z (2010) Photocatalytic removal of 2,4,6-trichlorophenol from water exploiting commercial ZnO powder. Desalination 263:176–182

Huang W, Kuhn JN, Tsung C, Zhang Y, Habas SE, Yang P, Somorjai GA (2008) Dendrimer templated synthesis of one nanometer Rh and Pt particles supported on mesoporous silica: catalytic activity for ethylene and pyrrole hydrogenation. Nano Lett 8:2027–2034

Jin XUE, Huang X, Hoek EMV (2009) Role of specific ion interactions in seawater RO membrane fouling by alginic acid. Environ Sci Technol 43:3580–3587

Kuvarega AT, Krause RWM, Mamba BB (2011) Nitrogen/palladium-codoped TiO_2 for efficient visible light photocatalytic dye degradation. J Phys Chem C 115:22110–22120

Lee HS, Im SJ, Kim JH, Kim HJ, Kim JP, Min BR (2008) Polyamide thin-film nanofiltration membranes containing TiO_2 nanoparticles. Desalination 219:48–56

Li N, Wei X, Mei Z, Xiong X, Chen S, Ye M, Ding S (2011) Synthesis and characterization of a novel polyamidoamine–cyclodextrin crosslinked copolymer. Carbohydr Res 346:1721–1727

Lianchao L, Baoguo W, Huimin T, Tianlu C, Jiping X (2006) A novel nanofiltration membrane prepared with PAMAM and TMC by in situ interfacial polymerization on PEK-C ultrafiltration membrane. J Membr Sci 269:84–93

Liu LF, Zhang PH, Yang FL (2010) Adsorptive removal of 2 4-DCP from water by fresh or regenerated chitosan/ACF/TiO_2 membrane. Sep Purif Technol 70:354–361

Malinga SP, Arotiba OA, Krause RW, Mapolie SF, Mamba BB (2012) Synthesis and characterisation of generation 2 and 3 poly(propyleneimine) dendrimer capped nanoalloy. Mater Lett 68:324–326

Meyer DE, Bhattacharyya D (2007) Impact of membrane immobilization on particle formation and trichloroethylene dechlorination for bimetallic Fe/Ni nanoparticles in cellulose acetate membranes. J Phys Chem B 111:7142–7154

Mun CH, Ng WJ, He J (2008) Acidogenic sequencing batch reactor start-up procedures for induction of 2,4,6-trichlorophenol dechlorination. Water Res 42:1675–1683

Park S, Cheedrala K, Diallo MS, Kim C, Kim IS, Goddard AW (2012) Nanofiltration membranes based on polyvinylidene fluoride nanofibrous scaffolds and crosslinked polyethyleneimine networks. J Nanopart Res. doi:10.1007/s11051-012-0884-7

Sarkar A, Carver PI, Zhang T, Merrington A, Bruza KJ, Rousseau JL, Keinath SE, Dvornic PR (2010) Dendrimer-based coatings for surface modification of polyamide reverse osmosis membranes. J Membr Sci 349:421–428

Schrick B, Blough JL, Jones AD, Mallouk TE (2002) Hydrodechlorination of trichloroethylene to hydrocarbons using bimetallic nickel-iron nanoparticles. Chem Mater 14:5140–5147

Scott RWJ, Wilson OM, Oh S, Kenik EA, Crooks RM (2004) Bimetallic palladium–gold dendrimer-encapsulated catalysts. J Am Chem Soc 4:7448–7453

Singh K, Ingole PG, Bhrambhatt H, Bhattachayra A, Bajaj HC (2011) Preparation, characterization and performance evaluation of chiral selective composite membranes. Sep Purif Technol 78:138–146

Smuleac V, Bachas L, Bhattacharyya D (2010) Aqueous-phase synthesis of PAA in PVDF membrane pores for nanoparticle synthesis and dichlorobiphenyl degradation. J Membr Sci 346:310–317

Smuleac V, Varma R, Sikdar S, Bhattacharyya D (2011) Green synthesis of Fe and Fe/Pd bimetallic nanoparticles in membranes for reductive degradation of chlorinated organics. J Membr Sci 379:131–137

Vassilev K, Turmanova S, Dimitrova M, Boneva S (2009) Poly (propylene imine) dendrimer complexes as catalysts for oxidation of alkenes. Eur Polym J 45:2269–2278

Wei X, Zhu L, Deng H, Xu Y, Zhu B, Huang Z (2008) New type of nanofiltration membrane based on crosslinked hyperbranched polymers. J Membr Sci 323:278–287

Weir M, Knecht M, Frenkel A, Crooks R (2010) Structural analysis of PdAu dendrimer-encapsulated bimetallic nanoparticles. Langmuir 26:1137–1146

Xu J, Dozier A, Bhattacharyya D (2005) Synthesis of nanoscale bimetallic particles in polyelectrolyte membrane matrix for reductive transformation of halogenated organic compounds. J Nanopart Res 7:449–467

Yang L, Lv L, Zhang S, Pan B, Zhang W (2011) Catalytic dechlorination of monochlorobenzene by Pd/Fe nanoparticles immobilized within a polymeric anion exchanger. Chem Eng J 178:161–167

DOI 10.1007/978-3-319-05041-6_5
Reprinted from the *Journal of Nanoparticle Research*, DOI 10.1007/s11051-013-1548-y

RESEARCH PAPER

A new approach for determination of fouling potential by colloidal nanoparticles during reverse osmosis (RO) membrane filtration of seawater

Ji Yeon Park · Sungil Lim · Kihong Park

Received: 10 December 2012 / Accepted: 26 February 2013 / Published online: 12 March 2013

Abstract A direct measurement of number concentration of colloidal nanoparticles (15–450 nm) in water was made with the membrane filtration-differential mobility analyzer technique, and its corresponding flux decline rate (FDR) was determined by laboratory-scale RO fouling test unit using varying number concentrations of silica nanoparticles in artificial seawaters. This relationship was used to predict fouling potential of colloidal nanoparticles in reverse osmosis (RO) membrane process of seawaters in RO plant. It was found that the FDR linearly increased with the increasing number of colloidal nanoparticles for the given concentration range and that the relationship between the number concentration and the FDR also depended on RO membrane surface properties. Data for estimated FDR values for natural seawaters after pretreatment showed a clear difference among samples, which is contrary to the pre-existing index such as silt density index and modified fouling index. Our data suggest that measurement of colloidal nanoparticles is useful for selection of proper pretreatment and successful operation of RO membrane process along with other particle fouling predictors accounting for large particles (>450 nm).

Keywords Colloidal nanoparticles · Counting · Fouling · Reverse osmosis · Membrane

Special Issue Editors: Mamadou Diallo, Neil Fromer, Myung S. Jhon

This article is part of the Topical Collection on Nanotechnology for Sustainable Development

J. Y. Park · S. Lim · K. Park (✉)
School of Environmental Science and Engineering, Gwangju Institute of Science and Technology (GIST), 1 Oryongdong, Buk-gu, Gwangju 500-712, Republic of Korea
e-mail: kpark@gist.ac.kr

Introduction

Particles and colloids in seawaters have been considered as one of major fouling sources during membrane filtration and reverse osmosis (RO) desalination processes, causing permeate flux decline at constant pressure filtration, increase in applied pressure at constant flux filtration, and decrease in membrane lifetime (Belfort et al. 1994; Zhu and Elimelech 1997; Vrijenhoek et al. 2001; Ng and Elimelech 2004). Microfiltration (MF) or ultrafiltration (UF) membrane filtration of seawaters for removal of particles and colloids was recently used as a pretreatment step during RO membrane desalination process (Zhang and Song 2000). However, the pretreated water still contained a significant amount of colloidal nanoparticles which were able to pass through the pre-filtration membranes (Luo and Wang 2001; Chua et al. 2003) and to be accumulated with other foulants on the RO

membrane surface due to concentration polarization, aggregation, and precipitation (Howe and Clark 2002), affecting the RO membrane fouling. The fouling limits the life of RO membrane and deteriorates its performance with decreasing permeate flux, requiring more energy and economical costs to keep a constant permeate flux (Howe and Clark 2002). A successful operation of the RO membrane process with adequate selection of pretreatment requires an accurate prediction of fouling by the colloidal nanoparticles.

A lot of effort has been made to predict membrane fouling by colloidal particles by developing fouling indices such as silt density index (SDI) (Belfort et al. 1994; Zhu and Elimelech 1997), which is a standard method, and modified fouling index (MFI) (Ng and Elimelech 2004). Since these methods used a 0.45-μm microfilter (Vrijenhoek et al. 2001), it was difficult to account for fouling caused by particles smaller than ~0.45 μm. It was also reported that colloidal fouling still occurred although such indices met (Butt et al. 1997; Van Paasen et al. 1998), suggesting that the SDI or MFI test would not be adequate for predicting fouling by colloidal nanoparticles smaller than 0.45 μm. Schippers et al. (1981) reported that colloidal nanoparticles smaller than 50 nm played a significant role in flux decline through RO membranes. In additional to the concentration of particles, the geometric properties (particle diameter, porosity, and so on) of cake on the membrane are also important factors to control fouling potential of water. Boerlage et al. (2002) developed a MFI–UF index which used the UF membrane instead of MF membrane to account for colloidal particles based on cake filtration (Boerlage et al. 2002). However, it took a longer time to determine the MFI–UF compared to the SDI and MFI, and a direct and real-time measurement of the colloidal nanoparticles in the feed water could not be performed by the MFI–UF method. Also, the MFI–UF used a dead-end flow mode, which was different from a cross flow mode employed in actual RO membrane desalination process.

The amount (i.e., number concentration) of colloidal nanoparticles could be considered as one of important water quality parameters and one of indicators for fouling potential, which has been little studied until now, due to difficulty in direct quantification of colloidal nanoparticles in water. In this study, on-line measurements of the number of colloidal nanoparticles in water were conducted. The colloidal nanoparticles were defined as insoluble solid nanoparticles not dissolved in water regardless of their chemical composition. The membrane filtration-differential mobility analyzer (MF-DMA) technique, which has been developed in our previous studies (Park et al. 2009a, b, 2011) was applied to determine the number and size of colloidal nanoparticles from 15 to 450 nm (particles/ml) (i.e., it is a on-line measurement technique having multipoint sampling capability). Then, we determined a relationship between the number concentration and fouling potential (i.e., the flux decline rate, FDR) of the colloidal nanoparticles (<450 nm) in the actual RO membrane filtration system by using silica nanoparticles with varying number concentrations in artificial seawaters. In addition to the quantification of colloidal nanoparticles in the feed water, it is essential to determine interaction between colloidal nanoparticles and RO membrane in the actual RO membrane process to better predict their fouling potential. Several commercial RO membranes having different surface properties were tested to investigate the interaction between colloidal nanoparticles and RO membranes. Further, the method was applied for natural seawaters sampled in several locations in Korea, and pretreated by various methods in RO pilot units. The measured fouling potential was also compared with pre-existing fouling indices. The developed relationship between N of colloidal nanoparticles (15–450 nm) and FDR should be useful for predicting a fouling potential caused by colloidal nanoparticles in the actual RO membrane processes, while the existing SDI and MFI could be used to predict fouling potential of large particles (>450 nm).

Experimental method

Figure 1a shows a schematic of the MF-DMA system to determine number concentration of insoluble nanoparticles (15–450 nm) in water. The details for the MF-DMA technique were described well in our previous paper (Park et al. 2011). Briefly, it separates insoluble colloidal particles from dissolved species by a series of MF and UF membrane filtration, and each solution before and after UF filtration was aerosolized by a constant output atomizer, and the aerosolized droplets were dried out by evaporating water leading to airborne particles (Ling et al. 2010). Then, particle

concentration in the air was subsequently measured with an aerosol measurement technique. The size and number of aerosolized particles were measured with the DMA and condensation particle counter (CPC). The established relationship between number concentrations of particles in air and in water by using various laboratory-generated particles of a known size or concentration was used to determine number concentrations of colloidal particles in water. Since seawaters typically contained a mixture of insoluble colloidal particles and dissolved species, their separation by MF and UF membranes was essential, and the effect of dissolved species on the quantification of insoluble nanoparticles was determined in our previous report. Thus, the MF-DMA technique was able to measure number concentration of insoluble suspended particles (particles/ml) ranging from 15 to 450 nm and mass concentration of dissolved species (ppm) in water almost in real time.

Figure 1b shows a laboratory-scale RO filtration unit to measure FDR (i.e., the FDR for water solutions with varying concentrations of colloidal nanoparticles in artificial or natural seawaters). A cross-flow mode was employed in the lab-scale RO fouling unit to simulate the actual RO membrane filtration process. The size of RO membrane was 14 cm long and 9.5 cm wide with a surface area of 125 cm^2. The feed water was circulated and pressurized by a high-pressure pump (Warner, USA) with a cross flow rate of 500 ml/min and an applied pressure at 5.5 MPa, respectively. The temperature of feed water was maintained at 25 °C by using a circulating cooling bath (J-LTB, JISICO, Korea). A high purity deionized (DI) water was first circulated through the RO membrane to remove any impurities from the membrane surface and to stabilize flow and pressure in the RO unit before test. Commercial RO membranes (TM-820, Toray, Japan), SWC-5 (Hydranautics, USA), and SW-30HR (Dow-Filmtec, USA) having different surface properties (roughness, surface charge, and contact angle) were tested in this study. All membranes were made of aromatic polyamide thin-film composite (TFC) with a salt rejection rate of more than 99 %. The membranes were stored in the DI water at 4 °C. The surface properties of these membranes, such as root mean square (RMS) roughness, surface charge, and contact angle, were summarized in Table 1 (Yang et al. 2009).

To derive a relationship between fouling potential and concentration of colloidal nanoparticles (15–450 nm), we used a mixture of an artificial seawater, mainly consisting of sea salt species (Sigma-Aldrich, USA) (the measured total dissolved solids is ~25,000 ppm), and insoluble silica particles (spherical particles with a density of 1.32 g/cm^3) (Nissan chemical, Japan) with varying concentrations. Measurement of their size distribution with the DMA and CPC showed that silica particles peaked at 121 nm (a high number of particles smaller than 100 nm with low number of particles larger than 300 nm) with a geometric standard deviation of 1.5–1.6. Natural seawaters were sampled from Pohang (Eastern Sea), Taean (Western Sea), Yeosu (Southern Sea), Mokpo (Western Sea), Gijang (Eastern Sea), and Changwon (Eastern Sea) in Korea. The artificial and natural seawaters were pre-filtered through 0.45-μm MF membrane (Advantec, Japan, Millipore, USA) to consider only small particles less than 0.45 μm, and concentrations of dissolved solids in artificial seawaters were measured with the TDS meter (OAKTON, Singapore). Our previous studies showed that after the 0.45-μm MF membrane filtration of the seawaters, insoluble particles larger than 0.45 μm were removed, while most of dissolved species passed through it (Park et al. 2009a, b, 2011). Also, natural seawaters pretreated by various methods (dissolved air flotation, DAF; double media filte, DMF; submerged MF membrane; and pressurized MF membrane] employed in actual RO pilot units were tested.

Measurements of SDI and MFI, which have been used for particle fouling indices, were also made by using an auto SDI test kit (GE Osmonics, USA) employing MF membranes (0.45 μm) (HAWP 04700, Millipore, USA) with a constant pressure at 206 kPa maintained by a booster pump (GE water tech, USA). For measurement of the MFI–UF, the dead-end membrane filtration unit with a polyethersulfone (PES)-UF membrane (GE Osmonics, USA) was used under a constant pressure of 1,241 kPa.

Results and discussion

Mixtures of silica nanoparticles with varying concentrations (a similar concentration range to pretreated natural seawaters by MF membrane) in artificial seawaters at a constant concentration of total dissolved solids (~25,000 ppm) were produced, and number concentrations of colloidal silica nanoparticles in

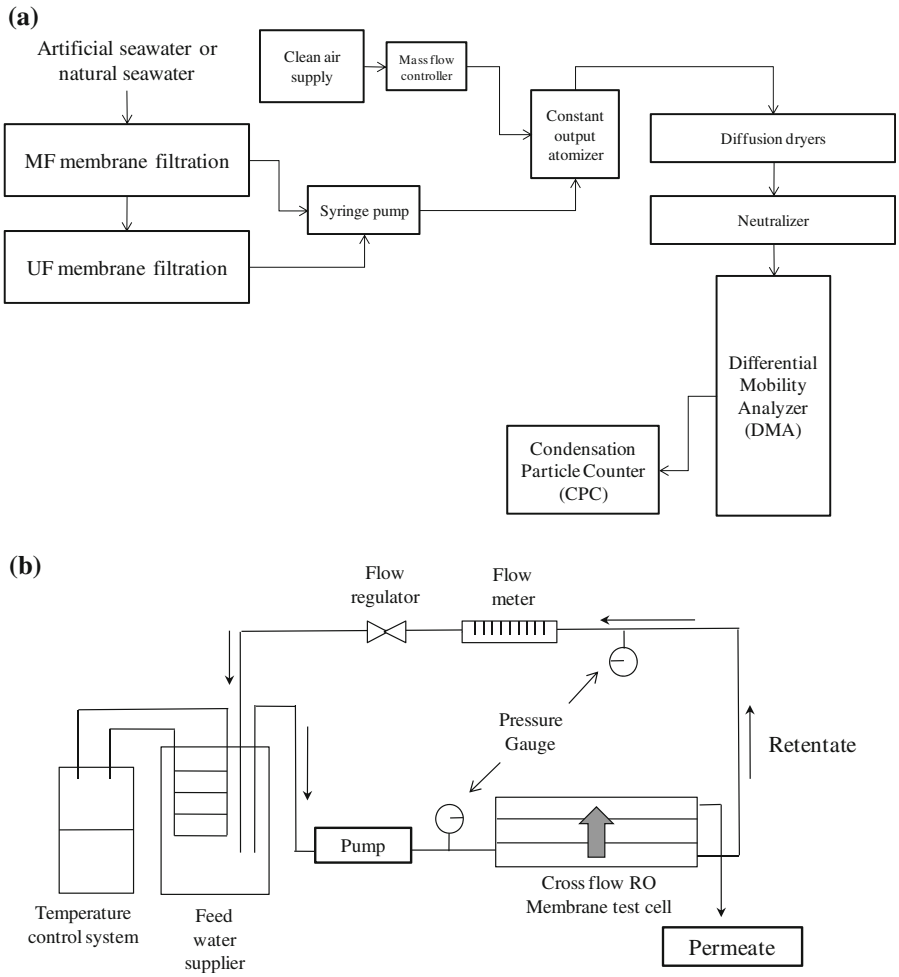

Fig. 1 Schematics for **a** the MF-DMA system and **b** laboratory-scale RO membrane fouling test unit

Table 1 Surface properties (surface roughness, surface charge, and contact angle) of the RO membranes tested in this study

[a] RO membrane used for natural seawaters

RO membrane model name	Surface roughness (nm)	Surface charge (mV)	Contact angle (°)
TM-820	77.56	−18.31	79.00
SWC-5	127.42	−21.71	72.40
SW-30HR	87.31	−30.11	24.00
LP-4040[a]	192.91	−29.45	70.40

water were determined by the MF-DMA technique. Also, above mixtures were sent to laboratory-scale RO filtration unit to determine permeate flux as a function of time. The permeate flux changes as a function of time for different samples through RO membrane (SWC-5) are shown in Fig. 2a. Data showed that the permeate flux decreased most rapidly for the mixture having the highest silica concentration (i.e., 1.75×10^{12} particles/ml), while for artificial seawater sample without silica nanoparticles the flux decreased slowly. The initial permeate flux was found to be strongly dependent on the concentration of silica nanoparticles. By using the permeate flux data at the initial time period, the FDR can be calculated by a non-linear fitting of the data developed in previous studies (Wang et al. 2007; Choi et al. 2009). Figure 2b shows the FDRs for solutions having different number concentration of silica particles (particles/ml) in

artificial seawater. It is evident that the FDR increased with increasing concentration of insoluble silica particles, suggesting that the number of colloidal nanoparticles (15–450 nm), which could be considered as one of important feed water quality parameters, can play a role in the RO fouling.

In addition to the water quality parameter (i.e., number concentration of colloidal nanoparticles in water), surface properties of the RO membrane, which was exposed to interact with particles, may affect fouling during the RO filtration process. To examine this, several RO membranes (TM-820, SWC-5, and SW-30HR) having different surface properties were tested. The surface properties of RO membranes used here were shown in Table 1. We found that as the number concentration of silica particles increased, the FDR increased, and that the slopes varied for different types of RO membranes as shown in Fig. 3a. As shown in Fig. 3b and Table 1, we found that the FDR (i.e., fouling potential caused by colloidal silica nanoparticles) was much higher for the SWC-5 RO membrane having the highest surface roughness among tested RO membranes. Also, we found that the FDR was lower for the RO membrane (SW-30HR) having a high negative surface charge and a low contact angle (i.e., hydrophilic). Our results are consistent with previous reports although their focus was not colloidal nanoparticles (Brauns et al. 2002; Song et al. 2004; Khirani et al. 2006; Li and Elimelech 2006; Yu et al. 2010). The membrane with the higher

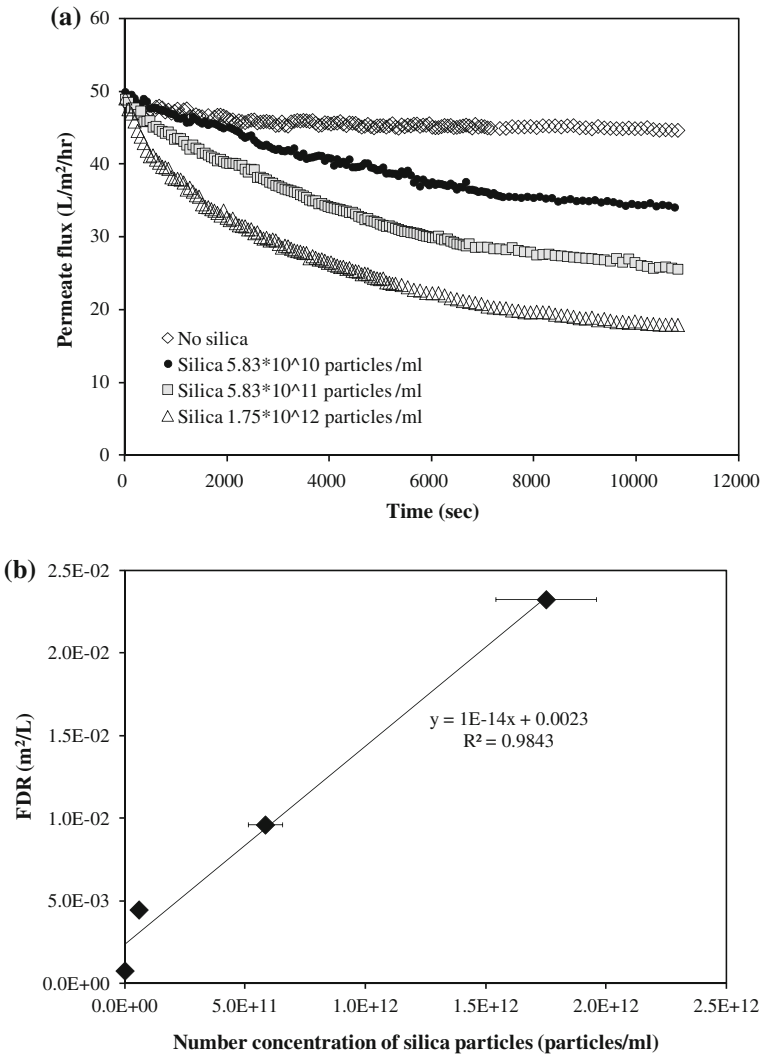

Fig. 2 **a** Time-dependent permeate fluxes through RO membrane (SWC-5) for mixtures of silica particles with varying number concentrations and artificial seawaters with a constant concentration of total dissolved solids (25,000 ppm), and **b** FDR versus number concentration

surface roughness caused more colloidal fouling due to the valley clogging than that having the smooth surface (Boussu et al. 2007). Membrane with high negative surface charge had a low fouling potential because of the repulsive force between the foulants having negative charge and membrane surface (Yang et al. 2009). In addition, a strong hydrophobic interaction between the foulants and membrane surface could cause multi-fouling layers on the membrane surface leading to increase fouling potential (Yang et al. 2009; Boussu et al. 2007).

Since the relationship between the number concentration of silica nanoparticles (15–450 nm) and their fouling potential also depended on RO membrane surface properties, the *N* was further normalized by values of surface roughness, surface negative charge, and contact angle. It was found that for current RO membranes tested here, the normalization of the number by the inverse of surface roughness and surface negative charge [i.e., *N*/(1/roughness × charge)] led to less dependence of the FDR on RO membrane surface properties as shown in Fig. 3b. Our data suggested that in addition to the feed water quality parameter, the consideration of surface property of the RO membrane accounting for the interaction between nanoparticles and the specific RO membrane is important to predict RO fouling in RO plant using various types of RO membranes. This might occur because cake filtration, which is also one of important particle fouling mechanisms in RO membrane filtration, may be affected by the roughness and surface charge of the membrane especially in early

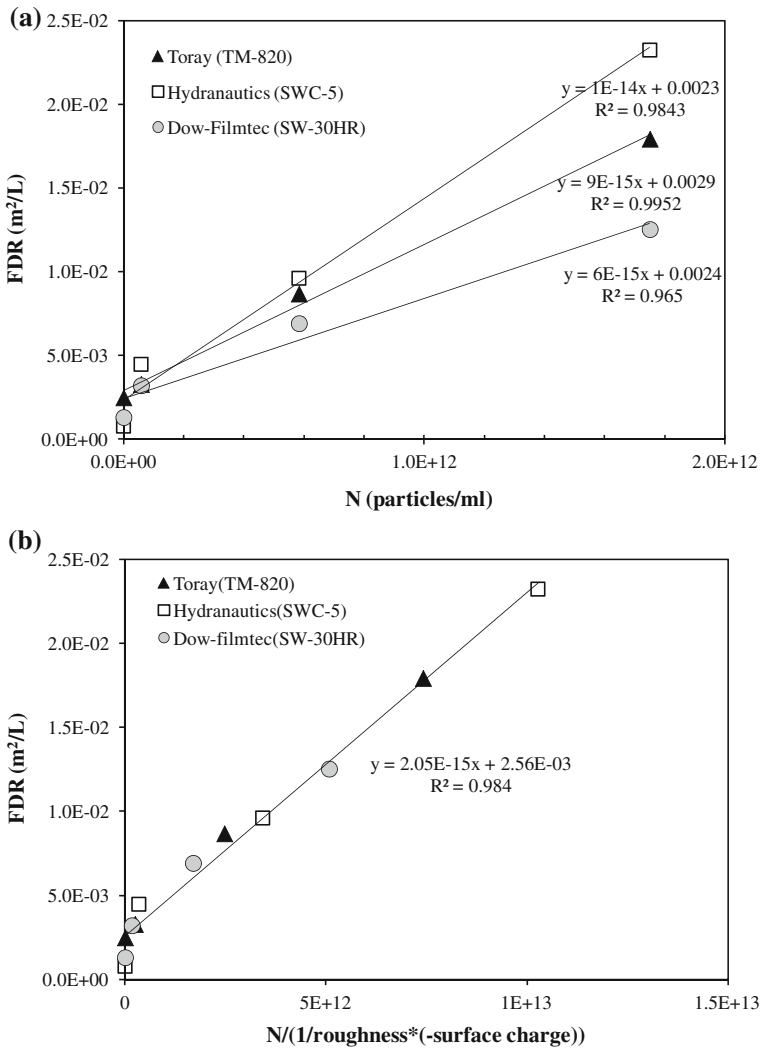

Fig. 3 **a** FDR versus *N* through RO membranes having different surface properties and **b** FDR versus *N* normalized by the inverse of surface roughness and charge of RO membranes

stages of filtration. The size distribution of particles can also play a role in the cake formation with concentration polarization, having an impact on the extent of membrane fouling. Throughout this study, the fouling potential of colloidal nanoparticles less than 450 nm was investigated.

The FDR values for MF membrane-filtered natural seawaters sampled at the Eastern Sea (Pohang), Western Sea (Taean), and Southern Sea (Yeosu) around the Korean peninsula were determined by using measured number concentrations (*N*) of insoluble nanoparticles, as shown in Fig. 4. The FDR of seawater sampled from Pohang was approximately two times higher than those from Taean and Yeosu, while mass concentrations of total dissolved solids among seawaters were invariant (23,358–24,640 ppm) within 3 %. Data suggest that the seawater from Pohang had the highest fouling potential by colloidal nanoparticles. Compared to other sites, the Pohang sampling site was located near heavy industrial complex where probably anthropogenic sources for colloidal nanoparticles would be abundant. As shown in Fig. 4, the MFI–UF also had a similar trend to the FDR, which has been known to better predict fouling potential of colloidal nanoparticles than the SDI and MFI, although it took much longer time to determine the MFI–UF compared to the *N*. In addition to the estimated FDR from the *N*, the actual FDR was measured for several samples, which also took a longer time compared to the *N*. The correlation coefficient between the estimated and measured ones was 0.93. However, there is a significant difference in the FDR values between the estimated and measured ones. Note that the FDR was estimated by using the relationship obtained from the silica particles in the artificial seawater (see Fig. 3). A new relationship should be needed by using various natural seawaters to have a value close to the measured FDR.

The MFI and SDI (5 min data) for natural seawaters before and after pretreatment (MF membrane-filtered) were measured. Without pretreatment, a distinct difference of the SDI and MFI was observed among different sampling sites. For example, the MFI was 98.5, 425.6, and 5.7 for natural seawaters from Pohang, Taean, and Yeosu, respectively. The SDI was 12.1 and 8.6 for natural seawaters sampled Pohang and Yeosu, respectively. The SDI was not available for the Taean sample due to high concentration of large particles. Data suggest that the SDI and MFI are adequate to predict fouling potential of large particles (>450 nm). After pretreatment that removed particles larger than 450 nm, the low values of SDI and MFI were found, and no significant difference among sites was observed, as shown in Fig. 5. However, the FDR estimated from the measured *N* varied significantly among seawaters sampled in different sites. Data suggest that the *N* should be useful to predict RO fouling caused by such small colloidal nanoparticles that can exist after pretreatment, which is difficult to be predicted by the SDI and MFI.

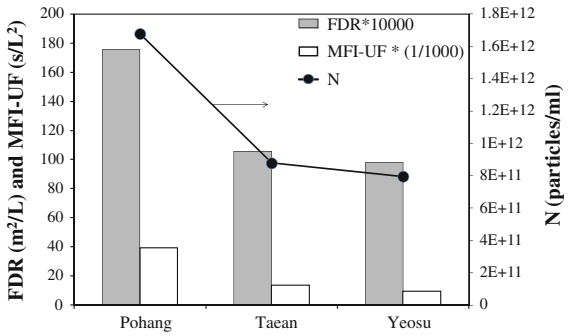

Fig. 4 Comparison of FDR, MFI–UF, and *N* for MF membrane-filtered natural seawaters sampled in Pohang, Taean, and Yeosu sampling sites in Korea

Effects of pretreatment methods (DAF, DMF, submerged MF membrane, and pressurized MF membrane methods employed in actual RO pilot units (Gijang and Changwon RO pilot units in Korea) on FDR were investigated (Fig. 6). FDR values were determined by using the measured *N* of the colloidal nanoparticles (15–450 nm) for pretreated seawaters. As shown in Fig. 6, the use of pressurized MF membrane method had the lowest fouling potential.

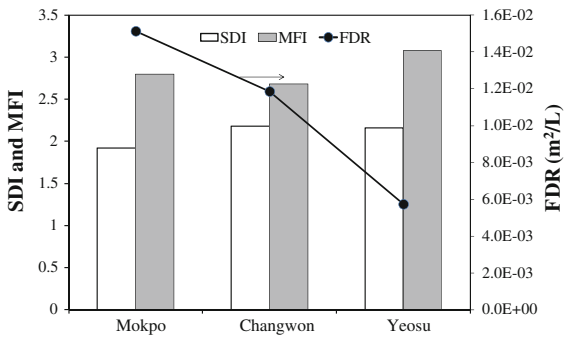

Fig. 5 Comparison of SDI, MFI, and FDR for MF membrane-filtered seawaters sampled in Mokpo, Changwon, and Yeosu sampling sites in Korea

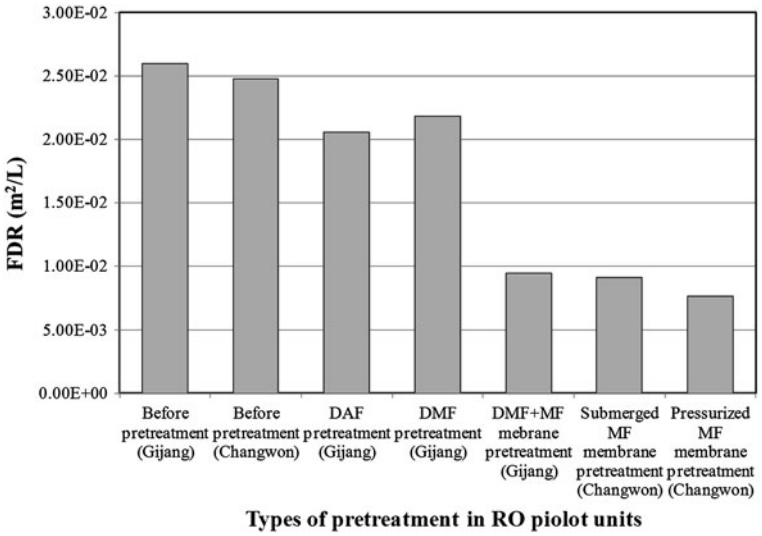

Fig. 6 FDR values for pretreated seawaters by various methods such as dissolved air flotation (DAF), double media filter (DMF), submerged MF membrane, and pressurized MF membrane systems employed in actual RO pilot units (Gijang and Changwon RO pilot units in Korea)

Our data suggest that the current measurement method should be useful to rapidly evaluate various pretreatment techniques in RO desalination processes and that the membrane filtration should be the most useful pretreatment method to remove nanoparticles.

Conclusions

A direct measurement of number concentration of colloidal nanoparticles (15–450 nm), which can be considered as one of important feed water quality parameters, was made, and then the relationship between the measured *N* and FDR in the actual RO membrane filtration system was determined, leading to rapidly predict fouling potential of colloidal nanoparticles. It was found that the relationship between the *N* and their fouling potential also depended on RO membrane surface properties, and that the normalization of *N* by the inverse of surface roughness and surface negative charge provided better prediction of colloidal nanoparticle fouling in the actual RO membrane process using various RO membranes. Results for FDR for various natural seawaters suggested that along with other particle fouling index accounting for large particles (>450 nm), the *N* can be used as a useful tool for real-time monitoring of colloidal nanoparticles in feed water, the selection of proper pretreatment, and the successful operation of RO membrane desalination process in RO plant.

Acknowledgments The research described in this paper was supported by the Center for Seawater Desalination (B01-05-03) and by the National Research Foundation of Korea (NRF) Grant (National Leading Research Laboratory) funded by the Korea Government (No. 2012-0006318). We appreciate Dr. Youngbaem Yu (Korea University, Seoul, Korea) for his assistance on the FDR measurement.

References

Belfort G, Davis RH, Zydney AL (1994) The behavior of suspensions and macromolecular solutions in crossflow microfiltration. J Membr Sci 96(1–2):1–58

Boerlage SFE, Kennedy MD, Dickson MR, El-Hodali DEY, Schippers JC (2002) The modified fouling index using ultrafiltration membranes (MFI-UF), characterization, filtration mechanisms and proposed reference membrane. J Membr Sci 197(1–2):1–21

Boussu K, Belpaire A, Volodin A, Van Haesendonck C, Van der Meeren P, Vandecasteele C, Van der Bruggen B (2007) Influence of membrane and colloid characteristics on fouling of nanofiltration membranes. J Membr Sci 289(1–2):220–230

Brauns E, Hoff EV, Molenberghs B, Dotremont C, Doyen W, Leysen R (2002) A new method of measuring and presenting the membrane fouling potential. Desalination 150(1–3):31–43

Butt FH, Rahman F, Baduruthamal U (1997) Characterization of foulants by autopsy of RO desalination membranes. Desalination 114(1):51–64

Choi J-S, Hwang T-M, Lee S, Hong S (2009) A systematic approach to determine the fouling index for a RO/NF membrane process. Desalination 238(1–3):117–127

Chua KT, Hawlader MNA, Malek A (2003) Pretreatment of seawater: results of pilot trials in Singapore. Desalination 159(1):225–243

Howe KJ, Clark MM (2002) Fouling of microfiltration and ultrafiltration membranes by natural waters. Environ Sci Technol 36(16):3571–3576

Khirani S, Aim RB, Manero M (2006) Improving the measurement of the Modified Fouling Index using nanofiltration membranes (NF-MFI). Desalination 191(1–3):1–7

Li Q, Elimelech M (2006) Synergistic effects in combined fouling of a loose nanofiltration membrane by colloidal materials and natural organic matter. J Membr Sci 278(1–2):72–82

Ling TY, Wang J, Pui DY (2010) Measurement of retention efficiency of filters against nanoparticles in liquids using an aerosolization technique. Environ Sci Technol 44:774–779

Luo M, Wang Z (2001) Complex fouling and cleaning-in-place of a reverse osmosis desalination system. Desalination 141(1):15–22

Ng HY, Elimelech M (2004) Influence of colloidal fouling on rejection of trace organic contaminants by reverse osmosis. J Membr Sci 244:215–226

Park J, Cho J, Park K (2009a) Evaluation of quantitative performance of the membrane filtration-differential mobility analyzer (MF-DMA) counting technique to determine suspended particles and dissolved solids in water. Desalination 247(1–3):316–325

Park K, Park J, Lee S, Cho J (2009b) Measurement of size and number of suspended and dissolved nanoparticles in water for evaluation of colloidal fouling in RO membranes. Desalination 238(1–3):78–89

Park J, Lim S, Han S, Park K (2011) Quantification of a mixture of insoluble submicrometer particles and dissolved solids in water using membrane filtration and aerosolization method. Aerosol Sci Technol 45(8):1010–1018

Schippers JC, Hannemaayer JH, Smolders CA, Kostense A (1981) Predicting flux decline in reverse osmosis membrane. Desalination 38:339–348

Song L, Chen KL, Ong SL, Ng WJ (2004) A new normalization method for determination of colloidal fouling potential in membrane processes. J Colloid Interface Sci 271(2):426–433

Van Paasen JAM, Kruithof JC, Bakker SM, Schoonenberg Kegel F (1998) Integrated multi-objective membrane systems for surface water treatment: pretreatment of nanofiltration by riverbank filtration and conventional ground water treatment. Desalination 118(1–3):239–248

Vrijenhoek EM, Hong S, Elimelech M (2001) Influence of membrane surface properties on initial rate of colloidal fouling of reverse osmosis and nanofiltration membranes. J Membr Sci 188(1–2):115–128

Wang Z, Chu J, Zhang X (2007) Study of a cake model during stirred dead-end microfiltration. Desalination 217(1–3):127–138

Yang J, Lee S, Lee E, Lee J, Hong S (2009) Effect of solution chemistry on the surface property of reverse osmosis membranes under seawater conditions. Desalination 247(1–3):148–161

Yu Y, Lee S, Hong K, Hong S (2010) Evaluation of membrane fouling potential by multiple membrane array system (MMAS): measurements and applications. J Membr Sci 362(1–2):279–288

Zhang M, Song L (2000) Mechanisms and parameters affecting flux decline in cross-flow microfiltration and ultrafiltration of colloids. Environ Sci Technol 34(17):3767–3773

Zhu X, Elimelech M (1997) Colloidal fouling of reverse osmosis membranes: measurements and fouling mechanisms. Environ Sci Technol 31(12):3654–3662

DOI 10.1007/978-3-319-05041-6_6
Reprinted from the *Journal of Nanoparticle Research*, DOI 10.1007/s11051-012-0776-x

RESEARCH PAPER

Multiwalled carbon nanotubes decorated with nitrogen, palladium co-doped TiO_2 (MWCNT/N, Pd co-doped TiO_2) for visible light photocatalytic degradation of Eosin Yellow in water

Alex T. Kuvarega · Rui W. M. Krause · Bhekie B. Mamba

Received: 14 November 2011 / Accepted: 10 February 2012 / Published online: 24 March 2012

Abstract Multiwalled carbon nanotube (MWCNT/N), Pd co-doped TiO_2 nanocomposites were prepared by calcining the hydrolysis products of the reaction of titanium isopropoxide, $Ti(OC_3H_7)_4$ containing multiwalled carbon nanotubes with aqueous ammonia. The prepared samples were characterised by Fourier transform infrared spectroscopy, Raman spectroscopy, thermogravimetric analysis, diffuse reflectance UV–Vis spectrophotometry (DRUV–Vis), XRD, scanning electron microscopy (SEM) and transmission electron microscopy (TEM). DRUV–Vis analysis confirmed the red shift in the absorption edge at lower MWCNT percentages. SEM and TEM images showed the complete coverage of the MWCNTs with clusters of anatase TiO_2 at low MWCNT percentages. Higher MWCNT levels led to their aggregation and consequently poor coverage by N, Pd co-doped TiO_2. The photocatalytic activities of the nanocomposites were monitored by photodegradation of Eosin Yellow under simulated solar and visible light irradiation ($\lambda > 450$ nm). Irradiation with simulated solar radiation gave higher dye-degradation rates compared to visible radiation. The optimum MWCNT weight percentage in the composites was found to be 0.5. High degradation-rate constants of 3.42×10^{-2} and 5.18×10^{-3} min^{-1} were realised for the 0.5% MWCNT/N, Pd co-doped TiO_2 composite, using simulated solar light and visible light, respectively.

Keywords Nanocomposite · Photocatalysis · Photodegradation · Visible light · Solar light · Sustainable nanotechnology

Special Issue Editors: Mamadou Diallo, Neil Fromer, Myung S. Jhon

This article is part of the Topical Collection on Nanotechnology for Sustainable Development

A. T. Kuvarega · R. W. M. Krause (✉) · B. B. Mamba
Department of Applied Chemistry, UJ Center for Nanomaterials Science, University of Johannesburg, P. O. Box 17011, Doornfontein, Johannesburg 2028, South Africa
e-mail: rkrause@uj.ac.za

R. W. M. Krause
DST/NRF Centre of Excellence in Strong Materials, University of the Witwatersrand, Private Bag 3, Wits, Johannesburg 2050, South Africa

Introduction

Carbon nanotubes (CNTs) exhibit excellent mechanical, electrical and magnetic properties as well as nanometre-scale diameter and high aspect ratio, which make them suitable candidates to mitigate the ever-increasing environmental challenges. They can be considered as good supports for semiconductors with photocatalytic properties because of their chemical stability, high mechanical strength and nanoporous character, which favour the diffusion of reacting agents. They also show great potential for sensor application, composites and as membrane materials (Baughman et al. 2002; Kim et al. 2007). To date,

many types of inorganic and organic molecules have been successfully decorated on CNTs using various methods. These composites not only exhibit unique intrinsic properties, such as electronic, mechanical, adsorption and thermal properties, but also display cooperative or synergetic effects (An et al. 2007).

The published literature on CNT/TiO_2 nanocomposites has attracted the attention of scientists because of their many and varied applications, inter alia, the purification of contaminated water (An et al. 2007; Gao et al. 2009; Wang et al. 2005). CNTs can efficiently adsorb pollutants in water and also increase the photocatalytic activity of TiO_2 by acting as electron traps, thus stabilising the charge carriers and suppressing the rate of electron–hole recombination. Accordingly, CNTs/TiO_2 composites can be used as promising materials for environmental cleaning. The coupling of TiO_2 with CNTs has been shown to provide a cooperative and synergistic effect which can enhance the overall efficiency of the photocatalytic process. The conductive structure of the CNT scaffold is believed to favour the separation of the photo-generated electron–hole pairs through the formation of heterojunctions (Schottky barrier) at the CNT/TiO_2 interface. TiO_2 is an n-type semiconductor; however, in the presence of CNTs, photogenerated electrons may move freely towards the CNT surface, which may have a lower Fermi level, leaving an excess of valence band holes in the TiO_2 to migrate to the surface and react. Under such circumstances, the TiO_2 effectively behaves as a p-type semiconductor, which is highly photoactive. CNTs can provide spatial confinement of TiO_2 and large supporting surface areas, leading to faster photocatalytic redox reactions (Gao et al. 2009; Woan et al. 2009).

Photocatalysis by TiO_2-based semiconductors has received lots of attention in the past few decades with the final goal of efficiently converting solar light energy into useful chemical energy. The effective utilisation of clean, safe and abundant solar energy should lead to promising solutions not only for energy issues due to the exhaustion of natural energy sources, but also for environmental pollution remediation (Anpo and Takeuchi 2003). In general, researchers are focussing on two aspects in order to improve the performance of TiO_2: improving the photocatalytic efficiency and extending the absorption edge of the semiconductors from the UV to the visible region (Kafizas et al. 2009). The photocatalytic reactivity of semiconducting TiO_2 is remarkably enhanced by the doping of small amounts of transition metals such as Fe, Cu, V, Mo or Ni and noble metals such as Pt, Pd, Os, Ir, Ru or Rh. The Fermi levels of these metals are lower than that of TiO_2, therefore photoexcited electrons can be transferred from the conduction band to metal particles deposited on the surface of TiO_2. These metals reduce the possibility of electron–hole recombination, resulting in efficient charge separation and higher photocatalytic reaction rates (Anpo and Takeuchi 2003; Rupa et al. 2009).

One of the most promising and widely investigated materials for visible photocatalysis is nitrogen-doped TiO_2, although other anions such as F, B, C, P and S have also been found to enhance the photocatalytic activity of TiO_2 in the visible range. This is because the nitrogen atom has a similar size to oxygen atom as well as low ionization energy so it can easily substitute O in TiO_2. This results in band gap narrowing as oxygen atoms are substituted by nitrogen due to mixing of the N 2*p* orbital with O 2*p* orbital or creation of additional N 2*p* states within the band gap of titania. Nitrogen-doped TiO_2 has been shown to exhibit higher photocatalytic activity under visible light irradiation (Lin et al. 2005), although there are still many theories on the modification mechanism of TiO_2 doped with nitrogen.

There are a number of methods that can be used to fabricate CNT/TiO_2 composite materials including, mechanical mixing of TiO_2 and CNTs, sol–gel synthesis of TiO_2 in the presence of CNTs, electro-spinning methods, electrophoretic deposition and chemical vapour deposition (Gao et al. 2009; Woan et al. 2009; Jitianu et al. 2004; Fan et al. 2006; Yu et al. 2005). The uniformity of the oxide coating and the physical properties of the composite materials may vary depending on the preparation method used. Though uniform coating of TiO_2 on CNTs may be achieved by chemical vapour deposition and electro-spinning methods, these techniques are not simple. They require specialised equipment and it may be difficult to quantify the ratio between composite compounds. Sol–gel methods are still the most preferred, although they usually lead to a heterogeneous, non-uniform coating of CNTs by TiO_2, showing bare CNT surfaces and random aggregation of TiO_2 onto the CNT surfaces (Gao et al. 2009).

The photocatalytic properties of CNT/TiO_2 composite photocatalysts still remain largely unexplored although considerable efforts have been devoted to the coating of TiO_2 nanoparticles on CNTs. There are only a few reports on coating non-metal–metal co-doped

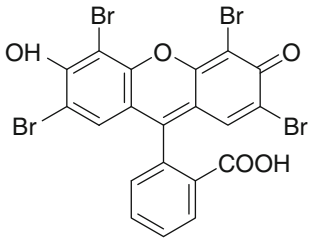

Fig. 1 Chemical structure of Eosin Yellow

TiO_2 on CNTs (Woan et al. 2009; Kang et al. 2007) for applications in water decontamination. To the best of our knowledge, there are no reports on supporting N, Pd co-doped TiO_2 on MWCNTs. Such nanocomposites have the potential to show the synergetic effect of the combination of N, Pd and MWCNTs on the catalytic performance of the TiO_2 on oxidative decomposition of organic pollutants in water using solar radiation. Yadav et al. (2011) demonstrated enhanced methyl orange degradation on MWCNT–TiO_2 nanohybrid catalysts prepared by click chemistry. They reported that the MWCNT–TiO_2 nanohybrid catalyst had an enhanced photocatalytic activity resulting from the synergistic effect due to strong covalent bonds between MWCNTs and TiO_2 nanoparticles (Yadav et al. 2011).

In this study, MWCNT/N, Pd co-doped TiO_2 composite photocatalysts were prepared by a modified sol–gel method. The materials were found to be active in the visible region of the solar spectrum. The photocatalytic degradation efficiency of the composite catalysts for a model synthetic dye was evaluated using Eosin Yellow (EY) (Fig. 1) in aqueous solution as a probe molecule.

Experimental details

Preparation of MWCNTs

The preparation, purification, functionalization and characterization of the MWCNTs were carried out in our laboratories. MWCNTs were synthesized using the nebulised-spray-pyrolysis method followed by acid functionalisation. Ferrocene (2.00 g) was added to toluene (50 ml) and placed into an atomisation chamber. This solution was nebulised using a high-frequency ultrasonic beam with a frequency of 1.54 MHz. A geyser resulted at the surface that generated a spray which was carried into the quartz tube placed in the furnace. The temperature of the furnace was maintained at 900 °C. Ultra-pure argon was used as a carrier gas and the gas flow rate was maintained at 500 cm^3 min^{-1} using a flow controller. The pyrolysis was carried out for 45 min. After the reaction, the flow rate of argon was reduced to 80 cm^3 min^{-1}. A black film of MWCNTs was formed in the inner surface of the tubing which was removed with a brush after the tube had cooled down.

Purification of MWCNTs

The MWCNTs were purified by heating them in air at 500 °C for 1 h to remove amorphous carbon and multi-shell carbon nanocapsules. The black product was allowed to cool and then immersed in concentrated hydrochloric acid (100 ml) to remove most of the iron particles. The product was then washed with distilled water and thereafter dried in an oven at 150 °C for 12 h.

Functionalization of MWCNTs

Purified MWCNTs were functionalized by heating under reflux in concentrated nitric acid (50 ml) for 6 h. This procedure removed the remaining iron particles and introduced some functional groups onto the surface of the MWCNTs. The functional groups included the hydroxyl and carboxyl groups. After the acid treatment, MWCNTs were washed with distilled water until the pH of the filtrate approached 7. The resulting MWCNTs were then filtered and dried at 60 °C overnight in air and further used for the preparation of the nanocomposites.

Preparation of materials

The following method was used to prepare 0.5% MWCNT/N, Pd co-doped TiO_2 (0.5% Pd): an appropriate weighed amount of purified MWCNTs was dispersed in a mixture of 2-propanol C_3H_8O, (50 ml) (99.8%, Sigma Aldrich, Germany) and titanium isopropoxide $Ti(OC_3H_7)_4$ (10 ml) (97%, Sigma Aldrich, Germany) to give a MWCNT:TiO_2 percentage of 0.5. The mixture was sonicated for 30 min to improve MWCNT dispersion. An appropriate amount of palladium diamine dichloride, $Pd(NH_3)_2Cl^{2-}$, (45% Pd, PGM Chemicals, RSA), to give a Pd:Ti ratio of 0.5% was dissolved in aqueous ammonia (3 ml) (25%,

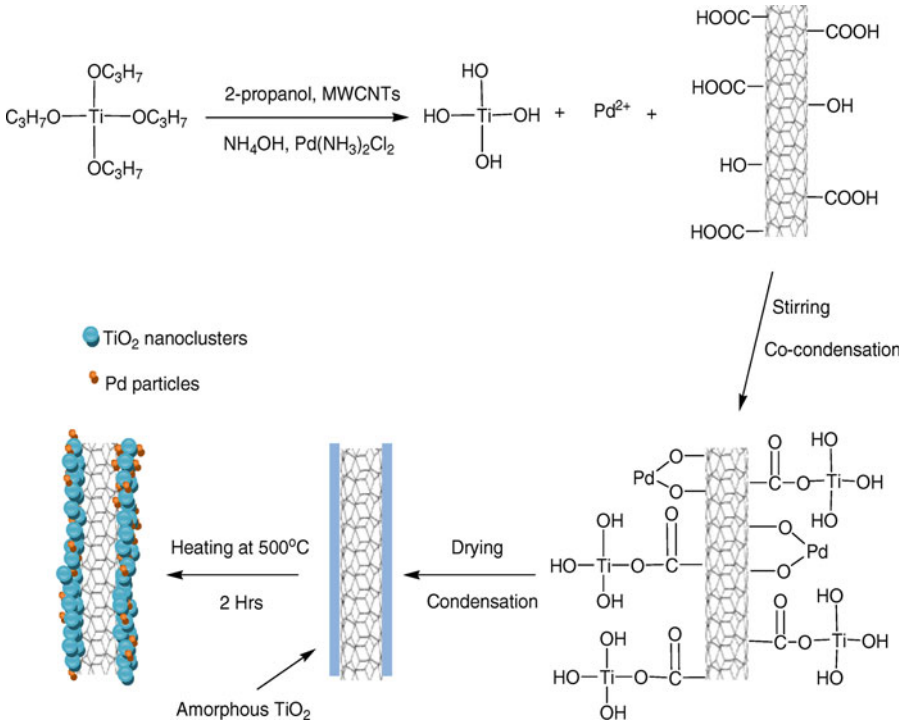

Fig. 2 Illustration of the synthesis of N, Pd co-doped TiO_2 decorated MWCNTs

Merck, Germany). The solution was added drop-wise to the MWCNT/2-propanol/titanium isopropoxide mixture while stirring vigorously for 30 min. After a further hour of stirring, the suspension was dried overnight in an oven set at 80 °C. The resulting light-grey powder was calcined for 2 h at 500 °C in air in an electric furnace and characterised by various techniques. In addition, 1, 2, 5 and 10% MWCNT samples were prepared by following the same procedure and weighing appropriate amounts of functionalised MWCNTs, respectively. A sample without MWCNTs was prepared for comparison. Figure 2 shows the synthetic route for the MWCNT/N, Pd co-doped TiO_2 nanocomposites.

Characterisation

FT-IR spectra were obtained on a Perkin Elmer (FT-IR Spectrum 100) spectrophotometer with 4 cm^{-1} resolution averaging 30 scans. Samples were analysed in their powder form using a ZnSe/diamond composite as the key component of the universal attenuated total reflectance sample holder.

Raman spectra, excited by a red diode laser (785 nm), were recorded on a Czerny-Turner micro-Raman spectrometer (Perkin Elmer Raman microscope) equipped with a cooled charged coupled device (CCD) detector set at −50 °C and an Olympus microscope. Measurements were done with the beam path set at 50× magnification.

X-ray diffraction (XRD) measurements were performed using an X-ray diffractometer (Philips PAN-analytical X'pert) operated at 40 kV and 40 mA. The Cu Kα radiation beam ($\lambda = 0.15406$ nm), Ni filtered (0.02 mm) and masked (11.6 mm), was collimated by Soller slits (0.04 rad). Measurements were performed in the range 20°–80° (2θ). Samples in their powder form were mounted on a Si sample holder using a bracket sample stage. Data analysis was performed using an X'pert data collector software. The crystallite sizes were estimated by applying the Scherer equation to the full width at half maxima (FWHM) data of the (101) peak of the anatase phase.

Optical properties were investigated using diffuse reflectance UV–Vis absorption spectrophotometry (DRUV–Vis) on a Shimadzu UV-2540 with an IRS 240 integrating sphere. $BaSO_4$ was used as a reference.

Scanning electron microscopy (SEM) images were obtained on a NOVA FEI/FIB Instrument, equipped with an INCA EDS analyser.

Transmission electron microscopy (TEM) analysis was performed under bright field on a Tecnai G^2 Spirit

TEM microscope to observe surface morphology, structure and grain size of the nanoparticles.

Thermogravimetric analysis (TGA) was carried out on a Perkin Elmer Pyris thermal analyser at a heating rate of 10 °C min^{-1} under nitrogen flow over a range of 30–900 °C in order to obtain thermal stability data.

Evaluation of photocatalytic activity

The photocatalytic performance of the N, Pd co-doped TiO_2 decorated MWCNTs was quantified by measuring the rate of degradation of EY under simulated solar radiation and visible light irradiation filtered using a dichroic UV filter ($\lambda > 450$ nm). The catalyst (0.1 g) was suspended in 100 ml of EY solution (100 ppm) under simulated solar radiation and visible light irradiation. A solar simulator (Oriel, Newport), equipped with an Oriel 500 W Xenon lamp, was employed as a source of radiation. The power output was set to 450 W in order to give an irradiance of 1,000 Wm^{-2} at 25 °C, using an Air Mass1.5 Global Spectral Filter. A dichroic UV filter ($\lambda > 450$ nm) was used for visible light irradiation. An Oriel PV reference cell system equipped with a 2 × 2 cm monocrystalline silicon photovoltaic cell and a Type K thermocouple was used to set the simulator irradiance to 1 sun. Before photocatalytic reactions, the suspensions were ultra-sonicated for 20 min and then magnetically stirred in the dark for 1 h to allow for adsorption equilibrium before illumination. Aliquots (3 ml) of the suspension were withdrawn at 15 min intervals using a 6 ml Neomedic disposable syringe and filtered through a 0.2 μm Pall Acrodisc PSF membrane filter for at least 120 min. Variations in the concentration of EY under illumination were monitored using a Shimadzu UV-2450 spectrophotometer (Japan) at $\lambda = 515$ nm.

Results and discussion

FT-IR studies were performed in order to determine the presence of functional groups and to study the surface changes on the nanocomposites (Fig. 3). The presence of OH groups and water on the surface of the particles was confirmed by the appearance of a broad band at 3,360 cm^{-1} for all samples. Another peak associated with O–H bending appeared around 1,640 cm^{-1}. The presence of hydroxyl groups on composite surfaces plays an important role in photocatalytic degradation. The functional groups on the composites were mainly from surface groups on the TiO_2. No characteristic peaks of the CNTs were observed due to the low percentage of MWCNTs in the nanocomposites. The band due to stretching and bending modes of Ti–O and O–Ti–O appeared as a highly intense broad band centred at approximately 500 cm^{-1} (Yu et al. 2011).

Raman analyses confirmed the presence of TiO_2 and MWCNTs in the nanocomposites (Fig. 4). Anatase TiO_2 shows six Raman active fundamental modes at 144 cm^{-1} (E_g), 197 cm^{-1} (E_g), 397 cm^{-1} (B_{1g}), 518 cm^{-1} ($A_{1g} + B_{1g}$) and 640 cm^{-1} (E_g) (Anpo and Takeuchi 2003). Well-resolved Raman peaks were observed at 145 cm^{-1} (E_g), 399 cm^{-1} (B_{1g}), 517 cm^{-1} ($A_{1g} + B_{1g}$) and 640 cm^{-1} (E_g) cm^{-1} in the spectra of all the samples calcined at 500 °C indicating the presence of anatase as the predominant phase (Ou et al. 2006).

Peaks characteristic of MWCNTs also appeared at about 1,311 cm^{-1} (D band) and at 1,578 cm^{-1} (G band or E_{2g}) (Yan et al. 2005) in the nanocomposites (Fig. 5). The D band corresponds to defect sites in the hexagonal framework of the MWCNTs due to disorder induced by sp^3 hybridization, whereas the G band indicates the presence of ordered sp^2 hybridization, a feature related to the structural integrity of the nanotubes. The ratio of D-band (I_D) to G-band (I_G) intensities is sensitive to the surface character of MWCNTs. The intensity ratio (I_D/I_G) values for 2%

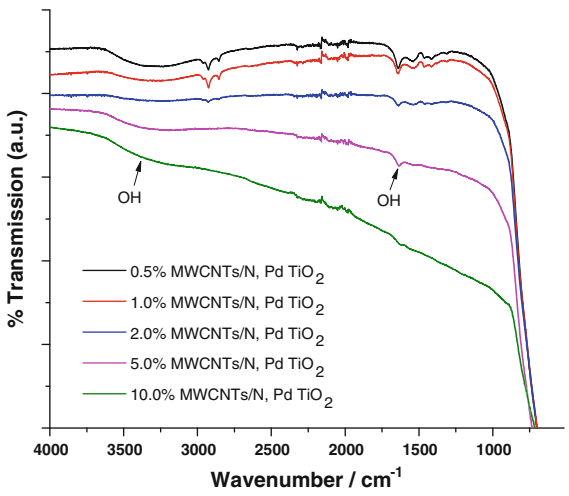

Fig. 3 FT-IR spectra of MWCNT/N, Pd co-doped TiO_2 with different MWCNT ratios

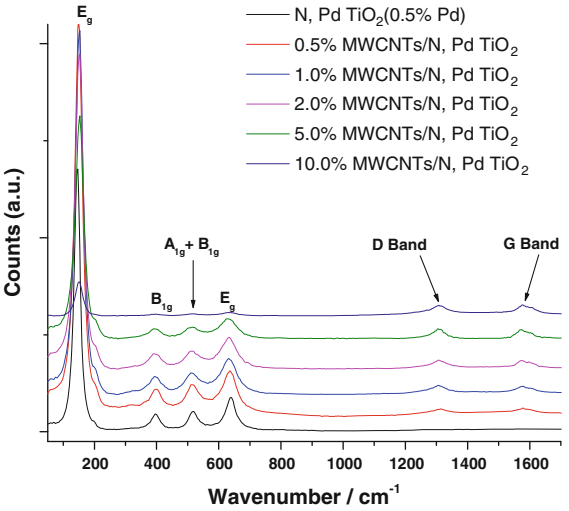

Fig. 4 Raman spectra of MWCNT/N, Pd co-doped TiO_2 with different MWCNTs ratios

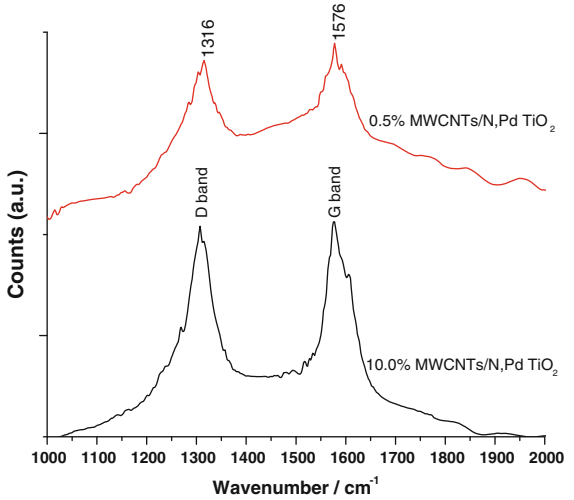

Fig. 5 Raman spectra of MWCNT/N, Pd co-doped TiO_2 showing the D and G bands

MWCNT/N, Pd co-doped TiO_2 and 5% MWCNT/N, Pd co-doped TiO_2 were found to be 0.986 and 0.942, respectively. These values suggest increased defects on CNTs resulting in increased D-band intensity, signalling the change of the hybridization of C atoms on the nanotubes from sp^2 to sp^3. A weak shoulder (D' band), which is also associated with the defects and disorder in the MWCNTs, appears at about 1,613 cm^{-1} in the nanostructure (Hirano et al. 2003). These observations provide evidence for covalent functionalization of N, Pd TiO_2 nanoparticles on MWCNTs (Yadav et al. 2011).

The intensity of these Raman peaks increases with increasing amounts of MWCNTs in the nanocomposites. The low intensity at low MWCNTs levels may be explained by the total coverage of the CNTs by the co-doped TiO_2 particles. At high MWCNT levels, the coverage by co-doped TiO_2 was lower due to aggregation and poor dispersion in 2-propanol, thus some of the MWCNTs were bare leading to more intense Raman peaks. These results are in agreement with SEM and TEM observations.

XRD analysis was performed to investigate the effect of MWCNTs on the crystallisation of different samples (Fig. 6). The XRD patterns of the nanocomposites may be as a result of the formation of pure anatase crystallites in the composites. Peaks at 2θ values of 25.3, 37.6, 48.2, 53.9, 54.8, 62.7 and 75.2 corresponding to the (101), (004), (200), (105), (211), (204) and (215) planes, respectively, can be indexed to the anatase phase (Ou et al. 2006). The characteristic peaks of the MWCNTs can hardly be identified from the pattern of the nanocomposite catalysts at low MWCNT percentages. The absence of aggregated MWCNTs in the composites containing low percentages of MWCNT led to a homogeneous dispersion of N, Pd TiO_2 on MWCNTs, further confirming the absence of the MWCNT characteristic peaks in the XRD patterns. There is a possibility of overlap of the intense peak of the MWCNTs (101) with the anatase (101) reflection (Gao et al. 2009). This feature is clearly visible by the appearance of a shoulder on the (101) anatase reflection of the 5% MWCNT/N, Pd co-doped TiO_2 and 10% MWCNT/N, Pd co-doped TiO_2. The crystallite size was calculated by X-ray line-broadening analysis using the Scherer equation:

$$D = \frac{k\lambda}{\beta \cos\theta}$$

where D is crystallite particle size, k is a constant of 0.9, λ is the wavelength (nm) of characteristic X-ray applied, β is the FWHM of the anatase (101) peak obtained by XRD and θ is Bragg angle (Maicu et al. 2011).

Results of particle sizes are shown in Table 1. There are no major differences in particle size with increasing amounts of MWCNTs. A general slight increase in particle size with increasing MWCNT content may be attributed to the rate of hydrolysis and condensation reactions on the support. At low

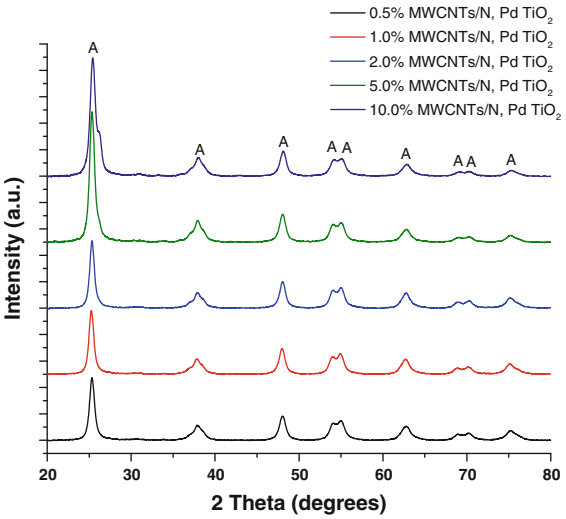

Fig. 6 XRD patterns of MWCNT/N, Pd co-doped TiO_2 with different MWCNT ratios (A = anatase phase)

Table 1 Effect MWCNTs on average particle size

Sample	Particle size (nm)
N, Pd co-doped TiO_2 (0.5% Pd)	16.41
0.5% MWCNT/N, Pd co-doped TiO_2 (0.5% Pd)	17.92
1.0% MWCNT/N, Pd co-doped TiO_2 (0.5% Pd)	15.21
2.0% MWCNT/N, Pd co-doped TiO_2 (0.5% Pd)	17.89
5.0% MWCNT/N, Pd co-doped TiO_2 (0.5% Pd)	18.64
10.0% MWCNT/N, Pd co-doped TiO_2 (0.5% Pd)	19.60

MWCNT levels, the condensation reaction is complete within a short period of time as few carboxylate sites are available for the reaction. The rapid hydrolysis of the titanium precursor occurred before or while the reaction products anchored on the nanotube supports leading to smaller particle sizes (Gao et al. 2009). Zhang and Oh (2010) reported an average particle size of 5 nm for MWCNT/TiO_2 composites prepared by the sol–gel method (Hirano et al. 2003). All the samples were still 100% in the anatase phase after calcination at 500 °C.

SEM images of the MWCNT/N, Pd co-doped TiO_2 nanocomposites (Fig. 7) show coverage of the MWCNTs with N, Pd TiO_2. Figure 7a shows coated MWCNTs in clusters of highly agglomerated N, Pd TiO_2 nanoparticles. Coverage is not continuous for some of the nanocomposites (Fig. 7b), with small bare gaps in the nanometre range on the MWCNTs. This might be due to the calcination leading to loss of water, carbon and nitrogenous material. This creates a strain on the nanoclusters resulting in a gap being created. The nanoclusters are formed by the hydrolysis and co-condensation of isopropyl titanate under alkaline conditions in the presence of MWCNT-COOH and Pd ions. The amorphous N, Pd TiO_2 obtained at room temperature was transformed to crystalline anatase after heat treatment at 500 °C. At higher MWCNT levels, aggregation becomes a problem, leading to poor dispersion of MWCNTs in 2-propanol and eventually poor coverage by the nanoparticles (Fig. 7d).

Elemental composition of the nanocomposites was probed and confirmed by EDS analysis (Fig. 8). Results indicated the presence of Ti, O, C and Pd. Presence of Na and S was also detected which may have originated from containers or sample-handling contamination. The C signal most certainly emanates from the MWCNTs.

Figure 9 shows the TEM images of the N, Pd co-doped TiO_2 alone and of MWCNT/N, Pd co-doped TiO_2 nanocomposites. TEM images confirm the presence of Pd deposits on the surface of the N-doped TiO_2 (Fig. 9a). Pd deposits are well dispersed on many of the TiO_2 particles and have diameters ranging from 1 to 2 nm. The particles are agglomerated and nearly spherical in shape. The size of the TiO_2 particles is approximately in the range of 15–20 nm, consistent with XRD measurements. The images also reveal a composite microstructure consisting of TiO_2 agglomerates with embedded MWCNTs confirming the intimate contact between the MWCNTs and co-doped TiO_2. All the CNTs were covered uniformly with a layer of co-doped TiO_2 at low MWCNT/co-doped TiO_2 ratio (Fig. 9b, c). However at 5% MWCNT/co-doped TiO_2 and 10% MWCNT/co-doped TiO_2, the distribution of the clusters is far from being homogeneous. Some of the MWCNTs are completely bare or show poor coverage (Fig. 9d, f). Pd particles sitting on MWCNTs are clearly visible on the poorly covered MWCNTs (Fig. 9f). The aggregation of co-doped TiO_2 nanoparticles on MWCNTs indicates the supporting role of the MWCNTs as centres for the deposition and growth of hydrolysis products as well as support for spatial confinement of the co-doped TiO_2 clusters (Gao et al. 2009). The thickness of the N, Pd TiO_2 layer on the MWCNTs was estimated to be 10–20 nm (at least one layer). Furthermore, it can be noted that the open ends of the tubular structure are

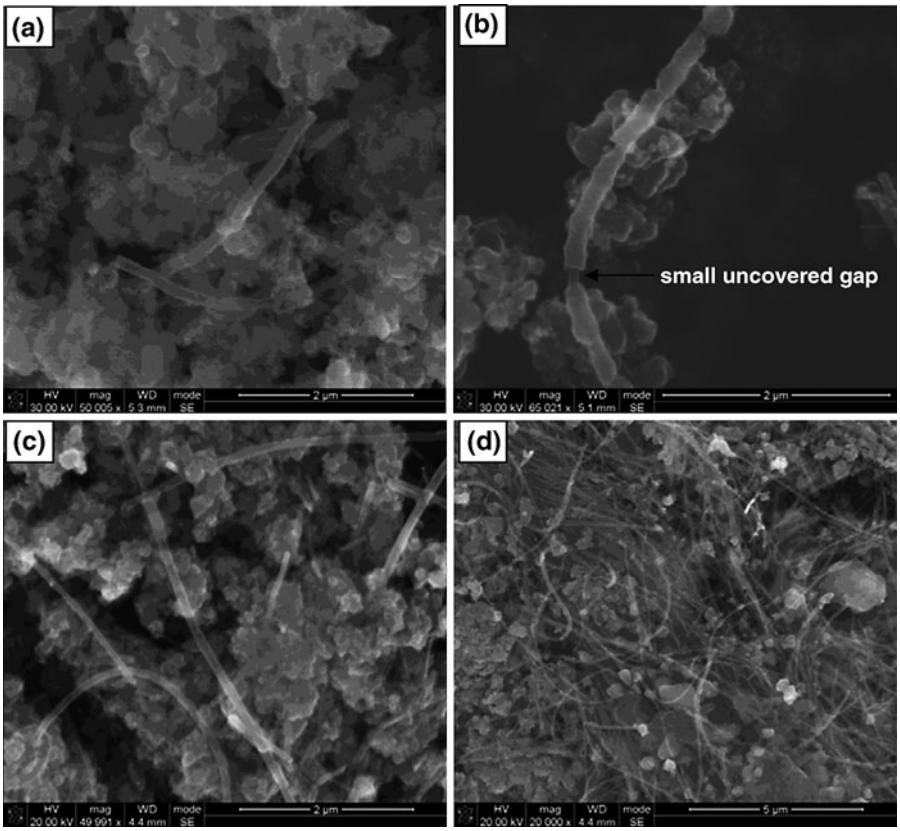

Fig. 7 SEM images of **a** 0.5% MWCNT/N, Pd TiO_2, **b** N, Pd TiO_2 decorated MWCNT showing a small uncovered gap, **c** 5% MWCNT/N, Pd TiO_2 and **d** aggregation in 10% MWCNT/N, Pd TiO_2

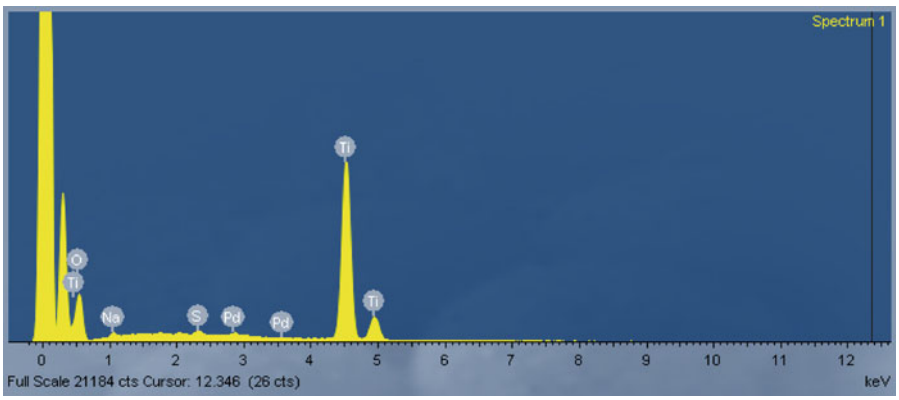

Fig. 8 Full-scale EDS scan of 2% MWCNT/N, Pd co-doped TiO_2

also covered by co-doped TiO_2, suggesting the presence of functional groups on the sidewalls and at the open ends of the functionalised MWCNTs (Fig. 9e, f).

TGA analysis was carried out to investigate the thermal stability and to estimate the CNT content in the nanocomposites. The results of weight loss as a function of temperature for 0.5% MWCNT/N, Pd co-doped TiO_2 to 10.0% MWCNT/N, Pd co-doped TiO_2 nanocomposites are shown in Fig. 10. A weight loss at a temperature of between 50 and 100 °C is attributed to the loss of water adsorbed onto the surface of the nanocomposites. Another weight loss at about 250 °C could be due to loss of any carbon or nitrogen-related

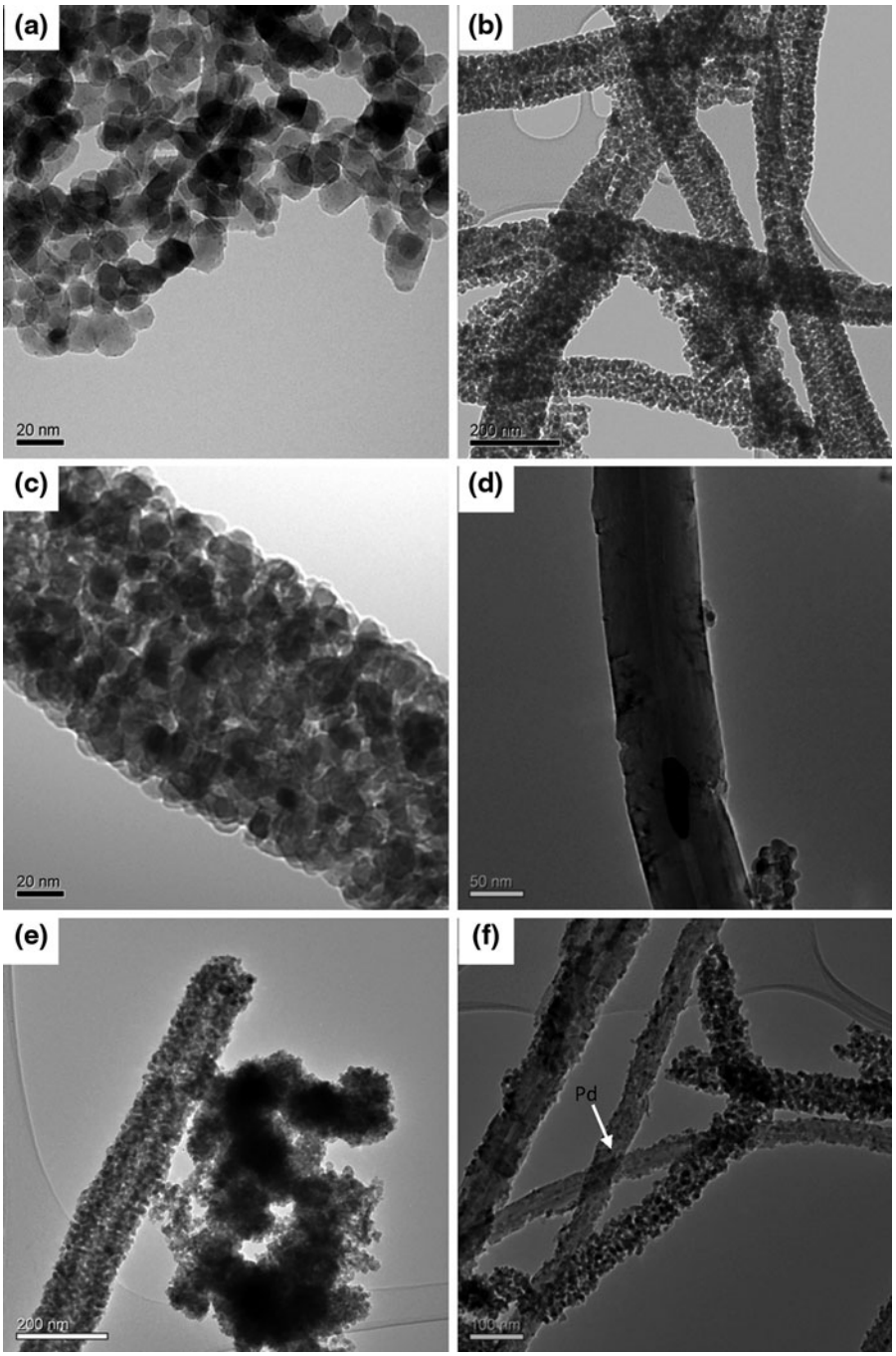

Fig. 9 TEM images of **a** N, Pd co-doped TiO_2 (0.5% Pd), **b** and **c** 0.5% MWCNT/N, co-doped Pd TiO_2 showing MWCNTs completely covered with N, Pd co-doped TiO_2, **d** MWCNT with N, Pd co-doped TiO_2 particle as well as aggregates, **e** MWCNT covered with N, Pd co-doped TiO_2 and N, Pd co-doped TiO_2 aggregates and **f** unevenly covered MWCNTs (5.0% MWCNT/N, Pd co-doped TiO_2) showing some Pd particles

material. The weight loss above 500 °C indicates the decomposition of CNTs. The weight ratio of MWCNTs over TiO_2 was estimated by correlating the mass loss with temperature. The weight loss above 500 °C, of approximately 1, 2, 5 and 12% for the 1, 2, 5 and 10% MWCNT/N, Pd co-doped TiO_2, respectively,

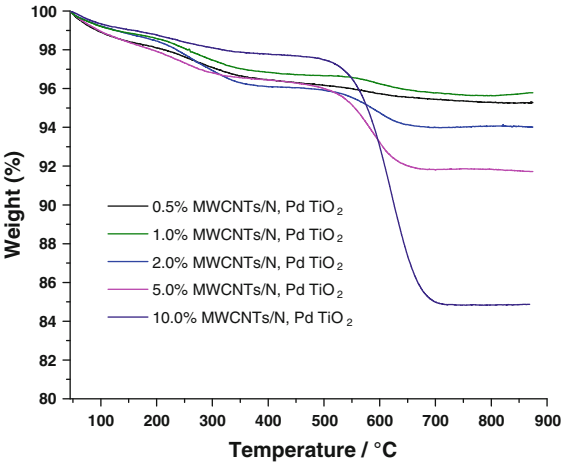

Fig. 10 TGA curves of MWCNT/N, Pd co-doped TiO_2 with different MWCNT ratios

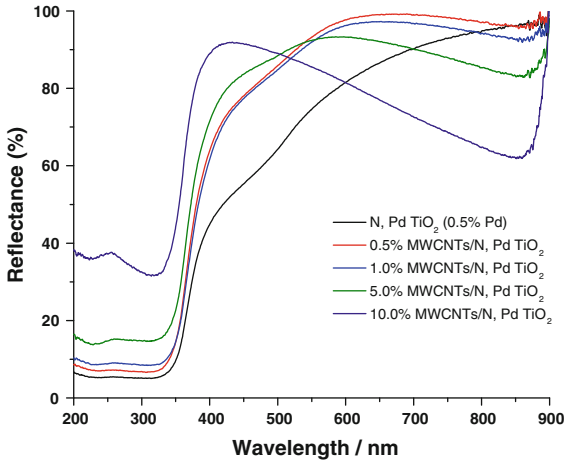

Fig. 11 UV–Vis diffuse reflectance spectra of different MWCNT/N, Pd co-doped TiO_2 nanocomposites

suggests that the MWCNT/N, Pd co-doped TiO_2 ratios used during synthesis of the nanocomposites are in close agreement with results obtained from TGA analyses. This observation points to negligible losses of MWCNTs during the composite-preparation procedure. The decomposition temperature of functionalised MWCNTs was found to be 570 °C. It occurs over a narrow temperature range of between 520 and 580 °C. However, the decomposition of nanocomposites occurs at a higher temperature of about 600 °C and over a wider temperature range with the onset at nearly 530 °C for the 5% MWCNT/N, Pd co-doped TiO_2 sample, ending at about 680 °C. The decomposition starts at 540 °C for the 2% MWNCT/N, Pd co-doped TiO_2 and at 560 °C for the 1% MWCNT/N, Pd co-doped TiO_2, respectively. This shift in the onset of the decomposition appears to be related to the level of coating of N, Pd TiO_2 on the MWCNTs as shown by the TEM images. The shift may be ascribed to the presence of the co-doped TiO_2 coated on the MWCNTs which may slightly restrain heat transfer resulting in delayed oxidation of MWCNTs.

The DRUV–Vis spectra of the different nanocomposites are shown in Fig. 11. The spectra are characterised by an intense fundamental absorption due to anatase TiO_2 in the region of between 350 and 400 nm. There is a red shift in the absorption edge for MWCNT/N, Pd co-doped TiO_2 nanocomposites that can be correlated to the amount of MWCNTs in the high-wavelength visible region. There is an increase in the absorption edge for the 0.5 and 1.0% MWCNT/N, Pd co-doped TiO_2 centred on 475 nm. At 2.0, 5.0 and 10% MWCNT/N, Pd co-doped TiO_2 there is a decrease in the absorption at around 475 nm but an increase is observed at between 700 and 900 nm.

An increase in MWCNTs was accompanied by a decrease in absorbance in the UV region (200–350 nm). This is due to a decrease or non-uniform coverage of MWCNTs in agreement with TEM and SEM observations. The nanocomposites showed the combined features of MWCNTs and co-doped TiO_2 with new properties, which are favourable for applications in the visible light region. The characteristics of the co-doped TiO_2 and MWCNTs were altered due to the interaction of TiO_2 nanoparticles with the MWCNTs, which may modify the process of the electron/hole pair formation under visible light irradiation (Wang et al. 2005; Kang et al. 2007). This unique structure of the MWCNT/TiO_2 composites might have led to the high catalytic activity reported for phenol degradation (An et al. 2007).

The DRUV–Vis spectra were plotted as the Kubelka–Munk function, $F(R)$, versus wavelength based on the Kubelka–Munk equation:

$$F(R) = \frac{(1-R)^2}{2R}$$

where reflectance, $R = R_{\text{sample}}/R_{\text{reference}}$ (Fig. 12).

The plot shows a decrease in the absorption coefficient with increasing amounts of MWCNTs in the UV region. The Kubelka–Munk plot can be transformed to a Tauc plot—a plot of $[F(R)\cdot hv]^n$

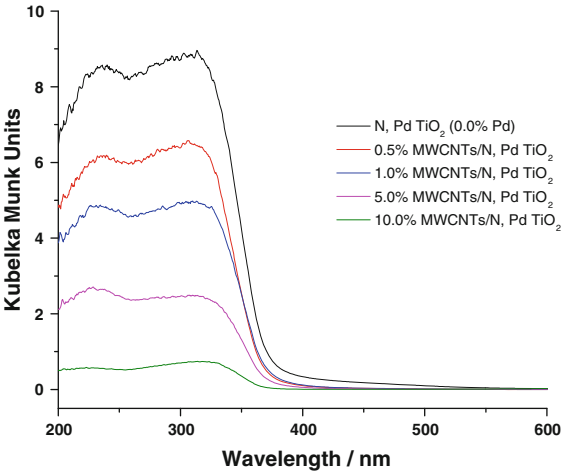

Fig. 12 Kubelka–Munk plots of different MWCNT/N, Pd co-doped TiO_2 nanocomposites

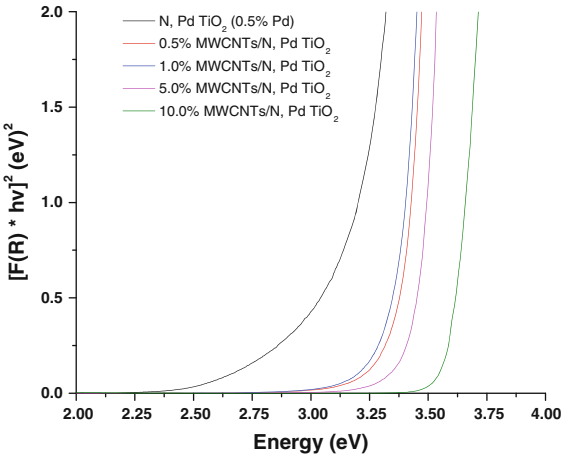

Fig. 13 Tauc plots of MWCNT/N, Pd co-doped TiO_2 nanocomposites

versus *hv*. The type of transition in TiO_2-based semiconductors is not well understood (Li et al. 2007); however, for a direct band-gap semiconductor the plot with $n = {}^1/_2$ gives a linear Tauc region just above the optical absorption edge. Extrapolation of this straight line to the photon energy axis yields the semiconductor band gap, a key indicator of its light-harvesting efficiency under solar illumination. Indirect band gap materials give a Tauc region with $n = 2$ (Serpone et al. 1995).

The band gaps (eV) for all the nanocomposites were determined from the lines' point of contact with the energy axis (Fig. 13) (Wu et al. 2010). Assuming an indirect band gap for all the samples, there was an increase in band-gap energy with increasing amounts of MWCNTs (Table 2). This can be ascribed to low levels of N and Pd available for doping with TiO_2. The N and Pd tend to associate more with the CNTs than with the TiO_2, causing an increase in band gap with increasing loadings of MWCNTs.

Figure 14a shows the results of the degradation of (EY) under simulated solar irradiation, in the presence of N, Pd TiO_2 alone and with the MWCNT/TiO_2 composites. There is a decrease in the degradation efficiency of the nanocomposites with increasing amounts of MWCNTs. The optimum MWCNT/TiO_2 ratio in the composites was found to be 0.5% by weight under the experimental conditions investigated. Reduced efficiency in the nanocomposites could be explained by partial agglomeration of the N, Pd TiO_2 on the MWCNTs as shown in the SEM and

Table 2 Effect of MWCNTs on band gap in MWCNT/N, Pd co-doped TiO_2 nanocomposites

Sample	Direct band gap (eV)
N, Pd co-doped TiO_2 (0.5% Pd)	2.30
0.5% MWCNT/N, Pd co-doped TiO_2 (0.5% Pd)	2.84
1.0% MWCNT/N, Pd co-doped TiO_2 (0.5% Pd)	2.93
5.0% MWCNT/N, Pd co-doped TiO_2 (0.5% Pd)	3.06
10.0% MWCNT/N, Pd co-doped TiO_2 (0.5% Pd)	3.42

TEM images (Figs. 7, 9). The remarkable thickness of the coating layer on some MWCNTs can be attributed to the continuous adsorption of titania particles on the initially formed TiO_2 coating layer, forming multi-layers on the MWCNT surfaces resulting in compromised photodegradation efficiency. Heterogeneous, non-uniform coating of N, Pd TiO_2 on MWCNTs, showing bare CNT surfaces and random aggregation of the nanoparticles onto the MWCNTs surface could also explain the observed trend (Gao et al. 2009). However, the supporting role of the MWCNTs as centres for the deposition and growth of hydrolysis products as well as support for spatial confinement of the TiO_2 clusters was noted.

The photodegradation of EY using visible light is shown in Fig. 14b. Simulated solar irradiation gave higher degradation rates compared to visible light irradiation because of the presence of a small percentage, (3–5%), of high-energy UV radiation in solar radiation. Irradiation of the composites with

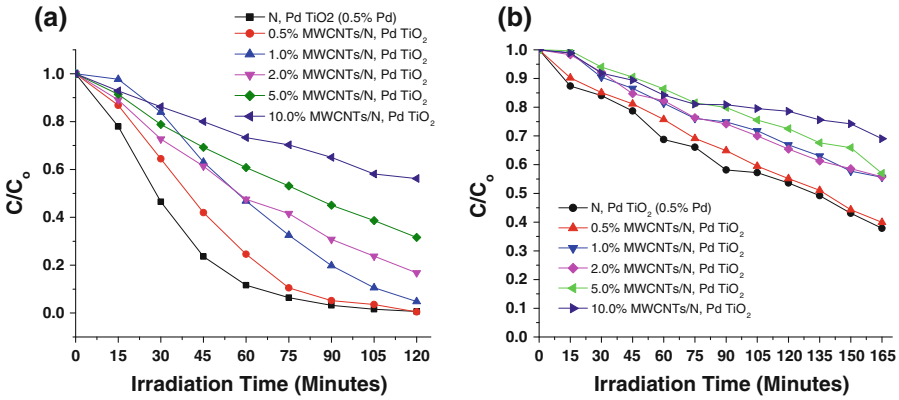

Fig. 14 Photodegradation of EY on N, Pd TiO_2 and MWCNT/N, Pd co-doped TiO_2 nanocomposites under **a** simulated solar light irradiation and **b** visible light irradiation ($\lambda > 450$ nm)

Table 3 Dye adsorption and EY photodegradation under simulated solar radiation

Sample	Dye adsorption (%)	Degradation after 120 min (%)
N, Pd co-doped TiO_2 (0.5% Pd)	23.39	99.30
0.5% MWCNT/N, Pd co-doped TiO_2	15.75	99.55
1.0% MWCNT/N, Pd co-doped TiO_2	15.36	95.21
2.0% MWCNT/N, Pd co-doped TiO_2	13.40	83.18
5.0% MWCNT/N, Pd co-doped TiO_2	29.06	68.36
10.0% MWCNT/N, Pd co-doped TiO_2	27.09	43.84

radiation of wavelengths greater than 450 nm resulted in reduced light-harvesting capability by TiO_2, with the MWCNTs acting as photosensitisers for the photocatalytic process. MWCNTs themselves tend to absorb very well in the visible region because of their colour. Their synergistic effects are governed by the ability to trap electrons before channelling them to the conduction band of the TiO_2.

The highest degradation efficiency under simulated solar irradiation was observed for the 0.5% MWCNT/N, Pd co-doped TiO_2 composite (99.55%). There was a decrease in the degradation efficiency of the nanocomposites with increasing amounts of MWCNTs, with the 1.0, 2.0, 5.0 and 10% MWCNT/N, Pd co-doped TiO_2 composites showing values of 95.21, 83.18, 68.36 and 43.84%, respectively (Table 3). This trend correlates very well with the increase in band gaps observed in the Tauc plots (Fig. 13). The presence of low levels of MWCNTs caused an increase in dye-degradation efficiency probably due to the synergistic effects of MWCNTs and N, Pd TiO_2 on the entire photodegradation process. There was no correlation between dye adsorption and photodegradation as observed with the 10% MWCNT/N, Pd co-doped TiO_2 which could adsorb 27.09% of the dye but only showed a degradation efficiency of 43.84%, a value lower than that for 0.5% MWCNT/N, Pd co-doped TiO_2 which showed an adsorption of only 15.75%. This can be explained by the uneven coating of the MWCNTs as well as their aggregation at higher percentages. A similar trend was observed for experiments performed under visible radiation (Table 4).

The photodegradation of EY in aqueous suspensions containing MWCNT/N, Pd co-doped TiO_2 nanocomposites obeyed first-order kinetics (Fig. 15):

$$\ln(C_o/C) = f(t).$$

The rate constants for EY photodegradation under simulated solar radiation are much higher than those for the experiments under visible radiation. Incorporation of N and Pd had a profound effect on the degradation efficiency of the nanocomposites. N reduces the TiO_2 band gap by forming states in the inter-gap region whilst Pd can trap photogenerated electrons, thereby enhancing electron–hole separation on the surface of the photocatalyst and increasing photocatalytic activity.

Wang et al. (2005) reported rate constants of 1.8 and 2.0×10^{-3} min^{-1} for neat TiO_2 and 5% MWCNT/TiO_2 composite catalyst, respectively. These values are lower than the values shown in

Table 4 Dye adsorption and EY photodegradation under visible radiation ($\lambda > 450$ nm)

Sample	Dye adsorption (%)	Degradation after 165 min (%)
N, Pd co-doped TiO_2 (0.5% Pd)	27.71	62.13
0.5% MWCNT/N, Pd co-doped TiO_2	14.76	60.07
1.0% MWCNT/N, Pd co-doped TiO_2	12.49	44.42
2.0% MWCNT/N, Pd co-doped TiO_2	15.64	44.22
5.0% MWCNT/N, Pd co-doped TiO_2	18.49	43.03
10.0% MWCNT/N, Pd co-doped TiO_2	27.82	30.99

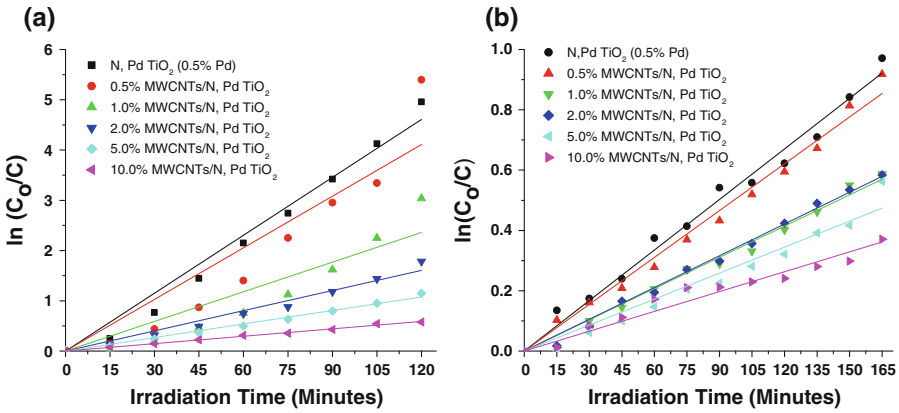

Fig. 15 Kinetics of EY degradation under **a** simulated solar radiation and **b** visible light

Table 5 for nanocomposites containing lower levels of MWCNTs at $\lambda > 450$ nm. In another study, Wang et al. (2009) reported on photodegradation of phenol using neat TiO_2 and 20% MWCNT/TiO_2 nanocomposites and obtained values of 0.68 and 1.55×10^{-3} min^{-1}, respectively. Oh et al. (2009) reported on photocatalytic degradation of methylene blue (MB) in an aqueous solution containing 5% MWCNT/TiO_2 composite photocatalysts, under ultraviolet light irradiation and recorded a rate constant value of 9.5×10^{-3} min^{-1} which was higher than 8.0×10^{-3} min^{-1} for pristine TiO_2 (Oh et al. 2009). Tian et al. (2011) synthesised MWCNT/TiO_2 hybrid nanostructures via solvothermal synthesis and sol–gel method with benzyl alcohol as a surfactant and tested them for visible light ($\lambda > 420$ nm) MB degradation. The sol–gel MWCNT/TiO_2 (20%) significantly enhanced the degradation of MB, compared to the pure TiO_2 and the mechanical mixture of MWCNTs and TiO_2. However, owing to the uniform distribution of TiO_2 nanocrystals on the CNT surface the MWCNT/TiO_2 (20%), prepared by solvothermal synthesis, showed even higher photocatalytic activity than sol–gel MWCNT/TiO_2 (20%). A first-order rate constant of 0.001 min^{-1} was observed for the MWCNT/TiO_2 (20%) prepared by solvothermal synthesis at a catalyst loading of 0.2 g l^{-1} and an MB concentration of 10 mg l^{-1} (Tian et al. 2011). Once again, these values are lower than those displayed in Table 5. These observations point to the increased efficiency of the nanocomposites prepared by the modified sol–gel method for EY degradation.

A proposed mechanism for the enhanced photocatalysis of the MWCNT/N, Pd co-doped TiO_2 composites is shown schematically in Fig. 16. Under visible light illumination, photo-excited electrons from the dispersed MWCNTs are injected into the conduction band of the N, Pd TiO_2 through the Ti–C bonds. The generated positively charged MWCNTs will in turn capture electrons from the valence band of N, Pd TiO_2 leaving holes behind in the N, Pd TiO_2. Holes can react with surface hydroxyl ions or water to produce hydroxyl radicals ($OH^{\bullet}$), while electrons can be trapped by the Pd before they react with adsorbed molecular oxygen yielding superoxide radicals ($O_2^{\bullet}$), which scavenge water molecules to form highly reactive $OH^{\bullet}$ radicals. The $OH^{\bullet}$ radicals are highly oxidising and are capable of degrading the EY to carbon dioxide and water.

When N, Pd TiO_2 forms a heterojunction with another semiconductor or metal (e.g., MWCNT), a

Table 5 EY photodegradation rate constants under simulated solar radiation and visible radiation

Sample	Rate constant, k (min^{-1}) (solar simulator)	Rate constant, k (min^{-1}) visible light ($\lambda > 450$ nm)
N, Pd co-doped TiO_2 (0.5% Pd)	3.84×10^{-2}	5.59×10^{-3}
0.5% MWCNT/N, Pd co-doped TiO_2	3.42×10^{-2}	5.18×10^{-3}
1.0% MWCNT/N, Pd co-doped TiO_2	1.97×10^{-2}	3.45×10^{-3}
2.0% MWCNT/N, Pd co-doped TiO_2	1.34×10^{-2}	3.51×10^{-3}
5.0% MWCNT/N, Pd co-doped TiO_2	8.98×10^{-3}	2.87×10^{-3}
10.0% MWCNT/N, Pd co-doped TiO_2	4.92×10^{-3}	2.19×10^{-3}

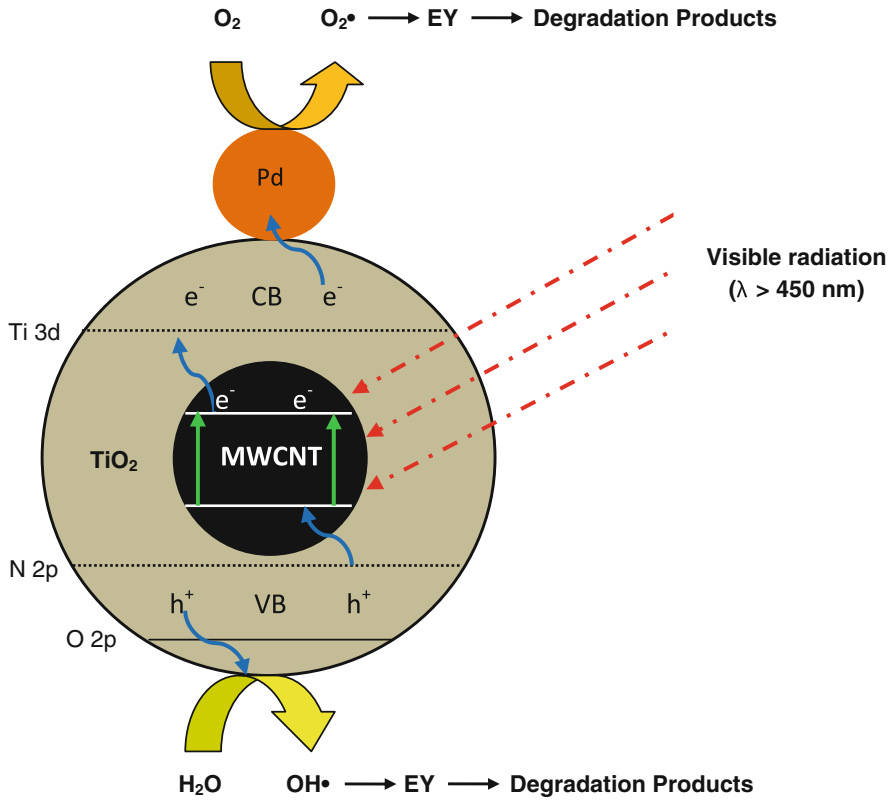

Fig. 16 Excitonic processes for the MWCNT/N, Pd co-doped TiO_2 catalysts under visible light irradiation

charge space ranging from several tens to hundreds of nanometres would be formed near the junction to equalise the Fermi levels. This will result in reduced band-gap energy within the MWCNT/N, Pd TiO_2 heterojunction. Formation of an interior electric field of the charge space within the nanocomposite can separate the photogenerated pairs which results in reduction of the recombination rate of the pairs. This mechanism suggests that the photocatalytic performance of MWCNT/N, Pd co-doped TiO_2 materials should be optimum at some specific value of the MWCNT content (Akhavan et al. 2010). Wang et al. (2009) recently reported 5 wt% of MWCNT content in MWCNT/TiO_2 composite photocatalysts as the optimum value for visible light-induced photocatalytic degradation of 2,6-dinitro-*p*-cresol (Wang et al. 2009).

The superoxide radicals act as oxidizing agents or as an additional source of hydroxyl radicals to catalyse the dye degradation (Zhang and Oh 2010). Theoretically, pure TiO_2 cannot be excited by visible light because of its large band gap. The positive effect of N, Pd co-doping coupled with incorporation of MWCNTs leads to enhanced photoreactivity due to synergistic effects.

Conclusion

MWCNT/N, Pd co-doped TiO_2 composite materials prepared through a modified sol–gel route displayed a rather homogeneous coverage of N, Pd TiO_2 over MWCNT and less agglomeration of TiO_2 nanoparticles on MWCNT surface. Particles were small (10–20 nm) and in the anatase form. At higher MWCNTs levels, coverage was compromised by aggregation of the nanotubes. Incorporation of N led to reduced TiO_2 band gap whilst the Pd acted as a sink for photogenerated electrons. Consistent with the shift of the UV–Vis absorption of the composites to longer wavelengths, there was a synergistic effect on the photocatalytic removal of EY at low MWCNT levels using visible light irradiation source. This effect showed that MWCNT can act as potential photosensitisers besides their role as adsorbents and dispersing agents. Simulated solar radiation gave higher degradation rates compared to visible light irradiation ($\lambda > 450$ nm). The highest photodegradation efficiency was observed for the 0.5% MWCNT/N, Pd co-doped TiO_2 under simulated solar radiation. Higher MWCNT loadings led to reduced dye-degradation efficiency with the 10% MWCNT/N, Pd co-doped TiO_2 degrading 43.84% in 2 h under simulated solar radiation. These observations confirm the unique properties of the MWCNT/N, Pd co-doped TiO_2 nanocomposites as potential functional water-purification materials.

Acknowledgments Funding from the University of Johannesburg and the Centre of Excellence in Strong Materials is appreciated.

References

Akhavan O, Azimirad R, Safa S, Larijani MM (2010) Visible light photo-induced antibacterial activity of CNT-doped TiO_2 thin films with various CNT contents. J Mater Chem 20:7386–7392

An G, Ma W, Sun Z, Liu Z, Han B, Miao S, Miao Z, Ding K (2007) Preparation of titania/carbon nanotube composites using supercritical ethanol and their photocatalytic activity for phenol degradation under visible light irradiation. Carbon 45:1795–1801

Anpo M, Takeuchi M (2003) The design and development of highly reactive titanium oxide photocatalysts operating under visible light irradiation. J Catal 216:505–516

Baughman RH, Zakhidov AA, De Heer WA (2002) Carbon nanotubes—the route toward applications. Science 297: 787–792

Fan W, Gao L, Sun J (2006) Anatase TiO_2-coated multi-wall carbon nanotubes with the vapor phase method. J Am Ceram Soc 89:731–733

Gao B, Chen GZ, Puma GL (2009) Carbon nanotubes/titanium dioxide ($CNTs/TiO_2$) nanocomposites prepared by conventional and novel surfactant wrapping sol–gel methods exhibiting enhanced photocatalytic activity. Appl Catal B 89:503–509

Hirano M, Nakahara C, Ota K, Tanaike O, Inagaki M (2003) Photoactivity and phase stability of ZrO_2-doped anatase-type TiO_2 directly formed as nanometer-sized particles by hydrolysis under hydrothermal conditions. J Solid State Chem 170:39–47

Jitianu A, Cacciaguerra T, Benoit R, Delpeux S, Beguin F, Bonnamy S (2004) Synthesis and characterization of carbon nanotubes–TiO_2 nanocomposites. Carbon 42(5–6): 1147–1151

Kafizas A, Kellici S, Jawwad A, Darr JA, Parkin IP (2009) Titanium dioxide and composite metal/metal oxide Titania thin films on glass: a comparative study of photocatalytic activity. J Photochem Photobiol A 204:183–190

Kang SZ, Cui Z, Jin Mu J (2007) Composite of carboxyl-modified multi-walled carbon nanotubes and TiO_2 nanoparticles: preparation and photocatalytic activity. Fuller Nanotub Carbon Nanostruct 15:81–88

Kim S, Jinschek JR, Chen H, Sholl DS, Marand E (2007) Scalable fabrication of carbon nanotube/polymer nanocomposite membranes for high flux gas transport. Nano Lett 7(9):2806–2811

Li Q, Xie R, Shang JK, Mintz EA (2007) Effect of precursor ratio on synthesis and optical absorption of TiON photocatalytic nanoparticles. J Am Ceram Soc 90(4):1045–1050

Lin Z, Orlov A, Lambert RM, Payne MC (2005) New insights into the origin of visible light photocatalytic activity of nitrogen-doped and oxygen-deficient anatase TiO_2. J Phys Chem B 109:20948–20952

Maicu M, Hidalgo MC, Colon G, Navio JA (2011) Comparative study of the photodeposition of Pt, Au and Pd on pre-sulphated TiO_2 for the photocatalytic decomposition of phenol. J Photochem Photobiol A 217:275–283

Oh WC, Jung AR, Ko WB (2009) Characterization and relative photonic efficiencies of a new nanocarbon/TiO_2 composite photocatalyst designed for organic dye decomposition and bactericidal activity. Mater Sci Eng C 29:1338–1347

Ou Y, Lin J, Fang S, Liao D (2006) MWNT–TiO_2:Ni composite catalyst: a new class of catalyst for photocatalytic H_2 evolution from water under visible light illumination. Chem Phys Lett 429:199–203

Rupa AV, Divakar D, Sivakumar T (2009) Titania and noble metals deposited titania catalysts in the photodegradation of tartrazine. Catal Lett 132:259–267

Serpone N, Lawless D, Khairutdinov R (1995) Size effects on the photophysical properties of colloidal anatase TiO_2 particles: size quantization versus direct transitions in this indirect semiconductor. J Phys Chem 99:16646–16654

Tian L, Ye L, Deng K, Zan L (2011) TiO_2/carbon nanotube hybrid nanostructures: solvothermal synthesis and their visible light photocatalytic activity. J Solid State Chem 184:1465–1471

Wang W, Serp P, Kalck P, Faria JL (2005) Visible light photodegradation of phenol on MWNT-TiO_2 composite

catalysts prepared by a modified sol–gel method. J Mol Catal A 235:194–199

Wang H, Wang HL, Jiang WF (2009) Solar photocatalytic degradation of 2,6-dinitro-*p*-cresol (DNPC) using multi–walled carbon nanotubes (MWCNTs)–TiO_2 composite photocatalysts. Chemosphere 75:1011–1105

Woan K, Pyrgiotakis G, Sigmund W (2009) Photocatalytic carbon nanotube–TiO_2 composites. Adv Mater 21:2233–2239

Wu Y, Zhang J, Xiao L, Chen F (2010) Properties of carbon and iron modified TiO_2 photocatalyst synthesised at low temperature and photodegradation of acid orange 7 under visible light. Appl Surf Sci 256:4260–4268

Yadav SK, Madeshwaran SM, Cho JW (2011) Synthesis of a hybrid assembly composed of titanium dioxide nanoparticles and thin multi-walled carbon nanotubes using ''click chemistry''. J Colloid Interface Sci 358:471–476

Yan MC, Chen F, Zhang JL, Anpo M (2005) Preparation of controllable crystalline titania and study on the photocatalytic properties. J Phys Chem B 109:8673–8678

Yu Y, Yu JC, Chan CY, Che YK, Zhao JC, Ding L, Ge WK, Wong PK (2005) Enhancement of adsorption and photocatalytic activity of TiO_2 by using carbon nanotubes for the treatment of azo dye. Appl Catal B 61:1–11

Yu J, Ma T, Liu S (2011) Enhanced photocatalytic activity of mesoporous TiO_2 aggregates by embedding carbon nanotubes as electron-transfer channel. Phys Chem Chem Phys 13:3491–3501

Zhang K, Oh WC (2010) Kinetic study of the visible light-induced sonophotocatalytic degradation of MB solution in the presence of Fe/TiO_2-MWCNT catalyst. Bull Korean Chem Soc 31(6):1589–1595

DOI 10.1007/978-3-319-05041-6_7
Reprinted from the *Journal of Nanoparticle Research*, DOI 10.1007/s11051-012-0790-z

RESEARCH PAPER

Synthesis and characterization of carbon-covered alumina (CCA) supported TiO_2 nanocatalysts with enhanced visible light photodegradation of Rhodamine B

Mphilisi M. Mahlambi · Ajay K. Mishra · Shivani B. Mishra · Rui W. Krause · Bhekie B. Mamba · Ashok M. Raichur

Received: 16 November 2011 / Accepted: 21 February 2012 / Published online: 14 March 2012

Abstract The anatase phase of titania (TiO_2) nanophotocatalysts was prepared using a modified sol gel process and thereafter embedded on carbon-covered alumina supports. The carbon-covered alumina (CCA) supports were prepared via the adsorption of toluene 2,4-diisocyanate (TDI) on the surface of the alumina. TDI was used as the carbon source for the first time for the carbon-covered alumina support system. The adsorption of TDI on alumina is irreversible; hence, the resulting organic moiety can undergo pyrolysis at high temperatures resulting in the formation of a carbon coating on the surface of the alumina. The TiO_2 catalysts were impregnated on the CCA supports. X-ray diffraction analysis indicated that the carbon deposited on the alumina was not crystalline and also showed the successful impregnation of TiO_2 on the CCA supports. In the Raman spectra, it could be deduced that the carbon was rather a conjugated olefinic or polycyclic hydrocarbons which can be considered as molecular units of a graphitic plane. The Raman analysis of the catalysed CCAs showed the presence of both the anatase titania and D and G band associated with the carbon of the CCAs. The scanning electron microscope micrographs indicated that the alumina was coated by a carbon layer and the energy dispersive X-ray spectra showed the presence of Al, O and C in the CCA samples, with the addition of Ti for the catalyst impregnated supports. The Brunauer Emmet and Teller surface area analysis showed that the incorporating of carbon on the alumina surface resulted in an increase in surface area, while the impregnation with TiO_2 resulted in a further increase in surface area. However, a decrease in the pore volume and diameter was observed. The photocatalytic activity of the nanocatalysts was studied for the degradation of Rhodamine B dye. The CCA-TiO_2 nanocatalysts were found to be more photocatalytically active under both visible and UV light irradiation compared to the free TIO_2 nanocatalysts.

Keywords Carbon-covered alumina · Toluene 2, 4-diisocyanate · Carbon coating · Equilibrium adsorption · TiO_2 · Impregnation · Olefinic · Sustainable development

Special Issue Editors: Mamadou Diallo, Neil Fromer, Myung S. Jhon

This article is part of the Topical Collection on Nanotechnology for Sustainable Development

M. M. Mahlambi · A. K. Mishra (✉) · S. B. Mishra · R. W. Krause · B. B. Mamba
Department of Chemical Technology, University of Johannesburg, P.O. Box 17011, Doornfontein 2028, South Africa
e-mail: amishra@uj.ac.za

A. M. Raichur
Department of Materials Engineering, Indian Institute of Science, Bangalore 560012, India

Introduction

Titanium dioxide (TiO_2 or titania) is a metal oxide semiconductor that has been extensively studied and

thus as a photocatalyst it has been used in coating self-cleaning surfaces, as environmental purifiers and in antifogging mirrors (Hoffmann et al. 1995; Mori et al. 2008; Foster et al. 2011). Owing to its peculiar and fascinating physicochemical properties, titania is a very important environmental and energy material with a wide variety of potential applications in diverse fields including gas sensors, part of photovoltaic devices, dielectric ceramics and catalysts for thermal or photo induced processes. Its properties which include, among others, long-term stability, non-toxicity, low price and superior photo-reactivity has led to TiO_2 gaining more prominence over most semiconductors (Ahn et al. 2007; Yu et al. 1997; Zhu et al. 2005; Tian et al. 2009; Li et al. 2008; Colmenares et al. 2006; Foglia et al. 2009; Yu and Zhang 2010). Various parameters like crystallinity, impurities, surface area and density of surface reactive sites results in an enhanced photocatalytic activity; however, crystallinity is the most important factor (Fu et al. 2005; Ao et al. 2008). The photocatalytic reactions are initiated when the TiO_2 semiconductor absorbs energy (a photon or hv) resulting in an excitement of an electron from the valence band to the conduction band. Electron can only be excited if the energy of the photon is equal to or exceeds the band gap (E_{bg} = 3.0–3.2 eV) of the titania semi-conductor (Hoffmann et al. 1995; Bessekhouad et al. 2003; Zhu et al. 2008). The electron (e^-) and the hole (h^+) act as the redox pair, and separation of these charges is imperative to result in enhanced oxidation and reduction, respectively (Fu et al. 2005; Hoffmann et al. 1995; Wang et al. 2008). The separated two charge carriers (e^- and h^+) therefore propel the photo-electrochemical red-ox reactions with the redox molecules at the semiconductor surface (Bessekhouad et al. 2003; Chen and Mao 2007). However, to increase the photocatalytic activity and recoverability of titania from aqueous media, these catalysts can be embedded on catalysts' supports.

Carbon and alumina are the mostly widely used for support materials. However, their exclusive use as catalysts' supports has some major drawbacks. Alumina, for instance, is an acidic support upon calcination reacts with the promoter ions (e.g. Co and Ni) resulting in the formation of unwanted metal oxides resulting in reduced the catalysts activity (Vissers et al. 1988; Boorman and Chong 1993; Zheng et al. 2008). Carbon supports, on the other hand, are either microporous or have poor mechanical strength and hence are not favourable support materials as they easily crush and have low bulk density (Boorman and Chong 1993; Błachnio et al. 2007). Also, metals catalysts supported on carbon can be deposited on the micropores of the carbon supports hence making their catalytic activity trivial (Błachnio et al. 2007).

However, both alumina and carbon supports have desirable properties. For instance, alumina supports have the ability to disperse up to 20% of the active metal phase, have high surface area as well as good mechanical properties (Vissers et al. 1988; Zheng et al. 2008). Carbon supports have mild interactions with the supported metals, a neutral surface, good thermal conductivity, high surface area with controlled pore volume, reduced coking propensity, resistance to nitrogen poison and variable surface functional groups which give carbon a tremendous scope for use as catalyst support material (Zheng et al. 2008; Boorman and Chong 1993).

A support is very important for a catalyst since it determines the catalytic activity of the catalyst. However, the exclusive use of carbon or alumina as catalyst supports can result in the loss of the catalytic activity of the catalysts; hence, a support system that exploits the merits of both substances can provide an ideal support system which overcomes the shortcomings of both. In this system, the alumina is coated with a thin layer of carbon before catalyst impregnation resulting in a support material that possesses both the textural and mechanical properties of alumina and the favourable surface properties of carbon (Boorman and Chong 1993; Błachnio et al. 2007; Zheng et al. 2008). The utilisation of these carbon-covered alumina materials as catalyst supports has gained an increasing interest in recent years (Błachnio et al. 2007; Boorman and Chong 1992; Lin et al. 2005a, b; Maity et al. 2009; Polyánszky and Petró 1990; Sharanda et al. 2006; Shashikala et al. 2007; Vissers et al. 1988; Zheng et al. 2008).

Carbon-covered alumina supports have been mostly used as supports for hydrotreating catalysts (Vissers et al. 1988; Boorman and Chong 1992; Maity et al. 2009) and ammonia synthesis (Rao et al. 1990). Recently, supports have found a lot of useful applications. For instance, CCA been used as a high surface area packing material for high performance liquid chromatography (Paek et al. 2010), and has also been prepared in various forms like carbon-coated alumina foams (Jana and Ganesan 2011). CCA-supported catalysts have hardly been used in remediation of

environmental burdens. According to literature, only nano-silver catalyst has been supported on CCA to monitor microorganisms in drinking water (Shashikala et al. 2007). Also, according to our best knowledge, TiO_2 nanocatalysts have never been supported on carbon-covered alumina supports. In this research, titania nanoparticles will be supported on CCA supports. This is expected to enhance the visible light photo response of the catalysts and also help to prevent the agglomeration of the nanoparticles when subjected to photocatalytic experiments. Supporting these CCA-supported TiO_2 nanocatalysts therefore plays a major part of this research and is expected to pave way for the use of renewable solar energy for environmental photocatalytic processes. The use of nanocatalysts (especially titanium dioxide or titania or TiO_2) has gained wide recognition since they have the potential to tackle the 'difficult-to-remove' contaminants and thus are expected to play an important role in solving many serious environmental and pollution problems. Titania catalysts not only show excellent catalytic performance with some of the highest selectivities known in the literature so far, but also its lower price in comparison to other catalysts increases its attractiveness as catalyst for use in environmental applications (Ulgen and Hoelderich 2011; Calandra et al. 2010). Also, the controllable synthesis of anatase titanium dioxide is another add-on to the wide investigation of TiO_2 for important industrial and environmental applications (Fang et al. 2011). In this study, we report on the synthesis and characterizations of the physical and textural properties of nano anatase TiO_2 catalysts supported on carbon-covered alumina.

Experimental

Materials and methods

Titanium (IV) tetraisopropoxide (TTIP) (99%) was obtained from Sigma-Aldrich (Germany) and used without further purification. Formic acid (98%) was purchased at Merck and AR grade *n*-propanol was sourced from SD's Fine Chem (Pty) Ltd., and was distilled before usage. γ-Alumina was purchased from Sigma-Aldrich and was calcined at 500 °C for 3 h in a muffle furnace to remove any organic impurities that might have been present. Toluene 2,4-diisocyanate was supplied by Industrial Polyurethanes (Edenvale, South Africa) and was used without purification. *n*-Xylene (AR grade) was purchased from Sigma-Aldrich and was dried on calcium hydride fro 24 h before usage.

Synthesis of catalysts and supports

Synthesis of TiO_2 nanocrystalline photocatalysts

For the synthesis of the anatase rich titania nanocatalysts, TTIP was hydrolysed through an esterification reaction between formic acid and propanol (Zhu et al. 2005) TTIP (10 mL, 0.334 mol) was dissolved in propanol (48 mL, 0.642 mol) and the reaction mixture was stirred for 20 min. Formic acid (13 mL, 0.535 mol) was gradually added while stirring gently. After stirring the reaction mixture for about 20 min, a white precipitate (titanium hydroxide) was gradually formed. This mixture was then stirred for a further 2-h period, aged at room temperature for another 2 h and filtered. The filtered residue was then repeatedly washed with copious amounts of propanol and deionized water; thereafter it was dried overnight in an oven at 80 °C. It was then ground into fine powder in a mortar and pestle and then calcined at 450 °C to obtain nanocrystalline TiO_2 catalysts.

Synthesis of carbon-covered alumina supports

CCA supports were synthesized by modification of an equilibrium adsorption method by Sharanda et al. (2006). A mixture of γ-alumina (5 g) and 1% TDI in *n*-xylene (115 mL) was occasionally shaken for 24 h at room temperature. The reaction mixture was filtered and washed with *n*-xylene (100 mL). A white fluffy precipitate was obtained. This was dried in an oven at 80 °C overnight. The obtained precipitate was then ground in a pestle and mortar and placed into a quartz cell. The temperature was slowly increased to 700 °C under 30 mL min^{-1} flow of nitrogen and the temperature was held at that temperature for 3 h in order to complete the pyrolysis of TDI and remove volatile products.

Impregnation experiments

To impregnate the CCA supports with the nanocatalysts, TiO_2 nanocatalysts were dissolved in distilled water to form a colloidal suspension. These were sonicated for 30 min at room temperature. CCA

supports were then added on the TiO_2 suspensions. The impregnated CCA supports were then sonicated for 1 h and left at room temperature for 24 h to dry. These were further dried in an oven at 80 °C for 12 h (overnight). After drying, these were then ground in a pestle and mortar and calcined at 450 °C for 3 h in a muffle furnace to afford the TiO_2-impregnated CCA supports.

Characterization

XRD spectroscopy analysis

The XRD measurements were carried out using an X'Pert Pro MPD PANalytical powder diffractometer operating in the reflection mode with CuKα radiation. The XRD chromatograms were recorded over an angular range of 20–80 °C (2θ) and with a step size of 0.02° and a collection time of 0.3 s ($\lambda =$ 0.154060 nm). A shape factor K is used in X-ray diffraction and crystallography to correlate the size of sub-micrometer particles, or crystallites. The Debye–Scherrer equation, $D = K\lambda/B \cos\theta$, was used to correlate the particle size, where the constant $K = 0.89$, $\lambda = 0.154060$ nm is the X-ray wavelength, B is the full width half maximum (FWHM) of the catalyst, and θ is the diffracting angle. The JCPDS XRD library software was used to confirm the Miller planes of the CCA supports.

Raman spectroscopy

For Raman analysis, a PerkinElmer Raman Micro 200 was used. This was equipped with a laser lamp operating at a wavelength of 785 nm and had a maximum output of 250 mW. For analysis, the sample was placed on a quartz slide on the stage of the microscope and the focus was adjusted manually to obtain the best image. This was then switched to the dark field and the beam was passed on the sample to record the spectrum.

SEM, TEM and EDX spectroscopy

A quanta FEI-SIRION SEM was used to analyse and visualise the surface morphology of the nanocatalysts. The powder samples were placed on a carbon tape and analysed without gold coating. A JEOL J2100 F TEM was used to study the microstructure of the nanocatalysts. The sample powders were dispersed in ethanol and sonicated for 10 min before analysis. A drop of the suspension was then placed on a carbon-coated copper grid and dried in air before visualisation. Both the SEM and TEM were coupled with an EDX detector, which was used to determine the identity of the alumina, the free carbon-covered alumina and the TiO_2-impregnated carbon-covered alumina supports.

BET surface area and pore size distribution measurements

To study the surface area (S_{BET}), pore volume and pore size distributions of the synthesized CCA supports, a Micromeritics ASAP 2020 Surface area and Porosity Analyzer was used. The samples were degassed in nitrogen under vacuum for 24 h at 200 °C before determination of the surface area. Typically, the samples were heated to 90 °C at a heating rate of 5 °C min^{-1} and the temperature was held at 90 °C for 180 min. The samples were then evacuated at a pressure of 50 mmHg for 30 min. The samples were then ramped to 180 °C at a heating rate of 10° min^{-1} and degassed for 24 h under nitrogen. Surface area is believed to be an important parameter when studying the catalytic efficiency of the nanocatalysts embedded on CCA supports (CCA-TiO_2) since a high surface area means more active sites for extensive catalysis.

Photocatalytic degradation studies

A Newport 9600 Full Spectrum Solar Simulator equipped with 150 W ozone free xenon lamp which produces a collimated beam of 33-mm diameter, an equivalent of 1.3 suns was used to study the degradation Rhodamine B by the titania photocatalysts. The distance between the solar simulator and the experimental set up was set such that the beam power was equivalent to 1 sun (about 10 cm). A high-pressure 125 W mercury vapour lamp (Samson, India) was used as the UV irradiation source. The photocatalytic activity of these nanophotocatalysts was studied using 100 mL (10 mg L^{-1}) Rhodamine B. The CCA-supported titania nanoparticles (100 mg nanoparticles per 100 mL of 10 mg L^{-1} dye) were used in suspension to determine the photoactivity of the nanoparticles. The solution was stirred with a magnetic stirrer for 1 h before irradiation with the solar light to establish an

adsorption–desorption equilibrium between the dye and the catalyst surface. Aliquots of 2 mL were extracted from the reaction chamber at 30-min intervals to study the extent of the degradation. The entire photo reactor setup was set inside a 100 cm × 70 cm wooden box. The set up was the same for the free (unsupported) titania nanocatalysts.

Results and discussions

XRD spectroscopy analysis

From the XRD patterns (Fig. 1), the CCA supports (A) do not show peaks associated with carbon and this means that characterisation of the CCAs with XRD did not reveal any peaks associated with the ordered carbon structures (Sharanda et al. 2006). The only peaks that could be seen are those associated with the alumina at $2\theta = 37.5$ (311), 39.5 (222), 42.9 (321) 45.6 (400) and 67.5 (411). These peaks concur with XRD data obtained from the JCPDS library catalogue number 04-0880. This therefore means that the presence of either amorphous carbon layer or a thin graphitic layer can only be assumed due to the black colour observed. Graph (A) shows peaks associated with pure anatase phase. The XRD peaks obtained at calcination temperatures of 450 °C corresponds to the tetragonal anatase titania phase of the titania and this was confirmed by cross referencing with the JCPDS CAS No. 21-1272 (JCPDS catalogue). The peaks that were observed at $2\theta = 25.2$ (101), $2\theta = 37.9$ (004), $2\theta = 48.0$ (200), $2\theta = 53.9$ (106) and $2\theta = 62.7$ (215) indicate the successful synthesis of the anatase phase of TiO_2. The peaks $2\theta = 27.5$ (a rutile-phase peak) due to the (110) reflection and $2\theta = 30.8$ (121) which is a brookite phase, and this is an indication of the absence of these phases in our synthesized titania (Navio et al. 1999; Anandan et al. 2008). Graph (B), which is of the TiO2-embedded CCA supports exhibit both the peaks associated with TiO_2 and CCA. This is an indication that embedding the TiO_2 nanocatalysts on the CCAs did not alter the core of the titania phase (anatase) or the CCA supports.

Raman spectroscopy

The UV Raman spectrum of the CCA supports is shown in Fig. 2 (insert). Two peaks that were assigned to the D and G bands were observed at 1318 and 1607 cm^{-1}, respectively, and are due to the sp^2 carbon species (Zheng et al. 2008; Lin et al. 2005b). These two peaks are common for various forms of disordered, noncrystalline and amorphous carbons observed in the Raman spectra. The D (disorder) band is related to the breathing modes of the sp^2 carbon atoms in the ring, while the G band is due to bond stretching of the sp^2 carbon atoms. The widths, dispersions and intensities of these peaks are different for various carbons and hence provide powerful information for differentiating carbon species (Lin et al. 2005b). The D peak can be fitted into three peaks which are observed at 1165, 1318 and 1386 cm^{-1}. The G band was observed at

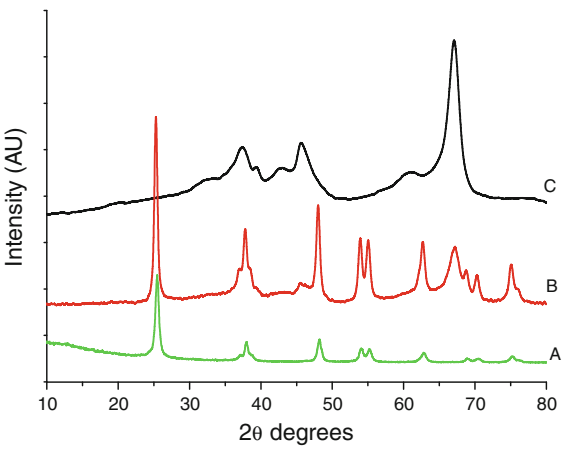

Fig. 1 XRD patterns of TiO_2 (*A*), TiO_2 impregnated CCA (CCA-TiO_2) (*B*) and CCA (*C*)

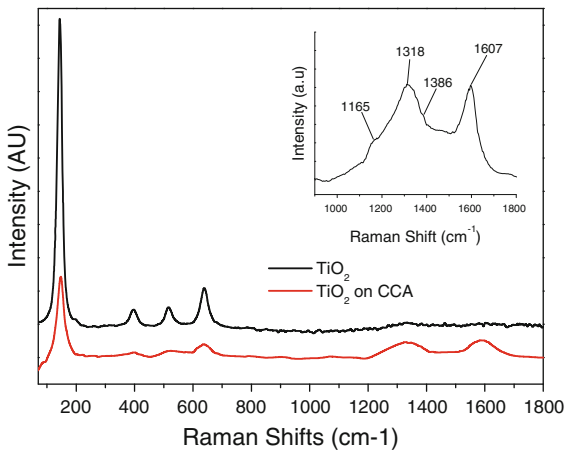

Fig. 2 UV Raman Spectra of the titania impregnated CCA supports

1607 cm^{-1}, and this is an indication that the carbon layer on the CCAs was possibly related to conjugate olefinic species or polycyclic aromatic hydrocarbons. This peak usually appears at lower wavelengths of 1582 cm^{-1} when the carbon layer is crystalline graphite (Lin et al. 2005b). This means that the carbon layer deposited on the alumina surface is not crystalline. It is therefore reasonable to speculate that the Raman analysis explains why there are no carbon peaks observed on the XRD chromatograms.

The Raman spectra of the titania in Fig. 2 show that the titania is anatase phase. The peaks observed are associated with the primitive unit cell of the anatase titania phase. It is tetragonal and has fifteen (15) irreducible optical modes which are represented by $1A_{1g} + 1A_{2u} + 2B_{1g} + 1B_{2u} + 3E_g + 2E_u$. The A_{1g}, B_{1g} and E_g modes are Raman active, while the A_{2u} and E_u are infra red active (Ohsaka et al. 1978). From Fig. 3, the two Raman bands at 516 and 399 cm^{-1} are the B_{1g} stretching modes while the three Raman bands at 639, 197 and 144 cm^{-1} are assigned to the A_{1g} modes, which are the stretching modes of the anatase phase of the titania. It should be noted that the frequency of the 144 cm^{-1} band is very intense and sharp and is nearly equal to that of the rutile phase, which is at 143 cm^{-1}. However, the difference is that the rutile phase band is sharp but weak (Ohsaka et al. 1978; Lei et al. 2001). This is important because it confirms that doping the TiO_2 with metal ions does not alter the phase, which is a very important feature when studying the degradation of organic pollutants by photo active semi-conductors.

The Raman peaks associated with both the anatase phase and the CCA modes both appear in the graph of the TiO_2 supports. This is an indication that the impregnation of the CCA supports by the TiO_2 was successful. However, the intensities of the peaks associated with the titania show that TiO_2 might be suppressed. This could be due to the surface modification of titania by the presence of carbon. Carbon can easily disperse on the surface of titania, a special property that might result in an improved catalytic activity of the titania (Lin et al. 2005a, b).

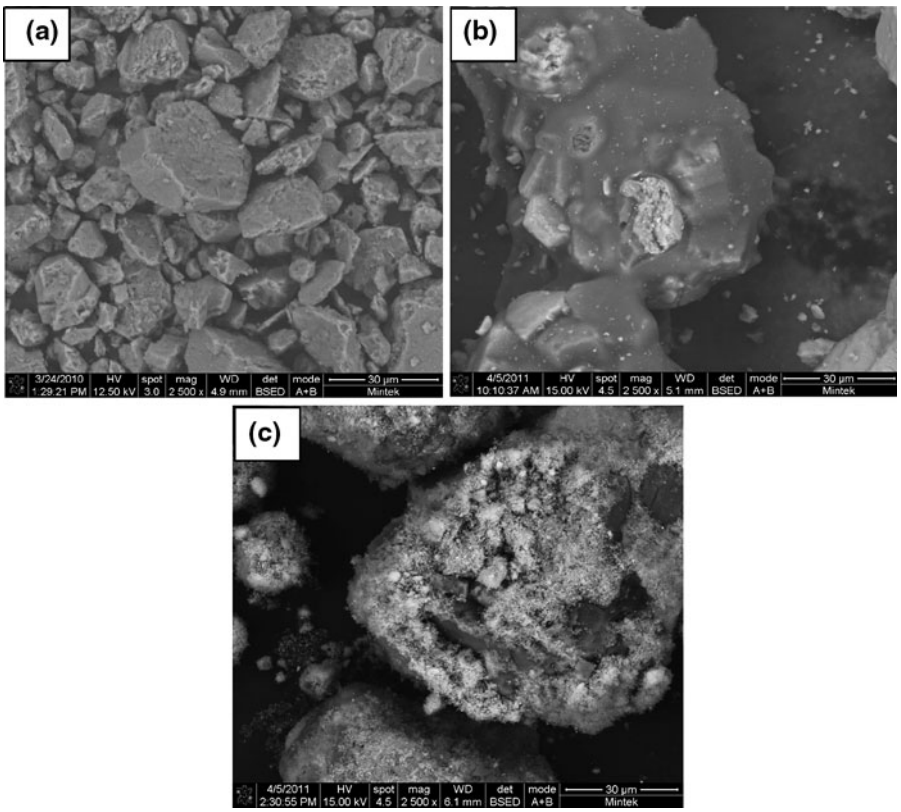

Fig. 3 SEM micrographs of **a** alumina, **b** CCA and **c** CCA-TiO_2

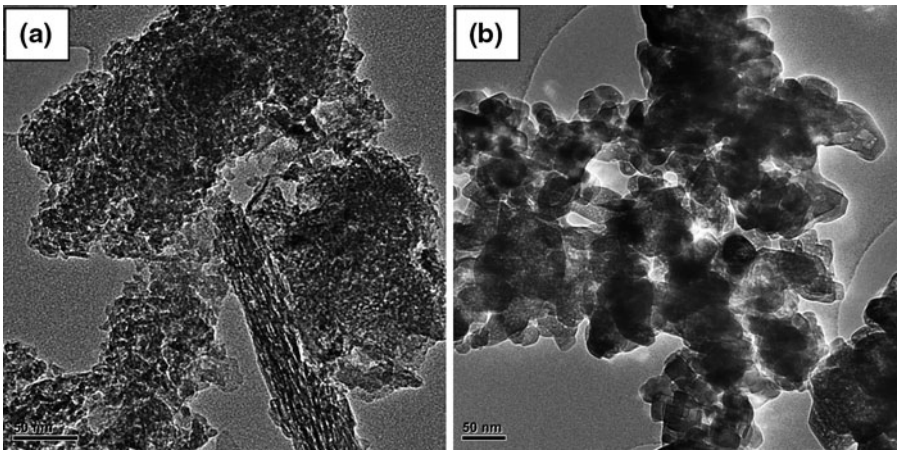

Fig. 4 TEM micrographs of alumina (**a**), CCA (**b**) and CCA-TiO_2

SEM, TEM and EDX spectroscopy

The SEM micrographs (Fig. 3) show the physical morphology of the alumina (a), CCA (b) and CCA-TiO_2 (c). The SEM micrographs show that a carbon layer has been deposited on the alumina support. The carbon layer appears to be homogeneously distributed on the surface of the alumina. Also, the alumina and CCA support surfaces appear to be porous and hence provide a large surface area for use as catalysts supports. Fig. 3c shows the TiO_2 nanocatalysts that are embedded on the CCA support surface. The titania nanocatalysts appear embedded on the pores of the CCA supports, hence giving the idea that they can be used in catalysis without falling away from the supports. Figure 4 shows TEM micrographs of the CCA supports (a) and the TiO_2 embedded supports (b). The CCA supports appear microporous and fluffy, an effect of carbon coating. Figure 4b shows the TEM micrograph of the TiO_2 embedded supports. The supported titania catalysts still appear to have not lost their crystallinity, and hence the assumption that the catalytic activity of the catalysts has not been altered, but an improvement might be expected. To identify the elemental composition of the synthesized catalyst and supports, the EDX spectra for the alumina (Fig. 5a), CCA (Fig. 5b) and CCA-TiO_2 (Fig. 5c) were also studied. These showed that the alumina was composed of only Al and O, while the CCA has C as an extra element. The CCA-TiO_2 spectrum shows the presence of Al, O, C and Ti. The EDX spectra therefore not only indicate the successful incorporation of carbon on the surface of alumina but also the successful impregnation of the CCA with the TiO_2 nanocatalysts.

BET surface area and pore size distribution measurements

The nitrogen adsorption–desorption isotherms were measured to understand the influence of carbon loading on the surface of the alumina as well as the effect of embedding the TiO_2 nanocatalysts on the CCA (Figs. 6, 7, 8). Figure 6 shows the adsorption–desorption isotherm of γ-alumina and the insert graph shows the pore size distribution graphs of the γ-alumina. Figure 7 shows the adsorption–desorption isotherm of the CCA support with the pore size distribution graph shown as an insert and Fig. 8 shows the adsorption–desorption isotherm of CCA-TiO_2 with the insert showing the pore size distribution graph. According to the Brunauer–Emmett–Teller (BET) classification, these adsorption–desorption isotherms can be classified as type IV. This type of isotherm describes the process of nitrogen adsorption on the adsorbent surface. Pure alumina, CCA and CCA-TiO_2 were all found to possess a heterogeneous pore structure. These microporous pores were filled up with the adsorbate (nitrogen) at small pressures and as the adsorbate concentration increases, pores of larger diameters were also filled up resulting in the formation of a multimolecular adsorption layer. Evidence of the occurrence of open pores in the alumina, CCA

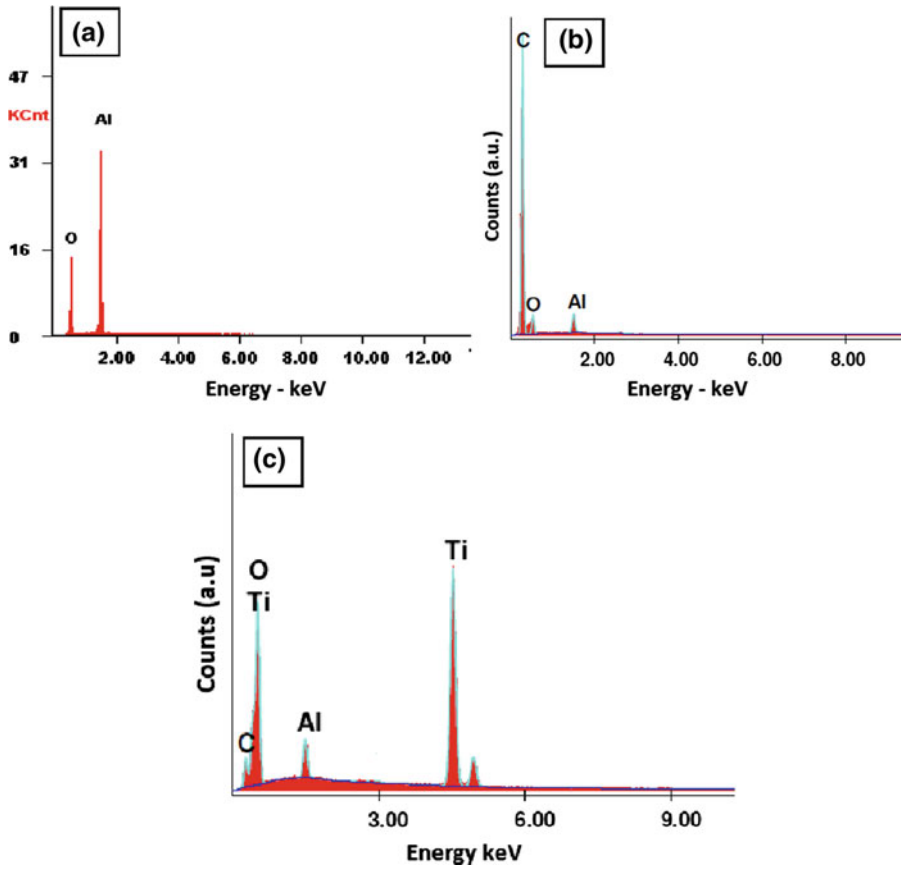

Fig. 5 EDX spectra of **a** alumina and **b** CCA and **c** CCA-TiO_2

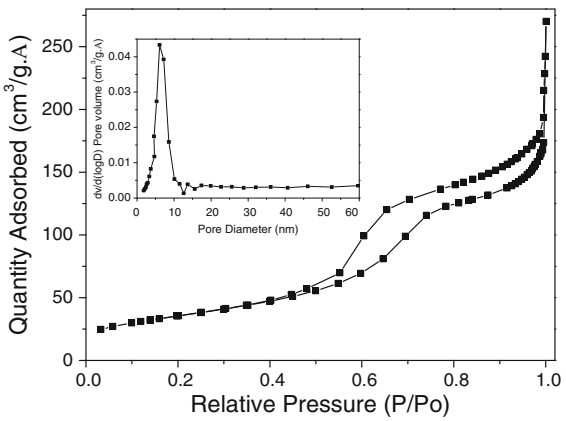

Fig. 6 Nitrogen adsorption–desorption isotherm of the initial alumina support

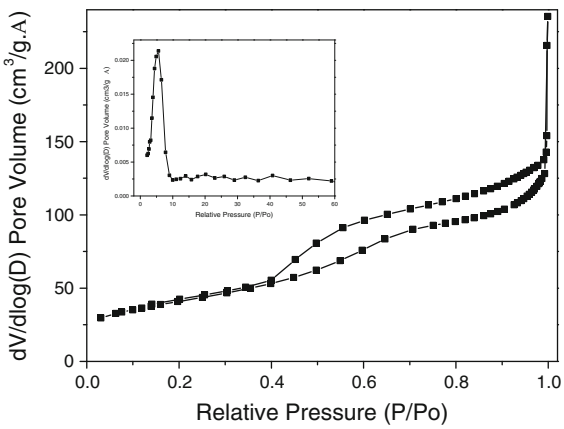

Fig. 7 Nitrogen adsorption–desorption isotherm of the CCA support

supports and CCA-TiO_2 are shown by the presence of the hysteresis loop in the diagrams.

To further study the texture and surface properties of alumina and the synthesized CCA supports, specific surface area, pore volume, pore size and pore size distribution were analysed according to the BJH method (insert graphs in Figs. 6, 7, 8) and are summarised in Table 1. The addition of the carbon layer on the surface of the alumina resulted in a significant increase in the surface area from

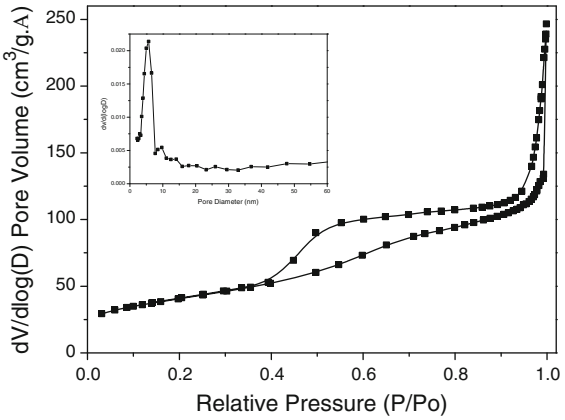

Fig. 8 Nitrogen adsorption–desorption isotherm of the CCA-TiO_2

Table 1 Textural properties of the CCA support

Sample	S_{BET} (N_2) ($m^2\ g^{-1}$)	Total pore volume ($cm^3\ g^{-1}$)	Mean pore diameter (nm)
Al_2O_3	128	0.27	8.36
CCA	146	0.20	5.41
CCA-TiO_2	149	0.21	5.69

128 $m^2\ g^{-1}$ (pure alumina), 146 $m^2\ g^{-1}$ (CCA) and 149 $m^2\ g^{-1}$ for the CCA-TiO_2. This increase is a result of the creation of new pore structures after the modification of the alumina surface (Błachnio et al. 2007). There is however a decrease on the pore volume (0.27–0.20 $cm^3\ g^{-1}$) and mean diameter of the pores (8.36–5.41 nm) for the alumina and the CCA. This can be attributed to the formation of a uniform carbon layer on the alumina surface (Sharanda et al. 2006). This is an indication that carbon occupied the inner pores of the alumina, hence the decrease (Zheng et al. 2008). However, the addition of the nanocatalysts on the CCA resulted in no noticeable difference between the sizes of the pore volumes. A slight increase in diameter (from 5.41 to 5.69 nm) was observed for the CCA and CCA-TiO_2. Furthermore, the shape of the pore size distribution graphs fits a Gaussian curve distribution with peak maxima at 6.4 nm for alumina, 5.4 nm for the CCA support and 5.6 nm for the CCA-TiO_2.

Photodegradation of Rhodamine B

For the photodegradation studies, the dye was illuminated with visible light in the absence of the catalyst (photolysis) to determine the extent of degradation under visible light. This was done since rhodamine B has been reported to absorb light which is in the range of 400–600 nm (He et al. 2009; Natarajan et al. 2011). The reaction mixture was first stirred in the dark for 1 h to reach equilibrium between the catalyst and the dye before illumination with either the UV or visible light, and the concentration was monitored. It was found that there was only about 2% adsorption of the dye on the catalysts when the equilibrium was reached. Photodegradation of rhodamine B was tested using the free and CCA-supported titania catalysts both under UV light and visible light irradiation for comparison purposes.

The results obtained showed that photolysis had an average of about 4% degradation of Rhodamine B after about 4.5 h. As shown in Fig. 9, both the CCA-TiO_2 and the free titania nanocatalysts achieved complete degradation after 270 min. From these results, the CCA-TiO_2 nanocatalysts show a higher reaction rate than the free anatase titania. Unsupported titania could only degrade about 20% Rhodamine B under visible light illumination in 270 min compared to complete degradation under UV light irradiation. The results obtained (Fig. 9) also show that CCA-TiO_2 nanocatalysts were photocatalytically active under both visible and UV light, although it was more photocatalytically active under visible light. Under visible light irradiation the photodegradation of Rhodamine was complete within 180 min compared to about 240 min observed under UV light irradiation. Also, The CCA-supported TiO_2 nanocatalysts

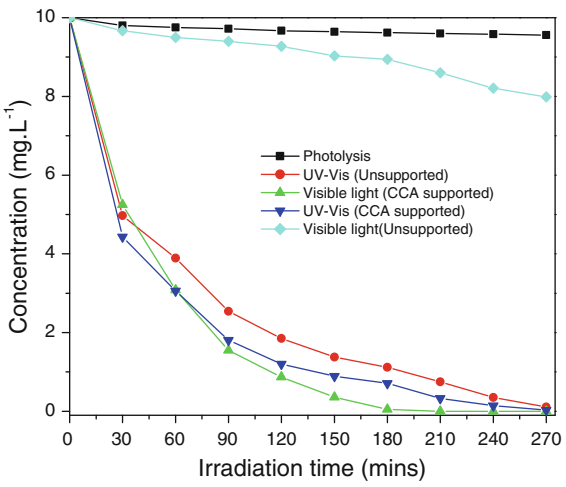

Fig. 9 Graph showing photodegradation of rhodamine B by free titania CCA-T under UV and visible light illumination

generally showed high photocatalytic activity than the unsupported titania nanocatalysts both under UV and visible light irradiation.

Conclusions

From this research study, the TiO_2 nanocatalysts were successfully embedded on CCA supports that were synthesized by exploiting the reactivity of the N=C=O groups of toluene 2,4 diisocyanate. The successful synthesis of the TiO_2 nanocatalysts-impregnated CCA supports was confirmed by UV Raman spectroscopy which showed the presence of the D and G olefinic carbon bands at 1318 and 1607 cm^{-1}, respectively, as well as the anatase TiO_2 peaks at 516 399, 639, 197 and 144 cm^{-1}. The SEM confirmed the presence of a uniform carbon layer on the surface of the alumina and the successful impregnation of the titania catalysts on the CCA supports. The EDX spectral analysis confirmed the elemental composition of the alumina, CCA supports as well as the CCA-TiO_2. Further analysis of the adsorption–desorption isotherms revealed that the presence of the carbon layer on the alumina surface resulted in an increase in surface area and a decrease in pore size and pore volume. This is a result of a formation of a uniform carbon layer on the alumina surface and also an indication that the carbon was modifying the pores of the alumina. However, although impregnating the supports with TiO_2 did result in an increase in surface area, there was no observable difference between the pore volume and pore diameter between the CCA supports and the CCA-TiO_2. Overall, for the first time the TiO_2 catalysts were successfully embedded on the CCA supports. The CCA-TiO2 nanocatalysts were found to be more photocatalytically active under visible light irradiation compared to their unsupported counterparts and this provides a great stride towards the use of the renewable solar energy for water treatment purposes.

Acknowledgments The authors are grateful to the University of Johannesburg for financial support and the Indian Institute of Science, Bangalore, India for providing the infrastructure to carry out some of this research work.

References

Ahn W-Y, Sheeley SA, Rajh T, Cropek DM (2007) Photocatalytic reduction of 4-nitrophenol with arginine-modified titanium dioxide nanoparticles. Appl Catal B Environ 74:103–110. doi:10.1016/j.apcatb.2007.01.016

Anandan S, Kumar PS, Pugazhenthiran N, Madhavan J, Maruthamuthu P (2008) Effect of loaded silver nanoparticles on TiO_2 for photocatalytic degradation of Acid Red 88. Sol Energy Mater Sol Cells 92:929–937. doi:10.1016/j.solmat.2008.02.020

Ao Y, Xu J, Fu D, Yuan C (2008) Preparation of Ag-doped mesoporous titania and its enhanced photocatalytic activity under UV light irradiation. J Phys Chem Solids 69:2660–2664. doi:10.1016/j.jpcs.2008.06.100

Bessekhouad Y, Robert D, Weber JV (2003) Synthesis of photocatalytic TiO_2 nanoparticles: optimization of the preparation conditions. J Photochem Photobiol A Chem 157:47–53. doi:10.1016/s1010-6030(03)00077-7

Błachnio M, Staszczuk P, Grodzicka G, Lin L, Zhu YX (2007) Adsorption and porosity properties of carbon-covered alumina surfaces. J Therm Anal Calorim 88(2):601–606. doi:10.1007/s10973-006-8067-3

Boorman PM, Chong K (1992) A comparative gas oil hydroprocessing study of alumina, carbon, and carbon-covered alumina supported Ni–Mo catalyst: effect of quinoline, thiophene, and vanadium spiking. Energy Fuels 6:300–307. doi:10.1021/ef00033a10

Boorman P, Chong K (1993) Preparation of carbon-covered alumina using fluorohydrocarbons: a new acidic support material. Appl Catal A Gen 95:197–210. doi:10.1016/0926-860x(93)85074-y

Calandra P, Lombardo D, Pistone V, Liveri T, Trusso C (2010) Structural and optical properties of novel surfactant-coated Yb@TiO_2 nanoparticles. J Nanopart Res. doi:10.1007/s11051-010-0133-x

Chen X, Mao SS (2007) Titanium dioxide nanomaterials: synthesis, properties, modifications, and applications. Chem Rev 107:2891–2959. doi:10.1021/cr0500535

Colmenares JC, Aramendia MA, Marinas A, Marinas J, Urbano F (2006) Synthesis, characterization and photocatalytic activity of different metal-doped titania systems. Appl Catal A Gen 306:120–127. doi:10.1016/j.apcata.2006.03.046

Fang WQ, Zhou JZ, Liu J, Chen ZG, Yang C, Sun CH, Qian GR, Zou J, Qiao SZ (2011) Hierarchical structures of single-crystalline anatase TiO_2 nanosheets dominated by 001 facets. Chem Eur J 17:1423–1427. doi:10.1002/chem.201002582

Foglia FD, Losco T, Piseri P, Milani P, Selli E (2009) Photocatalytic activity of nanostructured TiO_2 films produced by supersonic cluster beam deposition. J Nanopart Res 11:1339–1348. doi:10.1007/s11051-009-9691-1

Foster HA, Ditta IB, Varghese S, Steele A (2011) Photocatalytic disinfection using titanium dioxide: spectrum and mechanism of antimicrobial activity. Appl Microbiol Biotechnol 90:1847–1868. doi:10.1007/s00253-011-3213-7

Fu W, Yang H, Li M, Li M, Yang N, Zou G (2005) Anatase TiO_2 nanolayer coating on cobalt ferrite nanoparticles for magnetic photocatalyst. Mater Lett 59:3530–3534. doi:10.1016/j.matlet.2005.06.071

He Z, Sun C, Yang S, Ding Y, He H, Wang Z (2009) Photocatalytic degradation of rhodamine B by Bi_2WO_6 with electron accepting agent under microwave irradiation: mechanism and pathway. J Hazard Mater 162:1477–1486. doi:10.1016/j.jhazmat.2008.06.047

Hoffmann MR, Martin ST, Choi W, Bahnemannt DW (1995) Environmental applications of semiconductor photocatalysis. Chem Rev 95:69–96. doi:10.1016/j.ces.2007.06.030

Jana P, Ganesan V (2011) The production of a carbon-coated alumina foam. Carbon 49:3292–3298. doi:10.1016/j.carbon.2011.04.005

Lei Y, Zhang LD, Fan JC (2001) Fabrication, characterization and Raman study of TiO_2 nanowire arrays prepared by anodic oxidative hydrolysis of $TiCl_3$. Chem Phys Lett 338:231–236. doi:10.1021/s0009-2614(01)00263-9

Li X, Xiong R, Wei G (2008) S–N Co-doped TiO_2 photocatalysts with visible-light activity prepared by sol–gel method. Catal Lett 125:104–109. doi:10.1007/s10562-008-9521-6

Lin L, Lin W, Zhu YX, Zhao BY, Xie YC, He Y, Zhu YF (2005a) Uniform carbon-covered titania and its photocatalytic property. J Mol Catal 236:46–53. doi:10.1016/j.molcata.2005.04.028

Lin L, Lin W, Zhu YX, Zhao BY, Xie YC, Jia GQ, Li C (2005b) Uniformly carbon-covered alumina and its surface characteristics. Langmuir 21(11):5040–5046. doi:10.1021/la047097d

Maity SK, Flores L, Ancheyta J, Fukuyama H (2009) Carbon-modified alumina and alumina-carbon supported hydrotreating catalysts. Ind Eng Chem Res 48:1190–1195. doi:10.1021/ie800606p

Mori K, Maki K, Kawasaki S, Yuan S, Yamashita H (2008) Hydrothermal synthesis of TiO_2 photocatalysts in the presence of NH_4F and their application for degradation of organic compounds. Chem Eng Sci 63:5066–5070. doi:10.1016/j.ces.2007.06.030

Natarajan TS, Thomas M, Natarajan K, Bajaj HC, Tayade RJ (2011) Study on UV-LED/TiO_2 process for degradation of Rhodamine B dye. Chem Eng J 169:126–134. doi:10.1016/j.cej.2011.02.066

Navio JA, Colon G, Macias M, Real C, Litter MI (1999) Iron-doped titania semiconductor powders prepared by a sol-gel method. Part I: synthesis and characterization. Appl Catal A Gen 177:111–120. doi:10.1016/s0926-860x(98)00255-5

Ohsaka T, Izumi F, Fujiki Y (1978) Raman spectrum of anatase TiO_2. J Raman Spectrosc 7(6):321–324. doi:10.1002/jrs.1250070605

Paek C, Mccormick AV, Carr PW (2010) Preparation and evaluation of carbon coated alumina as a high surface area packing material for high performance liquid chromatography. J Chromatogr A 1217:6475–6483. doi:10.1016/j.chroma.2010.08.037

Polyánszky É, Petró J (1990) Relationship between selectivity and hydrogen sorption of carbon-supported palladium catalysts. Appl Catal 62:335–347. doi:10.1016/s0166-9834(00)82256-3

Rao KSR, Rao PK, Masthan SK, Kaluschnaya L, Shur VB (1990) New type of carbon coated alumina supports for the preparation of highly active ruthenium catalysts for ammonia synthesis. Appl Catal 62:L19–L22. doi:10.1016/s0166-9834(00)82229-0

Sharanda LF, Plyuto YV, Babich IV, Plyuto IV, Shpak AP, Stoch J, Moulijn JA (2006) Synthesis and characterisation of hybrid carbon-alumina support. Appl Surf Sci 252:8549–8556. doi:10.1016/j.apsusc.2005.11.078

Shashikala V, Kumar VS, Padmasri AH, Raju BD, Mohan SV, Sarma KS, Rao KSR (2007) Advantages of nano-silver-carbon covered alumina catalyst prepared by electrochemical method for drinking water purification. J Mol Catal A Chem 268:95–100. doi:10.1016/j.molcata.2006.10.019

Tian G, Fu H, Jing L, Tian C (2009) Synthesis and photocatalytic activity of stable nanocrystalline TiO_2 with high crystallinity and large surface area. J Hazard Mater 161:1122–1130. doi:10.1016/j.jhazmat.2008.04.065

Ulgen A, Hoelderich WF (2011) Conversion of glycerol to acrolein in the presence of WO_3/TiO_2 catalysts. Appl Catal A Gen 400:34–38. doi:10.1016/j.apcata.2011.04.005

Vissers J, Mercx F, Bouwens S, de Beer V, Prins R (1988) Carbon-covered alumina as a support for sulfide catalysts. J Catal 114:291–302. doi:10.1016/0021-9517(88)90033-4

Wang J, Li R, Zhang Z (2008) Degradation of hazardous dyes in wastewater using nanometer mixed crystal TiO_2 powders under visible light irradiation. Water Air Soil Pollut 189:225–237. doi:10.1007/s11270-007-9570-2

Yu J, Zhang J (2010) A simple template-free approach to TiO_2 hollow spheres with enhanced photocatalytic activity. Dalton Trans 39:5860–5867. doi:10.1039/c0dr00053a

Yu JC, Lin J, Kwok RWM (1997) Enhanced photocatalytic activity of $Ti_{1-x}V_xO_2$ solid solution on the degradation of acetone. J Photochem Photobiol A Chem 111:199–201. doi:1010-6030(97)00207-4

Zheng M, Shu Y, Sun J, Zhang T (2008) Carbon-covered alumina: a superior support of noble metal-like catalysts for hydrazine decomposition. Catal Lett 121:90–96. doi:10.1007/s10562-007-9300-9

Zhu J, Zhang J, Chen F, Iino K, Anpo M (2005) High activity TiO_2 photocatalysts prepared by a modified sol–gel method: characterization and their photocatalytic activity for the degradation of XRG and X-GL. Top Catal 35(3–4):261–268. doi:10.1007/s11244-005-3833-1

Zhu J, Yang D, Geng J, Chen D, Jiang Z (2008) Synthesis and characterization of bamboo-like CdS/TiO_2 nanotubes composites with enhanced visible-light photocatalytic activity. J Nanopart Res 10:729–736. doi:10.1007/s11051-0007-9301-z

DOI 10.1007/978-3-319-05041-6_8
Reprinted from the *Journal of Nanoparticle Research*, DOI 10.1007/s11051-012-1227-4

RESEARCH PAPER

Improvement of the structural, morphology, and optical properties of TiO_2 for solar treatment of industrial wastewater

M. Saif · S. M. K. Aboul-Fotouh · S. A. El-Molla · M. M. Ibrahim · L. F. M. Ismail

Received: 2 July 2012 / Accepted: 26 September 2012 / Published online: 25 October 2012

Abstract Hydrothermal preparation of pure anatase TiO_2 with hybrid nano and micro-morphologies directly from titania sol under acidic condition in the absence of any additives or templates has rarely been reported. The present work has found that the post-hydrothermal treatment at 200 °C for different times (6, 12, 24, and 36 h) of titania sol under an acidic environment affected strongly on the structural, morphology, and optical properties of TiO_2. A single-crystalline anatase phase with high surface area was obtained. The TEM results showed that shape of TiO_2 nanoparticles could be manipulated by post-hydrothermal treatment. The increasing of hydrothermal time (pH 2.5) significantly altered the morphology of TiO_2 from pure aggregated nanospherical shape (6 h) into branched micro-flowers as a major shape in addition to nanorod, nanocube, and nanosphere shapes (24 h). Shape-controlled TiO_2 nanoparticles showed a red shift in UV–Vis light reflectance spectra as compared to TiO_2 nanoparticles obtained without any hydrothermal treatment. The photoluminescence measurements confirm that hydrothermal treatment significantly decrease the electron–hole recombination chance in the obtained TiO_2. The fluorescent probe method was used for evaluation of the photo-oxidative activity of different TiO_2 nanomaterials. The highly active TiO_2 nanoparticle (hydrothermally treated for 24 h) was applied for industrial wastewater treatment using solar radiation as a renewable energy source.

Keywords TiO_2 · Sol–gel · Hydrothermal · Fluorescence · Wastewater

Special Issue Editors: Mamadou Diallo, Neil Fromer, Myung S. Jhon

This article is part of the Topical Collection on Nanotechnology for Sustainable Development

Electronic supplementary material The online version of this article (doi:10.1007/s11051-012-1227-4) contains supplementary material, which is available to authorized users.

M. Saif (✉) · S. M. K. Aboul-Fotouh · S. A. El-Molla · M. M. Ibrahim
Department of Chemistry, Faculty of Education, Ain Shams University, Roxy, Cairo 11711, Egypt
e-mail: mona_saif1@yahoo.com

L. F. M. Ismail
Department of Chemistry, Faculty of Science (Girls), Al-Azhar University, Nasr City, Cairo, Egypt

Introduction

In recent years, the semiconductor heterogeneous photocatalysis technique has attracted significant attention for solving the increasingly serious problems of environmental pollution. Among the inorganic semiconductors employed, TiO_2 is known to be a good photocatalyst because of its high photosensitivity, nontoxicity, easy availability, strong oxidizing power, and long-term stability (Fox and Dulay 1993; Shankar et al.

2004; Chena et al. 2007). Nevertheless, there are several limitations which have to be considered when using TiO_2, e.g., its high energy band gap, recombination of photo-induced electron/hole pairs and low interfacial charge transfer (Asal et al. 2011).

Improving of photo-oxidative efficiency of TiO_2 as example of inorganic semiconductors has become of significant importance for many research groups worldwide to meet the requirements of environmental protection (Saif and Abdel-Mottaleb 2007; Hafez et al. 2009, 2011). Many approaches have been pursued to promote the photo-oxidative activity of TiO_2 such as the choice of synthesis methods and the doped TiO_2 nanomaterials. Varieties of synthesis techniques have been developed to produce TiO_2 in different forms since its various properties strongly depend on its structures, including the crystal size, phase, morphology, and surface area. The most widely used methods to synthesize TiO_2 nanoparticles are thermal hydrolysis (Zhong et al. 2005; Seery et al. 2007; Lu and Wen 2008), sol–gel (Burda et al. 2005; Tayade et al. 2006), hydrothermal processes (Cheng et al. 1995; Tang et al. 2000; Eiden-Assmann et al. 2004), and microemulsion processes (Kim and Hahn 2001; Andersson et al. 2002). The sol–gel method is most widely used due to its possible capability in controlling the textural and surface properties of composite oxides. This method is mainly based on the hydrolysis and polycondensation of a metal alkoxide, which ultimately yields hydroxide or oxide under certain conditions. In these methods, sol–gel-derived precipitates are amorphous in nature. So calcination in air is inevitable for the transformation from amorphous to anatase phase. The calcination process frequently leads to serious particle agglomeration, grain growth, and small surface area which all decrease the photo-oxidative activity of TiO_2 (Li et al. 2005).

Hydrothermal approach to ceramic materials synthesis, also in form of nanosized powders, is a well-known method which takes advantage of a direct preparation at low crystallization temperatures without any additional calcination steps (Roy and Ghose 2000; Piticescu et al. 2003; Carotta et al. 2007). The hydrothermal method using water as reaction medium is environmentally friendly because the reactions are carried out in a closed system (Byrappa and Yoshimura 2001; Kolen'ko et al. 2004a, b; Yu et al. 2007). In the hydrothermal treatment, grain size, particle morphology, crystalline phase, and surface chemistry can be controlled via processing variables such as sol composition, pH, reaction temperature and pressure, aging time, and nature of solvent and additive. Most of published research focused on using hydrothermal method in basic medium for preparation of TiO_2 with different morphologies and phases (Kolen'ko et al. 2004a, b, 2006; Yu et al. 2006a, b; Nian and Teng 2006; Han et al. 2007; Zhang et al. 2008; D'Elia et al. 2011; Morgan et al. 2011). Also, several researches focused on preparation of anatase TiO_2 with rod shape using sodium titanate nanotube or nanowire as a precursor under acidic environment (Zhu et al. 2004, 2005; Yu and Xu 2007). This approaches are complicated due to a long progression of preparation steps and the use of several reactants and additives, which influence the time and cost. Hydrothermal preparation of pure anatase TiO_2 with hybrid morphologies directly from titania sol under acidic condition in the absence of any additives or templates has rarely been reported. All the more, no attempts of studding the effect of hydrothermal reaction time on the different properties of the TiO_2 in acidic medium.

In this work, the synthesis of single-crystalline anatase TiO_2 with hybrid micro-flowers/nanorod/nanocube/nanosphere morphologies through a facile hydrothermal treatment of titania sol in aqueous acetic/nitric acid is reported. The influence of the hydrothermal time on the structural, morphology, optical and photo-oxidative properties of TiO_2 is also investigated.

Experimental

Preparation of TiO_2 nanomaterials

All the chemicals were of analytical grade and used without further purification. For synthesis of TiO_2 nanoparticles, 1 ml Titanium(IV) isopropoxide, $Ti[O(C_3H_7)]_4$ (TTIP) solution was added dropwise under vigorous stirring into aqueous acetic/nitric solution (20 ml at pH 2.5) for 4 h at 70–80 °C. The resulting semi-transparent colloidal solution was transferred into a Teflon lined stainless steel autoclave which was sealed and maintained at 200 °C for 6, 12, 24, and 36 h. After cooling down at room temperature, the products were taken out and washed with DI-water and alcohol for five times till being neutral to remove some existing ions and impurities. The washed precipitates were dried in oven at 80 °C and finally ground to obtain TiO_2 samples. For comparison, TiO_2

sample was prepared by the same way (sol–gel) followed by calcinations at 450 °C for 90 min without any further hydrothermal treatment.

The following labels are used throughout the text: 6 h, 12 h, 24 h, and 36 h refer to TiO_2 prepared by hydrothermal treatment of the titania sol for 6, 12, 24, and 36 h, respectively; 0hsol refers to the TiO_2 prepared with sol–gel method followed by calcinations at 450 °C without hydrothermal treatment; 24 hC refers to the TiO_2 prepared by hydrothermal treatment of titania sol for 24 h and calcinated at 450 °C for 90 min.

Characterization

X-ray diffraction (XRD) measurements were made with a Philips diffractometer equipped with a CuKα_1 radiation ($k = 1.54056$ Å) as X-ray source, operated at 40 kV and emission current of 30 mA in the range of $2\theta = 10°$–$70°$. TiO_2 morphology was investigated using transmission electron microscope (TEM) equipped with energy dispersive spectroscopic (EDS) microanalysis system (JEM-2100CX (JEOL). The Brunauer–Emmett–Teller (BET) specific surface area was performed by surface area analyzer. UV–Visible absorbance and diffuse reflectance spectroscopy (UV–Vis/DR) was carried out on JASCO V-550 spectrometer (Japan) equipped with an integrating sphere accessory for diffuse reflectance spectra. Barium sulfate was used as a reference in case of diffuse reflectance measurements. The FT-IR spectrum was recorded using Nicolet IS10 FT-IR 430 spectrometer (USA). Illumination of the prepared TiO_2 nanoparticles were carried out using UV photoreactor (Photon Co., Egypt), air cooled. The UV photoreactor lamps emitted the photons in the range from 320 to 410 nm. The intensity of UV radiation was found to be 0.9 mW/cm^2. The COD value of the wastewater samples before and after illumination determined using multiparameter bench photometer with COD accompanied with COD test tube bench heater model C-99 from HANNA Company. The photoluminescence spectra were measured using LS55 spectrofluorometer (Perkin Elemr, USA).

Determination of $^{\bullet}$OH radicals using fluorescent probe method

Evaluation of the photo-oxidative activity of the prepared powders using fluorescent probe method was carried out as follows: 0.1 g of TiO_2 nanoparticles was added to coumarin solution (1.0×10^{-3} M) and illuminated with UV light under vigorous stirring. The fluorescence spectrum ($\lambda_{ex} = 332$ nm) for the coumarin solution was measured every 1.5 min of illumination. The apparent rate constant was calculated using the slope of the fluorescence intensity–illumination time curves. They can indirectly represent the apparent rate constant, but not the real values of the rate constant. It should be noted that the blank experiment at the same conditions but without TiO_2 was carried out, which showed that the coumarin without TiO_2 nanoparticles was totally inactive under UV illumination.

Real wastewater treatment

The highly active TiO_2 nanoparticles (24 h) was applied for degradation of real factory wastewater at pH 1.56 in sun light as a light source. The intensity of UV radiation was found to be 3.42 mW/cm^2 and visible light 1043 mW/cm^2.

The decoloration and mineralization efficiencies of the real wastewater using highly active sample (24 h) at time t, can be expressed as (Neamtu et al. 2004):

$$\text{Decolorization efficiency} = 100 \times (A_0 - A_t)/A_0$$

where A_0 and A_t are the initial and at time t absorbance values of the wastewater solution.

$$\text{Mineralization efficiency} = 100 \times (\text{COD}_0 - \text{COD}_t)/\text{COD}_0$$

where COD_0 and COD_t are the initial and at time t COD values of the wastewater solution.

Results and discussion

Characterization of as-prepared TiO_2 nanoparticles

XRD

Figure 1 presents the XRD patterns of the as-prepared TiO_2 nanoparticles. Crystal parameters of nanocrystals are listed in Table 1. All the TiO_2 nanoparticles exhibit anatase phase ($2\theta = 25.68°$, 37.77°, 48.03°, 55.08°, and 62.56°) (JCPDS 21-1272). No peaks corresponding to rutile and brookite phases are detected in the XRD patterns of 0hsol, 6 h, 12 h, 24 h, 36 h, and 24 hC,

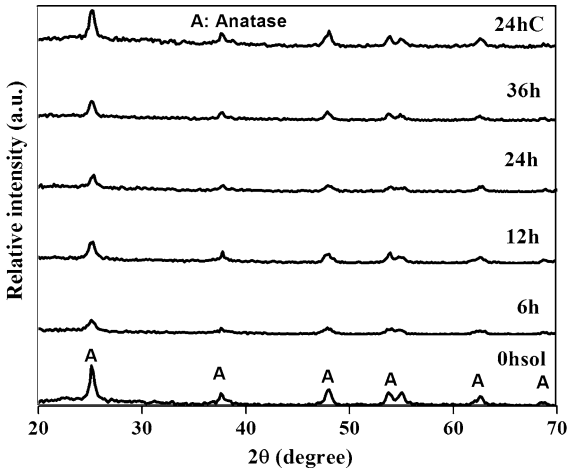

Fig. 1 XRD pattern of different prepared TiO_2 nanoparticles

Table 1 XRD analysis, surface and optical properties of different TiO_2 nanoparticles

Samples	L (nm)	FWHM	S_{BET} (m^2/g)	V_m (cm^3/g)	E_g (eV)
0hsol	29	0.49	66.6	15.3	3.4
6 h	10	1	282.9	64.9	3.36
12 h	12	0.75	317.9	73.0	3.35
24 h	20	0.5	604.6	138.9	3.31
36 h	22	0.5	372.9	85.7	3.39
24 hC	31	0.49	111.1	25.5	3.33

which indicates that there is no additional phase present in the prepared nanoparticles, at least within the limit of X-ray detection. It can be seen that the full width at half maximum value (FWHM) of the TiO_2 decrease as a result of increasing of hydrothermal time (6–36 h) and come close to the FWHM value of 0hsol nanoparticle (Table 1). As a consequence, the average crystal size (L) is increased with increasing hydrothermal time. These results confirm that the hydrothermal treatment can appreciably influence the TiO_2 crystallinity similar to calcinations treatment but at low temperature. This is assigned to the fact that longer hydrothermal time promoted Ostwald ripening and growth of nanocrystalline TiO_2 particles (Ng et al. 1996; Yu et al. 2007). It can be seen that, The TiO_2 crystallinity and crystallite size (L) slightly increase in case of 24 hC in comparison with 24 h. These results prove that further calcination for the hydrothermally treated nanoparticles leads to conglomeration and crystal growth (Yang et al. 2007; Zhang et al. 2012). During the hydrothermal process, the hydrous gel gradually develops into crystalline titania grains with further hydrolysis/polycondensation reactions and structural rearrangements. This is a very different process from crystallization via calcinations, which involves rapid purification and thermal transformation of hydrous gel that has not yet fully reacted which leads to agglomeration (Nagliati et al. 2006).

TEM

Figure 2a–g shows typical TEM images of different TiO_2 nanoparticles. The aggregates of uniform spherical nanoparticles with average diameter 16.7 nm are observed in 0hsol powder, as shown in Fig. 2a, b shows the TEM image of the TiO_2 obtained after 6 h, which reveals the products are highly aggregated spherical nanoparticle. These aggregated nanoparticles exist in cluster format. When the reaction time is prolonged to 12 h (Fig. 2c), different morphologies (nanosphere, nanorod, nanocube, and nanoring-like consisting of rod-like nanocrystals) are observed. After hydrothermal treatment for 24 h (Fig. 2d, e), the branched micro-flowers are observed as a major shape in addition to the other morphologies which already obtained in case of 12 h nanoparticles. The average diameter and length of nanorod are 7 and 11 nm, respectively.

Further increase in hydrothermal time to 36 h or calcination of 24 h powder at 450 °C leads to disappear of the branched micro-flowers and a mixture of small rods and spherical shapes are observed. This means that further heat treatment lead degrade the micro-flower to these major shapes as shown in (Fig. 2f–g).

The oriented attachment (OA) mechanism was recently found to be significant in the growth of nanomaterials as an approach for the preparation of complex nanostructures (Penn 2004; Xu et al. 2008; Li et al. 2009). In this synthesis, titanium isopropoxide is fast hydrolyzed in excess water forming a white precipitate followed by peptization under acidic and heat conditions (Zhang et al. 2000; Penn 2004; Xu et al. 2008; Li et al. 2009). The peptization process destroys agglomerates during precipitation. This is attributed to that the surface of TiO_2 have a net positive charge under our acidic condition (pH 2.5), which is less than the isoelectric point of anatase (pH_{IEP} 4.7–6.7), yielding a well-dispersed and highly

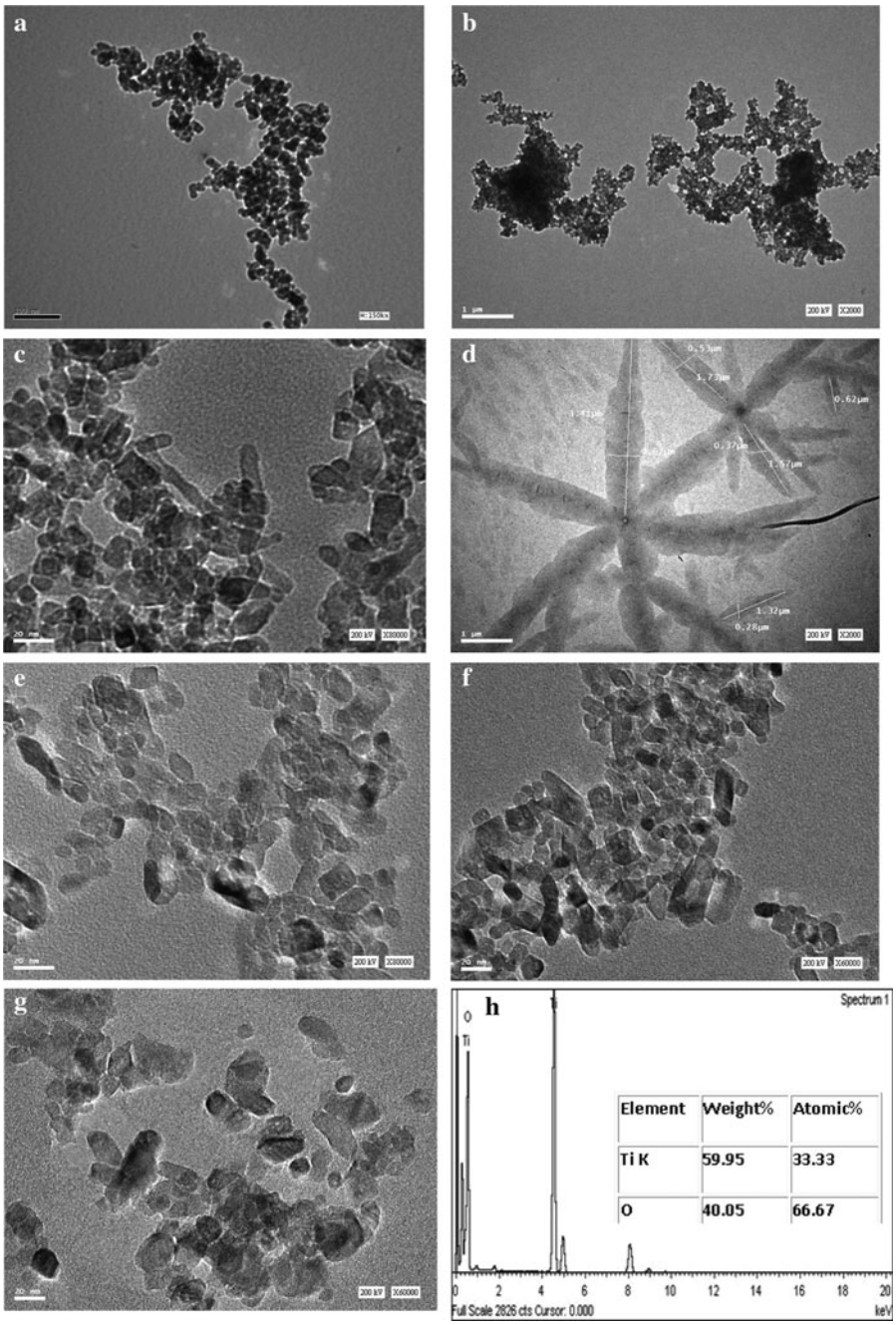

Fig. 2 TEM images of 0hsol (**a**), 6 h (**b**), 12 h (**c**), 24 h (**d**, **e**), 36 h (**f**) and 24 hC (**g**) nanoparticles; and EDS of 24 h (**h**)

transparent sol (Bischof and Anderson 1995; Li et al. 2009).

During autoclaving, the primary particles can somewhat grow through the dissolution–reprecipitation process under hydrothermal conditions, leading to some coarsening of the crystallite size. At the early time of hydrothermal treatment (6 h), some anatase TiO_2 nanocrystals in a finer size may dissolve under the Ostwald ripening mechanism, which produces the dissolved $[TiO_6]$ octahedral. The $[TiO_6]$ octahedral arranged via face-shared bonding formed spiral chains, creating anatase TiO_2 with spherical shape (Bischof and Anderson 1995; Li et al. 2009). These nanocrystals start to aggregate under hydrothermal treatment, forming gel-like precipitate. By increasing hydrothermal autoclaving time (12 h), some primary aggregated

nanocrystals underwent nucleation, and growth to obtain secondary nanoparticles with nanocube, nanorod, and nanoring-like consisting of rod-like shapes. The rod shape consists of zigzag ribbons of edge-sharing TiO_6 octahedra in which the octahedral share edges along the [100] direction (Yu and Xu 2007). More complex structure for the OA growth is expected by elongation the hydrothermal time (24 h). Indeed, the longer rod-like nanocrystals and branched micro-flower nanocrystals structures were formed. So the morphology of the products depends strongly on the reaction time.

Energy dispersive spectroscopy (EDS) was performed to further confirm the composition of the prepared nanoparticles. The EDS results of 24 h nanoparticles (Fig. 2h) proved the presence of titanium and oxygen elements. The atomic percentages of Ti and O in TiO_2 at a particular region are 33.33 and 66.67, respectively (Fig. 2h inset).

BET analysis

Gas adsorption measurements are widely used for determining the surface area of a variety of different solid materials, the measurement of adsorption at the gas/solid interface also forms an essential part of many fundamental and applied investigations of the nature and behavior of solid surfaces (Rouquerol et al. 1994).

Table 1 shows that the specific surface area (S_{BET}) and monolayer volume (V_m) of all hydrothermally treated TiO_2 nanoparticles (6 h, 12 h, 24 h, 36 h, and 24 hC) are higher than TiO_2 nanomaterials prepared by sol gel method without any hydrothermal treatment (0hsol). Moreover, by increasing the hydrothermal time, the S_{BET} and V_m increase till 24 h, then decrease again in case of 36 h nanoparticle. The highest S_{BET} and V_m are observed for 24 h nanoparticles. The obtained hybrid micro/nano-shapes in case of 24 h sample lead to increase the porosity of the TiO_2 surface and as a consequence its surface area.

Optical properties

The effect of hydrothermal treatment in acidic condition on the optical properties of TiO_2 nanoparticles was studied. Figure 3 shows the optical reflectance, R, in the wavelength range 200–750 nm for the prepared TiO_2 nanoparticles. The optical properties of the prepared powders are collected in Table 1. The broad intense absorption edge from ~400 nm to lower wavelengths region is associated with the intrinsic band gap absorption of the TiO_2 in which the Ti presence as a tetrahedral Ti(VI) (Yu et al. 2002, 2006a, b; Sreethawong et al. 2005). This absorption band is generally associated with the electronic excitation of the valence band O 2*p* electron to the conduction band Ti 3*d* level (Fuerte et al. 2002; Sreethawong et al. 2005). Besides, the absorption wavelength of TiO_2 red shifts from ~364.7 to ~374.6 nm after hydrothermal treatment from 0 to 24 h, indicating the decreasing of the optical band gap (Fig. 3, Table 1). Further heat treatment as in case of 36 h and 24 hC causes a slightly blue shift in the absorption band edge relative to 24 h nanoparticles. The smaller band gap energy in case of 24 h means a wider light response range of this sample i.e., absorb more photons. This would contribute to an enhanced photo-oxidative activity.

The band gap (E_g) of the prepared TiO_2 nanoparticles was estimated by extrapolation of the linear portion of $(\alpha h\nu)^2$ versus photon energy ($h\nu$) plots using the relation (Liu et al. 2006; Kumar et al. 2010; Jaleha et al. 2011),

$$\alpha h\nu = A\,(h\nu - E_g)^{1/2}$$

where $\alpha = 2.303 \times \ln (I_o/I)/t$, here $\ln (I_o/I)$, absorbance and t, thickness of the sample. A is a constant for a direct transition, and hν is photon energy of the incident radiation. Inset of Fig. 3 shows the $(\alpha h\nu)^2$ versus ($h\nu$) plot of different nanomaterials.

It can be seen that the band gap of TiO_2 decreased to a minimum value of 3.31 eV at hydrothermal time

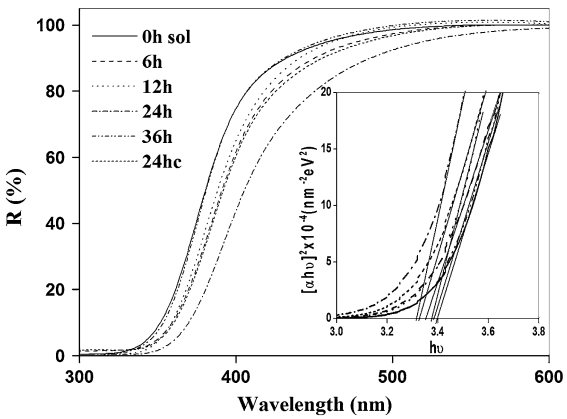

Fig. 3 UV–Vis/DR spectra of different prepared TiO_2. *Inset*: Plot of $(\alpha h\nu)^2$ versus photon energy ($h\nu$) for different nanoparticles

equal 24 h. The highest band gap energy is observed in case of 0hsol (3.4 eV) and 36 h (3.39 eV). The observed values are higher than the band gap of bulk anatase phase (3.18 eV). The higher band gap values observe in our case can be associated with the nano crystalline nature of the prepared TiO_2. Shape and size have a significant impact on the optical band gap of the nanoparticles (Liao and Liao 2007). With the morphologies shown in Fig. 2, the size difference of the nanoparticles is not the main reason for the lower band gap energy for the shape-controlled TiO_2 nanoparticles. According to Monticone et al. (2000), it seems that the quantum size effect is rather limited on anatase, due to a very small exciton Bohr radius (1.5 nm). According to the XRD and TEM analysis, the sizes of the prepared TiO_2 were larger than the size range of the quantum size effect related to the E_g of TiO_2. Thus, the quantum size effect could be excluded. The obtained different band gap energies can be attributed to the different morphologies and surface microstructures of the nanoparticles. This trend in the E_g values is in good agreement with the shape estimations from TEM measurements.

The photoluminescence (PL) emission spectra of the prepared TiO_2 were studied to disclose the separation efficiency of charge carriers, because PL emission results from the recombination of free carrier (Li et al. 2005; Saif and Abdel-Mottaleb 2007). The PL emission spectra of TiO_2 samples were examined in the range of 350–600 nm and shown in Fig. 4. It can be seen that the PL intensity of TiO_2 prepared by hydrothermal method

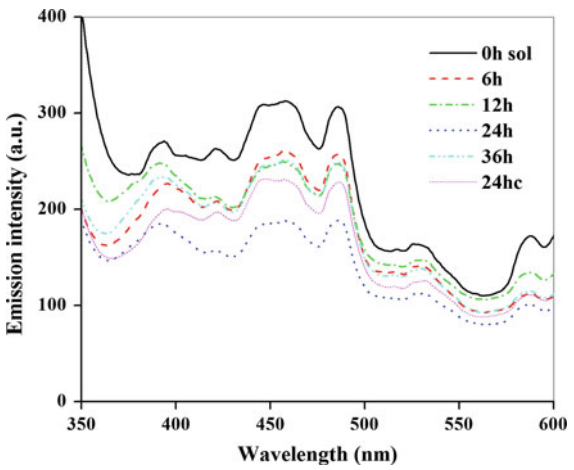

Fig. 4 The PL emission spectra of different prepared TiO_2 ($\lambda_{ex} = 325$ nm)

was significantly decreased in comparison with the TiO_2 prepared with sol–gel only (0hsol). Moreover, increasing hydrothermal time, the PL intensity decrease till 24 h then increase again in case of sample 36 h. The lower PL intensity indicates fewer recombinations between generated electrons and holes (Li et al. 2005; Saif and Abdel-Mottaleb 2007).

Hence, the hydrothermal treatment of the titania sol in aqueous acetic/nitric has enhanced the absorption of solar radiation with less energy and electron–hole separation.

Supplementary 1 shows the FT-IR spectrum of the 24 h powder. In the high wave number, spectral range a broad band between 3600 and 3100 cm^{-1} was assigned to stretching vibration of different surface hydroxyl groups (free or bounded). The band at 1633 cm^{-1} is related to molecular water (Asal et al., 2011). Also, the FT-IR show bands at 1519 cm^{-1} and 1384 cm^{-1} assigned to the asymmetric and symmetric stretching vibrations of the adsorbed acetic acid carboxylic group coordinated to Ti (Saif et al. 2012). In the low frequency region (below 1000 cm^{-1}) the absorption of titania was observed (Asal et al. 2011).

The obtained results indicate that 24 h sample have suitable structural, morphological, and optical properties for industrial wastewater mineralization.

Evaluation of the TiO_2 photo-oxidative activity using fluorescent probe method

There are several methods for evaluation of the photo-oxidative activity of self-cleaning materials. The most public methods are the dye method, the stearic acid method, and the contact angle method (Guan et al. 2008). All these methods have disadvantages of time consuming, low sensitivity, and high manipulation cost. Fluorescent probe is a novel method to evaluate the performance of TiO_2 materials and overcome on the above disadvantages. In this new method, the hydroxyl radicals ($^{\bullet}OH$) produced on the surface of nano-semiconductors under UV illumination can quantitatively convert coumarin of non-fluorescence to 7-hydroxycoumarin of fluorescence (Ishibashi et al. 2000).

As shown in Fig. 5, the generation of 7-hydroxycoumarin increases due to prolonged irradiation time. These results suggest that fluorescent products formed using 24 h sample are due to the specific reaction between $^{\bullet}OH$ radicals and coumarin (Xiao et al. 2008).

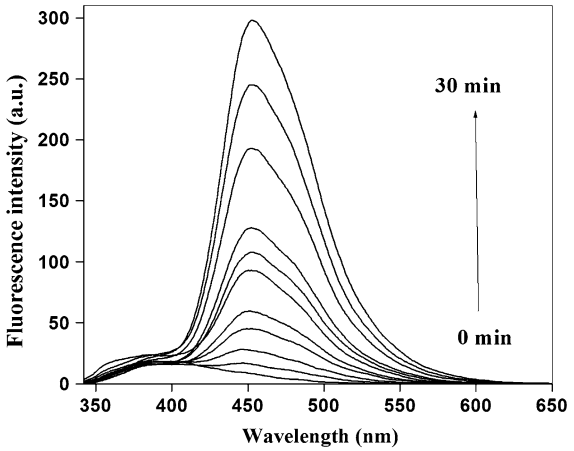

Fig. 5 Fluorescence spectral changes observed during illumination of 24 h nanopariticles immersed in coumarin solution (1.0×10^{-3} M) ($\lambda_{ex} = 332$ nm)

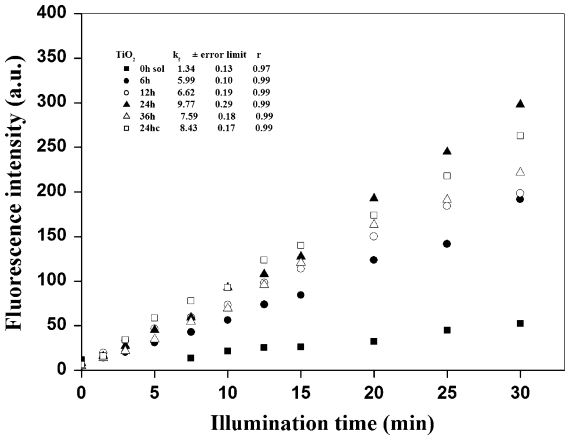

Fig. 6 Plots of the induced fluorescence intensity at 460 nm against irradiation time for coumarin using different TiO_2 nanoparticles

Figure 6 shows the plots of increase in fluorescence intensity against illumination time at 460 nm. The fluorescence intensity of 7-hydroxycoumarin by UV light illumination increases almost linearly against time. Consequently, we can conclude that $^{\bullet}OH$ radicals formed from the TiO_2 nanoparticles are in proportional to the light illumination time obeying pseudo-zero-order reaction rate kinetics. TiO_2 nanoparticles with better photo-oxidative activity yield faster generation of 7-hydroxycoumarin. Therefore, the slope (k_f) of the lines in Fig. 6 can be used to represent the apparent rate constant for the photooxidation of coumarin, which in turn is able to represent the photocatalytic activity of the prepared TiO_2 nanoparticles. The lower k_f value is observed in case of TiO_2 prepared by sol–gel without any hydrothermal treatment (0hsol). It also shows that the k_f increases from 5.99 to 9.77 with increasing the time of post-hydrothermal treatment in acidic medium from 6 to 24 h and then decreases again to 7.59 after 36 h of treatment.

These results suggest that the hydrothermal treatment at of the titania sol at different times in acidic medium enhanced the formation rate of $^{\bullet}OH$ radicals, and there is an optimum time for hydrothermal of the TiO_2.

Absorption of a photon with energy greater than the band gap energy resulted in the formation of conduction band electron and valence band hole, according to reaction (1). It was commonly accepted that the hole was quickly converted to the hydroxyl radical upon oxidation of surface water and surface hydroxyl group, according to reaction (2, 3), and that the hydroxyl radical was the major reactant, which was responsible for oxidation of organic substrates. The yield of $^{\bullet}OH$ radicals depended on the competition between oxidation of surface water or hydroxyl group by the holes (reaction (2, 3)) and electron–hole recombination according to reaction (4). Therefore, the greater the formation rate of $^{\bullet}OH$ radicals was, the higher separation efficiency of electron–hole pairs was achieved. All above-mentioned results demonstrated that hydrothermal treatment could effectively enhance the separation efficiency of electron–hole pairs via increase in the content of hydroxyl group on the TiO_2 particles, as a consequence increase the $^{\bullet}OH$ radicals produced from the nanomaterial. Moreover, the increase of amount of hydroxyl after hydrothermal treatment not only increase the trapping sites for photogenerated holes, but also can increase the trapping sites for photogenerated electrons by adsorbing more oxygen molecules (Salvador and Gutierrez 1982; Yu et al. 2007; Guan et al. 2008). This results lead to decrease the recombination rate of electron–hole pairs. In this study, the optimum preparation conditions was found in case of 24 h nanoparticle, at which the recombination of photo-induced electrons and holes could be the most effectively inhibited. Moreover, further heat treatment via hydrothermal and/or calcinations decrease the hydroxyl content as seen in case of 24 hC and 36 h nanoparticles. This is because the specific surface areas of the prepared samples decrease, the crystallite size increase and the crystallization enhance. Furthermore, some

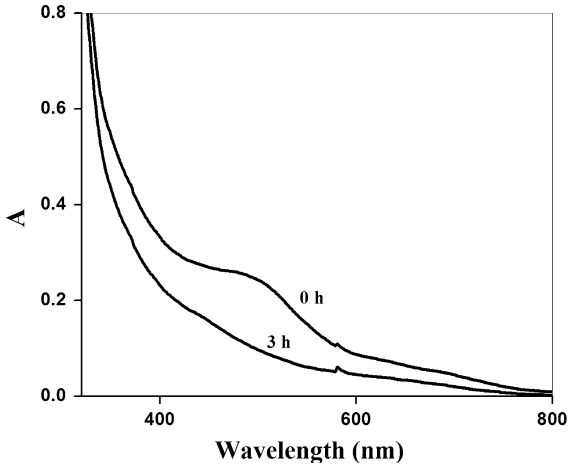

Fig. 7 The UV–Vis spectra of industrial wastewater sample in aqueous medium at 0 and 3 h sun light irradiation (*reaction conditions*: 0.1 g of TiO_2 (24 h), pH 1.56, and air atmosphere, the intensity of UV radiation was found to be 3.42 mW/cm^2 and visible light 1043 mW/cm^2)

Table 2 Solar decolorization and mineralization parameters of the real industrial wastewater in the presence of TiO_2 (24 h)

Irradiation time (h)	Decolorization (%)	COD value (mg/l)	Mineralization (%)
0	–	1694	–
3	64	729	57

adsorbed hydroxyl groups will dehydrate to form Ti–O–Ti (Ti–OH + HO–Ti) Ti–O–Ti + H_2O by further heat treatment (Yu et al. 2007).

$$TiO_2 + h\nu \rightarrow h^+ + e^- \quad (1)$$

$$h^+ + H_2O_{ads} \rightarrow {}^{\bullet}OH_{ads} + H^+ \quad (2)$$

$$h^+ + OH^- \rightarrow {}^{\bullet}OH \quad (3)$$

$$h^+ + e^- \rightarrow TiO_2 \quad (4)$$

Solar degradation of real industrial wastewater

The highly active nanoparticles (24 h) were applied for solar degradation of real industrial wastewater sample. Figure 7 shows the decolorization of the real wastewater sample after 3 h of sunlight illumination using 24 h nanoparticles. The solar decolorization and mineralization data of the wastewater sample are collected in Table 2. Figure 7 shows the reduction in main absorption peak of real wastewater sample in the presence of TiO_2 (24 h), which indicated that the real factory wastewater undergo decolorization. The decolorization and mineralization efficiency reached to 64 and 57 %, respectively, after passing 3 h from irradiation. So, the factory wastewater studied was not only decolorized but can degrade as well by TiO_2 sample. Therefore, TiO_2 prepared by hydrothermal treatment of titania sol for 24 h in acidic medium is a promising photocatalyst under solar light.

Conclusions

In summary, single-crystalline anatase TiO_2 with hybrid nano- and micro-morphologies have been synthesized by controlling the reaction time through a hydrothermal reaction of titania sol in acidic condition. The crystal structure, morphology, and optical properties of the obtained TiO_2 were studied. The photo-oxidative activity of these materials was evaluated using fluorescent probe method and the TiO_2 treated hydrothermally for 24 h achieves the highest one. The highly active nanoparticle (24 h) was applied for solar degradation of real industrial wastewater.

References

Andersson M, Osterlund L, Ljungstrom S, Palmqvist A (2002) Preparation of nanosize anatase and rutile TiO_2 by hydrothermal treatment of microemulsions and their activity for photocatalytic wet oxidation of phenol. J Phys Chem B 106:10674–10679

Asal S, Saif M, Hafez H, Mozia S, Heciak A, Moszyński D, Abdel-Mottaleb MSA (2011) Photocatalytic generation of useful hydrocarbons and hydrogen from acetic acid in the presence of lanthanide modified TiO_2. Int J Hydrogen Energy 36:6529–6537

Bischof BL, Anderson MA (1995) Peptization process in the sol gel preparation of porous anatase (TiO_2). Chem Mater 7:1772–1778

Burda C, Chen X, Narayanan R, El-Sayed MA (2005) The chemistry and properties of nanocrystals of different shapes. Chem Rev 105:1025–1102

Byrappa K, Yoshimura M (2001) Handbook of hydrothermal technology. William Andrew Publishing, New York

Carotta MC, Gherardi S, Malagù C, Nagliati M, Vendemiati B, Martinelli G, Sacerdoti M, Lesci IG (2007) Comparison between titania thick films obtained through sol–gel and hydrothermal synthetic processes. Thin Solid Films 515:8339–8344

Chena L-C, Huang C-M, Tsai F-R (2007) Characterization and photocatalytic activity of K^+-doped TiO_2 photocatalysts. J Mol Catal A Chem 265:133–140

Cheng H, Ma J, Zhao Z, Qi L (1995) Hydrothermal preparation of uniform nanosize rutile and anatase particles. Chem Mater 7:663–671

D'Elia D, Beauger C, Hochepied J-F, Rigacci A, Berger M-H, Keller N, Keller-Spitzer V, Suzuki Y, Valmalette J-C, Benabdesselam M, Achard P (2011) Impact of three different TiO_2 morphologies on hydrogen evolution by methanol assisted water splitting: nanoparticles, nanotubes and aerogels. Inter J Hydrogen Energy 36:14360–14373

Eiden-Assmann S, Widoniak J, Maret G (2004) Synthesis and characterization of porous and nonporous monodisperse colloidal TiO_2 particles. Chem Mater 16:6–11

Fox MA, Dulay MT (1993) Heterogeneous photocatalysis. Chem Rev 93:341

Fuerte A, Hernández-Alonso MD, Maira AJ, Martinez-Arias A, Fernández-Garcia M, Conesa JC, Soria J, Munuera G (2002) Nanosize Ti–W mixed oxides: effect of doping level in the photocatalytic degradation of toluene using sunlight-type excitation. J Catal 212:1–9

Guan H, Zhu L, Zhou H, Tang H (2008) Rapid probing of photocatalytic activity on titania-based self-cleaning materials using 7-hydroxycoumarin fluorescent probe. Analytica chim acta 608:73–78

Hafez H, Saif M, Mcleskey JT Jr, Abdel-Mottaleb MSA, Yahia IS, Story T, Knoff W (2009) Hydrothermal preparation of Gd^{3+}-doped titanate nanotubes: magnetic properties and photovoltaic performance. Int J Photoenergy 2009:1–8. doi:10.1155/2009/240402

Hafez H, Saif M, Abdel-Mottaleb MSA (2011) Down-converting lanthanide doped TiO_2 photoelectrodes for efficiency enhancement of dye-sensitized solar cells. J Power Sources 196:5792–5796

Han T-Y, Wu C-F, Hsieh C-T (2007) Hydrothermal synthesis and visible light photocatalysis of metal-doped titania nanoparticles. J Vac Sci Technol B 25:430–435

Ishibashi K-i, Fujishima A, Watanabe T, Hashimoto K (2000) Quantum yields of active oxidative species formed on TiO_2 photocatalyst. J Photochem Photobiol A Chem 134:139–142

Jaleha B, Shayegani Madada M, Farshchi Tabrizib M, Habibia S, Golbedaghic R, Keymaneshd MR (2011) UV-degradation effect on optical and surface properties of polystyrene-TiO_2 nanocomposite film. J Iran Chem Soc 8:S161–S168

Kim EJ, Hahn SH (2001) Microstructural changes of microemulsion-mediated TiO_2 particles during calcination. Mater Lett 49:244–249

Kolen'ko YV, Churagulov BR, Kunst M, Mazerolles L, Colbeau-Justin C (2004a) Photocatalytic properties of titania powders prepared by hydrothermal method. Appl Catal B Environ 54:51–58

Kolen'ko YV, Maximov VD, Garshev AV, Meskin PE, Oleynikov NN, Churagulov BR (2004b) Hydrothermal synthesis of nanocrystalline and mesoporous titania from aqueous complex titanyl oxalate acid solutions. Chem Phys Lett 388:411–415

Kolen'ko YV, Kovnir KA, Gavrilov AI, Garshev AV, Frantti J, Lebedev OI, Churagulov BR, Tendeloo GV, Yoshimura M (2006) Hydrothermal synthesis and characterization of nanorods of various titanates and titanium dioxide. J Phys Chem B 110:4030–4038

Kumar S, Nigam N, Ghosh T, Dutta PK, Singh SP, Datta PK, An L, Shi TF (2010) Preparation, characterization and optical properties of a novel azo-based chitosan biopolymer. J Mater Chem Phys 120:361–370

Li Z, Hou B, Xu Y, Wu D, Sun Y, Hu W, Deng F (2005) Comparative study of sol–gel-hydrothermal and sol–gel synthesis of titania–silica composite nanoparticles. J Solid State Chem 178:1395–1405

Li S, Li Y, Wang H, Fan W, Zhang Q (2009) Peptization–hydrothermal method as a surfactant-free process toward nanorod-like anatase TiO_2 nanocrystals. Eur J Inorg Chem 2009:4078–4084

Liao DL, Liao BQ (2007) Shape, size and photocatalytic activity control of TiO_2 nanoparticles with surfactants. J Photochem Photobiol A Chem 187:363–369

Liu Z, Jin Z, Liu X, Fu Y, Liu G (2006) Fabrication of ordered TiO_2 porous thin films by sol-dipping PS template method. J Sol-Gel Sci Technol 38:73–78

Lu C-H, Wen M-C (2008) Synthesis of nanosized TiO_2 powders via a hydrothermal microemulsion process. J Alloys Compd 448:153–158

Monticone S, Tufeu R, Kanaev AV, Scolan E, Sanchez C (2000) Quantum size effect in TiO_2 nanoparticles: does it exist? Appl Surf Sci 162–163:565–570

Morgan DL, Triani G, Blackford MG, Raftery NA, Frost RL, Waclawik ER (2011) Alkaline hydrothermal kinetics in titanate nanostructure formation. J Mater Sci 46:548–557

Nagliati M, Carotta MC, Gherardi S, Lesci IG, Martinelli G (2006) TiO_2 nanopowders for sensing applications; a comparison between traditional and hydrothermal synthesis way. Adv Sci Technol 45:205–208

Neamtu M, Yediler A, Siminiceanu I, Macoveanu M, Kettrup A (2004) Decolorization of disperse red 354 azo dye in water by several oxidation processes—a comparative study. Dyes Pigments 60:61–68

Ng JD, Lorber B, Witz J, Theobald-Dietrich A, Kern D, Giege R (1996) The crystallization of biological macromolecules from precipitates: evidence for Ostwald ripening. J Cryst Growth 168:50–62

Nian J-N, Teng H (2006) Hydrothermal synthesis of single-crystalline anatase TiO_2 nanorods with nanotubes as the precursor. J Phys Chem B 110:4193–4198

Penn RL (2004) Kinetics of oriented aggregation. J Phys Chem B 108:12707–12712

Piticescu RM, Piticescu RR, Taloi D, Badilita V (2003) Hydrothermal synthesis of ceramic nanomaterials for functional applications. Nanotechnology 14:312–317

Rouquerol J, Avnir D, Fairbridge CW, Everett DH, Haynes JH, Pernicone N, Ramsay JDF, Sing KSW, Unger KK (1994) Recommendations for the characterization of porous solids. Pure Appl Chem 66:1739–1758

Roy S, Ghose J (2000) Synthesis of stable nanocrystalline cubic zirconia. Mater Res Bull 35:1195–1203

Saif M, Abdel-Mottaleb MSA (2007) Titanium dioxide nanomaterial doped with trivalent lanthanide ions of Tb, Eu and Sm: preparation, characterization and potential applications. Inorg Chim Acta 360:2863–2874

Saif M, Mashaly MM, Eid MF, Fouad R (2012) Synthesis, characterization and thermal studies of binary and/or mixed ligand complexes of Cd(II), Cu(II), Ni(II) and Co(III) based on 2-(Hydroxybenzylidene) thiosemicarbazone: DNA binding affinity of binary Cu(II) complex. Spectrochim Acta A 92:347–356

Salvador P, Gutierrez C (1982) The role of surface state in the electroreduction of dissolved and/or photogenerated oxygen on n-TiO_2 electrodes. Chem Phys Lett 86:131–134

Seery MK, George R, Floris P, Pillai SC (2007) Silver doped titanium dioxide nanomaterials for enhanced visible light photocatalysis. J Photochem Photobiol A Chem 189: 258–263

Shankar MV, Anandan S, Venkatachalam N, Arabindoo B, Murugesan V (2004) Novel thin-film reactor for photocatalytic degradation of pesticides in aqueous solutions. J Chem Technol Biotechnol 79:1258–1279

Sreethawong T, Suzuki Y, Yoshikawa S (2005) Photocatalytic evolution of hydrogen over mesoporous TiO_2 supported NiO photocatalyst prepared by single-step sol–gel process with surfactant template. Int J Hydrogen Energy 30: 1053–1062

Tang J, Mei S, Ferreira MF (2000) Hydrothermal synthesis of nano-TiO_2 powders: influence of peptisation and peptising agents on the crystalline phases and phase transitions. J Am Ceram Soc 83:1361–1368

Tayade RJ, Kulkarni RG, Jasra RV (2006) Photocatalytic degradation of aqueous nitrobenzene by nanocrystalline TiO_2. Ind Eng Chem Res 45:922–927

Xiao Q, Si Z, Zhang J, Xiao C, Tan X (2008) Photoinduced hydroxyl radical and photocatalytic activity of samarium-doped TiO_2 nanocrystalline. J Hazard Mater 150:62–67

Xu JX, Li LP, Yan YJ, Wang H, Wang XX, Fu XZ, Li GS (2008) Synthesis and photoluminescence of well-dispersible anatase TiO_2 nanoparticles. J Colloid Interface Sci 318:29–34

Yang Y, Ma J, Qin Q, Zhai X (2007) Degradation of nitrobenzene by nano-TiO_2 catalyzed ozonation. J Mol Catal A Chem 267:41–48

Yu Y, Xu D (2007) Single-crystalline TiO_2 nanorods: highly active and easily recycled photocatalysts. Appl Catal B 73:166–171

Yu JC, Yu JG, Ho WK, Jiang ZT, Zhang LZ (2002) Effects of F^- doping on the photocatalytic activity and microstructures of nanocrystalline TiO_2 powders. Chem Mater 14:3808–3816

Yu H, Yu J, Cheng B, Zhou M (2006a) Effects of hydrothermal post-treatment on microstructures and morphology of titanate nanoribbons. J Solid State Chem 179:349–354

Yu J, Yu H, Cheng B, Zhao X, Zhang Q (2006b) Preparation and photocatalytic activity of mesoporous anatase TiO_2 nanofibers by a hydrothermal method. J Photochem Photobiol A Chem 182:121–127

Yu J, Wang G, Cheng B, Zhou M (2007) Effects of hydrothermal temperature and time on the photocatalytic activity and microstructures of bimodal mesoporous TiO_2 powders. Appl Catal B Environ 69:171–180

Zhang QH, Gao L, Guo JK (2000) Effect of hydrolysis conditions on morphology and crystallisation of nanosized TiO_2 powder. J Eur Ceram Soc 20:2153–2158

Zhang Y, Lan D, Wang Y, Wang F (2008) Hydrothermal synthesis of 2D ordered macroporous ZnO films. Front Chem China 3:229–234

Zhang W, Yang B, Chen J (2012) Effects of calcination temperature on preparation of boron-doped TiO_2 by sol-Gel method. Int J Photoenergy Article ID: 528637

Zhong Z, Ang T-P, Luo J, Gan H-C, Gedanken A (2005) Synthesis of one-dimensional and porous TiO_2 nanostructures by controlled hydrolysis of titanium alkoxide via coupling with an esterification reaction. Chem Mater 17:6814–6818

Zhu H, Gao X, Lan Y, Song D, Xi Y, Zhao J (2004) Hydrogen titanate nanofibers covered with anatase nanocrystals: a delicate structure achieved by the wet chemistry reaction of the titanate nanofibers. J Am Chem Soc 126:8380–8381

Zhu H, Lan Y, Gao X, Ringer S, Zheng Z, Song D, Zhao J (2005) Phase transition between nanostructures of titanate and titanium dioxides via simple wet-chemical reactions. J Am Chem Soc 127:6730–6736

DOI 10.1007/978-3-319-05041-6_9
Reprinted from the *Journal of Nanoparticle Research*, DOI 10.1007/s11051-012-1346-y

RESEARCH PAPER

Shape-controlled synthesis of α-Fe_2O_3 nanostructures: engineering their surface properties for improved photocatalytic degradation efficiency

S. Bharathi · D. Nataraj · K. Senthil · Yoshitake Masuda

Received: 13 July 2012 / Accepted: 28 November 2012 / Published online: 16 December 2012

Abstract α-Fe_2O_3 nanostructures with well-defined morphology: nanostructured dendrites, nanorods, nanospindles, and nanocubes were successfully synthesized by forced hydrolysis/reflex condensation and hydrothermal methods. The specific surface area and pore size distribution analysis of the different nanostructures prepared in this study confirms that these surface properties can be systematically improved and controlled by varying the precursors and preparatory conditions. The enhancement in surface properties was utilized to efficiently degrade relatively high concentration of synthetic organic effluent Rhodamine (RhB) at a faster rate using minimum quantity of the catalyst. The observed enhancement in the photocatalytic performance of iron oxide nanostructures is explained based on the inherent catalytic properties of iron oxide, and the improvement in surface area and porosity tailored by the preparatory method and conditions.

Keywords Shape-controlled synthesis · Surface porosity · Photocatalysis · Iron oxide nanostructures

Special Issue Editors: Mamadou Diallo, Neil Fromer, Myung S. Jhon

This article is part of the Topical Collection on Nanotechnology for Sustainable Development

S. Bharathi · D. Nataraj
Thin Films and Nanomaterials Lab,
Department of Physics, Bharathiar University,
Coimbatore 641046, India

S. Bharathi · D. Nataraj
DRDO-BU Centre for Life Sciences,
Bharathiar University, Coimbatore 641046, India

Present Address:
S. Bharathi (✉)
Texas Sustainable Energy Research Institute,
University of Texas, San Antonio, TX, USA
e-mail: bharathi.subramaniasiva@utsa.edu

Introduction

Controlling the shape, size, and surface properties at the nanoscale has become a throbbing area of research by contemporary material scientists due to the unique shape- and surface-dependent physical/chemical properties exhibited by anisotropic morphologies (Sajanlal et al. 2011). In particular, inorganic

K. Senthil
School of Advanced Materials Science & Engineering,
Sungkyunkwan University (Suwon Campus),
Cheoncheon-dong 300, Jangan-gu Suwon 440-746,
South Korea

Yoshitake Masuda
National Institute of Advanced Industrial Science and
Technology (AIST), Nagoya 463-8560, Japan

nanomaterials with anisotropic morphologies are studied for their enhanced electronic, magnetic, photonic, and catalytic properties (Jana et al. 2007). Among the various inorganic materials, iron and its oxides are the important class of materials with versatile fundamental and technological applications. Of all the iron oxides, hydroxides and oxyhydroxides that occur ubiquitously in nature, α-Fe_2O_3 (hematite) is the most stable iron oxide from the thermodynamic point of view. In particular, α-Fe_2O_3 nanostructures with well-defined shape and surface properties have shown improved performance suitable for applications such as light-induced water splitting, photocatalysis, sensors, and so on. Especially for applications like photocatalytic degradation of organic effluents, which rely on factors like band gap and stability of the photocatalyst in aqueous solution, hematite demonstrates exceptional capabilities. It is an n-type semiconductor with an indirect band gap of $\sim$2.2 eV, allowing it to absorb ultraviolet light as well as majority of visible light during photocatalysis.

For semiconductor-mediated heterogeneous photocatalysis, many factors like pH, temperature, concentration of catalyst, etc., manipulate the effectiveness of a catalyst in promoting the catalytic process (Beydoun et al. 1999; Akpan and Hameed 2009; Ahmed et al. 2010; Zhang et al. 2011). In addition to the aforementioned parameters, heterogeneous catalysis is largely influenced by the chemical composition and the surface properties of the catalyst. Highly porous nanostructures are promising candidates for heterogeneous catalysis as they possess large specific surface area for the photocatalytic reaction. So far, many groups (Yu and Kudo 2006; Testino et al. 2007; Chen et al. 2012; Bharadwaj et al. 2012) have demonstrated the remarkable effect of particle size and morphology on their photocatalytic performance. Although the shape- and surface-dependent physical/chemical properties of nanomaterials are understood and utilized extensively in photocatalytic applications, synthesis strategies to tailor the surface properties of nanostructures and to systematically unravel the shape-guiding process and the growth mechanism responsible for their enhanced functionalities, still remains a challenge. This demands comprehensive understanding of various interdependent parameters like intrinsic crystal structure of the material, nature of precursors, concentration of precursors, preparatory method, experimental conditions like temperature, reaction duration, and so on (Xia et al. 2003).

Recently, our group involved in the synthesis of different nanostructures including dendrites, nanorods, nanospindles, and nanocubes of hematite using simple wet chemical methods by precisely controlling the nature of precursor and experimental conditions. In the previous works reported by us elsewhere (Bharathi et al. 2010a, b), we have elaborated the effect of the precursors and preparatory methods in the formation and growth of these of nanostructures. In this study, we have analyzed the variations in surface properties exhibited by these different morphologies of iron oxide and have examined the role of reaction intermediates responsible for determining the surface properties of these nanostructures. In addition, we have studied the photocatalytic degradation efficiency of these nanostructures towards a model organic effluent Rhodamine B (RhB). Previous reports on the photocatalytic degradation of RhB (Fu et al. 2005; Qiu et al. 2008; Zeng et al. 2008; Lodha et al. 2011; Zhang et al. 2011) are based on either low initial concentration (10^{-5} M) of RhB or use of higher quantity of the material catalyst for complete degradation of RhB. In this study, we have attempted to efficiently degrade relative higher concentration of RhB (10^{-3} M) using minimum quantity of catalyst by enhancing the specific surface area and porosity. This quantitatively confirms the enhancement in photocatalytic properties of nanostructures based on improvement in their specific surface area and pore size distribution tailored by the preparatory conditions.

Experimental procedure

Synthesis of different nanostructures of α-Fe_2O_3

Different nanostructures of α-Fe_2O_3 were synthesized by forced hydrolysis–reflux condensation method and hydrothermal method separately using different precursors and experimental conditions. Three different sets of controlled experiments that were quite straightforward and repeatable were carried out to study the effect of preparatory method and conditions in determining the morphology of the final product.

In the first set of experiment, nanostructured dendrites of iron oxide were synthesized by the slow dissociation of $K_3[Fe(CN)_6]$ under hydrothermal condition as reported by us elsewhere (Bharathi et al. 2010a). In the typical experiment, 0.01 M $K_3[Fe(CN)_6]$

was hydrothermally treated at 180 °C for 12 h. The resulting precipitate was washed and dried at 80 °C for 24 h.

Second set of experiments were performed to selectively synthesize nanorods and nanospindles of iron oxide by forced hydrolysis and reflux condensation of Fe^{3+} ions in the presence of mineralizer $(NH_2)_2CO$. For the preparation of nanorods, the precursor solution was prepared with 0.25 M of $FeCl_3{\cdot}6H_2O$ and 1 M of $(NH_2)_2CO$. The reaction mixture was then refluxed at 90–95 °C for 12 h. The as-obtained yellow colored precipitate was washed with distilled water and dried at 80 °C for 24 h, and then calcined in air at 300 °C for 1 h. The same experimental condition was repeated by replacing the source of Fe^{3+} ions, namely $FeCl_3{\cdot}6H_2O$ with $Fe(NO_3)_3{\cdot}9H_2O$ to obtain iron oxide nanospindles.

In addition, third set of experiment was carried out for the preparation of iron oxide nanocubes by hydrothermal method. In this process, the same precursor used in the forced hydrolysis and reflux condensation method for the synthesis of nanorods, namely 0.25 M of $FeCl_3{\cdot}6H_2O$ and 1 M of $(NH_2)_2CO$ was hydrothermally treated at 180 °C for 12 h. The resulting precipitate was washed and dried at 80 °C overnight.

Characterization

The X-ray powder diffraction patterns of the samples were measured on PANalytical X'Pert Pro X-ray diffractometer with Cu $K\alpha_1$ radiation ($\lambda = 1.5406$ Å), with an operating voltage and current maintained at 40 kV and 40 mA. The morphology of the samples was studied using scanning electron microscopy (SEM, JSM 6700FM), field-emission scanning electron microscopy (FESEM, JSM 6335FM) and high-resolution transmission electron microscopy (HRTEM, JEOL JEM 2100). N_2 adsorption–desorption isotherms were obtained using Autosorb 1 Quantachrome. The specific surface area was calculated using Brunauer–Emmett–Teller (BET) and pore size distribution on the surface of the samples were evaluated from the desorption branches of the nitrogen isotherms using the Barret–Joyner–Halenda (BJH) model. Prior to the analysis, the powders were degassed at 100 °C for 1 h.

Photocatalytic degradation experiment

The photocatalytic activity was evaluated against the organic dye Rhodamine B (RhB) ($C_{28}H_{31}ClN_2O_3$). It is one of the most important xanthene dyes used as biological stain, tracing agent, solar collector, paper, and laser dye. It is a common organic pollutant resistant to biodegradation and direct photolysis (Yu et al. 2004; Yu and Qi 2009). In a typical experiment, 50 mg of the nanostructured catalyst was dispersed in 100 ml of freshly prepared 1 mM aqueous solution of RhB. The suspension containing the catalyst and dye solution was stirred in dark to establish adsorption/desorption equilibrium between the catalyst and the Rhodamine dye molecules. The solution was then illuminated by a 2 mW UV source ($\lambda = 365$ nm) to induce photochemical reaction. During the exposure of dye solution to the UV source, aliquots were taken out at frequent intervals of 15 min and the concentration of RhB solution was determined using UV–Vis spectrophotometer (3600, Shimadzu).

Results and discussion

Structural analysis

The crystallinity, phase, and purity of the different nanostructures were analyzed from their X-ray diffractograms as shown in Fig. 1. It could be seen that, the XRD pattern of all the nanostructures prepared in this study are in conformity with that of the

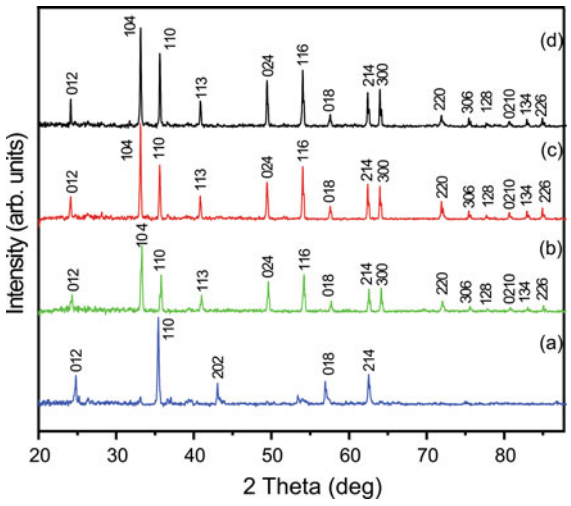

Fig. 1 XRD pattern of (**a**) nanostructured dendrites, (**b**) nanospindles, (**c**) nanorods, and (**d**) nanocubes of α-Fe_2O_3

rhombohedral α-Fe_2O_3 phase of iron oxide (JCPDS card # 33-0664 corresponding to the powder diffraction pattern of standard hematite). No diffraction peaks arising from the possible impurity of hydroxide or Fe_3O_4 phase could be observed in any of the samples.

Morphological analysis

The morphology of all the four samples prepared in this study was analyzed using FESEM, TEM, and HRTEM images.

Selective formation of nanostructured dendrites of α-Fe_2O_3

The FESEM image of the sample obtained by the hydrothermal treatment of 0.01 M $K_3[Fe(CN)_6]$ at 180 °C for 12 h (Fig. 2a, b) shows the formation of nanostructured dendritic micropines. The dendritic structure had a hierarchical arrangement of branches of length 2–2.5 μm symmetrically arranged on a main trunk of length 6–7 μm. The branches were composed of sub-branches of alternating length in the range of 100–300 nm oriented along specific crystallographic directions. The growth direction of the main trunk, branches, and sub-branches, leading to the formation of the entire dendritic shape, were analyzed using HRTEM images and selected area electron diffraction (SAED) pattern shown in Fig. 2c, d. The lattice spacing calculated from the lattice image (Fig. 2c) was found to be ~0.251 nm corresponding to the distance between adjacent $[\bar{1}100]$ planes. The SAED pattern of the dendritic structure clearly indicates the single crystalline nature of the sample with the central spot in the diffraction pattern representing the [0001] orientation and the other spots representing $\pm[10\bar{1}0]$, $\pm[1\bar{1}00]$, and $\pm[0\bar{1}10]$ orientations as indexed in Fig. 2d. These six crystallographically equivalent planes are the low

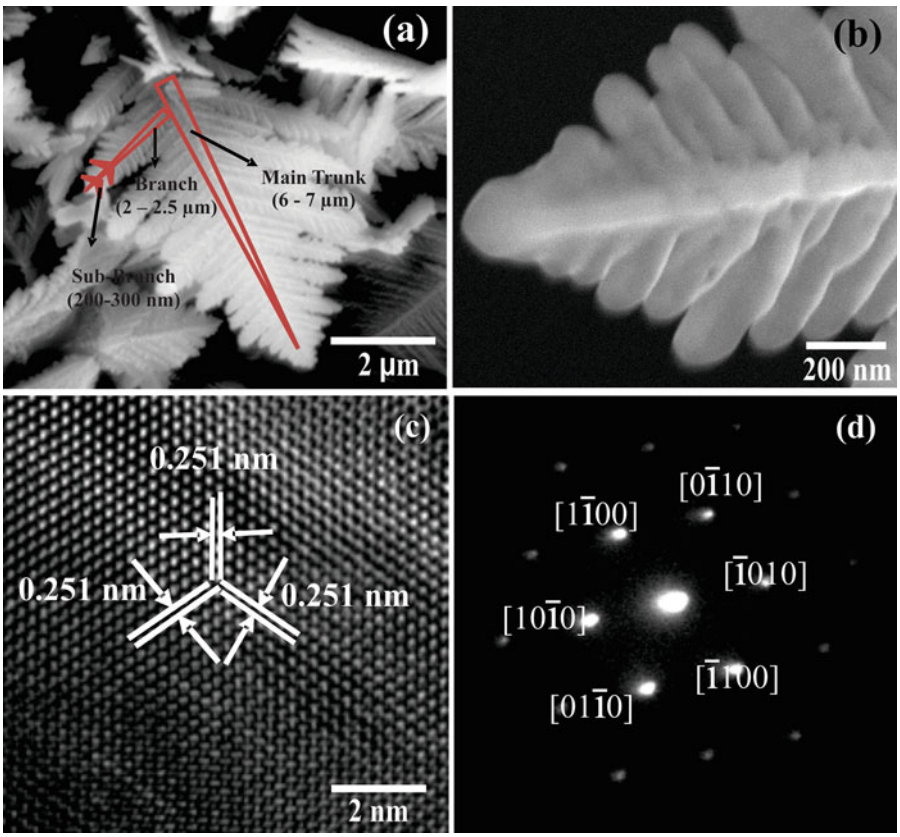

Fig. 2 (**a**) FESEM Image of nanostructured dendrites obtained by hydrothermal treatment of 0.01 M $K_3[Fe(CN)_6]$ at 180 °C for 12 h, showing main trunk with branches and sub-branches; (**b**) magnified view of the branches and sub-branches indicating the growth direction; (**c**) HRTEM image of the lattice pattern taken in the marked region of the dendrite; (**d**) corresponding SAED pattern

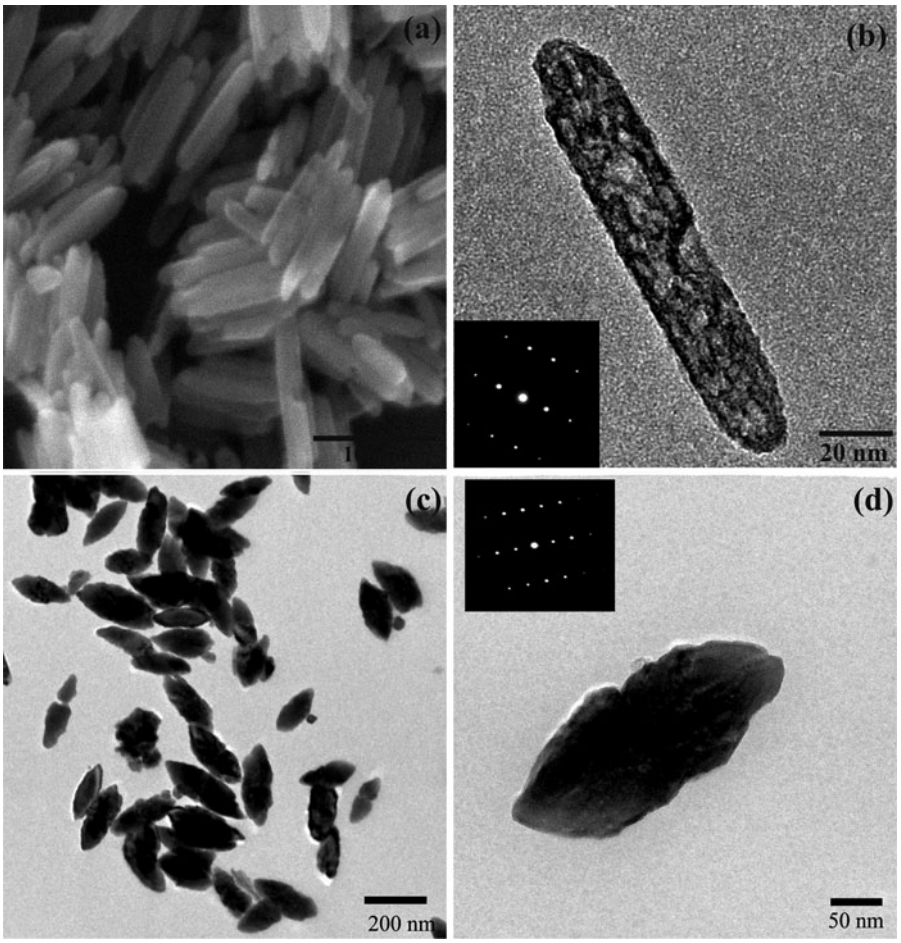

Fig. 3 (**a**) SEM image of nanorod obtained by forced hydrolysis of $FeCl_3 \cdot 6H_2O$ and annealing at 300 °C for 1 h; (**b**) TEM image of individual nanorod showing porous structure (*inset* shows the SAED pattern); (**c**) SEM image of nanospindle obtained by forced hydrolysis of $Fe(NO_3)_3 \cdot 9H_2O$ and annealing at 300 °C for 1 h; (**d**) TEM image of individual nanospindle showing rough surface (*inset* shows the corresponding SAED pattern)

energy facets for a hexagonal crystal lattice, which is the intrinsic crystal structure of hematite. We have reported a detailed analysis on the preparation of dendritic nanostructures, the effect of the nature of precursor, different growth directions, and growth mechanism elsewhere (Bharathi et al. 2010a).

Precursor-dependent formation of nanorods and nanospindles of α-Fe_2O_3

The morphology of the sample obtained in the second set of experiments, synthesized by the forced hydrolysis of $FeCl_3 \cdot 6H_2O$ and urea for 12 h, followed by annealing at 300 °C for 1 h, is shown in Fig. 3. The FESEM image of the sample shows the formation of rod-like nanostructures of diameter ~20 nm and length ~125 nm (Fig. 3a). The alternate bright and dark regions in the TEM image (Fig. 3b) signify the variations in the surface thickness of the nanorods. This can be considered as the presence of pores on the surface of the nanorods. The discrete spots in the SAED pattern shown as inset in Fig. 3b reveal the single crystalline nature of the hematite nanorods.

Further, to understand the importance of the initial precursor in determining the morphology, the refluxing experiment was repeated by replacing $FeCl_3 \cdot 6H_2O$ by $Fe(NO_3)_3 \cdot 9H_2O$. The SEM and TEM images of the 12 h refluxed and annealed sample (Fig. 3c, d) show the formation of spindle-shaped α-Fe_2O_3 nanostructures of length ~200 nm and diameter ~100 nm. This confirms unambiguously that the initial source of Fe^{3+} ions plays an important role in determining the

morphology. The atoms on different crystallographic facets have different adsorption capabilities, leading to preferential growth along certain facets. This might be one of the reasons for the selective growth of nanorods and nanospindles on varying the nature of precursor, though the exact mechanism for the formation of spindle-like morphology is still unclear. From the TEM image of a single spindle-like structure (Fig. 3d), it can be found that the surface is rather rough, which is again an indication of porous surface. In case of both the nanorods and nanospindles, the surface pores have been believed to have originated on annealing the as-prepared sample during the dehydroxylation of FeOOH to form α-Fe_2O_3 and also due to the removal of surface-adsorbed residual CO_2 formed due to the decomposition of urea in the reaction. A detailed study on the reaction intermediates, the possible reactions involved, and the role of urea in the formation of porous nanorods has already been reported by us elsewhere (Bharathi et al. 2010b).

Preparatory method-dependent formation of nanocubes of α-Fe_2O_3

In the above-mentioned forced hydrolysis and refluxing condition, the maximum reaction temperature that could be maintained was 95 °C, since water was used as the solvent under atmospheric pressure. But the hydrothermal method (which we have used in the first set of experiment) offers the advantage of crystallizing nanomaterials from aqueous solutions under elevated temperature and pressure. This technique is especially suitable for preparing metal oxides directly from

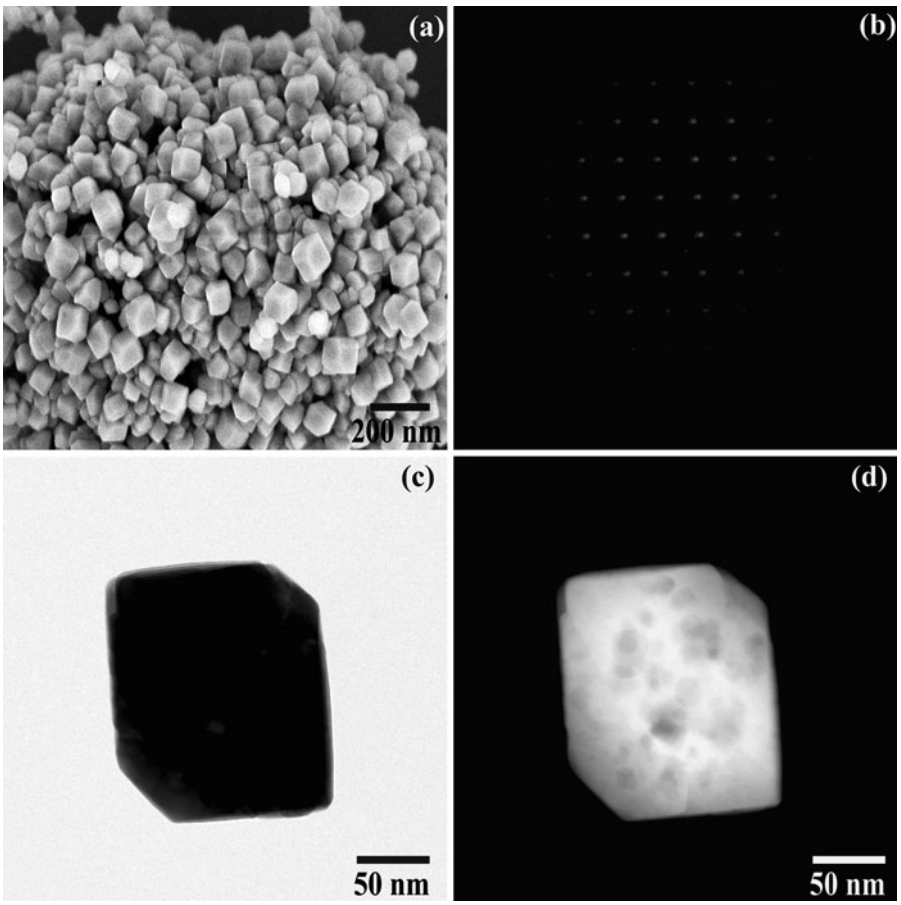

Fig. 4 (**a**) FESEM image of the nanocubes obtained by hydrothermal treatment of $FeCl_3 \cdot 6H_2O$ and urea at 180 °C for 12 h, (**b**) corresponding SAED pattern, (**c**) bright-field TEM image and (**d**) dark-field TEM image of the prepared iron oxide nanocubes showing deeply entrenched mesopores on the surface

solution, without any post-annealing treatments. So in this study, an effort was taken to utilize the advantages of both the hydrothermal method as well as the mild mineralizer urea for preparing porous α-Fe_2O_3 nanocrystals. In this method, the precursors and the concentration of the reactants were the same as used in the second set of experiments for the synthesis of nanorods. The only difference was that the experiment was carried out under hydrothermal condition at an elevated temperature of 180 °C for 12 h. The SEM image of the sample thus obtained (Fig. 4a) shows the formation of uniform, monodisperse nanocubes of edge length ~100 nm. The bright- and dark-field TEM images (Fig. 4c, d) of the nanocubes show the formation of deep entrenched pores of different sizes distributed on its surface. The SAED pattern (Fig. 4b) taken from a single nanocube ascertains that the nanocubes are single crystalline in nature. The growth of nanocubes can be understood based on the chemical reaction between the ferric chloride precursor and urea under hydrothermal condition. The initial stages of the reaction namely the decomposition of urea (Eqs. 1 and 2) and hydrolysis of ferric chloride (Eq. 4) are similar to the reactions involved in the forced hydrolysis and reflux condensation method (Bharathi et al. 2010b). However, the CO_2 formed during the decomposition of urea cannot be released under the closed hydrothermal condition unlike the reflux condensation condition.

$$(NH_2)_2CO + H_2O \rightarrow 2NH_3 + CO_2 \quad (1)$$

$$NH_3 + H_2O \rightarrow NH_4^+ + OH^- \quad (2)$$

$$CO_2 + H_2O \rightarrow 2H^+ + CO_3^{2-} \quad (3)$$

$$Fe^{3+} + 3OH^- \rightarrow Fe(OH)_3 \leftrightarrow FeOOH + H_2O \quad (4)$$

$$Fe^{3+} + CO_3^{2-} + H_2O \rightarrow Fe_2(CO)(OH) \quad (5)$$

$$2FeOOH \xrightarrow{\text{Hydrothermal Condition}} Fe_2O_3 + H_2O \quad (6)$$

$$Fe_2(CO_3)(OH) \xrightarrow{\text{Hydrothermal Condition}} Fe_2O_3 + 3CO_2 \quad (7)$$

Hence, the CO_2 released in the reaction would have reacted with the water to form H^+ and CO_3^{2-} ions (Eq. 3), which subsequently reacts with the available Fe^{3+} ions to form $Fe_2(CO_3)(OH)$ (Eq. 5). As the hydrothermal reaction was carried out at a higher temperature of 180 °C for a prolonged time of 12 h, both the FeOOH and $Fe_2(CO_3)(OH)$ would have decomposed to form the highly porous nanocubes of α-Fe_2O_3 (Eqs. 6, 7).

Specific surface area analysis

The fact that makes the study of these different nanostructures interesting is the variations in their surface properties, which is one of the most utilized functionality of nanostructures. Especially for catalytic applications, surface porosity enhances the separation and transfer of photoinduced electron–hole pair, which otherwise would recombine, limiting the photocatalytic efficiency (Yu et al. 2007; Wei et al. 2008). It also provides active sites for the incoming molecules to adsorb and interact with the semiconductor surface. Hence, determination of the specific surface area and pore size distribution in the nanostructure forms an important part in analyzing their catalytic properties.

In this study, the specific surface area and pore size distribution of the prepared hematite nanostructures were measured by the nitrogen adsorption–desorption isotherm using Brunauer-Emmett-Teller (BET) and Barrett-Joyner-Halenda (BJH) methods. Figure 5a–d shows the typical adsorption–desorption isotherms of the prepared nanostructures. The inset in each figure maps the corresponding pore size distribution calculated using BJH method. The nature and type of the hysteresis loop were categorized based on IUPAC standards (Sing et al. 1985). Figure 5a shows the specific surface area and pore size distribution in the nanostructured dendrites. The isotherm is characterized by a distinct hysteresis loop in the region 0.1–1 P/P_0, which can be categorized as Type IV isotherm. The shape of hysteresis exhibited by these particles is of H3 type characterized by slit-shaped pores. The specific surface area of the sample calculated using the BET equation was found to be 40.3 m^2/g. The pore size distribution in the nanostructured dendrites as calculated using BJH method represents the presence of mesopores of size 16 nm on the surface of the sample.

Figure 5b, c shows the isotherms recorded from the nanospindles and nanorods. The distinct hysteresis loop from 0.9 to 1 P/P_0 and 0.7 to 1 P/P_0 in case of nanospindles and nanorods can be categorized as Type V and Type IV isotherms, respectively. The nanospindles had a surface area of 66.8 m^2/g and narrow mesopore distribution of 2–3 nm. The hysteresis

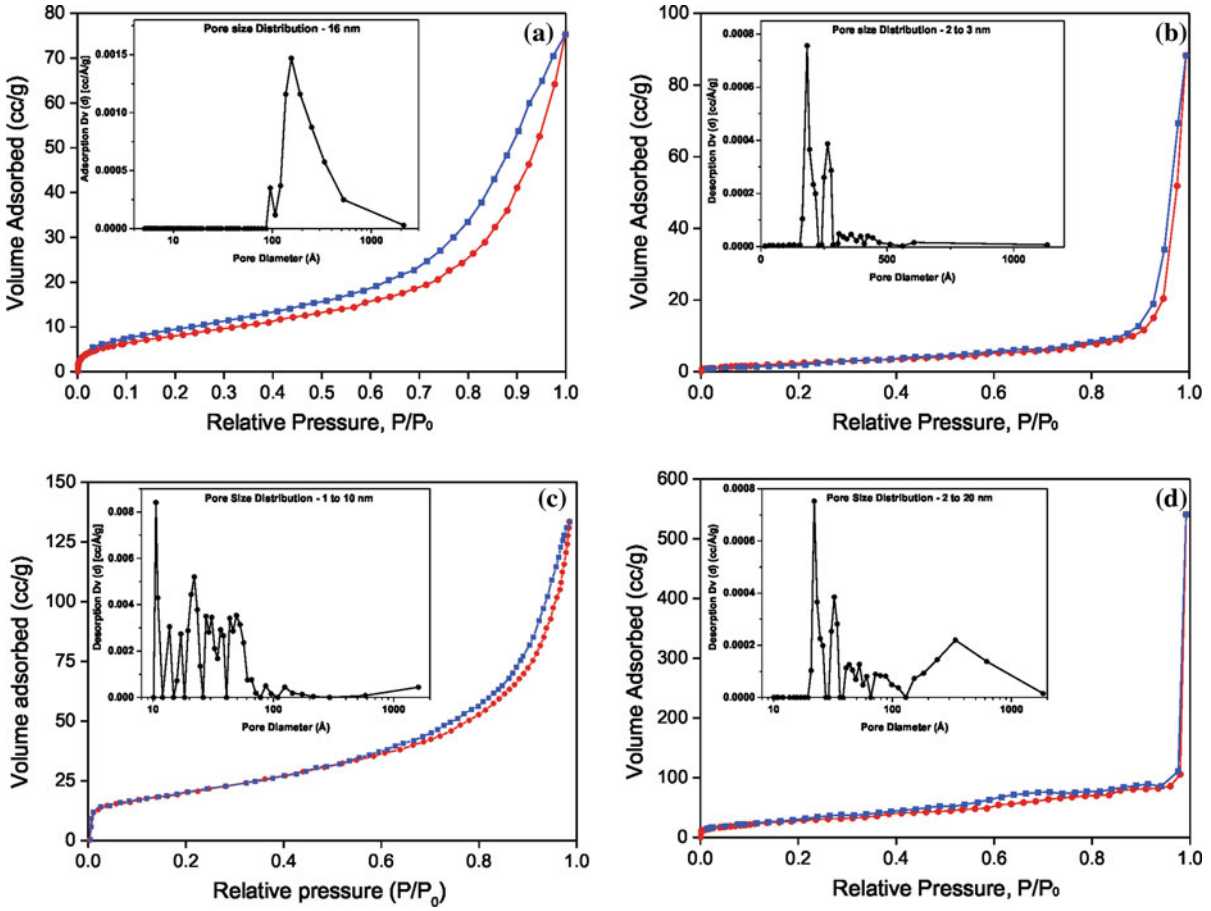

Fig. 5 Nitrogen adsorption–desorption isotherm of the prepared iron oxide: (**a**) nanostructured dendrites, (**b**) nanospindles, (**c**) nanorods, (**d**) nanocubes and (*insets*) the corresponding pore size distribution

shown by nanospindles is of H1 type, indicating uniform spherical pores in the surface of the sample. However, the nanorods had a relatively high specific surface area of 82.6 m^2/g and broad mesopore distribution of 1–10 nm. From the shape of the hysteresis loop, they were found to be of H3 type, which is again characterized by slit-shaped pores.

Figure 5d shows the nitrogen adsorption–desorption isotherm of the nanocubes of Type V with hysteresis of H1 type. Of all the nanostructures prepared in this study, iron oxide nanocubes had a very high specific surface area of 117 m^2/g. The pore size distribution curve shows that the dominant peaks are in the mesoporous range of 2–20 nm. It can also be observed that the pores are bimodal, signified by the presence of smaller and larger mesopores on the surface of the sample.

Origin of pores in urea-assisted reactions

On comparison of the specific surface area and pore size distribution of all the four morphologies (dendrites, nanospindles, nanorods, and nanocubes), it can be realized that preparatory method, precursors used, and the experimental conditions have a strong influence on the surface properties. Of all the morphologies investigated in this study, nanostructured dendrites showed relatively lower surface area because of the nature of precursor used in preparing the sample. On contrary, the other morphologies like nanospindles, nanorods, and nanocubes were prepared in the presence of mild mineralizer urea. The inorganic salt urea plays a dual role in the urea-assisted reactions. It alters the growth kinetics and is also responsible for the formation of pores on the surface of the sample. Urea-

assisted synthesis of inorganic materials is based on the dehydrolyzation of urea at temperatures above 70 °C (Lian et al. 2004). This leads to uniform concentration gradient and homogeneous precipitation in aqueous solution, unlike conventional heterogeneous precipitation methods. During the hydrolyzation of urea, hydroxides, and carbonates of the metal ions are formed. When these metal carbonates and hydroxides decompose to form stable oxide phase either under hydrothermal condition or during post-annealing treatment as in the case of forced hydrolysis method, they leave behind plenty of pores on the surface of the sample. Obviously, the specific surface area and the pore size distribution in the sample increases in urea-assisted reactions. This is the reason behind the origin of different types of isotherms and pore distribution as seen in the N_2 adsorption–desorption isotherms of the samples prepared under different experimental conditions.

Photocatalytic studies

To understand the influence of specific surface area on the catalytic properties of iron oxide, photocatalytic degradation activity of the prepared nanostructures were evaluated toward the synthetic dye Rhodamine B (RhB). The photodegradation was carried out in the absence of catalyst (blank experiment) and in the presence of different α-Fe_2O_3 nanostructures (dendrites, nanospindles, nanorods, and nanocubes) prepared in this study. In the absence of catalyst, UV irradiation of RhB solution showed almost negligible variation in the characteristic absorbance maximum at 554 nm. However, when hematite nanostructures were used as photocatalyst, the absorption maximum steadily decreased upon UV irradiation without any obvious peak shift of the absorption maximum. It was accompanied by a gradual change in color of the dye solution from pink color to almost a colorless solution. This marks the complete degradation and decolourization of aqueous RhB due to the degradation activity of the hematite photocatalyst activated under UV irradiation.

In case of nanostructured dendrites as catalyst, the absorbance showed maximum value of 2.66 before UV exposure and decreased to a value of 0.47 after 210 min (i.e., 3½ h) of UV exposure (Fig. 6a). When nanospindles were used as catalyst, the photodegradation and decolorization activity was slightly enhanced. The absorbance with an initial value of 2.66, decreased to 0.45 after 165 min (i.e., 2¾ h) as shown in Fig. 6b. In case of nanorods as catalyst, the intensity of absorbance maximum decreased to 0.4, after 135 min (2¼ h) of UV exposure (Fig. 6c), showing a relatively faster degradation rate. The degradation and decolorization rate of the RhB solution was prominently improved when nanocubes were used as catalyst. The absorbance maximum drastically decreased from 2.66 to 0.4 within 90 min (1½ h) of UV exposure as shown in Fig. 6d. There was no further decrease or change in the absorbance value, when the UV exposure was prolonged even up to 3 h. This marks the completion of the photodegradation as early as 90 min using iron oxide nanocubes.

After the completion of the photocatalytic degradation experiments, all the nanostructured α-Fe_2O_3 particles used as catalyst in this study were separated out by filtration, washed, and dried in oven. The so-used catalysts were reused to degrade a new solution of RhB with the same experimental conditions. The process was repeated three times to check the reusability of the nanoparticle catalysts. It was observed that the catalysts showed similar response every time they were reused. This confirms that the degradation activity was highly repeatable.

The UV–Vis absorbance spectra of the RhB solution during the different stages of photocatalytic reaction using the various iron oxide nanostructures are shown in Fig. 6a–d. Absorption spectrum was obtained by a plot between absorbance versus irradiation time and the decolourization efficiency was determined in terms of change in intensity of absorption maximum of the dyes. The decolourization efficiency was calculated (Wu and Zhang 2004) using the formula:

$$\frac{A_0 - A_t}{A_0} \times 100 \tag{8}$$

where A_0 is the absorption maximum at $t = 0$, A_t is the absorption maximum after t min taken for complete degradation. The apparent rate constant was determined by considering the absorbance values, before and after degradation and from the time required for degrading the dye completely. The regression curve of the natural logarithm of RhB concentration versus the reaction time was almost a straight line. This implies that the photodegradation of RhB followed pseudo-first-order kinetics in the presence of the catalyst.

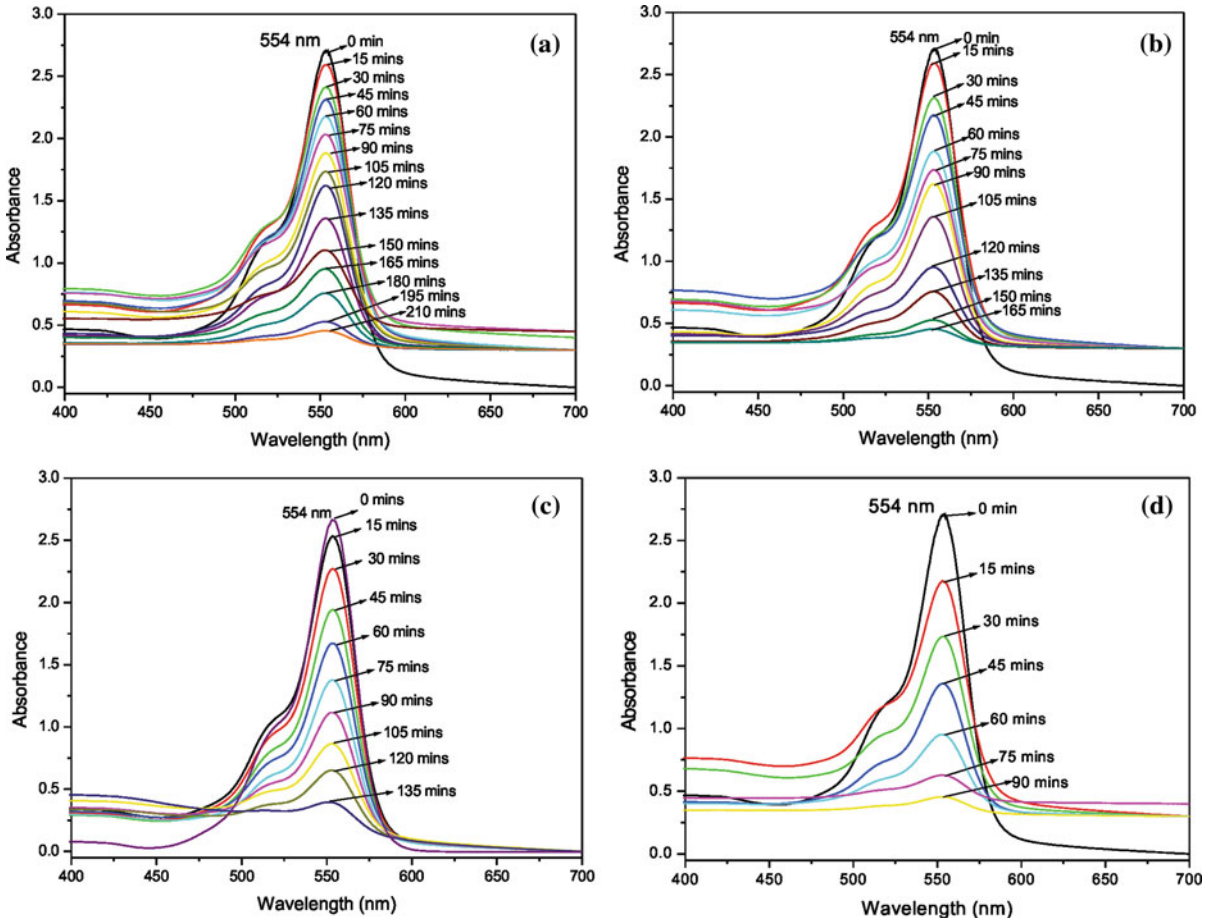

Fig. 6 UV–Vis absorbance spectra of RhB during photocatalytic reaction by (**a**) nanostructured dendrites, (**b**) nanospindles, (**c**) nanorods, and (**d**) nanocubes

Hence, the apparent rate constant of the photocatalytic degradation reaction was calculated (Yu and Qi 2009) using the formula:

$$\ln \frac{A_0}{A_t} = kt, \tag{9}$$

where k is the rate constant of the reaction, A_0, A_t are the absorbance maxima at $t = 0$ and $t =$ minimum time required for complete degradation, respectively.

The overall degradation trend of the different nanostructures in degrading the dye RhB is shown in Fig. 7. The Table 1 lists out the decolourization efficiency, degradation rate of the different nanostructured catalysts prepared in this study and their corresponding specific surface area and pore size distribution. The results obtained in this study show significant improvement in the photocatalytic degradation of highly concentrated

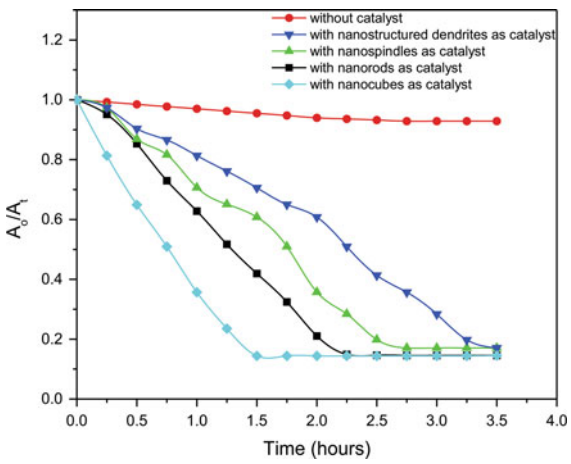

Fig. 7 Degradation trend of RhB as a function of irradiation time

solution of RhB using the prepared iron oxide nanostructures.

The observed enhancement in the photocatalytic performance of iron oxide nanostructures can be justified based on the catalytic properties of iron oxide, particle size, improvement in surface area, and porosity tailored by the preparatory method and conditions. Various researchers have carried out the heterogeneous photocatalytic degradation of RhB using TiO_2 and ZnO as photocatalysts (Barka et al. 2008; Zhang et al. 2011; Byrappa et al. 2006; Zhao and Wang 2011). Though these semiconductors were reported to have high photosensitivity, from the standpoint of application, there are some drawbacks associated with these semiconductors pertaining to faster charge carrier recombination, specific spectral activation due their large band gap, and their reusability/stability in aqueous solution (Sakthivel et al. 2002). These challenges were addressed in this study by considering the catalytic properties of α-Fe_2O_3. The indirect band gap ($\sim$2.2 eV) of α-Fe_2O_3 allows it to absorb ultraviolet light as well as the majority of visible light. Also, it is an n-type semiconductor in which the Fermi level is closer in energy to the conduction band than to the valence band. The relatively high energy of electrons in an n-type semiconductor causes a small number of electrons to be transferred to water when placed in electronic contact with it (Kay et al. 2006). This results from equilibration of the electronic energy levels of the semiconductor (the Fermi level) with the electronic energy levels of water (as measured by the water redox potential). The transfer of these few electrons from the semiconductor to the water sets up an electric field at the surface and results in the upward bending of the conduction and valence bands as they approach the surface. If the photon is absorbed near the surface of the hematite (within the band-bending region), the electric field drives the hole toward the surface and the electron away from it. At the surface, the hole can oxidize the organic molecules. The electron efficiently separated from the hole reduces the organic molecules adsorbed on the surface. This accounts for the enhanced catalytic properties as well as the stability of iron oxide in aqueous media.

In addition to the inherent catalytic properties, the effect of particle size and surface properties also has a profound influence in photocatalytic reactions. During photodegradation, photo-generated electrons (e^-) and holes (h^+) migrate to the surface of the catalyst and undergo redox reaction with the adsorbed reactants. The recombination of the photoexcited electron–hole pair needs to be retarded for an efficient charge transfer process to occur on the photocatalyst surface. This could be accomplished by enhancing intermediate charge carrier trapping. This charge trapping is more pronounced in case of nanocrystals with defects and pores on the surface because the surface irregularities like defects and pores are associated with surface electron states that differ in their energy from the bands present in the bulk semiconductor. The surface electron states serve as charge carrier traps and help to suppress the recombination of electrons and holes (Yu et al. 2007). Thus, nanomaterials with high specific surface area and pore size distribution show enhanced degradation efficiency when compared to their counterparts with relatively low specific surface area. This trend has been quantitatively proved in this study.

From the experimental observations presented in Table 1, it can be observed that the degradation rate can be directly correlated to the specific surface area and pore size distribution in the nanostructures. Among the four different morphologies of iron oxide evaluated for their photocatalytic efficiency, the dendrites sample showed a relatively lower photocatalytic activity. In

Table 1 Experimental observations of the decolourization efficiency, degradation rate of the different nanostructured catalysts prepared in this study and their corresponding specific surface area and pore size distribution

Catalyst	Time required for complete degradation (t, min)	Decolourization efficiency (%)	Rate constant	Specific surface area (m^2/g)	Pore size distribution (nm)
Dendrite	210	82.7	0.322	40.3	16
Nanospindle	165	83.08	0.589	66.8	2–3
Nanorod	135	84.96	0.8505	82.6	1–10
Nanocube	90	84.96	0.876	117	2–20

other words, the dendrite sample with relatively lower specific surface area took longer time to degrade the dye, whereas the nanocube sample with a relatively high specific surface area when compared to the other morphologies showed the highest photocatalytic degradation efficiency. The other morphologies namely nanorods and nanospindles also followed the same trend according to their specific surface area. The high specific surface area resulted in more unsaturated surface coordination sites exposed to the dye molecules. Hence, it can be ascertained that specific surface area has a straightforward influence on the photocatalytic activity. In addition to specific surface area, pore size distribution is another factor, which improves the degradation rate of the nanostructures. It has been reported (Zhang et al. 2008) that presence of smaller and larger mesopores facilitates efficient transport of reactant molecules onto the active sites, enhancing the efficiency of photocatalysis. In this study, though all the samples were mesoporous, the distribution of smaller and larger mesopores was found only in nanorods and nanocubes. This might be another reason for high photocatalytic degradation capability observed in the nanorods and nanocubes.

Conclusion

We have developed simple and environmentally benign methods for controlled synthesis of α-Fe_2O_3 nanostructures with well-defined shapes and tailored surface properties. By varying the nature of precursors and the preparatory conditions, we could achieve a precise control over the reaction kinetics and hence the shape and surface properties of the nanostructures. N_2 adsorption–desorption isotherms have shown a drastic improvement in specific surface area and pore size distribution in urea-assisted reactions. The photocatalytic degradation efficiency of the prepared nanostructures evaluated against RhB was found to have straightforward dependence on specific surface area. α-Fe_2O_3 nanocubes of relatively high specific surface area (117 m^2/g) and mesoporosity showed a faster degradation rate compared to other morphologies prepared in this study. This study quantitatively demonstrates a new strategy for improving photodegradation performance based on structure and surface property optimization.

Acknowledgments One of the authors SB acknowledge Defense Research and Development Organisation, Government of India for providing financial support and fellowship to carry out the research work. The authors thank Prof. K. Swaminathan, Prof & Head, Department of Microbial Biotechnology, Bharathiar University, Coimbatore, for extending UV–Vis spectrophotometer facility.

References

Ahmed B, Rasul MG, Martens WN, Brown R, Hashib MA (2010) Heterogeneous photocatalytic degradation of phenols in wastewater: a review on current status and developments. Desalination 261(1–2):3–18

Akpan UG, Hameed BH (2009) Parameters affecting the photocatalyticdegradation of dyes using TiO_2-based photocatalysts: a review. J Hazard Mater 170(2–3):520–529

Barka N, Qourzal S, Assabbane A, Nounah A, Ait-Ichou Y (2008) Factors influencing the photocatalytic degradation of Rhodamine B by TiO_2-coated non-woven paper. J Photochem Photobiol A 195:346–351

Beydoun D, Amal R, Low G, McEvoy S (1999) Role of nanoparticles in photocatalysis. J Nanopart Res 1:439–458

Bharadwaj L, Bharadwaj M, Sharma MK (2012) An analysis of Fe_2O_3 assisted photocatalytic degradation of Congo red dye. Toxicol Environ Health Sci 4(1):62–69

Bharathi S, Nataraj D, Seetha M, Mangalaraj D, Ponpandian N, Masuda Y, Senthil K, Yong K (2010a) Controlled growth of single-crystalline, nanostructured dendrites and snowflakes of α-Fe_2O_3: influence of the surfactant on the morphology and investigation of morphology dependent magnetic properties. Cryst Eng Commun 12:373–382

Bharathi S, Nataraj D, Mangalaraj D, Masuda Y, Senthil K, Yong K (2010b) Highly mesoporous α-Fe_2O_3 nanostructures: preparation, characterization and improved photocatalytic performance towards Rhodamine B (RhB). J Phys D 43:015501, p 9

Byrappa K, Subramani AK, Ananda S, Lokanatha Rai KM, Dinesh R, Yoshimura M (2006) Photocatalytic degradation of rhodamine B dye using hydrothermally synthesized ZnO. Bull Mater Sci 29(5):433–438

Chen D, Yoo SH, Huang Q, Ali G, Cho SO (2012) Sonochemical synthesis of Ag/AgCl nanocubes and their efficient visible-light-driven photocatalytic performance. Chem A Eur J 18(17):5192–5200

Fu H, Pan C, Yao W, Zhu Y (2005) Visible-light-induced degradation of Rhodamine B by nanosized Bi_2WO_6. J Phys Chem B 109:22432–22439

Jana S, Basu S, Pande S, Ghosh SK, Pal T (2007) Shape-selective synthesis, magnetic properties, and catalytic activity of single crystalline β-MnO_2 nanoparticles. J Phys Chem C 111:16272–16277

Kay A, Cesar I, Gratzel M (2006) New benchmark for water photooxidation by nanostructured α-Fe_2O_3 films. J Am Chem Soc 128(49):15714–15721

Lian S, Wang E, Kang Z, Bai Y, Gao L, Jiang M, Hu C, Xu L (2004) Synthesis of magnetite nanorods and porous hematite nanorods. Solid State Commun 129(8):485–490

Lodha S, Jain A, Punjabi PB (2011) A novel route for waste water treatment: photocatalytic degradation of rhodamine B. Arab J Chem 4(4):383–387

Qiu X, Li G, Sun X, Li L, Fu X (2008) Doping effects of Co^{2+} ions on ZnO nanorods and their photocatalytic properties. Nanotechnology 19:215703, p 8

Sajanlal PR, Sreeprasad TS, Samal AK, Pradeep T (2011) Anisotropic nanomaterials: structure, growth, assembly and functions. Nano Rev 2:5883

Sakthivel S, Geissen SU, Bahnemann DW, Murugesan V, Vogelpohl A (2002) Enhancement of photocatalytic activity by semiconductor heterojunctions: α-Fe_2O_3, WO_3 and CdS deposited on ZnO. J Photochem Photobiol A 148:283–293

Sing KSW, Everett DH, Haul RAW, Moscou L, Pierotti RA, Rouquerol J, Siemieniewska T (1985) Reporting physisorption data for gas/solid systems with special reference to the determination of surface area and porosity. Pure Appl Chem 57(4):603–619

Testino A, Bellobono IR, Buscaglia V, Canevali C, D'Arienzo M, Polizzi S, Scotti R, Morazzoni F (2007) Optimizing the photocatalytic properties of hydrothermal TiO_2 by the control of phase composition and particle morphology. A systematic approach. J Am Chem Soc 129(12):3564–3575

Wei Q, Zhang Z, Li Z, Zhou Q, Zhu Y (2008) Enhanced photocatalytic activity of porous α-Fe_2O_3 films prepared by rapid thermal oxidation. J Phys D 41:202002, p 4

Wu JM, Zhang TW (2004) Photodegradation of rhodamine B in water assisted by titania films prepared through a novel procedure. J Photochem Photobiol A 162(1):171–177

Xia Y, Yang P, Sun Y, Wu Y, Mayers B, Gates B, Yin Y, Kim F, Yan H (2003) One-dimensional nanostructures: synthesis, characterization, and applications. Adv Mater 15(5): 353–389

Yu J, Kudo A (2006) Effects of structural variation on the photocatalytic performance of hydrothermally synthesized $BiVO_4$. Adv Funct Mater 16(16):2163–2169

Yu J, Qi L (2009) Template-free fabrication of hierarchically flower-like tungsten trioxide assemblies with enhanced visible-light-driven photocatalytic activity. J Hazard Mater 169(1–3):221–227

Yu D, Cai R, Liu Z (2004) Studies on the photodegradation of Rhodamine dyes on nanometer-sized zinc oxide. Spectrochim Acta Part A 60(7):1617–1624

Yu H, Yu J, Cheng B, Liu S (2007) Novel preparation and photocatalytic activity of one-dimensional TiO_2 hollow structures. Nanotechnology 18(6):065604, p 8

Zeng S, Tang K, Li T, Liang Z, Wang D, Wang Y, Qi Y, Zhou W (2008) Facile route for the fabrication of porous hematite nanoflowers: its synthesis, growth mechanism, application in the lithium ion battery, and magnetic and photocatalytic properties. J Phys Chem C 112(13):4836–4843

Zhang J, Shi F, Lin J, Chen D, Gao J, Huang Z, Ding X, Tang C (2008) Self-assembled 3-D architectures of BiOBr as a visible light-driven photocatalyst. Chem Mater 20(9): 2937–2941

Zhang W, Li Y, Wang C, Wang P (2011) Kinetics of heterogeneous photocatalytic degradation of rhodamine B by TiO_2-coated activated carbon: roles of TiO_2 content and light intensity. Desalination 266(1–3):40–45

Zhao J, Wang L (2011) Degradation of Rhodamine B in aqueous solution by the UV/ZnO photocatalytic process. IEEE Conf Mater renew Energy Environ 2:1397–1400

DOI 10.1007/978-3-319-05041-6_10
Reprinted from the *Journal of Nanoparticle Research*, DOI 10.1007/s11051-012-1194-9

RESEARCH PAPER

Protein-functionalized magnetic iron oxide nanoparticles: time efficient potential-water treatment

Chuka Okoli · Magali Boutonnet · Sven Järås · Gunaratna Rajarao-Kuttuva

Received: 16 April 2012 / Accepted: 10 September 2012 / Published online: 22 September 2012

Abstract Recent advances in nanoscience suggest that the existing issues involving water quality could be resolved or greatly improved using nanomaterials, especially magnetic iron oxide nanoparticles. Magnetic nanoparticles have been synthesized for the development and use, in association with natural coagulant protein for water treatment. The nanoparticles size, morphology, structure, and magnetic properties were characterized by transmission electron microscope, X-ray diffraction, and superconducting quantum interference device magnetometry. Purified *Moringa oleifera* protein was attached onto microemulsions-prepared magnetic iron oxide nanoparticles (ME-MION) to form stable protein-functionalized magnetic nanoparticles (PMO+ME-MION). The turbidity removal efficiency in both synthetic and surface water samples were investigated and compared with the commonly used synthetic coagulant (alum) as well as PMO. More than 90 % turbidity could be removed from the surface waters within 12 min by magnetic separation of PMO+ME-MION; whereas gravimetrically, 70 % removal in high and low turbid waters can be achieved within 60 min. In contrast, alum requires 180 min to reduce the turbidity of low turbid water sample. These data support the advantage of separation with external magnetic field (magnetophoresis) over gravitational force. Time kinetics studies show a significant enhancement in ME-MION efficiency after binding with PMO implying the availability of large surface of the ME-MION. The coagulated particles (impurities) can be removed from PMO+ME-MION by washing with mild detergent or cleaning solution. To our knowledge, this is the first report on surface water turbidity removal using protein-functionalized magnetic nanoparticle.

Keywords Magnetic separation · Microemulsions · Magnetophoresis · Purified *Moringa oleifera* · Coagulant protein · Surface water

Special Issue Editors: Mamadou Diallo, Neil Fromer, Myung S. Jhon

This article is part of the Topical Collection on Nanotechnology for Sustainable Development

C. Okoli · G. Rajarao-Kuttuva
Environmental Microbiology, Royal Institute of Technology (KTH), 106 91 Stockholm, Sweden

C. Okoli · M. Boutonnet · S. Järås
Chemical Technology, Royal Institute of Technology (KTH), 100 44 Stockholm, Sweden

G. Rajarao-Kuttuva (✉)
School of Biotechnology, Albanova University Center, Roslagstullsbacken 21, 106 91 Stockholm, Sweden
e-mail: gkr@kth.se

Introduction

Functionalized nanomaterials are known to display novel and significant physical, chemical, and biological properties due to their structure, size, and large specific

surface area (Liao and Chen 2002; Mikhaylova et al. 2004; Grecu et al. 2008). For this reason, device that encompasses nanomaterials/nanotechnology has the potential to improve water quality, viability, and accessibility of potable water (Li et al. 2008; Liu et al. 2008; Theron et al. 2008). The use of natural materials like coagulant protein from *Moringa oleifera* associated with eco-friendly compounds may represent another possible solution to the existing concerns in water treatment process. The availability of the natural material and competing food source is often a risk for long-term solution. The functionalization of magnetic iron oxide nanoparticle with protein is appealing; especially because of its several advantages; such as, low cost of materials, high efficiency, reduction of chemical usage including sludge volume, and fast separation due to its magnetophoretic properties (Okoli et al. 2011a). This method also has great potential for material recycling, which makes it very advantageous for large-scale treatment process. Moreover, natural protein incorporated on magnetic nanoparticles constitutes an excellent alternative for chemical usage in water treatment process.

Availability of clean and safe water is a major problem in both developed and developing countries. At present, the world is facing difficult challenges in meeting the increasing demands of potable water due to population growth, increasing pollution of water bodies from several industrial and agricultural activities, drought, and competing demands from a variety of users (Vorosmarty et al. 2000; Lee and Schwab 2005; Moe and Rheingans 2006; Coetser et al. 2007; Theron et al. 2008).

There are concerns regarding the quality and quantity of water globally. However, to provide potable drinking water, various technologies have been developed and used over a century (Cloete 2010).

The conventional method for water treatment involves the use of mechanical, physical, and some chemical approaches. The choice of chemicals in water treatment is decisive. The treatment process may add substances to the water, which can increase the risk of diseases to human health. Moreover, high impact on the production of large volume of sludge, increase in water pH as well as scarcity of foreign currency for importing these chemicals especially in third world countries are of great concern (Sanchez-Martin et al. 2010). Even though different treatment processes exist to improve the water quality, disease outbreaks is often reported worldwide.

Considering the importance of potable drinking water globally, and keeping in mind concerns regarding the viability of recent practices of meeting the rising water demands, there is a pressing need to develop novel technologies and materials that will tackle the challenges associated with safe drinking water. While new technologies are being developed today for example nanofiltration, reverse osmosis, etc., (Cloete 2010) the need to have cost-effective, user-friendly, robust, and more efficient systems than the existing techniques for the removal of contaminants from drinking water either in water treatment process or in situ are considered paramount. The emergence of nanoscience has been identified as a promising technology that could play a major role in solving several complications involving water treatment and quality (Theron et al. 2008).

In this study, the development and application of magnetic iron oxide nanoparticles prepared from microemulsion that incorporates natural protein for coagulation/flocculation in water treatment is reported. The magnetic nanoparticles were characterized by transmission electron microscope (TEM), X-ray diffraction (XRD), and superconducting quantum interference device magnetometry (SQUID). Purified *Moringa oleifera* (PMO) coagulant protein was incorporated onto the magnetic nanoparticles to form PMO+ME-MION. The comparison of coagulation activity in terms of turbidity reduction for synthetic and surface waters (high and low turbidity) using PMO+ME-MION, PMO, bare ME-MION, and aluminum sulfate (alum) was also investigated. Effect of separation with magnetic field and force of gravity was compared and reported. Regeneration potential of the PMO+ME-MION was evaluated and discussed.

Materials and methods

Microemulsion-prepared magnetic iron oxide nanoparticles

The synthesis of ME-MION was carried out by *water-in-oil* microemulsion method. Two microemulsions were mixed (Fig. 1). Each microemulsion system consists of a surfactant, cetyl trimethyl ammonium bromide (CTAB), a co-surfactant (1-butanol), oil phase (hexanol), iron precursors ($FeCl_3$ and $FeCl_2$), precipitating agent (32 % NH_3), and water (Milli-Q

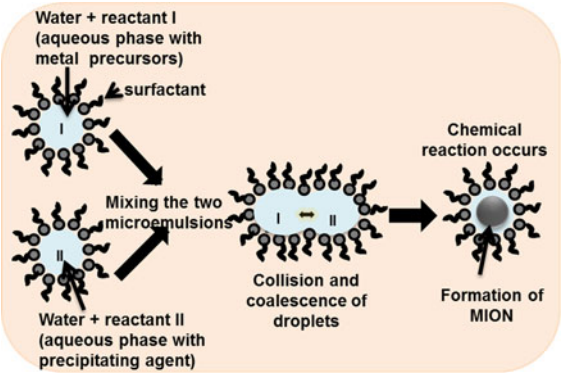

Fig. 1 Scheme for the preparation of ME-MION by *w/o* microemulsion reaction approach mixing two microemulsions of identical composition except for reactant I (metal precursors) and reactant II (precipitating agent)

water). The first microemulsion consists of aqueous solution of iron precursor while the second microemulsion contains a precipitating agent (aq.NH_3). Both microemulsion mixtures were homogenized. Precipitation of ME-MION was achieved by adding the first microemulsion into the latter at room temperature upon vigorous stirring for 1 h. The obtained ME-MION was washed and either dried at 70 °C or suspended in Milli-Q water until further use. More detailed synthetic procedures are given (Okoli et al. 2011a).

Characterization techniques

The size and morphology of the ME-MION were examined by high-resolution transmission electron Microscopy (HRTEM), which was carried out using a field emission transmission electron microscope, JEM-2200FS, 200 kV, with 0.19 nm resolution in TEM mode. For this purpose, dry powder sample was dispersed in isopropanol and deposited onto a formvar carbon copper grid. Selected area electron diffraction patterns (SAED) of the nanoparticles were also investigated from the electron micrographs (data not shown). X-ray diffraction data of the microemulsion-prepared nanoparticles were performed between 20 and 70° on Siemens D5000 diffractometer using Cu Kα radiation. Room temperature magnetic hysteresis loops of the nanoparticles were measured using a superconducting quantum interference device (SQUID) magnetometer, quantum design MPMS XL. The magnetic moments of the particles were determined in field over a range ±60kOe.

Analytical water source

The water samples for this study were collected from different lakes in Sweden. Raw surface waters with initial turbidity ranging from 7 to 17 NTU were collected in autumn from Lake Mälaren, west of Stockholm. Arboga (Västmanland) and Vättern-Lake (Götaland) water were collected during spring. The choice of seasonal variation in the collection of raw water samples is essential to evaluate the performance of coagulants with different turbidity/contaminants. The samples once collected were stored at 4 °C to prevent any bacteria growth. The model water sample was prepared from kaolin clay [14] with initial turbidity range of 150–170 NTU for comparison purposes. Aluminum sulfate (alum) was prepared (5 %) and used as a control. All experiments were carried out in a batch system.

Binding of PMO onto ME-MION

The purification of *Moringa oleifera* coagulant protein was achieved according to the method already described (Okoli et al. 2011a; Okoli et al. 2011b). Purified *Moringa oleifera* protein was used for the binding assay. Briefly, ME-MION was equilibrated with 10 mM ammonium acetate buffer, pH 6.7. The binding of PMO protein onto the ME-MION was performed in ammonium acetate buffer followed by 1–2 h incubation period in a rotary mixer (20 rpm) at room temperature. The PMO was adsorbed to the ME-MION. The supernatant was removed by magnetic separation and the resultant PMO+ME-MION was washed with ammonium acetate three times to remove the non-adsorbed protein and other impurities. The protein-functionalized ME-MION was suspended in ammonium acetate buffer and this was termed PMO+ME-MION system.

Turbidity removal study with PMO+ME-MION

The turbidity removal efficiency of the PMO+ME-MION has been examined in synthetic turbid water (clay solution). In a typical experimental setup, PMO+ME-MION was added to clay suspension and then mixed instantly. Absorbance at 500 nm was measured with Thermo Spectronic UV–visible spectrophotometer at time 0 and after 60 min settling time. In order to estimate the percentage turbidity removal

for different samples after sedimentation by force of gravity, the following equation was used:

$$\text{Turbidity removal } (\%) = \frac{I_T - F_T}{I_T} \times 100 \quad (1)$$

where I_T is the initial turbidity and F_T is the finial turbidity.

Time kinetics investigation

A simple and quick method to verify the performance of PMO+ME-MION in turbid waters has been developed. This technique was utilized for easy screening of active coagulant from different coagulant samples over a range of time. The following coagulant agents *i.e.*, alum, PMO, PMO+ME-MION, and bare ME-MION were investigated.

For the kinetic study, each coagulant agent was mixed with the turbid water source in a vial. The sample solution in each vial was mixed rapidly at 50 rpm for 5 min to allow the optimal contact between the sample waters and the coagulants. Initial turbidity of the solution was measured. The measurements were carried out periodically (0–240 min) during their settling time to monitor the optimal time needed to achieve good turbidity reduction. The synthetic clay solution, different surface water samples, and bare ME-MION was used as a negative control.

Separation by magnetic field or force of gravity

The magnetization effect of PMO+ME-MION was compared with the force of gravity (alum) in coagulation/flocculation of particles in turbid water samples. For this reason, a quick method was developed to achieve efficient turbidity reduction and separation with the aforementioned system over a short period of time using applied external magnetic field. Synthetic clay solution and natural surface water samples (SW1; 7 NTU and SW2; 17 NTU) from Lake Mälaren were used. PMO+ME-MION and alum were added to the turbid water sample and mixed instantly; the initial turbidity of the mixture was measured. The resultant mixture was allowed to interact for 10 min at room temperature. After the interaction time, an external magnetic field was applied for 1–2 min to separate the clean water solution from the PMO+ME-MION system while the water samples containing alum were decanted due to settling by gravity. Final turbidity of the treated water was measured.

Regeneration of PMO+ME-MION

The possibility of regenerating the PMO+ME-MION system was investigated in this work. Reusability potential of PMO+ME-MION (*i.e.*, after removal of flocculated impurities) was studied in three successive reuse. PMO+ME-MION were cleaned from the impurities adsorbed in turbid water sample (synthetic clay solution) by washing with mild detergent or cleaning solution. Two different cleaning agents were compared (20 % ethanol and 0.1 wt% Tween 20 in water). The mixture was left for 10 min at room temperature. The supernatant was removed by magnetic separation and the washing was repeated once again followed by 2× wash with 10 mM ammonium acetate buffer. The turbidity removal assay was performed as described before (Eq. 1). The regeneration step was repeated twice; the control sample was calculated initial percent turbidity removed using PMO+ME-MION in water sample before cleaning.

Results and discussion

Synthesis and characterization techniques

The formation of ME-MION in *w/o* microemulsions can be achieved by mixing two *w/o* microemulsions of identical composition, one comprising the inorganic salt precursor and another one comprising the precipitating agent in the aqueous phase nano-droplets. The size, morphology, and agglomeration of prepared ME-MION were examined by HRTEM (Okoli et al. 2011a). The obtained data depicts that ME-MION consisted mainly of elongated, rod-like morphologies with widths ranging from 5 to 10 nm (Okoli et al. 2011a). Diffraction pattern of the dry powder indicates the presence of a magnetic phase of either Fe_3O_4 or γ-Fe_2O_3; which is quite typical at 35° for (311) and 63° for (440). The XRD pattern of ME-MION (Fig. 2a) shows that the nanoparticles correspond to crystalline magnetite which reflects to the well matching of the diffraction peaks with magnetite pattern (Deng et al. 2005; Okoli et al. 2011a).

Magnetic moment of the ME-MION was determined at room temperature (300 K) in field over a range ±60kOe. It can be clearly seen that the magnetization curve for ME-MION displayed no magnetic remanence and coercivity, confirming a

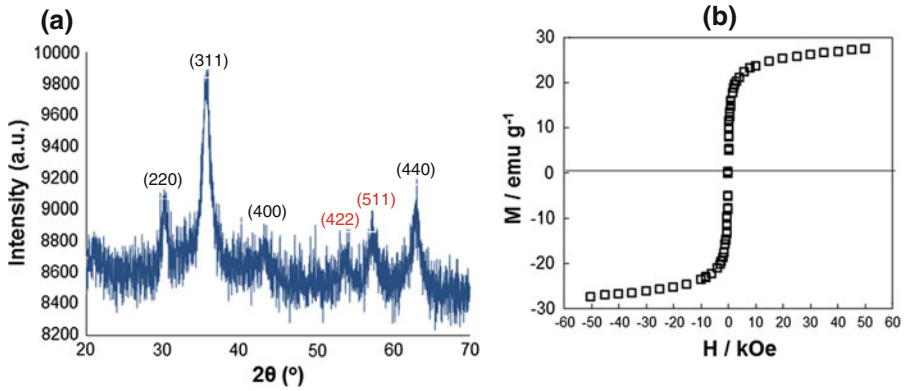

Fig. 2 X-ray diffraction pattern (**a**); and SQUID showing magnetization as a function of magnetic field (**b**); of ME-MION

superparamagnetic behavior and nanoscale dimensions of the particles (Fig. 2b). The recorded saturation magnetization (M_S) value for ME-MION is 30 emu/g.

Turbidity removal study with PMO+ME-MION

The PMO+ME-MION and PMO demonstrated significant coagulation capacity when assayed on the synthetic water sample. The efficiency of PMO+ME-MION improved after binding with PMO. Formation of flocs and reduction in turbidity of the clay suspension indicate better performance of the coagulants. The weight effect of PMO+ME-MION improved the separation speed of the flocs as the magnetized flocs formed around them are much heavier than suspended particles. Results from Fig. 3 also suggest that bare ME-MION can aggregate and flocculate the suspended particles in turbid water samples. Larger flocs can be formed by the collisions of bare nanoparticles with the turbid water sample, resulting in high density mass of ME-MION.

Time kinetics investigation

The present study was carried out to elucidate the performance of some coagulant agents in raw surface waters during different seasons. Results showing the optimal time required to achieve an efficient turbidity reduction with different coagulant agents have been shown in Fig. 4. The PMO+ME-MION showed a significant decrease in turbidity when tested on both synthetic clay solution (Fig. 4a) and natural water

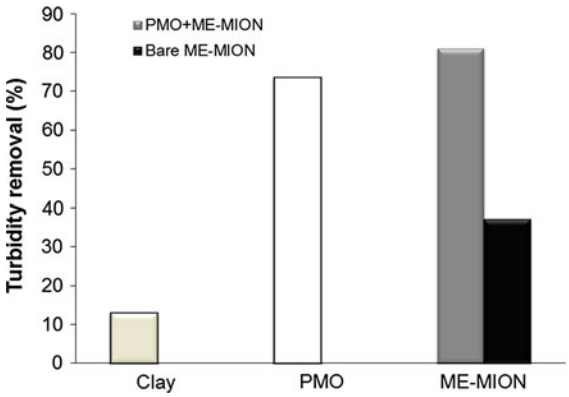

Fig. 3 Results showing turbidity removal at 60 min of separation time with purified moringa protein (PMO) and PMO+ME-MION in synthetic clay solution. Clay solution and bare ME-MION was used as controls

samples (Fig. 4b–d). The efficacy of the coagulant agents depend on the initial turbidity of the water sample (Ghebremichael et al. 2005; Sanchez-Martin et al. 2010). In this study, it is observed that the efficiency of PMO+ME-MION is not influenced by the initial turbidity of the water sample; for instance in 60 min, PMO+ME-MION showed approximately 80 % removal efficiency in both waters collected during autumn and spring seasons. However, it was evident that the high density mass of the magnetized flocs induced by electrostatic interaction resulted in fast flocculation of impurities in the water sample. On the contrary, alum and PMO were found to be less effective, especially in water sample collected during autumn season (Fig. 4b). However, alum and PMO were effective on surface waters collected during spring season (Fig. 4c, d). In addition, it can be

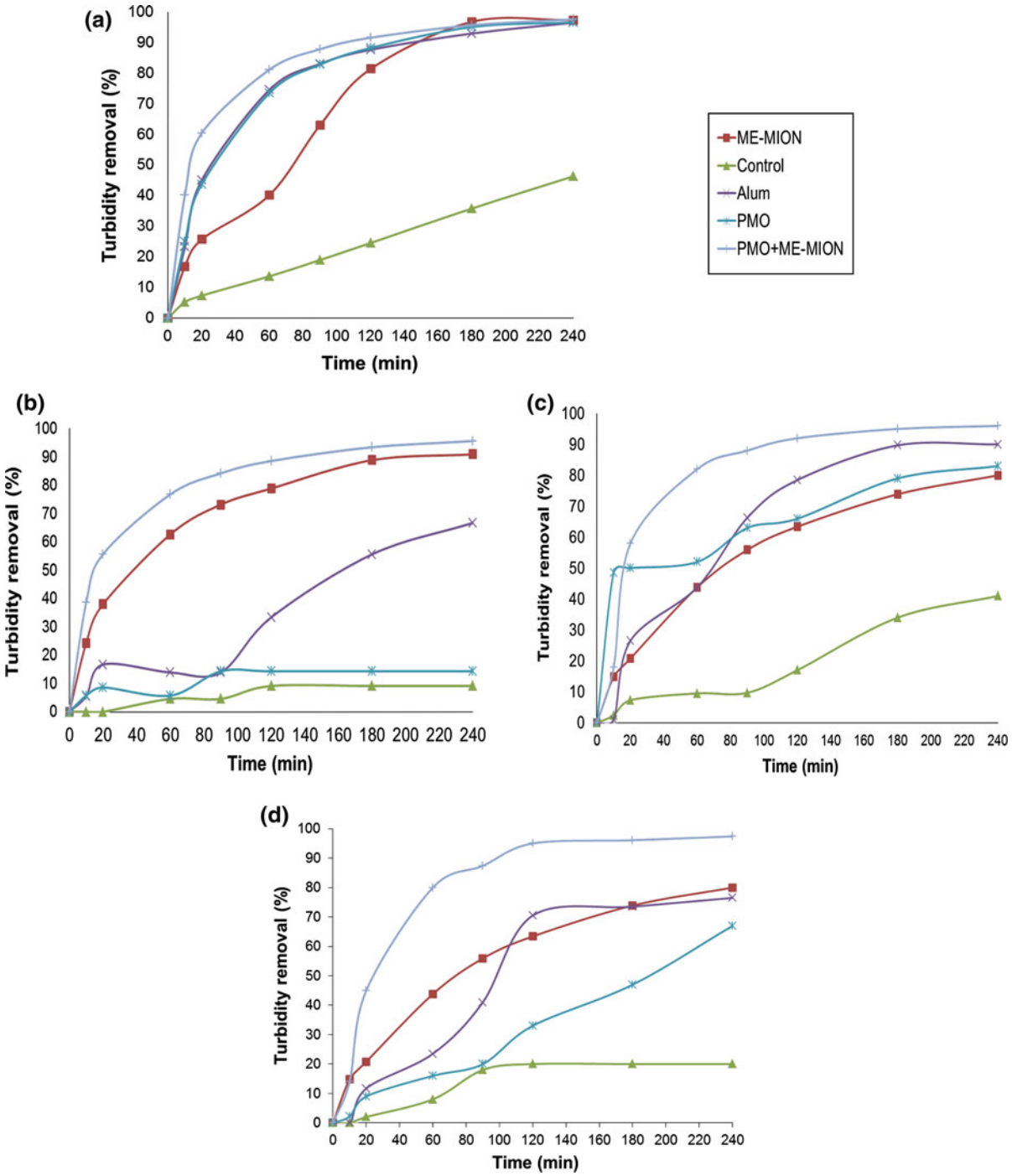

Fig. 4 Kinetic studies showing percent turbidity removal with: **a** synthetic clay solution and surface waters from **b** Lake Mälaren (autumn season), **c** Arboga water (spring season), and **d** Vättern-Lake (spring season). Control represents water sample without coagulant agents

observed that the efficiency of alum and PMO during spring season also depends on the composition of the source water. For instance, both alum and PMO showed 40–50 % turbidity removal with Arboga water (Fig. 4c) in 60 min; whereas, 10–20 % removal was observed with Vättern-Lake (Fig. 4d) in 60 min.

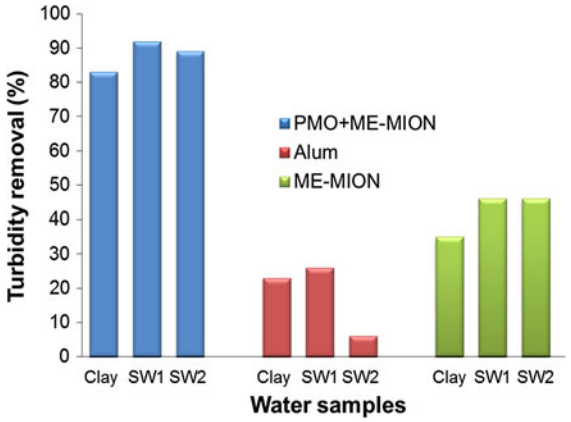

Fig. 5 Turbidity removal result showing the effect of magnetic field separation of suspended particles in natural and synthetic turbid water samples, with PMO+ME-MION and alum after 10 min interaction time and 2 min separation. SW1 and SW2 represent surface water (7 and 17 NTU, respectively) from Lake Mälaren. ME-MION was used as control

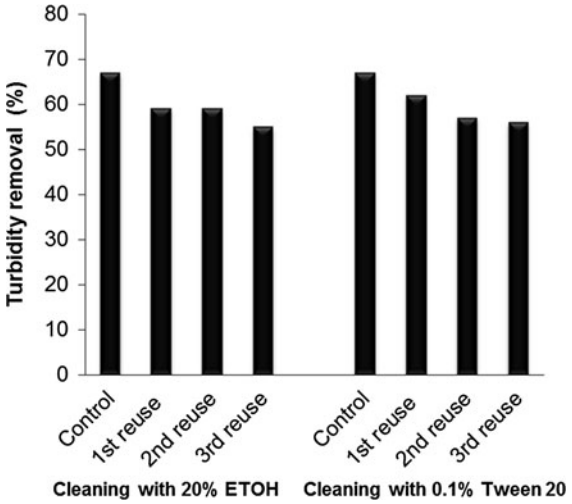

Fig. 6 Regeneration of PMO+ME-MION after turbidity removal assay with clay solution. Cleaning capacity of 20 % EtOH and 0.1 % Tween 20 were compared after 90 min of coagulation activity test. Control sample represents the initial coagulation activity of PMO+ME-MION before cleaning

Experimental results indicate that the performance of PMO+ME-MION, alum, PMO, and bare ME-MION follow a similar trend in natural surface waters while the bare ME-MION showed lower removal performance in synthetic clay solution. Nonetheless, bare ME-MION showed good performance in water collected during autumn season than that collected during the spring season. From this study, it can be established that the PMO+ME-MION is very efficient irrespective of the season or composition of the raw water. The experimental data clearly depicts that the developed PMO+ME-MION may serve as a viable complementary coagulant agent in water treatment process.

Separation by magnetic field or force of gravity

The influence of external magnetic field in the performance of protein-functionalized nanoparticles has been compared with gravitational force, in the clarification of turbid waters (Fig. 5). Experimental results show that PMO+ME-MION tested on natural water samples exhibit good turbidity removal. With PMO+ME-MION, turbidity removal of 75–90 % can be achieved within 12 min, due to the effect of magnetic field. According to magnetization curve theories, when nanoparticles are placed within a steady external magnetic field, the internal magnetic moment will spin in the same direction as the external magnetic field. This magnetophoretic occurrence will boost the magnetic properties of the nanoparticles thereby causing the aggregation of the water impurities (Lu et al. 2007; Faraji et al. 2010). The existence of this dynamics will induce the aggregation of the water contaminants by nanoparticles. The combination of PMO+ME-MION and applied magnetic field enhanced the effectiveness of the system in coagulating/flocculating impurities in different turbid water samples. Bare ME-MION showed lower turbidity removal as compared to PMO+ME-MION. This suggests that the binding of the protein onto the ME-MION was critical in enhancing their performance. Comparing the time kinetics study and separation by magnetic field (Figs. 4, 5), the time efficient removal of turbidity with PMO+ME-MION was evident. Moreover, in contrast to aluminum sulfate (alum), the turbidity removal of PMO+ME-MION presented high level of consistency in all the assayed water samples.

Regeneration of PMO+ME-MION

In order to examine the reusability of the PMO+ME-MION, the developed system was washed with mild detergent or cleaning solution after separation. Turbidity removal assay reveals that it is possible to reuse the PMO+ME-MION three times (Fig. 6). In comparison with the control sample (initial percentage

removal of PMO+ME-MION before washing), cleaning with 20 % EtOH and 0.1 % Tween 20 showed almost similar turbidity removal in the clay solution. PMO+ME-MION, on cleaning with both ethanol and Tween 20, showed a small reduction in performance (removal efficiency) after the first wash; however, a high level of consistency is seen in the successive washing. The most probable reason for the slight reduction in removal efficiency after first cleaning step could be that the clay particles were not completely removed from PMO+ME-MION. However, it is unlikely that the detergent or cleaning solution will desorb the electrostatic interaction between the negatively charged nanoparticles and the positively charged protein. Results from this investigation indicate that 20 % EtOH and 0.1 % Tween 20 have the capacity to regenerate the PMO+ME-MION after several reuses. More investigation is being conducted to fully understand the mechanism of cleaning to improve the efficiency of the system. One advantage of this technique is the reduction in cost of materials and treatment process.

Conclusions

The prepared magnetic nanoparticles size, morphology, structure, and magnetic properties were characterized by TEM, XRD, and SQUID. The development of protein-functionalized magnetic nanoparticles from microemulsion-prepared nanoparticles (ME-MION) and PMO protein have demonstrated creditable potential in the treatment of high and low turbid surface water samples irrespective of the season or source of water. The present investigation underscores the advantages of water treatment approach that encompasses magnetic nanoparticles with natural coagulant, which offers a novel water treatment approach; since the usage of chemical will be reduced by more than 60 % during the water treatment process. The treatment of surface waters with PMO+ME-MION showed better turbidity removal efficiency when compared to either alum or PMO. In contrast to alum and PMO, reduction in water turbidity is not affected by the initial turbidity of the water sample. The PMO+ME-MION could effectively remove more than 90 % of turbidity in surface waters under the influence of an external magnetic field within 12 min. The combination of PMO+ME-MION and magnetic field enhanced the effectiveness of the system in coagulating/flocculating impurities in different turbid water samples. Present investigation also suggests the possibility of regenerating PMO+ME-MION in more than three consecutive steps after turbidity removal assay.

The PMO+ME-MION developed in the work will be the first report, to our knowledge, that could potentially offer a cost-effective, robust, and environmentally friendly water treatment process.

Acknowledgments The authors are grateful for the financial support provided by the Swedish research funding agency, Formas.

References

Cloete TE (2010) Nanotechnology in water treatment applications. Caister Academic, Norfolk

Coetser SE, Heath RGM, Ndombe N (2007) Diffuse pollution associated with the mining sectors in South Africa: a first-order assessment. Water Sci Technol 55(3):9–16. doi:10.2166/Wst.2007.066

Deng YH, Wang CC, Hu JH, Yang WL, Fu SK (2005) Investigation of formation of silica-coated magnetite nanoparticles via sol-gel approach. Colloid Surface A 262(1–3):87–93. doi:10.1016/j.colsurfa.2005.04.009

Faraji M, Yamini Y, Rezaee M (2010) Magnetic nanoparticles: synthesis, stabilization, functionalization, characterization, and applications. J Iran Chem Soc 7(1):1–37

Ghebremichael KA, Gunaratna KR, Henriksson H, Brumer H, Dalhammar G (2005) A simple purification and activity assay of the coagulant protein from *Moringa oleifera* seed. Water Res 39(11):2338–2344. doi:10.1016/j.watres.2005.04.012

Grecu VV, Constantinescu S, Grecu MN, Olar R, Badea M, Turcu R (2008) Magnetic characterization of some nanometric iron oxides. Hyperfine Interact 183(1–3):205–214. doi:10.1007/s10751-008-9753-2

Lee EJ, Schwab KJ (2005) Deficiencies in drinking water distribution systems in developing countries. J water health 3(2):109–127

Li QL, Mahendra S, Lyon DY, Brunet L, Liga MV, Li D, Alvarez PJJ (2008) Antimicrobial nanomaterials for water disinfection and microbial control: potential applications and implications. Water Res 42(18):4591–4602. doi:10.1016/j.watres.2008.08.015

Liao MH, Chen DH (2002) Characteristics of magnetic nanoparticles-bound YADH in water/AOT/isooctane microemulsions. J Mol Catal B 18(1–3):81–87

Liu JF, Zhao ZS, Jiang GB (2008) Coating Fe3O4 magnetic nanoparticles with humic acid for high efficient removal of heavy metals in water. Environ Sci Technol 42(18):6949–6954. doi:10.1021/Es800924c

Lu AH, Salabas EL, Schuth F (2007) Magnetic nanoparticles: synthesis, protection, functionalization, and application.

Angew Chem Int Ed 46(8):1222–1244. doi:10.1002/anie.200602866

Mikhaylova M, Kim DK, Bobrysheva N, Osmolowsky M, Semenov V, Tsakalakos T, Muhammed M (2004) Superparamagnetism of magnetite nanoparticles: dependence on surface modification. Langmuir 20(6):2472–2477. doi:10.1021/La035648e

Moe CL, Rheingans RD (2006) Global challenges in water, sanitation and health. J water health 4(Suppl 1):41–57

Okoli C, Boutonnet M, Mariey L, Jaras S, Rajarao G (2011a) Application of magnetic iron oxide nanoparticles prepared from microemulsions for protein purification. J Chem Technol Biot 86(11):1386–1393. doi:10.1002/Jctb.2704

Okoli C, Fornara A, Qin J, Toprak MS, Dalhammar G, Muhammed M, Rajarao GK (2011b) Characterization of superparamagnetic iron oxide nanoparticles and its application in protein purification. J Nanosci Nanotechnol 11(11):10201–10206. doi:10.1166/jnn.2011.5007

Sanchez-Martin J, Ghebremichael K, Beltran-Heredia J (2010) Comparison of single-step and two-step purified coagulants from Moringa oleifera seed for turbidity and DOC removal. Bioresour Technol 101(15):6259–6261. doi:10.1016/j.biortech.2010.02.072

Theron J, Walker JA, Cloete TE (2008) Nanotechnology and water treatment: applications and emerging opportunities. Crit Rev Microbiol 34(1):43–69. doi:10.1080/10408410701710442

Vorosmarty CJ, Green P, Salisbury J, Lammers RB (2000) Global water resources: vulnerability from climate change and population growth. Science 289(5477):284–288

DOI 10.1007/978-3-319-05041-6_11
Reprinted from the *Journal of Nanoparticle Research*, DOI 10.1007/s11051-012-0828-2

RESEARCH PAPER

Fabrication of amine-functionalized magnetite nanoparticles for water treatment processes

Candace C. P. Chan · Hervé Gallard · Peter Majewski

Received: 25 August 2011 / Accepted: 13 March 2012 / Published online: 30 March 2012

Abstract Amine-functionalized magnetite nanoparticles are synthesized by a one pot water based process using *N*-[3-(trimethoxysilyl)propyl]diethylenetriamine (TRIS) as surfactant. The prepared functionalised nanoparticles are characterised by BET surface area measurements, X-ray diffraction, zeta potential measurement, and X-ray photoelectron spectrometry (XPS). The results clearly show the presence of TRIS on the surface of the nanoparticles. XPS analysis indicates the presence of very small amounts of maghemite on the surface of the magnetite nanoparticles. Water treatment test shows that the prepared nanoparticles are capable to remove natural organic matter (NOM) from natural water samples. The removal of NOM by the prepared particles is characterized by analysing the dissolved organic carbon (DOC) content and UV absorbance at 254 nm (UV_{254}) after the treatment of the water samples at various doses and treatment times.

Keywords Magnetite nanoparticles · X-ray photoelectron spectrometry · Amine functionalization · Water treatment · Sustainable development

Special Issue Editors: Mamadou Diallo, Neil Fromer, Myung S. Jhon

This article is part of the Topical Collection on Nanotechnology for Sustainable Development

C. C. P. Chan
Ian Wark Research Institute, University of South Australia, Mawson Lakes, Adelaide, SA 5095, Australia

H. Gallard
Laboratoire de Chimie et Microbiologie de l'Eau (LCME)—UMR CNRS 6008, Université de Poitiers, 40 Avenue du Recteur Pineau, 86022 Poitiers Cedex, France

P. Majewski (✉)
School of Advanced Manufacturing and Mechanical Engineering, Mawson Institute, University of South Australia, Mawson Lakes, Adelaide, SA 5095, Australia
e-mail: peter.majewski@unisa.edu.au

Introduction

In recent years, functionalised nanostructured materials are of great interest for researchers due to its unique electrical, structural, chemical, and magnetic properties allowing their use in a variety of novel applications, including electronic, optoelectronics, information storage, biosensing application, and biomedical engineering (Jordan et al. 1999; Todorovic et al. 1999; Rutnakornpituk et al. 2002; Goya et al. 2003; Lu et al. 2007; Majewski and Thierry 2007a, b, 2008; Thierry et al. 2009). Magnetite nanoparticles have attracted considerable attention because bulk Fe_3O_4 has a high Curie temperature (T_c—850 K) and nearly full spin polarization at room temperature, whereas magnetite nanoparticles show superparamagnetic properties (Goya et al. 2003) (Maity and Agrawal 2007).

Among different magnetic oxides, iron oxides nanoparticles, such as magnetite (Fe_3O_4) and

maghemite (γ–Fe_2O_3), have drawn most interest due to their magnetic, catalytic, conducting, and biological properties, which could find applications in many fields, including magnetic storage devices, ferrofluids, magnetic refrigeration systems, magnetic carriers for drug targeting, cancer diagnosis, separation of biochemical products, and catalysis (Tavakoli et al. 2007).

Research studies also show that magnetite nanoparticles are effective in arsenic removal, where Fe_3O_4 suspension was passed through a stainless-steel wool column that is equipped with a magnetic separator on the side wall (Mayo et al. 2007).

All of these applications demand nanomaterials of specific shapes, sizes, surface characteristics, and magnetic properties (Teja and Koh 2009). Magnetic nanoparticles have been synthesized with a number of different compositions and phases, including iron oxide, such as Fe_3O_4 (magnetite) and γ-Fe_2O_3 (maghemite), pure metals, such as Fe and Co, spine-type ferromagnets of $MgFe_2O_4$, $MnFe_2O_4$, and $CoFe_2O_4$, and alloys, such as $CoPt_3$ and FePt (Levent and George 2009). Several popular methods including co-precipitation, thermal decomposition and/or reduction, micelle synthesis, hydrothermal synthesis, and laser pyrolysis techniques can all be applied for the synthesis of high-quality magnetic nanoparticles of different functionality (Lu et al. 2007; Majewski and Thierry 2007a, b).

The most widely used synthesis route for iron oxide nanoparticles is based on precipitation from solutions (Majewski and Thierry 2007a, b). The method involves co-precipitation from iron (II) and iron (III) aqueous salt solution in a basic aqueous medium. The chemical reaction can be written as follows (Maity and Agrawal 2007):

$$Fe^{2+} + 2\ Fe^{3+} + 8OH^- \rightarrow Fe_3O_4 + 4\ H_2O \qquad (1)$$

With this classical co-precipitation method (Faraji et al. 2010), the size and size distribution of iron oxide nanoparticles in a homogeneous aqueous medium are hard to control due to the unlimited growth of the nanoparticles after their nucleation cannot be prevented (Tao et al. 2006). However, for applications in water treatment, the size of magnetite nanoparticles do not necessarily have to be particularly small, such as less than 10 nm, as bigger particles are much easier to collect with an applied magnetic field after the treatment.

The common problems that usually encountered from water sources are the aquatic organic materials. Natural organic matter (NOM) is the aquatic organic materials that stains water yellow to brownish as a result of intensive leaching of surrounding watersheds, the withering material from plants and animals in the terrestrial environment as well as in aquatic systems (Marhaba and Van 2000).

NOM represent a major problem in water treatment due to its role as a precursor to the formation of toxic disinfection by-products (DBP), such as trihalomethanes, haloacetic, and other halogenated organics (Collins et al. 1985). Not only forming DBPs, it also acted as a carbon food source for bacterial growth in distribution systems (Wang et al. 2000; Chow et al. 2008). Previous studies have shown that NOM can be removed from water by the traditional clarification treatment processes, such as coagulation, flocculation, and sand filtration (Clever et al. 2000; Zularisam et al. 2006; Pelekani et al. 1999; Tambo and Kamei 1998).

Studies have also shown that NOM, *Escherichia coli* (*E. coli*) bacteria, and MS2 bacteriophage virus (MS2) can be removed by amine-functionalised silica powder or quartz sand having particles sizes between 1 and 500 microns (Majewski 2007). Other organic species such as albumin and the protozoan parasite *Cryptosporidium parvuum* (*C. parvuum*) can be removed by the same category of amine-functionalised silica powder (Majewski and Chan 2008). However, depending on particles size, the removal of silica powder after water treatment requires different filter systems and related maintenance of the filters. Furthermore, as the removal of organic matter only occurs on the surface of the particles, the efficiency of functionalised silica with large particles sizes (e.g., quartz sand) is significantly reduced that requires the need of large doses. The application of very fine particles and nanoparticles may significantly reduce the required dose as they provide much larger surface area per volume. However, the removal of functionalized silica nanoparticles from water would require sophisticated and expensive filter systems, such as nanofiltration, which would render the use of functionalized silica as unnecessary, as nanofiltration alone is capable to remove a large range of organic contaminants from water. The use of magnetic nanoparticles, such as magnetite, however, would only require magnetic fields for their removal which may be an economically more feasible alternative (Zhang et al. 2007).

In this study, amine-functionalised magnetite nanoparticles are prepared through co-precipitation of iron

(II) and iron (III) salt in the presence of ammonium solution and subsequent functionalization with *N*-[3-(trimethoxysilyl)propyl]diethylenetriamine, ($C_{10}H_{27}N_3O_3Si$, TRIS in short), without the use of any organic solvents. TRIS functionalization was used, as it has already shown its potential to remove organic matter from water when attached to silica particles (Chan et al. 2011).

Dissolved organic carbon (DOC) measurement and high-performance size exclusion chromatography (HPSEC) with UV detection (HPSEC/UV) were also performed to demonstrate potential applications of the material for the removal of NOM in natural water resources.

Experimental section

Sample preparation

Analytical grade of ferrous chloride tetrahydrate ($FeCl_2{\cdot}4H_2O$ >99 % purity), ferric chloride hexahydrate ($FeCl_3{\cdot}6H_2O$ >99 % purity), and ammonium hydroxide (NH_4OH, 30 % of ammonia) were obtained from Aldrich. All aqueous solutions were prepared with ultra-pure Milli Q (MQ) grade water (18.2 MΩ cm). The surface functionalization of the particles was performed by using *N*-[3-(trimethoxysilyl)propyl]diethylenetriamine, $(CH_3O)_3Si(CH_2)_3NHCH_2CH_2NHCH_2CH_2NH_2$), TRIS, 97 % purity, Novachem (Fig. 1). All chemicals were used as received. A stock solution with a Fe^{3+}:Fe^{2+} ratio of 1.82:1 was prepared and used for the synthesis of magnetite nanoparticles. A volume of 0.106 M $FeCl_3 \times 6H_2O$ and 0.058 M $FeCl_2 \times 4H_2O$ were dissolved in 50 mL of pure water each of which was deoxygenated by bubbling N_2 gas in the water for 1 h prior to the use. The iron chloride solutions were then separately heated up to 70 °C for 1 h and subsequently mixed while using a mechanical stirrer.

Under vigorous and continuous stirring, 50 mL of NH_4OH (30 %) solution was added as a precipitant agent. Subsequently after adding NH_4OH solution, the color of the mixture turned from yellow to black that indicates the formation of magnetite. To remove excess iron salt and NH_4OH solution and to resuspend the particles in neutral water, the prepared magnetite particles were collected at the bottom of the beaker by a permanent magnet and the solution was decanted.

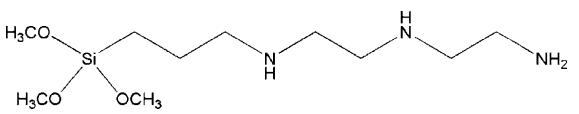

Fig. 1 The molecule *N*-[3-trimethoxysilyl)propyl]diethylenetriamine, ($C_{10}H_{27}N_3O_3Si$, TRISt)

The deposition of the TRIS on the magnetite nanoparticles can be easily performed by adding TRIS surfactant to the nanoparticle suspension with rapid stirring for 1 h. Samples with two TRIS concentrations were prepared by adding 50-μL (0.194 $mmol_{TRIS}/mol_{Fe}$) and 710-μL TRIS (2.75 $mmol_{TRIS}/mol_{Fe}$), respectively to the nanoparticles suspension after the formation of the magnetite nanoparticles.

Finally, the functionalised powder was isolated by again applying an external magnetic field and the supernatant was removed from the precipitate by decantation. The particles were then dried at 45 °C for 24 h.

Structural morphology and information

Transmission electron microscopy (TEM) and X-ray diffraction (XRD)

All the characterization of the sample was done in solid phase. The size and surface morphology of the magnetite nanoparticles were determined by using TEM. TEM images were acquired using a Philips CM200 operating at 200 kV. For sample preparation, the prepared TRIS-coated magnetite nanoparticles were diluted, subsequently dropped onto the copper grid surface, and dried for 1 h. Powder X-ray diffraction (XRD) pattern was collected using a Phillips PW1730 X-ray generator fitted with a Sietronics SIE112 automation system, with Co-Kα radiation ($\lambda = 1.7902$ Å) between a 2θ range from 6 to 90° in 0.02° steps at 0.1° per minute.

Zeta potential measurement

The zeta potential of pure and TRIS-coated magnetite nanoparticles was measured with Zetasizer Nano ZS instrument (Malvern). Measurements were made at different pH ranging from pH 1.80 to 12.00. The pH of the solution was adjusted using nitric acid and potassium hydroxide with a range of concentration (10^{-1} to 10^{-3} M). The ionic concentration was kept at

10^{-2} M KNO_3 as a background electrolyte. Average values from three measurements were used as a representative value.

X-ray photoelectron spectroscopy analysis (XPS)

X-ray photoelectron spectrometry of pure and TRIS-coated magnetite nanoparticles was performed on an AXIS Ultra spectrometer (Kratos Analytical Ltd.) equipped with a monochromatised Al Kα source with energy 1486.6 eV. The pressure in the analysis chamber was typically 5×10^{-9} mbar. The measurements were based on photoelectrons with a takeoff angle of 90 ^{o} to the detector. The elemental composition was obtained from survey spectra with pass energy of 160 eV while high-resolution spectra were collected with a pass energy of 20 eV. All binding energies were referenced to the C 1s neutral carbon peak at 284.9 eV. The intensities were calculated from the peak areas by the fitting program based on CasaXPS software.

Jar test apparatus and analytical methods for water treatment

Raw surface water was collected from Pinail Reservoir water, Poitiers, France. The experiments were carried out using a laboratory flocculator (Bioblock Fisher Scientific 11198 flocculator) equipped with 1-Liter beakers. Jar test is a classical method of simulating a full-scale water treatment process, providing a reasonable idea of the way a treatment chemical will behave and operate with various types of raw water and thus evaluate the performance of treatment process (Wang et al. 2002; Humbert et al. 2005; Qin et al. 2006; Yan et al. 2009).

A series of experiment was conducted using TRIS-coated magnetite nanoparticles for Pinail pond water. The experiment was carried out focusing on kinetic test and dosage test. The experiment was set to cover various collection points for kinetic test at a dose of 0.8 g of TRIS-coated magnetite nanoparticles in 1 L of Pinail surface water. The dosage concentration was then set at 0, 0.2, 0.6, 0.8, and 1.6 g of dry functionalised magnetite nanoparticles in 1 L for a contact time of 5 min. The samples were contained in a beaker where the stirring speed was set at 200 rpm. Aliquots of the samples were taken with a 50-mL syringe, filtered with 0.45-μm filter membrane and analysed. Treated water samples were analysed by means of its DOC content, UV_{254}, and HPSEC/UV.

The DOC content was analysed using a Shidmadzu TOC Vcsh analyzer, and UV absorbance at 254 nm was measured with a UV–VIS spectrophotometer SAFAS DES (Double Energy System) 190 with a 1-cm quartz cell.

HPSEC was performed on a REPROSIL 200 SEC 5 μm 300 × 8 mm column coupled with a UV–Visible detector (WATERS 996, $\lambda = 254$ nm), flow rate at 1.0 mL/min, mobile phase at 10-mM acetate pH 7.0. Solutions of PSS (polystyrene sulfonate with molecular weight of 13,000, 6,800, 4,300, and 1,400 Da) were used as calibration standards. A linear equation of log (MW) $= -0.5092 \times$ RT $+ 7.75$ with $R^2 > 0.99$, was obtained based on HPSEC calibration, where MW = Daltons and RT = retention time in min. In HPSEC analysis, organic molecules are separated primarily on the basis of differing molecular size so that largest molecules are eluted first in the column, whereas the smallest molecules are eluted last. This method has been proven and reported by previous studies to be an effective technique in evaluating various water treatment processes by comparing NOM profile before and after treatment (Pelekani et al. 1999; Drikas et al. 2003; Chow et al. 2008).

Results and discussions

TEM and XRD

The BET measurements of the prepared magnetite nanoparticles show that the particles have a surface area of 154 m^2/g. Figure 2 displays an XRD pattern of TRIS-coated Fe_3O_4 nanoparticles with a concentration of 2.75 mmol (710 μL of TRIS). The diffraction peak at the 2θ values of 30.0^{o}, 35.4^{o}, 43.1^{o}, 57.0^{o}, and 62.6^{o} can be attributed to (220), (331), (400), (511), and (440) crystal planes of cubic magnetite, respectively. However, diffraction analysis alone cannot distinguish between the cubic magnetite and maghemite, because of the similarity in structure and lattice parameters (Martínez Mera et al. 2007; Shi et al. 2010).

Therefore, XPS analysis was performed to identify Fe_3O_4 and γ-Fe_2O_3, as the components have characteristic iron $Fe2p_{3/2}$ and $Fe2p_{1/2}$ and oxygen O1s peaks (Zhang et al. 2004; Pana et al. 2005; Yamashita and Hayes 2008). Figure 3 shows the spectrum of the

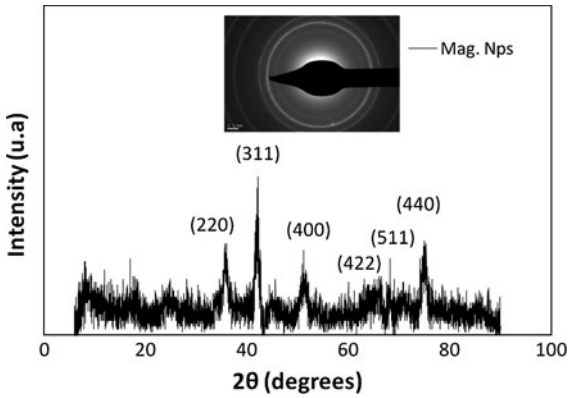

Fig. 2 XRD patterns of magnetite nanoparticles corresponding to sample with 2.75 mmol of TRIS-coated nanoparticles. Peak identification points to a chemical composition containing maghemite/magnetite iron oxide phases

prepared magnetite nanoparticles coated with a TRIS concentration of 2.75 $mmol_{TRIS}/mol_{Fe}$. Besides peaks for iron and oxygen, additional peaks for carbon and nitrogen can be identified. As carbon and nitrogen are essential components of TRIS, carbon and nitrogen on the surface of the particles is an evidence for the presence of TRIS coating of the particles.

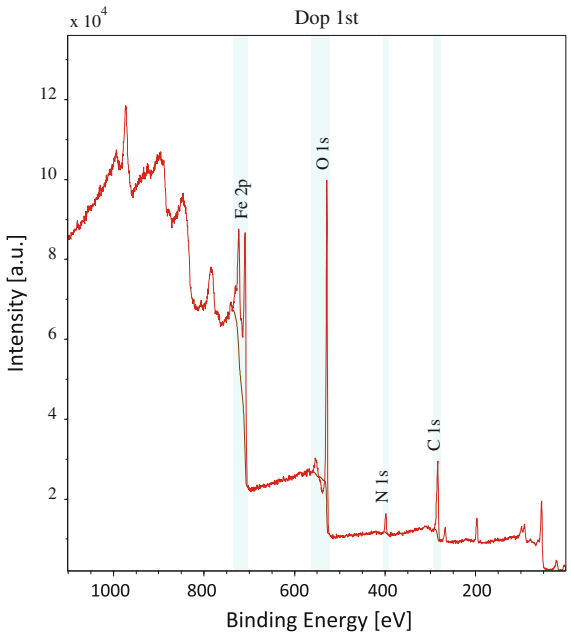

Fig. 3 XPS spectrum of TRIS-coated magnetite nanoparticles (TRIS concentration: 2.75 $mmol_{TRIS}/mol_{Fe}$)

XPS

In Table 1, the concentration of the analysed elements is listed. As expected from TRIS structure, the nitrogen content on the surface of the particles increases with increasing TRIS concentration. Considering that all analysed nitrogen belongs to amine of TRIS, a concentration of about 0.42 mmol TRIS per gram magnetite at a TRIS concentrations of 2.75 $mmol_{TRIS}/mol_{Fe}$ during synthesis of TRIS-coated magnetite nanoparticles can be calculated from the analysis listed in Table 1. This concentration is slightly less than of the value calculated for TRIS-coated silica (Chan et al. 2011). However, it is impossible to assess whether saturation of TRIS on the surface of the nanoparticles has been achieved at this TRIS concentration, as titration could not be applied. The carbon concentration on the surface of all samples is slightly higher than expected only from TRIS coating and, therefore, is believed to consist of the carbon component of TRIS as well as residues from the synthesis process or contamination from handling.

Figure 4 shows the high-resolution XPS pattern for the $Fe2p_{3/2}$ and $Fe2p_{1/2}$ peaks that have binding energies at 710.1 and 723.7 eV, respectively. These binding energies correlate with binding energies for $Fe2p_{3/2}$ and $Fe2p_{1/2}$ of magnetite as reported in the literature (Zhang et al. 2004; Pana et al. 2005; Yamashita and Hayes 2008). $Fe2p_{3/2}$ and $Fe2p_{1/2}$ binding energies of γ-Fe_2O_3 usually have higher binding energies of about 711 and 725 eV, respectively (Tahir et al. 2009). However, the spectrum also shows small satellite peaks at about 719 and 732 eV in the vicinity of the $Fe2p_{3/2}$ and $Fe2p_{1/2}$ peaks that are known to indicate γ-Fe_2O_3 (Tahir et al. 2009).

The high-resolution oxygen O1s spectrum of the sample is shown in Fig. 5. The O1s peak can be divided into three sub-peaks at 529.4, 530.4, and 532.5 eV. The two strongest peaks at binding energies of 529.4 and 530.4 eV clearly belong to magnetite (Wagner et al. 2003). However, the peak at the binding

Table 1 Surface analysis of pure and TRIS-coated magnetite nanoparticles (values in at%)

	Fe	O	N	C
Pure	36.0	52.0	–	12.0
50-μL TRIS	34.9	51.1	1.49	12.5
710-μL TRIS	32.5	51.4	3.56	12.6

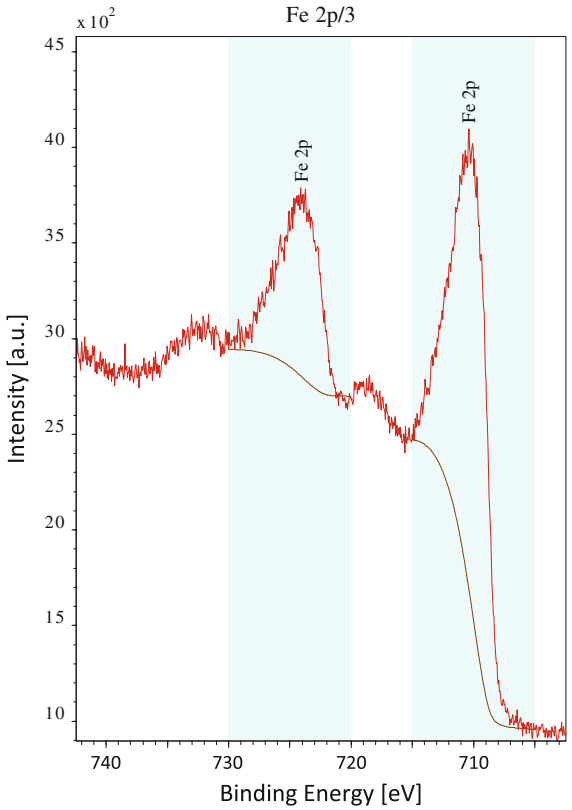

Fig. 4 High-resolution XPS spectrum of iron $Fe2p_{1/2}$ (*right*) and $Fe2p_{3/2}$ (*left*) peaks of TRIS-coated magnetite nanoparticles (TRIS concentration: 2.75 $mmol_{TRIS}/mol_{Fe}$)

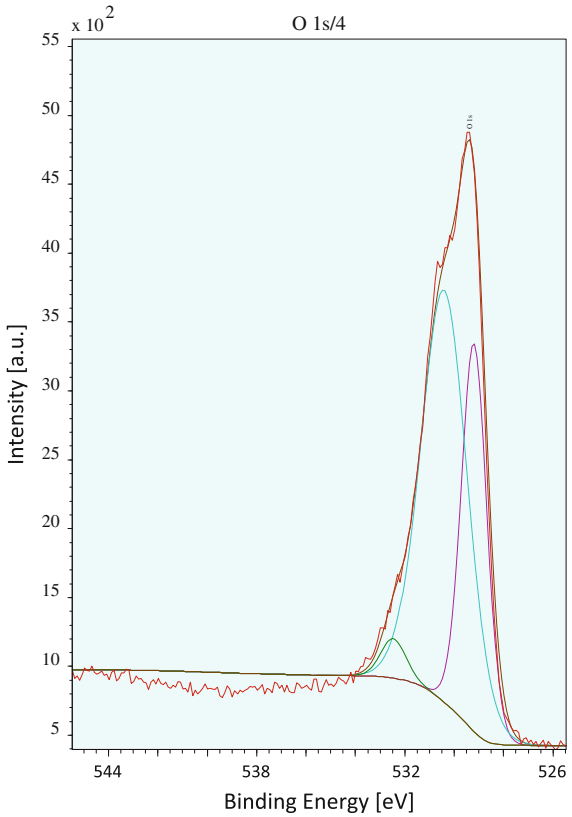

Fig. 5 High-resolution XPS spectrum of the oxygen O1s peak of TRIS-coated magnetite nanoparticles (TRIS concentration: 2.75 $mmol_{TRIS}/mol_{Fe}$)

energy of 529.4 eV may also belong to Fe_2O_3 (Wagner et al. 2003). The smaller peak at binding energies of 529.2 eV, however, cannot be attributed to any iron oxide and belongs to SiO_x which is believed to be caused by the binding of TRIS to the particles via Si–O–Fe bonds providing another evidence for the presence of TRIS on the surface of the particles (Wagner et al. 2003).

The C1s peak of the sample is shown in Fig. 6. Also the C1s peak can be divided into three sub-peaks at binding energies of 284.6 eV indicating C=C bonds, 286.3 eV indicating C–OH bonds, and 287.7 eV indicating C=O bonds. The observation of C=C bonds is another evidence of the presence of TRIS as C=C bonds are a main component of the molecule, whereas C–OH and C=O bonds cannot be attributed to TRIS and may be due to local oxidation of the TRIS molecule or contaminants from handling of the powder.

Overall, the XPS study of the sample give clear evidence that the sample mainly consists of magnetite that is coated with TRIS. However, the presence of small amounts of γ-Fe_2O_3, either as individual particles or on the surface of magnetite particles due to local oxidation of the magnetite particle, cannot fully be excluded.

CTEM analysis of sample with TRIS-coated is shown in Fig. 7a and b. The Fe_3O_4 nanoparticles have an unevenly sizes containing semispherical shape with average sizes of about 20–100 nm.

The zeta potentials of uncoated magnetite nanoparticles and TRIS-coated as a function of pH values are shown in Fig. 8. The pure magnetite nanoparticles have an isoelectric point (iep) of 8.0 with a value of about −17 mV at pH 9, which is consistent with published values for bare magnetite nanoparticles (Zhang and Bai 2002; Majewski 2007). In contrast, the zeta potential for the TRIS-coated magnetite nanoparticles

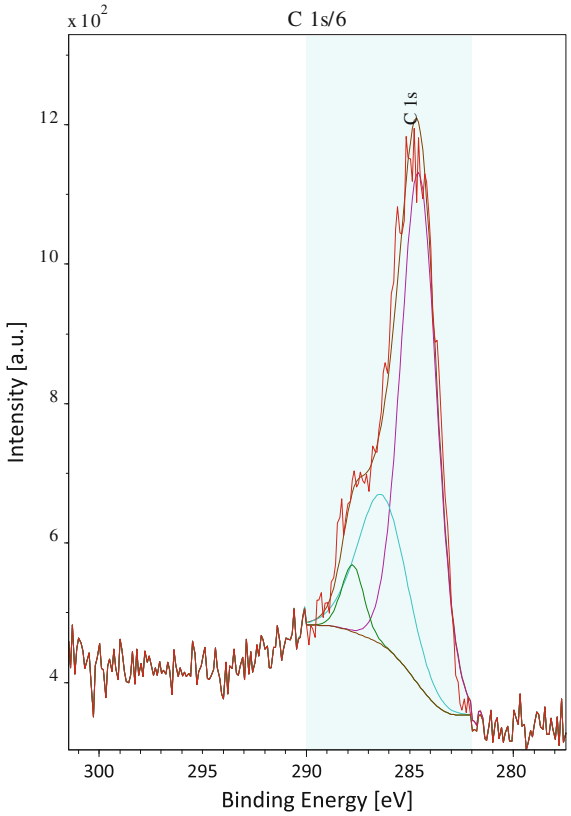

Fig. 6 High-resolution XPS spectrum of the carbon C1s peak of TRIS-coated magnetite nanoparticles (TRIS concentration: 710 μL)

(TRIS concentration 2.75 $mmol_{TRIS}/mol_{Fe}$) has an iep of 10.20 with a surface charge of +16.5 mV at pH 9. The reason for this difference in surface charge at the pH value of 9 is believed to be due to the presence of amine functional groups of the TRIS coating. The chemistry of the amine is dominated by the ability of the lone pair on the nitrogen atom to capture protons forming NH_3^+ groups. This phenomenon is the reason for the positive charge of the particles coated with NH_2-SAM at pH values less than about 10. Contrary to that, at pH values greater than about 10, the hydrogen of the amines is sufficiently acidic to undergo deprotonation forming negatively charged NH-groups, which is the reason for the negative surface charge of the NH_2-SAM-coated particles at pH values greater than about 10.

Detailed magnetic characterization of the prepared nanoparticles was not performed, so it cannot be claimed that the prepared nanoparticles are superparamagnetic. However, simple tests using a 0.2 T permanent magnet show that the prepared nanoparticles are magnetic and can be removed from water by applying a magnetic field (Fig. 9).

NOM removal: DOC and UV_{254} analyses on dosage test

Figure 10a and b shows the kinetic test and dosage test of DOC and UV absorbance at 254 nm by TRIS-coated magnetite nanoparticles. The DOC content and UV_{254} absorbance of the water sample rapidly decreases with increasing contact time, especially during the first 5 to 10 min, and then remain almost constant for 50 min. The reason for this is presumably a very fast uptake of organic matter by the TRIS-coated nanoparticles and saturation of the removal capacity of the particles as it was also observed for the TRIS-coated silica particles.

Dosage tests from 0 to 0.8 g/L show that removal of NOM increases with increasing concentration of TRIS-coated magnetic nanoparticles, which indicates that removal is limited by adsorption capacity of particles. For a dosage of 0.8 g/L, about 20 % of the DOC content and 36 % of the UV_{254} absorbance were removed after 5 min of contact time, as shown in Fig. 10b. The removal of UV-absorbing components in the water samples is more pronounced than the removal of DOC that indicates the preferential sorption of aromatic category molecules by TRIS-coated iron oxide.

High-performance size exclusion chromatography with UV profile

HPSEC has been widely used to determine the molecular weight (MW) distribution of aquatic humic substances. HPSEC separates the constituents based on differential permeation process, according to the sizes of the organic substances (Anu et al. 2002). Figures 11 and 12 compare the HPSEC/UV chomatograms of Pinail water before and after treatment with three different doses of TRIS-coated magnetite nanoparticles and contact time, respectively. HPSEC/UV chromatograms confirm that UV-absorbing organic molecules are progressively adsorbed when dosage increases from 0 to 1.6 g/L (Fig. 11). HPSEC/UV chromatograms in Fig. 12 also confirm that adsorption is fast and occurs within the first 5 min of contact time.

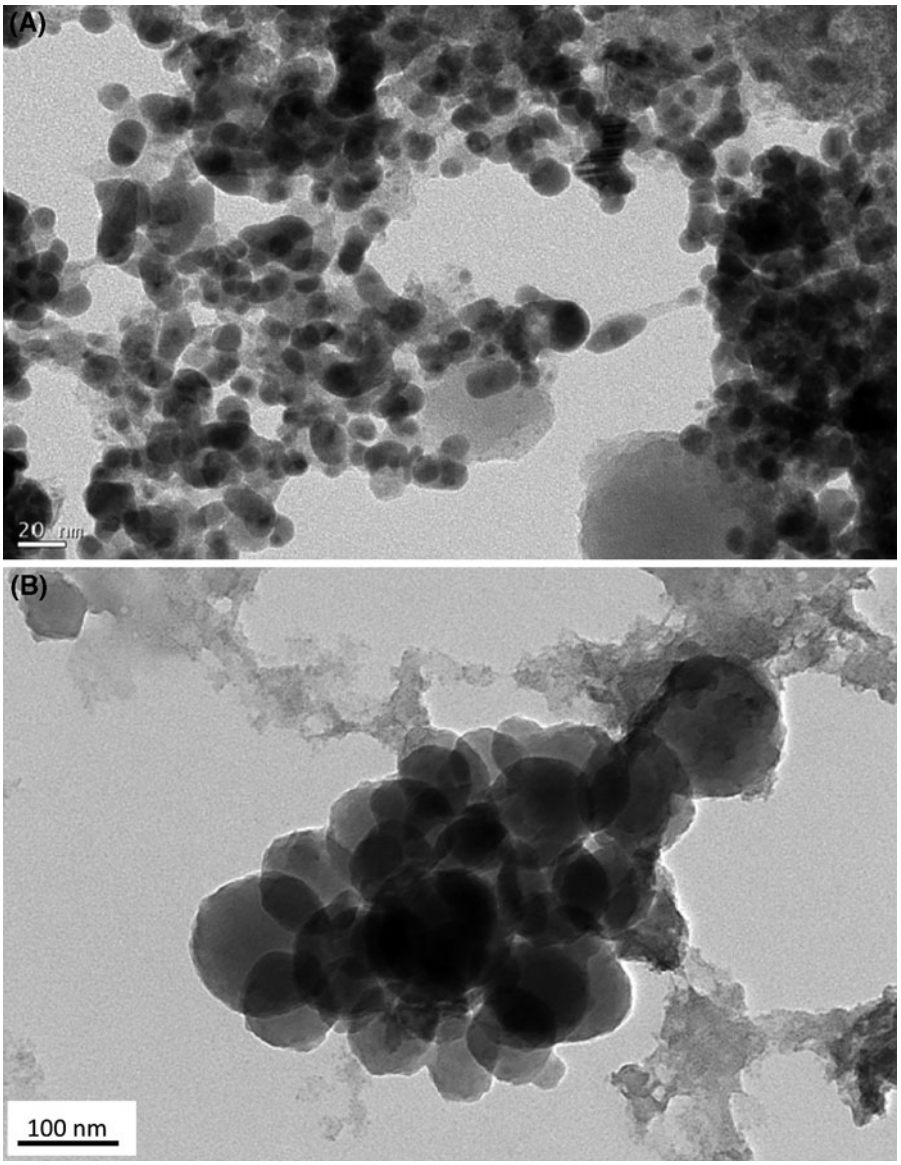

Fig. 7 **a** CTEM image of magnetite nanoparticles prepared as described in this study. **b** CTEM image of magnetite nanoparticles prepared as described in this study

Both dosage and kinetic tests show that colloidal material with MW >5 kDa and low molecular weight organic molecules (i.e., <200 Da) are less removed than molecules with mean MW of 1,000 Da and usually associated to humic-like molecules.

Conclusions

The study has shown that functionalised magnetite nanoparticles can be prepared using silane-based surfactants in aqueous solutions similar to our synthesis route for functionalised silica. It can, therefore, be expected that the reaction between the TRIS molecule and the surface of magnetite nanoparticles follows the same route like that with silica where the hydrolysed bonding group of TRIS reacts with hydroxyl groups on the surface of magnetite particles forming covalent $Fe_{magnetite}$–O–Si_{silane} bonds as observed via XPS analysis of the samples. The achieved TRIS concentration on the surface of the magnetite nanoparticles of 0.85 mmol per gram

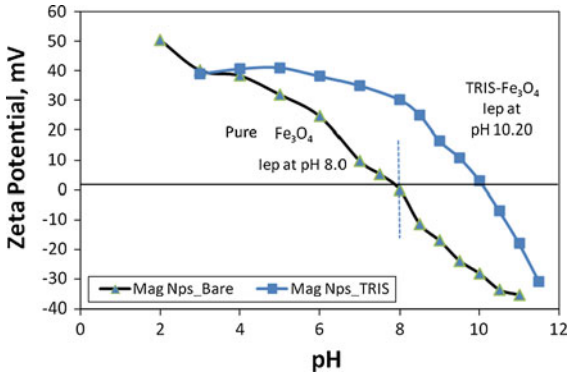

Fig. 8 Zeta potential of pure and TRIS-coated magnetite nanoparticles (710-µL TRIS concentration), background electrolyte 10^{-2} M KNO_3

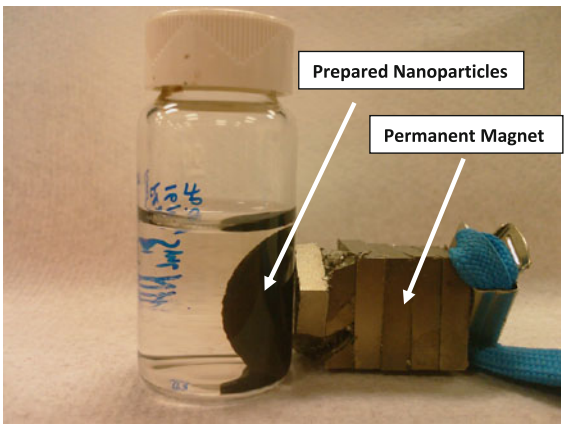

Fig. 9 Response of TRIS-coated magnetite nanoparticles (710-µL TRIS concentration) to a 0.2 T strong permanent magnet

magnetite is equivalent to results achieved for silica (Chan et al. 2011).

As an example for the application of silane-functionalised magnetite nanoparticles, water treatment tests were performed. The tests show that organic contaminants can be removed from water by TRIS-coated magnetite particles. This is to be expected as the capability of TRIS to remove organic matter from water has been studied with silica particles. The removal capacity of the prepared functionalised magnetite nanoparticles is slightly greater than 2 mg of DOC per gram of magnetite nanoparticles that correlates with the results obtained with TRIS functionalised silica (Chan et al. 2011).

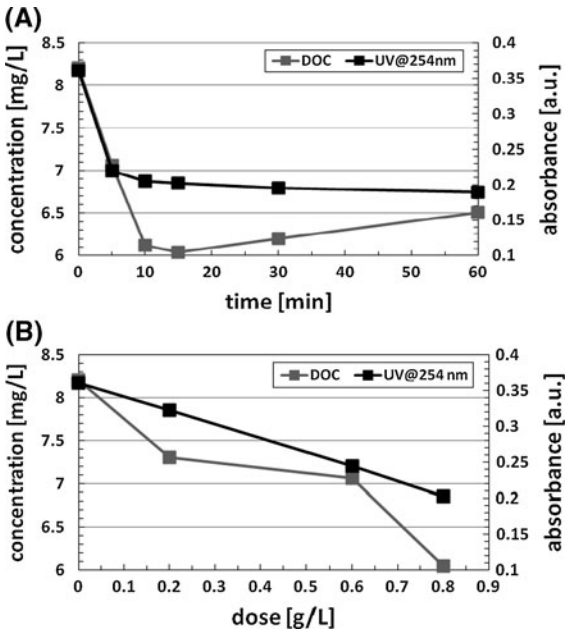

Fig. 10 **a** Kinetic test at 0.8 g/L of magnetite nanoparticles and **b** dosage test at 5-min contact time of DOC and UV absorbance at 254 nm by TRIS-coated magnetite nanoparticles (TRIS concentration 2.75 $mmol_{TRIS}/mol_{Fe}$)

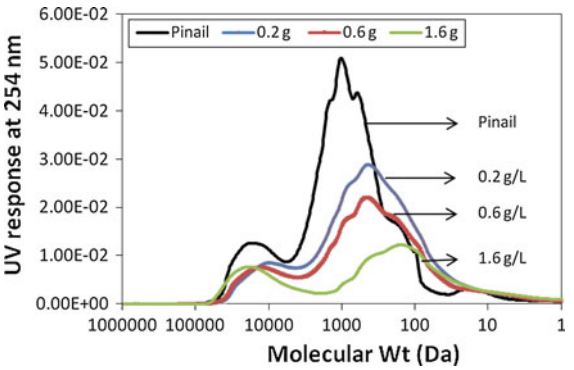

Fig. 11 HPSEC/UV dosage chromatograms of Pinail raw water by TRIS-coated magnetite nanoparticles (TRIS dose: 0.2 g/L, 0.6 g/L, and 1.6 g/L, respectively; contact time: 15 min; TRIS concentration 2.75 $mmol_{TRIS}/mol_{Fe}$)

The observation that magnetite nanoparticles can be functionalised by silane-based surfactants is of significance, as a wide range of silanes with a multitude of functional groups are commercially available. This allows preparing magnetite nanoparticles with a wide range of functionalities to address requirements for various applications, such as in water treatment.

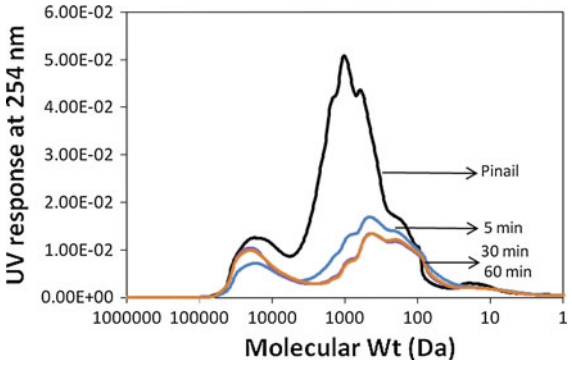

Fig. 12 HPSEC/UV kinetic chromatograms of Pinail raw water and treated water by TRIS-coated magnetite nanoparticles at fixed dose, 1 g/L and at various contact time: 5, 30, and 60 min, respectively. TRIS concentration 2.75 $mmol_{TRIS}/mol_{Fe}$

Acknowledgments The author would like to thank United Water International (UWI), Adelaide, Australia. This research is proudly supported by United Water as a part of its commitment to innovation and responsible water management. Author also would like to acknowledge Australian Research Council Nanotechnology Network (ARCNN) for granted an Overseas Travel Fellowships in research activities carried out in University of Poitiers, France.

References

Anu M, Niina L, Susanna K, Tuula T (2002) Removal of NOM in the different stages of the water treatment process. Environ Int 28(6):457–465

Chan CP, Choudhury N, Majewski P (2011) Fabrication of self-assembled monolayers of *N*-[3-(trimethoxysilyl)propyl]diethylenetriamine on silica particles. Colloids Surf A 257:2576–2580

Chow CWK, Fabris R, Leeuwen Jv, Wang D, Drikas M (2008) Assessing natural organic matter treatability using high performance size exclusion chromatography. Environ Sci Technol 42(17):6683–6689

Clever M, Jordt F, Knauf R, Rabiger N, Rudebusch M, Hilker-Scheibel R (2000) Process water production from river water by ultrafiltration and reverse osmosis. Desalination 131(1–3):325–336

Collins MR, Amy GL, King PH (1985) Removal of organic matter in water treatment. J Environ Eng 111(6):850–864

Drikas M, Chow CWK, Cook D (2003) The impact of recalcitrant organic character on disinfection stability, trihalomethane formation and bacterial regrowth: an evaluation of magnetic ion exchange resin (MIEX®) and alum coagulation. J Water supply Res T 52(7):475–487

Faraji M, Yamini Y, Rezaee M (2010) Magnetic nanoparticles: synthesis, stabilization, functionalization, characterization, and applications. J Iran Chem Soc 7(1):1–37

Goya GF, Berquó TS, Fonseca FC, Morales MP (2003) Static and dynamic magnetic properties of spherical magnetite nanoparticles. J Appl Phys 94(5):3520

Humbert H, Gallard H, Suty H, Croué J-P (2005) Performance of selected anion exchange resins for the treatment of a high DOC content surface water. Water Res 39(9):1699–1708

Jordan A, Scholz R, Wust P, Schirra H, Thomas S, Schmidt H, Felix R (1999) Endocytosis of dextran and silan-coated magnetite nanoparticles and the effect of intracellular hyperthermia on human mammary carcinoma cells in vitro. J Magn Magn Mater 194(1–3):185–196

Levent C, George CH (2009) Chemically synthesized FePt nanoparticles with controlled particle size, shape and composition. Nanotechnology 20(48):485602

Lu AH, Salabas E, Schüth F (2007) Magnetic nanoparticles: synthesis, protection, functionalization, and application. Angew Chem Int Ed 46(8):1222–1244

Maity D, Agrawal DC (2007) Synthesis of iron oxide nanoparticles under oxidizing environment and their stabilization in aqueous and non-aqueous media. J Magn Magn Mater 308(1):46–55

Majewski PJ (2007) Removal of organic matter in water by functionalised self-assembled monolayers on silica. Sep Purif Technol 57(2):283–288

Majewski PJ, Chan CP (2008) Removal of *Cryptosporidium parvum* by silica coated with self-assembled monolayers. J Nanosci Nanotechnol 8(11):1–4

Majewski P, Thierry B (2007a) Functionalized magnetite nanoparticles: synthesis, properties, and bio-applications. Crit Rev Solid State Mater Sci 32(3):203–215

Majewski P, Thierry B (2007b) Functionalized magnetite nanoparticles: synthesis, properties, and bio-applications. Crit Rev Solid State Mater Sci 32:203–215

Majewski P, Thierry B (2008) Superparamagnetic magnetite (Fe_3O_4) nanoparticles for bio-applications. Recent Pat Mater Sci 1:116–127

Marhaba TF, Van D (2000) The variation of mass and disinfection by-product formation potential of dissolved organic matter fractions along a conventional surface water treatment plant. J Hazard Mater 74(3):133–147

Martínez Mera I, Espinosa Pesqueira ME, Pérez Hernández R, Arenas Alatorre J (2007) Synthesis of magnetite (Fe_3O_4) nanoparticles without surfactants at room temperature. Mater Lett 61(23–24):4447–4451

Mayo JT, Yavuz C, Yean S, Cong L, Shipley H, Yu W, Falkner J, Kan A, Tomson M, Colvin VL (2007) The effect of nanocrystalline magnetite size on arsenic removal. Sci Technol Adv Mater 8(1–2):71–75

Pana L, Zhanga G, Fana C, Qiua H, Wua P, Wanga F, Zhang Y (2005) Fabrication and characterization of Fe_3O_4 thin films deposited by reactive magnetron sputtering. Thin Solid Films 473:63–67

Pelekani C, Newcombe G, Snoeyink VL, Hepplewhite C, Assemi S, Beckett R (1999) Characterization of natural organic matter using high performance size exclusion chromatography. Environ Sci Technol 33(16):2807–2813

Qin J–J, Oo MH, Kekre KA, Knops F, Miller P (2006) Impact of coagulation pH on enhanced removal of natural organic matter in treatment of reservoir water. Sep Purif Technol 49(3):295–298

Rutnakornpituk M, Thompson MS, Harris LA, Farmer KE, Esker AR, Riffle JS, Connolly J, St Pierre TG (2002) Formation of cobalt nanoparticle dispersions in the

presence of polysiloxane block copolymers. Polymer 43(8):2337–2348

Shi D, Cheng JP, Liu F, Zhang XB (2010) Controlling the size and size distribution of magnetite nanoparticles on carbon nanotubes. J Alloy Compd 502(2):365–370

Tahir AA, Wijayantha KGU, Saremi-Yarahmadi S, Mazhar M, McKee V (2009) Nanostructured r-Fe_2O_3 thin films for photoelectrochemical hydrogen generation. Chem Mater 21:3763–3772

Tambo N, Kamei T (1998) Coagulation and flocculation on water quality matrix. Wat Sci Tech 37(10):31–41

Tao K, Dou H, Sun K (2006) Facile interfacial coprecipitation to fabricate hydrophilic amine-capped magnetite nanoparticles. Chem Mater 18(22):5273–5278

Tavakoli A, Sohrabi M, Kargari A (2007) A review of methods for synthesis of nanostructured metals with emphasis on iron compounds. Chem Pap 61(3):151–170

Teja AS, Koh PY (2009) Synthesis, properties, and applications of magnetic iron oxide nanoparticles. Prog Cryst Growth Charact Mater 55(1–2):22–45

Thierry B, Brown M, Al-Ejeh F, Griesser H, Majewski P (2009) Immunotargeting of functional nanoparticles for MRI detection of apoptotic tumor cells. Adv Mater 21:541–545

Todorovic M, Schultz S, Wong J, Scherer A (1999) Writing and reading of single magnetic domain per bit perpendicular patterned media. Appl Phys Lett 74(17):2516–2518

Wang G-S, Hsieh S-T, Hong C-S (2000) Destruction of humic acid in water by UV light-catalyzed oxidation with hydrogen peroxide. Water Res 34(15):3882–3887

Wang G-S, Kang S-F, Yang H-J, Pai S-Y, Chen H-W (2002) Removal of dissolved natural organic matter from source water with alum coagulation. Environ Technol 23(12): 1415–1423

Wagner CD, Naumkin AV, Kraut-Vass A, Allison JW, Powell CJ, John R, Rumble J (2003) NIST X-ray photoelectron spectroscopy database. NIST standard reference database 20, version 3.5. National Institute of Standards and Technology, Gaitherburgh, USA

Yamashita T, Hayes P (2008) Analysis of XPS spectra of Fe^{2+} and Fe^{3+} ions in oxide materials. Appl Surf Sci 254:2441–2449

Yan M, Wang D, Ni J, Qu J, Ni W, Van Leeuwen J (2009) Natural organic matter (NOM) removal in a typical North-China water plant by enhanced coagulation: targets and techniques. Sep Purif Technol 68(3):320–327

Zhang X, Bai R (2002) Adsorption behavior of humic acid onto polypyrrole-coated nylon 6,6 granules. J Mater Chem 12(9):2733–2739

Zhang D, Liu Z, Han S, Li C, Lei B, Stewart MP, Tour JM, Zhou C (2004) Magnetite (Fe_3O_4) core–shell nanowires: synthesis and magnetoresistance. Nano Lett 4(11):2151–2155

Zhang JL, Srivastava RS, Misra RDK (2007) Core–shell magnetite nanoparticles surface encapsulated with smart stimuli-responsive polymer: synthesis, characterization, and LCST of viable drug-targeting delivery system. Langmuir 23(11):6342–6351

Zularisam AW, Ismail AF, Salim R (2006) Behaviours of natural organic matter in membrane filtration for surface water treatment: a review. Desalination 194(1–3):211–231

DOI 10.1007/978-3-319-05041-6_12
Reprinted from the *Journal of Nanoparticle Research*, DOI 10.1007/s11051-012-1272-z

RESEARCH PAPER

Manganese-incorporated iron(III) oxide–graphene magnetic nanocomposite: synthesis, characterization, and application for the arsenic(III)-sorption from aqueous solution

Debabrata Nandi · Kaushik Gupta · Arup Kumar Ghosh · Amitabha De · Sangam Banerjee · Uday Chand Ghosh

Received: 2 July 2012 / Accepted: 30 October 2012 / Published online: 15 November 2012

Abstract High specific surface area of graphene (GR) has gained special scientific attention in developing magnetic GR nanocomposite aiming to apply for the remediation of diverse environmental problems like point-of-use water purification and simultaneous separation of contaminants applying low external magnetic field (<1.0 T) from ground water. Fabrication of magnetic manganese-incorporated iron(III) oxide ($Mn_x^{2+}Fe_{2-x}^{3+}O_4^{2-}$) (IMBO)–GR nanocomposite is reported by exfoliating the GR layers. Latest microscopic, spectroscopic, powder X-ray diffraction, BET surface area, and superconducting quantum interference device characterizations showed that the material is a magnetic nanocomposite with high specific surface area (280 $m^2\ g^{-1}$) and pore volume (0.3362 $cm^3\ g^{-1}$). Use of this composite for the immobilization of carcinogenic As(III) from water at 300 K and pH ~7.0 showed that the nanocomposite has higher binding efficiency with As(III) than the IMBO owing to its high specific surface area. The composite showed almost complete (>99.9 %) As(III) removal (≤10 μg L^{-1}) from water. External magnetic field of 0.3 T efficiently separated the water dispersed composite (0.01 g/10 mL) at room temperature (300 K). Thus, this composite is a promising material which can be used effectively as a potent As(III) immobilizer from the contaminated groundwater (>10 μg L^{-1}) to improve drinking water quality.

Keywords Arsenic(III) · Graphene nanocomposite · Magnetic separation · Sorption

Special Issue Editors: Mamadou Diallo, Neil Fromer, Myung S. Jhon

This article is part of the Topical Collection on Nanotechnology for Sustainable Development

Electronic supplementary material The online version of this article (doi:10.1007/s11051-012-1272-z) contains supplementary material, which is available to authorized users.

D. Nandi · K. Gupta · A. K. Ghosh · U. C. Ghosh (✉)
Department of Chemistry and Biochemistry, Presidency University, 86/1 College Street, Kolkata 700073, India
e-mail: ucghosh@yahoo.co.in

A. De
Chemical Science Division, Saha Institute of Nuclear Physics, 1/AF Bidhannagar, Kolkata 700064, India

S. Banerjee
Surface Physics Division, Saha Institute of Nuclear Physics, 1/AF Bidhannagar, Kolkata 700064, India

Introduction

Graphene (GR) comprises monolayer of sp^2-hybridized carbon atoms decorated in a two-dimensional hexagonal (honeycomb) lattice, which has attracted special attention in scientific community since last few years owing to its superlative properties like mechanical strength, thermal conductivity, electrical conductivity, specific surface area etc. (Geim and Novoselov

2007; Avouris and Dimitrakopoulos 2012; Ramanathan et al. 2008). Thus, modified GR and hybrid GR materials have been developed and tailored to wide applications in super capacitance, drug delivery, magnetic resonance imaging, and surface science (Novoselov et al. 2004; Kim et al. 2009; Kim and Kim 2008; Gao et al. 2011a, b; Sreeprasad et al. 2011; Chandra et al. 2010; Schedin et al. 2007; Wang et al. 2008; Yu et al. 2009; Yang et al. 2009; Marcano et al. 2010). Graphene oxide (GO) is synthesized via oxidation followed by exfoliation of graphite layers by modified Hummer's method (Marcano et al. 2010) with additional $KMnO_4$ and used as precursor for GR and graphene composite (GC) synthesis. The presence of a large number of oxygenated functional groups makes GO hydrophilic (Fan et al. 2011), indicating the possibility to apply it in aquatic and biological environments. In recent times, it has been reported to use GO and GR as adsorbent for scavenging toxic chemicals and compounds (Seredych and Bandosz 2007; Matsuo et al. 2008; Chandra and Kim 2011; Yang et al. 2010, 2011; Gao et al. 2011a, b) from contaminated water/environment.

Occurrence of arsenic much exceeding the tolerance limit (10 μg L^{-1}) in groundwater is a global problem, and posed an ever-increasing degree of chronic arsenic toxicity (arsenicosis). A review report indicated (Smedley and Kinniburgh 2002) the arsenic pollution in USA, China, Chile, Bangladesh, Taiwan, Mexico, Argentina, Poland, Canada, Hungary, New Zealand, Japan, and India especially the Bengal delta. The arsenic content in ground waters as reported (Smedley and Kinniburgh 2002) is wide in range (West Bengal in India: <10–3,200 μg L^{-1} and Bangladesh: <0.5–2,500 μg L^{-1}). The cause of arsenic accumulation in groundwater in this Bengal delta region is an anoxic environment around its alluvial deposits of geogenic arsenic pyrites and iron oxyhydroxide with adsorbed arsenic undergoing microbial reduction (Nickson et al. 1998; McArthur et al. 2001; Harvey et al. 2002). The aquifers thus become rich in this reduced As(III) and Fe(II). The reported ratios of $As(III)/As_{total}$ at a depth of 30–40 m in these aquifers are in the range of 0.6–0.9 (Harvey et al. 2002), which is a matter of great concern as As(III), being more toxic and mobile (Roberts et al. 2004) than As(V), has much greater immobilization affinity with the thiol (–SH) part of the protein residue due to soft–soft acid–base reaction and shows adverse health impact of arsenic toxicity. This had forced the researchers to undertake challenges for developing materials to reduce arsenic levels below or equal to the permissible value (0.01 mg L^{-1}) in the last two decades by immobilization. Consequently, several technologies such as oxidation–precipitation, coagulation/electro coagulation/precipitation, membrane filtration and surface sorption, ion exchange, etc., were reported (Smedley and Kinniburgh 2002; Mondal et al. 2006; Mohan and Pittman 2007). However, the arsenic removal by surface sorption is well accepted for the treatment of high arsenic groundwater owing to simple operation, low recurring cost, high removal efficiency, and low sludge generation. Numerous materials (Smedley and Kinniburgh 2002; Mondal et al. 2006; Mohan and Pittman 2007), for example activated carbon, agricultural products and byproducts, biomasses, and metal oxides or metal ion-loaded biomaterials had been reported for the treatment by immobilization of high arsenic ground waters and industrial effluents. Some nanostructured bimetal oxides investigated in our laboratory (Basu et al. 2010; Gupta et al. 2008, 2011, 2012, 2010) showed higher arsenic binding capacity than the single metal oxides. Inorganic nanooxides combined with carbon base materials like activated carbon (Zhang et al. 2010a, b), carbon nanotube (Mauter and Elimelech 2008; Miyamoto et al. 2005), GO (Gao et al. 2011a, b), and reduced GO (Sreeprasad et al. 2011; Chandra et al. 2010) have created much interest to the researchers involved in the adsorption field owing to their much higher specific surface area as well as water dispersibility than pure oxides. Arsenic removal from contaminated drinking water had been investigated using GO-cross linked ferric hydroxide (Zhang et al. 2010a, b) magnetite-reduced GO (Chandra et al. 2010) etc.

The synthesis of GR and modified GR offers potentially low cost and large-scale production of GR-based materials (Yang et al. 2009; Marcano et al. 2010). This low production cost of GR makes itself a very interesting material in water treatment technology. However, use of such material for water treatment is somewhat inconvenient because of the separation problem. Here, magnetic separation appears to be a modern efficient technique applied to diverse problems, like water purification and simultaneous separation of sorbent. Incorporation of magnetic materials into the GR layers in GC may be a remediation of this critical problem as magnetic separation can easily be applied with such materials.

This manuscript thus reports the fabrication of reduced GO-based magnetic nanocomposite (GC) made from GO and manganese-incorporated magnetic iron(III) oxide (IMBO) with characterizations of IMBO, GR, and GC using the analytical techniques like powder X-ray diffraction (XRD), scanning electron microscopy (SEM), transmission electron microscopy (TEM), atomic force microscopy (AFM), Raman spectroscopy, Fourier transform infrared spectroscopy (FT-IR), Brunauer–Emmett–Teller (BET) surface area, and superconducting quantum interference device (SQUID). Finally, the investigation of application possibility of GC for the As(III) removal from the contaminated aqueous solution is reported with an insight of adsorption mechanism.

Experimental section

Chemicals

The chemicals used for this study are shown in Supporting information.

GO synthesis

GO was prepared based on the modified Hummer's method (Marcano et al. 2010) using additional $KMnO_4$ followed by exfoliation. Concentrated H_2SO_4 (50 mL) was added to a mixture of graphite flakes (2.0 g) and $NaNO_3$ (1.0 g) and stirred it at 0 °C in ice bath. $KMnO_4$ (6.0 g) was added in portion under vigorous stirring so that the temperature should not exceed 20 °C for 6 h. Next, additional $KMnO_4$ (6.0 g) was added in the pasty light brownish mixture and stirred it for 12 h at room temperature. Then 300 mL of ice-cold distilled water was added slowly to the mixture with the addition of 30 % H_2O_2 dropwise to reduce the excess $KMnO_4$ to terminate further oxidation. As reaction progressed, the suspension turned brown to light yellow. To purify, this mixture was washed with 5 % of HCl and warm water thoroughly. The obtained mass was dried, and dispersed in distilled water by 1 h sonication to exfoliate the oxidized graphite layers. Then it was centrifuged at 5,000 rpm for 30 min to remove large heavy particles. The resulting supernatant was filtered through 0.45 μm pore size membrane and washed thoroughly with 50 % ethanol to isolate GO mass. The obtained mass was dried under vacuum at 60 °C and collected pure GO as a brown solid product.

GR synthesis

Hydrazine hydrate (99 %) was added dropwise to the aqueous suspension of GO at 95 °C and stirred it for 12 h to reduce bonds like C=O, C–OH, C–O etc. (Harvey et al. 2002). As reaction progressed, the mixture was turned brown to black. The obtained mass was washed thoroughly with 50 % ethanol and centrifuged to isolate solid black mass of GR in the form of reduced GO.

Manganese-incorporated iron(III) oxide (IMBO) synthesis

It was synthesized by mixing aqueous 0.5 M ammonium iron(III) sulfate hexahydrate and aqueous 0.1 M manganese(II) chloride tetra hydrate (v/v = 1:1). Co-precipitation was done by adding 0.1 M ammonium carbonate solution slowly with constant stirring at room temperature to raise pH to 9.0 and kept it for 24 h with supernatant liquid. The settled precipitate was filtered and washed thoroughly with 50 % ethanol and dried at 60 °C under vacuum.

Fabrication of IMBO–graphene nanocomposite (GC)

To prepare GR-based IMBO composite, aqueous 0.5 M ammonium iron(III) sulfate hexahydrate and aqueous 0.1 M manganese(II) chloride tetrahydrate were mixed (v/v = 1:1) into the colloidal dispersion of GO with constant stirring for about half an hour. To this suspension, aqueous 0.1 M ammonium carbonate solution was added slowly with constant stirring at room temperature to raise the pH to 9.0 and aged it for 24 h with stock solution to settle down the solid mass. The solid mass was filtered and washed thoroughly with 50 % ethanol, and dried at 60 °C under vacuum. The dry solid mass was dispersed well in distilled water, and then it was treated with hydrazine hydrate (99 %) at 95 °C for reduction. The black solid material was isolated by centrifugation (5,000 rpm), and washed thoroughly with 50 % ethanol. It was dried at 60 °C in vacuum to get desired GC.

Stock As(III) solution

Preparation and preservation of As(III) solution are given in the Supplementary information. Arsenic

analysis in samples was done by the standard method (Supplementary information) (Clesceri et al. 1998).

Material characterization

The analytical tools used for the characterization of materials are given in the Supplementary information.

The pH for zero-point surface charge (pH_{zpc}) of the sample was analyzed by a method reported (Babic et al. 1999).

Experiments for the As(III) sorption

Experimental procedures for the batch sorption experiments conducted are discussed in the Supplementary information. Arsenic loaded water dispersed composite (GC) particles (10 mg/10 mL water) was separated by applying external magnetic field of ~0.3 T (Fig. 1).

As(III) sorption capacity

The mass balanced relation used for the calculation of As(III) immobilization amount by GC is given in the Supplementary information.

Results and discussion

Powder XRD patterns of calcined IMBO (4 h) at five different temperatures 373, 473, 573, 673, and 773 K are shown in Fig. S1A (Supplementary information). It has been seen that there is no alteration of peak positions of the samples indicating the stability of the material up to 773 K. The XRD patterns had shown well similarity with α-Fe_2O_3 phase of hematite. Major peaks at 2θ(°) = 24.2, 33.18, 35.64, 40.88, 49.5, 54.1, 62.48, 64.04, and 72.1 correspond to the planes of [*hkl*] values [102], [104], [110], [113] [024], [116], [124], [300], and [1010], respectively. No peak for manganese oxide mineral was detected in the XRD patterns indicating incorporation of manganese ions into the crystal structure of α-Fe_2O_3. However, the intensity of the peaks increased with increasing calcined temperature without changing the position of peaks. This indicated the gradual increase of crystallites size with increasing calcined temperature. The average size (nm) of particles calculated by inserting XRD data into the Scherer's equation (Nandi et al. 2012) ranged 9–20 and 50–80 for the calcined samples at 373 and 773 K, respectively. The unit cell parameters estimated by the analysis of XRD patterns at 373 K are $a = 8.563$ Å and $c = 13.868$ Å. Both these values are larger than those reported in JCPDS file (Card No. 89-8104) for α-Fe_2O_3, indicating the incorporation of larger Mn^{2+} replacing the smaller Fe^{3+} ions. Both the high-spin Mn^{2+} ($r = 97.0$ pm) and Fe^{2+} ($r = 92.0$ pm) are larger than the high-spin Fe^{3+} ($r = 78.5$ pm). Thus, the replacement of Fe^{3+} of α-Fe_2O_3 by smaller Fe^{2+} or Mn^{2+} ions increases (Lai et al. 2004) the size of unit cell. Incorporation of Mn^{2+} in α-Fe_2O_3 crystallite gives rise to a new spinel phase $Mn_x^{2+}Fe_{2-x}^{3+}O_4^{2-}$ ($x = 0.33$). This type of spinel structure is thermodynamically stable and reported previously (Lee 1988). As the oxide is synthesized by ammonium carbonate treatment, there is very little chance of oxidation of Mn^{2+} to Mn^{3+} state because such oxidation is usually

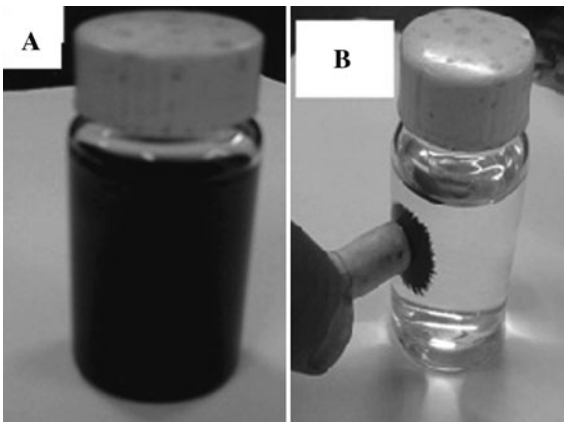

Fig. 1 **A** Dispersion of GC in water during experiment. **B** Low-field magnetic separation of dispersed GC from the experimented solution at room temperature

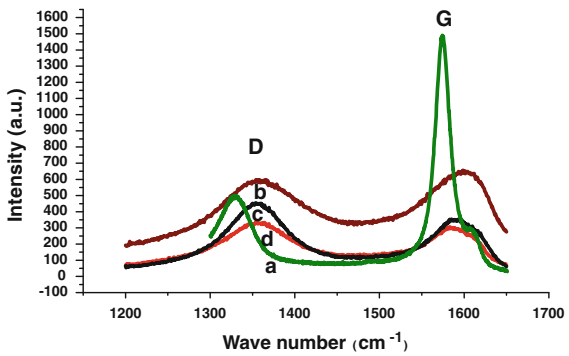

Fig. 2 Raman spectroscopy study of **A** graphite flake, **B** GO, **C** GR, and **D** GC

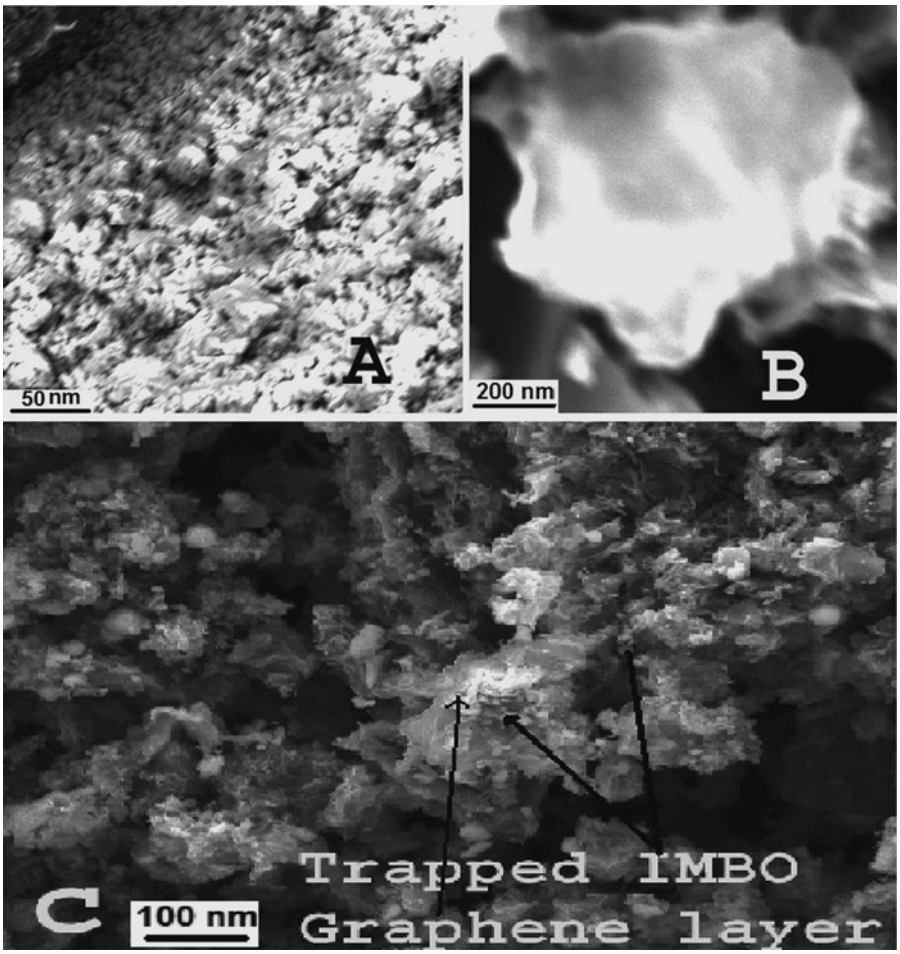

Fig. 3 SEM micrograph of **A** IMBO, **B** exfoliated GR, and **C** GC

taken place at highly alkaline medium (pH $\geq$ 9). Thus, in the spinel structure $Mn_x^{2+}Fe_{2-x}^{3+}O_4^{2-}$, the Mn^{2+} ions occupied the tetrahedral and the Fe^{3+} ions occupied the octahedral close packed sites formed by oxide ions (Kuo et al. 2007; Osmokrovi et al. 2006). Figure S1B in Supplementary information shows the XRD patterns of GO, GR, and GR–IMBO composite (GC). A broad peak at $2\theta(^\circ) = 10.6$ with larger *d*-spacing ($d = 8.22$ Å) was observed in the XRD pattern of GO corresponding to (001) diffraction plane, which is the characteristics of pure GO (Lian et al. 2010). This is attributed to the oxygen-containing functional group and water molecule insertion between the GO layers (Pan et al. 2009). When it was reduced to GR, the broad peak is observed at $2\theta(^\circ) = 26.2$. This is a characteristics peak of GR having the *d*-spacing 3.4 Å. When this GR underwent composite formation with the metal oxide, the characteristics GR peak at 23.7° shifted to the lower $2\theta(^\circ)$ region with higher *d*-spacing 3.7 Å, indicating entrapment of IMBO particles between exfoliated GR layers. The size of crystallites decreased in GC compared to that of pure IMBO, implying the increase of surface area and active sites in GC formation (Nesbitt et al. 1998). The XRD pattern of the composite is almost similar to that of GR (Fig. S1B). This is due to the fact that the metal oxide peak pattern is overlaid by GR peaks.

Raman spectra (488 nm excitation) (Fig. 2) displayed significant structural changes which took place owing to chemical reactions during conversion of graphite flake to GO to GR and GC. Graphite displayed two peaks at wave number (ν, cm^{-1}) 1,330 and 1,574, which are corresponding to the well-documented D and G bands, respectively. Here, the G band is corresponding to the first-order

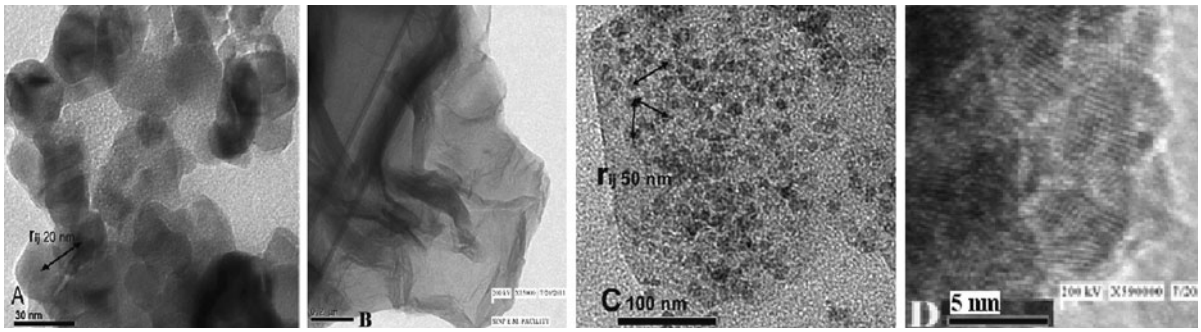

Fig. 4 TEM images of **A** IMBO, **b** GR, **c** GC, and d HRTEM of IMBO

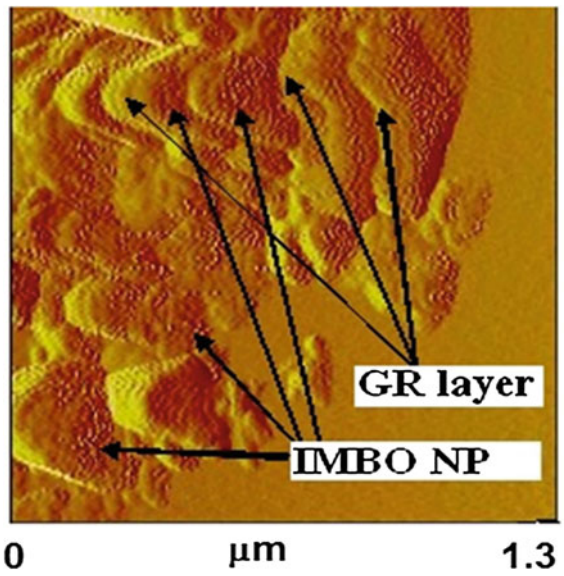

Fig. 5 AFM image of GC in 2D view

scattering of the E_{2g} mode associated with sp^2 domains. In GO, G band is broadened and shifted to $\nu = 1{,}596\ \mathrm{cm}^{-1}$ and the prominent D band is associated with reduction in size of the in-plane sp^2 domains, presumably due to the extensive oxidation by $KMnO_4$ in the presence of concentrated H_2SO_4 and rapid thermal exfoliation. The Raman spectra of GR and GC exhibited pronounced broad D and G bands at ν (cm^{-1}) = 1,356 and 1,586, respectively. A universal observation is that higher disorder in graphite leads to a broader G band as well as to a broad D band of higher relative intensity compared to that of the G band. Therefore, the intensity ratio of D band to G band usually signifies higher degree of disorderness associated with exfoliation (Tuinstra and Koenig 1970). The intensity ratio ($r_i = I_D{:}I_G$) for GR (1.30) and GC (1.14) showed a remarkable enhanced value compared to that for pure graphite (0.33) and GO (0.90) also, indicating the exfoliation of layers was initiated in GO stage (Gupta et al. 2009). The peaks intensity of GC decreased slightly with respect to GR due to the plausible penetration of reflection in electronic structure in GR layers by metal oxide. This change of peak intensity is observed due to the changes of reflection in electronic structure from the stacking of successive layers (Gupta et al. 2009). This type of significant change in intensity, location, and shape implies the decrease in number of layers (Ferrari et al. 2006).

The SEM images (Fig. 3) show the surface morphology of IMBO (A), GR (B), and GC (C). In image a of pure IMBO, the surface showed porous agglomeration of grain-like particles with rough surface morphology. The image B of pure GR displayed an exfoliated layer just like the outer scales of onion which is the intrinsic property of GR, a curled morphology (Meyer et al. 2007). The image C showed the trapped IMBO nanoparticles into the GR layers, indicating the increase of surface roughness due to composite formation.

To investigate size, shape, and morphology, the TEM images (Fig. 4) were taken for IMBO (a), GR (b), and GC (c). The image d in Fig. 4 represents the HRTEM of IMBO. The image a showed that the particle shape is almost hexagonal which is comparable with the α-Fe_2O_3 structure and particle size lies in the range of 15–25 nm which is also comparable with the size obtained by XRD data analysis. It is evident that magnetic particle of size less than 30 nm holds superparamagnetism (Hu et al. 2007). The particles were agglomerated somewhat, which are indicated by the black spots in the image. The estimated inter particle distance (r_{ij}) is found to be $\approx$20 nm. The image B

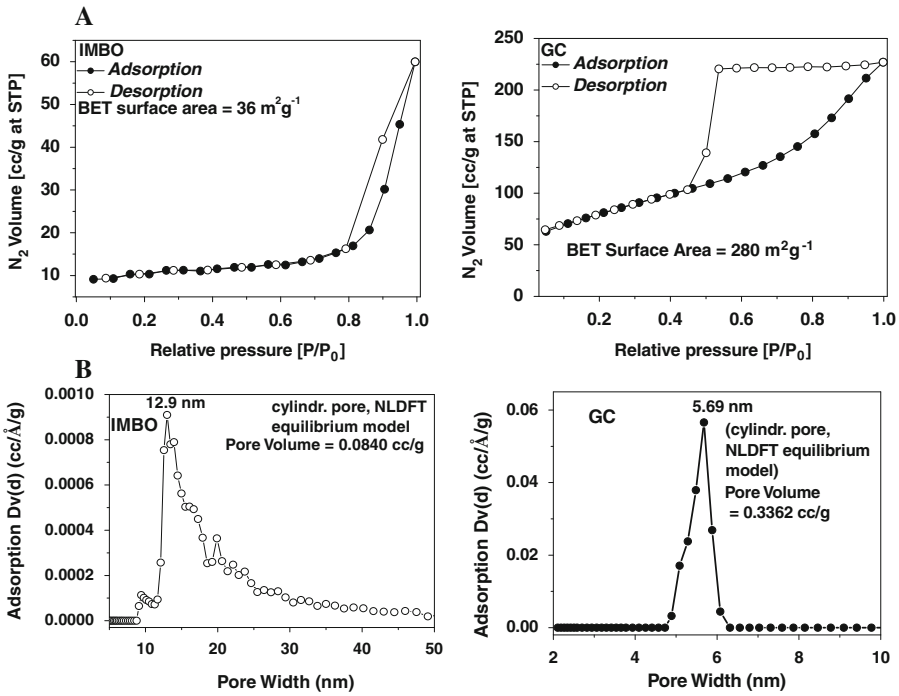

Fig. 6 **A** Nitrogen adsorption–desorption isotherms for IMBO and GC. **B** Pore size distribution curve for IMBO and GC with calculated pore volume

showed a thin wrinkled paper-like as well as rippled structure as a result of deformation and disorderness at the time of exfoliation (Lian et al. 2010). The image c revealed that after composite formation the colloidal nanoparticles (IMBO) are found to be entrapped between the GR sheets. The black spots (image C) in GR sheet indicated the presence of trapped IMBO particles, which are distributed well into this composite with respect to pure IMBO and r_{ij} increases to $\approx$50 nm. One can thus assume the weak magnetic interparticle interaction in the composite with respect to pure IMBO is responsible for lowering of magnetization value. Apart from that our experimental data strongly support our conceptualized preparation route in which metal oxide nanoparticles are entrapped inside the GR sheets. The image D shows nanocrystalline state with distinct lattice fringes ($d = 2.836$ Å) along the direction of [104] plane.

Figure 5 shows the AFM image of GC in 2D view. The image is very interesting one, because it clearly showed the attachment of very small IMBO particles within the layers of GR. The distinct layer with honeycomb-like architecture of GR having the length of several micrometers is also supportive with SEM image (Fig. 3B).

Figure S2 (Supplementary information) shows FT-IR spectra of all the samples. No characteristic peak is observed in the spectra of graphite flakes. When these flakes are transformed into the GO, a number of strong absorption peaks appeared. A broad peak having a center at 3,380 cm^{-1} and a sharp peak at 1,624 cm^{-1} appeared mainly due to the –OH stretching and bending mode of vibration, respectively, indicating the presence of surface hydroxyl groups on GO (Moon et al. 2011). The peaks at 1,230 and 1,401 cm^{-1} are mainly due to the epoxy C–O and C–OH vibrations (Compton et al. 2011). The presence of C=O group in carboxylic acid and carbonyl moieties is indicated by the sharp peaks at 1,726 cm^{-1}. Small peaks at 1,051 and 988 cm^{-1} are mainly due to the vibration of S=O bond and C–S–C bonds indicating the presence of $–SO_3H$ groups on GO surface (Si and Samulski 2008). After reduction with hydrazine hydrate the peaks at 1,230 and 1,401 cm^{-1} are almost disappeared, indicating the complete removal of epoxy and C–OH groups attached to the basal GR layers. The IR spectrum of GR shows the appearance of a new peak at 1,556 cm^{-1}, which is due to the skeletal stretching vibration of GR layer (Nethravathi and Rajamathi 2008). The weak band in IR spectrum at 1,207 cm^{-1} may be due to the presence of small number of unchanged epoxy groups at the vertices. The peaks corresponding to $–SO_3H$ groups on GO surface are completely absent in the IR spectra of GR. Thus, complete reduction of GO is obtained by

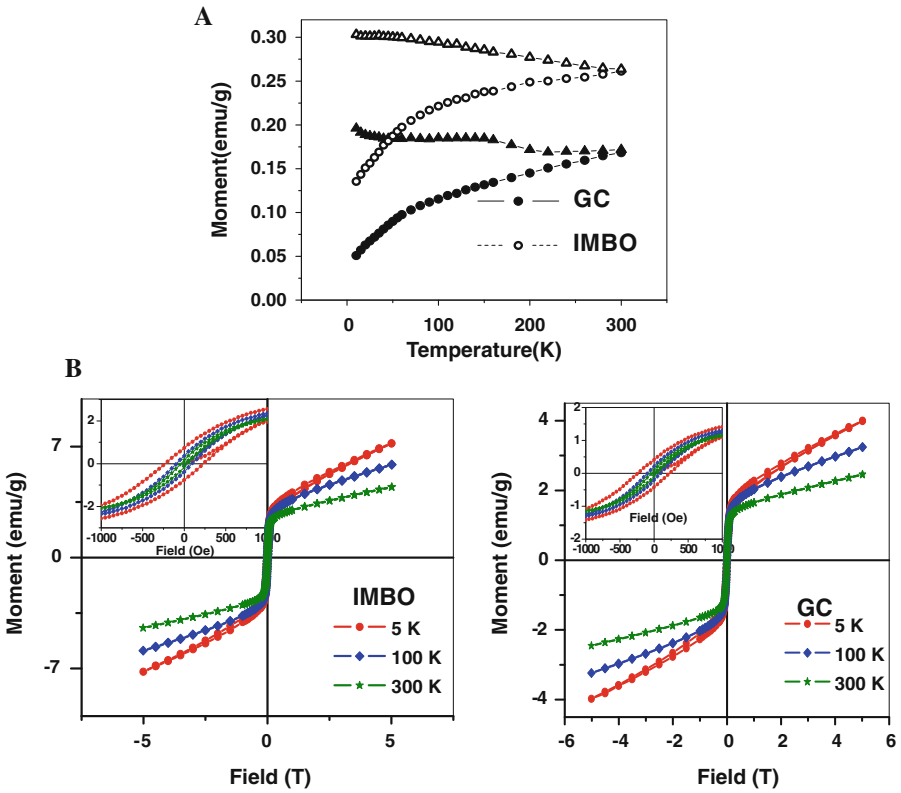

Fig. 7 **A** FC and ZFC curves as a function of temperature for IMBO and GC. **B** Hysteresis curves of pure IMBO and GC at 5, 100, 300 K (close observation of the hysteresis loops, *inset*)

Table 1 Comperative study of saturation magnetization (MS), remnant magnetization (MR), coercive field (H_C) at 5, 100, and 300 K for pure IMBO and GC

Temperatures (K)	Magnetic properties					
	Coercive field (H_C) (Oe)		Remanence (M_R) (emu g^{-1}		Saturation magnetization (M_S) (emu g^{-1})	
	IMBO	GC	IMBO	GC	IMBO	GC
5	232	230	0.77	0.42	7.3	3.9
100	96	92	0.36	0.21	5.8	3.2
300	38	32	0.17	0.09	4.5	2.4

hydrazine hydrate. In IMBO, a sharp peak observed at 548 cm^{-1} is mainly due to the Fe–O–Mn bond vibration. The oxide is hydrous in nature shown by the presence of a broad peak at 3,410 cm^{-1} for the –OH stretching vibration of surface hydroxyl groups. However, the IR spectrum of composite material (GC) is completely different from that of GR and IMBO. No characteristics peak of IMBO is observed in the IR spectrum of the composite. A peak, however, is observed at 1,580 cm^{-1} which is due to the skeletal stretching vibration of GR layers (Nethravathi and Rajamathi 2008). Thus, IMBO particles are incorporated into the GR layers by strong interacting forces which are overlaid by the layers and the characteristics peaks of the oxide are absent in the IR spectrum of the composite.

To investigate the specific surface area (Fig. 6A) and pore size distribution with pore volume (Fig. 6B) for IMBO and GC, N_2 (vapor) adsorption–desorption isotherm were carried out, respectively. For IMBO, the

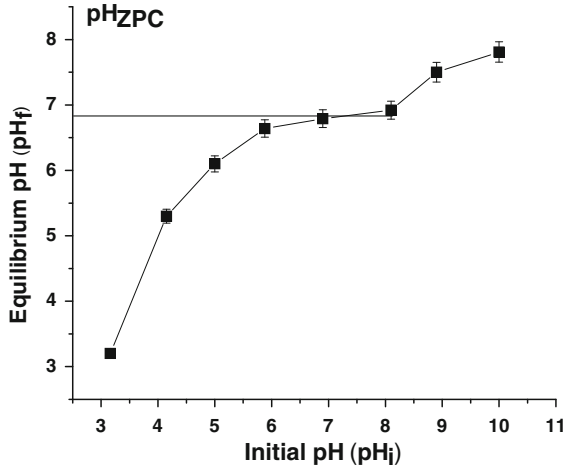

Fig. 8 Plot of pH_f versus pH_i to evaluate pH_{zpc} of GC

Table 2 Physicochemical properties of the composite (GC)

Name of the properties	Value of the parameters
Specific surface area of the sorbent ($m^2\ g^{-1}$)	180
Pore diameter (nm)	5.69
Pore volume (cc g^{-1})	0.3362
pH_{ZPC} of the sorbent	6.8 (±0.1)
Magnetic flux required to separate sorbent (10 mg/10 mL water) at room temperature (T)	0.3

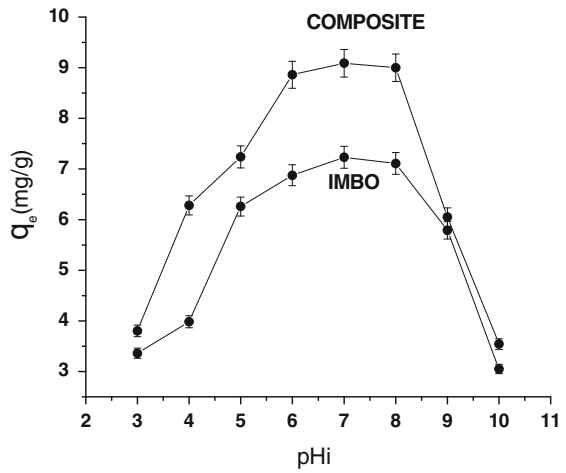

Fig. 9 As(III) sorption capacity versus initial pH (pH_i) of composite (GC) and IMBO. C_i of As(III) 5.0 mg L^{-1} and $T = 300$ (±1.0) K

N_2 (vapor) adsorption hysteresis is very small (Fig. 6A). Thus, the BET surface area and pore volume obtained are only 36 $m^2\ g^{-1}$ and 0.0840 cc g^{-1}

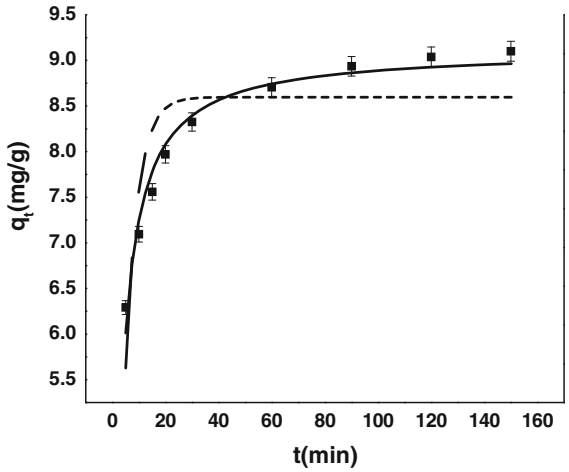

Fig. 10 Variation of q_t (mg g^{-1}) against time t (min) and a nonlinear fit of data with pseudo-first-order and pseudo-second-order equations at 5 mg L^{-1} As(III) solution and $T = 300$ (±1.0) K

(Fig. 6B), respectively, indicating low adsorption efficiency. But for the GC, the adsorption hysteresis is prominent (Fig. 6A), the BET surface area is 280 $m^2\ g^{-1}$ and pore volume is 0.3362 $cm^3\ g^{-1}$ (Fig. 6B) indicating hierarchical porous structure as well as superior adsorption capacity, indicating good possibility of the material to be used as a surface adsorber. Although both the samples show mesoporous structure but have remarkable different values in BET surface area and pore volume presumably due to the fact that magnetic nanoparticles themselves have strong magnetic interactions and could easily be aggregated together in IMBO.

Magnetic properties of the pure metal oxide (IMBO) and the composite (GC) had been investigated with SQUID. Figure 7a shows the zero field cooling (ZFC) and field cooling (FC) measurement of the temperature-dependant magnetization irreversibility at 100 Oe fields. The bifurcation of the ZFC–FC curves represents the super paramagnetic nature of the pure oxide nanoparticles and the composite. The blocking temperature (T_B) of both the samples is above 300 K. An interesting magnetization upturn has been found for GC but not for pure oxide in FC curve which is presumably due to free independent paramagnetic spin contribution from GR layer. Figure 7b shows the pattern of hysteresis loops of the GC at 5, 100, and 300 K with an applied magnetic field sweeping from −5 to +5 kOe. The saturation magnetization (M_S), remnant magnetization (M_R), and

Table 3 Kinetic parameters estimated for the As(III)-sorption by composite (GC) (C_i = 5.0 mg As(III) L^{-1}, pH 7.0 ± 0.1, and T = 300 ± 1.0 K)

As sample	Pseudo-first order				Pseudo-second order			
	k_1 (min^{-1})	q_t (mg g^{-1})	R^2	χ^2	k_2 (L g^{-1} min^{-1})	q_t (mg g^{-1})	R^2	χ^2
As(III)	0.212 ± 0.030	8.597 ± 0.203	0.96	0.253	0.042 ± 0.003	9.118 ± 0.084	0.99	0.025

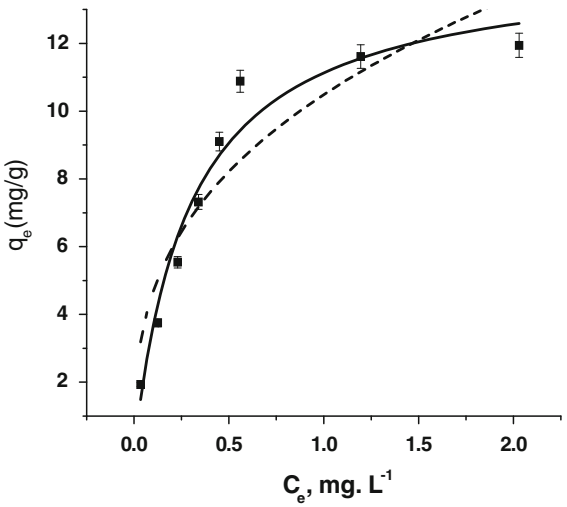

Fig. 11 Plots of equilibrium sorption capacity (q_e) versus equilibrium concentration (C_e) of As(III) and nonlinear fits of the data with Langmuir and Freundlich isotherm models for the sorption of As(III) by composite (GC) for 150 min at pH 7.0 ± 0.1, T = 300 ± 1.0 K

coercivity (H_C) for IMBO and GC are summarized in Table 1. All the magnetic hysteresis loops are S-like curves indicating super paramagnetic behavior of the samples (He and Gao 2010). As the sample has high surface to volume ratio, the magnetic contribution of the samples studied is mainly governed by the surface magnon. Above all at room temperature (300 K), the GC (sorbent) can easily be separated by external magnetic field to fulfill our objective.

The zero-point surface charge (pH_{ZPC}) of the composite (GC) was analyzed and found to be 6.8 (±0.1) (Fig. 8), which means that the composite surface (S) is positively charged below this pH and negatively charged above this pH. Thus, it can be given as

$$S\text{--}OH_2^+ \quad (pH < 6.8), \quad S\text{--}O^- \quad (pH > 6.8)$$

The characterizations of GC reveal that the properties like specific surface area, water dispersibility, magnetism, and pH_{ZPC} are prominently retained simultaneously in the composite (GR:IMBO = 1:1). Therefore, it has thus been tested for the As(III) immobilization by sorption from the aqueous phases with separation of dispersed material by applying external magnetic field strength. The physicochemical properties of the composite (GC) are summarized in Table 2.

The As(III)-sorption affinity of GC from aqueous phases depends upon the solution pH as the nature of the solid surface and the solute species changes with solution pH. Figure 9 demonstrates the variation of the immobilized As(III) amount by sorption on IMBO and GC separately with increasing initial solution pH (pH_i). It shows that the As(III)-sorption amount (q_e, mg g^{-1}) increased with increasing pH_i up to 6.0, and the q_e remained almost constant up to pH_i 8.0. A sharp decrease of q_e was observed with increasing pH_i from 8.0. The results indicated that the q_e by the composite is higher than by the oxide in the pH_i range 3.0–8.0, which is owing to greater specific surface area of GC than that of IMBO. The pH_{ZPC} (~6.8) (Fig. 8) value indicated that the surface charge nature of the composite material should be predominantly positive at pH < 6.8 and negative at pH > 6.8. The aqueous As(III) species exists as $As(OH)_3$ (pK_1 = 9.18) up to pH < ~9.2, and adsorption occurs via electrostatic attraction between positive surface sites on GC and negative end of $(HO)_2As^{III}–O^{\delta-}–H^{\delta+}$ (Lin and Wu 2001; Chandra et al. 2010). However, the increase of q_e (mg g^{-1}) with rising pH from 3.0 to 6.0 is presumably owing to the decrease of electrostatic repulsion between solute $H^{\delta+}$ and positive sites on GC surface as the later one should decrease with increasing pH. Again, the composite surface will be near to neutral at pH range 6.0–8.0, and q_e remains almost constant. Increase of the solution pH beyond 8.0, the negative surface sites of GC repels the $(HO)_2As–O^-$ giving an account for the decrease of q_e (Fig. 9).

Kinetic study of the As(III) immobilization reaction with GC is very important for determining the rate and other kinetic parameters including contact time. Figure 10 demonstrates the As(III) sorption amount

Table 4 Equilibrium parameters estimated for the As(III)-sorption reaction with composite (GC) (equilibrium time 150 min, pH 7.0 ± 0.1, and $T = 300 \pm 1.0$ K

As sample	Langmuir isotherm				Freundlich isotherm			
	R^2	χ^2	q_e (mg g^{-1})	K_a (L mg^{-1})	R^2	χ^2	K_F (mg g^{-1})	n
As(III)	0.96	0.648	14.42 ± 1.01	3.38 ± 0.7	0.86	2.183	2.84 ± 0.53	10.48 ± 0.67

Table 5 Comparison of maximum monolayer sorption capacity with some reported value

Name of the adsorbent	pH at which isotherm experiment performed	Maximum monolayer sorption capacity	References
Mn-substituted iron oxyhydroxide ($Mn_{0.13}Fe_{0.87}OOH$)	7.0	4.58	Lakshmipathiraj et al. (2006)
Fe_3O_4–Mn_3O_4	7.0	14.00	Silva et al. (2012)
RGO–Fe_3O_4 composite	7.0	12.22	Chandra et al. (2010)
Fe_3O_4-reduced graphite oxide–MnO_2 nanocomposites	7.0	14.04	Luoa et al. (2012)
Present composite	7.0	14.42	This study

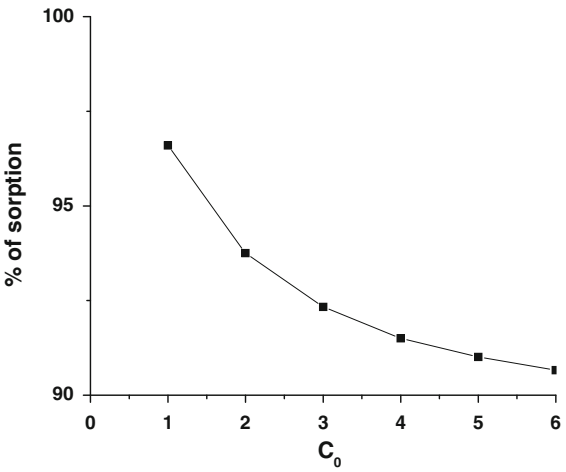

Fig. 12 Plots of adsorption percentage versus initial concentration (C_i) of As(III) for 150 min at pH 7 ± 0.1 and $T = 300 \pm 1.0$ K

(q_t, mg g^{-1}) by GC with increasing reaction time (t, min) at pH$_i$ 7.0 (±0.1) and $T = 300$ (±1.0) K. It shows that the time required is about 50 min to reach equilibrium indicated by plateau appearance (Fig. 10), which is lower than that reported previously for As(III) (Mohan and Pittman 2007). Rapid uptake of As(III) took place by the GC in initial 30 min, and that reduces with increasing contact time, which is due to the decrease of active available sites and the Columbic inhibition between the solute species on surface and the solute species available at solid–liquid interface. The kinetic data of the present reaction are modeled with pseudo-first-order equation (1) and pseudo-second order equation (2):

$$q_t = q_e[1 - \exp(-k_1 t)] \quad (1)$$

$$q_t = k_2 q_e^2 t/(1 + k_2 q_e t), \quad (2)$$

where q_e and q_t are the As(III)-sorption amount (mg g^{-1}) at equilibrium and at time t (min), respectively; and k_1 (min^{-1}) and k_2 (g mg^{-1} min^{-1}) are the rate constants for the respective equations. The kinetic parameters estimated from the nonlinear analysis of the data using Eqs. (1, 2) are summarized in Table 3. The R^2 and χ^2 values (Table 3) indicated that the kinetics of As(III) immobilization by sorption reaction obeyed better with the pseudo-second order equation (2) than the pseudo-first-order equation (1) under the conditions of present reaction. The rate constant k_2 obtained (Table 3) is high enough for As(III) uptake than those reported previously (Chandra et al. 2010), indicating rapid As(III)-immobilization by the composite (GC).

Figure 11 shows isotherm for the As(III)-sorption reaction with GC in the concentration range 1.0–8.0 mg L^{-1} at pH 7.0 and $T = 300$ K. The data obtained are modeled with Langmuir and Freundlich isotherm equations (3, 4). The isotherm model parameters estimated are summarized in Table 4.

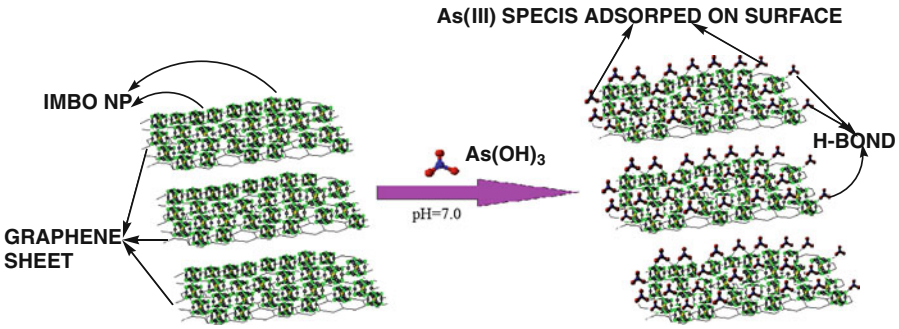

Fig. 13 Modeling of As(III) sorption on composite (GC) surface

$$\text{Langmuir equation}: q_e = (q_m K_a C_e)/(1 + K_a C_e), \quad (3)$$

$$\text{Freundlich equation}: \; q_e = K_F C_e^{(1/n)}, \quad (4)$$

where q_e (mg g^{-1}) and C_e (mg L^{-1}) are the As(III)-sorption amount by GC and the concentration at equilibrium, respectively; q_m and K_a are the Langmuir monolayer capacity (mg g^{-1}) and Langmuir constant (L mg^{-1}), respectively. K_F and n are the Freundlich constant, respectively. From the values of R^2 or χ^2 values, it can be said that the sorption process for As(III) immobilization described the Langmuir model (3) better than the Freundlich (4). The maximum monolayer capacity (q_m) of the composite (GC) is 14.42 mg g^{-1} which is compared with some previous reports in Table 5. However, the q_m is dependent on the concentration range used, which is quite low for the present case. This indicated that the composite material can be applied as a medium in the low concentration range of As(III) and practicable for natural As(III)-contaminated water treatment.

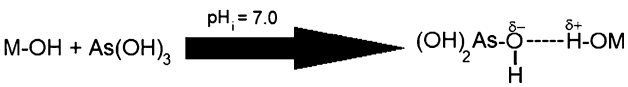

It was noteworthy that the percentage of sorption efficiency increased exponentially down to the low As(III) concentration. The percentage of immobilization by sorption increased rapidly from 90.6 to 96.5 with decreasing As(III) concentration from 6.0 to 1.0 mg L^{-1} (Fig. 12). Hence, it can be presumed that the composite (GC) showed almost complete (99.9 %) sorption of As(III), which should have practical application for filtration of high As(III)-contaminated ground water to minimize fast growing arsenicosis. The As(III) species in aqueous solution at pH $\sim$ 7.0 exists as $As(OH)_3$ and the composite surface is predominantly neutral at that pH ($pH_{ZPC} \sim 6.8$) (Fig. 8). When As(III) is sorbed on GC surface at solution pH 7.0, a small decrease of equilibrium solution pH was noticed indicating outer sphere surface complex formation reaction. The Dubinin-Raduskevich (D-R) isotherm modeling of the equilibrium data showed that the energy of sorption (E_{DR}) is $\sim$7.80 kJ mol^{-1}, implying physical nature of the reaction. Figure S3 (Supplementary information) shows the FT-IR spectra of pure GC- and As(III)-saturated GC. A new peak at 434 cm^{-1} is observed in the spectra of As(III)-rich composite, which may be due to the formation of weak chemical bond between surface –OH groups and $As(OH)_3$. Two broad peaks at $\nu \sim 797$ and 836 cm^{-1} appeared in the spectrum of adsorbed composite are owing to the vibration of As–O bonds (Nakamoto 1986). On the basis of the above facts, a mechanistic model (Fig. 13) on As(III) species attachment by the GC surface at $pH_i = 7.0$ is proposed below:

Conclusions

We have presented a facile and easy approach to synthesize a novel magnetic metal oxide–GC which displays remarkable magnetization retaining high specific surface area, a versatile property of GR. Apart from that the agglomeration of magnetic oxide nanoparticles is prevented by incorporating it into GR layers, which enhanced the opening of more active sorption sites. Use of this GC for the As(III)-sorption

indicated its high arsenic removal efficiency (>99.9 % within 10 μg L^{-1}) from the ground water at room temperature with an advantage of low-field magnetic separation of the dispersed solid to improve water quality. In addition, the As(III)-sorption mechanism modeling indicated physical nature of attachment with the composite material via outer surface complexation. Thus, this study opens a new avenue in the realm of sorption science to get rid of toxic element like As(III) from the contaminated ground water with the help of this potent magnetic GC to improve water quality.

Acknowledgments Authors sincerely acknowledge the Council of Scientific and Industrial Research (CSIR), New Delhi (INDIA) for providing financial support of this work, and also the Head, Department of Chemistry and Biochemistry and the Vice-Chancellor of Presidency University, Kolkata for laboratory facilities.

References

Avouris P, Dimitrakopoulos C (2012) Graphene: synthesis and applications. Mater Today 15:86–97

Babic BM, Milorjic SK, Polovina MJ, Koludieronic BV (1999) Point of zero charge and intrinsic equilibrium constants of activated carbon cloth. Carbon 37:477–480

Basu T, Gupta K, Ghosh UC (2010) Equilibrium and thermodynamics on arsenic(III) sorption reaction in the presence of background ions occurring in groundwater with nanoparticle agglomerates of hydrous iron(III) + chromium(III) mixed oxide. J Chem Eng Data 55:2039–2047

Chandra V, Kim KS (2011) Highly selective adsorption of Hg^{2+} by a polypyrrole-reduced graphene oxide composite. Chem Commun 47:3942–3944

Chandra V, Park J, Chun Y, Lee JW, Hwang I, Kim KS (2010) Water dispersible magnetite-reduced graphene oxide composites for arsenic removal. ACS Nano 4:3979–3986

Clesceri LS, Greenberg AE, Eaton AD (1998) Standard methods for the examination of water and waste water, 20th edn. APHA, AWWA & WEF, American Public Health Association, American Water Work Association, Water Environment Federation, Washington DC

Compton OC, Jain B, Dikin DA, Abouimrane A, Amine K, Nguyen ST (2011) Chemically active reduced graphene oxide with tunable C/O ratios. ACS Nano 5:4380–4391

Fan Z-J, Kai W, Yan Jun Y, Wei Tong W, Zhi L-J, Feng J, Ren YM, Song LP, Wei F (2011) Facile synthesis of graphene nanosheets via Fe reduction of exfoliated graphite oxide. ACS Nano 5:191–198

Ferrari AC, Meyer JC, Scardaci V, Casiraghi C, Lazzeri M, Mauri F, Piscanec S, Jiang D, Novoselov KS, Roth S, Geim AK (2006) Raman spectrum of grapheme and grapheme layers. Phys Rev Lett 97:187401–187404

Gao W, Majumdar M, Alemani LB, Narayanan TN, Ibarra MA, Pradhan BK, Ajayan PM (2011a) Graphene oxide also used for heavy metal adsorption; engineered graphite oxide materials for application in water purification. ACS Appl Mater Interfaces 3:1821–1826

Gao Y, Li Y, Zhang L, Huang H, Hu J, Shah SM, Su X (2011b) Adsorption and removal of tetracycline antibiotics from aqueous solution by grapheme oxide. J Colloid Interface Sci 368:540–546

Geim AK, Novoselov KS (2007) The rise of graphene. Nat Mater 6:183–191

Gupta K, Biswas K, Ghosh UC (2008) Nanostructure iron(III)–zirconium(IV) binary mixed oxide: synthesis, characterization and physicochemical aspects of arsenic(III) sorption from the aqueous solution. Ind Eng Chem Res 47:9903–9912

Gupta A, Chen G, Joshi P, Tadigadapa S, Eklund PC (2009) Raman scattering from high frequency phonons in supported *n*-graphene layer films. Nano Lett 6:2667–2673

Gupta K, Maity A, Ghosh UC (2010) Manganese associated nanoparticles agglomerate of iron(III) oxide: synthesis, characterization and arsenic(III) sorption behavior with mechanism. J Hazard Mater 184:832–842

Gupta K, Bhattacharya S, Chattopadhyay D, Mukhopadhyay A, Biswas H, Dutta J, Ray NR, Ghoah UC (2011) Ceria associated manganese oxide nanoparticles: synthesis, characterization and arsenic(V) sorption behavior. Chem Eng J 172:219–229

Gupta K, Bhattacharya S, Nandi D, Dhar A, Maity A, Mukhopadhyay A, Chattopadhyay D, Ray NR, Sen P, Ghosh UC (2012) Arsenic(III) sorption on nanostructured cerium incorporated manganese oxide (NCMO): a physical insight into the mechanistic pathway. J Colloid Interface Sci 377:269–276

Harvey CF, Swartz CH, Bhaduzzaman ABM, Keon-Blute N, Yu W, Ali MA, Ray J, Beckie R, Niedon V, Brabander D (2002) Arsenic mobility and groundwater extraction in Bangladesh. Science 298:1602–1606

He HK, Gao C (2010) Supraparamagnetic conductive and processable multifunctional grapheme nanosheets coated with high density Fe_3O_4 nanoparticles. ACS Appl Mater Interfaces 2:3201–3210

Hu J, Irena MCL, Chen G (2007) Comparative study of various magnetic nanoparticles for Cr(VI) removal. Sep Purif Technol 56:249–256

Kim WY, Kim KS (2008) Prediction of very large values of magnetoresistance in a graphene nanoribbon device. Nat Nanotechnol 3:408–412

Kim KS, Zhao Y, Jang H, Lee SY, Kim JM, Kim KS, Ahn JH, Kim P, Choi JY, Hong BH (2009) Large-scale pattern growth of graphene films for stretchable transparent electrodes. Nature 457:706–710

Kuo SL, Lee JF, Wu NL (2007) Study on pseudocapacitance mechanism of aqueous $MnFe_2O_4$ supercapitor. J Electrochem Soc 154:A34–A38

Lai J, Shafi KVPM, Ulman A, Loos K, Yang N, Cui MH, Estournès TVC, Locke DC (2004) Mixed iron–manganese oxide nanoparticles. J Phys Chem B 108:14876–14883

Lakshmipathiraj P, Narasimhan BRV, Prabhakar S, Raju BB (2006) Adsorption studies of arsenic on Mn-substituted iron oxyhydroxide. J Colloid Interface Sci 304:317–322

Lee M-T (1988) Catalytic behaviors of Fe–Mn mixed oxides, National Science Council, Republic of Chaina. PB 90140971, 1–52

Lian P, Zhu X, Liang S, Li Z, Wang W, Wang H (2010) Large reversible capacity of high quality grapheme sheets as an anode material for lithium ion batteries. Electrochem Acta 55:3909–3914

Lin TF, Wu JK (2001) Adsorption of arsenite and arsenate within activated alumina grains: equilibrium and kinetics. Water Res 35:2049–2057

Luoa X, Wanga C, Luoa S, Donga R, Tua X, Zenga G (2012) Adsorption of As(III) and As(V) from water using magnetite Fe_3O_4-reduced graphite oxide–MnO_2 nanocomposites. Chem Eng J 187:45–52

Marcano DC, Kosynkin DV, Berlin JM, Sinitskii A, Sun Z, Slesarev A, Alemany LB, Lu W, Tour JM (2010) Improved synthesis of graphene oxide. ACS Nano 4:4806–4814

Matsuo Y, Nishino Y, Fukutsuka T, Sugie Y (2008) Removal of formaldehyde from gas phase by silylated graphite oxide containing amino groups. Carbon 46:1162–1163

Mauter MS, Elimelech M (2008) Environmental applications of carbon-based nanomaterials. Environ Sci Technol 42: 5843–5859

McArthur JM, Ravenscroft P, Saifiullah S, Thirwall MF (2001) Arsenic in groundwater: testing pollution mechanisms for sedimentary aquifers in Bangladesh. Water Res 37: 109–117

Meyer JC, Geim AK, Katsnelson MI, Novoselov KS, Booth TJ, Roth S (2007) The structure of suspended grapheme sheets. Nature 446:60–63

Miyamoto J, Kanoh H, Kaneko K (2005) The addition of mesoporosity to activated carbon fibers by a simple reactivation process. Carbon 43:855–857

Mohan D, Pittman CU Jr (2007) Arsenic removal from water/wastewater using adsorbents—a critical review. J Hazard Mater 147:1–53

Mondal P, Majumder CB, Mohanty B (2006) Laboratory based approaches for arsenic remediation from contaminated water: recent developments. J Hazard Mater B137: 464–479

Moon G, Park Y, Kim W, Choi W (2011) Photochemical loading of metal nanoparticles on reduced graphene oxide sheets using phosphotungstate. Carbon 49:3454–3462

Nakamoto K (1986) Infrared and Raman spectra of inorganic and coordination compounds, 4th edn. Wiley, New York, p 74

Nandi D, Ghosh AK, Gupta K, De A, Sen P, Duttachowdhury A, Ghosh UC (2012) Polypyrrole–titanium(IV) doped iron(III) oxide nanocomposites: synthesis, characterization with tunable electrical and electrochemical properties. Mater Res Bull 47:2095–2103

Nesbitt HW, Canning GW, Bancroft GM (1998) XPS study of reductive dissolution of 7 Å-birnessite by H_3AsO_3, with constraints on reaction mechanism. Geochim Cosmochim Acta 62:2097–2110

Nethravathi C, Rajamathi M (2008) Chemically modified graphene sheets produced by the solvothermal reduction of colloidal dispersions of graphite oxide. Carbon 46: 1994–1998

Nickson RT, McArthur JM, Burgess WG, Ravenscroft P, Ahmed KM, Rahaman M (1998) Arsenic poisoning in Bangladesh groundwater. Nature 395:338

Novoselov KS, Geim AK, Morozov SV, Jiang D, Zhang Y, Dubonos SV, Grigorieva IV, Firsov AA (2004) Electric field effect in atomically thin carbon films. Science 306:666–669

Osmokrovi P, Jovaleki C, Manojlovi D, Pavlovi MB (2006) Synthesis of $MnFe_2O_4$ nanoparticles by mechanochemical reaction. J Optoelectron Adv Mater 8:312–314

Pan D, Wang S, Zhao B, Wu M, Zhang H, Wang Y, Jiao Z (2009) Storage properties of disordered graphene nanosheets. Chem Mater 21:3136

Ramanathan T, Abdala AA, Stankovich S, Dikin DA, Alonso MH, Piner RD, Adamson DH, Schniepp HC, Chen X, Ruoff RS et al (2008) Functionalized graphene sheets for polymer nanocomposites. Nat Nanotechnol 3:327–331

Roberts LC, Hug SJ, Ruettimann T, Billah M, Khan AW, Rahman MT (2004) Arsenic removal with iron(II) and iron(III) in waters with high silicate and phosphate concentrations. Environ Sci Technol 38:307–315

Schedin F, Geim AK, Morozov SV, Hill EW, Blake P, Katsnelson MI, Novoselov KS (2007) Detection of individual gas molecules adsorbed on graphene. Nat Mater 6:652–655

Seredych M, Bandosz TJ (2007) Removal of ammonia by graphite oxide via its intercalation and reactive adsorption. Carbon 45:2130–2132

Si Y, Samulski ET (2008) Synthesis of water soluble graphene. Nano Lett 8:1679–1682

Silva GC, Almeida FS, Ferreira AM, Ciminelli VST (2012). Preparation and application of a magnetic composite (Mn_3O_4/Fe_3O_4) for removal of As(III) from aqueous solutions. Mater Res 15(3):403–408

Smedley PL, Kinniburgh G (2002) A review of the source, behaviour and distribution of arsenic in natural waters. Appl Geochem 17:517–568

Sreeprasad TS, Maliyekkal SM, Lisha KP, Pradeep T (2011) Reduced graphene oxide–metal/metal oxide composites: facile synthesis and application in water purification. J Hazard Mater 186:921–931

Tuinstra F, Koenig JL (1970) Raman spectrum of graphite. J Chem Phys 53:1126–1130

Wang X, Zhi L, Mullen K (2008) Transparent, conductive graphene electrodes for dye-sensitized solar cells. Nano Lett 8:323–327

Yang X, Zhang X, Ma Y, Huang Y, Chen Y, Wang Y (2009) Superparamagnetic graphene oxide Fe_3O_4 nanoparticles hybrid for controlled targeted drug carriers. J Mater Chem 19:2710–2714

Yang S-T, Chang Y, Wang H, Liu G, Chen S, Wang Y, Liu Y, Cao A (2010) Folding/aggregation of graphene oxide and its application in Cu^{2+} removal. J Colloid Interface Sci 351:122–127

Yang S-T, Chen S, Zhang L, Huang J, Chen F, Yang Z, Yao J, Zhang Z (2011) Controlled assembly of Fe_3O_4 magnetic nanoparticles on graphene oxide. Nanoscale 3:1446–1450

Yu YJ, Zhao Y, Ryu S, Brus L, Kim KS, Kim P (2009) Charge transfer chemical doping of few layer graphenes: charge distribution and band gap formation. Nano Lett 9:3430–3434

Zhang S, Li X, Chen JP (2010a) Preparation and evaluation of a magnetite-doped activated carbon fiber for enhanced arsenic removal. Carbon 48:60–67

Zhang K, Dwivedi V, Chi CY, Wu JS (2010b) Graphene oxide/ferric hydroxide composites for efficient arsenate removal from drinking water. J Hazard Mater 182:162–168

DOI 10.1007/978-3-319-05041-6_13
Reprinted from the *Journal of Nanoparticle Research*, DOI 10.1007/s11051-012-0881-x

RESEARCH PAPER

Arsenic removal by magnetic nanocrystalline barium hexaferrite

Hasmukh A. Patel · Jeehye Byun · Cafer T. Yavuz

Received: 13 November 2011 / Accepted: 18 April 2012 / Published online: 28 June 2012

Abstract Nanoscale magnetite (Fe_3O_4) (<15 nm) is known to remove arsenic efficiently but is very difficult to separate or require high magnetic fields to separate out from the waste water after treatment. Anisotropic hexagonal ferrite ($BaFe_{12}O_{19}$, BHF) is a well-known permanent magnet (i.e., fridge magnets) and attractive due to its low cost in making large quantities. BHF offers a viable alternative to magnetite nanocrystals for arsenic removal since it features surfaces similar to iron oxides but with much enhanced magnetism. Herein, we employ BHF nanocrystalline materials for the first time in arsenic removal from wastewater. Our results show better (75 %) arsenic removal than magnetite of the similar sizes. The BHF nanoparticles, 6.06 ± 0.52 nm synthesized by thermolysis method at 320 °C do not show hexagonal phase, however, subsequent annealing at 750 °C produced pure hexagonal BHF in >200 nm assemblies. By using BHF, we demonstrate that nanoparticle removal is more efficient and fixed bed type cartridge applications are more possible.

Keywords Hexaferrites · Nanoparticles · Magnetic · Arsenic removal · Adsorption · Magnetite · Sustainable development · Water resources

Special Issue Editors: Mamadou Diallo, Neil Fromer, Myung S. Jhon

This article is part of the Topical Collection on Nanotechnology for Sustainable Development

H. A. Patel · J. Byun · C. T. Yavuz (✉)
Graduate School of EEWS, Korea Advanced Institute of Science and Technology (KAIST), Daejeon 305-701, Republic of Korea
e-mail: yavuz@kaist.ac.kr
URL: http://yavuz.kaist.ac.kr/

Introduction

Arsenic is one of the most toxic contaminants found in the environment and has been recognized as a toxic element for centuries. Arsenic contamination has become a worldwide epidemic, especially in developing countries where a significant percentage of the population depends on groundwater for drinking. Elevated concentrations of arsenic in groundwater are found in many countries such as India, Bangladesh, Vietnam, and Chile (Mohan and Pittman 2007; Acharyya et al. 1999; Sharma and Sohn 2009).

The toxicity of arsenic to human health ranges from skin lesions to cancer of the brain, liver, kidney, and stomach. A wide range of arsenic toxicity has been determined that depends on arsenic speciation. Generally inorganic arsenic species are more toxic than organic forms to living organisms, including humans and other animals. To minimize the health impact of arsenic, the United States Environmental Protection Agency adopted a new maximum contaminant level of 10 μg/L in drinking water on January 22, 2001 (Pena et al. 2005). Arsenic is naturally present in groundwater

in the forms of arsenite (AsO_3^{3-}) and arsenate (AsO_4^{3-}). These anions resemble phosphite (HPO_3^{2-}) and phosphate (PO_4^{3-}) ions, and it is this similarity that is the dominant source of their toxicity: arsenite and arsenate block ATP → ADP conversions by permanently replacing phosphate groups (Yavuz et al. 2010).

Among methods developed to remove the arsenic from contaminated water such as coagulation and flocculation, precipitation, ion exchange, and membrane filtration, adsorption is the most widely used because it is simple, cost-effective, and sludge-free. The effectiveness of adsorption primarily depends on the characteristics of the adsorbent; therefore, there has been considerable interest in identifying the proper adsorbents for arsenic removal. So far, many adsorbents such as zirconium based gel (Biswas et al. 2008), agricultural residue (Ranjan et al. 2009; Shipley et al. 2011), iron modified bauxite (Bhakat et al. 2006), porous materials (Li et al. 2007), modified carbon black (Borah et al. 2009) and polymeric materials (Cumbal et al. 2003; Lim et al. 2009) have been developed for the removal of arsenic. Magnetically activated adsorbents, especially magnetite nanoparticles have been extensively studied as a promising adsorptive material and offer new opportunities for enhanced separation in complex environmental systems due to their durability, resistance to oxidation, less susceptibility to fouling by natural organic matters, high isoelectric point, high surface area, and selectivity for arsenic species (Beker et al. 2010; Tang et al. 2011; Yavuz et al. 2006; Yean et al. 2005; Mayo et al. 2007; Yavuz et al. 2010; Yavuz et al. 2009; Yean et al. 2005). As(III) is more mobile and toxic (25–60 times) than As(V). This elevated toxicity is due to its preferential reaction with sulfhydryl groups in mammalian enzymes (Pena et al. 2005). As(III) is also known to prefer neutral species (H_3AsO_3) at conventional water pH ranges i.e., pH 6–8, unlike As(V), making it more difficult to remove as shown in Table 1.

Nanoscale magnetic iron oxides show great promise in applications such as magnetic data storage, water treatment, ferrofluids, medical imaging, drug targeting, and catalysis, because of their inexpensive, non-toxic and high temperature stability (Kwon and Hyeon 2008; Zeng et al. 2002; Yavuz et al. 2006; Zhao et al. 2011). Among magnetic iron oxides, the hexagonal ferrites, especially barium hexaferrite ($BaFe_{12}O_{19}$, BHF) receive the widest commercial interest due to their availability and high magnetocrystalline anisotropy (1.7 T), featuring high coercivity, remanent magnetization and ferromagnetic resonance (Tucek et al. 2010). The enhanced magnetism identifies BHF as an improved magnetic adsorbent since its parent iron oxide, magnetite shows significant arsenic removal (Yavuz et al. 2006).

Table 1 Effect of pH on the ionic state of As(III) and As(V)

For As(III)	
$H_3AsO_3 \rightarrow H_2AsO_3^- + H^+$	$pK_{a1} = 9.22$
$H_2AsO_3^- \rightarrow HAsO_3^{2-} + H^+$	$pK_{a2} = 12.13$
$HAsO_3^{2-} \rightarrow AsO_3^{3-} + H^+$	$pK_{a3} = 13.40$
For As(V)	
$H_3AsO_4 \rightarrow H_2AsO_4^- + H^+$	$pK_{a1} = 2.2$
$H_2AsO_4^- \rightarrow HAsO_4^{2-} + H^+$	$pK_{a2} = 6.97$
$HAsO_4^{2-} \rightarrow AsO_4^{3-} + H^+$	$pK_{a3} = 11.53$

Though there have been a number of attempts to synthesize nanoparticles of BHF by various techniques (Junliang et al. 2010), such as thermolysis, reverse micro-emulsion, co-participation, hydrothermal process, sol–gel route, none resulted in highly monodisperse nanocrystals. On the contrary, monodisperse transition metal-based ferrite nanoparticles, $MnFe_2O_4$, $CoFe_2O_4$, $NiFe_2O_4$, $FeFe_2O_4$, are well documented, where high temperature aging of metal–surfactant complexes are commonly employed (Hyeon et al. 2002; Bao et al. 2007).

In this brief communication, we attempt to utilize barium hexaferrites for the removal of As(III) from contaminated waters. To the best of our knowledge this is the first report in BHF-mediated arsenic removal. By using BHF, we demonstrate that nanoparticle removal is more efficient and fixed bed type cartridge applications are more probable. BHFs were synthesized by a successful thermolysis of ferric hydroxide, barium hydroxide, oleic acid in 1-octadecene and subsequent annealing.

Experimental

Materials

1-Octadecene (technical grade, 90 %) and oleic acid (99 %) were obtained from Sigma-Aldrich, USA. Iron(III) hydroxide (90 %), barium hydroxide octahydrate (97 %), *n*-hexane (99.5 %), magnetite (50–100 nm) and ethyl alcohol (99.5 %) were

obtained from SAMCHUN, South Korea. As(III) standard solution (1,000 mg/L) was purchased from Fluka.

Synthesis of BHF ($BaFe_{12}O_{19}$)

0.979 g (11 mmol) Iron (III) hydroxide and 0.31 g (0.96 mmol) barium hydroxide octahydrate were mixed and powdered using mortar-pestle. This mixture, 11.3 g (40 mmol) oleic acid and 25 g 1-octadecene were transferred into a 100 mL three-neck round bottom flask equipped with condenser, magnetic stirrer, thermocouple, and heating mantle. The reaction mixture was heated under vigorous stirring at 5 °C/min up to 320 °C and kept at this temperature for 90 min under dinitrogen environment. Subsequently, the resulted black mixture was cooled down to room temperature and washed several times with ethyl alcohol. The wax-like black material was then dispersed into *n*-hexane for further characterization and designated as BHF. The BHF nanoparticles were annealed at 550 and 750 °C at a heating rate of 5 °C/min and the temperature were maintained for 2 h. The annealed samples are designated as BHF-550 and BHF-750.

As(III) adsorption and desorption study

Arsenic adsorption experiments were performed with 0.1, 0.5, 1, 5, and 10 mg/L of As(III) solutions, prepared in an electrolyte solution containing 0.01 M NaCl, 0.01 M tris(hydroxymethylamino)methane buffer, and 0.01 M NaN_3 at pH 8. All experiments were performed in batches with 10 mg of sample/L of solution. Equilibrium time was 24 h, with constant tumbling. The solution was separated from BHF by a strong magnet and aliquots were analyzed for As(III) concentration by ICP-AES and ICP-MS. The data of arsenic adsorption was analyzed by Langmuir and Freundlich isotherm models. Desorption was conducted as batch experiments in aqueous alkaline solution of sodium hydroxide (pH 13). After adsorption cycle, BHF-750 was separated, dispersed in 10 mL of alkaline solution and allowed for tumbling for 24 h at room temperature. The particles were magnetically removed and solutions were acidified by dilute nitric acid for arsenic measurement.

Characterization

TEM images were collected by Field Emission Transmission Electron Microscope (FE-TEM, 200 kV, Tecnai F20). Samples for TEM investigations were prepared by putting an aliquot of *n*-hexane solution of nanoparticles onto an amorphous carbon substrate supported on a copper grid. The excess liquid was then removed, and the grid was allowed to dry at room temperature. In order to investigate the morphology of annealed BHF particles, sample loaded on Si(100) wafer were characterized by scanning electron microscopy (SEM, Magellan400). X-ray diffraction analyses were carried out using Micro-area X-ray diffractometer (Rigaku, D/MAX-2500). The quantitative analyses of Iron, barium, and arsenic were measured by inductively coupled plasma atomic emission spectroscopy (ICP-AES) or inductively coupled plasma atomic mass spectroscopy (ICP-MS). BHF was digested in concentrated nitric acid for elemental analysis.

Results and discussion

The powder XRD patterns (Fig. 1) of the BHF synthesized at different temperatures clearly reveal that hexaferrites phase is formed after annealing at 750 °C. The diffraction peaks at 2 θ value of 30.34°, 32.31°, 34.17°, 37.15°, 56.8°, and 63.16° correspond to diffraction planes (110), (107), (114), (203), (2011) and (2200), respectively. These patterns can be ascribed to hexagonal $BaFe_{12}O_{19}$ phase (JCPDS # 84-0757). The BHF-750 is in single phase with hexagonal structure without showing any detectable impurities. The as-made BHF contains Fe_2O_3 and Fe_3O_4 as major phases (JCPDS # 86-0550 and 79-0417) therefore it was annealed at 550 and 750 °C. Annealing below 750 °C does not result in hexagonal phase, as evident from XRD patterns. The crystallite size of BHF-750 has been calculated from the Debye–Scherrer formula (Hessien et al. 2008; Patel et al. 2008), using the full width at half maximum (FWHM) value of the most intense peak (114) in the X-ray patterns using,

$$\text{Crystallite size} = K\lambda/W\cos\theta$$

where $W = W_b - W_s$ and W_b is the broadened profile width of experimental sample and W_s is the standard profile width of reference silica sample.

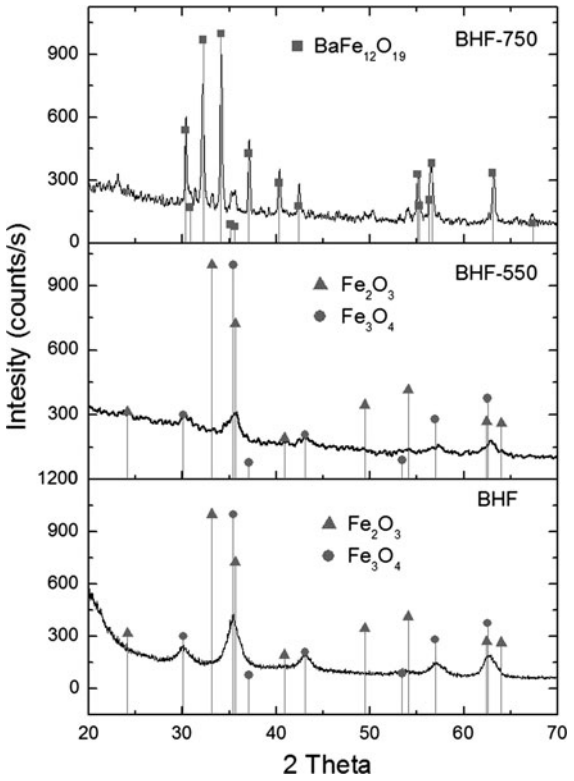

Fig. 1 X-ray diffraction patterns of as-synthesized BHF and annealed BHF-550, BFH-750

The crystallite size of BHF-750 is 61.7 nm, however, the particle size of BHF-750 varies from 200–550 nm.

TEM image (Fig. 2a) showed particles of spherical shapes, uniform in size with an average particle diameter of 6.06 ± 0.52 nm for BHF. The particle sizes are consistent throughout the sample as observed from TEM images. The chemical compositions measured by ICP-AES show Fe/Ba molar ratio is 11.6, fit well with the theoretical ratio in corresponding barium and strontium hexaferrite compounds. Although Fe/Ba = 11.6 is observed in BHF, XRD pattern suggest that there is no evidence of hexagonal phase formation. This implies that barium is not integrated and it requires higher temperature for inclusion of barium into hexagonal phase. The annealing of BHF nanoparticles distorted size, which resulted agglomeration and size of BHF-750 increased substantially. The SEM image reveals agglomerated particles of BHF-750 (Fig. 2b) with particle size varies from 200–550 nm.

We use As(III) as a typical contaminant to investigate the potential application of BHF in environment pollution control. As one of the most toxic and carcinogenic chemical elements, arsenic has been recorded as a priority issue by the World Health Organization (WHO). Today, perhaps more than 100 million people in India, Bangladesh, Vietnam, Nepal, China, and possibly other countries are drinking water with arsenic concentrations up to 100 times the WHO guideline of 10 μg/L. Batch experiments were conducted to determine As(III) removal efficiency for BHF-750. In batch experiment, 10 mg/L of BHF was interacted with As(III) solutions of 0.1, 0.5, 1, 5, and 10 mg/L. Figure 3 shows the As(III) removal with respect to various concentration. Initially, adsorption of As(III) occurred rapidly up to As(III) concentration of 1 mg/L. The arsenic removal efficiency at this point is 0.88 mg/g. After this, saturation begins, indicates equilibrium of As(III) was started and attained complete saturation at 10 mg/L where arsenic removal efficiency is 2.37 mg/g.

The isotherm models of Langmuir and Freundlich were used to fit the experimental adsorption equilibrium data of arsenic on BHF-750 (Zhao et al. 2010; Mayo et al. 2007). Adsorption isotherms, which are the presentation of the amount of solute adsorbed per unit of adsorbent as a function of equilibrium concentration in solution at constant temperature, were also studied. The Langmuir isotherm is valid for single-layer adsorption. It is based on the assumption that all the adsorption sites have equal affinity for molecules of the adsorbate and there is no transmigration of the adsorbate in the plane of the surface. Langmuir isotherm is presented as,

$$q_e = \frac{q_m K_L C_e}{1 + K_L C_e}$$

The Freundlich equation deals with physico-chemical adsorption on heterogenous surfaces (indicates the adsorptive capacity or loading factor) and is presented as,

$$q_e = K_F C_e^{1/n}$$

where C_e (mg/L) is the concentration of arsenic at equilibrium, K_L (L/mg), and q_m (mg/g) are the Langmuir constants related to the energy of adsorption and maximum capacity, respectively; K_F ($mg^{1-(1/n)}\ L^{1/n}\ g^{-1}$) and 1/n are the Freundlich constants

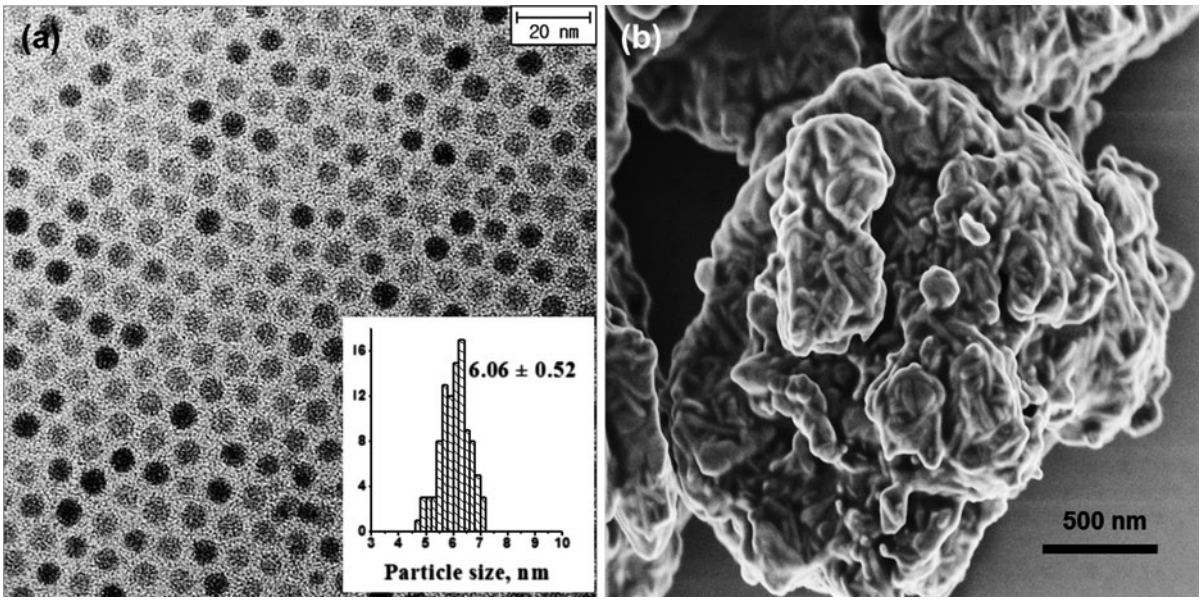

Fig. 2 **a** TEM image and particle size distribution of BHF, and **b** SEM image of annealed BHF-750

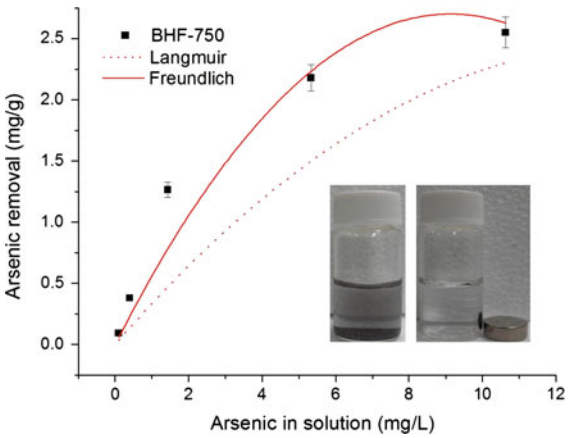

Fig. 3 Arsenic adsorption studies with nanocrystalline BHF-750 (*Inset* easy separation of BHF-750 from wastewater)

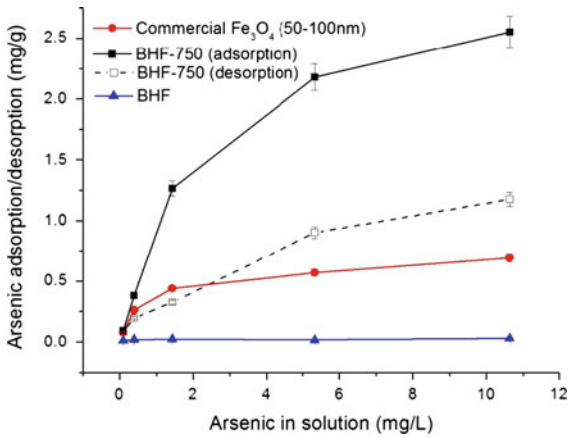

Fig. 4 Arsenic adsorption/desorption studies on BHF-750, arsenic adsorption studies on commercial Fe_3O_4 (50–100 nm) and uncalcined BHF

related to the adsorption capacity and intensity, respectively; and q_e (mg/g) is the mass of arsenic adsorbed per mass of adsorbent. Regression coefficients (r^2) for Langmuir and Freundlich isotherm is 0.92 and 0.96, indicating that both the models fit reasonably well with As(III) adsorption. The maximum monolayer adsorption capacity (q_m) obtained for BHF-750 is 2.27 mg/g which is comparable with experimental capacity of 2.55 mg/g. The Freundlich adsorption intensity parameters (n) is 3.8, also supporting the favorable adsorption of As(III) on BHF-750.

As(III) removal efficiency of BHF-750 is higher than the capacity of commercial magnetite, Fe_3O_4 (0.25 mg/g) of 300 nm size (Yavuz et al. 2006). Furthermore, commercial Fe_3O_4 (50–100 nm) and BHF (non-calcined sample) were also studied for As(III) removal under identical conditions as shown in Fig. 4. The As(III) removal capacity for commercial Fe_3O_4 and BHF is 0.7 and 0.03 mg/g. This behavior

Table 2 Recovery efficiencies of BHF-750 after As(III) adsorption tests

As(III) concentration (mg/L)	Initial dosage of BHF-750 (g)	Residual BHF (after treatment) (g)	%	Remarks
0.1	0.0098	0.0113	115	Residual BHF-750 was weighed after drying for 3 h at 90 °C
0.5	0.012	0.0098	82	
1	0.0099	0.0095	96	
5	0.01	0.014	140	
10	0.0098	0.0121	123	

suggests that hexaferrites of nanodimensional sized gave better arsenic removal efficiency than commercial Fe_3O_4 nanoparticles. The arsenic adsorption was reduced significantly at high pH and arsenic was desorbed from the magnetite at alkaline pH (Yean et al. 2005; Phu et al. 2009). After arsenic adsorption, BHF-750 were treated with alkaline solution of pH 13 for desorption of arsenic (Fig. 4). It was found that 55 % of the arsenic was desorbed from BHF-750.

Recovery of BHF-750 after arsenic removal was calculated by measuring post-treatment weight of magnetically separated adsorptive media (Table 2). The sorbents were dried for 3 h at 90 °C to make sure no water remained adsorbed. The recoveries were mostly found to exceed quantitative amounts, suggesting that adsorbed species tend to immobilize on the surface in the form of arsenites or hydroxylates.

Conclusions

In summary, we found that BHF nanoparticles offer better arsenic capacity and much versatile handling than their magnetite counterparts. This behavior proves useful when the removal of arsenic by magnetic nanoparticles are taken to the actual field operations. However, it is found to be difficult to form barium hexaferrite hexagonal phase at low temperatures. Only, the subsequent annealing at 750 °C of BHF nanoparticles synthesized by solvothermal method resulted hexagonal phase. Size control and monodispersity of BHF nanoparticles are lost after annealing, as expected. Arsenic removal efficiency of annealed BHF (BHF-750) is 75 % which is quite higher than magnetite nanoparticles of similar size. This proves that metal hexaferrites are potential materials for heavy metal removal application from wastewater. Moreover, hard magnetic behavior of metal hexaferrites may solve the problem of separation of treated nanoparticles from water at low magnetic field. When attempted to recycle the adsorbent, it was found that 55 % of the arsenic was desorbed from BHF-750 in aqueous alkaline solution.

Acknowledgments This study is supported by KAIST EEWS Initiative 2011–2013 for the development of enhanced water treatment technologies by nanoscale ferrites and their carbon assemblies. This work was also supported by the National Research Foundation of Korea Grant funded by the Korean Government (MEST) (NRF-2012-C1AAA001-M1A2A2026588).

References

Acharyya SK, Chatraborty P, Lahiri S, Raymahashay BC, Guha S, Bhowmik A (1999) Arsenic poisoning in the Ganges delta. Nature 401:545–546

Bao N, Shen L, Wang Y, Padhan P, Gupta A (2007) A facile thermolysis route to monodisperse ferrite nanocrystals. J Am Chem Soc 129:12374–12375

Beker U, Cumbal L, Duranoglu D, Kucuk I, Sengupta AK (2010) Preparation of Fe oxide nanoparticles for environmental applications: arsenic removal. Environ Geochem Health 32:291–296

Bhakat PB, Gupta AK, Ayoob S, Kundu S (2006) Investigations on arsenic(V) removal by modified calcined bauxite. Colloids Surf A 281:237–245

Biswas BK, Inoue J, Inoue K, Ghimire KN, Harada H, Ohto K, Kawakita H (2008) Adsorptive removal of As(V) and As(III) from water by a Zr(IV)-loaded orange waste gel. J Hazard Mater 154:1066–1074

Borah D, Satokawa S, Kato S, Kojima T (2009) Sorption of As(V) from aqueous solution using acid modified carbon black. J Hazard Mater 162:1269–1277

Cumbal L, Greenleaf J, Leun D, SenGupta AK (2003) Polymer supported inorganic nanoparticles: characterization and environmental applications. React Funct Polym 54:167–180

Hessien MM, Rashad MM, El-Barawy K (2008) Controlling the composition and magnetic properties of strontium hexaferrite synthesized by co-precipitation method. J Magn Magn Mater 320:336–343

Hyeon T, Chung Y, Park J, Lee SS, Kim Y-W, Park BH (2002) Synthesis of highly crystalline and monodisperse cobalt ferrite nanocrystals. J Phys Chem B 106:6831–6833

Junliang L, Yanwei Z, Cuijing G, Wei Z, Xiaowei Y (2010) One-step synthesis of barium hexaferrite nano-powders via microwave-assisted sol–gel auto-combustion. J Eur Ceram Soc 30:993–997

Kwon SG, Hyeon T (2008) Colloidal chemical synthesis and formation kinetics of uniformly sized nanocrystals of metals, oxides, and chalcogenides. Acc Chem Res 41(12):1696–1709

Li Z, Beachner R, McManama Z, Hanlie H (2007) Sorption of arsenic by surfactant-modified zeolite and kaolinite. Microporous Mesoporous Mater 105:291–297

Lim S-F, Zheng Y-M, Paul Chen J (2009) Organic arsenic adsorption onto a magnetic sorbent. Langmuir 25(9):4973–4978

Mayo JT, Yavuz C, Yean S, Cong L, Shipley H, Yu W, Falkner J, Kan A, Tomson M, Colvin VL (2007) The effect of nanocrystalline magnetite size on arsenic removal. Sci Technol Adv Mater 8:71–75

Mohan D, Pittman CU Jr (2007) Arsenic removal from water/wastewater using adsorbents—a critical review. J Hazard Mater 142(1–2):1–53

Patel HA, Bajaj HC, Jasra RV (2008) Synthesis of Pd and Rh metal nanoparticles in the interlayer space of organically modified montmorillonite. J Nanopart Res 10:625–632

Pena ME, Korfiatis GP, Patel M, Lippincott L, Meng X (2005) Adsorption of As(V) and As(III) by nanocrystalline, Titanium dioxide. Water Res 39:2327–2337

Phu ND, Phong PC, Chau N, Luong NH, Hoang LH, Hai NH (2009) Arsenic removal from water by magnetic $Fe_{1-x}Co_xFe_2O_4$ and $Fe_{1-y}Ni_yFe_2O_4$ nanoparticles. J Exp Nanosci 4(3):253–258

Ranjan D, Talat M, Hasan SH (2009) Biosorption of arsenic from aqueous solution using agricultural residue 'rice polish'. J Hazard Mater 166:1050–1059

Sharma VK, Sohn M (2009) Aquatic arsenic: toxicity, speciation, transformations, and remediation. Environ Int 35:743–759

Shipley HJ, Engates KE, Guettner AM (2011) Study of iron oxide nanoparticles in soil for remediation of arsenic. J Nanopart Res 13:2387–2397

Tang W, Li Q, Li C, Gao S, Shang JK (2011) Ultrafine α-Fe_2O_3 nanoparticles grown in confinement of in situ self-formed ''cage'' and their superior adsorption performance on arsenic(III). J Nanopart Res 13:2641–2651

Tucek J, Zboril R, Namai A, Ohkoshi S (2010) ε-Fe_2O_3: an advanced nanomaterial exhibiting giant coercive field, millimeter-wave ferromagnetic resonance, and magnetoelectric coupling. Chem Mater 22:6483–6505

Yavuz CT, Mayo JT, Yu WW, Prakash A, Falkner JC, Yean S, Cong L, Shipley HJ, Kan A, Tomson M, Natelson D, Colvin VL (2006) Low-field magnetic separation of monodisperse Fe_3O_4 nanocrystals. Science 314:964–967

Yavuz CT, Prakash A, Mayo JT, Colvin VL (2009) Magnetic separations: from steel plants to biotechnology. Chem Eng Sci 64:2510–2521

Yavuz CT, Mayo JT, Suchecki C, Wang J, Ellsworth AZ, D'Couto H, Quevedo E, Prakash A, Gonzalez L, Nguyen C, Kelty C, Colvin VL (2010) Pollution magnet: nanomagnetite for arsenic removal from drinking water. Environ Geochem Health 32:327–334

Yean S, Cong L, Yavuz CT, Mayo JT, Yu WW, Colvin VL, Tomson MB (2005) Effect of magnetite particle size on adsorption and desorption of arsenite and arsenate. J Mater Res 20(12):3255–3264

Zeng H, Li J, Liu JP, Wang ZL, Sun S (2002) Exchange-coupled nanocomposite magnets by nanoparticles self-assembly. Nature 420:395–398

Zhao X, Wang J, Wub F, Wang T, Cai Y, Shi Y, Jiang G (2010) Removal of fluoride from aqueous media by Fe_3O_4@Al$(OH)_3$ magnetic nanoparticles. J Hazard Mater 173:102–109

Zhao X, Guo X, Yang Z, Liu H, Qian Q (2011) Phase-controlled preparation of iron (oxyhydr)oxide nanocrystallines for heavy metal removal. J Nanopart Res 13:2853–2864

DOI 10.1007/978-3-319-05041-6_14
Reprinted from the *Journal of Nanoparticle Research*, DOI 10.1007/s11051-012-0846-0

RESEARCH PAPER

Removal of heavy metals from aqueous solutions using Fe_3O_4, ZnO, and CuO nanoparticles

Shahriar Mahdavi · Mohsen Jalali · Abbas Afkhami

Received: 6 October 2011 / Accepted: 22 March 2012 / Published online: 5 July 2012

Abstract This study investigated the removal of Cd^{2+}, Cu^{2+}, Ni^{2+}, and Pb^{2+} from aqueous solutions with novel nanoparticle sorbents (Fe_3O_4, ZnO, and CuO) using a range of experimental approaches, including, pH, competing ions, sorbent masses, contact time, scanning electron microscopy, transmission electron microscopy, and X-ray diffraction. The images showed that Fe_3O_4, ZnO, and CuO particles had mean diameters of about 50 nm (spheroid), 25 nm (rod shape), and 75 nm (spheroid), respectively. Tests were performed under batch conditions to determine the adsorption rate and uptake at equilibrium from single and multiple component solutions. The maximum uptake values (sum of four metals) in multiple component solutions were 360.6, 114.5, and 73.0 mg g^{-1}, for ZnO, CuO, and Fe_3O_4, respectively. Based on the average metal removal by the three nanoparticles, the following order was determined for single component solutions: $Cd^{2+} > Pb^{2+} > Cu^{2+} > Ni^{2+}$, while the following order was determined in multiple component solutions: $Pb^{2+} > Cu^{2+} > Cd^{2+} > Ni^{2+}$. Sorption equilibrium isotherms could be described using the Freundlich model in some cases, whereas other isotherms did not follow this model. Furthermore, a pseudo-second order kinetic model was found to correctly describe the experimental data for all nanoparticles. Scanning electron microscopy, energy dispersive X-ray before and after metal sorption, and soil solution saturation indices showed that the main mechanism of sorption for Cd^{2+} and Pb^{2+} was adsorption, whereas both Cu^{2+} and Ni^{2+} sorption were due to adsorption and precipitation. These nanoparticles have potential for use as efficient sorbents for the removal of heavy metals from aqueous solutions and ZnO nanoparticles were identified as the most promising sorbent due to their high metal uptake.

Keywords Nanoparticles · Heavy metals · Removal · Aqueous solutions · Environmental and health effects · Sustainability

Special Issue Editors: Mamadou Diallo, Neil Fromer, Myung S. Jhon

This article is part of the Topical Collection on Nanotechnology for Sustainable Development

S. Mahdavi (✉) · M. Jalali
Department of Soil Science, College of Agriculture, Bu-Ali Sina University, Hamedan, Iran
e-mail: smahdaviha@yahoo.com

M. Jalali
e-mail: jalali@basu.ac.ir

A. Afkhami
Department of Analytical Chemistry, College of Chemistry, Bu-Ali Sina University, Hamedan, Iran
e-mail: afkhami@basu.ac.ir

Introduction

Industrial activities can lead to heavy metal contamination of surface and groundwater. Heavy metals are toxic to humans and they persist in the environment,

the need for processes to remove heavy metals has received increasing attention (Afkhami et al. 2010; Chen and Li 2010; Ezoddina et al. 2010).

Recent approaches for the removal of heavy metals from wastewaters have mainly included chemical precipitation, adsorption, oxidation–reduction, evaporation, ionic exchange, electrochemical treatment, and membrane separation techniques (Mobasherpour et al. 2011a; Flores and Cabassud 1999; Rahmani et al. 2010). Some of these methods may be more effective than adsorption under certain conditions, but adsorption is considered the most attractive technique, because it is simple and the most cost-effective. It is also feasible to implement adsorption in full-scale applications and the process methods are rapid (Rahmani et al. 2010; Blanchard et al. 1984). There has been a recent emphasis on the use of alternative low-cost materials as potential sorbents for the removal of heavy metals. Thus, several inorganic and organic adsorbents have been proposed for use in adsorption methods, including zeolites, clay minerals, fly ash, biosorbents, and activated carbon (Savage and Diallo 2005; Abollino et al. 2003; Sheng et al. 2004; Wingenfelder et al. 2005; Ghorbel-Abid et al. 2009; Afkhami et al. 2011; Ahmadzadeh Tofighy and Mohammadi 2011). There is also a large amount of interest in the use of nanoparticles for the removal of heavy metals (Afkhami et al. 2010; Yantasee et al. 2007; Feng et al. 2011). Nanoparticles have several special properties, such as high surface area and adsorption capacity, unsaturated surfaces, simple operation, and simple production (Afkhami et al. 2010; Rahmani et al. 2010; Navrotsky 2000). Nanomaterials such as Nanoscale zero-valent iron (Fe^0), Fe_2O_3, Fe_3O_4, TiO_2, SiO_2, and Al_2O_3 are the most commonly used materials that have been applied as adsorbents (Afkhami and Norooz-Asl 2009; Chen and Li 2010; Rahmani et al. 2010; Hu et al. 2006; Sharma and Srivastava 2010; Recillas et al. 2011). Of these nanoparticles, Fe_3O_4 is the classical nanoparticle that is most widely used in wastewater treatment (Hu et al. 2006; Sharma and Srivastava 2010; Panneerselvam et al. 2011). Few studies have investigated the performance and mechanism of cationic heavy metal uptake by ZnO and CuO (Martinson and Reddy 2009; Singh et al. 2010). Thus, we selected one commonly used (Fe_3O_4) and two uncommonly used (CuO, ZnO) nanoparticles to evaluate the nature and properties of nanoparticles when applied to heavy metal removal. The aim of this research was therefore to investigate the kinetics and equilibria of the uptake efficiency of Cd^{2+}, Cu^{2+}, Ni^{2+}, and Pb^{2+} from aqueous solutions under batch conditions using nanostructured Fe_3O_4, ZnO, and CuO in single and multiple component solutions.

Materials and methods

Chemicals and methods for the characterization of nanoparticles

Solutions used for the metal sorption experiments were prepared as their chloride salts (Merck, Germany). Nanostructured Fe_3O_4, CuO, and ZnO were purchased (purity, 99.5 %) from Tecnan (www.tecnan-nanomat.es , Spain) and Nabond (www.nabond.com, China). Heavy metal analysis was conducted using a Varian SpectrAA 220 atomic absorption spectrophotometer. The crystallinity and phase identification of the adsorbent powders was determined by XRD (Seifert 300 diffractometer) with CuKα as the radiation source and Ni as the filter in the range $2\theta = 10$–$70°$. Scanning electron microscope–energy dispersive X-ray (SEM–EDX) measurements were made using a Philips XL30 to determine the nanoparticle morphology. The shape and dimensions of the adsorbents were determined by transmission electron microscopy (TEM) (Philips CM10, high tension at 100 kV). TEM samples were prepared by drop casting on carbon-coated copper TEM grids and the solvent was allowed to evaporate at room temperature. The surface area and average adsorption pore width of the selected fraction of nanostructures was determined by Brunauer–Emmett–Teller (BET)-nitrogen gas analysis using a Belsorp-mini II (BelJapan) for chemisorption measurement. A pH meter (Jenway 3510) was used for pH measurements.

Heavy metal adsorption analysis

Kinetic and adsorption capacity experiments were conducted in a series of 50 mL Falcon tubes containing 0.05 g (2 g L^{-1}) of the nanostructured materials (Fe_3O_4, ZnO, and CuO) with 25 mL of 100 mg L^{-1} metal ions solution at their native pH. The suspensions were shaken (100 rpm) at 25 °C. Solid/liquid phases were then separated by centrifugation (4,000 rpm) before samples were filtered through a 0.22 μm filter membrane (super pure filter, Sartorius Company). The concentration of heavy metals was measured by atomic absorption spectroscopy. The percentage removal was calculated as:

$$\%\text{Removal} = \left(\frac{C_0 - C_e}{C_0}\right) \times 100 \quad (1)$$

where C_0 and C_e are the initial and final concentration of heavy metals in the solution phase. All adsorption experiments were conducted in triplicate and the mean of three values was expressed in the results. The standard deviation was <5 %.

Effect of pH

The pH was adjusted by adding NaOH or HCl in a pH range from 2 to 7, while other conditions remained the same as the adsorption studies.

Effect of contact time

Batch experimental procedures were conducted with different shaking times of: 10, 20, 30, 40, 50, 60, 90, 120, and 180 min (with the exception of Fe_3O_4), and 24 h, while other conditions remained the same as the adsorption studies.

Kinetics modeling study

Linearized equations of pseudo-first order (Rahmani et al. 2010; Zhou et al. 2009; Chen and Li 2010) and pseudo-second order (Rahmani et al. 2010; Zhou et al. 2009; Chen and Li 2010) kinetic models were used to investigate the mechanism and rate of the metal adsorption process. The pseudo-first order kinetic model is given as:

$$\log(q_e - q_t) = \log q_e - \frac{K_1}{2.303} t \quad (2)$$

where q_e and q_t are the amounts of the metal ions adsorbed on the adsorbent in mg g^{-1} at equilibrium and at time t, respectively, while K_1 is the constant of first-order adsorption in 1/min. The pseudo-second order kinetic model statistical analysis is given as:

$$\frac{1}{q_t} = \frac{1}{K_2 q_e^2} + \frac{t}{q_e} \quad (3)$$

where K_2 is the rate constant of second-order adsorption in g mg^{-1} min^{-1}.

Effect of sorbent dosage

Batch experiments were conducted by mixing different sorbents masses of 0.5, 1, 2, 3, 4, and 5 g L^{-1}, while other conditions remained the same as the adsorption studies.

Adsorption isotherms

Adsorption isotherm experiments were conducted with Cd^{2+}, Cu^{2+}, Ni^{2+}, and Pb^{2+} solutions at different initial heavy metal concentrations (0, 10, 20, 30, 60, 100, 200, and 300 mg L^{-1}) at 25 °C, with 0.05 g (2 g L^{-1}) nanostructured materials and 25 mL of adsorbate at different concentrations, with 0.01 M $NaNO_3$ as the background salt. Isotherms were determined on the basis of batch analysis in single and competitive modes. The equilibrium heavy metal concentration in the liquid phase was determined using a standard atomic absorption spectroscopy method. To insure equilibrium and guarantee full adsorption, the nanoparticle suspensions were centrifuged after 24 h of equilibration. Freundlich and Langmuir equations (Afkhami et al. 2010; Rahmani et al. 2010; Afkhami and Norooz-Asl 2009; Afkhami and Moosavi 2010; Mobasherpour et al. 2011b) were fitted to data. The Freundlich equation is an empirical equation for describing the surface heterogeneity of a sorbent and it is commonly represented as:

$$\text{Log } q_e = \text{Log } k_F + 1/n \text{ Log } C_e \quad (4)$$

where q_e is the amount of heavy metal adsorbed per unit weight of adsorbent at a specified equilibrium (mg g^{-1}), C_e is the equilibrium concentration of the solution (mg L^{-1}), k_F is the Freundlich constant representing the adsorption capacity (mg g^{-1}), and n is a constant representing the adsorption intensity (dimensionless) where $n \ll 1$ indicates that the adsorbate was unfavorably adsorbed on the adsorbent and $1 < n < 10$ indicates that the adsorption was favorable. The Langmuir equation is based on an assumption of a structurally homogeneous adsorbent, and it is described using the following equation:

$$\frac{C_e}{q_e} = \frac{C_e}{q_0} + \frac{1}{q_0 b} \quad (5)$$

where q_e and C_e have the same definitions as in Eq. (4), q_0 (q_{max}) is the maximum adsorption at monolayer coverage (mg g^{-1}), and b (K_L) is the Langmuir constant related to the energy of adsorption that quantitatively reflects the affinity of the binding sites (L mg^{-1}).

Desorption procedure

Desorption experiments were performed immediately after the completion of the sorption experiments. After

removal of the supernatant and washing adsorbents three times with deionized water, 25 mL of 0.01 M $CaCl_2$ solutions were added to the centrifuge tubes. The centrifuge tubes were vortexed to disperse the adsorbent pellets and suspensions were mechanically shaken for 24 h. The suspensions were then centrifuged for 20 min

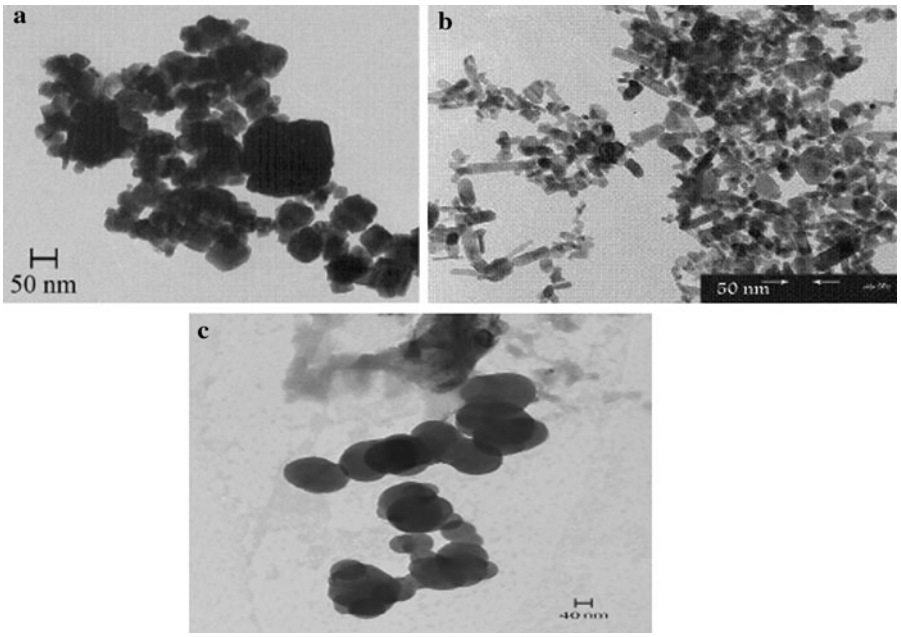

Fig. 1 TEM image of **a** Fe_3O_4, **b** ZnO, and **c** CuO nanoparticles

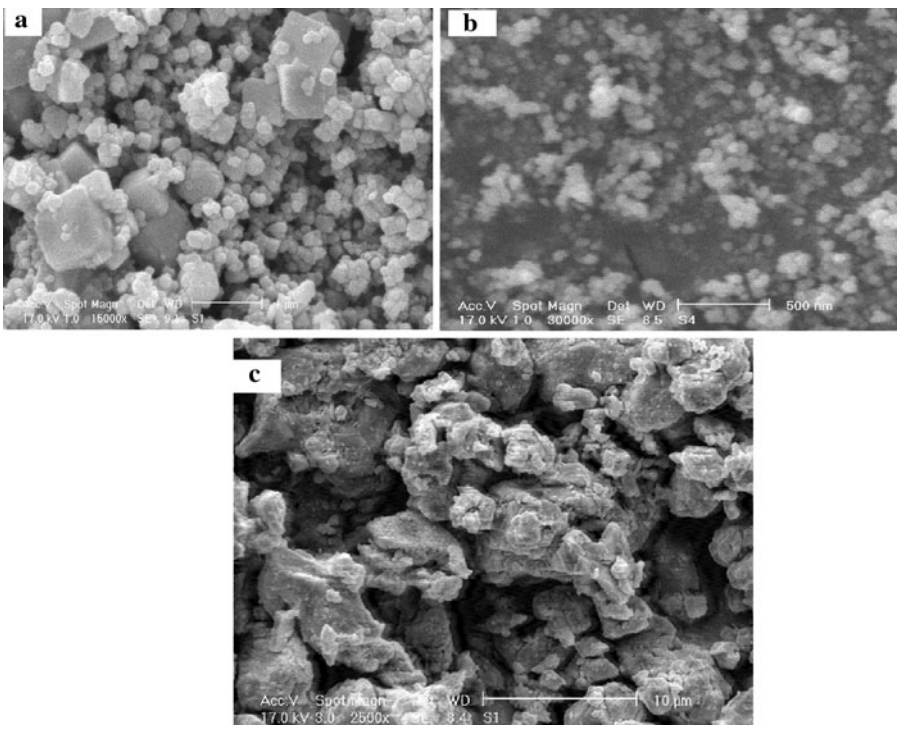

Fig. 2 SEM image of **a** Fe_3O_4, **b** ZnO, and **c** CuO nanoparticles

at 5,000 rpm before measuring the equilibrium concentrations of Cd^{2+}, Cu^{2+}, Ni^{2+}, and Pb^{2+} in the supernatant solutions. Desorbed Cd^{2+}, Cu^{2+}, Ni^{2+}, and Pb^{2+} was calculated at the desorption stage.

Saturation indices (SI) and the speciation of heavy metals

The SI and speciation of heavy metals in isotherm leachate (at final concentration = 300 mg L^{-1}) were calculated using the geochemical speciation model Visual MINTEQ version 2.3. MINTEQ is an equilibrium speciation model that can be used to calculate the equilibrium composition of dilute aqueous solutions in the laboratory or natural aqueous systems (Allison and Novo-Gradac 1991; Jalali and Arfania 2010).

The SI for each solid is defined as: log IAP (logarithm of the ion activity product)—log K_s (K_s is the temperature-corrected solubility constant). Oversaturation is indicated if SI > 0, whereas the solution is undersaturated with respect to the solid if SI < 0. There is an apparent equilibrium with respect to the solid when SI = 0 (or more correctly $-0.5 <$ SI < 0.5) (Jalali and Arfania 2010).

Results and discussion

Characteristics of the adsorbents

TEM micrographs were used to examine the shape and particle sizes of the adsorbents (Fig. 1). The images showed that Fe_3O_4, ZnO, and CuO particles had mean diameters of about 50 nm (spheroid), 25 nm (rod shape), and 75 nm (spheroid), respectively. SEM was also used to examine the surface morphology of adsorbents (Fig. 2). SEM images showed that Fe_3O_4 particles differed in size to some extent. ZnO had

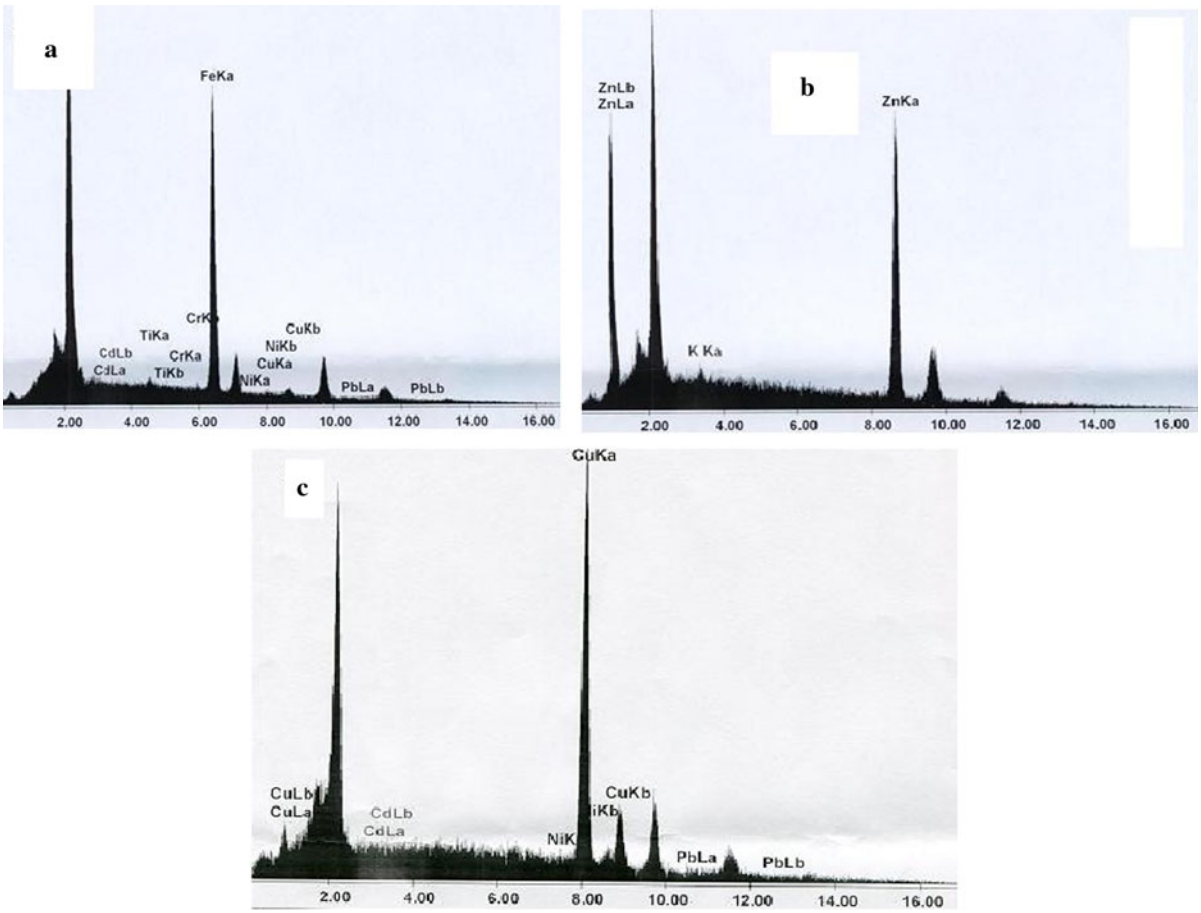

Fig. 3 SEM-EDX spectrum of **a** Fe_3O_4, **b** ZnO, and **c** CuO nanoparticles on Au substrate

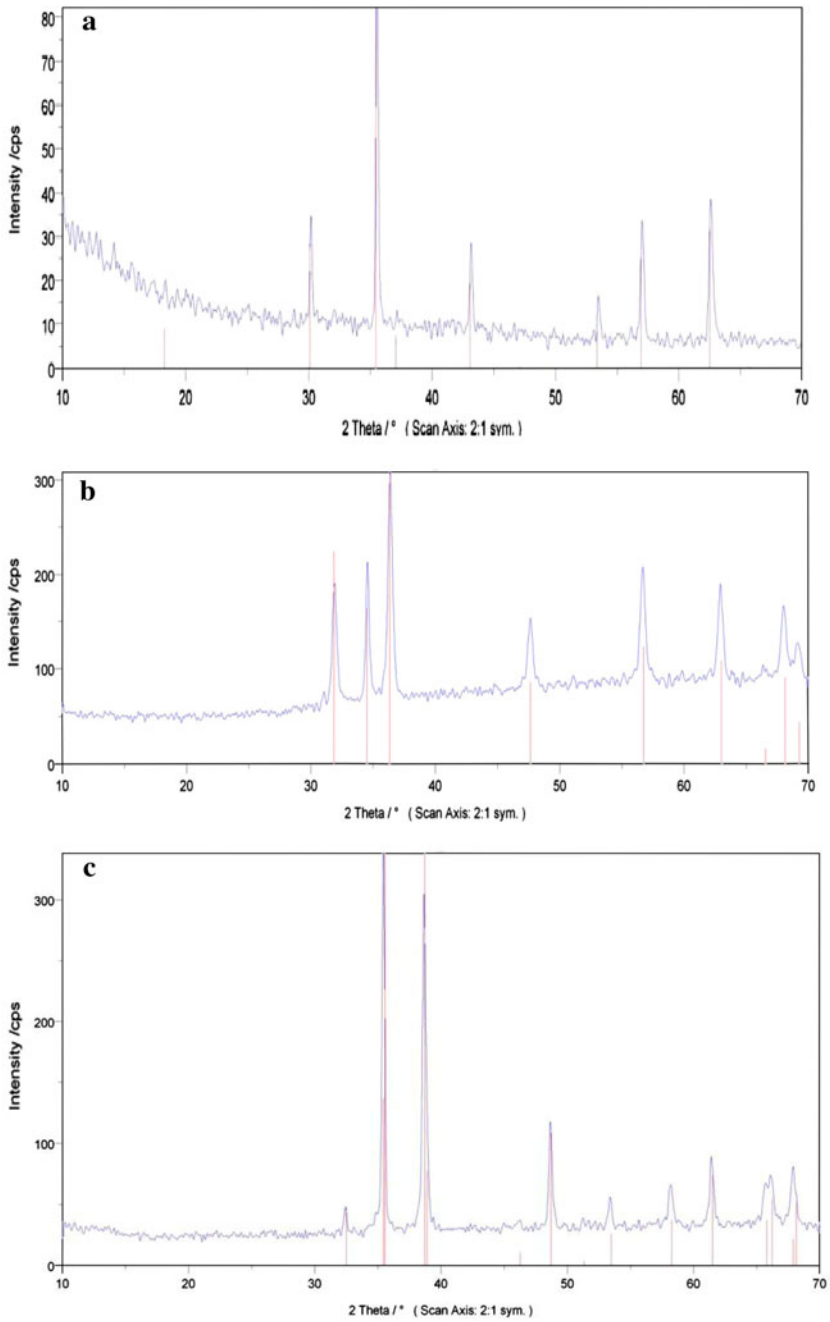

Fig. 4 X-ray diffraction patterns of **a** Fe_3O_4, **b** ZnO, and **c** CuO nanoparticles

Table 1 Structural properties of nanoparticles

Adsorbent	BET ($m^2\ g^{-1}$)	Pore volume ($cm^3\ g^{-1}$)	Pore size (nm)	Crystallite size (nm)[a]	Particle size (nm)[b]
Fe_3O_4	24.8	8.8×10^{-2}	25.71	36.88	50
ZnO	31.2	12.0×10^{-2}	15.81	16.70	25
CuO	12.1	3.15×10^{-2}	54.11	31.50	75

[a] Data calculated from the XRD pattern according to Scherrer equation

[b] Data from TEM analysis

homogeneous surfaces with a highly porous morphology and a small pore size. CuO had low surface porosity with a large pore size. Figure 3 shows a typical EDX elemental analysis of adsorbents indicating the degree of purity on the particle surfaces. Typical XRD profiles of nanoparticles are shown in Fig. 4, indicating that similar peak characteristics were shared by Fe_3O_4, ZnO, and CuO in their powder diffraction files (JCPDS PDF data numbers 79–419, 75–576, and 45–937, respectively). We calculated the crystallite size measurements from the XRD patterns, according to Scherrer's equation:

$$D = 0.9\lambda/(b\cos\theta) \quad (6)$$

This equation uses the reference peak width at angle θ (radian), where λ is the wavelength of the incident X-ray (1.5418 Å), b is the width of the XRD peak at half height, and 0.9 is a shape factor (Nagappa and Chandrappa 2007; Rezaei et al. 2011) (Table 1). It should be noted that the particle dimension obtained by TEM was higher than the corresponding crystallite size. This difference may be explained by the presence of aggregates in the TEM grain that consisted of several crystallites and/or poor crystallinity (Afkhami and Moosavi 2010; Zhang et al. 2008).

Table 1 shows the results of the N_2 sorption experiments and the estimated crystallite diameters based on the XRD and TEM data. The specific surface area, total pore volume, and pore size distribution of the materials were calculated using the BET equation. The results indicated that ZnO had a much greater surface area than Fe_3O_4 and CuO (Table 1).

Effect of initial pH

The pH value played a very important role in the use of nano-adsorbents as supports in the metal ion adsorption process. Figure 5 shows the effects of pH on the adsorption of heavy metals by adsorbents. As expected, higher acidity conditions correlated with lower adsorption of metal ions. This may be due to the protonation of functional groups. The functional groups in metal oxides generally covered with hydroxyl groups that vary in forms at different pH. In addition, FT-IR results

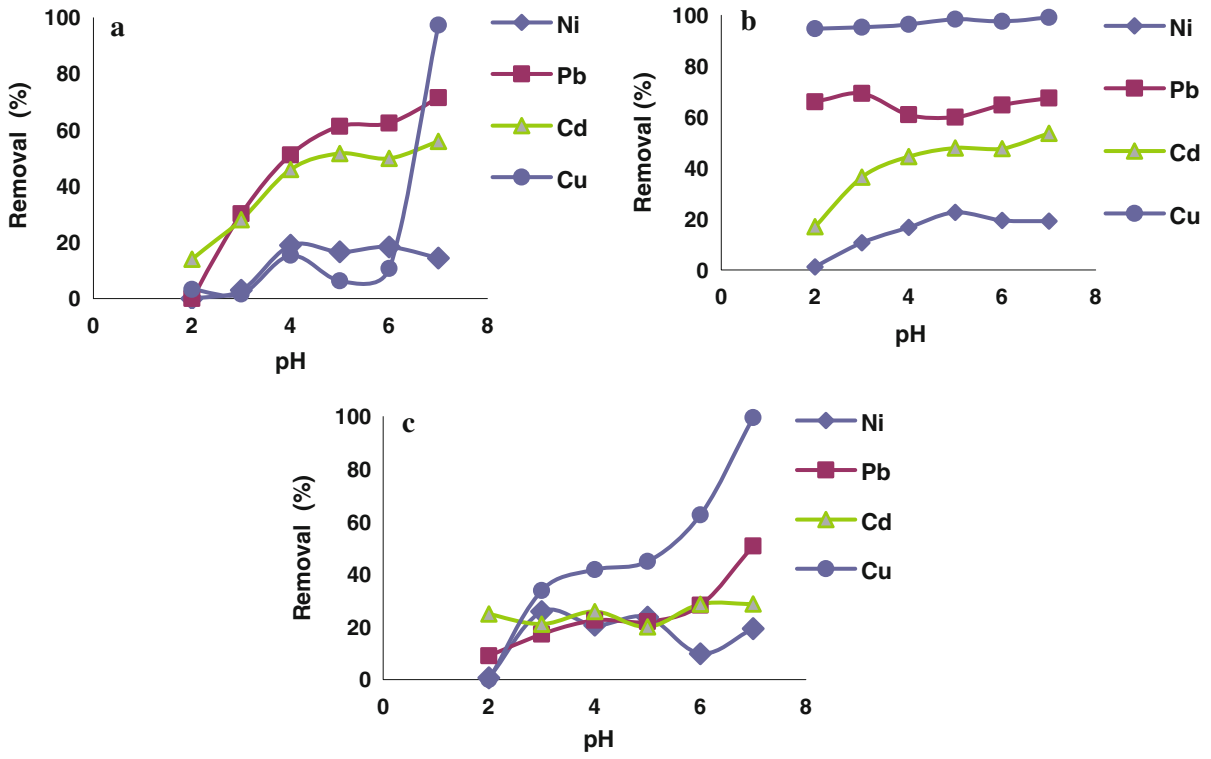

Fig. 5 Effect of pH on percentage removal of metals in **a** Fe_3O_4, **b** ZnO, and **c** CuO nanoparticles (initial concentration = 100 mg L^{-1}, adsorbent dosage: 2 g L^{-1}, 100 rpm)

in many cases revealed that OH and O groups in surfaces of these adsorbents (Afkhami and Moosavi 2010; Panneerselvam et al. 2011; Bian et al. 2011; Banerjee and Chen 2007). The surfaces of these adsorbents are neutral at pH_{zpc} (the pH of zero point charge). The pH_{zpc} of Fe_3O_4, ZnO, and CuO is about 6.9, 9.2, and 9.4, respectively (Essington 2004; Zhang et al. 2008; Martinson and Reddy 2009). As the pH of solution increased the adsorption increased due to the successive deprotonation of hydroxyl groups on the adsorbent and electrostatics attraction between negative sites on adsorbent and metals. When the pH decreased, there was competitive adsorption between H^+ ions and strongly competing heavy metals in solution. The binding sites of the nano-adsorbent were dominated by H^+ ions at a low pH value, which led to protonated functional groups, thus adsorption is reduced (Afkhami and Moosavi 2010). The number of adsorption sites available for heavy metal ions decreased as the number of protonated metal-binding absorbent groups increased. Figure 5 shows that the maximum removal of the four ions occurred at pH 6 with all adsorbents, as in all cases this pH is below the pH_{zpc} of the adsorbent. Therefore, removal is increased at pH > 6. This may be due to the formation of metal complexes (covalent or ionic bonding) and/or precipitation and/or electrostatic attraction (Afkhami et al. 2010). Preference of these mechanisms in each adsorbent and metal to some extent related to nature of functional groups, chemistry of metal and solution. For example for Cu in ZnO adsorbent the dominant mechanism may be complexes and precipitation (Fig. 5).

Effects of the amount of adsorbent

The effect of nanoparticle dosage is shown in Fig. 6. Removal increased with the increase in the sorbent mass (Fig. 6a, b, c). An increase in the absorbent dosage from 0.5 to 5 g L^{-1} led to an increase in the removal efficiency of Cd^{2+}, Cu^{2+}, Ni^{2+}, and Pb^{2+} from 9.2 to 41.3, 24.0 to 33.0, 8.1 to 15.0, and 23.7 to 81.5 %, respectively, as shown in Fig. 6 for the Fe_3O_4 sorbent. Other nanoparticles showed the same trend (Fig. 6). This was apparently due to the increasing number of binding sites with the increased amount of absorbent (Lazaridis and Charalambous 2005; Chen and Yang 2006). The maximum adsorption of heavy metals with almost all adsorbents was obtained with an

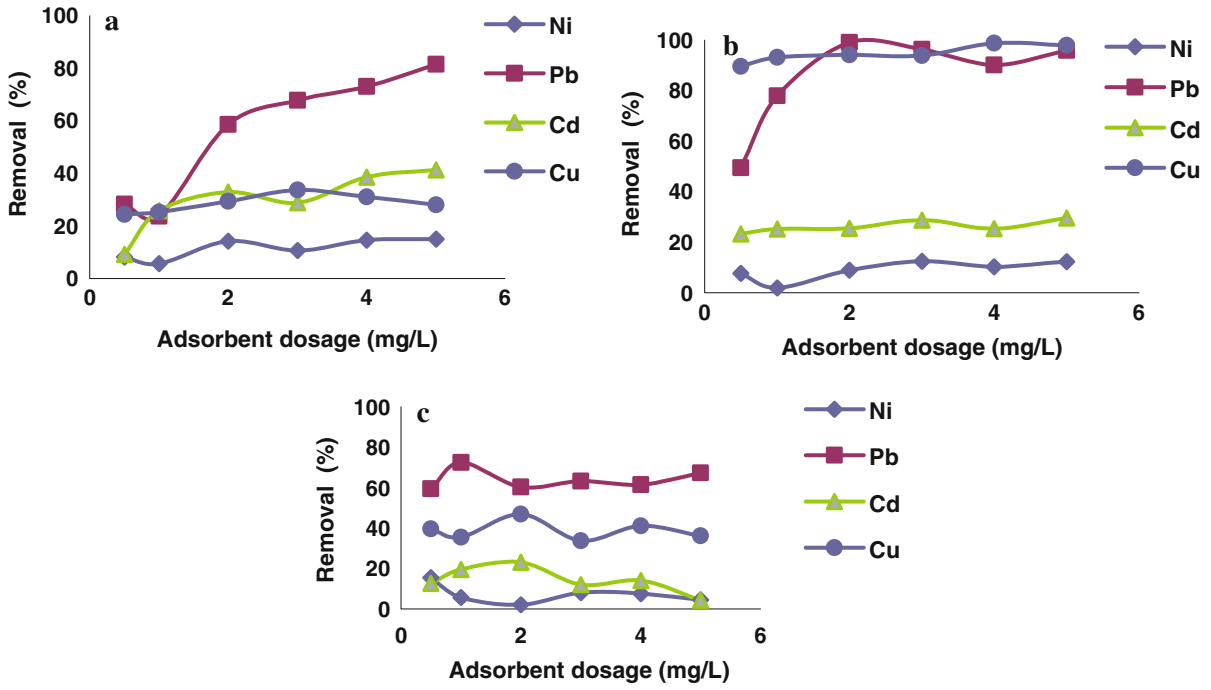

Fig. 6 Effect of adsorbent dose on removal of heavy metals on adsorbents (**a** Fe_3O_4, **b** ZnO, **c** CuO). Condition: initial concentration 100 mg L^{-1}, pH native, rpm 100

adsorbent dosage of 2 g L^{-1}. Thus, 2 g L^{-1} (0.05 g) was considered the optimum dosage.

Effect of contact time

The adsorption of heavy metals by nano-adsorbents was investigated as a function of contact time (10–1,440 min) at 100 mg L^{-1} initial concentrations, with at their native pH heavy metal removal increased with time and Fig. 7 shows that the removal efficiency of the four ions reached maximum values after 120–180 min with almost all ions and adsorbents. No significant increases occurred between 180 min and 24 h. Based on the adsorption kinetics analysis, a contact time of 24 h (greater confidence) was selected for subsequent isotherm studies of all four metals and all nanoparticles.

The best fit model was selected based on the match between the experimental and theoretical values and the linear correlation coefficient. A pseudo-first order model did not fit the experimental data, whereas Table 2 and Fig. 8 show that the pseudo-second order kinetics plots of heavy metal sorption were well fitted to the experimental data for all three adsorbents. The

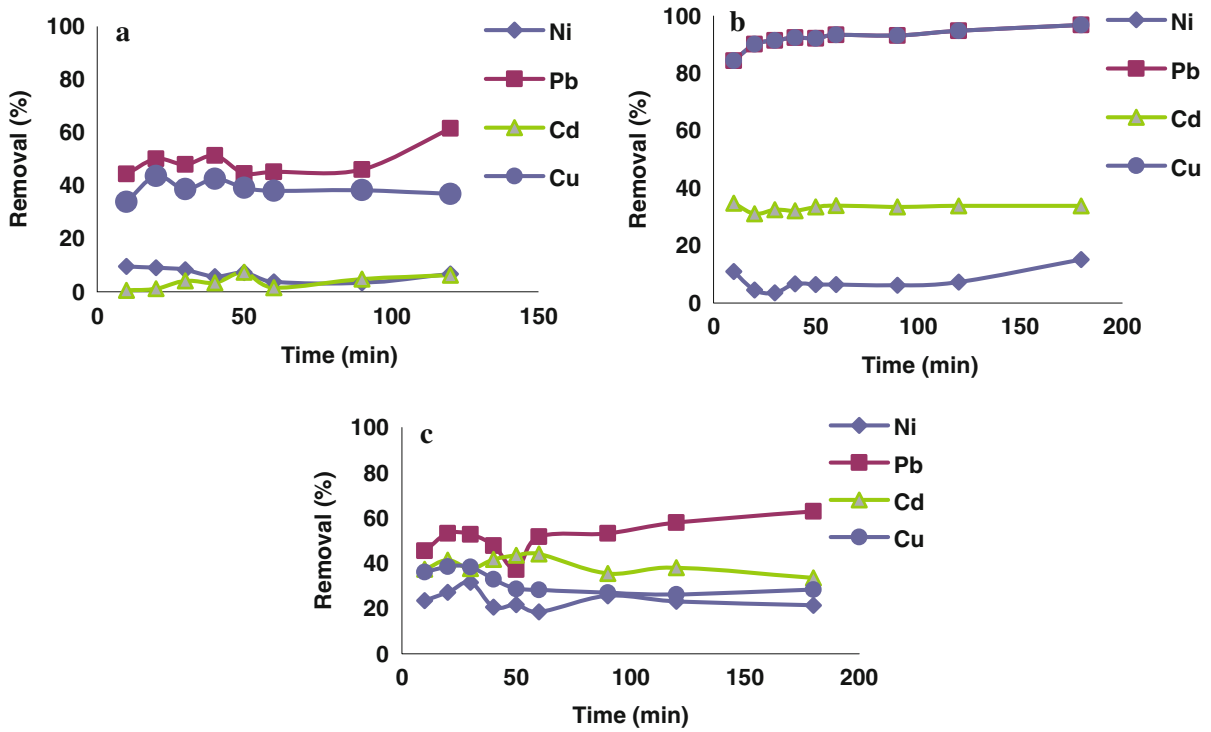

Fig. 7 Effect of contact time on adsorption of heavy metals on to adsorbents: **a** Fe_3O_4, **b** ZnO, and **c** CuO nanoparticles (initial concentration = 100 mg L^{-1}, adsorbent dosage: 2 g L^{-1}, 100 rpm)

Table 2 The pseudo-second-order kinetics model constant (at concentration 100 mg L^{-1})

Metals	Fe_3O_4			ZnO			CuO		
	q_e (mg g^{-1})	K_2 (g mg^{-1} min^{-1})	R^2	q_e (mg g^{-1})	K_2 (g mg^{-1} min^{-1})	R^2	q_e (mg g^{-1})	K_2 (g mg^{-1} min^{-1})	R^2
Ni	4.440	0.006	0.998	7.87	0.002	0.998	1.66	0.019	0.995
Pb	30.310	0.003	0.998	50.00	0.011	1	2.95	0.052	0.999
Cd	2.330	0.010	0.998	19.23	0.006	0.999	1.74	−0.122	0.999
Cu	20.830	0.011	0.999	50.00	0.011	1	1.77	0.031	0.997

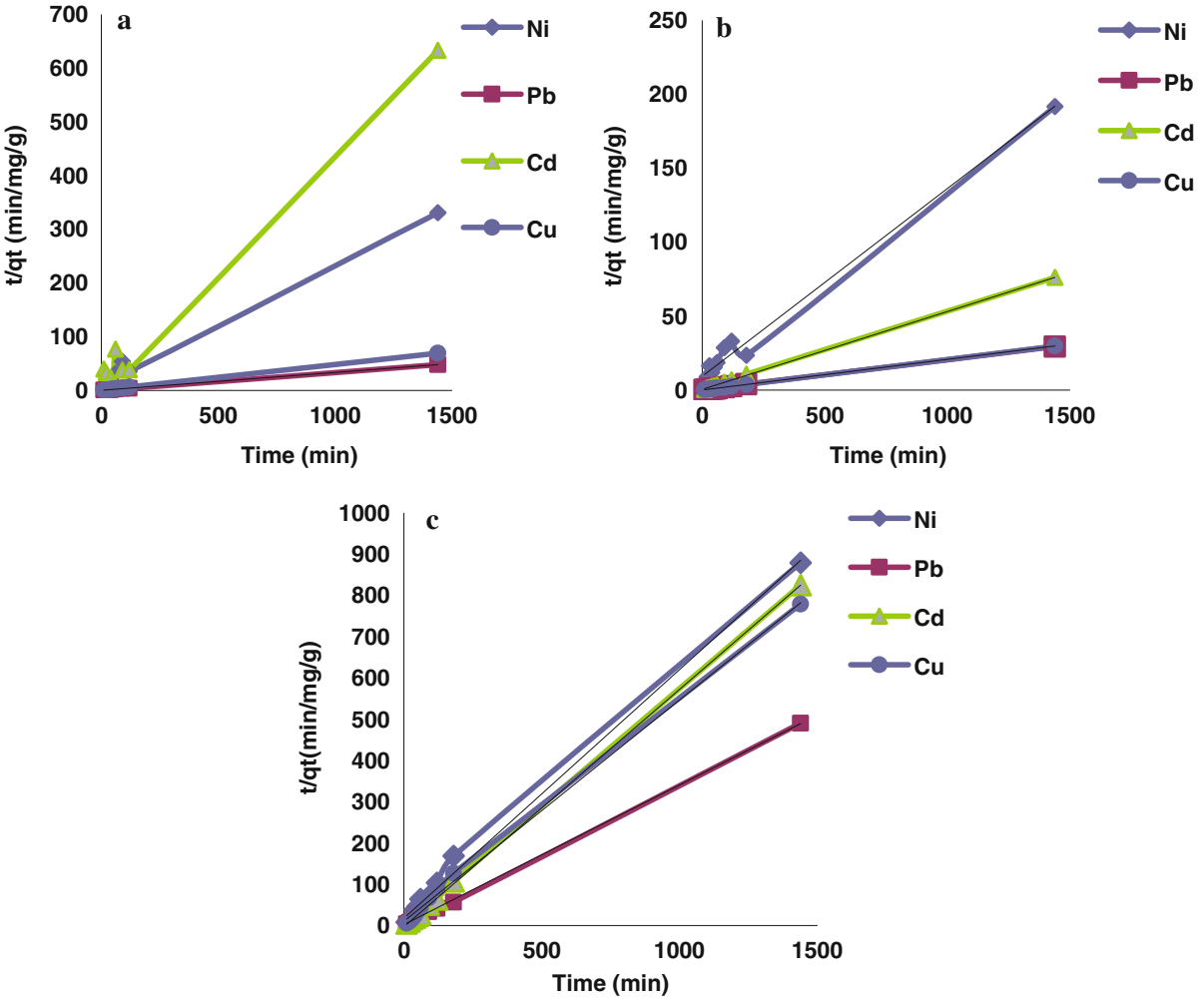

Fig. 8 Pseudo-second-order kinetics plots of sorption of heavy metals on adsorbents: **a** Fe_3O_4, **b** ZnO and **c** CuO nanoparticles

rate equations and related values are given in Table 2. The rates of the pseudo-second order reactions may be dependent on the amount of solute adsorbed on the surface of adsorbent and the amount adsorbed at equilibrium. The best fit of the pseudo-second order kinetic model in the present system suggested that the adsorption behavior of the heavy metal ions onto the nanoparticles occurred by a chemisorption mechanism via electrostatic attraction (Keyhanian et al. 2011; Song et al. 2011).

Adsorption isotherms

The removal of Cd^{2+}, Cu^{2+}, Ni^{2+}, and Pb^{2+} by nanoparticles as a function of their concentration was studied at constant temperature (25 ± 0.1 °C) by varying the metal concentration from 10 to 300 mg L^{-1}, while keeping all other parameters constant. The sorption results of Cd^{2+}, Cu^{2+}, Ni^{2+}, and Pb^{2+} using nanoparticles are shown in Fig. 9. Cd^{2+}, Cu^{2+}, Ni^{2+}, and Pb^{2+} sorption and the equilibrium solution Cd^{2+}, Cu^{2+}, Ni^{2+}, and Pb^{2+} concentration increased with increasing amounts of metals added. Using Fe_3O_4 nanoparticles and based on the maximum amount of metal adsorption, the maximum metal adsorption capacity was evaluated as 122.5, 101.4, 35.6, and 14.7 mg g^{-1} for Cd^{2+}, Pb^{2+}, Ni^{2+}, and Cu^{2+}, respectively. In the same manner, the following order was found: Cu^{2+} (137.5) > Cd^{2+} (119.1) > Pb^{2+} (112.7) > Ni^{2+} (48.6 mg g^{-1}) for ZnO, and Cd^{2+} (118.3) > Cu^{2+} (54.1) > Ni^{2+}

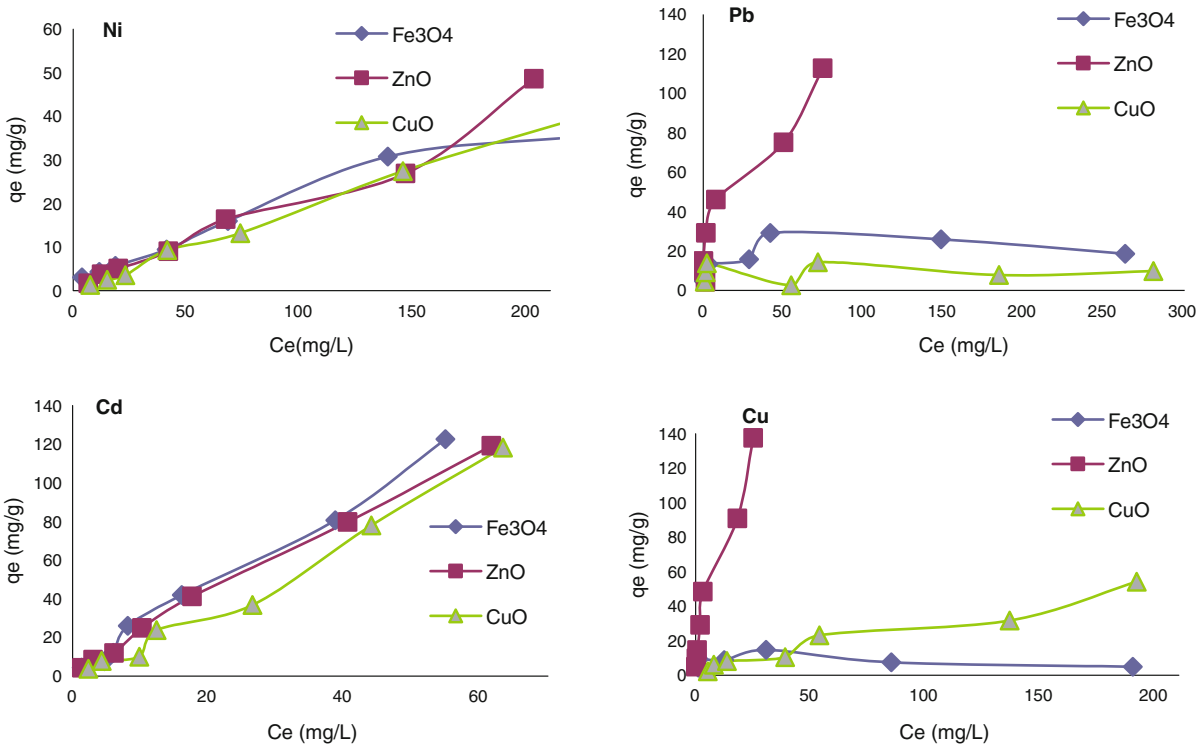

Fig. 9 Adsorption isotherms of Cd^{2+}, Cu^{2+}, Ni^{2+} and Pb^{2+} in single component solution using Fe_3O_4, ZnO and CuO nanoparticles

(39.4) > Pb^{2+} (14.2 mg g^{-1}) for CuO. The electronegativity of the cations is an important factor in determining which of the trace metals chemisorb with the highest performance. The more electronegative metals should form the strongest covalent bond with O atoms on nanoparticles surfaces. According to the electronegativity, the order of adsorption should have been $Cu^{2+} > Ni^{2+} > Pb^{2+} > Cd^{2+}$ but, on the basis of electrostatics, the strongest bound should be performed by the metals with the greatest charge-to-radius ratio. This would produce a different order of performance for the same metals: $Ni^{2+} > Cu^{2+} > Cd^{2+} > Pb^{2+}$ (McBridge 1994). Thus, the series based on the electronegativity and electrostatics differed from the series obtained experimentally. The differences observed were considered to be due to the specificities of the ion exchange material and to differences in the experimental techniques used (Inglezakis et al. 2003). This selectivity may vary according to the sources of adsorbents, the types of metals, and the experimental conditions (Ok et al. 2007). The difference order of the series may be an indicator that adsorption is not necessarily the only mechanism responsible for the removal of heavy metal ions from solution, because precipitation of metal hydroxides may also have a significant influence on the nanoparticle treatment process.

In the multiple component solutions, metals exhibited competitive adsorption on nanoparticles. The amount of cations sorbed from multiple component solutions (Fig. 10) was mainly lower than those sorbed from single component solutions, which agreed with results reported by other authors (Panayotova and Velikov 2002; Vidal et al. 2009; Jalali and Moharrami 2007). The maximum adsorption of Cd^{2+} was 31.5, 51.3, and 42 mg g^{-1} with Fe_3O_4, ZnO, and CuO nanoparticles, respectively, which was approximately 74, 57, and 64 % less when compared with the single component system. With Fe_3O_4, ZnO and CuO nanoparticles, the adsorption of Ni^{2+} was decreased compared with the single component system (56, 75, and 35 %, respectively), whereas the adsorption of Pb^{2+} increased by 24 % with ZnO and by 65 % with CuO, although it decreased by 85 % with Fe_3O_4.

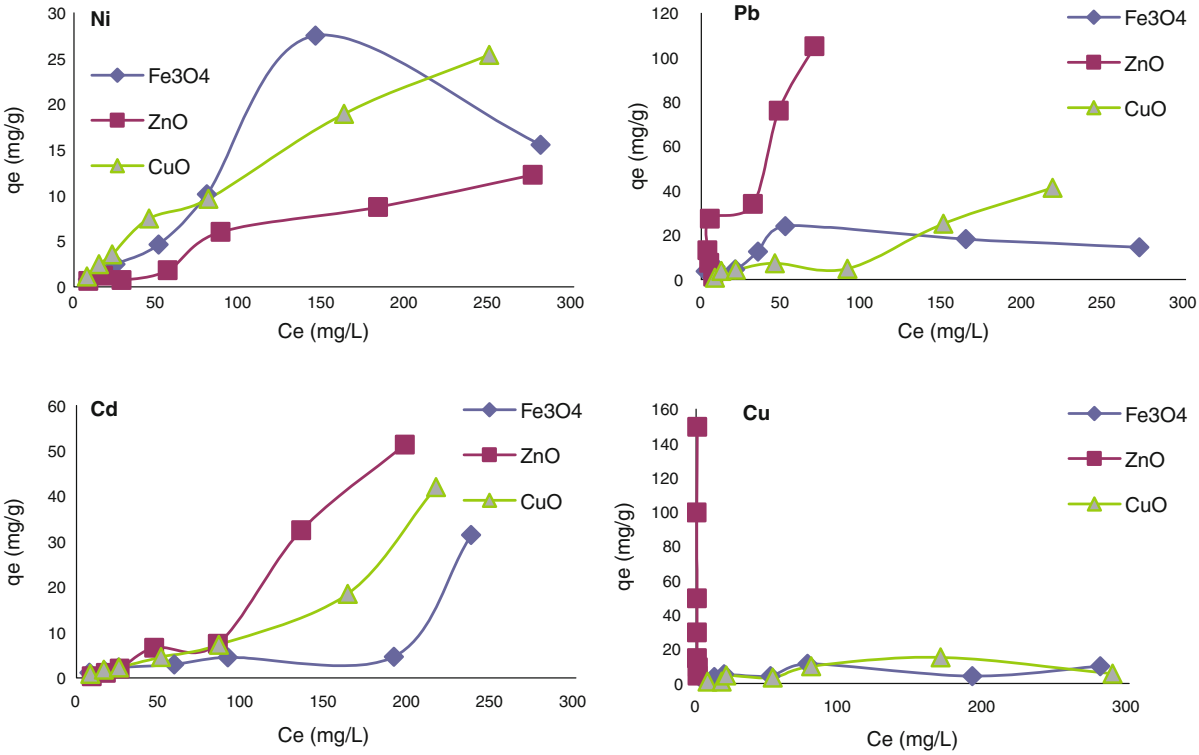

Fig. 10 Adsorption isotherms of Cd^{2+}, Cu^{2+}, Ni^{2+}, and Pb^{2+} in multi component solutions using Fe_3O_4, ZnO, and CuO nanoparticles

Table 3 Freundlich constant for Ni^{2+} and Cd^{2+} adsorption on the NPs in single and competitive isotherms

Freundlich parameters	Fe_3O_4			ZnO			CuO		
	n	K_F (mg g^{-1})	R^2	n	K_F	R^2	n	K_F	R^2
Single									
Ni^{2+}	1.550	0.995	0.996	1.086	0.319	0.991	0.972	0.162	0.992
Cd^{2+}	1.06	2.71	0.961	1.130	3.030	0.992	0.978	1.500	0.972
Competitive									
Ni^{2+}	0.744	0.036	0.971	1.136	0.083	0.951	1.146	0.223	0.991
Cd^{2+}	1.37	0.203	0.955	0.628	0.011	0.982	0.907	0.073	0.971

Cu^{2+} adsorption increased (8 %) with ZnO, but it decreased with CuO (89 %) and Fe_3O_4 (22 %) nanoparticles. This suggests that metal adsorption was different on nanoparticles in the multiple component system compared with the single component system.

ZnO had the highest metal uptake capacity of 360 mg g^{-1} (sum of the four adsorbed metals), followed by CuO (114.5 mg g^{-1}) and Fe_3O_4 (73 mg g^{-1}). Thus, the adsorption capacity of the ZnO was significantly higher than that of Fe_3O_4 and CuO in both single and multiple component solutions. There are no published data on the maximum adsorption capacities of ZnO and CuO, so these results cannot be compared. However, Recillas et al. (2011) reported that the maximum adsorption of Pb^{2+} by Fe_3O_4 nanoparticles was 82.6 mg g^{-1}. Two equilibrium models were analyzed to investigate the sorption isotherms, i.e., the Langmuir and Freundlich isotherm models. Neither of these two models fitted the Cu^{2+} and Pb^{2+} isotherms in single and multiple component solutions. Cd^{2+} and Ni^{2+} sorption on nanoparticles produced a good trend in the Freundlich model, with

high correlation coefficients in single and multiple component solutions (Table 3). The higher correlation coefficient indicated that there was a strong positive relationship with the data and that the Cd^{2+} and Ni^{2+} experimental sorption data with all nanoparticles was well fitted to the Freundlich model.

The regenerability of the loaded adsorbent is a key factor for improving the economy of the adsorption process. In this study, metals adsorbed in batch experiments were effectively eluted by using 10 mM $CaCl_2$ as a desorbent. The highest efficiency of desorption (82.5 %) was obtained with Cd^{2+} and ZnO nanoparticles in both single and multiple component solutions, followed by Pb^{2+} (55.6 and 60.1 % in single and multiple component solutions, respectively) and CuO nanoparticles (Fig. 11).

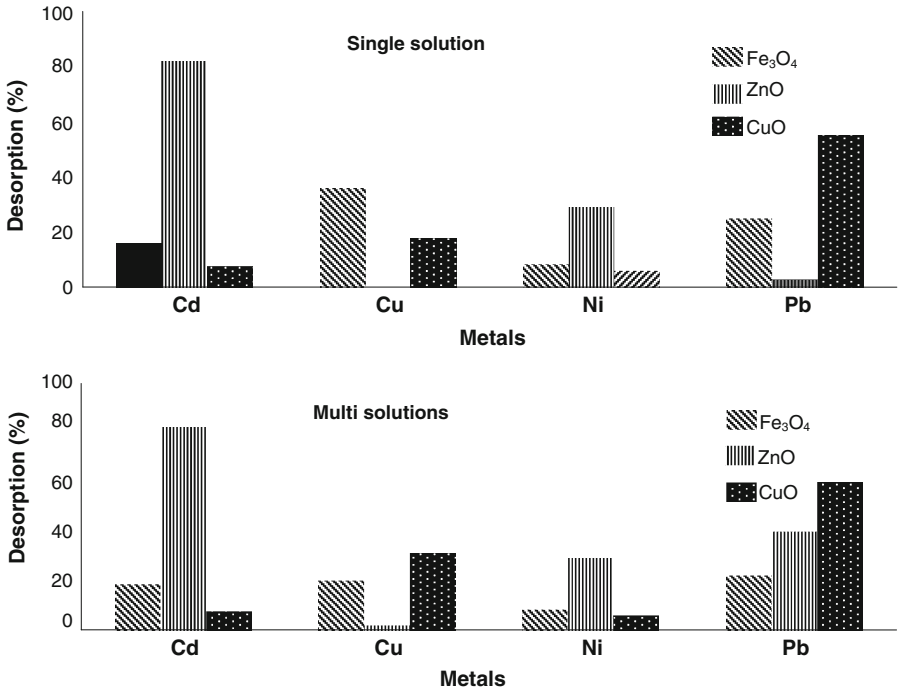

Fig. 11 Desorption of Cd^{2+}, Cu^{2+}, Ni^{2+}, and Pb^{2+} in single and multi component solutions using Fe_3O_4, ZnO, and CuO nanoparticles

Table 4 Speciation of metals in equilibrium solution in contact with Fe_3O_4, ZnO, and CuO using Visual MINTEQ model in single component solution

Adsorbents	Species (frequency)							
	Cd^{2+}	%	Cu^{2+}	%	Ni^{2+}	%	Pb^{2+}	%
Fe_3O_4	Cd^{2+}	75	Cu^{2+}	96.4	Ni^{2+}	98	Pb^{2+}	85.5
	$CdCl^{1+}$	22.5	$CuCl^{+}$	1	$NiNO_3^{+}$	1.3	$PbNO_3^{+}$	7.4
	$CdNO_3^{+}$	1.5	$CuNO_3^{+}$	1.6			$PbCl^{+}$	5.6
	Cd^{2+}	75	Cu^{2+}	20.5	Ni^{2+}	98.1	Pb^{2+}	76
ZnO	$CdCl^{+}$	22.4	$Cu_2(OH)_2^{+}$	28.6	$NiNO_3^{+}$	1.2	$PbCl^{+}$	5.4
	$CdNO_3^{+}$	1.4	$Cu_3(OH)_4^{2+}$	47.5			$PbOH^{+}$	8.8
	Cd^{2+}	76.9	Cu^{2+}	95	Ni^{2+}	98.4	Pb^{2+}	86.2
CuO	$CdCl^{+}$	21.3	$CuCl^{+}$	1	$NiNO_3^{+}$	1.3	$PbNO_3^{+}$	7.5
	$CdNO_3^{+}$	1.4					$PbCl^{+}$	5.5

Table 5 Speciation of metals in equilibrium solution in contact with Fe_3O_4, ZnO, and CuO using Visual MINTEQ model in multi component solutions

Adsorbents	Species (frequency)							
	Cd^{2+}	%	Cu^{2+}	%	Ni^{2+}	%	Pb^{2+}	%
Fe_3O_4	Cd^{2+}	44	Cu^{2+}	95.7	Ni^{2+}	98.4	Pb^{2+}	65
	$CdCl^{1+}$	51.4	$CuCl^{+}$	2.3	$NiNO_3^{+}$	1	$PbNO_3^{+}$	4.2
	$CdCl_2$	3.8	$CuNO_3^{+}$	1.3			$PbCl^{+}$	28.9
	Cd^{2+}	43.6	Cu^{2+}	87	Ni^{2+}	98.4	Pb^{2+}	62.1
ZnO	$CdCl^{+}$	51.6	$Cu_2(OH)_2^{+}$	6.7	$NiNO_3^{+}$	1.1	$PbCl^{+}$	31.3
	$CdCl_2$	3.8	$CuCl^{+}$	2.1			$PbCl_2$	1.3
	Cd^{2+}	44	Cu^{2+}	95	Ni^{2+}	98.4	Pb^{2+}	65
CuO	$CdCl^{+}$	51.4	$CuCl^{+}$	2.3	$NiNO_3^{+}$	1.3	$PbNO_3^{+}$	4.2
	$CdCl_2$	3.8	$CuNO_3^{+}$	1.3			$PbCl^{+}$	28.9

Table 6 Saturation indices of metals in equilibrium solution in contact with Fe_3O_4, ZnO, and CuO using Visual MINTEQ model in single component solutions

Adsorbents	Single							
	Cd minerals	SI	Cu minerals	SI	Pb minerals	SI	Ni minerals	SI
Fe_3O_4	$Mg_2(OH)_3Cl$	−40	$Mg_2(OH)_3Cl$	−44	$Mg_2(OH)_3Cl$	−44	$Mg_2(OH)_3Cl$	−38
	Brucite	−19	Periclase	−27	Periclase	−27	$Mg(OH)_2$	−20
	Periclase	−12.4	Brucite	−22	Brucite	−22	Brucite	−18
			Atacamite(Cu)	1.2	$Pb(OH)_2$	0.83		
	$Mg(OH)_2$	−20	$Mg_2(OH)_3Cl$	−40	Lime	−20	Lime	−20
ZnO	Lime	−20	Periclase	−24	Brucite	−18	Brucite	−18
	Brucite	−18	Brucite	−19.7	$Pb(OH)_2$	0.953	$Mg_2(OH)_3Cl$	−38
			Atacamite	3.2			$Ni(OH)_2$	1.47
			$Cu_2(OH)_3NO_3$	1.4				
			Tenorite(Pb)	1.3				
CuO	Lime	−25	$Mg_2(OH)_3Cl$	−45	Lime	−25.5	Lime	−22
	$Mg(OH)_2$	−24	$Mg(OH)_2$	−24.8	Brucite	−22.5	Brucite	−20
	Brucite	−22	Brucite	−22.9			$Mg_2(OH)_3Cl$	−40
			Atacamite	0.55				

Table 7 Saturation indices of metals in equilibrium solution in contact with Fe_3O_4, ZnO, and CuO using Visual MINTEQ model in multi component solutions

Adsorbents	Minerals (SI)					
Fe_3O_4	Lime	$Mg_2(OH)_3Cl$	Brucite	Atacamite		
	−25	−20	−10	0.831		
ZnO	$Mg(OH)_2$	$Mg_2(OH)_3Cl$	Brucite	Atacamite	$Cu_2(OH)_3NO_3$	$Pb_2(OH)_2Cl_2$
	−23.3	−22	−21.6	3.2	0.9	0.51
CuO	Lime	$Mg_2(OH)_3Cl$	Brucite	Atacamite		
	−25.4	−19.9	−10.6	1.17		

Effect of sorbents on the speciation and precipitation of heavy metals

The speciation of metals in solution was a result of competition between different metal complexes, metal chelates, and free metal ions. Visual MINTEQ 2.3 software was used to calculated the distribution of Cd^{2+}, Cu^{2+}, Ni^{2+}, and Pb^{2+} chemical species in the equilibrium supernatant and the possibility of mineral precipitation at the highest added concentration (300 mg L^{-1}) of Cd^{2+}, Cu^{2+}, Ni^{2+}, and Pb^{2+}. Tables 4 and 5 show the frequencies of the heavy metal chemical species. In single component solutions, free metal ions mainly dominated in solutions of all nanoparticles (Table 4). The majority of the Cu^{2+} in solution was predicted to be present as OH^- complexes, while about 23 % of the Cd^{2+} in solution was predicted to be present as $CdCl^+$ with ZnO and Fe_3O_4 nanoparticles, respectively. The percentage of free ion species was reduced in multiple component solutions (Table 5). In multiple component solutions, the majority of Ni^{2+}, Pb^{2+}, and Cu^{2+} ions in solution were predicted to be present as free species, while about 51 % of the Cd^{2+} in solution was predicted to be present as $CdCl^+$ (Table 5). Pederson (2002) reported similar results for Cd^{2+} and Cu^{2+} (Pederson 2002), where the majority of the Cd in solution was predicted to be present as Cl^- complexes, while about 90 % of the Cu in solution was predicted to be present as positively charged species (Cu^{2+}, $CuCl^+$, and $CuOH^+$).

Furthermore, chemical modeling predicted that the solution SI values for all MINTEQ database Cd^{2+} and Pb^{2+} minerals were below zero in both single and multiple component solutions. Therefore, the main mechanism involved in removing Cd^{2+} and Pb^{2+} from

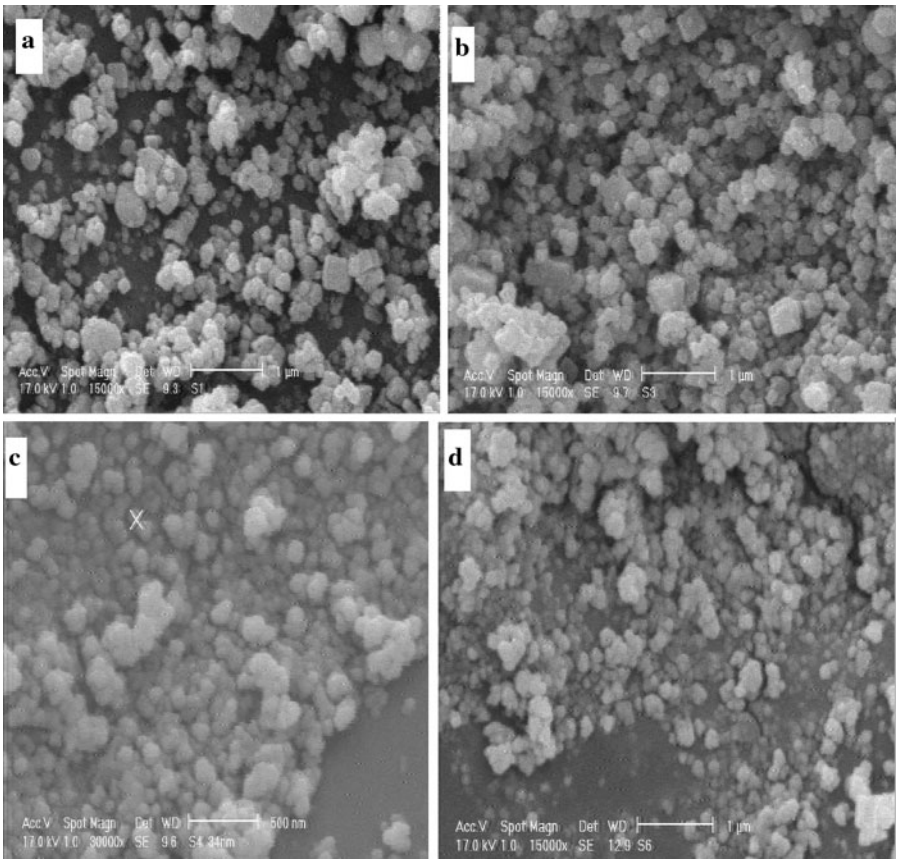

Fig. 12 SEM image of **a** Fe_3O_4; **c** ZnO after treatment with single (Ni) and **b** Fe_3O_4; **d** ZnO after treatment with multiple heavy metal solutions

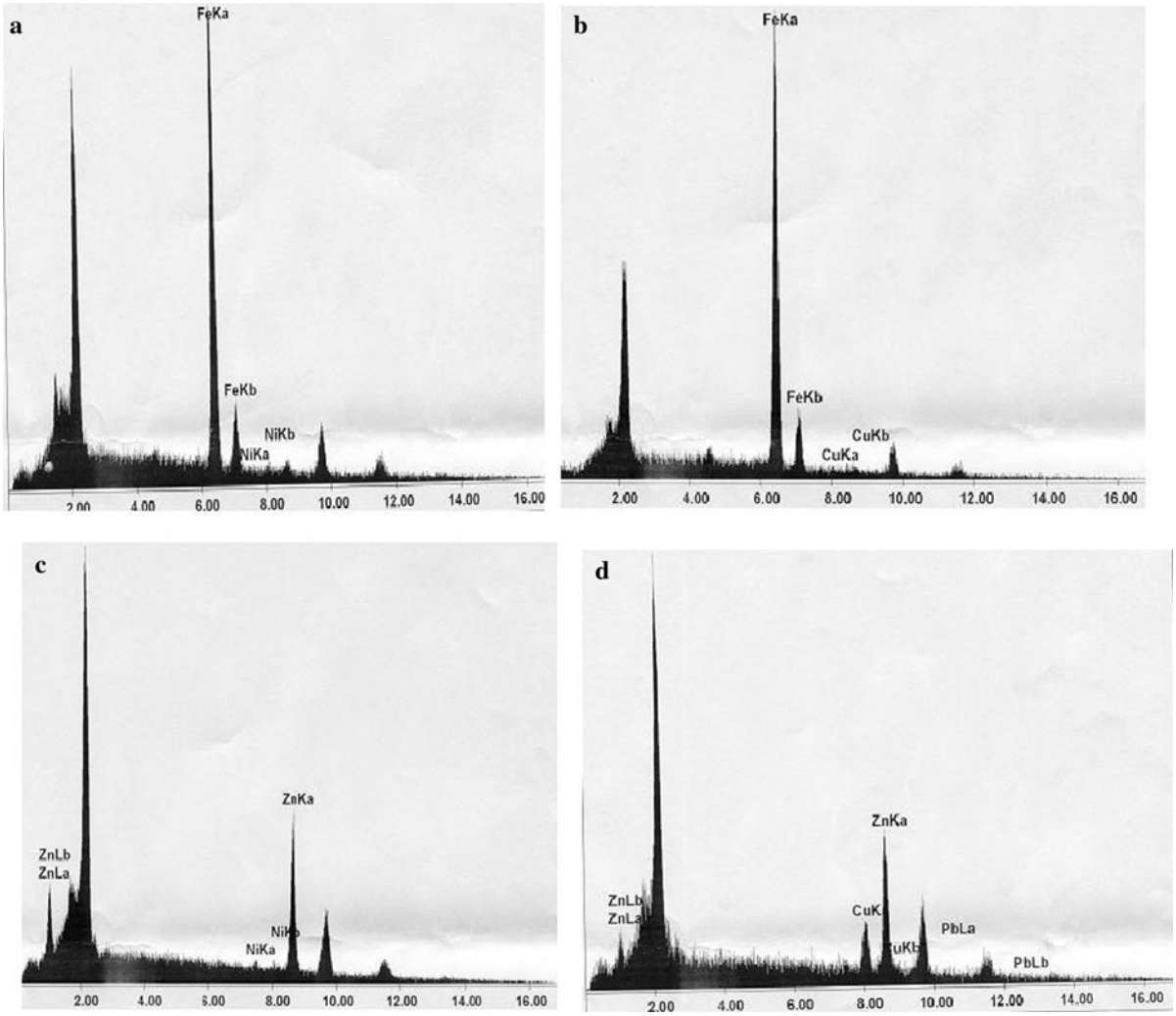

Fig. 13 EDX image of **a** Fe_3O_4; **c** ZnO after treatment with single (Ni) and **b** Fe_3O_4; **d** ZnO after treatment with multiple heavy metal solutions

solution was adsorption on the surface of nanoparticles. Geochemical modeling predicted that Cu^{2+} was mainly precipitated as Atacamite in both single and multiple component solutions for all nanoparticles (Tables 6, 7). MINTEQ predicted that Ni precipitated as Ni $(OH)_2$ in both single and multiple component solutions.

Formation of Cu^{2+} and Ni^{2+} precipitates on nanoparticles in single and multiple component solutions was further supported by SEM-EDX images (Figs. 12, 13). Scanning electron microscope images revealed the association and accumulation of Ni^{2+} with nanoparticles particularly in Fe_3O_4 and ZnO by changing the morphology of nanoparticles (Fig. 12), as well as EDX analysis revealed increase amount of Ni, Cu, and Pb in the surfaces of sorbents (Fig. 13) thereby indicating the possibility of their precipitation onto nanoparticles.

Conclusion

Nanoparticles provide an efficient technique for the removal of toxic heavy metals from wastewater. This study investigated the removal of Cd^{2+}, Cu^{2+}, Ni^{2+}, and Pb^{2+} using nanoparticles (Fe_3O_4, ZnO and CuO) as novel sorbents. Metal removal depended on the pH of the medium and maximum adsorption occurred at

pH 6. A second order model described the kinetic data well. Metal uptake decreased with decreasing pH, thereby indicating the competition of protons for binding to acidic sites. The Freundlich isotherm fitted some equilibrium data, whereas other data were not well fitted. Our results showed that ZnO nanoparticles had a much higher metal adsorption capacity compared with the other nanoparticles tested.

References

Abollino O, Aceto M, Malandrino M, Sarzanini C, Mentasti E (2003) Sorption of heavy metals on Na-montmorillonite effect of pH and organic substances. Water Res 38: 1619–1627

Afkhami A, Moosavi R (2010) Adsorptive removal of Congo red, a carcinogenic textile dye, from aqueous solutions by maghemite nanoparticles. J Hazard Mater 174:398–403

Afkhami A, Norooz-Asl R (2009) Removal, preconcentration and determination of Mo (VI) from water and wastewater samples using maghemite nanoparticles. Colloids Surf A 346:52–57

Afkhami A, Saber-Tehrani M, Bagheri H (2010) Simultaneous removal of heavy-metal ions in wastewater samples using nano-alumina modified with 2,4-dinitrophenylhydrazine. J Hazard Mater 181:836–844

Afkhami A, Bagheri H, Madrakian T (2011) Alumina nanoparticles grafted with functional groups as a new adsorbent in efficient removal of formaldehyde from water samples. Desalination 281:151–158

Ahmadzadeh Tofighy M, Mohammadi T (2011) Adsorption of divalent heavy metals ions from water using carbon nanotube sheets. J Hazard Mater 185:140–147

Allison J, Novo-Gradac K (1991) MINTEQA2/PRODEFA2, A Geochemical assessment model for Environmental system: version 3.11 databases and version 3.0. User Manual. USEPA, Environmental Research Laboratory, Athens, GA

Banerjee SS, Chen DH (2007) Fast removal of copper ions by gum Arabic modified magnetic nano-adsorbent. J Hazard Mater 147:792–799

Bian SW, Mudunkotuwa IA, Rupansinghe T, Grassian VH (2011) Aggregation and dissolution of 4 nm ZnO nanoparticles in aqueous environment: influence of pH, ionic strength, size, and adsorption of humic acid. Langmuir 27:6059–6068

Blanchard G, Maunaye M, Martin G (1984) Removal of heavy metals from waters by means of natural zeolites. Water Res 18:1501–1507

Chen YH, Li FA (2010) Kinetics study on removal of Cu^{2+} using goethite and hematite nano-photocatalysts. Colloid Inter Sci 347:277–281

Chen JP, Yang L (2006) Study of a previous term heavy metal next term biosorption onto raw and chemically modified Sargassum sp. via spectroscopic and modeling analysis. Langmuir 22:8906–8914

Essington ME (2004) Soil and water chemistry: an integrative approach. CRC Press, Boca Raton

Ezoddina M, Shemirania F, Abdib Kh, Khosravi Saghezchia M, Jamalic MR (2010) Application of modified nano-alumina as a solid phase extraction sorbent for the preconcentration of Cd and Pb in water and herbal samples prior to flame atomic Absorption spectrometry determination. J Hazard Mater 178:900–905

Feng Y, Gong J-L, Zeng J-MNiu Q-Y, Zhang H-Y, Niu Ch-G, Deng J-H, Yan M (2011) Adsorption of Cd (II) and Zn (II) from aqueous solutions using magnetic hydroxyapatite nanoparticles as adsorbents. Chem Eng J 162:487–494

Flores V, Cabassud C (1999) A hybrid membrane process for Cu(II) removal from industrial wastewater, comparison with a conventional process system. Desalination 126: 101–108

Ghorbel-Abid I, Jrad A, Nahdi K, Trabelsi-Ayadi M (2009) Sorption of chromium (III) from aqueous solution using bentonitic clay. Desalination 246:595–604

Hu J, Chen G, Lo MC (2006) Selective removal of heavy metals from industrial waste water using maghemite nanoparticles: performance and mechanism. J Environ Eng 132: 702–715

Inglezakis VJ, Loizidou MD, Grigoropoulou HP (2003) Ion exchange of Pb^{2+}, Cu^{2+}, $Fe^{3.+}$, and Cr^{3+} on natural clinoptilolite: selectivity determination and influence of acidity. J Colloid Inter Sci 261:49–54

Jalali M, Arfania H (2010) Leaching of heavy metals and nutrients from calcareous sandy-loam soil receiving municipal sewage sludge. J Plant Nutr Soil Sci 173: 407–416

Jalali M, Moharrami, S (2007) Competitive adsorption of trace metals in calcareous soils of western Iran. Geoderma 140:156–163

Keyhanian F, Shariati Sh, Faraji M, Hesabi M (2011) Magnetite nanoparticles with surface modification for removal of methyl violet from aqueous solutions. Arab J Chem (in press)

Lazaridis NK, Charalambous C (2005) Sorptive removal of trivalent and hexavalent chromium from binary aqueous solutions by composite alginate–goethite beads. Water Res 39:4385–4396

Martinson CA, Reddy KJ (2009) Adsorption of arsenic(III) and arsenic(V) by cupric oxide nanoparticles. J Colloid Inter Sci 336:406–411

McBridge MB (1994) Environmental chemistry of soils. Oxford University Press, New York

Mobasherpour I, Salahi E, Pazouki M (2011a) Removal of nickel (II) from aqueous solutions by using nano-crystalline calcium hydroxyapatite. J Saudi Chem Soc 15: 105–112

Mobasherpour I, Salahi E, Pazouki M (2011b) Removal of divalent cadmium cations by means of synthetic nanocrystallite hydroxyapatite. Desalination 266:142–148

Nagappa B, Chandrappa GT (2007) Mesoporous nanocrystalline magnesium oxide for environmental remediation. Microporous Mesoporous Mater 106:212–218

Navrotsky A (2000) Nanomaterials in the environment, agriculture, and technology (NEAT). J Nanoparticles Res 2:321–323

Ok YS, Yang JE, Zhang Y-S, Kim SJ, Chung DY (2007) Heavy metal adsorption by a formulated zeolite-portland cements mixture. J Hazard Mater 147:91–96

Panayotova M, Velikov B (2002) Kinetics of heavy metal ions removal by use of natural zeolite. J Environ Sci Health Part A 37:139–147

Panneerselvam P, Morad N, Tan KA (2011) Magnetic nanoparticle (Fe_3O_4) impregnated onto tea waste for the removal of nickel (II) from aqueous solution. J Hazard Mater 186:160–168

Pederson AJ (2002) Evaluation of assisting agents for electrodialytic removal of Cd, Pb, Zn, Cu and Cr from MSWI fly ash. J Hazard Mater B95:185–198

Rahmani A, Zavvar Mosavi H, Fazli M (2010) Effect of nanostructure alumina on adsorption of heavy metals. Desalination 253:94–100

Recillas S, García A, González E, Casals E, Puntes V, Sánchez A, Font X (2011) Use of CeO_2, TiO_2 and Fe_3O_4 nanoparticles for the removal of lead from water: toxicity of nanoparticles and derived compounds. Desalination 277: 213–220

Rezaei M, Khajenoori M, Nematollahi B (2011) Preparation of nanocrystalline MgO by surfactant assisted precipitation method. Mater Res Bull 46:1632–1637

Savage N, Diallo MS (2005) Nanomaterials and water purification : opportunities and challenges. J Nanoparticles Res 7:331–342

Sharma YC, Srivastava V (2010) Separation of Ni (II) ions from aqueous solutions by magnetic nanoparticles. J Chem Eng Data 55:1441–1442

Sheng P, Ting YP, Chen JP, Hong L (2004) Sorption of lead, copper, cadmium, zinc, and nickel by marine algal biomass: characterization of biosorptive capacity and investigation of mechanisms. J Colloid Inter Sci 275:131–141

Singh J, Im J, Whitten JE, Soares JW, Steeves DM (2010) Chemisorption of a thiol-functionalized ruthenium dye on zinc oxide nanoparticles: implications for dye-sensitized solar cells. Chem Phys Lett 497:196–199

Song J, Kong H, Jang J (2011) Adsorption of heavy metal ions from aqueous solution by polyrhodanine-encapsulated magnetic nanoparticles. J Colloid Inter Sci 359:505–511

Vidal M, Santos MJ, Abrao T, Rodriguez J, Rigol A (2009) Modeling competitive metal sorption in a mineral soil. Geoderma 149:189–198

Wingenfelder U, Hansen C, Furrer G, Schulin R (2005) Removal of heavy metals from mine waters by natural zeolites. Environ Sci Technol 39:4606–4613

Yantasee W, Warner CL, Sangvanich T, Addleman RS, Carter TG, Wiacek RG, Fryxell GE, Timchalk C, Warner MG (2007) Removal of heavy metals from aqueous systems with thiol functionalized superparamagnetic nanoparticles. Environ Sci Technol 41:5114–5119

Zhang Y, Chen Y, Westerhoff P, Hristovski K, Crittenden JC (2008) Stability of commercial metal oxide nanoparticles in water. Water Res 42:2204–2212

Zhou YT, White CB, Nie HL, Zhu LM (2009) Adsorption mechanism of Cu^{2+} from solution by chitosan-coated magnetic nanoparticles modified with α-ketoglutaric acid. Colloids Sur B 74:244–252

DOI 10.1007/978-3-319-05041-6_15
Reprinted from the *Journal of Nanoparticle Research*, DOI 10.1007/s11051-012-0899-0

RESEARCH PAPER

Kaolin-supported nanoscale zero-valent iron for removing cationic dye–crystal violet in aqueous solution

Zheng-xian Chen · Ying Cheng · Zuliang Chen · Mallavarapu Megharaj · Ravendra Naidu

Received: 1 October 2011 / Accepted: 3 May 2012 / Published online: 5 July 2012

Abstract The degradation of crystal violet in aqueous solution was investigated using kaolin-supported zero-valent iron nanoparticles (K-nZVI). It was found that K-nZVI with a ratio of kaolin:zero-valent iron nanoparticles (nZVI) at 1:1 was most effective in removing crystal violet. Batch experiments show that more than 97.29 % crystal violet was degraded using K-nZVI, while only 24.36 % was removed using nZVI after reacting for 7 min, where the solution contained 100 mg L^{-1} crystal violet at pH 6.5. This is due to a decrease in aggregation of Fe^0 nanoparticles and enhanced their reactivity in the presence of kaolin, which was confirmed by the characterization using scanning electron microscopy. X-ray diffraction shows the formation of iron oxide and hydroxide, while UV–Vis spectral shows that the absorption peak of crystal violet was reduced, as well as Fourier transform infrared shows that new bands were formed after K-nZVI reacting with crystal violet. These suggest that degradation of crystal violet by K-nZVI include the oxidation of iron, the adsorption of crystal violet onto the K-nZVI, the transformation of crystal violet to leuko-crystal violet, and finally the cleavage of C=C bond.

Keywords Kaolin · Decoloration · Nanoscale zero-valent iron · Crystal violet Water filtration · Sustainable development

Special Issue Editors: Mamadou Diallo, Neil Fromer, Myung S. Jhon

This article is part of the Topical Collection on Nanotechnology for Sustainable Development

Z. Chen · Y. Cheng · Z. Chen
School of Chemistry and Material Sciences, Fujian Normal University, Fuzhou 350007, Fujian, China

Z. Chen (✉) · M. Megharaj · R. Naidu
Centre for Environmental Risk Assessment and Remediation, University of South Australia, Mawson Lakes, SA 5095, Australia
e-mail: zuliang.chen@unisa.edu.au

Z. Chen · M. Megharaj · R. Naidu
Cooperative Research Centre for Contamination Assessment and Remediation of Environments, Mawson Lakes, SA 5095, Australia

Introduction

In recent years, nanoscale zero-valent iron (nZVI) has been often used in groundwater treatment and site remediation due to its higher reactivity (Li et al. 2006; Theron et al. 2008). However, nZVI particles have a strong tendency to aggregate because nZVI agglomeration results from van der Waals forces of attraction (Choe et al. 2000). To prevent particle aggregation, a wide variety of stabilizers have been proposed to modify nZVI particle surface characteristics (Ponder et al. 2000; He and Zhao. 2005). Resin-supported nZVI particles were employed to remove Cr(VI) and Pb(II) from aqueous solutions where apparent rates of

removal for Cr(VI) and Pb(II) were enhanced 5-and 18-fold, respectively (Ponder et al. 2000). More recently, kaolinite-supported nZVI (Zhang et al. 2010) and bentonite-supported nZVI (Shi et al. 2010) have been used to remove aqueous Pb(II) and Cr(VI) and reduce the extent of their aggregation. These results suggest that implementing stabilized nZVI particles may represent an effective method for in situ remediation of groundwater or industrial effluents.

For treatment of dye wastewater, reports have been published concerning the use of nZVI to remove azo dyes. The reduction of Acid Black 24 in aqueous solution using nZVI showed that more than 97 % dye was removed in 30 min using an initial 100 mg L^{-1} dye solution (Shu et al. 2007). Removal of methyl orange using nZVI suggested that the main roles played by nZVI particles in the decolorization process were those of adsorption and reduction (Fan et al. 2009). The degradation of Orange G in aqueous solutions using Fe–Ni bimetallic nanoparticles revealed that this degradation mechanism proceeds through a reductive cleavage of the azo linkage, resulting in the formation of aniline and surface-adsorbed naphthol amine derivatives (Bokare et al. 2008). However, use of supported nZVI to remove cationic dye such as crystal violet in aqueous solution to significantly improve their aggregation and reactivity has not been reported. In addition, as cationic dyes are used widely in industrial applications for dyeing of silk, leather, paper, wool and cotton (Liu et al. 2010), it has not emerged that removing crystal violet using nZVI and the mechanism for removing crystal violet by nZVI are still unknown. This is because crystal violet is a cationic dye, which could distinguish it from azo dyes.

Furthermore, kaolin, which is a low-cost and efficient adsorbent, has great potential in removing crystal violet from wastewaters because it is abundant, has chemical and mechanical stability, high adsorption ability, and unique structural properties. Kaolin, furthermore, has been confirmed as an effective adsorbent in the removal of crystal violet and brilliant green from aqueous medium (Nandi et al. 2009). This study explores the possibility of removing crystal violet using kaolin-supported zero-valent iron nanoparticles (K-nZVI) and understanding its mechanism for doing this. In addition, the study also investigates whether K-nZVI improves nZVI aggregation and results in significantly increased reactivity. Therefore, this paper reports on two major issues: (1) the synthesis of K-nZVI and comparing the removal of crystal violet using kaolin, nZVI and K-nZVI; and (2) characterization of K-nZVI and the proposed degradation mechanism.

Materials and methods

Materials and chemicals

Kaolin was supplied by Taojinfeng Co. Ltd, which operates in Fujian, China. The chemical composition of the kaolin materials was as follows: SiO_2 50.67 %, Al_2O_3 44.02 %, Fe_2O_3 0.10 %, TiO_2 0.21 %, CaO 0.00 %, MgO 0.17 %, K_2O 0.21 %, Na_2O 0.00 %. After drying at a temperature of 70 °C for over 12 h, kaolin was ground and sieved with a 200 mesh screen before experimentation. All the reagents used in this study were of analytical reagent grade without further purification. Crystal violet solution was prepared by dissolving it in various amounts using distilled water to the desired concentrations. The chemicals used in this study include $NaBH_4$, $FeCl_3{\cdot}6H_2O$, and crystal violet ($C_{25}H_{30}N_3$, MW = 407.979 g mol^{-1}, characteristic wavelength 588 nm, Aldrich Chemical, USA).

Synthesis of nZVI and supported nZVI

nZVI and K-nZVI were synthesized as described in our previous study (Zhang et al. 2010), where liquid-phase reduction was used with kaolin as a supported material. In brief, 100 mL 0.179 M of Fe(III) solution was prepared by dissolving $FeCl_3{\cdot}6H_2O$ into a mixture of ethanol and water (30 %, v/v). The solution was added to a three-necked flask containing kaolin (4 g) and the contents were mixed uniformly under nitrogen using an electronic stir bar. Then an equal volume of $NaBH_4$ (1.610 M) was added drop-wise into the stirred mixture. The reduction reaction is given as an Eq. (1). The black solid produced was vacuum filtrated (Buchner funnel, Whatman filter paper, grade no. 1) and washed three times with 50 mL of 0.1 M HCl, distilled water and ethanol, respectively. The solid was then dried under N_2 atmosphere overnight and kept in a nitrogen atmosphere before use (Zhang et al. 2010).

$$4Fe^{3+} + 3BH_4^- + 9H_2O \rightarrow 4Fe^0_{(s)} \downarrow + 3B(OH)_3 + 9H^+ + 6H_2 \uparrow \quad (1)$$

Unsupported nZVI and K-nZVI with different mass ratios of kaolin versus nZVI, theoretically calculated to be 0:1, 1:1, 2:1, and 4:1, were then prepared by varying the initial kaolin loadings at the beginning of the synthesis.

Characterizations and measurements

The morphology and size of the kaolin, nZVI, and K-nZVI were observed using scanning electron microscopy (SEM) (Philips-FEI XL30 ESEM-TMP, Philips Electronics Co., Eindhoven, Netherlands). The operating voltage was set at 20 kV, and the current was 40 mA.

The specific surface areas (SSA) of nZVI, K-nZVI (1:1), and kaolin were measured using the BET-N_2 adsorption method (the Brunauer–Emmett–Teller isotherm) via Micromeritics' ASAP 2020 Accelerated Surface Area and Porosimetry Analyzer (Micromeritics Instrument Corp., GA).

X-ray diffraction (XRD) patterns concerning before and after K-nZVI reacted with crystal violet were done using a Philips-X'Pert Pro MPD (Netherlands) with a high-power Cu-Kα radioactive source ($\lambda = 0.154$ nm).

Fourier transforms infrared spectra (FTIR) concerning before and after K-nZVI reacted with crystal violet was obtained employing a Fourier transform infrared spectroscope (FTIR Nicolet 5700, Thermo Corp., USA). Samples for FTIR measurement were prepared by mixing 1 % (w/w) specimen with 100 mg of KBr powder and pressed into a sheer slice. An average of 9 scans was collected for each measurement with a resolution of 2 cm^{-1}.

Crystal violet concentration was measured using a UV-Spectrophotometer (722 N, Shanghai, China) at 588 nm. The removal efficiency of crystal violet using K-nZVI was calculated using the following equation (Shu et al. 2007):

$$\eta = \frac{C_0 - C_e}{C_0} \times 100\,\% \qquad (2)$$

where η (%) = the crystal violet removal efficiency, C_0 = the initial crystal violet concentration in the solution (mg L^{-1}), C_e = the crystal violet concentration at equilibrium (mg L^{-1}).

Batch experiments

To compare crystal violet removal efficiency using various materials, batch experiments were carried out using various materials added to a solution of 100 mg L^{-1} (25 mL). Mixtures were placed on a rotary shaker at 35 °C and then left at their initial pH. The mixed solutions were filtered through 0.45 μm membranes at different time intervals to determine the residual concentration of crystal violet. All these experiments were undertaken in duplicate.

Results and discussion

Mass ratios of kaolin/nZVI used to remove crystal violet

Figure 1 illustrates the removal efficiencies of crystal violet using K-nZVI, which had been prepared using different mass ratios of K-nZVI (1:1, 2:1, and 4:1). It can be seen that the removal efficiency of crystal violet varied according to the mass ratios of K-nZVI, which decreased as the mass ratio rose from 1:1 to 4:1. The highest removal efficiency of crystal violet was approximately 99.63 % using K-nZVI with a mass ratio of K-nZVI (1:1). However, an increase in the mass ratio of K-nZVI led to a decline in the removal efficiency of crystal violet. In the meantime the mass ratios of K-nZVI rose from 1:1 to 4:1. However, the removal efficiencies were equally poor when the mass ratio of K-nZVI rose to 4:1, where only 42.89 % crystal violet was removed using K-nZVI with a mass ratio of K-nZVI (4:1). This is due to the fact that the high content of kaolin blocked the formation of nZVI during the synthesis, and consequently resulted in a decline in the dispersion of iron nanoparticles on the kaolin as shown in Fig. 2 (Ponder et al. 2000; Zhang et al. 2010).

SSA can be used to evaluate the reactivity of nanoparticles, which was determined using the BET-N_2 adsorption–desorption method. The SSA for K-nZVI with various mass ratios of 1:1, 2:1, and 4:1 were 19.84, 17.92, and 15.99 $m^2\ g^{-1}$, respectively, while the SSA of nZVI was 35.16 $m^2\ g^{-1}$. This indicates that the SSA for K-nZVI decreased as the content of kaolin in K-nZVI increased, resulting in differences in crystal violet removal efficiency (Zhang et al. 2010). However, the surface area of K-nZVI is lower than that of nZVI, but its removal of crystal violet is higher than that of nZVI, suggesting that the aggregation of Fe^0 declined while the dispersion increased. Consequently its reactivity improved when

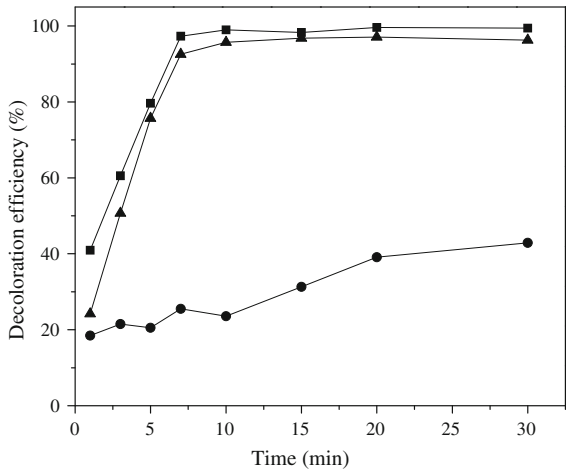

Fig. 1 Removal efficiencies of crystal violet using K-nZVI with different mass ratios of kaolin: nZVI. Conditions: dose: 1.0 g L^{-1} (the same mass of nZVI); 2.0 g L^{-1} K-nZVI; $C_0 = 100$ mg L^{-1}; 30 mL; 25 °C ± 1; pH = 6.5; shaking speed: 250 rpm. [*Triangle* using K-nZVI (1:1); *square* using K-nZVI (2:1); *circle* using K-nZVI (4:1)]

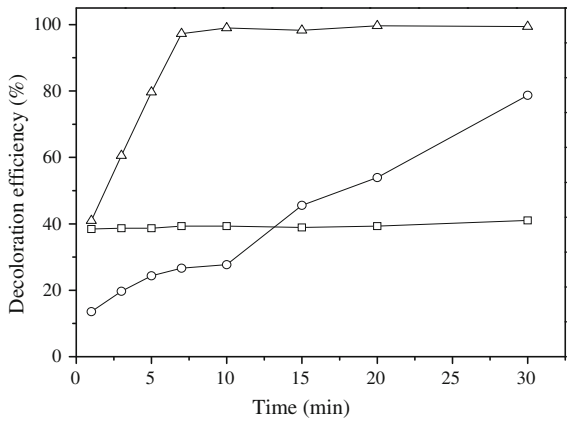

Fig. 2 Decolorization of crystal violet by various materials. Conditions: dose: 1.0 g L^{-1} (Kaolin, nZVI, respectively), 2.0 g L^{-1} K-nZVI; $C_0 = 100$ mg L^{-1}; 30 mL; 25 °C ± 1; pH = 6.5; shaking speed: 250 rpm. (*Square* using kaolin; *triangle* using K-nZVI; *circle* using nZVI)

the kaolin was used as a support material (Smuleac et al. 2010). In addition, a lower surface area resulted from the incorporation of kaolin (6.03 m^2 g^{-1}) as a support material, suggesting that kaolin not only dispersed and stabilized Fe^0 nanoparticles (Lin et al. 2009), but also played a role in adsorbing crystal violet from aqueous solution onto the kaolin (Nandi et al. 2009). This finding is confirmed by what is described in the following section. Hence, K-nZVI (1:1) was used in the subsequent study.

Degradation of crystal violet using various materials

Figure 2 shows the removal efficiency of crystal violet from an aqueous solution containing an initial concentration of 100 mg L^{-1} using kaolin (0.035 g), nZVI (0.035 g), and K-nZVI (0.070 g). It can be seen that the removal of crystal violet using K-nZVI reached at equilibrium was less than 7 min and more than 97.23 % K-nZVI was removed, while only 78.72 % was removed using nZVI and more than 30 min was required to reach equilibrium using nZVI. In addition, kaolin was an effective adsorbent for removing crystal violet from aqueous medium as the 39.33 % crystal violet was removed by the kaolin (Nandi et al. 2009). K-nZVI significantly improved the removal rate of crystal violet compared to that using nZVI despite the fact that K-nZVI has a lower surface area (19.84 m^2 g^{-1}) than that of nZVI (35.16 m^2 g^{-1}). It suggests that kaolin as a support material could first, stabilize and disperse nZVI and second, prevent nZVI from aggregation and consequently increase the reactivity of the nZVI. Previous SME images of K-nZVI have confirmed this. Less efficient removal of crystal violet using nZVI could be attributed to the fact that nZVI was prone to aggregate as shown, leading to a decrease in its specific surface area and reaction activity (Choe et al. 2000; Zhang et al. 2010) despite the low adsorption of cationic dye onto the Fe^0, Fe_2O_3, and Fe_3O_4 being reported (Noubactep 2009).

Figure 2 shows that the adsorption of crystal violet onto kaolin had occurred, where 39.22 % crystal violet was removed despite the kaolin having a low surface area (6.03 m^2 g^{-1}). This agrees with a study of kaolin as an effective adsorbent for removing crystal violet and from aqueous solution (Nandi et al. 2009). As the removal of cationic species using kaolin is based on ion exchange, where small amounts of Fe species could result in a significant change in the surface charge (Zeta potential of kaolin was 6.00 by the measurement) and adsorption mechanisms and kaolin has a relative low cation-exchange capacity (Nandi et al. 2009; Jiang et al. 2010), this made it favorable in adsorbing cationic dye such as crystal violet because of electrostatic attraction. On the basis

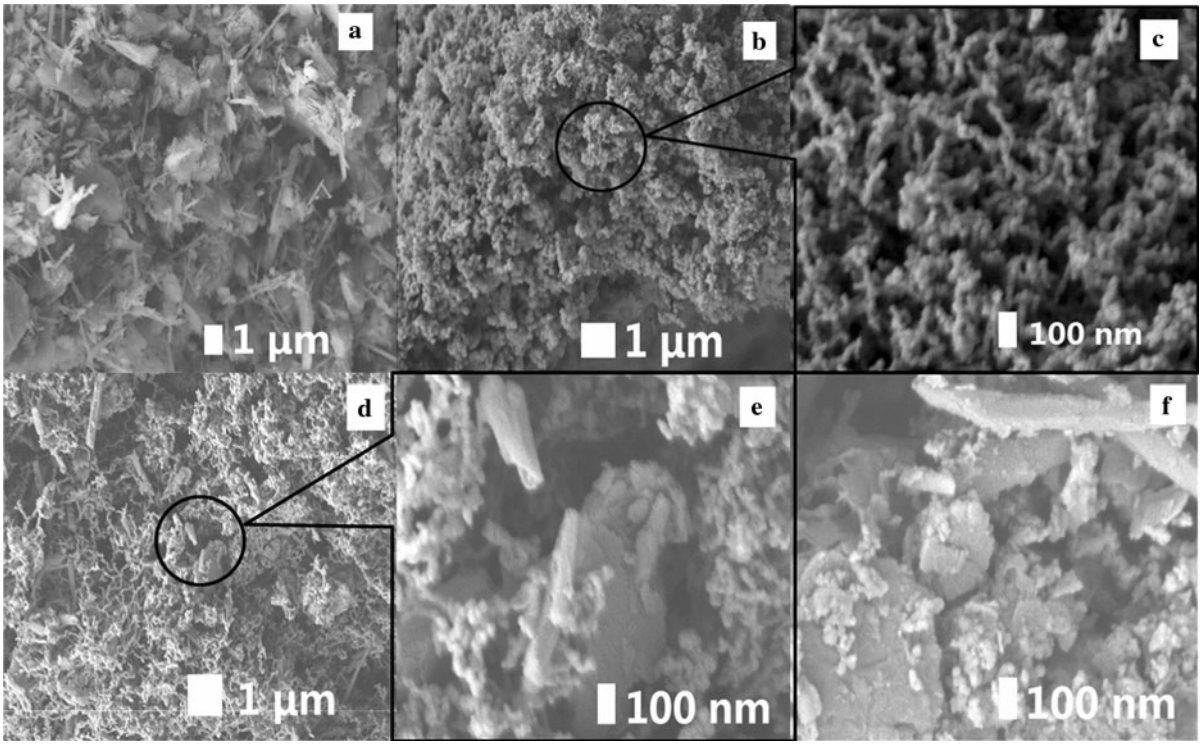

Fig. 3 SEM images of nZVI and K-nZVI. **a** Kaolin (×10,000), **b** nZVI (×10,000), **c** nZVI (×50,000), **d** K-nZVI (1:1) before reaction (×10,000), **e** K-nZVI (1:1) before reaction (50000), **f** K-nZVI (1:1) after reaction (×50,000)

of the results for removing crystal violet using various materials, it is concluded that kaolin in K-nZVI plays both an adsorption role of crystal violet and dispersant role of nZVI. In the meantime the nZVI (as a reducer) in K-nZVI provides the electron, and for this reason the crystal violet decreased (Noubactep 2009). This explains why K-nZVI is able to remove a high amount of crystal violet from aqueous solution.

Characterizations

SEM of various materials

The morphologies of kaolin, nZVI, K-nZVI before and after reacting with crystal violet were characterized by SEM as shown in Fig. 3. As observed in SEM image (Fig. 3a), the kaolin was formed by sheets and every sheet clung closely to each other. In addition, the kaolin showed some white particles on the surface of the mineral; these are likely to be non-clay minerals such as sodium, potassium, calcium, and magnesium (Galan et al. 1996). The synthesized nZVI were mostly spherical and existed in the form of prominent chain-like aggregates (Fig. 3b, c). However, Fig. 3d, e was obtained from sample prepared with mass ratios of kaolin to iron (1:1), the aggregation of nZVI seems to decrease compared to that in Fig. 3b, c. This was also observed when kaolin was used as a support material for nZVI to remove Pb(II), Cu(II), and Co(II) (Üzüm et al. 2009; Zhang et al. 2010). However, as shown in Fig. 3f, the dimensions of iron nanoparticles increased distinctively after being used to remove the crystal violet. This results from the formed passive iron oxides layers [Fe_3O_4, Fe_2O_3, $Fe(OH)_3$, and FeOOH] and subsequently coated the surface of the nanoparticles (Mielczarski et al. 2005), which was further confirmed by the XRD.

XRD spectrogram

The XRD patterns of kaolin, K-nZVI before and after reacting with crystal violet are presented in Fig. 4. It can be seen that a characteristic peak at $2\theta = 44.9°$ confirmed the existence of zero-valent iron (α-Fe^0) in freshly prepared K-nZVI (Fig. 4a) (Fan et al. 2009). The peak in Fig. 4b indicated the presence of maghemite (γ-Fe_2O_3) ($2\theta = 35.68°$), and magnetite (Fe_3O_4)

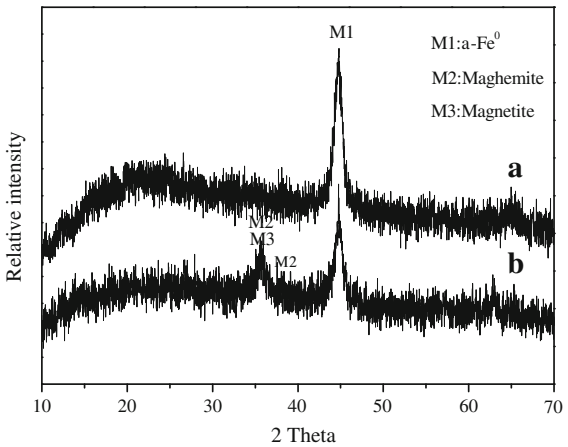

Fig. 4 X-ray diffraction spectral of K-nZVI. **a** Before the reaction, **b** after the reaction

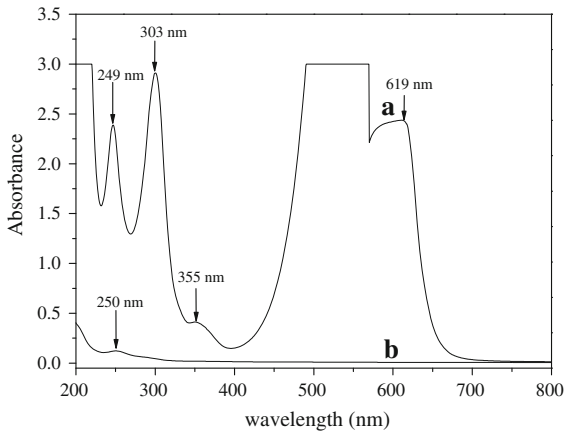

Fig. 5 UV–Visible spectral. **a** Before the reaction with K-nZVI, **b** after reaction with K-nZVI. Conditions: dose: 2.0 g L^{-1} K-nZVI (1:1); C_0 = 100 mg L^{-1}; 30 mL; 25 °C ± 1; pH = 6.5; shaking speed: 250 rpm

($2\theta = 35.45°$) in the K-nZVI after reacting with crystal violet, while the zero-valent iron's peak was obviously reduced and the iron oxide's peak had increased (Mielczarski et al. 2005; Üzüm et al. 2009). It can therefore be concluded that iron oxides formed as a result of K-nZVI reducing the crystal violet, where nZVI as the electron donor provided the electron and the crystal violet accepted the electron to form the leuko-crystal violet (Noubactep 2009). Hence, this is the reason why the dimensions of iron nanoparticles increased after K-nZVI reacted with the crystal violet as observed by the SEM images.

Figure 5 illustrates the UV–Vis spectra of crystal violet using a standard solution containing an initial concentration of 100 mg L^{-1}, where the band at 619 nm originated from the –C=C– bond, and bands at 249, 303, and 355 nm related to aromatic rings were observed (Fan et al. 2009). In contrast, the band at 619 nm fell significantly when the K-nZVI was added to the solution containing 100 mg L^{-1} crystal violet when the colorless leuko- crystal violet was formed (Noubactep 2009). This indicates that the degradation of the crystal violet was thought to form the leuko-crystal violet as the crystal violet was reduced by the K-nZVI.

FTIR analysis

Kaolin, nZVI, K-nZVI before and after reacting with crystal violet were scanned in the range of 4,000–400 cm^{-1} wave numbers using a FTIR with spectra shown in Fig. 6a–d. The FTIR spectra for kaolin in Fig. 6a shows the bands at 3623.60 and 3697.80 cm^{-1}, which corresponds to O–H vibration of H_2O molecule in the kaolin mesosphere (Kakali et al. 2001). The bands at 1,045 and 916 cm^{-1} suggest the presence of Al–O–H bands (Ryan and Huertas 2009), while the band peaks at 3623.60 cm^{-1} and 3697.80 cm^{-1} correspond to O–H vibration of H_2O molecule in the kaolin mesosphere (Kakali et al. 2001; Ryan and Huertas 2009). The O–H vibration in kaolin octahedron was significantly reduced, which was due to the partial destruction of the Si–O and Al–O bond. This resulted from the reaction of $NaBH_4$ and H_2O

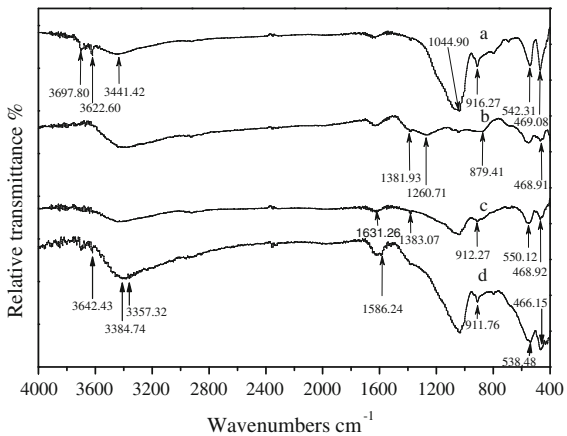

Fig. 6 FTIR spectral. **a** Kaolin, **b** nZVI, **c** K-nZVI before reaction, **d** K-nZVI after reaction

introduced during the preparation of nZVI (Yuan et al. 2008). In addition, the bands at 469.00 and 540.60 cm^{-1} corresponding to Fe–O stretch of Fe_2O_3 and Fe_3O_4 were observed in Fig. 6c, d, which agrees well with the nZVI spectra bands (Fig. 6c). This indicates that the part of the nZVI in K-nZVI was oxidized (Zhu et al. 2010). Furthermore, new bands at 1586.24 cm^{-1} correspond to C=O stretching vibrations, and 911.76 cm^{-1} corresponds to symmetric out of plane bending of the ring hydrogens (Ayed et al. 2010).

As shown in Fig. 2, the 39.33 % crystal violet was removed by the kaolin from aqueous solution, indicating that crystal violet is absorbed onto the kaolin. In addition, SEM (Fig. 3) and XRD (Fig. 4) display that the formation of maghemite (γ-Fe_2O_3), and magnetite (Fe_3O_4) after reaction, where crystal violet can be adsorbed onto the oxide iron as previously reported (Noubactep 2009; Zhu et al. 2010). The UV–Visible spectral at 619 nm originated from the –C=C– bond was nearly disappeared completely (Fig. 5), indicating that the crystal violet was reduced by K-nZVI, where K-nZVI was first oxidized and provided electron, and then the dye molecule accepted electron. The possible mechanism is summarized as below

$$\text{Crystal violet} + \text{Kaolin} \rightarrow \text{Crystal violet} - \text{Kaolin (adsorption)} \quad (3)$$

$$Fe^0 + 2H_2O \rightarrow Fe^{2+} + H_2 + 2OH^- + 2e^- \text{(inbasic solution)} \quad (4)$$

$$Fe^0 + 2H^+ \rightarrow Fe^{2+} + H_2 + 2e^- \text{(in acid solution)} \quad (5)$$

$$4Fe^0 + 2H_2O + O_2 \rightarrow \gamma - Fe_2O_3 \text{ and } Fe_3O_4 \quad (6)$$

$$\text{Crystal violet} + \gamma - Fe_2O_3 \text{ and } Fe_3O_4 \rightarrow \text{Crystal violet} - \text{iron oxides} \quad (7)$$

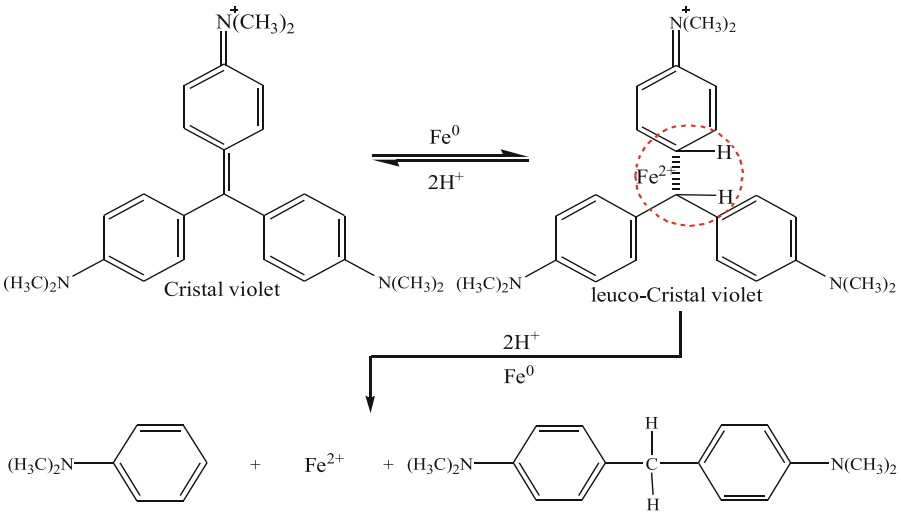

(8)

Conclusion

In this study, it emerged that K-nZVI can be used to remove a high concentration of crystal violet from aqueous solution when the surface area of K-nZVI is enhanced (26.11 $m^2\ g^{-1}$) and the nZVI aggregation is reduced. The results obtained from SEM indicate that nZVI loaded onto kaolin was well dispersed and this helped aggregation to decrease. XRD analyses demonstrated that Fe in the K-nZVI was oxidized and provided an excellent level of efficiency in removing crystal violet. In describing the mechanism of K-nZVI to remove crystal violet, it can be concluded that crystal violet in aqueous solution was absorbed by K-nZVI, and following this the crystal violet formed leuko-crystal violet. Last, the C=C bond cleavage was broken by the reduction.

Acknowledgments The project was supported by a Fujian "Minjiang Fellowship" from Fujian Normal University.

References

Ayed L, Chaie K, Cheref A, Bakhrouf A (2010) Biodegradation and decolorization of triphenylmethane dyes by *Staphylococcus epidermidis*. Desalination 260:137–146

Bokare A, Chikate R, Rode C, Paknikar K (2008) Iron–nickel bimetallic nanoparticles for reductive degradation of azo dye Orange G in aqueous solution. App Catal B 79:270–278

Choe S, Chang Y, Hwang K, Khim J (2000) Kinetics of reductive denitrification by nanoscale zero-valent iron. Chemosphere 41:1307–1311

Fan J, Guo Y, Wang J, Fan M (2009) Rapid decolorization of azo dye methyl orange in aqueous solution by nanoscale zerovalent iron particles. J Hazard Mater 166:904–910

Galan E, Aparicio P, Miras A, Michailidis K, Tsirambides A (1996) Technical properties of compounded kaolin sample from Griva (Macedonia, Greece). Appl Clay Sci 10: 477–490

He P, Zhao D (2005) Preparation and characterization of a new class of starch stabilized bimetallic nanoparticles for degradation of chlorinated hydrocarbons in water. Environ Sci Technol 39:3314–3320

Jiang M, Jin X, Lu X, Chen Z (2010) Adsorption of Pb(II), Cd(II), Ni(II) and Cu(II) onto natural kaolinite clay. Desalination 252:33–39

Kakali G, Perraki T, Tsivilis S, Badogiannis E (2001) Thermal treatment of kaolin: the effect of mineralogy on the pozzolanic activity. Appl Clay Sci 20:73–80

Li X, Elliott D, Zhang W (2006) Zero-valent iron nanoparticles for abatement of environmental pollutants: materials and engineering aspects. Crit Rev Solid State Mater Sci 31: 111–122

Lin C, Liou Y, Lo S (2009) Supported Pd/Sn bimetallic nanoparticles for reductive dechlorination of aqueous trichloroethylene. Chemosphere 74:314–319

Liu Q, Wang L, Xiao A, Guo J, Ding W, Yu H, Huo J, Ericson M (2010) Templated preparation of porous magnetic microspheres and their application in removal of cationic dyes from wastewater. J Hazard Mater 181:586–592

Mielczarski J, Atenas G, Mielczarski E (2005) Role of iron surface oxidation layers in decomposition of azo-dye water pollutants in weak acidic solutions. Appl Catal B 56: 289–303

Nandi B, Goswama I, Purkait M (2009) Removal of cationic dyes from aqueous solution by kaolin: kinetic and equilibrium studies. Appl Clay Sci 42:583–590

Noubactep C (2009) Characterizing the discoloration of methylene blue in Fe_0/H_2O systems. J Hazard Mater 166:79–87

Ponder S, Darab J, Mallouk T (2000) Remediation of Cr(VI) and Pb(II) aqueous solutions using supported, nanoscale zero-valent iron. Environ Sci Technol 34:2564–2569

Ryan P, Huertas F (2009) The temporal evolution of pedogenic Fe–smectite to Fe-kaolin via interstratified kaolin–smectite in a moist tropical soil chronosequence. Geoderma 151: 1–15

Shi L, Zhang X, Chen Z (2010) Bentonite-supported nanoscale zero-valent iron used to remove Cr(VI) from wastewater. Water Res 45:886–892

Shu H, Chang M, Yu H, Chen W (2007) Reduction of an azo dye acid black 24 solution using synthesized nanoscale zero-valent iron particles. J Colloid Interface Sci 314:89–97

Smuleac V, Bachas L, Bhattacharyya D (2010) Aqueous-phase synthesis of PAA in PVDF membrane pores for nanoparticle synthesis and dichlorobiphenyl degradation. J Membr Sci 346:310–317

Theron J, Walker J, Cloete T (2008) Nanotechnology and water treatment: applications and emerging opportunities. Crit Rev Microbiol 34:43–69

Üzüm Ç, Shahwan T, Eroğlu A, Hallam K, Scott T, Lieberwirth I (2009) Synthesis and characterization of kaolinite-supported zero-valent iron nanoparticles and their application for the removal of aqueous Cu^{2+} and Co^{2+} ions. Appl Clay Sci 43:172–181

Yuan P, Annabi-Bergaya F, Tao Q, Fan M, Liu Z, Zhu J, He H, Chen T (2008) A combined study by XRD, MR, TG and HRTEM on the structure of delaminated Fe-intercalated/pillared clay. J Colloid Interface Sci 324:142–149

Zhang X, Lin S, Lu X, Chen Z (2010) Removal of Pb(II) from water using natural kaolin loaded with synthesized nanoscale zero-valent iron. Chem Eng J 163:243–248

Zhu H, Jiang R, Xiao L, Li W (2010) A novel magnetically separable Fe_2O_3 crosslinked chitosan adsorbent: preparation, characterization and adsorption application for removal of hazardous azo dye. J Hazard Mater 119: 251–257

DOI 10.1007/978-3-319-05041-6_16
Reprinted from the *Journal of Nanoparticle Research*, DOI 10.1007/s11051-012-0900-y

RESEARCH PAPER

Aqueous phosphate removal using nanoscale zero-valent iron

Talal Almeelbi · Achintya Bezbaruah

Received: 22 December 2011 / Accepted: 3 May 2012 / Published online: 28 June 2012

Abstract Nanoscale zero-valent iron (NZVI) particles have been used for the remediation of a wide variety of contaminants. NZVI particles have high reactivity because of high reactive surface area. In this study, NZVI slurry was successfully used for phosphate removal and recovery. Batch studies conducted using different concentrations of phosphate (1, 5, and 10 mg PO_4^{3-}-P/L with 400 mg NZVI/L) removed ~96 to 100 % phosphate in 30 min. Efficacy of the NZVI in phosphate removal was found to 13.9 times higher than micro-ZVI (MZVI) particles with same NZVI and MZVI surface area concentrations used in batch reactors. Ionic strength, sulfate, nitrate, and humic substances present in the water affected in phosphate removal by NZVI but they may not have any practical significance in phosphate removal in the field. Phosphate recovery batch study indicated that better recovery is achieved at higher pH and it decreased with lowering of the pH of the aqueous solution. Maximum phosphate recovery of ~78 % was achieved in 30 min at pH 12. The successful rapid removal of phosphate by NZVI from aqueous solution is expected to have great ramification for cleaning up nutrient rich waters.

Keywords Phosphate · Nanoscale zero-valent iron (NZVI) · Microscale zero-valent iron (MZVI) · Phosphate removal · Phosphate recovery · Adsorption · Eutrophication · Environmental remediation · Sustainable development

Special Issue Editors: Mamadou Diallo, Neil Fromer, Myung S. Jhon

This article is part of the Topical Collection on Nanotechnology for Sustainable Development

T. Almeelbi · A. Bezbaruah (✉)
Department of Civil Engineering, Nanoenvirology Research Group, Fargo, ND 58108, USA
e-mail: a.bezbaruah@ndsu.edu

T. Almeelbi
Environmental and Conservation Sciences Program, North Dakota State University, Fargo, ND 58108, USA

Introduction

Phosphorus (P) exists in water in both particulate and dissolved forms. The usual forms of P in aqueous solutions are orthophosphates, polyphosphates, and organic phosphates (Mezenner and Bensmaili 2009). Phosphorus is necessary for the growth of organisms and plants and is an indicator of surface water quality. Excessive P present in natural waters is known to cause eutrophication (Penn and Warren 2009). Eutrophication results in the depletion of oxygen that leads to fish death and affects other aquatic life forms adversely. The major point sources that contribute to P built up in aquatic environment include municipal and industrial wastewaters. Run-offs from agriculture, including animal agriculture, are the major non-point

sources. The amount of P compounds in these sources should be controlled to prevent eutrophication in lakes and other surface waters. Accelerated eutrophication not only affects the aquatic life but indirectly hinders the economic progress of communities that depend on aquatic food and other resources (Cleary et al. 2009). Dissolved phosphate of ~0.02 mg/L is considered to have potential that lead to profuse algal growth in waters (USEPA 1995).

On the other hand, phosphorus is one of the required nutrients for plants. P-based fertilizers are extensively used in food crops and it is intricately related to global food security. Phosphorous for fertilizer production comes predominantly from select mines from Morocco, Western Saharan region, and China (Cordell et al. 2009). Phosphorus is a nonrenewable resource. While an assessment of future consumption of phosphorus fertilizers indicates that natural phosphate (PO_4^{3-}) deposits will last for approximately 60–240 years (Cornel and Schaum 2009), P production rate is predicted to decline sometime in year 2035 while the demand for P-based fertilizers is on the rise (Cordell et al. 2011). Short supply of P-fertilizer is a major concern in food security area. It is, therefore, essential recover P from 'wastes' for possible reuse in agriculture.

Chemical precipitation (de Bashan and Bashan 2004), physico-chemical processes (Mishra et al. 2010), and enhanced biological phosphate removal (Gouider et al. 2011) are the frequently used techniques to remove aqueous phosphate. Among them chemical treatment methods for aqueous phosphate removal are widely practiced using chemicals like lime (Ahn and Speece 2006), alum (Babatunde and Zhao 2010), and ferric chloride (Caravelli et al. 2010). However, the high cost of chemicals and problems associated with sludge management make these methods unattractive for waters containing high amounts of phosphate (for example, wastewater with a typical total P of 4–14 mg/L, Tchobanoglous et al. 2003).

Sorption has emerged as a viable option for phosphate removal from aqueous media. In the recent years considerable amount of emphasis has been put on the use of low cost (ad)sorbents. Cost effectiveness is identified as the prime criterion in the selection of a sorption technology whether it uses synthetic or natural sorbents (Mishra et al. 2010). Phosphate can be removed from water using sorbents such as oxides of iron, natural ores like calcite, and goethite (FeOOH), active red mud, and activated carbon. One of the problems encountered with these sorbents is that they have very low sorption capacities. For example, sorption capacities of iron oxides are 11.2 mg PO_4^{3-}/g (Yan et al. 2010a) and 19.02 mg PO_4^{3-}-P/g (Cordray 2008). Similarly, natural ores like calcite were reported to have a sorption capacity of 0.1 mM PO_4^{3-}/g (i.e., 3.1 mg PO_4^{3-}-P/g, Karageorgiou et al. 2007). Goethite (FeOOH, 17.3 mg PO_4^{3-}-P/g, Chitrakar et al. 2006), active red mud (9.8 PO_4^{3-}-P/g, Yue et al. 2010), and activated carbon (3.02 mg PO_4^{3-}-P/g, Hussain et al. 2011) are so far tried for P removal.

In the last two decades nanoscale zero-valent iron (NZVI) particles have received a lot of attention because of their unique reactive and sorbtive characteristics (Bezbaruah et al. 2009, 2011; Li et al. 2006). NZVI particles show good sorbtive characteristics owing to their high surface to volume ratio (Yan et al. 2010b). However, most of the reported work on sorption by NZVI has been on metalloids and heavy metals including some actinides (Giasuddin et al. 2007; Kanel et al. 2005; Klimkova et al. 2011; Scott et al. 2011) and, to the best of the authors' knowledge, there is no literature on phosphate removal using NZVI and subsequent recovery of phosphate.

The objective of this study is to investigate the efficacy of NZVI particles for phosphate removal and recovery from aqueous solutions. Phosphate removal was tried under different environmental conditions (temperature, ionic strength), and in the presence of interfering ions and organic compounds. The effect of NZVI particle size on phosphate removal was studied. Batch experiments were conducted under different pH conditions to investigate the optimal pH conditions for phosphate recovery from NZVI.

Materials and methods

Chemicals and reagents

Iron(III) chloride hexahydrate ($FeCl_3 \cdot 6H_2O$, 98 %, Alfa Aesar), sodium borohydride ($NaBH_4$, 98 %, Aldrich), methanol (production grade, BDH), calcium chloride ($CaCl_2$, ACS grade, BDH), monopotassium phosphate (KH_2PO_4, 99 %, EMD), potassium nitrate (KNO_3, 99 %, Alfa Aesar), sodium hydroxide (5 N NaOH, Alfa Aesar), potassium sulfate (K_2SO_4, ACS grade, HACH), natural organic matter (Suwannee

River NOM, RO isolation, IHSS), and humic acid (H1452, Spectrum) were used as received unless and otherwise specified.

Synthesis of NZVI

NZVI particles were synthesized using sodium borohydride reduction method (Eq. 1, Huang and Ehrman 2007).

$$2FeCl_3 + 6NaBH_4 + 18H_2O \rightarrow 2Fe^0 + 21H_2 + 6B(OH)_3 + 6NaCl \quad (1)$$

Ferric chloride hydrate (1.35 g) was dissolved in 40 mL of deoxygenated de-ionized (DI) water (solution A), and 0.95 g of sodium borohydride was dissolved in 10 mL of deoxygenated DI water in a separate beaker (solution B). Then solution A was added drop wise to solution B under vigorous stirring conditions (using a magnetic stirrer). The resultant black precipitates (NZVI) were centrifuged and washed with copious amount of deoxygenated DI water. The NZVI in slurry form was then stored in 20 mL vials in methanol to prevent oxidation, and used for experiments later. NZVI slurry in the vials was withdrawn using a pipette after vigorous stirring. The average weight of dry NZVI present in 1 mL well stirred slurry was measured to be 20 mg ± 0.6 mg ($n = 25$).

Phosphate removal batch studies

Batch experiments were conducted using (a) NZVI and (b) microscale zero-valent iron (MZVI) particles. Phosphate solution (50 mL of 1, 5, 10 mg PO_4^{3-}-P/L) with 20 mg of NZVI (i.e., 400 mg/L) in multiple 50 mL polypropylene plastic vials fitted with plastic caps (reactors). The reactors were rotated end-over-end at 28 rpm in a custom-made shaker to reduce mass transfer resistance. One of the reactors was withdrawn at specific time interval (0, 10, 20, 30, 60 min) and the content was centrifuged at 4,000 rpm. Bulk solution from this reactor was collected for phosphate analysis and reactor was sacrificed or the spent NZVI was used for phosphate recovery study (see "Phosphate recovery batch studies"). Ascorbic acid method (Eaton et al. 2005) was used for phosphate analysis. This method depends on the formation phosphomolybdic acid during the reaction between orthophosphate and molybdate. Ascorbic acid reduces phosphomolybdic to form a blue complex. The color was measured in a UV–vis spectrophotometer (HACH, DR 5000) at wavelength of 880 nm. A five-point calibration was done routinely.

Effect of initial NZVI concentration

Batch studies were conducted with seven different NZVI concentrations (80, 160, 240, 320, 400, 480, 560 mg/L) for an initial bulk PO_4^{3-}-P concentration of 5 mg/L. The experimental procedure described earlier (see "Phosphate removal batch studies") was followed. Samples were withdrawn for phosphate analysis at 30 min.

Interference studies

The effects ionic strength, presence of selected anions and cations, and humic substances were examined. Batch studies were conducted in room temperature (22 ± 2 °C) using 400 mg NZVI/L and 40 mL of solution with an initial bulk phosphate concentration of 5 mg PO_4^{3-}-P/L. Sampling frequency was maintained as described earlier (see "Phosphate removal batch studies").

The ionic strength was varied from 0 to 10 mM by adding specific amounts of $CaCl_2$ to the phosphate solution. The range of ionic strength was selected to represent groundwater conditions. The possible interference due to the presence of other important ions was also studied using two important anions (sulfate and nitrate). Potassium sulfate was used as the source of SO_4^{2-} (0, 100, 500, 900 mg/L). The effect of NO_3^- (0, 1, 5, 10 mg NO_3^--N /L) was studied by adding KNO_3. Humic substances present in water may affect phosphate removal by NZVI, and to evaluate such impacts Suwannee River (USA) natural organic matter (0, 1, 10, 50 mg/L) and humic acids (0, 1, 10, 50 mg/L) were used in separate batch experiments. The batch experiments were conducted as described earlier (see "Phosphate removal batch studies").

Effect of temperature

Experiments were conducted under different temperatures conditions (4, 22, 60 °C) to find out the effect of temperature change on phosphate removal by NZVI. The temperature of phosphate solution was first adjusted to the desired temperature by keeping it in the specific environment for long enough periods

(~24 h). NZVI particles (400 mg/L) were added to phosphate solution (40 mL, 5 mg/L) once the specific temperature was reached. Samples were shaken at 100 rpm under temperature-controlled environment using an incubator-cum-orbital shaker (Thermo Scientific, MaxQ4000).

Effect of particle size

Effect of zero-valent iron (ZVI) particle size on phosphate removal was evaluated using NZVI particles synthesized within this research and MZVI particles purchased from a supplier (Aldrich, 99.9 % purity, used as received). ZVI reactions are known to be surface mediated (Thompson et al. 2010), and as such it was ensured that the same surface area concentrations were used in the experiments conducted with NZVI and MZVI. The NZVI particles used in this experiment had a surface area of ~25 m^2/g (Bezbaruah et al. 2009) and MZVI had a surface area of ~2 m^2/g (reported by the manufacturer). NZVI and MZVI surface area concentration of 10 m^2/L (400 mg/L NZVI and 5 g/L MZVI) was used in the study.

Phosphate recovery batch studies

An initial batch study was conducted to find out the pattern of desorption (recovery) of phosphate into water from NZVI used for phosphate removal. Batch experiments were run first in 50 mL plastic vials fitted with plastic caps (reactors) with 400 mg/L NZVI and 50 mL of 5 mg PO_4^{3-}-P/L to get the phosphate sorbed onto NZVI. The batch reactors were withdrawn after 60 min and centrifuged to separate the spent NZVI (i.e., NZVI particles with phosphate sorbed onto them). The bulk solution was decanted out and phosphate concentration was measured. A 50 mL volume of DI water was added to the spent NZVI and the pH was manipulated (2–12) with either 0.1 N HCl or NaOH. The reactors were closed and rotated end-over-end for 30 min. The reactors with the samples were then centrifuged and concentration of phosphate was measured in the bulk solution. The optimal pH for phosphate recovery (i.e., when maximum phosphate recovery) was determined based on this initial batch study results, and the rest of the phosphate recovery experiments were conducted at that particular (optimal) pH.

Additional batch studies were conducted in sacrificial reactors at the optimal pH, and phosphate recovery was monitored over time (0, 10, 20, 30 min). The data obtained from the removal experiments were normalized with respect to the original bulk phosphate concentration. For the data sets from the recovery studies, the initial phosphate concentration was calculated based on the mass of phosphate sorbed onto the NZVI and the data were normalized with respect to that.

NZVI characterization

X-ray diffraction (XRD) was done to find out NZVI composition. The samples were placed in stainless steel sample holders and XRD patterns were recorded using Cu Kα radiation ($\lambda = 1.5418$ Å) on a Philips X'Pert diffractometer operating at 40 kV and 40 mA between 5° and 90° (2θ) at a step size of 0.0167° (Xi et al. 2010).

High-resolution transmission electron microscopy (HRTEM, JEOL JEM-2100-LaB6 TEM) was used to observe the shape of NZVI particles and determine their particle size. NZVI particles were vacuum dried and the dry particles were placed in ethanol and sonicated for 5 min to achieve proper dispersion. Drops of the resulting solution were placed onto lacey carbon grids (Electron Microscopy Sciences, USA) and allowed to dry. Images were taken using a Gatan ORIUS large format CCD camera.

Quality control

All experiments were done in triplicates during this research and the average values are reported along with the standard deviations. Blanks with only phosphate (without NZVI/MZVI) were run along with the NZVI and MZVI experiments. The analytical instruments and tools were calibrated before the day's measurements. One-way analysis of variance (ANOVA) tests were performed to compare the variance between data sets as needed. Additionally, Dunnett Method was used to compare control with rest of the treatment data. Minitab 16 software (Minitab, USA) was used for all statistical analyses.

Results and discussion

NZVI synthesis and characterization

NZVI synthesized (Fig. 1a) during this research were mostly spherical in shape and had particle size

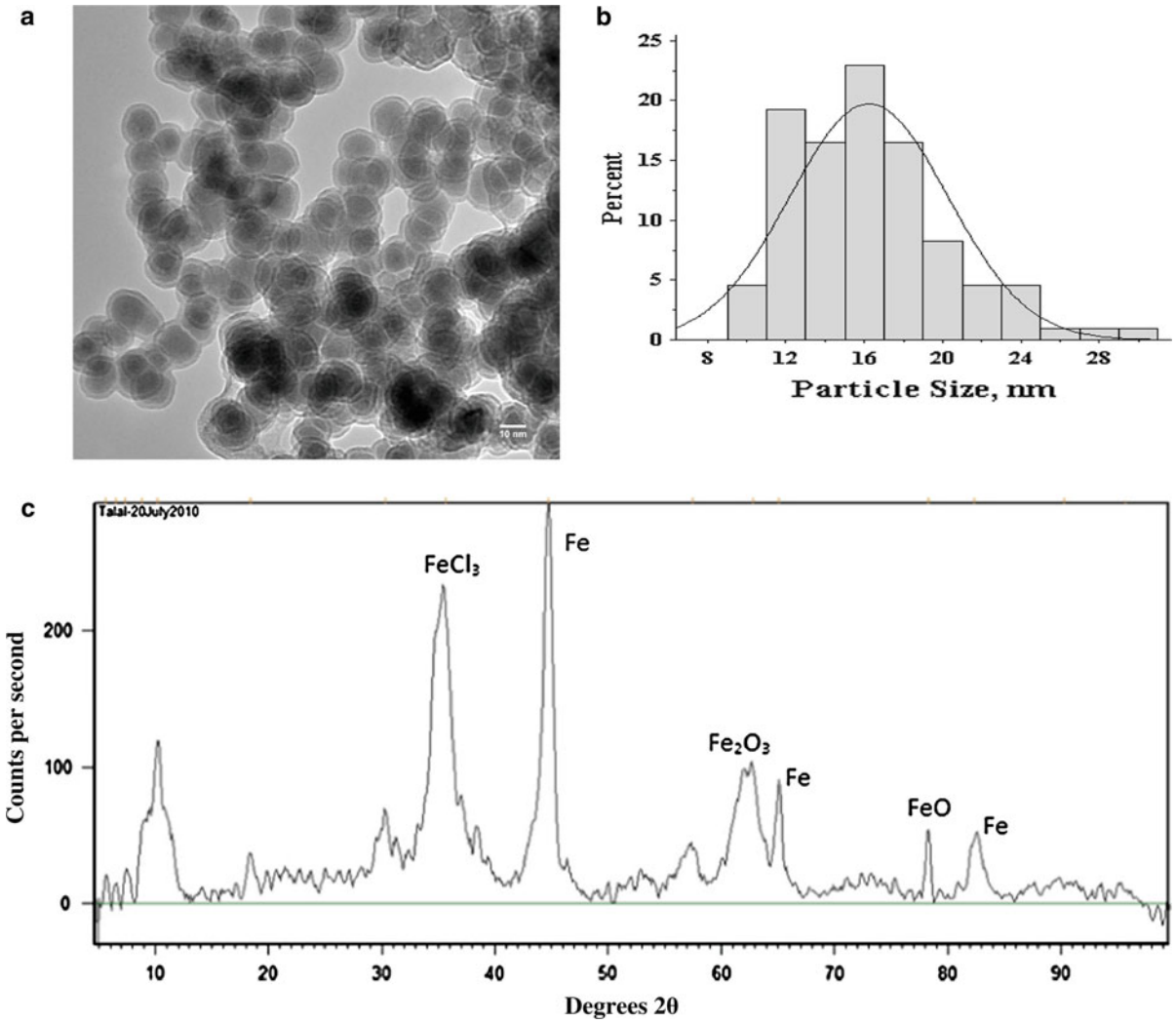

Fig. 1 **a** High-resolution transmission electron microscopy (HRTEM) image of NZVI. **b** Particles size distribution of the nanoparticles synthesized was 10–30 nm with an average size of 16.24 ± 4.05 nm ($n = 109$). **c** X-ray diffraction (XRD) spectrum of NZVI with prominent peaks for Fe^0. Peaks for oxides are from Fe-oxide layer on the NZVI, and the $FeCl_3$ peak is from residuals of raw materials used in NZVI synthesis

distribution from 10 to 30 nm with an average size of 16.24 ± 4.05 nm ($n = 109$, Fig. 1b). Huang and Ehrman (2007) reported particle size of 20 nm using the same method. The XRD spectrum (Fig. 1c) for the particles synthesized during this study shows three peaks of zero-valent iron (Fe^0). A couple of iron oxide peaks were also observed which might be because of exposure of the particles to air during the XRD experiment. During the synthesis of NZVI, the particles were not bleed with air (as in Bezbaruah et al. 2009, 2011) but there is still a possibility that a thin oxide layer around the particles was formed due to reaction with atmospheric oxygen. A peak for iron chloride was also observed which might be from the left over reactants used for the synthesis of NZVI (see Eq. 1).

Phosphate removal

Batch experiments were conducted for phosphate removal using 400 mg/L NZVI and different phosphate concentrations (1, 5, 10 mg PO_4^{3-}-P/L). Rapid phosphate removal was observed in the first a few minutes of the experiment for all three concentrations.

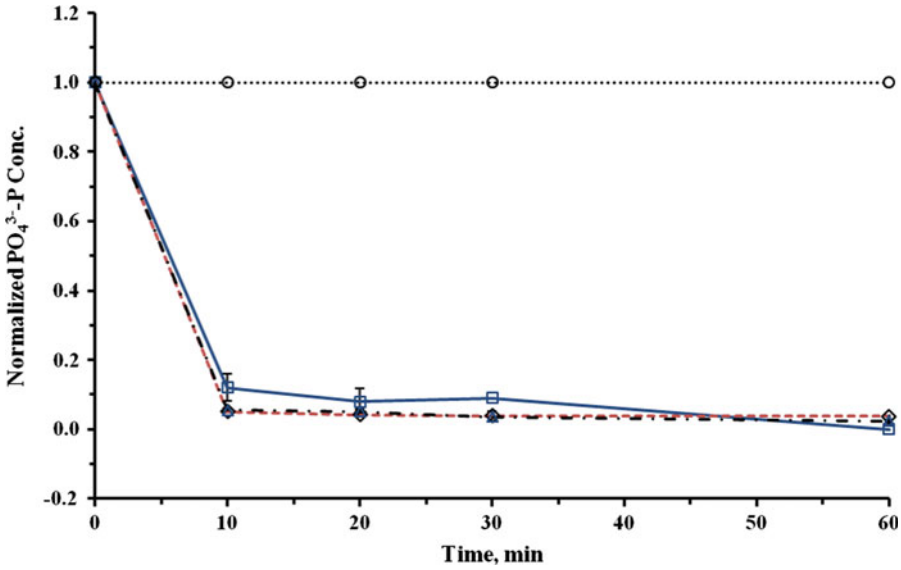

Fig. 2 Phosphate removal by NZVI/L from bulk solutions with different initial phosphate concentrations (*triangle* 10 mg PO_4^{3-}-P/L, *diamond* 5 mg PO_4^{3-}-P/L, *square* 1 mg PO_4^{3-}-P/L, *circle* Blank). NZVI = 400 mg/L

Table 1 Different iron-based adsorbents used for phosphate removal and their performance data

Type of iron	Type of water/phosphate	Removal (%, time)	% Recovery	Source
Hydroxy-iron	DI/KH_2PO_4	90 %, 5.83 h	–	Yan et al. (2010a)
Iron ore	Wastewater	97 %, 15 d	–	Guo et al. (2009)
Iron hydroxide–eggshell waste	Distilled water/KH_2PO_4	73 %, 3.67 h		Mezenner and Bensmaili (2009)
Steel slag	Distilled water/KH_2PO_4	71–82 %, 2 h	–	Xiong et al. (2008)
Synthetic Goethite	NaH_2PO_4	40–100 %, 2–8 h	~82%	Chitrakar et al. (2006)
Akaganeite	NaH_2PO_4	15–100 %, 4–8 h	~90 %	Chitrakar et al. (2006)
Synthetic Goethite	Sea water/NaH_2PO_4	60 %, 24 h	–	Chitrakar et al. (2006)
Akaganeite	Sea water/NaH_2PO_4	30 %, 24 h	–	Chitrakar et al. (2006)
Iron oxide tailing	DI/KH_2PO_4	71 %, 24 h	13–14 %	Zeng et al. (2004)
Biogenic iron oxide	DI/KH_2PO_4	100 %, 24 h	49 %	Cordray (2008)
This study-NZVI	DI/KH_2PO_4	96–100 %, 60 min	~80 %	

About 88–95 % of phosphate was removed within the first 10 min and only minimal removal was observed beyond that (Fig. 2). Blanks did not show any removal of phosphate. Three consecutive data points (20, 30, and 60 min) showed no major change (maximum 2.7 % variation) in phosphate removal for the two higher concentrations (5 and 10 mg PO_4^{3-}-P/L) while a much larger variation (~7.8 % from 20 to 60 min) was observed for 1 mg PO_4^{3-}-P/L. While complete (100 %) phosphate removal was observed for 1 mg PO_4^{3-}-P/L solution, 96.29 ± 0.13 and 97.53 ± 0.16 percent removals were observed for 5 and 10 mg PO_4^{3-}-P/L, respectively. The sorption capacities at 60 min were found to be 2.27 ± 0.00, 12.00 ± 0.02, and 24.38 ± 0.04 mg/g for 1, 5, and 10 mg PO_4^{3-}-P/L, respectively. The sorption capacity increased linearly ($R^2 = 0.9999$) with the increase in phosphate concentration.

For 5 mg PO_4^{3-}-P/L, 30 min was found to be long enough time to achieve equilibrium with 400 mg NZVI/L. As such all experimental data for 5 mg PO_4^{3-}-P/L and 400 mg NZVI/L were collected up to 30 min. Iron-based removal techniques are reported by others where 15–100 % phosphate removal has been achieved (Table 1). Hydroxides of iron were found to be most effective in the removal process but a wide range of efficiency (15–100 %) has been reported (Chitrakar et al. 2006; Cordray 2008; Mezenner and Bensmaili 2009; Yan et al. 2010a). Synthetic goethite (α-FeOOH) was found to remove

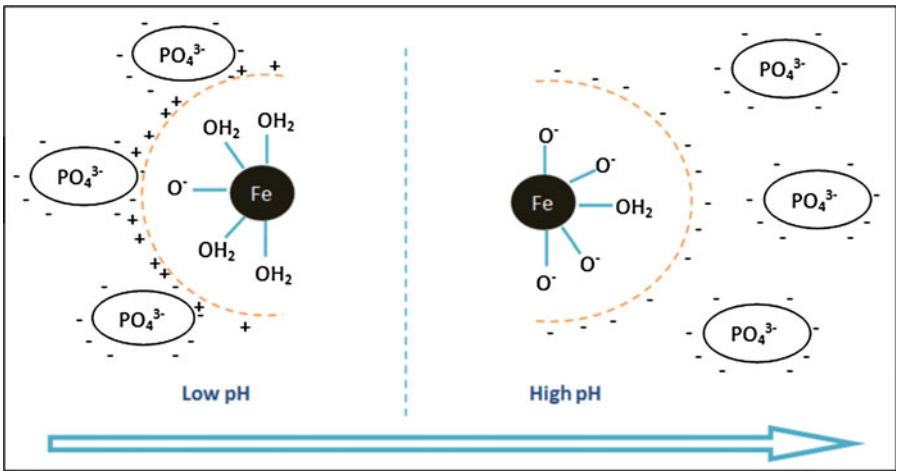

Fig. 3 Phosphate sorption by NZVI under various pH conditions (after Cordray 2008). Lower pH is more conducive for phosphate adsorption while desorption is the dominant phenomenon at higher pH

up to 1 mg P/L completely (100 %) from NaH_2PO_4 solution (Chitrakar et al. 2006). Again 100 % phosphate removal was observed with akaganeite (β-FeOOH) up to 0.3 mg P/L. It took 2–8 h to reach equilibrium in most of the reported phosphate removal experiments done with DI/distilled/wastewater (Mezenner and Bensmaili 2009; Chitrakar et al. 2006; Xiong et al. 2008; Yan et al. 2010a) but took 24 h to reach equilibrium in seawater (Chitrakar et al. 2006). It is pertinent here to discuss treatment time in other sorption systems for comparison purposes. Hussain et al. (2011) reported 95 % removal of phosphate with granular activated carbon over a 150-min period. Sorption of ~95 % of phosphate on calcite in 45 min was reported by Karageorgiou et al. (2007).

In the present study, very fast removal of phosphate (88–95 % in 10 min) was achieved, and that makes this research very relevant for continuously flowing (pumped) water (i.e., required contact time will be short). The sorption capacities of NZVI after 10-min interaction with the aqueous solution containing phosphate were found to be 2.20 ± 0.06, 11.87 ± 1.20, and 23.62 ± 0.11 mg/g for 1, 5, and 10 mg PO_4^{3-}-P/L solutions, respectively. The sorption capacities of 3.02–19.02 mg PO_4^{3-}-P/g reported by others (Chitrakar et al. 2006; Cordray 2008; Hussain et al. 2011; Karageorgiou et al. 2007; Yan et al. 2010a, b) are comparable to the sorption capacities achieved for the NZVI in this study. However, the reaction time is much shorter with NZVI.

The mechanism of phosphate removal by NZVI in the present study can be explained based on point of zero charge (PZC) and ligand exchange (Eq. 2, Karageorgiou et al. 2007, and Fig. 3). PZC for NZVI is around 7.7 (Giasuddin et al. 2007), and when pH is less than PZC the surface of NZVI is positively charged which makes the surface suitable for anion (PO_4^{3-}) sorption. The initial pH of the test solutions used in this study was ~4.0 and final pH after 60 min reaction was ~7.5 which was still lower than the PZC of NZVI. The pH environment maintained in the reactor was ideal for PO_4^{3-} sorption and that is why 97.53–100 % removal was achieved in this study.

$$-\mathrm{Fe}-\mathrm{OH} + \mathrm{X}^- \xrightarrow{\mathrm{H}^+} -\mathrm{Fe}-\mathrm{O}^{\delta-}\cdots\mathrm{X}^- \quad (\mathrm{pH} < \mathrm{PZC}) \qquad (2)$$

Effect of initial NZVI concentration

The removal of phosphate (C_0 = 5 mg/L) was found to increase with increase in the initial NZVI concentration (Fig. 4) and followed a linear trend (R^2 = 0.9539) as NZVI concentration increased from 0 to 560 mg/L. NZVI concentration beyond 400 mg/L did not improve PO_4^{3-} removal significantly. Phosphate removal of 100 % was obtained with 560 mg NZVI/L. When the initial NZVI concentration was increased from 80 to 560 mg/L, the removal of phosphate increased by ~78 %. The increase in phosphate removal efficiency with the increase in NZVI concentration was expected as the contaminant removal by NZVI is a surface area mediated process. When NZVI concentration increased from 0 to 560 mg/L the reactive iron surface area in solution

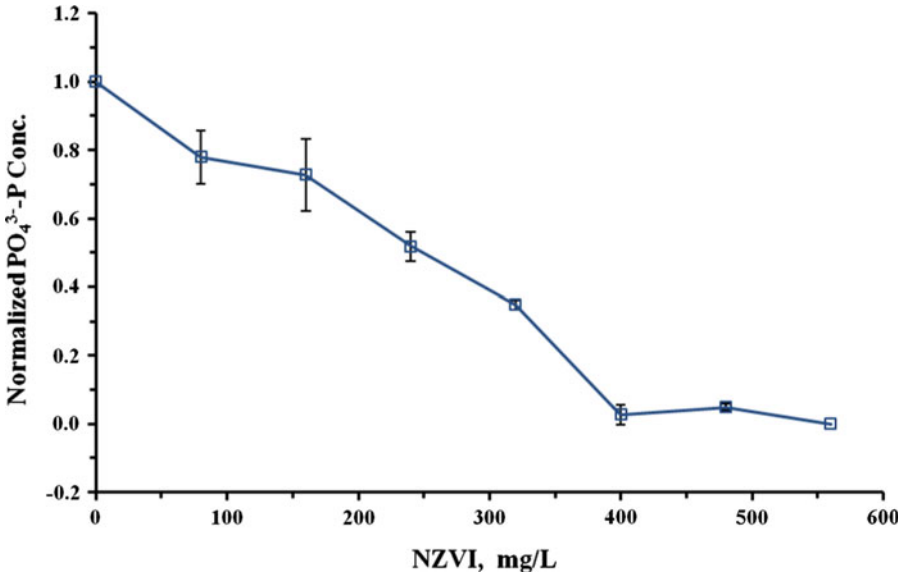

Fig. 4 Effect of initial NZVI concentration on phosphate removal. Initial PO_4^{3-}-P = 5 mg/L

increased from 0 to 14 m^2/L (NZVI surface area = 25 m^2/g). The observations are consistent with findings by others with sorption media where surface area controls the sorption of phosphate (Mezenner and Bensmaili 2009).

Interference studies

The interferences of various ions and organic matters on phosphate removal were studied with an objective to understand how NZVI is going to behave during real field applications. Ionic strength (varied from 0 to 10 mM) did not have any statistically significant effect on phosphate (C_0 = 5 mg/L) removal by NZVI (Fig. 5a, $\alpha = 0.005$, $p = 0.225$). However, ANOVA tests showed statistically significant differences in the treatment data for nitrate ($\alpha = 0.005$, $p = 0.001$), sulfate (0–900 mg/L, $\alpha = 0.005$, $p = 0.00$), humic acid (0–50 mg/L, $\alpha = 0.005$, $p = 0.00$), and NOM (0–50 mg/L, $\alpha = 0.005$, $p = 0.00$). Dunnett method was used to further compare the control with rest of the treatment data. All nitrate concentrations (1, 5, 10 mg NO_3^--N/L, Fig. 5b) were found to significantly interfere in phosphate removal from aqueous solution. However, this statistically significant increase in phosphate removal (1.40–2.77 %) may not have any practical significance bring very marginal. Again, the treatment data were significantly different from the control for all sulfate concentrations (100, 500, 900 mg/L). Phosphate removal by NZVI decreased by 5.16–6.27 % in the presence of sulfate in the solution (Fig. 5c). While the presence of NOM (1, 10, 50 mg/L, Fig. 5d) decreased phosphate removal by 6.01–11.03 % (all statistically significant), the presence of humic acid showed mixed results. The presence of 1 mg/L humic acid (Fig. 5e) significantly reduced (13.86 %) phosphate removal but interference was not statistically significant when humic acid concentration was increased (10 and 50 mg/L).

Liu et al. (2011) have reported interference due to ionic strength during phosphate removal with lanthanum-doped activated carbon fiber. They increased ionic strength from 0 to 10 mM and observed an 8.1 % drop in phosphate removal (from 98.8 to 90.7 %). Even 10 mM ionic strength did not affect the phosphate removal efficiency in the present study, and a removal of 96.0–98.5 % was achieved in all cases (ionic strength varied from 0 to 10 mM). Introducing competing anions was expected to have negative effects on phosphate adsorption (Liu et al. 2011). Fe^0 was successfully used by others to remove nitrate from aqueous solution (Bezbaruah et al. 2009; Hwang et al. 2011) and so it was expected that nitrate will compete with phosphate for reactive/sorption sites on NZVI. Nitrate was found to interfere in phosphate removal in layered double hydroxides (Das et al. 2006) and ~12 % reduction in phosphate removal in the presence of nitrate was reported. Xue et al. (2009), however, did not find any interference of NO_3^- during phosphate removal using basic oxygen furnace slag. In the present

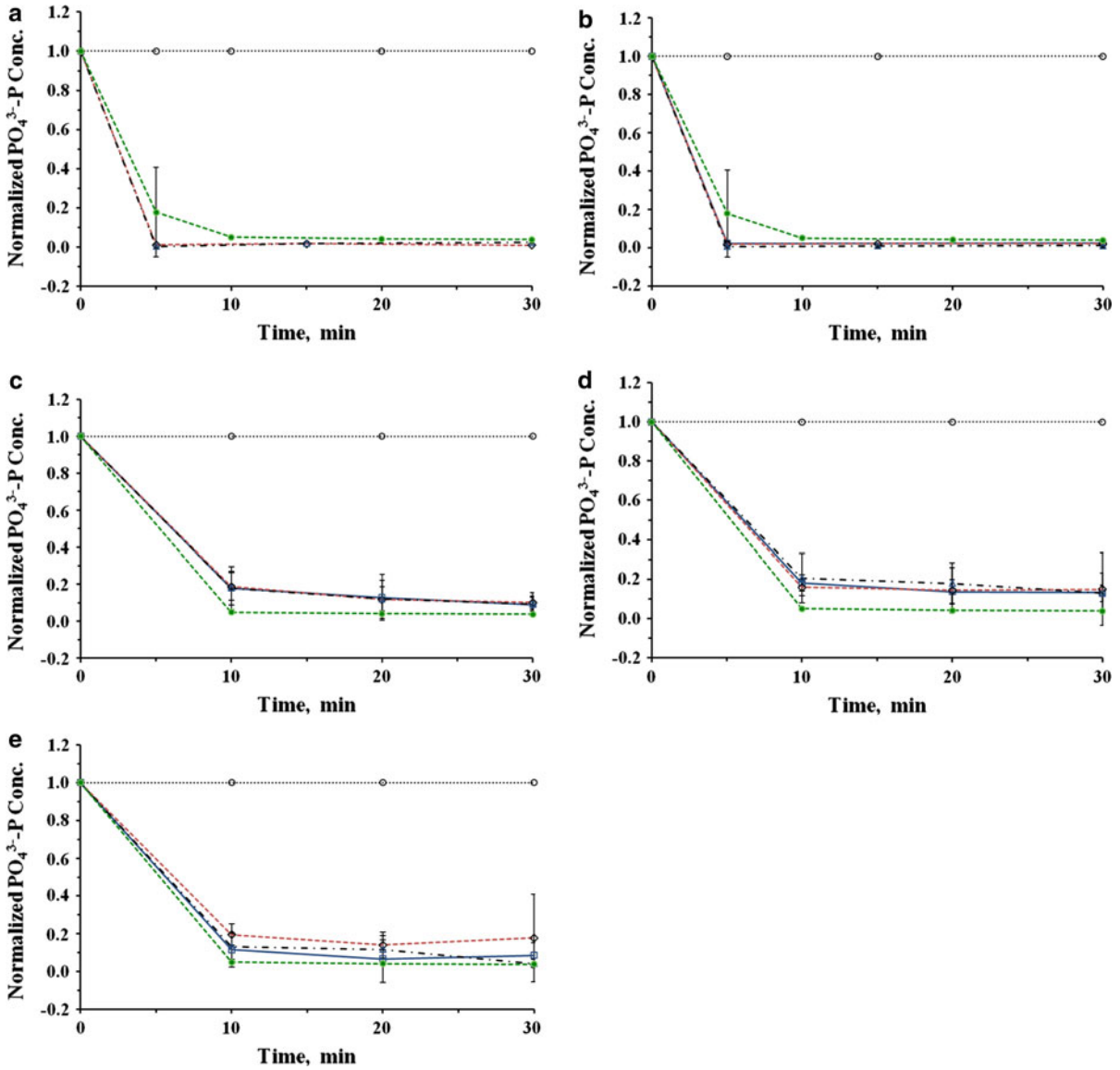

Fig. 5 **a** Phosphate removal under different ionic strength conditions (*filled circle* 0 mM ionic strength, *diamond* 5 mM ionic strength, *triangle* 10 mM ionic strength). **b** Phosphate removal in the presence of nitrate (*filled circle* 0 mg NO_3^--N/L, *square* 1 mg NO_3^--N/L, *diamond* 5 mg NO_3^--N/L, *triangle* 10 mg NO_3^--N/L). **c** Phosphate removal in the presence of sulfate (*filled circle* 0 mg SO_4^{2-}/L, *square* 100 mg SO_4^{2-}/L, *diamond* 500 mg SO_4^{2-}/L, *triangle* 900 mg SO_4^{2-}/L). **d** Phosphate removal in the presence of natural organic matter (*filled circle* 0 mg NOM/L, *square* 1 mg NOM/L, *diamond* 10 mg NOM/L, *triangle* 50 mg NOM/L). **e** Phosphate removal in the presence of humic acids (*filled circle* 0 mg/L, *square* 1 mg/L, *diamond* 10 mg/L, *triangle* 50 mg/L). For all figures: *open circle* Blank, NZVI = 400 mg/L, Initial PO_4^{3-}-P = 5 mg/L

study slight increase (1.40–2.77 %) in phosphate removal (though not environmentally significant) was observed. Further research would be needed to find out the possible reason for this increase but the authors would like to hypothesis that nitrate reacted with NZVI to produce iron (hydr)oxides with a higher affinity for phosphate. Sulfate was also reported to interfere with phosphate and reduced phosphate removal by 24.5 % in layered double hydroxides (Das et al. 2006). In this study, sulfate retarded the phosphate removal process and reduced removal efficiency as high 6.27 %. The adsorption of phosphate in presence of humic acid was studied by Antelo et al. (2007) and found that phosphate adsorption onto the surface of goethite decreased by 45

and 25 % in the presence of humic acid at pH of 4.5 and 7, respectively. This can be explained by the competition of the humic acids functional groups with phosphate for the sorption sites where the humic acid outcompeted the phosphate. Also, the sorption sites on the surface could be blocked by the relatively large size of humic acids (~15 Å in diameter, Simeoni et al. 2003), thus less sorption sites will be available for phosphate (~2.56 Å in diameter) (Antelo et al. 2007). Similar results were reported by others (Shuai and Zinati 2009). In the present study only low concentration (1 mg/L) of humic acid affected phosphate removal while higher concentration did not. This happened possibly because of increased sorption of phosphate onto NZVI due to lowering of solution pH (see Fig. 3) at higher humic acid concentrations. Additional experiments are needed to investigate why the presence of the humic substances did not adversely affect phosphate removal by NZVI, the authors feel that NZVI reacts very fast with phosphate in the first 10 min or so the possible inferring compounds are not competitive enough. In this study, phosphate removal in the presence of Suwannee River NOM (1, 10, 50 mg/L) was found to be significantly different from the control (without NOM). Phosphate removal efficiency of NZVI reduced by 9.01–11.03 % in the presence of NOM. This result was expected as NOM negatively impacts NZVI reactivity. Li et al. (2010) reported the minimum concentration of NZVI that inhibited *E. coli* growth after 24 h exposure as 5 mg NZVI/L. However, in the presence of NOM, the NZVI concentration had to be increased to 100 mg/L to achieve the same degree of inhibition. This happened possibly because the NZVI particles' reactive surfaces were covered with NOM and, thus, reducing the overall reactivity of NZVI. Chen et al. (2011) also observed a 23 % reduction in trichloroethylene (TCE) degradation by NZVI in the presence of Suwannee River NOM.

Effects of temperature

Experiments were conducted at 4, 22, and 60 °C during this study. The removal of phosphate at 4 and 22 °C was relatively slower than the removal at 60 °C. However, after 30 min, the removal was the more or less same (91.4–95.3 %) for all temperatures (Fig. 6) and there was no significant differences between the values (one-way ANOVA: $\alpha = 0.005$, $p = 0.144$). This is in contrast to findings by others. Increasing the temperature from 25 to 45 °C increased the phosphate adsorption capacity of granular ferric hydroxide from 3.6 to 5.1 M P/g (i.e., 0.11–0.16 mg/g, Saha et al. 2010). Liu et al. (2011) also reported increase adsorption capacity in lanthanum-doped activated carbon fibers from 8.54 to 9.41 mg/g of with the increase of temperature from 20 to 50 °C. Mezenner and Bensmaili (2009) reported ~60 % increase in phosphate adsorption onto iron hydroxide–eggshell waste when the temperature was increased from 20 to

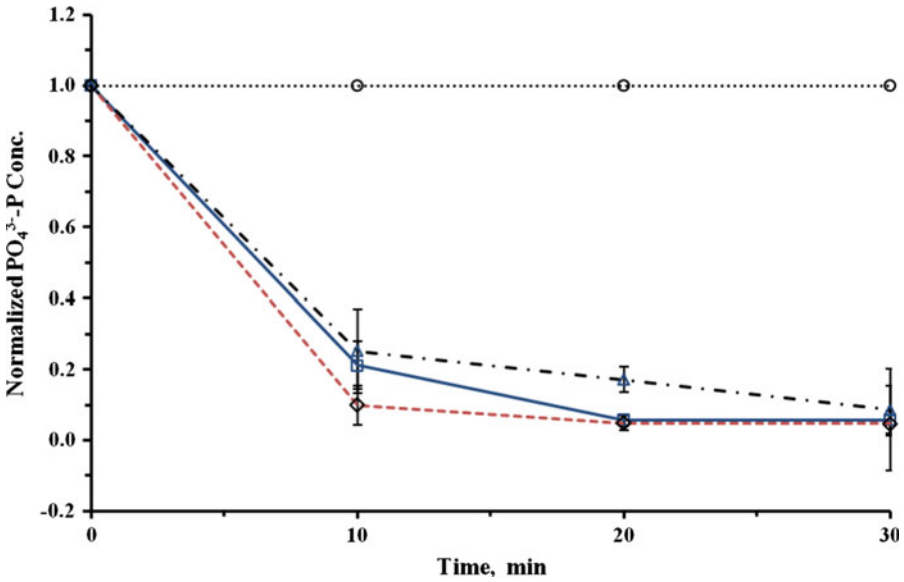

Fig. 6 Effect of temperature on phosphate removal by NZVI, (*square* 4 °C, *triangle* 22 °C, *diamond* 60 °C, *circle* Blank with only PO_4^{3-} solution). NZVI = 400 mg/L, Initial PO_4^{3-}-P = 5 mg/L. Blank shown here is for 22 °C only. The blanks at other temperatures followed similar trends and are not shown here to maintain clarity

45 °C. Fast phosphate removal that takes place within the first 10 min may be the reason why no distinction could be made between removal achieved in three different temperatures.

Effect of particle size

Sorption is dependent on surface area and, hence, in this study the same surface area (10 m^2/L) was used for the comparison of phosphate removal by NZVI (particle size ~16 nm) and MZVI (<10 μm). MZVI removed only 23 % of phosphate (C_0 = 5 mg PO_4^{3-}-P/L) in 30 min whereas NZVI removed ~96 % of phosphate over the same time period (Fig. 7). NZVI was 13.9 times more efficient than MZVI in removing aqueous phosphate. Others reported similar observations with NZVI for other contaminants. Surface area normalized rate constant (k_{sa}) of NZVI (surface area ~30–35 m^2/g) for tetrachloromethane degradation was reported as over two orders of magnitude higher than that of MZVI (Li et al. 2006). Also, removal capacity of Cr(VI) using NZVI was more than 100 times that of the removal capacity using MZVI (Li et al. 2006). Kanel et al. (2005) reported that the k_{sa} for As(III) removal by NZVI was 1–3 orders of magnitude higher than MZVI. While using NZVI, k_{sa} of alachlor degradation was found to be ~10 times that with MZVI ($k_{sa\text{-}NZVI} = 38.5 \times 10^{-5}$ and $k_{sa\text{-}MZVI} = 3.8\text{–}7.7 \times 10^{-5}$ L h^{-1} m^{-2}, Thompson et al. 2010).

Phosphate recovery

In the initial batch study ran to find out the optimal pH for phosphate recovery maximum phosphate recovery was achieved at pH 12, and the recovery was minimal at acidic pH (data not shown). In the follow up phosphate desorption (recovery) batch studies conducted at pH 12, 78.4 % phosphate recovery was obtained (Fig. 8). The 78.4 % recovery is based on the mass of phosphate sorbed onto NZVI during removal experiment. If the recovery is calculated based on the mass of the phosphate present in the original bulk solution from which removal was achieved than the phosphate removal is 74.5 %. In terms of practical applications, if 5 mg/L phosphate is present in bulk solution 4.80 mg/L (96 % removal, see "Phosphate removal" under "Results and discussion") will be removed by NZVI and 3.73 mg/L (74.5 % recovery) can be recovered back from the NZVI. Better phosphate recovery at higher pH was achieved possibly because of the abundantly present hydroxide ions at a higher pH. The presence of these hydroxide ions would result in a net negative surface charge to which few phosphate anions would be bound. The opposite phenomena would occur at a lower pH which would result in more sorption. Poor recovery of phosphate at pH 4 and 6 supports the previously proposed mechanism where an electrostatic attraction between the phosphate ions and the surface of NZVI occur resulting in phosphate sorption on the surface of

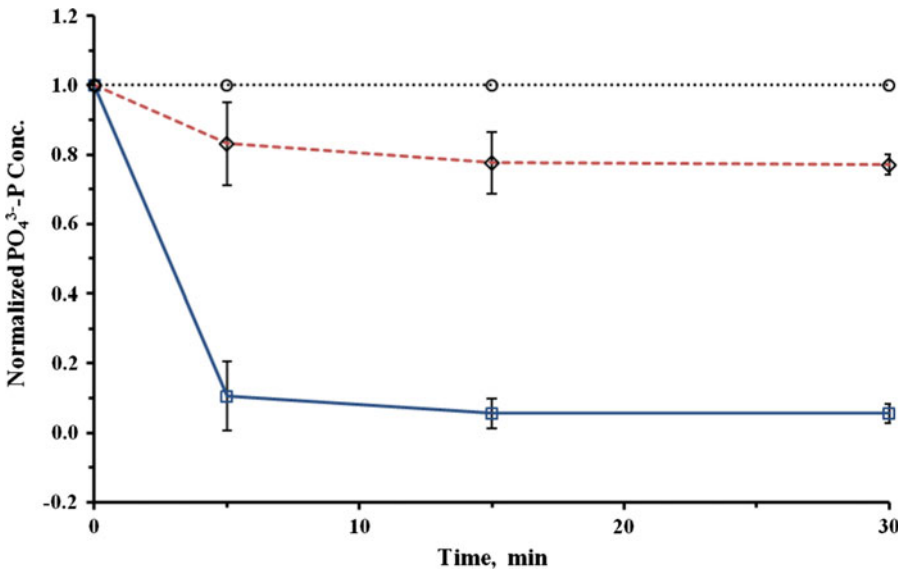

Fig. 7 Effect of ZVI particles size on phosphate removal (*diamond* Micro-ZVI, *square* NZVI, *circle* Blank). MZVI = 5 g/L; NZVI = 400 mg/L; Equal ZVI surface area concentrations (10 m^2/L) were used for both MZVI and NZVI, Initial PO_4^{3-}-P = 5 mg/L

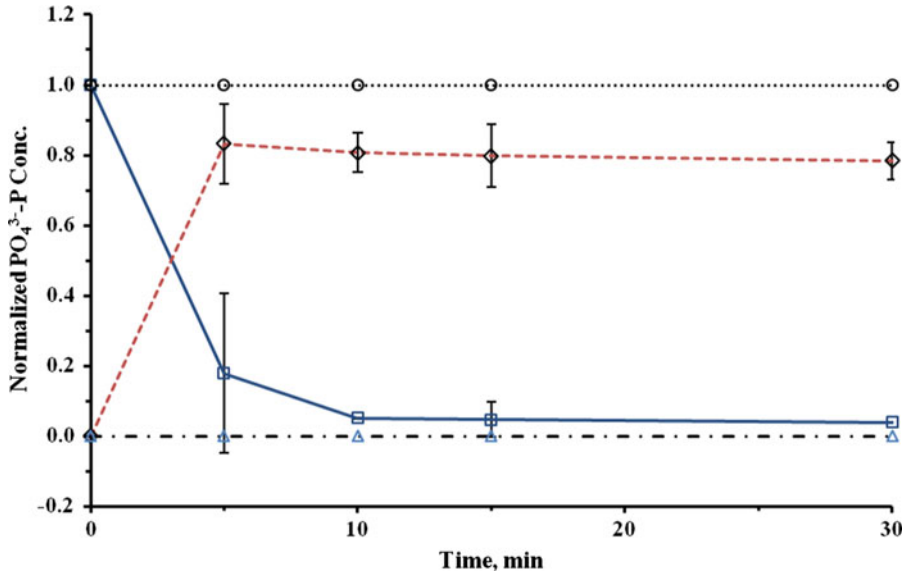

Fig. 8 Phosphate removal and recovery using NZVI (*square* Removal, *circle* Blank in removal experiment (PO_4^{3-} solution), *diamond* Recovery, *triangle* Control in recovery experiment (pH adjusted DI water + fresh NZVI)). NZVI = 400 mg/L, Initial PO_4^{3-}-P = 5 mg/L. Control for the removal experiment was DI water with NZVI; no phosphate was detected in the sample, and the data points coincided with the control for the recovery experiment

NZVI. Also, pH 12 is higher than PZC of NZVI and particles are negatively charged resulting in desorption of phosphate (Eq. 3, Karageorgiou et al. 2007 and Fig. 3). Research indicate that phosphate can be recovered from sorptive media under high pH conditions (Babatunde and Zhao 2010; Cordray 2008; Karageorgiou et al. 2007; Liu et al. 2011). Similar results were reported by others using other forms of iron oxides (Yan et al. 2010a; Zeng et al. 2004).

$$\equiv Fe-OH + X^- \xrightarrow{OH^-} \equiv Fe-\bar{O} + X^- + H_2O \quad (pH > PZC) \qquad (3)$$

Conclusions

Results from the batch studies conducted during this research demonstrate the effectiveness of NZVI for phosphate removal and recovery with different initial phosphate concentrations (1, 5, 10 mg PO_4^{3-}-P/L). Phosphate removal of 88–95 % was achieved in the first 10 min itself and 96–100 % removal was achieved after 30 min. Increase in phosphate removal efficiency improved with the increase in initial NZVI concentration use and followed a linear trend ($R^2 = 0.9539$). When the initial NZVI concentration was increased from 80 to 560 mg/L, the removal of phosphate increased by ~78 % ($C_0 = 5$ mg/L). Little interference was observed in phosphate removal due to ionic strength and temperature change. Sulfate and natural organic matters had statistically significant negative impacts but nitrate marginally improved phosphate removal. The phosphate removal efficiency was also not affected by high concentrations of humic acid. Phosphate sorbed onto NZVI was successfully recovered (~78 %). The phosphate recovery process was found to be pH dependent with maximum recovery achieved at pH 12.

Environmental significance

Phosphate removal using NZVI has potential applications in wastewater treatment plants, where phosphate removal is otherwise not very efficient. The speed of phosphate removal using NZVI (88–95 % removal in the first 10 min) gives the nanoparticles an advantage over other sorbents. The high speed of phosphate removal by NZVI can be used to engineer a commercially viable treatment process with low detention time and minimal infrastructure. More research is needed to

optimize the recovery of phosphate from NZVI as pH 12 may not be a practical value from economic and hazard perspectives.

Acknowledgments This project was completed with support from Civil Engineering Department at North Dakota State University. Fellowship offered to Almeelbi by the Saudi Arabian Cultural Mission to the US is thankfully acknowledged. The help from the members of Nanoenvirology Research Group (NRG) and Environmental Engineering Laboratory of North Dakota State University is thankfully acknowledged.

References

Ahn YH, Speece RE (2006) Waste lime as a potential cation source in the phosphate crystallization process. Environ Technol 27:1225–1231. doi:10.1080/09593332708618739

Antelo J, Arce F, Avena M, Fiol S, Lopez R, Macias F (2007) Adsorption of a soil humic acid at the surface of goethite and its competitive interaction with phosphate. Geoderma 138:12–19. doi:10.1016/j.geoderma.2006.10.011

Babatunde AO, Zhao YQ (2010) Equilibrium and kinetic analysis of phosphorus adsorption from aqueous solution using waste alum sludge. J Hazard Mater 184:746–752. doi:10.1016/j.jhazmat.2010.08.102

Bezbaruah AN, Krajangpan S, Chisholm BJ, Khan E, Bermudez JJE (2009) Entrapment of iron nanoparticles in calcium alginate beads for groundwater remediation applications. J Hazard Mater 166:1339–1343. doi:10.1016/j.jhazmat.2008.12.054

Bezbaruah AN, Shanbhogue SS, Simsek S, Khan EE (2011) Encapsulation of iron nanoparticles in alginate biopolymer for trichloroethylene remediation. J Nanopart Res 13:6673–6681. doi:10.1007/s11051-011-0574-x

Caravelli AH, Contreras EM, Zaritzky NE (2010) Phosphorous removal in batch systems using ferric chloride in the presence of activated sludges. J Hazard Mater 177:199–208. doi:10.1016/j.jhazmat.2009.12.018

Chen JW, Xiu ZM, Lowry GV, Alvarez PJJ (2011) Effect of natural organic matter on toxicity and reactivity of nano-scale zero-valent iron. Water Res 45:1995–2001. doi:10.1016/j.watres.2010.11.036

Chitrakar R, Tezuka S, Sonoda A, Sakane K, Ooi K, Hirotsu T (2006) Phosphate adsorption on synthetic goethite and akaganeite. J Colloid Interface Sci 298:602–608. doi:10.1016/j.jcis.2005.12.054

Cleary J, Slater C, Diamond D (2009) Analysis of phosphate in wastewater using an autonomous microfluidics-based analyser. World Acad Sci Eng Technol 52:196–199

Cordell D, Drangert JO, White S (2009) The story of phosphorus: global food security and food for thought. Glob Environ Change-Human Policy Dimens 19:292–305. doi:10.1016/j.gloenvcha.2008.10.009

Cordell D, Rosemarin A, Schroder JJ, Smit AL (2011) Towards global phosphorus security: a systems framework for phosphorus recovery and reuse options. Chemosphere 84:747–758. doi:10.1016/j.chemosphere.2011.02.032

Cordray A (2008) Phosphorus removal characteristics on biogenic ferrous iron oxides. Master's Thesis, Washington State University, USA

Cornel P, Schaum C (2009) Phosphorus recovery from wastewater: needs, technologies and costs. Water Sci Technol 59:1069–1076. doi:10.2166/wst.2009.045

Das J, Patra BS, Baliarsingh N, Parida KM (2006) Adsorption of phosphate by layered double hydroxides in aqueous solutions. Appl Clay Sci 32:252–260. doi:10.1016/j.clay.2006.02.005

de Bashan LE, Bashan Y (2004) Recent advances in removing phosphorus from wastewater and its future use as fertilizer (1997–2003). Water Res 38:4222–4246. doi:10.1016/j.watres.2004.07.014

Eaton AD, Franson MAH, Association AWW, Federation WE (2005) Standard methods for the examination of water and wastewater, 21st edn. American Public Health Association, Washington, DC, USA

Giasuddin ABM, Kanel SR, Choi H (2007) Adsorption of humic acid onto nanoscale zerovalent iron and its effect on arsenic removal. Environ Sci Technol 41:2022–2027. doi:10.1021/es0616534

Gouider M, Mlaik N, Feki M, Sayadi S (2011) Integrated physicochemical and biological treatment process for fluoride and phosphorus removal from fertilizer plant wastewater. Water Environ Res 83:731–738. doi:10.2175/106143011x12928814444772

Guo CH, Stabnikov V, Kuang SL, Ivanov V (2009) The removal of phosphate from wastewater using anoxic reduction of iron ore in the rotating reactor. Biochem Eng J 46:223–226. doi:10.1016/j.bej.2009.05.011

Huang KC, Ehrman SH (2007) Synthesis of iron nanoparticles via chemical reduction with palladium ion seeds. Langmuir 23:1419–1426. doi:10.1021/la0618364

Hussain S, Aziz HA, Isa MH, Ahmad A, Van Leeuwen J, Zou L, Beecham S, Umar M (2011) Orthophosphate removal from domestic wastewater using limestone and granular activated carbon. Desalination 271:265–272. doi:10.1016/j.desal.2010.12.046

Hwang YH, Kim DG, Shin HS (2011) Mechanism study of nitrate reduction by nano zero valent iron. J Hazard Mater 185:1513–1521. doi:10.1016/j.jhazmat.2010.10.078

Kanel SR, Manning B, Charlet L, Choi H (2005) Removal of arsenic(III) from groundwater by nanoscale zero-valent iron. Environ Sci Technol 39:1291–1298. doi:10.1021/es048991u

Karageorgiou K, Paschalis M, Anastassakis GN (2007) Removal of phosphate species from solution by adsorption onto calcite used as natural adsorbent. J Hazard Mater 139:447–452. doi:10.1016/j.jhazmat.2006.02.038

Klimkova S, Cernik M, Lacinova L, Filip J, Jancik D, Zboril R (2011) Zero-valent iron nanoparticles in treatment of acid mine water from in situ uranium leaching. Chemosphere 82:1178–1184. doi:10.1016/j.chemosphere.2010.11.075

Li XQ, Elliott DW, Zhang WX (2006) Zero-valent iron nanoparticles for abatement of environmental pollutants: materials and engineering aspects. Crit Rev Solid State 31:111–122. doi:10.1080/10408430601057611

Li ZQ, Greden K, Alvarez PJJ, Gregory KB, Lowry GV (2010) Adsorbed polymer and NOM limits adhesion and toxicity

of nano scale zerovalent iron to *E. coli*. Environ Sci Technol 44:3462–3467. doi:10.1021/es9031198

Liu J, Wan L, Zhang L, Zhou Q (2011) Effect of pH, ionic strength, temperature on the phosphate adsorption onto lanthanum-doped activated carbon fiber. J Colloid Interface Sci 364:490–496. doi:10.1016/j.jcis.2011.08.067

Mezenner NY, Bensmaili A (2009) Kinetics and thermodynamic study of phosphate adsorption on iron hydroxide–eggshell waste. Chem Eng J 147:87–96. doi:10.1016/j.cej.2008.06.024

Mishra SP, Das M, Dash UN (2010) Review on adverse effects of water contaminants like arsenic, fluoride and phosphate and their remediation. J Sci Ind Res 69:249–253

Penn CJ, Warren JG (2009) Investigating phosphorus sorption onto kaolinite using isothermal titration calorimetry. Soil Sci Soc Am J 73:560–568. doi:10.2136/sssaj2008.0198

Saha B, Griffin L, Blunden H (2010) Adsorptive separation of phosphate oxyanion from aqueous solution using an inorganic adsorbent. Environ Geochem Health 32:341–347. doi:10.1007/s10653-010-9305-y

Scott TB, Popescu IC, Crane RA, Noubactep C (2011) Nanoscale metallic iron for the treatment of solutions containing multiple inorganic contaminants. J Hazard Mater 186(280):287. doi:10.1016/j.jhazmat.2010.10.113

Shuai XF, Zinati G (2009) Proton charge and adsorption of humic acid and phosphate on goethite. Sci Soc Am J 73:2013–2020. doi:10.2136/sssaj2009.0119

Simeoni MA, Batts BD, McRae C (2003) Effect of groundwater fulvic acid on the adsorption of arsenate by ferrihydrite and gibbsite. Appl Geochem 18:1507–1515. doi:10.1016/s0883-2927(03)00074-x

Tchobanoglous G, Burton FL, Stensel HD, Metcalf & Eddy (2003) Wastewater engineering: treatment and reuse, 4th edn. McGraw-Hill, New York

Thompson JM, Chisholm BJ, Bezbaruah AN (2010) Reductive dechlorination of chloroacetanilide herbicide (Alachlor) using zero-valent iron nanoparticles. Environ Eng Sci 27:227–232. doi:10.1089/ees.2009.0147

USEPA (1995) Ecological restoration: a tool to manage stream quality, Report EPA 841-F-95-007. US EPA, Washington, DC, USA

Xi YF, Mallavarapu M, Naidu R (2010) Reduction and adsorption of Pb(2+) in aqueous solution by nano-zero-valent iron-A SEM, TEM and XPS study. Mater Res Bull 45:1361–1367. doi:10.1016/j.materresbull.2010.06.046

Xiong JB, He ZL, Mahmood Q, Liu D, Yang X, Islam E (2008) Phosphate removal from solution using steel slag through magnetic separation. J Hazard Mater 152:211–215. doi:10.1016/j.jhazmat.2007.06.103

Xue YJ, Hou HB, Zhu SJ (2009) Characteristics and mechanisms of phosphate adsorption onto basic oxygen furnace slag. J Hazard Mater 162:973–980. doi:10.1016/j.jhazmat.2008.05.131

Yan LG, Xu YY, Yu HQ, Xin XD, Wei Q, Du B (2010a) Adsorption of phosphate from aqueous solution by hydroxy-aluminum, hydroxy-iron and hydroxy-iron-aluminum pillared bentonites. J Hazard Mater 179:244–250. doi:10.1016/j.jhazmat.2010.02.086

Yan WL, Herzing AA, Kiely CJ, Zhang WX (2010b) Nanoscale zero-valent iron (nZVI): aspects of the core–shell structure and reactions with inorganic species in water. J Contam Hydrol 118:96–104. doi:10.1016/j.jconhyd.2010.09.003

Yue QY, Zhao YQ, Li Q, Li WH, Gao BY, Han SX, Qi YF, Yu H (2010) Research on the characteristics of red mud granular adsorbents (RMGA) for phosphate removal. J Hazard Mater 176:741–748. doi:10.1016/j.jhazmat.2009.11.098

Zeng L, Li XM, Liu JD (2004) Adsorptive removal of phosphate from aqueous solutions using iron oxide tailings. Water Res 38:1318–1326. doi:10.1016/j.watres.2003.12.009

DOI 10.1007/978-3-319-05041-6_17
Reprinted from the *Journal of Nanoparticle Research*, DOI 10.1007/s11051-012-0845-1

RESEARCH PAPER

Poly(vinyl chloride)-*g*-poly(2-(dimethylamino)ethyl methacrylate) graft copolymers templated synthesis of mesoporous TiO_2 thin films for dye-sensitized solar cells

Rajkumar Patel · Sung Hoon Ahn · Jin Ah Seo · Sang Jin Kim · Jong Hak Kim

Received: 16 August 2011 / Accepted: 22 March 2012 / Published online: 17 June 2012

Abstract A poly(vinyl chloride) (PVC) main chain was grafted with poly(2-(dimethylamino)ethyl methacrylate) (PDMAEMA) containing a quaternary amine group using atom transfer radical polymerization. The successful synthesis of a PVC-*g*-PDMAEMA graft copolymer was confirmed by Fourier transform infrared, nuclear magnetic resonance, thermogravimetric analysis, and transmission electron microscopy. The PVC-*g*-PDMAEMA graft copolymer was used as a structure-directing agent (SDA) for the fabrication of a mesoporous thin film containing a titanium dioxide (TiO_2) layer. To control the porosity of the resultant inorganic layer, the ratio of SDA to TTIP as well as the concentration of the sol–gel was varied. The structure and porosity of the mesoporous film were characterized by XRD and SEM analysis. The mesoporous TiO_2 film fabricated on the FTO surface was used as a photoanode for the dye-sensitized solar cell (DSSC). DSSC performance was the greatest when using TiO_2 film with a higher porosity and lower interfacial resistance. The highest energy conversion efficiency reached 3.2 % at 100 mW/cm^2, which was one of the highest reported values for a quasi-solid-state DSSC with 600-nm-thick TiO_2 film.

Keywords Graft copolymer · Atom transfer radical polymerization · TiO_2 · Dye-sensitized solar cell · Sol–gel · Energy conversion · Sustainability

Special Issue Editors: Mamadou Diallo, Neil Fromer, Myung S. Jhon

This article is part of the Topical Collection on Nanotechnology for Sustainable Development

R. Patel · S. H. Ahn · J. A. Seo · S. J. Kim · J. H. Kim (✉)
Department of Chemical and Biomolecular Engineering, Yonsei University, 262 Seongsanno, Seodaemun-gu, Seoul 120-749, South Korea
e-mail: jonghak@yonsei.ac.kr

Introduction

Dye-sensitized solar cells (DSSC) are one of the many technologically interesting applications of nanocrystalline titania (TiO_2) and was introduced in 1991 (O'Reagan and Grätzel 1991). An 11 % energy conversion efficiency in DSSC was observed for organic liquid-based redox electrolytes. In order to overcome the disadvantage of liquid electrolytes, alternative solid-state or quasi-solid-state DSSC using hole conductors (Beltran et al. 2006; Kroeze et al. 2006; Tan et al. 2004a, b; Li et al. 2006), gel electrolytes (Wu et al. 2007; Xia et al. 2006; Wang et al. 2002), quasi-solid (Wang et al. 2003; Sakaguchi et al. 2004; Lu et al. 2007), or solid polymer electrolytes (Kim et al. 2004; Kang et al. 2007; Kalaignan et al. 2006) have been developed. The electron diffusivity of TiO_2 photoelectrodes depends mainly on the structural and morphological behaviors of TiO_2 nanoparticle layers.

TiO_2 nanoparticles with controlled size, morphology, and crystallinity are prepared mainly through a hydrothermal/solvothermal process and sol–gel

method. The hydrothermal/solvothermal process is a conventional method in which the TiO_2 nanoparticles are synthesized, followed by a coating of the synthesized nanoparticles onto fluorine-doped tin oxide (FTO) glass using a binder. A sol–gel process is a simple one-step process where the size and shape of the nanoparticles can be controlled while maintaining the interconnectivity as well as the mesoporous structure of the TiO_2 layer. In the sol–gel process, the structure-directing agent (SDA) plays the most unique and important role since its hydrophilic part interacts with the TiO_2 precursor, resulting in the inhibition of TiO_2 nanoparticle growth during the calcination step (Forster and Antonietti 1998; Kim et al. 2001; Urbas et al. 2002; Yeh et al. 2003; Fahmi et al. 2003; Liang et al. 2004; Melde et al. 2005; Lee et al. 2008; Koh et al. 2009).

An amphiphilic block copolymer was used as an SDA to fabricate the well-organized nanostructural materials. For example, the polystyrene-*b*-poly(ethylene oxide) diblock copolymer (PS-*b*-PEO) was used for the preparation of CdS quantum dot nanoparticles (Yeh et al. 2003).The polystyrene-*block*-poly(4-vinylpyridine) (PS-P4VP) was used for the formation of metal nanowire (Fahmi et al. 2003) and porous carbon film (Liang et al. 2004). Poly(styrene-*block*-methyl methacrylate) (PS-*b*-PMMA) was also templated for the preparation of silica (SiO_2) thin films (Melde et al. 2005).

An amphiphilic copolymer includes a graft copolymer as well as a block copolymer. A graft copolymer is advantageous over a block copolymer due to its economical and simple synthetic method. Our research group has been focused on the synthesis of novel graft copolymers which can be used as SDAs for the fabrication of a TiO_2 mesoporous layer. Poly(vinylidene fluoride-*co*-chlorotrifluoroethylene)-*graft*-poly(oxyethylene methacrylate) (P(VDF-*co*-CTFE)-*g*-POEM) (Koh et al. 2010), poly(vinyl chloride)-*graft*-poly(oxyethylene methacrylate) (PVC-*g*-POEM) (Ahn et al. 2010, 2011a, b; Kim et al. 2011), and poly(vinyl chloride)-*graft*-poly(*N*-vinyl caprolactam) (PVC-*g*-NVCL) (Patel et al. 2012) were used as an SDA to synthesize mesoporous TiO_2 film. However, the thickness of SDA-templated TiO_2 film is often limited to the submicron scale due to crack formation during calcination, resulting in low efficiency.

The hydrogen bonding interaction between the ether group of poly(ethylene oxide) (PEO) and the TiO_2 precursor such as titanium(IV) isopropoxide (TTIP) leads to the use of PEO-based block copolymers, e.g., polystyrene-*block*-poly(ethylene oxide) (PS-*b*-PEO) (Cheng and Gutmann 2006) and polyisoprene-*block*-poly(ethylene oxide) (PI-*b*-PEO) (Nedelcu et al. 2009). Yoshitake et al. (2002) also reported that the interaction between TTIP and the amine group can lead to the formation of the worm-like structure of TiO_2 film. It is also known that the hydrogen bonding of the amine group (29 kJ/mol) is stronger than that of the ether group (21 kJ/mol).

In this study, novel amphiphilic graft copolymers of poly(vinyl chloride)-*graft*-poly(2-(dimethylamino) ethyl methacrylate) (PVC-*g*-PDMAEMA) containing a quaternary amine group were synthesized using atom transfer radical polymerization (ATRP). The hydrophilic properties arise from the quaternary amine of PDMAEMA containing a lone pair which interacts with the hydroxyl group of the titanium surface through hydrogen bonding. The stronger hydrogen bonding between amine and TiO_2 was triggered to utilize the PVC-*g*-PDMAEMA graft copolymer as a template for the formation of the mesoporous TiO_2 layer. The synthesis of the graft copolymers was confirmed by proton nuclear magnetic resonance (^{1}H-NMR), Fourier transfer infrared (FT-IR) spectroscopy, and thermogravimetric analysis (TGA), and its microphase-separated structure was analyzed by transmission electron microscopy (TEM). The graft copolymers were combined with aTiO_2 precursor, i.e., TTIP, and calcinated at a high temperature to form mesoporous TiO_2 thin films. The porosity and crystallinity of the TiO_2 film were characterized using scanning electron microscopy (SEM) and X-ray diffraction (XRD), respectively. Quasi-solid-state DSSC were fabricated using mesoporous TiO_2 film and polymer electrolytes. The performances and electrochemical impedance spectroscopy (EIS) properties of DSSCs are also reported.

Experimental

Materials

N,*N*-dimethylamino-2-ethyl methacrylate (DMAEMA), PVC (M_n = 22,000 g/mol, M_w = 45,000 g/mol), 1,1,4,7,10,10-hexamethyltriethylene tetramine (HMTETA,99 %), copper(I) chloride (CuCl, 99 %),

lithium iodide (LiI), iodine (I_2), titanium(IV) bis(ethyl acetoacetato) diisopropoxide, chloroplatinic acid hexahydrate (H2PtCl6), titanium(IV) isopropoxide (TTIP, 97 %), fumed silica nanoparticles (SiO_2, 14 nm), poly(ethylene glycol dimethyl ether) (PEGDME, $M_n = 500$ g/mol), hydrogen chloride solution (HCl, 35 wt%), and sodium hydroxide solution (NaOH, 0.1 N) were procured from Aldrich. 1-Methyl-3-propyl imidazolium iodide (MPII) and ruthenium dye (535-bisTBA, N719) were purchased from Solaronix, Switzerland. High purity solvents of tetrahydrofuran (THF), butanol, acetonitrile, 2-propanol, chloroform, and ethanol were purchased from J.T. Baker. FTO conducting glass substrate (TEC8, 8 Ω/sq, 2.3-mm thick) was purchased from Pilkington, France.

Synthesis of the PVC-*g*-PDMAEMA graft copolymer

A predetermined amount of PVC was dissolved in 60 mL of NMP in a round-bottom flask. DMAEMA was added to the above solution and mixed well. The ratio of DMAEMA was increased to produce graft copolymers with different grafting ratios. To this homogeneous mixture, 0.08 g of the CuCl catalyst and 0.22 mL of the HEMTA ligand were added and deoxygenated with nitrogen for 30 min. The temperature of the reaction mixture was slowly increased to 90 °C in an oil bath and stirred for over 40 h. The viscous solution was diluted with THF, passed through an activated Al_2O_3 column to remove the catalyst, and then precipitated in methanol. The products were purified by dissolution in THF and re-precipitated in methanol several times. Finally, the resultant product was dried in a vacuum oven overnight at 50 °C.

Preparation of the mesoporous TiO_2 thin films

The FTO glass was cleaned by sonication in isopropanol and then in chloroform. A layer of titanium(IV) bis (ethyl acetoacetato) diisopropoxide was spin coated on the clean FTO glass followed by sintering at 450 °C for 30 min. To prepare the sol–gel solution, 0.05 g of PVC-*g*-PDMAEMA graft copolymer was dissolved in 1.5 mL of THF and mixed with TTIP (0.2 mL) containing 0.1 mL of HCl (37 %). The prepared solution was stirred for 3 h at ambient temperature. Graft copolymers with different grafting degrees were used for the fabrication of the mesoporous TiO_2 film, i.e., TiO_2-1, TiO_2-2, TiO_2-3, and TiO_2-4, which were synthesized using PVC-*g*-PDMAEMA graft copolymers with a 1:1, 1:3, 1:5, and 1:7 wt ratio, respectively. The above sol–gel solution was spin coated on the blocked FTO glass at 2,000 rpm for 30 s by a SMSS Delta 80BM spin coater. In order to eliminate the organic part of the solution, it was calcinated at 500 °C for 30 min to generate the mesoporous TiO_2 thin film. 10^{-4} mol/dm^3 of the alcoholic N719 dye solution was adsorbed onto the TiO_2 layer at 50 °C for over 2 h under dark conditions. To remove the unadsorbed dye, the film was washed with absolute ethanol and dried in a vacuum oven.

Preparation of the counter electrode

Conductive FTO coated with platinum was used as a counter electrode. The counter electrodes were prepared by spin coating 4 wt% H_2PtCl_6 propanol solutions onto the clean conductive FTO glass and sintering at 450 °C for 30 min.

Fabrication of DSSC

The active area of 0.16 cm^2 of the photoelectrode was coated with polymer electrolyte solution and covered with platinum counter electrode, according to the previously reported process (Ahn et al. 2010, 2011a, b; Park et al. 2010; Roh et al. 2010). PEGDME, SiO_2, MPII, and I_2 were dissolved in THF for the preparation of the polymer electrolyte. The mole ratio of ether oxygen to iodide was 20, and the iodine concentration was 10 wt% with respect to salt (Roh et al. 2010). In order to achieve good penetration of the electrolyte solution into the TiO_2 layer, the solvent was evaporated very slowly. The polymer electrolyte was sandwiched between the photoelectrode and counter electrode. Finally, the solvent was evaporated completely by placement in a vacuum oven for 1 day. Five identical DSSCs were assembled and characterized. The average estimated error of efficiency was ±5 %.

The photovoltaic performance measures of short-circuit current (J_{sc}, mA/cm^2), open-circuit voltage (V_{oc}, V), fill factor (FF), and overall energy conversion efficiency (η) were measured using a Keithley Model

2400 source meter and a 1,000 W xenon lamp (Oriel, 91193). The light was homogeneous up to an 8 × 8 inch^2 area, and its intensity was calibrated with a Si solar cell (Fraunhofer Institute for Solar Energy System, Mono-Si+KG filter, Certificate No. C-ISE 269) to a one sun light intensity (100 mW/cm^2). The intensity was verified with a NREL-calibrated Si solar cell (PV Measurements Inc.). Photoelectrochemical performance was calculated using the following equations:

$$\mathrm{FF} = \frac{V_{\max} \cdot J_{\max}}{V_{\mathrm{oc}} \cdot J_{\mathrm{sc}}} \quad (1)$$

$$\eta\,(\%) = \frac{V_{\max} \cdot J_{\max}}{P_{\mathrm{in}}} \times 100 \; = \frac{V_{\mathrm{oc}} \cdot J_{\mathrm{sc}} \cdot ff}{P_{\mathrm{in}}} \times 100 \quad (2)$$

where J_{sc} is the short-circuit current density (mA/cm^2), V_{oc} is the open-circuit voltage (V), P_{in} is the incident light power, and $J_{\max}$ (mA/cm^2) and $V_{\max}$ (V) are the current density and voltage in the *J*–*V* curve, respectively, at the point of maximum power output.

Characterization

^{1}H-NMR measurements were performed with a 600-MHz, high-resolution NMR spectrometer (Avance 600-MHz FT-NMR spectrometer, Bruker, Ettlingen, Germany). FT-IR spectra of the samples were collected with an Excalibur series FT-IR instrument (DIGLAB Co., Hannover, Germany) in the frequency range of 4,000–600 cm^{-1} with an attenuated total reflection facility. XRD measurements were carried out on a Rigaku RINT2000 wide-angle goniometer with a Cu cathode operated at 40 kV and 300 mA. UV–Visible spectroscopy was performed with a spectrophotometer (Shimazu) in the range of 200–800 nm. The thermal properties of the materials were determined by TGA (Mettler Toledo TGA/SDTA 851e, Columbus, OH) from room temperature to 800 °C at a heating rate of 20 °C/min in a nitrogen atmosphere. EF-TEM pictures were obtained using a Philips CM30 microscope operating at 300 kV after drop casting the dilute solution onto a standard copper grid. Morphological characterization for the mesoporous TiO_2 film was carried out using FE-SEM (S-4700, Hitachi).

Results and discussion

Synthesis of the PVC-*g*-PDMAEMA graft copolymers

The reaction for the synthesis of PVC-*g*-PDMAEMA graft copolymers via ATRP is illustrated in Scheme 1. PVC-*g*-PDMAEMA graft copolymers were designed to have amphiphilic properties from hydrophobic PVC main chains and hydrophilic PDMAEMA side chains. In particular, the quaternary amine of PDMAEMA has strong interactions with a TiO_2 precursor, which provides a basis for the effective morphology control of the mesoporous TiO_2 films.

The FT-IR spectra of the PVC-*g*-PDMAEMA graft copolymers synthesized with different amounts of added DMAEMA monomers are presented in Fig. 1. The stretching vibration bands at 1,724 and 1,150 cm^{-1} represent the carbonyl group (C=O) and tertiary amine group (C–N stretching), respectively, indicating the grafting of PVC by PDMAEMA. The PVC-*g*-PDMAEMA graft copolymer was also characterized using ^{1}H-NMR spectroscopy, as presented in Fig. 2. The methyl group protons (a) appeared at 2.42 ppm,

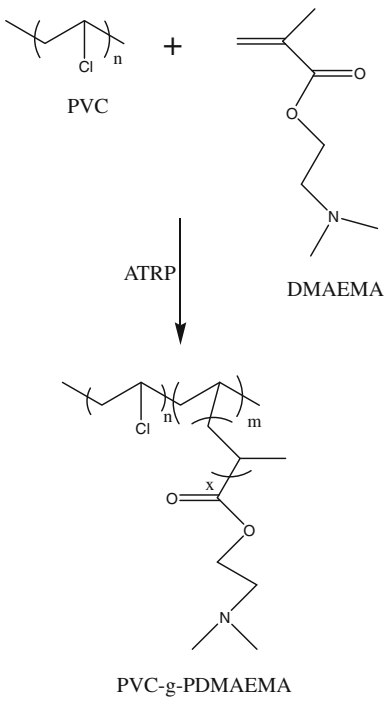

Scheme 1 ATRP synthesis of the PVC-*g*-PDMAEMA graft copolymer

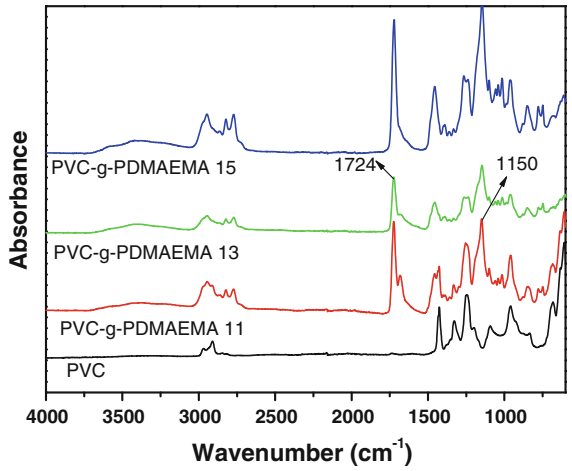

Fig. 1 FT-IR spectra of the PVC-*g*-PDMAEMA graft copolymers with various compositions

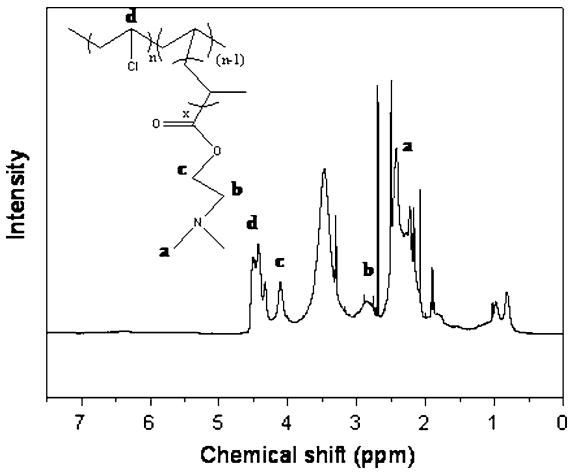

Fig. 2 ^{1}H NMR spectrum of PVC-*g*-PDMAEMA 11

which is a higher field than that of the methylene proton (b) due to the higher shielding effect. The methylene protons (b) adjacent to the amine group appear at 2.84 δ. The methylene proton (c) adjacent to the ester group appeared at 4.11 ppm due to the deshielding effect by the electron-withdrawing ester group. The chloro-substituted methylene proton (d) of the main chain PVC appeared at 4.42 ppm and can be attributed to the electron-withdrawing deshielding effect of the chlorine group. The overall spectrum indicated that the PVC main chains were successfully grafted by the PMDAEMA side chains.

Figure 3 shows the TEM images of PVC-*g*-PDMAEMA graft copolymers prepared with THF solution. It shows a microphase-separated structure consisting of bright and dark regions. The darker region represents the PVC main chains of the graft copolymer, whereas the bright region indicates PDMAEMA side chains due to the higher electron density in the former region. The darker dots inside the bright PDMAEMA regions are presumed to be due to the residual copper ions that are in situ reduced during the TEM measurement. With the increase in grafting degree, the bright regions became larger, indicating an increased portion of the PDMAEMA side chains (Fig. 3b).

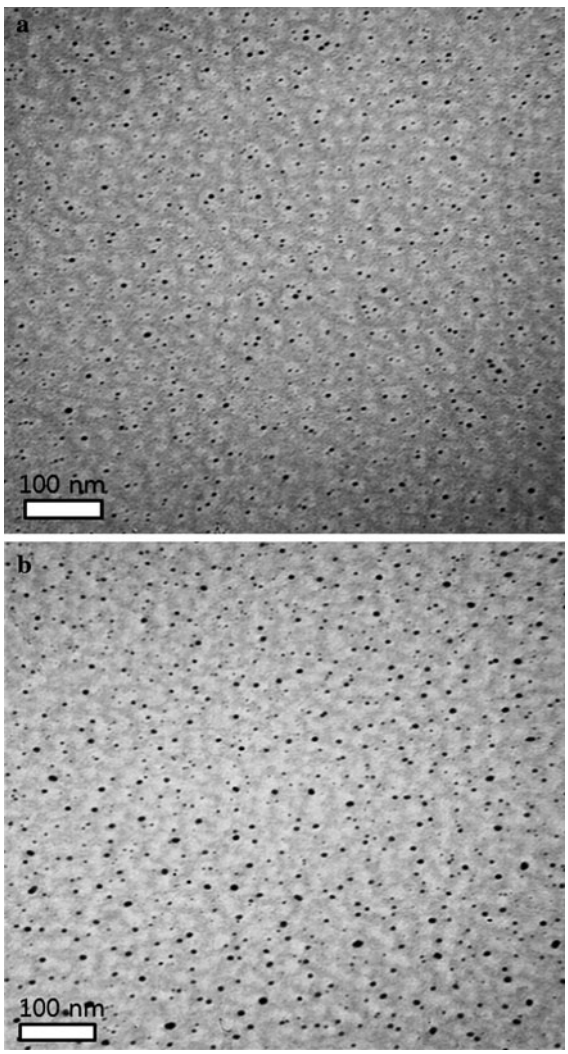

Fig. 3 TEM micrographs of the **a** PVC-*g*-PDMAEMA 11 and **b** PVC-*g*-PDMAEMA 13 graft copolymers

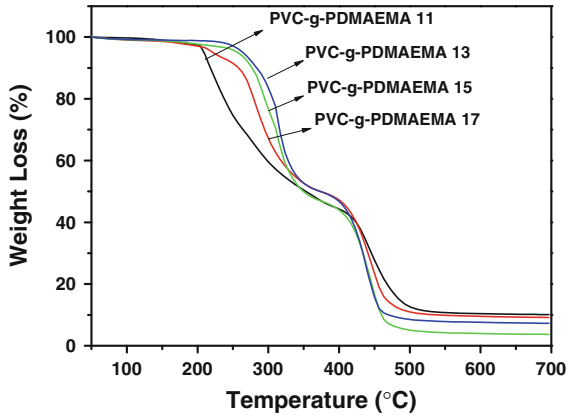

Fig. 4 TGA data of the PVC-*g*-PDMAEMA graft copolymers with various compositions

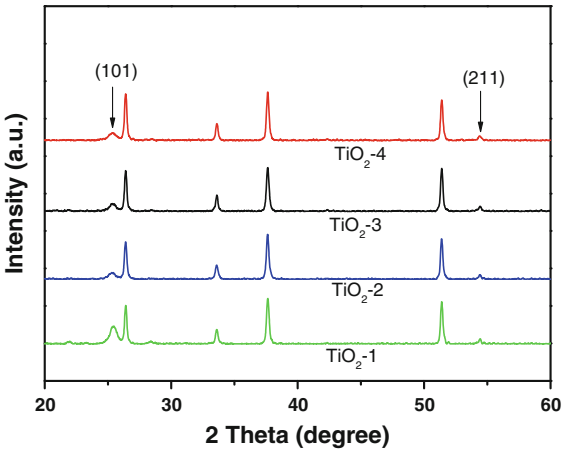

Fig. 5 XRD patterns of the mesoporous TiO_2 thin films templated by the PVC-*g*-PDMAEMA graft copolymer

The TGA plots in Fig. 4 shows two degradation steps of the graft copolymers. The first step of degradation occurred in the temperature range of 240–300 °C and might be due to the loss of the labile chlorine atom from the main PVC chain. With the increase in grafting ratio, the first degradation temperature increased due to the decreased number of chlorine groups available. The 5 wt% degradation temperatures were arranged in the order of PVC-*g*-PDMAEMA 11 (210 °C) < PVC-*g*-PDMAEMA 13 (223 °C) < PVC-*g*-PDMAEMA 15 (256 °C) < PVC-*g*-PDMAEMA 17 (263 °C). This indicates that the degradation temperature increased from 210 °C for PVC-*g*-PDMAEMA11 to 263 °C for the PVC-*g*-PDMAEMA17 sample. This results from the reduction of the content of labile chlorine atoms with an increase in the grafting ratio, which requires a higher temperature for the evolution of HCl. The second degradation step was observed in the temperature range of 440–460 °C and may be due to the degradation of the main chain as well as the grafted chains of the PVC-*g*-PDMAEMA copolymer. The graft copolymers were almost completely removed after calcination above 500 °C.

Preparation of the mesoporous TiO_2 thin films

Synthesized PVC-*g*-PDMAEMA graft copolymers with various grafting degrees were used as SDAs to synthesize mesoporous TiO_2 films through a sol–gel process using a titanium precursor, i.e., TTIP. Upon calcination at 500 °C, mesoporous TiO_2 thin films obtained as TTIP were selectively incorporated into the hydrophilic PDMAEMA domains. TiO_2 crystallites were formed in situ during calcination, originating from favorable interactions between TTIP and PDMAEMA. The structural patterns of crystallized mesoporous TiO_2 films templated by PVC-*g*-PDMAEMA were characterized by XRD analysis, as presented in Fig. 5. The sharp crystalline peaks at 25.3° and 54.5° (2θ) were assigned to the (101) and (211) planes, respectively, of the anatase TiO_2 phase (Nedelcu et al. 2009, Falaras et al. 2008). The remaining peaks arose from the bare FTO glass. This result indicates the structural changes and phase transformation of TiO_2 to crystalline anatase.

Figure 6 shows the SEM images of mesoporous TiO_2 thin films templated by PVC-*g*-PDMAEMA graft copolymers, which involved a sol–gel process based on the hydrolysis and condensation of TTIP and calcination at 500 °C. The cylindrical, worm-like micelles formed around the PVC chains were burned during calcination to form pores. In the TiO_2-1 sample (Fig. 6a), the pore size was larger than 50 nm, which was gradually reduced to <50 nm in the TiO_2-2 film. As the grafting degree increased, the portion of hydrophobic PVC main chains that could generate pores upon calcination decreased. Therefore, the pore size was gradually reduced as the grafting degree increased. The thickness of the mesoporous TiO_2 film was approximately 600 nm, as determined by the cross-sectional SEM image (Fig. 6e). The magnified images of the TiO_2 films are presented in Fig. 7 where the more clear mesoporous and interconnected structures of TiO_2 were observed. The porosity and pore

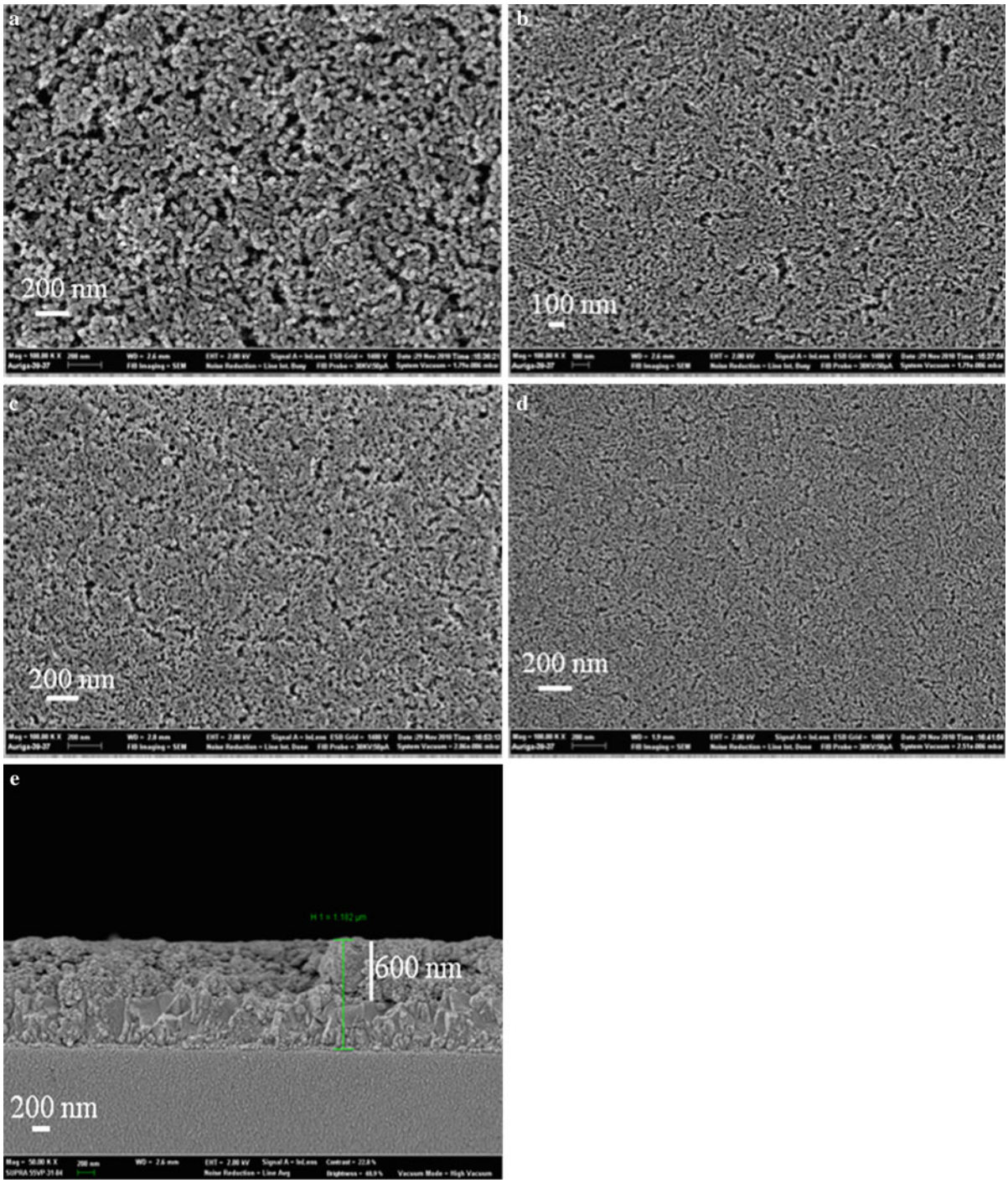

Fig. 6 SEM surface images of mesoporous TiO_2 film templated by the PVC-*g*-PDMAEMA graft copolymer: **a** TiO_2-1, **b** TiO_2-2, **c** TiO_2-3, **d** TiO_2-4, and **e** cross-sectional image of TiO_2-1 film

size of the TiO_2 films gradually decreased with increasing grafting degree of the PVC-*g*-PDMAEMA graft copolymer. The pictures of TiO_2 photoelectrodes are shown in Fig. 8. The transparency through photoelectrodes increased with decreasing pore size, i.e., TiO_2-1 < TiO_2-2 < TiO_2-3 < TiO_2-4. In general, as

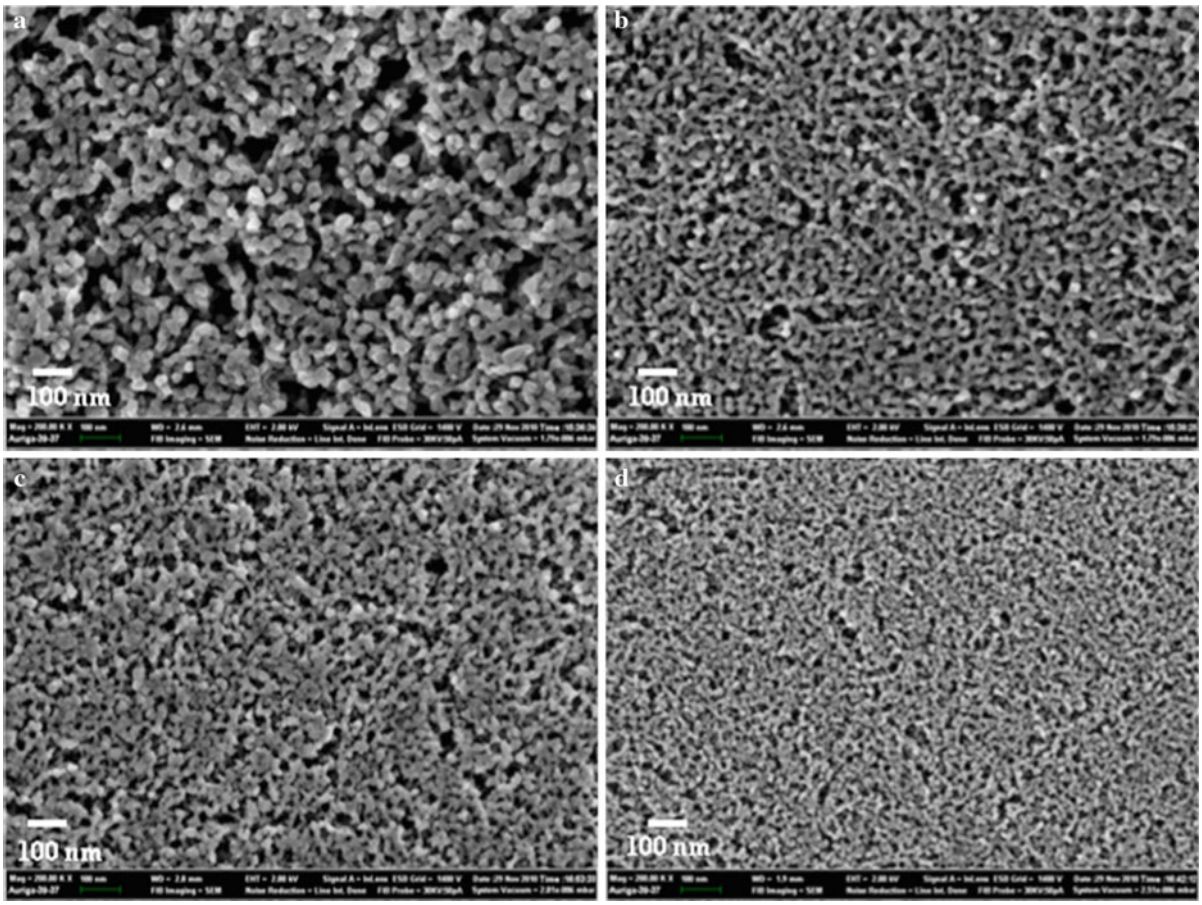

Fig. 7 Magnified SEM images of mesoporous TiO_2 film templated by the PVC-*g*-PDMAEMA graft copolymer: **a** TiO_2-1, **b** TiO_2-2, **c** TiO_2-3, and **d** TiO_2-4

the transparency of the photoelectrodes increased, the scattering of sunlight decreased, resulting in the decrease in solar cell efficiency, which is consistent with the following *J*–*V* results.

Performances of DSSCs

There are some advantages of quasi-solid-state DSSCs over liquid-based versions in terms of flexibility, lightness, and long-term stability. Thus, polymer electrolytes consisting of PEGDME, SiO_2, MPII, and I_2 were employed to fabricate solar cells. The cell performance was measured using linear sweep voltammetry, as presented in Fig. 9. The performances of the DSSCs measured as V_{oc}, J_{sc}, FF, and efficiency (η) are summarized in Table 1. The performances were strongly dependent on the morphology of the TiO_2 film. The DSSC fabricated with TiO_2-1 film exhibited the highest efficiency (3.2 %) with a J_{sc} of 9.1 mA/cm^2, V_{oc} of 0.72 V, and FF of 48 % at 100 mW/cm^2. This is one of the highest efficiency values ever reported for quasi-solid-state DSSC with 600-nm-thick TiO_2 film. For example, Nedelcu et al. (2009) reported 1.5 % efficiency solid-state DSSC using PI-*b*-PEO block copolymer and 860-nm-thick mesoporous TiO_2 films. Ahn et al. (2010) reported 2.2 % efficiency solid-state DSSC with PVC-*g*-POEM graft copolymer 700-nm-thick mesoporous TiO_2 films. The obtained efficiencies were also compared with the dye adsorption values, as presented in Table 1 and Fig. 10. It was found that the dye adsorption of the TiO_2-1 photoelectrode was the highest compared to the other TiO_2 photoelectrodes. This is attributed to the higher porosity as well as the larger surface area of the TiO_2-1 photoelectrode, resulting in a higher J_{sc} value.

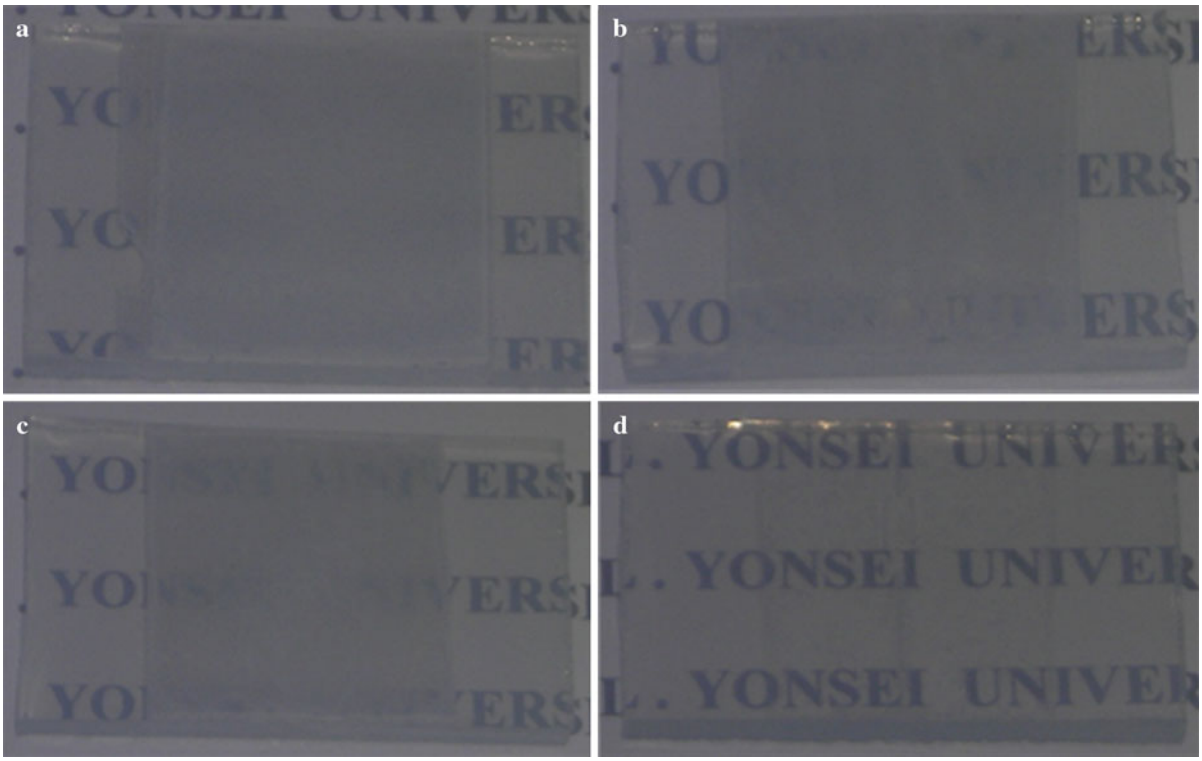

Fig. 8 Photographs of the TiO_2 photoelectrodes: **a** TiO_2-1, **b** TiO_2-2, **c** TiO_2-3, and **d** TiO_2-4

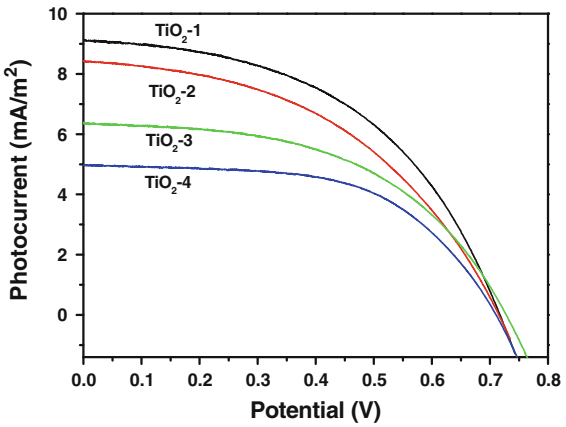

Fig. 9 *J–V* curves for DSSCs fabricated with mesoporous TiO_2 films templated by the PVC-*g*-PDMAEMA graft copolymer and a polymer electrolyte consisting of PEODME/SiO_2/MPII/I_2 at 100 mW/cm^2

The internal resistances and electron transport kinetics in DSSCs were studied using EIS analysis. Figure 11a shows the Nyquist plots of EIS for the DSSCs with different photoelectrodes measured at 100 mW/cm^2. The Bode phase plots of EIS for DSSCs with different photoelectrodes are also shown in Fig. 11b. Electrochemical parameters determined from EIS analysis, namely resistance values (R_s, R_1, R_2, and W_s) and lifetime of electrons for recombination (τ_r), are presented in Table 1. The impedance spectra can be interpreted and modeled using equivalent circuits, with each component explained below. Each equivalent circuit consisted of several components: ohmic resistance (R_s), charge transfer resistance at the counter electrode/electrolyte (R_1), charge transfer resistance at the photoelectrode/electrolyte (R_2), resistance at the Warburg diffusion of redox I^-/I_3^- couple in the electrolyte (W_s), constant phase element of capacitance corresponding to R_1 (CPE1), and constant phase element of capacitance corresponding to R_2 (CPE2). The characteristic frequency is related to the inverse of τ_r in the TiO_2 film. The charge transport resistance at the TiO_2/dye/electrolyte interface increased from TiO_2-1 to TiO_2-4. This is because the porosity and interconnectivity of TiO_2-1 were the greatest, whereas those of TiO_2-4 were the lowest. This results in better electron transport and lower charge recombination. Consequently, the TiO_2-1

Table 1 Photovoltaic performances, dye adsorption, and EIS parameters of DSSCs fabricated with mesoporous TiO_2 films templated by PVC-*g*-PDMAEMA and a polymer electrolyte consisting of PEODME/SiO_2/MPII/I_2 at 100 mW/cm^2

TiO_2 electrode	V_{oc} (V)	J_{sc} (mA/cm^2)	FF	η (%)	R_s (Ω)	R_1 (Ω)	R_2 (Ω)	Ws (Ω)	Dye loading (nmol/cm^2)	τ_r (ms)
TiO_2-1	0.72	9.1	0.48	3.2	16.4	20.7	55.5	14.4	17.1	156.2
TiO_2-2	0.73	8.4	0.48	2.7	21.4	18.0	63.2	41.8	15.3	105.2
TiO_2-3	0.76	6.3	0.51	2.4	20.7	20.4	67.9	21.4	13.1	92.5
TiO_2-4	0.74	5.0	0.56	2.0	19.0	26.5	66.9	16.7	8.2	56.8

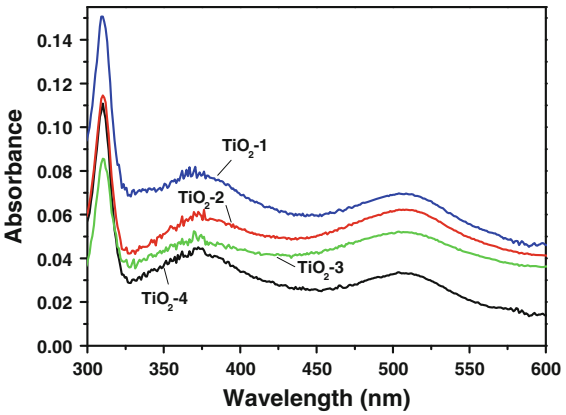

Fig. 10 UV–Visible spectra of dye adsorption onto TiO_2 photoelectrodes

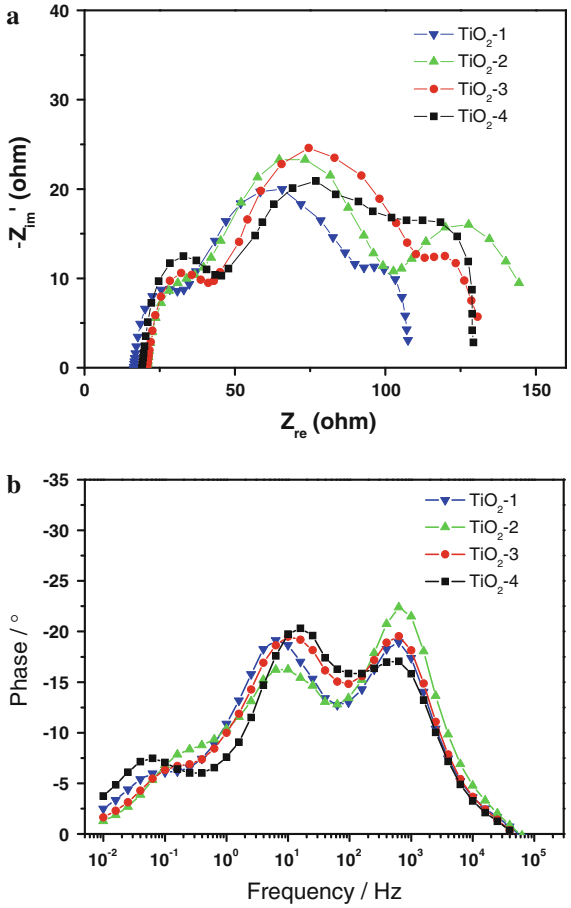

Fig. 11 **a** Nyquist plots and **b** Bode phase plots of DSSCs fabricated with mesoporous TiO_2 films templated by PVC-*g*-PDMAEMA and a polymer electrolyte consisting of PEODME/SiO_2/MPII/I_2 at 100 mW/cm^2

electrode with the lowest resistance exhibited the highest τ_r value (156.2 ms), leading to the highest efficiency among the samples. These results are in agreement with the DSSC performance results where the TiO_2-1 photoelectrode has the highest efficiency, resulting from higher porosity and lower interfacial resistance.

Conclusions

PVC-*g*-PDMAEMA graft copolymers with different grafting ratios were synthesized through the ATRP method and characterized by FT-IR and NMR spectroscopy. The self-assembly behavior of the graft copolymer was analyzed by TEM analysis. TGA data show that the PVC-*g*-PDMAEMA graft copolymers were nearly degraded above 500 °C, indicating their applicability as a template to synthesize mesoporous TiO_2 films. The structure and morphology of anataze TiO_2 films were characterized by XRD, TEM, and SEM analyses. The resultant porous TiO_2 thin films were efficiently used as a photoelectrode for fabricating quasi-solid-state DSSCs employing the polymer electrolyte consisting of PEODME, nano-sized silica, MPII, and I_2. The maximum energy conversion efficiency reached 3.17 % at 100 mW/cm^2 for the TiO_2-1 photoelectrode with higher porosity and lower interfacial resistance. This is one of the highest

efficiencies ever reported for quasi-solid-state DSSCs with 600-nm-thick TiO_2 film.

Acknowledgments This study was supported by a National Research Foundation (NRF) grant funded by the Korean government (MEST) through the Pioneer Research Center Program (2008-05103) and the Korea Center for Artificial Photosynthesis (KCAP) located at Sogang University (NRF-2009-C1AAA001-2009-0093879). This work is financially supported by the Ministry of Knowledge Economy (MKE) and Korea Institute for Advancement in Technology (KIAT) through the Workforce Development Program in Strategic Technology.

References

Ahn SH, Koh JH, Seo JA, Kim JH (2010) Structure control of organized mesoporous TiO_2 films templated by graft copolymers for dye-sensitized solar cells. Chem Commun 46:1935–1937

Ahn SH, Park JT, Koh JK, Roh DK, Kim JH (2011a) Graft copolymer directed synthesis of micron-thick organized mesoporous TiO_2 films for solid-state dye-sensitized solar cells. Chem Commun 47:5882–5884

Ahn SH, Jeon H, Son KJ, Ahn H, Koh WG, Ryu DY, Kim JH (2011b) Efficiency improvement of dye-sensitized solar cells using graft copolymer-templated mesoporous TiO_2 films as an interfacial layer. J Mater Chem 21:1772–1779

Beltran EL, Prené P, Boscher C, Belleville P, Buvat P, Lambert S, Guillet F, Boissière C, Grosso D, Sanchez C (2006) Nanostructured hybrid solar cells based on self-assembled mesoporous titania thin films. Chem Mater 18:6152–6156

Brinker CJ, Scherer GW (1990) Sol–gel science: the physics and chemistry of sol–gel processing. Academic Press, Boston

Cheng YJ, Gutmann JS (2006) Morphology phase diagram of ultrathin anatase TiO_2 films templated by a single PS-*b*-PEO block copolymer. J Am Chem Soc 128:4658–4674

Cozzoli PD, Kornowski A, Weller H (2003) Low-temperature synthesis of soluble and processable organic-capped anatase TiO_2 nanorods. J Am Chem Soc 125:14539–14548

Fahmi AW, Braun HG, Stamm M (2003) Fabrication of metalized nanowires from self-assembled diblock copolymer templates. Adv Mater 15:1201–1204

Falaras P, Stergiopoulos T, Tsoukleris DS (2008) Enhanced efficiency in solid-state dye-sensitized solar cells based on fractal nanostructured TiO_2 thin films. Small 4:770–776

Forster S, Antonietti M (1998) Amphiphilic block copolymers in structure-controlled nanomaterial hybrids. Adv Mater 10:195–217

Kalaignan GP, Kang M, Kang YS (2006) Effects of compositions on properties of PEO–KI–I_2 salts polymer electrolytes for DSSC. Solid State Ionics 177:1091–1097

Kang MS, Kim JH, Won J, Kang YS (2007) Oligomer approaches for solid-state dye-sensitized solar cells employing polymer electrolytes. J Phys Chem C 111:5222–5228

Kern R, Sastrawan R, Ferber J, Stangl R, Luther J (2002) Modeling and interpretation of electrical impedance spectra of dye solar cells operated under open-circuit conditions. Electrochim Acta 47:4213–4225

Kim HC, Jia X, Stafford CM, Kim DH, McCarthy TJ, Tuominen M, Hawker CJ, Russell TP (2001) A route to nanoscopic SiO_2 posts via block copolymer templates. Adv Mater 13:795–797

Kim JH, Kang MS, Kim YJ, Won J, Park NG, Kang YS (2004) Dye-sensitized nanocrystalline solar cells based on composite polymer electrolytes containing fumed silica nanoparticles. Chem Commun 14:1662–1663

Kim J, Koh JK, Kim B, Ahn SH, Ahn H, Ryu DY, Kim JH, Kim EK (2011) Enhanced performance of I_2-free solid-state dye-sensitized solar cells with conductive polymer up to 6.8%. Adv Funct Mater 21:4633–4639

Koh JK, Seo JA, Koh JH, Kim JH (2009) Templated synthesis of Ag loaded TiO_2 nanostructures using amphiphilic polyelectrolyte. Mater Lett 63:1360–1362

Koh JH, Seo JA, Ahn SH, Kim JH (2010) Templated synthesis of porous TiO_2 thin films using amphiphilic graft copolymer and their use in dye-sensitized solar cells. Thin Solid Films 519:158–163

Kotani Y, Matoda T, Matsuda A, Kogure T, Tatsumisago M, Minami T (2001) Anatase nanocrystal-dispersed thin films via sol–gel process with hot water treatment: effects of poly(ethylene glycol) addition on photocatalytic activities of the films. J Mater Chem 11:2045–2048

Kroeze JE, Hirata N, Schmidt-Mende L, Orizu C, Ogier SD, Carr K, Gratzel M, Durrant JR (2006) Parameters influencing charge separation in solid-state dye-sensitized solar cells using novel hole conductors. Adv Funct Mater 16:1832–1838

Lee KJ, Park JT, Goh JH, Kim JH (2008) Synthesis of amphiphilic graft copolymer brush and its use as template film for the preparation of silver nanoparticles. J Polym Sci A 46:3911–3918

Li B, Wang L, Kang B, Wang P, Qiu Y (2006) Review of recent progress in solid-state dye-sensitized solar cells. Sol Energy Mater Sol Cells 90:549–573

Liang C, Hong K, Guiochon GA, Mays JW, Dai S (2004) Synthesis of a large-scale highly ordered porous carbon film by self-assembly of block copolymers. Angew Chem Int Ed 116:5785–5789

Lu YF, Ganguli R, Drewien CA, Anderson MT, Brinker CJ, Gong WL, Guo YX, Soyez H, Dunn B, Huang MH, Zink JI (1997) Continuous formation of supported cubic and hexagonal mesoporous films by sol–gel dip-coating. Nature 389:364–368

Lu S, Koeppe R, Gunes S, Sariciftci NS (2007) Quasi-solid-state dye-sensitized solar cells with cyanoacrylate as electrolyte matrix. Sol Energy Mater Sol Cells 91:1081–1086

Melde BJ, Burkett SL, Xu T, Goldbach JT, Russell TP, Hawker CJ (2005) Silica nanostructures templated by oriented block copolymer thin films using pore-filling and selective-mineralization routes. Chem Mater 17:4743–4749

Nedelcu M, Lee J, Crossland EJW, Warren SC, Orilall MC, Guldin S, Huttner S, Ducati C, Eder D, Wiesner U, Steiner U, Snaith HJ (2009) Block copolymer directed synthesis of mesoporous TiO_2 for dye-sensitized solar cells. Soft Matter 5:134–139

O'Reagan B, Grätzel M (1991) A low-cost, high-efficiency solar cell based on dye-sensitized colloidal TiO_2 films. Nature 353:737

Park JT, Roh DK, Patel R, Kim E, Ryu DY, Kim JH (2010) Preparation of TiO_2 spheres with hierarchical pores via

grafting polymerization and sol–gel process for dye-sensitized solar cells. J Mater Chem 20:8521–8530

Patel R, Ahn SH, Chi WS, Kim JH (2012) Poly(vinyl chloride)-graft-poly(*N*-vinyl caprolactam) graft copolymer: synthesis and use as template for porous TiO_2 thin films in dye-sensitized solar cells. Ionics. doi:10.1007/s11581-011-0641-4

Roh DK, Park JT, Ahn SH, Ahn H, Ryu DY, Kim JH (2010) Amphiphilic poly(vinyl chloride)-*g*-poly(oxyethylene methacrylate) graft polymer electrolytes: Interactions, nanostructures and applications to dye-sensitized solar cells. Electrochim Acta 55:4976–4981

Sakaguchi S, Ueki H, Kato T, Kadoa T, Shiratuchi R, Takashima W, Kaneto K, Hayase S (2004) Quasi-solid dye sensitized solar cells solidified with chemically cross-linked gelators control of TiO_2/gel electrolytes and counter Pt/gel electrolytes interfaces. J Photochem Photobiol A 164:117–122

Schlichthorl G, Huang SY, Sprague J, Frank AJ (1997) Band Edge movement and recombination kinetics in dye-sensitized nanocrystalline TiO_2 solar cells: a study by intensity modulated photovoltage spectroscopy. J Phys Chem B 101:8141–8155

Schlichthorl G, Park NG, Frank AJ (1999) Evaluation of the charge-collection efficiency of dye-sensitized nanocrystalline TiO_2 solar cells. J Phys Chem B 103:782–791

Tan S, Zhai J, Wan M, Meng Q, Li Y, Jiang L, Zhu D (2004a) Influence of small molecules in conducting polyaniline on the photovoltaic properties of solid-state dye-sensitized solar cells. J Phys Chem B 108:18693–18697

Tan S, Zhai J, Xue B, Wan M, Meng Q, Li Y, Jiang L, Zhu D (2004b) Property influence of polyanilines on photovoltaic behaviors of dye-sensitized solar cells. Langmuir 20:2934–2937

Urbas AM, Maldovan M, DeRege P, Thomas EL (2002) Bicontinuous cubic block copolymer photonic crystal. Adv Mater 14:1850–1853

Wang P, Zakeeruddin SM, Exnar I, Gratzel M (2002) High efficiency dye-sensitized nanocrystalline solar cells based on ionic liquid polymer gel electrolyte. Chem Commun 2972–2973

Wang P, Zakeeruddin SM, Comte P, Exnar I, Gratzel M (2003) Gelation of ionic liquid-based electrolytes with silica nanoparticles for quasi-solid-state dye-sensitized solar cells. J Am Chem Soc 125:1166–1167

Wang ZS, Kawauchi H, Kashima T, Arakawa H (2004) Significant influence of TiO_2 photoelectrode morphology on the energy conversion efficiency of N719 dye-sensitized solar cell. Coord Chem Rev 248:1381–1389

Wu J, Lan Z, Lin J, Huang M, Hao S, Sato T, Yin S (2007) A novel thermosetting gel electrolyte for stable quasi-solid-state dye-sensitized solar cells. Adv Mater 19:4006–4011

Xia J, Li F, Huang C, Zhai J, Jiang L (2006) Improved stability quasi-solid-state dye-sensitized solar cell based on polyether framework gel electrolytes. Sol Energy Mater Sol Cells 90:944–952

Yang PD, Zhao DY, Margolese DI, Chmelka BF, Stucky GD (1998) Generalized syntheses of large-pore mesoporous metal oxides with semicrystalline frameworks. Nature 396:152–155

Yang PD, Zhao DY, Margolese DI, Chmelka BF, Stucky GD (1999) Block copolymer templating syntheses of mesoporous metal oxides with large ordering lengths and semicrystalline framework. Chem Mater 11:2813–2826

Yeh SW, Wei KH, Sun YS, Jeng US, Liang KS (2003) Morphological transformation of PS-*b*-PEO diblock copolymer by selectively dispersed colloidal CdS quantum dots. Macromolecules 36:7903–7907

Yoshitake H, Sugihara T, Tatsumi T (2002) Preparation of wormhole-like mesoporous TiO_2 with an extremely large surface area and stabilization of its surface by chemical vapor deposition. Chem Mater 14:1023–1029

DOI 10.1007/978-3-319-05041-6_18
Reprinted from the *Journal of Nanoparticle Research*, DOI 10.1007/s11051-012-0983-5

RESEARCH PAPER

SnO_2, IrO_2, Ta_2O_5, Bi_2O_3, and TiO_2 nanoparticle anodes: electrochemical oxidation coupled with the cathodic reduction of water to yield molecular H_2

Jina Choi · Yan Qu · Michael R. Hoffmann

Received: 15 March 2012 / Accepted: 8 June 2012 / Published online: 18 July 2012

Abstract In recent years, the search for environmentally friendly alternative energy sources with reduced carbon footprints has increased. The coupling of photovoltaic power sources with advanced electrolysis systems for hydrogen production via water splitting using organic contaminants as sacrificial electron donors has been considered to a be viable alternative. In this report, we demonstrated the feasibility of a scaled-up rooftop prototype of the proposed hybrid photovoltaic-electrolysis system, which utilizes semiconductor nanoparticles coated on to metal substrates as electrodes for the generation of hydrogen coupled with the oxidation of wastewater. Application of an anodic bias of >2.0 V to bismuth-doped TiO_2 (BiO_x–TiO_2) on Ti metal anodes with a sequential under-coatings of nanoparticulate SnO_2, IrO_2, Ta_2O_5, and Bi_2O_3 results in the electrochemical degradation of a variety of organic chemical contaminants in water (i.e., rhodamine B (Rh.B), methylene blue (MB), salicylic acid, triclosan, and phenol) and actual wastewater from a chemical manufacturing plant, while at the same time, molecular hydrogen is produced at stainless steel (SS) cathodes. The kinetics of the anodic substrates oxidation is investigated as a function of the cell current (I_{cell}), substrate concentration, and background electrolyte composition (e.g., NaCl, Na_2SO_4, or seawater). Average current efficiencies were found to be in the range of 4–22 %, while the cathodic current and energy efficiencies for hydrogen production were found to be in the range of 50–70 % and 20–40 %, respectively.

Keywords Semiconductor composites · Nanoparticle coatings · Electrochemical oxidation · Wastewater treatment · Hydrogen production · Organic compound oxidation · Sustainable development

Special Issue Editors: Mamadou Diallo, Neil Fromer, Myung S. Jhon

This article is part of the Topical Collection on Nanotechnology for Sustainable Development

J. Choi · Y. Qu · M. R. Hoffmann (✉)
Linde-Robinson Laboratories, California Institute of Technology, Pasadena, CA 91125, USA
e-mail: mrh@caltech.edu

Present Address:
J. Choi
KRICT, Korea Research Institute of Chemical Technology, Yuseong 305-600, Daejeon, Republic of Korea

Introduction

In recent years, there has been increasing interest in developing electrochemical methods for wastewater treatment because of its advantages, which may include versatility, energy efficiency, amenability to automation, and robustness (Juttner et al. 2000; Chen 2004; Anglada et al. 2009). Electrochemical treatment

has been explored for treating various synthetic wastewaters containing specific target compounds such as dyes and phenolic compounds (Comninellis and Nerini 1995; Iniesta, Michaud et al. 2001; Shen, Yang et al. 2005; Panizza, Barbucci et al. 2007) and more recently attention has focused on the treatment of actual wastewaters including domestic wastewaters, industrial wastewaters, and landfill leachates (Vlyssides et al. 2002; Vaghela et al. 2005; Urtiaga et al. 2009). However, one of the primary objections to electrochemical wastewater treatment is the relatively high operating cost incurred because of a relatively high electric energy consumption rate.

Hydrogen from electrochemical water splitting is considered to be a viable alternative method of industrial energy production and a possible renewable energy resource to help combat climate change because of the emission of green-house gases (DOE 2008). Hydrogen is mainly produced by steam methane reforming (SMR), which produces large carbon emissions and because of the competitive uses for methane as a fuel. Given this conflicting situation, the electrolytic production of hydrogen via water electrolysis or electrochemical water splitting has the potential to produce large quantities of hydrogen that are free of direct carbon emissions. However, the primary disadvantage of water electrolysis for hydrogen generation are the high electricity consumption rates, especially in larger-scale applications as compared with SMR using natural gas.

During the past decades, electrochemical applications for water splitting and for the wastewater treatment have been independently studied. However, we propose using a dual-purpose hybrid electrolysis system that couples wastewater treatment with hydrogen generation as a useful by-product. In a hybrid electrolysis system, the electrochemical oxidation of organic contaminants takes place at an anode while reduction simultaneously takes place at an appropriate cathode, which results in hydrogen production from electron transfer to water or protons. In previous studies, our group successfully demonstrated hybrid electrochemical cells consisting of BiO_x–TiO_2/Ti(0) anodes coupled with stainless steel (SS) cathodes for the complete oxidation of phenol with the simultaneous hydrogen production (Park et al. 2008a, b, 2009).

In this study, we have scaled up our hybrid electrolysis system to a subpilot-scale size (with a volume of 20 L) with metal oxide anodes with an over-coating of BiO_x–TiO_2/Ti(0) and SS cathodes to investigate the feasibility of practical applications of this approach. The kinetics of oxidative degradation of a variety of target substrates including methylene blue (MB), rhodamine B (Rh.B), phenol, salicylic acid, triclosan, and organic waste contained in actual domestic and industrial wastewater with corresponding simultaneous generation of hydrogen was investigated. We also demonstrate in this study a solar-powered hybrid electrolysis system employing a commercial photovoltaic (PV) panel as the source of applied potential across the electrode array.

Experimental details

Electrode preparation

The composite semiconductor anodes were coupled with stainless steel (SS, Hastelloy C-22) cathodes. The anode consists of a sequential series of metal oxide coatings on a titanium metal plate: (a) a Ti metal substrate, (b) an anti-passivation layer consisting of a mixture of IrO_2 and Ta_2O_5, (c) an intermediated layer (a sealing coat) of SnO_2 and Bi_2O_3, (d) a slurry undercoating of nanoparticles of TiO_2 doped with Bismuth (Bi), and finally (e) an over-coating mixture of nanoparticulate TiO_2 and Bi_2O_3. The undercoating layer and over-coating layer together form the electrocatalytically active outer layer of the anode and each coating step requires a specific heat treatment at different temperatures and time durations of the annealing process. Further details of the preparation procedure are provided elsewhere (Park et al. 2008a, b; Weres 2009). This electrode has been shown to have excellent stability and a long service life (Weres 2009). The surface area of each electrode plate is about 800 cm^2; the prototype pilot-scale reactor consists of five anodes and six cathodes that face to each other at an inter-electrode distance of 2 mm.

Electrolysis experiments

Electrolysis experiments were carried out in the subpilot-scale reactor with a total volume of 20 L. A schematic diagram of the 20-L electrochemical reactor is shown in Fig. 1. The electrode array is immersed in 20 L of laboratory water to which NaCl (J.T.Baker) is added as a primary supporting electrolyte over the range

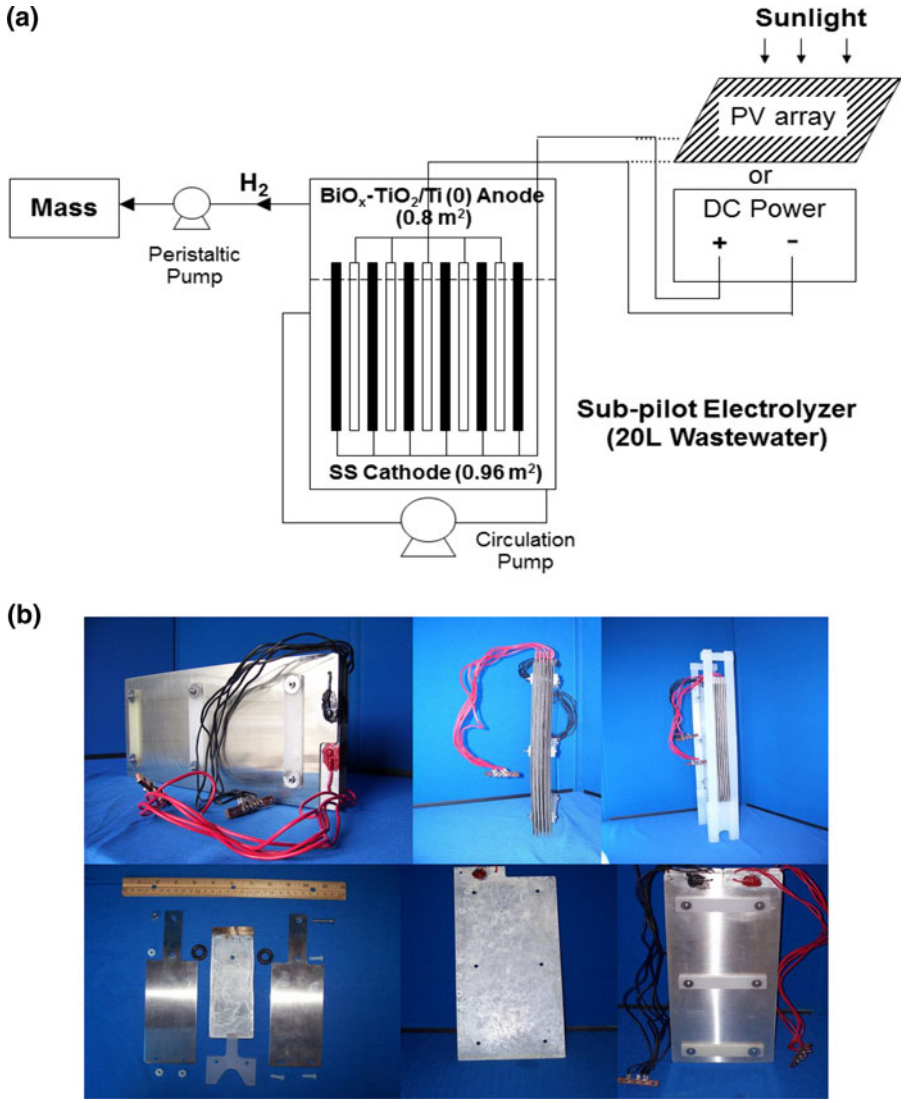

Fig. 1 **a** Schematic diagram of a subpilot electrochemical reactor and overall hybrid system. **b** Photographs of the electrode arrays showing the anodic semiconductor coatings on the Ti-metal base support

of 0–75 mM (typically 50 mM). For comparison, Na_2SO_4 (EMD) was used an alternative electrolyte. Seawater, which was collected from Santa Monica Bay directly off of the Los Angeles shoreline, was also employed as an alternative background electrolyte. Target substrates or electron donors such as methylene blue (MB, J.T.Baker), rhodamine B (Rh.B, Aldrich), salicylic acid (SA, Aldrich), phenol (PhOH, Mallinckrodt), and 5-chloro-2-(2,4-dichlorophenoxy)phenol (triclosan, Fluka) were added into a background electrolyte solution for water treatment testing. The substrate solutions were continuously mixed throughout the 20-L volume by a circulation pump connected to the bottom of reactor. The majority of experiments were carried out near circum-neutral pH. The oxidation of triclosan was investigated at pH 12 because of the low solubility of triclosan at lower pH values. The electrochemical degradation of industrial wastewater from a chemical manufacturing plant located in Minnesota was also investigated. The chemical plant wastes contained the following organic compounds: acetone, diisopropyl ether, MEK, 2-propanol, 2-butyl alcohol, MIBK, and a complex mixture of C4 to C12 perfluorosulfonic and perfluorocarboxylic acids. The original wastewater

samples were diluted with tap water to give a COD concentration for laboratory experiments in the range of 150–300 ppm. Constant current over the range between 7.5 and 40 A (typically 25 A) and voltage range of 3–4 V was applied to the electrode pairs with a DC power supply (HP 6260B). The cell voltages (E_{cell}) and cell currents (I_{cell}) were measured during electrolysis by multi-meter (Fluka).

Solar-powered electrolysis experiments

In the case of solar-powered electrolysis, a commercial polycrystalline silicon solar photovoltaic (PV) panel (Silicon Solar Inc.) with a peak power output of 180 W ($E_{peak} = 25.9$ V and $I_{peak} = 6.95$ A) and with an exposed surface area of 1.50 m^2 (dimensions: 0.95 m × 1.57 m) was employed in roof-top experiment on top of the Keck Laboratories building on the Caltech campus in Pasadena, CA. Solar PV panel was connected to the rooftop reactor to provide the potential bias to drive the oxidative degradation of various wastewaters containing target organic substrates; the electrons released by oxidation are then transferred to the metal cathode resulting in the simultaneous production of molecular hydrogen from water reduction. Either a 50-mM NaCl solution or a 10 volume percent (v/v %) filtered seawater solution were used as the primary source of supplemental background electrolytes added to the wastewater samples. In addition to the measurement of the cell potential, E_{cell}, and cell current, I_{cell}, solar radiation was monitored using a pyranometer (Apogee) coupled with a digital data-logger (Campbell Scientific).

Analytical methods

Sample aliquots were withdrawn from the solution intermittently during electrolysis. The disappearance or bleaching of the color of the dyes was monitored by measuring the absorbance at 665 and 550 nm for MB and Rh-B, respectively, with a UV/Vis spectrophotometer. The concentrations of phenol, salicylic acid, and triclosan were measured by a HPLC (Agilent 1100 series) equipped with a C18 column and a UV detector. The mobile phase of HPLC mixture contained 45 % acetonitrile, 55 % Milli-Q water, and 0.1 wt % acetic acid. For actual authentic wastewater samples, the chemical oxygen demand (COD) was measured using COD reagent vials (Hach), which utilize dichromate as the oxidant in an acidic solution at 150 °C for 2 h. $AgNO_3$ (Aldrich) was added into sample solution before measuring COD to eliminate the chloride interference when NaCl was used as the electrolyte. In addition, the COD of the other test substrates was also measured to determine the current efficiencies for the anodic oxidations.

Molecular hydrogen (H_2) produced from water during electrolysis was detected by a quadruple mass spectrometry (MS, Balzers). As shown in Fig. 1, the reactor was sealed and the headspace gas of the reactor was extracted with a peristaltic pump and pushed into a quadruple MS with 70 eV electron ionization energy via a turbo pump (Pfeiffer; 5.0×10^{-6} Torr). The production rate of H_2 was calculated from the volume percent of H_2 in the headspace gas, which was measured assuming that it was directly proportional to the percentage of ion current of H_2 in total ion currents measured by MS.

Current efficiency and energy efficiency

The instantaneous current efficiency (ICE) for anodic oxidation was calculated using the following equation introduced by Comninellis and Pulgarin (1991) and Comninellis and Nerini (1995):

$$\mathrm{ICE}(\%) = \left(\frac{[\mathrm{COD}_0 - \mathrm{COD}_t]FV}{8It}\right) \times 100, \qquad (1)$$

where COD_0 and COD_t are the COD (in g O_2/L) before and after electrolysis, respectively, F is the Faraday constant (96487 C/mol), V is volume of the electrolyte (L), I is the current (A), t is the reaction time (s).

Because the ICE decreases with time during electrolysis and finally approaches zero, the electrochemical oxidation index (EOI), which expresses the average current efficiency, was also calculated by following equation:

$$EOI(\%) = \frac{\int ICE}{\tau}, \qquad (2)$$

where τ is the time of electrolysis at which ICE is almost zero.

The cathodic current efficiency (CE) for H_2 production was calculated by the following equation:

$$\mathrm{CE}(\%)\text{for } \mathrm{H_2} = \left(\frac{2 \times \text{numbers of } \mathrm{H_2} \text{ molecules produced}}{\text{numbers of electron flew}}\right) \times 100. \quad (3)$$

The overall energy efficiency (EE) for H_2 production is calibrated using the heating value of H_2 (HHV = 39 Wh/g) and the energy consumed by the system:

$$\mathrm{EE}(\%)\text{for } \mathrm{H_2} = \left(\frac{39\mathrm{Wh/g} \times \mathrm{H_2} \text{ production rate(mol/h)}}{E_{\mathrm{cell}}(\mathrm{V}) \times I_{\mathrm{cell}}(\mathrm{A})}\right) \times 100. \quad (4)$$

In the case of our solar-powered electrolysis system, the energy efficiencies were calculated using the following equations:

$$\text{Solar to } \mathrm{PV_{cell}EE}(\%) = \left(\frac{E_{\mathrm{cell}}(\mathrm{V}) \times I_{\mathrm{cell}}(\mathrm{A})}{\text{solar flux } (\mathrm{W/m^2}) \times \text{PV area}(\mathrm{m^2})}\right) \times 100, \quad (5)$$

$$\text{Solar to } \mathrm{H_2EE}(\%) = \frac{\mathrm{H_2EE}(\%) \times \text{Solar to } \mathrm{PV_{cell}EE}(\%)}{100}. \quad (6)$$

Results and discussion

Electrochemical water treatment

Figure 2a shows the typical E_{cell}–I_{cell} output for the BiO_x–TiO_2/Ti(0) composite semiconductor anode coupled to a stainless steel cathode in the subpilot reactor in presence of sodium chloride or sodium sulfate as the supporting electrolytes. The current generation is initiated near 2.0 V of applied voltage and increases linearly >2.5 V of E_{cell}. The utilization of Na_2SO_4 as a supporting electrolyte generates a higher current density than that obtained with NaCl at the same applied voltage.

Figure 2b shows the current density as a function of the electrolyte concentration at +3 V of applied voltage. The current density increases with the addition of more electrolyte, but it does not increase much at high concentrations of electrolyte (i.e., >50 mM). Therefore, the concentration of the background

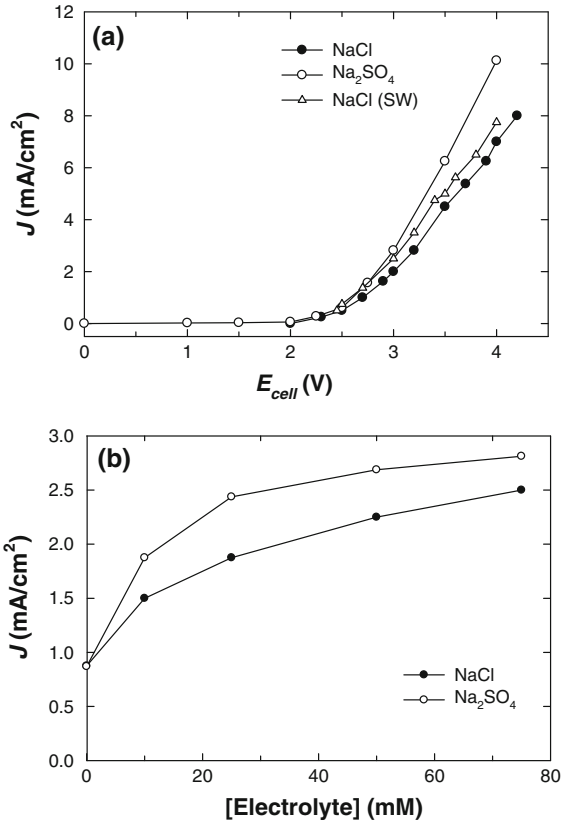

Fig. 2 **a** Current–voltage curves in the presence of 50 mM NaCl or Na_2SO_4 as a supporting electrolyte. NaCl (SW) is a seawater sample diluted to 10 v/v %. **b** The current density (J_{cell}) as a function of the concentration of the electrolyte (mM) at applied cell voltage of E_{cell} = 3.0 V

electrolytes was fixed 50 mM (or 10 v/v % of diluted seawater) in the subsequent experiments. We also measured E_{cell}–I_{cell} curve in the presence of 10 v/v % seawater instead of adding NaCl, as seawater typically contains 0.5 M NaCl. The current density in diluted seawater (10 v/v %) was slightly higher than in the case of 50-mM NaCl. This increase may be attributed to the presence of the additional ionic components present in seawater beyond Na^+ and Cl^-. The conductivity of diluted seawater solution was 5.3–5.6 mS/cm.

Figure 3 shows the effect of applied current density on the electrochemical degradation of organic substrates when NaCl or Na_2SO_4 was used as supporting electrolytes in the pilot reactor. Figure 3a shows the electrochemical degradation (i.e., color removal) of MB at different applied cell current in the presence of 50-mM NaCl. As expected, an increase in the current

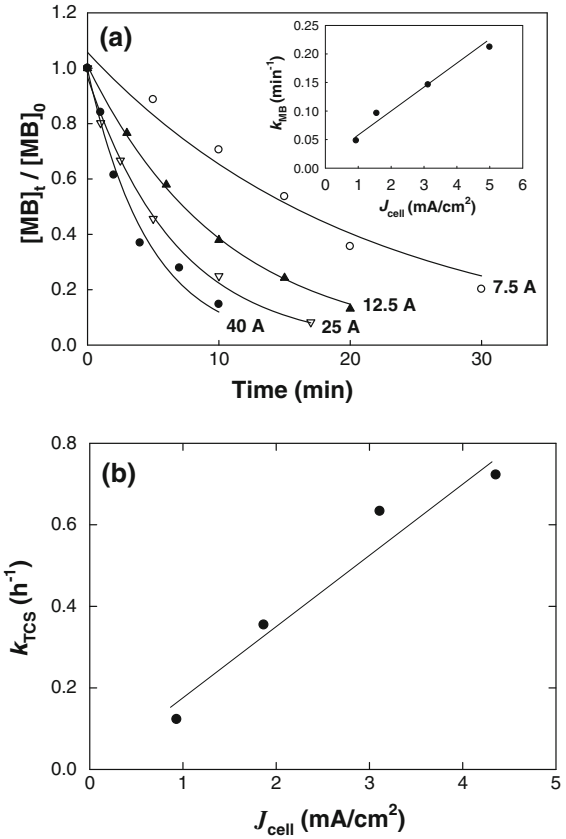

Fig. 3 Electrochemical degradation of organic substrates as a function of applied current density: **a** The degradation of methylene blue ($[MB]_0 = 10$ μM) in 50 mM NaCl. **b** Degradation of triclosan ($[TCS]_0 = 100$ μM) in 50 mM Na_2SO_4

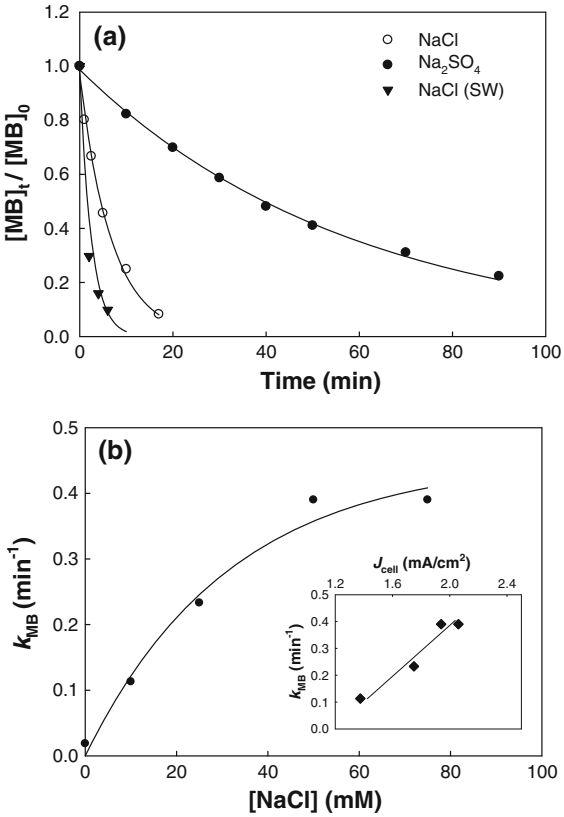

Fig. 4 **a** Electrochemical degradation of methylene blue (MB) as a function of background electrolyte at $I_{cell} = 25$A, $[MB]_0 = 10$ μM, 50 mM NaCl, 50 mM Na_2SO_4, and 10 v/v % seawater (NaCl, SW). **b** The color removal (i.e., bleaching) rate constant of MB as a function of the concentration of NaCl (SW) electrolyte at $E_{cell} = 3$ V, $[MB]_0 = 10$ μM

density resulted in a faster bleaching and degradation of MB because of the larger rate of $OH^{\bullet}$ radical (i.e., hydroxyl radical) generation and because of the production of higher yields of reactive chlorine species (e.g., HOCl, Cl_2^-, and $Cl^{\cdot}$). The bleaching of MB follows first-order kinetics with an apparent degradation rate constant of MB (k_{MB}) that is proportional to the current density (Fig. 3a, inset). Figure 3b also shows that the degradation rate constant for triclosan (k_{TCS}) is increased when higher current densities are applied in the presence of 50-mM Na_2SO_4.

Figure 4a shows that the MB degradation rate in the presence of NaCl was much faster than in the presence of Na_2SO_4, although the measured current density in the presence of NaCl was somewhat lower than in the case of Na_2SO_4 (Fig. 2). The same relative tendencies were observed during the degradation of the other target organic substrates such as Rhodamine B (Rh.B) and salicylic acid (SA) as shown in Table 1. In the presence of 50-mM NaCl, the half-lives ($t_{½}$) of RhB and SA were found to be less than 2 min. However, in the Na_2SO_4 electrolyte solution, the corresponding half-lives increased to 27 min for RhB and 77 min for SA, respectively. NaCl is known to enhance the electrochemical degradation efficiencies of various organic substrates (e.g., MB, phenol, glucose, and 17 β–estradiol) as compared with Na_2SO_4 (Comninellis and Nerini 1995; Bonfatti et al. 2000; Murugananthan et al. 2007; Panizza et al. 2007). It is believed that there are three pathways for electrochemical degradation of organic substrates: (1) direct oxidation on the anode surface (Eq. 7), (2) indirect oxidation mediated by $OH^{\bullet}$ radicals (Eq. 8), and (3) indirect oxidation mediated by electro-generated oxidants from electrolyte solution such as Cl, Cl_2^-, and OCl^- in the presence of NaCl:

Table 1 The degradation rate constants for anodic oxidation of several organic substrates: 20 L subpilot reactor, $I_{cell} = 25$ A applied, (electrolyte) = 0.05 M

Substrate	Conc. (μM)	Electrolyte	k_{obs} (min^{-1})	$t_{½}$ (min)	k_{COD} (min^{-1})
MB	5	NaCl	0.192	3.6	
	10	NaCl	0.146	4.7	0.130
	50	NaCl	0.136	5.1	
	100	NaCl	0.129	5.4	0.056
	250	NaCl	0.095	7.3	
PhOH	100	NaCl	2.320	0.3	0.124
	250	NaCl	1.190	0.6	
	1000	NaCl	0.360	1.9	
Rh.B	100	NaCl	0.379	1.8	0.259
	100	Na_2SO_4	0.026	27	
S.A.	100	NaCl	0.420	1.7	
	100	Na_2SO_4	0.009	77	

$$\text{Reduced organic compound} \rightarrow \text{Oxidized organic compound} + e^- \quad (7)$$

$$H_2O \rightarrow OH\cdot + H^+ + e^- \quad (8)$$

$$Cl^- \rightarrow Cl\cdot + e^- \quad (9)$$

$$Cl^- + Cl\cdot \rightarrow Cl_2^{\cdot -} \quad (10)$$

$$Cl_2\cdot^- + H_2O \rightarrow HOCl + Cl^- + H^+ + e^- \quad (11)$$

$$Cl_2\cdot^- + OH\cdot \rightarrow HOCl + Cl^- \quad (12)$$

$$HOCl \leftrightarrow OCl^- + H^+ (pKa = 7.2) \quad (13)$$

Chlorine species such as $Cl^{\cdot}$, $Cl_2^{\cdot -}$, and OCl^- (i.e., chlorine atom, the chlorine radical anion, and hypochlorite) are generated at the anode surface from the oxidation of Cl^-. They serve as secondary oxidants during electrolysis which results in a faster observed oxidation rates of the target substrates as compared with other electrolytes.

In our previous study, $Cl_2^{-\bullet}$ was assumed to be the primary oxidant among various active chlorine species because the observed degradation rates are found to be proportional only to the bimolecular rate constants of $Cl_2^{\bullet -}$ with specific substrates (Park et al. 2009). At the same time, the indirect oxidation by $OH^{\bullet}$ radicals and $SO_4^{-\bullet}$ radicals (Eq. 8) can take place when using Na_2SO_4 as electrolyte as well. However, substrate oxidation rates with Na_2SO_4 are found to be quite low. This result implies either that lower steady-state concentrations of $OH^{\bullet}$ radicals are produced in Na_2SO_4 solutions or that $SO_4^{-\bullet}$ radicals are not generated at a sufficient steady-state level. Most likely, $SO_4^{-\bullet}$ radicals produced at the semiconductor anode surface self-react to produce peroxydisulfate (or persulfate, Eq. 15):

$$SO_4^{2-} \rightarrow SO_4^{\cdot -} + e^- \quad (14)$$

$$SO_4^{\cdot -} + SO_4^{\cdot -} \rightarrow S_2O_8^{2-} \quad (15)$$

The substrate oxidation rates in 10 v/v % seawater were found to be higher than that in 50-mM NaCl solutions. This result indicates that seawater should be suitable as an alternative source of ionic conductivity and chloride as shown in Fig. 4a. In the absence of an added NaCl or seawater, MB was degraded slowly ($k_{MB} \sim 1.8 \times 10^{-2}$ min^{-1}). However, in the presence of NaCl, the MB degradation rate increased by an order of magnitude ($k_{MB} = 1.1$–3.9×10^{-1} min^{-1}); although, higher degradation rates were not obtain with further increases in the background NaCl concentration. This observation is consistent with the change in current density as a function of the concentration of the background electrolyte (Fig. 2b). The inset in Fig. 4b shows the linear relationship between the observed degradation rates and current densities generated by adding different concentration of NaCl.

In Table 1, we summarize the measured degradation rate constants for several different organic compounds. In the case of MB, the initial concentration of MB has little effect on the measured MB degradation rate. For example, k_{MB} at $[MB]_0 = 5$ μM was larger than at higher concentrations of MB; however, k_{MB} did not decrease very much over the range of 10–250 μM (see Fig. 5a, inset). The half-life life ($t_{½}$) for MB degradation at $[MB]_0 = 10$ and 250 μM was determined to be 5 and 7 min, respectively. However, the initial concentration of phenol significantly affected

the apparent degradation rate of phenol. For example, k_{PhOH} decreased at higher initial phenol concentrations. This may have been the results of competition for surface sites on the anode or to the formation of chlorinated and hydroxylated intermediates.

In the case of the electrochemical kinetics of MB degradation, the COD removal rate was found to be slower than the rate of color loss (Fig. 5). However, k_{COD} was similar to k_{obs} when $[MB]_0 = 10$ μM, and two times higher than k_{obs} when $[MB]_0 = 100$ μM (Table 1). In the specific case of phenol degradation, the substrate was completely eliminated within 2 min, but the COD reduction process continued for more than 10 min (i.e., $k_{COD} >> k_{obs}$ in Fig. 5b).

In Fig. 6, the current efficiencies (i.e., ICE) for the anodic oxidations were also measured in terms of COD reduction. Figure 6a shows that the current efficiency was higher at the initial stages (e.g., 85 % for MB oxidation) and decreased with time during electrolysis. The observed current efficiency clearly depends on the nature of the substrate and on the applied current density. Low initial concentrations result in higher current efficiencies. For example, with low initial concentrations of MB, higher current efficiency is obtained than at higher initial concentrations. In addition, the observed current efficiency increases at low applied current density, whereas the substrate removal efficiency increases at higher current densities. The current efficiency for phenol oxidation at an applied cell current, I_{cell}, of 8 A was higher than that obtained at $I_{cell} = 25$ A. Average current efficiencies (i.e., EOI) for the tested substrates are shown in Fig. 6b. The average current efficiencies were found to be in the range of 10–20 % in descending order of MB > Rh.B > phenol at the same initial concentration.

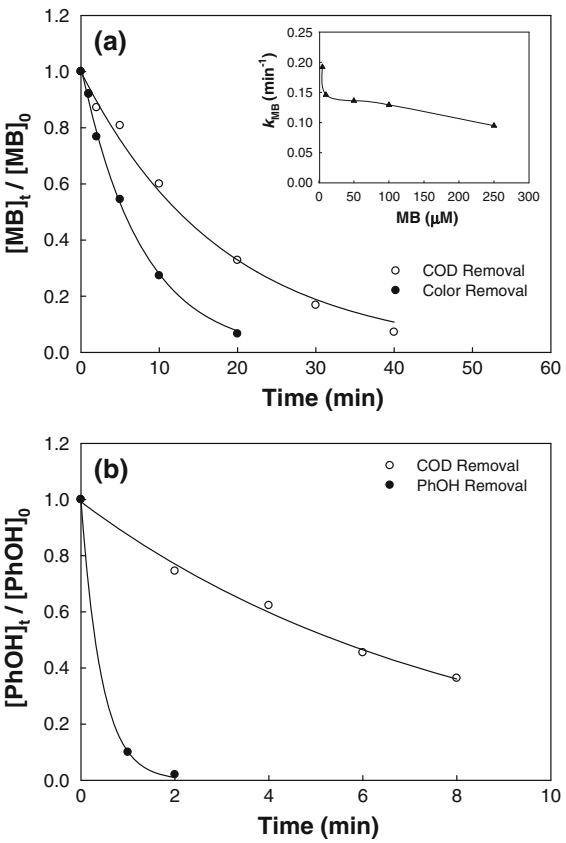

Fig. 5 Electrochemical degradation of organic substrates versus COD removal for **a** MB and **b** phenol at applied $I_{cell} = 25$ A in the presence of 50 mM NaCl ($[MB]_0 = 10$ or 100 μM, $[PhOH]_0 = 100$ μM)

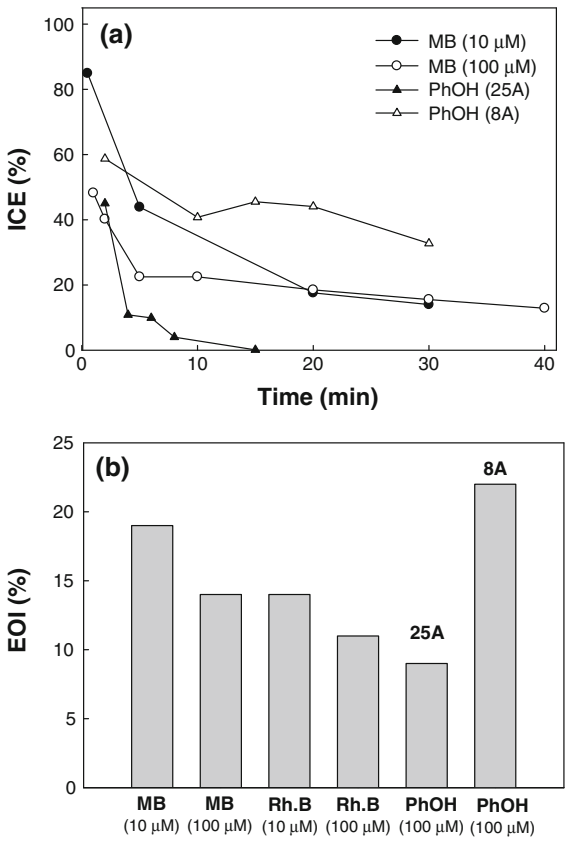

Fig. 6 **a** Time profile of current efficiencies (ICE) and **b** average current efficiencies (EOI) for substrates oxidations: $[MB]_0 = 10$ or 100 μM, $[Rh.B]_0 = 10$ or 100 μM, $[PhOH]_0 = 100$ μM, [NaCl(SW)] = 50 mM, $I_{cell} = 25$ A applied except in the case of phenol, where $I_{cell} = 8$ A

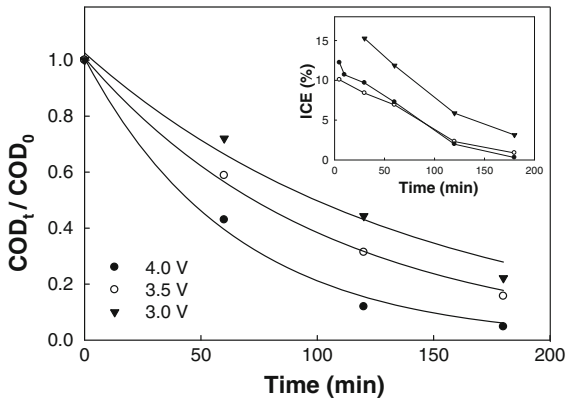

Fig. 7 Electrochemical oxidation of industrial wastewater samples (COD_0 = 100–150 ppm) at different applied voltages. Seawater, 10 v/v % (2 L), was used as the background electrolyte. Inset graph shows the current efficiencies where the average current efficiency was determined to be 4 %

Figure 7 illustrates the concentration versus time profiles for the electrochemical oxidation of actual wastewater obtained from a major chemical industry. The COD was reduced during electrolysis while the removal efficiency was found to increase with increasing applied voltage. The average current efficiency was near 4 %. The efficiency obtained with a complex mixture of chemical wastes was lower than the average current efficiencies (10–20 %) for the test substrates.

In conclusion, our prototype electrochemical reactor system appears to provide a suitable approach to achieve complete oxidation and, in many cases, total mineralization (i.e., conversion of the organic compounds to CO_2) of a variety of environmental organic pollutants and real wastewater as well. NaCl was shown to be the most effective background electrolyte for wastewater treatment, although diluted seawater is even better.

Simultaneous H_2 production via water electrolysis

Table 2 shows that significant amounts of H_2 were produced during water electrolysis at the stainless steel cathode in the electrochemical reactor under various conditions. For pure water splitting in the absence of organic substrates, H_2 production rates were in the range of 3–5 L/h and current efficiencies (CE) and energy efficiencies (EE) were about 50–60 % and 20–35 %, respectively. As expected, the prototype reactor was less efficient compared with a much smaller sized reactor which had an EE of 35–60 %. The current efficiency and energy efficiency for H_2 production also decreased with increasing applied power, which showed same tendency as substrates oxidation at anode. In addition, the direct comparison of NaCl, seawater, and Na_2SO_4 was carried out. These comparisons showed that Na_2SO_4 was better than NaCl for net H_2 production rates. This could be attributed to the higher current densities generated in dissociated Na_2SO_4 solutions compared with the same concentrations of NaCl (Fig. 2). On the other hand, in NaCl solutions, active chlorine species are clearly produced at anode surfaces and then reduced again at the cathode. Thus, fewer electrons are available for proton or water reduction, which in turn lowers the H_2 production rates at cathode.

In the presence of organic substrates such as MB and phenol, the observed H_2 production rates were measured at 5–6 L/h during the simultaneous oxidation of the substrates at the anodes. The H_2 production rates were found to be relatively stable before and after

Table 2 The rate, cathodic current efficiency (CE), and energy efficiency (EE) of hydrogen production: 20-L subpilot reactor, constant current applied, 0.05 M of electrolyte used

Substrate	I_{cell} (A)	E_{cell} (V)	Electrolyte	H_2 Production (L/h)	CE (%)	EE (%)
Water only	12.5	2.85	NaCl	3.2	60	35
	20	3.00	NaCl	4.0	48	23
	25	3.23	NaCl	4.3	42	19
	25	3.26	sw	5.0	48	21
	25	3.27	Na_2SO_4	5.2	50	22
MB	25	3.25	sw	5.3	51	23
PhOH	25	3.22	sw	5.7	56	25
Wastewater	25	3.22	sw	5.4	52	23
Wastewater (PV)	7	2.82	sw	2.2	74	38

sw 10 v/v % of seawater

adding organic substrates. Similar H_2 production rates were obtained with industrial wastewater also; this indicates that the presence of organic wastes in solution did not have a negative effect on cathodic H_2 production rate. In previous studies, we have shown that some specific organic substrates can actually increase H_2 production energy efficiencies by 30–50 % by quenching active chlorine species. At the same time, active chlorine species were found to be in competition with H_2 production (Park et al. 2008a, b, 2009). The reactive chlorine species effectively functions as electron shuttles between the anode and cathode (i.e., chloride can be recycled between the anode and cathode). However, organic substrates can be rapidly oxidized by the reactive chlorine species; this has the net effect of making more electrons available at the cathodes for water reduction (Park et al. 2009).

In a separate set of experiments, we compared the H_2 production rates to the corresponding hypochlorite (OCl^-) production rates. In a smaller-sized electrochemical reactor, H_2 production rates of 100–300 μM/min were found to be in a similar range to the OCl^- production over the range of 100–150 μM/min. However, in the larger pilot reactor, the H_2 production rate was increased to 3–5 mM/min, whereas the OCl^- production rate remained relatively constant at 200 μM/min.

Solar-powered hybrid electrolysis systems

Figure 8 shows the results of solar-powered photovoltaic-electrolysis experiments using our 20-L reactor, which was performed on the rooftop of W. M. Keck Laboratories at Caltech in August 2009. The electrochemical reactor was directly connected to the output of a 180 W_{peak} commercial PV panel with a surface area of 1.50 m^2. In Fig. 8a, we illustrate a typical time profile for the incident solar light radiation as measured with a pyranometer; this is matched with the corresponding measured values of E_{cell}, and I_{cell} on typical sunny days in Pasadena. The peak of incident solar radiation energy was near 1,000 W/m^2 around noontime, although the incident flux decreased to 600 W/m^2 in the late afternoon because of the larger solar zenith angle. The cell voltage, E_{cell}, was determined to be +3.3 V in the presence of diluted seawater. This value decreased to 3.0 V in the afternoon as incident solar irradiation flux

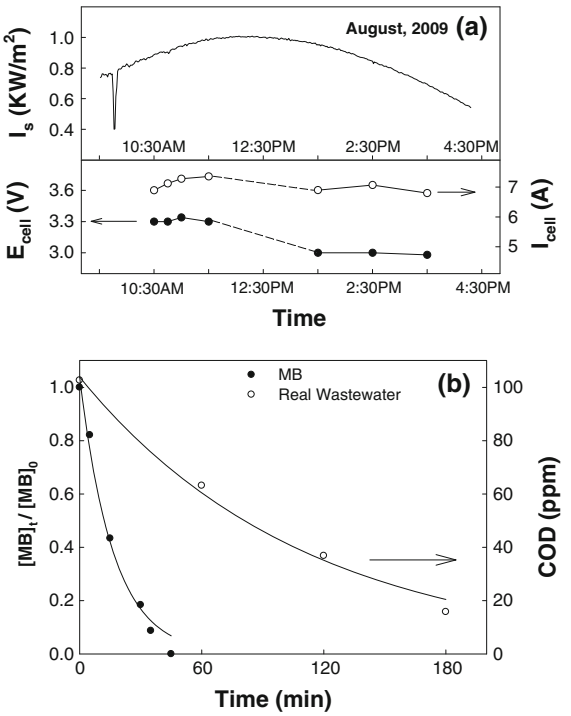

Fig. 8 Solar-powered rooftop experiment: **a** solar intensity, cell current, and cell voltage, which are measured during daytime, **b** degradation of MB ($[MB]_0 = 100$ μM) and COD removal of chemical industry wastewater ($COD_0 = 100$ ppm). Seawater, 10 v/v % (2 L), was used as the background electrolyte

decreased. The cell current, I_{cell}, was found to be close to 7 A both in the morning and in the late afternoon. The values for E_{cell} and I_{cell} were measured over several days including a partly cloudy day in August 2009. Over this span, the corresponding values remained relatively constant over the ranges of 2.7–3.3 V and 6–7 A. The actual PV power output was measured as 23 W, which was only 13 % of the PV_{peak} power output reported by the supplier. The apparent loses may be because of resistive losses in the wiring, higher temperatures during testing, and the resistive losses because of the coupling to the electrolyzer. The solar-to-PV_{cell} energy efficiency was determined to be 1.6–2 % for the larger panel, whereas for a smaller area PV panel, the energy efficiency was 2.5 % for a system panel rated at 6.4 W_{peak} (area = 0.13 m^2) and a smaller electrolyzer using the same composition of the anodes and cathodes (V = 200 mL).

Figure 8b shows that MB and industrial wastewater were effectively treated in spite of lower power

outputs. For example, the apparent pseudofirst-order rate constant for COD reduction (k_{COD}) of industrial wastewater with solar-driven system by PV array operating at 21 W ($E_{cell} \times I_{cell} = 3.0$ V $\times$ 7 A) was estimated to be 9.0×10^{-3} min^{-1}, which is similar to k_{COD} for DC-powered oxidation at 45 W ($E_{cell} \times I_{cell} = 3.0$ V $\times$ 15 A). The average current efficiency for the chemical wastewater oxidation was 15 % in the solar-powered system, which is almost four times higher under DC-powered oxidation. The higher observed efficiency may be attributed to photo-assisted electrochemical (i.e., photo-electrochemical, PEC) reactions taking place in the solar-powered rooftop experiments. The prototype PV-electrolyzer was directly exposed to solar-light that is capable of catalytically activating the doped-TiO_2 particles coated on anode surface. Preliminary results of laboratory experiment with a medium size of electrochemical reactor illuminated with a UV lamp showed that the electrochemical oxidation rates of phenol were increased with direct exposure to UV light irradiation indicating that the PEC processes actually take place on BiO_x–TiO_2/Ti(0).

In solar-driven hybrid electrolysis system, H_2 was continuously produced during the simultaneous oxidation of the organic substrates present in the chemical plant wastewater. The H_2 production rate was 2.2 L/h, which was smaller than observed in the DC-powered system (Table 2). In spite of relatively low power, however, CE and EE values were increased to 74 and 38 %, respectively. Similar to the anodic oxidation results, higher CE and EE for H_2 production in the solar-powered electrolysis system can be ascribed to the secondary photocatalytic activity of TiO_2 on anode surface. In DC-powered electrolysis using a medium sized electrolyzer, we also found that the photo-electrochemical (PEC) H_2 production rates under simultaneous UV light irradiation were approximately two times higher than in the absence of UV light. The solar-to-H_2 energy efficiency was determined 0.8 %.

Potential practical applications

The preceding results provide a practical example of a prototype hybrid photovoltaic-electrolysis system, which has a dual purpose for both wastewater treatment and H_2 production. In the PV-powered experiments, the solar-to-H_2 energy efficiency was estimated to be less than 1 %, which was lower than other commercial PV-electrolysis systems in the range of 2–10 % (Lehman et al. 1997; Hollmuller et al. 2000; Ahmad and El Shenawy 2006; Gibson and Kelly 2008). However, our hybrid PV-electrolysis system has several advantages for practical applications. First, our hybrid PV-electrolysis system can be operated under mild conditions, whereas other types of PV-electrolysis systems referenced earlier are only operated at much harsher conditions (e.g., pH 0 or pH 14). For example, in the case of alkaline water electrolyzers, which are operated at very high pH (i.e., 6–7 M KOH) to obtain optimal activity. In addition, the operational temperatures are in the range of 70–80 °C under elevated pressures to minimize the overall energy requirements (Srinivasan 2006). However, the hybrid PV-electrolysis system can be effectively operated under near-neutral pH conditions with relatively low concentrations of background electrolytes (e.g., 50 mM NaCl). Furthermore, our PV-electrolysis system can be employed for the dual purpose of wastewater treatment coupled and H_2 production. The combined approach to convert waste to energy should make this approach economically feasible with further optimization. High-concentration alkaline electrolyzers or proton exchange membrane electrolyzers would be impractical for applications in water or wastewater treatment.

The PV-electrolysis system can be further distinguished from other electrochemical water treatment systems in that a composites of multiple semiconductors electrodes are employed as anodes. For example, boron-doped diamond electrodes (BOD) are often promoted as suitable anodes for wastewater treatment because of their stability, wide potential range for water stability, and relatively low background current (Cabeza et al. 2007; Jiang et al. 2008). Jiang et al. also observed that the decomposition of waste organics and simultaneous hydrogen production are feasible with a boron-doped diamond (BOD) electrode (Jiang et al. 2008; Montanaro et al. 2008; Montanaro and Petrucci 2009; Petrucci and Montanaro 2011). However, pilot-scale application are limited because of (1) the high price of the boron-doped diamonds and (2) to limitations of reactor scale-up given that production of BOD electrodes requires chemical vapor deposition (CVD) or high-pressure–high-temperature (HPHT) processes (Kraft 2007). On the other hand, the Bi-doped TiO_2 anodes employed herein can be easily manufactured at a relatively low cost (Weres 2009). In addition, PV-

electrolysis systems for environmental applications (i.e., water treatment) has been proposed to reduce the operating costs of water treatment (Jiang et al. 2008).

In conclusion, we have demonstrated a practical, low-cost, subpilot-scale, prototype PV-electrolysis system for water and wastewater treatment. The reactor system presented herein appears to have a synergic effect on the extent of water treatment when powered by sunlight as compared with the same system powered by direct current (DC power). The synergistic effect is the direct result of the added effect of the direct absorption of photons by the composite semiconductor leading to photocatalytic oxidation.

Acknowledgments We are grateful to the Bill and Melinda Gates Foundation for support of our solar toilet project under the Reinventing the Toilet Project, Grant: OPP1037491 "Development of a Self-Contained, PV-Powered Domestic Toilet and Wastewater Treatment System."

References

Ahmad GE, El Shenawy ET (2006) Optimized photovoltiac system for hydrogen production. Renew Energ 31:1043–1054

Anglada A, Urtiaga A, et al (2009) Contributions of electrochemical oxidation to waste-water treatment: fundamentals and review of applications. J Chem Technol Biotechnol. doi:10.1002/jctb.2214

Bonfatti F, Ferro S et al (2000) Electrochemical incineration of glucose as a model organic substrate—II. Role of active chlorine mediation. J Electrochem Soc 147:592–596

Cabeza A, Urtiaga AM et al (2007) Electrochemical treatment of landfill leachates using a boron-doped diamond anode. Ind Eng Chem Res 46:1439–1446

Chen GH (2004) Electrochemical technologies in wastewater treatment. Sep Purif Technol 38:11–41

Comninellis C, Nerini A (1995) Anodic-oxidation of phenol in the presence of NaCl for waste-water treatment. J Appl Electrochem 25:23–28

Comninellis C, Pulgarin C (1991) Anodic-oxidation of phenol for waste-water treatment. J Appl Electrochem 21:703–708

DOE (2008) International energy outlook 2006; DOE/EIA = 0484(2008). Energy Information Administration

Gibson TL, Kelly NA (2008) Optimization of solar powered hydrogen production using photovoltaic electrolysis devices. Int J Hydrogen Energy 33:5931–5940

Hollmuller P, Joubert JM et al (2000) Evaluation of a 5 kW(P) photovoltaic hydrogen production and storage installation for a residential home in Switzerland. Int J Hydrogen Energy 25:97–109

Iniesta J, Michaud PA et al (2001) Electrochemical oxidation of phenol at boron-doped diamond electrode. Electrochim Acta 46:3573–3578

Jiang JY, Chang M et al (2008) Simultaneous hydrogen production and electrochemical oxidation of organics using boron-doped diamond electrodes. Environ Sci Technol 42:3059–3063

Juttner K, Galla U et al (2000) Electrochemical approaches to environmental problems in the process industry. Electrochim Acta 45:2575–2594

Kraft A (2007) Doped diamond: a compact review on a new, versatile electrode material. Int J Electrochem Sci 2:355–385

Lehman PA, Chamberlin CE et al (1997) Operating experience with a photovoltaic-hydrogen energy system. Int J Hydrogen Energy 22:465–470

Montanaro D, Petrucci E (2009) Electrochemical treatment of Remazol Brilliant Blue on a boron-doped diamond electrode. Chem Eng J 153:138–144

Montanaro D, Petrucci E et al (2008) Anodic, cathodic and combined treatments for the electrochemical oxidation of an effluent from the flame retardant industry. J Appl Electrochem 38:947–954

Murugananthan M, Yoshihara S et al (2007) Electrochemical degradation of 17 beta-estradiol (E2) at boron-doped diamond (Si/BDD) thin film electrode. Electrochim Acta 52:3242–3249

Panizza M, Barbucci A et al (2007) Electrochemical degradation of methylene blue. Sep Purif Technol 54:382–387

Park H, Vecitis CD et al (2008a) Solar-powered production of molecular hydrogen from water. J Phys Chem C 112:885–889

Park H, Vecitis CD et al (2008b) Solar-powered electrochemical oxidation of organic compounds coupled with the cathodic production of molecular hydrogen. J Phys Chem A 112:7616–7626

Park H, Vecitis CD et al (2009) Electrochemical water splitting coupled with organic compound oxidation: the role of active chlorine species. J Phys Chem C 113:7935–7945

Petrucci E, Montanaro D (2011) Anodic oxidation of a simulated effluent containing Reactive Blue 19 on a boron-doped diamond electrode. Chem Eng J 174:612–618

Shen ZM, Yang J et al (2005) Dual electrodes oxidation of dye wastewater with gas diffusion cathode. Environ Sci Technol 39:1819–1826

Srinivasan S (2006) Fuel cells: from fundamentals to applications. Springer, New York

Urtiaga A, Rueda A et al (2009) Integrated treatment of landfill leachates including electrooxidation at pilot plant scale. J Hazard Mater 166:1530–1534

Vaghela SS, Jethva AD et al (2005) Laboratory studies of electrochemical treatment of industrial azo dye effluent. Environ Sci Technol 39:2848–2855

Vlyssides AG, Karlis PK et al (2002) Electrochemical treatment in relation to pH of domestic wastewater using Ti/Pt electrodes. J Hazard Mater 95:215–226

Weres O (2009) Electrode with surface comprising oxides of titanium and bismuth and water purification process using this electrode, US 7494583 B2

DOI 10.1007/978-3-319-05041-6_19
Reprinted from the *Journal of Nanoparticle Research*, DOI 10.1007/s11051-013-1781-4

RESEARCH PAPER

Preparation of proton conducting membranes containing bifunctional titania nanoparticles

Ayşe Aslan · Ayhan Bozkurt

Received: 22 February 2013 / Accepted: 5 June 2013 / Published online: 16 June 2013

Abstract Throughout this work, the synthesis and characterization of novel proton conducting nanocomposite membranes including binary and ternary mixtures of sulfated nano-titania (TS), poly(vinyl alcohol) (PVA), and nitrilotri(methyl phosphonic acid) (NMPA) are discussed. The materials were produced by means of two different approaches where in the first, PVA and TS (10–15 nm) were admixed to form a binary system. The second method was the ternary nanocomposite membranes including PVA/TS/NMPA that were prepared at several compositions to get PVA–TS–$(NMPA)_x$. The interaction of functional nano particles and NMPA in the host matrix was explored by FT-IR spectroscopy. The homogeneous distribution of bifunctional nanoparticles in the membrane was confirmed by SEM micrographs. The spectroscopic measurements and water/methanol uptake studies suggested a complexation between PVA and NMPA, which inhibited the leaching of the latter. The thermogravimetry analysis results verified that the presence of TS in the composite membranes suppressed the formation of phosphonic acid anhydrides up to 150 °C. The maximum proton conductivity has been measured for PVA–TS–$(NMPA)_3$ as 0.003 S cm^{-1} at 150 °C.

Keywords Nanocomposites · Functional nanoparticles · PEMFC membrane · TGA · DSC · Proton conductivity

Special Issue Editors: Mamadou Diallo, Neil Fromer, Myung S. Jhon

This article is part of the Topical Collection on Nanotechnology for Sustainable Development

A. Aslan (✉) · A. Bozkurt
Department of Chemistry, Fatih University, 34500 Büyükçekmece-Istanbul, Turkey
e-mail: ayseaslan44@gmail.com

A. Bozkurt
e-mail: bozkurt@fatih.edu.tr

Introduction

Polymer composite membranes containing inorganic moieties have attracted great attention because of their dual nature stemming from the flexibility of the organic polymer backbone, and the thermal and chemical stability of the inorganic additive (Celik et al. 2012; Gray 1997; Babir and Gomez 1996; Aslan et al. 2009).

The inorganic additive, TiO_2, is believed to be the most promising material at present due to its powerful oxidation strength, high photostability, and nontoxicity (Chen et al. 2007; Carbone et al. 2008). However, upon embedding TiO_2 into polymer matrices, proton conductivity usually decreases with an increase in filler content due to the rather low proton conductivity of the fillers themselves and their considerable dilution effect on the proton-exchange groups in the original polymer matrix. To overcome this problem, modified nanoparticles possessing different functional groups

were employed. Bifunctional nanoparticles, having been embedded into polymers, play a role in the construction of novel nanocomposite membranes with enhanced proton conductivities (Wang et al. 2002; Munakata et al. 2005; Nogami et al. 2000). In the previous work, we proved that the presence of acidic functional units enhanced the proton conductivity of polymer membranes, and according to the XRD results, the size of sulfated titania nanoparticles was 10–15 nm (Aslan and Bozkurt 2012, 2013).

Poly(vinyl alcohol) (PVA), one of the most commonly used matrices, has extensively been investigated with different kinds of nanofillers (Godovsky 2000; Qian et al. 2001; Kumar et al. 2001). These studies showed that the introduction of nanosized particles into PVA altered its physicochemical properties. For example, incorporation of magnetite nanoparticles, synthesized by a sonochemical method, into PVA (Baglio et al. 2005) was found to reduce the glass transition temperature of PVA by 15 °C and the thermal stability by 28 °C. However, in the presence of montmorillonite (MMT) nanofiller, glass transition increased by 25 °C and the thermal degradation was unaffected up to 50 % of initial weight loss (Strawhecker and Manias 2000; Yu et al. 2003; Schaffer and Windle 1999). More recently, PVA-based nanocomposites have been developed to improve the properties of the polymer for use in a variety of applications (Nakane et al. 1999; Lin et al. 2003; Ione et al. 2001).

In addition, inclusion of TiO_2 filler into PVA matrix has effectively reduced the swelling ratio of the composite polymer membrane (Yang and Lin 2002; Yang 2007; Venckatesh et al. 2012; Tuncer et al. 2007). Furthermore, Yang (Gasa et al. 2006; Boroglu et al. 2011) synthesized a crosslinked PVA composite polymer membrane to be applied in alkaline DMFCs. Their results showed that the morphological properties of the filler played a major role in the performance of the composite membranes at higher operating temperatures.

Recently, proton conducting membranes including functional nano-titania have been reported (Smitha et al. 2004; Zhou et al. 2010). High concentration of phosphonic acid groups, which were bonded by oxygen bridges with acid-modified nano-titania, increased the proton conductivity and thermal stability of the nanocomposite membranes.

In this paper, we report on the preparation and characterization of novel proton conducting super acid nanocomposite polymer membranes. Sulfated nano-titania (TS) was synthesized by hydrolysis and precipitation of titanyl sulfate. Several binary system membranes were produced on the basis of a complexation reaction between PVA and TS. Ternary systems with a variety of compositions were also prepared by mixing TS, PVA, and NMPA (Fig. 1). Physicochemical properties of the composite membranes were investigated using instrumental techniques.

Experimental

Materials and preparation

The solvents, methanol (Sigma-Aldrich), and dimethylformamide (DMF; Merck) were used as received.

Sulfated nano-titania was produced according to a previously reported procedure (Aslan and Bozkurt 2012). Firstly, 5 g of titanyl sulfate ($TiOSO_4 \cdot nH_2O$, $n = 1$–2) was dissolved in 200 mL of water and stirred for about 50 min. The solution temperature was slowly increased up to 70 °C, and the white precipitate was collected by suction filtration and washed several times with distilled water. The obtained powder was carefully dried and stored in a glove box. In the powder sample, the amount of sulfate groups was calculated by acid–base titration, which was about 1×10^{-3} mol/g.

Binary and ternary proton-conductive polymer nanocomposite membranes were produced using two different procedures. According to previous studies, at higher

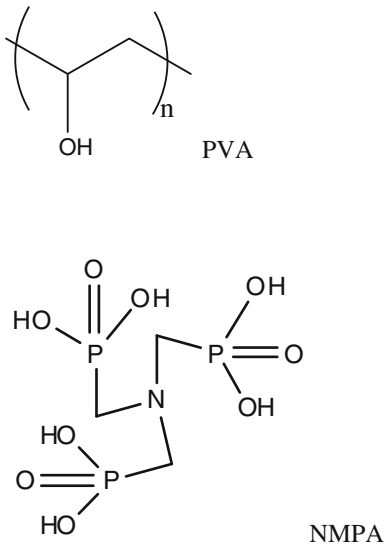

Fig. 1 Structure of PVA and NMPA

contents (10–20 %) of additive materials (TS), the proton conductivity decreased because of their blocking effect as well as interactions between host–guest systems and additive materials. The former membranes were prepared by mechanical mixing of TS (5 % (w/w)) and PVA in DMF, while the latter ones were obtained by addition of the dopant nitrilotri(methyl triphosphonic acid) (NMPA) into PVA/TS system at several stoichiometric ratios. The homogeneous solutions were stirred overnight at ambient temperature. The membranes were prepared by casting of the solution on a polished poly(tetrafluoro ethylene), and the solvent was slowly evaporated at 80 °C for 24 h. To ensure complete solvent removal, the membranes were placed under vacuum at 80 °C for 48 h. Homogeneous and yellowish free-standing films were obtained.

Characterizations

The FTIR spectra of the samples were obtained on a Bruker Alpha-P ATR spectrometer in the range 4,000–400 cm^{-1}, with 4 cm^{-1} resolution.

The surface morphology of blend membranes was investigated by scanning electron microscopy (SEM, Philips XL30S-FEG). All the samples were sputtered with gold for 150 s before SEM measurements.

Thermal stabilities of the complex polymer electrolytes were examined by thermogravimetry analysis (TGA) with a Perkin Elmer STA 6000. The samples ($\sim$10 mg) were heated from room temperature to 700 °C under N_2 atmosphere at a heating rate of 10 °C min^{-1}.

Differential scanning calorimetry (DSC) data were derived using Perkin Elmer JADE DSC instrument. The measurements were done at a rate of 10 °C min^{-1} under a nitrogen flow.

Water uptake (WU) values were determined by the weight difference between the fully hydrated membranes and the dried ones. The dried membranes (W_{dry}) were weighed and then wetted until the weight remained constant. The wet or saturated weights of the membranes (Wwet) were measured quickly after removing or wiping out any remaining surface water with a piece of tissue paper. The WU was calculated according to the formula (1):

$$\text{Water uptake (WU)} = \frac{W_{wet} - W_{dry}}{W_{dry}} \times 100\,\%, \qquad (1)$$

The alternating current (ac) conductivity studies of the samples were performed using a Novocontrol dielectric impedance analyzer. The samples were sandwiched between platinum-blocking electrodes, and the conductivities were measured in the frequency range from 0.1 Hz to 3 MHz at 10 °C intervals.

Results and discussions

Characterizations

Figure 2 shows the FT-IR spectra of PVA–TS and TS. FT-IR spectrum of sulfated titania PVA showed a very strong and broad peak centered at 3,300 cm^{-1} attributed to the hydroxyl (–OH) group and a peak at 2,900 cm^{-1} that correspond to the CH_2 asymmetric stretching (Daniliuc et al. 1992). FT-IR spectra of TS showed characteristic peaks around 1,650 cm^{-1} and at 980–1,250 cm^{-1}. The peaks at 980–1,250 cm^{-1} were attributed to bidentate sulfate coordination on the titania surface (980–990, 1,040, 1,130–1,150, and 1,210–1,230 cm^{-1}). The S=O vibration at 1,393 cm^{-1} can be clearly observed from the sample TS (Sakai et al. 2010; Jiang et al. 2003; Arata and Hino 1990; Navarrete et al. 1996; Celik et al. 2008).

Figure 3 is the FT-IR of the ternary system where the peak at 1,150 cm^{-1} corresponds to P=O stretching of NMPA. As can be seen in the PVA–TS–NMPA spectrum, the weak peak between 910 and 1,100 can be attributed to the P–O–Ti and P–O stretching vibrations.

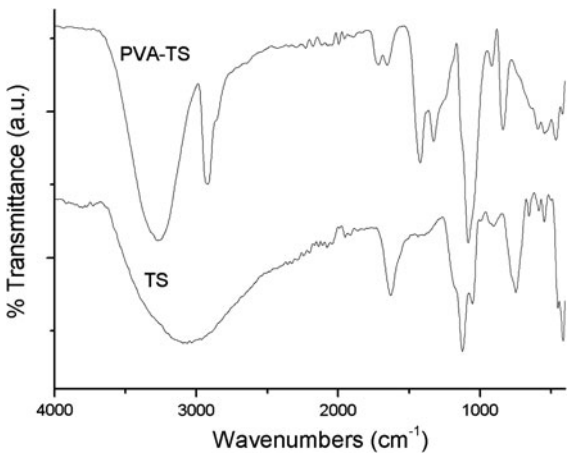

Fig. 2 FT-IR spectra of the PVA–TS and sulfated titania composite membranes

The bands at 1,330 and 1,427 cm^{-1} can be attributed to the weak phosphoryl (PO) frequency and P–C stretching vibrations, respectively (Zhou et al. 2010). It could be deduced from these results that NMPA had replaced the original bidentate position of SO_3H and formed chemical bonds with the Ti atom at the titania surface via phosphonate groups. NMPA shows strong bands at 950 cm^{-1} that belong to asymmetric stretching vibrations of the P–OH group, at 1,150 cm^{-1} that corresponds to P=O stretching, and a weak peak around 3,500 cm^{-1} was attributed to O–H stretching (Chen et al. 2007). The characteristic peaks of TS at 980–990, 1,040, 1,130–1,150, and 1,210–1,230 cm^{-1} are overlapped with the corresponding peaks of phosphonic acid units of host matrix and became more intense. Between 3,500 and 2,000 cm^{-1}, a broadening of the band can be related to hydrogen-bonding network formation. Within 1,500–800 cm^{-1} region, the peaks near 1,150 and 960 cm^{-1} are attributed to characteristic absorptions in the formation of anion NMPA as a consequence of SO_3H interaction (Ma et al. 2008). These results confirm successful embedding of bifunctional nano-titania in the PVA host matrix.

Morphology

The micro-topography of PVA–TS and PVA–TS–NMPA composite membranes was studied by SEM as shown in Fig. 4. In Fig. 4a, it was observed that TS were homogenously dispersed and embedded in the PVA matrix.

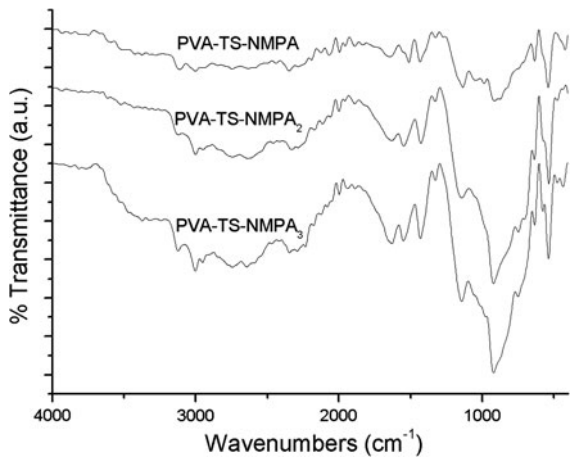

Fig. 3 FT-IR spectra of the PVA–TS–NMPA composite membranes

The SEM micrograph indicates that there was no obvious agglomeration of TS nanoparticles. In comparison with the pure PVA (Peng et al. 2005), the surface of the PVA–TS–NMPA nanocomposite was smoother (Fig. 4b). Additionally, due to strong interactions between sulfonic acid groups of sulfated titania and phosphonic acid units of NMPA, no phase separation was observed during solvent evaporation. Although micro-domain formation regarding PVA–TS–NMPA complex might have been expected in the final dry membrane, such domains did not appear in the SEM micrographs. Figure 4b indicates a very good compatibility between PVA and NMPA. Consequently, the micrographs showed that homogeneous films were successfully produced.

Thermal analysis

Table 1 lists the glass transition temperatures of the PVA–TS–$NMPA_x$ composite membranes. PVA exhibits a glass transition located at around 72 °C (Peng et al. 2005). In the presence of TS, the T_g of PVA shifts to 150 °C which indicated that TS prevented segmental motion of the PVA. The membrane materials PVA–TS–NMPA, PVA–TS–$NMPA_2$, and PVA–TS–$NMPA_3$ have definite obvious glass transition temperatures of 118, 100, and 92 °C, respectively. Clearly, the results indicated that the glass transition temperatures of the samples shift to lower temperatures as the quantity of NMPA increases. This behavior can be described by the softening effect of NMPA.

Figure 5 shows the thermogravimetry (TG) results of the composite membranes recorded under N_2 atmosphere. The TG graphs show an elusive weight loss up to 150 °C, which can be attributed to anhydride formation (Park et al. 2005). It is clear that the dried polymers are thermally stable up to approximately 250 °C, after which, they decompose. The PVA–TS thermograms indicated that the sulfated titania nanoparticles enhanced the thermal stability of the composite membranes. The degradation temperature of PVA–TS–NMPA nanocomposite polymer membranes is approximately 200 °C, i.e., slightly lower than that of PVA–TS.

Water uptake

The WU of the membranes is a major parameter influencing proton conductivity, mechanical property,

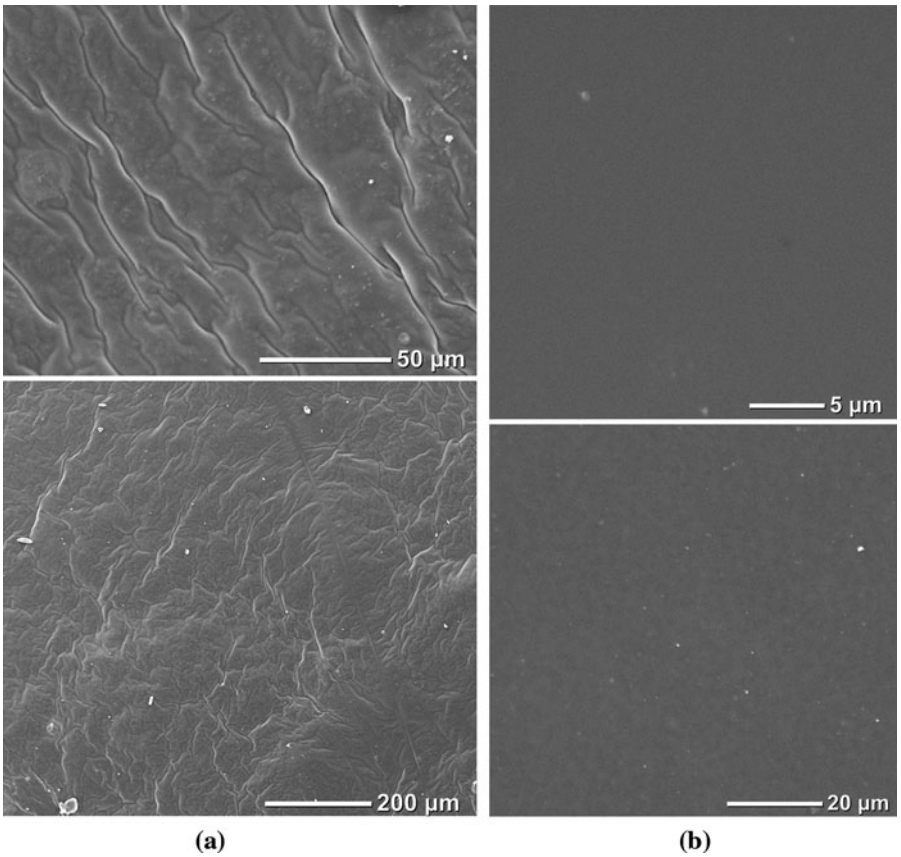

Fig. 4 SEM micrographs of the surface of composite membranes. **a** PVA–TS, **b** PVA–TS–NMPA

Table 1 Maximum proton conductivity and T_g (°C) values for all the membranes

Sample name	Molar Ratio (PVA/NMPA)	T_g (°C)	Maximum proton conductivity (S cm^{-1})
PVA–TS	–	151	2×10^{-6} at 150 °C
PVA–TS–NMPA	1:1	118	8.5×10^{-6} at 150 °C
PVA–TS–$NMPA_2$	1:2	100	3.1×10^{-4} at 150 °C
PVA–TS–$NMPA_3$	1:3	92	0.003 at 150 °C

and stability. WUs of the PVA–TS–NMPA samples are shown in Fig. 6. As can be seen, WU decrease with increasing NMPA content. The sample PVA–TS has the highest WU value (70 %). This result showed that the decreasing swelling character with NMPA content enhanced the mechanical strength, and almost no NMPA dissolved in the solution. The result indicated that the complexation of PVA–TS with NMPA prevented the loss of guest polymer (PVA) to the solution.

Conductivity measurement

Alternating current conductivities, σ_{ac} (ω) of the polymers, were studied at various temperatures using an impedance analyzer. The frequency-dependent AC conductivities (σ_{ac} (ω)) were calculated using Eq. (2);

$$\sigma'(\omega) = \sigma_{ac}(\omega) = \sigma''(\omega)\omega\varepsilon_o \quad (2)$$

where $\sigma'(\omega)$ is the real part of conductivity, $\omega = 2\pi f$ is the angular frequency, ε_o is the vacuum permittivity, and ε'' is the imaginary part of complex dielectric permittivity (ε^*). The proton conductivities of PVA–TS and PVA–TS–NMPA anhydrous nanocomposite polymer electrolytes were measured between 20 and 150 °C. The AC conductivity of PVA–TS–$NMPA_2$ composite membrane is shown in Fig. 7. The graph

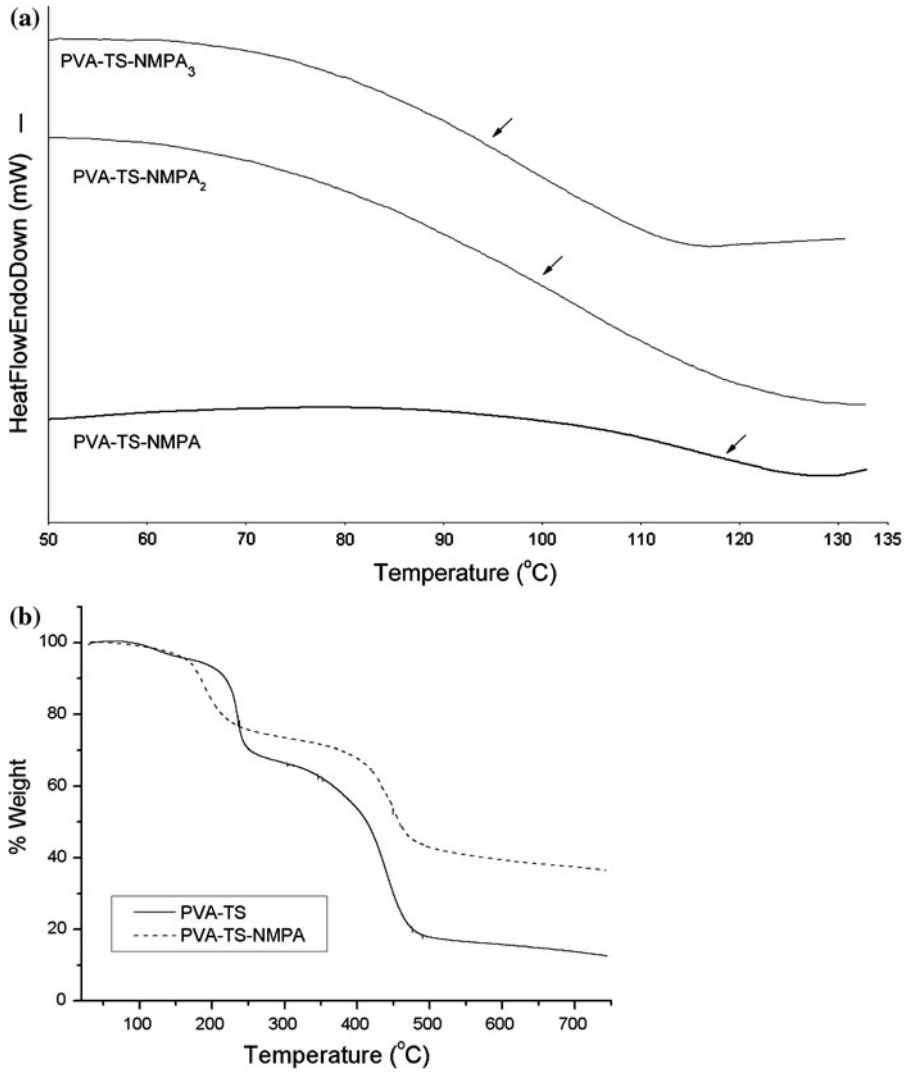

Fig. 5 Thermal analysis of the composite membranes. **a** DSC curves of PVA–TS–NMPA composite membranes under nitrogen atmosphere at a heating rate of 10 °C min^{-1}. **b** TG analysis of PVA–TS–NMPA composite membranes under nitrogen atmosphere at a heating rate of 10 °C min^{-1}

includes several regions which are typical for ion-conducting polymers. The irregularities between 80 and 150 °C at the low-frequency side correspond to polarization blocking the electrode–electrolyte interface, and the conductivity increase at high temperature and high frequencies results from the regular dispersion in polymer electrolytes (Acar et al. 2009). The DC conductivities of anhydrous samples were derived from the plateau regions which are compared in Fig. 8.

Clearly, the proton conductivity of PVA–TS system increases linearly (Arrhenius behavior) with increasing temperature. Max conductivity of PVA with 5 % TS is 2×10^{-6} at 150 °C.

Previously, it was reported that organophosphorylated titania and chitosan composite membranes exhibit an increased proton conductivity to an acceptable level of 0.01 S cm^{-1} (RH = 80 %) for DMFC (Zhou et al. 2010). These organophosphorylated titania nanoparticles enhanced the proton conductivity when they were dispersed in the membranes at low temperatures in humidified conditions. In this study, we combined the advantages of phosphonic acid units

and sulfonic acid units on the titania surface, which enhanced the proton diffusion under anhydrous conditions.

The conductivity isotherm of PVA–TS–NMPA composite membranes strongly depends on temperature as well as the ratio of NMPA. The proton conductivity of PVA–TS nanocomposite membrane is lower than that of composite membranes with NMPA. The DC conductivity illustrated that the NMPA content increases the conductivity for PVA–TS–NMPA composite membranes. The maximum proton conductivity was measured for PVA–TS–$NMPA_3$ and found to be 0.003 (S cm^{-1}) at 150 °C, in the dry state. The material with $x = 3$ was considered to be the optimum composition for these series of composite membranes. Conductivity results showed that the NMPA composition is highly effective on the proton conductivity of the samples in the PVA–TS–NMPA systems.

In the current system, proton transfer can be facilitated by the additional phosphonic acid groups on NMPA. From the FT-IR of composite membranes

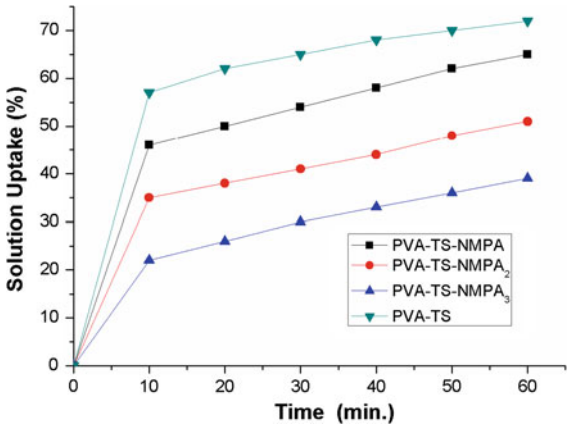

Fig. 6 Water/methanole uptake of PVA–TS–NMPA composite membranes

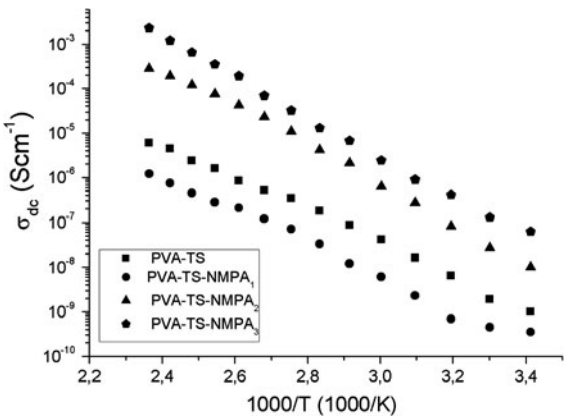

Fig. 8 DC conductivity measurements of PVA–TS–NMPA composite membranes versus reciprocal temperature

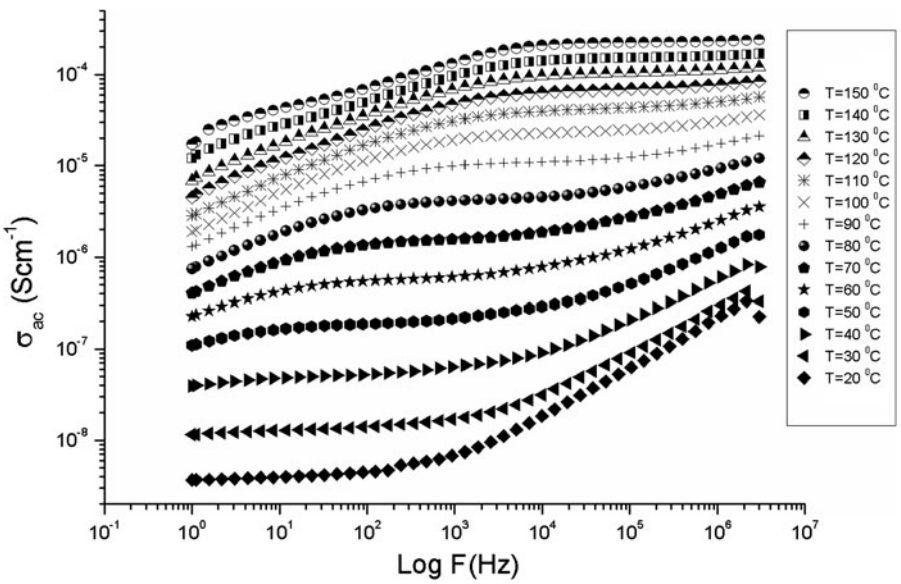

Fig. 7 AC conductivity of PVA–TS–$NMPA_2$ composite membranes

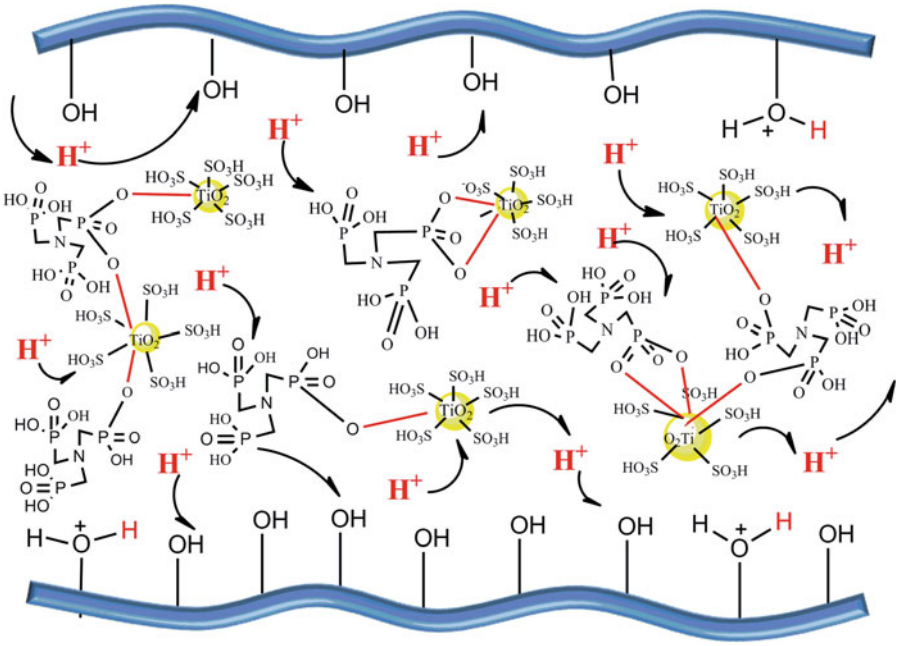

Fig. 9 Proton transport mechanism of the PVA–TS–NMPA composite membranes

as well as the conductivity data, it can be concluded that a Grotthuss mechanism (structural diffusion) is the possible pathway for the total proton diffusion. This continuous pathway may convey proton mobility over the –P-OH, and sulfonic acid groups may reduce the energy barrier for proton transport (Fig. 9). The protons could travel through the ionic functional groups (Salgado 2007; Smitha et al. 2004).

Conclusions

In the present work, composite membranes of PVA and bifunctional nano-titania were produced. FT-IR data confirmed the formation of super acid and the strong interaction between the modified inorganic nanoparticle and host polymer matrix. WU study showed that WU increased with decreasing NMPA content. The TGA results verified that the presence of TS in the composite membranes enhanced thermal stability up to approximately 250 °C. DSC results illustrated that the T_g of the materials shifted to lower temperatures with increasing NMPA content. In the anhydrous state, the proton conductivity of PVA–TS–NMPA was found to be 0.003 S cm^{-1} at 150 °C. In dried samples, the proton diffusion is expected to occur by the transport of the protons through phosphonic acid units up to a certain threshold composition of NMPA. The synthesized composite materials have ability to form free-standing films with improved mechanical strengths and, therefore, can be suggested for use in proton-exchange membrane fuel cell (PEMFC) applications.

Acknowledgments This work was supported by Fatih University Research Foundation under the contract number P50021005_G and partially supported by Turkish academy of sciences (TÜBA).

References

Acar O, Sen U, Bozkurt A (2009) Ata proton conducting membranes based on poly(2,5-benzimidazole) (ABPBI)–poly(vinylphosphonic acid) blends for fuel cells. Int J Hydrogen Energy 34:2724

Arata K, Hino M (1990) Mater Chem Phys 26:213–237

Aslan A, Bozkurt A (2012) Nanocomposite polymer electrolyte membranes based on poly (vinylphosphonic acid)/sulfated nano-titania. J Power Sources 217:158–163

Aslan A, Bozkurt A (2013) An investigation of proton conductivity of nanocomposite membranes based on sulfated nano-titania and polymer. Solid State Ionics 239:21–27

Aslan A, Ünal Ş, Ayhan B (2009) Preparation, properties, and characterization of polymer electrolyte membranes based on poly(1-vinyl-1,2,4 triazole) and poly(styrene sulfonic acid). J Electrochem Soc 156:B1112–B1116

Babir F, Gomez T (1996) Efficiency and economics of proton exchange membrane (PEM) fuel cells. Int J Hydrogen Energy 21:891–901

Baglio V, Aricò AS, Blasi AD, Antonucci V, Antonucci PL, Licoccia S (2005) Nafion–TiO_2 composite DMFC membranes: physico-chemical properties of the filler versus electrochemical performance. Electrochim Acta 50:1241–1246

Boroglu SM, Celik SU, Bozkurt A, Ismail B (2011) The synthesis and characterization of anhydrous proton conducting membranes based on sulfonated poly(vinyl alcohol) and imidazole. J Memb Sci 375:157–164

Carbone A, Sacca A, Gatto I, Pedicini R, Passalacqua E (2008) Investigation on composite S-PEEK/H-BETA MEAs for medium temperature PEFC. Int J Hydrogen Energy 33:3153–3158

Celik SU, Akbey U, Graf R, Bozkurt A, Spiess HW (2008) Anhydrous proton conducting properties of copolymer membranes: a combined study with MAS NMR. Phys Chem Chem Phys 10:6058–6066

Celik SÜ, Bozkurt A, Hosseini SS (2012) Alternatives toward proton conductive anhydrous membranes for fuel cells: heterocyclic protogenic solvents comprising polymer electrolytes. Prog Polym Sci 37:1265–1291

Chen SY, Han CC, Tsai CH, Huang J, Chen YW (2007) Effect of morphological properties of ionic liquid-templated mesoporous anatase TiO_2 on performance of PEMFC with Nafion/TiO_2 composite membrane at elevated temperature and low relative humidity. J Power Sources 171:363–372

Daniliuc L, Kesel CD, David C (1992) Intermolecular interactions in blends of poly(vinyl alcohol) with poly(acrylic acid) FTIR and DSC studies. Eur Polym J 28:1365–1371

Gasa JV, Boob S, Weiss RA, Shaw MT (2006) Proton-exchange membranes composed of slightly sulfonated poly(ether ketone ketone) and highly sulfonated crosslinked polystyrene particles. J Memb Sci 269:177–186

Godovsky DY (2000) Applications of polymer-nanocomposites. Adv Polym Sci 153:165–205

Gray FM (1997) Polymer electrolytes. Royal Society of Chemistry Monographs, Cambridge

Ione C, Daniel L, Angel A, Carmen M (2001) Dynamic mechanical and dielectrical properties of poly(vinyl alcohol) and poly(vinyl alcohol)-based nanocomposites. J Polym Sci Part B Polym Phys 39:1968–1975

Jiang XC, Herricks T, Xia YN (2003) One-dimensional nanostructures: synthesis, characterization, and applications. Adv Mater 15:1205–1209

Kumar RV, Elgamiel R, Diamant Y, Gedanken A (2001) Sonochemical preparation and characterization of nanocrystalline copper oxide embedded in poly(vinyl alcohol) and its effect on crystal growth of copper oxide. Langmuir 17:1406–1410

Lin H, Watanabe Y, Kimura M (2003) Preparation of magnetic poly (vinyl alcohol) (PVA) materials by in situ synthesis of magnetite in a PVA matrix. J Appl Polym Sci 87:1239–1247

Ma TY, Zhang XJ, Shao GS, Cao JL, Yuan ZY (2008) Ordered macroporous titanium phosphonate materials: synthesis, photocatalytic activity, and heavy metal ion adsorption. J Phys Chem C 112:3090–3096

Munakata H, Chiba H, Kanamura K (2005) Enhancement on proton conductivity of inorganic–organic composite electrolyte membrane by addition of sulfonic acid group. Solid State Ionics 176:2445

Nakane K, Yamashita T, Iwakuka K, Suzuki F (1999) Thermal properties and morphology of a poly(vinyl alcohol)/silica nanocomposite prepared with a self-assembled monolayer technique. J Appl Polym Sci 74:133

Navarrete J, Lopez T, Gomez R (1996) Surface acidity of sulfated TiO_2-SiO_2 Sol-Gels. Langmuir 12:4385–4390

Nogami M, Matsushita H, Goto Y, Kasuga T (2000) A sol–gel-derived glass as a fuel cell electrolyte. Adv Mater 12:1370–1372

Park HB, Shin HS, Lee YM, Rhim JW (2005) Annealing effect of sulfonated polysulfone ionomer membranes on proton conductivity and methanol transport. J Memb Sci 247:103

Peng Z, Kong LX, Li SD (2005) Thermal properties and morphology of a poly(vinyl alcohol)/silica nanocomposite prepared with a self-assembled monolayer technique. J Appl Polym Sci 96:1436–1442

Qian XF, Yin J, Huang JC, Yang YF, Guo XX, Zhu ZK (2001) The preparation and characterization of PVA/Ag_2S nanocomposite. Mater Chem Phys 68:95–97

Sakai T, Kajitani S, Kim S, Hamagami J, Oda H, Matsuka M, Matsumoto H, Ishihara T (2010) Proton conduction properties of hydrous sulfated nano-titania synthesized by hydrolysis of titanyl sulfate. Solid State Ionics 181:1746–1749

Salgado JR (2007) Study of basic biopolymer as proton membrane for fuel cell systems. Electrochim Acta 52:3766–3778

Schaffer MSP, Windle AH (1999) Fabrication and characterization of carbon nanotube/poly(vinyl alcohol) composites. Adv Mater 11:937–941

Smitha B, Sridhar S, Khan AA (2004) Polyelectrolyte complexes of chitosan and poly(acrylic acid) as proton exchange membranes for fuel cells. Macromolecules 37:2233–2239

Strawhecker KE, Manias E (2000) Structure and properties of poly(vinyl alcohol)/Na^+ montmorillonite nanocomposites. Chem Mater 12:2943–2949

Tuncer E, Sauers I, James DR, Ellis AR, Paranthaman MP, Goyal A, More KL (2007) Enhancement of dielectric strength in nanocomposites. Nanotechnology 18:32–39

Venckatesh R, Balachandaran K, Sivaraj R (2012) Synthesis and characterization of nano TiO_2–SiO_2: PVA composite-a novel route. Int Nano Lett 2:15–20

Wang H, Holmberg BA, Huang L, Wang Z, Mitra A, Norbeck JM, Yan Y (2002) Nafion-bifunctional silica composite proton conductive membranes. J Mater Chem 12:834–837

Yang CC (2007) Synthesis and characterization of the cross-linked PVA/TiO_2 composite polymer membrane for alkaline DMFC. J Memb Sci 288:51–60

Yang CC, Lin SJ (2002) Preparation of composite alkaline polymer electrolyte. Mater Lett 57:873–881

Yu YH, Lin CY, Yeh JM, Lin WH (2003) Preparation and properties of poly(vinyl alcohol)–clay nanocomposite materials. Polymer 44:3553–3560

Zhou WW, Wang Y, Xiao L, Jiang Z (2010) Preparation and properties of hybrid direct methanol fuel cell membranes by embedding organophosphorylated titania submicrospheres into a chitosan polymer matrix. J Power Sources 195:4104–4113

DOI 10.1007/978-3-319-05041-6_20
Reprinted from the *Journal of Nanoparticle Research*, DOI 10.1007/s11051-012-0853-1

RESEARCH PAPER

Nanotechnology convergence and modeling paradigm of sustainable energy system using polymer electrolyte membrane fuel cell as a benchmark example

Pil Seung Chung · Dae Sup So · Lorenz T. Biegler · Myung S. Jhon

Received: 10 January 2012 / Accepted: 29 March 2012 / Published online: 3 July 2012

Abstract Developments in nanotechnology have led to innovative progress and converging technologies in engineering and science. These demand novel methodologies that enable efficient communications from the nanoscale all the way to decision-making criteria for actual production systems. In this paper, we discuss the convergence of nanotechnology and novel multi-scale modeling paradigms by using the fuel cell system as a benchmark example. This approach includes complex multi-phenomena at different time and length scales along with the introduction of an optimization framework for application-driven nanotechnology research trends. The modeling paradigm introduced here covers the novel holistic integration from atomistic/molecular phenomena to meso/continuum scales. System optimization is also discussed with respect to the reduced order parameters for a coarse-graining procedure in multi-scale model integration as well as system design. The development of a hierarchical multi-scale paradigm consolidates the theoretical analysis and enables large-scale decision-making of process level design, based on first-principles, and therefore promotes the convergence of nanotechnology to sustainable energy technologies.

Keywords Nanotechnology convergence · Sustainable energy · Membrane · Fuel cell · Multi-scale modeling

Special Issue Editors: Mamadou Diallo, Neil Fromer, Myung S. Jhon

This article is part of the Topical Collection on Nanotechnology for Sustainable Development

P. S. Chung · D. S. So · L. T. Biegler · M. S. Jhon (✉)
Department of Chemical Engineering, Carnegie Mellon University, Pittsburgh, PA, USA
e-mail: mj3a@andrew.cmu.edu

D. S. So
National Nanotechnology Policy Center, Korea Institute of Science and Technology Information, Seoul 130-741, Korea

M. S. Jhon
School of Advanced Materials Science and Engineering, Sungkyunkwan University, Suwon 440-746, Korea

Introduction

Over the past decade, demands for sustainability have rapidly increased and become a major global challenge (Serrano et al. 2009). Compared with conventional energy resources that include fossil energy, sustainable energy sources are one of the most promising alternatives; they offer higher efficiency, reliable operation, and instantaneous rechargeable capabilities, as well as significant environmental sustainability with near-zero green house emission during the energy production/conversion processes. The tremendous progress in nanotechnology has provided an understanding of nanoscale physics in order to control system properties and find new materials and technologies applicable to novel energy

systems. These advances include high-porosity nanostructured materials for energy conversion/storage and nanocomposite membranes and sorbents for resource purification. Moreover, various analytic approaches, which span multiple time and length scales, have been developed to satisfy the demand for tuning physical properties, chemical structures, and functionalities of new materials within specific time and length scales. As nanotechnology research evolves toward application-driven fundamental investigations, the key technical goal is convergence of novel nanotechnologies and development of frameworks that lead to optimization and scale-up for a variety of applications (Roco et al. 2011). Therefore, advances in nano-analysis direct us to the critical issue of the multi-scale interactions that are often described via a hierarchy of scale-specific models. In this paper, we present a multi-scale modeling strategy that integrates complex engineering systems over a broad range of time and length scales. This enables atomistic synthesis of materials as well as optimization of converging technologies, as demonstrated via the fuel cell system.

Commercialization of fuel cell systems has increased rapidly, with an expected market share of over 30 % of sustainable energy production in 2020. While fuel cells range from power sources for portable electronic devices to power plant applications, this technology still requires a major breakthrough for broader commercialization. Novel nanoparticle research enables replacement of conventional platinum catalyst and nano tailoring for electrolyte and porous materials. Consequently, it allows a number of existing nanotechnologies to converge to overcome technological barriers. Most components of the fuel cell system comprise multi-phenomena at different time and length scales; these often can be described through a hierarchy of scale-specific models. Moreover, scale-specific models use specific numerical techniques to solve the governing equations. To achieve cutting-edge technology that satisfies stringent design and performance requirements, it is necessary to use holistic multi-scale integration models, as these insure that knowledge generated at one scale is transmitted to the others. Here, we develop a multi-scale modeling method with an optimization framework for nanotechnology convergence in a hydrogen polymer electrolyte membrane fuel cell (PEMFC) (Fig. 1). It should be noted that other fuel cells, including solid oxide fuel cells, can also be described through a similar mathematical framework. The modeling paradigm based on this PEMFC benchmark includes atomistic/molecular phenomena as well as meso/continuum scale integration with system optimization, which have barely been investigated

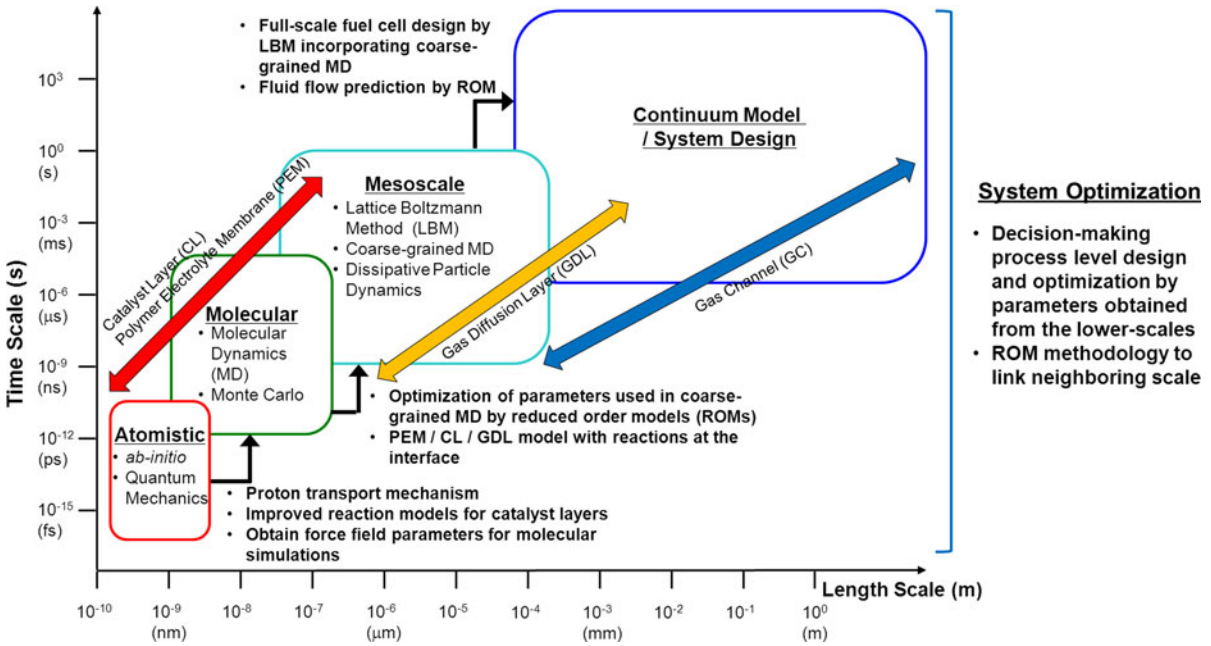

Fig. 1 Strategy and framework for multi-scale approach on PEMFC with system optimization

(Goddard et al. 2006). The development of our hierarchical multi-scale paradigm consolidates the theoretical analysis and enables large-scale decision-making for the process level design, and therefore promotes nanotechnology convergence with fuel cell technology.

Nanotechnology in sustainable PEMFC

As the need for renewable energy systems increases, fuel cells have attracted considerable attention as a potential replacement for the massive power generation and portable systems for home/office/transportation. Since the PEMFC consists of nanoscale subsystems with multi-physics, an accurate system model is needed to design PEMFC with optimal performance. Therefore, fundamental understanding of electrochemistry, materials, and heat and mass transport phenomena is critical to develop accurate models that lead to high performance and reliability for fuel cells. The hydrogen PEMFC, which directly converts chemical energy into electrical energy, will be used in future green car technology in parallel with plug-in and hybrid electric vehicles. The hydrogen PEMFC device comprises a hydrogen source and a gas compressor supplying air in a stack, which consists of multiple PEMFCs connected in series. An individual PEMFC (Fig. 2a) comprises two gas channels (GCs), two gas diffusion layers (GDLs), and two catalyst layers (CLs) each on the anode and cathode sides, as well as a central polymer electrolyte membrane (PEM). The GCs are bipolar plates that are hollow chambers for fluid inlet and outlet. They also serve as a connection between adjacent cells. The GDLs are porous materials which support the CL, provide uniform distribution of gases, and act as a medium for electron transport from the CL (where the electrochemical reactions typically occur with a platinum (Pt) catalyst) to the external current collectors. The PEM acts as a proton transport passage from anode to the cathode, and the conductivity of the PEM is a strong function of its water uptake. Humidified hydrogen and air are fed to the anode and cathode inlets, respectively.

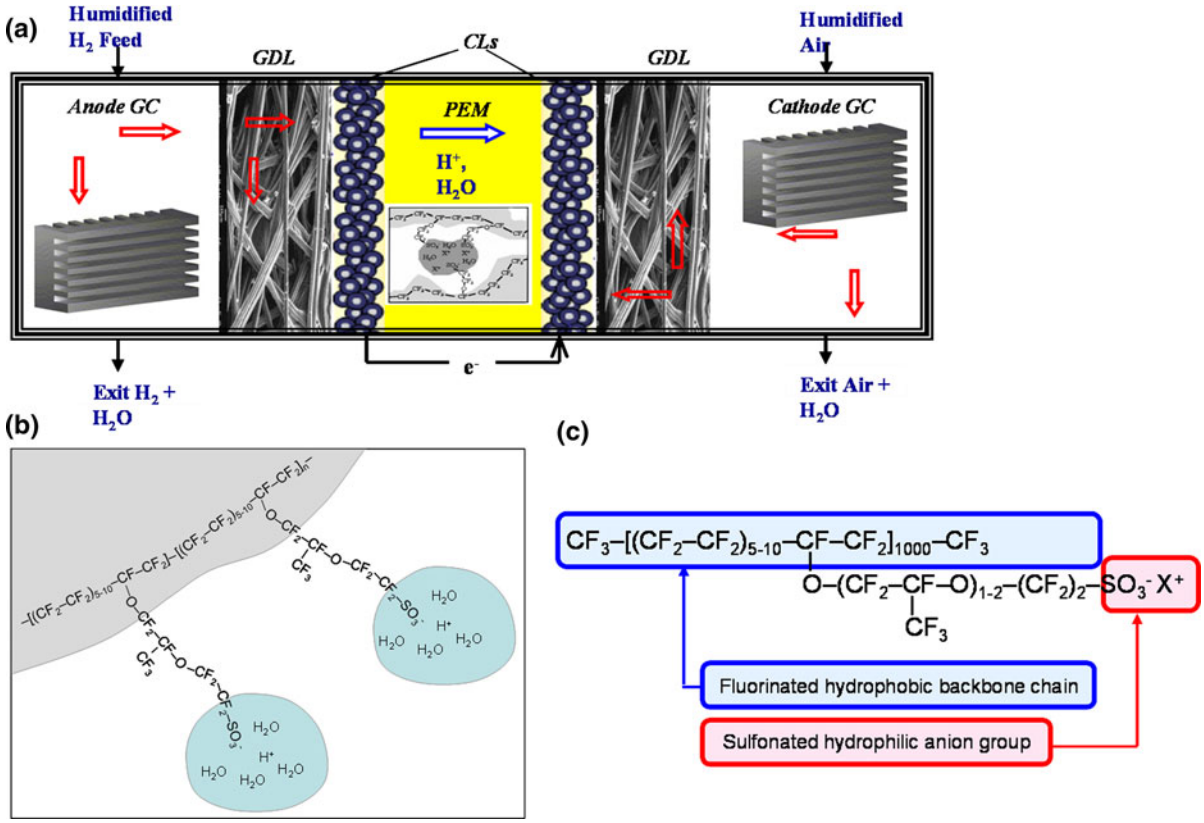

Fig. 2 **a** Components of a single stack hydrogen PEMFC. **b** PEM structure with Nafion®, and **c** chemical structure of Nafion®

The species undergo transport processes in both the GCs and the porous GDLs, after which they reach the anode/cathode CLs. Within the CLs, hydrogen and oxygen undergo electrochemical reactions, and the water molecules are transported across the PEM from anode to the cathode. The protons released in the oxidation reaction at the anode are transported across the PEM, and electrons released reach the cathode via an external circuit. On reaching the cathode the protons and electrons combine with the oxygen in the reduction reaction to generate water as the product. The direct methanol fuel cell (DMFC) is another type of PEMFC, which uses a solution of methanol and water as a fuel instead of humidified hydrogen gas. Compared to hydrogen fuel cells, DMFCs are advantageous for their ease of fuel delivery and storage, lack of humidification requirement, and reduced design complexity. Owing to the absence of ancillary equipment (i.e., fuel reformer), the DMFC is ideally suited for portable electronic devices such as laptops or mobile phones (Mench et al. 2004).

A PEM is a semipermeable membrane generally made from ionomers and designed to conduct protons while being impermeable to gases such as oxygen or hydrogen. This is their essential function for a PEM fuel cell: separation of reactants and transport of protons. One of the most commonly and commercially available PEM materials is Nafion® (Fig. 2b, c), which is produced by DuPont. While Nafion is an ionomer with a perfluorinated backbone like Teflon, there are many other structural motifs used to make ionomers for PEMs. Many use polyaromatic polymers while others use partially fluorinated polymers. Nafion® has received a considerable amount of attention as a proton conductor for PEM fuel cells because of its excellent thermal and mechanical stability. The chemical basis of Nafion®'s superior conductive properties remains a focus of research. As far as reported, protons on the $SO_3^-H^+$ (sulfonic acid) groups hop from one acid site to another. This membrane structure allows movement of cations but the membranes do not conduct anions or electrons. Nafion® can be manufactured with various cationic conductivities. To function, the membrane must conduct hydrogen ions (protons) but not electrons, as this would in effect "short circuit" of the fuel cell. The membrane must also not allow gas to pass to the other side of the cell, a problem known as fuel crossover (Baxter et al. 1999; Dohle et al. 2000, Ren et al. 2000), and must be resistant to the reducing environment at the anode and the harsh oxidative environment at the cathode. Although the PEMFC is a prime energy source candidate for small-scale applications, water management is critical to performance, as power output requires optimized water uptake in the membrane. Water management is a very difficult subject in PEM systems; several water management solutions exist, including integration of electro-osmotic pumps. Furthermore, the Pt catalyst on the membrane is easily poisoned by carbon monoxide (less than one part per million is usually acceptable) and the membrane is sensitive to materials like metal ions, which can be introduced by corrosion of metallic bipolar plates. The commercial viability of this device is currently hampered due to its high cost, power density, and low durability.

Since characteristics of sub-components emphasize nanoscale transport and chemical reaction phenomena, which depend on the nano structures of PEM, CLs, and GDLs, key issues that are addressed for the breakthrough in PEMFC technology are: (i) novel materials, obtained through computational chemistry calculations (possessing high temperature operability and low cost), and electrocatalysts for high reduction reaction kinetics and tolerance to carbon monoxide. These materials require increased durability (an order of magnitude higher) and meet requirements of environment, safety, and health; (ii) optimal design parameters for GDLs (porosity and hydrophobicity), CLs (thickness, composition, and particle-size distribution) as well as determination of operating and design conditions (i.e., optimal temperature, pressure, current density, humidity, geometric parameters, flow characteristics, and arrangements, etc.); (iii) analysis of the interfaces in PEM-CL (including catalytic reactions and proton transport) as well as in CL–GDL/GDL–GC, where multi-phase transport occurs. This entire PEMFC design can be envisioned as an ultra-large integration of sub-models and an optimization problem with the objective of maximizing performance, and minimizing the cost, with a given durability. As a hierarchy of governing equations containing a large set of parameters to be optimized and conditions to be satisfied, multi-scale, -physics models are bound to play a pivotal role in achieving the design goals, in synergy with the experimentation. Moreover, the development of breakthrough technologies in the PEMFC can further advance research in other applications of nanotechnology such as

membrane separation technology based on Pd-alloy for advanced coal conversion processes (O'Brien et al. 2011). This membrane may enable separation of H_2 in CO_2-rich gas streams, reduce energy and cost composed to conventional solvent and cryogenic methods and provide additional fuel resources for PEMFC. In addition, the investigation of transport phenomena and reactions at the mesoscopic level for nanostructured geometry will lead to synergetic advances in nano energy research.

Hierarchical equations in multi-scale modeling

During the past few decades, various theoretical models have been developed to explain the physical properties and to find key parameters for the prediction of the system behaviors. Recent technological issues demand the integration of subsystem models at various scales, which entails examining nano physical properties, subsystem size, and scale-specified numerical analysis methods on system level performance. Multi-scale modeling components including quantum mechanical (i.e., density functional theory (DFT) and ab initio simulation), mesoscopic (i.e., Monte Carlo (MC), molecular dynamics (MD), and lattice Boltzmann method (LBM)), and macroscopic (i.e., LBM, computational fluid mechanics, and system optimization) have also gained tremendous attention. Here, we introduce a few modeling methodologies and the structure of hierarchical equations, which are broadly utilized in multi-scale approaches including the fuel cell system.

Atomistic-molecular level

Atomistic-molecular level simulations are utilized to investigate bottom level scale phenomena such as membrane conformation and proton conduction mechanisms in PEM and reaction kinetics on the CLs. First-principle theoretical model at the bottom level (quantum mechanics) plays a critical role in the multi-scale modeling strategy, since the techniques build the theoretical fundamentals for empirical knowledge on upper level calculations (Fig. 3). At this level, the molecular system is described by utilizing various ab initio quantum mechanical calculations, which are currently available to solve many body wave-function problems represented by the Schrödinger equation (Jensen 1989). The density functional theory (DFT) is an alternative method to provide the computational efficiency via energy functional depending on the electron density (Parr and Yang 1994). In this calculation, the ground-state electronic energy is determined by the electron density (Hohenberg and Kohn 1964). Although the quantum level calculation promises accuracy since the model is based on fundamental, non-empirical rules, the calculation demands a huge computational cost. As a consequence the technique cannot be utilized for the upper level of the scale represented as massive molecular systems, which are more than ~1,000 atoms. Therefore, quantum level models are generally utilized with a combination of molecular level theories, which have been extensively investigated. Most recently, this approach has evolved into a correlated

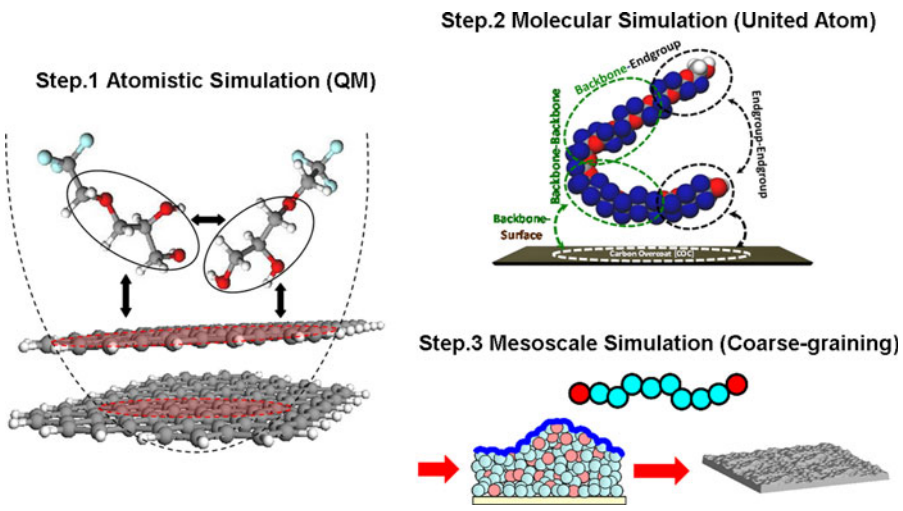

Fig. 3 Force-field parameter implementation from *bottom level* (QM) to *upper level* (coarse-grained molecular simulations)

quantum/statistical mechanical approach based on improvements with real-time, time-dependent density functional theory (RTTDDFT), and pseudo-atomistic MC/molecular dynamics (PAMCMD) calculations (Dalton 2009). At this level, we can obtain first-principles prediction of properties with non-adjustable parameters. This study provides a proof-of-concept that detailed quantum mechanical methods can be used to inform macroscale experimental systems, producing new materials with dramatically improved properties. In PEMFC modeling, Goddard et al. developed the multi-scale simulation with reactive force field (ReaxFF), which simultaneously captures reactive and transport processes at the interface between polymer electrolyte membrane (PEM) and electrode (Goddard et al. 2006).

Classical molecular simulation methods such as MC and molecular dynamics (MD) represent atomistic/molecular level modeling, which discards the electronic degrees of freedom while utilizing parameters transferred from quantum level simulation as force-field parameters. A molecule in the simulation is composed of beads which represent atoms, where the interactions are described by classical potential energy functions. To model the electrochemical effects, the nonbonding interactions were modified by the combination of van der Waals interaction and the electrostatic Coulombic interactions:

$$U_{\mathrm{LJ}-C}(r_{ij}) = 4\varepsilon_{ij}\left[\left(\frac{\sigma}{r_{ij}}\right)^{12} - \left(\frac{\sigma}{r_{ij}}\right)^{6}\right] + \frac{q_i q_j \mathrm{e}^2}{4\pi\varepsilon_0}\frac{1}{r_{ij}}, \tag{1}$$

where σ is the diameter of beads, ε_{ij} corresponds to the well depth of LJ interaction, r_{ij} denotes the distance between two beads i and j, ε_0 is the dielectric constant in vacuum, e represents elementary electric charge, and q_i and q_j are the charge parameters for Coulombic interaction. Apart from the Coulombic interaction, the molecular system of PEMFC is analogous to the oligomer/solid surface system, which was investigated within the framework of nano lubrication area (Chung et al. 2012). From here on, we choose these types of interactions to illustrate the bottom levels in multi-scale modeling for PEMFC. The difference between two systems is that the short range interactions between oligomer/surface is replaced by long range Coulombic interaction, which makes it easier to illustrate molecular level coarse-graining procedure. Chemical bond potential energy between adjacent beads and bend potential energy between adjacent bonds are commonly represented by harmonic potential energy (Leach 2001). Alternatively, anharmonic finitely extensible nonlinear elastic (FENE) springs connect the adjacent beads separated by a distance of r_{ib}:

$$U_{\mathrm{FENE}}(r_{\mathrm{ib}}) = \begin{cases} -\frac{1}{2}kR_0^2 \ln\left[1 - \left(\frac{r_{\mathrm{ib}}}{R_0}\right)^2\right] & r_{\mathrm{ib}} < R_0 \\ \infty & \text{otherwise} \end{cases}. \tag{2}$$

Here, r_{ib} denotes the interbead distance (i.e., the bond length between two adjacent beads), k is the spring constant which quantifies the rigidity of the bond, and R_0 is the maximum extensibility of the spring. The form of torsional potential parameters, describing four bonded atoms, is:

$$U_\phi = k\sum_{n=0}^{N-1} A_n \cos^n \phi, \tag{3}$$

where U_ϕ is the torsional potential, k is a constant, A_n are the coefficients, and ϕ is the torsional angle. To incorporate classical potential functions with quantum mechanical calculations, eigenvalue analysis is developed to calculate stretching and bending parameters from the ab initio Hessian matrix for the harmonic potential form, and the torsional potential parameters are calculated by generating the ab initio torsional energy profiles via a series of constrained geometry optimization.

From the equilibrium geometries in quantum mechanical models, the atomistic intramolecular force-field parameters, which are potential parameters in atomistic MD simulation, can be obtained by using the method of Seminario (1996). With the combination of atomistic MD simulation, quantum mechanical properties of the materials have provided the advances in the study of the fundamental nanoscale phenomena. However, processes at the device or system level occur above the microscale, which the quantum and atomistic levels cannot cover. Therefore, the development of a coarse-graining procedure, which simplifies the detailed structure of molecules, while retaining fundamental phenomena from quantum/atomistic level models, becomes one of the critical issues in atomistic/molecular level modeling.

The molecular motion in MD simulation is deterministic by solving a Hamiltonian system (Allen and

Tildesley 1996). However, for the dissipative dynamic description for the coarse-grained model, Langevin dynamics (Grest 1996) can also be employed, where the force acting on the ith bead in the αth molecule can be calculated by the following equation:

$$m\frac{\mathrm{d}^2\mathbf{r}_{\alpha i}}{\mathrm{d}t^2} = -\frac{\partial U}{\partial \mathbf{r}_{\alpha i}} - \zeta \cdot \frac{\mathrm{d}\mathbf{r}_{\alpha i}}{\mathrm{d}t} + f^*_{\alpha i}(t). \tag{4}$$

Here, m and $\mathbf{r}_{\alpha i}$ are the mass and position vector of beads, respectively. ζ is the friction tensor, which is assumed to be isotropic for simplicity in our simulation, i.e., $\zeta = \Gamma I$, where I is the unit dyad and $\Gamma = 0.5\tau^{-1}$ ($\tau = \sigma(m/\varepsilon)^{0.5}$), where ε is the well depth of LJ interaction. Further, $f^*_{\alpha i}$ is the Brownian random force, which obeys the Gaussian white noise, and is generated according to the fluctuation–dissipation theorem:

$$\left\langle f^*_{\alpha i}(t) f^*_{\beta j}(t') \right\rangle = 2k_{\mathrm{B}}T\,\Gamma\delta_{\alpha\beta}I\delta_{ij}\delta(t-t'), \tag{5}$$

where the angular bracket denotes an ensemble average. $\delta_{\alpha\beta}$ and δ_{ij} are Kronecker deltas, and $\delta(t - t')$ is a Dirac's delta function. Γ quantifies the magnitude of Brownian force. k_{B} and T are the Boltzmann constant and absolute temperature, respectively.

The coarse-graining method was introduced to determine the force-field parameters from atomistic information through a variational minimization procedure (Izvekov and Voth 2005a, b), and the method has been applied to the study of various material systems (Wang et al. 2006; Iuchi et al. 2007; Zhou et al. 2007; Shi et al. 2006). Further, the coarse-graining framework was expanded with a statistical mechanical theory by introducing the many-body potential of the mean force, which enables coarse-graining model consistent with atomistic models. The coarse-grained sites are constructed by clusters of atoms where the mass of the coarse-grained site is the sum of the included atoms. The new coarse-grained bond lengths are calculated from the distance between the centers of mass of the clusters of atoms as shown in Fig. 4.

The method aims to pass the distribution of structural parameters from the atomistic to the coarse-grained structure. The procedure involves performing an atomistic MD simulation and calculating the equilibrium probability distributions of the corresponding coarse-grained bond lengths, bond angles, and torsional angles. A Boltzmann distribution is fit to the distribution determined from the MD simulation by varying the parameters of the bonded potential:

$$P(\mathbf{r}) \propto \exp(-U_{\mathrm{r}}(\mathbf{r})/k_{\mathrm{B}}T), \tag{6}$$

where P is the probability distribution of bond lengths, and U_{r} is the bond potential, and T is absolute temperature. A similar approach is used for the bond angles and torsions. In order to correct for any error in the parameter calculation due to fitting a Boltzmann distribution to a condensed phase simulation, a coarse-grained MD simulation is run by using the parameter from the fit, and a new probability distribution is calculated. An updated Boltzmann distribution is fit to the distribution, generating another set of potential parameters. Parameters determined from both the atomistic and the coarse-grained simulations are used

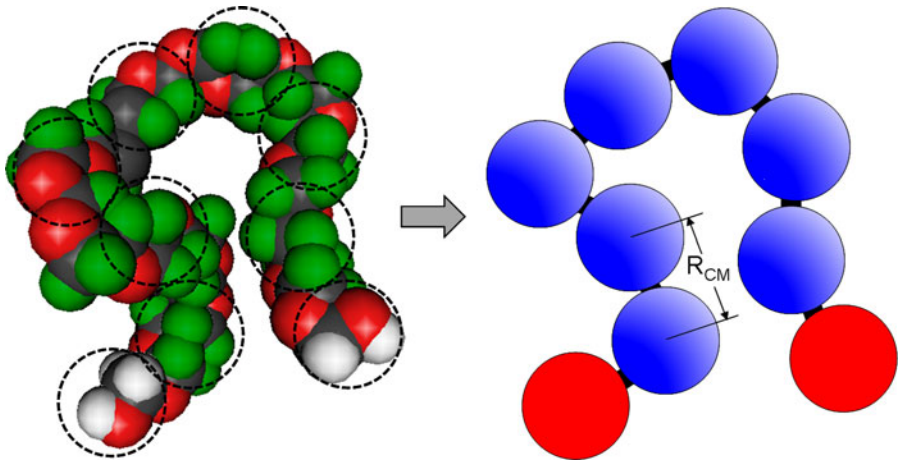

Fig. 4 Mapping of atomistic clusters onto coarse-grained sites. $\mathbf{R}_{\mathrm{CM}}$ represents the bond (backbone) between coarse-grained sites, where the sites are the centers of mass of the atomistic clusters

to calculate the final coarse-grained potential parameters as shown in Eqs. (7) (8):

$$K_{\mathrm{r}}^{I} = (K_{\mathrm{r}}^{II})^2 / K_{\mathrm{r}}^{III}, \tag{7}$$

$$r_{\mathrm{o}}^{I} = 2r_{\mathrm{o}}^{II} - r_{\mathrm{o}}^{III}, \tag{8}$$

where *I* denotes the final coarse-grained parameter, *II* denotes a parameter determined from the atomistic simulation, and *III* denotes a parameter determined from the coarse-grained simulation. A similar approach can be applied to the bond angle and torsional potentials.

Mesoscale–continuum level

In the fuel cell system, mesoscale–continuum simulations are used to investigate the fuel flows in GC and GDL, and predict the fuel distribution on the CL through GDL depending on the pore structures. Continuum models including conservation law and constitutive relations has been widely utilized here. However, these methodologies fail to capture the complex flow within nano/microstructural geometry. LBM was recently introduced as an alternative mesoscale/continuum level modeling tool, which has the advantages in capturing clear physics in the system with complex geometry and nanoscale physics. Since LBM covers a broad range of the system scale and is based on the particle assumption, the method is considered as a multi-scale method from mesoscale to continuum scale including buffer region simulation substituting computational fluid dynamics. It is a promising candidate for hierarchical integration with atomistic/molecular level models. Physical phenomena in air-bearing/viscoelastic liquid-bearing nano-tribological system and nanoscale heat transfer phenomena have been modeled via LBM (Kim et al. 2005; Ghai et al. 2006). Due to the convenience of the complex geometry manipulation, LBM is suitable for modeling flow through porous media, which can be utilized for GDL simulation in PEMFC.

LBM has emerged as a promising numerical tool for simulating fluid flows and thermal management with complex physics (Chen and Doolen 1998). Numerous advantages, including clear physical pictures, an inherently transient nature, multi-scale simulation capabilities, and fully parallel algorithms, make LBM an attractive candidate as a multi-scale simulation tool. Kim et al. have developed a novel LBM by adopting a spatially dependent relaxation time model to predict the nanoscale air bearing performance (Kim et al. 2005). Unlike conventional numerical methods, which discretize the macroscopic equations, LBM constructs simplified kinetic models incorporating the essential physics of microscopic processes so that the macroscopic properties obey the desired equations. The two-dimensional, lattice Boltzmann kinetic equation (LBKE) with Bhatnagar–Gross–Krook (BGK) approximation can be written as (Mei et al. 2000):

$$f_i(x + c_i\Delta t, t + \Delta t) = f_i(x,t) - \frac{1}{\tau}[f_i(x,t) - f_i^{\mathrm{eq}}(x,t)] \quad \text{for } i = 0, 1, \ldots, N, \tag{9}$$

where τ is the relaxation time which controls the rate of approach to equilibrium; $f_i(x,t)$ is the discrete one particle distribution function, which is the probability of finding a particle with the velocity c_i at (x,t); Δt is the time step; N is the number of discrete particle velocities in each node direction; $f_i^{\mathrm{eq}}(x,t)$ is the discrete equilibrium distribution function given as:

$$f_i^{\mathrm{eq}}(x,t) = w_i\rho\left[1 + \frac{\mathrm{e}\cdot v}{c^2} + \frac{vv:(\mathrm{e}_i\mathrm{e}_i - c^2 I)}{2c^4}\right], \tag{10}$$

$$\text{with } w_i = \begin{cases} 4/9, & i = 0 \\ 1/9, & i = 1, \ldots, 4 \\ 1/36, & i = 5, \ldots, 8 \end{cases},$$

where v is the fluid velocity, $c \equiv \Delta s/\Delta t = \sqrt{3k_{\mathrm{B}}T/m}$ is the lattice speed, and Δs is the lattice spacing, and ρ is the density. The nine discrete velocities in D2Q9 model (Fig. 5) are given by

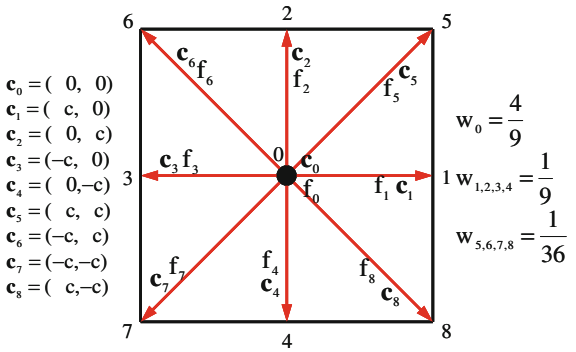

Fig. 5 A lattice node of D2Q9 model (2D lattice with nine directions of streaming)

$$c_i = \begin{cases} (0,\,0), & i = 0 \\ (\pm 1,\,0)c,\ (0,\,\pm 1)c, & i = 1,\ldots,4 \\ (\pm 1,\,\pm 1)c, & i = 5,\ldots,8. \end{cases} \tag{11}$$

The ρ and v are calculated by

$$\rho(x,\,t) = \sum_i f_i \quad \text{and} \quad v(x,\,t) = \frac{1}{\rho(x,t)} \sum_i c_i f_i. \tag{12}$$

Multi-scale system integration

Multi-scale modeling provides effective hierarchical analysis and simulation strategies linking various models in different scales, where each level addresses specific physical phenomena. The classical concept of the multi-scale modeling method is straightforward integration among the various scale levels, which utilizes the simultaneous description of all-scale subsystems. This method provides real-time multi-scale observation yet the computational time depends on the slowest calculation. To overcome the disadvantage in the computational cost while retaining multi-scale advantages, the hierarchical multi-scale model, which utilizes parameters in lower level of scale to obtain new parameters for the upper level degrees of freedom, has been developed (Ulherr and Theodorou 1998; Theodorou 2005). The hierarchical multi-scale model allows each level of calculation to be performed independently, and the input parameters can be estimated from other scale level models, which discard unnecessary calculations during the bridging procedure between different scales (Doi 2003; Glotzer and Paul 2002; Delle Site and Kremer 2005). Recently, the focus of multi-scale modeling strategy is on developing bridging methodology connecting quantum–atomistic/molecular–mesoscale–continuum levels (Laio et al. 2002; Csanyi et al. 2004; Faller 2004; Delgado-Buscalioni and Coveney 2003; Broughton et al. 1999; Rafii-Tabar et al. 1998; Smirnova et al. 1999; O'Connell and Thompson 1995; Hadjiconstantinou 1999; Neri et al. 2005; Villa et al. 2004; Li et al. 1998; Flekkoy et al. 2000).

The bridging procedure finds reduced order parameters for upper level scale models. As shown in Fig. 6, reduced order models (ROMs) are introduced to capture the predictive behavior of the lower-scale model and provide the links to capturing behavioral information from all of the lower scales, while allow the integrated formulation to be tractable. The major role of multi-scale ROMs is that they allow feasible realizations of complex domain models (consistency) and capture accurate complex model behavior over a wide range of the decision space (performance). With the development of ROMs at each level, modeling and optimization formulations at a given level will capture

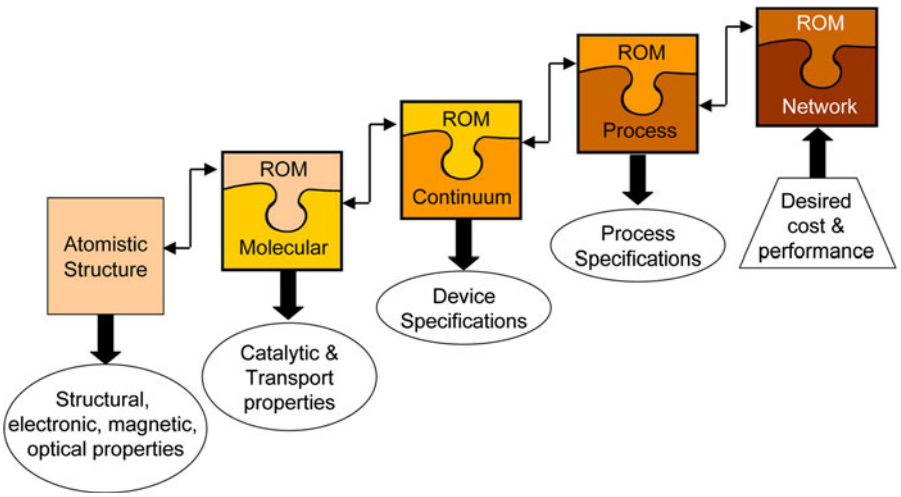

Fig. 6 Linking models at various scales using ROMs and deriving lower-scale specifications through an inverse optimization formulation. The ROM included at each scale is a reduced representation of the model at the scale below that could range from a set of parameters such as, for example, elementary rate constants to complex models derived from proper orthogonal decomposition and perhaps even to the full lower scale model. This is symbolised by *coloring* the ROM box with the same color as that of the box representing the adjacent lower scale model

performance and feasibility at neighboring levels. By allowing this communication between levels, accurate and efficient decision-making can be made. Also note that the bidirectional flow between levels in Fig. 6 easily allows us to develop and generalize ideas of reverse engineering and inverse problems.

The coupling of models at different scales is a challenging subject in the integration procedure, yet it is most important for the accuracy of the multi-scale models. Especially the computational cost associated with large-scale calculations often precludes their integration over time and length scales, while rigorous models are now widely applied at all modeling scales. As an essential tool to overcome this barrier, ROM plays a critical role to link detailed phenomena at all modeling scales. While ROMs are applied over the entire modeling spectra, their development is usually done as a one-time activity at an ad hoc level. In the development of a multi-scale modeling with optimization framework, it is required to develop a systematic approach for ROM development and integration. This will lead to the development of a single framework that promises much more detailed predictions of system-level simulations with high accuracy and interdependencies for large-scale decision-making.

Depending on the particular length and time scale and the application domain, ROMs take a variety of different forms. Often, physics-based analytic models are derived from simplified, limiting behaviors of transport, reaction and equilibrium phenomena and conservation laws. At the process engineering level, these lead to a rich and widely applied model library, which must nevertheless be extended to newer technologies in reaction and separation. Examples of these include macroscopic models for rate laws, vapor liquid equilibrium and thermodynamic properties used at the level of process networks. In addition, process models are often derived that consist of semi-empirical functional forms fitted with data including reactor models and process models derived from data-derived correlations. At the device level, which is dominated by models in continuum mechanics, ROMs take a variety of forms, ranging from reduced order solutions involving proper orthogonal decomposition, variable resolutions models on meshes with varying degrees of refinement, variable-fidelity physics models such as inviscid, irrotational, and incompressible flow for Navier–Stokes equations. Lastly, at atomistic and molecular levels, the task is to infer thermodynamic and kinetic properties and constants that are later used in macroscopic physics-based models. Often these calculations are used directly to regress to physics-based ROMs, such as with cluster expansion and kinetic MC modeling. Moreover, for complex device or molecular models, such as time consuming continuum mechanics and probabilistic models with little or no structural information, general regression-based models are derived that apply data-driven regression approaches (e.g., principle component analysis, compressed sensing, neural nets, wavelets). At all of these levels, ROMs have approximation errors that prevent their direct integration for multi-scale decision-making. As a result, there is a clear need to develop uncertainty bounds as part of the development for all of these models. Such bounds are statistically derived and lead to confidence regions in the parameter space of the ROM. Consequently, a key task in the application of ROMs is the derivation of corresponding uncertainty bounds. Moreover, as the underlying model changes, provisions must be added to update models and error bounds and explore uncertainty ranges (Lang et al. 2009; Agarwal et al. 2009; Lang et al. 2011).

The overall approach is termed a data-model fusion which leads to challenges in numerical methods, error estimates, and linking with physics-based models. Moreover, with the availability of ROMs across the spectrum of relevant problem scales, one can develop multi-scale optimization formulations that act as the "glue" toward their integration, leading to the entire model.

Process scale level

Process-scale models represent the behavior of reaction, separation and momentum, heat and mass transfer at the process flowsheet level, or for a network of process flowsheets. Whether based on first principles or empirical relations, the model equations for these systems typically consist of conservation laws, physical, and chemical equilibrium among species and phases, and additional constitutive equations that describe the rates of chemical transformation or transport of mass and energy. These process models are often represented by a collection of individual unit models (the so-called unit operations) that usually correspond to major pieces of process equipment, which, in turn, are captured by device-level models. These unit models are assembled within a process

flowsheet that describes the interaction of equipment either for steady state or dynamic behavior. As a result, models can be described by algebraic or differential equations. For example, steady state process flowsheets are usually described by lumped parameter models described by algebraic equations. Similarly, dynamic process flowsheets are described by lumped parameter models described by differential–algebraic equations. Models that deal with spatially distributed models are frequently considered at the device level, with partial differential equations that model fluid flow, heat and mass transfer and reactions. On the other hand, they are usually computationally intensive to incorporate within an overall process model. Process flowsheeting models, embodied in commercial process simulators such as ASPEN Plus®, HYSYS®, or PRO-II®, have become the accepted standard to describe and evaluate process engineering systems, for petroleum refineries, and chemical processes and power plants. Not only do they provide quantitative information on the flow of material and energy throughout a process network, but they are used extensively to assess and analyze the current state of the process, improve the operation of existing processes, and guide and validate the design of new processes. As a result of their applications in all of these engineering tasks, these process models have also become the medium of communication for crucial technical material shared among networks of project teams that participate in any engineering operation. On the other hand, simplifications used in process models (e.g. equilibrium-based, lumped parameter, and other short-cut models) often lead to inaccuracies and performance limitations. Consequently, these models often require model tuning through semi-empirical correlations and data integration. Such tasks are time-consuming and problem specific as they often require information from additional experiments and pilot plant trials, with missing information leading to start-up and operational risks. Clearly the incorporation of more accurate multi-scale phenomena captured by ROMs will overcome these limitations (Lang et al. 2011).

Technological applications of hierarchical methodologies

Hierarchical modeling methods introduced in the previous section are specified for the each sub-component; atomistic/molecular simulations (i.e., ab initio, DFT, and MD) for the PEM, CL, and GDL, and mesoscale/continuum simulation (i.e., LBM) for GDL and GC. In addition to the model integration, each level of modeling provides the detailed properties in the fuel cell system with scale-specific analysis. Here, we present the scale-specific modeling for each sub-component of PEMFC, and introduce the system optimization in the device scale and ROM for the multi-scale integration, which has not been pioneered yet.

Polymer electrolyte membrane

The PEM generally consists of polytetrafloroethylene chains with hydrophilic perflorosulfonate side groups. The water molecules within the system agglomerate in the vicinity of hydrophilic groups (i.e., sulfonic ion groups) and form hydrophilic clusters. A network of these clusters forms passages for proton conduction within PEM which is critical to PEMFC performance. Hence a detailed relationship between PEM structure, water uptake, and proton conduction is necessary for synthesis of novel membrane materials, which overcome the limitations of state-of-the-art PEMs. Ab initio models of PEM have been studied to explain the first-principle dynamics of proton conduction mechanism in hydrated PEM (Habenicht et al. 2010; Choe et al. 2010). Quantum mechanical calculations are incorporated to atomistic MD simulations by providing accurate potential energy functions as inputs to MD simulations. The atomistic MD exhibits the correspondence to the experimental data and provides PEM structural information and proton transfer mechanisms in PEM (Jinnouchi and Okazaki 2003). Particle- and field-based simulation techniques (i.e., integration of atomistic MD and dynamic DFT) was utilized to investigate the processes of self-organization in the systems of sulfonated poly(ether ether ketone)s in the presence of water (Komarov et al. 2010). Goddard et al. (2006) used similar overlapping simulation methodologies for the PEM as well as CL and successfully applied a reactive force field from quantum mechanical calculations to larger-scale MD simulations retaining the accuracy. The molecular level model can be also applied for different electrocatalyst materials to determine atomistic or molecular mechanisms for electrochemical reactions and degradation of the electrode. Franco et al. (2009) analyzed

degradation mechanisms of cathode CL in PEMFC by using multi-scale mechanistic models.

Atomistic MD models can be extended to the coarse-grained level, which is determined by the dimension of the backbone chain and branch. For the precise description of water molecular behavior, a simple point charge (SPC) model was adopted (Krishnan et al. 2001), which can be used to simulate complex composition systems and quantitatively express vibrational spectra of water molecules in vapor, liquid, and solid states. The six-parameter (D_{OH}, α, β, $L_{\gamma\theta}$, $L_{\gamma\gamma}$, and $L_{\theta\theta}$) SPC potential used for the water molecules is shown in Eq. (13):

$$U_{123} = D_{OH}[(1-\exp[-\alpha\Delta r_{12}])^2 + (1-\exp[-\alpha\Delta r_{13}])^2] + \left[L_{rr}\Delta r_{12}\Delta r_{13} + L_{\gamma\theta}(\Delta r_{12}+\Delta r_{13})\Delta r_{23} + \frac{L_{\theta\theta}(\Delta r_{23})^2}{2}\right]\exp\{-\beta[(\Delta r_{12})^2+(\Delta r_{13})^2]\} \quad (13)$$

with $\Delta r_{ij} = r_{ij} - r_{e,ij}$,

where $r_{e,ij}$ is the equilibrium distance between the ith and jth atoms. The subscripts 1, 2, and 3 correspond to the oxygen and the two hydrogen atoms, respectively. The water uptake in the electrolyte was examined from 1 to 14.3 H_2O/SO_3^-. Note that the electrolyte in the state of water uptake at 14.3 H_2O/SO_3^- is almost identical to the immersed proton form of the electrolyte in this simulation.

One of the most important phenomena related to the electrolyte structure is water uptake variation in the PEM. The electrolyte swells upon water uptake, and the density of the electrolyte decreases in a humidified atmosphere. Swelling deformation has been considered as forming transport paths for the cluster of water molecules and protons. We first calculated the density of the PEM system for various amounts of water uptake. The squares and diamonds in Fig. 7a indicate the experimental and simulated density for the dry and hydrated proton form of electrolyte (Jinnouchi and Okazaki 2003; Gierke et al. 1981). As water content increases, the PEM density decreases in the simulations as well as experiments, and predicted values are in good agreement with experimental values, indicating that swelling phenomena of the electrolyte can be captured through this simulation. This swelling phenomena of Nafion® molecules is also illustrated via Fig. 7b, which shows that the radius of gyration among the simulation species increases when the number of water molecules in the system increases. This indicates that as the area occupied by water molecules around the end of the side-chain increases, the Nafion® molecules tend to stretch-out geometrically. Haubold et al. (2001) found that side-chain

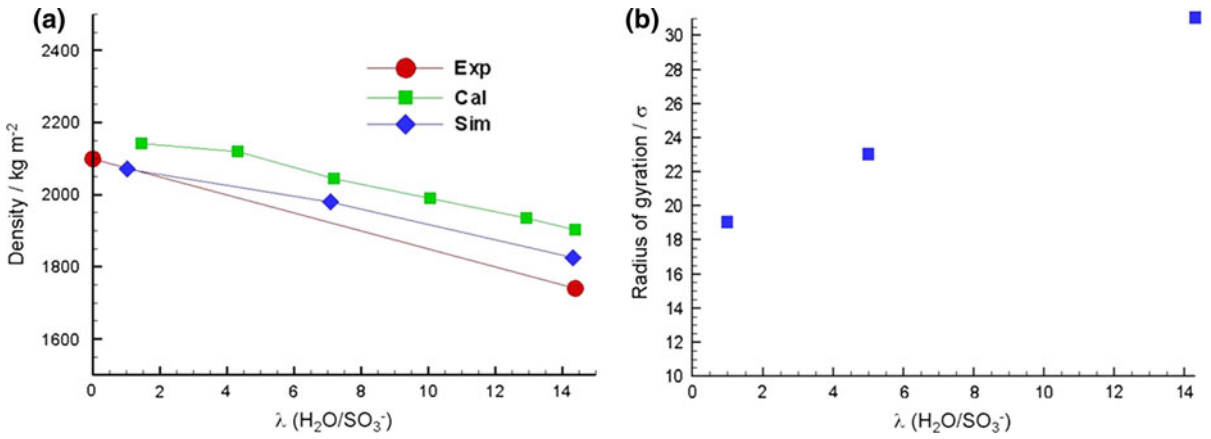

Fig. 7 **a** Density of electrolyte (*circle* experiment by Gierke et al. (1981), *square* calculation by Jinnouchi and Okazaki (2003), *diamond* our model) and **b** Water uptake dependence of radius of gyration of Nafion® molecules

unfolding of the polymer can be observed when the water content increases. In this simulation, we observed that increase in clustered regions of water not only affects the side-chain conformations but also the conformation of the backbone chain, making the polymer backbone chain stretched.

The evidence of water–water cluster generation in the wet electrolyte has been provided through several experimental techniques such as small-angle X-ray scattering, transmission electron microscopy, and Fourier transform infrared spectroscopy (FTIR) (Roche et al. 1981; Porat et al. 1995; Falk 1980). It has been reported that polar particles (water and protons) cohere in the electrolyte. We also confirmed such phenomena in this simulation via radial distribution functions (RDFs = the number of atoms between radii r and $r + \Delta r$/the number of atoms in an ideal gas between r and $r + \Delta r$) among the species (Fig. 8). The sharp peak in RDFs between polar species indicates that almost all the protons and the water molecules always exist within the clustered region. However, we did not observe significant peaks between the polar and nonpolar particles. These results indicate that polar particles cohered in our simulations as well. Figure 9 illustrates the two-dimensional snapshot of water density distribution within the simulation cell for various amounts of water content (H_2O/SO_3^-). It is clearly observed that the high-water density region increases as the water content increases. This high-water density region corresponds to the clusters observed in previous experimental studies. The increase of the high-water density region implies an increase of the number of the transport paths for polar particles. The alignment of these clusters is disorderly, and highly tortuous transport pathways are constructed in our electrolyte model.

Researchers have shown that protons and water molecules move together through the clusters constructed in electrolytes. Although several theoretical methods using macroscopic modeling have been proposed based on the information of the electrolyte structure, there is no model that estimates transport

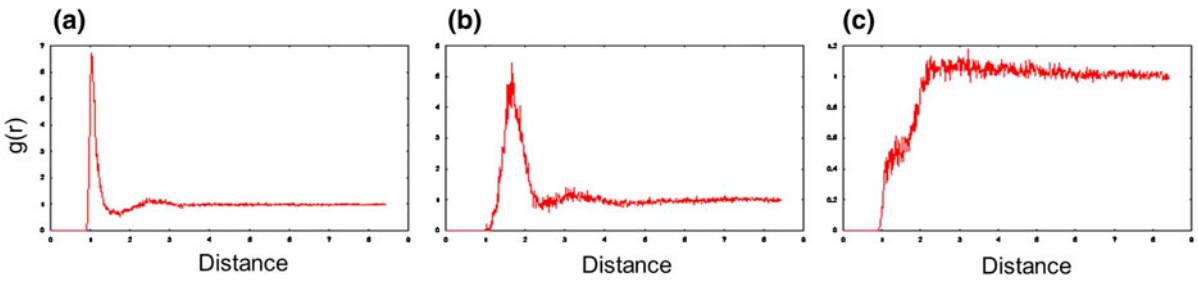

Fig. 8 RDF: of **a** H^+-H_2O, **b** H^+-S, and **c** H^+-CF_2

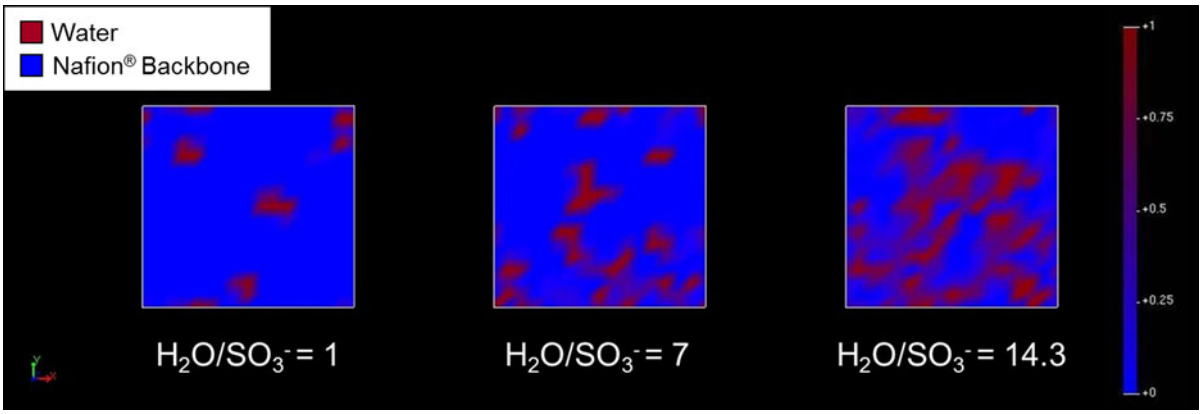

Fig. 9 Water density distributions in a cross section of the system

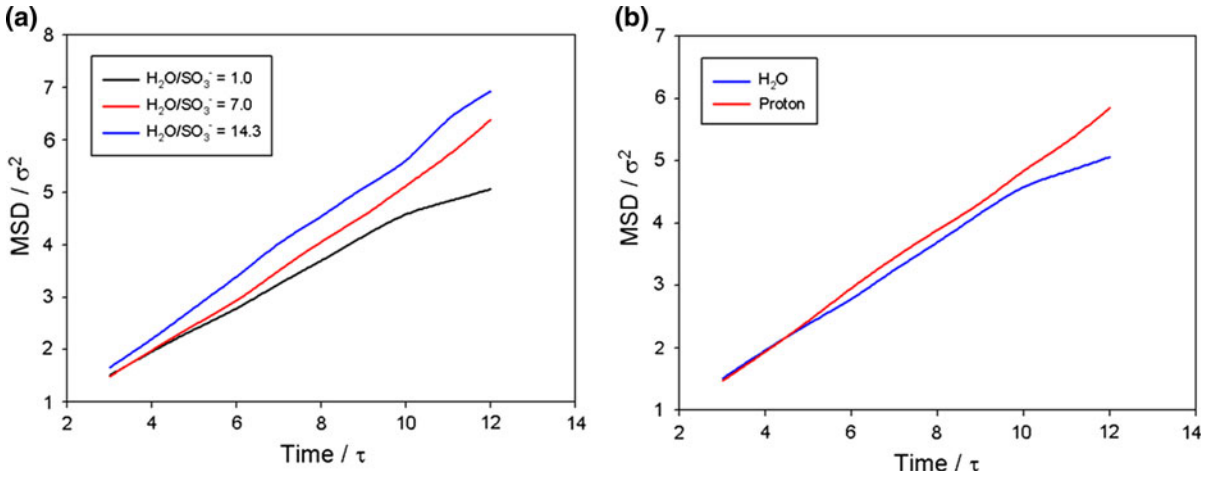

Fig. 10 **a** Water content dependence of MSD of protons and **b** MSD of protons and water molecules (H_2O/SO_3^-:1)

properties from the sub-continuum modeling viewpoint. From Fig. 10a, we observe that the mean-square displacement (MSD) of protons increases as the water content increases. In other words, the diffusivity of the protons (proportional to the gradient of MSD) increases as the water content increases. Thus, the diffusion of protons in the PEM depends on the water content. This phenomenon can be explained in terms of the electrolyte structure. As discussed before, the water molecules and ions cohere with each other and construct hydrophilic clusters in a humidified electrolyte. These clusters join with each other and form transport pathways for the protons and water molecules. Evidence that the protons and water molecules move through this cluster region has been obtained from the RDF. Hence, we can conclude that the cluster region is the transport path for protons and water molecules. The shape parameters of the clustered region, such as the cluster size and clusters connectivity, can strongly affect the transport properties in the electrolyte. The low diffusivity in the electrolyte is due to the tortuous shape of the cluster region. The ions and water molecules in an electrolyte solution can move freely in all directions, but particles in the PEM cannot, due to the tortuous hydrophobic wall. Figure 10b illustrates the comparison between diffusivity of water molecules and protons. We observe that the diffusion coefficient of the protons is smaller than that of the water molecule, and the activation energy of protons is higher than that of water molecule. This indicates that the resistance to transport of protons is higher than the water molecules.

Multi-physics in gas diffusion layer

An entire PEMFC model has been successfully investigated via continuum mechanics, which does not have detailed molecular structural information or simulate complex multi-phase, -physical phenomena. Phase separation at GC–GDL and GDL–CL interfaces may reduce the efficiency of the fuel distribution through GDL and reaction rates inside the CL. Conventional continuum mechanics has a barrier to simulate the complex two-phase gas–liquid flow phenomena within the porous GDL. To overcome this issue, LBMs can be introduced. This method is specifically useful for simulating multi-phase flows as well as hybridizing molecular with continuum level theories. Since the LBM covers from mesoscale to continuum levels, it is straight-forward to combine GDL (mesoscale/continuum level) and GC (continuum level) models.

For the porous media flow simulation, LBM can be applied on the manipulated complex geometry of porous media due to its advantages on the complex geometry. However, in spite of this convenience, the calculation cost will be drastically increased as the system size increases up to the device level approximately in millimeter scale and above. To develop larger scale buffer simulation, the representative elementary volume (REV) method was invented,

where a single lattice represents the volume of porous media. The fuel flowing in the porous electrode can be described by a continuity equation and the Brickman–Forchheimer-extended Darcy equations (Nithiarasu et al. 1997):

$$\nabla \cdot v = 0, \tag{14}$$

and

$$\frac{\partial v}{\partial t} + (v \cdot \nabla)\left(\frac{v}{\phi}\right) = -\frac{1}{\rho}\nabla(\phi P) + v\nabla^2 v + F, \tag{15}$$

where ϕ is porosity, P is cell total pressure, and v is kinematic viscosity. F represents total body force due to the presence of the porous medium and other external force fields, expressed by:

$$F = -\frac{\phi v}{K}v - \frac{\phi F_\phi}{\sqrt{K}}|v|v + \phi G, \tag{16}$$

where G is the body force induced by an external force, and F_ϕ and K are, respectively, the geometric function and permeability, which can be estimated from Ergun's experimental results and expressed by (Ergun 1952; Vafai 1984):

$$F_\phi = \frac{1.75}{\sqrt{150\phi^3}} \quad \text{and} \quad K = \frac{\phi^3 d_p^2}{150(1-\phi)^2}, \tag{17}$$

where d_p is the effective average diameter of the solid in the porous electrode.

In general, the Boltzmann transport equation with single relaxation time approximation can be written as Eq. (18). In order to simulate flow through the porous media, we consider the drag effect of the medium and present the LBM equation by the following statistical average form:

$$\bar{f}_i(x + c_i\Delta t, t + \Delta t) = \bar{f}_i(x,t) - \frac{1}{\tau}[\bar{f}_i(x,t) - \bar{f}_i^{eq}(x,t)] + F_i\Delta t\,. \tag{18}$$

where $\bar{f}_i(x,t)$ and $\bar{f}_i^{eq}(x,t)$ are volume-averaged distribution and equilibrium distribution function at REV scale, respectively (From now on, the overbars will be omitted for the sake of convenience). F_i is the force term for ith particle of fluid. F_i is chosen as (Cancelliere et al. 1990):

$$F_i = \omega_i\rho\left(1 - \frac{1}{2\tau}\right)\left(\frac{e_i \cdot F}{c^2} + \frac{(e_i \cdot v)(e_i \cdot F)}{\phi c^4} - \frac{v \cdot F}{\phi c^2}\right). \tag{19}$$

The density and velocity of the fluid are defined by

$$\rho(x,t) = \sum_i f_i \quad \text{and} \quad v(x,t) = \frac{1}{\rho(x,t)}\sum_i c_i f_i + \frac{\Delta t}{2}F \tag{20}$$

The macroscopic equations for fluid flowing through porous media may be recovered by Taylor expansion and Chapman–Enskog expansion, which become

$$\frac{\partial \rho}{\partial t} + \nabla \cdot (\rho v) = 0, \tag{21}$$

and

$$\frac{\partial(\rho v)}{\partial t} + \nabla \cdot \left(\frac{\rho v v}{\phi}\right) = -\nabla P + \nabla \cdot [\rho\nu(\nabla v + v\nabla)] + F. \tag{22}$$

We see that above equations recover Eqs. (14) and (15) for incompressible flow. Note that as $\phi = 1$, Eqs. (15) or (22) are reduced to the standard LBKE for the fluid flows in the absence of porous media.

Xu et al. have successfully introduced the Brickman–Forcher extended Darcy equation in order to solve the performance of molten carbonate fuel cell (Xu et al. 2006). As a verification of REV method, Poiseuille flow profiles were simulated in the porous media modifying LBM with Brickmann–Forcher extended Darcy equation. The porosity is set to be 0.1, Reynolds number (Re) ranges from 0.01 to 100, and the Darcy number (Da) ranges from 10^{-6} to 10^2. The lattice used is an 80×80 square mesh, and the relaxation time is set to be 0.8. Periodic boundary conditions are applied to the entrance and the exit. The velocity field is initialized to be zero at each lattice node with a constant density $\rho = 1.0$, and the distribution function is set to be its equilibrium at $t = 0$. In Fig. 11a, the numerical results of the REV LBM are compared with the finite difference results, which were solved by Guo and Zhao (2002). Excellent agreement is observed between REV LBM and the finite-difference solutions, which confirms the validity of the REV LBM for the continuum scale exhibiting that velocity profiles tend to be unity when the finer porous media is used with same porosity. REV LBM is also compared to the standard LBM with manipulated porous media geometry in same parameter conditions as a verification of REV LBM at lower scale level.

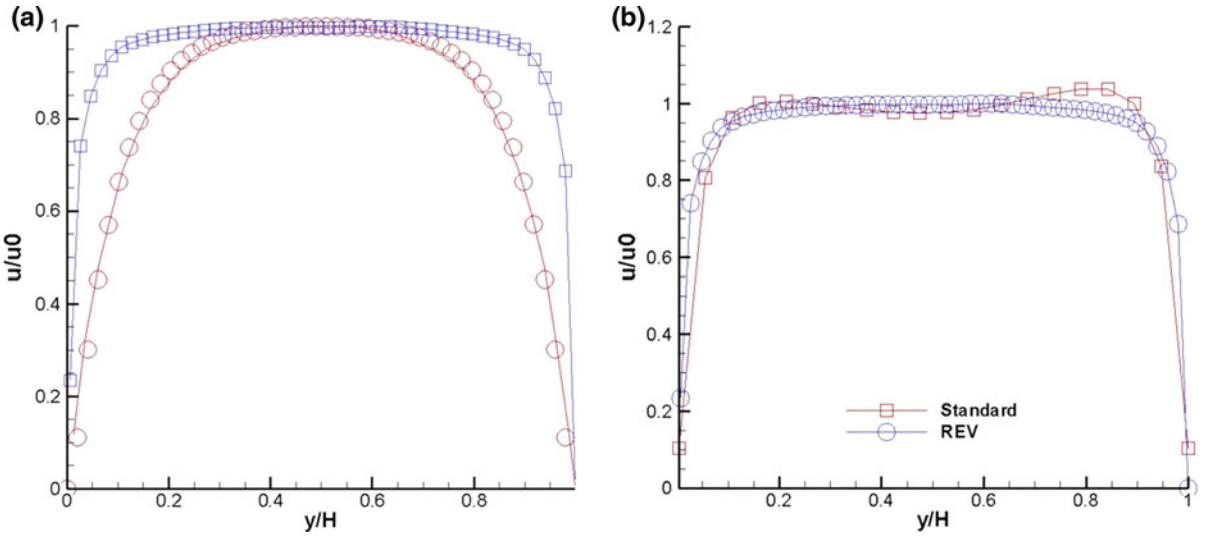

Fig. 11 **a** Comparison of normalized velocity profile ($Re = 0.1$); *solid line* analytical solution, *symbol* LBM; *blue* $Da = 10^{-4}$, *red* $Da = 10^{-3}$, $\phi = 0.1$, and **b** comparison of REV (*blue*) and standard (*red*) methods: $Re = 0.1$, $Da = 10^{-4}$, $\phi = 0.1$. (Color figure online)

Figure 11b shows that the standard LBM with porous geometry shows behavior similar to the results from REV LBM. Since the flow in PEMFC is multi-component/-phase, which results in clogging effects, the details of porous media geometry cannot be discarded for an accurate GDL model. Therefore, multi-scale integration in GDL can be obtained via combining REV LBM and LBM with the porous media geometry.

LBKE can be further modified to capture the multi-component/-phase phenomena in GDL as well as GC. This modification also allows modeling the hydrophilic effect such as bubble transport phenomenon. Bubble phenomenon in situ was visualized by using the hydrophilic carbon cloth since it has more regularly distributed pores than the hydrophobic one. Therefore, the hydrophilic diffusion layer is more preferred to remove bubbles. In order to simulate a multi-component, -phase flow in the fuel cell, we need to solve the same number of LBKEs as the number of components. The additional effects from the multi-phase flow, such as the surface tension, the fluid–solid force, and the buoyancy force can be treated as external forces for the momentum equation. Therefore, the modified LBM equation can be expressed as

$$\rho^{\sigma}(x,t)v^{\sigma}(x,t) = \sum_{i} f_i^{\sigma}(x_i,t)c_i + F^{\sigma}_{\text{total}}(x,t), \tag{23}$$

for the multi-component, -phase flow. In Eq. (23), $F^{\sigma}_{\text{total}}(x,t)$ represents the total external force parameter (momentum per volume) of the component σ contributed by the surface tension, the fluid–solid interaction force, and the buoyancy force:

$$F^{\sigma}_{\text{total}}(x,t) = F^{\sigma}_{\text{surface tension}}(x,t) + F^{\sigma}_{\text{fluid-solid}}(x,t) + F^{\sigma}_{\text{buoyancy}}(x,t). \tag{24}$$

To model the surface tension force in the multi-component fluid, an interaction potential $\phi(x,x')$ was defined as

$$\phi(x,x') = G^{\sigma\sigma'}\psi^{\sigma}(x)\psi^{\sigma'}(x'), \tag{25}$$

where $\psi^{\sigma}(x)$ is a function of the mass density of the species σ at the position vector x; and $G^{\sigma\sigma'}$ is set to be the interaction strength between the species σ and the other species σ'. For simplicity, we assume that $G^{\sigma\sigma'}$ only accounts for the nearest–neighbor interactions. The rate of change of the momentum per volume for the multi-component fluid becomes,

$$\frac{\mathrm{d}F^{\sigma}_{\text{surface tension}}}{\mathrm{d}t}(x,t) = -\Psi^{\sigma}(x,t)\sum_{\sigma'} G^{\sigma\sigma'} \times \sum_{i} \Psi^{\sigma'}(x + \mathrm{e}_i\Delta t, t)\mathrm{e}_i. \tag{26}$$

Hence, the force parameter contributed by the surface tension can be approximated by the following equation:

$$F^{\sigma}_{\text{surface tension}}(x,t) = -\tau^{\sigma}\left[\Psi^{\sigma}(x,t)\sum_{\sigma'}G^{\sigma\sigma'}\sum_{i}\Psi^{\sigma'}(x+\mathrm{e}_i\Delta t,t)\mathrm{e}_i\right], \tag{27}$$

where τ^{σ} is the collision time for the species σ.

The interaction force at the fluid–solid interaction can be expressed by

$$F^{\sigma}_{\text{fluid}-\text{solid}}(x,t) = -\rho^{\sigma}\sum_{i}G^{\sigma}_{i}s(x+\mathrm{e}_i\Delta t)\mathrm{e}_i, \tag{28}$$

where G^{σ}_{i} is the fluid–solid interaction potential parameter; s is a function of the position of the particle, $s = 0$ when the particle is in the fluid, and $s = 1$ when the particle is at the fluid/solid interface. The angle between the fluid and the wall, due to the hydrophilicity, can be controlled by adjusting the fluid–solid interaction potential parameter G^{σ}. The angle increases with larger G^{σ}. When the contact angle increases, the wall is less hydrophilic. The momentum contributed by the buoyancy force can be expressed by:

$$F^{\sigma}_{\text{buoyancy}}(x,t) = -g\sum_{i}\rho^{\sigma}(x+\mathrm{e}_i\Delta t,t)\mathrm{e}_i, \tag{29}$$

where g is the gravitational constant.

By modifying LBM, the multi-physical models can be realized with the combination of the thermal effects on the nanoscale systems, which effectively describes nanoscale thermal phenomena due to its broad length and time scale coverage. Since electrons as well as phonons play a vital role in the energy transport in the nanoscale system, the thermal behavior of both electrons and phonons needs to be simultaneously considered to accurately predict the transient sub-continuum thermal transport. LBM can successfully resolve such complicated systematic problems since the complexity of the collision term in the BTE can be significantly reduced by using the single relaxation time approximation (Ghai et al. 2006). LBKEs for heat transfer obtained from the BTEs are written as:

$$\mathrm{e}_{\text{elec},i}(\mathbf{x}+\Delta\mathbf{x}_{\text{elec}},t+\Delta t) = (1-w_{\text{elec}})\mathrm{e}_{\text{elec},i}(\mathbf{x},t) + w_{\text{elec}}\,\mathrm{e}^{0}_{\text{elec},i}(\mathbf{x},t) - Q_{\text{elec}-\text{p}}\Delta t/D + S\Delta t/D\,, \tag{30}$$

and

$$\mathrm{e}_{\text{p,i}}(\mathbf{x}+\Delta\mathbf{x}_{\text{p}},t+\Delta t) = (1-w_{\text{p}})\,\mathrm{e}_{\text{p},i}(\mathbf{x},t) + w_{\text{p}}\,\mathrm{e}^{0}_{\text{p},i}(\mathbf{x},t) + Q_{\text{elec}-\text{p}}\Delta t/D\,. \tag{31}$$

The subscripts elec, p, i, and D represent electron, phonon, a specific direction in the lattice, and the number of propagation directions in the lattice, respectively. $w \equiv \Delta t/\tau$ and $\mathrm{e}_i(\mathbf{x}, t)$ are the dimensionless relaxation time and the discrete energy distributions of an energy carrier, respectively. $\Delta\mathbf{x}_i$ is related to the time step (Δt) as $\Delta\mathbf{x}_i = c_i\Delta t$. S is the energy density absorbed by the electrons per unit time and $Q_{\text{elec-p}}$ is the coupling term which represents the energy transfer between electrons and phonons. The total energy density and the equilibrium energy distribution are given by

$$\mathrm{e}(\mathbf{x},t) = \sum_{i=1}^{D}\mathrm{e}_i(\mathbf{x}_i,t) \quad \text{and} \quad \mathrm{e}^{0}_{i}(\mathbf{x},t) = \mathrm{e}(\mathbf{x},t)/D. \tag{32}$$

The study of multi-scale approach from atomistic/molecular to mesoscale/continuum levels still has challenges for the systems such as non-equilibrium dynamics and thermally sensitive systems since the communication between scales drastically increases. To resolve the issue, we need to develop more effective intermediate level or bridging methods, which can also be incorporated to the multi-physics analysis.

Device-scale/process scale level

A more physically accurate representation includes space–time dependencies on physical parameters via conservation laws as well as electrochemistry based on irreversible thermodynamics. This model for PEMFC system consists of an integrated assembly of several interacting physical components, each comprising multi-dimensional, -physical transport, and electrochemical reaction processes. There are seven chambers in the model, the GCs, the GDLs, and the CLs both on anode and the cathode sides, and a central PEM region. This device-level model is based on multi-phase continuum mechanics model coupled with species, and energy conservation along with electrochemistry. The descriptive equations for various sub-components are integrated and incorporated

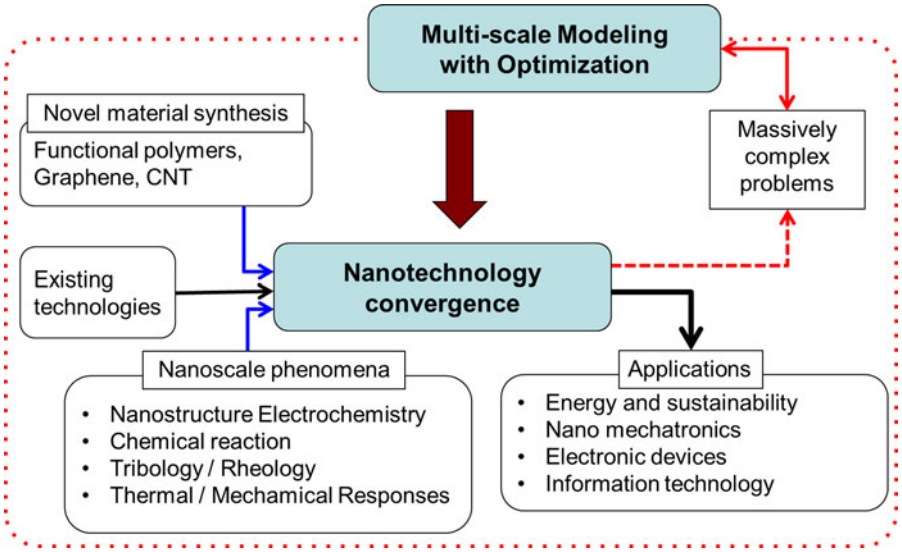

Fig. 12 The multi-scale approach with the system optimization procedure and nanotechnology convergence

into the optimization framework. Although this approach primarily originated from continuum mechanics, one can obtain spatial dependencies and temporal resolution of physical parameters through an optimization scheme. The process level comprises three subsystems (1) fuel processing, (2) PEMFC stack, and (3) post-combustion. The design questions at this level are sensitivity and risk analyses and optimization of network connections of these subsystems and the individual components within each subsystem. In addition, the process operation requires handling external disturbances, model uncertainties, future upgrades and the ability to incorporate technological advances. State-of-the-art flowsheet optimization strategies based on black-box or phenomenological models have some predictive capabilities, but these are usually limited to early stage decision-making and not detailed design (Biegler et al. 1997). Nevertheless, this limitation can be remedied through integration with ROMs (Lang et al. 2011). This provides motivation for stepping down each level toward the "bottom," where the bottom-most level is electronic/atomistic. The multi-scale approach combined with the system design procedure will provide the optimized solution for complex combinatorial problems of nanotechnology development resulting from the convergence of existing technologies and novel nanotechnology, and will address the broad range of applications utilizing nanoscale materials and phenomena (Fig. 12).

Summary and conclusions

A holistic strategy in hierarchical modeling, which enables communication among physical phenomena at different length and time scales and provides understanding of system properties with nanoscale parameters, has been presented in this paper in the context of the PEMFC benchmark system. Through representative modeling methods at each scale, physical phenomena in each subsystem have been explained and possibilities for integrating different scale methods were provided. As explained in the benchmark system, bridging methodologies, which enable an organic linkage of subsystems, were discussed as a key to build the successful multi-scale model. Here, molecular to continuum scales can be bridged by introducing LBM, which characterizes a broad range from mesoscale to continuum level behavior. Moreover, molecular level models with quantum level parameters can be incorporated to LBM via coarse-graining procedure using ROM, which simplifies detailed molecular structures while transferring relevant physical parameters to upper scale levels. The parameters in coarse-grained model include nanoscopic information obtained stochastically from sequential coarse-graining procedures that include ab initio and bead-spring models.

The development of the hierarchical multi-scale paradigm consolidates theoretical analysis methods

and extends to large-scale design and decision-making at the process level, with models based on first-principles. Although the current integration method still has topics to be explored, recent significant advances in multi-scale modeling for each application will bring profound understanding of complex systems and lead to the multidisciplinary impact on the entire science and engineering fields. When molecular architecture becomes important, nanotechnology and convergence applications that deal with optimization can be resolved through the modeling paradigm presented in this paper.

Acknowledgements This study was supported by Korea Science & Engineering Foundation through the WCU Project.

References

Agarwal A, Biegler LT, Zitney SE (2009) Simulation and optimization of pressure swing adsorption systems using reduced-order modeling. Ind Eng Chem Res 48:2327–2343

Allen MP, Tildesley DJ (1996) Computer simulation of liquids. Clarendon, Oxford

Baxter SF, Battaglia VS, White RE (1999) Methanol fuel cell model: anode. J Electrochem Soc 146:437–447

Biegler LT, Grossman IE, Westerberg AW (1997) Systematic methods of chemical process design. Prentice-Hall, Upper Saddle River

Broughton JQ, Abraham FF, Bernstein N, Kaxiras E (1999) Concurrent coupling of length scales: methodology and application. Phys Rev B 60:2391–2403

Cancelliere A, Chang C, Foti E, Rothman DH, Succi S (1990) The permeability of a random medium: comparison of simulation with theory. Phys Fluids A 2:2085–2088

Chen S, Doolen GD (1998) Lattice Boltzmann method for fluid flows. Annu Rev Fluid Mech 30:329–364

Choe YK, Tsuchida E, Ikeshoji T, Ohira A, Kidena K (2010) An ab initio modeling study on a modeled hydrated polymer electrolyte membrane, sulfonated polyethersulfone (SPES). J Phys Chem B 114:2411–2421

Chung PS, Smith R, Vemuri SH, Jhon YI, Tak K, Moon I, Biegler LT, Jhon MS (2012) Multi-scale/multi-physical modeling in head/disk interface of magnetic data storage. J Appl Phys 111:07B712

Csanyi G, Albaret T, Payne MC, De Vita A (2004) "Learn on the fly": a hybrid classical and quantum-mechanical molecular dynamics simulation. Phys Rev Lett 93:175503

Dalton LR (2009) Theory-inspired development of organic electro-optic materials. Thin Solid Films 518:428–431

Delgado-Buscalioni R, Coveney PV (2003) Continuum-particle hybrid coupling for mass, momentum, and energy transfers in unsteady fluid flow. Phys Rev E 67:046704

Delle Site L, Kremer K (2005) Multiscale modeling of polymers on a surface: from ab initio density functional calculations of molecular adsorption to large scale properties. Int J Quantum Chem 101:733–739

Dohle H, Divisek J, Jung R (2000) Process engineering of the direct methanol fuel cell. J Power Sour 86:469–477

Doi M (2003) OCTA (Open computational tool for advanced material technology). Macromol Symp 195:101–108

Ergun S (1952) Fluid flow through packed column. Chem Eng Prog 48:89–94

Falk M (1980) An infrared study of water in perfluorosulfonate (Nafion) membranes. Can J Chem 58:1495–1501

Faller R (2004) Automatic coarse graining of polymers. Polymer 45:3869–3876

Flekkoy EG, Wagner G, Feder J (2000) Hybrid model for combined particle and continuum dynamics. Europhys Lett 52:271–276

Franco AA, Passot S, Fugier P, Anglade C, Billy E, Guetaz L, Guillet N, Vito ED, Mailley S (2009) PtxCoy catalysts degradation in PEFC environments: mechanistic insights I. Multiscale modeling. J Electrochem Soc 156:B410–B424

Ghai SS, Chung PS, Kim WT, Amon CH, Jhon MS (2006) Thermal modeling of a multilayered film via Taylor series expansion- and least squares-based-lattice Boltzmann method. IEEE Trans Magn 42:2474–2476

Gierke TD, Munn GE, Wilson FC (1981) The morphology in nafion perfluorinated membrane products, as determined by wide- and small-angle X-ray studies. J Polym Sci 19:1687–1704

Glotzer SC, Paul W (2002) Molecular and mesoscale simulation of polymers. Annu Rev Mater Res 32:401–436

Goddard W III, Merinov B, Van Duin A, Jacon T, Blanco M, Molinero V, Jang SS, Jang YH (2006) Multi-paradigm multi-scale simulations for fuel cell catalysts and membranes. Mol Simulat 32:251–268

Grest GS (1996) Grafted polymer brushes in polymeric matrices. J Chem Phys 105:5532–5541

Guo ZL, Zhao TS (2002) Lattice Boltzmann model for incompressible flows through porous media. Phys Rev E 66: 036304

Habenicht BF, Paddison SJ, Tuckerman ME (2010) The effects of the hydrophobic environment on proton mobility in perfluorosulfonic acid systems: an ab initio molecular dynamics study. J Mat Chem 20:6342–6351

Hadjiconstantinou NG (1999) Combining atomistic and continuum simulations of contact-line motion. Phys Rev E 59:2475–2478

Haubold HG, Vad T, Jungbluth H, Hiller P (2001) Nanostructure of NAFION: a SAXS study. Electrochim Acta 46:1559–1563

Hohenberg P, Kohn W (1964) Inhomogeneous electron gas. Phys Rev 136:B864–B871

Iuchi S, Izvekov S, Voth GA (2007) Are many-body electronic polarization effects important in liquid water? J Chem Phys 126:124505

Izvekov S, Voth GA (2005a) A multiscale coarse-graining method for biomolecular systems. J Phys Chem B 109: 2469–2473

Izvekov S, Voth GA (2005b) Multiscale coarse graining of liquid-state systems. J Chem Phys 123:134105–134117

Jensen F (1989) Introduction to computational chemistry. Wiley, Chichester

Jinnouchi R, Okazaki K (2003) Molecular dynamics study of transport phenomena inperfluorosulfonate ionomer membranes for polymer electrolyte fuel cell. J Electrochem Soc 150:E66–E73

Kim WT, Jhon, Zhou Y, Staroselsky I, Chen H (2005) Nanoscale air bearing modeling via lattice Boltzmann method. J Appl Phys 97:10P304

Komarov PV, Veselov IN, Chu PP, Khalatur PG, Khokhlov AR (2010) Atomistic and mesoscale simulation of polymer electrolyte membranes based on sulfonated poly(Ether Ether Ketone). Chem Phys Lett 487:291–296

Krishnan M, Verma A, Balasubramanian S (2001) Synthesis of agarose-metal/semiconductor nanoparticles having superior bacteriocidal activity and their simple conversion to metal-carbon composites. Proc Indian Acad Sci (Chem Sci) 113:579–586

Laio A, VandeVondele J, Röthlisberger U (2002) A Hamiltonian electrostatic coupling scheme for hybrid car-parrinello simulations. J Chem Phys 116:6941–6948

Lang Y-D, Malacina A, Biegler LT, Munteanu S, Madsen JI, Zitney SE (2009) Reduced order model based on principal component analysis for process simulation and optimization. Energy Fuel 23:1695–1706

Lang Y-D, Zitney SE, Biegler LT (2011) Optimization of IGCC processes with reduced order CFD models. Comp Chem Eng 35:1705–1717

Leach AR (2001) Molecular modeling: principles and applications. Longman, Harlow

Li J, Liao D, Yip S (1998) Coupling continuum to molecular-dynamics simulation: reflecting particle method and the field estimator. Phys Rev E 57:7259–7267

Mei R, Shyy W, Yu D, Luo L (2000) Lattice Boltzmann method for 3-D flows with curved boundary. J Comp Phys 161:680–699

Mench MM, Wang CY, Thynell S (2004) Direct dimethyl ether polymer electrolyte fuel cells for portable applications. J Electrochem Soc 151:A144–A150

Neri M, Anselmi C, Cascella M, Maritan A, Carloni P (2005) Coarse-grained model of proteins incorporating atomistic detail of the active site. Phys Rev Lett 95:218102

Nithiarasu P, Seetharamu KN, Sundararajan T (1997) Natural convective heat transfer in a fluid saturated variable porosity medium. Int J Heat Mass Tran 40:3955

O'Brien CP, Miller JB, Morreale BD, Gellman AJ (2011) The kinetics of H_2-D_2 exchange over Pd, Cu, and PdCu surfaces. J Phys Chem C 115:24221–24230

O'Connell ST, Thompson PA (1995) Molecular dynamics–continuum hybrid computations: a tool for studying complex fluid flows. Phys Rev E 52:R5792–R5795

Parr RG, Yang W (1994) Density-functional theory of atoms and molecules. Oxford University, New York

Porat Z, Fryer JR, Huxham M, Rubinstein I (1995) Electron microscopy investigation of the microstructure of nafion films. J Phys Chem 99:4667–4671

Rafii-Tabar H, Hua L, Cross M (1998) A multi-scale atomistic-continuum modeling of crack propagation in a two-dimensional macroscopic plate. J Phys Condens Matter 10:2375–2387

Ren X, Springer T, Zawodzinski T, Gottesfeld S (2000) Methanol transport through the Nafion membranes. Electro-osmotic drag effects on potential step measurements. J Electrochem Soc 147:466–474

Roche EJ, Pineri M, Duplessix R, Levelut AM (1981) Small-angle scattering studies of nafion membranes. J Polym Sci Polym Phys Ed 19:1–11

Roco MC, Mirkin CA, Hersam MC (2011) Nanotechnology research directions for societal needs in 2020. Springer, Berlin

Seminario JM (1996) Calculation of intramolecular force fields from second-derivative tensors. Int J Quantum Chem 60:1271–1277

Serrano E, Rus G, Garcia-Martinez J (2009) Nanotechnology for sustainable energy. Renew Sust Energy Rev 13:2373–2384

Shi Q, Izvekov S, Voth GA (2006) Mixed atomistic and coarse-grained molecular dynamics: simulation of a membrane-bound ion channel. J Phys Chem B 110:15045–15048

Smirnova JA, Zhigilei LV, Garrison BJ (1999) A combined molecular dynamics and finite element method technique applied to laser induced pressure wave propagation. Comput Phys Commun 118:11–16

Theodorou DN (2005) Hierarchical modeling of amorphous polymers. Comput Phys Commun 169:82–88

Ulherr A, Theodorou DN (1998) Hierarchical simulation approach to structure and dynamics of polymers. Curr Opin Solid State Mater Sci 3:544–551

Vafai K (1984) Convective flow and heat transfer in variable porosity media. J Fluid Mech 147:233–259

Villa E, Balaeff A, Mahadevan L, Schulten K (2004) Multiscale method for simulating protein-DNA complexes. Multiscale Model Sim 2:527–553

Wang YT, Izvekov S, Yan TY, Voth GA (2006) Multiscale coarse-graining of ionic liquids. J Phys Chem B 110: 3564–3575

Xu YS, Liu Y, Zu XZ, Huang GX (2006) Lattice Boltzmann simulation of molten carbonate fuel cell performance. J Electrochem Soc 153:A607–A613

Zhou J, Thorpe IF, Izvekov S, Voth GA (2007) Coarse-grained peptide modeling using a systematic multiscale approach. Biophys J 92:4289–4303

DOI 10.1007/978-3-319-05041-6_21
Reprinted from the *Journal of Nanoparticle Research*, DOI 10.1007/s11051-012-0949-7

REVIEW

Thermally rearranged (TR) polymer membranes with nanoengineered cavities tuned for CO_2 separation

Seungju Kim · Young Moo Lee

Received: 3 January 2012 / Accepted: 23 May 2012 / Published online: 23 June 2012

Abstract Membrane gas separation technology has been rapidly growing for industrial applications such as air separation, carbon dioxide (CO_2) separation from natural gas production, hydrogen separation, etc. Needs for CO_2 separation are increasing as carbon capture technology has been recognized as an essential part when combating the global warming issue. Membrane gas separation technology deals with mass transport phenomena through the membrane engineered on a sub-nanoscale controlling transport properties of small gas molecules such as CO_2, N_2, O_2, H_2, etc. In this review, we will report on the recent developments in capture technologies utilizing various membranes including nano-engineered thermally rearranged (TR) polymers. TR polymer membranes show high gas permeability as well as good separation properties, especially in CO_2 separation processes such as from post-combustion flue gas and natural gas sweetening.

Keywords Polymer membrane · CO_2 capture · Gas separation · Sustainable development

Special Issue Editors: Mamadou Diallo, Neil Fromer, Myung S. Jhon

This article is part of the Topical Collection on Nanotechnology for Sustainable Development

S. Kim · Y. M. Lee (✉)
School of Chemical Engineering, College of Engineering, Hanyang University, Seoul 133-791, Korea
e-mail: ymlee@hanyang.ac.kr

Y. M. Lee
WCU Department of Energy Engineering, Hanyang University, Seoul 133-791, Korea

Introduction

Global warming has been an important issue with climate change caused by greenhouse gases (Marchant and White 2011). The emission of carbon dioxide (CO_2), one of the most effective greenhouse gases, is rapidly growing with recent industrial development for the last several decades. However, fossil fuels, which have been used in most major industrial fields producing CO_2, are still the most efficient energy source. Carbon capture and storage (CCS) technology was introduced to reduce CO_2 concentration in the atmosphere and has been investigated for substantial installation. The CO_2 separation process is the challenging part known to be about 70 % of the total cost of the CCS process (Pires et al. 2011). The capture cost can be reduced by developing efficient CO_2 separation processes (Chu 2009; Gibbins and Chalmers 2008; Herzog 2001). Among CO_2 emission sources such as transportation or industrial activities, the emission from power generation, especially from coal-fired power plants, is regarded as the major source (Chu 2009). In post-combustion CO_2 capture, the CO_2 separation process is applied at the final stage of the

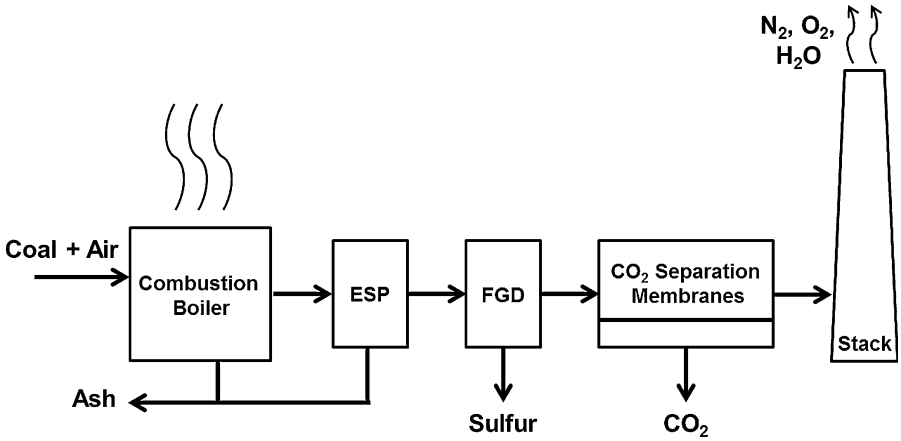

Fig. 1 Schematic of a flue gas cleanup train for a coal-fired power plant (Merkel et al. 2010)

power generation process after desulfurization as shown in Fig. 1. The post-combustion capture process is appropriate for existing facilities, so it can effectively reduce CO_2 emission (Pires et al. 2011; Terry 2007; Zhao et al. 2008).

Carbon capture technology

Post-combustion flue gas from coal-fired power plants mainly consists of carbon dioxide and nitrogen (N_2). The flue gas component consists of about 14 % CO_2 and ~80 % N_2 with a small amount of oxygen (O_2) and water vapor (H_2O) (<5 %) (Herzog 2001; Zhao et al. 2008). CO_2 in flue gas can be separated by means of various technology and materials using physical properties and/or chemical affinities of CO_2 molecules. The chemical absorption process uses CO_2 sorption properties of amine solvent. Monoethanolamine (MEA) solvent is the most well-known and applicable chemical agent for this technology. The absorption process uses chemical affinity of CO_2 molecules with sorbent. It has been developed for more than 60 years and many demonstration projects are in progress (Idem et al. 2005; Pires et al. 2011; Rao and Rubin 2002). Recently, rigid materials with intrinsic porosity are under investigation for the CO_2 separation process such as zeolites (Gramm et al. 2006; Pham et al. 2011; Shin et al. 2009), zeolitic imidazolate framework (ZIF) (Banerjee et al. 2008; Venna and Carreon 2009), polyhedral oligomeric silsesquioxanes (POSS) (Dasgupta et al. 2010; Li and Chung 2010), and metal–organic frameworks (MOFs) (Bae and Snurr 2011; Rosi et al. 2003; Rowsell et al. 2004, 2005). These materials possess well-defined three-dimensional micropores suitable for molecular sieving materials. Gas transport is based on gas diffusion into microporous structure, and thus CO_2 separation rate is dependent on pore size and porosity.

Membrane processes

A membrane is a selectively permeable material which can separate mixtures based on physical and chemical properties such as size, vapor pressure, affinity, etc. Membranes are usually thin layers with small holes or cavities which allow some molecules to pass through, while other molecules cannot (Brunetti et al. 2010; Mulder 1996). Gas separation membranes, which separate small gas molecules, control transport of gas molecules mainly by size and transport rate differences of gas molecules. Gas transport in membranes is described as both diffusion and sorption mechanism (Bernardo et al. 2009; Koros and Fleming 1993).

Permeation properties of gas molecules through membranes can be elucidated from diffusion and sorption which is described as

$$P = D \cdot S \tag{1}$$

where P, D, and S are permeation, diffusion, and solubility coefficient (Mulder 1996). Gas transport rate is usually based on a solution-diffusion mechanism: sorption of penetrant into the membrane, diffusion through the membrane, and desorption from the opposite side of the membrane. Transport rate is mainly determined by kinetic diameter of gas molecules and chemical affinity with membranes. Gas transport mechanism of polymer membranes is

dominated by the properties of polymers. For rubbery polymers such as poly(dimethyl siloxane) (PDMS), solubility-based permeation is dominant although it has an amorphous and rubbery structure and reasonable gas diffusion. However, for glassy polymers such as poly(1-trimethylsilyl-1-propyne) (PTMSP) or polyimides (PI), diffusion-based permeation is appropriate to explain the gas transport mechanism due to gas diffusion through free volume element in glassy polymers.

Gas permeability and selectivity are two important factors. Permeability, which is described in Barrer and GPU units (1 Barrer $= 10^{-10}$ cm^3 (STP) cm cm^{-2} s^{-1} cmHg^{-1}, 1 GPU $= 10^{-6}$ cm^3(STP) cm^{-2} s^{-1} cmHg^{-1}), interprets how fast gas molecules pass through the membrane. Selectivity is a membrane property that selectively picks target molecules (Mulder 1996). Selectivity of gases is defined as,

$$\alpha_{i/j} = \frac{P_i}{P_j} = \frac{D_i}{D_j} \cdot \frac{S_i}{S_j} \quad (2)$$

where P is permeability and $\alpha_{i/j}$ is selectivity in gas mixture i and j.

As shown in Fig. 2, some gas molecules have fast transport rates and some have slow rates determined by kinetic diameter and chemical affinity. For CO_2/N_2 separation application, their size difference is quite small (only 0.03 nm) so that gas separation for CO_2/N_2 is difficult unless high pressure is applied as a driving force. However, application of high pressure requires high energy cost in the flue gas separation process, increasing capture cost and lowering competitiveness of membrane is an option for capture technology. Membrane processes have many advantages such as small footprint, environmental suitability, economic efficiency, etc. In spite of its advantages, the membrane process is regarded as a minor process in current CCS technology because of low permeability particularly at low driving force (Baker 2002). It is important to have the right cavity size in polymer membranes, between 0.3 and 0.4 nm, in order to have high gas permeability and selectivity (Park et al. 2007). Diffusion selective membranes from glassy polymers have been developed for promising membrane materials with high performance for gas separation processes. Thermally rearranged (TR) polymer membranes, which will be discussed in the following section, have been investigated for diffusion selective membranes with nanoengineered free volume elements.

Many institutes and companies that have researched the development of membrane materials and processes have demonstrated membrane processes. Research Institute of Innovative Technology for the Earth (RITE) in Japan has reported on CCS technology including membrane separation. RITE reported a hollow fiber membrane module which has CO_2 permeance of 1,000 GPU and CO_2/N_2 selectivity of 40 (Kazama 2004).

Membrane Technology & Research Inc. in the US has reported membrane modules called Polaris^{TM} for CO_2 separation from flue gas (Merkel et al. 2010). They developed membrane materials as well as membrane processes and verified efficiency of membrane processes in energy consumption and total cost. Polaris^{TM} membranes were demonstrated in a coal-fired power plant for CO_2 separation from flue gas.

Polymers with intrinsic microporosity (PIMs) have been reported as a microporous glassy polymer and developed for membrane materials (Budd et al. 2006; Du et al. 2011; McKeown et al. 2006; McKeown and Budd 2010).

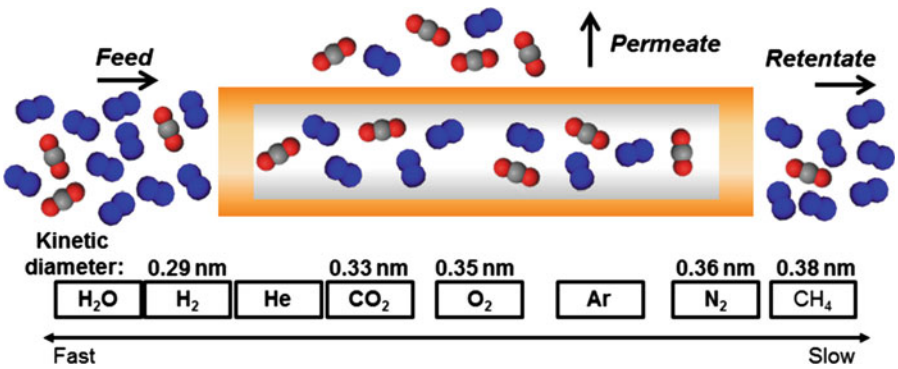

Fig. 2 Gas transport in membrane modules and kinetic diameters of small gas molecules (Freeman et al. 2006)

The membrane process is a good candidate to retrofit the CO_2 separation process from post-combustion flue gas (Powell and Qiao 2006). Currently, the chemical absorption process is the most available technology for practical application. However, the process cost is high due to the cost of amine solvent and excessive heat energy to regenerate CO_2 from solvent. Its long-term stability is poor with degradation, but the reason for the degradation is still an unsolved problem (Rochelle 2009). The membrane process is a desirable future technology to overcome the limit of the absorption process.

TR polymer membranes

Conventional polymeric membranes have been applied for many gas separation processes due to the advantage of manufacturing such as low cost, easy handling, and processability despite its poor chemical and thermal stability (Baker 2002). However, aromatic glassy polymers interconnected with heterocyclic rings such as polybenzoxazoles (PBO), polybenzothiazoles (PBZ), polypyrrolone (PPL), and polybenzimidazoles (PBI) have excellent chemical and thermal stability even in harsh conditions. These properties make the materials attractive for many applications; however, they also reduce the processability. This kind of polymer cannot be dissolved in common organic solvents for membrane formation and can only be dissolved in strong acids (Imai et al. 1965).

Recently, TR polymers have been studied as membrane materials. TR polymers are aromatic polymers with heterocyclic rings prepared by in situ thermal conversion of polyimides with *ortho*-functional groups (PIOFG). The thermal conversion mechanism of TR polymers was studied by Tullos's group (Tullos and Mathias 1999; Tullos et al. 1999) and has been studied for membrane materials by Lee's group (Calle and Lee 2011; Choi et al. 2010; Han et al. 2010a, b; Jung et al. 2010; Park et al. 2007). TR polymer has an aromatic structure with a rigid polymer backbone, so it does not have processability. However, the precursor polymer for TR polymer is an aromatic polyimide which is widely used for many industrial applications and easily dissolved in common organic solvents. Therefore, it is easy to form into any shape such as flat film and hollow fibers. TR polymer membranes can be prepared by simple thermal rearrangement after membrane formation with precursor polymers. Figure 3 describes the thermal conversion reaction from PIOFG to TR polymer. *Ortho*-functional group can be hydroxyl (–OH), thiol (–SH), and amine ($–NH_2$) groups and resulting TR polymers have PBO, PBZ, and polypyrrolone (PPL) structures. PBI structure can also be prepared from PPL (Han et al. 2010a). Those TR polymers are chemically and thermally stable aromatic polymers which have exceptional gas transport properties. During the thermal rearrangement process in solid state, a microporous structure is obtained. Thermal conversion results in the evolution of interconnected microcavities with a narrow cavity size distribution which is accessible for small gas molecules. TR polymers are novel microporous membrane materials with large free volume elements and narrow cavity sizes, and they induce fast mass transport of gas molecules and good separation properties. By conversion in solid state, free volume in PIOFG is dramatically increased when converted to TR polymer. This unusual free volume structure accounts for permeability with fast diffusion of gases. CO_2 permeability of TR polymer membranes is enhanced by more than two orders of magnitude over those of precursor polymers and typical glassy polymers.

From TR polymers, various PBO membranes have been studied (Han et al. 2010b; Jung et al. 2010; Park et al. 2007, 2010). The precursor of TR-PBO was prepared by conventional polycondensation reaction of dianhydride and diamine with hydroxyl function group in common polar aprotic solvents such as *N*-methyl-2-pyrrolidione (NMP), and hydroxyl group containing poly(amic acid) (HPAAc) was obtained. HPAAc was converted to hydroxyl polyimide (HPI) by various imidization methods such as thermal, chemical, and azeotropic imidizations, based on dehydration reaction of poly(amic acid) structure. The final thermal rearrangement of HPI for TR-PBO was followed at a high temperature of about 450 °C in inert atmosphere after membrane formation. The physical properties of TR-PBO membranes, such as gas permeability and selectivity, were distinguished by polymer backbone structures as well as the imidization method (Han et al. 2010b).

Polymer backbone structure influences physical properties as well as membrane performance. Commercial polyimides such as Matrimid® and P84® have

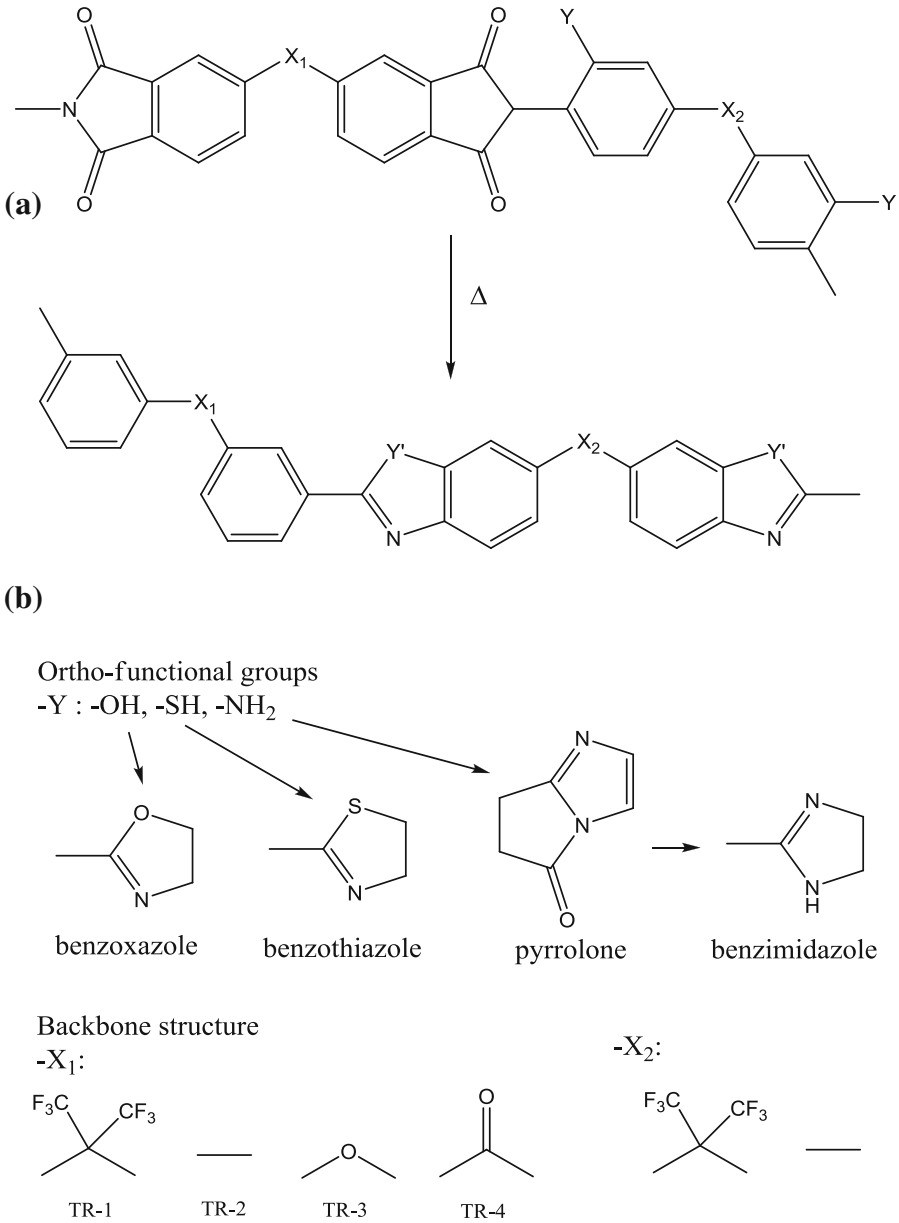

Fig. 3 Mechanism of thermal rearrangement from PIOFG to TR polymer: **a** chemical structure of PIOFG, **b** TR polymers

carbonyl linkage, and these membranes show good mechanical properties and high gas permeability due to free volume created by bulky carbonyl group (Bos et al. 2001; Tin et al. 2004). Bulkier fluorine-containing group can create larger free volume in polymers and improve membrane gas permeation properties. Many fluorine-containing polyimide membranes have been reported for gas separation membranes and showed better performance for gas separation (Cui et al. 2011; Das and Koros 2010; Wang et al. 2008). TR polymer membranes that have been prepared with fluorine group containing monomers (TR-1) in dianhydride and diamine presented the highest gas permeation properties with good selectivity. However, TR polymer membranes with ether linkage (TR-3) showed the lowest gas permeation properties due to packing effect caused by flexible ether linkage in the polymer backbone.

Positron annihilation lifetime spectroscopy (PALS) is commonly used to determine the cavity size distribution and relative intensity of free volume elements, which are critical for gas separation

materials. PALS provides polymer structures by the estimate of the free volume elements of polymers (Ammala et al. 2002). A positron, which is emitted from a radioactive ^{22}Na source injected into the sample, forms a spin parallel bound state with an electron called *ortho* positron (*o*Ps) and annihilates with an antiparallel electron. In the annihilation, *r*-photons are set free and detected. The lifetime of *o*Ps relies on the electron density and the free volume elements. For analysis of membrane materials, PALS measurement is appropriately used to investigate free volume element and cavity size distribution. Moreover, it can provide an explanation of the transport mechanism of small gases. Compared to diffraction analysis using X-ray, PALS measurement can detect cavity size of various materials, even amorphous polymer, more accurately (Anderson et al. 2008; Merkel et al. 2003).

Table 1 describes physical properties and free volume characterization of representative highly permeable polymers such as PTMSP, PIMs, and TR polymers. By calculation of τ_3 and τ_4, cavity size in bimodal systems can be determined. Typical glassy polymers such as polyimide (PI) and polysulfone (PSf), which have low fractional free volume, are depicted as only unimodal cavity distribution. However, highly permeable polymers, as shown in Table 1, are described with bimodal cavity distribution. Larger cavity size of TR polymers was about 8–10 Å (1 Å = 0.1 nm), which was efficient for fast mass transport and high permeability. Small cavity size of TR polymer membranes was about 3 Å, which was suitable for CO_2 separation. Note that kinetic diameter of CO_2 is 3.3 Å. Moreover, PALS data explain free volume increase during thermal rearrangement by relative intensity increase. Large free volume elements resulted in extraordinarily high gas permeability especially for CO_2 molecules (Han et al. 2010b).

Gas permeation properties of TR polymer membranes and their copolymer membranes are summarized and compared in Table 2. Typical glassy polymer membranes such as PI show diffusion-enhanced gas permeation. Therefore, smaller gas molecules such as H_2 and CO_2 show higher permeability compared with larger molecules such as N_2 and CH_4, but relatively low permeability for all the gas molecules. However, TR polymer membranes show very high gas permeability for smaller gas molecules such as H_2 due to enlarged free volume element. Nanoengineered and well-tuned cavities with <0.38 nm in cavity size, a little larger than kinetic diameter of CO_2 molecules (0.33 nm) and similar to that of CH_4 (0.38 nm), lead to fast gas transport of CO_2 and good selectivity over N_2 and CH_4. CO_2 permeability of TR polymer membranes presents over a few thousand Barrer, which is the highest level of permeability of typical glassy polymers reported.

Gas permeation properties of TR polymer membranes can be controlled by degree of thermal rearrangement, which is determined by thermal treatment conditions (Park et al. 2010). Thermal rearrangement of PIOFG was generated at around 300–350 °C and fully converted to TR polymer at around 450 °C. When PIOFG were thermally treated below 450 °C, partially rearranged TR polymers had an imide part as well as a benzoxazole part. Consequently, the gas permeation properties of those polymers were dependent on the degree of thermal conversion. Thermally kinetic studies of TR polymers were also carried out. The gas permeability and selectivity were tunable by degree of thermal conversion for specific gas separation applications.

Table 1 Comparison of physical properties and cavity characterization of highly permeable polymers (Han et al. 2010b; Staiger et al. 2008; Thomas et al. 2009)

Sample	Physical properties		Cavity characterization					
	Density (g/cm^3)	FFV	τ_3 (ns)	I_3 (%)	τ_4 (ns)	I_4 (%)	Cavity diameter (Å$_3$)	Cavity diameter (Å$_4$)
PTMSP	0.75	0.34	1.7	7.4	8.8	34	5.1	12.4
PIM-1	1.13	–	2.06	6.15	6.28	18.6	5.8	10.6
TR-tPBO	1.17	0.28	1.2	5.0	5.26	6.0	4.0	9.7
TR-aPBO	1.38	0.22	1.1	7.1	3.9	12.7	3.5	8.4
TR-cPBO	1.15	0.35	1.0	5.3	5.00	3.7	3.4	9.5

Table 2 Gas permeability and selectivities of TR polymer membranes

Sample code	Permeability (Barrer)					Selectivities		
	H_2	CO_2	O_2	N_2	CH_4	O_2/N_2	CO_2/N_2	CO_2/CH_4
TR-PBO series (Park et al. 2007, 2010)								
TR-1	2,774	4,045	747	156	73	4.8	26	55
TR-2	444	597	93	20	15	4.7	30	41
TR-3	91	73	14	2.3	1	6.1	31	58
TR-4	356	469	81	15	10	5.4	31	41
TR-PBI (Han et al. 2010a)								
PAI	36	24	3	0.7	0.3	4.1	35	92
PPL	376	234	65	13.0	8.0	4.9	18	29
TR-PBI	1,779	1,624	337	62.0	35	5.4	26	46
PBO–PPL copolymer (Choi et al. 2010)								
TR-PBO	4,194	4,201	1,092	284	151	3.9	15	28
PBO–PPL 8:2	1,989	1,874	421	94	50	4.5	20	37
PBO–PPL 5:5	2,895	1,805	475	85	46	5.6	21	39
PBO–PPL 2:8	1,680	525	132	18	6.7	7.3	29	78
PPL	376	234	65	13	8.1	4.9	18	29
PBO–PI copolymer (Jung et al. 2010)								
TR-PBO	1,228	1,014	220	48	41	4.6	21	24
PBO–PI 8:2	623	389	90	18	14	4.9	21	27
PBO–PI 5:5	47	25	4.8	0.82	0.65	5.8	31	39
PBO–PI 2:8	38	11	2.2	0.4	0.3	5.7	29	38
PI	14	2.7	0.72	0.09	0.03	7.7	30	91

TR polymers with various monomers in dianhydride and diamine have shown different gas permeation properties. Commercial monomers such as 4,4′-hexafluoroisopropylidene diphthalic anhydride (6FDA), 1,2,3,5-benzentetra carboxylic dianhydride (PMDA), etc., as a dianhydride, and 2,2-bis(3-amino-4-hydroxyphenyl)hexafluoropropane (bisAPAF), etc., as a diamine were used to prepare precursor of TR polymers. Synthetic monomers, which were not commercially available, such as bis(*o*-aminophenol) monomer [e.g., 2,2-bis(4-(4-amino-3-hydroxyphenoxy)phenyl)-hexafluoropropane (6FBAHPP)] (Calle and Lee 2011), were also introduced. Because TR polymer membranes with bulky hexafluorine groups present the highest gas permeation properties as well as fractional free volume, a monomer with bulky fluorine groups and with ether linkages was introduced. TR poly(ether-benzoxazole) (TR-PEBO) membrane was prepared to observe the effect of chain flexibility on physical properties and gas permeation properties (Calle and Lee 2011). TR polymers with flexible polymer backbone showed large rotational freedom. Thermal rearrangement of those polymers occurred at lower temperature and mild conditions. The full conversion to TR polymers was achieved at 400 °C, which was lower than the conventional TR temperature.

Copolymerization was introduced to control physical properties as well as to confirm the effect of thermal rearrangement. Poly(benzoxazole-*co*-imide) membranes were obtained from the thermal rearrangement of poly(hydroxyl imide-*co*-imide) (Jung et al. 2010). From TR-PBO-*co*-PI membranes, gas permeability and selectivity were easily controlled by varying composition of the imide part during copolymerization. Size and distribution of free volume elements and cavities were created during thermal rearrangement. Another copolymer of TR polymers was studied with ladder-type polymer, polypyrrolone (PPL). Poly(benzoxazole-*co*-pyrrolone) was obtained by thermal rearrangement of precursors of polyimides with hydroxyl group for the benzoxazole part and

amino group for the pyrrolone part (Choi et al. 2010). PPL was introduced as a selective site due to its well-packed structure, and copolymers showed relatively high selectivity. TR PBO–PPL copolymer presented structural synergy effect for selectivity and permeability. As PPL contents increased, as a selective part, selectivity increased. Rigid PPL structure improved molecular sieving effect and overcame original material selectivity. As described in Table 2, gas separation properties of TR copolymer membranes can be tuned with well-defined nanoengineered free volume element or cavities. PBI was prepared by a thermal rearrangement process (Han et al. 2010a). Conventional PBI shows very high thermal and chemical stability as well as a high glass transition temperature; therefore, PBI has been used in applications with harsh conditions. However, due to its strong chemical stability, it is difficult to prepare PBI membranes using conventional solvent (Allcock et al. 2003). TR-PBI was prepared from TR-PPL precursor. PPL has rigid and strong backbone structure, but imide linkage in PPL is weak at alkaline condition. TR-PBI was prepared by simple thermal treatment after alkaline hydrolysis of TR-PPL. During thermal rearrangement, microporous characteristics were obtained and gas permeation properties were enhanced compared to the precursors. TR-PBI membranes show much higher gas transport performance than conventional PBI membranes and are widely applicable for various gas separation processes.

Figure 4 shows the relationship of permeability and selectivity for CO_2/N_2 separation, which was introduced in data collection from literature to describe the trade-off relationship of gas permeability and selectivity (Robeson 2008). Robeson plotted gas permeability and selectivity data for various gas separation applications. From data collection, he demonstrated the upper bound as a performance limit of membrane materials. Many polymeric membrane materials have been developed in the last several decades; however, only some of the materials pass through the upper bound. However, as shown in Fig. 4, all TR polymer membranes are located near and some of them are beyond the upper bound. TR polymer membranes show much higher performance than any of the polymeric membranes.

Various TR polymer membranes were fabricated into hollow fiber membrane modules as shown in Fig. 5. Hollow fibers are a typical membrane type for

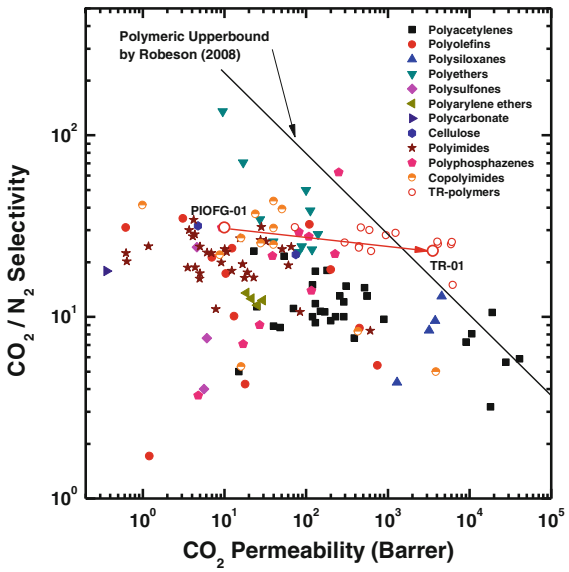

Fig. 4 Upper bound correlation for CO_2/N_2 separation

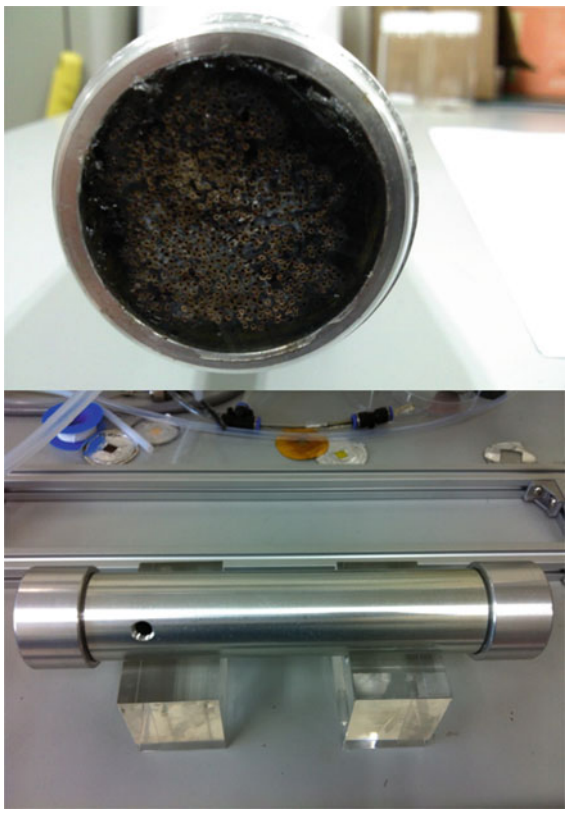

Fig. 5 TR polymer membrane modules (hollow fiber type)

gas separation modules. Hollow fiber membrane fabricated with the phase separation method has large membrane area per volume and packing density.

Therefore, many commercial membrane modules for gas separation are made of hollow fiber membrane modules (Clausi and Koros 2000; Kosuri and Koros 2008; Lin et al. 2002). TR polymers can be prepared into hollow fiber membranes from HPIs followed by a thermal rearrangement process (Kim et al. 2012). Laboratory scale TR-PBO hollow fiber membrane module showed CO_2 permeance of about 2,000 GPU with selectivity over nitrogen of about 13. Development of high performance membrane modules made of TR hollow fiber membranes will lead to effective CO_2 separation, and thus capture technology with TR membranes will be a promising option for CCS technology with low capture cost.

Conclusions

TR polymer membranes have recently made significant progress for gas separation applications. Gas permeability of TR polymer membranes was enhanced by two orders of magnitude over typical glassy polymer membranes; therefore, it can significantly reduce the industrial process cost and CO_2 capture cost. Microporous structures and gas transport properties of TR polymers are tunable by different thermal protocols and backbone structure of precursor polymers. Suitable TR membranes can be produced for specific gas separation applications by tuning the right cavity size. In particular, TR polymer membranes are engineered for CO_2 transport through polymer free volume elements and show extraordinarily high permeability with proper selectivity of CO_2 over N_2. TR polymer membranes can be one of the promising options for CCS technology with low carbon capture cost over conventional absorption and adsorption technology currently trying to scale up.

Acknowledgments This work was financially supported by Korea CCS R&D Center (KCRC), funded by the Ministry of Education, Science and Technology in Korea. YML appreciates support from WCU (World Class University) program, National Research Foundation (NRF) of the Korean Ministry of Science and Technology (No. R31-2008-000-10092-0), which we gratefully acknowledge.

References

Allcock HR, Lampe FW, Mark JE (2003) Contemporary polymer science. Pearson Education Inc., Upper Saddle River

Ammala A, Hill AJ, Meakin P, Pas SJ, Turney TW (2002) Degradation studies of polyolefins incorporating transparent nanoparticulate zinc oxide UV stabilizers. J Nanopart Res 4:167–174

Anderson CJ, Pas SJ, Arora G, Kentish SE, Hill AJ, Sandler SI, Stevens GW (2008) Effect of pyrolysis temperature and operating temperature on the performance of nanoporous carbon membranes. J Membr Sci 322: 19–27

Bae YS, Snurr RQ (2011) Development and evaluation of porous materials for carbon dioxide separation and capture. Angew Chem Int Ed 50:11586–11596

Baker RW (2002) Future directions of membrane gas separation technology. Ind Eng Chem Res 41:1393–1411

Banerjee R, Phan A, Wang B, Knobler C, Furukawa H, O'Keeffe M, Yaghi OM (2008) High-throughput synthesis of zeolitic imidazolate frameworks and application to CO_2 capture. Science 319:939–943

Bernardo P, Drioli E, Golemme G (2009) Membrane gas separation: a review/state of the art. Ind Eng Chem Res 48:4638–4663

Bos A, Pünt I, Strathmann H, Wessling M (2001) Suppression of gas separation membrane plasticization by homogeneous polymer blending. AIChE J 47:1088–1093

Brunetti A, Scura F, Barbieri G, Drioli E (2010) Membrane technologies for CO_2 separation. J Membr Sci 359: 115–125

Budd PM, McKeown NB, Fritsch D (2006) Polymers of intrinsic microporosity (PIMs): high free volume polymers for membrane applications. Macromol Symp 245–246: 403–405

Calle M, Lee YM (2011) Thermally rearranged (TR) poly(ether-benzoxazole) membranes for gas separation. Macromolecules 44:1156–1165

Choi JI, Jung CH, Han SH, Park HB, Lee YM (2010) Thermally rearranged (TR) poly(benzoxazole-*co*-pyrrolone) membranes tuned for high gas permeability and selectivity. J Membr Sci 349:358–368

Chu S (2009) Carbon capture and sequestration. Science 325:1599

Clausi DT, Koros WJ (2000) Formation of defect-free polyimide hollow fiber membranes for gas separations. J Membr Sci 167:79–89

Cui L, Qiu W, Paul DR, Koros WJ (2011) Physical aging of 6FDA-based polyimide membranes monitored by gas permeability. Polymer 52:3374–3380

Das M, Koros WJ (2010) Performance of 6FDA–6FpDA polyimide for propylene/propane separations. J Membr Sci 365:399–408

Dasgupta B, Sen SK, Banerjee S (2010) Aminoethylaminopropylisobutyl POSS—polyimide nanocomposite membranes and their gas transport properties. Mater Sci Eng B 168:30–35

Du N, Park HB, Robertson GP, Dal-Cin MM, Visser T, Scoles L, Guiver MD (2011) Polymer nanosieve membranes for CO_2-capture applications. Nat Mater 10:372–375

Freeman B, Yampolskii Y, Pinnau I (2006) Materials science of membranes for gas and vapor separation. Wiley, Chichester

Gibbins J, Chalmers H (2008) Carbon capture and storage. Energy Policy 36:4317–4322

Gramm F, Baerlocher C, McCusker LB, Warrender SJ, Wright PA, Han B, Hong SB, Liu Z, Ohsuna T, Terasaki O (2006) Complex zeolite structure solved by combining powder diffraction and electron microscopy. Nature 444:79–81

Han SH, Lee JE, Lee KJ, Park HB, Lee YM (2010a) Highly gas permeable and microporous polybenzimidazole membrane by thermal rearrangement. J Membr Sci 357:143–151

Han SH, Misdan N, Kim S, Doherty CM, Hill AJ, Lee YM (2010b) Thermally rearranged (TR) polybenzoxazole: effects of diverse imidization routes on physical properties and gas transport behaviors. Macromolecules 43:7657–7667

Herzog HJ (2001) Peer reviewed: what future for carbon capture and sequestration? Environ Sci Technol 35:148A–153A

Idem R, Wilson M, Tontiwachwuthikul P, Chakma A, Veawab A, Aroonwilas A, Gelowitz D (2005) Pilot plant studies of the CO_2 capture performance of aqueous MEA and mixed MEA/MDEA solvents at the University of Regina CO_2 capture technology development plant and the boundary dam CO_2 capture demonstration plant. Ind Eng Chem Res 45:2414–2420

Imai Y, Taoka I, Uno K, Iwakura Y (1965) Polybenzoxazoles and polybenzothiazoles. Die Makromol Chem 83:167–178

Jung CH, Lee JE, Han SH, Park HB, Lee YM (2010) Highly permeable and selective poly(benzoxazole-*co*-imide) membranes for gas separation. J Membr Sci 350:301–309

Kazama S (2004) In: CO_2 separation with molecular gate membrane. GCEP Energy Workshops, Stanford, Palo Alto, CA

Kim S, Han SH, Lee YM (2012) Thermally rearranged (TR) polybenzoxazole hollow fiber membranes for CO_2 capture. J Membr Sci 403–404:169–178

Koros WJ, Fleming GK (1993) Membrane-based gas separation. J Membr Sci 83:1–80

Kosuri MR, Koros WJ (2008) Defect-free asymmetric hollow fiber membranes from Torlon®, a polyamide-imide polymer, for high-pressure CO_2 separations. J Membr Sci 320:65–72

Li Y, Chung T-S (2010) Molecular-level mixed matrix membranes comprising Pebax® and POSS for hydrogen purification via preferential CO_2 removal. Int J Hydrogen Energy 35:10560–10568

Lin K-Y, Wang D-M, Lai J-Y (2002) Nonsolvent-Induced gelation and its effect on membrane morphology. Macromolecules 35:6697–6706

Marchant G, White A (2011) An international nanoscience advisory board to improve and harmonize nanotechnology oversight. J Nanopart Res 13:1489–1498

McKeown NB, Budd PM (2010) Exploitation of intrinsic microporosity in polymer-based materials. Macromolecules 43:5163–5176

McKeown NB, Gahnem B, Msayib KJ, Budd PM, Tattershall CE, Mahmood K, Tan S, Book D, Langmi HW, Walton A (2006) Towards polymer-based hydrogen storage materials: engineering ultramicroporous cavities within polymers of intrinsic microporosity. Angew Chem Int Ed 45:1804–1807

Merkel TC, He Z, Pinnau I, Freeman BD, Meakin P, Hill AJ (2003) Effect of nanoparticles on gas sorption and transport in poly(1-trimethylsilyl-1-propyne). Macromolecules 36:6844–6855

Merkel TC, Lin H, Wei X, Baker R (2010) Power plant post-combustion carbon dioxide capture: an opportunity for membranes. J Membr Sci 359:126–139

Mulder M (1996) Basic principles of membrane technology. Kluwer Academic Publishers, Dordrecht

Park HB, Jung CH, Lee YM, Hill AJ, Pas SJ, Mudie ST, Van Wagner E, Freeman BD, Cookson DJ (2007) Polymers with cavities tuned for fast selective transport of small molecules and ions. Science 318:254–258

Park HB, Han SH, Jung CH, Lee YM, Hill AJ (2010) Thermally rearranged (TR) polymer membranes for CO_2 separation. J Membr Sci 359:11–24

Pham TCT, Kim HS, Yoon KB (2011) Growth of uniformly oriented silica MFI and BEA zeolite films on substrates. Science 334:1533–1538

Pires JCM, Martins FG, Alvim-Ferraz MCM, Simões M (2011) Recent developments on carbon capture and storage: an overview. Chem Eng Res Des 89:1446–1460

Powell CE, Qiao GG (2006) Polymeric CO_2/N_2 gas separation membranes for the capture of carbon dioxide from power plant flue gases. J Membr Sci 279:1–49

Rao AB, Rubin ES (2002) A technical, economic, and environmental assessment of amine-based CO_2 capture technology for power plant greenhouse gas control. Environ Sci Technol 36:4467–4475

Robeson LM (2008) The upper bound revisited. J Membr Sci 320:390–400

Rochelle GT (2009) Amine scrubbing for CO_2 capture. Science 325:1652–1654

Rosi NL, Eckert J, Eddaoudi M, Vodak DT, Kim J, O'Keeffe M, Yaghi OM (2003) Hydrogen storage in microporous metal-organic frameworks. Science 300:1127–1129

Rowsell JLC, Millward AR, Park KS, Yaghi OM (2004) Hydrogen sorption in functionalized metal–organic frameworks. J Am Chem Soc 126:5666–5667

Rowsell JLC, Yaghi OM, Chen B, Ockwig NW, Millward AR, Contreras DS (2005) Cover picture: strategies for hydrogen storage in metal–organic frameworks/high H_2 adsorption in a microporous metal–organic framework with open metal sites. Angew Chem Int Ed 44:4647

Shin J, Camblor MA, Woo HC, Miller SR, Wright PA, Hong SB (2009) PST-1: a synthetic small-pore zeolite that selectively adsorbs H_2. Angew Chem Int Ed 121:6775–6777

Staiger CL, Pas SJ, Hill AJ, Cornelius CJ (2008) Gas separation, free volume distribution, and physical aging of a highly microporous spirobisindane polymer. Chem Mater 20: 2606–2608

Terry FW (2007) Combustion processes for carbon capture. Proc Combust Inst 31:31–47

Thomas S, Pinnau I, Du N, Guiver MD (2009) Pure- and mixed-gas permeation properties of a microporous spirobisindane-based ladder polymer (PIM-1). J Membr Sci 333:125–131

Tin PS, Chung T-S, Liu Y, Wang R (2004) Separation of CO_2/CH_4 through carbon molecular sieve membranes derived from P84 polyimide. Carbon 42:3123–3131

Tullos G, Mathias L (1999) Unexpected thermal conversion of hydroxy-containing polyimides to polybenzoxazoles. Polymer 40:3463–3468

Tullos GL, Powers JM, Jeskey SJ, Mathias LJ (1999) Thermal conversion of hydroxy-containing imides to benzoxazoles: polymer and model compound study. Macromolecules 32:3598–3612

Venna SR, Carreon MA (2009) Highly permeable zeolite imidazolate framework-8 membranes for CO_2/CH_4 separation. J Am Chem Soc 132:76–78

Wang L, Cao Y, Zhou M, Liu Q, Ding X, Yuan Q (2008) Gas transport properties of 6FDA-TMPDA/MOCA copolyimides. Eur Polym J 44:225–232

Zhao L, Riensche E, Menzer R, Blum L, Stolten D (2008) A parametric study of CO_2/N_2 gas separation membrane processes for post-combustion capture. J Membr Sci 325:284–294

DOI 10.1007/978-3-319-05041-6_22
Reprinted from the *Journal of Nanoparticle Research*, DOI 10.1007/s11051-012-0793-9

RESEARCH PAPER

Local intermolecular interactions for selective CO_2 capture by zeolitic imidazole frameworks: energy decomposition analysis

Ji Young Park · Yoon Sup Lee · Yousung Jung

Received: 29 September 2011 / Accepted: 22 February 2012 / Published online: 24 March 2012

Abstract Intermolecular energy decomposition analysis (EDA) is reported for the binding of CO_2 with zeolitic imidazole frameworks (ZIF) to provide a molecular level interpretation of the recent capacity and selectivity measurements of several ZIFs and to suggest a theoretical guideline to improve their performance further, using 1 nm size of organic linker fragment of the ZIFs as a target molecule. The EDA suggests that the local electronic interaction of CO_2 and the substituent groups, mainly frozen density and polarization interactions with little charge transfer, is the primary binding interaction, but the electron correlation effects can be equally or more important depending on the binding geometry and functional groups. The present correlated calculations identify the preferred ZIF binding sites for various gases including CO_2 to be mostly near the benzene substituent groups rather than the plane of imidazole rings. We predict that the NH_2-substituted ZIF would have an enhanced capacity of CO_2 as compared to the NO_2-substituted ZIF that was recently synthesized and reported to be one of the materials with the best capacity results along with high gas selectivity. The present calculations may imply that the local functionality of the linking organics, rather than detailed framework structures, may be of primary importance in designing certain high capacity MOF or ZIF materials.

Keywords CO_2 capture · Zeolitic imidazole frameworks · Intermolecular interactions · Nanostructures · Sustainable development

Special Issue Editors: Mamadou Diallo, Neil Fromer, Myung S. Jhon

This article is part of the Topical Collection on Nanotechnology for Sustainable Development

Electronic supplementary material The online version of this article (doi:10.1007/s11051-012-0793-9) contains supplementary material, which is available to authorized users.

J. Y. Park · Y. S. Lee
Department of Chemistry, KAIST, 335 Gwahak-ro, Yuseong-gu, Daejeon, Korea
e-mail: yslee@kaist.edu

Y. Jung (✉)
Graduate School of Energy, Environment, Water, and Sustainability (EEWS), KAIST, 335 Gwahak-ro, Yuseong-gu, Daejeon, Korea
e-mail: ysjn@kaist.ac.kr

Introduction

In addition to generating and storing new eco-friendly and renewable energy sources (Yang et al. 2007; Samanta et al. 2006; Mueller and Ceder 2005; Mulder et al. 2005; Sagara et al. 2004), direct removal of carbon dioxide from vehicles or fossil fuels is an important global problem to be addressed urgently due to the global climate changes. Recently, new porous crystalline materials (Kitagawa et al. 2004; Brant et al. 2006; Park et al. 2006; Hayashi et al. 2007; Wang et al.

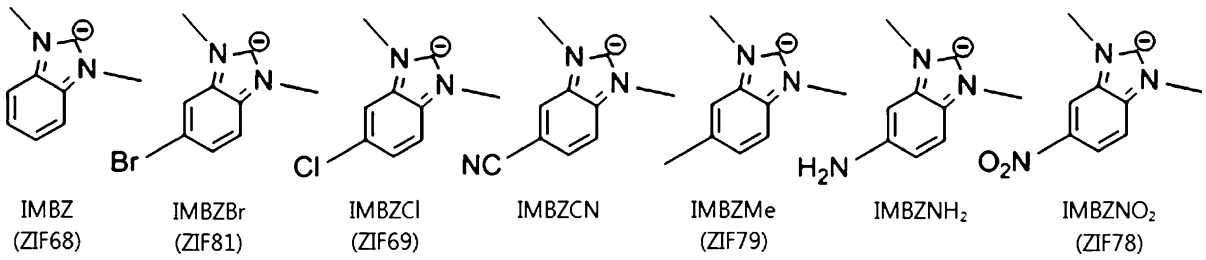

Fig. 1 Ditopic imidazolates considered in this work. IMBZ(ZIF68), IMBZBr(ZIF81), IMBZCl(ZIF69), IMBZMe(ZIF79) and $IMBZNO_2$(ZIF78) are used in the study of Banerjee et al. (2009) and IMBZCN and $IMBZNH_2$ are additionally suggested in this work

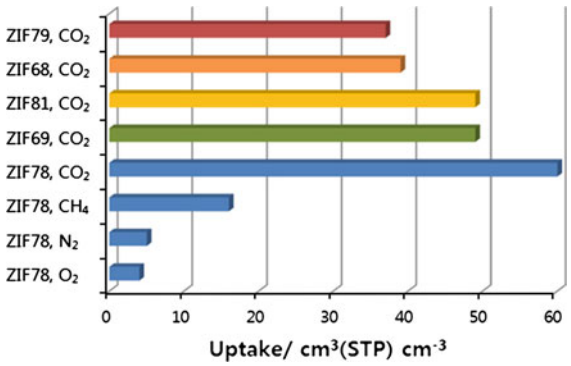

Fig. 2 The experimental adsorption isotherms data from Banerjee et al. (2009) for various ZIFs for different gases, CO_2, N_2, O_2, and CH_4 under 298 K and 800 Torr

2008; Banerjee et al. 2008) have been developed with stable tetrahedral networks that have large CO_2 adsorption capacities. Among them, zeolitic imidazole frameworks (ZIFs) (Hayashi et al. 2007; Wang et al. 2008; Banerjee et al. 2008, 2009) are promising ones that are composed of Zn and functionalized ditopic imidazolates (Fig. 1) linkers, each of them substituting the Si and O atoms of zeolites. Compared with metal organic frameworks (MOF) that are widely explored as hydrogen or CO_2 storage materials, ZIFs have higher thermal and chemical stability (Banerjee et al. 2009; Furukawa et al. 2010). The ZIF also shows remarkable CO_2 selectivity among various gases (Fig. 2) (Banerjee et al. 2008). Recently, MOFs that have high gas adsorption capacity but are also thermally and mechanically stable have been reported (Furukawa et al. 2010). Research efforts are thus being focused on finding new ways to increase capacities by controlling the pore size or introducing new functional groups, both experimentally and theoretically. As the pore size becomes larger, more gases can be placed in the pore. By a rough estimate, less than 10 carbon dioxide molecules can be placed in a 15.9 Å diameter pore at 77 K and 40 bar for some ZIFs (Banerjee et al. 2008). In this case, even for the high pressure given, only 1 or 2 molecules can be attached on the linker. When one carbon dioxide is bound on the linker, induced dipole moment may attract another carbon dioxide to be around and, resulting in storing more carbon dioxides in the pore. In general, synthesizing structures with larger pore size (precombustion) and more effective linker with stronger affinity (postcombustion) would be important for high capacity but application dependent. Of course, another issue for gas storage is gas selectivity among various gas mixtures. MOFs with open metal sites (Park et al. 2012) or amidoxime functionalities (Zulfigar et al. 2011) are another promising candidates for high capacities and selectivities.

Recently, as a large capacity CO_2 capture material, the Yaghi group synthesized (Banerjee et al. 2008) ZIF-78 (NO_2; nitrobenzoimidazolate) that has a large adsorption capacity as well as high CO_2 selectivity among N_2, O_2, and CH_4 gases, even though it has a relatively small surface area among other synthesized ZIFs. The ZIF-82 (CN; cyanideimidazolate) also showed a large capacity. From the fact that ZIF-78 and 82 have large CO_2 capacities, it was suggested that the dipole–quadrupole interactions between ZIFs and gases may be important because both ZIF-78 and ZIF-82 have lone pair electrons on N atoms of substituent groups.

Molecular dynamics simulations (Babarao and Jiang 2009; Liu et al. 2009; Rankin et al. 2009; Liu and Smit 2010; Pérez-Pellitero et al. 2010) and quantum chemical calculations were performed to provide insights into the CO_2 capture by porous materials. Molecular dynamics simulation studies suggested the possible binding sites of CO_2 to be near the substituent groups. Although these MD studies provided potentially useful insights into the possible binding modes of CO_2 in ZIFs, the results would depend critically on the empirical force field (FF)

used. For example, the FF used in the study of Pérez-Pellitero et al. (2010), namely Universal Force Field (UFF) (Rappe et al. 1992) is a general force field that is not optimized for the ZIF systems under consideration. Quantum chemical calculations are also performed by many groups. Vogiatzis et al. (2009) showed that lone pair electrons of nitrogen are a binding site in the general imidazole group in the context of ZIF systems. But in experimental ZIFs, both lone pair electrons are used in making conjugate orbitals on the imidazole ring because of the zinc coordinations, making these model systems not suitable to study ZIFs. Negri and Sendig (2007) studied the binding of CO_2 with conjugated ring systems, and more recently, Torrisi et al. (2009, 2010) also calculated the interactions between CO_2 with functionalized benzenes. The latter authors found various energy minimum structures and analyzed the origins of binding of CO_2 with C_6H_6, $C_6H_5NO_2$, $C_6H_5NH_2$, $C_6H_4(OH)_2$, $C_6H_5SO_3H$, and C_6H_5COOH. They found that the molecules that have lone pair electrons or polar groups involving acidic hydrogens have large CO_2-ligand affinity.

In this work, we explore various model systems that can best describe the experimental ZIF system while maintaining the size of systems under computational feasibility, and using them, attempt to provide the molecular level interpretation of the CO_2 binding of ZIF systems as well as binding sites. Although at high pressures the pore volume becomes important, the experimental conditions we are comparing our calculations with are measured at 1 bar (Banerjee et al. 2009) where there was no direct correlation between the pore metric and CO_2 update, and the CO_2 uptake was rather influenced primarily by functionality effects. To this end, we perform energy decomposition analysis and identify the key intermolecular interactions that are responsible for the strong binding and selectivity. On the basis of these understanding, we propose a new functional group that could have larger capacity and selectivity.

Methodology

Computational details

The minimum energy structures were optimized by B3LYP/6-311+G*, and reoptimized using RIMP2/VDZ(d) using the development version of QCHEM software package (Shao et al. 2006) to allow the long range correlation effects in the nonbonding interactions of CO_2 with various model ZIFs. For improved energetics on the optimized geometries (i.e., single point energy evaluation), we used scaled MP2 methods, SOSMP2 (Jung et al. 2004; Lochan et al. 2005; Jung and Head-Gordon 2006) and SCSMP2 (Grimme 2003), to correct usual overestimation trends of the conventional MP2. Indeed our results indicate that SOSMP2 and SCSMP2 systematically lower the binding strengths predicted in RIMP2. The VDZ(d) basis for zinc and cc-pVTZ basis (Peterson and Puzzarini 2005) for all other elements were used for correlated single point energy calculations (Hill and Platts 2008; Yousaf and Peterson 2009). Frozen core approximation was used in MP2 calculations.

Using the absolutely localized molecular orbitals (ALMO) energy decomposition analysis (Khaliullin et al. 2007), we decompose intermolecular interactions into the geometric distortion (GD), frozen density component (FRZ), polarization (POL), and the charge-transfer (CT) terms (Wu et al. 2009a, b).

$$\Delta E_{BINDING} = (\Delta E_{GD} + \Delta E_{FRZ} + \Delta E_{POL} + \Delta E_{CT} + \Delta E_{HF-BSSE}) + \Delta E_{CORR} \quad (1)$$

In Eq. 1, the first five terms in the parenthesis are calculated and analyzed using the Hartree–Fock wave function and the last term, ΔE_{CORR}, is the BSSE (basis set superposition error)-corrected correlation energy contribution that is computed at the scaled MP2 level in this study. The GD denotes the geometric distortion, and the frozen density term (FRZ) is understood by the energy associated with the interaction of two fragments under its isolated density when brought to a supermolecule complex without any density relaxation of fragments. Polarization (POL) and charge transfer (CT) lower the energy by allowing the fully relaxed electron densities, where POL corresponds to the intramolecular density relaxation and CT includes the intermolecular density relaxation and fully optimized delocalized MOs. The CT term is further divided as a sum of the charge transfer from ZIFs to gas, and from gas to ZIFs, plus higher order charge transfer correction terms which are typically negligible (Figgen et al. 2005). The HF-BSSE term is the BSSE correction for the HF energy. We note that to quantitatively compare with experiments in general, it is more appropriate to consider free energy rather than an electronic energy. However, in the present case, since the main purpose is to consider various model substituents, and predict the functional groups with

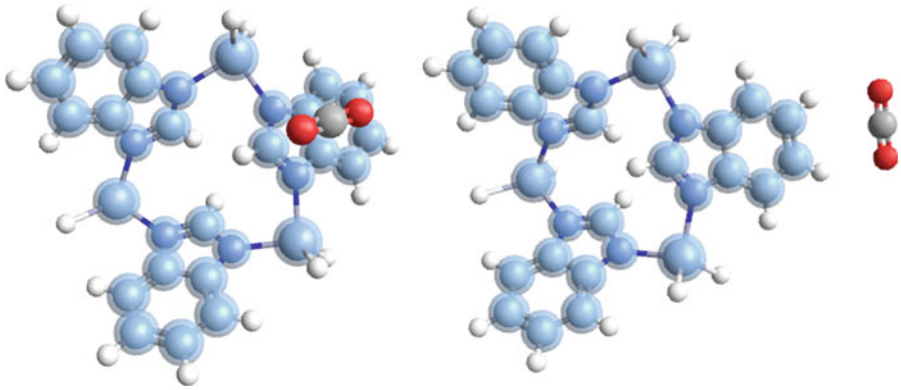

Fig. 3 The simplest cyclic building unit (REF) of the experimental ZIF (IMBZ) taken from the X-ray crystal structure database, interacting with CO_2. Atoms in *blue* are fixed during geometry optimization while CO_2 was fully relaxed. Shown *left* is the optimized ONIM structure, and shown *right* is the optimized NRSB structure. (Color figure online)

the higher *relative* binding affinity, we suppose the consideration of just the electronic energy contribution is sufficient. The latter reasoning is because a missing component in the free energy estimation of binding in our case is mainly the entropy of free CO_2 gas molecule and cage which is roughly the same for all model systems compared, adding only a constant in our predicted relative energetics.

Model system

Due to the large size of the basic building blocks of ZIFs, we used smaller models to simplify the system. In the experiment, the bridging imidazolate group has a −1 formal charge (Banerjee et al. 2008, 2009; Wu et al. 2009a, 2009b) with the oxidation state of Zn +2 to neutralize the framework. Each Zn atom is fully coordinated by imidazolate linkers in a tetrahedral manner, and thus the main role of Zn is regarded as supporting flat structures around imidazolate with negligible interactions with CO_2, unlike in the open metal sites of other MOFs that interact directly with CO_2. Geometry optimization of the [CO_2 + REF] complex, where REF denotes the fixed cyclic geometry taken from the X-ray crystal structure database of ZIF-68 shown in Fig. 3, supported this structural role of Zn, in which CO_2 was optimized geometrically near the center of imidazole ring or the substituent group, but remote from the Zn atom. Therefore, in our model, we decided to terminate Zn with hydrogen atoms after testing terminations with –H, –ZnH, –ZnH_2, –ZnH_3, –$Zn(CH_4)_2$, and –$Zn(CH_4)_3$. Some of the model structures were found to be unstable or did not yield a flat structure in the gas phase, but among them, the negatively charged –ZnH_2 model yielded the correct flat structure, similar natural bond orbital (NBO) charges

Table 1 The –ZnH_2 model system considered in this study to study the local binding with CO_2 with experimental ZIF systems, and calculated natural bond orbital (NBO) charges for the key atoms in the framework

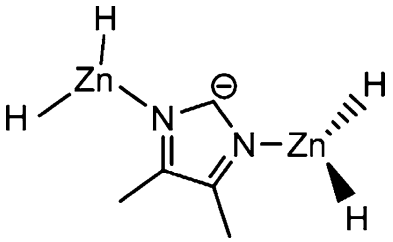

Targets	NBO charge			
	C	N	Zn	H
ZnH_2	0.20	−0.65	0.63	−0.41
REF*	0.24	−0.60	0.53	−0.44

Structures are optimized by B3LYP/6-31+G* level

* NBO charges of the reference ZIF unit obtained from the crystal structure (Wang et al. 2008). This consists of circularly connected three Zn-imidazolate units and is the smallest symmetric structure. The C is the carbon atom sandwiched between two nitrogens

as compared with REF (Table 1), negative formal charge on the imidazole ring, and remained stable with and without complexation with CO_2. Therefore, –ZnH_2 model was used for all calculations reported here.

To validate the chosen model, we compared the binding energies of CO_2 with the model and REF (Fig. 3) systems, which yielded −11.2 and −4.5 kJ/mol (model structure) versus −19.0 and −7.1 kJ/mol (reference structure) at RIMP2/cc-pVTZ for two different binding modes ONIM and NRSB, respectively (acronyms ONIM and NRSB are described in the next section). Although there is some quantitative difference between the reference and model calculations, the trends of the two binding modes are the

same, supporting the validity of the model. As will be described in "Results and discussion" section, our model also reproduces the experimental trend (ordering) of adsorption capacities of five different ZIFs with different substituents in excellent agreement, again justifying the validity of the model used in this paper. The fact that there are no experimental changes in properties of the frame upon binding of CO_2 is consistent with our calculations with weak and physical adsorption.

Results and discussion

Binding on the imidazole ring (ONIM)

In general, two binding sites can be considered in ZIFs, one on the imidazole ring (ONIM) and the other near the edge of imidazole or benzene substituent group (NRSB). Binding of CO_2 near Zn is generally not favorable because of the steric crowdedness from the neighboring linkers. In this section we consider ONIM configurations, and the NRBZ cases are considered in the next section.

When the carbon dioxide binds to the imidazole ring, the center of CO_2 carbon directs to the negatively charged carbon center of imidazole (Fig. 4). All of seven optimized structures considered in this study are similar and ZIF68 is shown in Fig. 4 as a representative. For all structures, there is no noticeable structural distortion on CO_2, and binding distances between the carbon center of CO_2 and the carbon center of imidazole ring range between 3.14 and 3.31 Å, indicating van der Waals complexes.

From the small orbital overlap under this binding distance, one might expect the dominant binding nature of carbon dioxide to be mainly the dispersion force and some electrostatic interactions between the quadrupole moment of CO_2 and local functionalities of the imidazole ring. The fact that the binding does not occur at the Hartree–Fock (HF) level and the binding occurs after the correlation treatment at the RIMP2 level, however, indicates that dispersion interactions are the main intermolecular interactions for this type of binding since the electrostatic interaction is usually well described at the HF level. The results are summarized in Table 2. All seven functional groups have similar interaction energies both at the HF and RIMP2 level, roughly +10 and −11 kJ/mol, respectively. Using the SCS-MP2 (or SOS-MP2) method which we regard as the most accurate energetics in the present study, the binding strength decreases by approximately 5 kJ/mol. A sharp difference in the capacity observed experimentally depending on different functional groups is thus not explained by considering the ONIM modes of binding alone.

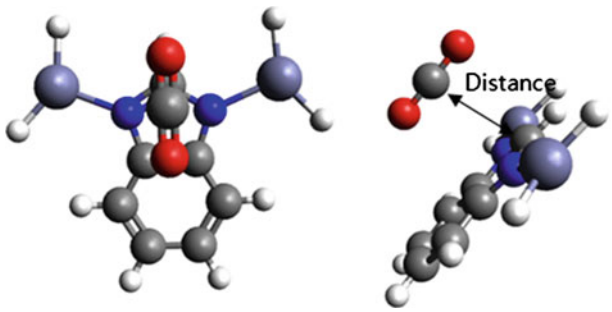

	Distance (Å)
BZ	3.15
Br	3.15
Cl	3.15
CN	3.31
CH_4	3.27
NH_2	3.16
NO_2	3.14

Fig. 4 *Top view* (*left*) and *side view* of IMBZ. Distance between C center of CO_2 and ZIFs are shown in a *side table*

Table 2 The interaction energies of CO_2 for the ONIM case: CO_2 binds to the center of imidazole ring of target molecules as in Fig. 3

	BZ	Br	Cl	CN	CH_4	NH_2	NO_2
HF (kJ/mol)	9.5	9.6	9.8	10.3	8.7	9.4	10.2
RIMP2 (kJ/mol)	−11.2	−11.0	−10.4	−10.5	−11.6	−11.3	−10.7
SOSMP2 (kJ/mol)	−4.1	−3.9	−3.4	−3.4	−4.6	−4.1	−3.6
SCSMP2 (kJ/mol)	−6.5	−6.3	−5.7	−5.8	−6.9	−6.5	−6.0

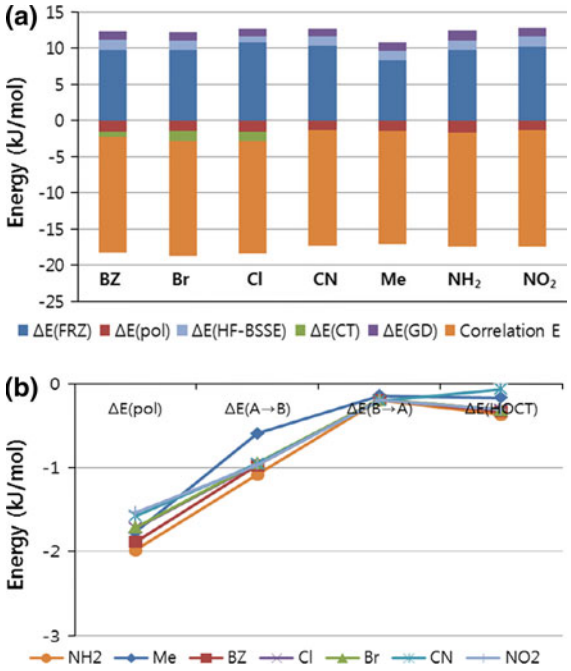

Fig. 5 **a** EDA results for the case of binding 'on the imidazole ring (ONIM)'. **b** More details about the polarization and charge transfer terms. The ΔE(A → B) means charge transfer from ZIFs to CO_2, ΔE(B → A) means charge transfer from CO_2 to ZIFs, and ΔE(HOCT) means higher order charge transfer terms

The energy decomposition analysis is summarized in Fig. 5. The largest unfavorable interaction component is frozen density term that arises from bringing the two monomer densities without relaxing the orbitals, but is recovered by the large dispersive correlation effects due to the parallel stacking geometry. There are some polarization effects and charge-transfer interactions, but their magnitudes are small, 1–2 kJ/mol and less than 1 kJ/mol, respectively. The relative importance of various interaction terms (FRZ, POL, and CT terms) is similar throughout different functional groups.

Binding near the substituted benzene groups (NRSB)

Optimized structures for the NRSB modes of binding are summarized in Fig. 6. Depending on the substituent groups, the binding distance from the carbon center of CO_2 to the center atom of substitute groups varies from 2.79 to 3.45 Å. There are also possibilities of weak hydrogen bonding between the oxygen of CO_2 and C–H groups of benzene rings, and they are indicated in Fig. 6 as arrows with the distances explicitly shown. The internal geometry of CO_2 after binding is more or less intact throughout different functional groups, with the largest bending of 4.1 occurring for NH_2.

The binding energetics for the NRSB cases are summarized in Table 3 and their decomposition analysis is summarized in Fig. 8. Unlike the ONIM modes of binding, the binding of CO_2 occurs for NRSB even at the HF level for all functional groups considered in this study except for the bare benzene case. The EDA indicates that those molecules with local dipole moments at the substituent site (CN, NH_2, and NO_2) all bind CO_2 at the HF level due to their electrostatic interaction with the quadrupole moment of CO_2. Electronegative atomic substituents such as Br and Cl also bind CO_2 molecule, but to a much smaller extent. These mainly electrostatic binding interactions at the HF level are then strengthened after correlation treatments by 3–10 kJ/mol at the SCS-MP2 level.

The order of SCS-MP2 binding strength is given as $NH_2 > NO_2 > CN > Br \approx Cl > Bz \approx Me$, among which NO_2, Br, Cl, Me, and BZ are synthesized and measured experimentally in the study of Banerjee et al. (2009). The capacity measurements (Banerjee et al. 2008) showed the binding order of $NO_2 > Br \approx Cl > Bz \approx Me$, in excellent agreement with our computed binding affinity order. From this agreement, we can suggest that the experimental capacity results reflect the binding affinity of CO_2, and the primary binding interaction and sites are the local interactions of CO_2 with the benzene substituent groups, rather than with the imidazole rings, consistent with experimental interpretations (Banerjee et al. 2008). A further examination of the pore structure of these ZIFs suggests that places where the imidazole rings reside may be spatially too tight for CO_2 to be stored. Since the binding distance of CO_2 with the imidazole rings is about 3.2 Å, at least the spherical space of about 6 Å in diameter may be needed as drawn in Fig. 7. The crystal structure implies that CO_2 would barely fit in a region where the imidazole rings can interact with CO_2, consistent with our finding that the capacity order agrees well with the NRSB modes of binding. The previous MD simulations also predicted the NRSB as possible and primary binding sites (Rankin et al. 2009). By contrast, spaces near the benzene substituents are open pores that are readily accessible to CO_2.

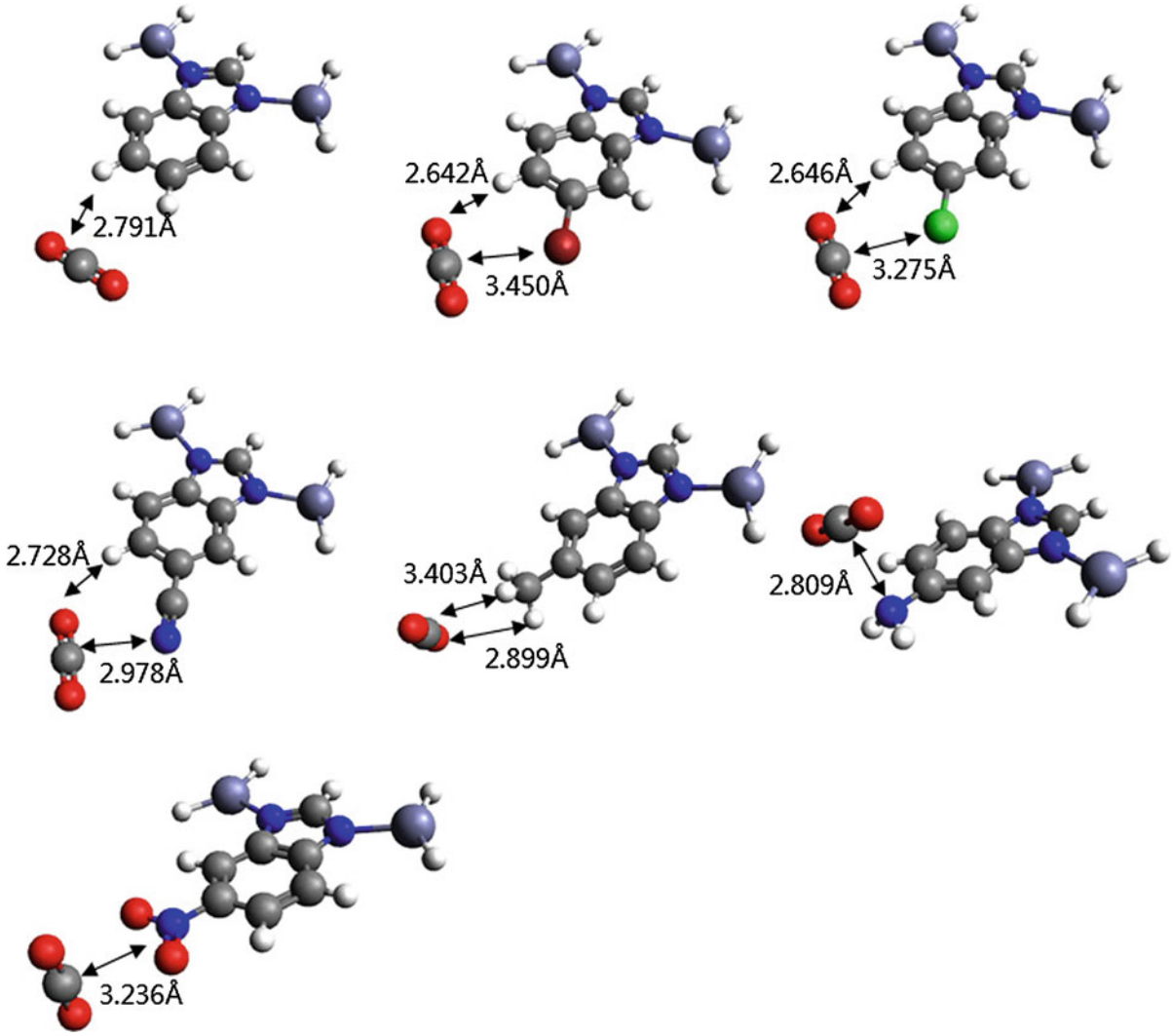

Fig. 6 Optimized geometries of CO_2 binding 'near the benzene substitute groups (NRBZ)'. From *left* to *right*; IMBZ, IMBZBr, IMBZCl (*1st row*), IMBZCN, IMBZMe, $IMBZNH_2$ (*2nd row*), and $IMBZNO_2$ (*3rd row*)

Table 3 The interaction energies of CO_2 for the NRSB case: CO_2 binds near the substituent groups of target molecules as in Fig. 5

	BZ	Br	Cl	CN	CH_4	NH_2	NO_2
HF (kJ/mol)	1.5	−0.8	−1.2	−4.4	1.5	−3.4	−8.2
RIMP2 (kJ/mol)	−4.5	−7.7	−7.5	−10.5	−4.2	−16.5	−12.6
SOSMP2 (kJ/mol)	−2.3	−4.5	−4.5	−7.1	−2.2	−10.6	−9.2
SCSMP2 (kJ/mol)	−3.0	−5.5	−5.5	−8.2	−2.9	−12.6	−10.3

The binding affinities of CO_2 with the ZIF model systems calculated here are in good agreement with the previous study of interactions of CO_2 with the isolated functionalized benzene molecules as shown in Table 3 (Torrisi et al. 2009, 2010). This important agreement suggests that in ZIFs the local interaction of substituted groups with CO_2 is most important to determine the binding strength without much perturbation from the

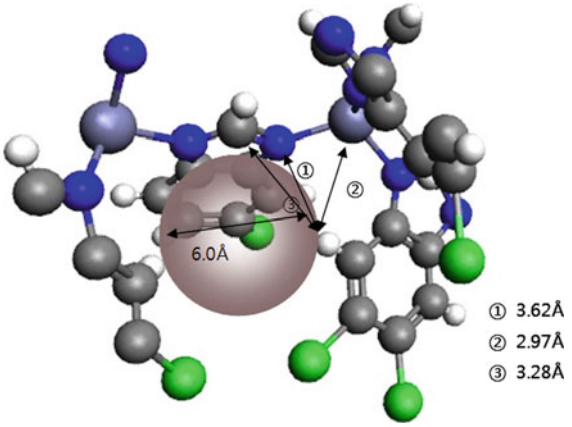

Fig. 7 The near-imidazole pore space of the experimental crystal structure of IMBZCl that may be accessible to CO_2 (Wang et al. 2008). The *shaded sphere* in *pink* is too crowded for CO_2 to be adsorbed. (Color figure online)

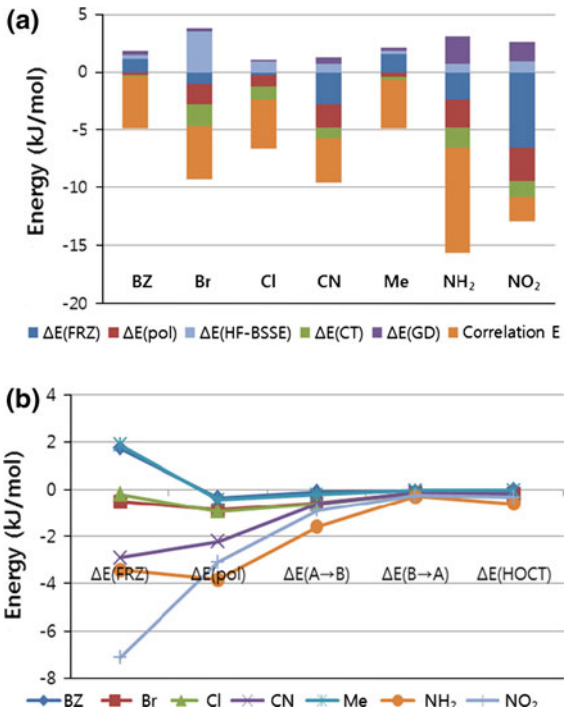

Fig. 8 **a** EDA results for the case of binding 'near the benzene substitute groups (NRBZ)'. **b** More details about the polarization and charge transfer terms

linker framework or the presence of metals. In other words, in the design of MOFs or ZIFs for higher CO_2 storage capacity, the present calculations suggest that the detailed structural effects may be secondary and the local functionality is of primary importance.

The EDA is summarized in Fig. 8. Again, electrostatic effects on the binding can be seen from the HF results: only the functional groups that are electronegative or have local dipole moments bind CO_2 at the HF level, with the NO_2 group having the strongest binding. The functionality that is predicted to have the highest binding strength is NH_2 which is bound by -3.4 kJ/mol at the HF level but by -12.6 kJ/mol at the SCS-MP2 level. This can be compared with the experimental NO_2 group, that is bound by -8.2 kJ/mol at the HF and by -10.3 at the SCS-MP2 level. Therefore, the stronger interaction of CO_2 with the NH_2 group as compared to NO_2 is largely a correlation effect. Frozen density and polarization effects account for 12%, charge transfer accounts for 8%, and the correlation effects (mainly dispersion) are responsible for 73% of the total interaction energy, unlike NO_2 where the largest contribution is electrostatic interactions.

In a very recent report of ZIFs that have large surface area and high CO_2 capacity, Morris et al. (2010) reported that the amine-substituted imidazole (direct attachment) has a high uptake for CO_2, but the system is different from the one considered in this study (6 in Fig. 1). In a computational interpretation for the measured high uptake, the authors suggested that the functionality's asymmetry and polarizability significantly influences the CO_2 uptake capacity, that is, imidazoles with asymmetric functionalization have greater capacity as compared with those with symmetric functionalization. We note that the symmetric frameworks that showed low capacity in the latter interpretation incidentally had functional groups with low local binding affinities toward CO_2 (i.e., methyl or chloride substituents), and therefore whether the observed low uptakes are due to the symmetry aspect or to the low local binding strength seems unclear. Additional computational interpretations and insights would be helpful.

Gas selectivity

Gas selectivity is considered in this section. In particular in the study of Banerjee et al. (2009), ZIF78 (with NO_2 group) showed a remarkable selectivity toward the CO_2 capture in a mixture of various other gases, CH_4, O_2, and N_2. We explain its molecular origin here.

Gases have local minimum between the benzene ring and the nitrogen center of the NO_2 substitute

Table 4 The calculated interaction energies of various gases (selectivity) for $IMBZNO_2$ (ZIF78): gases bind near the NO_2 groups of $IMBZNO_2$ (ZIF78), with optimized structures shown in Supporting Information

	CO_2	N_2	O_2	CH_4
HF (kJ/mol)	−8.2	10.5	9.1	9.1
RIMP2 (kJ/mol)	−12.6	−5.3	−3.9	−7.0
SOSMP2 (kJ/mol)	−9.2	−0.6	0.8	−1.8
SCSMP2 (kJ/mol)	−10.3	−2.1	−0.8	−3.5

group. Optimized structures are shown in Supporting Information. Binding distances are 3.24 Å(CO_2), 3.31 Å(N_2), 3.31 Å(O_2), and 3.47 Å(CH_4). In Table 4, our model system for the ZIF78 predicts that the decreasing order of binding strength is CO_2 (−10.3 kJ/mol) > CH_4 (−3.5) > N_2 (−2.1) > O_2 (−0.8), in reasonable agreement with experiment ($CO_2 > CH_4 > N_2 \approx O_2$). Using these SCS-MP2 energetics and a simple Boltzmann distribution, the CO_2/CH_4 (selectivity of CO_2 over CH4), CO_2/N_2 and CO_2/O_2 can be estimated to be 16, 27, and 45, respectively, which can be compared with estimated 10, 50, and 48, respectively, based on experiments (Banerjee et al. 2008). These simple estimates suggest that although there are quantitative differences between the experimental and calculated selectivities, the adsorption isotherms can be roughly understood by considering binding energy differences among gases.

The EDA analysis is shown in Fig. 9. Among various gases tested, only CO_2 molecule has negative interaction energy of isolated densities, perhaps due to specific interactions of the lone pair electrons of nitrogen of amino group and the electron deficient carbon of CO_2 (Torrisi et al. 2009), as well as the large quadrupole moment of CO_2. However, quadrupole moments alone cannot explain the overall adsorption trend since CH_4 has a zero quadrupole moment but has a larger capacity than O_2 and N_2 with nonzero quadrupole moments (Rallapalli et al. 2010). It was also suggested (Rallapalli et al. 2010) that there is a strong correlation between the polarizability of gases and the adsorption capacity of gas molecules in some metal–organic frameworks. Our EDA analysis, however, indicates that the frozen density, FRZ, term (in the absence of polarizability) is relatively more important than the intra and intermolecular electronic relaxation (POL, CT) and correlation effects, terms that are related to polarizability.

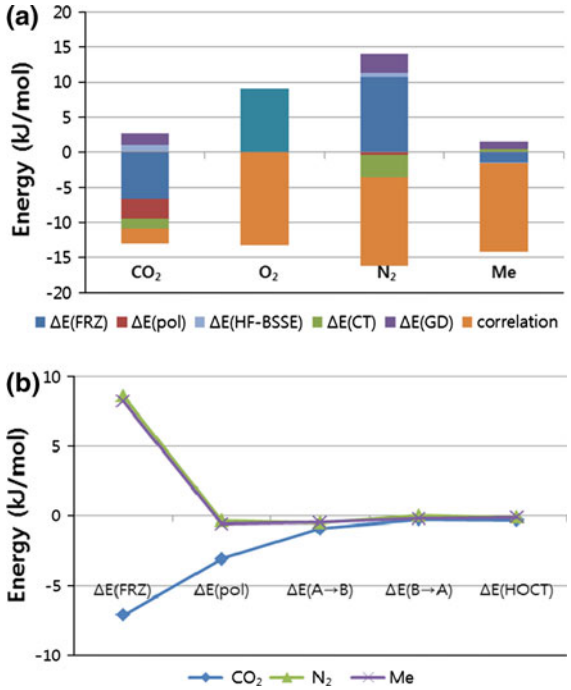

Fig. 9 **a** EDA results for the binding of various gases to the NO_2-substituted ZIF system. **b** More details about the frozen density, polarization, and charge transfer terms (The ALMO EDA is not implemented for a triplet ground state, and for O_2 only a separation of the total interaction energy into the positive HF and negative correlation contribution is thus given)

For the NO_2-substituted model, CO_2 is bound by −8.2 kJ/mol while the other gases are unbound by about 10 kJ/mol at the HF level. Due to the lack of favorable electrostatic interaction of the NO_2 substitute group with the other gases (N_2, O_2, CH_4), the latter gas molecules move between the benzene ring and the substitute group for rich electron density and favorable dispersion interactions (Fig. 9). For these gases, the optimized structures have relatively large face-to-face overlap between the gas molecules and the benzene rings or substituents. On the other hand, CO_2 prefers the position near the benzene substitute group to experience larger frozen density, polarization, and charge transfer effects. From the comparison of binding energy and energy decomposition analysis, polarization or charge transfer is larger for the NRSB case than for the ONIM case.

We also predicted the binding selectivity for the NH_2 case, which offers the tightest binding. The optimized binding sites are depicted in Supporting Information. Binding distances are 3.24 Å(CO_2), 3.13 Å(N_2), 3.20 Å(O_2), and 3.48 Å(CH_4). The

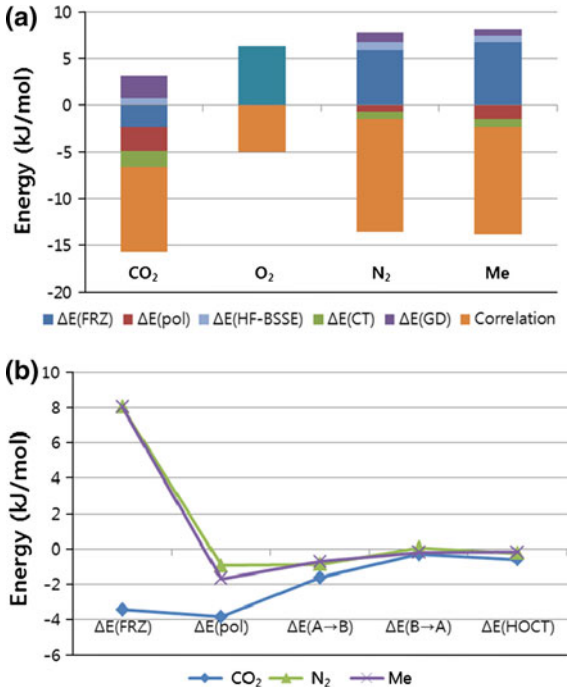

Fig. 10 **a** EDA results for the binding of various gases to the NH_2-substituted ZIF system (predicted). **b** More details about the frozen density, polarization, and charge transfer terms. See also the caption of Fig. 8

Table 5 The predicted interaction energies of various gases (selectivity) for $IMBZNH_2$: gases bind near the NH_2 groups of $IMBZNH_2$, with optimized structures shown in Supporting Information

	CO_2	N_2	O_2	CH_4
HF (kJ/mol)	−3.4	7.3	6.3	5.8
RIMP2 (kJ/mol)	−16.5	−8.1	−1.2	−9.2
SOSMP2 (kJ/mol)	−10.6	−3.1	2.5	−4.0
SCSMP2 (kJ/mol)	−12.6	−4.8	1.3	−5.7

binding sites of all gases are similar and on the lone pair electrons of the N center of NH_2. The EDA summarized in Fig. 10 indicates that there is a substantial correlation effect between the NH_2 group and CO_2, N_2 and CH_4, but large electrostatic effects are found only for CO_2. The FRZ term is favorable for binding only for CO_2.

Using the Boltzmann factor, we can calculate expected ratio of adsorbed gases for the NH_2 substituted case. From the calculation employing the SCSMP2 level binding energy in Table 5, we obtain 12 (CO_2/CH_4), 23 (CO_2/N_2), and 85 (CO_2/O_2). These results are comparable to or better than the NO_2-substituted case, namely, 16, 27, and 45. From these results, we suggest that the NH_2 substitute will result in a better adsorption capacity for CO_2 and also the good selectivity among N_2, O_2, and CH_4 gases than the NO_2 substituent group.

Conclusions

Based on the comparison of NBO charges and structural features with experimental ZIF system, we developed a model system that is terminated with ZnH_2 and captures the experimental binding energetics quite well. The most likely binding sites that reproduce the experimental binding capacity data are near the benzene substitute groups, rather than on the imidazole rings, consistent with previous MD simulations and experimental interpretations (Banerjee et al. 2009). The sterics of the confined space of the ZIF structures also suggest that the places near the imidazole rings may be too congested to be a capable binding site, unlike near the benzene substituents that are found in open pores and readily accessible to CO_2. The binding order of different functional groups observed experimentally is well reproduced in our calculations with the chosen model/method, justifying the analysis presented in this paper. The energy decomposition analysis suggests that the local electrostatic interaction between CO_2 and the substituent groups is the primary binding interaction, but the correlation effects can be equally or more important depending on the binding geometry and functional groups.

An excellent gas selectivity of ZIF78 toward CO_2 and the selectivity order among N_2, O_2, and CH_4 gases observed experimentally are reasonably reproduced computationally, where the primary interaction responsible for the selectivity is identified to be the electrostatic interaction of CO_2 with the local NO_2 group. The NH_2 group is then predicted to have the strongest binding for CO_2 among the ones tested in this work along with the high selectivity in a gas mixture due mainly to dispersion-like correlated effects. The present calculations may imply that the local functionality of the linking organics, rather than detailed framework structures, may be of primary importance in designing certain high capacity MOF or ZIF materials.

Acknowledgments YJ acknowledges the support of Basic Science Research Program (2010-0023018) and WCU (NRF R-31-2008-000-10055-0) program funded by the Korea Ministry of Education, Science and Technology. YSL is supported by grants (2010-0016243, 2010-0001632) funded by NRF and the EEWS program of KAIST.

References

Babarao R, Jiang J (2009) Unprecedentedly high selective adsorption of gas mixtures in *rho* zeolite-like metal-organic framework: a molecular simulation study. J Am Chem Soc 131:11417–11425

Banerjee R, Phan A, Wang B, Knobler C, Furukawa H, O'Keeffe M, Yaghi OM (2008) High-throughput synthesis of zeolitic imidazolate frameworks and application to CO_2 capture. Science 319:939–942

Banerjee R, Furukawa H, Britt D, Knobler C, O'Keeffe M, Yaghi OM (2009) Control of pore size and functionality in isoreticular zeolitic imidazolate frameworks and their carbon dioxide selective capture properties. J Am Chem Soc 131:3875–3877

Brant JA, Liu Y, Sava DF, Beauchamp D, Eddaoudi M (2006) Single-metal-ion-based molecular building blocks (MBBs) approach to the design and synthesis of metal-organic assemblies. J Mol Struct 796:160–164

Figgen D, Rauhut G, Dolg M, Stoll H (2005) Energy-consistent pseudopotentials for group 11 and 12 atoms: adjustment to multi-configuration Dirac–Hartree–Fock data. Chem Phys 311:227–244

Furukawa H, Ko N, Go YB, Aratani N, Choi SB, Choi E, Yazaydin AÖ, Snurr RQ, O'keeffe M, Kim J, Yaghi OM (2010) Ultrahigh porosity in metal-organic frameworks. Science 329:424–428

Grimme S (2003) Spin-component-scaled Møller–Plesset (SCS-MP) perturbation theory: a generalization of the MP approach with improved properties. J Chem Phys 118:9095

Hayashi H, Côté AP, Furukawa H, O'Keeffe M, Yaghi OM (2007) Zeolite a imidazolate frameworks. Nat Mater 6:501–506

Hill JG, Platts JA (2008) Auxiliary basis sets for density fitting-MP2 calculations: nonrelativistic triple-ζ all-electron correlation consistent basis sets for the 3*d* elements Sc–Zn. J Chem Phys 128:044104

Jung Y, Lochan R, Dutoi T, Head-Grodon M (2004) Scaled opposite spin second order Møller-Plesset correlation energy: an economical electronic structure method. J Chem Phys 121:9793

Jung Y, Head-Gordon M (2006) A fast correlated electronic structure method for computing interaction energies of van der Waals complexes applied to the fullerene-porphyrin dimer. Phys Chem Chem Phys 8:2831

Khaliullin RZ, Cobar EA, Lochan RC, Bell AT, Head-Gordon M (2007) Unravelling the origin of intermolecular interactions using absolutely localized molecular orbitals. J Phys Chem A 111:8753–8765

Kitagawa S, Kitaura R, Noro S (2004) Functional porous coordination polymers. Angew Chem Int Edn 43: 2334–2375

Liu B, Smit B (2010) Molecular simulation studies of separation of CO_2/N_2, CO_2/CH_4, and CH_4/N_2 by ZIFs. J Phys Chem C 114:8515–8522

Liu D, Zheng C, Yang Q, Zhong C (2009) Understanding the adsorption and diffusion of carbon dioxide in zeolitic imidazolate frameworks: a molecular simulation study. J Phys Chem C 113:5004–5009

Lochan R, Jung Y, Head-Gordon M (2005) Scaled opposite spin second order Møllet-Plesset theory with improved physical description of long-range dispersion interactions. J Phys Chem A 109:7598

Morris W, Leung B, Furukawa H, Yaghi OK, He N, Hayashi H, Houndonougbo Y, Asta M, Laird BB, Yaghi OM (2010) A combined experimental–computational investigation of carbon dioxide capture in a series of isoreticular zeolitic imidazolate frameworks. J Am Chem Soc 132:11006–11008

Mueller T, Ceder G (2005) A density functional theory study of hydrogen adsorption in MOF-5. J Phys Chem B 109: 17974–17983

Mulder FM, Dingermans TJ, Wagemaker M, Kearley GJ (2005) Modelling of hydrogen adsorption in the metal organic framework MOF5. Chem Phys 317:113–118

Negri F, Saendig N (2007) Tuning the physisorption of molecular hydrogen: binding to aromatic, hetero-aromatic and metal-organic framework materials. Theor Chem Acc 118: 149–163

Park J, Kim H, Han SS, Jung Y (2012) Tuning metal–organic frameworks with open-metal sites and its origin for enhancing CO_2 affinity by metal substitution. J Phys Chem Lett 3:826

Park KS, Ni Z, Côté AP, Choi JY, Huang RD, Uribe-Romo FJ, Chae HK, O'Keeffe M, Yaghi OM (2006) Exceptional chemical and thermal stability of zeolitic imidazolate frameworks. Proc Natl Acad Sci USA 103:10186–10191

Pérez-Pellitero J, Amrouch H, Siperstein FR, Pirngruber G, Nieto-Draghi C, Chaplais G, Simion-Masseron A, Bazer-Bachi D, Peralta D, Bats N (2010) Adsorption of CO2, CH4, and N2 on zeolitic imidazolate frameworks: experiments and simulations. Chem Eur J 16:1560–1571

Peterson KA, Puzzarini C (2005) Systematically convergent basis sets for transition metals. II. Pseudopotential-based correlation consistent basis sets for the group 11 (Cu, Ag, Au) and 12 (Zn, Cd, Hg) elements. Theor Chem Acc 114:283–284

Rallapalli P, Prasanth KP, Patil D, Somani RS, Jasra RV, Bajaj HC (2010) An alternative activation method for the enhancement of methane storage capacity of nanoporous aluminium terephthalate, MIL-53(Al). J Porous Mater 17:523–528

Rankin RB, Liu J, Kulkarni AD, Johnson JK (2009) Adsorption and diffusion of light gases in ZIF-68 and ZIF-70: a simulation study. J Phys Chem C 113:16906–16914

Rappe AK, Casewit CJ, Colwell KS, Goddard WA III, Skiff WM (1992) UFF, a full periodic table force field for molecular mechanics and molecular dynamics simulations. J Am Chem Soc 114:10024–10035

Sagara T, Klassen J, Ganz E (2004) Computational study of hydrogen binding by metal-organic framework-5. J Chem Phys 121:12543

Samanta A, Furuta T, Li J (2006) Theoretical assessment of the elastic constants and hydrogen storage capacity of some

metal-organic framework materials. J Chem Phys 125: 084714

Shao Y, Molnar LF, Jung Y, Kussmann J, Ochsenfeld C, Brown ST, Gilbert ATB, Slipchenko LV, Levchenko SV, O'Neill DP, DiStasio RA, Lochan RC, Wang T, Beran GJO, Besley NA, Herbert JM, Lin CY, Van Voorhis T, Chien SH, Sodt A, Steele RP, Rassolov VA, Maslen PE, Korambath PP, Adamson RD, Austin B, Baker J, Byrd EFC, Dachsel H, Doerksen RJ, Dreuw A, Dunietz BD, Dutoi AD, Furlani TR, Gwaltney SR, Heyden A, Hirata S, Hsu CP, Kedziora G, Khalliulin RZ, Klunzinger P, Lee AM, Lee MS, Liang W, Lotan I, Nair N, Peters B, Proynov EI, Pieniazek PA, Rhee YM, Ritchie J, Rosta E, Sherrill CD, Simmonett AC, Subotnik JE, Woodcock HL, Zhang W, Bell AT, Chakraborty AK, Chipman DM, Keil FJ, Warshel A, Hehre WJ, Schaefer HF, Kong J, Krylov AI, Gill PMW, Head-Gordon M (2006) Advances in methods and algorithms in a modern quantum chemistry program package. Phys Chem Chem Phys 8:3172–3191

Torrisi A, Mellot-Draznieks C, Bell RG (2009) Impact of ligands on CO_2 adsorption in metal-organic frameworks: first principles study of the interaction of CO_2 with functionalized benzenes. I. Inductive effects on the aromatic ring. J Chem Phys 130:194703

Torrisi A, Mellot-Draznieks C, Bell RG (2010) Impact of ligands on CO_2 adsorption in metal-organic frameworks: first principles study of the interaction of CO_2 with functionalized benzenes. II. Effect of polar and acidic substituents. J Chem Phys 132:044705

Vogiatzis KD, Mavrandonakis A, Klopper W, Froudakis GE (2009) Ab initio study of the interactions between CO_2 and N-containing organic heterocycles. ChemPhysChem 10:374–383

Wang B, Côté AP, Furukawa H, O'Keeffe M, Yaghi OM (2008) Colossal cages in zeolitic imidazolate frameworks as selective carbon dioxide reservoirs. Nature 453:207–212

Wu T, Zhang J, Zhou C, Wang L, Bu X (2009a) Zeolite RHO-type net with the lightest elements. J Am Chem Soc 131:6111–6113

Wu Q, Ayers PW, Zhang Y (2009b) Density-based energy decomposition analysis for intermolecular interactions with variationally determined intermediate state energies. J Chem Phys 131:164112

Yang Z, Xia Y, Mokaya R (2007) Enhanced hydrogen storage capacity of high surface area zeolite-like carbon materials. J Am Chem Soc 129:1673–1679

Yousaf KE, Peterson KA (2009) Optimized complementary auxiliary basis sets for explicitly correlated methods: aug-cc-pVnZ orbital basis sets. Chem Phys Lett 476:303–307

Zulfigar S, Faradas F, Park J, Stucky GD, Jung Y, Atilhan M, Yavuz CT (2011) Amidoximes: promising candidates for CO_2 capture. Energy Env Sci 4:4528

DOI 10.1007/978-3-319-05041-6_23
Reprinted from the *Journal of Nanoparticle Research*, DOI 10.1007/s11051-013-2011-9

PERSPECTIVES

Nanotechnology and clean energy: sustainable utilization and supply of critical materials

Neil A. Fromer · Mamadou S. Diallo

Received: 20 June 2013 / Accepted: 13 September 2013 / Published online: 10 October 2013

Abstract Advances in nanoscale science and engineering suggest that many of the current problems involving the sustainable utilization and supply of *critical materials* in clean and renewable energy technologies could be addressed using (i) nanostructured materials with enhanced electronic, optical, magnetic and catalytic properties and (ii) nanotechnology-based separation materials and systems that can recover *critical materials* from non-traditional sources including mine tailings, industrial wastewater and electronic wastes with minimum environmental impact. This article discusses the utilization of nanotechnology to improve or achieve materials sustainability for energy generation, conversion and storage. We highlight recent advances and discuss opportunities of utilizing nanotechnology to address materials sustainability for clean and renewable energy technologies.

Keywords Critical materials · Clean energy · Nanotechnology · Urban mining

Special Issue Editors: Mamadou Diallo, Neil Fromer, Myung S. Jhon

This article is part of the Topical Collection on Nanotechnology for Sustainable Development

N. A. Fromer
Resnick Sustainability Institute, California Institute of Technology, Pasadena, CA, USA
e-mail: nafromer@caltech.edu

M. S. Diallo (✉)
Graduate School of Energy, Environment, Water and Sustainability (EEWS), Korea Advanced Institute of Science and Technology (KAIST), 373-1 Guseong Dong, Yuseong Gu, Daejeon 305-701, Republic of Korea
e-mail: diallo@wag.caltech.edu; mdiallo@kaist.ac.kr

M. S. Diallo
Environmental Engineering and Science, Division of Engineering and Applied Science, California Institute of Technology, Pasadena, CA, USA

Introduction

Global climate change is one of the greatest challenges facing the world in the twenty-first century [Intergovernmental Panel on Climate Change (IPCC) 2007]. During the past two decades, a consensus has gradually emerged that increasing emissions of greenhouse gases such as carbon dioxide (CO_2) from the combustion of fossil fuels (e.g. coal and petroleum) are the key drivers of global climate change (IPCC 2007). Meeting the growing demand for energy while significantly reducing CO_2 emissions will require the deployment of orders of magnitude more clean and renewable energy systems than what is now in place as the world population reaches 8–10 billion by 2050 (Fromer et al. 2011; Diallo et al. 2013). However, there is a growing realization that the development and large-scale implementation of clean and renewable energy systems will require sizeable amounts of technology

metals (Diallo and Brinker 2011; Fromer et al. 2011; Diallo et al. 2013). Like energy and water, the availability of metals derived from minerals and other sources is critical to the world economy and global sustainability. Recent stresses in the global market of rare-earth elements (REEs) have brought the sustainable supply of technology metals to the forefront (Diallo and Brinker 2011; Fromer et al. 2011). In addition to REEs and platinum group metals (PGMs), significant amounts of copper, silver, cobalt, nickel, gold, magnesium, lithium, titanium, gallium, molybdenum and tungsten will be needed to build the clean and renewable energy technologies of the twenty-first century including (i) solar cells, (ii) wind turbines, (iii) electrical vehicles, (iv) batteries and (v) energy-efficient lighting devices [Fromer et al. 2011; Department of Energy (DOE) 2011]. The United States (US) National Research Council (NRC) published one the first comprehensive studies of critical minerals/materials in 2008. In this seminal study, the NRC developed the concept of "criticality matrix" and showed that a mineral/material must be both *essential in use* and subject to *supply restriction* to be deemed *critical* [NRC 2008]. The NRC subsequently applied its criticality matrix to eleven elements and mineral groups including PGMs and REEs. They reported that metals with the *highest degree of criticality* included indium, manganese, niobium, PGMs and REEs (NRC 2008). Recently, the role of *critical materials* in energy generation, conversion and storage has been the subject of several reports (Fromer et al. 2011; Moss et al. 2011; DOE 2011).

As nanotechnology looks toward the next 10 years and beyond, two key questions arise:

- Can nanotechnology address the challenges of achieving or improving materials sustainability for clean and renewable energy technologies?
- Can nanotechnology help augment the supply of *critical materials* required for clean and renewable energy technologies technologies?

This perspective article highlights and discuss opportunities of using nanotechnology to address materials sustainability in clean and renewable energy technologies. The focus is on selected areas where nanotechnology is likely to have the greatest impact over the next decade: (1) solar photovoltaics, (2) solid state lighting, (3) wind turbines, (4) electric vehicles, (5) solar fuels and (6) batteries. Following the "Introduction", "Nanotechnology and clean energy: opportunities for improving materials sustainability" section gives an overview of recent advances in the development of nanostructured materials with enhanced electronic, optical, magnetic and catalytic properties that can reduce or eliminate the utilization of *critical materials* in energy generation, conversion and storage. "Nanotechnology and clean energy: opportunities for improving the supply of critical materials" section highlights advances in the development of nanotechnology-based separation materials and systems that can efficiently recover *critical materials* from non-traditional sources including mine tailings, industrial wastewater and electronic wastes with minimum environmental impact. "Summary and outlook" section provides a summary and outlook of the utilization of nanotechnology to improve or achieve materials sustainability in clean and renewable energy technologies.

Nanotechnology and clean energy: opportunities for improving materials sustainability

As noted above, meeting the world's growing demand for clean and renewable energy will require not only substantial amounts of technology metals, the REEs being foremost, but also PGMs, indium, lithium, gallium, tellurium and precious metals (e.g. silver). Although the current industrial demand for these technology metals is small in terms of tonnage, they are deemed essential for a number of energy applications, including (i) permanent magnets for wind turbines and EVs, (ii) metal alloys for batteries, (iii) light absorbers and emitters for photovoltaics, (iv) light emitting diodes (LEDs) and (v) catalysts for solar-fuel generation. In 2010, clean and renewable energy technologies consumed about 20 % of the global supply of technology metals, and this is likely to increase significantly in the future (Fromer et al. 2011; DOE 2011; Diallo et al. 2013). To address materials criticality in clean and renewable energy technologies, several new programs supported by both the public and private sectors have been initiated. These programs aim to both (1) increase materials supply through investments in mining, exploration and materials recycling and (2) reduce demand using various mechanisms including the initiation of research and development (R&D) programs by the

Advanced Research Projects Agency-Energy (ARPA-E) of the US DOE to replace REEs in motors and turbines (ARPA-E 2011). More recently, DOE has established the Critical Materials Institute, an Energy Innovation Hub led by Ames National Laboratory to address materials sustainability for clean and renewable energy technologies (http://cmi.ameslab.gov/about_home.html).

In order to address the critical nature of technology metals, it is important to understand the nature of their criticality. Clean and renewable energy technologies often use large quantities of metals such dysprosium, gallium and platinum due to some unique functionality that each of these metals provides including superior magnetic, optical and catalytic properties (Fromer et al. 2011; DOE 2011). In some cases, the required functionality (e.g. magnetism) can be replaced both at the system level (e.g. using induction motors that do not rely on high coercivity magnets) and at the bulk material level (e.g. using niobium–titanium superconducting magnets that do not require REEs). In many cases, however, a decrease in the usage of a critical material or a reduction of its criticality will depend to a large extent on finding new ways to re-engineer the required material functionality using substitutes. For every application in which this could be achieved, the criticality of a material could be lowered thereby reducing its importance for those applications. Ideally, the new material would exhibit superior performance in terms of functionality as well. But even if that would not always be the case, this could still ease criticality by replacing the material in other applications where a decrease or loss of functionality would be acceptable. Nanotechnology provides unprecedented opportunities to address materials sustainability in clean and renewable energy technologies. As we become more proficient at manipulating and controlling matter at the atomic scale, we will also become more successful at preparing new functional materials "by design" with the required electronic, optical, magnetic and catalytic properties while utilizing little or none of the *critical elements* that are currently required in clean and renewable energy technologies. Below, we discuss selected areas where nanostructured materials are emerging as viable alternatives to reduce or eliminate the utilization of *critical materials* in energy generation, conversion and storage. Table 1 highlights selected examples and strategies for reducing materials criticality in clean and renewable energy technologies.

Photovoltaics and solid state lighting

In PV and solid-state lighting, the optical properties of *critical materials* are their key attributes. The increase in the use of semiconductor lasers and LEDs in commercial applications over the past several decades has been largely driven by our ability to fabricate high-quality nanostructures (quantum wells and now quantum dots) with enhanced optical properties, most notably in III–V devices. These nanostructures are providing new opportunities to tune the absorption properties of photovoltaic materials. It is worth mentioning that companies such as Cyrium Technologies and QuantaSol (acquired in 2011 by JDSU) are already using semiconductor nanocrystals (or quantum dots) and quantum wells to fabricate high-efficiency multi-junction solar cells for concentrating photovoltaics (CPV) applications (Valdivia et al. 2010). The improvement in efficiency enables these new CPV systems to compete on a cost basis with flat panel solar cells while using much less amounts of active semiconductor material (i.e. 1/1000th) and silver. Ordered films/arrays of photoactive semiconductor nanocrystals are also being employed to fabricate more efficient thin-film solar cells that are directly tuned to the solar spectrum (Gur et al. 2005; Ma et al. 2009). This is in turn providing new opportunities to reduce materials criticality through the utilization of earth-abundant elements or non *critical materials* (Guo et al. 2010). Nanotechnology could also help find solutions to the so-called "green gap" in semiconductor LEDs (O'Donnell et al. 2012). A conventional semiconductor lighting device generates "white" light by mixing blue or UV light produced by an InGaN LED with that emitted by a yellow-orange (amber) AlInGaAsP LED. However, in both cases the efficiency drops off as the materials are tuned towards the green region of the spectrum. Nanotechnology offers potential solutions to this problem through the fabrication of quantum-dot LEDs that do not require REEs (Zhang et al. 2011). Finally, we would like to mention that advances in plasmonics and nanophotonics are providing new opportunities to develop more efficient optical materials for renewable and clean energy technologies. Plasmonic or photonic nanostructures assembled on a periodic lattice with unit length comparable to the wavelength of light have the capability to alter the optical properties of materials by inducing light to couple into guided

Table 1 Nanotechnology and materials criticality reduction strategies in clean and renewable energy systems

Systems	Components	Critical materials	Materials criticality reduction strategies
Wind turbines	Generators	Neodymium, dysprosium	Develop nanostructured REPMs that utilize less amounts of neodymium and dysprosium
			Use non-critical materials and earth-abundant elements to develop nanocomposite "exchange spring magnets" by coupling nanoparticles with hard and soft magnetic domains to achieve high energy density and coercivity
Electric vehicles	Motors	Neodymium, dysprosium	Same strategy as above
	LIB	Lithium, cobalt	Use electrospun nanofibers made of earth-abundant elements to prepare more efficient anodes, cathodes and separators for LIB
	NiMH Batteries	REEs, cobalt	Develop magnesium batteries and new batteries using nanomaterials based on earth-abundant elements
Solar cells	Thin film	Tellurium, gallium, germanium, indium, silver, cadmium	Find new nanostructured and absorbing materials that match the solar spectrum without using critical materials
			Exploit quantum confinement to tune and improve the optical properties of solar cells materials built using non critical materials
			Exploit advances in nanophotonics and plasmonics to build thin-film solar cells that utilize orders of magnitude less active materials
Solid state lighting devices	LED devices	Gallium, indium	See strategy as above
			Utilize nanoparticles and quantum confinement to improve light emitting efficiency throughout the visible spectrum
	Phosphors	Yttrium, europium, terbium, other REEs	Switch from fluorescent lights to LED lights to decrease the use of phosphors (REEs) by an order of magnitude
			Utilize nanoparticle light emitters to reduce or replace REEs in phosphors
Solar fuel generators	Catalysts	Platinum, palladium, iridium, yttrium	Develop hydrogen/oxygen evolution catalysts using nanomaterials based on earth-abundant elements
			Optimize grain size and exploit quantum size effects to tune band energies, surface states, and thermal properties to increase catalyst activity and reactivity

modes or absorb much more strongly than in standard thin films, thereby enabling the use of orders of magnitude less materials in solar cells and semiconductor LEDs (Deceglie et al. 2012; Callahan et al. 2012; Grandidier et al. 2012).

Wind turbine and Electric vehicles

High-power rare earth permanent magnets (REPMs) have been at the core of the growth in the size and efficiency of wind turbines over the past decade. They are also commonly used in the motors for Electric vehicles (EVs) because they provide better power/weight ratios. There is a renewed interest in materials that can achieve comparable energy density and coercivity as the REPMs with no or little amounts of REEs. Several strategies are being implemented to achieve this objective. These range from a simple reduction in the grain size of REPM magnets (Shen et al. 2006) to the development of entirely new systems including coupled "exchange-spring magnets" (Kneller and Hawig 1991; Liu et al. 2011). These consist of hybrid nanostructures with two functional nanoparticles of different chemistry (e.g. FePt and $Fe_{0.8}Ni_{0.2}$) that are selected for their hard or soft magnetic properties and coupled together to produce permanent magnets with high energy density and coercivity (Kneller and Hawig 1991; Liu et al. 2011). Finally, we would like to mention that the ARPA-E REACT program is supporting several projects focused on the development of high-performance magnets based on nanostructured materials from earth-abundant elements including cerium, iron, nitrogen, manganese and aluminum (ARPA-E 2011).

Solar fuels

Because solar radiation is intermittent, the large-scale implementation of solar power will require efficient systems that convert solar energy into high-density chemical fuels. One of the great challenges in clean energy technology is to build an efficient and scalable photo-electrochemical reactor that combines solar energy with water and CO_2 to generate fuels such as hydrogen and methanol (Lewis and Nocera 2006). To achieve high efficiency, the first generation of bench scale solar fuel generators employed PGMs (e.g. platinum and iridium) as base metals for their hydrogen and oxygen evolution catalysts. PGMs are among the most *critical* and expensive technology metals on Earth. Thus, the discovery and optimization of non-platinum based catalysts is a critical step in the development of an industrial scale solar fuel generator. Recent work has shown that molybdenum sulfide and nickel–molybdenum alloy based nanomaterials hold promise as new hydrogen evolution catalysts (Vrubel et al. 2012; Mckone et al. 2013). It is worth mentioning that progress on the development of oxygen evolution catalysts has been slower. However, recent work points to the possibility of optimizing the nanoscale structures of perovskite oxide materials for this purpose (Suntivich et al. 2011). This work is a major thrust of the Joint Center for Artificial Photosynthesis (JCAP), a Department of Energy innovation hub dedicated to the development of a prototype solar fuel generator (http://solarfuelshub.org/). JCAP has initiated an extensive research program to discover new catalysts for solar-fuel generation based on earth-abundant elements. This program combines high-throughput combinatorial search for new catalysts with experimental and theoretical investigations of fundamental reaction pathways and mechanisms.

Batteries

In industrialized countries such as the United States, transportation is responsible for approximately 67 % of oil consumption and 33 % of CO_2 emissions (Davis et al. 2013; EPA 2008). Electricity is the cleanest and most versatile source of energy for meeting the world's growing demand for energy while significantly reducing CO_2 emissions. Thus, increase in the usage of EVs and plug-in hybrid electric vehicles (PIHEVs) could result in significant decreases in both oil consumption and CO_2 emissions. Because lithium-ion batteries (LIB) currently provide the best combinations of energy density ($\sim$100 Wh/kg) and power density ($\sim$200 W/kg) at the lowest cost (See http://www.allaboutbatteries.com/Battery-Energy.html), they have emerged as the most widely employed electricity storage media for EVs and PIHEVs during the past 10 years. However, EVs and PIHEVs will need to have batteries "with twice the energy storage of today's state-of-the-art LIB at 30 % of the cost" to be competitive with gasoline-powered cars (ARPA-E 2010). Nanotechnology provides new opportunities to improve the performance of LIB including energy density, power density, size, weight, stability and safety while reducing their costs (Aricò et al. 2005; Brinker and Ginger 2011). A significant development in battery technology is the emergence of electrospun nanofibers as versatile classes of nanomaterials for the preparation of high-performance anodes and cathodes for LIB using earth-abundant elements such as silicon, magnesium, vanadium, carbon and sulfur (Cavaliere et al. 2011; Raghavan et al. 2012). Electrospinning is also being employed to develop more efficient separators for LIB (Cavaliere et al. 2011; Raghavan et al. 2012) using polyvinylidene fluoride (PVDF) and polyacrylonitrile as base polymers (Cavaliere et al. 2011; Raghavan et al. 2012).

Nanotechnology and clean energy: opportunities for improving the supply of critical materials

Most of the technology metals that are currently being utilized in clean and renewable energy technologies are produced through the mining, extraction and processing of virgin ores (DOE 2011; Fromer et al. 2011). Because there is a significant time lag between the discovery and processing of new virgin ores, current and future shortages of technology metals cannot be addressed by just opening new mines and mineral/metal processing facilities. Thus, there is a critical need for a multipronged strategy to augment the supply of technology metals for clean and renewable energy technologies. Such strategy will include (i) improvements in extraction efficiency and process yields, (ii) extraction and recovery from non-traditional sources and (iii) recycling. Because the recovery

of REEs from virgin ores such monazite and bastnasite requires a multistep extraction/purification process, a 20 % improvement of the yield of each of the five basic unit processes could double the production (Fromer et al. 2011). During the past two decades, advances in industrial ecology (e.g. material flow analysis) have established that industrial waste streams are important and largely untapped sources of technology metals including wastewater (Allen and Behmanesh 1994), mine tailings (Bian et al. 2012) and electronic wastes (Johnson et al. 2007; Reck and Graedel 2012). This has led to the emergence of "urban mining" as a potentially viable technology for augmenting the supply of technology metals (Nakamuro and Sato 2011).

The overall goal of urban mining is to extract valuable metals/elements from wastes. The National Institute for Materials Science of Japan has estimated the total reserves of gold, silver and indium in Japanese urban mines to be, respectively, equal to 6800, 60000 and 1700 tons (Nakamuro and Sato 2011). With funding from the recently established DOE Critical Materials Institute (http://cmi.ameslab.gov/about_home.html), the Idaho National Laboratory has initiated an urban mining research program to extract REEs from consumer electronic products (Stricker 2013). It is worth mentioning that many of the technology metals in waste streams "have concentrations that are more enriched than minimum profitable ore grades" (Johnson et al. 2007). Figure 1 shows a generic process flow diagram for a processing facility designed to recover metals from liquid wastes (e.g. industrial wastewater and mining effluents) and solid wastes (e.g. mine tailings and electronic wastes). This metal recovery system is structured around four core unit operations and processes: (1) pretreatment, (2) extraction and concentration, (3) recovery and purification and (4) post treatment. The pretreatment system is designed to process the waste streams into metal-laden solutions that can be subsequently utilized to extract the technology metals of interest with high rate of recovery and minimum environmental impact (e.g. zero liquid discharge through water reuse). Following pretreatment, the metal-laden solutions are sent to the extraction/concentration and recovery/purification units where the target metals of interest are selectively recovered and converted to pure metals or metal oxides, etc. depending on the product end-uses. Allen and Shonnard (2008) have shown that there are no fundamental thermodynamic limitations (i.e. entropy barrier) in recovering metals from solid and liquid wastes. Thus, the key bottleneck to metal extraction from waste streams is the availability of energy-efficient, cost-effective and environmentally acceptable separation technologies. A broad range of separations processes could be coupled together to recover metals from solutions including solvent extraction, ion exchange, membrane filtration, electrorefining and crystallization (DOE 2006). Nanotechnology has emerged an enabling platform for a new generation of high-performance separation materials and systems for metal extraction from solutions (Diallo and Brinker 2011). Below, we highlight selected areas where nanotechnology-based separation materials and systems have great potential to advance urban mining and the sustainable recovery of *critical materials* from waste solutions: (1) Dendrimer-based ligands and metal recovery systems, (2) anion exchange and chelating resins and (3) nanofiltration (NF) membranes.

Dendrimer-based ligands and metal recovery systems

In aqueous solutions, metal ions exist as cationic species depending on metal and background electrolyte concentrations (Stumm and Morgan 1996). Technology metal ions that are often present as cationic species in aqueous solutions include REEs, copper, nickel, cobalt and lithium (Martell and Hancock 2006). Chelating agents are the most effective ligands for cationic metal species in solutions (Martell and Hancock 2006). Thus, a *Grand Challenge* in urban mining and metal recovery from wastes is to design and synthesize high-capacity, selective, recyclable and stable chelating ligands that (i) can operate efficiently in complex aqueous solutions (e.g., highly acid or basic media) under continuous mixing and (ii) are easily and efficiently separated from aqueous solutions using low-pressure and room-temperature separation technologies. Metal ion complexation is an acid–base reaction that depends on several parameters including (i) metal ion size and acidity, (ii) ligand basicity and molecular architecture and (iii) solution physical–chemical conditions. Three milestones in coordination chemistry were the discoveries of the *Hard and Soft Acids and Bases principle*, the *chelate effect* and the *macrocyclic effect* (Martell and Hancock 1996). Although macrocycles and polydentate ligands

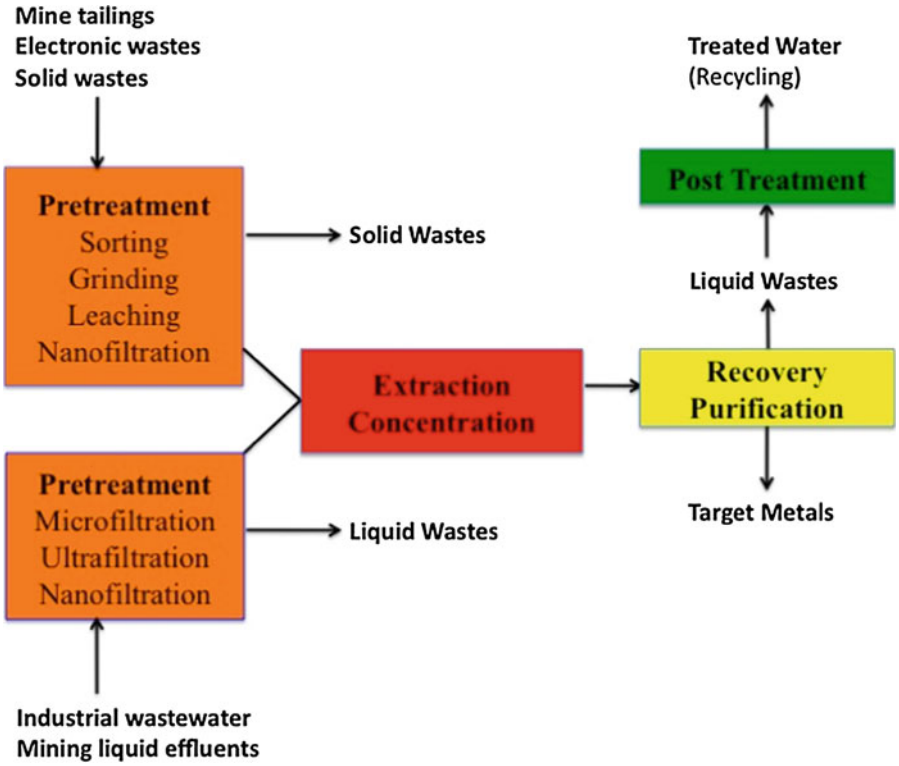

Fig. 1 Conceptual process flow diagram of a generic processing facility designed to extract technology metals from waste streams

have been shown to form stable complexes with a variety of metal ions, their limited binding capacity (i.e. 1:1 complexes in most cases) is a major impediment to their utilization as high-capacity chelating agents for industrial and environmental separations. Their relatively low molecular weights also preclude their effective recovery from industrial wastewater streams by low-pressure membrane filtration.

The invention of dendritic macromolecules is another milestone in ligand architecture and coordination chemistry. Dendritic macromolecules, which include random hyperbranched polymers, dendrigraft polymers, dendrons and dendrimers, consist of 3-D globular nanostructures with characteristic sizes (e.g. diameter) ranging from 1 to 20 nm (Fréchet and Tomalia 2002; Tomalia and Diallo 2012). Dendritic macromolecules can be designed and functionalized to serve as high-capacity, selective and recyclable ligands for metal ions in aqueous and nonaqueous solutions. Poly(amidoamine) (PAMAM) dendrimers were the first classes of commercially available dendrimers. They provide good model systems for probing metal ion complexation with dendrimer-based ligands. Figure 2a depicts a 2-D structure of a generation 4 PAMAM dendrimer (G4-NH_2) with terminal primary amine groups. The G4-NH_2 PAMAM is a globular macromolecule with a molar mass of 14215 Dalton and a hydrodynamic diameter of 5 nm (Dvornic and Uppuluri 2002). This dendrimer has 64 primary amine groups, 62 tertiary amine groups and 124 amide groups. Molecular dynamics simulations by Maiti et al. (2005) have shown that a G4-NH_2 PAMAM can encapsulate $\sim$201 water molecules at pH 7.0. This unique combination of high density of ligands and globular/open structure with a high number of trapped water molecules provide a key advantage of dendrimer-based ligands such as the G4-NH_2 PAMAM over open-chain multidentate ligands and macrocycles; that is the covalent attachment of nitrogen and oxygen donors to flexible PAMAM chains enclosed within a water-soluble globular nanostructure ($\sim$5.0 nm in diameter) results in a macroligand field with multiple binding sites and large binding capacity/selectivity for transition metal ions, lanthanides and actinides including Cu(II), Pd(II), Pt(II), Ag(I), Au(I), Gd(III) or U(VI) (Cohen et al. 2001; Diallo et al. 2004, 2008; Scott et al. 2005).

Because dendrimers such as the G4-NH_2 PAMAM (Fig. 2a) have persistent globular shapes and relatively large molecular weights, they are readily separated from solutions using low-pressure

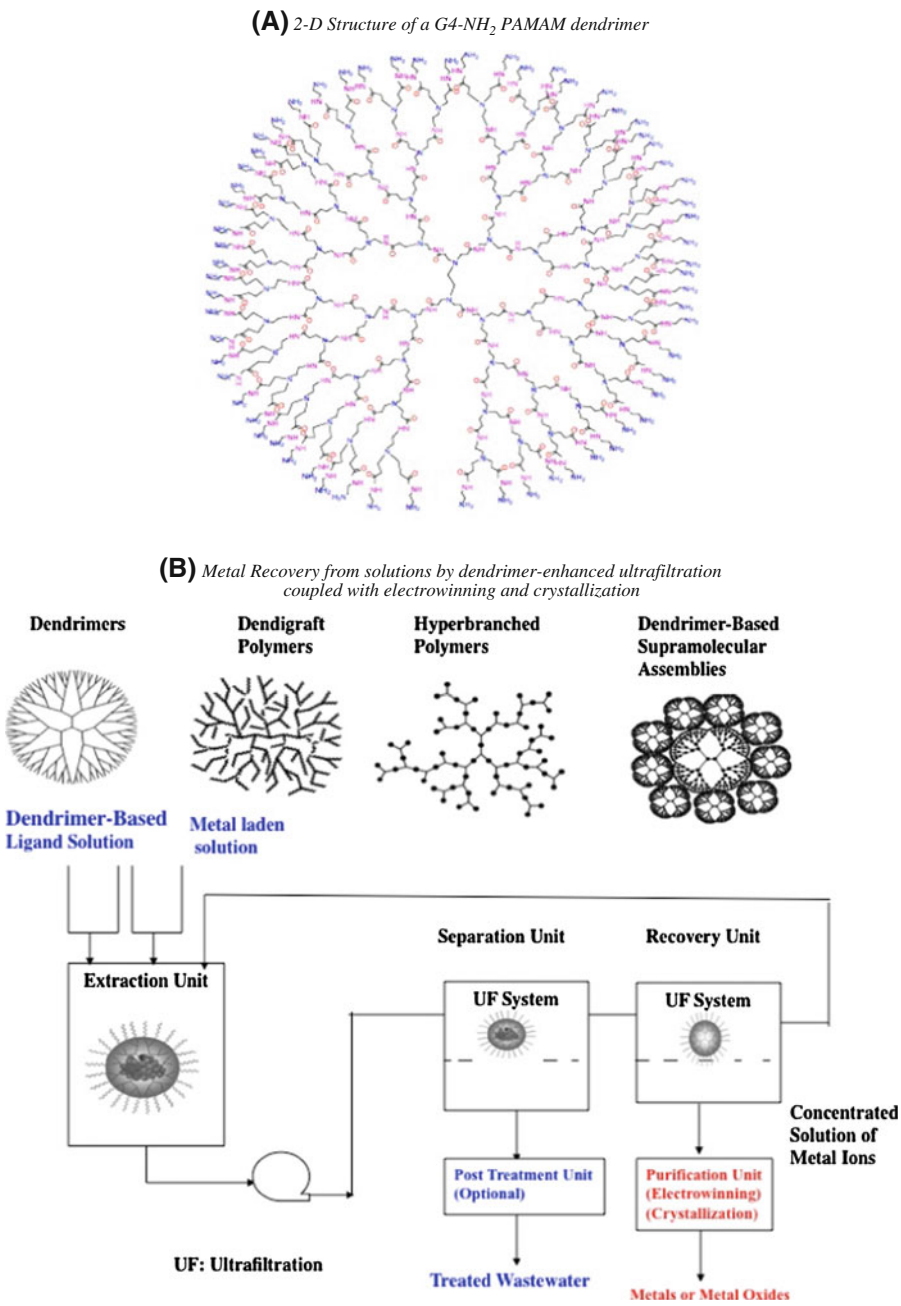

Fig. 2 Dendrimer-based chelating agents and separation systems for metal extraction and purification from solutions

membrane ultrafiltration (UF) (Diallo et al. 2005, Diallo 2008). Figure 2b shows a conceptual depiction of the utilization of dendrimer-based ligands in a metal recovery system that couples a *dendrimer enhanced* UF [DEUF] (Diallo et al. 2005; Diallo 2008) process with the well-established metal purification process of *electrowinning and crystallization*. This new metal recovery system is structured around four unit processes with an optional post-treatment unit designed to produce "clean" water for reuse or dischargeable "effluent" water (Fig. 2). In the extraction unit, a solution of a dendrimer-based ligand with large molecular weight (e.g. $M_w > 10000$ Da) is mixed with a metal laden solution containing the target metal ions (Fig. 2b). Following complexation, the solution of dendrimer-based ligand + bound metal ions is sent to the separation unit where it is filtered using low-pressure UF. The metal ion-rich membrane retentate is

subsequently sent to the recovery unit. For most metal ions, a change in solution acidity and/or salt concentration will cause the dendrimer-based ligand to release their bound metal ions. Thus, a low-pressure UF membrane system could also be used as recovery unit to separate the dendrimer-based ligand following the release of the bound metal ions. In the final step, the concentrated solution of metal ions is sent to the purification unit to extract and purify the target metals. By integrating the DEUF process with well-established purification technologies such as *electrowinning* and *crystallization* (Fig. 2b), it should be possible to develop and optimize a new generation cost-effective and environmentally sound processes that can recover a broad range of technology metals from waste solutions including industrial wastewater, mining aqueous effluents and solid-waste leaching solutions (Fig. 1).

Although dendrimers have shown great potential as high-capacity, selective and recyclable chelating agents for many technology metals used in clean and renewable energy technologies, they are expensive due to the multiple steps required for their synthesis and purification (Fréchet and Tomalia 2002; Tomalia and Diallo 2012). Hyperbranched polymers (HBP) have emerged as viable and low-cost alternatives to dendrimers in industrial applications (Fréchet and Tomalia 2002; Seiler 2006; Zhao et al. 2013). Unlike dendrimers, HBP are readily synthesized via one-step reactions using various AB_n monomers. Branched polyethyleneimine (BPEI) macromolecules have emerged as low-cost alternatives to dendrimers with amine groups such PAMAM for a broad range of industrial applications (Krämer et al. 2004; Seiler 2006). BPEI macromolecules consist of primary, secondary and tertiary amines linked by C_2 alkyl chains (Fig. 3a). Two very attractive features of BPEI macromolecules as chelating agents for metal ions are (i) their high contents of functional amine groups (18–20 mol/kg) and (ii) the availability of industrial-scale quantities of BPEI macromolecules with molecular weights (M_w) ranging from about 2000 to several millions Dalton. Moreover, BPEI macromolecules can be functionalized with groups various to synthesize ion-selective ligands (Krämer et al. 2004). Thus, they have great potential as low-cost alternatives to dendrimers for the synthesis of high-capacity, selective and recyclable chelating agents for metal extraction from waste solutions by DEUF (Fig. 2b). Finally, we would like to mention the recent development of a "vinyl oligomer combination" strategy to the synthesis of HPB by Zhao et al. (2013). The authors believe that this new approach will "allow facile synthesis of highly branched polymeric materials from readily available multi-vinyl monomers" (Zhao et al. 2013). The optimization of this new synthetic method could provide additional opportunities to develop high-performance chelating agents for metal recovery from solutions by DEUF (Fig. 2b).

Anion exchange and chelating resins from dendritic macromolecules

In aqueous solutions, metal ions can also exist as anionic species (Stumm and Morgan 1996; Martell and Hancock 1996). Technology metal ions that form anionic species in aqueous solutions include uranium, platinum, gold and oxyanions of various important metals including molybdenum, vanadium, tungsten and germanium. Thus, the availability of efficient, cost-effective and environmentally acceptable anion separation technologies will be critical to the urban mining and extraction of technology metals from waste solutions. The design of selective ligands and sorbents for anions is a challenging undertaking. Anions have a variety of geometries [e.g., spherical for chloride (Cl^-) and tetrahedral for molybdate] (Moyer and Bonnesen 1997; Gloe et al. 2003). The charge-to-radius ratios of anions are also lower than those of cations (Gloe et al. 2003). Thus, anion binding to ligands and sorbents through electrostatic interactions tends to be weaker than cation binding. The anion binding capacity and selectivity of ligands and sorbents also depend on (i) the extent of ion solvation, (ii) solvent polarity and (iii) host preorganization (Moyer and Bonnesen 1997; Gloe et al. 2003). During the past two decades, significant progress has been made in the supramolecular chemistry of anions. A variety of hosts including calixarenes, tripodal ligands, azacrowns and dendritic macromolecules have been designed and synthesized for the selective recognition, complexation and extraction of anions from solutions (Moyer and Bonnesen 1997; Gloe et al. 2003). Despite these important advances, anion exchange and chelating resins will remain the most widely utilized separation media for anion extraction from solutions in the foreseeable future.

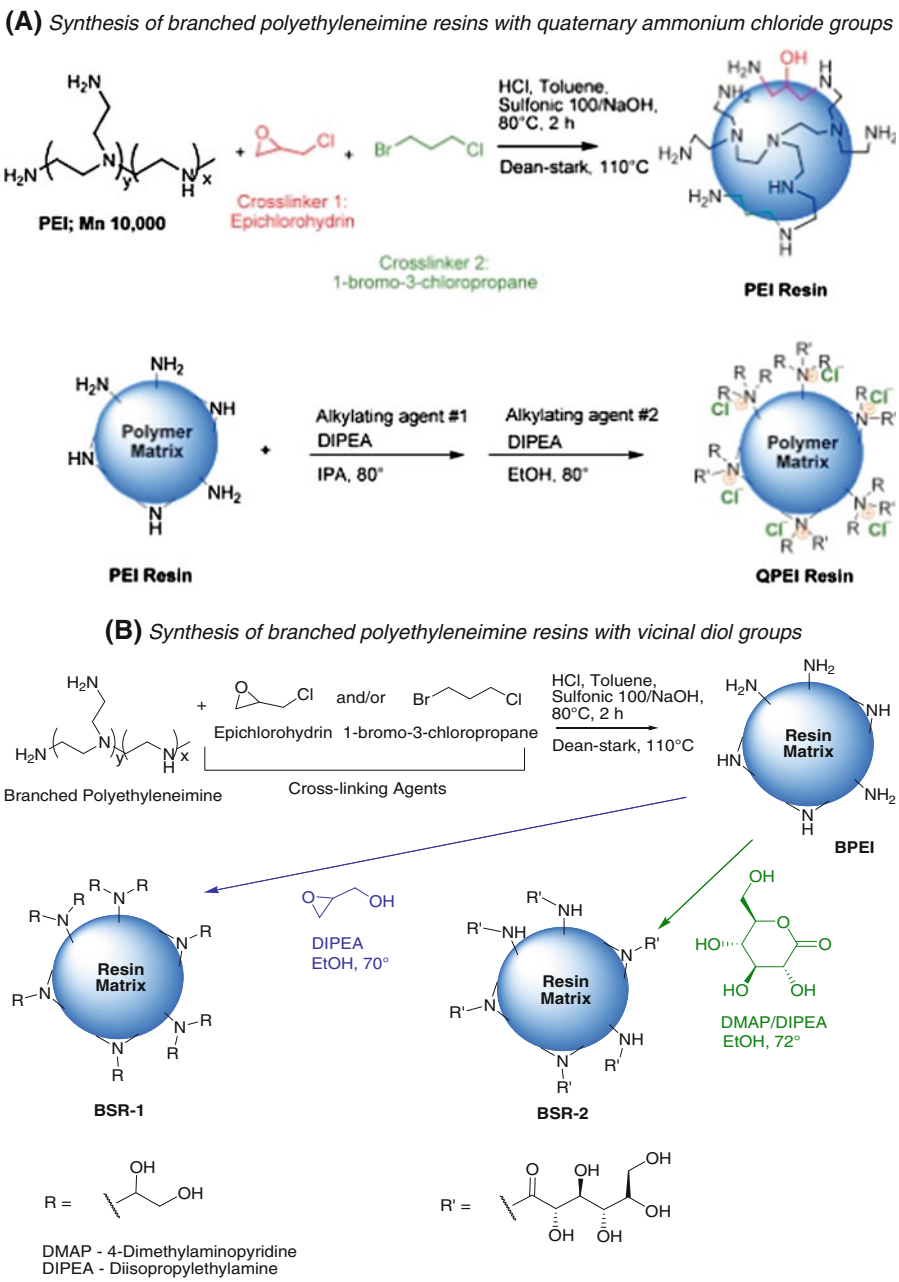

Fig. 3 Anion exchange and chelating resins from dendritic macromolecules (Chen et al. 2012; Mishra et al. 2012). The resin shown in **b** contains vicinal diol groups that can selectively chelate oxyanions ions in solutions including borate, vanadate, molybdate and tungstate

Ion exchange (IX) is the reversible exchange between ions from a solution and fixed ions from a resin as the solution passes through the medium. For example, strong-base resins with ammonium Cl^- exchange sites can be utilized to extract gold from mining leach liquors (Gomes et al. 2001). In contrast, chelating resins are employed to selectively extract PGMs from solutions (Harland 1994). Most metal extraction processes by IX from mining leach solutions and industrial wastewater are carried out in columns (Harland 1994). In these applications, the exchange/binding capacity (EC)—defined as the number of exchange/binding sites in equivalents (Eq) per unit volume (L) of swollen resin bed—is the key performance parameter. Today, the vast majority of commercial anion exchange and chelating resins are prepared by functionalization of crosslinked styrene–divinylbenzene (STY–DVB) beads (Harland 1994).

However, commercial anion exchange and chelating resins have limited exchange/binding capacities with a maximum EC of 1.4 eq/L (Cl^-) for STY–DVB resins with methyl quaternary ammonium Cl^- groups (Chen et al. 2012). For STY–DVB chelating resins with n-methylglucamine, the EC is 0.7 eq/L (Mishra et al. 2012). Because of this, current commercial anion exchange and chelating resins have limited operational capacity in column-based separation processes that are used to recover metals from mining leach solutions and industrial wastewater.

Dendritic macromolecules are providing new opportunities to develop high-capacity anion exchange and chelating resins for metal extraction from solutions (Chen et al. 2012; Mishra et al. 2012). Chen et al. (2012) have shown that BPEI macromolecules can be used as building blocks to synthesize anion exchange resins (Fig. 4a) with exchange capacities that are 1.5–2 times larger than those of commercial STY–DVB resins. To achieve this, the authors first reacted BPEI macromolecules with a mixture of crosslinkers [epichlorohydrin (ECH) + 1-bromo-3-chloropropane] using an inverse suspension process to produce spherical beads (Fig. 4a). The PEI beads were subsequently alkylated to afford anion exchange resins with methyl ammonium Cl^- exchange sites and EC_v reaching 2.7 eq/L (Chen et al. 2012). BPEI macromolecules can also be used as precursors to synthesize chelating resins that can selectively extract oxyanions from solutions. Mishra et al. (2012) reacted BPEI beads with glucono-1,5-D-lactone to afford a resin (BSR-2) with high density of vicinal diol groups (Fig. 4b). Because boron can selectively complex with ligands containing vicinal diol groups, the authors tested the boron sorption capacity/selectivity of the BSR-2 PEI resin. Mishra et al. (2012) reported that the new resin has a boron sorption capacity of 1.93 ± 0.04 mmol/g in deionized water and 0.1 M NaCl solution, which is 66 % larger than that of standard commercial boron-selective resins with *n*-methylglucamine groups. The authors also reported that the PEI BSR-2 resin shows excellent regeneration efficiency using a standard acid with a 1.0 M HCl solution followed by neutralization with a 0.1 M NaOH solution (Mishra et al. 2012). Finally, we would to mention that oxyanions of a number of critical metals (e.g. molybdenum, vanadium, tungsten and germanium) can also selectively complex with resins/sorbents containing vicinal diol groups (Matejka et al. 2004). Thus, the optimization and successful optimization of PEI-based resins with vicinal diol groups could provide a new family of high-performance chelating resins for metal extraction from waste solutions.

NF membranes from polymeric nanofibers and dendritic macromolecules

Pressure-driven membrane processes such microfiltration (MF), UF, NF and reverse osmosis (RO) have become the key components of a broad range of environmental and industrial separation processes including water purification, wastewater treatment, biochemical separations, chemical processing and metal recovery (Strathmann 2011; Schäefer et al. 2005). UF and MF membranes have large pore sizes (e.g., 10–100 nm) allowing them to operate at much reduced pressures (e.g., 0.3–5.0 bar). However, they can only retain particles/colloids and are not effective at retaining or extracting dissolved ions from solutions. In contrast, RO membranes are very effective at retaining dissolved ions in solutions while allowing pure water to pass through. However, they require large pressures to operate (Strathmann 2011; Schäefer et al. 2005). NF is increasingly being used as alternative to RO in water reclamation, industrial wastewater treatment and metal/acid recovery from solutions (Schäefer et al. 2005). NF membranes have larger pores (e.g. 1.0–3.0 nm) and thus require much less pressure than RO membranes. Because of this, NF is increasingly being used in industrial separation processes including the recovery of metals, acids and bases from mining leach liquors and metal finishing solutions (Soldenhoff et al. 2005).

Today, the vast majority of commercial NF membranes are thin-film composite (TFC) membranes with three components: (1) a nonwoven poly(ethylene terephthalate) support, (2) a microporous polysulfone support and (3) a thin separation layer consisting of crosslinked polyamide (PA) prepared by interfacial polymerization of trimesyl Cl^- with an aromatic amine (e.g. m-phenylene diamine) or an aliphatic amine (e.g. piperazine) (Vankelecom et al. 2005). TFC PA NF membranes have small pores (e.g. 0.5–1.5 nm) and are negatively charged (Schäefer et al. 2005). Their mechanisms of ion rejection include (i) size exclusion, (ii) Donnan exclusion and (iii) dielectric exclusion (Vezzani and Bandini 2002; Escoda et al.

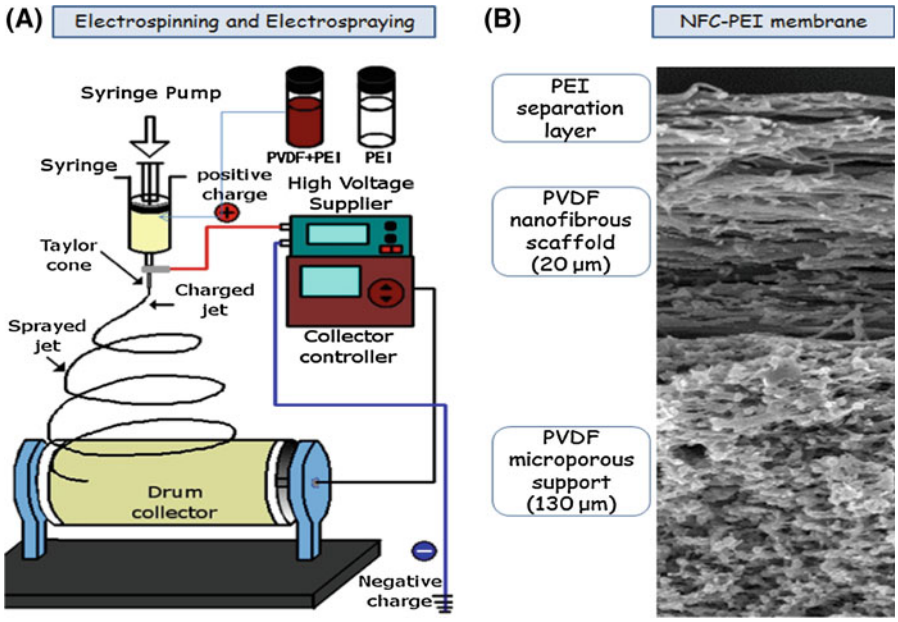

Fig. 4 Low-pressure and ion selective nanofibrous composite membranes (Park et al. 2012). This class of membranes could be used to extract and concentrate metal ions from solutions

2010; Déon et al. 2011). Although TFC–PA NF membranes are effective in most cases at retaining (>90 %) negatively charged divalent anions (e.g. SO_4^{2-} and PO_4^{3-}), they tend to exhibit lower rejection for positively charged metal species of technology metals including Cu^{2+}, Ni^{2+}, Co^{2+} and Zn^{2+} (Cheng et al. 2011; Ji et al. 2011; Ba et al. 2009). Thus, there is a need for novel and positively charged NF membranes to expand the applicability of NF by improving its viability as a cost-effective and environmentally sound process to (i) separate/concentrate technology metals from mining leach liquors and (ii) reclaim water from acid/basic mining leach liquors, industrial wastewater and mining liquid effluents (Fig. 1).

The convergence between membrane technology, polymer nanofiber technology and dendrimer nanotechnology is providing new opportunities to develop low-pressure and positively charged NF membranes. Park et al. (2012) have recently described the preparation of a new family of low-pressure and positively charged NF membranes consisting of crosslinked BPEI separation layers supported by PVDF nanofibrous scaffolds that are deposited onto commercial PVDF MF membrane supports (Fig. 4). To prepare these new membranes, the authors first utilized electrospinning to deposit blends of PVDF/BPEI nanofibers onto commercial PVDF MF membranes (Fig. 4). Following completion of the electrospinning process, Park et al. (2012) electrosprayed solutions of BPEI + methanol onto the PVDF nanofibrous scaffolds (Fig. 4a). The BPEI-laden nanofibrous PVDF scaffolds were subsequently reacted with solutions of trimesoyl Cl^- (TMC), 1,3-dibromopropane and ECH, respectively, to produce NFC membranes with crosslinked PEI separation layers (Fig. 4). Park et al. (2012) used a broad range of analytical tools/assays to characterize the morphology, composition, hydrophobicity and surface charge of the new NFC membranes. They also measured the ion rejection and permeate flux of the new membranes by carrying cross-flow filtration experiments at constant pressure of 7.0 bar using aqueous solutions (2,000 mg/L) of four salts (NaCl, $MgCl_2$, Na_2SO_4, and $MgSO_4$). The overall results of the characterization and filtration experiments indicate that the NFC–PVDF–PEI membrane with TMC crosslinker has good potential to serve as a low-pressure and positively charged NF membrane for metal recovery from waste solutions (Fig. 1). This membrane is hydrophilic with a surface charge (zeta potential) of ~40 mV at pH 6.0 and a water contact angle of ~39.0° that is lower than those of commercial TFC–PA NF membranes, which have contact angles of 50–60° (Park et al. 2012). The filtration experiments showed that the NCF–PVDF membrane with a separation layer of BPEI macromolecules crosslinked with TMC has a high water flux (~30 L m^{-2} h^{-1}) and high rejections for $MgCl_2$ (~88 %) and NaCl (~65 %) at pH 6 using a pressure

of 7 bar. The optimization of the NFFC–PVDF–PEI membranes could provide new opportunities to develop efficient NF pretreatment membranes that can extract and concentrate technology metals from waste solutions (Fig. 1) to improve their selective recovery and purification using DEUF (Fig. 2b) or chelating resins (Fig. 4).

Summary and outlook

Energy is a major challenge of the twenty-first century, and meeting the world's growing demand for energy while significantly reducing CO_2 emissions will require the deployment of orders of magnitude more clean and renewable energy systems than what is in place now. There is a growing realization, however, that the implementation of clean and renewable energy systems will require sizeable amounts of technology metals including *critical materials* such as REEs and PGMs. Nanotechnology provides unprecedented opportunities to address materials criticality in clean and renewable energy technologies. Nanomaterials are particularly attractive as functional materials for clean and renewable energy systems due their large surface areas and size and shape-dependent optical, electronic, magnetic and catalytic properties. Thus, nanomaterials based on non *critical materials* and earth-abundant elements are increasingly being optimized and evaluated as components and building blocks of energy generation, conversion and storage systems. The most promising applications of nanostructured materials in clean and renewable energy technologies include (i) solar cells, (ii) wind turbines, (iii) EVs, (iv) batteries, (v) energy-efficient lighting devices and (vi) solar fuel generation. Nanotechnology can also help augment the supply of critical materials for clean and renewable energy technologies. Nanomaterials can be processed into various form factors including water-soluble ligands, particles, fibers and membranes. These unique properties of nanomaterials are being utilized to develop new more effective separation materials and systems for the selective recovery of technology metals from non-traditional sources including mine tailings, industrial wastewater and electronic wastes with minimum environmental impact.

In summary, nanotechnology has great potential to help improve or achieve materials sustainability for clean and renewable energy technologies as we become more proficient at manipulating matter at the atomic scale to prepare functional materials "by design" with the required electronic, optical, magnetic and catalytic properties while utilizing little or none of the *critical elements* that are currently required in energy generation, conversion and storage. However, a key challenge will be to process/integrate nanomaterials into systems with demonstrated added values including (i) terawatt-scale electricity generation from solar radiation at cost comparable to that of electricity from fossil fuels and (ii) batteries and motors that enable EVs to be cost-competitive with gasoline-powered cars. Moreover, it is important to keep in mind that energy technologies are materials intensive and that criticality is not a fixed property of a material. As we discover, invent and optimize new energy materials and technologies (e.g. more efficient thermoelectric materials for terawatt-scale electricity generation using waste heat), almost any material could find its way onto a critical list. Thus, scientists, engineers, policy makers and business leaders need to approach energy innovation with this in mind and adopt a holistic approach to achieve materials sustainability in clean and renewable energy technologies including (i) materials substitution and/or system design to reduce or eliminate criticality, (ii) recycling, (iii) improvements in metal extraction efficiency and yields from existing mines and (iv) recovery from non-traditional sources such as mine tailings, industrial wastewater and electronic wastes.

Acknowledgments Neil A. Fromer thanks the Resnick Sustainability Institute, as well as the LMI-EFRC, Rod Eggert, and Jack Lifton and the other attendees of the Resnick Institute critical materials workshop for helpful discussions. Mamadou Diallo thanks the EEWS Initiative (Grant # NT080607C0209721), the National Research Foundation of Korea (NRF) [MEST grant No. 2012M1A2A2026588] and the National Science Foundation (NSF) of United States [CBET grants 0948485 and 0506951] for funding his research on sustainable chemistry, engineering and materials (SusChEM).

References

Aricò AS, Bruce P, Scrosati B, Tarascon JM, van Schalkwijk W (2005) Nanostructured materials for advanced energy conversion and storage devices. Nat Mat 4:366–377

ARPA-E (Advanced Research Projects Agency-Energy) (2011) Rare earth alternatives in critical technologies (REACT). http://arpa-e.energy.gov/?q=arpa-e-programs/react

Ba C, Langer J, Economy J (2009) Chemical modification of P84 copolyimide membranes by polyethylenimine for nanofiltration. J Membr Sci 327:49–58

Bian Z, Mia X, Lei S, Chen SE, Wang W, Stuthers S (2012) The challenges of reusing mining and mineral-processing wastes. Science 337:702–703

Brinker JC, Ginger D (2011) Nanotechnology for sustainability: energy conversion, storage, and conservation. In: Roco MC, Mirkin MC, Hersham M (eds) Nanotechnology research directions for societal needs in 2020: retrospective and outlook. Springer, New York, pp 261–303

Callahan DM, Munday JN, Atwater HA (2012) Solar cell light trapping beyond the ray optic limit. Nano Lett 12:214–218

Cavaliere S, Subianto S, Savych I, Jones DJ, Rozière J (2011) Electrospinning: designed architectures for energy conversion and storage devices. Energy Environ Sci 4:4761–4785

Chen DP, Yu CJ, Chang C-Y, Wan Y, Frechet JMJ, Goddard WA, Diallo MS (2012) Branched polymeric media: perchlorate-selective resins from hyperbranched polyethyleneimine. Environ Sci Technol 46:10718–10726

Cheng S, Oatley DL, Williams PM, Wright CJ (2011) Positively charged nanofiltration membranes: review of current fabrication methods and introduction of a novel approach. Adv Colloid Interface Sci 164:12–20

Cohen SM, Petoud S, Raymond KN (2001) Synthesis and metal binding properties of salicylate-, catecholate-, and hydroxypyridinonate-functionalized dendrimers. Chemistry-A 7:272–279

Deceglie MG, Ferry VE, Alivisaos AP, Atwater HA (2012) Design of nanostructured solar cells using coupled optical and electrical modeling. Nano Lett 12:2894–2900

Déon S, Escoda A, Fievet P (2011) A transport model considering charge adsorption inside pores to describe salts rejection by nanofiltration membranes. Chem Eng Sci 66:2823–2832

Diallo MS (2008) Water treatment by dendrimer enhanced filtration. US Patent 7,470,369

Diallo MS, Brinker JC (2011) Nanotechnology for sustainability: environment, water, food, minerals and climate. In: Roco MC, Mirkin MC, Hersham M (eds) Nanotechnology research directions for societal needs in 2020: retrospective and outlook. Science policy reports. Springer, New York, pp 221–259

Diallo MS et al. (2013) Implications: convergence of knowledge and technology for a sustainable society. In: Roco MC, Bainbridge WS, Tonn B, Whitesides G (eds) Convergence of knowledge, technology, and society: beyond convergence of nano-bio-info-cognitive technologies. Science Policy Reports, Springer, Dordrecht

Diallo MS, Christie S, Swaminathan P, Balogh L, Shi X, Um W, Papelis L, Goddard WA, Johnson JH (2004) Dendritic chelating agents 1. Cu(II) binding to ethylene diamine core poly(amidoamine) dendrimers in aqueous solutions. Langmuir 20:2640–2651

Diallo MS, Christie S, Swaminathan P, Johnson JH, Goddard WA (2005) Dendrimer enhanced ultrafiltration. 1. Recovery of Cu(II) from aqueous solutions using G*x*–NH_2 PAMAM dendrimers with ethylene diamine ore. Environ Sci Technol 39:1366–1377

Diallo MS, Wondwossen A, Johnson JH, Goddard WA (2008) Dendritic chelating agents 2. U(VI) binding to poly(amidoamine) and poly(propyleneimine) dendrimers in aqueous solutions. Environ Sci Technol 42:1572–1579

DOE (Department of Energy) (2006) Basic research needs for advanced nuclear energy systems. http://science.energy.gov/bes/news-and-resources/reports/abstracts/#ANES

DOE (Department of Energy) (2011) Critical materials strategy. http://energy.gov/pi/office-policy-and-international-affairs/downloads/2010-critical-materialsstrategy

Dvornic PR, Uppuluri S (2002) Rheology and solution properties of dendrimers. In: Fréchet JMJ, Tomalia DA (eds) Dendrimers and other dendritic polymers. Wiley, New York

Escoda A, Lanteri Y, Fievet P, Déon S, Szymczyk A (2010) Determining the dielectric constant inside pores on nanofiltration membranes from membrane potential measurements. Langmuir 26:14628–14635

Fréchet JMJ, Tomalia DA (2002) Dendrimers and other dendritic polymers. Wiley, New York

Fromer N, Eggert RG, Lifton J (2011) Critical materials for sustainable energy applications. Resnick Institute Report, California Institute of Technology. http://resnick.caltech.edu/programs/critical-materials/index.html

Gloe K, Stephan H, Grotjahn M (2003) Where is the anion extraction going? Chem Eng Technol 26:1107–1117

Gomes CP, Almeida MF, Loureiro JM (2001) Gold recovery with ion exchange used resins. Sep Purif Technol 24:35–57

Grandidier J, Callahan DM, Munday JN, Atwater HA (2012) Gallium arsenide solar cell absorption enhancement using whispering gallery modes of dielectric nanospheres. IEEE J Photovolt 2:123–128

Guo Q, Ford GM, Yang WC, Walker BC, Stach EA, Hillhouse HW, Agrawal R (2010) Fabrication of 7.2% efficient CZTSSe solar cells using CZTS nanocrystals. J Am Chem Soc 132:17384–17386

Gur I, Fromer NA, Geier ML, Alivisatos AP (2005) Air-stable all inorganic nanocrystal solar cells processed from solution. Science 310:462–465

Harland CE (1994) Ion-exchange: theory and practice, 2nd edn. Royal Society of Chemistry, London

IPCC (Intergovernmental Panel on Climate Change) (2007) Solomon, S, Quin, D, Manning, M, Chen, Z, Marquis, M, Averyt, KB, Tignor, M, Miller, HL (eds) Climate change 2007: the physical science basis. Cambridge University Press, Cambridge

Ji Y, An Q, Zhao Q, Chen H, Gao C (2011) Preparation of novel positively charged copolymer membranes for nanofiltration. J Membr Sci 376:254–265

Johnson J, Harper EM, Lifset R, Graedel TE (2007) Dining at the periodic table: metals concentration as they relate to recycling. Environ Sci Technol 41:1759–1765

Kneller EF, Hawig R (1991) The exchange-spring magnet—a new material principle for permanent-magnets. IEEE Trans Magn 27:3588–3600

Krämer M, Stumbé JF, Grimm G, Kaufmann B, Krüger U, Webe M, Haag R (2004) ChemBioChem 5:1081–1087

Lewis NS, Nocera DG (2006) Powering the planet: chemical challenges in solar energy utilization. Proc Natl Acad Sci 103:15729–15735

Liu XQ, He SH, Qiq JM, Wang JP (2011) Nanocomposite exchange-spring magnet synthesized by gas phase method: from isotropic to anisotropic. Appl Phys Lett 98:222507

Ma W, Luther JM, Zhend HM, Wu Y, Alivisatos AP (2009) Photovoltaic devices employing ternary PbS_xSe_{1-x} nanocrystals. Nano Lett 9:1699–1703

Maiti PK, Lin T, Cagin ST, Goddard WA (2005) The effect of solvent and pH on the structure of PAMAM dendrimers. Macromolecules 38:979–991

Martell AE, Hancock RD (1996) Metal complexes in aqueous solutions. Plenum Press, New York

Matejka Z, Parschova H, Ruszova P et al (2004) Selective uptake and separation of oxoanions of molybdenum, vanadium, tungsten, and germanium by synthetic sorbents having polyol moieties and polysaccharide-based biosorbents. In: Moyer BA, Singh P (eds) Fundamentals and applications of anion separations. Kluwer Academic/Plenum Publishers, New York

Mckone J, Sadtler B, Werlang C, Lewis NS, Gray HB (2013) Ni–Mo nanopowders for efficient electrochemical hydrogen evolution. ACS Catal 3:166–169

Mishra H, Yu, CJ, Chen DP, Dalleska NF, Hoffmann MR, Goddard, WA, Diallo MS (2012) Branched polymeric media: boron-chelating resins from hyperbranched polyethyleneimine. Environ Sci Technol 46:8998–9004

Moss R, Tzimas E, Kara H, Willis P, Kooroshy J (2011) Critical metals in strategic energy technologies. Publications Office of the European Union. http://publications.jrc.ec.europa.eu/repository/handle/111111111/22726

Moyer BA, Bonnesen PV (1997) Physical factors in anion separations. In: Bianchi A, Bowman-James K, García-Espana E (eds) Supramolecular chemistry of anions. VCH, New York, pp 1–44

Nakamuro E, Sato K (2011) Managing the scarcity of chemical elements. Nat Mat 10:158–161

NRC (National Research Council) (2008) Minerals, critical minerals, and the U.S. economy. ISBN: 0-309-11283

O'Donnell KP, Maur MAD, Di Carlo A, Lorenz K (2012) It's not easy being green: strategies for all-nitrides, all colour solid state lighting. Phys Stat Solidi 6:49–52

Park S-J, Cheedrala RK, Diallo MS, Kim CH, Kim IS, Goddard WA (2012) Nanofiltration membranes based on polyvinyldene fluoride nanofibrous scaffolds and crosslinked polyethyleimine networks. J Nanopart Res 14:884

Raghavan P, Lim DH, Ahn JH et al (2012) Electrospun polymer nanofibers: the booming cutting edge technology. React Funct Polym 72:915–930

Reck BK, Graedel TE (2012) Challenges in metal recycling. Science 337:690–695

Schäefer A, Fane AG, Waite TD (2005) Nanofiltration: principles and applications. Elsevier, New York

Scott RWJ, Wilson OM, Crooks RM (2005) Synthesis, characterization and applications of dendrimer-encapsulated manoparticles. J Phys Chem B 109:692–704

Seiler M (2006) Hyperbranched polymers: phase behavior and new applications in the field of chemical engineering. Fluid Phase Equilib 241:155–174

Shen Y, Huang MQ, Lee D, Bauser S, Higgins A, Chen C, Liu S (2006) Hybrid nanograin rare earth magnets with improved thermal stability. J Appl Phys 99:08B520

Soldenhoff K, McCulloh J, Manis A, Macintosh P (2005) Nanofiltration in metal and acid recovery. In: Schäefer A, Fane AG, Waite TD (eds) Nanofiltration: principles and applications. Elsevier, New York, pp 459–477

Strathmann H (2011) Introduction to membrane science and technology. Wiley-VCH, Weinheim

Stricker N (2013) Reverse mining: scientists extract rare earth materials from consumer products. https://inlportal.inl.gov/portal/server.pt/community/newsroom/257/feature_story_details/1269?featurestory=DA_606590)

Stumm W, Morgan JJ (1996) Aquatic chemistry: chemical equilibria and rates in natural waters, 3rd edn. Wiley, New York

Suntivich J, May K, Gasteiger H, Goodenough J, Shao-Horn Y (2011) A perovskite oxide optimized for oxygen evolution catalysis from molecular orbital principles. Science 334:1383–1385

Tomalia DA, Diallo MS (2012) Dendrimers: synthetic science to controlled organic nanostructures and a window to a new systematic framework for unifying nanoscience. In: Goddard WA, Brenner DW, Lyshevski SE, Iafrate GJ (eds) Handbook of nanoscience, engineering and technology, 3rd edn. CRC Press, Boca Raton, pp 413–467

Valdivia CE, Chow S, Fafard S, et al. (2010) Measurement of high efficiency 1 cm^2 AlGaInP/InGaAs/Ge solar cells with embedded InAs quantum dots at up to 1000 suns continuous concentration. In: Proceedings of the 35th IEEE photovoltaic specialists conference (PVSC), pp 1253–1258

Vankelecom IFJ, De Smet K, Gevers LEM, Jacobs PA (2005) Nanofiltration membrane materials and preparation. In: Schäefer A, Fane AG, Waite TD (eds) Nanofiltration: principles and applications. Elsevier, New York, pp 34–65

Vezzani D, Bandini S (2002) Donnan equilibrium and dielectric exclusion for characterization of nanofiltration membranes. Desal 149:477–483

Vrubel H, Merki D, Hu X (2012) Hydrogen evolution catalyzed by MoS3 and MoS2 particles. Energy Environ Sci 5:6136–6144

Zhang Y, Xie C, Su H et al (2011) Employing heavy metal-free colloidal quantum dots in solution-processed white light-emitting diodes. Nano Lett 11:329–332

Zhao T, Zheng Y, Poly J, Wang W (2013) Controlled multivinyl monomer homopolymerization through vinyl oligomer combination as a universal approach to hyperbranched architectures. Nat Commun 4:1873. (http://www.nature.com/ncomms/journal/v4/n5/full/ncomms2887.html)

DOI 10.1007/978-3-319-05041-6_24
Reprinted from the *Journal of Nanoparticle Research*, DOI 10.1007/s11051-012-0869-6

RESEARCH PAPER

Recovery of silica from electronic waste for the synthesis of cubic MCM-48 and its application in preparing ordered mesoporous carbon molecular sieves using a green approach

Tzong-Horng Liou

Received: 5 October 2011 / Accepted: 11 April 2012 / Published online: 19 June 2012

Abstract The electronics industry is one of the world's fastest growing manufacturing industries. However, e-waste has become a serious pollution problem. This study reports the recovery of e-waste for preparing valuable MCM-48 and ordered mesoporous carbon for the first time. Specifically, this study adopts an alkali-extracted method to obtain sodium silicate precursors from electronic packaging resin ash. The influence of synthesis variables such as gelation pH, neutral/cationic surfactant ratio, hydrothermal treatment temperature, and calcination temperature on the mesophase of MCM-48 materials is investigated. Experimental results confirm that well-ordered cubic MCM-48 materials were synthesized in strongly acidic and strongly basic media. The resulting mesoporous silica had a high surface area of 1,317 m^2/g, mean pore size of about 3.0 nm, and a high purity of 99.87 wt%. Ordered mesoporous carbon with high surface area (1,715 m^2/g) and uniform pore size of CMK-1 type was successfully prepared by impregnating MCM-48 template using the resin waste. The carbon structure was sensitive to the sulfuric acid concentration and carbonization temperature. Converting e-waste into MCM-48 materials not only eliminates the disposal problem of e-waste, but also transforms industrial waste into a useful nanomaterial.

Keywords E-waste · Silica · MCM-48 · CMK-1 · Textural characterization · Nanotechnology · Sustainable development

Special Issue Editors: Mamadou Diallo, Neil Fromer, Myung S. Jhon

This article is part of the Topical Collection on Nanotechnology for Sustainable Development

T.-H. Liou (✉)
Department of Chemical Engineering, Ming Chi University of Technology, 84 Gungjuan Rd., Taishan, New Taipei 24301, Taiwan
e-mail: thliou@mail.mcut.edu.tw

Introduction

Silica-based mesoporous materials, designated M41s, have attracted much attention because these materials exhibit a high surface area, large pore volume, and adjustable pore size. Mesoporous silica with pore sizes ranging from 2 to 50 nm has found many applications, including catalysts (Ying et al. 2011), nanocomposites (Kim et al. 2009), storage and recovery of H_2 and CO_2 (Prasanth et al. 2010; Jang et al. 2009), and biotechnological applications (Liu et al. 2010). The main members of the M41's family are MCM-41, MCM-48, and MCM-50, which have hexagonal, cubic, and unstable lamellar structures, respectively. Because MCM-48 material has a three-dimensional pore system that helps reduce pore blockage and provides more efficient mass transfer kinetics, it is a better candidate for catalytic and adsorption applications than with MCM-41 materials (Zhao et al. 2010a). The

channel structure of MCM-48 silica consists of an interconnected pore system that acts as a template for ordered mesoporous carbon (OMC) synthesis (Ryoo et al. 2001). The ordered mesoporous carbon with large adsorption capacity is highly favorable for the development of advanced materials in CH_4 and H_2 storage (Peng et al. 2008), adsorbents for removal of organic pollutants (Hao et al. 2010), carbon composite films for supercapacitor (Dai et al. 2011), fuel cells (Salgado et al. 2010), and biomedical materials (Kim et al. 2008). However, owing to its very sensitive synthetic conditions, relatively few studies investigate MCM-48. Electronic packaging resin waste is rich in silica. Thus, achieving high-quality MCM-48 and OMC materials with well-ordered mesoporous structure by a green approach and electronic waste has important economic and environmental implications.

Over the past decades, the electronics industry has developed rapidly around the world. Estimations of the worldwide revenue of the semiconductor industry exceeded US 226 billion in 2009, and this figure is expected to grow by 13 % each year (Kim et al. 2010). However, the disposal of electronic and electrical waste (e-waste) has become a serious environmental problem as a result of the huge amounts of electronic goods being produced. The current annual production of e-waste, including old computers, mobile phones, television sets, stereos, and radios, is estimated to be approximately 20–50 million tons (Chen et al. 2011). Taiwan's Environmental Protection Administration (EPA) established its *Scrap Home Appliances and Computers Recycling Regulation*, based on the Waste Disposal Act (WDA), to require manufacturers and importers to take back their products (Shih 2001). Electronic packaging materials are widely used in many types of electrical and electronic equipment. This material is used to protect electronic products such as integrated circuits (IC). Electronic packaging material is generally a mixture of epoxy resin, phenol resin, silica, and additives (Liou 2003). In present, the treatment of e-waste includes reuse, remanufacturing, and recycling, along with incineration and landfilling (Cui and Zhang 2008). Because plastic materials are essentially non-biodegradable, putting them in landfill is not a viable long-term solution. The chemical composition of packaging resin waste is approximately 80 wt% silica (Liou 2004), which is useful for the mass production of MCM-48 mesoporous molecular sieves. Therefore, using recycled industrial resin waste offers benefits in terms of waste treatment and the recovery of valuable materials.

Numerous studies indicate the synthesis and characterization of mesoporous MCM-41 materials by adding an appropriate surfactant to the silica precursor (Bhagiyalakshmi et al. 2010a; Lelong et al. 2008). However, the use of e-waste to prepare MCM-48 materials is generally neglected in the literature. The phase characteristics of MCM-48 are strongly influenced by its synthesis time, temperature, silica source, and type of surfactant template (Peña et al. 2001; Petitto et al. 2005). Doyle et al. (2006) studied the evolution of phases during MCM-48 synthesis and found that increasing reaction time or temperature alters the overall phase transformations from MCM-41/MCM-50 to MCM-48 to MCM-50. Wei et al. (2010) synthesized MCM-48 with mixed surfactants of cethyltrimethylammonium bromide (CTAB) and Triton X-100 (TX-100), showing that TX-100/CTAB ratio is crucial to the formation of a pure MCM-48 structure. Solid wastes, such as coal fly ash and rice husk, provided the silicon sources for the synthesis of mesoporous silica materials, SBA-15 and SBA-16 (Chandrasekar and Ahn 2008; Bhagiyalakshmi et al. 2010b). These mesoporous silica materials were impregnated with sucrose in the presence of sulfuric acid solution and then were pyrolyzed in inert gas to obtain ordered mesoporous carbon.

The recovery of valuable metals from e-waste has been well studied in the literature (Cui and Zhang 2008). However, little attention has been paid to the recovery and utilization of silica from e-waste. The current study investigates MCM-48 prepared using a sodium silicate precursor obtained from recycled electronic packaging resin wastes. The commercial fabrication of sodium silicate from quartz sand and sodium carbonate at 1,300 °C requires a lot of energy (Brinker and Scherer 1990). In contrast, using cheap inorganic silica sources from e-wastes can improve the industrial scale production of MCM-48 materials. Previous studies provide a detailed analysis of the recovery of packaging resin ash and its application in preparing MCM-41 materials (Liou 2003; 2004; 2011). The aim of this study is to synthesize highly ordered MCM-48 using cationic and neutral surfactant mixture. The high-quality MCM-48 produced in this study is suitable as a template for the synthesis of ordered mesoporous carbons. The synthesis of MCM-48 and ordered mesoporous carbon by a green approach enables the effective use of e-waste resources.

Experimental

Materials

The electronic packaging resin waste used in this study was obtained from an electronic packaging mill (Siliconwave Precision Co., Taiwan). The basic constituents and properties of this material were described in a previous report (Liou 2003). Commercially available surfactants, including cetyltrimethylammonium bromide (CTAB, $C_{16}H_{33}(CH_3)_3NBr$, Acros organics) and polyethylene glycol dodecyl ether ($C_{12}(EO)_4$, Sigma-Aldrich), served as organic templates. Analytical grade sulfuric acid (H_2SO_4), hydrochloric acid (HCl), hydrofluoric acid (HF), and sodium hydroxide (NaOH) were used as acid and base treatments (Merck, Germany). Sucrose ($C_{12}H_{22}O_{11}$) and glucose ($C_6H_{12}O_6$) were used as the carbon precursors (Sigma-Aldrich). High purity air and N_2 were used as the reaction gas and purge gas, respectively (Sun Fu Co., 99.995 %).

Extraction of silica from electronic packaging resin waste

Resin wastes were first ground and fine powders were obtained by sieving to below 45 μm. The packaging resin ash (denoted as PRA) was used as a raw material for preparing mesoporous silica by Liou's method (Liou 2004). For each heat-treated sample, the powdered resin of approximately 5.0 g was heated at 800 °C in air. The amount of ash produced is 4.1 g. After the heating period, the ash was refluxed using HCl solution to remove any metallic impurities. The remaining solid was washed with distilled water several times to remove acid from the filtrate, and then dried in an oven at 105 °C for 24 h.

The dissolution of silica from PRA was performed by an alkali-extracting method (Liou 2011). The 50 g of acid-leached PRA powder was added to a flask containing a 4.0 M 325 ml of NaOH solution and boiled at 100 °C for 6 h with constant stirring. This process converted the silica into a sodium silicate solution. The solution was centrifuged to separate the suspended particles, and then filtered through a glass filter (Whatman plc, England) to remove any metal or carbon residue. This filtration process was repeated several times and finally obtained a colorless, transparent solution. The concentration of alkali-extracting solution was diluted with deionized water from 4.0 M to 2.0 M.

Synthesis of mesoporous silica molecular sieves

By a typical synthesis procedure, 1.82 g of CTAB and 0.27 g of $C_{12}(EO)_4$ were dissolved in 32 ml of deionized water. The 10 ml of sodium silicate solution was mixed with the CTAB/$C_{12}(EO)_4$ solution with constantly stirring. A 1.0 M H_2SO_4 solution was titrated slowly into the silicate solution. The mixture pH was monitored with a S20-K pH meter (Metter Toledo) to control pH at a constant value of 1–11. The gel was transferred into PTFE-lined stainless steel autoclave and allowed to hatch at a constant temperature for 48 h. The precipitates were water-washed, filtered, and dried. The dried powders were calcined in air at a 1 °C/min heating rate and then maintained at 450–850 °C for 6 h.

Preparation of mesoporous carbon molecular sieve

The OMC synthesis method reported by Ryoo et al. (2001) was adopted. Essentially, MCM-48 was impregnated with sucrose and water in the presence of H_2SO_4. The impregnated silica was dried in an oven at 100 °C for 6 h, and then dried at 160 °C for 6 h. The impregnation and drying steps were repeated once. The obtained sample was placed in a tubular reactor and was heated to 500–900 °C at a temperature rate of 10 °C/min in N_2. After carbonization, the silica template was removed in an aqueous HF solution. Finally, the OMC was obtained by washing the solid sample repeatedly with deionized water and drying it in air at 105 °C for 24 h.

Characterization of the mesoporous silica and mesoporous carbon samples

The amounts of metallic impurities were estimated using an inductively coupled plasma-mass spectrometer (Kontrin Plasmakon, model S-35). A Heraeus elemental analyzer was used to determine the amount of fundamental organic element. The adsorption–desorption isotherms of N_2 at −196 °C were measured using a Micrometric ASAP 2010 instrument.

The mesophase of samples was analyzed using a small angle X-ray scattering (SAXS) system (Osmic, model PSAXS-USH-WAXS-002). The crystalline

structure of the samples was identified using powder X-ray diffractometer (PANalytical, model X'pert pro system). The FTIR spectra of samples were obtained using a Shimadzu FTIR-8300 spectrometer. The surface morphology of samples was studied using a JEOL JSM-6700F field-emission scanning-electronic microscope (FE-SEM). The mesoporous structure of powders was observed by high-resolution transmission electron microscopy (JEOL, model JEM-1200CX II). The remaining amount (W/W_o) of samples were recorded using a thermogravimetric apparatus (Mettler, model TGA/SDTA851e). Each sample was heated at a 10 °C/min heating rate in air.

Results and discussion

Analysis of metallic impurities of silica molecular sieve

The amounts of metallic ingredients present in PRA and mesoporous silica samples were analyzed by ICP-MS (Table 1). When silica was synthesized from alkali-extracted PRA at pH 7 without the addition of a surfactant, the sample possessed a higher proportion of Na impurities. This is because Na salts are embedded in the silica gel during precipitation and are not easily removed from the gel (Liou 2011). No Na impurities appeared in the mesoporous silica samples, which were synthesized from alkali-extracted PRA by adding a surfactant. This is due to the well-dispersed silica particles in the surfactant solution. The Na ions can easily diffuse out of the silica matrix and be removed by a water-washing procedure. Comparing silica samples synthesized at various pH values shows that the total impurity content produced under strongly acidic (pH 1) and strongly basic (pH 11) conditions is relatively lower than neutral (pH 7) and weakly acidic (pH 3 and pH 5) conditions. The silica synthesized at pH 5 has highest impurity content. The remaining masses for thermal decomposition of as-synthesized silica in air are in the order of pH 5>pH 3>pH 7>pH 1>pH 9>pH 11 (in subsequent TGA observations). This suggests that when silica materials are synthesized in the neutral and weakly acidic media, it results in a higher degree of poly-condensation of the silicate species. As a result, trace amounts of metal may be cached in the silica matrix and cannot be removed by a water-washing procedure. The purity of PRA-MCM-48 silica synthesized at pH 11 is as high as 99.87 wt%.

Synthesis conditions of silica molecular sieve

Effects of gelation pH value

Figure 1a shows that a maximum surface area of 1,153 m^2/g at pH 11. According to SAXS analysis (Fig. 1c, d), the three diffraction peaks at (211), (220), and (332) appeared when the solution pH was adjusted to pH 1 or pH 11. The two SAXS patterns correspond to the characteristics of the MCM-48 material (Han et al. 2004; Doyle and Hodnett 2003). This result can

Table 1 Metallic ingredients analysis of PRA and mesoporous silica samples synthesized at various pH values

	Metallic ingredients as oxides, ppm										
	Na	Sb	K	P	Au	Fe	Mg	Al	Cr	Ag	Total
PRA[a]	87	6,100	8	75	8	92	101	501	9	8	6,989
pH 7[b]	7,181	812	ND	9	ND	48	4	888	2	ND	8,944
pH 1[c]	ND	1,277	ND	5	ND	ND	ND	394	3	ND	1,679
pH 3[c]	ND	1,495	ND	3	ND	ND	ND	363	ND	ND	1,861
pH 5[c]	ND	1,457	ND	12	ND	25	ND	447	ND	ND	1,941
pH 7[c]	ND	1,213	ND	8	ND	138	ND	416	20	ND	1,795
pH 9[c]	ND	1,090	ND	9	ND	133	ND	413	ND	ND	1,645
pH 11[c]	ND	759	ND	2	ND	124	ND	430	3	ND	1,318

[a] Raw resin was burnt in air at 5 °C/min heating rate

[b] Silica sample was prepared from alkali-extracted PRA without the addition of surfactant

[c] Silica sample was prepared from alkali-extracted PRA by adding the neutral/cationic surfactants

ND means not detected

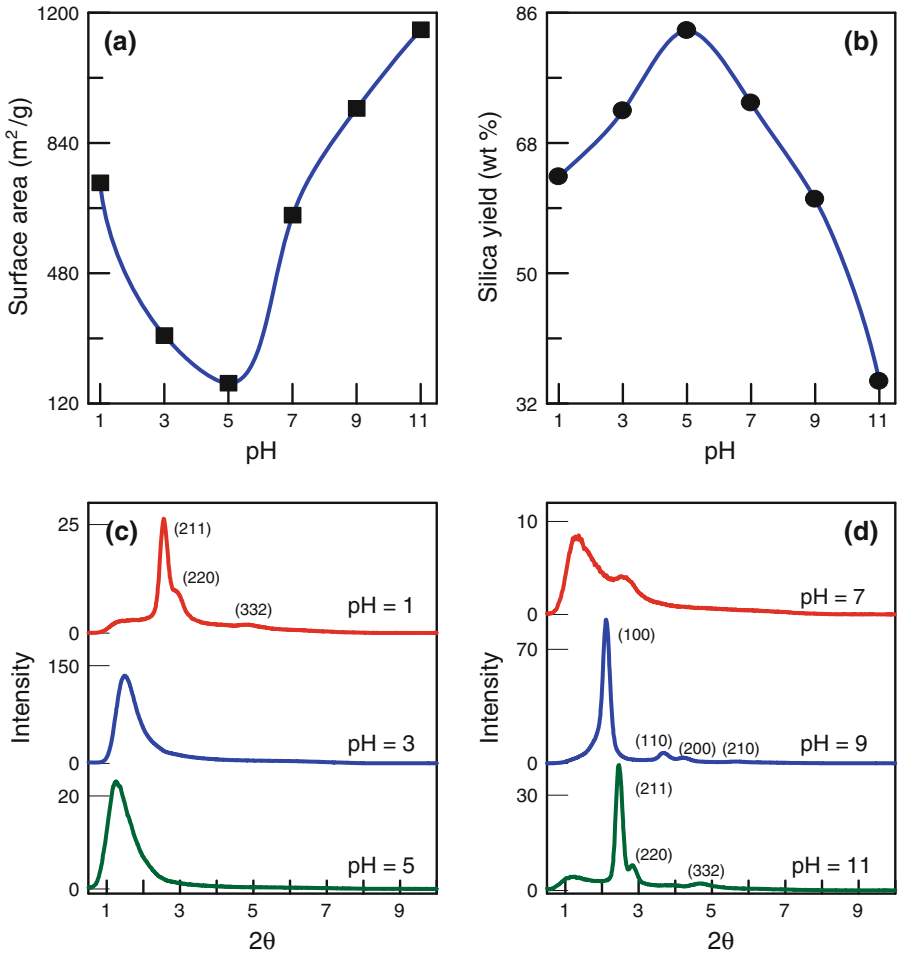

Fig. 1 Effect of gelation pH values on **a** surface area, **b** silica yield, and **c**, **d** phase characteristic of mesoporous silica samples

be explained by the electrostatic attraction between charged silica species and surfactant micelles (Zhao et al. 2010b). At a high pH (pH 11), the negatively charged silica interacted with positively charged CTA^+ micelles, leading to the formation of a cubic framework. Therefore, the silica possessed a high surface area. At a low pH (pH 1), an ordered mesophase was constructed through reversal arrangement of cationic silica and neutral micelles (Liou 2011). This situation also increases the surface area of the products. At pH 3–7, the SAXS patterns show mainly one diffraction peak at 1.26°. This indicates that the surfactant micelle may be destroyed, converting the pore structure into a less ordered structure. Consequently, the surface area steeply decreases. The SAXS pattern for pH 9 sample shows an intense diffraction (100) peak and three higher order (110), (200), and (210) reflections at 2Θ values below 10°, indicating the hexagonal arrangement of a MCM-41 mesoporous structure (Samadi-Maybodi et al. 2011). Figure 1b shows that the silica yield has the opposite tendency as surface area analysis. The silica yield from PRA was defined as (weight of mesoporous silica produced after calcination)/(weight of PRA sample) × 100. For further comparison, Table 2 shows the relationship between gelation pH and the amount of organic element in the as-synthesized samples. The silica phase at pH 5 is approximately 82 wt%, and at pH 1 and pH 11 has wt% only around 64 and 40, respectively. These observations indicate that the higher proportion of silicate species in the surfactant solution under neutral and weakly acidic conditions increases the silica yield for pH 7 and pH 5 samples.

Table 2 Elemental content of as-synthesized silica samples prepared at various pH values

	Composition (wt%)				
	C	H	O[a]	N	Ash
pH 1	24.39	4.85	5.77	0.96	64.03
pH 5	12.34	3.33	2.54	0.23	81.56
pH 7	21.97	5.91	4.14	0.75	67.23
pH 11	38.84	7.23	12.66	1.47	39.80

Silica samples were un-calcined

[a] By difference

Effects of neutral/cationic surfactant ratio

Figure 2a shows the surface area of mesoporous silica obtained by changing the neutral-to-cationic surfactant ratio, where a fraction of the neutral surfactant, f_n, varied from 0 to 1. The highest surface area of 1,317 m^2/g appeared at a fraction of 0.04. Based on SAXS observations (does not show here), typical hexagonal phase MCM-41 products appeared without the addition of neutral surfactant ($f_n = 0$) (Ryoo et al. 1999). A pure mesophase MCM-48 was obtained as f_n increased to 0.04 and 0.13. When the f_n was 0.26, the product was lamellar. Further increasing f_n beyond 0.40, the mesophase transformed to a poor structural order. Therefore, the surface area steeply reduced. This observation indicates that excessive neutral surfactant can dilute the CTA^+ concentration, causing the micelles to gradually disappear and transforming the lamellar phase to the disordered phase.

Effects of hydrothermal treatment temperature

Figure 2b shows that the surface area increases with increasing hydrothermal treatment temperature from 25 to 75 °C is due to the progressive formation of ordered mesophase silica. However, the surface area decreases with increasing temperature from 75 to

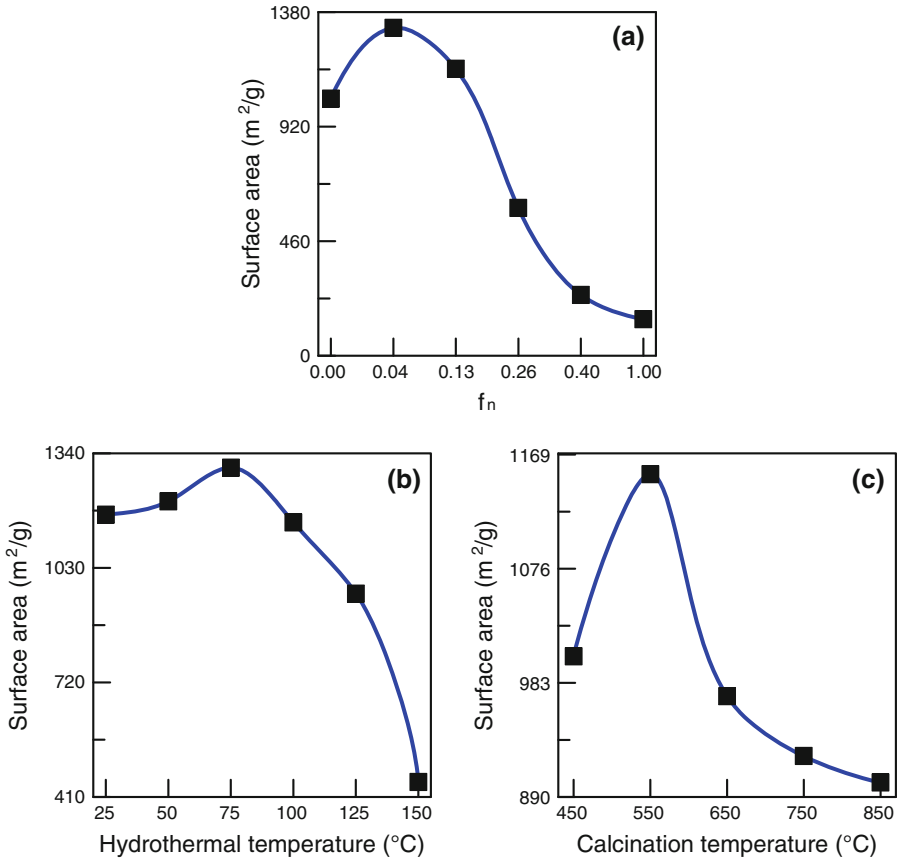

Fig. 2 Effect of **a** neutral/cationic surfactant ratio, **b** hydrothermal treatment temperature, and **c** calcination temperature on the surface area of mesoporous silica samples synthesized at pH 11

150 °C due to silica pore shrinkage. This suggests that increasing the hydrothermal treatment temperature can accelerate the silicate condensation on the silica wall, which subsequently thickens the silica framework (Wang et al. 2000). Mesoporous silica obtained at a low temperature (25–75 °C) has the characteristics of a hexagonal MCM-41 structure. At high temperature (100–125 °C), the silica shows the characteristics of a cubic MCM-48 structure. When the hydrothermal temperature is 150 °C, the material structure transforms to the disordered phase accompanied by a significant decrease in surface area.

Effects of calcination temperature

The purpose of calcination is to remove the organic template from silica/surfactant composite, leaving the porous surface of product. Figure 2c shows that the maximum of the BET surface area appears at 550 °C. The surface areas increase as the calcination temperature increases from 450 to 550 °C due to the release of organic volatiles. However, the surface areas decrease when the calcination temperature exceeds 550 °C is probably caused by the collapse of the gel structure due to the rapid release of water from the pores.

Analysis of silica product characteristics

Pore structure analysis of mesoporous silica molecular sieve

Figure 3 shows the N_2 adsorption–desorption isotherms of silica samples. The isotherms for samples synthesized at pH 1–5 (Fig. 3a) show a type IV isotherm, typical characteristics of mesoporous solids. The sample at pH 5 shows a hysteresis loop similar to H3 (Sing et al. 1985). The isotherm for the pH 3 sample is similar to that of the pH 5 sample. The sample synthesized at pH 1 shows a type H2 hysteresis loop and an obvious increase in adsorbed volume. Figure 3b shows the pore size distribution of silica samples produced in acidic conditions. The silica produced at pH 1 shows a narrow pore distribution

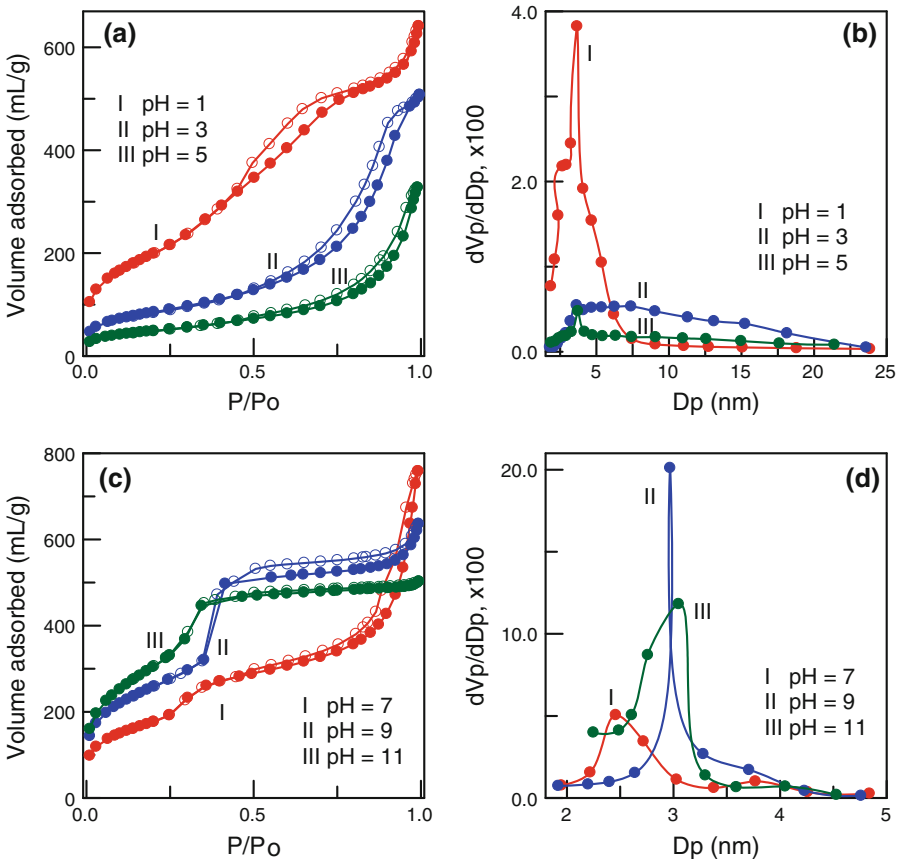

Fig. 3 Nitrogen adsorption–desorption isotherm and differential pore size distribution of mesoporous silica samples synthesized at various pH values: **a**, **b** pH 1–5; **c**, **d** pH 7–11

with average size of 3.7 nm. The samples synthesized at pH 3 and pH 5 have a wide pore size distribution and larger pore diameter, showing that the pore structure is not uniform.

The isotherms of samples obtained at pH 7–11 are type IV (Fig. 3c). These pores may come from the primary pores of silica framework and the voids between particles (Han et al. 2004). The isotherm of the sample synthesized at pH 7 shows a hysteresis loop similar to H3. The pH 9 and pH 11 samples show a sharp increase in adsorbed volume at $P/P_o = 0.2–0.4$ due to the capillary condensation of nitrogen, implying a uniform size of the pore channels (Liu et al. 2009). One H2 hysteresis loop appears at $0.4 < P/P_o < 1.0$ due to the formation of a mesoporous structure. The pore size distribution of silica samples synthesized at pH 7–11 is shown in Fig. 3d. The maximum pore distribution ranges from 2.5 to 3.1 nm increases with pH.

Table 3 lists the specific surface area, pore volume, and average pore diameter of PRA and mesoporous silica samples. In acidic media (pH 1–5), the surface area and pore volume decreased with the increase of the pH values. In neutral and basic media (pH 7–11), the surface area increased and pore volume decreased with the increase of the pH value. The maximum pore volume was 0.985 cm^3/g at pH 7 and the minimum pore volume was 0.444 cm^3/g at pH 5.

Table 3 Specific surface area, pore volume, and average pore diameter of PRA and mesoporous silica samples synthesized at various pH values

	S_{BET} (m^2/g)	V_t (cm^3/g)	V_{mic} (cm^3/g)	V_{meso} (cm^3/g)	V_{meso}/V_t (%)	D_p (nm)
PRA[a]	2.72	0.006	0.000	0.001	16.67	51.10
pH 1[b]	730	0.916	0.022	0.894	97.60	3.67
pH 3[b]	308	0.762	0.003	0.759	99.61	3.65
pH 5[b]	176	0.444	0.003	0.441	99.32	3.74
pH 7[b]	641	0.985	0.022	0.963	97.77	2.46
pH 9[b]	936	0.907	0.021	0.886	97.68	2.97
pH 11[b]	1,153	0.851	0.000	0.851	100.00	3.05

S_{BET} BET surface area, V_t total pore volume, V_{mic} micropore volume, V_{meso} mesopore volume. D_p average pore diameter

[a] Raw resin was burnt in air at 5 °C/min heating rate

[b] Silica samples were prepared from alkali-extracted PRA by adding the neutral/cationic surfactants

Analysis of thermal characteristic, chemical constitution, and crystalline structure

Figure 4a shows the TG and DTG curves of as-synthesized samples obtained in acidic media. The mass loss occurs in two temperature zones, revealing an initial mass loss for temperatures up to ~400 °C due to the decomposition and thermodesorption of the cationic surfactant. The first peak temperature at approximately 228 °C is related to the Hoffmann elimination (giving alkene and trimethylamine) and subsequent trimethylamine desorption (Zhao et al. 2005). The second and third peaks at approximately 275 and 330 °C can be associated with further thermal decomposition of surfactant intermediates. The mass loss increased as the pH decreased. This is because the content of organic substance in the as-synthesized samples increased with decreasing the pH values (Table 2). The mass loss in the range of 400–800 °C may be attributed to the release of water via condensation of silanol group (Kruk et al. 2000). Figure 4b shows the TG and DTG curves of as-synthesized samples produced in neutral and basic media. This figure reveals two major mass loss regions: ~330 °C, 330–800 °C. The DTG curves reveal two peak temperatures at 179–249 and 305 °C for pH 7–9. This mass loss is due to the decomposition and desorption of the organic templates and the water loss due to the condensation of silanols in the silica framework. The mass loss of sample increased as the pH increased because the content of organic substance in the as-synthesized sample increased.

Figure 5a shows the FTIR spectra of the MCM-48 silica obtained from PRA at various calcination temperatures. The bands appearing between 450 and 1,300 cm^{-1} are due to the presence of silica (Liou and Wu 2010). The bands at approximately 475 cm^{-1} correspond to the Si–O–Si vibrations. The peak at 970 cm^{-1} is related to the Si–OH bond, while the peak at 1,115 cm^{-1} is related to Si–O stretching vibrations. Surface silanols and adsorbed water molecules create the broad band appearing in the region between 3,200–3,700 cm^{-1}. The peak position does not change when the temperature exceeds 550 °C, indicating that the combustion reaction is complete. Figure 5b shows the XRD pattern of MCM-48 with a wide range scan, revealing only a broad peak in the region 2Θ greater than 10^o, which suggests the presence of disordered cristabolite (Liou and Yang 2011).

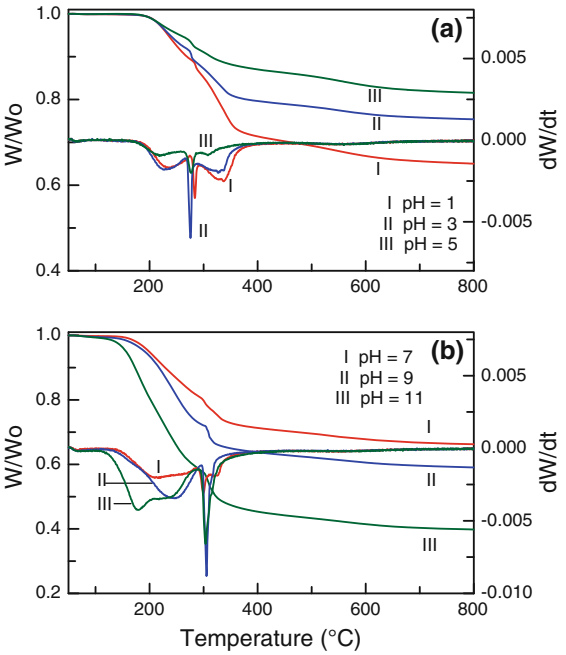

Fig. 4 TG and DTG thermograms of as-synthesized silica samples at various pH values: **a** pH 1–5; and **b** pH 7–11

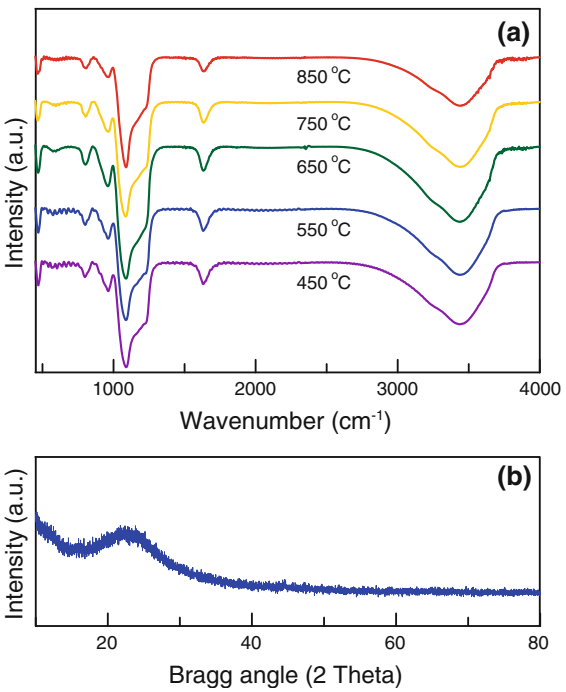

Fig. 5 MCM-48 samples synthesized at pH 11: **a** Fourier transform infrared spectra obtained at various calcination temperatures; and **b** X-ray diffraction pattern obtained at calcination temperature of 550 °C

Synthesis of ordered mesoporous carbon molecular sieve

Experimental results indicate that the optimal procedure for synthesizing MCM-48 is to employ a neutral-to-cationic surfactant ratio of 0.04–0.13 at pH 11 with a hydrothermal temperature of 100 °C and a calcination temperature of 550 °C. Therefore, this study conducts the remaining experiments for preparing a MCM-48 template by these reaction conditions.

Figure 6 displays the SAXS patterns for carbons prepared by impregnation of the MCM-48 template with sucrose. As shown in Fig. 6a, the carbon sample obtained without the addition of sulfuric acid ($H_2SO_4 = 0$ g) did not have an ordered porous structure. However, adding varying amounts of sulfuric acid obtained CMK-1 carbons predominantly containing two sharp low-angle reflections typical of cubic structure (Hussain and Ihm 2009). This was caused by sucrose's hydrophilic nature; it does not easily enter pores surrounded by a hydrophobic silica framework (Joo et al. 2001). However, adding a sulfuric acid catalyst transformed the sucrose into a less hydrophilic substance. As a result, the sucrose successfully penetrated the silica pore. When the amount of sulfuric acid was higher than 0.28 g (for each gram of sucrose), sulfuric acid occupying proportions of the silica pore volume may have caused the decreased SAXS intensity. Some carbons also formed outside the silica pores. Figure 6b shows the carbon sample obtained at 500 °C demonstrated weak diffraction intensities, indicating a poorly ordered mesoporous structure. When carbonization temperatures were in the range of 600 to 1,000 °C, these samples revealed characteristics of ordered mesoporous carbon with CMK-1 structure. The relative intensities of the diffraction peaks increased with increasing carbonization temperatures. Higher carbonization temperature facilitates the formation of carbons with enhanced framework and structural ordering. However, at a carbonization temperature of 1,000 °C, contraction or collapse of pores may have caused the resulting decrease in SAXS intensity (Liou and Wu 2009).

Following carbonization of the sucrose/MCM-48 composites, removal of the MCM-48 templates by leaching using HF solution obtained pure mesoporous carbon products. The TG curves in Fig. 7 shows the effects of HF concentration on the amounts of silica

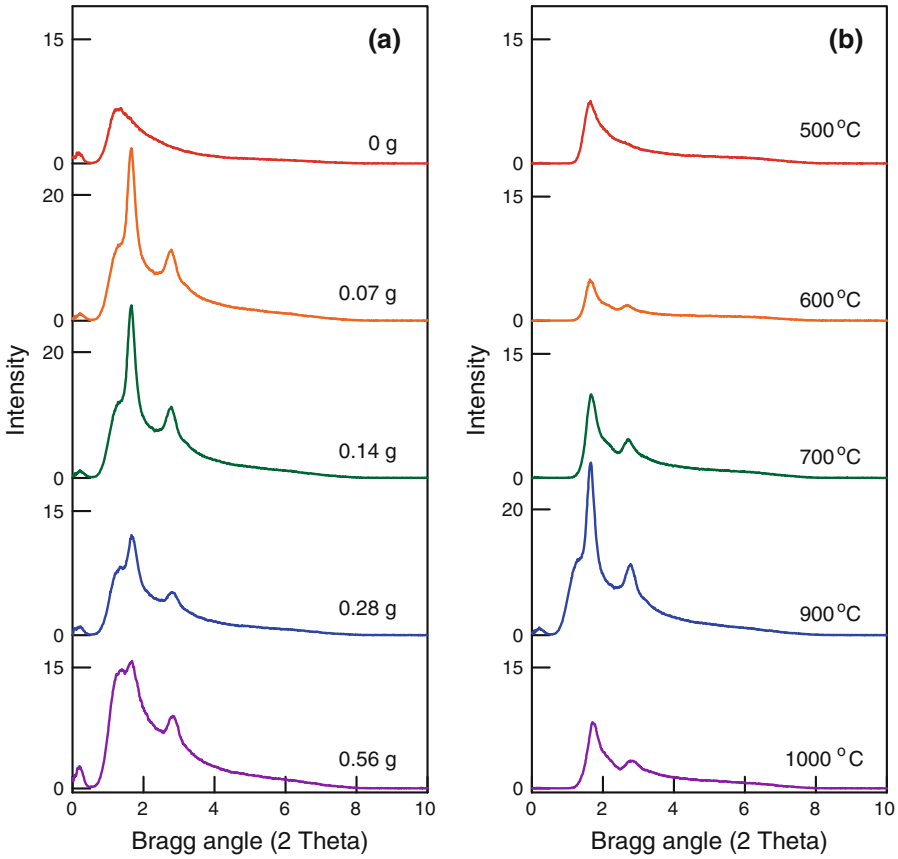

Fig. 6 SAXS pattern for carbons synthesized by: **a** various amounts of H_2SO_4 for each grain of sucrose; and **b** various carbonization temperatures

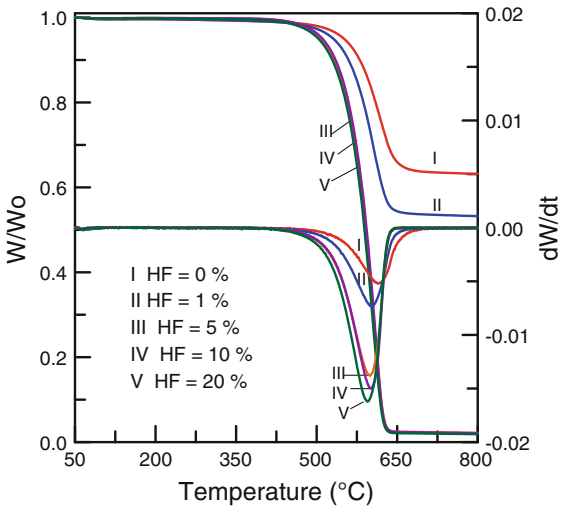

Fig. 7 Effect of HF concentration on the remaining amount of ash for carbon sample burnt in air. The carbon samples were obtained from pyrolysis of sucrose/MCM-48 composite in N_2 at 900 °C

template remaining after burning samples in air. The remaining silica decreased as the HF concentration increased. HF concentration of 5 wt% was sufficient for complete removal of the MCM-48 template. As revealed in the DTG curves in Fig. 7, the peak height increased with increasing HF concentrations, indicating that leaching of silica templates with high HF concentrations had the effect of increasing oxidation.

Figure 8a, b show the N_2 adsorption–desorption isotherm and pore size distribution for carbon obtained without the addition of sulfuric acid. The isotherm displayed the carbon sample including both microporous and mesoporous structures (Liou 2010). A narrow peak in pore size distribution occurred at 3.9 nm. The carbon sample exhibited a low BET surface area of approximately 877 m^2/g and a total pore volume of 0.680 cm^3/g. Figure 8c shows the N_2 adsorption–desorption isotherm of CMK-1 carbon with carbonization temperature of 900 °C. The isotherm exhibits two capillary condensation steps at $P/P_o = 0.2$–0.3 and 0.4–1.0. These well-pronounced capillary condensation steps indicate a high uniformity in pore size.

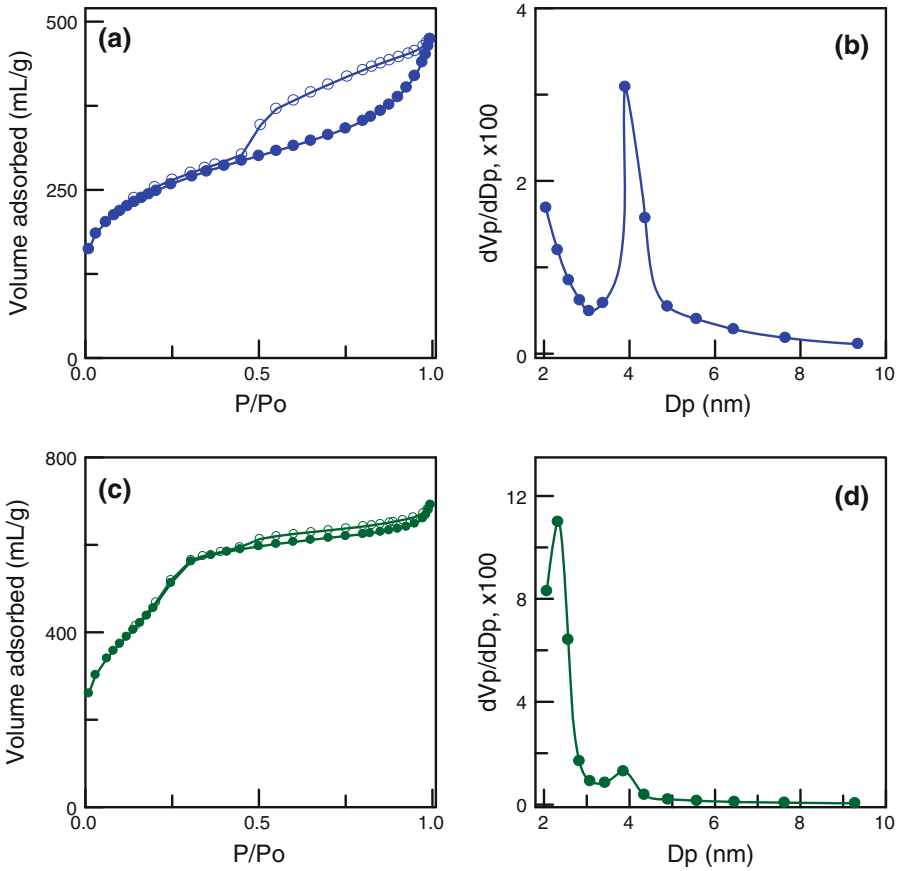

Fig. 8 Nitrogen adsorption–desorption isotherm and differential pore size distribution of mesoporous carbon samples prepared by the impregnation of MCM-48 template with sucrose: **a**, **b** without the addition of sulfuric acid; **c**, **d** addition of sulfuric acid

The pore size distribution displayed in Fig. 8d reveals a bimodal mesoporous structure. Two narrow peaks appear at a pore diameter of approximately 2.3 and 3.9 nm. The CMK-1 sample exhibits a high BET surface area of 1,715 m^2/g and total pore volume of 1.02 cm^3/g.

Observation of surface morphology of silica and carbon products

Figure 9a–g shows the surface morphologies of mesoporous silica obtained at pH 1–11. The silica sample synthesized at pH 1 consists of very fine grains with a mean size smaller than 5 nm, while the silica synthesized at pH 3 has a like-sponge porous tissue. The silica synthesized at pH 5 shows semi-sphere grains, while that formed at pH 7 shows an aggregate of fine grains. The MCM-41 sample synthesized at pH 9 shows irregularly shaped particles. The surface morphology of MCM-48 synthesized at pH 11 shows mainly rectangular particle shapes (Sayari 2000). Figure 9g shows the lamellar structure of silica synthesized at a neutral/cationic ratio of 0.26. The micrometer-sized spherical particles consist chiefly of thin platelets measuring 20-nm thick and 0.5-μm wide. Figure 9h–l shows the surface morphologies of mesoporous carbon samples. Figure 9h illustrates the direct synthesis of mesoporous carbon from as-synthesized MCM-48 silica nanocomposite. The proposed method uses CTAB/$C_{12}(EO)_4$ surfactants as a carbon precursor to substitute sucrose. SEM analysis shows that this carbon material is a hollow and spherical solid. SAXS confirms that this carbon material did not have an ordered porous structure (data not shown here). This observation indicates that the surfactant mixtures were unable to completely penetrate the silica pores. The surface area of direct synthesis of carbon material is only 750 m^2/g. The surface morphology of carbon material in Fig. 9i obtained from the MCM-41 template resembles nanotubes without an ordered arrangement. The same result was also confirmed by SAXS analysis (data not shown). This observation indicates that MCM-41 silica was unsuitable as a template for OMC synthesis (Ryoo et al. 2001). Figure 9j–l shows the carbon samples

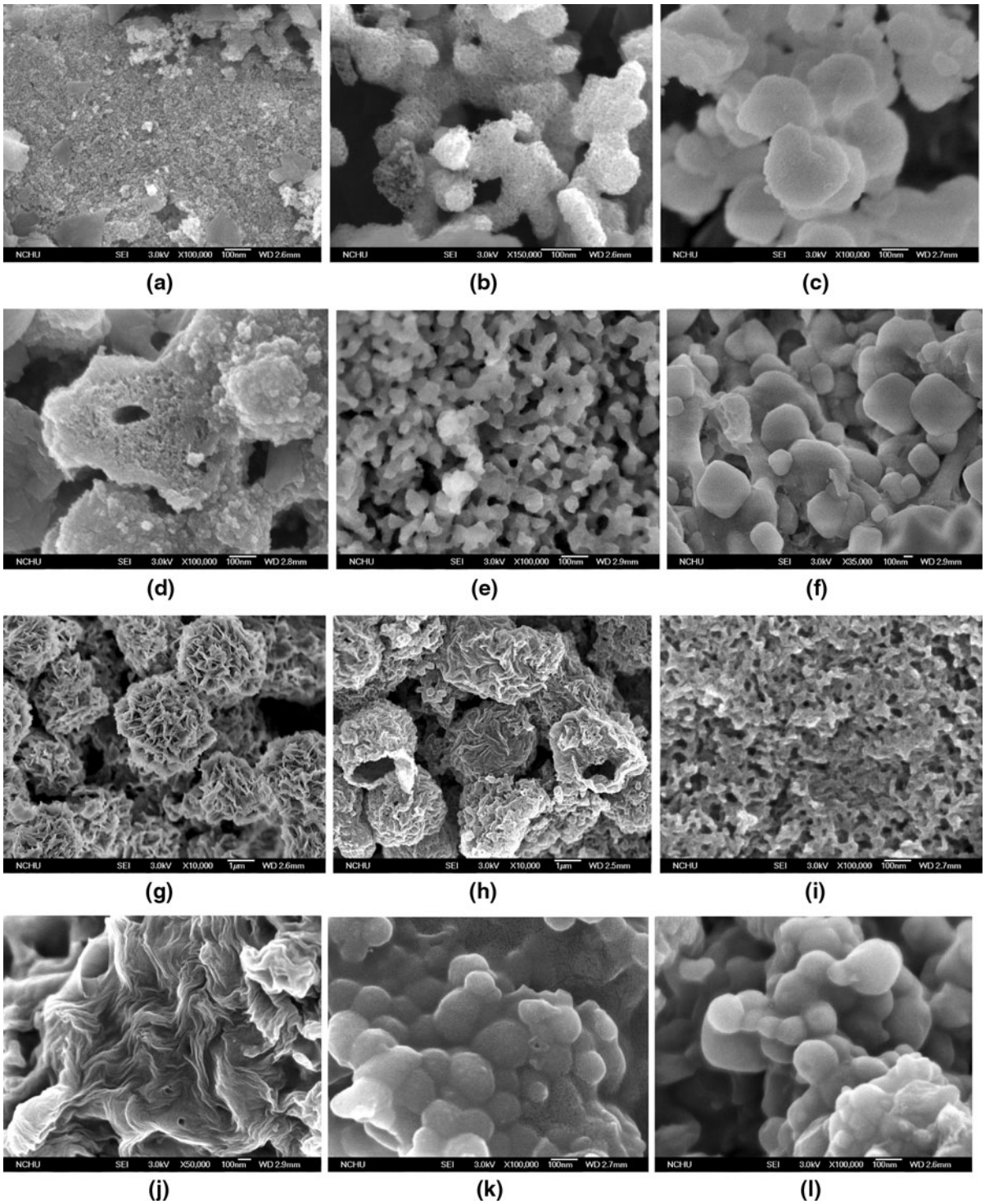

Fig. 9 FE-SEM images of samples: **a–f** mesoporous silica samples synthesized at various gelation pH values of 1, 3, 5, 7, 9, and 11, respectively; **g** mesoporous silica with lamellar structure; **h** carbon sample obtained from direct carbonization of as-synthesized MCM-48 composite; **i** carbon sample obtained using a MCM-41 as template; **j** carbon sample obtained without the addition of sulfuric acid; and **k–l** carbon samples obtained using sucrose and glucose as carbon precursors, respectively

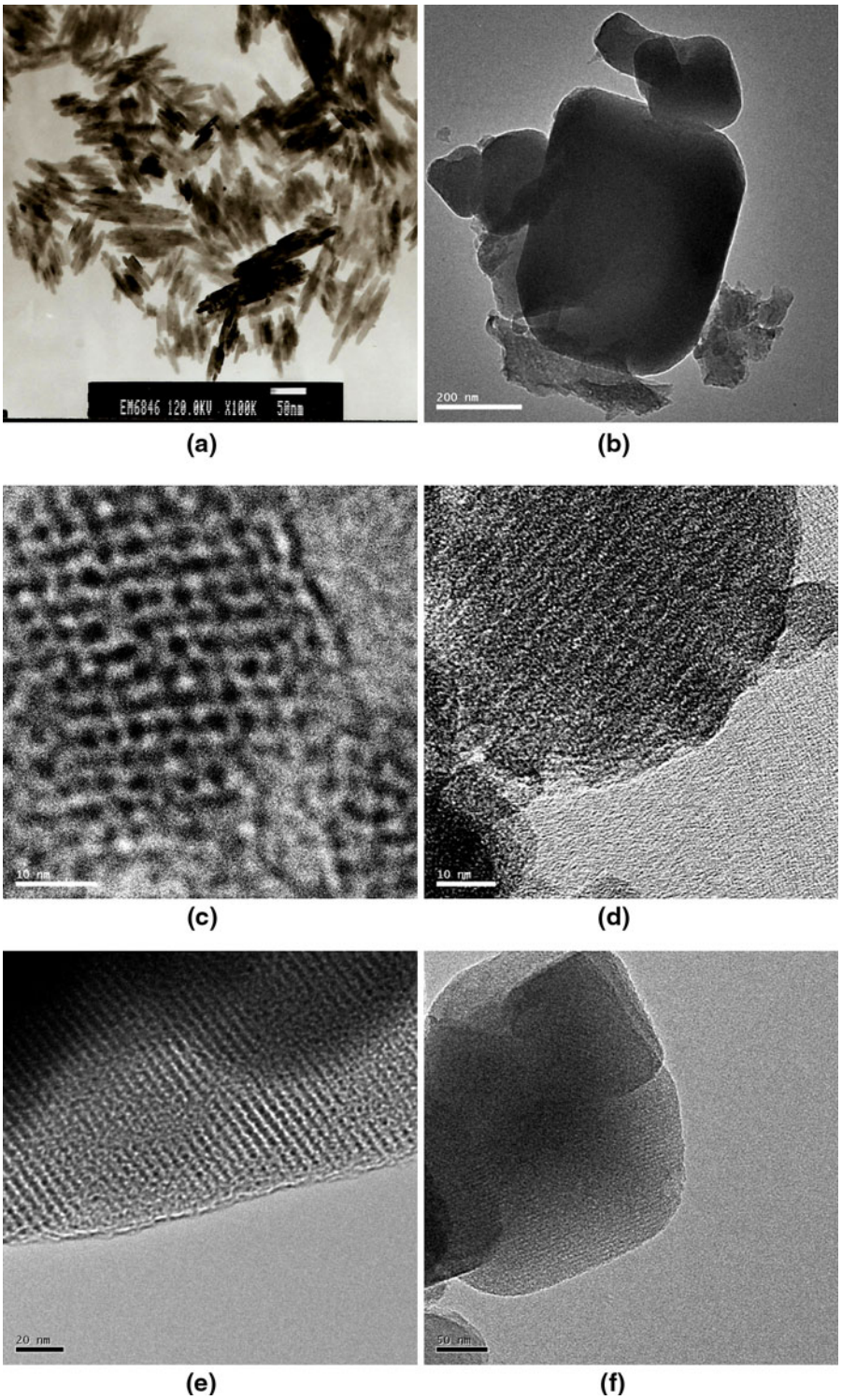

Fig. 10 High-resolution TEM images of samples: **a** PRA, **b** particle morphology of MCM-48, **c**, **d** MCM-48 synthesized at pH 11, **e**, **f** CMK-1 carbon

obtained using a MCM-48 as template. The carbon formed without the addition of sulfuric acid reveals a corrugated tissue (Fig. 9j). The carbon deposition on the sample surface indicated that sucrose does not easily penetrate the silica pores. Figure 9k, l shows the CMK-1 carbons obtained using sucrose and glucose as carbon precursors by adding a sulfuric acid catalyst. The appearance of the two carbon materials is similar to MCM-48 silica (Kaneda et al. 2002). As expected from the results of SAXS analysis in Fig. 6, H_2SO_4 pre-treatment successfully converted sucrose and glucose to ordered mesoporous carbons.

Figure 10a shows the typical PRA powder after burning the packaging resin waste in air. The size of the particles was approximately 60-nm long and 10-nm wide. Figure 10b is a low-resolution TEM image of MCM-48 particles, showing a well-defined edge and a rectangular particle shape. Figure 10c, d shows the high-resolution TEM images of MCM-48 particles. The sample shows a regular array of mesopores along the (111) direction (Fig. 10c), and a uniform pore structure along the (100) direction (Fig. 10d). These images indicate that the cubic mesostructure of MCM-48 is well developed, which is in agreement with the results of SAXS (Fig. 1d). Wang et al. (Wang et al. 2005) observed similar morphologies. Typical HR-TEM images of OMC samples are shown in Fig. 10e, f. Figure 10e shows a pattern of parallel stripes with black and white in sharp contrast. The carbon materials consisted of highly ordered mesopores. Figure 10f shows rectangular edges of the carbon particles with a uniform pore distribution. No carbon deposition is apparent on the external surface of OMC, indicating that the amount of sucrose was just sufficient to fill the internal cellular pores of MCM-48.

Conclusion

MCM-48 mesoporous molecular sieves free of Na impurities were synthesized using cheap, recycled silica from electronic packaging resin ash. The structure of silica samples achieved using different pH media, hydrothermal temperatures, and ratios of surfactant changed continuously from hexagonal to cubic to lamellar. Results confirm that ordered CMK-1 carbon can be successfully synthesized from the MCM-48 template using sucrose as a carbon precursor. The conversion of packaging resin ash into MCM-48 offers a better alternative for recycling and utilization of e-waste. Both MCM-48 and CMK-1 materials reveal a high surface area and uniform pore size, rendering them suitable for the development of advanced materials in energy and green application.

Acknowledgments The author expresses thanks to the National Science Council of Taiwan for its financial support under Project No. NSC 96-2221-E-131-001.

References

Bhagiyalakshmi M, Yun LJ, Anuradha R, Jang HT (2010a) Utilization of rice husk ash as silica source for the synthesis of mesoporous silicas and their application to CO_2 adsorption through TREN/TEPA grafting. J Hazard Mater 175:928–938

Bhagiyalakshmi M, Lee JY, Jang HT (2010b) Synthesis of mesoporous magnesium oxide: Its application to CO_2 chemisorption. Int J Greenh Gas Control 4:51–56

Brinker CJ, Scherer GW (1990) Applications. In: Sol–gel science, the physics and chemistry of sol–gel processing. Academic Press, Inc., San Diego

Chandrasekar G, Ahn WS (2008) Synthesis of cubic mesoporous silica and carbon using fly ash. J Non-Cryst Solids 354:4027–4030

Chen D, Bi X, Liu M, Huang B, Sheng G, Fu J (2011) Phase partitioning, concentration variation and risk assessment of polybrominated diphenyl ethers (PBDEs) in the atmosphere of an e-waste recycling site. Chemosphere 82:1246–1252

Cui J, Zhang L (2008) Metallurgical recovery of metals from electronic waste: a review. J Hazard Mater 158:228–256

Dai M, Song L, LaBelle JT, Vogt BD (2011) Ordered mesoporous carbon composite films containing cobalt oxide and vanadia for electrochemical applications. Chem Mater 23:2869–2878

Doyle A, Hodnett BK (2003) Stability of MCM-48 in aqueous solution as a function of pH. Microporous Mesoporous Mater 63:53–57

Doyle AM, Ahmed E, Hodnett BK (2006) The evolution of phases during the synthesis of the organically modified catalyst support MCM-48. Catal Today 116:50–55

Han S, Xu J, Hou W, Yu X, Wang Y (2004) Synthesis of high-quality MCM-48 mesoporous silica using gemini surfactant dimethylene-1,2-bis(dodecyldimethylammonium bromide). J Phys Chem B 108:15043–15048

Hao GP, Li WC, Wang S, Zhang S, Lu AH (2010) Tubular structured ordered mesoporous carbon as an efficient sorbent for the removal of dyes from aqueous solutions. Carbon 48:3330–3339

Hussain M, Ihm SK (2009) Synthesis, characterization, and hydrodesulfurization activity of new mesoporous carbon supported transition metal sulfide catalysts. Ind Eng Chem Res 48:698–707

Jang HT, Park YK, Ko YS, Lee JY, Margandan B (2009) Highly siliceous MCM-48 from rice husk ash for CO_2 adsorption. Int J Greenh Gas Control 3:545–549

Joo SH, Jun S, Ryoo R (2001) Synthesis of ordered mesoporous carbon molecular sieves CMK-1. Microporous Mesoporous Mater 44–45:153–158

Kaneda M, Tsubakiyama T, Carlsson A, Sakamoto Y, Ohsuna T, Terasaki O, Joo SH, Ryoo R (2002) Structural study of mesoporous MCM-48 and carbon networks synthesized in the spaces of MCM-48 by electron crystallography. J Phys Chem B 106:1256–1266

Kim TW, Chung PW, Slowing II, Tsunoda M, Yeung ES, Lin VSY (2008) Structurally ordered mesoporous carbon nanoparticles as transmembrane delivery vehicle in human cancer cells. Nano Lett 8:3724–3727

Kim H, Karkamkar A, Autrey T, Chupas P, Proffen T (2009) Determination of structure and phase transition of light element nanocomposites in mesoporous silica: case study of NH_3BH_3 in MCM-41. J Am Chem Soc 131:13749–13755

Kim HJ, Han B, Kim YJ, Yoa SJ (2010) Characteristics of an electrostatic precipitator for submicron particles using nonmetallic electrodes and collection plates. J Aerosol Sci 41:987–997

Kruk M, Jaroniec M, Ryoo R, Joo SH (2000) Characterization of MCM-48 silicas with tailored pore sizes synthesized via a highly efficient procedure. Chem Mater 12:1414–1421

Lelong G, Bhattacharyya S, Kline S, Cacciaguerra T, Gonzalez MA, Saboungi ML (2008) Effect of surfactant concentration on the morphology and texture of MCM-41 materials. J Phys Chem C 112:10674–10680

Liou TH (2003) Pyrolysis kinetics of electronic packaging material in a nitrogen atmosphere. J Hazard Mater 103:107–123

Liou TH (2004) Kinetics study of thermal decomposition of electronic packaging material. Chem Eng J 98:39–51

Liou TH (2010) Development of mesoporous structure and high adsorption capacity of biomass-based activated carbon by phosphoric acid and zinc chloride activation. Chem Eng J 158:129–142

Liou TH (2011) A green route to preparation of MCM-41 silicas with well-ordered mesostructure controlled in acidic and alkaline environments. Chem Eng J 171:1458–1468

Liou TH, Wu SJ (2009) Characteristics of microporous/mesoporous carbons prepared from rice husk under base- and acid-treated conditions. J Hazard Mater 171:693–703

Liou TH, Wu SJ (2010) Kinetics study and characteristics of silica nano-particles produced from biomass-based material. Ind Eng Chem Res 49:8379–8387

Liou TH, Yang CC (2011) Synthesis and surface characteristics of nanosilica produced from alkali-extracted rice husk ash. Mater Sci Eng B-Adv 176:521–529

Liu X, Du Y, Guo Z, Gunasekaran S, Ching CB, Chen Y, Leong SSJ, Yang Y (2009) Monodispersed MCM-41 large particles by modified pseudomorphic transformation: direct diamine functionalization and application in protein bioseparation. Microporous Mesoporous Mater 122:114–120

Liu A, Han S, Che H, Hua L (2010) Fluorescent hybrid with electron acceptor methylene viologen units inside the pore walls of mesoporous MCM-48 silica. Langmuir 26:3555–3561

Peña ML, Kan Q, Corma A, Rey F (2001) Synthesis of cubic mesoporous MCM-48 materials from the system SiO_2:CTAOH/Br:H_2O. Microporous Mesoporous Mater 44–45:9–16

Peng X, Cao D, Wang W (2008) Heterogeneity characterization of ordered mesoporous carbon adsorbent CMK-1 for methane and hydrogen storage: GCMC simulation and comparison with experiment. J Phys Chem C 112:13024–13036

Petitto C, Galarneau A, Driole MF, Chiche B, Alonso B, Renzo FD, Fajula F (2005) Synthesis of discrete micrometer-sized spherical particles of MCM-48. Chem Mater 17:2120–2130

Prasanth KP, Raj MC, Bajaj HC, Kim TH, Jasra RV (2010) Hydrogen sorption in transition metal modified mesoporous materials. Int J Hydrogen Energy 35:2351–2360

Ryoo R, Joo SH, Kim JM (1999) Energetically favored formation of MCM-48 from cationic—neutral surfactant mixtures. J Phys Chem B 103:7435–7440

Ryoo R, Joo SH, Kruk M, Jaroniec M (2001) Ordered mesoporous carbons. Adv Mater 13:677–681

Salgado JRC, Alcaide F, Alvarez G, Calvillo L, Lazaro MJ, Pastor E (2010) Pt–Ru electrocatalysts supported on ordered mesoporous carbon for direct methanol fuel cell. J Power Sources 195:4022–4029

Samadi-Maybodi A, Teymouri M, Vahid A, Miranbeigi A (2011) In situ incorporation of nickel nanoparticles into the mesopores of MCM-41 by manipulation of solvent-solute interaction and its activity toward adsorptive desulfurization of gas oil. J Hazard Mater 192:1667–1674

Sayari A (2000) Novel synthesis of high-quality MCM-48 silica. J Am Chem Soc 122:6504–6505

Shih LH (2001) Reverse logistics system planning for recycling electrical appliances and computers in Taiwa. Resour Conserv Recycl 32:55–72

Sing KSW, Everett DH, Haul RAW, Moscou L, Pierotti RA, Rouquerol J, Siemieniewska T (1985) Reporting physisorption data for gas/solid systems with specific reference to the determination of surface area and porosity. Pure Appl Chem 57:603–619

Wang LZ, Shi JL, Yu J, Zhang WH, Yan DS (2000) Temperature control in the synthesis of cubic mesoporous silica materials. Mater Lett 45:273–278

Wang L, Shao Y, Zhang J (2005) Short-time formation of well-ordered cubic mesoporous MCM-48 molecular sieve with the aid of fluoride ions. Mater Lett 59:3604–3607

Wei FY, Liu ZW, Lu J, Liu ZT (2010) Synthesis of mesoporous MCM-48 using fumed silica and mixed surfactants. Microporous Mesoporous Mater 131:224–229

Ying F, Wang S, Au CT, Lai SY (2011) Highly active and stable mesoporous Au/CeO_2 catalysts prepared from MCM-48 hard-template. Microporous Mesoporous Mater 142: 308–315

Zhao W, Hao Z, Hu C (2005) Synthesis of MCM-48 with a high thermal and hydro-thermal stability. Mater Res Bull 40: 1775–1780

Zhao D, Budhi S, Rodriguez A, Koodali RT (2010a) Rapid and facile synthesis of Ti-MCM-48 mesoporous material and the photocatalytic performance for hydrogen evolution. Int J Hydrogen Energy 35:5276–5283

Zhao W, Li Q, Wang L, Chu J, Qu J, Li S, Qi T (2010b) Synthesis of high quality MCM-48 with binary cationic—nonionic surfactants. Langmuir 26:6982–6988

DOI 10.1007/978-3-319-05041-6_25
Reprinted from the *Journal of Nanoparticle Research*, DOI 10.1007/s11051-013-1831-y

RESEARCH PAPER

Sustained release of fungicide metalaxyl by mesoporous silica nanospheres

Harrison Wanyika

Received: 30 March 2013 / Accepted: 30 June 2013 / Published online: 10 July 2013

Abstract The use of nanomaterials for the controlled delivery of pesticides is nascent technology that has the potential to increase the efficiency of food production and decrease pollution. In this work, the prospect of mesoporous silica nanoparticles (MSN) for storage and controlled release of metalaxyl fungicide has been investigated. Mesoporous silica nanospheres with average particle diameters of 162 nm and average pore sizes of 3.2 nm were prepared by a sol–gel process. Metalaxyl molecules were loaded into MSN pores from an aqueous solution by a rotary evaporation method. The loaded amount of metalaxyl as evaluated by thermogravimetric analysis was about 14 wt%. Release of the fungicide entrapped in the MSN matrix revealed sustained release behavior. About 76 % of the free metalaxyl was released in soil within a period of 30 days while only 11.5 and 47 % of the metalaxyl contained in the MSN carrier was released in soil and water, respectively, within the same period. The study showed that MSN can be used to successfully store metalaxyl molecules in its mesoporous framework and significantly delay their release in soil.

Keywords Mesoporous silica nanoparticles · Metalaxyl · Loading · Sustained release

Special Issue Editors: Mamadou Diallo, Neil Fromer, Myung S. Jhon

This article is part of the Topical Collection on Nanotechnology for Sustainable Development

H. Wanyika (✉)
Department of Chemistry, Jomo Kenyatta University of Agriculture & Technology, P.O. Box 62000, Nairobi 00200, Kenya
e-mail: hwanyika@gmail.com

Introduction

Globally, only ~10 % of the applied pesticides realizes their intended purpose, otherwise, the rest is lost to the environment through various modes, such as, drift during application, as run-off, leaching, volatilization, and degradation by photolysis, hydrolysis and by microbial action (Ghormade et al. 2011). This has led to periodic application of the pesticides so as to achieve threshold concentration for effective crop protection. A direct and negative consequence of the prevailing phenomena is the unprecedented high cost of agricultural production and heavily polluted environment. Emerging pesticide application technologies need to be harnessed in order to improve efficacy, reduce the amounts applied, and provide better control of the agrichemicals, thus, make agriculture sustainable and the environment greener.

A successful pesticide formulation is one that possesses the following properties: remains potent for a significant period of time even in harsh environment, is pest/pathogen specific with less ecotoxicity, does not suffer pest resistance, is economically viable and is benign to plants and mammals (Nair et al. 2010).

Most of such requirements may be achieved by a state-of-the-art pesticide delivery system. In the last decade, scientists have put considerable efforts in studying suitable systems for the controlled release of drug molecules. Amongst the widely investigated techniques are the use of polymeric materials and liposomes. Zheng and co-worker suggested polymeric nanocapsules as vehicles for the pesticides ivermectin and acetamiprid (Zheng and Shang 2005). Liu et al. (2001) controllably released fungicides tebuconazole and chlorothalonil from polyvinylpyridine and polyvinylpyridine-*co*-styrene matrix. However, the commercialization of most reported potential pesticide carriers has not been realized due to low drug payload, scale-up difficulties, regulatory limitations and structural instability.

Recently, nanomaterials have been identified as potential targeted delivery carriers for pesticides. In particular, MSN attributes include well defined and tunable pore sizes (2–50 nm), large pore volumes, high surface areas, chemical stability, resistance to microbial attack, nanostructures that can be tailored, easily modified surface properties, biocompatibility, and aqueous degradability (Al-Kady et al. 2011; Ambrogio et al. 2011). In addition, MSN protect-loaded guest molecules against environmentally induced enzymatic degradation since no swelling or porosity changes occur in response to external stimuli, such as, pH and temperature (Yang 2011). Furthermore, MSN are excellent pesticide delivery carriers, as their structural properties can be modified to either enhance or slow down release kinetics (Ukmar et al. 2011). Arguably, MSN offers great promise for the fabrication of stimulus responsive and targeted pesticide delivery scaffolds. Indeed, various attempts have been made to study the suitability of siliceous materials for storage and sustained release (SR) of pesticides. Experimental results have shown that porous hollow silica nanoparticles (PHSNs) are excellent carriers for the SR of avermectin; an oil-soluble pesticide (Wen et al. 2005). Moreover, they can protect avermectin from photodegradation (Li et al. 2006). The pesticide molecules were loaded into PHSNs by simple immersion loading (SIL) and supercritical fluid loading (SFL) technologies, respectively. Liu et al. (2006) employed SFL method to entrap a different molecule, validamycin; a water-soluble pesticide into PHSNs, they observed a multi-stage release pattern from the nanocarrier.

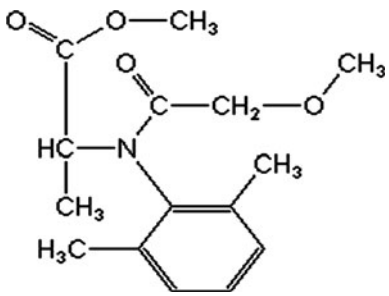

Fig. 1 Structure of metalaxyl

Metalaxyl, [methyl-*N*-(2,6-dimethylphenyl)-*N*-(2-methoxyacetyl)alaninate] (Fig. 1) is an acylanilide fungicide with residual and systemic activity against fungi of the order Peronosporales, which attack a wide range of crops. Its application may be foliar, soil incorporation, surface spraying (broadcast or band), drenching, sprinkler or drip irrigation, soil mix or seed treatment (Sukul and Spiteller 2001).

In this study, MSN with honeycomb like structure were loaded with fungicide metalaxyl by rotar vapor method. Metalaxyl was chosen as a model pesticide molecule due to nature of its use. Sustained release profiles of metalaxyl–MSN composites (RMSN) were investigated in water and in soil. Our results epitomize a novel application of MSN as sustained release carrier for fungicides.

Materials and methods

Cetyltrimethylammonium bromide (CTAB), tetraethylorthosilicate (TEOS), NaOH, Metalaxyl were purchased from Sigma-Aldrich Company. All chemicals used in this study were analytical grade. Nano pure water was used for the analysis.

Synthesis of mesoporous silica nanoparticles

MSN were synthesized under basic conditions using CTAB as the structure-directing agent, and TEOS as the silica source. In summary, TEOS (24.0 mL) was slowly added into a homogeneous surfactant solution-containing 4.0 g CTAB/1920 mL water/14 mL NaOH (2.0 M) that had been heated to 80 °C at a stirring rate of 1,000 rpm. After stirring for 2 h, the resulting precipitate was filtered and washed with water, then, oven dried at 120 °C for 4 h and finally calcined at 550 °C for 5 h in air.

Loading of metalaxyl into mesoporous silica nanoparticles

To entrap the pesticide into MSN, metalaxyl (14.0 mg) was homogenously dissolved in 20.0 mL of water by sonication for 15 min. Then, 220 mg of MSN was added and suspended in the solution by magnetic stirring at RT for 12 h. The solvent was then slowly evaporated under reduced pressure (0.085 mPa) in water bath at 50 °C for 2 h using a rotary evaporator. The metalaxyl-loaded MSN denoted as RMSN was dried at RT for 24 h and used for further tests.

Characterization

The crystallinity and structural properties of the MSN and RMSN samples were characterized with XRD diffractometer (LR 39487C XRD) using nickel filtered CuKα ($\lambda = 1.542$ Å) radiation operated at 40 kV/40 mA in the range 0.5–10° with a step size of 0.002° 2θ.

The adsorption of metalaxyl was examined by Infrared (IR) spectroscopy. IR spectra were recorded on a FT-IR spectrophotometer (SPECTMM ONE B) using KBr discs in the range 400–4,000 cm^{-1}.

The morphology and size of MSN and RMSN were observed by a scanning electron microscope (SEM, Hitachi S4800) and transmission electron microscope (TEM, Tecnai G^2 20 S-TWIN).

The quantification of the relative amount of the loaded metalaxyl was carried out by thermal analysis, that is, thermal gravimetric analysis (TGA), and differential thermal analysis (DTA) at a heating rate of $3min^{-1}$ with N_2 using thermal gravimetric analyzer (TGA-7) from RT to 800 °C. The nitrogen adsorption/desorption isotherms were collected on Micromeritics equipment (ASAP 2020). Specific surface areas and pore volumes were determined by standard BET and BJH methods, respectively, from adsorption branches of the isotherms.

Sorption–desorption studies

Sorption isotherms were measured using a batch equilibration method. Triplicates of 20 mg of MSN were treated with 6 mL of solutions containing 0.2–0.8 mg mL^{-1} initial concentrations (C_i) of metalaxyl in water. The suspensions were shaken at 25 ± 2 °C for 24 h and centrifuged at 10,000 rpm for 10 min. Supernatants were filtered through 0.22 μm diameter nylon filters and equilibrium concentrations (C_e) determined by UV spectrophotometry scan in the range 330–200 nm. The UV absorption peak at 270 nm was used to monitor concentration changes. Standard concentrations of metalaxyl ranged from 0.05 to 0.8 mg mL^{-1}. The amount of fungicide adsorbed (C_s) was calculated from the difference between the initial (C_i) and the equilibrium (C_e) solution concentrations. Adsorption isotherms were fitted to the logarithmic form of the Freundlich equation:

$$\log C_s = \log K_f + {}^{1}/_{n_f} \log C_e$$

where C_s (mg kg^{-1}) is the amount of herbicide adsorbed at the equilibrium concentration C_e (mg l^{-1}) and K_f ($mg^{1-n} l^n g^{-1}$) and n_f (unitless) are the empirical Freundlich constants.

Desorption was followed immediately after adsorption using the 0.8 mg mL^{-1} metalaxyl concentrations by replacing 3 mL of the supernatant with 3 mL of pure water. This desorption procedure was repeated three times for each sample. Desorption isotherms were also fitted to Freundlich equation and desorption coefficients calculated. A desorption hysteresis coefficient was calculated as the percentage of ratio between the sorption and desorption isotherms slopes (Fernandes et al. 2003):

$$H = \frac{nf_{ads}}{nf_{des}} \times 100$$

Release measurements

Batch release kinetics in water

The release of metalaxyl from RMSN was carried out by suspension of 4.0 mg of RMSN in 4.0 ml of water contained in glass bottles and sealed with screw caps for different time periods. Different experiments for the different periods of time were set up simultaneously. In all cases, the release kinetics was obtained in triplicate. After each time lapse, the bottles were hand-shaken, and centrifuged at 10,000 rpm for 10 min. The supernatant were filtered, and analyzed by high performance liquid chromatography (HPLC). The following HPLC conditions were used: detector, UV, $\lambda = 220$ nm; column, supelcosil LC-18 5 μm,

250 × 4.6 mm^2; temperature, 30 °C; mobile phase, acetonitrile/water (50/50 v/v); injection volume, 10 μL; flow rate 1.0 ml min^{-1}; run time, 10 min.

Release in soil

The controlled release characteristics of the RMSN were determined with soil-filled glass separating funnels with a volume of 25 cm^3. Pure metalaxyl (7.0 mg) corresponding to the amount entrapped in the controlled release systems was used as control. The soil columns were settled by the addition of 20 ml of water, 50 mg of RMSN were placed on top of the soil column and 10 ml of pure water was applied on a 3 days interval for 1 month to the tubes. The elute was filtered through 0.22 μm syringe filters and analyzed for metalaxyl content by HPLC method previously described.

Results and discussion

Loading and characterization of samples

Rotavapor-loading method was employed, a driving concentration gradient was generated by evaporating the solvent slowly but steadily. Metalaxyl was driven into the MSN pores in a fashion similar to immersion loading method which requires utilization of high drug concentration (Limnell et al. 2011).

Powder SAXRD patterns for MSN and RMSN samples are shown in Fig. 2. For MSN, three diffraction peaks at 2θ (2.4°, 4.1°, and 4.7°) were observed, which could be indexed as (100), (110), and (200) reflections based on the hexagonal unidirectional structure system. XRD of RMSN reveals a similar pattern with the intensity of the peaks greatly reduced, indicating reduced scattering contrast between the pore walls and pore space of silica due to successful loading of metalaxyl (Popovici et al. 2011). It is clear that loading efficiency was improved by increasing the metalaxyl: MSN particle ratio from 1:16 to 1:10 w/w. However, the presence of d_{100} reflection suggests that the mesoporous structure of MSN was retained after loading with the fungicide molecules.

A comparison of Fourier transform-IR (FT-IR) spectra (Fig. 3) of free metalaxyl, MSN and RMSN reveals that the metalaxyl characteristic stretching frequencies of the di-substituted amide and carbonyl ester groups at 1,457 and 1,735 cm^{-1}, respectively, are depicted in RMSN spectrum without any significant bond shift. This corroborates the XRD results. MSN

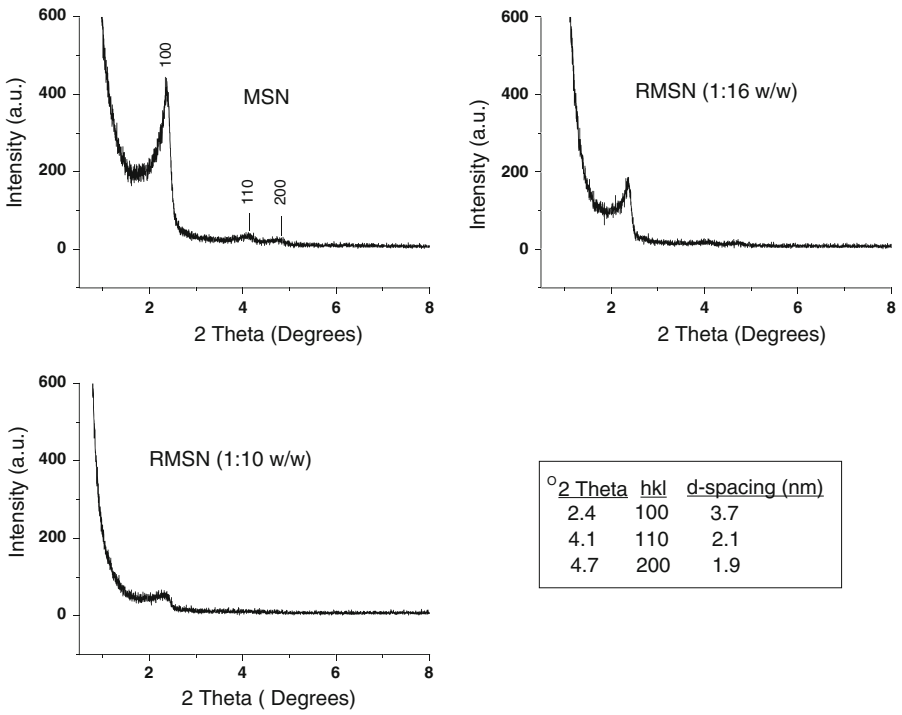

Fig. 2 SAXRD patterns of MSN and RMSNs with different metalaxyl: MSN particle ratios

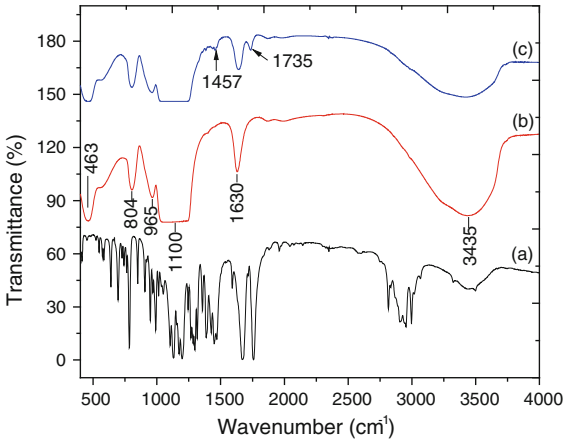

Fig. 3 IR spectra of *a* metalaxyl, *b* MSN, and *c* RMSN

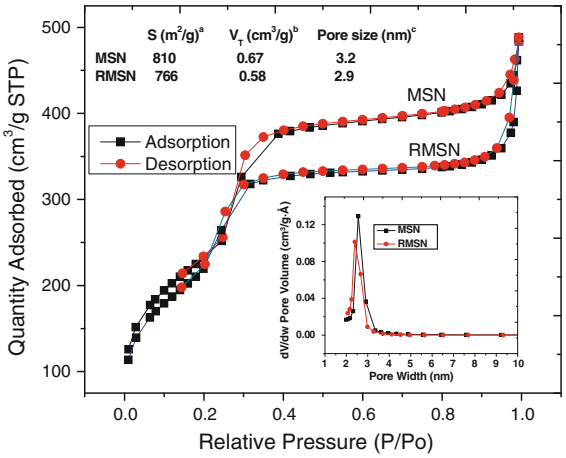

Fig. 4 Nitrogen adsorption–desorption isotherms of MSN, RMSN and (*inset*) pore width distribution (*figure*) and physical parameters (*table*) of the samples

exhibits characteristic absorption bands corresponding to $Si–OH_{Stretching}$ (3,435 cm^{-1}), $SiO–H_{Bending}$ (1,630 cm^{-1}), $Si–O–Si_{Stretching}$ (1,100 cm^{-1}), $Si–OH_{Bending}$ (965 cm^{-1}), and $SiO–H_{Stretching}$ (804 cm^{-1}).

Moreover, the absence of new peaks that cannot be ascribed to either metalaxyl or MSN in the RMSN spectrum suggests MSN–metalaxyl interactions through noncovalent bonding in the adsorption process. Weak van der Waals forces and hydrogen bonds describe the kind of host–guest chemistry observed in the entrapment of metalaxyl molecules into the MSN pores.

N_2 sorption studies resulted in type-IV isotherms (Fig. 4) typical of mesoporous materials according to the International Union of Pure and Applied Chemistry (IUPAC) convention. Both isotherms depicted a type H3 hysteresis loop in the high pressure region. This indicates existence of mesoporosity. A sharp inflection point at $P/P_O = 0.3$ is indicative of narrow pore-size distribution as confirmed by the inset figure. The amount of nitrogen adsorbed by RMSN was reduced while the shape of the hysteresis loop was not altered, which indicated that some adsorptive sites in MSN were already occupied by metalaxyl and the loading process had no significant effect on the pore shape. Single point surface area of MSN reduced from 810 to 766 m^2g^{-1} while total pore volume and adsorption average pore size reduced from 0.67 to 0.58 cm^3g^{-1} and 3.2 to 2.9 nm, respectively, after loading with metalaxyl (inset). The reduction in sorption parameters confirmed further the successful entrapment of the fungicide onto the nanocarrier.

Electron microscopy was used to examine the effect of the entrapment of metalaxyl on physical and morphological characteristics of the MSN. The SEM and TEM images of MSN and RMSN are shown in Fig. 5. Particle diameters were estimated from SEM images using a nano measurer 1.2 software and an average of 70 randomly selected particles calculated. Respective particle sizes for MSN and RMSN are averaged at ~160 and ~162 nm with a narrow distribution (inset in Fig. 5a, c). Positions of mesopores on the TEM images are indicated by arrows. All materials show highly ordered honeycomb-like porous system typical of mesoporous silica. Evidently, the structural integrity of MSN was preserved after the loading process.

The amount of metalaxyl entrapped in MSN was estimated by thermogravimetry. TGA curves (Fig. 6) revealed that, MSN and RMSN showed a weight loss of 10 % (Fig. 6a) and 24 % (Fig. 6b), respectively, after heating to 800 °C. The difference of 14 wt% was taken to be the amount of metalaxyl loaded in MSN. The greatest weight loss happened at <300 °C since far beyond this temperature range, metalaxyl which has a melting point of ~73 °C and a boiling point of ~296 °C in pure state had decomposed. Adsorbed water and surface silanol groups contribute to extra weight loss at low and high temperature, respectively. The amount of fungicide loaded was considered significant cognisant to the fact that application of metalaxyl active ingredient is in very minute amounts, typically, in the range of 0.151–8.970 kg ha^{-1} for

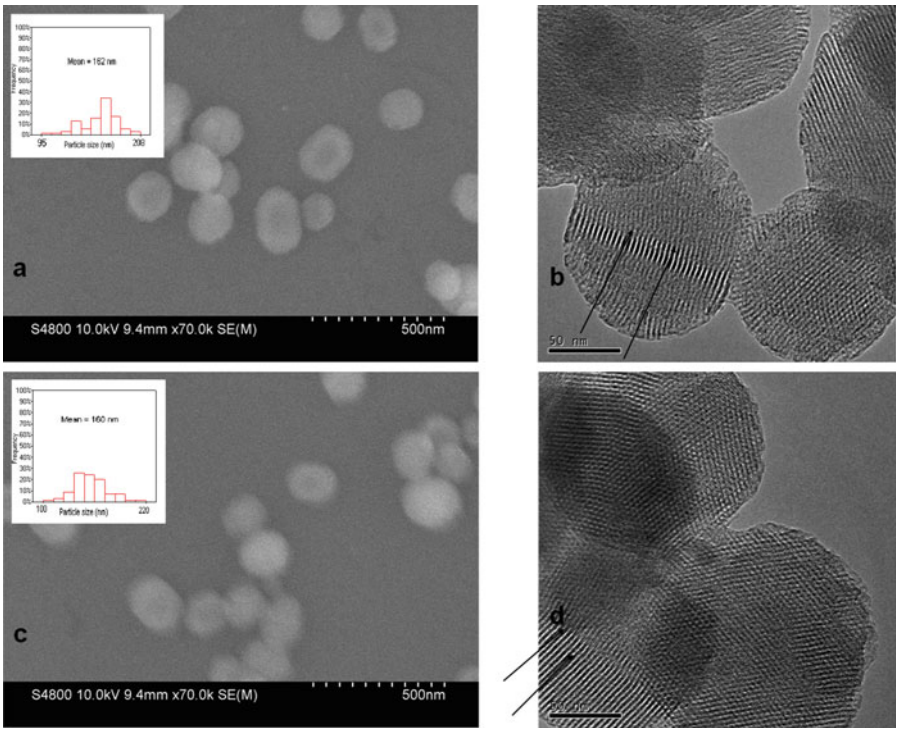

Fig. 5 SEM and corresponding TEM images of MSN (**a**, **b**) and metalaxyl–MSN hybrid (**c**, **d**). *Inset* particle-size distributions

agricultural crops, 0.154–0.700 g kg^{-1} for seed treatment, and 1.00–8.07 kg ha^{-1} for ornamental trees and plants (Monkiedje et al. 2002). However, the amount of fungicide loaded in the MSN carrier matrix could be increased by increasing the concentration of the pesticide solution as demonstrated by XRD studies.

Sorption studies

UV spectra of metalaxyl standard concentrations and corresponding calibration curve are exhibited in Fig. 7. The spectra express two distinct absorption peaks of equal intensity at 270 and 247 nm, the absorbance values of the peaks varied proportionally with concentration. The peaks were ascribed to the R- and S-enantiomers of metalaxyl which is a racemic mixture of the two. The absorbance values of the peak at 270 nm were used for quantification. R^2 value ratified the analysis method.

Metalaxyl sorption isotherms and corresponding Freundlich curves are shown in Fig. 8. Type L-isotherms (Fig. 8a) according to Giles classification (Giles et al. 1960) are exhibited which suggested that sorption occurred by physical forces. The adsorption and desorption isotherms fitted the Freundlich sorption equation with R^2 values of 0.99 and 0.93, respectively (Fig. 8b) which indicated a strong linear relationship between equilibrium concentration (C_e) and amount sorbed (C_s). Values of Freundlich adsorption–desorption coefficients are inset in Fig. 8b. Low value of K_f implied that the fungicide was adsorbed in low amounts while the low n_f value suggested broad distribution of adsorption site types on the MSN surface (Rodrıguez-Cruz et al. 2008). Low fungicide payload was attributed to low metalaxyl concentration in the loading solution. The finding on availability of multiple adsorption sites on MSN resonated well with its structural nature of having outer and inner surfaces. A much lower K_{fd} than K_f value confirmed desorption. A n_{fd} value that approached zero implied desorption process involving multiple stages. Low value of the desorption hysteresis coefficient (H) value verified reversibility of the sorption process. Reversibility is sine-qua-non for sustained release application of any carrier matrix.

Fungicide release studies

The amount of metalaxyl released from RMSN was determined using high performance liquid chromatography. The metalaxyl standards calibration curve and HPLC chromatogram are displayed in Fig. 9.

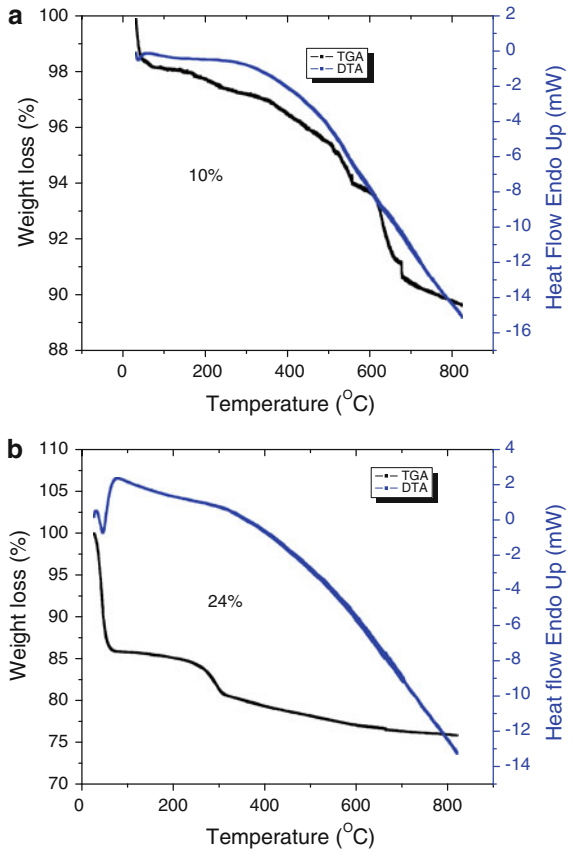

Fig. 6 TGA and DTA curves for **a** MSN and **b** RMSN

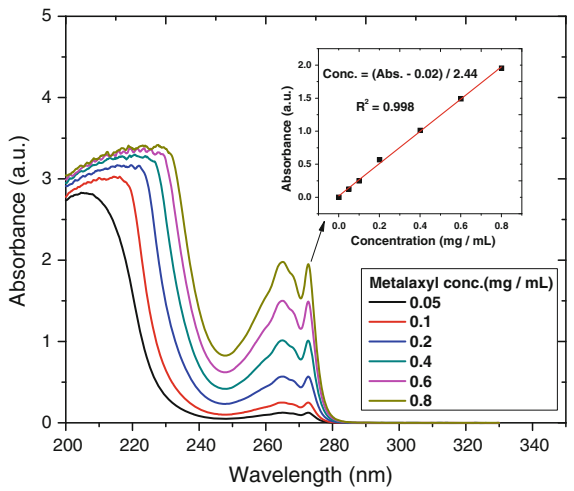

Fig. 7 UV absorption spectra for metalaxyl calibration standards and (*inset*) calibration curve showing a linear relationship between the fungicide concentrations and UV absorbance

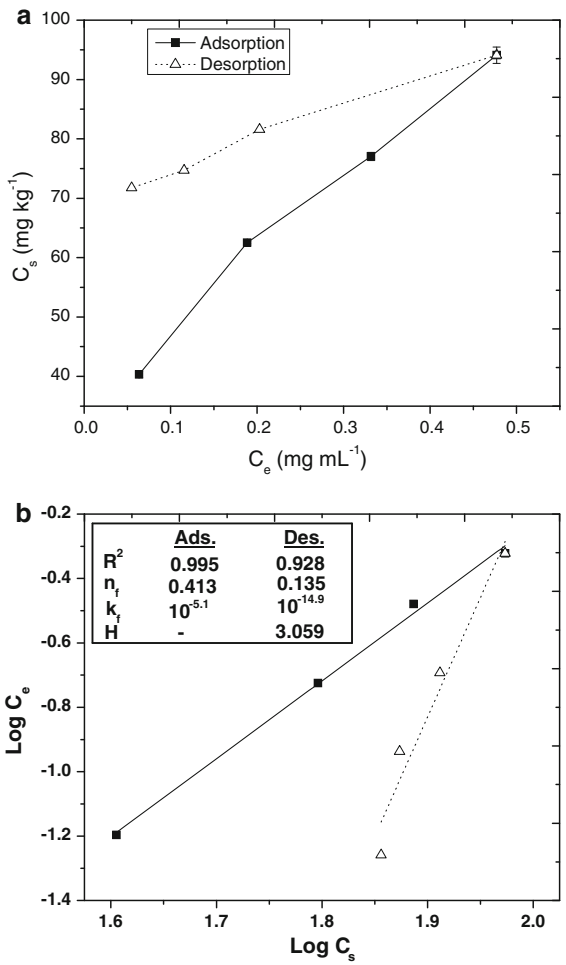

Fig. 8 **a** Metalaxyl adsorption and desorption isotherms in MSN. **b** Freundlich curves and (*inset*) constants for the sorption process

Correlation coefficient (R^2) value demonstrated linear relationship between peak areas and metalaxyl concentration. The release profiles are shown in Fig. 10. Slow and sustained release behavior was manifested with 47 and 11.5 % of the loaded metalaxyl been released in water (Fig. 10a) and soil (Fig. 10b), respectively, within a period of 30 days. Application of free metalaxyl in soil (control) resulted in 76 % release. The results demonstrated ~7 times delay in the release of metalaxyl into the soil from the MSN matrix. This would facilitate long periods of soil protection and treatment using the same quantity of the fungicide. MSN are inorganic and water insoluble materials that do not leach in soil. However, their efficiency as fungicide carriers could also be improved

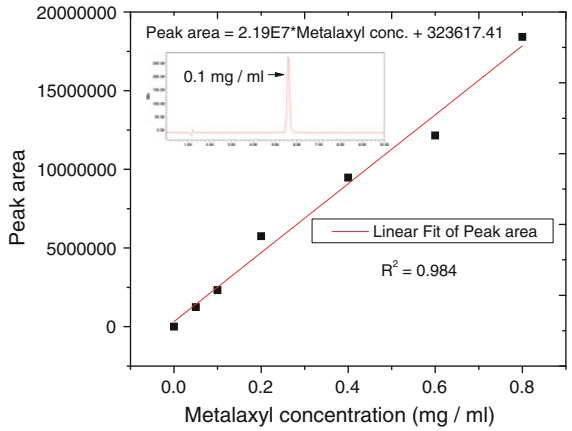

Fig. 9 Curve of best fit for metalaxyl standard concentrations and (*inset*) HPLC chromatogram

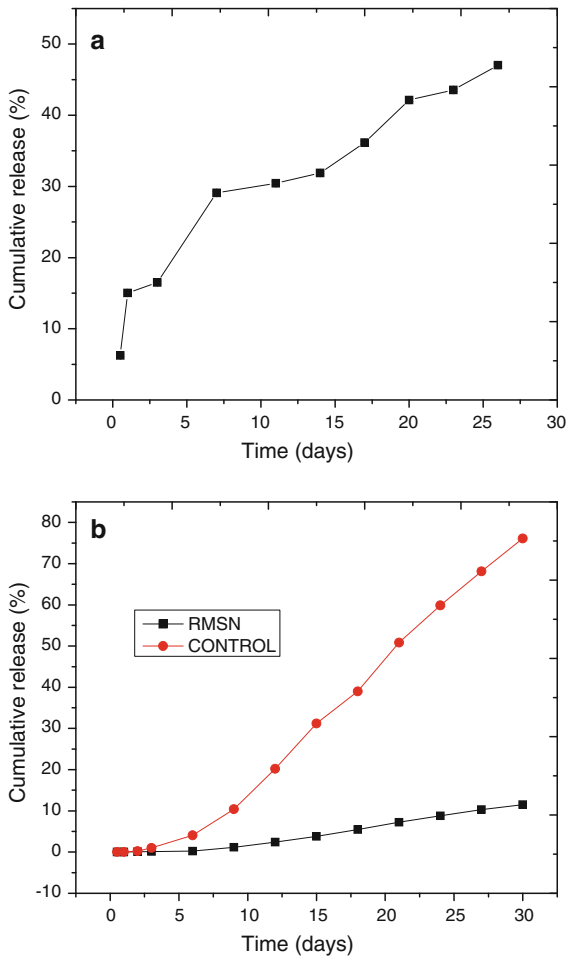

Fig. 10 Sustained release profiles for RMSN in **a** water and **b** soil

by functionalizing them with moieties that would make them "achor" to the plant roots. Moreover, future studies should aim at determining the long term residual levels of various pesticide molecules loaded in the siliceous nanoscale delivery vehicles.

Conclusion

Metalaxyl was successfully loaded into MSN mesoporous framework; payload was significant at 14 % w/w. A slower and more sustained release of metalaxyl was realized from the nanoscale carrier compared with free fungicide. It is demonstrated that MSN can provide an efficient means to deliver pesticides in a controlled fashion thus reducing wastage and environmental hazard. We envisage that, in future, MSN will find application in smart pesticide delivery systems not only for slow release but also capable of detecting an early stress or infection and offer targeted treatment.

Acknowledgments This research was supported by the German Academic Exchange Service (DAAD) and Jomo Kenyatta University of Agriculture and Technology (JKUAT).

References

Al-Kady AS, Gaber M, Hussein MM, Ebeid EM (2011) Nanostructure-loaded mesoporous silica for controlled release of coumarin derivatives: a novel testing of the hyperthermia effect. Eur J Pharm Biopharm 77:66–74

Ambrogio MW, Thomas CR, Zhao Y-L, Zink JI, Stoddart JF (2011) Mechanized silica nanoparticles: a new frontier in theranostic nanomedicine. Acc Chem Res 44(10):903–913. doi:10.1021/ar200018x

Fernandes MC, Cox L, Hermosin MC, Cornejo J (2003) Adsorption–desorption of metalaxyl as affecting dissipation and leaching in soil role of mineral and organic components. Pest Manag Sci 59:545–552

Ghormade V, Deshpande MV, Paknikar KM (2011) Perspectives for nano-biotechnology enabled protection and nutrition of plants. Biotechnol Adv 29:792–803

Giles CH, Mac Ewan TH, Nakhwa SN, Smith D (1960) Studies in adsorption. Part XI. A system of classification of solution adsorption isotherms, and its use in diagnosis of adsorption mechanisms and in measurement of specific surface areas of solids. J Chem Soc 111:3973–3993

Li Z-Z, Xu S-A, Wen L-X, Liu F, Liu A-Q, Wang Q, Sun H-Y, Yu W, Chen J-F (2006) Controlled release of avermectin from porous hollow silica nanoparticles: influence of shell thickness on loading efficiency, UV-shielding property and release. J Controlled Release 111:81–88

Limnell T, Santos HA, Makila E, Heikkila T, Salonen J, Murzin DY, Kumar N, Laaksonen T, Peltonen L, Hirvonen J (2011) Drug delivery formulations of ordered mesoporous silica: comparison of three drug loading methods. J Pharm Sci 100(8):3294–3306. doi:10.1002/jps.22577

Liu Y, Yan I, Heiden P, Laks P (2001) Use of nanoparticles for controlled release of biocides in solid wood. J Appl Polym Sci 79:458–465

Liu F, Wen L-X, Li Z-Z, Yu W, Sun H-Y, Chen J-F (2006) Porous hollow silica nanoparticles as controlled delivery system for water-soluble pesticide. Mater Res Bull 41:2268–2275

Monkiedje A, Ilori MO, Spiteller M (2002) Soil quality changes resulting from the application of the fungicides mefenoxam and metalaxyl to a sandy loam soil. Soil Biol Biochem 34:1939–1948

Nair R, Varghese SH, Nair BG, Maekawa T, Yoshida Y, Kumar DS (2010) Nanoparticulate material delivery to plants. J Plant Sci 179:154–163

Popovici RF, Seftel EM, Mihai GD, Popovici E, Voicu VA (2011) Controlled drug delivery system based on ordered mesoporous silica matrices of captopril as angiotensin-converting enzyme inhibitor drug. J Pharm Sci 100(2): 704–714

Rodrıguez-Cruz MS, Andrades MS, Sanchez-Martın MJ (2008) Significance of the long-chain organic cation structure in the sorption of the penconazole and metalaxyl fungicides by organo clays. J Hazard Mater 160:200–207

Sukul P, Spiteller M (2001) Influence of biotic and abiotic factors on dissipating metalaxyl in soil. Chemosphere 45:941–947

Ukmar T, Maver U, Planinsek O, Kaucic V, Gaberscek M, Godec A (2011) Understanding controlled drug release from mesoporous silicates: theory and experiment. J Controlled Release 155:409–417

Wen L-X, Li Z-Z, Zou H-K, Liu A-Q, Chen J-F (2005) Controlled release of avermectin from porous hollow silica nanoparticles. Pest Manag Sci 61:583–590

Yang Y-W (2011) Towards biocompatible nanovalves based on mesoporous silica nanoparticles. Med Chem Commun 2:1033–1049. doi:10.1039/c1md00158b

Zheng H, Shang Q (2005) Water suspension acetamiprid nanocapsule preparation and its repairing method. Chem. Abs. 143:73729

DOI 10.1007/978-3-319-05041-6_26
Reprinted from the *Journal of Nanoparticle Research*, DOI 10.1007/s11051-013-1984-8

PERSPECTIVES

Nanomanufacturing and sustainability: opportunities and challenges

Ahmed A. Busnaina · Joey Mead · Jacqueline Isaacs · Sivasubramanian Somu

Received: 6 July 2013 / Accepted: 28 August 2013 / Published online: 15 September 2013

Abstract New nanomanufacturing technologies, although still in research labs, present a great opportunity to drastically reduce the cost of making nanostructures on a large scale and at high-rates. Such new bottom-up directed assembly-based approaches involve adding materials selectively thereby both reducing waste and the number of required processes. Directed assembly-based processes are conducted at room pressure and temperatures which significantly reduces the cost of nanomanufacturing equipment and tools, ensuring long-term sustainability by reducing energy, consumables, and waste costs. This paradigm shift in nanomanufacturing will unleash not only a wave of creativity in sustainable nanomanufacturing but lessons learnt along the way can be used in various other sectors. Along with the exquisite technological promise that nanotechnology holds, nano-enabled products are heralded as a means for energy and resource reduction, resulting in potential manufacturing cost reductions and further, for potential improvements to environmental remediation. Sustainable nanomanufacturing will, by dramatically lowering current nanomanufacturing barriers, spur innovation, and the creation of entirely new industries by leveling the playing and ultimately leading to the democratization of nanomanufacturing.

Keywords Nanomanufacturing · Sustainability · Directed assembly · Nanomaterials

Special Issue Editors: Mamadou Diallo, Neil Fromer, Myung S. Jhon

This article is part of the Topical Collection on Nanotechnology for Sustainable Development

A. A. Busnaina (✉) · J. Isaacs · S. Somu
NSF Nanoscale Science and Engineering Center for High-rate Nanomanufacturing, Northeastern University, Boston, MA 02115, USA
e-mail: BUSNAINA@COE.NEU.EDU

J. Mead
University of Massachusetts Lowell, Lowell, MA 01854, USA

Introduction

Considerable investment and progress have been made in nanotechnology over the last decade. Much of the initial investment was justifiably focused on fundamental research, resulting in significant advancement in nanomaterials, new manufacturing processes capable of making 2D and 3D nanoscale structures, and new device concepts. However, most of today's products involving fabricated nanostructures are made using top down conventional technologies such as semiconductor manufacturing. Today, a semiconductor fabrication facility that manufactures consumer electronics containing nanoscale features costs $7–10 billion to construct. Semiconductor processing equipment cost ranges from a few hundred thousand dollars to a few million with

some lithography equipment exceeding $50 million. This high cost entry barrier completely shuts out small- and medium-sized businesses. In addition, such large facilities have a huge environmental impact; for example, these facilities consume more than 4 million gallons of water per day. Dramatically lowering such barriers will spur innovation and the creation of entirely new industries. Imagine if a company of any size could manufacture nanoscale systems and devices at a small fraction (e.g., one hundredth) of today's cost. It would unleash a wave of creativity by making nanoscale manufacturing accessible and affordable for a range of industries in the same way as the advent of PC technology did for the computing industry, and in the process revitalize manufacturing.

Manufacturing is the process of adding or removing materials at the macro, micro, or nanoscales. Current micro and nanoscale manufacturing involves deposition (thin film using chemical or physical processes), etching, polishing, assembly, packaging, and wire bonding. Successful nanoscale manufacturing that leads to commercialization of nano-enabled products requires robust, additive, and multiscale nanomanufacturing systems that can be used to make a diverse array of applications. There are already signs of the shift in manufacturing of devices and other products from vacuum-based processes. For example, some photovoltaic manufacturers use screen-printing, and some display applications (already commercialized) use inkjet printing of circuit patterns. Recently, the use of 3D and electronic printing additive technologies is on the rise, however, they are slow and are only capable of microscale resolutions, so products requiring higher resolution or large sizes take a very long time. In addition, these printing technologies are top down processes and cannot be scaled down to enable the manufacturing of nanostructures. Even with today's slow electronic printing and lower resolution, they still offer significant savings compared to conventional (semiconductor manufacturing based) electronics. For example, the cost of a printed integrated sensor-plus-digital-readout device is 1/10–1/100th the cost of current silicon-based systems (Ernst 2012).

Of course, success of an emerging technology is not dependent on the technology alone. Ethical, legal, and societal implications (ELSI) for nano-enabled products must be weighed with the technological advantages. Unintended implications of nanotechnology to human health and the environment should be avoided by early examination of the effects of nanoparticle releases throughout the product lifecycle. Many organizations and research labs are striving to find safe practices for working with nanomaterials in light of the uncertainties of exposure (Murashov and Howard 2011; NIOSH Workplace Safety and Health Topics, National Institute of Occupational Safety and Health, Center for Disease Control and Prevention, http://www.cdc.gov/niosh/topics/nanotech/, Accessed July 5 2013; OECD series on the safety of manufactured nanomaterials, organisation for economic co-operation and development, http://www.oecd.org/science/nanosafety/publicationsintheseriesonthesafetyofmanufacturednanomaterials.htm Accessed July 5 2013). The environmental health and safety (EHS) implications remain paramount to the responsible commercialization of nano-enabled products.

Sustainable nanomanufacturing opportunities

New nanomanufacturing technologies, although still in research labs, present a great opportunity to address these manufacturing challenges. New directed assembly (Vossmeyer et al. 1997; Polleux et al. 2004; Park et al. 2001; Davis et al. 2001; Zirbs et al. 2005) and transfer approaches (Allen et al. 2006; Ahn et al. 2006; Kim et al. 2010) involves adding materials selectively such that no material removal is needed; thereby both reducing waste and the number of required processes. These directed assembly processes offer high-rate, bottom-up, directed, and precise assembly of nanoelements (such as carbon nanotubes, nanoparticles, and polymer nanostructures). These techniques are capable of making nanoscale systems and devices with unique properties that harness the individual and synergistic properties of underlying nanomaterials. Most of the directed assembly and transfer processes are conducted at room pressure and temperatures. This drastically reduces the cost of nanomanufacturing equipment and tools, ensuring long-term sustainability by reducing energy, consumables, and waste costs.

Such a nanomaterials-based nanomanufacturing system could be built for a fraction of today's fab cost. So why is the directed assembly-based nanomanufacturing approach lower in cost? The processes used are operated at room temperature and pressure (no vacuum or high temperature), which will provide a significant cost reduction in equipment, energy, and

maintenance costs. Most of the tools used to conduct the directed assembly processes are simple—mostly dip coating or spinning-based processes—significantly reducing tool and operation costs. Also, with reduction of the number of process required the consumption of water, material, and energy would be significantly reduced. Many of the directed assembly and transfer processes are scalable and high-rate.

Opportunities exist at the initial stages of product design to create environmentally benign products, beginning with assessment of nanomanufacturing practices (Eckelman et al. 2012; Dahlben et al. 2013). The economic and environmental assessment of products during their manufacture, use and end-of-life disposal is encouraged to establish best practices now—while the processes are under development—instead of after intended consequences arise.

Sustainable nanomanufacturing processes

Various processes for large scale manufacturing of nano-enabled products have been developed. In this paper, the author will focus on efforts developed at the NSF Nanoscale Science and Engineering Center for high-rate nanomanufacturing (CHN). The CHN efforts focused on processes that utilize directed assembly and transfer for assembling various types of nanoelements on different substrates with precise addressing and orientation. Pre-patterned templates are used to direct the assembly of nanoparticles (as small as 2 nm), conducting polymers (Wei et al. 2006), and single wall carbon nanotubes (SWCNTs) (Xiong et al. 2005). CHN has also developed damascene templates to provide a uniform electrophoretic force throughout the template for any pattern size enabling reliable assembly over large areas. These techniques enabled the directed assembly of nanoparticles (Xiong et al. 2006) and SWCNTs into nanoscale patterns in 1 min and over a large area (in inches) (Makaram et al. 2007a). Moreover these assembly techniques are used to assemble more than one type of nanomaterial on the same substrate for increased functionality and performance.

Truly 3D integrated circuits based on conventional CMOS technology are hindered by fabrication related challenges. Introduction of nanomaterials into preexisting systems and architectures can result in superior performance. However, techniques developed to selectively place nanometer-sized materials (Nihei et al. 2004; Chen et al. 2006) are restricted to planar substrates. CHN has developed a hybrid technique combining both bottom-up dielectrophoresis and top-down microfabrication techniques to enable low temperature integration of SWNTs (Makaram et al. 2007b; Selvarasah et al. 2011) and gold nanoparticles (Yilmaz et al. 2010) into three-dimensional architectures. In addition, CHN demonstrated the assembly of SWCNTs into exiting CMOS platforms to create highly robust sensors for the detection of various chemicals (Chen et al. 2009, 2010).

An emerging area of commercial importance is flexible electronics, but they suffer from a significant performance drawback when compared to standard CMOS devices. Unprecedented advantages can be realized if nanomaterials are used as active elements in flexible electronics. To addresses this issue CHN has demonstrated directed assembly of SWNT structures on soft polymer substrates using a surface controlled fluidic assembly (Selvarasah et al. 2010; Xiong et al. 2009). Polymer structures patterned in non-uniform geometries, such as sharp 90° bends and T-junctions (Stoykovich et al. 2007) have also been shown. Directed assembly of polymer blends into non-uniform structures (Wei et al. 2009; Fang et al. 2010), with multiple length scales on a single template (Chiota et al. 2009) and into arbitrary structures at a high-rate has been demonstrated by CHN (Fig. 1).

Transfer of assembled nanoelements from one surface to another is important for the integration of nanoscale processes. The CHN has demonstrated the successful transfer of conducting polymers and CNTs to a number of polymer substrates (Kumar et al. 2008; Wei et al. 2006). By combining template-guided fluidic SWNT assembly (Xiong et al. 2007; Jaber-Ansari et al. 2009a, b; Somu et al. 2010) and transfer techniques (Li et al. 2011a, b) researchers at CHN has created horizontally organized SWNTs network architectures at nano/microscale on diverse substrates with enhanced functionality.

Sustainable nanomanufacturing challenges

There are many challenges facing this new nanomanufacturing technology, some of the challenges are technical and some are cultural. For example, the electronics industry has spent hundreds of billions of dollars on fabrication facilities and will not entertain

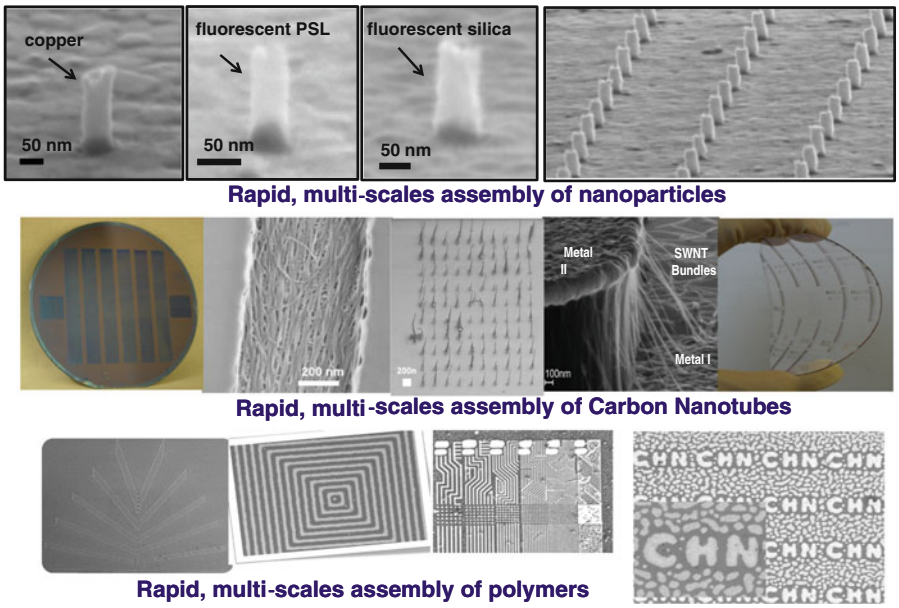

Fig. 1 Assembly of various nanoelements, including nanoparticles, carbon nanotubes, and polymers in different configuration and orientation

or consider a new manufacturing technology unless there is a remarkable enhancement over existing performance in addition to low cost.

Most of the technical challenges deal with scalability while maintaining the nanoscale properties. In macroscopic systems comprising nanomaterials, the absence of nanomaterial properties at macroscopic length scales is a huge challenge. In order to achieve this, control of surface properties over large areas while maintaining the necessary forces at the nanoscale needs to be achieved thus enabling multiscale, heterogeneous, and monolithic nanomanufacturing that is scalable, fast, and repeatable with high yield. Hence compatibility and flexibility of the developed processes for a wide range of nanomaterials-substrates needs to be addressed. In a multilayered process, i.e., where several directed assembly and transfer process are sequentially conducted for creating a fully functional device the effect of surface tension, solvent, and viscosity of suspension/solution used in individual/subsequent processes on assembly needs to be addressed. For processes involving multiple transfers, the effect of substrate compliance (for flexible substrates) on assembly, contact area, adhesion, and transfer need to be addressed.

These innovations will lead to products with embedded nanomaterials—the health and environmental impacts of which must be established throughout their life cycles. The US National Nanotechnology Initiative Strategic Plan advocates the responsible development of nano-enabled products as central to promoting scalable nanomanufacturing and product commercialization, calling for more effective use of life cycle analysis in decision-making as nanomanufacturing scales to commercial production. Given the uncertain potential hazards, it is important to identify the likely workplace and environmental exposures during manufacture, functionalization, use, and end-of-life management including recycling and disposal—to avoid any unintended consequences. Only with broader perspectives of the systems into which nano-enabled products are inserted can nanomanufacturing succeed in becoming sustainable.

Conclusion and outlook

Many applications such as sensors, electronics, energy harvesting or storage, medical devices or functional structures can be made entirely through directed assembly and transfer process platform encompassing various nanoelements with specific functionality. Concerted efforts from scientist and engineers are needed to realize this manufacturing capability. This paradigm shift in manufacturing of nano-enabled products will unleash not only a wave of creativity in sustainable nanomanufacturing but lessons learnt along the way can be used in various other sectors.

Along with the exquisite technological promise that nanotechnology holds, nano-enabled products are heralded as a means for energy and resource reduction, resulting in potential manufacturing cost reductions and further, for potential improvements to environmental remediation. A systems approach to implementation will allow for responsible and effective commercialization of these emerging industries. Sustainable nanomanufacturing will, by dramatically lowering current nanomanufacturing barriers, spur innovation and the creation of entirely new industries by leveling the playing and ultimately leading to the democratization of nanomanufacturing.

References

Ahn JH, Kim HS, Lee KJ, Jeon S, Kang SJ, Sun Y, Nuzzo RG, Rogers JA (2006) Heterogeneous three-dimensional electronics by use of printed semiconductor nanomaterials. Science 314:1754–1757

Allen AC, Sunden E, Cannon A, Graham S, King W (2006) Nanomaterial transfer using hot embossing for flexible electronic devices. Appl Phys Lett 88:083112

Chen Z, Cao G, Lin Z, Koehler I, Bachmann PK (2006) A self-assembled synthesis of carbon nanotubes for interconnects. Nanotechnology 17:1062–1066

Chen CL, Yang CF, Agarwal V, Sonkusale S, Busnaina A, Chen M, Dokmeci M R (2009) SS-DNA-decorated single-walled carbon nanotubes integrated on CMOS circuitry for high sensitivity gas sensing. In: Solid-state sensors, actuators and microsystems conference, Transducers 2009 International pp.1477–1480

Chen CL, Yang CF, Agarwal V, Kim T, Sonkusale S, Busnaina A, Chen M, Dokmeci MR (2010) DNA-decorated carbon-nanotube-based chemical sensors on complementary metal oxide semiconductor. Nanotechnology 21(9):095504

Chiota J, Shearer J, Wei M, Barry C, Mead J (2009) Multiscale directed assembly of polymer blends using chemically functionalized nanoscale-patterned templates. Small 5:2788–2791

Dahlben LJ, Eckelman MJ, Hakimian A, Somu S, Isaacs JA (2013) Environmental life cycle assessment of a carbon nanotube-enabled semiconductor device. Environ Sci Technol. doi:10.1021/es305325y

Davis SA, Breulmann M, Rhodes KH, Zhang B, Mann S (2001) Template-directed assembly using nanoparticle building blocks: a nanotectonic approach to organized materials. Chem Mater 13:3218–3226

Eckelman MJ, Mauter M, Isaacs JA, Elimelech M (2012) New perspectives on nanomaterial aquatic ecotoxicity production impacts equal direct exposure impacts for carbon nanotubes. Environ Sci Technol 46:2902–2910

Ernst J (2012) Printed electronics memory: challenges of logic and integration. EDN Network www.edn.com. Accessed 9 Apr 2012

Fang L, Wei M, Barry C, Mead J (2010) Effect of spin speed and solution concentration on the directed assembly of polymer blends. Macromolecules 43:9747–9753

Jaber-Ansari L, Hahm M, Kim T, Somu S, Busnaina A, Jung Y (2009a) Large scale highly organized SWNTs networks for electrical devices. Appl Phys A96:373–377

Jaber-Ansari L, Hahm M, Somu S, Echegoyen Y, Busnaina A, Jung YJ (2009b) Mechanism of very large scale assembly of SWNTs in template guided fluidic assembly process. JACS 131:804–808

Kim S, Wu J, Carlson A, Jin SH, Kovalsky A, Glass P, Liud Z, Ahmede NN, Elgane SL, Chen FW, Ferreirae PM, Sittig M, Huangb Y, Rogers JA (2010) Microstructured elastomeric surfaces with reversible adhesion and examples of their use in deterministic assembly by transfer printing. Proc Natl Acad Sci 107:17095–17100

Kumar A, Wei M, Barry CMF, Orroth S, Busnaina A, and Mead J (2008) Transfer of template patterned carbon nanotubes to a polymer surface using the thermoforming process. In: Society of plastics engineers annual technical conference

Li B, Jung HY, Wang H, Kim YL, Kim T, Hahm M, Busnaina A, Upmanyu M, Jung YJ (2011a) Ultra-thin SWNTs films with tunable, anisotropic transport Properties. Adv Funct Mater 2:1810–1815

Li B, Hahm MG, Kim YL, Kar HS, Jung YJ (2011b) Highly organized two- and three-dimensional single-walled carbon nanotubes-polymer hybrid architectures. ACS Nano 5:4826–4834

Makaram P, Somu S, Xiong X, Busnaina A, Jung YJ, McGruer N (2007a) Scalable nanotemplate assisted directed assembly of single walled carbon nanotubes for nanoscale devices. Appl Phys Lett 90:243108–243111

Makaram P, Selvarasah S, Xiong X, Chen C-L, Busnaina A, Khanduja N, Dokmeci MR (2007b) Three-dimensional assembly of single-walled carbon nanotube interconnects using dielectrophoresis. Nanotechnology 18:395204

Murashov V, Howard J (eds) (2011) Nanotechnology standards. Springer, Newyork. ISBN: 978-1-4419-7852-3 (Print) 978-1-4419-7853-0 (Online)

Nihei M, Horibe M, Kawabata A, Awano Y (2004) Simultaneous formation of multiwall carbon nanotubes and their end-bonded ohmic contacts to Ti electrodes for future ULSI interconnects. Jpn J Appl Phys 43:1856–1859

NIOSH workplace safety and health topics, National Institute of Occupational Safety and Health, Center for Disease Control and Prevention. http://www.cdc.gov/niosh/topics/nanotech/. Accessed 5 Jul 2013

OECD Series on the safety of manufactured nanomaterials, Organisation for economic co-operation and development, http://www.oecd.org/science/nanosafety/publicationsintheseriesonthesafetyofmanufacturednanomaterials.htm Accessed 5 Jul 2013

Park SJ, Lazarides AA, Mirkin CA, Letsinger RL (2001) Directed assembly of periodic materials from protein and oligonucleotide-modified nanoparticle building blocks. Angew Chem 113:2993–2996

Polleux J, Pinna N, Antonietti M, Niederberger M (2004) Ligand-directed assembly of preformed titania nanocrystals into highly anisotropic nanostructures. Adv Mater 16:436–439

Selvarasah S, Busnaina A, Dokmeci MR (2010) Parylene-C passivated carbon nanotube flexible transistors. Appl Phys Lett 97:153120

Selvarasah S, Busnaina A, Dokmeci MR (2011) Design, fabrication, and characterization of three-dimensional single-walled carbon nanotube assembly and applications as thermal sensors. IEEE Trans Nanotechnol 10:13–20

Somu S, Wang H, Kim Y, Jaberansari L, Hahm M-G, Li B, Kim T, Xiong X, Jung YJ, Upmanyu M, Busnaina A (2010) Topological transitions in carbon nanotube networks via nanoscale confinement. ACS Nano 4:4142–4148

Stoykovich MP, Kang HM, Daoulas KC, Liu GL, Liu CC, DiPablo JJ, Muller M, Nealey PF (2007) Directed self-assembly of block copolymers for nanolithography fabrication of Isolated features and essential integrated circuit geometries. ACS Nano 1:168–175

Vossmeyer T, DeIonno E, Heath JR (1997) Light-directed assembly of nanoparticles. Angew Chem, Int Ed Engl 36:1080–1083

Wei M, Tao Z, Xiong X, Kim M, Lee J, Somu S, Sengupta S, Busnaina A, Barry C, Mead J (2006) Fabrication of patterned conducting polymer on insulating polymeric substrates by electric-field-assisted assembly and pattern transfer. Macromol Rapid Commun 32:1826–1832

Wei M, Fang L, Lee J, Somu S, Xiong X, Barry C, Busnaina A, Mead J (2009) Directed assembly of polymer blends using nanopatterned templates. Adv Mater 21:794–798

Xiong X, Makaram P, Bakhtari K, Somu S, Busnaina A, Small J, McGruer N, Park J (2005) Directed assembly of nanoelements using electrostatically addressable templates. Mater Res Soc Symp Proc 901:19–23

Xiong X, Makaram P, Busnaina A, Bakhtari K, Somu S, McGruer N, Park J (2006) Large scale directed-assembly of nanoparticles using nanotrench templates. Appl Phys Lett 89:193108–193111

Xiong X, Jaber-Ansari L, Hahm M, Busnaina A, Jung YJ (2007) Building highly organized SWNT networks using template guided assembly. Small 3:2006–2010

Xiong X, Chen C-L, Ryan P, Busnaina AA, Jung YJ, Dokmeci MR (2009) Directed assembly of high-density single-walled carbon nanotube patterns on flexible polymer substrates. Nanotechnology 20:295302

Yilmaz C, Kim T-H, Somu S, Busnaina AA (2010) Large scale nanorods nanomanufacturing by electric field directed assembly For nanoscale device applications. IEEE Nano 9:653–658

Zirbs R, Kienberger F, Hinterdorfer P, Binder WH (2005) Directed assembly of Au nanoparticles onto planar surfaces via multiple hydrogen bonds. Langmuir 21:8414–8421

DOI 10.1007/978-3-319-05041-6_27
Reprinted from the *Journal of Nanoparticle Research*, DOI 10.1007/s11051-013-2031-5

RESEARCH PAPER

Synthesis, characterization and mechanistic insights of mycogenic iron oxide nanoparticles

Arpit Bhargava · Navin Jain · Manju Barathi L. · Mohd. Sayeed Akhtar · Yeoung-Sang Yun · Jitendra Panwar

Received: 3 June 2013 / Accepted: 26 September 2013 / Published online: 20 October 2013

Abstract In the present study, extracellular synthesis of iron oxide nanoparticles (IONPs) was achieved using *Aspergillus japonicus* isolate AJP01. The isolate demonstrated its ability to hydrolyze the precursor salt solution, a mixture of iron cyanide complexes, under ambient conditions. Hydrolysis of these complexes released ferric and ferrous ions, which underwent protein-mediated coprecipitation and controlled nucleation resulting in the formation of IONPs. Transmission electron microscopy, selected area electron diffraction pattern, energy dispersive spectroscopy and grazing incidence X-ray diffraction analysis confirmed the mycosynthesis of IONPs. The synthesized particles were cubic in shape with a size range of 60–70 nm with crystal structure corresponding to magnetite. Scanning electron microscopy analysis revealed the absence of IONPs on fungal biomass surface, indicating the extracellular nature of synthesis. Fourier transform infrared spectroscopy confirmed the presence of proteins on as-synthesised IONPs, which may confer their stability. Preliminary investigation indicated the role of proteins in the synthesis and stabilization of IONPs. On the basis of present findings, a probable mechanism for synthesis of IONPs is suggested. The simplicity and versatility of the present approach can be utilized for the synthesis of other nanomaterials.

Keywords Iron oxide nanoparticles · Biosynthesis · Soil fungi · Extracellular proteins · *Aspergillus japonicus* · Nanobiotechnology

Special Issue Editors: Mamadou Diallo, Neil Fromer, Myung S. Jhon

This article is part of the Topical Collection on Nanotechnology for Sustainable Development

Electronic supplementary material The online version of this article (doi:10.1007/s11051-013-2031-5) contains supplementary material, which is available to authorized users.

A. Bhargava · N. Jain · M. Barathi L. · J. Panwar (✉)
Centre for Biotechnology, Department of Biological Sciences, Birla Institute of Technology and Science, Pilani, India
e-mail: drjitendrapanwar@yahoo.co.in

Mohd. S. Akhtar
Department of Applied Microbiology, College of Natural Sciences, Jimma University, Jimma, Ethiopia

Y.-S. Yun
Division of Environmental and Chemical Engineering, Chonbuk National University, Chonbuk, South Korea

Introduction

The advent of nanotechnology has revolutionized science, economy and everyday life. Intrinsic properties with respect to bulk materials change drastically in the event of reduction of size to nanoscale-like quantum confinement in semiconductors, surface plasmon resonance in some metallic nanoparticles and

superparamagnetism in magnetic nanoparticles (Noguez 2007; Jun et al. 2008; Wu et al. 2008). As compared to the larger particles of the bulk material, nanoparticles exhibit completely new or improved properties based on their size, distribution and morphology. Changes in properties at nanoscale have been thoroughly used in various interesting applications involving optoelectrical, catalytic, photochemical and electrochemical phenomena (Fedlheim and Foss 2001).

Iron oxide nanoparticles (IONPs) have been consistently used in developing technologies related to data storage, environmental remediation, energy generation, water purification, etc. (Teja and Koh 2009). Narrowing our focus to applications of IONPs in biology, their amenable properties offer very useful and attractive potentials in biomedicine, viz. biomolecular targeting, hyperthermia, cell manipulations and as carrier/delivery molecule (Bhargava et al. 2011). As evident by the importance of IONPs, their synthesis has received considerable attention. Biosynthesis of nanoparticles presents an appealing approach which integrates material science and microbial biotechnology, potentially overcoming limitations associated with conventional physical and chemical methods of nanoparticle synthesis (Laurent et al. 2008). Presently, the biological method relies on the use of plants, bacteria and fungi for the synthesis of nanoparticles and became an eco-friendly, yet cost-effective alternative with the ability of controlling synthesis at the molecular level in certain cases. Molecular control can be well appreciated in the biosynthesis of magnetosomes by magnetotactic bacteria where the overall synthesis is regulated at the genetic level by a group of genes collectively called 'magnetosome island' which is a conserved gene cluster (Komeili 2007). Recently, Parikh et al. (2011) reported the presence of a gene homolog of a putative gene of the silver-binding protein (silE) from various strains of *Morganella* spp. that were tested for silver nanoparticles synthesis.

Fungi have emerged as potential candidates for the biosynthesis of nanoparticles because of their ease in handling, low cost maintenance as well as easy downstream processing, due to the predominantly extracellular nature of nanoparticle synthesis (Gade et al. 2010). Additionally, being a eukaryotic organism, fungi have been reported to secrete a versatile range of extracellular components in higher amounts as compared to prokaryotic organisms. This might be helpful in achieving significantly higher and desired productivity of various nanoparticles (Dhillon et al. 2011).

Appreciating the perspective that organisms isolated from metal-rich regions show improved ability for high metal tolerance as well as microbial activities that adapt to stressed environment, Jain et al. (2013) reported the efficiency of metal-tolerant fungal isolates toward extracellular synthesis of nanoparticles. In the present study, we report the mycosynthesis of IONPs utilizing *Aspergillus japonicus* isolate AJP01 isolated from iron-rich soil. The fungal isolate demonstrated its ability to hydrolyze the precursor salt solution, a mixture of iron cyanide complexes, under ambient conditions. Hydrolysis of these complexes releases ferric and ferrous ions, which possibly undergo protein-mediated coprecipitation and controlled nucleation resulting in the formation of IONPs as suggested by the experimental inferences. The IONPs were synthesised extracellularly and stabilized by proteins of fungal origin. Based on the preliminary molecular and biochemical investigations, the probable mechanism for synthesis and subsequent stabilization of IONPs is discussed.

Materials and methods

Materials

All chemicals used were of analytical grade and procured from Sigma-Aldrich (Sigma-Aldrich, St. Louis, MO, USA) or Merck Chemicals (Merck KGaA, Darmstadt, Germany) unless otherwise stated. Commercially available magnetite nanoparticles (637106) were purchased from Sigma-Aldrich. All culture media and molecular biology kits were purchased from HiMedia Laboratories (HiMedia Laboratories, Mumbai, India). Reagents and enzymes used in PCR reactions were obtained from Promega (Promega, Mannheim, Germany). The primers ITS1 and ITS4 were purchased from Sigma-Aldrich and Bt2a, Bt2b, CL1 and CL2A from Eurofins MWG Operon (Eurofins MWG Operon, Ebersberg, Germany).

Isolation and molecular identification of fungal isolate

The fungus was isolated from soil samples of iron-rich regions of Udaipur, Rajasthan, India. Briefly, the collected soil samples were serially diluted and plated

on Martin Rose Bengal Agar media (pH 7.2) supplemented with chloramphenicol at a final concentration of 30 μg/mL after autoclaving. Petri plates were incubated at 28 °C for 96 h under dark conditions. Individual and morphologically distinct fungal colonies were selected and further purified by repeated sub-culturing on potato dextrose agar (PDA) medium (pH 5.6). Glycerol stocks of the isolates were prepared and preserved at −70 °C.

Fungal DNA was extracted using HiPurA^{TM} plant genomic DNA miniprep purification spin kit with minor modifications. Amplification of the internal transcribed spacer (ITS) regions of ribosomal DNA was amplified using primers ITS1 (5′-TCCGTAGGTGAACCTGCGG) and ITS4 (5′-TCCTCCGCTTATTGATATGC) (White et al. 1990). Partial amplification of β-tubulin gene was performed using the primers Bt2a (5′-GGTAACCAAATCGGTGCTGCTTTC) and Bt2b (5′-ACCCTCAGTGTAGTGACCCTTGGC) (Glass and Donaldson 1995). In addition, partial amplification of the calmodulin gene was performed using the primers CL1 (5′-GARTWCAAGGAGGCCTTCTC) and CL2A (5′-TTTTTGCATCATGAGTTGGAC) (O'Donnell et al. 2000). PCR reactions were carried out in total volumes of 50 μL containing Taq Buffer A, 15 mM $MgCl_2$, 50 μM each of deoxynucleoside triphosphates, 50 pmol of each primers (30 pmol in case of partial β-tubulin gene amplification), 1 unit of TaqDNA polymerase and 4 μL of template genomic DNA. The reactions were carried out on a Veriti® Thermal Cycler (Applied Biosystems, Carlsbad, CA, USA). The PCR conditions followed for amplification of ITS regions were as follows: 2 min of preheating at 94 °C followed by 30 cycles of denaturation at 94 °C for 1 min, annealing at 57 °C for 1.5 min, extension at 72 °C for 2 min and a final extension of 4 min at 72 °C. The PCR conditions followed for amplification of partial β-tubulin gene were as follows: 5 min of preheating at 94 °C followed by 35 cycles of denaturation at 94 °C for 1 min, annealing at 60 °C for 45 s, extension at 72 °C for 1 min and a final extension of 7 min at 72 °C. The PCR conditions followed for amplification of partial calmodulin gene were as follows: 10 min of preheating at 94 °C followed by 35 cycles of denaturation at 94 °C for 50 s, annealing at 58 °C for 50 s, extension at 72 °C for 1 min and a final extension of 7 min at 72 °C. The PCR products were separated on 1.0 % (w/v) agarose gel including DNA ladder SM0241 (Fermentas Life Sciences, Burlington, ON, Canada) and purified using a HiPurA^{TM} PCR product purification spin kit.

The purified PCR products were sequenced using an ABI prism DNA sequencer by BigDye terminator method (Applied Biosystems, Foster City, CA, USA). The resulting nucleotide sequences were compared using Basic Local Alignment Search Tool (BLAST) network services of the National Center for Biotechnology Information (NCBI) database (http://www.ncbi.nlm.nih.gov/) and the most closely related species were determined. The sequences were further submitted to GenBank and the accession numbers were obtained.

Extracellular mycosynthesis of IONPs

All the fungal isolates were screened to check their ability to hydrolyze the precursor salt solution comprising freshly prepared potassium ferricyanide $K_3[Fe(CN)_6]$ and potassium ferrocyanide $K_4[Fe(CN)_6]$ in a millimolar ratio of 1:0.5 (data not shown). The isolate showing maximum hydrolysis was selected for further study. The fungal isolate was maintained on PDA slants (pH 5.6) with repeated sub-culturing on fresh media. From an actively growing culture, a loopful of spores was inoculated in 80 mL of MGYP medium (0.3 % malt extract, 1.0 % glucose, 0.3 % yeast extract, 0.5 % peptone; pH 7.0) in 250 mL Erlenmeyer flasks. The inoculated flasks were incubated at 28 °C for 72 h on a rotary shaker (120 rpm) under dark conditions. After incubation, the fungal biomass was separated from the culture medium by centrifugation (5,000 rpm) at 4 °C for 15 min and washed thrice with autoclaved Milli-Q water to remove all traces of media. Typically, 20 g of biomass (fresh weight) was resuspended in 100 mL of precursor salt solution in a 250 mL Erlenmeyer flask and incubated at 28 °C for 96 h on a rotary shaker (120 rpm) under dark conditions. After incubation, the biomass was separated by filtration using Whatman grade 1 filter paper (Whatman Inc., Florham Park, NJ, USA) and the cell-free filtrate containing IONPs was obtained for further characterization. Biomass in autoclaved Milli-Q water (without precursor salt solution) as positive control and pure precursor salt solution (without biomass) as negative control were also incubated simultaneously along with the experimental flasks in three replicates.

The growth (colony forming unit, CFU) and viability of fungus before and after exposure to

precursor salt solution were checked. For determination of CFU, the fungal biomass was cut into pieces (5 × 5 mm) and shaken with 0.02 % Tween 80 for 30 min on a rotary shaker (250 rpm). Suitable dilutions were spread on the surface of PDA medium (pH 5.6). CFU on the plates were counted after incubation at 28 °C for 72 h under dark conditions (Schnurer 1993). The fungus viability was observed by inoculating the exposed fungal biomass on PDA medium (pH 5.6). The inoculated Petri plates were incubated at 28 °C for 72 h under dark conditions.

A separate experiment was performed to examine the possibility of IONPs synthesis, solely by the fungal extracellular proteins. For this, 20 g (fresh weight) of fungal biomass was suspended in 100 mL of autoclaved Milli-Q water and incubated for 72 h in an Erlenmeyer flask in similar conditions as described earlier. After incubation, the cell-free filtrate containing extracellular proteins was recovered by filtration using Whatman grade 1 filter paper. The precursor salt solution at a final millimolar ratio of 1:0.5 was added to the flask containing cell-free filtrate and incubated on a rotary shaker (120 rpm) at 28 °C for 96 h under dark conditions. Cell-free filtrate (without precursor salt solution) as positive control and pure precursor salt solution (without cell-free filtrate) as negative control were also incubated simultaneously along with the experimental flasks in three replicates.

Characterization of mycosynthesized IONPs

Hydrolysis of iron cyanide complex was monitored by taking UV–visible absorption spectra of the culture supernatant at different time intervals. UV–visible measurements were carried out on a V-630 UV–visible spectrophotometer instrument (Jasco Corporation, Tokyo, Japan) at a resolution of 1 nm with a scan speed of 400 nm/min using a 1 cm path length quartz cuvette. Samples for transmission electron microscopy (TEM) imaging and selected area electron diffraction (SAED) pattern determination were prepared on a carbon-coated TEM grid by drop coating the cell-free filtrate containing IONPs after 30 min of sonication. TEM measurement and SAED pattern determination were carried out on a JEM-2100 instrument (JEOL, Tokyo, Japan) operated at an accelerating voltage of 80 and 200 kV for low- and high-resolution imaging, respectively. Energy dispersive spectroscopy (EDS) analysis was carried out using a H-7650 scanning electron microscope (SEM) instrument (Hitachi High-Technologies Corporation, Tokyo, Japan) equipped with Quantax EDS attachment (Bruker AXS Ltd., Coventry, UK) by freeze drying the cell-free filtrate containing IONPs followed by coating on a double-sided carbon tape attached to the grid surface. The crystalline phase of the iron oxide was identified by grazing incidence X-ray diffraction (GIXRD) measurements of thin layer of mycosynthesized IONPs on glass substrates carried out on an X'Pert PRO X-ray diffractometer instrument (PANalytical BV, Almelo, The Netherlands). The diffraction pattern was recorded between 20° and 80° (2θ) with the diffractometer operated at a voltage of 40 kV and a current of 30 mA with CuK_{α} radiation. The crystal phase was determined by comparing the calculated values of interplanar spacing and the corresponding intensities of diffraction peaks with theoretical values from the Joint Committee on Powder Diffraction Standards-International Centre for Diffraction Data (JCPDS-ICCD) database. Fourier transform infrared (FTIR) spectroscopy measurements of the freeze-dried IONPs diluted with potassium bromide in the ratio of 1:100 were recorded on an IR Prestige-21 FTIR instrument (Shimadzu, Nakagyo-ku, Japan) with a diffuse reflectance mode (DRS-8000) attachment. All measurements were carried out in wavenumber range of 400–4,000 cm^{-1} at a resolution of 4 cm^{-1}.

For scanning electron microscopy (SEM) analysis of the fungal biomass exposed to precursor salt solution, the biomass was fixed overnight at 4 °C with 2.5 % (v/v) glutaraldehyde in 0.1 M sodium phosphate buffer, pH 7.2. The specimen was rinsed in buffer, dehydrated in a series of 30–100 % ethanol and then dried in a desiccator under vacuum. An automatic Polaron OM-SC7640 sputter coater instrument (Quorum Technologies, Sussex, UK) was used for coating the specimens with gold particles. The specimen was examined using EVO 40 scanning electron microscope instrument (Carl Zeiss, Oberkochen, Germany).

Ferrozine assay for estimation of free iron

To estimate the free iron content in the solution after completion of reaction, ferrozine assay was performed in the cell-free filtrate (Gibbs 1976). The aliquot (1 mL) was treated with ferrozine at a final concentration of 1 mM and the absorbance was recorded at 562 nm against blank (1 mM ferrozine). Ferrous

sulfate solution (1 mM) was used as positive control, whereas cell-free filtrate (without precursor salt solution) and pure precursor salt solution (without cell-free filtrate) were used as negative controls. The experiment was performed in triplicate.

Protein purification and one-dimensional gel electrophoresis

Extracellular proteins from both the test (biomass exposed to precursor salt solution) and control (biomass in autoclaved Milli-Q water) were purified using ammonium sulfate precipitation. Solid ammonium sulfate was added slowly at a final concentration of 80 % (w/v) (Simpson 2004). The mixture was gently stirred for 4–5 h at 4 °C. The resulting precipitate was subsequently collected by centrifugation at 10,000 rpm for 20 min at 4 °C. The proteins obtained thereafter were resuspended in a minimum amount of 50 mM phosphate buffer, pH 7.2, and dialyzed using a Sigma-Aldrich 12-kDa cutoff dialysis bag pre-treated as per the manufacturer's instructions. Briefly, the precipitated protein was filled in the treated dialysis bag, which was then suspended in dialysis buffer (50 mM phosphate buffer, pH 7.2) and stirred slowly at 4 °C. The buffer was changed three to four times over a 12 h period. The total protein concentration in the dialyzed samples was estimated by the standard protocol of Lowry et al. (1951), using bovine serum albumin as standard.

The dialyzed protein fractions were separated on the basis of molecular weight by sodium dodecyl sulfate–polyacrylamide gel electrophoresis (SDS-PAGE) as per standard procedure with adequate modifications (Laemmli 1970). Samples were denatured in 2× sample buffer containing 60 mM Tris (pH 6.8), 25 % glycerol, 2 % SDS, 14.4 mM 2-mercaptoethanol and 0.1 % bromophenol blue, boiled for 5 min, followed by centrifugation at 8,000 rpm for 1 min at 4 °C. Unstained protein molecular weight marker SM0661 (Fermentas Life Sciences) was run along with samples. Electrophoresis was performed on a Mini Protean®3 Cell instrument (BioRad Laboratories, Hercules, CA, USA) at a constant voltage of 100 kV for 120 min. After electrophoresis, the gel was stained with Coomassie Brilliant blue G-250 stain and was observed in a BioRad Gel Doc™ XR imaging system.

Role of proteins in nanoparticle stability

The role of extracellular proteins in nanoparticle stabilization was investigated. For this, the cell-free filtrate containing extracellular proteins from positive control flask (without precursor salt solution) was recovered by filtration using Whatman grade 1 filter paper. The commercially available magnetite nanoparticles at a final concentration of 50 mg/mL was added to the cell-free filtrate and incubated on a rotary shaker (150 rpm) at 28 °C for 48 h under dark conditions. After this, zeta potential measurements were carried out on a Zetasizer Nano ZS (Malvern Instruments Ltd, Worcestershire, UK) at neutral pH. Magnetite nanoparticles (50 mg/mL) suspended in water were used as control.

Results

Molecular identification of fungal isolate

Fungi were isolated from soil samples of iron-rich regions of Udaipur, Rajasthan, India. Preliminary identification of fungi was performed on the basis of morphological parameters such as color, spore shape, arrangement and hyphal branching pattern after staining with cotton blue. A total of 16 fungal isolates were observed on the basis of distinct morphological parameters. After screening, the isolate showing maximum hydrolysis of precursor salt solution was identified at the molecular level by comparative sequence analysis of the ITS regions of ribosomal DNA as well as that of partial β-tubulin and partial calmodulin gene sequences. The sequencing of PCR products resulted in 540 bp (ITS region), 491 bp (partial β-tubulin gene) and 699 bp (partial calmodulin gene) long nucleotide sequences. These sequences were compared using BLAST algorithm. Isolate AJP01 showed the maximum similarity with *Aspergillus japonicus*. The derived fungal sequences were deposited in GenBank with the following accession numbers: JF770435 (ITS region), JX103558 (partial β-tubulin gene) and JX103559 (partial calmodulin gene). *Aspergillus japonicus* isolate AJP01 has been deposited in the Microbial Type Culture Collection and Gene Bank at the Institute of Microbial Technology, Chandigarh, India with the MTCC number 11733 and is available at public domain.

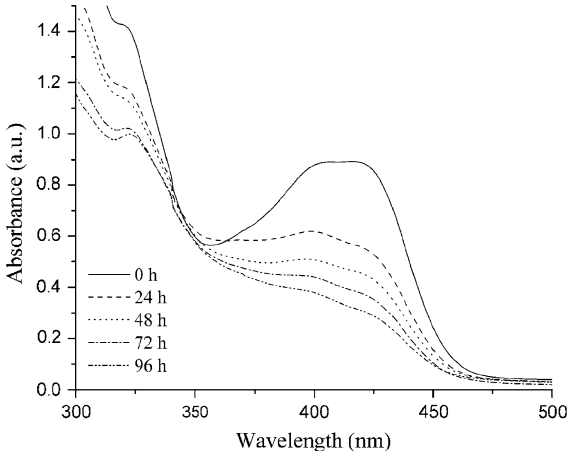

Fig. 1 UV–visible absorption spectrum of cell-free filtrate representing the gradual synthesis of IONPs as a function of time

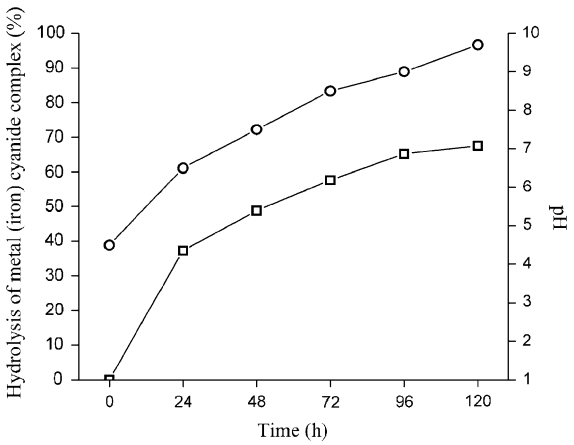

Fig. 2 Graphical representation of increase in the rate of hydrolysis of iron cyanide complex (in percent) observed at 420 nm (*open squares*) and increase in reaction pH (*open circles*) as a function of time

Characterization of mycosynthesized IONPs

The absorption spectra of precursor salt solution showed highly symmetric band absorption with peak maximum at 420 nm, which is attributed to the characteristic absorption maximum of potassium ferricyanide (Williams 1997). A steady decrease in intensity of peak as a function of time of reaction was observed during the reaction spanning 96 h (Fig. 1). The hydrolysis of iron cyanide complexes accounted for the highest magnitude (37.28 %) in the initial 24 h (Fig. 2). After 96 h of incubation, no significant increase was observed in the percent hydrolysis.

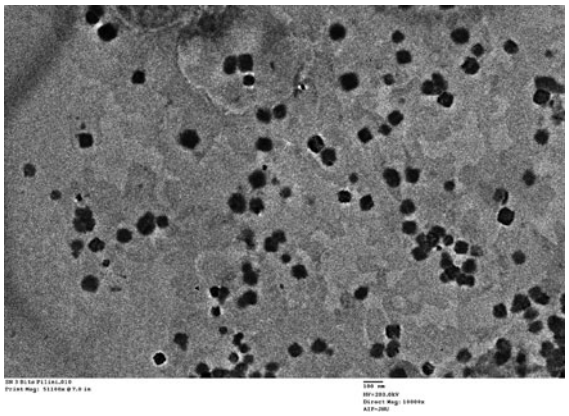

Fig. 3 TEM micrograph of mycosynthesized iron oxide nanoparticles (*scale bar* equivalent to 100 nm)

The size and morphology of mycosynthesized IONPs were determined by TEM measurements. A representative TEM micrograph (Fig. 3) revealed the particle morphology to be cubic in shape with strict control over particle size. The particle size distribution histogram obtained from TEM measurements (Fig. 4) showed that the maximum number of particles confined in the range of 60–70 nm and possessed an average size of 82.25 ± 5 nm. The SAED patterns (Fig. 5) confirmed the nanoparticles to be crystalline and the diffraction pattern data were found to be consistent with the typical structure characteristics of iron oxide (magnetite [Fe_3O_4] and maghemite [γ-Fe_2O_3]). On the basis of calculated d-values, the diffraction pattern analysis suggested that the particles belonged to magnetite (Sun et al. 2004). High-resolution TEM micrograph (Fig. 6) demonstrated the well-resolved interference fringe pattern attesting to the crystallinity of a typical magnetite nanoparticle with no sign of crystal defects. EDS analysis of freeze-dried sample was performed to determine the elemental composition of nanoparticles (Fig. 7). The EDS spectrum showed an optical absorption band at ~6.5 eV, which is representative of iron (Njagi et al. 2010). Figure 8 shows the XRD pattern of synthesised IONPs. Analysis of XRD spectra showed characteristic Bragg's diffraction peaks which are in good agreement with the standard magnetite pattern (JCPDS: 19-0629).

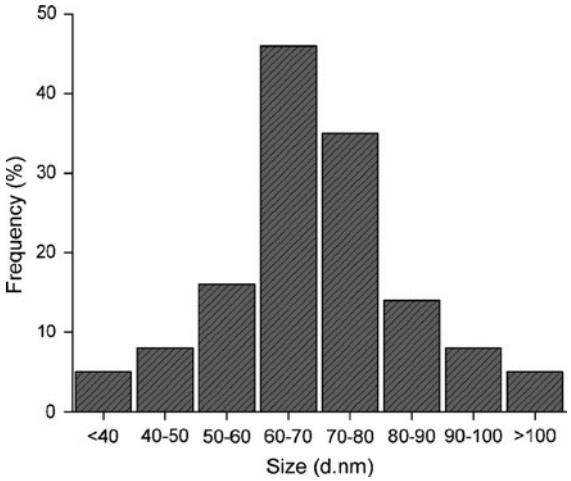

Fig. 4 Particle size distribution histogram of iron oxide nanoparticles extracted from TEM analysis

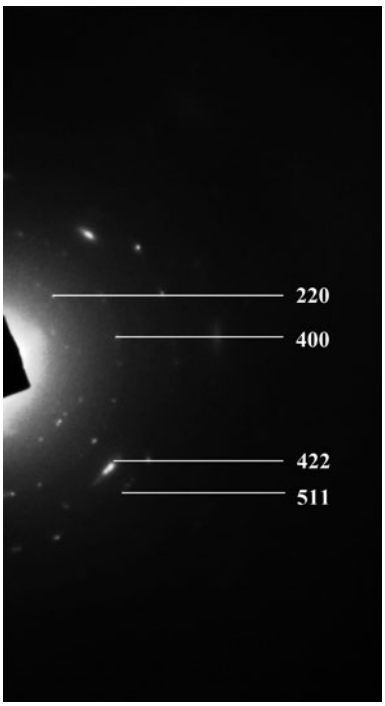

Fig. 5 SAED pattern from a single iron oxide nanoparticle. The diffraction rings corresponds to the allowed (511), (422), (400) and (220) Bragg's reflections

To examine the possibility of synthesis of IONPs bounded to the fungal biomass, SEM imaging of the fungal biomass exposed to the precursor salt solution was performed after completion of the reaction. A

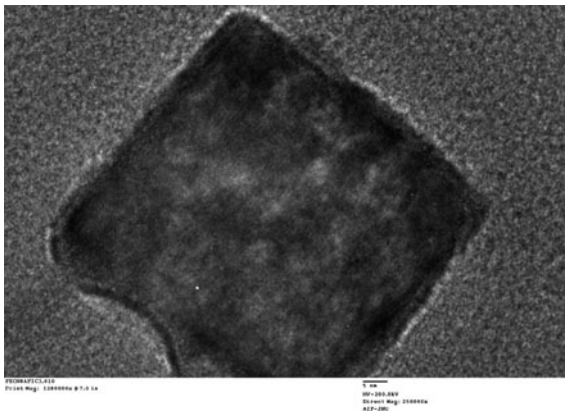

Fig. 6 High-resolution TEM micrograph of a single iron oxide nanoparticle (*scale bar* equivalent to 5 nm)

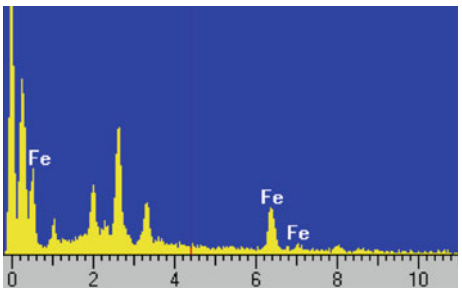

Fig. 7 EDS spectrum of freeze-dried cell-free filtrate containing mycosynthesized iron oxide nanoparticles

representative SEM micrograph of the exposed biomass (Fig. 9) showed the absence of IONPs on the fungal surface, signifying exclusively extracellular synthesis by this fungal isolate.

Ferrozine assay for qualitative estimation of free metal ions

The hydrolysis of the iron cyanide complex was further confirmed by the ferrozine assay, wherein ferrozine specifically binds with free ferrous ions. However, it may non-specifically bind to free ferric ions. The precursor salt solution exposed to fungal biomass for 96 h showed positive result in the ferrozine assay. However, the precursor salt solution failed to give positive results on reaction with ferrozine as metal ions were strongly bound with cyanide and remained in the form of iron cyanide complexes. In the absence of free metal ions, there was a negative result in the ferrozine assay.

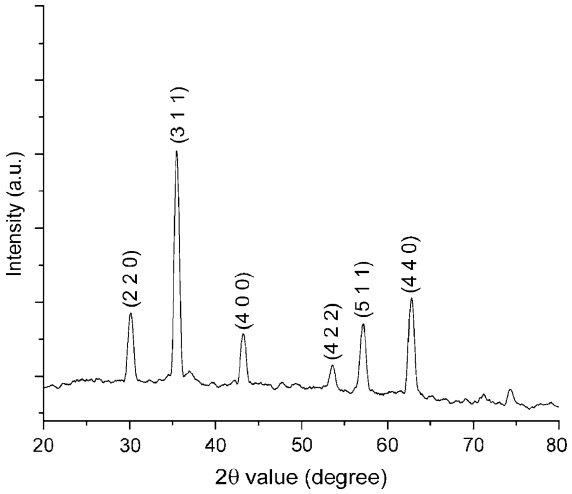

Fig. 8 Grazing incidence X-ray diffraction pattern of myco-synthesized iron oxide nanoparticles. The XRD pattern indicates Bragg's reflections corresponding to the magnetite structure

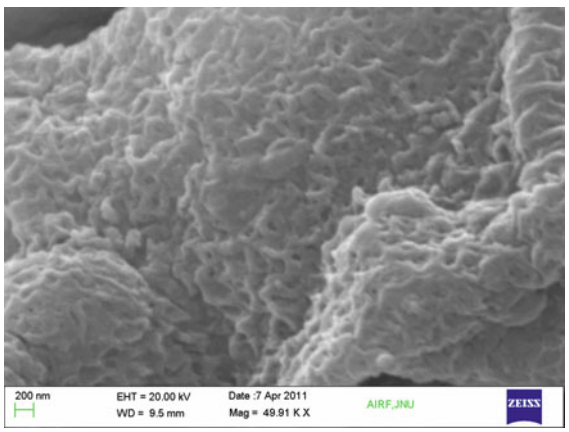

Fig. 9 SEM micrograph of fungal biomass exposed to precursor salts showing the absence of iron oxide nanoparticles on biomass surface (*scale bar* equivalent to 200 nm)

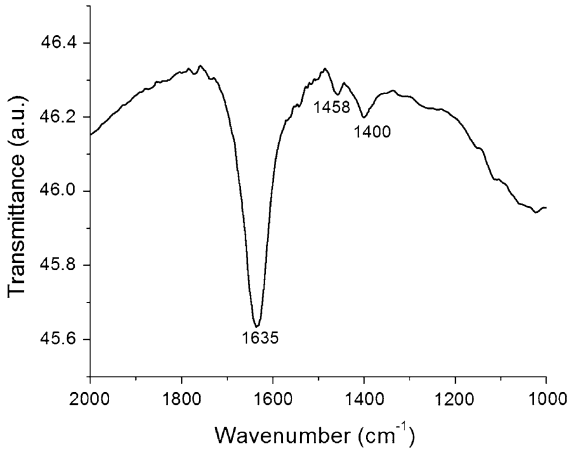

Fig. 10 FTIR spectrum of freeze-dried sample of iron oxide nanoparticles

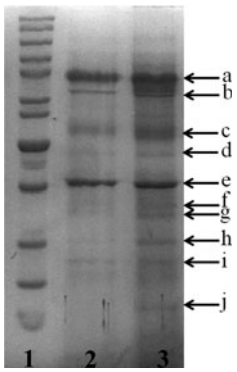

Fig. 11 SDS-PAGE analysis of purified extracellular proteins from *Aspergillus japonicus* isolate AJP01. *Lane 1* 10–200 kDa molecular size marker (Fermentas SM0661). Purified extracellular proteins obtained from unexposed (*lane 2*) and exposed (*lane 3*) fungal biomass to precursor salt solution. The *arrows* indicate extracellular proteins with molecular weight ca. 85 kDa (*a*), 76 kDa (*b*), 55 kDa (*c*), 49 kDa (*d*), 42 kDa (*e*), 38 kDa (*f*), 36.5 kDa (*g*), 31 kDa (*h*), 28 kDa (*i*) and 21 kDa (*j*)

Role of fungal proteins in synthesis and stabilization

Fourier transform infrared measurements were carried out to identify the possible interaction between fungal proteins and IONPs (Fig. 10). FTIR analysis of freeze-dried samples showed a prominent vibration band at wavenumber 1,635 cm^{-1} assigned to the amide I bond of proteins arising due to carbonyl stretch in proteins, wavenumber 1,458 cm^{-1} representing $–CH_2–$ bending mode characteristic of protein side chains and wavenumber 1,400 cm^{-1} indicating COO^- stretching (Macdonald and Smith 1996; Wang et al. 2006; Yang et al. 2007).

A significant difference was observed in the concentration of various extracellular proteins expressed from biomass exposed to the precursor salt solution as compared to the control (unexposed biomass). The concentration of extracellular proteins secreted by the fungal biomass exposed to the precursor salt solution was determined to be 1,125 ± 7.5 μg/mL, which was nearly twice the concentration of extracellular proteins (587 ± 2.3 μg/mL) secreted by the unexposed biomass as estimated by Lowry's assay.

To identify the active role of extracellular proteins secreted by fungal biomass in synthesis and/or stabilization of IONPs, the protein profiles were compared by one-dimensional SDS-PAGE (Fig. 11). The SDS-PAGE analysis revealed the presence of several extracellular proteins, ca. 85 kDa (a), 76 kDa (b), 55 kDa (c), 49 kDa (d), 42 kDa (e), 38 kDa (f), 36.5 kDa (g), 31 kDa (h), 28 kDa (i) and 21 kDa (j).

The role of fungal protein in stabilization was further proved in the context with commercially available magnetite nanoparticles. A zeta potential of −1.83 mV was observed in control having magnetite nanoparticles suspended in water, whereas a zeta potential value of −12.2 eV was observed for magnetite nanoparticles incubated with fungal extracellular proteins. The more negative zeta potential observed in the latter case signifies that the protein plays an important role in the stabilization of nanoparticles making them more dispersed and stable (Patil et al. 2007).

Discussion

Overall, 16 morphologically distinct fungi were isolated from iron-rich soil. In our earlier study, we have demonstrated the ability of metal-tolerant fungus in the biosynthesis of nanoparticles (Jain et al. 2013). A mixture of iron cyanide complex was chosen as the precursor salt solution for the extracellular synthesis of IONPs. All the fungal isolates were screened to check their ability to hydrolyze iron cyanide complexes. Isolate AJP01 showed the most promising results on the basis of UV–visible spectroscopic measurements and was selected for further studies. For harnessing the complete potential of the remarkable capabilities of any biological entity, it is a prerequisite to identify the organism which improves the possibility of constructive modification, both at the physiological and molecular levels (Jogler et al. 2009). On the basis of comparative sequence analysis of ITS regions of ribosomal DNA, partial β-tubulin and partial calmodulin gene sequences, isolate AJP01 was identified as *Aspergillus japonicus*.

The extracellular synthesis of IONPs was achieved by exposing fungal biomass to precursor salt solution under ambient conditions. As shown in Fig. 1, the fungus was successful in hydrolyzing iron cyanide complexes, as the intensity at 420 nm corresponding to the absorption maxima of potassium ferricyanide observed a progressive decrease as a function of time. Noteworthy is the development of a broad absorption band at ca. 330 nm corresponding to the formation of iron oxide (Sherman and Waite 1985). This indicates the concurrent synthesis of IONPs as the cell-free filtrate turned brown in color at the end of the reaction. A similar kind of observation regarding change in color of the cell-free filtrate has been reported by Bharde et al. (2006), wherein the synthesis of IONPs was achieved using *Fusarium oxysporum* and *Verticillium* species. The percent hydrolysis of iron cyanide complexes showed no increase after 96 h of reaction (Fig. 2). The subsequent decrease in the rate of hydrolysis with time may be credited to the increase in pH toward alkalinity apart from a decline in substrate concentration which might have affected fungal enzyme activity such as nitrilase/cyanide hydratase. Cyanide hydratase is primarily a fungal enzyme responsible for the hydrolysis of cyanide complexes forming formamide (Ebbs 2004). The hydrolysis may be attributed to cyanide biodegradation as a consequence of its availability as a sole source of carbon and nitrogen for the survival of fungus under nutrient-deprived stress conditions (Dumestre et al. 1997; Barclay et al. 1998).

The fungus was able to maintain its growth and viability as it showed significant increase in CFU values as well as good growth on PDA plates even after 96 h of exposure with precursor salt solution containing cyanide, proving the utilization and degradation of cyanide as an energy source (Supplementary Material, Table S1, Fig. S1).

It is notable that the size of mycosynthesized nanoparticles is less than 100 nm as characterized by TEM analysis (Fig. 3; Fig. 4). This amenable size makes them potential candidates for use in various bio-inspired applications, where particle size is an essential consideration (Arruebo et al. 2007). SAED, HR-TEM, EDS and XRD analysis in this study further confirmed the composition and crystallinity of the obtained IONPs, respectively (Figs. 5, 6, 7, 8). The SEM analysis depicts the absence of nanoparticles on fungal surface (Fig. 9). These results prove the exclusive extracellular synthesis of IONPs by *Aspergillus japonicus* isolate AJP01.

The exposure of fungal biomass to the precursor salt solution resulted in the release of metal ions from cyanide complexes, which were confirmed by the

positive results for ferrozine assay in the test samples as compared to pure precursor salt solution. In earlier reports, it has been clearly demonstrated that complexed iron does not react with ferrozine and requires to be released from its complex form (Riemer et al. 2004). Ferrozine assay clearly indicated the degradation of cyanide complexes by fungal isolate and subsequent release of free metal ions (Dumestre et al. 1997; Barclay et al. 1998).

The mycosynthesis of nanoparticles is a result of complex biochemical reactions which can be mediated by a number of metabolic intermediates (Durán et al. 2011). In an earlier study, we showed that mycosynthesized silver nanoparticles were individually coated with extracellular fungal proteins (Jain et al. 2011). In the present study, FTIR measurements showed close interactions between fungal proteins and IONPs (Fig. 10). The proteins are believed to be associated with nanoparticles in their native secondary structure, as indicated by the vibration band at wavenumber 1,635 cm^{-1} (Takekiyo et al. 2009). The concentration of extracellular proteins secreted by fungal biomass exposed to precursor salt solution was nearly twice the concentration of extracellular proteins secreted by unexposed biomass as estimated by Lowry's assay and also observed by SDS-PAGE (Fig. 11). These results indicate the elevated expression of various extracellular proteins in the presence of precursor salt solution, which may be responsible for the coprecipitation, controlled nucleation and/or stabilization of IONPs. However, the hydrolysis of iron cyanide complexes may not be attributed to these extracellular proteins, as synthesis of IONPs using only cell-free filtrate (containing extracellular proteins) exclusive of biomass failed to give positive results for hydrolysis of iron cyanide complexes. In this case, no change in the intensity at 420 nm which is attributed to the characteristic absorption maximum of potassium ferricyanide was observed as a function of time during the course of reaction spanning 96 h. These results clearly indicate the role of fungal membrane proteins in hydrolyzing iron cyanide complexes and releasing free ferric and ferrous ions, and expectantly subsequent hydrolysis of cyanide. Fungi are well known to

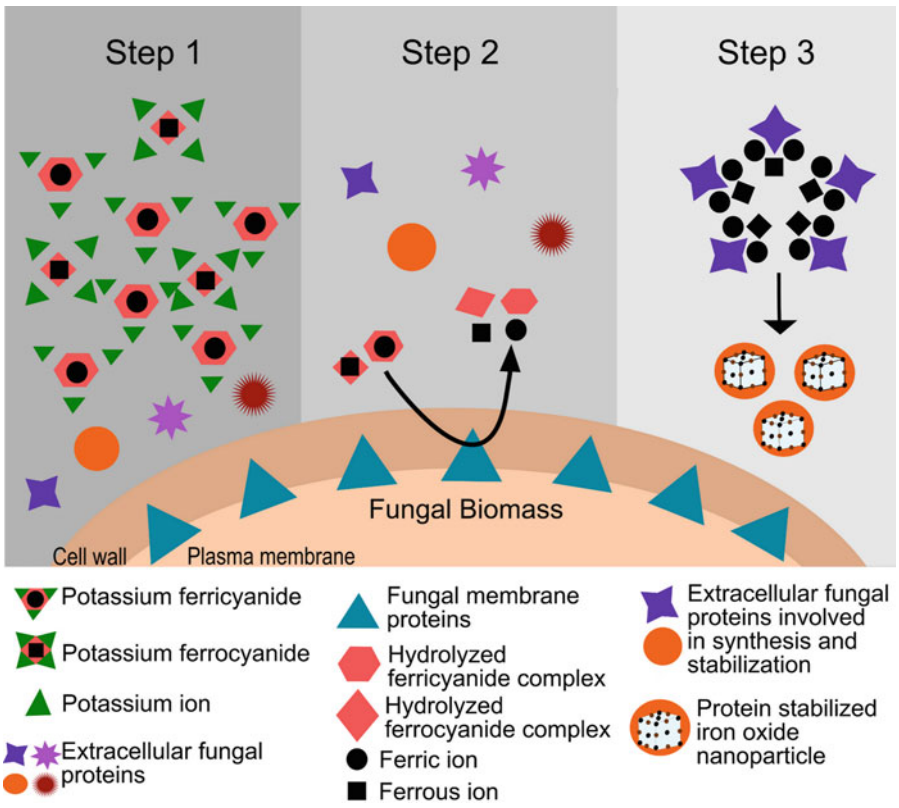

Fig. 12 Possible mechanism suggesting mycosynthesis of iron oxide nanoparticles

degrade (hydrolyze) metal cyanide complex by the action of enzymes such as cyanide hydratase or nitrilase, which hydrolyzes the metal cyanide bond, releasing the free metal moiety (Barclay et al. 1998; Ebbs 2004).

Based on the present experimental findings, a schematic presentation of the possible mechanism for synthesis of IONPs is speculated (Fig. 12). We hypothesized that the synthesis process occurs in three steps. The first step involves the immediate release of potassium ions from the ferricyanide and ferrocyanide complexes soon after the addition of precursor salts in solution. In the second step, the ferricyanide and ferrocyanide complexes undergo hydrolysis as supported by UV–visible spectroscopic analysis. This is possibly mediated by one or more of the fungal membrane proteins releasing ferric and ferrous ions as determined by the ferrozine assay during the present study. Expectantly, hydrolysis of cyanide may take place as being the only nutrient source for growth and survival of fungi under nutrient-deprived stress conditions during the experiment. The role of extracellular proteins in the hydrolysis of iron cyanide complexes can be disqualified as no observable results were obtained in the reaction with only cell-free filtrate. The third step involves the IONPs 'synthesis' by coprecipitation and controlled nucleation of ferric and ferrous ions available at millimolar ratio of 1:0.5, respectively. Progressing alkaline pH and interaction of one or more extracellular proteins may mediate the 'synthesis', followed by stabilization of mycosynthesized IONPs by other proteins, as suggested by the FTIR studies. The role of extracellular proteins in stabilization was further confirmed by the increase in zeta potential value of protein stabilized nanoparticles as compared to unstabilized ones.

Further investigations at the biochemical and molecular level regarding the hydrolysis of iron cyanide complexes, protein/polypeptide-mediated synthesis and stabilization of IONPs are in progress in our laboratory. Elucidation of the detailed mechanism behind biosynthesis of IONPs using fungi can lead to imperative modifications in the protocol for augmentation in the overall yield of IONPs. Genetic engineering implications to the present process can be achieved if the involved proteins and their respective genes can be identified making mycosynthesis comparable to commercially used physical and chemical methods of nanoparticle synthesis.

Acknowledgments This research was financially supported by the Indian Council of Agricultural Research, Government of India under the National Agricultural Innovation Project scheme (NAIP/C4/C-2032). Facilities provided by the Chonbuk National University, Jeonju, Republic of Korea, Advanced Instrumentation Research Facility, Jawaharlal Nehru University, New Delhi, India and Birla Institute of Technology and Science, Pilani, India are gratefully acknowledged. Arpit Bhargava and Navin Jain are thankful to the Indian Council of Agricultural Research and Council of Scientific and Industrial Research, Government of India, respectively, for providing research fellowship.

References

Arruebo M, Fernández-Pacheco R, Ibarra MR, Santamaría J (2007) Magnetic nanoparticles for drug delivery. Nano Today 2:22–32. doi:10.1016/S1748-0132(07)70084-1

Barclay M, Hart A, Knowles CJ, Meeussen JCL, Tett VA (1998) Biodegradation of metal cyanides by mixed and pure cultures of fungi. Enzyme Microb Technol 22:223–231. doi:10.1016/S0141-0229(97)00171-3

Bharde A, Rautaray D, Bansal V, Ahmad A, Sarkar I, Yusuf SM, Sanyal M, Sastry M (2006) Extracellular biosynthesis of magnetite using fungi. Small 2:135–141. doi:10.1002/smll.200500180

Bhargava A, Jain N, Panwar J (2011) Synthesis and application of magnetic nanoparticles: a biological perspective. In: Dhingra HK, Jha PN, Bajpai P (eds) Current topics in biotechnology and microbiology: recent trends. Lap Lambert Academic Publishing AG & Co Kg, Colne, pp 117–155

Dhillon GS, Brar SK, Kaur S, Verma M (2011) Green approach for nanoparticle biosynthesis by fungi: current trends and applications. Crit Rev Biotechnol 32:49–73. doi:10.3109/07388551.2010.550568

Dumestre A, Chone T, Portal J, Gerard M, Berthelin J (1997) Cyanide degradation under alkaline conditions by a strain of *Fusarium solani* isolated from contaminated soils. Appl Environ Microbiol 63:2729–2734

Durán N, Marcato P, Durán M, Yadav A, Gade A, Rai M (2011) Mechanistic aspects in the biogenic synthesis of extracellular metal nanoparticles by peptides, bacteria, fungi, and plants. Appl Microbiol Biotechnol 90:1609–1624. doi:10.1007/s00253-011-3249-8

Ebbs S (2004) Biological degradation of cyanide compounds. Curr Opin Biotechnol 15:231–236. doi:10.1016/j.copbio.2004.03.006

Fedlheim DL, Foss CA (2001) Metal nanoparticles: synthesis, characterization, and applications. CRC Press, Boca Raton

Gade A, Ingle A, Whiteley C, Rai M (2010) Mycogenic metal nanoparticles: progress and applications. Biotechnol Lett 32:593–600. doi:10.1007/s10529-009-0197-9

Gibbs CR (1976) Characterization and application of ferrozine iron reagent as a ferrous iron indicator. Anal Chem 48:1197–1201. doi:10.1021/ac50002a034

Glass NL, Donaldson GC (1995) Development of primer sets designed for use with the PCR to amplify conserved genes

from filamentous ascomycetes. Appl Environ Microbiol 61:1323–1330

Jain N, Bhargava A, Majumdar S, Tarafdar JC, Panwar J (2011) Extracellular biosynthesis and characterization of silver nanoparticles using *Aspergillus flavus* NJP08: a mechanism perspective. Nanoscale 3:635–641. doi:10.1039/C0NR00656D

Jain N, Bhargava A, Tarafdar JC, Singh SK, Panwar J (2013) A biomimetic approach towards synthesis of zinc oxide nanoparticles. Appl Microbiol Biotechnol 97:859–869. doi:10.1007/s00253-012-3934-2

Jogler C, Lin W, Meyerdierks A, Kube M, Katzmann E, Flies C, Pan Y, Amann R, Reinhardt R, Schüler D (2009) Toward cloning of the magnetotactic metagenome: identification of magnetosome island gene clusters in uncultivated magnetotactic bacteria from different aquatic sediments. Appl Environ Microbiol 75:3972–3979. doi:10.1128/AEM.02701-08

Jun YW, Seo JW, Cheon J (2008) Nanoscaling laws of magnetic nanoparticles and their applicabilities in biomedical sciences. Acc Chem Res 41:179–189. doi:10.1021/ar700121f

Komeili A (2007) Molecular mechanisms of magnetosome formation. Annu Rev Biochem 76:351–366. doi:10.1146/annurev.biochem.74.082803.133444

Laemmli UK (1970) Cleavage of structural proteins during the assembly of the head of bacteriophage T4. Nature 227:680–685. doi:10.1038/227680a0

Laurent S, Forge D, Port M, Roch A, Robic C, Vander Elst L, Muller RN (2008) Magnetic iron oxide nanoparticles: synthesis, stabilization, vectorization, physicochemical characterizations, and biological applications. Chem Rev 108:2064–2110. doi:10.1021/cr068445e

Lowry OH, Rosebrough NJ, Farr AL, Randall RJ (1951) Protein measurement with the folin phenol reagent. J Biol Chem 193:265–275

Macdonald IDG, Smith WE (1996) Orientation of cytochrome c adsorbed on a citrate-reduced silver colloid surface. Langmuir 12:706–713. doi:10.1021/la950256w

Njagi EC, Huang H, Stafford L, Genuino H, Galindo HM, Collins JB, Hoag GE, Suib SL (2010) Biosynthesis of iron and silver nanoparticles at room temperature using aqueous sorghum bran extracts. Langmuir 27:264–271. doi:10.1021/la103190n

Noguez C (2007) Surface plasmons on metal nanoparticles: the influence of shape and physical environment. J Phys Chem C 111:3806–3819. doi:10.1021/jp066539m

O'Donnell K, Nirenberg H, Aoki T, Cigelnik E (2000) A multigene phylogeny of the *Gibberella fujikuroi* species complex: detection of additional phylogenetically distinct species. Mycoscience 41:61–78. doi:10.1007/BF02464387

Parikh RY, Ramanathan R, Coloe PJ, Bhargava SK, Patole MS, Shouche YS, Bansal V (2011) Genus-wide physicochemical evidence of extracellular crystalline silver nanoparticles biosynthesis by *Morganella* spp. PLoS ONE 6:e21401. doi:10.1371/journal.pone.0021401

Patil S, Sandberg A, Heckert E, Self W, Seal S (2007) Protein adsorption and cellular uptake of cerium oxide nanoparticles as a function of zeta potential. Biomaterials 28:4600–4607. doi:10.1016/j.biomaterials.2007.07.029

Riemer J, Hoepken HH, Czerwinska H, Robinson SR, Dringen R (2004) Colorimetric ferrozine-based assay for the quantitation of iron in cultured cells. Anal Biochem 331:370–375. doi:10.1016/j.ab.2004.03.049

Schnurer J (1993) Comparison of methods for estimating the biomass of three food-borne fungi with different growth patterns. Appl Environ Microbiol 59:552–555

Sherman DM, Waite TD (1985) Electronic spectra of Fe (super 3+) oxides and oxide hydroxides in the near IR to near UV. Am Mineral 70:1262–1269

Simpson RJ (2004) Purifying proteins for proteomics: a laboratory manual. Cold Spring Harbor Laboratory Press, New York

Sun YK, Ma M, Zhang Y, Gu N (2004) Synthesis of nanometer-size maghemite particles from magnetite. Colloids Surf A 245:15–19. doi:10.1016/j.colsurfa.2004.05.009

Takekiyo T, Wu L, Yoshimura Y, Shimizu A, Keiderling TA (2009) Relationship between hydrophobic interactions and secondary structure stability for trpzip β-hairpin peptides. Biochemistry 48:1543–1552. doi:10.1021/bi8019838

Teja AS, Koh PY (2009) Synthesis, properties, and applications of magnetic iron oxide nanoparticles. Prog Cryst Growth Charact Mater 55:22–45. doi:10.1016/j.pcrysgrow.2008.08.003

Wang C, Zhang Y, Seng HS, Ngo LL (2006) Nanoparticle-assisted micropatterning of active proteins on solid substrate. Biosens Bioelectron 21:1638–1643. doi:10.1016/j.bios.2005.07.008

White TJ, Bruns T, Lee S, Taylor J (1990) Amplification and direct sequencing of fungal ribosomal RNA genes for phylogenetics. In: Innis MA, Gelfand DH, Sninsky JJ, White TJ (eds) PCR protocols a guide to methods and applications. Academic Press, San Diego, pp 315–322

Williams M (1997) The Merck Index, 12th Edition. CD-Rom Version 12.1. Drug Dev Res 41:108–108. doi:10.1002/(SICI)1098-2299(199706)41:2<108::AID-DDR9>3.0.CO;2-L

Wu Z, Neaton JB, Grossman JC (2008) Quantum confinement and electronic properties of tapered silicon nanowires. Phys Rev Lett 100:e246804. doi:10.1103/PhysRevLett.100.246804

Yang T, Li Z, Wang L, Guo C, Sun Y (2007) Synthesis, characterization, and self-assembly of protein lysozyme monolayer-stabilized gold nanoparticles. Langmuir 23:10533–10538. doi:10.1021/la701649z

DOI 10.1007/978-3-319-05041-6_28
Reprinted from the *Journal of Nanoparticle Research*, DOI 10.1007/s11051-012-1094-z

RESEARCH PAPER

Electrochemical synthesis of gold nanorods in track-etched polycarbonate membrane using removable mercury cathode

Manoj K. Sharma · Arvind S. Ambolikar · Suresh K. Aggarwal

Received: 2 February 2012 / Accepted: 23 July 2012 / Published online: 14 August 2012

Abstract The electrochemical template synthesis of gold nanorods within the cylindrical pores of track-etched polycarbonate (PC) membrane using a removable mercury cathode is reported. The novelty of this new approach is that it eliminates the requirement of coating an approximately 500 nm–1 μm-thick metallic layer, as conducting substrate, onto one surface of the insulating template membrane by the sputter deposition technique. A two-compartment electrochemical cell was designed and used for this work. The PC membrane was placed between the two compartments separating the aqueous solution of $HAuCl_4$ from mercury. Mercury, filled in one of the compartments, is in contact with one surface of the membrane (similar to sputter-deposited metallic layer) and serves as the conducting substrate/cathode for the electrochemical deposition of gold in the nanopores of track-etched PC membrane. Once the electrodeposition is completed, the mercury and the $HAuCl_4$ solution are removed from the compartments, and a malleable track-etched PC membrane embedded with free-standing gold nanorods is obtained. The ensemble of the metal nanorods grown in the template membrane is not attached to any conducting substrate, and gold nanorods can be freed from the template membrane after the dissolution. The Au-deposited PC membrane and free-standing Au nanorods were characterized by EDXRF, XRD, UV–Visible spectroscopy, AFM, and FEG-TEM. The EDXRF and XRD studies confirmed the deposition of the face-centered cubic phase of Au in the pores of the PC membrane. The TEM studies showed the formation of a cigar-shaped gold nanorod in the cylindrical pores of the PC membrane. The diameter of gold nanorods ranges from 100 to 200 nm. The new approach is simple, cost-effective, and saves time.

Keywords Track-etched membrane · Electrochemical synthesis · Removable mercury cathode · Gold nanorods · Two-compartment electrochemical cell

Introduction

Nanomaterials are of great interest to the research community because of their unique chemical and physical properties which are distinct from the bulk (Nalwa 2000; Hodes 2007; El-Sayed 2004). Nanomaterials have found a wide range of applications in almost every discipline of science and technology. Nanomaterials are touching many aspects of human life in the form of advanced materials for smart

Special Issue Editors: Mamadou Diallo, Neil Fromer, Myung S. Jhon

This article is part of the Topical Collection on Nanotechnology for Sustainable Development

M. K. Sharma (✉) · A. S. Ambolikar · S. K. Aggarwal
Fuel Chemistry Division, Bhabha Atomic Research Centre, Trombay, Mumbai 400 085, India
e-mail: mksaks@yahoo.com; mkumars@barc.gov.in

miniaturized devices, sensors, therapeutic agents, etc. (Cao et al. 2002; Elghanian et al. 1997; Couzin 2002). The properties of nanomaterials can be easily tuned by changing their shape and size (El-Sayed 2004; Schmidt et al. 1998; Ivanova and Zamborini 2010; Berry 1998; Sanchez-Sanchez et al. 2010). Therefore, the synthesis of shape- and size-controlled nanomaterials is still a subject of great interest to researchers (Reetz and Helbig 1994). Many template- and non-template-based methods for the synthesis of nanomaterials of various shapes and sizes are reported (Bale et al. 2007; Xia et al. 2003; Xiong and Xia 2007; Huang et al. 2000; Ahmadi et al. 1996; Sun and Xia 2002). The aqueous colloidal suspension of gold nanorods was synthesized via an electrochemical method by introducing a shape-inducing reagent in solution (Yu-Ying et al. 1997). Templates are more frequently used to tune the size and the shape of the nanomaterials. Porous anodized alumina and track-etched polycarbonate (PC) membranes are commercially available templates for chemical and electrochemical synthesis of one-dimensional (1D) nanomaterials–nanowires, nanorods and nanotubules of metals, semiconductors, and conducting polymers (Martin 1994; Schonenberger et al. 1997; Hernandez et al. 2007). Superior properties of 1D nanomaterial have been theoretically predicted and experimentally confirmed by the researchers.

The previously reported method of electrochemical template synthesis of nanowires, nanorods, and nanotubules in template membrane involves an indispensable and inevitable step of coating an approximately 500 nm–1 μm-thick metallic layer onto one surface of the insulating membrane by the sputter deposition technique. The schematic diagram in Fig. 1a shows the various experimental steps involved in the method. The coated metallic layer serves as the conducting substrate/cathode for electrodeposition of metal nanowires within the pores of the membrane. In some reports (Pena et al. 2002), sputter deposition was followed by the electrochemical deposition of metal to further increase the metallic layer thickness so that the coated metallic layer completely covers the pores that may not be blocked during the sputter deposition method. The membrane is then fixed on the conducting substrate (Au or Cu plate) with the cathodic metallic layer in contact with the substrate. The membrane fixed on the conducting substrate is mounted either as the working electrode in a three-electrode electrochemical cell or as the cathode in a two-electrode electrochemical cell. The ensemble of the metal nanowires grown in the template membrane is attached to the coated metallic layer and protrudes from its surface like the bristles of a brush after the dissolution of the template membrane (Schonenberger et al. 1997). Therefore, the nanowires grown in the template membranes are not free-standing. The free-standing nanowire can be obtained by detaching it from a coated metal film. It is impossible to prepare a malleable track-etched membrane embedded with free-standing gold nanorods due to the sputter-deposited metal coating on one surface. The sputter-deposited metallic layer completely blocks the mouth of the pores on one surface, and the availability of pores with an open mouth on the other surface depends on the electrodeposition time. If the electrodeposition time is lesser than the time required for complete filling of the cylindrical pores, a large number of pores with an open mouth are available on the surface of the template membrane due to the incomplete filling of the cylindrical pores. The incomplete filled cylindrical pores with an open mouth can be used for encapsulation of the desired chemical or biochemical species by functionalizing the gold nanorods within the pores.

In this work, we report the electrochemical synthesis of gold nanorods within the cylindrical pores of the track-etched PC membrane using a removable mercury cathode, and this new approach eliminates the requirement of sputter deposition of a metallic layer coating onto one surface of the template membrane. A simple two-compartment electrochemical cell was used and the track-etched PC membrane was placed between the two compartments separating the aqueous solution of $HAuCl_4$ from mercury as shown in Fig. 1b. Mercury, filled in one of the compartments, is in contact with one surface of the membrane (similar to sputter-deposited metallic layer) and serves as the conducting substrate/cathode for the electrochemical deposition of gold in the nanopores of the track-etched PC membrane. Once the electrodeposition is completed, the mercury and the $HAuCl_4$ solution are removed from the compartments, and the membrane is washed with an ample amount of water. A malleable track-etched PC membrane embedded with free-standing gold nanorods is obtained. The ensemble of the metal nanowires grown in the template membrane is not attached to any conducting substrate, and gold nanorods can be easily

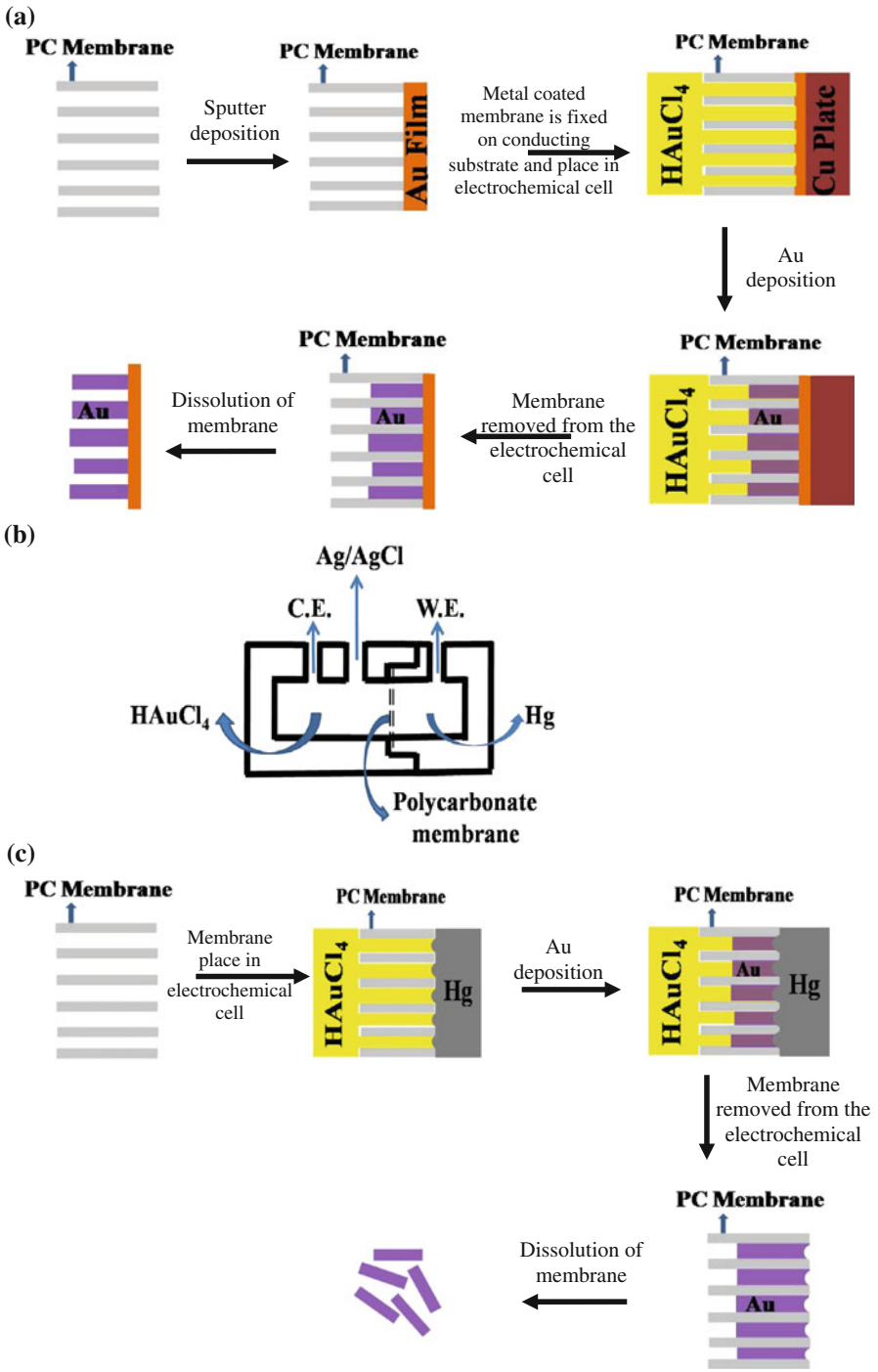

Fig. 1 **a** Schematic of electrochemical synthesis in insulating template membrane using sputter-deposited metallic layer as cathode. **b** Schematic of the two-compartment electrochemical cell (*W.E.* working electrode, *C.E.* counter electrode). **c** Schematic of electrochemical template synthesis in insulating template membrane using removable mercury cathode

freed from the template membrane after the dissolution in dichloromethane. The schematic diagram in Fig. 1c shows the various experimental steps involved in the method. The Au-deposited PC membrane and the gold nanorods obtained after the dissolution of PC membrane were characterized by EDXRF, XRD, UV–Visible spectroscopy, AFM, and FEG-TEM. The TEM studies showed the formation of a cigar-shaped gold nanorod in

the pores of the PC membrane. If the electrodeposition time is lesser than the time required for complete filling of the cylindrical pores, the surface of both the sides of the gold nanorods-embedded PC membrane shows pores with an open mouth (unlike the sputter-deposited metal film-coated template membrane). AFM studies showed that the PC membrane in which gold is electrodeposited for a short time has a large number of pores with an open mouth on the surface of both sides of the membrane.

The new approach is simple, cost-effective, and saves time. It can be used be used to prepare nanorods in other track-etched porous membranes without any change in the present experimental setup. The internal architecture of the pores will be reflected in the shape of the electrodeposited nanorods. Therefore, the template porous membranes should have well-defined cylindrical pores to prepare good-quality nanorods within the membrane. The incomplete filled cylindrical pores with an open mouth at the membrane surface can be used for encapsulation of the desired chemical or biochemical species by functionalizing the gold nanorods within the pores, and the functionalized track-etched PC membrane can be used to develop sensors based on the detection of analyte by surface-enhanced raman scattering (SERS) techniques (Ruan et al. 2007). These gold nanorods-containing track-etched membranes can also be used as smart surfaces/materials for catalytic and optical applications.

Experimental

All the reagents used were of analytical reagent grade. PVP-coated Nucleopore track-etched porous PC membrane with a pore diameter of 200 nm and thickness of 10 μm was obtained from Whatman Ltd. Deionised water (18 MΩ cm^{-1}) purified using the MilliQ water purifier system from Millipore was used throughout the present study. The porous PC membrane (diameter = 2 cm) was sonicated in water for 5 min. It was placed in the two-compartment electrochemical cell. Mercury and aqueous solution of 10 mM $HAuCl_4$ were filled in two different compartments separated by the PC membrane. The mercury in contact with one side of the membrane served as the cathode. The electrochemical deposition of gold within the pores of the PC membrane was carried out by applying a constant cathodic potential of −0.2 V on mercury. The electrochemical deposition time (t_d) was 1,000 and 3,000 s. Electrochemical experiments were performed using CHI 760D electrochemical workstation. The Ag/AgCl/3 M KCl aqueous and Pt wire were used as the reference electrode and the counter electrode, respectively. The membrane was then washed thoroughly in water and was allowed to dry in air. The deposition of gold in the PC membrane is also carried out by a galvanic reaction between $HAuCl_4$ and mercury for 1,000 s in a similar two-compartment cell as discussed above without applying the cathodic potential. An energy dispersive X-ray fluorescence (EDXRF) measurement of the membrane was carried out using Jordan Valley EX-3600 TEC EDXRF spectrometer with the Rh target operated at a voltage of 40 kV and a current of 170 μA. Rh K_α was used as the excitation for L_α and L_β lines of gold. X-ray diffraction (XRD) patterns were recorded on STOE XRD unit using Cu target (Cu K_α = 1.5406 Å) with graphite monochromator. Absorbance spectra of membrane were recorded in the transmittance mode using a UV–Vis spectrophotometer (QE65000, Ocean Optic Ltd). The absorbance spectra were measured in air by placing the membrane in a quartz cell. For atomic force microscopy (AFM) studies of the PC membrane samples, tapping mode AFM measurements were performed in air at ambient temperature conditions using a Nanosurf easyScan 2 AFM (Nanosurf, Switzerland) with 10 μm scanner head. The cantilevers used were NCLR-10 (Nano World) with a resonance frequency of 190 kHz and a force constant of 48 N m^{-1}. The scanned area was 2.4 × 2.4 μm. AFM data were analyzed by Nanosurf Report 4.1 software. FEG-TEM measurements were performed using a JEOL electron microscope (JEM 2100 F) operating at 200 kV. A sample preparation for TEM experiment was carried out by dissolving the Au-deposited PC membrane in dichloromethane and the solution was pipetted onto carbon-coated copper grids.

Results and discussion

AFM gives the surface morphology of the membrane with a nanometer or even atomic resolution by scanning the surface with a very sharp tip of atomic dimension. Figure 2a shows the 3-dimensional AFM image of the track-etched PC membrane surface before the electrodeposition of gold. The pores are

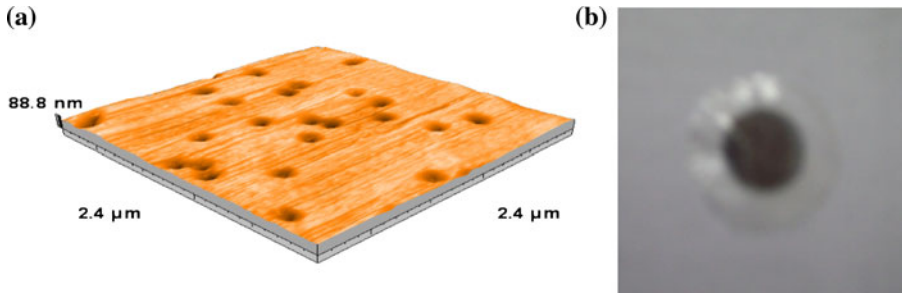

Fig. 2 **a** AFM images of the track-etched PC membrane surface before electrochemical deposition of gold. **b** Gold-deposited PC membrane

randomly distributed on the membrane surface as shown in Fig. 2a. As measured from the AFM image, the pore diameter ranges from 145 to 238 nm and the average diameter of the pore is about 194 nm. The overlapping of boundaries of two or more pores is observed at some places on the surface of the PC membrane. A number of pores in the membrane are not normal to the membrane surface, but instead make an angle with respect to the surface plane (Xia et al. 2003). The electrochemical deposition of gold within the cylindrical pores of the PC membrane was carried out by applying a constant cathodic potential −0.2 V on mercury. At −0.2 V, a hydrogen evolution reaction was not observed at the mercury working electrode. There is a lot of published literature which described the potentiostatic deposition/synthesis of gold nanostructures in the potential range of +0.5 to −0.5 V versus Ag/AgCl/saturated KCl aqueous electrode (Tian et al. 2006; Sakai et al. 2009). On applying the cathodic potential, the gold nanorods started growing almost simultaneously within all the cylindrical pores available in the membrane (as shown in schematic diagram in Figs. 1, 9). The nanorods grew along the direction of the pore axis and completely blocked the cylindrical pores within a very short duration of applying the cathodic potential. This would prevent the transport of water across the membrane. Therefore, there was an almost complete loss of water permeability due to the formation of gold nanorods within the track-etched PC membrane by means of the present method. However, in case of formation of metal nanotubules in the track-etched membranes, the metal electrodeposition occurs preferentially on the pores' wall leading to the pore constriction due to the decrease in the pore radius and reduces the water permeability. If the metal electrodeposition is continued for a longer time, the nanotubules close up to form solid metal nanorods, thus leading to an almost complete loss of water permeability.

Figure 2b shows the photograph of the track-etched PC membrane after electrochemical deposition of gold, and the dark colored circle of 1 cm diameter is the area in the PC membrane where gold was electrodeposited. EDXRF analysis was carried out to confirm the electrochemical deposition of gold in the pores of the PC membrane. The EDXRF spectrum of the potentiostatically deposited gold in the PC membrane (Fig. 3) shows the $L_{\alpha 1}$ and $L_{\beta 1}$ lines of the Au at 9.76 and 11.52 keV, respectively. The crystal structure of the electrochemically deposited gold in the pores of PC was investigated by XRD (Fig. 4). The broad peaks at the scattering angles (2θ) equal to 38.16°, 44.34°, and 64.52° correspond to the 111, 200, and 220 planes, respectively, of the face-centered cubic phase of the Au. The broadened peaks indicate that Au particles deposited in the pores of the PC membrane are nanocrystallites. Figure 5 shows the visible absorbance spectrum of the PC membrane

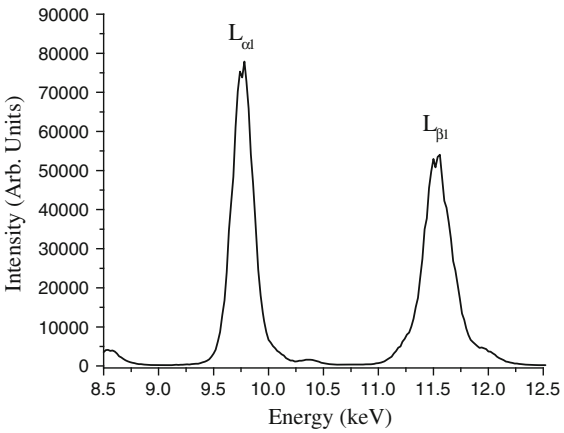

Fig. 3 EDXRF spectrum of Au-deposited PC membrane prepared by electrochemical deposition

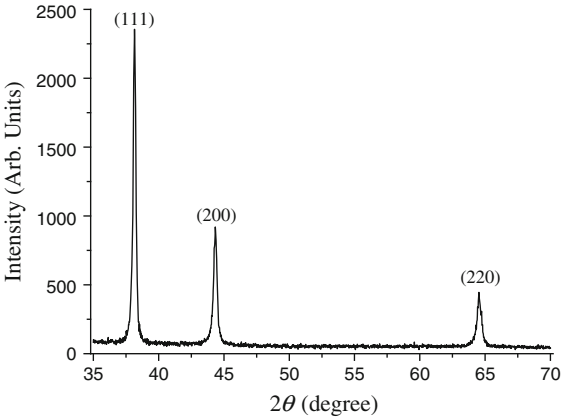

Fig. 4 XRD pattern of Au-deposited PC membrane prepared by electrochemical deposition

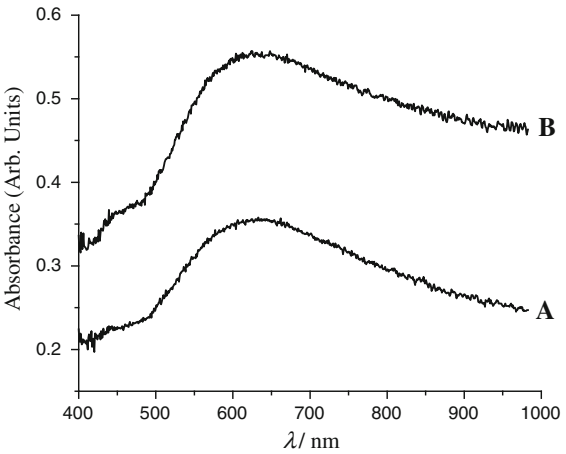

Fig. 5 Visible absorbance spectrum of Au-deposited PC membrane prepared by electrochemical deposition (*A*, t_d = 1,000 s and *B*, t_d = 3,000 s)

after electrochemical deposition of gold in its pores (for both t_d = 1,000 s and t_d = 3,000 s). A single red-shifted very broad peak was observed at around 636 nm. The nanostructured gold particles absorb light in the visible and/or near-infrared region due to the surface plasmon resonance (SPR), and the position of the SPR band(s) depends on particle size, shape, dielectric constant of the local surrounding medium, inter-particle coupling, etc. (Mayer and Hafner 2011; Halas et al. 2011; Eustis and El-Sayed 2006; Ghosh and Pal 2007).

As is evident from TEM images in Fig. 6a, b, the gold is electrodeposited as nanorods in pores of the PC membrane. The nanorods are cigar-shaped and their surface is rough. The physical characteristic (diameter, length, surface roughness, etc.) of the electrodeposited nanorods depends on the physical properties of the template membrane (pore radius, pore length, internal architecture of the pore, etc.) as well as on the parameters used for the electrodeposition (electrodeposition time, electrode potential, etc.). The length of the gold nanorods increases on increasing the electrodeposition time (Fig. 6a, b). Track-etched PC membranes are prepared by bombarding the PC sheets with high energy ions, nuclear particles, etc. The latent tracks produced by these ions are subjected to chemical etching in alkaline solution to enlarge the pore size which can be tuned by controlling the process parameters. The damaged sites in the polymeric chain are more reactive than the undamaged sites in the latent tracks; therefore, the etching and the enlargement of the pores along the length of the latent tracks are non-uniform. This leads to the surface roughness of the pore wall, and the diameter of the circular cross-section is non-uniform along the length of the pore; more often, the pores are cigar-shaped. Therefore, the metal nanorods or nanowires synthesized in such a pore often have a rough surface, which is the replica of the surface roughness of the pore wall. Prior to the development of this newly reported approach, we used to synthesize the nanorods or nanowires of noble metals in track-etched PC membranes by coating one surface of the template membrane using metal film, and we observed a similar rough surface morphology. Therefore, the observed rough surface morphology of gold nanorods in our present work is the replica of surface roughness of the pore wall in the PC membrane. There are reports on modification of the pores' wall by molecular anchors to synthesize the nanorods with a smooth surface (Hernandez et al. 2007). In the TEM experiments, we observed that some of the gold nanorods were branched. The branching of nanorods corroborates the AFM observations that a number of pores are not perpendicular to the surface of the membrane, but make an angle with respect to the surface plane, and the overlapping of two or more pores occurs in the membrane. Figure 6c shows a 2-nm resolution image with a lattice distance of about 0.232 nm, which is close to a lattice distance (d_{hkl}) of (111) plane of face-centered cubic structure of gold. From the SAED pattern (Fig. 6d), the diffraction spots were indexed to (111), (200), and (220) diffraction planes of the face-

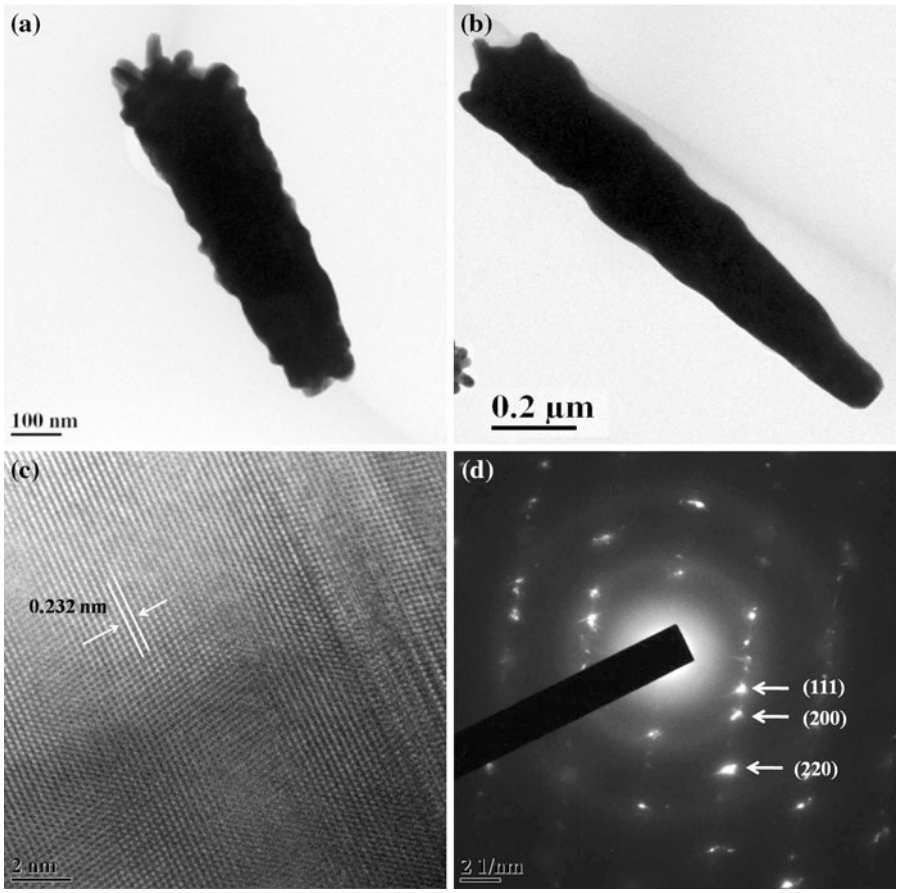

Fig. 6 FEG-TEM images of the gold nanorods after dissolution of the PC membrane **a** $t_d = 1{,}000$ s, **b** $t_d = 3000$ s, **c** 2-nm resolution image showing lattice distances, **d** SAED pattern

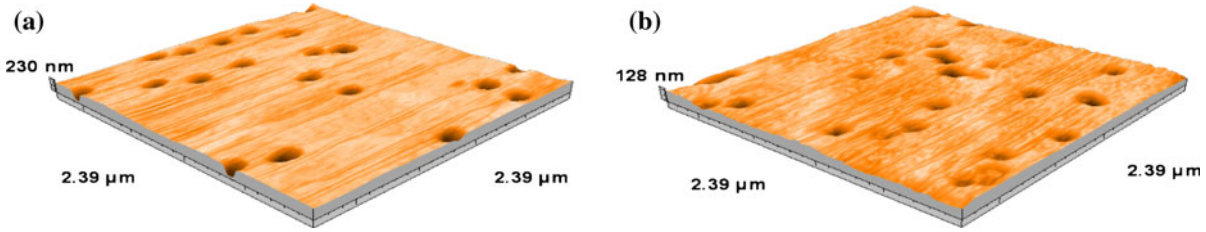

Fig. 7 AFM images of both the surfaces of the track-etched PC membrane after electrochemical deposition of gold ($t_d = 1{,}000$ s). Side 1 (**a**) and side 2 (**b**)

centered cubic structure of gold in agreement with the XRD pattern.

AFM analyses of the surface morphology of the PC membranes were done after the electrochemical deposition of gold in the pores of the PC membranes. Figures 7 and 8 show the surface morphology of both the sides of the track-etched PC membrane after carrying out the electrodeposition of gold for 1,000 s and 3,000 s, respectively. In Fig. 7, the randomly distributed pores are observed on both the sides of the membrane with almost the same number density. As evident from the Fig. 7, the pores in the PC membrane are not completely filled with the gold because the electrodeposition time of 1,000 s might not be sufficient. If the cathodic potential is applied for a longer time, the deposition of gold begins on the surface of the PC membrane once the pores are completely filled. After increasing the electrodeposition time to 3,000 s,

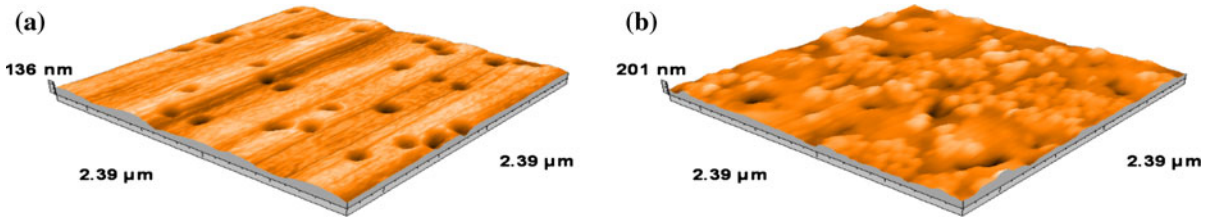

Fig. 8 AFM images of both the surfaces of the track-etched PC membrane after electrochemical deposition of gold (t_d = 3,000 s). Side 1 (**a**) and side 2 (**b**)

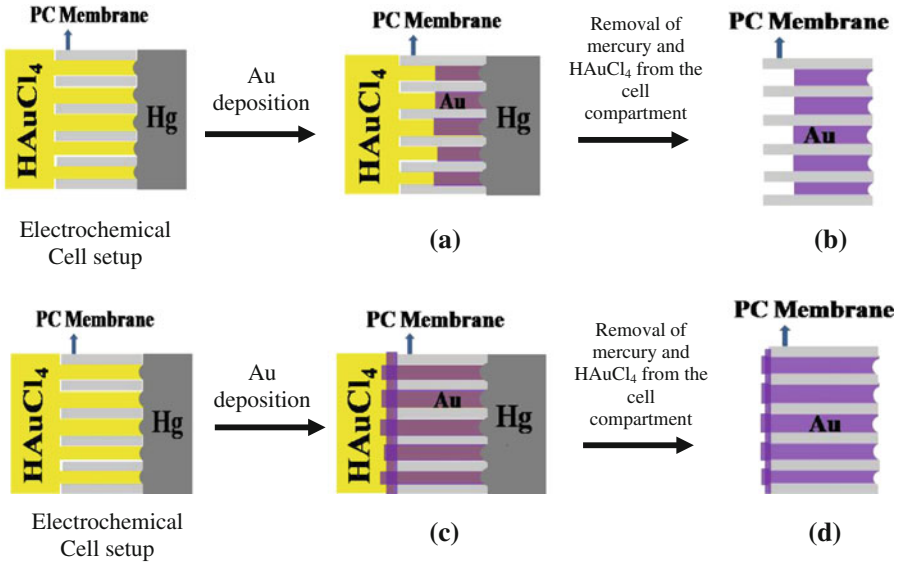

Fig. 9 Schematic of the growth of gold nanorods in the PC membrane using the removable mercury cathode in a two-compartment electrochemical cell for a shorter deposition time, t_d = 1,000 s, (**a**, **b**) and a longer deposition time, t_d = 3,000 s, (**c**, **d**). Gold-deposited membrane after removing the mercury and $HAuCl_4$ from the cell compartments and washing it with deionized water: (**b**, **d**)

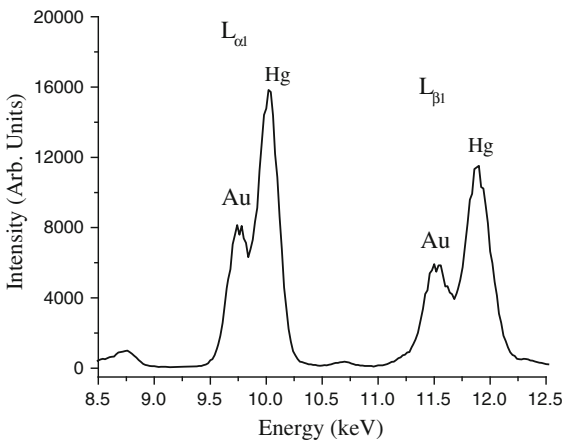

Fig. 10 EDXRF spectrum of Au-deposited PC membrane prepared by galvanic reaction

the surface morphologies of both the sides of the PC membrane were found to be completely different from one another as shown in Fig. 8. The surface morphology of one side, Fig. 8a, is almost similar to those in Figs. 2a and 7. As shown in Fig. 8b, a very small number of pores are visible on the surface of the other side of the PC membrane due to the complete filling of a large number of pores by the gold, and the gold deposits are also observed on the surface. Figure 9 shows a schematic diagram of the growth of gold nanorods in the PC membrane for shorter (a, b) and longer (c, d) deposition times to elucidate the AFM observations in Figs. 7 and 8.

In the absence of applied potential, the galvanic reaction occurs between $AuCl_4^-$ ion and the elemental Hg, leading to the formation of metallic gold,

mercurous chloride, and mercuric chloride as shown in the reactions below.

$$2AuCl_4^- + 6Hg \rightarrow 2Au + 3Hg_2Cl_2 + 2Cl^- \quad (1)$$

$$2AuCl_4^- + 3Hg_2Cl_2 \rightarrow 2Au + 6HgCl_2 + 2Cl^- \quad (2)$$

The EDXRF spectrum of the gold deposited in the PC membrane by the galvanic reaction (Fig. 10) shows the $L_{\alpha 1}$ and $L_{\beta 1}$ lines of Hg at 10.02 and 11.88 keV, respectively, along with the $L_{\alpha 1}$ and $L_{\beta 1}$ lines of Au at 9.76 and 11.52 keV, respectively. There are no lines for Hg in the EDXRF spectrum of the potentiostatically deposited gold nanorods in the PC membrane, thus ruling out the possible contamination of electrodeposited Au nanorods by Hg. These observations lead to a conclusion that the spontaneous galvanic reaction between $HAuCl_4$ and Hg is forbidden on applying the cathodic potential on Hg. The visible absorbance spectrum of the gold deposited in the PC membrane by the galvanic reaction shows two peaks with maxima at 456 and 571 nm. The peak with maxima at 571 nm can be attributed to the SPR of gold nanoparticles.

Conclusion

The gold nanorods were electrochemically synthesized within the pores of the track-etched PC membrane by a simple and cost-effective novel approach based on the use of mercury as a removable cathode. The novelty of this new approach is that it does not require the coating of a metallic layer on one surface of the template membrane by the sputter deposition technique. A malleable track-etched PC membrane with free-standing cigar-shaped gold nanorods in its pore was prepared. The gold-deposited PC membrane with a shorter deposition time has a large number of pores with an open mouth onto the surface of both the sides. The gold-deposited PC membrane with a longer deposition time has a large number of pores with an open mouth on the surface of one side only, and a significant decrease in the number of pores with an open mouth is observed on the surface of the other side. Further studies are in progress to biochemically functionalize the gold nanorods within the incomplete filled pores of the track-etched PC membrane with desired biochemical species to develop sensors based on the detection of analyte by the SERS techniques.

Acknowledgments The authors are thankful to Mr. B. T. Naidu Babu and Mr. L. S. Mombasawala for the FEG-TEM measurement in the Central Facility at SAIF, IIT Bombay. The authors also acknowledge the helpful discussions with Dr. A. K. Pandey, RCD, BARC.

References

Ahmadi TS, Wang ZL, Green TC, Henglein A, El-Sayed MA (1996) Shape-controlled synthesis of colloidal platinum nanoparticles. Science 272:1924–1926

Bale SS, Asuri P, Karajanagi SS, Dordick JS, Kane RS (2007) Protein-directed formation of silver nanoparticles on carbon nanotubes. Adv Mater 19:3167–3170

Berry RS (1998) Size is everything. Nature 393:212–213

Cao Y-WC, Jin R, Mirkin CA (2002) Nanoparticles with Raman spectroscopic fingerprints for DNA and RNA detection. Science 297:1536–1540

Couzin J (2002) Nanoparticles cut tumor's supply lines. Science 296:2314–2315

Elghanian R, Starhoff JJ, Mucic RC, Letsinger RL, Mirkin CA (1997) Selective colorimetric detection of polynucleotides based on the distance-dependent optical properties of gold nanoparticles. Science 277:1078–1081

El-Sayed MA (2004) Small is different: shape-, size- and composition-dependent properties of some colloidal semiconductor nanocrystals. Acc Chem Res 37:326–333

Eustis S, El-Sayed MA (2006) Why gold nanoparticles are more precious than pretty gold: noble metal surface plasmon resonance and its enhancement of the radiative and non-radiative properties of nanocrystals of different shapes. Chem Soc Rev 35:209–217

Ghosh SK, Pal T (2007) Interparticle coupling effect on the surface plasmon resonance of gold nanoparticles: from theory to applications. Chem Rev 107:4797–4862

Halas NJ, Lal S, Chang W-S, Link S, Nordlander P (2011) Plasmons in strongly coupled metallic nanostructures. Chem Rev 111:3913–3961

Hernandez SC, Chaudhuri D, Chen W, Myung NV, Mulchandani A (2007) Single polypyrrole nanowire ammonia gas sensor. Electroanalysis 19:2125–2130

Hodes G (2007) When small is different: some recent advances in concepts and applications of nanoscale phenomena. Adv Mater 19:639–655

Huang MH, Choudrey A, Yang P (2000) Ag nanowire formation within mesoporous silica. Chem Commun 12:1063–1064

Ivanova OS, Zamborini FP (2010) Size-dependent electrochemical oxidation of silver nanoparticles. J Am Chem Soc 132:70–72

Martin CR (1994) Nanomaterials: a membrane-based synthetic approach. Science 266:1961–1966

Mayer KM, Hafner JH (2011) Localized surface plasmon resonance sensors. Chem Rev 111:3828–3857

Nalwa HS (2000) Handbook of nanostructured materials and nanotechnology. Academic Press, New York

Pena DJ, Mbindyo JKN, Carado AJ, Mallouk TE, Keating CD, Razavi B, Mayer TS (2002) Template growth of photoconductive metal–CdSe–metal nanowires. J Phys Chem 106:7458–7462

Reetz MT, Helbig W (1994) Size-selective synthesis of nanostructured transition metal clusters. J Am Chem Soc 116:7401–7402

Ruan C, Luo W, Wang W, Gu B (2007) Surface-enhanced Raman spectroscopy for uranium detection and analysis in environmental samples. Anal Chim Acta 605:80–86

Sakai N, Fujiwara Y, Arai M, Yu K, Tatsuma T (2009) Electrodeposition of gold nanoparticles on ITO: control of morphology and plasmon resonance-based absorption and scattering. J Electroanal Chem 628:7–15

Sanchez-Sanchez CM, Solla-Gullon J, Vidal-Iglesias FJ, Aldaz A, Montiel V, Herrero E (2010) Imaging structure sensitive catalysis on different shape-controlled platinum nanoparticles. J Am Chem Soc 132:5622–5624

Schmidt M, Kusche R, von Issendorff B, Haberland H (1998) Irregular variations in the melting point of size-selected atomic clusters. Nature 393:238–240

Schonenberger C, van der Zande BMI, Fokkink LGJ, Henny M, Schmid C, Kruger M, Bachtold A, Huber R, Birk H, Staufer U (1997) Template synthesis of nanowires in porous polycarbonate membranes: electrochemistry and morphology. J Phys Chem B 101:5497–5505

Sun Y, Xia Y (2002) Shape-controlled synthesis of gold and silver nanoparticles. Science 298:2176–2179

Tian Y, Liu H, Zhao G, Tatsuma T (2006) Shape-controlled electrodeposition of gold nanostructures. J Phys Chem B 110:23478–23481

Xia Y, Yang P, Sun Y, Wu Y, Mayers B, Gates B, Yin Y, Kim F, Yan H (2003) One-dimensional nanostructures: synthesis, characterisation, and applications. Adv Mater 15:353–389

Xiong Y, Xia Y (2007) Shape-controlled synthesis of metal nanostructures: the case of palladium. Adv Mater 19: 3385–3391

Yu-Ying Yu, Ser-Sing Chang, Chien-Liang Lee, Wang CRC (1997) Gold nanorods: electrochemical synthesis and optical properties. J Phys Chem B 101:6661–6664

DOI 10.1007/978-3-319-05041-6_29
Reprinted from the *Journal of Nanoparticle Research*, DOI 10.1007/s11051-013-1709-z

RESEARCH PAPER

Filtration behavior of silver nanoparticle agglomerates and effects of the agglomerate model in data analysis

Jelena Buha · Heinz Fissan · Jing Wang

Received: 18 January 2013 / Accepted: 6 May 2013 / Published online: 20 June 2013

Abstract In many data evaluation procedures for particle measuring devices and in filtration models, spherical particles are assumed. However, significant fractions of aerosol particles are agglomerates of small primary spheres. The morphology of particles in filtration processes may not be known a priori and if the filtration data are processed with wrong assumption, errors can be induced. In this work, we have quantified such errors for the case of open-structured agglomerates. Filtration efficiency tests with polydisperse silver nanoparticle agglomerates and their sintered spheres were performed. After the sintering process, particles with a compact structure with the shape close to a sphere are obtained, which are referred to as sintered spheres in the present study. The testing method involved generation of particulate forms, passing the particles through the testing section, and measurement of the particle number concentrations and size distributions before and after the filter. Measurements of the aerosols upstream and downstream of the filter were conducted using scanning mobility particle sizers (SMPS, TSI Inc.), which covered the rage from 10 to 480 nm. Particles were additionally characterized from the electron microscopic images and the average primary particle size was determined to be 16.8 nm. The number-size distribution curves were obtained and used for penetration calculation. The penetration was dependent on the particle size and morphology. Silver-sintered spheres were captured with a lower efficiency than agglomerates with the same mobility diameter because of the stronger interception effect for agglomerates. Data analysis of the number-size distribution for agglomerates was processed based on sphere assumption and using the model for open-structured agglomerates developed by Lall and Friedlander. The efficiencies based on total concentrations

Special Issue Editors: Mamadou Diallo, Neil Fromer, Myung S. Jhon

This article is part of the Topical Collection on Nanotechnology for Sustainable Development

J. Buha (✉) · J. Wang (✉)
Analytical Chemistry, Empa, 8600 Dübendorf, Switzerland
e-mail: jelena.buha@empa.ch

J. Wang
e-mail: jing.wang@ifu.baug.ethz.ch

J. Buha · J. Wang
Institute of Environmental Engineering, ETH Zurich, 8093 Zurich, Switzerland

H. Fissan
Institute of Energy and Environmental Technology e.V. (IUTA), 47229 Duisburg, Germany

H. Fissan
Center for Nanointegration Duisburg-Essen (CeNIDE), 47057 Duisburg, Germany

of number, surface and volume were affected when the agglomerate model was used. The effect was weakest for the total number efficiency and strongest for the total volume efficiency. Filtration efficiency curves for agglomerates were additionally plotted as a function of the volume equivalent diameter or number of primary particles per agglomerate, because the latter parameters provide more information for the agglomerate structure.

Keywords Nanoparticle agglomerates · Silver · Filtration · TEM · Mobility diameter

Introduction

Many engineered nanoparticles (NP) and natural aerosols exist in the form of NP agglomerates. Accordingly, filtration of NP agglomerates is gaining more attention (Fu et al. 1990; Lange et al. 1999; Kim et al. 2009a, b; Cena et al. 2012). An important group of agglomerates consist of clusters or chains of nanosize spherules with point contacts. They are often produced by high temperature processes leading to a solid particulate. It has been suggested that particle surface area is the most important parameter in terms of NP toxicity (Oberdörster et al. 2005). Silver agglomerates, among the others, are a health concern; they are expected to be more toxic than spherical silver particles with the same mass due to larger surface area. The additional reason for choosing silver agglomerates for this study is the extensive number of reports on their generation and properties and the advantage of easy control over the morphology by adjusting the sintering temperature (Ku and Maynard 2006; Lall et al. 2006; Shin et al. 2009a, b).

There are some reports available quantifying the physical properties of agglomerates. Mobility is a fundamental property that can be readily measured and determines their transport and the kinetics of their growth (Sorensen 2011). While there have been a number of reports of the dynamic shape factor of regular 3-D structures such as ellipsoids, rods, and of multiplets (Kousaka et al. 1996; Song et al. 2005; Zelenyuk and Imre 2007), there have been few studies for larger agglomerates produced by high temperature processes. One of these was the study by Park et al. (2004) to measure the dynamic shape factor of diesel exhaust particles. They used a differential mobility analyzer (DMA) and electron microscopy (EM) to measure the dynamic shape factor, which is finally a function of only the mobility diameter and the volume equivalent sphere diameter. They were able to obtain dynamic shape factor measurements of diesel exhaust particulates with an uncertainty of 10–15 % over a mobility size range from 50 to 220 nm. In some studies, various predictions for the friction coefficient of large agglomerates were tested. In order to get reliable data, the friction coefficient of NP agglomerates as a function of the agglomerate size for agglomerates with primary sphere size in the free molecular regime was examined (Shin et al. 2009b).

So as to analyze agglomerates in detail, initial step is the determination of the primary particle size, which is an important structural parameter for open-structured agglomerates with most primary particles available for interaction with the suspending media and minimal necking among primary particles. It may be determined using electron microscopy, as presented in our study, or quasi-online using the instrument UNPA (Shin et al. 2010; Wang et al. 2010). The second important step is resolving the number of primary particles within the agglomerate. There have been a number of agglomerate studies on the relationship between the mobility radius and the radius of gyration and between the mobility radius and the number of primary particles in agglomerate. These include the studies for in-flame carbonaceous aerosols in the free molecular regime (Cai and Sorensen 1994), or an insightful review of other experimental studies covering a wide range of Knudson number (Wang and Sorensen 1999).

The present work focuses on filtration of agglomerates instead of detailed structural characterization. Particle collection in fibrous filters is a very complex problem in filtration theory, and therefore spherical particles are mainly considered. Nevertheless, real-world particles often have a complicated structure, which influences their deposition behavior. The study by Lange et al. (2000) showed that the concept of equivalent diameters can be used to predict filter penetration for nonspherical particles if relevant diameters have been measured, and if these are inserted into models for spherical particles. In a previous study by Lange et al. (1999), filter penetration was successfully predicted for the regime where diffusion and interception are the dominant deposition mechanisms. The measured penetrations agreed well with the calculations.

Air filtration tests are often performed by challenging the filter with testing aerosols and measuring the aerosol

concentrations upstream and downstream of the filter using a CPC for total efficiency and a SMPS for number distribution as function of mobility diameter. Kim et al. (2009a) measured filtration efficiency for monodisperse silver NP agglomerates in standard fiberglass media. In contrast, we tested polydisperse silver NP agglomerates in nanofiber filters in the present study. Polydisperse aerosols are frequently used since one test can provide the filtration efficiency curve for a wide range of particle sizes (Song and Park 2006; Japuntich et al. 2007). This approach requires accurate measurement of the number-size distribution of the aerosols. If polydisperse NP agglomerates are used as challenging aerosols in filtration experiments, the data evaluation for the measurement could be based on sphere assumptions or open-structured agglomerate assumptions, for example, using a model developed by Lall and Friedlander (2006). This model was validated and justified for open-structured silver agglomerates in the studies reported before (Shin et al. 2009a; Wang et al. 2010). We have examined the filtration data using silver NP agglomerates. The filtration efficiencies based on number, surface area and volume are further on computed with these different assumptions. Penetration of silver agglomerates through fibrous filters was predicted, using a model for spheres and suitable equivalent diameters for the agglomerates. The main results are presented in five folds: (1) Characterization of all silver particulate forms produced. (2) Experimental results using polydisperse aerosols, showing that the penetration of agglomerates was lower than that of sintered spheres with the same mobility diameter. (3) Modeling for filtration of sintered spheres and agglomerates and the comparison to the experimental results. (4) Analyses of the number-size distribution data based on sphere and open-structured agglomerate assumptions; the results show that using the correct structural parameters impacts calculation of the total filtration efficiency. (5) The filtration efficiency of agglomerates considered as function of structure-related parameters, e.g., the volume equivalent diameter and number of primary particles per agglomerate.

Materials, methods, and characterization

Experimental set-up

Silver primary particles were generated by the evaporation and condensation method with silver slugs (Alfa Aesar, 99.99 % metal based) within an electric tube furnace. One silver slug, with the dimensions of 6.35 mm (diameter and length), was placed in a ceramic boat and positioned in the middle of the first tube furnace, where the silver was heated to 1150 °C and further condensation led to silver NP. The particle generation system was stable during our experiments. Particle concentration at the peak and the standard deviation of the size distribution measured with SMPS varied within 20 %. The peak location varied by a few nanometers.

Silver agglomerates were produced by passing primary particles through an agglomeration chamber to increase the residence time needed for coagulation to take place. Nitrogen gas was used as the carrier gas with a flow rate of 1.5 lpm. The general methodology that was employed is similar to the ones reported before (Ku and Maynard 2006; Lall et al. 2006; Shin et al. 2009a, b). Silver NP, collided and attached to each other in the agglomeration chamber leading to NP agglomerates made up of a few up to hundreds primary particles.

Downstream of the agglomeration chamber, the NP agglomerates were sintered in a second tube furnace. The agglomerates were coalesced at 600 °C, which allowed direct comparison of the filtration behavior of the agglomerate to that of a sphere with the same mobility diameter and for the same material.

Schematic diagram of the experimental set-up is shown in Fig. 1. It consisted of an NP agglomerate generator (two electric tube furnaces), an agglomeration chamber (16 l volume capacity), a nanometer aerosol sampler for TEM sampling, a Kr-85 neutralizer, two SMPS systems for size distribution measurements, and a filter penetration measurement system (multiple layers of nanofiber filters and the filter holder). The testing method involved generation of silver particles, passing the particles through the testing section, and measurement of the particle concentrations and size distributions before and after the filter. Size distributions of the primary particles, as well as silver agglomerates and sintered agglomerates upstream and downstream of the test filter, were measured by SMPS systems. Each of the particulate form (primary particles, silver agglomerates, sintered silver spheres) was further on collected for the offline electron microscopy analysis. Face velocity was controlled with the flow meter and kept constant (5 cm/s) throughout all of the experiments.

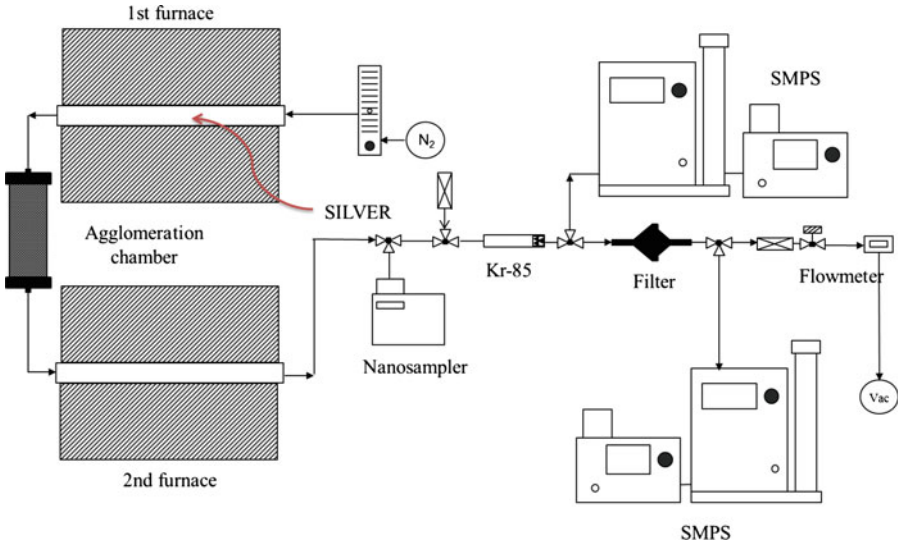

Fig. 1 Schematic of NP agglomerate synthesis and characterization set-up system

Instrumentation

The generated particles were characterized in the aerosol form by particle size distribution measurement and in the collected particle form by transmission electron microscopy (TEM). The particle size distribution was measured by an SMPS consisting of a DMA column (Model 3081, TSI, USA) and a condensation particle counter (CPC) (Model 3775, TSI, USA). The imaging was carried out using TEM (JEM-2200FS, JEOL, Japan). For TEM, the particles were collected on a copper grid covered by an amorphous carbon film with a nanometer aerosol sampler (NAS) (3089, TSI, USA).

Results and discussion

Characterization of silver agglomerates and sintered spheres

After producing silver NP from silver powder using the electric tube furnaces and the agglomeration chamber, SMPS measurements (Figs. 2, 4) and extensive electron microscopy studies were performed (Fig. 3). Size distributions of particles generated in the first furnace and measured at the outlet at room temperature (no agglomeration, no sintering) for three times, which qualitatively demonstrated the temporal stability and reproducibility. Respective SMPS results are presented in Fig. 2a, which give a representation of the primary particle size distribution since they do not adequately agglomerate before the agglomeration chamber. Primary particles were additionally identified from the TEM images of the open-structured silver agglomerates and their sizes were determined. The primary particle size was calculated out of 188 particles incorporated into agglomerates. It was ascertained that the average primary particles of silver agglomerates had an average diameter of 16.8 nm, with a standard deviation of 3.75 nm as shown in Fig. 2b. Primary particles were polydispersed as can be seen on the graph. They were fitted well with a Gaussian distribution function, as shown in the inset. The studies reported before show that the primary particle size of silver agglomerates in diameter was 15 nm in Schmidt-Ott (1988) and 18.5 nm in Lall et al. (2006).

TEM analysis was performed to characterize the primary particles, the agglomerates and the sintered spheres formed after the sintering process in the second furnace. All samples were collected for a short period of time to avoid particle overlapping due to the high concentrations. Figure 3a shows a TEM image of the primary spheres. Figure 3b is showing the open-structured agglomerates, sampled after the agglomeration chamber and the second furnace at room temperature. The image of the compact-structured particles formed by the sintering process at 600 °C is presented in Fig. 3c. This is a representative image out of 20 taken, and we notice a general trend of small particles being attached to the surface.

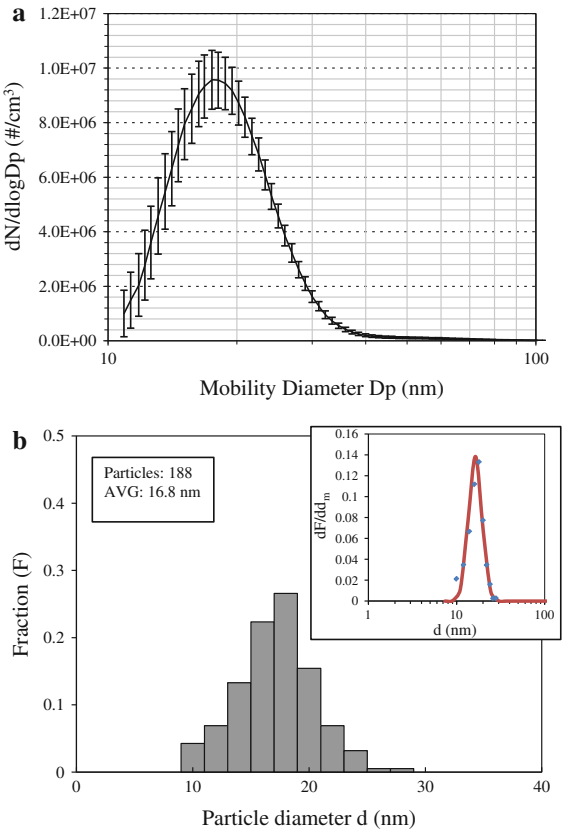

Fig. 2 **a** The size distributions of primary silver nanoparticles, produced after the first electrical tube furnace treatment at 1150 °C (SMPS results); **b** size distribution of the primary particles in open-structured agglomerates and fitted Gaussian distribution as *inset*

The melting temperature of silver is 962 °C which is higher than the temperature used in the sintering furnace. Thus, the sintered spheres are not totally coalesced, instead smaller particles are attached to the surface due to the heterogeneous coagulation. A number of previous studies (Schmidt-Ott 1988; Ku and Maynard 2006; Kim et al. 2009a; Cena et al. 2012) confirmed using SEM or low resolution TEM that the Ag particles sintered at 600 °C had shapes close to spheres. Our TEM analysis also showed the overall particle shape was close to a sphere, but the detailed structure of the small particles at the surface is for the first time reported. The detailed surface structure and the imperfect sphericity of the sintered particles have little effect on the filtration behavior, which is demonstrated by the good agreement between the theoretical model assuming perfect spheres and the experimental results in Sect. 3.3. Similarly, Kim et al. (2009a) and Cena et al. (2012) compared their filtration results using Ag particles sintered at 600 °C with models assuming perfect spheres. Significant size increase of spheres after the sintering process in the second tube furnace (Fig. 3c) is obvious when compared with the initial primary particles shown in Fig. 3a (scale bar is the same for all the images). Most likely, the grain boundary diffusion took place when spheres were formed out of the agglomerated NP during the sintering process. Primary size distribution was estimated from the TEM micrographs of silver agglomerates. During the collection of the silver NP agglomerates, directly after the agglomeration chamber, the sampling time was optimized to be able to distinguish the sizes and morphology of the agglomerates produced. Size of the particles determined from TEM images was in good agreement with the SMPS results obtained for primary particles (Fig. 2a).

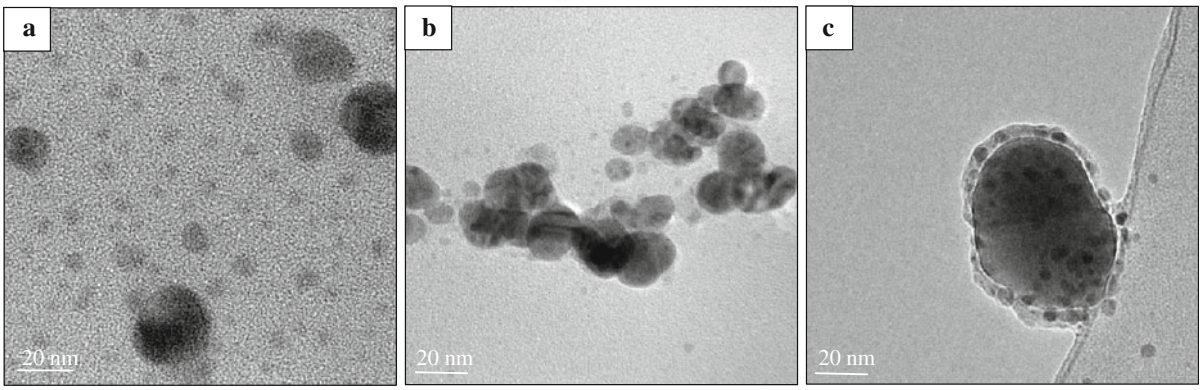

Fig. 3 Examples of TEM images of the silver particles used in the filtration tests: **a** primary silver particles; **b** silver agglomerates produced by the coagulation process; **c** silver-sintered spheres produced by the sintering process

Filtration tests of silver agglomerates and sintered spheres

Tests were performed on nanofiber filters composed of a layer of nanofibers on a substrate made of micrometer fibers. Nanofibers can improve the filtration performance compared to conventional filters in certain applications (Wang et al. 2008a, b). The substrate provides necessary support for the fragile nanofiber layer. Effective nanofiber solidity (α), which represents the solid fraction in the nanofiber layer, as well as the nanofiber efficiency (%) and pressure drop (Pa) were measured and calculated elsewhere (Wang et al. 2008b). We used three layers of the fibrous filter and the face velocity of 5 cm/s for all of the experiments presented.

Size distributions as function of mobility diameter of the silver agglomerates upstream (solid line) and downstream (dashed line) of the test filter were measured by SMPS (Fig. 4). As it can be seen from the diagram, the peak is shifted toward bigger particles in the downstream measurements, which is an indication that the chosen test filter is more effective for the smaller particles sizes at the selected face velocity.

Filtration efficiencies of silver-sintered spheres and agglomerates with the same mobility diameters are further on compared in Fig. 5. The slope and position of the efficiency curve for sintered spheres (Fig. 5) is between the curves for NaCl and agglomerates. The silver spheres have much higher density than NaCl, so the inertial impaction is stronger. The importance of inertial impaction is negligible for small sizes but increases with the size, which qualitatively agrees with the results. It is noticeable that for smaller sizes, up to 70 nm, the morphology of the particles does not play a significant role, whereas for bigger sizes the difference becomes more obvious. Diffusion is dominant and interception and inertial impaction have little effects for small particles, thus the particle density and morphology barely influence the filtration efficiency. As the particle size increases, both interception and inertial impaction come back to the play and the difference in the behavior of spherical particles and agglomerates (Fig. 5) becomes more obvious. This is most likely due to the larger interception length in comparison to spherical particles with the same mobility diameter.

Modeling of filtration efficiency

From the penetration curves presented in Fig. 5, it is obvious that agglomerate particles have lower penetration through filter when compared to spherical particles with the same mobility diameter. The difference in the deposition behavior of agglomerates and sintered spheres is governed by the relationship between the diffusion and interception equivalent diameters for particles with the same density.

Besides the sphere assumption (Fig. 6, dotted line), agglomerate model was used as well (Fig. 6, solid line). We considered diffusion, interception, and inertial impaction to calculate penetration of Ag agglomerates through the nanofiber filter (Wang et al. 2008b, 2011). Since the penetration P is related to the single fiber efficiency E, we chose the following expression for the single fiber efficiency due to the diffusion (Eq. 1),

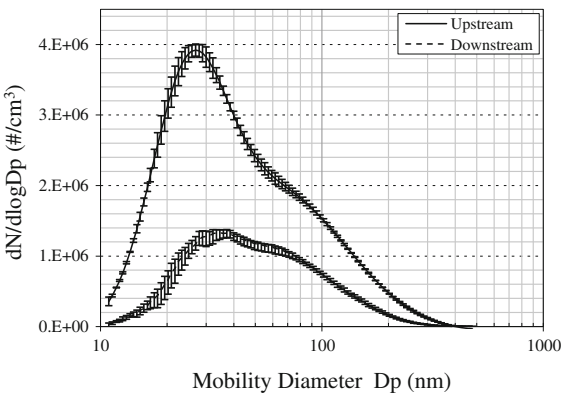

Fig. 4 The size distributions of the silver agglomerates upstream and downstream of the filter

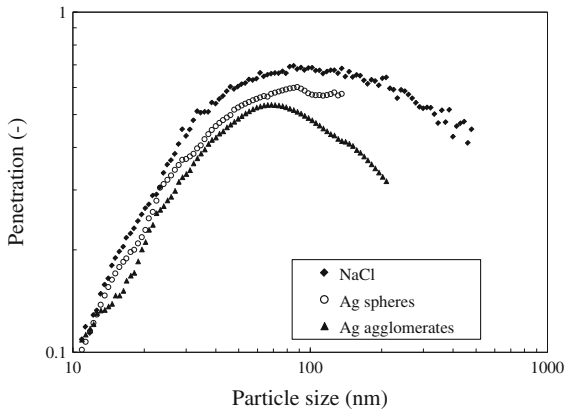

Fig. 5 Penetration curves of polydisperse NaCl, Ag sintered spheres and Ag agglomerates

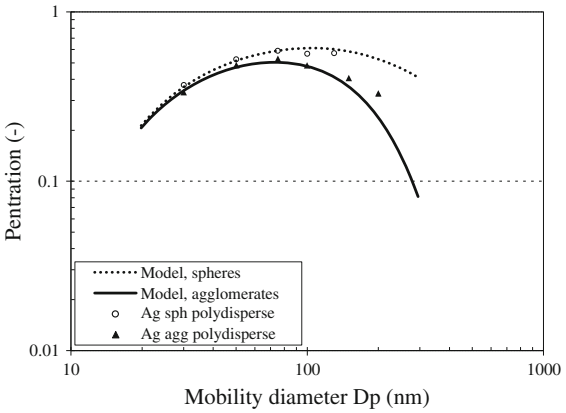

Fig. 6 Penetration curves of polydisperse silver sintered spheres and agglomerates compared with the spheres and agglomerates models, respectively

$$E_{\mathrm{D}} = 2.27 K_{\mathrm{u}}^{-\frac{1}{3}} P_{\mathrm{e}}^{-\frac{2}{3}} (1 + 0.62 K_{\mathrm{n}} P_{\mathrm{e}}^{\frac{1}{3}} K_{\mathrm{u}}^{-\frac{1}{3}}), \tag{1}$$

where $K_{\mathrm{u}} = -\ln\alpha/2 - 3/4 + \alpha - \alpha^2/4$ is the Kuwabara hydrodynamic factor; $P_{\mathrm{e}} = U_{\mathrm{f}} d_{\mathrm{f}}/D$ is the Peclet number with the diffusion coefficient (D), the face velocity of the air incident on the filter (U_{f}) and the fiber diameter (d_{f}); $K_{\mathrm{n}} = 2\lambda/d_{\mathrm{f}}$ is the Knudsen number, λ is the mean free path and α is the nanofiber solidity.

The efficiency due to the interception is as follows

$$E_{\mathrm{R}} = \frac{(1+R)^{-1} - (1+R) + 2(1+1.996K_{\mathrm{n}})(1+R)\ln(1+R)}{2(-0.75 - 0.5\ln\alpha) + 1.996K_{\mathrm{n}}(-0.5 - \ln\alpha)}, \tag{2}$$

For parameter R, the equation shown below was used for agglomerates,

$$R = B d_{\mathrm{m}}^{\gamma}/d_{\mathrm{f}}. \tag{3}$$

where B and γ are the factors for the maximum length calculation as reported by Kim et al. (2009a), (γ is found to be 1.268 and B 0.603 at room temperature), d_m is the mobility diameter.

The efficiencies due to the inertial impaction and interception of particles undergoing diffusion are presented, respectively:

$$E_{\mathrm{I}} = \frac{\mathrm{Stk}^3}{\mathrm{Stk}^3 + 0.77\mathrm{Stk}^2 + 0.22}, \tag{4}$$

$$E_{\mathrm{DR}} = \frac{1.24R^{2/3}}{(K_{\mathrm{u}}P_{\mathrm{e}})^{1/2}}. \tag{5}$$

The Stokes number ($\mathrm{Stk} = \tau U_{\mathrm{f}}/d_{\mathrm{f}}$) is the measure of inertia. $\mathrm{Stk} = \rho d^2 C_{\mathrm{c}} U_{\mathrm{f}}/18\eta d_{\mathrm{f}}$ is the Stokes number for the spherical particles. The relaxation time of the agglomerates is computed based on the mass (m) of the agglomerate reported elsewhere (Kim et al. 2009a). The resulting expression for the Stokes number is given as $\mathrm{Stk} = mC_{\mathrm{c}}U_{\mathrm{f}}/(3\pi\eta d_{\mathrm{m}} d_{\mathrm{f}})$, where η is the viscosity and C_{c} Cunningham slip correction factor.

The total efficiency can further on be computed as

$$E = E_{\mathrm{D}} + E_{\mathrm{R}} + E_{\mathrm{I}} + E_{\mathrm{DR}}, \tag{6}$$

The penetration of the nanofiber layer is presented as follows,

$$P^{\mathrm{N}} = \exp\left(-\frac{4\alpha E t}{\pi d_{\mathrm{f}}(1-\alpha)}\right), \tag{7}$$

where t is the thickness of the nanofiber layer.

To obtain the total penetration for the composite filter, we assume the nanofiber layer and the substrate act independently and in series to capture particles; the penetration through the substrate in the composite filter is the same as that through the bare substrate. Based on these assumptions, we can compute the total penetration as $P = P^{\mathrm{N}} \times P^{\mathrm{S}}$, where P^{N} and P^{S} are the penetrations through the nanofiber layer and the substrate, respectively. We compute the P^{N} from the modeling (Eq. 7) and P^{S} is assumed to give 94 % penetration for 30 nm particles and 99 % for all particles that are bigger than 30 nm (based on the data of Wang et al. 2008a). Out of these results, we can further on obtain P, presented in Fig. 6. For the comparison purpose, only selected sizes of polydisperse Ag sintered spheres and Ag agglomerates were chosen out of Fig. 5.

Analyses of the agglomerate filtration data

The SMPS scan results depend on the assumption of the particle morphology. In order to better understand the influence on the filtration data, we have performed the calculations for the number, surface area, and volume of agglomerates based on sphere assumption and open-structured agglomerate assumption.

The number concentration was corrected due to the different charging efficiencies for spheres and agglomerates. The charging efficiency for agglomerates (η_{agg}) is calculated from Eq. 8 (Wen et al. 1984), where d_{qe} is

the charging equivalent diameter (Eq. 9), e is the elementary charge, T is the temperature, k is the Boltzmann constant, N is the primary particle number, and q is the charge on the particle,

$$\eta_{\text{agg}} = \frac{e}{(\pi d_{\text{qe}} kT)^{1/2}} \exp\left(\frac{-q^2 e^2}{d_{\text{qe}} kT}\right), \tag{8}$$

$$d_{\text{qe}} = \frac{Nd}{\ln(2N)}. \tag{9}$$

The number concentration from SMPS, based on sphere, can further on be corrected taking in consideration respective charging efficiencies, as presented in Eq. 10,

$$n_{\text{agg}} = n_{\text{sph}} \frac{\eta_{\text{sph}}}{\eta_{\text{agg}}}. \tag{10}$$

In addition, for open-structured agglomerates, the surface area may be computed as the sum of surface area of primary particles,

$$A_{\text{agg}} = N(d_{\text{m}}) 4\pi d^2. \tag{11}$$

The number of primary particles according to Lall and Friedlander model is shown in Eq. 12, where c^* is the dimensionless drag force. Thus, the surface area is independent of the primary particle size (Eq. 13),

$$N(d_{\text{m}}) = \frac{12\pi\lambda}{c^* d^2} \frac{d_{\text{m}}}{C_{\text{c}}(d_{\text{m}})}, \tag{12}$$

$$A_{\text{agg}} = N(d_{\text{m}})(\pi d^2) = \frac{12\pi^2\lambda}{c*} \frac{d_{\text{m}}}{C_{\text{c}}(d_{\text{m}})}. \tag{13}$$

The volume of agglomerates may be computed as the sum of volume of primary particles and if the number of primary particles formula is introduced, it shows that it is dependent on the size of the primary particles,

$$V_{\text{agg}} = N(d)\left(\frac{1}{6}\pi d^3\right) = \frac{2\pi^2\lambda}{c*} \frac{d d_{\text{m}}}{C_{\text{c}}(d_{\text{m}})}. \tag{14}$$

The same SMPS scan can lead to significantly different volume distributions depending on the assumption of spheres or agglomerates with certain primary size. If the primary particle size increases, the volume increases. Spheres have significantly larger volumes than the agglomerates with the same mobility size (Fig. 7).

In the calculation for filtration efficiency, the upstream and downstream concentrations can be corrected assuming open-structured agglomerates (Eq. 15). The correction factor cancels out and the

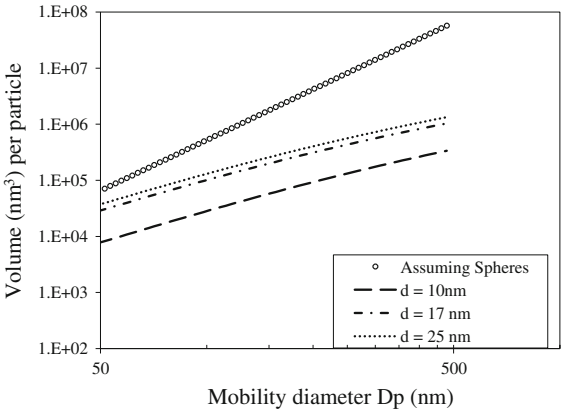

Fig. 7 Volume per particle computed for spheres and for agglomerates for different primary particle size assumption (10, 17, and 25 nm)

filtration efficiency E_{agg} is the same as computed assuming spheres E_{sph}. The filtration efficiency for surface area or volume is the same as for number. At each mobility diameter, the surface area or volume calculation is the same up- and down-stream and cancels out.

$$\begin{aligned} E_{\text{agg}} &= 1 - \frac{\text{downstream } n_{\text{agg}}(d_{\text{m}})}{\text{upstream } n_{\text{agg}}(d_{\text{m}})} \\ &= 1 - \frac{\text{downstream } n_{\text{sph}}(d_{\text{m}}) \frac{\eta_{\text{sph}}}{\eta_{\text{agg}}}}{\text{upstream } n_{\text{sph}}(d_{\text{m}}) \frac{\eta_{\text{sph}}}{\eta_{\text{agg}}}} = E_{\text{sph}}. \end{aligned} \tag{15}$$

However, the agglomerate correction does affect the filtration efficiency based on total concentrations because the correction is size dependent and its contribution to the total concentration cannot be canceled out. The filtration efficiencies based on total concentrations have wide applications, for example, the NIOSH-standard-compliant filter tester (TSI 8130), uses polydisperse NaCl particles and a photometer to measure total up- and down-stream concentrations and to evaluate respirator efficiency; the NP surface area monitor (NSAM) has been used to measure up- and down-stream surface area concentrations to evaluate filters (Stanley et al. 2010).

The results regarding the efficiencies based on total concentrations of number, surface area and volume, and the effects by the agglomerate correction are presented in Table 1. If agglomerates with $d = 17$ nm give the right filtration efficiency (microscopic study gave the average primary particle size of 16.8 nm), the error using the raw SMPS results (spheres) is $\sim$2 % for the number, 3 % for surface area, and 7 % for the volume

Table 1 Filtration efficiencies computed based on total concentrations of number, surface area and volume

Filtration efficiency	Spheres	Agg with $d = 10$ (nm)	Agg with $d = 17$ (nm)	Agg with $d = 25$ (nm)
Total number concentration	0.6373	0.6318	0.6143	0.5905
Total surface area concentration	0.6118	0.5924	0.5879	0.5831
Total volume concentration	0.5485	0.5924	0.5879	0.5831

Spheres and open-structured agglomerate assumption with different primary particle sizes used

(graphs not shown here). The results using $d = 10$, 17, and 25 nm are very close, which indicates that the value of the primary particle size is not critical for open-structured agglomerates in the calculation of total efficiency. The total efficiency is affected by the agglomerate correction. The effect is weakest for the total number efficiency, and strongest for the total volume efficiency.

We applied multiple charge correction based on sphere assumption to the size distributions of sintered spheres before and after the filter, then the penetrations with and without the multiple charge correction were compared. The maximum difference between the penetrations at each mid-point of the size channel was less than 1.8 %; the difference between the total number penetrations was 0.26 %. Thus, the effect of multiple charged fractions is negligible for silver-sintered spheres. The multiple charge fractions for agglomerates are different than spheres, however, they are in the same range (Wen et al. 1984). Thus, we expect the multiple charge fractions have insignificant effect on the penetration calculation.

Filtration efficiency of agglomerates as functions of structure-related parameters

Our results indicate that the agglomerate structure can affect calculation of the filtration efficiency. The primary particle size is an important structural parameter for open-structured agglomerates. The number-size distribution curve changes with the primary particle size. Since the electrical mobility diameter, as an equivalent diameter, does not describe the morphology of the agglomerate, filtration efficiency for NP agglomerates was additionally plotted as a function of volume equivalent diameter. The penetration results for both silver-sintered spheres and agglomerates are plotted in Fig. 8a. Three curves are presented; the first one using the volume equivalent diameter computed from the open-structured agglomerate model (dashed line), where the primary particle size is assumed to be 17 nm; the second one using the volume equivalent diameter from the sphere assumption (solid line); the third one showing the experimental results for the sintered spheres (dotted line). The electrical mobility diameter and the volume equivalent diameter are the same for spheres. Thus, the curve for sintered spheres in Fig. 8a, is the same as that in Fig. 5. This approach is to illustrate how much the curve is shifted depending on the assumption of the particle morphology. Since the volume equivalent diameter is smaller than the electrical mobility diameter for agglomerates, the curve is shifted to the left. Comparison between the curves for the sintered spheres and agglomerates reveals that for a fixed volume equivalent diameter less than about 40 nm, spheres have smaller mobility diameter, higher diffusivity, therefore lower penetration; for a fixed volume equivalent diameter larger than about 75 nm, agglomerates have larger interception length, therefore lower penetration.

The filtration efficiency is additionally plotted vs. the number of primary particles per agglomerate (Fig. 8b). Since the primary particle size may not be known, three different sizes for primary particle diameter d (10, 17 and 25 nm) are used. The curve corresponding to 17 nm represents the correct one. If the primary particle size increases, the number per agglomerate decreases, causing the curve to shift to the left. The choice of the primary particle size has significant effect on the curve.

Primary particle size is essential in data analysis and this information can be provided in different ways. We have chosen to analyze the TEM images and compare it to the SMPS results. Finally ascertained value is further on implemented in the models for the sphere and open-structured agglomerate assumption.

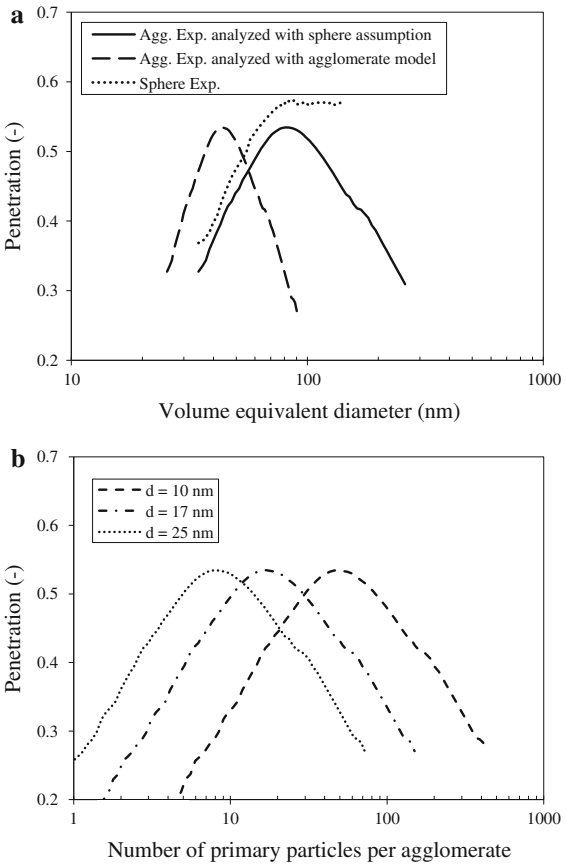

Fig. 8 **a** Computed filtration penetration curves based on sphere assumption or agglomerate model with 17 nm particle size and the sphere experiment curve when compared to the volume equivalent diameter; **b** filtration penetration curves for different primary size particles assumption when compared to the number of primary particles per agglomerate

Conclusions

Our study shows that agglomerate particles have lower penetration through filter when compared to spherical particles with the same mobility diameter. For smaller particles, diffusion dominates, sintered spheres, and agglomerates have similar filtration. For bigger sizes, interception becomes important; agglomerates have extended branches, therefore lower penetration. By sintering the agglomerates to a spherical shape, we were able to obtain a direct comparison of nanoparticle agglomerate filtration to compact structure nanoparticles of the same material. When the particle morphology is not known a priori, the filtration data may be processed with different assumptions. The curve of filtration efficiency versus mobility size is not affected by the assumption on particle morphology. However, the efficiency based on total concentrations is affected by the agglomerate correction. The effect is the weakest for the total number efficiency, and the strongest for the total volume efficiency. The filtration efficiency of open-structured agglomerates as a function of geometric parameters, such as volume per agglomerate, can only be characterized with information of the primary particle size. Primary particle size was ascertained with both SMPS and TEM. Such filtration efficiency data provide insight for the effect of particle structure on filtration.

Acknowledgments Financial support by the European Committee for Standardization in the frame of mandate M/461 "Standardization activities regarding nanotechnologies and nanomaterials" is acknowledged. The authors also thank the support of members of the Center for Filtration Research: 3M, Boeing Commercial Airplanes, Cummins Filtration, Donaldson Co., Inc., Entegris, Inc., Hollingsworth & Vose Co., MANN + HUMMEL, GMBH, MSP Corp., Samsung Electronics Co., Ltd, Shigematsu Works Co., Ltd, TSI Inc., and W. L. Gore & Associates, Inc. and affiliate member NIOSH.

References

Cai J, Sorensen CM (1994) Diffusion of fractal aggregates in the free molecular regime. Phys Rev E 50(5):3397–3400

Cena LG, Ku BK, Peters TM (2012) Particle collection efficiency for nylon mesh screens. Aerosol Sci Technol 46(2):214–221. doi:10.1080/02786826.2011.617401

Fu T-H, Cheng M-T, Shaw DT (1990) Filtration of chain aggregate aerosols by model screen filter. Aerosol Sci Technol 13(2):151–161. doi:10.1080/02786829008959433

Japuntich DA, Franklin LM, Pui DY, Kuehn TH, Kim S, Viner AS (2007) A comparison of two nano-sized particle air filtration tests in the diameter range of 10 to 400 nanometers. J Nanopart Res 9:93–107. doi:10.1007/978-1-4020-5859-2_10

Kim SC, Wang J, Emery MS, Shin WG, Mulholland GW, Pui DYH (2009a) Structural property effect of nanoparticle agglomerates on particle penetration through fibrous filter. Aerosol Sci Technol 43(4):344–355. doi:10.1080/02786820802653763

Kim SC, Wang J, Shin WG, Scheckman JH, Pui DYH (2009b) Structural properties and filter loading characteristics of soot agglomerates. Aerosol Sci Technol 43(10):1033–1041. doi:10.1080/02786820903131081

Kousaka Y, Endo Y, Ichitsubo H, Alonso M (1996) Orientation-specific dynamic shape factors for doublets and triplets of spheres in the transition regime. Aerosol Sci Technol 24(1):36–44

Ku BK, Maynard AD (2006) Generation and investigation of airborne silver nanoparticles with specific size and morphology by homogeneous nucleation, coagulation and sintering. J Aerosol Sci 37(4):452–470. doi:10.1016/j.jaerosci.2005.05.003

Lall AA, Friedlander SK (2006) On-line measurement of ultrafine aggregate surface area and volume distributions by electrical mobility analysis: I. Theoretical analysis. J Aerosol Sci 37(3):260–271. doi:10.1016/j.jaerosci.2005.05.021

Lall AA, Seipenbusch M, Rong W, Friedlander SK (2006) On-line measurement of ultrafine aggregate surface area and volume distributions by electrical mobility analysis: II. comparison of measurements and theory. J Aerosol Sci 37(3):272–282. doi:10.1016/j.jaerosci.2006.01.006

Lange R, Fissan H, Schmidt-Ott A (1999) Predicting the collection efficiency of agglomerates in fibrous filters. Part Part Syst Charact 16(2):60–65. doi:10.1002/(sici)1521-4117(199906)16:2<60:aid-ppsc60>3.0.co;2-a

Lange R, Fissan H, Schmidt-Ott A (2000) A new method for the determination of the interception equivalent diameter. J Aerosol Sci 31(2):221–231. doi:10.1016/s0021-8502(99)00050-6

Oberdörster G, Oberdörster E, Oberdörster J (2005) Nanotoxicology: an emerging discipline evolving from studies of ultrafine particles. Environ Health Perspect 113(7):823–839. doi:10.1289/ehp.7339

Park K, Kittelson DB, McMurry PH (2004) Structural properties of diesel exhaust particles measured by transmission electron microscopy (TEM): relationships to particle mass and mobility. Aerosol Sci Technol 38(9):881–889. doi:10.1080/027868290505189

Schmidt-Ott A (1988) New approaches to in situ characterization of ultrafine agglomerates. J Aerosol Sci 19(5):553–563. doi:10.1016/0021-8502(88)90207-8

Shin W, Wang J, Mertler M, Sachweh B, Fissan H, Pui D (2009a) Structural properties of silver nanoparticle agglomerates based on transmission electron microscopy: relationship to particle mobility analysis. J Nanopart Res 11(1):163–173. doi:10.1007/s11051-008-9468-y

Shin WG, Mulholland GW, Kim SC, Wang J, Emery MS, Pui DYH (2009b) Friction coefficient and mass of silver agglomerates in the transition regime. J Aerosol Sci 40(7):573–587. doi:10.1016/j.jaerosci.2009.02.006

Shin WG, Wang J, Mertler M, Sachweh B, Fissan H, Pui DYH (2010) The effect of particle morphology on unipolar diffusion charging of nanoparticle agglomerates in the transition regime. J Aerosol Sci 41(11):975–986. doi:10.1016/j.jaerosci.2010.07.004

Song CB, Park HS (2006) Analytic solutions for filtration of polydisperse aerosols in fibrous filter. Powder Technol 170(2):64–70. doi:10.1016/j.powtec.2006.08.011

Song DK, Lenggoro IW, Hayashi Y, Okuyama K, Kim SS (2005) Changes in the shape and mobility of colloidal gold nanorods with electrospray and differential mobility analyzer methods. Langmuir 21(23):10375–10382. doi:10.1021/la0513196

Sorensen CM (2011) The mobility of fractal aggregates: a review. Aerosol Sci Technol 45(7):765–779. doi:10.1080/02786826.2011.560909

Stanley N, Qi C, Pui DYH (2010) a new method of filter efficiency evaluation using the nanoparticle surface area monitor (NSAM) for a nanoparticle health relevant filter efficiency measure. Filtration 10(1):40–46

Wang GM, Sorensen CM (1999) Diffusive mobility of fractal aggregates over the entire knudsen number range. Phys Rev E 60(3):3036–3044

Wang J, Kim SC, Pui DYH (2008a) Figure of merit of composite filters with micrometer and nanometer fibers. Aerosol Sci Technol 42(9):722–728. doi:10.1080/02786820802249133

Wang J, Kim SC, Pui DYH (2008b) Investigation of the figure of merit for filters with a single nanofiber layer on a substrate. J Aerosol Sci 39(4):323–334. doi:10.1016/j.jaerosci.2007.12.003

Wang J, Shin WG, Mertler M, Sachweh B, Fissan H, Pui DYH (2010) Measurement of nanoparticle agglomerates by combined measurement of electrical mobility and unipolar charging properties. Aerosol Sci Technol 44(2):97–108. doi:10.1080/02786820903401427

Wang J, Kim SC, Pui DYH (2011) Carbon nanotube penetration through a screen filter: numerical modeling and comparison with experiments. Aerosol Sci Technol 45(3):443–452. doi:10.1080/02786826.2010.541531

Wen HY, Reischl GP, Kasper G (1984) Bipolar diffusion charging of fibrous aerosol particles—I. Charging theory. J Aerosol Sci 15(2):89–101. doi:10.1016/0021-8502(84)90029-6

Zelenyuk A, Imre D (2007) On the effect of particle alignment in the DMA. Aerosol Sci Technol 41(2):112–124. doi:10.1080/02786820601118380

DOI 10.1007/978-3-319-05041-6_30
Reprinted from the *Journal of Nanoparticle Research*, DOI 10.1007/s11051-012-1093-0

PERSPECTIVES

Nanotechnology for sustainability: what does nanotechnology offer to address complex sustainability problems?

Arnim Wiek · Rider W. Foley · David H. Guston

Received: 31 May 2012 / Accepted: 23 July 2012 / Published online: 21 August 2012

Abstract Nanotechnology is widely associated with the promise of positively contributing to sustainability. However, this view often focuses on end-of-pipe applications, for instance, for water purification or energy efficiency, and relies on a narrow concept of sustainability. Approaching sustainability problems and solution options from a comprehensive and systemic perspective instead may yield quite different conclusions about the contribution of nanotechnology to sustainability. This study conceptualizes sustainability problems as complex constellations with several potential intervention points and amenable to different solution options. The study presents results from interdisciplinary workshops and literature reviews that appraise the contribution of the selected nanotechnologies to mitigate such problems. The study focuses exemplarily on the urban context to make the appraisals tangible and relevant. The solution potential of nanotechnology is explored not only for well-known urban sustainability problems such as water contamination and energy use but also for less obvious ones such as childhood obesity. Results indicate not only potentials but also limitations of nanotechnology's contribution to sustainability and can inform anticipatory governance of nanotechnology in general, and in the urban context in particular.

Keywords Nanotechnology · Sustainability · Complex problems · Problem solving · Intervention research · Anticipatory governance

Special Issue Editors: Mamadou Diallo, Neil Fromer, Myung S. Jhon

This article is part of the Topical Collection on Nanotechnology for Sustainable Development

A. Wiek · R. W. Foley
School of Sustainability, Arizona State University, Tempe, AZ 85287-5502, USA

A. Wiek (✉) · R. W. Foley · D. H. Guston
Center for Nanotechnology in Society, Consortium for Science, Policy & Outcomes, Arizona State University, Tempe, AZ 85287, USA
e-mail: arnim.wiek@asu.edu

Introduction

Nanotechnology is often touted as an important contributor to sustainability. Nobel laureate Smalley (2006) spoke highly of nanotechnology's potential to cope with global challenges such as energy production for a growing world population. Karn (2005) states similarly high hopes that "nanotechnology can help with all these sustainability […] issues," including climate change, resource depletion, population growth, urbanization, social disintegration, and income inequality. Diallo et al. (2011) acknowledge that "global sustainability challenges facing the world are complex and involve multiple interdependent areas," but assert that nanotechnology is capable of mitigating many of those. Weiss and Lewis (2010)

reflect sentiments of the American Chemical Society in recognizing the "significant contributions that nanoscience is making toward sustainability." In light of these statements, it seems fair to conclude that Smith and Granqvist (2011) summarize a widely held position when stating: "Solutions to the urgent challenges of environment degradation, resource depletion, growth in population, and cities, and in energy use, will rely heavily on nanoscience." Even when the complexity of sustainability challenges is enumerated and the socially embedded nature of technology is acknowledged, nanotechnological optimism and even determinism prevail.

Such claims *seem* to align with the concept of sustainability science, an emerging field that is problem-focused and solution-oriented toward the long-term vitality and integrity of human societies (Kates et al. 2001; Clark and Dickson 2003; Komiyama and Takeuchi 2006; Jerneck et al. 2011; Wiek et al. 2012a). Over the last decade, sustainability science has laid theoretic and methodological foundations to comprehensively address "wicked" sustainability problems in light of systemic failures (Ravetz 2006; Seager et al. 2012; Wiek et al. 2012a). However, the claims and related studies above generally fail to acknowledge that sustainability problems are neither simple nor merely complicated, but are rather truly complex in structure—and thus require a complex approach to resolution. Such an oversight has multiple origins. First, analysts sometimes confuse sustainability problems with such natural resource problems as energy supply or water contamination, thus neglecting such numerous *non*-biophysical challenges as epidemics, violent conflicts, or economic exploitation that equally threaten human societies and are often fundamental to or accompany natural resource problems (Jerneck et al. 2011; Wiek et al. 2012a). Second, there is a lack of consideration given to the root causes of sustainability problems. For example, by means of nanotechnology to remediate water contamination is a typical "end-of-pipe" solution, which, while necessary, is doing nothing to stop the proliferation of Superfund sites that are often concentrated in low-income and minority communities (Lerner 2010). Third, nanotechnological solutions are often proposed as technological fixes without seriously considering alternatives. Yet, case studies demonstrate that other, non-technical solutions might be more effective and efficient (Sarewitz and Nelson 2008). Fourth, potentially negative side effects of these nanotechnologies are seldom considered. This is a particularly critical issue when addressing wicked problems, which often stem from previous solutions (Seager et al. 2012). Fifth, these studies suggest *real* progress although they usually focus on *potential* innovations to address the problem. Hypothesized impacts bias the perception of nanotechnology's real contribution to sustainability and draw attention away from urgent sustainability problems that nanotechnology might not be capable of mitigating or away from better positioned mitigation strategies. With the promise of substantial economic gains and increased sustainability-related awareness of consumers, a sixth origin could be the use of sustainability claims as pure marketing strategy similar to "greenwashing" campaigns (Jones 2007).

Sustainability problems are not just any kind of problem, but feature specific characteristics (Wiek et al. 2012a). They threaten the viability and integrity of societies or groups; they are urgent, requiring immediate attention for decisions to avoid irreversibility; they have projected long-term future impacts that necessitate consideration of future generations; they are place-based, which means causes and impacts can be observed within distinct localized area; they exhibit complexity at spatial levels (reaching from local to global levels) and cut across multiple sectors (social, economic, environmental); and they are often contested. Thus, complex sustainability problems are unlikely to be solved in the simple sense that a hammer can solve the problem of a nail sticking out—even considering the sophistication of hypothesized nanotechnologies. Instead, we use the language of *mitigation* to refer to interventions intended to ameliorate complex sustainability problem.

In light of these potential pitfalls, the study presented here conceptualizes sustainability problems as complex constellations (networked cause-effect chains) that present potential intervention points, amenable to different types of solution options. The study relies on interdisciplinary workshops and literature reviews to appraise specific contributions of nanotechnology to mitigating sustainability problems with four questions in mind:

1. Are *all* sustainability problems amenable to nanotechnological fixes? Which ones are and which ones are *not*?

2. How and where does nanotechnology intervene in such problem constellations?
3. Are nanotechnological solutions more effective and efficient than alternative mitigation options? Are there any potentially negative side effects associated with nanotechnological fixes (as experienced with other technological solutions)?
4. What is the evidence that the *potential* of nanotechnology for mitigating sustainability problems is being realized through actual implementation?

The study focuses on nanotechnologies designed to contribute to sustainability efforts, including applications for increasing the efficiency of solar panels, water purification, air purification, environmental remediation, etc. It is important, however, to recognize that these "green" uses represent <10 % of nanotechnology applications currently patented (Lobo and Strumsky 2011).

There is ample room here to select exemplary cases of historic claim making and subsequently create a hypothetical space to explore the nanotechnology claims as rhetoric bent on exhibiting nanotechnology's potential. Rather than taking that road, this study addresses the outlined questions in a specific context, namely, the *urban* context, within which we analyze the sustainability claims (cf. Jones 2007). Urban locales, containing more than 50 % of the world's population, are confronted with urgent sustainability challenges, and cities have started to take action on these challenges independently (Svara 2011). Cities are also the key hubs of innovation, as well as decision-making centers for larger regions, states, and nations. Their infrastructure, culture, and technological developments—embodied in a dynamic set of resources, institutions, and actions—represent society's general development path.

Phoenix, recently granted the disreputable distinction of being the world's least sustainable city (Ross 2011), is an excellent case for intervention research on urban sustainability problems. The commitment to a sustainable future and a strong partnership between researchers, city planners, and citizens has been developing since 2009, resulting in a sustainability-oriented draft General Plan with several accompanying and followup projects (Wiek et al. 2010; Wiek and Kay 2011). We build on these endeavors when exploring nanotechnology's potential in more detail for three exemplary urban sustainability problems prevalent in Phoenix: two obvious ones, *water contamination* and *non-renewable energy supply*, are presented along side one urban sustainability problem less obviously addressed (but claimed to) by technological solutions, *childhood obesity*. The selected issues receive considerable attention in scientific and political communities as recently summarized by Roco et al. (2011): "Global conditions that might be addressed by mass use of nanotechnology include […] constraints on using common resources such as water, food, and energy."

Our ultimate goal is to perform research that embeds nanotechnology in a suite of potential solutions to urban sustainability challenges that warrant consideration and assessment by experts and stakeholders. In doing so, the study contributes to anticipatory governance of emerging technologies in general, and nanotechnology in particular, through the lenses of urban systems and sustainability science (Barben et al. 2008; Guston 2008; Karinen and Guston 2010; Wiek et al. 2012b; Wiek et al. in press).

Research design

In this study, we conceptualize nanotechnology as the supply-side (technological solution options) to sustainability problems as the demand-side (societal needs). This supply–demand model follows Sarewitz and Pielke's (2007) proposed framework to assess a given technology (supply) with respect to a given societal need (demand) through an economics metaphor. The goal is to identify the overlap between demand and supply, or in other words, *reconcile* to what extent demand for solutions to sustainability problems and supply of nanotechnology match (Sarewitz and Nelson 2008), and thus to what extent we might reasonably expect nanotechnology that is currently being produced to contribute to their mitigation. Existing and proposed nanotechnologies have the potential to address a spectrum of challenges, but defining the overlap between demand and supply means identifying how nanotechnology "solves" specific problems with what impacts (intended and unintended), and whether or not other, more effective, efficient, or equitable alternatives exist (Wiek et al. in press).

To investigate specific intersections, we adopt basic ideas of intervention research methodology

(Fraser et al. 2009), namely to evaluate the effectiveness of strategies for positive change (improvements of social conditions). Accordingly, each nanotechnology application is considered a unique intervention into a complex problem constellation. We apply this methodology to appraise the effectiveness of exemplary nanotechnologies to mitigate urban sustainability problems. Previous technological interventions in complex socio-technical systems, such as cities, have not always led to the desired outcomes, and so it is also important to account for unintended consequences in the appraisal (Wiek et al. in press).

We conducted this study in three phases by means of a case study approach that relied on a set of mixed methods. The first phase began with *initial literature reviews* on urban sustainability challenges (demand) and nanotechnology applications (supply). We then conducted two *expert workshops* to deepen the supply–demand knowledge base through an exploration of urban challenges in metropolitan Phoenix (see case study details in the following section). One workshop was conducted with an interdisciplinary group of scholars ($n = 13$) from geography, urban planning, social sciences, civil engineering, and sustainability science with expertise in urban systems, transportation, energy systems, climate change, justice, poverty, and resilience. Participants generated a ranked list of sustainability problems and outlined for each of the ten highest ranked problems the problem constellation of root causes (drivers), causing activities, perceived benefits, negative impacts, and affected populations. The other workshop was conducted with an interdisciplinary group of scholars ($n = 9$) from physics, chemistry, electrical engineering, materials science, and energy systems engineering. The workshop validated and augmented materials gathered through the nanotechnology literature review. The participants ranked the nanotechnology solutions that would most likely contribute to urban sustainability.

The second phase of the research consisted of *in-depth literature reviews* to substantiate the nanotechnology applications and urban sustainability problems elicited in the expert workshops. One was a review of literature, documents, and datasets that provide evidence of specific urban sustainability problems in metropolitan Phoenix. The final literature review was a reconciliatory analysis of the amenability of technological solutions to sustainability problems. Specific quantitative evidence, estimations, and data were explored that apply to both the potential benefits and life cycle costs of selected nanotechnologies.

The third and final phase of the research was a set of three *walking audits* and reflections with a group of nanotechnology researchers (engineers and social scientists) and community members ($n = 20$) in the case study area (see description below). The walking audits explored the intersection of nanotechnologies and urban sustainability problems, focusing on water contamination, energy systems, and the food-health nexus. Participants discussed the prospect, possibility, and impact of nanotechnology interventions at specific places where those urban sustainability problems manifest.

In summary, we employed a case study approach (focusing on exemplary sustainability problems in a neighborhood in Phoenix) and gathered relevant data from literature and document reviews, as well as expert workshops and walking audits through participatory research. The results integrate evidence from published studies and official documents with insights from community and subject matter experts.

Case study—the Gateway Corridor Community in Phoenix, Arizona

In order to make the research more tangible, accessible, and relevant to stakeholders and decision-makers, we conducted a case study following the paradigm of place-based sustainability research (Wiek et al. in press). Based on a previous study (Wiek and Kay 2011), we selected the Gateway Corridor Community in metropolitan Phoenix for this study (see Fig. 1). The community name is not an official title but reflects the transportation and infrastructure corridor (coupled light rail, airport, automobile, and canal) with the Gateway Community College as central hub. The community is bounded to the north and east by state highways 202 and 143, to the south by Sky Harbor International Airport and to the west by 24th Street. The area is bisected from northwest to southeast by the Grand Canal with the only canal crossings at Van Buren Ave and Washington Ave. The community comprises industrial, commercial, educational, cultural, and residential areas. Recent socio-demographic data indicate that, of the 5,096 residents, 66 % are Hispanic or Latino (USCB 2010a). The American Community Survey (ACS) identifies that 43 % of the

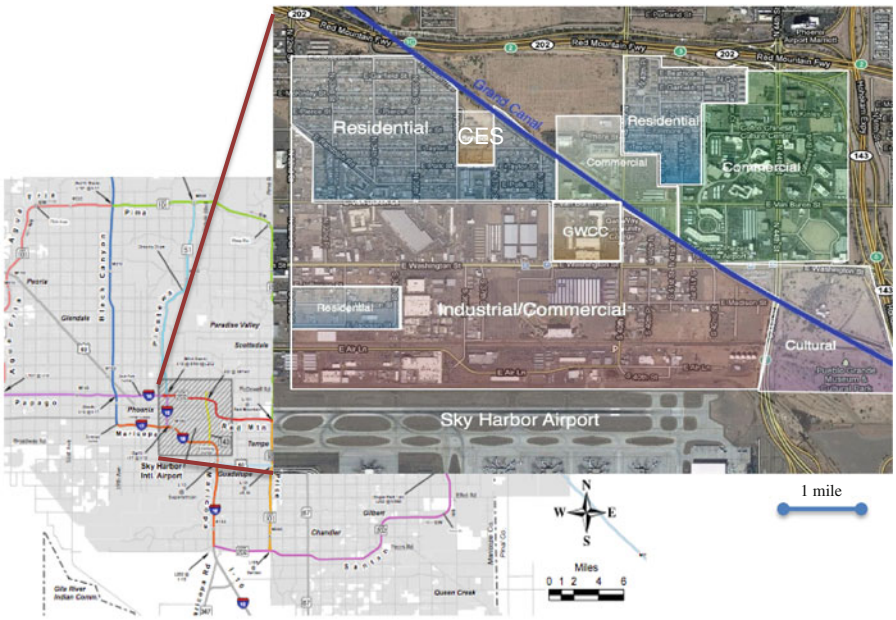

Fig. 1 Gateway Community Corridor in metropolitan Phoenix. *GWCC* Gateway Community College, *CES* Crockett Elementary School. *Note* The zoning demarcations are based on fieldwork and do not necessarily match published city records

population earns below established poverty levels, median household income is $33,392, and one-third of residents (33 %) do not have high school diplomas or equivalencies (USCB 2010b). These data provide a limited snapshot of the community; yet, they indicate significant needs and barriers to sustainable community development.

The selection of the Gateway Corridor was based on two factors: the diverse set of urban sustainability problems and the engagement in numerous intervention activities by university, city, and civic entities. The Gateway Corridor Community exhibits many of the sustainability challenges identified by the expert workshop, including: minimal economic opportunities for residents, reflected in underinvestment in building stock and deteriorating industrial base; a lack of amenities accessible by walking or cycling; urban heat island effects due to lack of vegetation cover and choice of construction materials; social isolation between the diverse (ethnic) sub-communities in the area; and historic groundwater contamination from industrial production. In response to these challenges, several synergistic efforts are underway in the area, including transit-oriented development along the new light rail route through the "Reinvent Phoenix" project funded by the U.S. Department of Housing and Urban Development (HUD) (Johnson et al. 2011), energy efficiency efforts for the built environment through "Energize Phoenix" funded by the U.S. Department of Energy (DOE) (Dalrymple and Bryck 2011), high-tech economic development in the area (Discovery Triangle 2011), proposals seeking to reinvent the water utility-oriented Grand Canal (Ellin 2009), Phoenix's General Plan update process, which brings citizen input to bear on the planning process (Wiek et al. 2010), and plans for a new community health care center expanding services into the community.

Results

Urban sustainability problems (demand)

Applying the concept of complex sustainability problems outlined above, experts identified a set of urban sustainability problems for metropolitan Phoenix, including lack of satisfactory economic opportunities, non-renewable and inefficient energy systems, automobile reliant mobility, poor air quality, overuse of water resources, environmental injustices, childhood obesity, waste, lack of social cohesion, and urban heat

island effects. The experts then initially explored the root causes (drivers), causing activities, perceived benefits, negative impacts, and affected populations. The detailed results of the workshop are presented elsewhere (Wiek and Foley 2011) and will be captured in an interactive database of urban sustainability problems (syndromes). We selected three of these urban sustainability problems for illustrative purposes here. The first two—water contamination and non-renewable energy supply—are seemingly amenable to technical solutions. The third, childhood obesity, appears not to be, and yet, emerging nanotechnology applications promise to address (childhood) obesity, too. We further analyzed the selected urban sustainability problems with respect to root causes (drivers), causing activities, perceived benefits, negative impacts and affected populations, based on expert input, recent study results (e.g., Wiek et al. 2010; Ross 2011; Svara 2011), and specified for the Gateway Corridor Community (as far as data were available). The key information on the three problem constellations is summarized in Table 1.

Water contamination

Stakeholders and researchers alike define the Motorola 52nd Street (M52) Superfund Site as an urban sustainability problem, literally underlying the community. The Motorola semi-conductor facility acknowledged the release of an estimated 93,000 gallons of tri-chloroethylene (TCE) in 1982 (ADEQ 2006). Numerous chlorinated and non-chlorinated hydrocarbons are found at the M52 site, but the 93,000 gallons of TCE is the only published estimate. The primary causes of the TCE releases were attributed to leaking tanks, improper hazardous waste disposal into on-site dry wells, and poor chemical management during the production of industrial goods. These were common practices in semi-conductor and metal-working facilities across the country (EPA 2011b). At the M52 Superfund Site, TCE migrated to the aquifer running west to east along the Salt River that flows directly beneath the Gateway Corridor. It is one of the only confirmed dense non-aqueous phase liquid (DNAPL)-contaminated fractured bedrock site beneath a large urban center. It is divided into three operable units (OU1, OU2, and OU3). OU1 and OU2 underlay the Gateway Corridor case study area (EPA 2011b). Root causes included cost cutting measures (the lack of preventative tank maintenance, improper disposal, and employee training on chemical handling); the absence of anticipatory chemical management regulations (before 1980); the perception that dry well disposal was a safe chemical management practice; and the drive to produce inexpensive electronics to support profits and national competitiveness. Inexpensive electronics meet deeper societal root causes such as consumer value, convenience, and utility maximization.

Adverse effects include an estimated 800 billion gallons of contaminated groundwater with unmeasured impacts on alluvial-based biota. Ingestion exposure risk for people was mitigated through the installation of city-provided drinking water (from surface water). Residents recall playing in contaminated water as children and complain of high cancer rates in families living in the community, but cancer cluster research has not produced statistically significant correlations (ADEQ 2011). Soil gas vapors, previously not considered a substantive risk, are migrating up from the fractured bedrock and alluvial soil layers, eventually intruding concrete foundation slabs of residents and businesses. Recently collected data validated by EPA, in an area adjacent to Gateway Corridor, show that more than 50 % of soil gas samples exceed the current risk-based screening levels (EPA 2011c). More recently, indoor air quality testing shows elevated chlorinated hydrocarbons derived from groundwater contaminants in 15 of 39 residences (EPA 2011d). This presents a direct inhalation risk to residents and workers and has triggered an extension of the indoor air quality testing. Citizens had implored state agencies, for years without success, to test soil gas vapors—until EPA assumed control of vapor intrusion and community involvement.

Twenty-eight years of poor information, unresponsive state agencies, and corporate-led remediation efforts fueled feelings by residents that there is an industry-agency alliance. Community members repeatedly questioned researchers conducting community surveys, for fear they represented government or corporate interests. This history of mistrust now plagues the ability of the regional EPA, while based in San Francisco, to operate in Phoenix. EPA cannot dedicate the requisite resources to rebuild community relationships and trust due to budgetary constraints. Diverse publics living in the Gateway Corridor are not well represented in the community involvement group

Table 1 Basic structure of urban sustainability problems

Title	Causing activities	Underlying drivers and actors	Adverse effects (AE) and impacted populations (IP)	Prevalence indicators and sources
Water Contamination	Industrial production of goods	Reactive government policies; lax standards for industrial production and accountability; perception of safety; lack of consumer activism; values of comfort; values of utility maximization and specialization	AE: Impacted groundwater, impacted air (vapor intrusion); biologic impacts; exposure risks (ingestion & inhalation); decreased property values; decreased trust; geographic stigmatization IP: Residents (vulnerable communities and societal groups), city administration (lost tax revenue), state and federal governments (remediation expenses)	Groundwater contaminated at M52 site: >800 billion gallons (annually >1 billion gallons are pumped and treated) Toxics released at M52 site: 93,000 TCE gallons (ADEQ 2006). Area atop contaminated groundwater (M52 site): 7,300 acres (EPA 2011a) People living on M52 site: 52,233 in that overlay site from McDowell to Buckeye & 7th Av to 52nd St (USCB 2010a)
Childhood Obesity	Malnutrition (convenience foods); Lack of exercise	Food deserts; industrial agriculture practices and policies; large-scale production and distribution system; marketing and branding foods; low recreational opportunity; values of convenience, comfort, and safety; lack of knowledge; economic constraints	AE: Early on-set diabetes; cardio-vascular diseases; psycho-social impacts; future educational opportunities and earning potential decreases; increased healthcare costs; increased morbidity and mortality IP: children, especially racial minorities and lower earning socio-economic; parents of obese children; society (supporting healthcare and lost productivity).	Percentage of overweight and obese children (16 years and older) (BMI >85th Percentile) in Arizona: 17.8 (Singh et al. 2010) Mean hours/week physical exercise for children ages 14–18 in Arizona: >33 % exercise less than once per week. [AzDHS recommendation: 100 % of children exercise most days of week (5 of 7 days)] Adults eating fruits (2) and vegetables (3) in Arizona: 30–34.9 % eat fruits, 20–24.9 % eat vegetables (Grimm et al. 2010) [AzDHS recommendation: 100 % of population consume fruits and vegetables (5) servings combined (AZDHS 2006)] Average daily intake of fats & oils as nation: 179 g (1,600 calories) (Hiza and Bente 2007) [USDA/HHS recommendation: 25–35 % of caloric intake or 500–1,120 based on recommended caloric intake below] Average caloric intake per person as nation: 3,900 cal (Hiza and Bente 2007) [USDA/HHS recommendation: 2,000 calories per person per day, up to 3,200 in adolescent males]

Table 1 continued

Title	Causing activities	Underlying drivers and actors	Adverse effects (AE) and impacted populations (IP)	Prevalence indicators and sources
Non-renewable Energy Supply	Centralized production, distribution and use of fossil and nuclear energy	Centralized planning; high consumption based on potentially unlimited supply; subsidizing fossil fuels; lack of knowledge about alternatives; larger homes and dwelling creating demand; rural electrification policy; culture of electrical consumption; path dependency; full life cycle costs not incorporated; building codes	AE: Vulnerability to power outages, based on dependence for heating, cooling, cooking, and water; decreased visibility; DALYs from poor air quality; increased carbon dioxide emissions; mining and extraction impacts; transmission impacts IP: Lower socio-economic groups; workers with direct exposure; children (lung development); elderly (increased stress on lungs)	Total Tons of COE/GDP: 4.95 MMTCO2E in Arizona (estimate) by ACCAG (2006) COE/capita: 7.0 MMTCO2E (estimate) by ACCAG (2006) Electricity Energy Production as Percentage of COE generation in Arizona: 38 % (ACCAG 2006) Percentage of renewable energy in Arizona: 2.8 % (not including hydropower) 6.2 % (including hydropower) (ACCAG 2006)

meetings. The Hispanic and Latino community faces a racially biased state immigration law, enforced in a manner recently deemed discriminatory by the US Justice Department (USDOJ 2011). This penumbra of discrimination overshadows attempts to bring the community (en mass) to public meetings. The M52 Superfund Site depresses local property values, as owners are required to disclose this fact to potential buyers, and undermines the City's property tax base. The M52 Superfund Site is not merely a natural resource or environmental justice issue, but is central to a larger constellation of causing activities, root causes, and effects (see Fig. 2).

Childhood obesity

The network of severe individual and societal impacts, as well as their intermediate and root causes, constitute childhood obesity as a complex global problem (Finegood et al. 2008; Brennan et al. 2011). Based on rudimentary data, childhood obesity is considered a prevalent problem in Arizona, where 17 % of children were obese and 30 % overweight in 2007 and which suffered the highest rate of increase in obesity (46 %) between 2003 and 2007 among all states (Singh et al. 2010). Obesity arises from two primary causing activities, a lack of exercise and overconsumption of (malnutritious) foods. A diverse set of root causes, including environmental and social factors, underlies these behaviors in the case study area (Wiek and Kay 2011). Residents in the Gateway Corridor must travel north under state highway 202 to get to the preferred shopping markets, Walmart and Food City. The only food stores within walking distance of residents are convenience stores and fast-food restaurants. (The Chinese Cultural Center within the case study area boundaries offers both dining and grocery services, but they are not preferred by many non-Asian community members.) Industrial-scale agricultural production, processing, and distribution networks supply large grocers, who provision low–cost and low-quality foods. Marketing and branding efforts successfully draw people into purchasing processed foods that are high in fats and oils. Transporting food by public transit in Phoenix's summer heat, with minimal shading structures for pedestrians, reinforces a reliance on automobile transportation and values of convenience. With highways and the airport walling the community off, the only unbarred path for foot

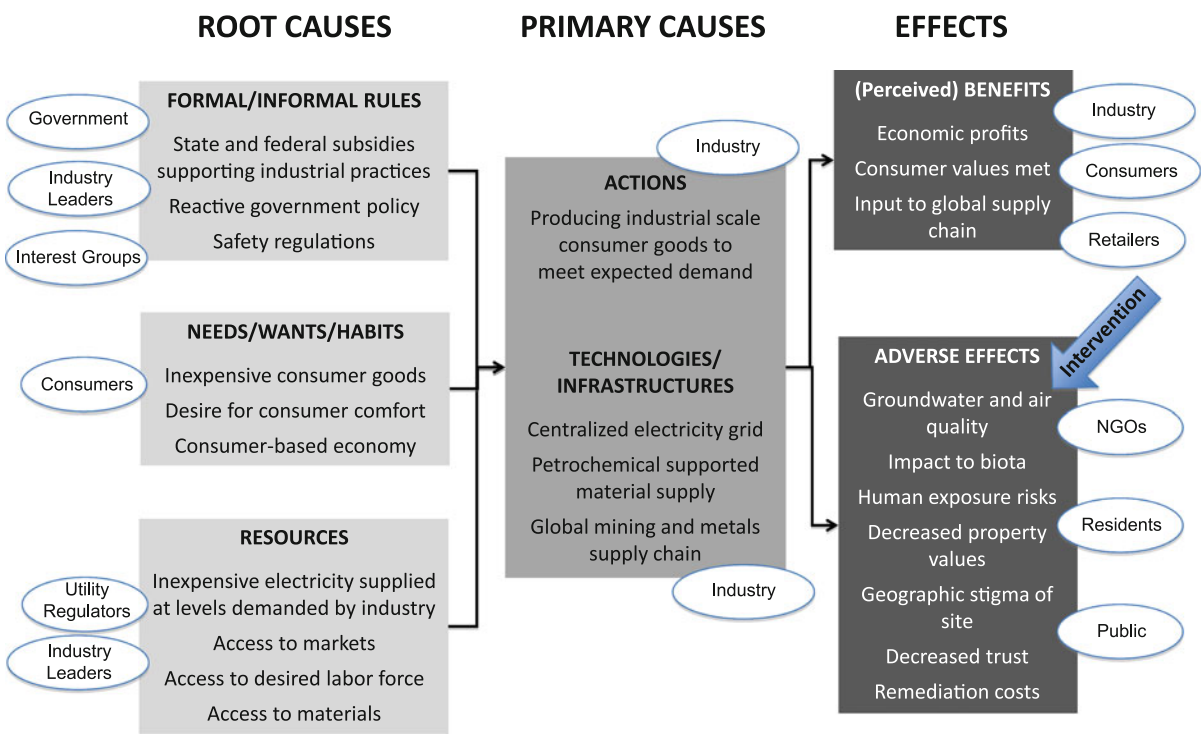

Fig. 2 Problem constellation of water contamination at the M52 superfund site with the proposed intervention point of water purification

traffic is west toward the state prison facility at 24th and Van Buren. Inmates in bright orange jumpsuits are seen through mesh fences confined in their yard. This stretch of Van Buren, Washington, and Jefferson avenues running west is known locally for prostitution, hourly motel room rentals, pornography stores, strip clubs, and narcotics distribution. Perceptions of roads and local canals as dangerous for children encourage indoor recreational activities. Local students often travel to the YMCA facility for safe and indoor recreation opportunities. There are no public parks in the Gateway Corridor and there are currently no plans to construct parks in the vacant lots due to shrinking city budgets.

Adverse effects, studied in comparable urban areas, range from increased morbidity and mortality to early onset type II diabetes to foot and knee pain that reduces mobility to psycho-social impacts observed in children and adults (see Dietz 1998; Freedman et al. 2005; Finegood et al. 2008; Biro and Wien 2010). The prevalence of childhood obesity is elevated in communities of color with African Americans and Hispanics having more than twice the likelihood as non-Hispanic white children (Singh et al. 2010). Macro-economic impacts are projected to reach an annual cost of $10 billion in 2035 (Lightwood et al. 2009).

Lack of renewable energy supply

Residential and commercial energy needs are met through a centralized production and distribution network. Arizona Public Services Co. (APS) provides electricity to residents in the Gateway Corridor with the following energy portfolio: 38 % coal, 27 % nuclear, 30 % natural gas, 3 % renewables, and 2 % energy efficiency (APS 2012). APS released their projected energy portfolio for 2025 revealing a 1 % decrease in coal and nuclear. Natural gas is estimated to increase 33 % and renewables and energy efficiency by 600 % (APS 2012). The primary development need expressed by APS officials is transmission capacity. A plan shows redundancies in centralized networks are emphasized through 2020 (APS 2011). This reflects root causes including, growing societal demand, path dependency in the infrastructure, electrical device connectivity, and standardization policies. Adverse effects include anthropogenic-based climate change with various subsequent effects such

Table 2 Profiles of nanotechnologies applicable to selected urban sustainability challenges (for details visit: http://nice.asu.edu)

Urban sustainability challenge	Nanotechnology function	Nanotechnology substance; and mechanism	Potential full-scale benefits	Potential full-scale life cycle impacts	Development stage	Substitute for:	Sources/references
Water contamination	Water decontamination	nZVI particle; active	nZVI is injected within a slurry to catalyze organo-chlorinated solvents in situ.	Life cycle analysis proposed by EPA and university researchers (Eason et al. 2011; Wiesner et al. 2009)	Engineering	Pump and treat with activated Carbon	Watlington (2005). Zhang (2005). Valli et al. (2010), EPA (2011e), Ela et al. (2011)
Water contamination	Water desalinization	Polydi-methyl-siloxane compound; passive	Ion polarization creates functional junction to separate desalinated water from enriched brine.	Life cycle analysis proposed by EPA and university researchers (Eason et al. 2011; Wiesner et al. 2009)	Scientific Proof of Concept	Macro-porous filters and evaporators	Kim et al. (2010), Tarabara (2010)
Air contamination	Air purification	Carbon nanotubes (CNTs) and TiO_2; passive	Cleans indoor air to remove contaminants.	Unknown Some evidence of lung impacts from air borne CNTs (Kimbrell 2009)	Scientific Proof of Concept	Macroporous filters	Woan et al. (2009), Oh et al. (2009)
Air contamination	Vapor detectors	SnO_2 metal oxide; passive	Contaminant gas surface reacts with metal oxide sensor.	Life cycle analysis proposed by EPA and university researchers (Eason et al. 2011; Wiesner et al. 2009).	Engineering	Electro-chemical gas sensors	Graf et al. (2006), Wang et al. (2010), Waitz et al. (2010)
Health	Food additives	TiO_2 particle; passive	Titanium dioxide is a transparent coating preventing microbial growth.	Oral ingestions of TiO_2 particles in lab mice has lead to health concerns about bio-distribution and acute toxicity (Wang et al. 2007)	Commercial	Shelf life expiration and product disposal	Mihee et al. (2007), Wang et al. (2004), Kuzma and Verhage (2006)
Health	Food additives	Nanocapsule structure; passive	Omega-3 fatty acids are encapsulated and inserted into carbohydrates.	Life cycle analysis proposed by EPA and university researchers (Eason et al. 2011; Wiesner et al. 2009)	Scientific Proof of concept	Balanced diet by varied food selection.	Siegrist Siegrist et al. (2007), Robson (2011), Eldaw (2011)
Energy efficiency	Energy storage	Fluorinated polymers (FPA) and alkaline metals; active	Energy storage with denser and non-aqueous (ionic air) electrolyte.	Life cycle analysis proposed by EPA and university researchers (Eason et al. 2011; Wiesner et al. 2009)	Scientific Proof of Concept	Aqueous phase electrolyte solutions.	Friesen and Buttry (2010), Salloum et al. (2008), Mickelson (2011)

Table 2 continued

Urban sustainability challenge	Nanotechnology function	Nanotechnology substance; and mechanism	Potential full-scale benefits	Potential full-scale life cycle impacts	Development stage	Substitute for:	Sources/references
Energy efficiency	Photo-voltaics	CdTe or GaAs; passive	Full-scale installation would produce demanded power required by Phoenix.	Life cycle CO2 equivalent emissions estimated at 90–300 times lower than coal-fired power plant in studies (Fthenakis et al. 2008)	Ubiquitous, but not available	Fossil, nuclear, and biomass combustion	Kato et al. (2001), Noufi and Zweibel (2006), Tetey et al. (2010)
Energy efficiency	Industrial catalysis	Zeolite L particle; active	Zeolite L nanoporous catalyzes bulk particles into reformed compounds.	Life cycle analysis proposed by EPA and university researchers (Eason et al. 2011; Wiesner et al. 2009)	Scientific Proof of Concept	Bulk Catalysts	Hu et al. (2011), Bernardo et al. (2009)
Energy efficiency	LED lighting (nano-enhanced)	Nonacene compound; passive	Organic light emitting diodes that can be affixed by printing on materials surface.	Proposed research on-going at Green Launching Pad (Brooks 2011)	Scientific Proof of Concept,	Fluorescent and filament lighting	Purushothaman et al. (2011), Gao et al. (2011), Kaur et al. (2010)

as water shortages in the desert southwest (Seager et al. 2007). Second, localized urban heat island effects are most likely to affect Hispanic residents and those in the Gateway Corridor (Chow et al. 2012). The electricity system from source to outlet encompasses sectorial dimensions of economics, natural resource, and social demands detailed in Table 1.

Nanotechnology applications (supply)

A broad literature review yielded a number of nanotechnologies directly applicable to urban sustainability problems. We validated the initial set of applications through expert workshops and interviews, which yielded a top ten list of nanotechnologies that held promise to alleviate urban sustainability problems in metropolitan Phoenix. From this set, we selected those applications that are pertinent to the three urban sustainability challenges described above. Table 2 reflects those applications, also captured in an online database entitled "Nanotechnology in City Environments" (NICE) that serves as a repository for information on the functionality, as well as the sustainability challenges these technologies are seeking to ameliorate and information on potential benefits and risks (http://nice.asu.edu).

Nanotechnology interventions in urban sustainability syndromes

To this point, we have analyzed three critical urban sustainability challenges facing metropolitan Phoenix and identified ten nanotechnologies that offer technical solutions to these sustainability challenges. Based on this systemic problem understanding and functional knowledge of potential nanotechnology solutions, our next and final step is to appraise the interventions of nanotechnology solutions into each of the three problem constellations. Table 3 details the case, the intervention point, mechanism, governing decision-makers, the decision process, barriers to intervention, potential resources required to intervene, effectiveness and efficacy (if known) of the nanotechnology, and restates the current intervention. We present the results for our three case studies as an initial attempt to *reconcile* nanotechnology applications (as supply) and sustainability challenges (as demand) to exemplarily

Table 3 Nanotechnology applications as intervention strategies for complex urban sustainability problems

Case study	Systemic intervention points	Mechanism	Decision-makers	Decision process	Barrier(s)	Required resources	Effectiveness	Efficacy	Current invention strategy	Sources/ references
Water contamination (M52 Superfund Site)	Remediate contaminated groundwater Provision air filtration	Contaminant removal post-release	Regulatory agencies, responsible parties, community members	Formal federal decision-making process	Decision-making Process; Test site validation; Acceptance by parties; Sunk costs in current technology;	Unknown energy and materials costs.	Pilot stage in situ testing for nZVI slurry. Lab scale proof of concept for CNT air filtration.	Pilot test reported 82–96 % reduction in TCE. No in situ testing of CNT air filters.	Both use known activated carbon based technology	Chang et al. (2010), EPA (2011e), Watlington (2005)
Childhood Obesity	Alleviate food deserts by lengthening storability Enhancement nutrition with food additives	Industrial packaging using titanium dioxide as bacteria disinfectant Insertion of omega-3 fatty acids into carbohydrates	Industrial agriculture packaging, distributers, consumers, and FDA	Formal regulations. FDA approved bulk-TiO_2 Nutritional supplements are not drugs: not regulated: informal decisions by individual consumers	Technology risks assessed by food industry; public perception of nano in food, toxicology reports indicate bio-distribution of oral transmission creates acute toxicity in lab mice	Retooling packaging plants to incorporate TiO_2 coated cellophane. Capsulation of omega-3 in carbohydrates. Unknown energy and materials costs	*E. coli*, *Salmonella typhimurium*, and *B. cereus* eliminated by TiO_2 encased fresh vegetables. Omega-3 fatty acids enhance nutritional content of carbohydrates.	*E. coli killed at* 95.67 %, 94.27 % and 91.61 % in 3.0, 5.0 and 7.0 pH solutions in combination with ultra-violet rays. Limited data on efficacy of omega-3 uptake.	Products are assigned expiration dates based on historic food safety issues (i.e., recalls) and product testing. Nutrition information based on historic tests.	Wang et al. (2004, 2007), Mihee et al. (2007), Kuzma and Verhage (2006), Siegrist et al. (2007)
Lack of renewable energy sources and energy efficiency.	Create utility scale and decentralized photovoltaic arrays Retrofit homes and businesses with nano-enhanced lighting	Semi-conductor converting light to energy in CdTe based thin-film LEDs provide high quality light with low energy demand	Utility regulators, utility operators, electricity distributors, consumers, financiers, and building inspectors	Regulatory mandates for utilities and regulated market based decisions. Home and business owners that see energy efficiency retrofits as valuable.	Cost parity with fossil fuels, technical feasibility, inconsistent subsidies, current reliability, return on investment of retrofits, available energy efficiency subsidies	Production, material costs, financing, political will, addition al storage capacity, and net energy are not all known.	Currently 7.3–10.2 efficiency is reported for thin-film photo-voltaic. Price point is two times existing sources. LEDs provides high quality lumens with reduced energy demand.	Constraints based on current US grid. Proven efficacy in product testing and measurable outcomes in residential buildings pending.	Regulated utilities must attain renewable energy standards set at 15 % by 2024. Meet Phoenix electrical codes.	Kato et al. (2001), Fthenakis et al. (2008), Noufi and Zweibel (2006), Tettey et al. (2010), Hatch-Miller et al. (2006)

answer the guiding question on what nanotechnology offers to address complex sustainability problems.

Addressing water contamination

The latent decision (made in 1986) was to address remediation through pump and treat methods (EPA 2011b). The annual average volume of water pumped per year between 2005 and 2010 was 844 million gallons in OU1 and OU2 (EPA 2011f). The annual average volume of TCE recovered per year from OU1 and OU2 was 115 gallons (EPA 2011f). The recovery rate of TCE (gallons) per million gallons of groundwater pumped per year from OU1 and OU2 between 2005 and 2010 is 0.14 gallons of TCE. A linear extrapolation of the current TCE removal rate suggests that the complete removal of TCE will occur after the year 3000. This timeframe is untenable for current and future residents.

The M52 Superfund Site appears to be amendable to a nanotechnology solution as current pump and treat technologies are neither efficient nor effective. The efficacy rate of nanoscale Zero-Valent Iron (nZVI) to remove TCE at the Goodyear-Phoenix Airport site is reported at 82–96 % in pilot tests (Chang et al. 2010). We must caution that the hydrology and geological structures at the Goodyear-Phoenix airport site are not directly comparable to the M52 site; however, these are promising results. The effectiveness for nZVI slurry jet injections into groundwater may eliminate the need for groundwater pumping. Three rounds of in situ nZVI slurry jet injections would theoretically reduce TCE (at 82 % efficacy) to approximately 0.5 % of current levels. From this rough appraisal, we can conclude that in situ remediation with nZVI may remove the TCE either sooner (in <1,000 years) and with less effort (pumping 844 millions gallons of groundwater annually). As for the filtration of contaminated air with CNTs, there is little evidence of in situ testing. Ideal conditions in laboratory experiments and placing devices in residences are different contexts. Significant work is needed to refine prototypes before testing CNT air filtration in non-laboratory settings.

There are issues with in situ nZVI slurry injections and CNT air filtration. First, the fate, transport, and toxicological assessments for both eco-toxicity and human health of full-scale application of jet-injected nZVI slurry have not been conducted. While deploying CNTs in residences to clean organic toxins from the air calls forth efforts to reduce fire risk with asbestos tiles. Ensuring asbestos-like nanoparticles are not released in homes is a critical issue (Philbrick 2010). Thereby, a potential unintended consequence from injecting nZVI quantities sufficient to remediate billions of gallons of contaminated groundwater could be anticipated, as could the release of CNTs into homes from design or user error. Second, the cost estimates to produce the quantities of nZVI slurry required to treat an estimated 800 billion gallons of contaminated groundwater or those for CNTs for filtration are not known. Net present value calculations discount any future benefits past 30 years to a value of zero, making the cost-benefit calculations appear negative. Current cost-benefit models that discount future generations will not support near-term and high-cost solutions. Further, the formalized decision-making structure, which cedes authority to EPA (with judicial review by the 9th Circuit Court), may further impede this intervention. Technical questions of the applicability of nZVI and CNTs aside, significant toxicological, financial, and decision-making hurdles remain.

Considering applied pilot-scale testing of nZVI slurry to remediate groundwater (EPA 2011e; Watlington 2005; Chang et al. 2010) and laboratory-scale application of CNTs, the evidence supports the rhetoric on environmental applications of nanotechnology (Karn 2005) in this case. The proposed nanotechnology intervention, although certainly needed to optimize the current solution, occurs downstream of the original incident (release of TCE) as depicted in Fig. 2. The intervention will not address upstream policies, values, or resources that influence the actions that caused this historic release, including potential health impacts from nZVI slurry or CNTs. In fact, there are similar industrial practices that continue to create new suites of large-scale environmental challenges potentially analogous to superfund sites, e.g., oil spills, hydraulic fracturing in natural gas fields, and unregulated nanoparticle disposal.

When considering interventions in wicked problems, silver bullets lack the ability to resolve all the complex problem elements (Seager et al. 2012). Rebuilding trust, co-producing visions of the community (with researchers, city planners, regulatory agencies, and citizens), and strategic investments in community assets are needed to transition the

Gateway Community toward a sustainable neighborhood consisting of vibrant businesses, lively parks, and urban gardens—as expressed in visioning workshops (Wiek and Kay 2011). A more profound approach would require a suite of interventions, including non-technical (institutional) interventions. Educating students at the nearby BioScience high school and engaging parents and administrators at Crockett Elementary School and planners at Gateway Community College are ways to communicate these issues to the next generation of citizens and decision-makers. Strategic planning efforts to co-construct a future vision of the community between citizens, city planners, researchers, and businesses are underway. A $10 M research proposal for long-term efforts toward clean-up and community sustainability that explores technical and non-technical solution options at the M52 Superfund Site is currently under review with the National Institutes of Health.

Addressing childhood obesity

Childhood obesity is currently a highly publicized issue of public health concern. From the Office of the President (Barnes 2010) to local parent and teacher associations, numerous interventions are being attempted. There are few evaluations of the effectiveness of these interventions (Brennan et al. 2011). The proposed nanotechnology interventions are twofold. First, the food packaging with TiO_2 that allows industrial-scale agricultural production and distribution to reduce microbial contamination of vegetables for longer a shelf life. The industry presents this intervention as a means to overcome costs associated with product loss (spoilage) and allow for greater profitability in retailing fresh vegetables wrapped in TiO_2-coated packaging (Robinson and Morrison 2009). The second intervention is the construction of nutritionally enhanced carbohydrates (a food staple in US diets) with omega-3 fatty acids (Robinson and Morrison 2009). This intervention is intended to induce a compound that will confound adiposity development at the cellular level.

Neither intervention is cognizant of physiologic, socio-economic, or cultural preferences. Wang et al. (2007) shows that TiO_2 ingested in laboratory animals is transported to a variety of organs, raising concerns of acute toxicity and biotoxicity. Omega-3 fatty acids are described as healthy fats at the rates currently consumed; however, current engineered methods to increase omega-3 levels are primarily observed in farm-raised fish. Elevated risks of mercury, organochlorine compounds, and polychlorinated biphenyls are being discovered in farm-raised fish (Hamilton et al. 2005; Domingo 2007). This stirs the question of whether unintended compounds will join the engineered omega-3 fatty acids encapsulated in carbohydrates.

To shift perspective, who is the targeted market for engineered carbohydrates, longer shelf life vegetables that cost less than organic vegetables and wild caught fish? Studies indicate that consumers' preference for engineered foods is lower than for non-engineered foods (Siegrist et al. 2007, 2009). Childhood obesity in the US is more likely in lower income groups (3.46 times), in neighborhood perceived as unsafe (1.61 times), in neighborhood with trash visible (1.44 times), and where no community recreation center is located (1.23 times) (Singh et al. 2010). The Gateway Corridor is primarily a low-income community that is perceived as unsafe, lacks a recreation center, and trash is visible on sidewalks and abandoned lots. This suggests that Gateway Corridor residents could be a considerable segment of the target market for products addressing childhood obesity, presumably against their preferences. The proposed nanotechnology interventions reinforce practices and norms of industrial-scale agriculture and distribution to automobile-oriented urban communities.

Residents and decision-makers have outlined more holistic and preventative interventions in collaborative visioning workshops (Wiek and Kay 2011). Such visions include community organizations (schools, neighborhood associations, and faith-based organizations) providing land for urban agriculture and skills training; a community center which provides childcare services, adult education, after school recreational and learning opportunities for all ages; and job and skill-oriented trainings offered through voluntary work supporting community-based small business initiatives. Mountain Park Health Center, a non-profit health care service provider, is funding community-based participatory research to develop innovative, effective, and comprehensive health care services together with the community. Administrators at both Gateway Community College and Crockett Elementary School are engaging with parents, students, and researchers to better understand the problems and

devise solutions in concert, rather than in top–down management fashion.

Addressing the lack of renewable energy

Cadmium-telluride photovoltaic (CdTePV) in printed thin-film applications would intervene at the point of power generation and nano-enhanced LEDs at the point of use. The life cycle impacts of CdTePV are 90–300 times less than coal-fired power plant impacts per watt of capacity (Fthenakis et al. 2008). The greatest benefits from CdTePV are realized in the power generation phase, where almost no emissions occur. The Cree Corporation in North Carolina produces nano-enhanced LEDs having long since invested in optimizing the production of 6H-SiC crystals (Edmond et al. 1993). No data are available for a life cycle analysis, as corporate secrets protect the crystal formation processes. Lighting retrofits are the lowest cost, highest return energy efficiency investment, and the most preferred by businesses engaged with the initiative "Energize Phoenix" (Dalrymple and Bryck 2011). Grid-scale solar electricity and energy storage at Solana Generating Station, currently under construction, will produce 280 megawatts. Solana relies on large-scale batteries that offer 4–6 h of storage (Mahrer 2011). Positive outcomes abound from these interventions.

However, there are unaddressed issues with both CdTePV and LEDs. The reliability and storability of CdTePV-generated energy may not meet user demands for constant uninterrupted power supply. Storing CdTePV-generated power in large-scale batteries (offering near 100 % reliability) is currently not cost effective (Mahrer 2011). The plan by Arizona Power Supply (APS) for distribution reinforces preferences for utility-scale solar, rather than addressing uncertainties that accompany rooftop solar. Costs to retrofit the electrical grid from a centralized to a decentralized model will be significant. Both the societal expectations for electricity and shortfalls in component technologies influence the adoption of these promising (yet unrealized) nanotechnology interventions. A deeper root cause of the problem constellation is the continued growth in the demand for inexpensive electricity to power our expected lifestyles, from entertainment to manufacturing capacity. This and other background drivers remain unaddressed in the proposed interventions.

More profound strategies to address the outlined lack of renewable energy problem require suites of interventions, including non-technical (institutional) interventions such as demand-side management. Recently, the "Energize Phoenix" grant was awarded to assist residents and businesses increase energy efficiency and support renewable energy provision in the Gateway Corridor (a subset of the Energize Phoenix Corridor). The grant exemplifies a partnership between city, businesses, and researchers. Initiated in 2010, seventeen commercial projects were completed in the first year with sixteen of the seventeen total projects were lighting retrofits for an estimated savings of 1.9 million kilowatt hours (kWh) across all the projects (Dalrymple and Bryck 2011). While businesses have leveraged subsidies and the commercial programs were launched before the residential programs, no residents participated in the first year; all completed energy efficiency projects occurred at commercial properties. A lack of awareness and education, issues of trust, language, and cultural barriers are some root causes preventing home owners from taking action. The issues of trust range from distrust in the idea of a "free lunch" to distrust of authority and fear of potential immigration enforcement action. Second, limited financial resources prevent residents from paying the $99 fee upfront for a subsidized energy assessment even though they are rebated the fee later. And, despite a grant to cover 60 % of the upgrade costs and a subsidized loan to cover the remaining 40 %, residents are hesitant to take on any debt on a property that may have limited or negative equity due to the real estate market, even as the savings in their utility bills are estimated to more than cover loan payments (Dalrymple and Bryck 2011). In the second year, overall participation in the residential programs increased to approximately 400 households, attributable to increased marketing awareness, outreach to and engagement with trusted community leaders and organizations, exposure to the participation of neighbors, door-to-door community surveying, and community events. However, participation by low-income residents and in the Gateway Corridor continues to lag considerably. This uneven participation response demonstrates that these complex problem constellations are challenging beyond technical feasibility, demanding coordinated efforts to affect change toward sustainability.

Discussion

Our study explored the potential of nanotechnology solutions as a means to mitigating urban sustainability problems. In two cases (contaminated water and energy systems), there is evidence that nanotechnologies can address existing problems. In the case of childhood obesity, the proposed interventions (food additives and food packaging) seem inappropriate in the face of the significant social drivers underlying childhood obesity, as well as the strong apprehension consumers hold against food additives. In all cases, the nanotechnology interventions fail to address root causes, such as demand for electricity, reactive policies addressing environmental contamination, and consumption of cheap convenience foods and sedentary indoor entertainment.

We are, however, focusing on intervention points and potential effectiveness. Admittedly, these are not technical feasibility assessments and this analysis is not fully inclusive of all decision-making, legal, and economic barriers that comprise robust intervention research. We are taking a broader sustainability perspective on the urban problems to understand just how nanotechnology might intervene and what problem components accompanying initiatives would need to address.

Here, we briefly discuss in how far this study provides insights into the four research questions posed at the beginning. First, over-simplified ideas about sustainability perpetuate the false image that nanotechnology will mitigate the majority of the pressing and complex challenges societies face around the world. It reproduces the technocratic proposition that dominates the progress narratives in industrialized and post-industrial societies (Pitkin 2001). Clearly, there are nanotechnologies that can intervene in urban sustainability problems, but we ought to be careful not to over-sell their problem-solving potential and capacity. Not all urban sustainability problems are amenable to nanotechnology interventions; in fact, most of them require a suite of interventions, of which technology in general and nanotechnology specifically provide but *one* stream of solutions. Informed by intervention research, we have argued in this study that a comprehensive problem understanding must inform the appraisal of this potential (Sarewitz and Nelson 2008).

Second, urban nanotechnological interventions are, at best, midstream interventions, but many are end-of-pipe (downstream) interventions. Systemic interventions that affect positive changes, especially through upstream interventions impacting key drivers and underlying social phenomena, are critical to long-term sustainable solutions (Midgley 2006; Schensul 2009). Social interventions might have significantly higher success rates than technical ones as they offer interventions that address the root causes of problem constellations. Addressing societal demand for cheap convenience foods, the lack of precautionary regulations managing chemicals, or the externalities from fossil fuels not priced into the current power supply—all these issues offer institutional interventions that demand attention on par with technological interventions.

Third, nanotechnology is an enabling technology (on top of other technologies) or a platform (below other technologies) to deliver complimentary technologies. The promised benefits are largely dependent on the distribution and breakthrough of parallel technologies. The unintended consequences that might result from the "hosting" technology as much as from the applied nanotechnology need to be explored through laboratory experimentation, small-scale pilot tests, and research. Nanotechnology will soon play a role in reducing the material requirement for precious metals in exhausts and increase profits in the automobile industry and thereby optimizing an ultimately flawed technology (SDC 2012). In addition to the traditional environmental, health, and safety concerns, research needs to anticipate the ethical, legal, and social implications, for instance, of pumping high volumes of nZVI slurry into groundwater contaminated with various toxins.

Fourth, there is evidence that LED lighting retrofits and photovoltaic panels will increasingly be introduced and incentivized. Industrial-scale production of TiO_2 awaits the anticipated demand for nanotechnology packaging. Field tests conducted with nZVI slurry show initially promising results to catalyze organic groundwater contaminants. Installing CNT-based air filters into homes and encapsulating nutritional supplements are still held within laboratory-scale experiments. We would argue, however, that these interventions do not address root causes (at all) and only in the energy production and efficiency intervention do they address causing behaviors. The other cases demonstrate the technological path dependencies and the conventional approach of optimization, not disruption and transformational change necessary for achieving sustainability.

Conclusions

Clearly, there is potential for nanotechnology to contribute to a sustainable future, but those interventions must be coupled with and embedded in systemic intervention strategies which are not solely reliant on nanotechnology as the silver bullet. The goal of the presented research is to support initiatives of anticipatory governance that integrate nanotechnology in comprehensive mitigation strategies to urban sustainability challenges that warrant approval by experts and stakeholders alike. Further research on how nanotechnology can be joined with other solution options to comprehensively address urban sustainability problems is necessary. There remains significant work to take a broader scan of all the potential interventions, assess potential pathways, and implement comprehensive strategies to transition these urban sustainability problems into a sustainable future.

Acknowledgments The authors would like to thank their colleagues at the Center for Nanotechnology in Society at Arizona State University (CNS-ASU) and Lauren Withycombe Keeler (School of Sustainability, ASU) for helpful comments on earlier versions of this article, as well as Richard Rushford (School of Sustainability), Evan Taylor (CNS-ASU), and Braden Kay (School of Sustainability) for research assistance. This research was undertaken with support by CNS-ASU, funded by the National Science Foundation (cooperative agreement #0531194 and #0937591). The findings and observations contained in this paper are those of the authors and do not necessarily reflect the views of the National Science Foundation.

References

Arizona Department of Environmental Quality (ADEQ) (2011) Motorola 52nd street site EPA national priorities list (NPL) site. http://www.azdeq.gov/environ/waste/sps/download/phoenix/m52.pdf. Accessed 6 April 2012

Arizona Climate Change Action Group (ACCAG) (2006) Final Arizona greenhouse gas inventory and reference case projects: appendix D: greenhouse gas emissions inventory and reference case projections 1990–2020. Arizona Climate Change Action Group, Phoenix

Arizona Department of Environmental Quality (ADEQ) (2006) Third five year review: operable unit 1—Motorola 52nd street superfund site. Arizona Department of Environmental Quality, Phoenix

Arizona Public Service (APS) (2011) Arizona Public Service Company 2011–2020 transmission plan. http://www.aps.com/files/siting/APS_2011_Ten_Year_Plan_BTA-11-0017_Plan_Only.pdf. Accessed 2 April 2012

Arizona Public Service (APS) (2012) APS will fuel Arizona with a clean, diverse, customer-powered energy mix. http://www.azenergyfuture.com/files/resourceplan.pdf Accessed 2 April 2012

Barben D, Fisher E, Selin C, Guston DH (2008) Anticipatory governance of nanotechnology: foresight, engagement, and integration. In: Hacket EJ, Amsterdamska O, Lynch M, Wajcman J (eds) The handbook of science and technology studies, 3rd edn. MIT Press, Cambridge, pp 979–1000

Barnes M (2010) Solving the problem of childhood obesity within a generation: White House task force on childhood obesity—report to the President. Office of the President, Washington, DC

Bernardo P, Drioli E, Golemme G (2009) Membrane gas separation: a review/state of the art. Ind Eng Chem Res 48:4638–4663

Biro FM, Wien M (2010) Childhood obesity and adult morbidities. Am J Clin Nutr 91(S):1499–1505

Brennan L, Castro S, Brownson RC, Claus J, Orleans CT (2011) Accelerating evidence reviews and broadening evidence standards to identify effective, promising, and emerging policy and environmental strategies for prevention of childhood obesity. Annu Rev Public Health 32:199–223

Brooks D (2011) Light heavyweight: a UNH spinoff company works on flexible white light sources. University of New Hampshire Magazine, USA

Chang PR, Pantaleoni AD, Shenk DJ (2010) Jet-assisted injection of nano-scale, zero-valent iron to treat TCE in a deep alluvial aquifer. ERM, Scottsdale

Chow WTL, Chuang W-C, Gober P (2012) Vulnerability to extreme heat in metropolitan Phoenix: spatial, temporal, and demographic dimensions. Prof Geogr 64:286–302

Clark WC, Dickson NM (2003) Sustainability science: the emerging research program. Proc Natl Acad Sci USA 100(14):8059–8061

Dalrymple M, Bryck D (2011) Energy efficiency on an urban scale. Global Institute of Sustainability, Tempe

Diallo M, Brinker CJ, Nel A, Shannon M, Savage N (2011) Nanotechnology for sustainability: environment, water, food, minerals, and climate. In: Roco MC, Mirkin C, Hersam MC (eds) Nanotechnology research directions for societal needs in 2020. Springer, London, pp 145–173

Dietz WH (1998) Health consequences of obesity in youth: childhood predictions of adult disease. Pediatrics 101: 518–525

Discovery Triangle (DT) (2011) About: discovery triangle. http://www.discoverytriangle.org/about/. Accessed 30 November 2011

Domingo JL (2007) Omega-3 fatty acids and the benefits of fish consumption: is all that glitters gold? Environ Int 33(7): 993–998

Eason T, Meyer DE, Curran MA, Upadhyayula VKK (2011) Guidance to facilitate decisions for sustainable nanotechnology. Environmental Protection Agency, Cincinnati

Edmond A, Kong H-S, Carter CH Jr (1993) Blue LEDs, UV photodiodes and high-temperature rectifiers in 6H-SiC. Phys B 185:453–460

Ela WP, Sedlak DL, Barlaz MA, Henry HF et al (2011) Towards identifying the next generation of superfund and hazardous waste site contaminants. Environ Health Perspect 119(1):6–10

Eldaw A (2011) Nanotechnology in elevation of the worldwide impact of obesity and obesity-related diseases: potential roles in human health and disease. J Diabetes Sci Technol 5(4):1005–1008

Ellin N (2009) Canalscape. Available at http://canalscape.org/exhibit-publication/publication/. Accessed 1 December 2011

Environmental Protection Agency (EPA) (2011a) Chemical report http://iaspub.epa.gov/triexplorer/tri_release.chemical. Accessed 15 January 2012

Environmental Protection Agency (EPA) (2011b) Site overview. Motorola, Inc. 52nd street plant. http://yosemite.epa.gov/r9/sfund/r9sfdocw.nsf/3dec8ba325236842882574 2600743733/22ac34863a99a86388257007005e9409!OpenDocument#documents. Accessed 12 October 2011

Environmental Protection Agency (EPA) (2011c) Results of soil gas sampling and next steps—community involvement group presentation. http://yosemite.epa.gov/r9/sfund/r9sfdocw.nsf/3dc283e6c5d6056f88257426007417a2/c32fcdd96847b354882578ae006f7a98/$FILE/June8_Community_Meeting_Final.pdf. Accessed 5 January 2012

Environmental Protection Agency (EPA) (2011d) October sampling event: OU1 validated indoor air and subslab data. http://yosemite.epa.gov/r9/sfund/r9sfdocw.nsf/3dc283e6c5d6056f88257426007417a2/b1c66d8fe3e7b64e88257998006b1ef2/$FILE/October%20Data%20Summary%20no%20addresses_02Feb2012.pdf. Accessed 6 April 2012

Environmental Protection Agency (EPA) (2011e) Selected sites using or testing nanoparticles for remediation media. Environmental Protection Agency, Washington, DC

Environmental Protection Agency (EPA) (2011f) Report: Motorola 52nd St. Superfund Site five-year review completed. Environmental Protection Agency, San Fransico

Finegood DT, Karanfil O, Matteson CL (2008) Getting from analysis to action: framing obesity research, policy and practice with a solution-oriented complex systems lens. Healthc Pap 9(1):36–41

Fraser MW, Richman JM, Galinsky MJ, Day SH (2009) Intervention research—developing social programs. Oxford University Press Inc, New York

Freedman DS, Khan LK, Serdula MK, Dietz WH et al (2005) The relation of childhood BMI to adult adiposity: the Bogalusa heart study. Pediatrics 115(1):22–27

Friesen CA, Buttry DA (2010) Metal-air low temperature ionic liquid cell. United States Patent and Trademark Office, Washington, DC

Fthenakis VM, Kim HC, Alsema E (2008) Emissions from photovoltaic life cycles. Environ Sci Technol 42(6): 2168–2174

Gao X, Hodgson JL, Jiang DE et al (2011) Open-shell singlet character of stable derivatives of nonacene, hexacene and teranthene. Org Lett 13(13):3316–3319

Graf M, Gurlo A, Barsan N, Weimar U, Hierlemann A (2006) Microfabricated gas sensor systems with sensitive nanocrystalline metal-oxide films. J Nanopart Res 8:823–839

Grimm KA, Blanck HM, Scanlon KS, Moore LV, Grummer-Strawn LM, Foltz JL (2010) State-specific trends in fruit and vegetable consumption among adults—United States, 2000–2009. Morb Mortal Wkly Rep 59(35):1125–1130

Guston DH (2008) Innovation policy: not just a jumbo shrimp. Nature 454:940–941

Hamilton MC, Hites RA, Schwager SJ, Foran JA et al (2005) Lipid composition and contaminants in farmed and wild salmon. Environ Sci Technol 39(22):8622–8629

Hatch-Miller J, Mundell WA, Gleason M, Mayes KK, Wong B (2006) Docket No. RE-00000C-05-0030. Arizona Corporation Commission

Hiza HAB, Bente L (2007) Nutrient content of the U.S. food supply, 1909–2004 a summary report. United States Department of Agriculture, Washington, DC

Hu EL, Davis SM, Davis R, Scher E (2011) Applications: catalysis by nanostructured materials. In: Roco MC, Mirken CA, Hersam MC (eds) Nanotechnology research directions for societal needs in 2020. Springer, London, pp 315–332

Jerneck A, Olsson L, Ness B et al (2011) Structuring sustainability science. Sustain Sci 6(1):69–82

Johnson C, Upton C, Wiek A, Golub A (2011). Reinvent Phoenix: cultivating equity, engagement, economic development and design excellence with transit-oriented development. City of Phoenix and Arizona State University

Jones R (2007) Can nanotechnology ever prove that it is green? Nat Nanotech 2:71–72

Karinen R, Guston DH (2010) Governing future technologies: nanotechnology and the rise of an assessment regime. In: Kaiser M, Kurath M, Massan S, Rehmann-Sutter C (eds) Toward anticipatory governance: the experience with nanotechnology. Springer, Dordrecht, pp 217–232

Karn B (2005) Overview of environmental applications and implications. How does nanotechnology related to the environment? Or why are we here? In: Karn B, Masciangioli T, Zhang WX, Colvin V, Alivisatos P (eds) Nanotechnology and the environment: application and implications. American Chemical Society, Washington, DC, pp 2–6

Kates RW, Clark WC, Corell R, Hall JM et al (2001) Sustainability science. Science 292(5517):641–642

Kato K, Hibino T, Komoto K, Ihara S, Yamamoto S, Fujihara H (2001) A life-cycle analysis on thin-film CdS/CdTe PV modules. Sol Energy Mater Sol Cells 67:279–287

Kaur I, Jazdzyk M, Stein NN, Prusevich P, Miller GP (2010) Design, synthesis, and characterization of a persistent nonacene derivative. J Am Chem Soc 132(4):1261–1263

Kim SJ, Ko SH, Kang KH, Han J (2010) Direct seawater desalination by ion concentration polarization. Nat Nanotechnol 5(4):297–301

Kimbrell G (2009) Governance of nanotechnology and nanomaterials: principles, regulation, and renogiating the social contract. J Law Med Ethics 37(4):706–723

Komiyama H, Takeuchi K (2006) Sustainability science: building a new discipline. Sustain Sci 1(1):1–6

Kuzma J, VerHage P (2006) Nanotechnology in agriculture and food production. Project on Emerging Technologies, Washington, DC

Lerner S (2010) Sacrifice zones—the front lines of toxic chemical exposure in the United States. The MIT Press, Cambridge

Lightwood J, Bibbins-Domingo K, Coxson P et al (2009) Forecasting the future economic burden of current adolescent overweight: an estimate of the coronary heart disease policy model. Am J Public Health 99(12):2230–2237

Lobo J, Strumsky D (2011) How green is my nano? Evidence from USPTO patents. 3rd Annual Society for the Study of Nanoscience and Emerging Technologies. Tempe

Mahrer E (2011) APS renewable energy overview. Greenhouse Gas, Renewable Energy, Green Building and Sustainability Seminar, Mesa

Mickelson L (2011) Surface stress during electro-oxidation of carbon monoxide and bulk stress evolution during electrochemical intercalcation of lithium. Dissertation, Arizona State University

Midgley G (2006) Systemic intervention for public health. Am J Public Health 96(3):466–472

Mihee C, Choi Y, Park H, Kim K, Woo GJ, Park J (2007) Titanium dioxide UV photocatalytic disinfection in fresh carrots. J Food Protect 70(1):97–101

Noufi R, Zweibel K (2006) High-efficiency CdTe and CIGS thin-film solar cells: highlights and challenges. IEEE 4th world conference on photovoltaic energy conversion, Waikoloa

Oh WC, Zhang FJ, Chen ML (2009) Preparation of MWCNT/TiO_2 composites by using MWCNTs and titanium(IV) Alkoxide precursors in benzene and their photocatalytic effect and bactericidal activity. Bull Korean Chem Soc 30(11):2637–2642

Philbrick M (2010) An anticipatory governance approach to carbon nanotubes. Risk Anal 30(11):1708–1722

Pitkin B (2001) A historical perspective of technology and planning. Berkeley Plan J 15:32–55

Purushothaman B, Bruzek M, Parkin SR, Miller AF, Anthony JE (2011) Synthesis and structural characterization of crystalline nonacenes. Angew Chem 123:7151–7155

Ravetz J (2006) Post-normal science and the complexity of transitions towards sustainability. Ecol Complex 3(4): 275–284

Robinson DKR, Morrison M (2009) Report on nanotechnology in agrifood. European Commission: ObservatoryNANO. http://www.observatorynano.eu/project/filesystem/files/Full%20Report%20Nanotechnology%20in%20Agrifood%20May%202009.pdf. Accessed 14 May 2012

Robson AA (2011) Food nanotechnology: water is the key to lowering the energy density of processed foods. Nutr Health 20(3–4):231–236

Roco MC, Harthorn B, Guston D, Shapira P (2011) Innovative and responsible governance of nanotechnology for societal development. J Nanopart Res. doi:10.1007/s11051-011-0454-4

Ross A (2011) Bird on fire: lessons from the world's least sustainable city. Oxford University Press Inc, New York

Salloum KS, Hayes JR, Friesen CA, Posner JD (2008) Sequential flow membrane less microfluidic fuel cell with porous electrodes. J Power Sources 180:243–252

Sarewitz D, Nelson R (2008) Three rules for technological fixes. Nature 456(7224):871–872

Sarewitz D, Pielke R Jr (2007) The neglected heart of science policy: reconciling supply of and demand for science. Environ Sci Policy 10(1):5–16

Schensul JJ (2009) Community, culture and sustainability in multilevel dynamic systems intervention science. Am J Community Psychol 43(3–4):241–256

SDC (2012) SDC Materials announces field trials for emission control catalysts. http://www.nanowerk.com/news/newsid=23902.php. Accessed 10 February 2012

Seager R, Ting M, Held I, Kushnir Y, Lu J, Vecchi G et al (2007) Model projections of an immanent transition to a more arid climate in southwestern North America. Science 316: 1181–1184

Seager T, Selinger E, Wiek A (2012) Sustainable engineering science for resolving wicked problems. J Agric Environ Ethics 25(4):467–484

Siegrist M, Cousin M-E, Kastenholz H, Wiek A (2007) Public acceptance of nanotechnology foods and food packaging: the influence of affect and trust. Appetite 49(2):459–466

Siegrist M, Stampfli N, Kastenholz H (2009) Acceptance of nanotechnology foods: a conjoint study examining consumers' willingness to buy. Br Food J 111(7):660–668

Singh GK, Kogan MD, van Dyck PC (2010) Changes in state-specific childhood obesity and overweight prevalence in the United States from 2003 to 2007. Arch Pediatr Adolesc Med 164(7):598–607

Smalley R (2006) Nanotechnology and our energy challenge. In: Foster L (ed) Nanotechnology: science, innovation, and opportunity. Pearson Education Inc, Upper Saddle River, pp 13–17

Smith GB, Granqvist CG (2011) Green nanotechnology: solutions for sustainability and energy in the built environment. CRC Press, Boca Raton

Svara JH (2011) The early stage of local government action to promote sustainability. In: Cotnoir PD (ed) The municipalities year book—2011. ICMA Press, Washington, DC, pp 43–60

Tarabara VV (2010) Nanotechnology and water purification. Nanotechnology thought leaders series. http://www.azonano.com/article.aspx?/ArticleID=2532. Accessed 12 October 2011

Tettey KE, Yee MQ, Lee D (2010) Photocatalytic and conductive MWCNT/TiO_2 nanocomposite thin films. Appl Mat Interfaces 2(9):2646–2652

United State Department of Justice (USDOJ) (2011) United States' Investigation of the Maricopa County Sheriff Office. http://www.justice.gov/crt/about/spl/documents/mcso_findletter_12-15-11.pdf. Accessed January 19 2012

United States Census Bureau (USCB) (2010a) Census 2010 summary file 1: Arizona block data. Prepared by the City of Phoenix

USCB (2010b) 2005–2009 American community survey Arizona. Prepared by the City of Phoenix

Valli F, Tijoriwala K, Mahapatra A (2010) Nanotechnology for water purification. Int J Nuc Desalt 4(1):49–57

Waitz T, Becker B, Wagner T, Sauerwald T, Kohl C, Tiemann M (2010) Ordered nanoporous SnO_2 gas sensors with high thermal stability. Sens Actuators B150:788–793

Wang J, Zhang XD, Han JT (2004) Study on catalyzing germicidal efficacy of ultrasound and nanometer titanium dioxide. Chin J Disinfect 02:3–7

Wang J, Zhou G, Chen C, Yu H, Li Y, Jiao F, Zhao Y et al (2007) Acute toxicity and biodistribution of different sized titanium dioxide particles in mice after oral administration. Toxicol Lett 168:176–185

Wang C, Yin L, Zhang L, Xiang D, Gao R (2010) Metal oxide gas sensors: sensitivity and influencing factors. Sensors 3(10):2088–2106

Watlington K (2005) Emerging nanotechnologies for site remediation and wastewater treatment. Thesis, North Carolina State University

Weiss PS, Lewis PA (2010) Sustainability through nanotechnology. ACS Nano 4(3):1249–1250

Wiek A, Foley R (2011) Urban sustainability challenges in metropolitan Phoenix. Workshop report. Center for Nanotechnology in Society, Arizona State University

Wiek A, Kay B (eds) (2011). Whose community, whose future? Sustainability efforts in a diverse community in Phoenix. Project report. School of Sustainability, Arizona State University

Wiek A, Selin C, Johnson C (eds) (2010) The future of Phoenix—crafting sustainable development strategies. Project Report. School of Sustainability, Arizona State University, Tempe

Wiek A, Ness B, Brand FS, Schweizer-Ries P, Farioli F (2012a) From complex systems thinking to transformational change: a comparative appraisal of sustainability science projects. Sustain Sci 7(Suppl 1):5–24

Wiek A, Guston DH, Frow E, Calvert J (2012b) Sustainability and anticipatory governance in synthetic biology. Int J Soc Ecol Sustain Dev 3(2):25–38

Wiek A, Guston DH, van der Leeuw S, Selin C, Shapira P (in press) The nano-enhanced city, sustainability challenges, and anticipatory governance. Urb Technol

Wiesner MR, Lowry GV, Jones KL, Hochella MF Jr, Giulio RT, Casman E, Bernhardt ES (2009) Decreasing uncertainties in assessing environmental exposure, risk, and ecological implications of nanomaterials. Environ Sci Technol 43(17): 6458–6462

Woan BK, Pyrgiotakis G, Sigmund W (2009) Photocatalytic carbon-nanotube—TiO_2 composites. Adv Mater 21: 2233–2239

Zhang WX (2005) Nanotechnology for water purification and waste treatment. Frontiers in nanotechnology US EPA millennium lecture series. Washington, DC

DOI 10.1007/978-3-319-05041-6_31
Reprinted from the *Journal of Nanoparticle Research*, DOI 10.1007/s11051-012-0854-0

PERSPECTIVES

Nanotechnology policy in Korea for sustainable growth

Dae Sup So · Chang Woo Kim · Pil Seung Chung · Myung S. Jhon

Received: 10 January 2012 / Accepted: 29 March 2012 / Published online: 31 May 2012

Abstract Korea has become one of the leading countries in nanotechnology along with the U.S., Japan, and Germany. Since 2001, the Korean Government established the "Nanotechnology Development Plan." Since then, the trend in nanotechnology is steadily changing from fundamental research to application-driven technologies. In this paper, we examine the nanotechnology development and policy during the past decade, which includes the investments in R&D, infrastructure, and education. The Third Phase (2011–2020) on clean nanotechnology convergence and integration in information, energy, and the environmental sector is also given. Furthermore, the program on long-term strategy dealing with sustainability in resolving future societal demand and plans for sustainable energy and environmental activities will be discussed in depth. The outcomes and national evaluations of research and education are also given.

Keywords Nanotechnology · Korea · Sustainability · Energy and environment · Governance · International perspective

Special Issue Editors: Mamadou Diallo, Neil Fromer, Myung S. Jhon

This article is part of the Topical Collection on Nanotechnology for Sustainable Development

D. S. So · C. W. Kim
National Nanotechnology Policy Center, Korea Institute of Science and Technology Information, Seoul 130-741, Korea

D. S. So · P. S. Chung · M. S. Jhon (✉)
Department of Chemical Engineering, Carnegie Mellon University, Pittsburgh, PA 15213, USA
e-mail: mj3a@andrew.cmu.edu

M. S. Jhon
School of Advanced Materials Science and Engineering, Sungkyunkwan University, Suwon 440-746, Korea

Introduction

During the past decade, nanotechnology has globally become a core technology, projecting the future direction of science and engineering as well as the industry (Serrano et al. 2009). Since 2001, when U.S. Government announced "National Nanotechnology Initiative (NNI)," the Korean Government has strategically supported development with their own "Nanotechnology Development Plan (NDP) (July, 2001)" to actively lead research and development in nanotechnology (Table 1) (Eighth National Science and Technology Commission 2001), in addition to establishing various roadmaps including "Nanotechnology Strategy for the Industry" and "Plan for the Training System in the Nanotechnology." The "Legislation on Nanotechnology Development" established in December 2002 expedites the progress of this development by providing the systemic legal foundation. The direction of NDP is regularly adjusted every 5 years (Second Phase NDP in 2005 and Third Phase in 2011). Unique from the

Table 1 NDP of Korea

Date	Projects	Korean Government Organization
04/2000	Agency for Tera-level Nanometerials Development	Ministry of Science and Technology[a]
07/2001	First NDP (Eighth National Science and Technology Commission)	Interministry
05/2002	Agency for Nanomaterials Technology Development	Ministry of Science and Technology
05/2002	Agency for Nanomechatronics	Ministry of Science and Technology
07/2002	Nano-Fab Center	Ministry of Science and Technology
12/2002	Legislation of Nanotechnology Development	Interministry
05/2003	Advanced Nano-Fab Center	Ministry of Science and Technology
07/2003	Support for Nanotechnology Information	Ministry of Science and Technology
01/2004	Nano Technology Research Society	Ministry of Science and Technology
08/2004	Nanotechnology Intergration Center	Ministry of Commerce, Industry, and Energy
12/2005	Second NDP	Interministry
10/2007	Roadmap for Nanotechnology Standard	Ministry of Knowledge Economy (MKE)
04/2008	Roadmap for Nanotechnology	Ministry of Education, Science, and Technology (MEST)
12/2008	Strategy for Nanotechnology Convergence	MEST; MKE
09/2009	Mid-term Strategy of Original Nanotechnology (747 Initiative)	MEST
11/2009	National Platform for the Safety, Certification, and Enhancement of Nanomaterials	MKE
12/2009	Mid- and Long-term Plan (2010–2014) for the Nanomaterials Safety	Ministry of Environment
08/2010	National Nanotechnology Policy Center	Interministry
04/2011	Third NDP	Interministry
10/2011	Nano Safety Program	Interministry

[a] Note that the Ministry of Science and Technology became MEST in 2008

programs in other countries, NDP provides the direction for the nanotechnology research and development as well as the infrastructure for the human resources. Since the initial investment from the Korean Government in constructing the framework, the National Nano-Fab Center and the Korea Advanced Nano-Fab Center were established in 2002 and 2003 for fundamental research, while the Nano Integration Center was established in 2004 for investigating the applications of nanotechnology. The Government has invested $ 693 million into these nanotechnology centers. To sustain the support of the Government, the Committee of Nanotechnology Experts was founded, which is affiliated with the National Science and Technology Commission.

The nanotechnology program strives to encourage collaborations between affiliated organizations, and to promote the safety aspect of nanotechnology. The Ministry of Education, Science, and Technology (MEST) suggested the roadmap for nanotechnology development by establishing "Strategy for the Nanotechnology Convergence (2008)," and also announced "Mid-term Strategy for the Original Nanotechnology." The Ministry of Environment presented "Mid to Long-term Plan (2010–2014) for Safety Control of the Nanomaterials" and the Government recently announced "Safety Control in Nanotechnology (October, 2011)". The central Government initiated the evaluation and correspondence of the societal impact of nanotechnology, which has gained increasing attention as developments in nanotechnology occur as given in the report on the effect of nanotechnology evaluated in 2006. As a result of these governmental programs, Lux Research projected Korea to become one of the most competitive leading countries in nanotechnology along with the U.S., Japan, and Germany (Nordan 2008).

In April 2011, the Korean Government evaluated the nanotechnology policies which have been enacted by the Government so far, and established "Third Phase NDP" reflecting the global trend and confirming the directions for the next decade (Korean Government 2011). This program illustrates the vision of the leading country in the nanotechnology emphasizing the creation of the new industrial area, the infrastructure for the human resources, and the criteria for the

ethical and societal responsibilities. For these purposes, the Government selected 30 future technologies in five major categories (Table 2), with investments up to $720 million by 2020. These major categories include the nanotechnology of energy and the environment for sustainable growth, and the development of the solar cell, secondary battery, fuel cell, membrane, thermo-electric, and piezo-electric systems with nanostructured materials were selected as the technologies primarily investigated.

The recent nanotechnology policy in Korea can be compared to the establishment of NANO2 policy in the U.S. for this decade (2011–2020) (Roco et al. 2011), which selected "safe and sustainable development of nanotechnology" as one of the primary objectives. Diallo et al. illustrated that a clean environment, water resources, food supply, mineral resources, green manufacturing, habitat, transportation, climate change and biodiversity especially including nanotechnology-based energy solutions are key technologies in this area. They defined the sustainability to be a technology satisfying societal, environmental, and economic aspects. In this paper, we provide the NDP outcomes on the research, education, and industries during the past decade, and a mid- and long-term nanotechnology plan for energy and environmental areas with sustainable growth and the details of major technological progress based on the "Third Phase NDP."

Nanotechnology development plan

Here, we provide the Korean national evaluation of the past investments on nanotechnology, including examples of research outcomes. The projects on establishing infrastructure are discussed along with the industrial and educational impacts, and future directions, which are the current projection by the Korean Government.

National investment and research outcomes

Since the Korean Government initiated NDP in 2001, $1,905 million had been invested in the research and development of the nanotechnology. Among the national institutions, MEST and Ministry of Knowledge Economy (MKE) have invested over 75 % of overall national investment on nanotechnology (Fig. 1), implying that fundamental research and educational activities were emphasized during the past decade.

The amount of the investment in nanotechnology has been drastically increased from $94 million in 2001 to $ 227 million in 2009 after NDP was established (Fig. 2a). The investment during the First Phase (2001–2005) NDP was $ 959 million with $ 674 million for research and development (R&D), $ 238 million for the infrastructure, and $ 47 million for the human resources (HR) in the nanotechnology area. During the Second Phase (2006–2010) NDP, $1,174 million was increased with $ 922 million for R&D, $ 186 million for the infrastructure, and $ 64 million for HR (Fig. 2b). This indicates that the investment for the R&D steadily increased, which represents the active R&D projects on nanotechnology were successfully achieved based on the infrastructure established during the First Phase NDP.

As a result, Korea has made a new leap forward to be in the top four countries in the nanotechnology area, and the NDP strategy and the governmental investment have led to fruitful success in nanotechnology with drastic advances in the practical applications. The selected highlight of scientific

Table 2 30 technologies in five major categories

Categories	Future technology
Nano devices	Nano memory device, nano CMOS logic device, ultrasmall nano sensor, nano electronic device, and nano flexible device
Nano bio	Nano-based food, nano wellbeing product, nano diagnosis, nano analysis of cell, and intelligent nano medicine
Nano energy/environment	Nanostructured solar cell, secondary battery, fuel cell, membrane, thermo-electrics, and piezo-electric systems
Nanomaterials	Mass production, functional material, printed electronic materials, energy harvesting, nanocatalyst/porous media, resource collection, and substitute
Nano manufacturing/measuring devices	Large-sized nanomaterial manufacturing, nanostructured patterning, measurement in nano manufacturing, nano thin film manufacturing, simulation, and smart manufacturing

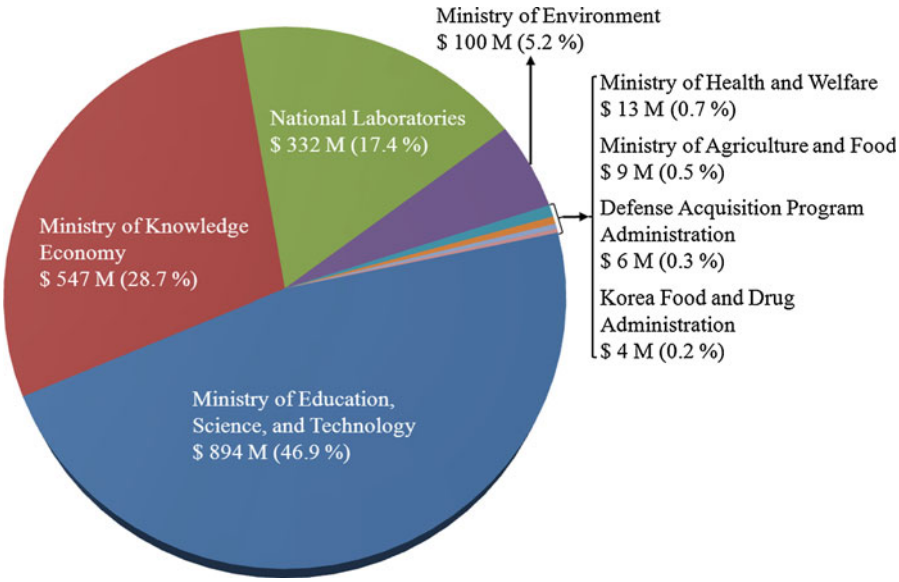

Fig. 1 Investment of the Korean Government on nanotechnology since 2001

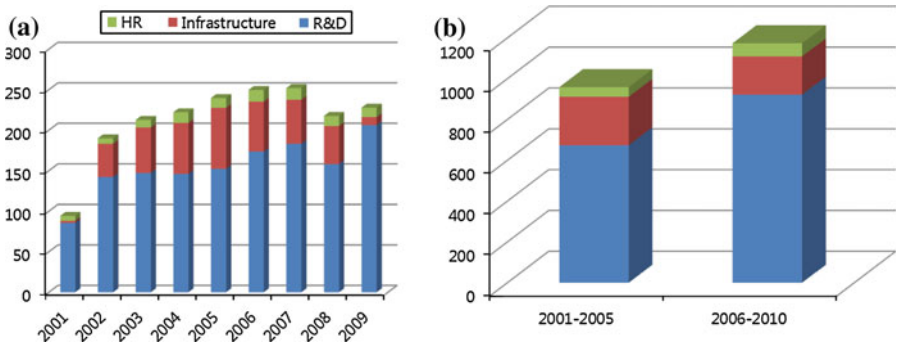

Fig. 2 **a** Annual investments and **b** the investment during the First and Second Phases NDP

achievements at the academic institution is given below. The novel methodology for large-scale pattern growth of graphene films for stretchable transparent electrodes, which enables an up to 30 inch transparent electrode by the roll-to-roll method, was developed by Sungkyunkwan University (SKKU), thereby breaking through the barrier to the practical application of graphene (Kim et al. 2009). In collaboration with MIT, Korea Advanced Institute of Science and Technology (KAIST) developed high-power lithium-ion batteries using multiple virus genes having affinity for single-walled carbon nanotubes (SWNT), which increase the electric conductivity by using the characteristics of nano-sized electrode materials (Lee et al. 2009a). Nano satellites, which communicate the information of the chemicals including proteins, and heavy metals within the cell, were investigated by Sogang University (Choi et al. 2009). The world's first nano-sized lens was invented by Pohang University of Science and Technology (POSTECH), which enables near-field focusing and magnification through self-assembled nanoscale spherical lenses (Lee et al. 2009b). Flexible memory, which enables achievement of highly integrable organic memory devices and other organic-based electronics with greatly increased cell density, was developed by Gwangju Institute of Science and Technology (GIST) (Song et al. 2010). In addition to these achievements, the number of the scientific publications in SCI journals has drastically increased from 196 in 2,000 to over 2,500 (China: 8,297, U.S.: 8,061, and Japan: 2,820) in 2008 with a citation per article of 9.9 (U.S.: 22.0, Germany: 16.6, UK: 16.1, France: 15.4, Japan, 12.7, and Italy: 12.5). Total share of the U.S. patents increased from 187 in 2001 to 2940 in 2009 (Fig. 3). Particularly, the number of the U.S. patents shared by Korea has increased by

50 % since 2005, when the Second Phase NDP was initiated.

Infrastructure, industries, and educations

From the Second Phase NDP, the Korean Government established six major nanotechnology infrastructures (Table 3), which supports the network between academia and industries, provide the special facilities and equipment for nanotechnology, and devise the nanotechnology R&D frames preventing overlapping investments and encouraging organized development plans. These infrastructures were evaluated to be highly impactive on the Korean economy with 7.28 benefit-cost ratio (BCR). Since the plan for these infrastructure projects will be terminated in a few years, the Korean Government is currently establishing alternative plans for organized collaborations among these six major infrastructures for synergetic development and securing steady investments with the replacement measure for old facilities and equipment. For the commercialization of nanotechnology in the next phase projects, the Government plans to establish research institutes or organizations, which investigate the toxicity of the nanomaterials on the human and the environment, which will be one of the most critical issues in the nanotechnology applications.

The share of nanotechnology in the world market is expected to reach $2.6 trillion within the next few years. In addition to the development of the nanomaterials, nano-devices recently became the major subject since nanotechnology made a transition from the fundamental to application-driven development (Table 4). In Korea, the industries have applied the nanotechnology to produce semiconductors, vehicles, display, and household devices and items. The industries including the small and medium-sized businesses are increasingly involved in the nanotechnology area (154 companies in 2005 and 184 in 2009 with 35.1 % of entire industries engaged in developing the applications of nanomaterials, 12.6 % in the nano-bio, and 8.7 % in the nano-device areas). As the Korean Government encouraged the collaboration between the industries and academia with the NDP strategy, the number of core researchers working in this area increased five times more than in 2000. In the education sector, 43 universities established the nanotechnology department with 7,385 students (B.S.: 6,084, M.S.: 887, and Ph.D.: 404) graduating in 2015, which will form the core R&D resources for the growing market of the nanotechnology.

Although broad scientific achievements with enormous investments have been made during the past decade, nanotechnology barely generated significant profitable returns. Therefore, the Korean government is attempting to shift the investment from the fundamental R&D to commercialization by reinforcing the collaboration between the industries and academia.

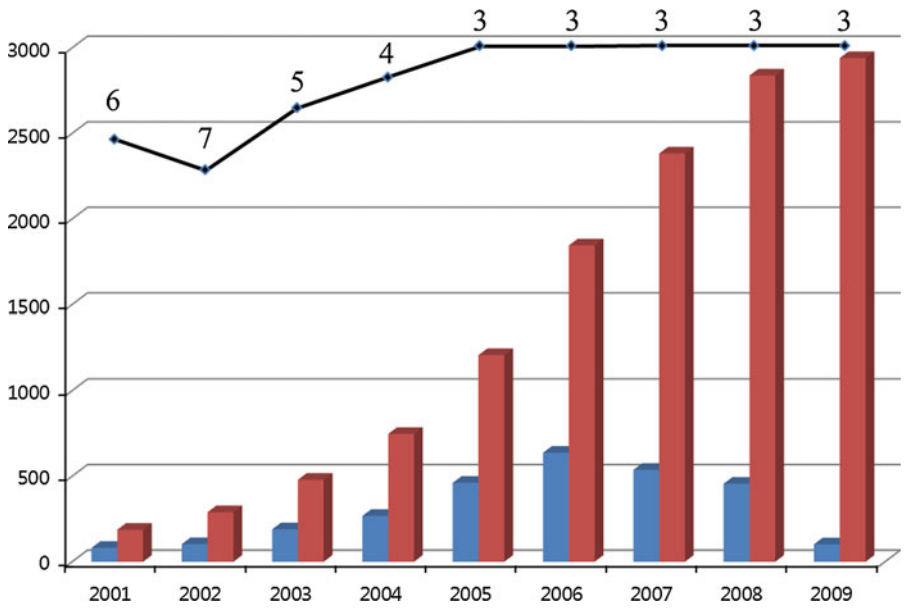

Fig. 3 Korean share of U.S. patents: (*blue*) annual number, (*red*) cumulative number, and (*black*) ranking

Table 3 Infrastructures of Nano-Fab Center and National Center for Nanomaterials Technology (NCNT) in Korea

	Institution	R&D area	Investment (million $)
MEST	National Nano-Fab Center	Si based nanomaterials, MEMS	Total: 260
			Government: 106
			Local: 154
	Korea Advanced Nano-Fab Center	Nanocomposite semiconductor, electronic materials, optical materials	Total: 147
			Government: 43
			Local: 104
MKE	NCNT (Pohang)	Semiconductor, display, nanomaterials	Total: 101
			Government: 38
			Local: 63
	NCNT (Jeonju)	Semiconductor, nano-patterning, etching	Total: 67
			Government: 21
			Local: 46
	NCNT (Gwangju)	Semiconductor, nano-deposition	Total: 71
			Government: 24
			Local: 47
	NCNT (Daegu)	Nanomaterials, energy materials	Total: 44
			Government: 30
			Local: 14

Table 4 Prospect of Nanotechnology in the World Market: billion $ (in %)

Category	2000	2010	2020
Nanomaterial	180.3 (42.6)	605.7 (38.2)	680.2 (27.7)
Nano-device	174.0 (41.1)	734.6 (46.3)	1,259.6 (51.2)
Bio and pharmacy	43.7 (10.3)	87.4 (5.5)	188.6 (7.6)
Environment and energy	11.6 (2.7)	106.4 (6.7)	230.3 (9.4)
Process, measurement, and facility	14.0 (3.3)	52.3 (3.3)	100.1 (4.1)
Total	423.7	1,586.2	2,458.8

The government encourages supporting the technology transfer from academia to the industry as well as the foundation of small business directly operated by the universities similar to programs such as SBIR/STTR in the U.S..

Nanotechnology Development Plan on Energy and Sustainability

Innovative progress in nanotechnology has tremendously contributed to the area of sustainable energy including energy production/conversion/storage as well as improvement in the environment by utilizing novel nano materials. This trend has become a core technology, which breaks through the technical barriers in sustainable energy systems with ultra-high efficiency and low cost for commercialization. For the power generation and conversion systems, nanostructured materials are investigated to increase the efficiency for the gas/liquid fuel separations, the polymer electrolyte fuel cell (PEFC), solid oxide fuel cell (SOFC), dye-sensitized solar cell (DSSC), thin film fuel cell (TFFC), organic solar cell (OSC), and bio fuels (Khan et al. 2011; Ermete 2011; Natalia and Alessandro 2011; Alvarez and Cervantes 2011). Research on the high density energy storage has also been advancing for lithium-ion and lithium polymer secondary batteries, super capacitor, and materials for hydrogen storage. Nanotechnology controls the environmental effects of current and future technologies by using nanoscale adsorption and separation phenomena

for toxic chemicals and inventing nano sensor for contamination detection.

Trends in the Nanotechnology

Most of the countries including the U.S., E.U., and Japan have focused on developing novel nano materials for electrolyte in fuel cells, which reduce the cost and provide enhanced stability and durability for commercialization. Consequently, new nano material alloys have been extensively investigated to reduce the usage of platinum catalyst in low temperature fuel cells through the interdisciplinary research activities in the U.S. national laboratories (e.g., Army Research Laboratory, Brookhaven National Laboratory, National Renewable Energy Laboratory) and universities (e.g., Brown, Georgia Tech). The nanostructured thin film solid oxide electrolytes and new materials and processes by using nano bionics for high temperature fuel cell have been developed especially by the E.U., Japan, U.S., and China. The E.U. has the most number of core patents in nano materials for the photoelectric transformation efficiency in solar cells (EPFL in Switzerland). For the DSSC, the nano material electrodes, dye synthesis, electrolytes, high performance conductors, and technologies for modulations are investigated to obtain high energy efficiency. For the OSC, various research activities have been performed to obtain the energy efficiency for commercialization via techniques for system design and orientation of materials, deterioration control, cell inosculation, and module processing.

The area of energy storage has significantly advanced by utilizing novel nanoscale materials and engineering for high energy efficiency. The U.S. is focusing on obtaining original technologies such as nanoscale design by computational methods and new types of electrodes, while Japan is intensively developing the process engineering for coating and surface modification. These technologies are further investigated for the energy storage systems with high speed charging and stability.

BASF in Germany and Engelhard in the U.S. have intensively investigated nano-sized pore catalysts for environmental technologies, and M. Haruta (Okumura et al. 2002) in Japan and D.W. Goodman (Choudhary and Goodman, 2005) in the U.S. lead the research on nano dispersed catalysts. The carrier, which harvests and purifies the resources from the contaminated environment, is also being developed, and the membrane coated by the nano-sized pore materials will enable resource separation with high efficiency.

Future directions

The global regulations of CO_2 demands the development and application of nanotechnology in the area of energy and sustainability technologies including energy production/conversion/storage with high efficiency, zero emission energy systems, and environmental devices, which detect, improve, and purify the contaminated resources. Also, the nanotechnological innovations converge to the existing technologies, where the development has been stunted due to insufficient performance. Nanotechnology convergence in the energy and sustainability will enable scientists to resolve the concerns of energy shortages and environmental issues via systems with zero emission and purification as well as high performance energy production and storage systems (e.g., high performance solar cell, fuel cell, and secondary battery).

Societal demand on the energy and environment

The global concern on energy comes from the shortage of the fossil energy resources, which is also the cause of pollution when the resources are combusted for energy. Therefore, the paradigm for the future energy system is focusing on developing clean energy systems such as fuel cells in motor vehicles and portable electronic devices, as well as the OSC and DSSC, so that the load on the nation wide power grid is reduced. Table 5 shows the societal demand on nanotechnology predicted for the next decade. The novel nano energy storage systems can also reduce the energy loss since society adopts ubiquitous frameworks, which demand small yet reliable power sources. In addition, the nanotechnology convergence systems (e.g., the power generator combining solar and thermoelectric powers) will maximize the efficiency of the energy conversion providing societal benefits in the aspects of energy cost as well as environment. Nanomaterials for the catalysts and membrane will be utilized for purification (e.g., micro/ultrafiltration, reverse osmosis, nano adsorbent) (Matsumoto et al. 2004; Zaidi et al. 1992; Vrijenhoek et al. 2001), and simultaneously for energy resource production (e.g., hydrogen separation for the fuel cell)

Table 5 The societal demand on nanotechnology

Area	Products	Market breadth		Market Share in 2020 (%)
		2010 (millon $)	2020 (millon $)	
Energy production/conversion	Fuel cell	6	37	30
	Photosynthesis	0	30	70
	OSC/DSSC	700	2,000	20
Energy storage	Secondary battery	23	170	60
	Super capacitor	5	270	70
Energy system with the convergence technology	Thermoelectric power (vehicle)	5	100	70
	Thermoelectric power (portable)	0	30	70
	Small scale energy harvesting	140	760	50
Environment purification	Air purification catalyst	30	55	80
	Nano adsorbent	24	44	80
	Catalysts for the power plant and motor vehicle	95	352	90
	Polymer/ceramic nano membrane	36	142	80
Resource recycling	Microfiltration	43	11	50
	Ultrafiltration	27	71	70
	Reverse osmosis membrane	31	80	80
Nanosensor for the environment	Portable sensor	2	40	45
	Ubiquitous sensor network (USN) system	10	40	30

(Sircar and Golden, 2000). Nano sensors will be invented for the inspection of the environment for the post-production stage.

Strategy for the nanotechnology for sustainability in Korea

The Korean government is striving to keep pace with the rapid changes in the nanotechnology area by establishing the long-term strategy for nanotechnology integration with the information, energy, and environmental sectors. Major research subjects on nanotechnology convergence selected by this strategy will expedite the commercialization of evolutionary technologies for energy and the environment, thereby increasing the market share of sustainable energy area to 15 % (Fig. 4) (Korea Institute of Science and Technology, 2011; Rockstrom et al. 2009). This national plan results in breakthroughs in energy production/conversion/storage promising high efficiency as well as water management. For instance, thermoelectric generation and energy harvesting in the submicron scale are being intensively investigated along with molecular recognition, which enables detection of the contaminant materials after production. Table 6 shows selected research subjects based on the current societal demand. The major technologies in energy/environmental areas are selected and evaluated to understand the current status of the subjects and find the direction for high efficiency energy systems with no environmental impact. Solar cells and secondary batteries are being evaluated as the stable stage in research bringing the impact on the industry to the near future, while the fuel cell system is still being developed, possibly contributing enormously to the energy production. Nanostructured solar cell systems are currently investigated through multiple exciton generation (MEG), organic/inorganic materials, and biomimetrics. Due to the high cost of fuel cell materials, alternative nano catalysts for platinum and new types of fuel cell systems are being developed. The applications of nanostructured membrane for purification, thermo-electric, and piezoelectric materials are identified motivating the fundamental research and application-driven development. This area emphasizes the research on nanostructured porous materials, which control the molecular scale separation and adsorption by modifying the membrane architecture. Figure 5 shows the plan for the selected research areas during the next decade.

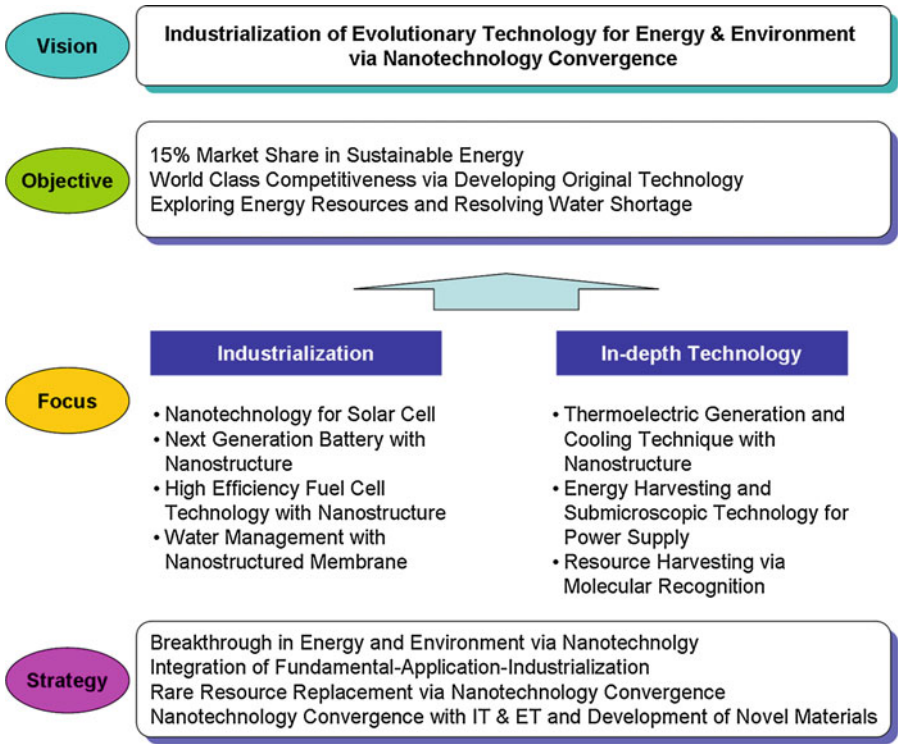

Fig. 4 Strategies for nanotechnology convergence in energy and environmental areas in Korea (Alvarez and Cervantes 2011)

Conclusions

From July 2001, as the Korean government established the strategy for nanotechnology, NDP and seven Korean governmental ministries including the MEST have invested about $ 1.9 billion in this program during the last decade. As a result, Korea is considered one of the top four countries in the area of nanotechnology with significant research outcomes. The Korean government found that the past investment on nanotechnology during the First and Second NDPs successfully led to research projects and the establishment of the infrastructure, which impacted the industrial and educational improvement of nanotechnology. Currently, the government has extended the program to "Third Phase (2011–2020)" to achieve the original technologies, which have enormous impacts on the industry and economy, and lead the growth with clean nanotechnology convergence information technology (IT), energy technology (ET), and biotechnology (BT), which produce the new paradigm in the industry. Furthermore, the program contributes by resolving the shortage in resources secured by nanomaterial-based systems for energy production/conversion/storage, and the use of nanoscale devices will enable medical treatment. For the energy and environmental areas, the evolutionary benefits from the nanotechnology such as high efficiency and low production cost will solve the issues of the societal and industrial demand (e.g., water management via nanostructured membrane) by focusing on the application-driven development. The Korean government is attempting to shift the investment from fundamental R&D to commercialization by reinforcing the collaboration between industries and academia. The Government encourages supporting the technology transfer from academia to industry as well as the foundation of small businesses directly operated by the universities, similar to programs such as SBIR/STTR in the U.S. The R&D on identifying and controlling the toxicity of nanomaterials is to be focused first, which is a globally discussed critical problem for commercialization. For these purposes, the government should provide the next generation nanotechnology policy, which encourages balanced investments from the Korean governmental ministries with active collaboration.

Table 6 Future research areas based on societal demand

Area	Products	Related Research Subjects
Energy production/conversion	Fuel cell	Developing nano materials for fuel cell systems
	Photosynthesis	Ion transport ceramic materials
	OSC/DSSC	High efficiency materials for OSC/DSSC
Energy storage	Secondary battery	Systems for fast charge/high output/high stability by using nano carbon materials
	Super capacitor	Lithium-ion/nanostructured carbon materials (e.g., graphene)
Energy system with the convergence technology	Thermoelectric power (vehicle)	Evacuated thermal insulation/recycling
	Thermoelectric power (portable)	Portable energy system using body heat
	Small scale energy harvesting	Piezo-electric energy harvesting technology
Environment purification	Air purification catalyst	Nano metal dispersed carbon porous materials
	Catalysts for the power plant and motor vehicle	Nanomaterials reducing pollutants
Resource recycling	Microfiltration/ultrafiltration	Antifouling and selectivity on the filtration
		Compound membranes with uniform pore size
	Reverse osmosis membrane	Flux and chemical stability on the membrane
Nanosensor for the environment	Portable sensor	Nanosensors and molecular recognition technology for air/water pollutions

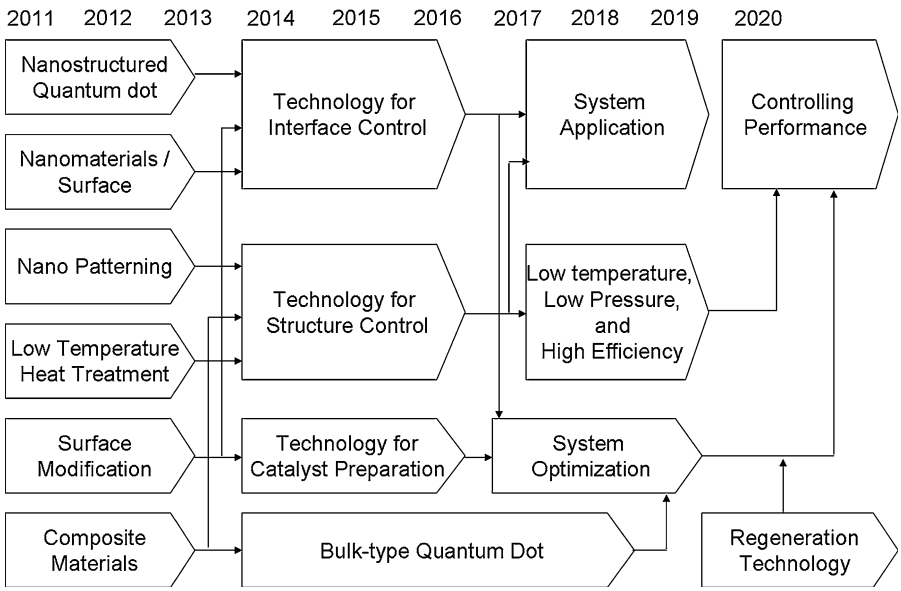

Fig. 5 Plan for the selected research areas in Korea during this decade

Acknowledgments

We acknowledge the support of the MEST, and related research contributed to this manuscript, which is based on the "Research on the Third Phase NDP." This study was also supported by the Korea Science & Engineering Foundation through the WCU Project.

References

Alvarez LH, Cervantes FJ (2011) (Bio)nanotechnologies to enhance environmental quality and energy production. J Chem Technol Biotechnol 86:1354–1363

Choi Y, Park Y, Kang T, Lee LP (2009) Selective and sensitive detection of metal ions by plasmonic resonance energy transfer-based nanospectroscopy. Nat Nanotechnol 4: 742–746

Choudhary TV, Goodman DW (2005) Catalytically active gold: the role of cluster morphology. Appl Cat A 291:32–36

Eighth National Science and Technology Commision (2001) July, 18th

Ermete A (2011) The stability of molten carbonate fuel cell electrodes: a review of recent improvements. Appl Energy 88:4274–4293

Khan MA, Sunden B, Yuan JL (2011) Analysis of multi-phase transport phenomena with catalyst reactions in polymer electrolyte membrane fuel cells—a review. J Power Sour 196:7899–7916

Kim KS, Zhao Y, Jang H, Lee SY, Kim JM, Kim KS, Ahn J-H, Kim P, Choi J-Y, Hong BH (2009) Large-scale pattern growth of graphene films for stretchable transparent electrodes. Nature 457:706–710

Korea Institute of Science and Technology Information (2011) Research on third phase nanotechnology development plan

Korean Government (2011) third phase national nanotechnology development plan of Korea

Lee YJ, Yi H, Kim WJ, Kang K, Yun DS, Strano MS, Ceder G, Belcher AM (2009a) Fabricating genetically engineered high-power Lithium-ion batteries using multiple virus genes. Science 324:1051–1055

Lee JY, Hong BH, Kim WY, Min SK, Kim Y, Jouravlev MV, Bose R, Kim KS, Hwang I-C, Kaufman LJ, Wong CW, Kim P, Kim KS (2009b) Near-field focusing and magnification through self-assembled nanoscale spherical lenses. Nature 460:498–501

Matsumoto T, Komatsu T, Nakano H, Arai K, Nagashima Y, Yoo E, Yamazaki T, Kijima M, Shimizu H, Takasawa Y, Nakamura J (2004) Efficient usage of highly dispersed Pt on carbon nanotubes for electrode catalysts of polymer electrolyte fuel cells. Catal Today 90:277–281

Natalia M, Alessandro T (2011) Theoretical studies of dye-sensitised solar cells: from electronic structure to elementary processes. Energy Environ Sci 4:4473–4495

Nordan MM (2008) Change required for the national nanotechnology initiative as commercialization eclipses discovery. Lux Research

Okumura M, Akita T, Haruta M (2002) Hydrogenation of 1,3-butadiene and of crotonaldehyde over highly dispersed Au catalysts. Catal Today 74:265–269

Rockstrom J, Steffen W, Noone K, Persson A, Stuart Chapin F, Lambin EF, Lenton TM, Scheffer M, Folke C, Schellnhuber HJ, Nykvist B, de Wit CA, Hughes T, van der Leeuw S, Rodhe H, Sorlin S, Snyder PK, Costanza R, Svedin U, Falkenmark M, Karlberg L, Corell RW, Fabry VJ, Hansen J, Walker B, Liverman D, Richardson K, Crutzen P, Foley JA (2009) A safe operating space for humanity. Nature 461:472–475

Roco MC, Mirkin CA, Hersam MC (2011) Nanotechnology research directions for societal needs in 2020. Springer, Berlin and Boston

Serrano E, Rus G, Garcia-Martinez J (2009) Nanotechnology for sustainable energy. Renew Sust Energy Rev 13:2373–2384

Sircar S, Golden TC (2000) Purification of hydrogen by pressure swing adsorption. Sep Sci Technol 35:667–687

Song S, Cho B, Kim T-W, Ji Y, Jo M, Wang G, Choe M, Kahng YH, Hwang H, Lee T (2010) Three-dimensional integration of organic resistive memory devices. Adv Mater 22:5048–5052

Vrijenhoek EM, Hong S, Elimelech M (2001) Influence of membrane surface properties on initial rate of colloidal fouling of reverse osmosis and nanofiltration membranes. J Mem Sci 188:115–128

Zaidi A, Simms K, Kok S (1992) The use of miro/ultrafiltration for the removal of oil and suspended solids from oilfield brines. Water Sci Technol 25:163–176